

SNAPSHOT of the EIC Yellow Report Document

November 19, 2020

SNAPSHOT 19 Nov. 2020

**Editors:**

add the list of PWG and DWG editors here

**Contributors:**

PROPOSED AUTHORSHIP REQUIREMENTS: The author team consists of an inclusive list of EICUG members who contributed to the Yellow Report studies and writing process. The author team will be listed once for the complete Yellow Report (or perhaps once per Volume for arXiv purposes), with no further authorship names in sections or sub-sections. This is meant to highlight that the YR report is a community effort giving explicit credit upfront to all individuals of the author team. Physics and detector sub-working group conveners should compile the authorship list by asking on a public, working group mailing list to respond to a call for author list compilation asking for the following information: Last Name, First Name, Email address, and Name of institution. Using Microsoft / Google Forms will ease the process of collecting and compiling an inclusive list. This list should then be forwarded to the physics and detector working group conveners who compile the final author team list, which should be as inclusive as possible acknowledging the work from any EICUG member who presented ideas, studies, and participated in the writing process.

SNAPSHOT 19

# Contents

<b>I</b>	<b>Executive Summary</b>	<b>1</b>
<b>1</b>	<b>The Electron-Ion Collider</b>	<b>2</b>
<b>2</b>	<b>Physics Measurements and Requirements</b>	<b>3</b>
<b>3</b>	<b>Detector Concepts</b>	<b>4</b>
<b>4</b>	<b>Opportunities for Detector Technology and Computing</b>	<b>5</b>
<b>II</b>	<b>Physics</b>	<b>9</b>
<b>5</b>	<b>Introduction</b>	<b>10</b>
<b>6</b>	<b>The EIC Physics Case</b>	<b>13</b>
<b>7</b>	<b>The EIC Measurements and Studies</b>	<b>16</b>
7.1	Global properties and parton structure of hadrons . . . . .	16
7.1.1	Unpolarized parton structure of the proton and neutron . . . . .	19
7.1.2	Spin structure of the proton and neutron . . . . .	26
	Neutron spin structure from inclusive and tagged DIS with polarized $^3\text{He}$ and $^2\text{H}$ . . . . .	30
7.1.3	Parton structure of mesons . . . . .	37
	Introduction . . . . .	37
	Sullivan Process . . . . .	38
	Theoretical Backgrounds in Extracting the Data . . . . .	39

	Kinematics of interest to address specific theory questions . . . . .	41
	Meson structure function projections . . . . .	41
	Impact on global QCD analysis . . . . .	42
	Complementarity with other facilities . . . . .	43
	Synergy with continuum and lattice QCD . . . . .	44
7.1.4	Origin of the hadron mass . . . . .	45
7.1.5	Multi-parton correlations . . . . .	47
	Introduction . . . . .	47
	$g_T^a(x)$ from inclusive DIS. . . . .	48
	$e^a(x)$ from semi-inclusive DIS. . . . .	49
7.1.6	Inclusive and hard diffraction . . . . .	51
	Inclusive diffraction . . . . .	51
	Diffractive dijets . . . . .	54
	Large $ t $ diffractive production of vector mesons . . . . .	56
7.1.7	Global event shapes and the strong coupling constant . . . . .	58
	Introduction . . . . .	58
	Theoretical Methods . . . . .	59
	Predictions . . . . .	63
	Fitting for $\alpha_S$ . . . . .	64
	Experimental projections . . . . .	65
	Jet measurement performance . . . . .	66
	$\tau_1^a$ measurement performance . . . . .	67
	Systematic Uncertainties and Unfolding . . . . .	68
	Discussion . . . . .	70
7.2	Multi-dimensional Imaging of Nucleons, Nuclei, and Mesons . . . . .	70
7.2.1	Nucleon and Meson form factors . . . . .	73
	Nucleon Form Factors . . . . .	73
	Meson Form Factors . . . . .	75
7.2.2	Imaging of quarks and gluons in impact-parameter space . . . . .	78

7.2.3	Imaging of quarks and gluons in momentum space . . . . .	86
	Unpolarized TMDs and TMD evolution . . . . .	87
	Quark Sivers and Collins measurements . . . . .	89
	Gluon TMD measurements . . . . .	90
	Chiral-odd distribution functions via di-hadron measurements . . .	93
7.2.4	Wigner Functions . . . . .	99
7.2.5	Light (polarized) nuclei . . . . .	101
	Coherent DVCS on light nuclei . . . . .	101
	Tensor polarized deuteron . . . . .	103
	Medium modification of azimuthal modulations in nuclear SIDIS . .	104
7.3	The Nucleus: A Laboratory for QCD . . . . .	107
7.3.1	High parton densities and saturation . . . . .	111
7.3.2	Diffraction . . . . .	115
7.3.3	Nuclear PDFs . . . . .	119
7.3.4	Particle propagation through matter and transport properties of nuclei	123
	Parton showers and energy loss in cold nuclear matter . . . . .	123
	Formation of hadrons in matter . . . . .	124
	Jet production and modification in $eA$ collisions . . . . .	124
7.3.5	Collective effects . . . . .	126
7.3.6	Special opportunities with jets and heavy quarks . . . . .	127
	Flavor-tagged jets and the jet charge . . . . .	127
	Light and heavy-flavor tagged jet angularities . . . . .	128
	Energy flow and quantum number correlations in jets . . . . .	129
7.3.7	Short-range correlations, origin of nuclear force . . . . .	130
	Diffraction J/psi production in electron-deuteron scattering at the EIC and its implication to short-range correlations . . . . .	130
	Studying Short-Range Correlations with an EIC . . . . .	135
7.3.8	Structure of light nuclei . . . . .	137
	Studying nucleon structure in $A=3$ nuclei using double spectators tagging . . . . .	138

	Coherent scattering off the lightest nuclei . . . . .	140
7.3.9	Coherent and incoherent photoproduction on heavy targets . . . . .	141
	Coherent photoproduction . . . . .	142
	Walker-Good and coherent photoproduction . . . . .	143
	Coherent Photoproduction . . . . .	144
	Incoherent Photoproduction . . . . .	145
	Separating Coherent and Incoherent Production . . . . .	146
7.4	Understanding Hadronization . . . . .	146
7.4.1	Hadronization in the vacuum . . . . .	147
	Light meson fragmentation functions and flavor sensitivity . . . . .	147
	Fragmentation into polarized $\Lambda$ hyperons . . . . .	148
	Partial wave decomposition of polarized and unpolarized di-hadron FFs including TMDs . . . . .	150
	Jet Substructure . . . . .	152
	Target fragmentation . . . . .	154
7.4.2	Hadronization in the nuclear environment . . . . .	154
	Collinear Nuclear Fragmentation functions for light hadrons . . . . .	154
	In medium evolution for light and heavy flavor mesons . . . . .	155
	Heavy meson reconstruction and physics projections . . . . .	156
	Heavy flavor-tagged jet substructure at the EIC . . . . .	158
7.4.3	Particle production for identified hadron species . . . . .	158
7.4.4	Production mechanism for quarkonia and exotic states . . . . .	158
	Precision quarkonium physics at the EIC . . . . .	159
	Production of quarkonia and exotics at in $eA$ collisions . . . . .	160
7.4.5	New particle production mechanisms . . . . .	162
	Odderon exchange . . . . .	163
	Exclusive backward ( $u$ -channel) production . . . . .	163
	$u$ -Channel Exclusive Meson Electroproduction . . . . .	165
	Three-gluon exchange and near-threshold production . . . . .	166
7.4.6	Spectroscopy . . . . .	166

7.4.7	Target Fragmentation . . . . .	168
7.5	Connections with Other Fields . . . . .	170
7.5.1	Electro-weak and BSM physics . . . . .	170
	Introduction . . . . .	170
	Weak Neutral Current Measurements . . . . .	171
	Charged Lepton Flavor Violation . . . . .	174
	Charged Current Chiral Structure . . . . .	176
	Heavy Photon and Neutral-Lepton Searches . . . . .	176
	General BSM Searches . . . . .	177
7.5.2	Neutrino physics . . . . .	178
	Cross sections and kinematical regions . . . . .	179
	Studies of (Anti)Neutrino-Nucleus Interactions . . . . .	180
	Measurements of the Strangeness Content of the Nucleon . . . . .	180
	Isospin Physics and Sum Rules . . . . .	181
	Electroweak measurements and the NuTeV anomaly . . . . .	181
	Possible GPD measurements in neutrino scattering . . . . .	182
7.5.3	Cosmic ray/astro-particle physics . . . . .	183
	Cosmic ray air showers . . . . .	183
	Astrophysical Neutrinos . . . . .	185
7.5.4	Other connections to pp, pA, AA . . . . .	186
7.5.5	The EIC and nuclear structure physics . . . . .	191
7.5.6	Interface to High-Energy Physics efforts . . . . .	194
7.6	Connected Theory Efforts . . . . .	197
7.6.1	Lattice QCD . . . . .	198
7.6.2	Radiative corrections . . . . .	200
<b>8</b>	<b>Detector Requirements</b>	<b>206</b>
8.1	Inclusive Measurements . . . . .	206
8.1.1	Reconstruction of kinematic variables . . . . .	206
8.1.2	Kinematic phase space . . . . .	208

8.1.3	Electron Acceptance and Particle Identification . . . . .	209
8.1.4	Resolution and bin migration effects in electron reconstruction. . . . .	214
8.1.5	Acceptance, resolution, and bin migration effects in Jacquet-Blondel reconstruction . . . . .	216
8.1.6	Generator Verification . . . . .	217
	Systematic Uncertainties for the Inclusive Pseudo-data . . . . .	220
8.2	Semi-Inclusive Measurements . . . . .	222
8.2.1	General SIDIS kinematics and requirements . . . . .	222
8.2.2	Hadron PID impact on 4D TMD measurements . . . . .	223
8.2.3	Using the hadronic final state to reconstruct SIDIS variables . . . . .	225
8.2.4	Requirements for di-hadron measurements . . . . .	227
8.2.5	Requirements for $\Lambda$ measurements . . . . .	229
8.2.6	Spectroscopy requirements for forward electron identification . . . . .	229
8.3	Jets and Heavy Quarks . . . . .	231
8.3.1	Simulation and Detector Modeling . . . . .	232
8.3.2	Kinematics Summary . . . . .	234
8.3.3	Tracking . . . . .	234
	Momentum Resolution . . . . .	235
	Vertex Resolution . . . . .	238
	Additional Considerations . . . . .	240
8.3.4	Particle Identification . . . . .	241
8.3.5	Calorimetry . . . . .	243
	Electromagnetic Calorimetry . . . . .	244
	Hadron Calorimetry . . . . .	245
	Coverage Continuity . . . . .	248
8.3.6	Summary . . . . .	249
8.4	Exclusive Measurements . . . . .	249
8.4.1	Deeply virtual Compton scattering and exclusive production of $\pi^0$ in $ep$ . . . . .	249
8.4.2	Neutron target . . . . .	252

8.4.3	Deeply virtual Compton scattering off helium . . . . .	254
	The Orsay-Perugia Event Generator (TOPEG) . . . . .	255
	Central detector . . . . .	255
	Forward detector . . . . .	256
	Overall performance . . . . .	256
8.4.4	Exclusive vector meson production in $ep$ . . . . .	257
	Detector requirements . . . . .	257
	Kinematic coverage . . . . .	262
8.4.5	Timelike Compton Scattering . . . . .	263
8.4.6	Exclusive vector meson production in $e+A$ . . . . .	268
	Event Generation and decay channels . . . . .	269
	Kinematic coverage . . . . .	269
	Beam effects . . . . .	270
	Impact of momentum resolution . . . . .	273
	Separating coherent and incoherent processes . . . . .	276
8.4.7	$u$ -channel exclusive electroproduction of $\pi^0$ . . . . .	279
8.4.8	Exclusive meson production by charged currents . . . . .	280
	Kinematics reconstruction . . . . .	281
	Photoproduction backgrounds . . . . .	283
8.4.9	Deep Exclusive $\pi^+$ production . . . . .	285
	Kinematics . . . . .	285
8.4.10	Diffraction dijets . . . . .	285
8.5	Diffraction Measurements and Tagging . . . . .	288
8.5.1	Requirements for exclusive vector meson production . . . . .	288
	Pseudorapidity acceptance . . . . .	288
	Soft kaons from $\phi$ decays . . . . .	289
	Momentum Resolution . . . . .	291
	Separating coherent and incoherent interactions . . . . .	292
8.5.2	Overview of Far Forward Region . . . . .	293

8.5.3	Meson structure . . . . .	294
	Sullivan process for pion structure: $e + p \rightarrow e' + X + n$ . . . . .	294
	Sullivan process for kaon structure: $e + p \rightarrow e' + X + \Lambda$ . . . . .	295
	Exclusive $p(e, e' \pi^+ n)$ events . . . . .	301
	Accelerator and Instrumentation requirements . . . . .	303
8.5.4	Deuteron DIS with spectator tagging: Free neutron structure and nuclear modifications . . . . .	304
8.5.5	Diffraction $J/\Psi$ production on the deuteron with spectator tagging . . . . .	305
8.5.6	Double Tagging In The Far Forward Region . . . . .	307
8.5.7	Short-Range Correlations and EMC Effect Studies . . . . .	307
8.5.8	Inclusive diffraction . . . . .	308
8.5.9	Summary of Far Forward Region Physics Requirements . . . . .	313
8.6	Summary of Requirements . . . . .	313
<b>III</b>	<b>Detectors</b>	<b>314</b>
<b>9</b>	<b>Introduction</b>	<b>315</b>
<b>10</b>	<b>Detector Challenges and Performance Requirements</b>	<b>316</b>
10.1	Beam Energies, Polarization, Versatility, Luminosities . . . . .	316
10.1.1	Integration with accelerator . . . . .	316
	Beam parameters and lattice . . . . .	316
	Beam pipe, vacuum, background . . . . .	316
10.2	Rate and Multiplicities . . . . .	319
10.3	Integrated Detector and Interaction Region . . . . .	319
10.4	Backgrounds . . . . .	319
10.5	Systematics and Ancillary Detectors . . . . .	319
10.5.1	Luminosity . . . . .	319
10.5.2	Polarimetry . . . . .	319
10.6	Physics Requirements . . . . .	319

<b>11 Detector Aspects</b>	<b>320</b>
11.1 Magnet	320
11.2 Tracking	322
11.2.1 Introduction	322
11.2.2 Main requirements and acceptance coverage	322
11.2.3 Technology survey	323
Silicon Detector Technologies for EIC	323
MAPS	324
65 nm MAPS SVT detector	326
Alternative Silicon Sensors	328
Gaseous Tracking Detector Technologies	330
Time Projection Chambers (TPC)	330
Micro Pattern Gaseous Detectors (MPGDs)	333
Drift Chambers & Straw Tubes (DCs)	334
Small-strip Thin Gap Chambers (sTGCs)	334
11.2.4 Comparison of Technology Choices	335
11.2.5 Detector concepts and performance studies	335
All-Silicon Tracking Option	335
Baseline All-Silicon Tracking Option (Barrel & End Caps)	335
Alternative Forward Tracking Option: Hadron End Cap with Si disk + MPGDs	341
11.2.6 Hybrid Tracking System	346
Barrel: Silicon Vertex + TPC	346
Barrel: Silicon Vertex + Cylindrical MPGDs	348
Hadron & Electron End Cap: MPGDs	352
11.2.7 Fast tracking Layers & Additional PID detectors	354
Fast Signal & High Resolution MPGDs for DIRC in the Barrel Region	354
MPGD-based-TRDs for Electron PID and Tracking in the End Caps	354
Readout structures for MPGDs	357
11.2.8 Integration issues	358

11.2.9	Material Budget Considerations . . . . .	358
11.3	Particle Identification . . . . .	359
11.3.1	Physics Requirements . . . . .	360
11.3.2	$\frac{dE}{dx}$ . . . . .	362
11.3.3	Cerenkov . . . . .	364
	Hadron Blind Detector (HBD) . . . . .	365
	CsI RICH . . . . .	366
	Dual RICH (dRICH) . . . . .	369
	Modular RICH (mRICH) . . . . .	373
	Detection of Internally Reflected Cerenkov (DIRC) . . . . .	374
11.3.4	Time Of Flight (TOF) . . . . .	376
	MPGD-based-TRDs for Electron PID and Tracking in the End Caps . . . . .	378
11.3.5	Photon Detection Technology Options . . . . .	382
11.3.6	Configuration for EIC . . . . .	384
	Hadron Arm . . . . .	384
	Central Arm . . . . .	385
	Electron Arm . . . . .	386
11.4	Electromagnetic Calorimetry . . . . .	388
11.4.1	Requirements and Overview . . . . .	388
11.4.2	ECAL: Requirements, Options and Features . . . . .	390
	Homogeneous Calorimeters . . . . .	391
	Sampling Calorimeters . . . . .	392
	ECAL technologies considered for EIC . . . . .	393
	Impact of the material in front of ECAL . . . . .	394
	Impact of the Cell Size and the Projective Geometry . . . . .	395
	Electron/pion separation . . . . .	397
	Lowest detectable energy . . . . .	401
	Readout Considerations . . . . .	401
	Discussion . . . . .	402

11.4.3	ECAL: Appendix . . . . .	403
	PbWO <sub>4</sub> crystals . . . . .	403
	Scintillating glass . . . . .	403
	Lead glass . . . . .	404
	Scintillating fibers embedded in absorber . . . . .	405
	Shashlyk . . . . .	406
11.5	Hadronic Calorimetry . . . . .	410
11.5.1	General consideration for Hadron Calorimeters . . . . .	410
11.5.2	Central detector consideration . . . . .	411
11.5.3	HCal Energy resolution . . . . .	412
11.5.4	eRD1 EIC R&D and STAR forward developments . . . . .	413
11.5.5	Alternative methods for high resolution HCal . . . . .	414
11.6	Far-Forward Detectors . . . . .	414
11.6.1	Introduction . . . . .	414
	General Layout of Far-Forward IR Region . . . . .	415
11.6.2	Roman Pots . . . . .	415
	Basic Requirements for Roman Pots . . . . .	417
	Silicon Sensors for Roman Pots . . . . .	418
	Summary of the Current Design Constraints . . . . .	420
11.6.3	Off-Momentum Detectors . . . . .	421
	Basic Design Considerations . . . . .	421
	Summary of the Off-Momentum Detector Considerations . . . . .	422
11.6.4	B0-spectrometer . . . . .	422
	Basic requirements for B0 . . . . .	422
	Silicon Sensors for B0-tracker . . . . .	423
	Pre-shower or EMCAL in the B0 spectrometer . . . . .	424
	Summary of the Current Design Constraints . . . . .	424
11.6.5	Zero-Degree Calorimeter (ZDC) . . . . .	425
	Basic requirements for the ZDC . . . . .	425

EMCAL technologies for ZDC . . . . .	426
HCAL technologies for ZDC . . . . .	426
Soft photon detection . . . . .	427
Scintillator Tracker Detector . . . . .	427
Summary of the current design . . . . .	428
11.6.6 Physics impact . . . . .	429
Simulation Details . . . . .	429
Deeply Virtual Compton Scattering (DVCS) . . . . .	429
Spectator Tagging in e+D Interactions . . . . .	431
Spectator Proton and Neutron Tagging in e+ <sup>3</sup> He and e+ <sup>3</sup> H Collisions . . . . .	432
Far-forward tagging ions . . . . .	434
Meson Structure and FF Lambda Decay . . . . .	434
11.6.7 Conclusions . . . . .	436
11.6.8 Appendix . . . . .	440
11.7 Far-Backward Detectors . . . . .	443
11.7.1 Far-Backward Photons . . . . .	443
Luminosity Measurement . . . . .	443
Bremsstrahlung Photon Detection Principles and Requirements . . . . .	445
Bremsstrahlung Photon Detector Implementation . . . . .	447
11.7.2 Far-Backward Electrons . . . . .	449
Far-Backward Electron Processes and Measurements . . . . .	449
11.8 Polarimetry . . . . .	452
11.8.1 Electron Polarimetry . . . . .	455
11.8.2 Hadron Polarimetry . . . . .	463
11.9 Readout Electronics and Data Acquisition . . . . .	466
11.9.1 Introduction . . . . .	466
11.9.2 Glossary . . . . .	467
Readout electronics terms . . . . .	467
Data acquisition system terms . . . . .	468

11.9.3	Overview on DAQ Structure . . . . .	469
11.9.4	Constraints and Environment . . . . .	471
11.9.5	Readout Electronics: Present State of the Art . . . . .	473
	Introduction . . . . .	473
	Front-end electronics . . . . .	473
	Digitization and data treatment . . . . .	474
	Examples of readout chips . . . . .	475
	Support system . . . . .	479
11.9.6	Possible Readout Chip Evolution and Future Technological Constraints	479
11.9.7	Existing streaming readout DAQ Systems for particle physics experiments . . . . .	481
	LHCb streaming readout DAQ . . . . .	481
	sPHENIX Hybrid DAQ . . . . .	482
	The RCDAQ Data Acquisition System . . . . .	482
	The ERSAP system . . . . .	483
11.9.8	A Progressive Approach toward the EIC DAQ System . . . . .	483
11.9.9	Experimental Validation of the Approach . . . . .	485
	Jefferson Laboratory efforts . . . . .	486
	BNL efforts . . . . .	488
11.10	Software, Data Analysis and Data Preservation . . . . .	488
11.11	Artificial Intelligence for the EIC Detector . . . . .	493
<b>12</b>	<b>The Case for Two Detectors</b>	<b>496</b>
<b>13</b>	<b>Integrated EIC Detector Concepts</b>	<b>497</b>
13.1	General Purpose Detector Concept . . . . .	497
13.1.1	Standard Layout . . . . .	497
13.1.2	Detector technology description . . . . .	497
13.1.3	Electronics, Data Acquisition and Computing technology description	497
13.1.4	Detector Integration . . . . .	497
	Hall infrastructure . . . . .	497

Safety and Environmental Protection . . . . .	499
Installation . . . . .	499
Detector Alignment . . . . .	504
Access and Maintenance . . . . .	505
Central Detector . . . . .	507
Forward and Backward Detector . . . . .	507
13.1.5 Systematics Discussion . . . . .	507
13.2 Second General Purpose Detector Concept . . . . .	507
13.2.1 Standard Layout . . . . .	507
13.2.2 Detector technology description . . . . .	507
13.2.3 Electronics, Data Acquisition and Computing technology description . . . . .	507
13.2.4 Detector Integration . . . . .	507
Central Detector . . . . .	507
Forward and Backward Detector . . . . .	507
13.2.5 Systematics Discussion . . . . .	507
<b>14 Detector Technology</b> . . . . .	<b>508</b>
14.1 Silicon-Vertex Tracking . . . . .	510
14.1.1 Monolithic Active Pixel Sensors (MAPS) . . . . .	510
14.1.2 Silicon-Sensor Tracking Fallback . . . . .	511
14.1.3 Services Reduction – Multiplexing and Serial-Fiber Off Detector Output . . . . .	512
14.1.4 Services Reduction - Serial Powering and/or DC-DC Converters for Powering of Detector Components . . . . .	512
14.2 Tracking . . . . .	513
14.2.1 Low-Mass Forward/Backward GEM Detectors . . . . .	513
14.2.2 Large Cylindrical $\mu$ RWELL Layer . . . . .	514
14.2.3 Large Micromegas Barrel Tracker . . . . .	515
14.2.4 R&D Needs for Planar $\mu$ RWELL Detectors . . . . .	516
14.2.5 MPGD Readout for a Time Projection Chamber . . . . .	517
GEM and MicroMegas . . . . .	517

Hybrid and Gating . . . . .	518
Readout Electronics . . . . .	518
14.3 Particle Identification . . . . .	519
14.3.1 A Modular RICH (mRICH) for Particle Identification . . . . .	519
14.3.2 A Dual-Radiator Ring Imaging Cherenkov Detector (dRICH) . . . . .	520
14.3.3 High-Performance DIRC . . . . .	521
14.3.4 Photosensor: MCP-PMT and LAPPD . . . . .	522
14.3.5 R&D Needs for GEM-TRD/Tracker in the Forward Direction . . . . .	523
14.3.6 Gaseous Single Photon Detectors Based on MPGD Technologies . . . . .	524
14.3.7 Fast Timing Silicon Sensor: LGADs . . . . .	525
14.4 Electromagnetic and Hadronic Calorimetry . . . . .	527
14.4.1 Tungsten Scintillator Calorimetry . . . . .	527
14.4.2 SciGlass for Electromagnetic Calorimetry . . . . .	528
14.4.3 Hadronic Calorimetry . . . . .	529
14.4.4 CSGlass for Hadronic Calorimetry . . . . .	530
14.5 Auxiliary Detectors . . . . .	531
14.5.1 Roman Pots and LGAD Technology . . . . .	531
14.5.2 Zero Degree Calorimeter . . . . .	532
14.5.3 Superconducting-Nanowire Particle Detectors . . . . .	534
14.6 Data Acquisition . . . . .	535
14.6.1 Streaming-Capable Front-End Electronics, Data Aggregation, and Timing Distribution . . . . .	535
14.6.2 Readout Software Architecture, Orchestration and Online Analysis . . . . .	536
14.7 Electronics . . . . .	537
14.7.1 R&D of High Precision Timing Distribution Over Large System . . . . .	537
14.7.2 R&D of FPGA Operation in Radiation Environment . . . . .	538
14.7.3 R&D of Micro-electronics, Optop-Electronics and Powering . . . . .	538
<b>Appendix A Deep Inelastic Scattering Kinematics</b>	<b>540</b>
A.1 Structure functions . . . . .	540

A.2 Invariants . . . . .	541
A.3 Laboratory frame . . . . .	543
A.4 Breit frame . . . . .	544
A.5 Helicity studies . . . . .	545

**References**

**R-1**

SNAPSHOT 19 Nov. 2020

**Part I**

**Executive Summary**

SNAPSHOT 19 Nov. 2020

## Chapter 1

# The Electron-Ion Collider

SNAPSHOT 19 Nov. 2020

## Chapter 2

# Physics Measurements and Requirements

SNAPSHOT 19 Nov. 2020

## Chapter 3

# Detector Concepts

SNAPSHOT 19 Nov. 2020

## Chapter 4

# Opportunities for Detector Technology and Computing

In parallel with a nearly two-decade-long community effort of EIC science development and refinement, as well as experimental equipment conceptualization, Brookhaven National Laboratory in association with TJNAF and the DOE Office of Nuclear Physics established in 2011 a highly successful generic EIC-related detector R&D program. This program both built bridges between various domestic and international research groups and scientific communities, and was successful in its own right towards detector R&D. Presently, 281 scientists are engaged in the generic EIC-related R&D program, from 75 institutions in 10 countries. Most of the efforts have been organizationally merged in groups of topical consortia, which can provide the seeds for the EIC detector collaboration(s).

Many of the supported projects, ongoing or completed, developed technologies that are now integral parts of existing detector concepts or are regarded as potential alternatives. The vertex detector R&D consortium aims to develop new improved Monolithic Active Pixel Sensors (MAPS) to meet the requirements demanded by the EIC requirements. Various Micro-Patter Gas Detector (MPGD) technologies, such as Gaseous Electron Multiplier (GEM), Micromegas, and  $\mu$ RWELL, have been pursued for low material tracking in barrel and forward regions as well as Time-Projection Chamber (TPC) readouts. New concepts like miniTPCs and integrated Cherenkov-TPCs had been developed and tested. Many options for electromagnetic, and recently, hadronic calorimetry have received R&D effort within the calorimetry consortium. From this grew the Tungsten-Scintillating Fiber (W-SciFi) calorimeter, scintillating fibers embedded in a W-powder composite absorber. In parallel, novel scintillating glasses (SciGlass) have been developed with unprecedented quality as cost-effective alternative to expensive lead-tungstate ( $\text{PbWO}_4$ ) crystals. The particle identification consortium is pursuing various technologies, such as Direct-Internally Reflected Cherenkov light (DIRC) detectors, Dual Ring-Imaging Cherenkov (RICH) detectors with gas and aerogel radiators. New coating materials like nano-diamonds to replace Cesium-Iodide (CsI) for RICH photo sensors are also under investigation. Time-of-Flight detectors, as well as Roman Pots for forward proton detection, require highly segmented

AC-coupled Low-Gas Avalanche Detector (AC-LGAD) sensors whose development has just started to get supported by the program. Besides hardware R&D the program has supported various vital projects such as machine background studies and simulation software developments to enable more accurate definition of the physics' requirements. Sartre and Beagle are two examples of Monte-Carlo event generators whose development was substantially boosted by the program. Both were intensively used in the context of this report.

In general, due to this longstanding generic EIC-related detector R&D program, and further support from Laboratory Directed Research & Development (LDRD) Programs within the US national laboratories, and many university groups both inside and outside the US, the detector technologies to implement a successful comprehensive Day-One EIC Science program exist. For this reason the EIC User Group can continue to consider various technologies for many of the different detector functions to implement, with an eye also to possible detector complementarity for a second detector. The EIC also benefitted substantially from synergetic R&D conducted for many high-energy and nuclear physics experiments, not only at BNL and JLab, but also for experiments such as ALICE and LHCb at CERN, PANDA at GSI and BELLE-II and KEK.

On the other hand, further opportunities do remain. These are driven both by pursuing alternative detector technologies for a complementary second fully integrated EIC detector and Interaction Region, and to prepare for future cost-effective detector upgrades to enhance capabilities addressing new nuclear physics opportunities. Furthermore, the EIC will be a two-decade Nuclear Physics facility after its construction is completed and will in this period likely require further detector upgrades driven by its science findings. It is expected that further physics opportunities enabled by new detector capabilities will already arise during the EIC design and construction phase.

Nuclear physics detection techniques typically need to cover a large range in energies. They can range from the MeV scale of nuclear binding energies and 100 MeV/c momentum scale below the Fermi momentum to isolate nuclear processes, all the way to the multiple tens of GeV scales to pinpoint the elementary sub-atomic quark-gluon processes and quark flavors. Due to this, Nuclear Physics drives detector technologies with often different demands than those in high-energy and particle physics. Examples are (i) particle identification techniques and their cost-effectiveness in readout (RICH, DIRC, ultra-low-precision TOF, electro-magnetic and hadronic calorimetry), (ii) those driving detector material minimization to detect the lowest-momentum particles (inner tracking solutions, gaseous-based radial TPCs), (iii) those pushing for specific material radiation tolerances (electro-magnetic rather than hadronic, high-power target areas, and low-energy nuclear fragments), and (iv) those related to spin or polarization (beam, targets, polarimetry).

Further opportunities for detector technology within these overarching Nuclear Physics areas exist in the EIC design, construction, and science operations era. These can best be considered in detector functionality areas such as particle identification, calorimetry, tracking, and readout electronics, to address how one can enhance the performance of the EIC detector(s) with target R&D projects in a year or more.

Examples of such detector opportunities include, but are not limited to, the following: material minimization in a possible all-Silicon tracker, particle identification reach at mid rapidity and at higher momenta, cost-effectiveness of readout of particle identification detectors by improvements to Silicon Photomultipliers (SiPMs) or to Incom's Large-Area Picosecond Photo-detectors (LAPPD). Furthermore, improvement of the achievable hadronic calorimetry resolutions, large-scale production and low-energy photon detection efficiency of possible glass-based electromagnetic calorimetry, new Application-Specific Integrated Circuit (ASIC) and front-end readout board needs required for streaming readout modes, or improved spatial and/or timing resolution of Zero-Degree Calorimeters driven by the imaging and diffractive science programs. It is crucial that this research for enhanced detector functionality continues and is recognized as driven by Nuclear Physics needs.

In parallel with these detector opportunities, unique opportunities exist to directly *integrate* modern computing and data analysis methods in the experiment. Efforts are underway to develop methods and production systems to establish a quasi-instantaneous high-level nuclear physics analysis based on modern statistics from a self-calibrated matrix of detector raw data synchronized to a reference time, without intermediate data storage requirements. This takes direct advantage of advances in micro-electronics and computing, and of artificial intelligence (AI) methods.

Micro-electronics and computing technologies have made order-of-magnitude advances in the last decades. Combined with modern statistical methods, it is now possible to analyze scientific data to rapidly expose correlations of data patterns and compare with advanced theoretical models. While many existing nuclear physics and high-energy physics experiments are taking advantage of these developments by upgrading their existing triggered data acquisition to a streaming readout model, these experiments do not have the luxury of an integrated systems from data acquisition through analysis, such as the EIC has. Hence, we aim to remove the separation of data readout and analysis altogether, taking advantage of modern electronics, computing and analysis techniques in order to build the next generation computing model that will be essential for probing the femto-scale science accessible at the EIC.

An integrated whole-experiment approach to detector readout and analysis towards scientific output will take advantage of multiple existing and emerging technologies. Amongst these are: "Streaming readout" where detectors are read out continuously, continuous data quality control and calibration, task-based high performance local computing, distributed bulk data processing at supercomputer centers, modern statistical methods that can detect differences among groups of data or associations among variables even under very small departures from normality, and systematic use of artificial intelligence (AI) methods at various stages.

To further elaborate on the latter, AI is becoming ubiquitous in Nuclear Physics, and EIC could be one of the first programs where AI is systematically employed from the start. AI already plays an important role in existing experiments such as LHCb at CERN, where machine learning algorithms make already the majority of the near-real-time decisions what physics data should be written or proceed to a higher level analysis.

Supported by the modern electronics able to continuously convert the analog detector signals, streaming readout can further the convergence of online and offline analysis: here the incorporation of high-level AI algorithms in the analysis pipeline can lead to better data quality control during data taking and shorter analysis cycles. AI could foster in the next years significant advances in the crucial area of fast calibration/alignment of detectors, greatly facilitating a data streaming readout approach.

For tracking, in Nuclear Physics experiments typically being characterized by most of the computing cycles spent in propagating the particles through inhomogeneous magnetic fields and material maps, AI can contribute to determine the optimal initial track parameters allowing to decrease the number of iterations needed. For particle identification, crucial for Nuclear Physics experiments, there recently has been a large growth of applications.

AI at the EIC is expected to play a role in high-level physics analysis such as searches for rare signatures which necessitates advanced techniques making strong use of machine learning to filter out events, the utilization of jets to empower taggers for boosted jets and quark flavors within the jets, and in the aid for construction of higher-level Wigner distributions from sparse and missing data. With the EIC detector design ongoing and opportunities for two detectors at the EIC, AI can be gainfully used for the design optimization process of the large and complex EIC detector systems that are based on computationally intensive simulations, for the optimization of the individual detector systems, and even the optimization of materials used within detectors to improved performance.

**Part II**  
**Physics**

SNAPSHOT 19 Nov. 2020

## Chapter 5

# Introduction

For more than a decade, the physics community studying quantum chromodynamics (QCD) has gathered to come up with the next experimental facility that can answer the outstanding questions about the inner structure of matter. A consensus developed towards the need of a machine that can explore hadrons using the electromagnetic probe at high center-of-mass energies: an electron-ion collider (EIC). Over the years, tremendous efforts have been devoted to making the physics case strong and defining the characteristics of such a collider. Important capabilities such as polarized beams, high luminosity, flexible center-of-mass energy, large variety of beam species are all essential for the success of the project. The physics case has been developed by the community in a White Paper [1] outlining the fundamental questions that an EIC would address.

Another major milestone was the recommendation in the US 2015 Long Range Plan for Nuclear Science of a high-energy high-luminosity polarized EIC as the highest priority for new facility construction. Since then, the interest in the community has continued to grow. An assessment of a US-based electron-ion collider science program was carried out by the National Academy of Sciences Engineering, and Medicine (NAS) in 2017, with a report produced in 2018 [2] and findings which concluded that its physics case is compelling, fundamental and timely. Crucial questions that could be addressed at an EIC include the origin of the mass of atomic nuclei, the origin of the spin of protons and neutrons, how gluons hold hadrons and nuclei together, and whether new emergent forms of matter made of gluons densely packed in phase space exist.

The NAS committee added that along with advancing nuclear science, an EIC would also benefit other areas such as astrophysics, particle physics, accelerator physics, and theoretical and computational modeling. It would also play a valuable role in sustaining the U.S. nuclear physics workforce in the coming decades. Moreover, it would have a significant role in advancing more broadly the technologies that would result from the research and development undertaken in the implementation and construction of an EIC in the U.S. The report emphasizes that an EIC is the only high-energy collider being planned for construction in the U.S. currently, and building such a facility would maintain U.S. leadership in accelerator collider science while benefiting the physical sciences.

Following the extremely positive assessment by the NAS, the US Department of Energy officially started the EIC project by establishing its CD-0 (mission need) in December 2019. In parallel to the DOE-driven activities and in order to prepare the EIC construction, the physics community, organized around an EIC Users Group, started an initiative to define the detector requirements needed to deliver the science spelled out in the EIC White Paper and new topics highlighted in the NAS report and other publications. The goal is to advance the state and detail of the documented physics studies and detector concepts in preparation for the realization of the EIC. The effort aims to provide the basis for further development of concepts for experimental equipment best suited for science needs towards future Technical Design Reports (TDRs). These efforts were carried out during the year 2020 and are summarized in this “Yellow Report”.

The “Yellow Report” term was first coined by the CERN physics community, where a series of workshops was organized to build on the previous groundwork in detector R&D, upgrades developments, progress made in the experimental analysis techniques, as well as theory advances. The goal was to morph these broad works into an extensive review of the LHC prospects in the high-luminosity era. Likewise, to advance both the physics case and the detector concepts in preparation for the EIC, the EIC Yellow Report effort has been initiated in December 2019 with a kick-off meeting hosted by the MIT. A total of 4 dedicated workshops, with an intermediate report to the community at the EIC Users Group meeting, were part of the program:

- 1st Workshop: March 19-21, 2020, Temple University, Philadelphia, PA
- 2nd Workshop: May 22-24, 2020, University of Pavia, Pavia, Italy
- Status reports at Summer EICUG Meeting: August 3-7, 2020, FIU, Miami, FL
- 3rd Workshop: September 17-19, 2020, CUA, Washington, DC
- 4th Workshop: November 19-21, 2020, UC Berkeley, Berkeley, CA

All workshops and meetings and the entire effort were open to the participation of anyone in the community. The Yellow Report initiative was thus set to prove a medium for broad community engagement, further the physics case, provide input to detector requirement, bring forward best available and emerging detector technologies and concepts, and document the progress towards EIC realizations. This Yellow Report represents the current state of affairs and is intended to be used by the scientific community as the basis for further studies and developments. It is hoped that this intellectual investment into the future of the EIC will then guide the design and development of the actual EIC detectors.

The physics case and physics-driven detector requirement studies were organized within the Physics Working group. In parallel, detector R&D efforts and detector technology choices were worked on within the Detector Working group. This Volume summarizes the Physics Working group efforts. It addresses the progress towards the effort main goal: carrying out a quantitative analysis of planned physics measurements for topics highlighted in the White Paper and new physics topics developed more recently, and document emerging implications for detector design. To focus and further organize this effort, the Physics

Working group was divided into smaller subgroups, organized by the physics processes, which provides a natural pathway for assessing detector requirements. These subgroups are: Inclusive Reactions, Semi-inclusive Reactions, Jets and Heavy Quarks, Exclusive Reactions, Diffractive Reactions & Tagging.

The working groups were in charge of defining and studying the physics processes that fall into the particular categories. Through simulations and by drawing from theoretical studies the goal was to specify the requirements for the detector which would ensure that the physics outlined in the White Paper and the NAS report could be performed successfully. The working groups also addressed more recent aspects that came to broader attention after the publication of the White Paper and the NAS report.

The summary of the detector requirements delivered by each of the Physics subgroups is documented in the corresponding section of Chapter 8. The physics studies that lead to these detector requirements and novel physics ideas and measurements proposed that may not yet provide input for the detector R&D are documented in Chapter 7.

SNAPSHOT 19 Nov. 2020

## Chapter 6

# The EIC Physics Case

The working groups began to organize with the Yellow Report kick-off meeting held in Dec. 2019 at MIT [3]. This would turn out to be the first and last in person meeting of the participants.

The science program of the future EIC was divided in 5 main topics, in a similar ways as it was articulated in the White Paper:

- Global properties and parton structure
- Internal imaging of the nucleon and nuclei
- Nuclear medium modifications
- Hadronization
- Connections with other fields

In order to best asses the detector requirements needed to fulfil this wide physics program, it was realized that it would be more suitable to organize working groups that would study similar processes. Indeed, the measurement of the same kind of process would generally lead to similar detector requirements, independently of the physics topic it may address. The different kind of physics measurements were grouped into the following categories:

- Inclusive reactions
- Semi-inclusive reactions
- Jets and heavy flavor measurements
- Exclusive reactions
- Diffractive processes and forward tagging

**Physics topics linked to processes & measurements** *White Paper & NAS measurements*

Processes+ ↓ Topics	Inclusive	Semi-Inclusive	Jets, Heavy Flavor	Exclusive	Diffractive, Forward Tagging
Global properties and parton structure	Incl. SF	h, hh	j, Q	excl. J/ψ, γ	Incl. diffr., tagged DIS on pol. D/He
Imaging		h	j, jj, j+h, Q+Qbar, [QQbar]	Excl-DIS: DVCS, DVMP (J/ψ, γ, ρ <sup>0</sup> , φ, π <sup>+</sup> , K, ρ <sup>+</sup> , K*...), Elastic scattering	
Nucleus	Incl. SF	h, hh	j, jj, Q, [QQbar]	coh. VM, jj, h, hh	Diffr. SF, incoh. VM, jj, h, hh D/He FF, nucl. fragments
Hadronization		h, hh, j+h	j, Q		
Other fields		CC DIS, γ-A total X-sec		γ-A elast. X-sec	γ-A diffr. X-sec <sub>5</sub>

**Figure 6.1:** Relationship between the EIC science topics (rows) and the categories of measurements (columns). Measurements already discussed in the White Paper or the NAS report are highlighted in red. Additional measurements and physics ideas have emerged since, and are also included in this table.

Figure 6.1 illustrates how the different categories of measurements above can address the different physics topics of the EIC.

The following two chapters of this volume are organized as follows. Chapter 7 gives an overview of EIC science, reviewing and updating the physics case previously presented in the White Paper and highlighted in the NAS report. In addition, new ideas emerged in the meantime and not discussed before are described in more detail. The sections of this chapter received contributions from a number of participants across working groups. Nucleon tomography – multidimensional imaging of the nucleon in position and momentum space (FFs, PDFs, TMDs, GPDs, Wigner functions) is covered in sections 7.2.1 to 7.2.4; the high-energy regime of non-linear color fields and the physics of gluon saturation is covered mainly in secs. 7.3.1; QCD diffraction and exclusive processes are covered in sec. 7.1.6, 7.3.2, and 7.3.9; the physics related to the origin of the spin and mass of the proton is described in sec. 7.1.2 and 7.1.4, respectively. These are the pillars of the QCD program at the EIC outlined in the White Paper [1] and reviewed in the NAS report [2].

This YR also addresses a number of recent topics which had not been covered in depth in the WP or the NAS report. These include the partonic structure of mesons in sec. 7.1.3, multi-parton correlations in sec. 7.1.5, short range correlations and the origin of the nuclear force in sec. 7.3.7, nuclear PDFs in sec. 7.3.3, the structure of light (polarized) nuclei in sec. 7.3.8, particle propagation through matter and transport properties of nuclei in sec. 7.3.4, as well as hadronization and spectroscopy of exotic states in sec. 7.4. These are exciting timely topics which further broaden the rich physics program to be pursued at the EIC.

The program pursued at the EIC is firmly focused on QCD. Nevertheless, it also connects to other fields, in particular to High Energy Physics. Specific aspects of electroweak and beyond the Standard Model physics, neutrino, cosmic ray & astroparticle physics, and the physics of proton-proton, proton-nucleus and nucleus-nucleus collisions studied at the RHIC and LHC accelerators which will benefit from the insight provided by the EIC have been outlined in sec. 7.5.

Finally, sec. 7.6 mentions theory efforts with ties to the program pursued at the EIC. These are the understanding of QED radiative corrections in electron scattering from a hadron or nucleus. And, Lattice QCD which is the only tool available for obtaining first principles, non-perturbative results from the quantum field theory of the strong interactions.

Chapter 7 describes the detector requirements from each of the categories of processes. The structure of this chapter details the studies performed by each of the physics working groups.

SNAPSHOT 19 Nov. 2022

## Chapter 7

# The EIC Measurements and Studies

### 7.1 Global properties and parton structure of hadrons

**Nucleon spin:** Global properties such as the spin and the mass are among the most important quantities characterizing any hadron. Getting a deeper understanding of those properties in QCD is among the key missions of the EIC. Starting with the spin, we recall that the spin- $\frac{1}{2}$  of the nucleon can be decomposed according to

$$\frac{1}{2} = S_q + S_g + L_q + L_g \quad (7.1)$$

into contributions from the quark plus antiquark (gluon) spin  $S_q$  ( $S_g$ ), as well as quark (gluon) angular momenta  $L_q$  ( $L_g$ ). For quite some time it was generally believed that  $S_q$  is largely responsible for making up the nucleon spin. It came therefore as a big surprise when in the late 1980s the EMC Collaboration reported a value for  $S_q$  that is consistent with zero within errors. This “nucleon spin crisis” initiated a large number of further experimental and theoretical activities. Presently available results suggest that about 25% of the nucleon spin is carried by the quark and antiquark spin. Mainly due to the RHIC spin program, we now also have clear evidence for a nonzero  $S_g$ . However, the values of both  $S_q$  and  $S_g$  still have very large uncertainties. The main reason for this situation lies in the fact that, in order to determine the parton spin contributions in Eq. (7.1), one in principle needs to know the corresponding helicity distributions (see below) for any parton momentum  $x$ , since their integral defines  $S_q$  and  $S_g$ . But the helicity distributions are presently only known for  $x \gtrsim 0.01$  with sufficient precision. Through measurements of polarized DIS [DIS sidebar?], the EIC will provide unprecedented information for the parton helicity distributions down to  $x \sim 10^{-4}$  — see Fig. 7.1. This will not only result in a much better understanding of both  $S_q$  and  $S_g$ , but also further constrain the sum  $L_q + L_g$  in Eq. (7.1), where we refer to Sec. 7.1.2 for more details. The EIC may actually be able to also provide, for the first time, direct information on the parton orbital angular momenta through measuring Wigner functions, as will be discussed below in Sec. 7.2.4.

**Nucleon mass:** Similarly to the nucleon spin, it is of crucial importance to understand how

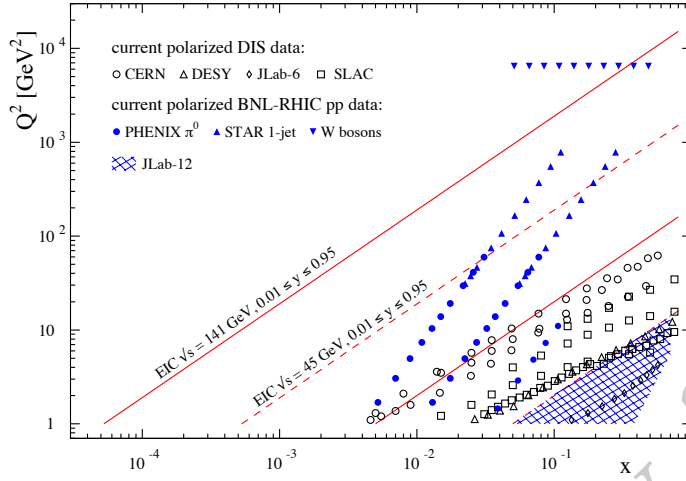


**Figure 7.1:** The kinematic coverage of the EIC for polarized inclusive DIS compared to that of previous experiments.

the nucleon mass can be decomposed in QCD into contributions from the partons. The mass of an atom is almost exactly equal to the sum of the masses of its constituents, that is, the nucleus and the electrons. Likewise the mass of an atomic nucleus is approximately given by the mass of the nucleons which make up the nucleus. On the other hand, the nucleon mass cannot even be computed roughly by adding the masses of its constituents, which are attributed to the Higgs mechanism. For instance, the sum of the masses of the valence quarks is just about 1% of the nucleon mass. In a proper QCD analysis, the quark mass contribution to the nucleon mass is much larger. Nevertheless, studies suggest that at least 75% of the nucleon mass must have a different origin. This bulk of the nucleon mass may be understood as the contribution from the quark and gluon energies. Alternatively, one can attribute it to the trace anomaly of the QCD energy momentum tensor which, by definition of an anomaly, is a quantum effect. The trace anomaly can also be decomposed into contributions from quarks and gluons. In Sec. 7.1.4 below we will briefly discuss studies which strongly suggest that the trace anomaly is measurable by means of threshold production of heavy quarkonia, a process that can be explored better than ever at the EIC. The EIC will therefore be able to deepen our understanding of the nucleon mass in QCD.

**Parton distributions:** Since the pioneering DIS experiments at SLAC in the late 1960s it is known that the nucleon has a partonic structure. The simplest quantities describing how the partons are distributed inside the nucleon are the (one-dimensional) PDFs, which depend on the fraction  $x$  of the nucleon's momentum that is carried by the parton. The most prominent ones are the twist-2 PDFs which have a density interpretation. For a spin- $\frac{1}{2}$  hadron like the nucleon one can define the three quark PDFs

$$f_1^q(x) = q(x), \quad g_1^q(x) = \Delta q(x), \quad h_1^q(x), \quad (7.2)$$

where  $f_1^q$  denotes the density of unpolarized quarks in an unpolarized nucleon, while  $g_1^q$  ( $h_1^q$ ) denotes the density of longitudinally (transversely) polarized quarks in a longitudinally (transversely) polarized nucleon. (In (7.2) the most commonly used notations for the unpolarized and helicity PDFs are shown.) Even though the unpolarized PDFs are rather well known by now, the EIC can still further this field as outlined in Sec. 7.1.1. The expected significant EIC potential for pinning down the helicity PDFs will be discussed in detail in Sec. 7.1.2, whereas the prospects for the transversity distribution are presented in Sec. 7.2 on multi-dimensional imaging since an important reaction for measuring  $h_1$  involves the (3D) TMDs.

**Meson structure:** Measurements at the EIC can also address the structure of mesons. Specifically, very detailed plans exist to explore pions, by far the lightest strongly interacting particles, as well as kaons. Since those mesons are unstable they cannot be probed directly in a DIS experiment. However, by considering suitable final states and kinematics in electron-proton scattering one is able to largely single out lepton scattering off the meson of interest. For instance, in order to explore DIS off a pion, the detection of a neutron is needed, in addition to the scattered lepton. Studies of light mesons are very interesting in their own right, but may also offer deeper insights into the generation of hadron masses. This aspect serves as an important driver behind those activities as explained in quite some detail in Sec. 7.1.3 and elsewhere.

**Multi-parton correlations:** The inclusive DIS process not only contains information about densities of single partons (twist-2 PDFs) but also about multi-parton correlations, which characterize the structure of hadrons at a new level. Specifically, the twist-3 structure function  $g_T$ , which is accessible in polarized DIS, is related to quark-gluon-quark correlations in the nucleon. Additional quark-gluon-quark correlations can be studied in lepton-nucleon scattering by considering other final states beyond the fully inclusive one. It is timely to explore how the EIC can contribute to this important field, which in the past has received very little attention in documents dealing with the EIC science case. In Sec. 7.1.5 the prospects in that regard are briefly discussed. Among other things, it is argued that the EIC would allow one, for the first time, to extract unambiguous information about quark-gluon-quark correlations from inclusive DIS over a large kinematical range.

**Inclusive diffraction:** About 10% of the inclusive DIS events observed at HERA are diffractive, that is, they show a large rapidity gap between the system  $X$  and the proton (or a low-mass excitation of the proton). Therefore diffraction became a major research topic in the HERA community. Since the proton is detected, diffractive events in DIS are characterized by additional kinematic variables beyond the standard variables  $x$  and  $Q^2$  [DDIS sidebar?]. The EIC holds promise to significantly extend our understanding of inclusive diffraction. In particular, as discussed in some detail in Sec. 7.1.6, the kinematic range that can be explored at the EIC shows a considerable complementarity relative to the HERA measurements.

### 7.1.1 Unpolarized parton structure of the proton and neutron

#### Inclusive NC and CC DIS

Historically, our knowledge of unpolarized collinear parton distribution functions (PDFs) has been driven by inclusive neutral current (NC) and charged current (CC) deep inelastic scattering (DIS) cross sections from protons and deuterons, together with high-energy scattering data from proton-antiproton collisions at the Tevatron and more recent measurements from proton-proton collisions at the LHC. A detailed description of the data set entering PDF determinations can be found at Refs. [4–6]. The existing DIS data cover an impressive range in the outgoing lepton kinematics with  $x$  down to  $10^{-5}$  and  $Q^2$  up to the order  $10^4$   $\text{GeV}^2$ . While there is a substantial kinematic overlap between the measurements at HERA and those in fixed-target experiments, they are complementary in accessing the small- $x$  and large- $x$  longitudinal hadron structure, respectively. The EIC, on the other hand, covers an overlapping kinematic range between HERA and the fixed-target experiments, with an instantaneous luminosity potentially 3 orders-of-magnitude larger than at HERA. The EIC, together with the Jefferson Lab 12 GeV program, will allow for a new era in the exploration of hadron structure in high definition.

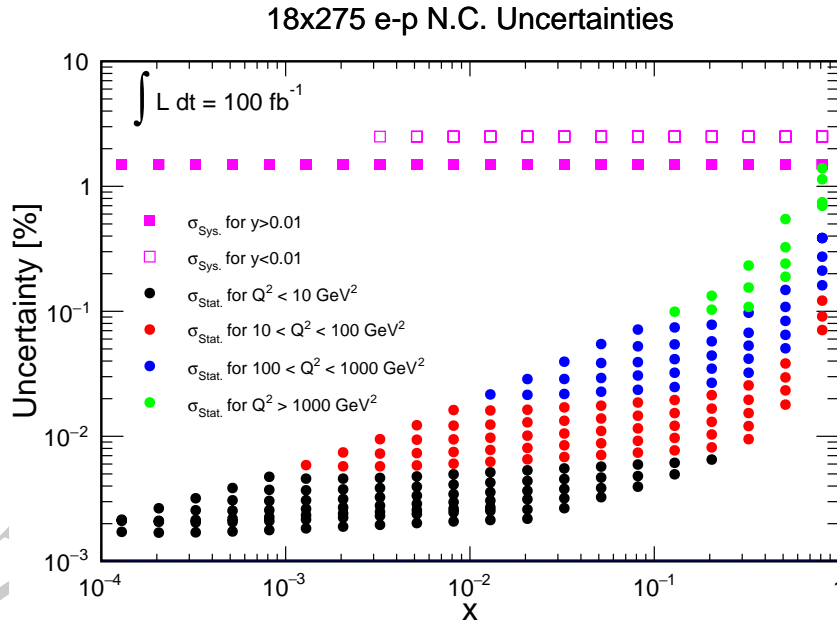


**Figure 7.2:** Simulated statistical and systematic uncertainties for  $eP$  NC DIS at  $\sqrt{s} = 140.7 \text{ GeV}$ .

In Fig. 7.2 we present relative statistical and systematic uncertainties for the EIC NC cross sections. While an integrated luminosity of  $100 \text{ fb}^{-1}$  provides an impressively small statistical uncertainty at small  $x$ , the overall uncertainties are estimated at present to be limited by the systematic uncertainties. Details for the projected uncertainties can be found in Sec. 8.1

Fig. 7.3 shows the impact of the EIC NC DIS data on our current knowledge of the differential cross sections computed using the NNPDF3.1 PDF set [7, 8]. Using a  $\chi^2$ -based hypothesis test, we assess the EIC constraining power at the single bin level with  $\mathcal{L} = 100 \text{ fb}^{-1}$  of pseudo data and point-by-point systematic uncertainties as described in section 8.1 (left panel), reduced by a factor 2 (central panel) and then 10 (right panel). The impact of the EIC pseudo data is quantified in terms of a Z-score that measures the statistical separation in units of standard deviation  $\sigma$  between two hypotheses of cross-sections. The figure shows that more than  $5\text{-}\sigma$  (Z-score  $\geq 5$ ) average discrimination power between cross-sections generated from the central PDF replica and non-central PDF replicas can be achieved across the entire EIC acceptance if the current projections for the systematic uncertainties are reduced by a factor of 10.

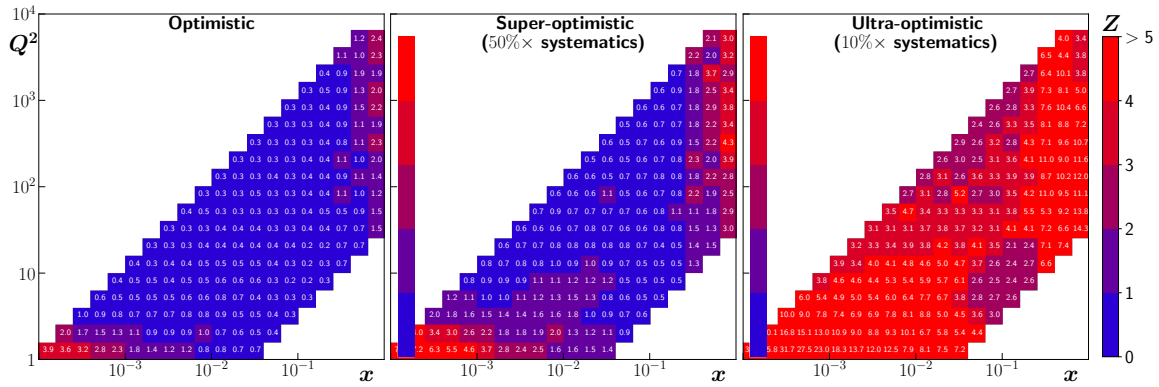


**Figure 7.3:** Z-analysis for different scenarios: original, half and tenth of the nominal systematic uncertainties, both correlated and uncorrelated. The Z-score uses the NNPDF3.1 proton PDFs [7] to compare the cross-sections generated from the central PDF replica (the null hypothesis) and non-central PDF replicas (the alternative hypothesis).

In order to assess the impact from different bins on the  $(x, Q^2)$  plane of the EIC data, we present in Fig. 7.4 (left) a parton level analysis i.e non perturbative quantities such as PDF combinations focusing in particular on the strange sector via  $R_s = (s + \bar{s})/(\bar{u} + \bar{d})$  using the Z-score technique. We select the strange sector since it is one of the most difficult PDFs to be extracted from data (see recent developments in Refs. [9, 10]) from inclusive NC and CC reactions that places stronger constraints on detector capabilities. The analysis is carried out using the NNPDF3.1 [7, 8] replicas and modifying the sea-quark PDFs requiring  $R_s = 0.5$  and  $R_s = 1$  in such a way that momentum conservation is not violated. The Z-scores profile shows that the strange sector can be discriminated up to  $3\text{-}\sigma$  at low- $x$  and low- $Q^2$  and  $2\text{-}\sigma$  in a narrow region of high- $x$  and high- $Q^2$ . The sensitivity in the moderate  $x$  are found to be marginal.

A complementary analysis done in the framework of PDFSense [11–13] shown in Fig. 7.4 (right) also illustrates a potential for modest sensitivity of the EIC  $e^-$  data to the behavior of the above-defined  $R_s$  PDF combination. This can be inferred based on the share of individual pseudodata with relatively larger values of the *sensitivity* parameter,  $|S_f|$ . The PDF-level pulls of the EIC pseudodata can be judged in context against the typical values

of  $|S_f|$  [11] for data fitted in the CT18 global analysis [14].

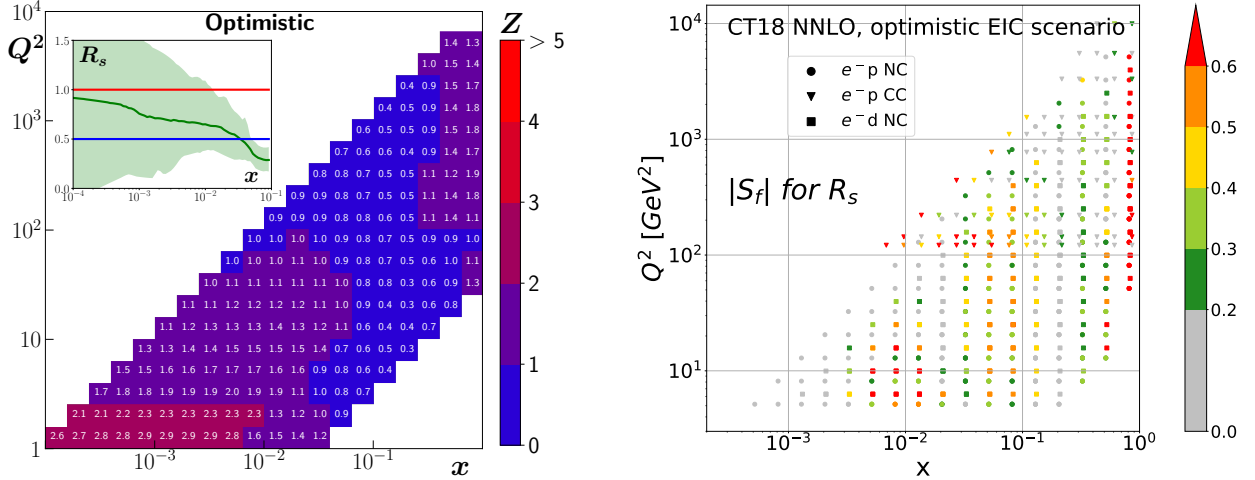


**Figure 7.4:** (left): Z-score analysis comparing the cross-sections generated from PDF replicas satisfying  $R_s = 0.5$  (the null hypothesis in blue) and  $R_s = 1$  (the alternative hypothesis in red). These two hypotheses are built by modifying the NNPDF3.1  $s$ ,  $\bar{s}$ ,  $\bar{u}$ ,  $\bar{d}$  distributions with an additive factor  $\kappa(x)$  in a way to conserve the sum rules. (right): The sensitivity,  $|S_f|$ , of the EIC  $e^-$  pseudodata to the  $R_s$  PDF ratio; redder points indicate those pseudodata with larger expected constraining power, as discussed in Ref. [11].

In Fig. 7.5 we examine the potential impact of EIC's NC and CC with incident electron beam colliding with proton and deuteron beams from a selection of PDF global analyzers (CJ [15], CT [14], JAM [10, 16], NNPDF [7, 9]). For proton beams we use  $\mathcal{L} = 100\text{fb}^{-1}$  with  $\sqrt{s} = 28.6, 44.7, 63.3, 140.7$  GeV for NC and 140.7 GeV for CC. For deuteron beams we use  $\mathcal{L} = 10\text{fb}^{-1}$  and consider only NC at  $\sqrt{s} = 28.6, 66.3, 89.0$  GeV. We stress that the various analyses are carried out under different conditions of data selection and PDF extraction methodologies. Focusing on the DIS data sets, all groups use the bulk of world DIS data from SLAC, BCDMS, NMC and HERA. While CT and NNPDF place strong cuts on  $W^2 \gtrsim 10\text{GeV}^2$  which excludes the very large- $x$  and low- $Q^2$  region, CJ and JAM use lower cuts of  $W^2 \gtrsim 4\text{GeV}^2$  allowing to include PDF constraints from JLab. In terms of methodologies, different groups have different approaches to carry out the Bayesian inference. CJ and CT use maximum likelihood augmented by the hessian approach to estimate the confidence regions for the PDFs while JAM and NNPDF utilizes Monte Carlo approaches to sample the posterior distribution of the parameter space of the associated PDFs. In order to attempt to remove the systematic effects stemming from the Bayesian inference adopted by each group in Fig. 7.5 we present relative uncertainties after EIC normalized to pre-EIC relative uncertainties for a selection of parton flavor combinations. The grey band built as an envelope from the various groups indicates the uncertainty on the impact study from the projected EIC data. The impact of EIC can be seen as the variations of the ratios away from unity which occurs in most of the regions to be explored at the EIC. We stress that the

ratios are not bound to be less than one since the inclusion of new data can change the relative strength of the flavor channels on the differential cross sections. On the other hand, the cross section uncertainties propagated from PDF uncertainties do decrease as expected on statistical grounds. The results show that there is strong impact on the valence sector where the uncertainties can decrease up to 80% which can give new insights on the  $d/u$  ratio. On the other hand the sea sector is predominately modified in the small- $x$  region as expected with decrease of uncertainties up to 50%. Overall we find that the current detector setup with systematic uncertainties as large as 2% can induce significant constraints on PDFs.

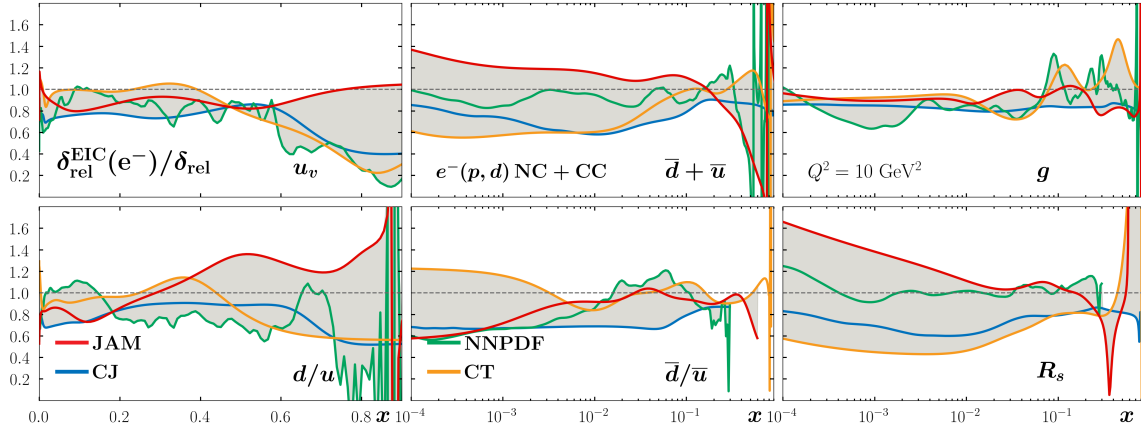


**Figure 7.5:** Comparison of relative uncertainties for unpolarized PDFs  $xf(x)$  for multiple flavors, before and after the inclusion of EIC data, evaluated at  $Q^2 = 10 \text{ GeV}^2$ . We include the analysis of different collaborations, limited to  $e^-$  datasets only.

### Positron beam

While the EIC has the main focus on an incident electron beam, the possibility of having a positron beam to measure NC and CC is a relevant complementarity that boosts the exploration of the nucleon's flavor structure. In particular, the differing charge of the exchanged  $W^+$  boson is such that positron CC interactions are capable of probing a unique combination of flavor currents inside the target hadron relative to an electron beam. This potentially offers significant additional constraints to the  $d$ -type PDFs, further constraining the  $d/u$  ratio. Beyond this, positron beams may also afford further access to other effects within the PDFs, such as the breaking of (anti)strange symmetry,  $s = \bar{s}$ , or parton-level charge-symmetry violation [17]. In Fig. 7.6 we present the impact of positron data on top of all the electron data as ratios of the relative uncertainties. Furthermore,  $e^+, d$  scattering allows improvements to the understanding of nuclear effects for the simplest of all nuclei in a region free of contamination from  $1/Q^2$  power corrections.

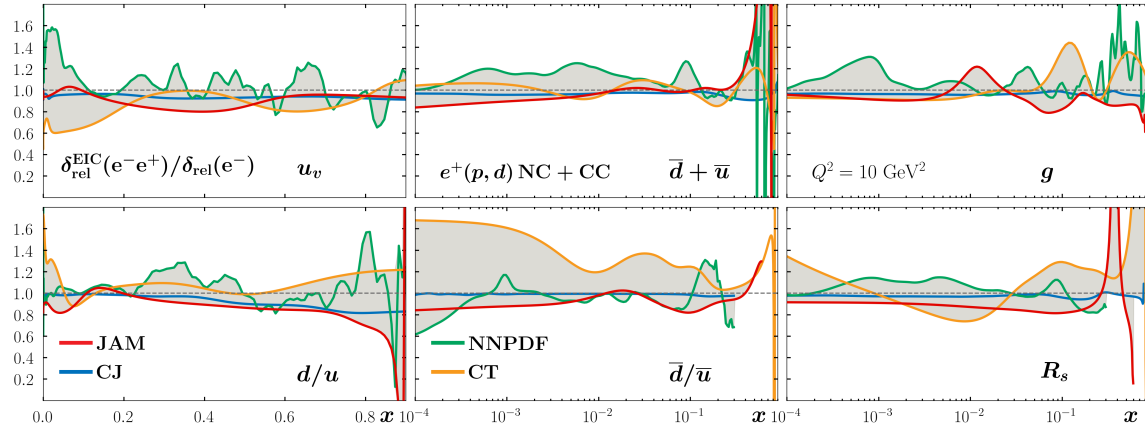


**Figure 7.6:** PDF relative uncertainties after inclusion of NC and CC  $e^+(p,d)$  data normalized to only electron case data.

### Parity-violating DIS

Parity-violating electron scattering asymmetry ( $A_{PV}$ ) is a unique observable accessible at the EIC where the dominant structure function  $F_1^{\gamma Z}$  receives flavor combinations without relative weights in contrast to the pure photon exchange that dominates the NC cross sections. In Fig. 7.7 we illustrate the strong impact on the strange-quark distribution  $x(s + \bar{s})$ , in particular, at low values of  $x$ .

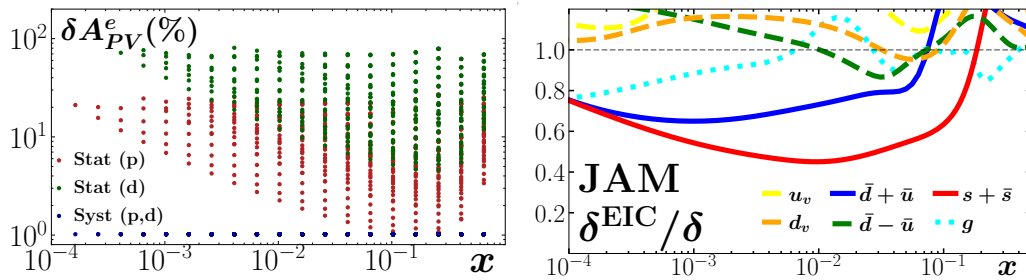


**Figure 7.7:** (Left):  $A_{PV}$  uncorrelated statistical and systematic percent errors for proton and deuteron beams. (Right): PDF uncertainties after the inclusion of  $A_{PV}$  normalized to no EIC baseline.

### Tagged DIS

Tagged DIS data (TDIS) offer a way to probe the structure of a barely off-shell neutron via semi-inclusive tagging of a slow proton spectator in  $e + D \rightarrow e' + p + X$  events. When these measurements are analyzed through the recently developed on-shell extrapolation technique, they provide one with an effective, free neutron DIS cross section. [18, 19]. Fig. 7.8 shows the improvement in the PDF relative uncertainty when using the EIC

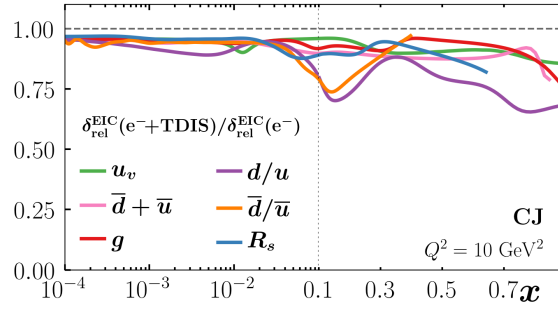


**Figure 7.8:** Impact of TDIS data on PDF determination within the CJ global fitting framework. The vertical axis displays the ratio of relative PDF errors obtained with the TDIS augmented EIC data set to those obtained with the baseline  $e^-p$  EIC data.

electron-induced DIS data set augmented with TDIS data [20]. The addition of this data improves in general the determination of all flavors over the whole  $x$  range, and even more for the  $d/u$  quark ratio at large  $x$ .

Within a global analysis framework the combination of inclusive deuteron data and “free” tagged neutrons will provide one with new opportunities for understanding the dynamics of nuclear binding and Fermi motion, as well as measuring the nucleon’s offshell quark and gluon structure [15, 21, 22]. Furthermore, the effective free neutron data will allow one for the first time to measure the  $D/(p+n)$  ratio with data from the same machine, following the pioneering BONUS measurement [23]. This will eventually lead to a better understanding of the EMC effect [24] starting from its very first manifestation in the nuclear deformation of a bound proton-neutron system compared to a free one.

### Sea quark PDFs via SIDIS measurements

As fragmentation functions provide additional access to the flavor of the fragmenting parton via their dependence on fractional energy  $z$  and the type of detected hadron, they are an excellent tool to gain further information on the flavor structure of the nucleon. While inclusive cross section measurements only provide limited access to the parton flavor via iso-spin symmetry and the different weights between neutral and charged current interactions, the semi-inclusive DIS (SIDIS) cross sections add sensitivity via the fragmentation functions  $D_1^{q,h}(z, Q^2)$  (in the case of unpolarized, single-hadron fragmentation). A detailed description of fragmentation functions and their expected sensitivities with the EIC data can be found in section 7.4.1, but here it should only be stressed, that the valence parton content of the detected hadron relates to the fragmenting parton flavor, particularly at high  $z$ . Kaons have a higher sensitivity to strange quark fragmentation than pions while negative pions have a higher sensitivity to d-quark fragmentation compared to positive pions. The combination of measurements of differently charged pion, kaon and other hadron SIDIS cross sections essentially allows to disentangle the different valence, sea and gluon unpolarized PDFs.

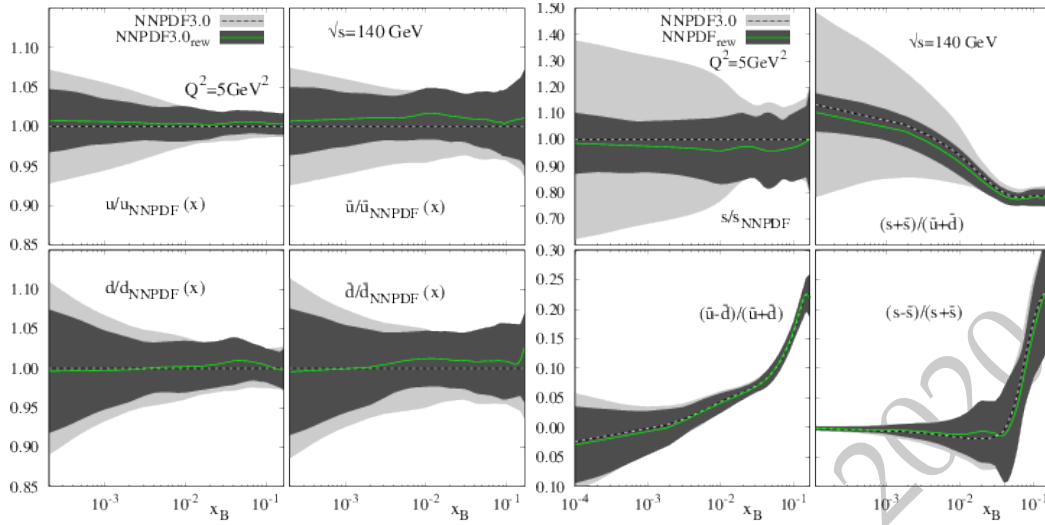


**Figure 7.9:** Expected impact on the unpolarized sea quark PDFs when adding SIDIS information from pions and kaons in  $e+p$  collisions. The baseline NNPDFs were taken from [29].

A recent study on the expected impact on the unpolarized and particularly sea quark PDFs using simulated pseudo-data that can be obtained at an EIC can be found in Ref. [25]. In this study PYTHIA 6 [26] MC simulations were performed at the expected c.m.s energies of  $\sqrt{s} = 140$  GeV and  $\sqrt{s} = 45$  GeV of an EIC and were extrapolated to  $10 \text{ fb}^{-1}$  of accumulated luminosity. The typical DIS selection criteria ( $Q^2 > 1 \text{ GeV}^2$ ,  $0.01 < y < 0.95$  and  $W^2 > 10 \text{ GeV}^2$ ) were augmented by selecting charged pions and kaons that would end up in a main EIC detector and at momenta where particle identification may be available. Using a reweighting technique [27,28] the impact was evaluated simultaneously for unpolarized PDFs and fragmentation functions. The impact on unpolarized sea quark PDFs can be seen in Fig. 7.9. While the impact on up, down, anti-up and anti-down quark PDFs is moderate as they are already very well determined, the far less well known strange PDFs gets constrained very substantially, particularly at lower  $x$ . In addition, the presently heavily debated strange to light sea-quark symmetry will be determined well at lower  $x$ .

### Nonperturbative charm

The question of a possible nonperturbative charm component in the nucleon wave function [30] has long challenged the field of hadronic physics. While numerous model calculations have been undertaken over the years, in addition to a significant number of QCD global analyses, a definitive signal has long been elusive, with most analyses [31,32] generally placing upper limits on the total nonperturbative charm momentum,  $\langle x \rangle_{c+\bar{c}}$ , at the scale  $Q = m_c$ . The EMC charm structure function measurements of 1983 [33] have been suggested as offering evidence for nonperturbative charm, but have been challenging to accommodate in a global fit. The kinematic region over which nonperturbative charm is expected to be especially visible in typical model calculations is high  $x$  and low-to-moderate  $Q^2$ . In Fig. 7.10, the size of the resulting effect in the charm structure function is plotted in

a typical model calculation [34] for two scenarios, highly suppressed [ $\langle x \rangle_{c+\bar{c}} = 0.1\%$ ] and intermediate [ $\langle x \rangle_{c+\bar{c}} = 0.35\%$ ]. Precision DIS data in this region,  $x \gtrsim 0.3$  and  $\langle Q^2 \rangle \sim 20 \text{ GeV}^2$ , would permit the direct measurement of the charm structure function and help resolve the proton's charm content. The most recent analysis carried out by the NNPDF collaboration [35] has demonstrated how  $F_2^c$  measurements at large  $x$  have great potential to unravel intrinsic charm and that the constraints of the EIC on a nonperturbative charm component would complement those provided at the LHC, eg via weak boson production in the forward region.

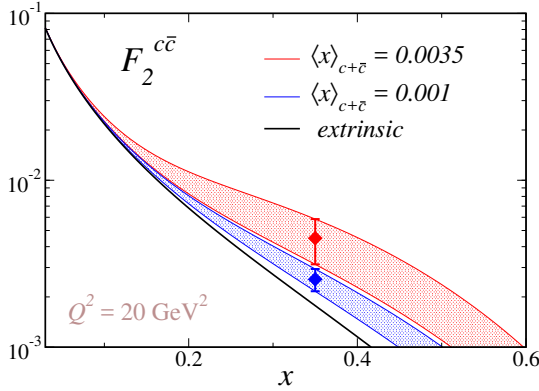


**Figure 7.10:** Two scenarios [34] for the potential magnitude of the *nonperturbative* charm contribution to the charm structure function of the proton,  $F_2^{c\bar{c}}$ . The presence of nonperturbative charm can be seen as a definite overhang in the charm structure function above the perturbative charm (black solid line) result.

## Charm jets

In addition to the moderate sensitivity to  $R_s$  from inclusive EIC measurements, data involving final-state tagging of a produced charm quark may also help discriminate among scenarios for the strange sea, as demonstrated in a recent analysis [36]. In Fig. 7.11, we illustrate the event-level variation in CC DIS production of charm jets for  $\sqrt{s} = 140 \text{ GeV}$  at the EIC, and find strong dependence on the input scenario for  $R_s$  [ $R_s = 0.325$  vs.  $R_s = 0.863$ , as obtained using extreme PDF sets in CT18(Z) NNLO]. This strong dependence suggests charm-jet production may be a sensitive channel to constrain nucleon strangeness and disentangle patterns of SU(3) symmetry breaking in the light-quark sea.

## 7.1.2 Spin structure of the proton and neutron

### Inclusive $A_{LL}$

In studying the spin structure of the nucleon, the double spin asymmetry  $A_{LL}$  has provided the bulk of the constraints on the spin-dependent collinear PDFs. In contrast to the unpolarized case, however, the existing  $A_{LL}$  data have a much more limited kinematic coverage ( $x \gtrsim 0.01$ ) compared with spin-averaged structure functions and cross sections. As the world's first polarized lepton-hadron (and lepton-nucleus) collider, the EIC will explore uncharted territory in spin physics. In addition to the sensitivity to the quark sector,

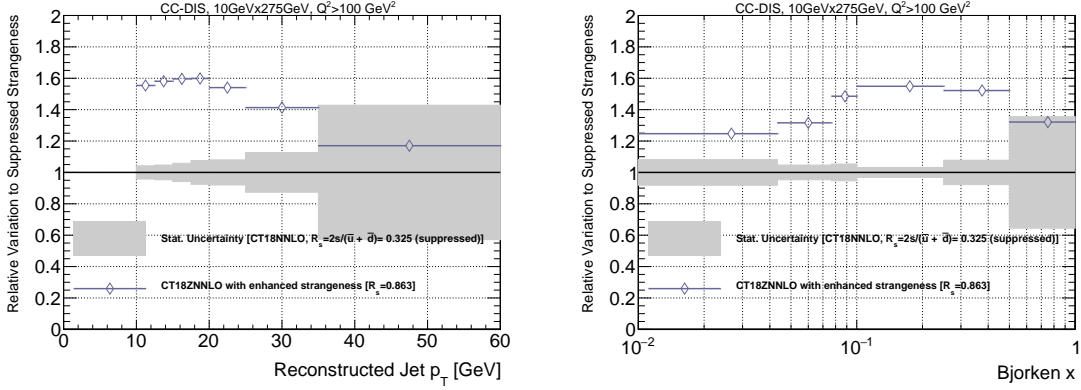


**Figure 7.11:** Comparison of charm-jet yields in electron-proton CC DIS under two scenarios for the behavior of nucleon strangeness and the light-quark sea:  $R_s = 2s/(\bar{u} + \bar{d}) = 0.325$  (CT18 NNLO with suppressed strangeness) and  $R_s = 0.863$  (CT18Z NNLO with enhanced strangeness). The gray band indicates the expected statistical error on the reconstructed and tagged charm jet  $p_T$  (left) or Bjorken  $x$  (right) spectrum for  $100 \text{ fb}^{-1}$  of data as simulated in Ref. [36]. The blue points indicate the relative difference in expected yields between the enhanced and suppressed strangeness cases,  $1 + (N_{0.863} - N_{0.325})/N_{0.325}$ . The relative magnitude of the blue points compared to the statistical uncertainty suggests that charm-jet measurements in CC DIS have strong sensitivity to the nucleon’s unpolarized strange PDF. While this calculation is from  $ep$ , similar discrimination power is expected for nuclear scattering as well.

the wide  $Q^2$  coverage of the EIC will probe scaling violations in the  $g_1$  structure function, offering significant constraints on the gluon helicity PDF, as demonstrated by the correlation and sensitivity maps across kinematics shown in Fig. 7.12 [37]. The EIC impact on the helicity distributions is illustrated in Fig. 7.13, and indicates that the uncertainty on the gluon helicity is significantly reduced relative to the DSSV14 [37, 38] baseline after the inclusion of the projected EIC pseudodata at  $\mathcal{L} = 10 \text{ fb}^{-1}$  with energies  $\sqrt{s} = 44.7$  and  $141.4 \text{ GeV}$ .

One of the challenges in accurately assessing the impact of the inclusive  $A_{LL}$  measurements at the EIC is the fact that the predictions for the rates are based on extrapolation from existing measurements that only extend down to  $x \sim 0.01$ . A study exploring the uncertainty on the helicity distributions associated with the extrapolation of  $A_{LL}$  for the EIC pseudodata is shown in Fig. 7.14. The analysis is carried out within the JAM global QCD analysis framework, including all existing data on  $A_{LL}$  and inclusive jet production from polarized  $pp$  scattering at RHIC [39], along with  $A_{LL}$  from EIC proton target pseudodata simulated with  $\mathcal{L} = 100 \text{ fb}^{-1}$ , 2.3% normalization uncertainty, and 2% point-by-point uncorrelated systematic uncertainties. To explore the impact of the extrapolation region, three sets of pseudodata were generated by shifting the unmeasured region at low  $x$  with  $\pm 1\sigma$  CL using existing helicity PDF uncertainties as well as the central predictions. In Fig. 7.14 the uncertainty bands for  $g_1^p$  before and after the three scenarios ( $\pm 1\sigma$  CL and central) at the EIC is shown, along with the truncated moments for  $\Delta g$  as a function of the lower limit of  $x$  integration,  $x_{\min}$ . The results show that, the uncertainty on  $\Delta g$  can

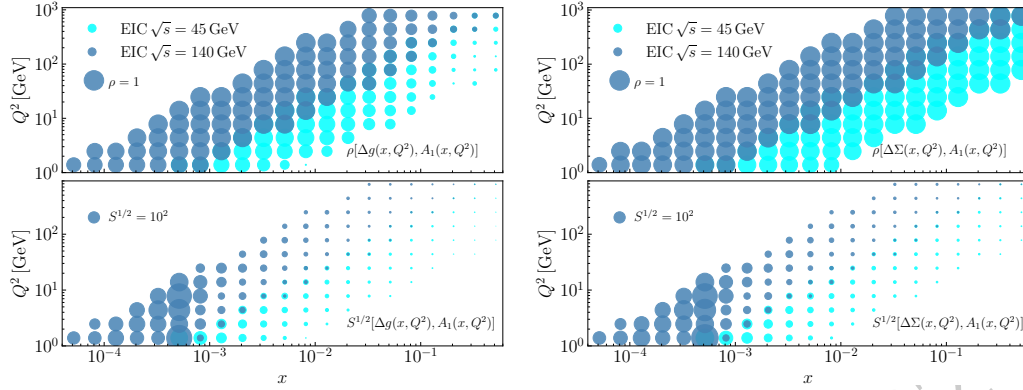


**Figure 7.12:** Correlation (upper panel) and sensitivity (lower panel) coefficients between the gluon helicity distribution  $\Delta g(x, Q^2)$  and the double spin asymmetry  $A_1$ , as well as between the singlet quark distribution  $\Delta \Sigma(x, Q^2)$  and  $A_1$ , as a function of  $\{x, Q^2\}$ . The lighter blue and darker blue circles represent the value of the correlation (sensitivity) coefficient for  $\sqrt{s} = 45$  GeV and 140 GeV, respectively. In all the cases the size of the circles is proportional to the value of the correlation (sensitivity) coefficient.

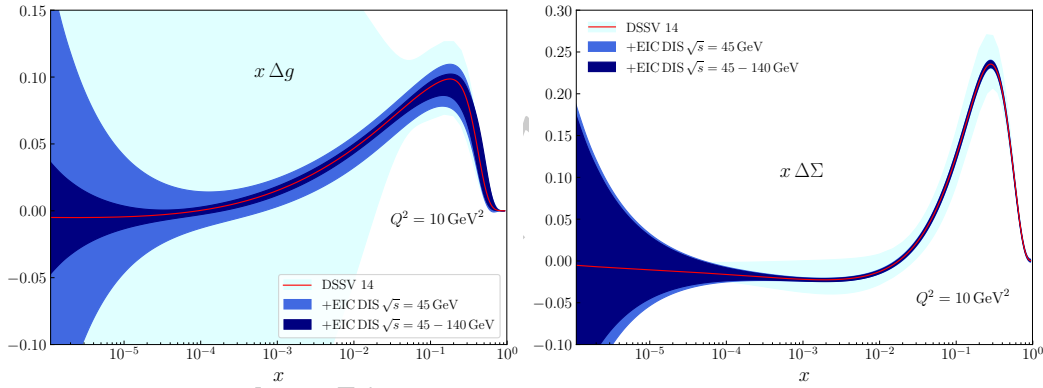


**Figure 7.13:** Impact of  $A_{LL}$  on the gluon helicity (left panel) and quark singlet helicity (right panel) distributions from the DSSV analysis [37].

improve from 40 – 80% depending on the low- $x$  behavior of  $g_1^p$  extrapolation. The impact on the quark singlet moment is however less dramatic if one uses proton data alone, since uncertainties on both the  $\Delta u$  and  $\Delta d$  flavors need to be reduced.

To better constrain the helicity distributions for individual quark flavors, information on the neutron structure function is required, in addition to the proton. The neutron can be obtained from either deuterium or  $^3\text{He}$  data, and in Fig. 7.15 we consider the impact on the  $\Delta \Sigma$  truncated moment uncertainties of both nuclei. Here the impact of EIC data, taking central values of  $A_{LL}$  at low  $x$ , with protons only versus with  $^3\text{He}$  or deuterium is shown for both the truncated moments of the quark singlet and gluon PDFs, compared with those from the JAM PDFs without EIC data. For proton EIC data alone, the impact on  $\Delta \Sigma$  is relatively modest, with uncertainties reduced by  $\sim 30\%$ . Addition of polarized deuterium or  $^3\text{He}$  EIC data, simulated with  $\mathcal{L} = 10 \text{ fb}^{-1}$ , 2.3% normalization uncertainty, and 2%

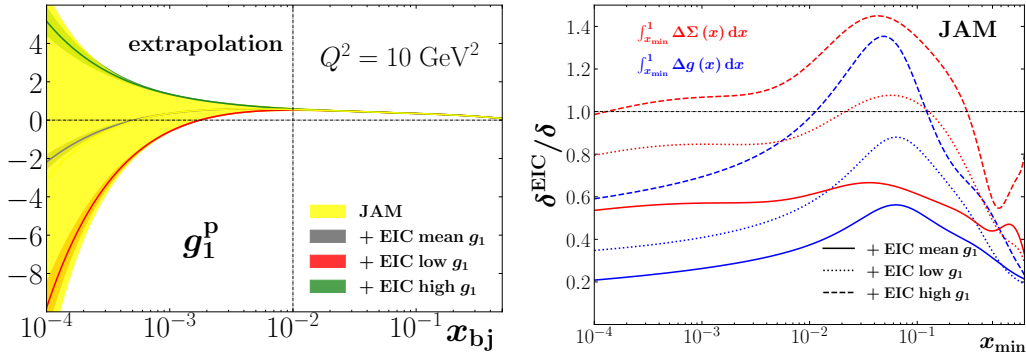


**Figure 7.14:** Impact of the  $g_1^p$  extrapolation on truncated moments of  $\Delta g$  and  $\Delta\Sigma$  as a function of  $x_{\min}$ . (Left): Impact of projected  $A_{LL}^p$  data at EIC kinematics on  $g_1^p$ , relative to the recent JAM global QCD analysis [39, 40] (yellow band) taking  $+1\sigma$  ("high  $g_1$ ", green band),  $-1\sigma$  ("low  $g_1$ ", red band) and central (grey band) uncertainties of  $A_{LL}^p$ . (Right): Uncertainty of the truncated quark singlet and gluon truncated moments with EIC data normalize to the baseline PDFs [39, 40], taking  $+1\sigma$  ("high  $g_1$ ", dashed line),  $-1\sigma$  ("low  $g_1$ ", dotted line) and central ("mean  $g_1$ ", solid line) uncertainties of  $A_{LL}^p$ .

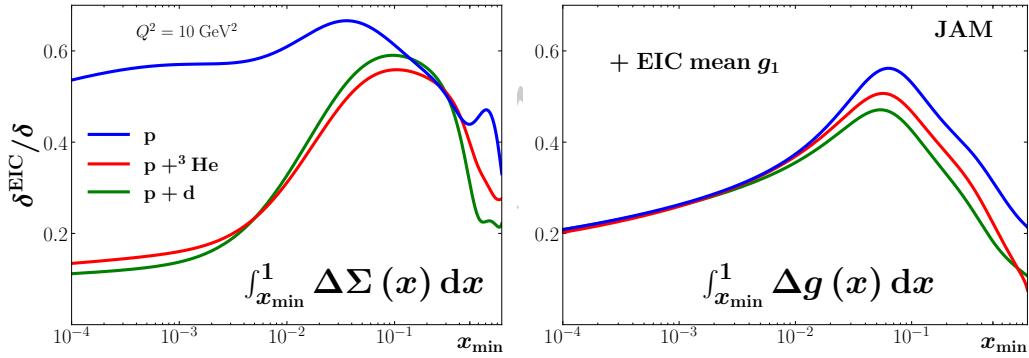
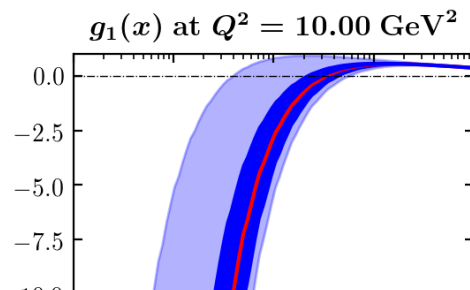


**Figure 7.15:** Ratio of uncertainties of the truncated quark singlet moment (left panel) and gluon moment (right panel) with EIC data to those without EIC data, for proton only new data (blue curves), proton +  $^3\text{He}$  (red curves), and proton + deuteron (green curves) using the central predictions for  $g_1$  in the unmeasured region.

point-by-point uncorrelated systematic uncertainty, gives a dramatic impact in the quark singlet moment, with uncertainties reduced 3–4 times compared to those with proton data alone. Deuteron and  $^3\text{He}$  data however, do not have significant impact in the uncertainty of the gluon truncated moment compared to proton data.

### Helicity and small $x$ dipole formalism

A prediction for the  $g_1$  structure function based on the novel small- $x$  evolution equations derived by Kovchegov, Pitonyak and Sievert (KPS) in [42–45]



is shown in Fig. 7.16. The KPS equations evolve the polarized color-dipole scattering amplitude toward small values of Bjorken  $x$ . At the leading order employed here, the KPS equations resum powers of  $\alpha_s \ln^2(1/x)$ , generating perturbative QCD predictions for the small- $x$  behavior of helicity PDFs and for the  $g_1$  structure function. The curve in Fig. 7.16 is obtained by using the large- $N_c$  LO KPS equations (along with their initial conditions) in the JAM framework [40, 46] to fit the existing world DIS data on  $A_1$  and  $A_{||}$  for  $x < 0.1$  and extrapolate the resulting  $g_1$  structure function to lower values of  $x$  using the same KPS evolution. The plot was constructed in [41] for fixed  $\alpha_s = 0.3$ . Clearly the EIC data will significantly shrink the uncertainty of this prediction from the light blue error band in Fig. 7.16 to the dark blue one, allowing for a much better constraint on the proton spin coming from the small- $x$  quarks and moving the community closer to the resolution of the proton spin puzzle.

### Neutron spin structure from inclusive and tagged DIS with polarized $^3\text{He}$ and $^2\text{H}$

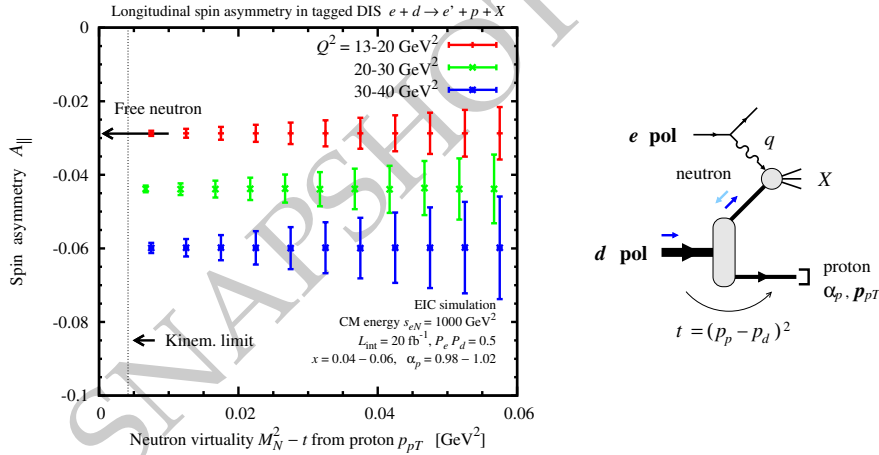


**Figure 7.17:** Simulated EIC measurements of the longitudinal double-spin asymmetry  $A_{||}$  in polarized deuteron DIS with proton tagging  $e + d \rightarrow e' + X + p$ . The asymmetry is shown as a function of the neutron virtuality  $t - M_N^2$ , which is kinematically fixed by the tagged proton momentum (light-cone momenta  $\alpha_p$  and  $p_{pT}$ ). In the limit  $t - M_N^2 \rightarrow 0$  (on-shell extrapolation) the tagged spin asymmetry coincides with the free neutron spin asymmetry  $A_{||n}$  [47, 48]. The uncertainties shown are statistical ( $L_{\text{int}} = 20 \text{ fb}^{-1}, P_e P_d = 0.5$ ).

Nucleon spin structure studies require measurements of polarized DIS on the neutron as

well as the proton [49–51]. Neutron and proton data together are needed to determine the flavor composition of the quark helicity distributions, to separate singlet and nonsinglet structures in QCD evolution and the extraction of gluon polarization ( $g_1^p - g_1^n$  and  $g_1^p + g_1^n$  are generally of the same order at  $x \gtrsim 10^{-3}$ ), and to evaluate the Bjorken sum rule. The extraction of neutron spin structure from DIS on polarized light nuclei must account for nuclear effects (neutron polarization, nuclear motion, dynamical modifications), which cause significant uncertainties and have been investigated theoretically [52–60]. The dynamical modifications of nucleon spin structure are themselves an object of study and provide insight into the emergence of nuclear interactions from QCD (see Sec. 7.3.8).

At EIC neutron spin structure will be measured using DIS on polarized  $^3\text{He}$ , and possibly polarized deuteron  $^2\text{H} \equiv d$ . Measurements will be performed using both inclusive DIS (cross sections, spin asymmetries) and DIS with partial or full detection of the nuclear breakup state (spectator tagging). Each of these methods brings unique advantages and challenges to neutron structure extraction. Their combination offers the prospect of substantial advances in the understanding of nuclear effects and the precision of neutron structure extraction, making the theoretical uncertainties commensurate with the projected experimental uncertainties of spin structure measurements at EIC.

Inclusive polarized DIS on  $^3\text{He}$  is the standard channel for neutron spin structure measurements at EIC. Their analysis has traditionally relied on the effective neutron polarizations inferred from non-relativistic nuclear structure [54, 61]. Significant nuclear modifications arise from the presence of  $\Delta$  isobars in the  $^3\text{He}$  nucleus at  $x \gtrsim 0.1$  [58, 59], and from spin-dependent nuclear antishadowing and shadowing at  $x \lesssim 0.1$ . The theoretical uncertainty resulting from these effects is expected to be the dominant uncertainty and should be reduced by further theoretical studies. DIS on  $^3\text{He}$  with spectator proton/neutron tagging has been explored and appears feasible with the EIC forward detectors (see Sec. 7.3.8). The theoretical analysis of these measurements requires the modeling of nuclear final-state interactions, for which corresponding methods have been developed [19, 62–65].

DIS on the polarized deuteron complements the measurements on  $^3\text{He}$  and offers several advantages [47, 48, 66]. In the deuteron  $\Delta$  isobars and other non-nucleonic degrees of freedom are suppressed in average nuclear configurations (nucleon momenta  $\lesssim 300$  MeV), so that the extraction of neutron spin structure from inclusive DIS is generally simpler and more accurate than for  $^3\text{He}$  [67].

In tagged DIS on the deuteron, the measured spectator momentum fixes the nuclear configuration and permits a differential treatment of nuclear effects, significantly improving the theoretical accuracy. The tagged proton momentum controls the strength of  $S$  and  $D$  waves in the deuteron wave function and thus the effective neutron polarization in DIS [47, 48]. On-shell extrapolation in the proton momentum eliminates nuclear modifications and final-state interactions and permits the extraction of the free neutron structure functions [18]. Simulations show that an accurate determination of the neutron double-spin asymmetry  $A_{\parallel n}$  is feasible using polarized tagged DIS with on-shell extrapolation (see Fig. 7.17). Further applications of tagged measurements are discussed in Sec. 7.3.8.

### Orbital angular momentum contribution to nucleon spin

The improved constraints on the net spin of quarks and gluons allow to study other contributions to the proton spin, such as those coming from the partons orbital angular momenta. Fig. 7.18 presents the potential of the EIC to constrain the spin contribution from orbital angular momentum, assuming that it can be identified with the difference between the net quark and gluon spin contribution and the actual proton spin  $1/2$ . The horizontal axis in Fig. 7.18 show the difference between  $1/2$  and the contribution from the spin of quarks and gluons for a momentum fraction down to  $x = 0.001$ . The remaining contributions would be the room left to the orbital angular momentum if the net spin contribution from partons with smaller momentum fractions is very small or even zero. But as the latter could actually be non negligible, and is currently very uncertain, we represent in the vertical axis their potential contribution to the proton spin. The colored areas show the constraints on these values coming from present data, in light cyan, and those that one would expect from the projected EIC measurements. The diagonal lines represent the combinations of low and high  $x$  contributions for which the resulting orbital angular momentum would be as large as the proton spin and parallel to it, vanishing, or exactly opposite. The EIC data would be able to discard at least one of these extreme scenarios, and perhaps two of them.

The quark contribution of orbital angular momentum to nucleon spin can further be isolated via the extraction of Generalised Parton Distributions (GPDs). These are functions which relate, on the light front, the longitudinal momentum fraction of a parton ( $x$ ) to its position in the transverse plane (impact parameter) [68]. As such, they carry sensitivity to the orbital angular momentum of partons, which is expressed in Ji's relation [69] connecting the total angular momentum of quarks to the second Mellin moment of two GPDs,  $H$  and  $E$ :

$$J^q = \frac{1}{2} - J^g = \frac{1}{2} \int_{-1}^1 x dx \{H^q(x, \xi = 0, t = 0) + E^q(x, \xi = 0, t = 0)\}, \quad (7.3)$$

where a similar relation holds for gluons. GPDs, which are discussed in more detail in section 7.2.2, are experimentally accessible in exclusive processes at low four-momentum transfer to the nucleon,  $t$  – where the nucleon remains intact – and high four-momentum transfer to the struck parton,  $Q^2$ . This typically results in the production of a high-energy photon (in deeply virtual Compton scattering, DVCS) or meson (in hard exclusive meson production), although other processes are possible – kinematic studies of these are pre-

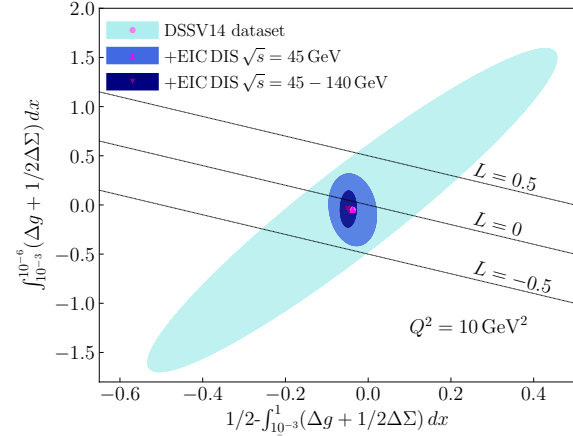


**Figure 7.18:** Room left for potential orbital angular momentum contributions to the proton spin at  $Q^2 = 10 \text{ GeV}^2$ , according to present data and future EIC measurements.

sented in section 8.4. The variable  $\xi$  encodes half the parton's longitudinal momentum-fraction change, as a result of the scattering. It is important to note that While  $J_i$ 's decomposition allows one to identify the orbital angular momentum contribution of quarks by subtracting the known contribution of intrinsic quark-spin from  $J^q$ , this cannot be done equivalently for the contribution of gluons using the measured value of gluon intrinsic spin,  $\Delta G$  – a discussion of the spin-decomposition controversy can be found in [70].

The range of  $x$  accessible at the EIC, combined with its high luminosity, will enable the GPDs  $H$  and  $E$  to be dramatically constrained – an impact study for the GPD  $E$  can be seen in section 7.2.2. While  $H$  is fairly well-known in the valence region, determined mainly from the fixed-target experiments at Jefferson Lab,  $E$  is almost entirely unknown. Both GPDs are virtually unmapped in the low- $x$  region accessible at the EIC. Different observables carry different sensitivity to the GPDs and measurements from multiple processes are needed for their flavour separation: thus DVCS on the proton and neutron will allow the extraction of the GPDs for  $u$ - and  $d$ -quarks, which can also be obtained via the hard exclusive production of different mesons. Vector meson production is sensitive, at leading-twist and order, to gluon GPDs. The programme of exclusive measurements at EIC will enable, for the first time, orbital angular momentum contributions from different flavour quarks as well as the total contribution of gluons to nucleon spin to be determined, providing crucial insights into what has been long known as the “proton spin puzzle”.

### Parity-violating DIS

Parity-violating DIS asymmetries with unpolarized electrons and polarized hadron beams can provide additional constraints on the spin-dependent PDFs due to its unique flavor sub-processes. In Fig. 7.19 we present the impact of  $A_{\text{PV}}^{\text{had}}$  at the EIC on helicity PDFs assuming a proton target with  $100 \text{ fb}^{-1}$  luminosity and an uncorrelated systematic uncertainty of 1% from the pion background. We find a moderate impact of around  $\approx 50\%$  for  $\Delta s$ , a more moderate impact of  $\approx 20\%$  for the valence quarks, and no impact on the gluon spin  $\Delta g$ . Correspondingly, the impact on the truncated quark singlet moment in Fig. 7.19 is found to be around 50% with the inclusion of EIC  $A_{\text{PV}}^{\text{had}}$  data.

### Sea quark Helicities via SIDIS

The sensitivity on the struck parton that fragmentation functions provide (see also section 7.4.1 concerning the fragmentation functions themselves) can be used to leverage the understanding of the helicity structure of the nucleon. In particular the access to the sea quark helicities can be substantially improved over inclusive DIS measurements via SIDIS measurements that additionally detect pions and kaons in the final state. Detailed impact studies that use PEPSI as polarized generator and follow the previous DSSV [38, 71, 72] extractions have been performed on the expected EIC measurements using various collision energies and polarized proton and  $He^3$  beams [37]. As can be seen in Fig. 7.20, the reduction in the uncertainties of all three sea quark helicities ( $\Delta\bar{u}$ ,  $\Delta\bar{d}$ ,  $\Delta s$ ) in comparison to the current level of understanding is substantial. Similar to the gluon polarization, the

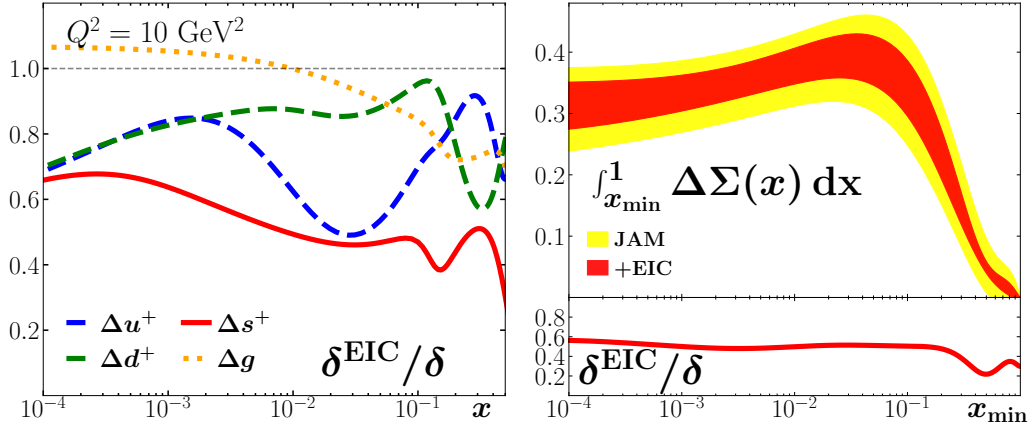


**Figure 7.19:** (Left panel) Ratio of uncertainties on the helicity PDFs including EIC data on the parity-violating DIS asymmetry  $A_{\text{PV}}^{\text{had}}$  to those without EIC data, at  $Q^2 = 10 \text{ GeV}^2$ . (Right panel) Impact of EIC  $A_{\text{PV}}^{\text{had}}$  data on the truncated moment of the quark singlet distribution,  $\int_{x_{\min}}^1 \Delta\Sigma(x) dx$ , as a function of  $x_{\min}$ .

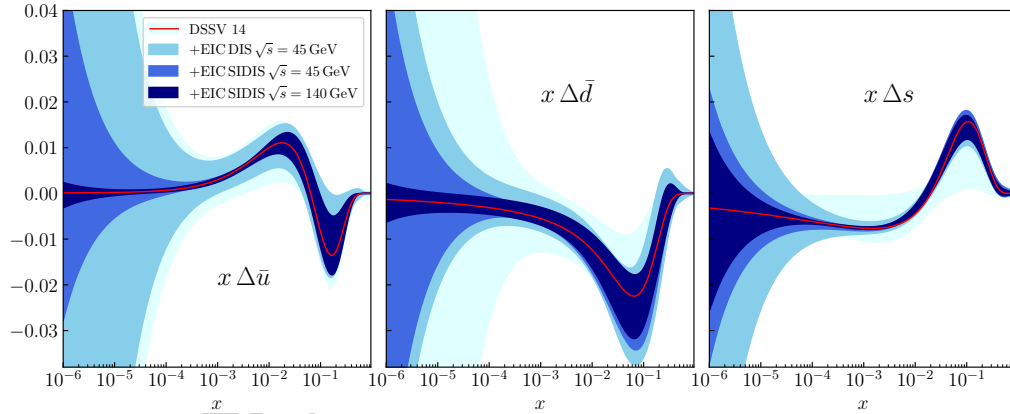


**Figure 7.20:** Impact of the EIC semi-inclusive measurements on the sea quark helicities  $x\Delta\bar{u}(x, Q^2)$ ,  $x\Delta\bar{d}(x, Q^2)$  and  $x\Delta s(x, Q^2)$  as a function of  $x$  at  $Q^2 = 10 \text{ GeV}^2$ .

highest impact at low  $x$  relates to the data at the highest collision energies while intermediate to higher  $x$  receive the biggest improvements already from the lower collision energies. One of the most important points that can be answered with the sea quark helicities are their contributions to the spin sum rule. In particular the strange sea polarization is in current fits forced to negative values at lower  $x$  due to the hyperon  $\beta$  decay constants and the assumption of  $\text{SU}(3)_F$  symmetry in conjunction with no indication of a negative polarization in the  $x$  range covered in the currently existing data [73,74]. The EIC SIDIS data will conclusively answer whether there is a nonzero strange polarization at  $x > 0.5 \cdot 10^{-5}$ . Further studies using similar pseudodata together with a re-weighting technique on the NNPDFpol [75,76] replicas come to similar conclusions about the improvements to the sea quark helicities [77].

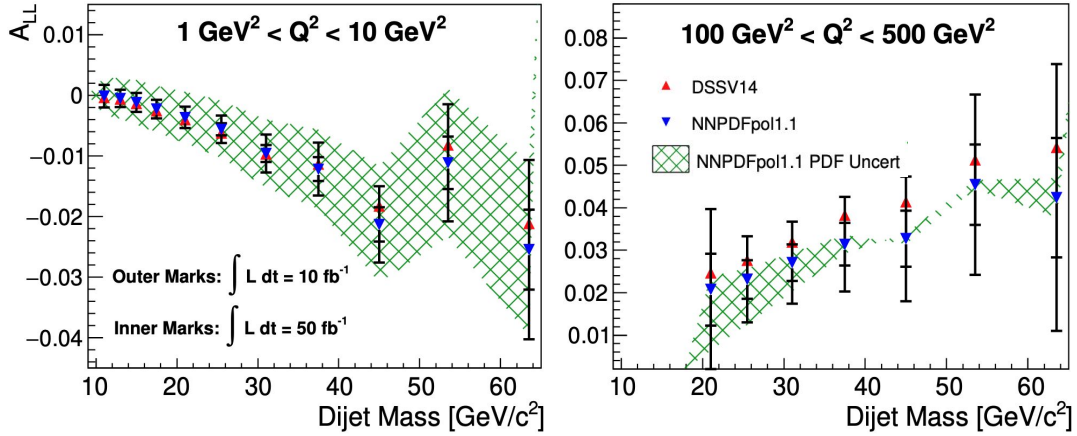


**Figure 7.21:** Dijet  $A_{LL}$  as a function of dijet invariant mass for the combined QCD and PGF subprocesses using the DSSV14 and NNPDF1.1 polarized PDFs in the 1-10  $\text{GeV}^2$  (top), 10-100  $\text{GeV}^2$  (middle), and 100-500  $\text{GeV}^2$  (bottom) two bins. Note that projected statistical uncertainties for the DSSV14 points are not shown for clarity, but are nearly identical to those from NNPDF1.1. (Figure from [79])

### $\Delta G$ from Dijet $A_{LL}$

As mentioned elsewhere in this section, the golden channel for the determination of  $\Delta G$  at the EIC will be the  $Q^2$  variation of the inclusive  $g_1$  structure function [78]. However, higher order processes such as photon gluon fusion (PGF) will provide direct access to the gluon and serve as an important cross check to the inclusive result. A signature of the PGF process is the production of back-to-back partons with large momentum transverse to the virtual quark - parton axis. Therefore, detecting dijets in the Breit frame can be used to tag PGF events. A feasibility study was recently conducted [79] which confirmed the viability of dijet reconstruction as a tag of PGF events, and also demonstrated the ability to use the dijet kinematics to reconstruct a number of relevant partonic quantities, such as the momentum fraction of the struck gluon. An estimation of the size of the expected dijet longitudinal double-spin asymmetry  $A_{LL}$ , which is sensitive to  $\Delta G$ , and associated statistical uncertainties was also performed following the procedure in [80] and compared to the uncertainties on the NNPDFpol1.1 [75] polarized PDF as shown in Fig. 7.21. While the expected statistical precision on  $A_{LL}$  given a moderate amount of integrated luminosity would improve on our present knowledge of the polarized PDFs, it is likely that the inclusive  $g_1$  measurement would provide superior constraining power. Even though, the dijet  $A_{LL}$  measurement will be important as a cross check to the inclusive measurement as it arises from a different subprocess and will have different experimental uncertainties.

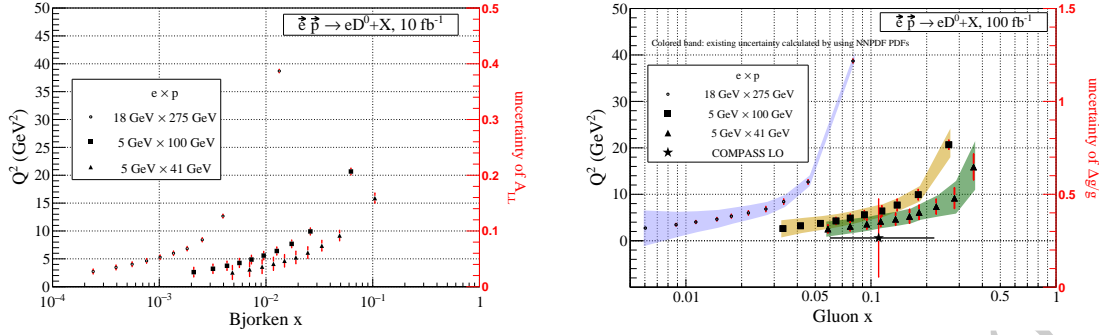


**Figure 7.22:** (left) The double longitudinal spin asymmetry  $A_{LL}$  in semi-inclusive DIS production of  $D^0$  mesons at  $x$  and  $Q^2$  of the measurements with the projected size of its statistical uncertainties and (right) illustrated precision, kinematic coverage, and leading-order impact compared with prior data and theory evaluation.

### $\Delta G$ from heavy quark $A_{LL}$

Heavy quark probes are versatile probes for studying different aspects of QCD and nucleon structure. An example for the EIC is the gluon polarization  $\Delta g(x, Q^2)$ . The most precise insights in  $\Delta g(x, Q^2)$  at the EIC will come indirectly from scaling violations of the inclusive structure function  $g_1(x, Q^2)$ . Heavy quark production forms a considerable contribution to the (polarized) cross section in lepton-nucleon DIS and hence to the corresponding structure functions. Heavy quark production is dominated by gluon-induced processes already at the Born level in perturbative QCD. In the case of lepton-nucleon DIS, only the photon-gluon fusion process contributes at Born level, which makes heavy-quark production particularly sensitive to the gluon distributions. The data on the charm contribution to the structure function  $F_2(x, Q^2)$  from HERA, for example, are used in most global analyses of unpolarized parton distribution functions. Corresponding measurements of longitudinally polarized DIS at the EIC will provide insights in  $\Delta g(x, Q^2)$ . The COMPASS collaboration at CERN has pioneered such a measurement. To assess the potential and impact for the EIC, studies were performed of the semi-inclusive DIS production of single  $D^0$  mesons and their subsequent decay into the charged  $K\pi$  branch. These studies were based on pythia-eRHIC and EIC fast simulations of detector response extended with vertex fitting and including selections based on topological reconstruction from the smeared (decay) tracks. Figure 7.22 (left) shows the contribution  $g_1^Q(x, Q^2)$  expressed as the asymmetry  $A_{LL}$  at Bjorken- $x$  and  $Q^2$  of the measurements with the size of their statistical uncertainties for the nominal EIC beam polarizations and an integrated luminosity of  $10 \text{ fb}^{-1}$ . pQCD contributions to the inclusive heavy quark production in polarized DIS are known [81] at next-to-leading order. Impact studies on equal footing with those of  $g_1(x, Q^2)$  are thus in principle possible in global analyses. However, they are not available as this report is being written. Instead, the impact of future EIC data was assessed in a leading-order approach following that of the pioneering COMPASS determination [82]. This impact is illustrated in Fig. 7.22 (right), which shows the leading order  $A_{LL} = \Delta g(x, Q^2)/g(x, Q^2)$  versus gluon- $x$  together with the prior COMPASS data and  $\Delta g(x, Q^2)/g(x, Q^2)$  based on the NNPDF (polarized) parton distributions.

### 7.1.3 Parton structure of mesons

#### Introduction

Pions and kaons are unique expressions of Standard Model dynamics, exhibiting a peculiar dichotomy. Namely, they are hadron bound states defined, like all others, by their valence quark and/or antiquark content; but the mechanism(s) which give all other hadrons their roughly 1 GeV mass-scale are obscured in these systems. The EIC, with its high-luminosity and wide kinematic range, offers an extraordinary new opportunity to increase knowledge on pion and kaon structure. There is much to be learned: pions and kaons are not point-like; their internal structure is more complex than is usually imagined; and the properties of these nearly-massless strong-interaction composites provide the clearest windows onto emergent hadronic mass (EHM) and its modulation by Higgs-boson interactions (see Sec. 7.1.4). In this section we summarize the experimental requirements for critical EIC measurements that tackle some outstanding questions in the study of meson (pion and kaon) mass and structure and show the impact the global knowledge of pion parton distributions. We then show how these measurements fit in with ongoing and foreseen programs efforts worldwide.

To facilitate this discussion, we translate current theory understanding of light meson structure and the EHM (and structure) mechanisms into a set of critical science questions. We note that not all of these science questions are theoretically rigorously defined but rather reflect our current state of understanding. They represent outstanding mysteries that require further experimental (and theoretical) examination, and illustrate the impact of a coherent study of pion and kaon structure yielding results similar to present studies of proton structure.

In Table 7.1 we present the key science questions along with specific measurements required to advance our understanding. We also present the high-level experimental needs, providing the minimum experimental requirements as well as improvements that could further expand these studies. Some interesting science questions that may be more challenging to address are listed in the bottom of the Table; they are considered more speculative as validating the reaction mechanism will be more challenging than other cases, due to considerations such as competing reaction and background mechanisms.

For all observables, a luminosity well above  $10^{33} \text{cm}^{-2} \text{sec}^{-1}$  is required to compensate for the (few times)  $10^{-3}$  fraction of the proton wave function related to the pion (kaon) Sullivan process. Also, a large range in  $x_L$  is required, up to  $x_L \sim 1$  for the  $e + p$  reactions and  $x_L$  at least  $\sim 0.5$  for the  $e + D$  reactions. In addition to the  $\pi^+$  channels listed in Table 7.1, data on  $\pi^-$  (e.g.  $e + D \rightarrow e' + X + p + p$ ) and on  $\pi^0$ -channels (e.g.  $e + p \rightarrow e' + X + p$ ) are crucial to constrain reaction mechanisms and theory backgrounds in extracting the physical pion (kaon) target information.

In facing these questions, unique insights can be drawn by focusing on the properties of QCD's (pseudo-)Nambu-Goldstone modes, i.e. pions and kaons; and diverse phenomenological and theoretical approaches (both in lattice and continuum QCD approaches) are now being deployed in order to develop a coherent image of these bound states. Complete

Science Question	Key Measurement[1]	Key Requirements[2]
What are the quark and gluon energy contributions to the pion mass?	Pion structure function data over a range of $x$ and $Q^2$ .	<ul style="list-style-type: none"> <li>• Need to uniquely determine <math>e + p \rightarrow e' + X + n</math> (low <math>-t</math>)</li> <li>• CM energy range <math>\sim 10</math>-100 GeV</li> <li>• Charged and neutral currents desirable</li> </ul>
Is the pion full or empty of gluons as viewed at large $Q^2$ ?	Pion structure function data at large $Q^2$ .	<ul style="list-style-type: none"> <li>• CM energy <math>\sim 100</math> GeV</li> <li>• Inclusive and open-charm detection</li> </ul>
What are the quark and gluon energy contributions to the kaon mass?	Kaon structure function data over a range of $x$ and $Q^2$ .	<ul style="list-style-type: none"> <li>• Need to uniquely determine <math>e + p \rightarrow e' + X + \Lambda/\Sigma^0</math> (low <math>-t</math>)</li> <li>• CM energy range <math>\sim 10</math>-100 GeV</li> </ul>
Are there more or less gluons in kaons than in pions as viewed at large $Q^2$ ?	Kaon structure function data at large $Q^2$ .	<ul style="list-style-type: none"> <li>• CM energy <math>\sim 100</math> GeV</li> <li>• Inclusive and open-charm detection</li> </ul>
Can we get quantitative guidance on the emergent pion mass mechanism?	Pion form factor data for $Q^2 = 10$ -20 (GeV/c) $^2$ .	<ul style="list-style-type: none"> <li>• Need to uniquely determine exclusive process <math>e + p \rightarrow e' + \pi^+ + n</math> (low <math>-t</math>)</li> <li>• <math>e + p</math> and <math>e + D</math> at similar energies</li> <li>• CM energy <math>\sim 10</math>-75 GeV</li> </ul>
What is the size and range of interference between emergent-mass and the Higgs-mass mechanism?	Kaon form factor data for $Q^2 = 10$ -20 (GeV/c) $^2$ .	<ul style="list-style-type: none"> <li>• Need to uniquely determine exclusive process <math>e + p \rightarrow e' + K + \Lambda</math> (low <math>-t</math>)</li> <li>• L/T separation at CM energy <math>\sim 10</math>-20 GeV</li> <li>• <math>\Lambda/\Sigma^0</math> ratios at CM energy <math>\sim 10</math>-50 GeV</li> </ul>
What is the difference between the impacts of emergent- and Higgs-mass mechanisms on light-quark behavior?	Behavior of (valence) up quarks in pion and kaon at large $x$	<ul style="list-style-type: none"> <li>• CM energy <math>\sim 20</math> GeV (lowest CM energy to access large-<math>x</math> region)</li> <li>• Higher CM energy for range in <math>Q^2</math> desirable</li> </ul>
What is the relationship between dynamically chiral symmetry breaking and confinement?	Transverse-momentum dependent Fragmentation Functions of quarks into pions and kaons	<ul style="list-style-type: none"> <li>• Collider kinematics desirable (as compared to fixed-target kinematics)</li> <li>• CM energy range <math>\sim 20</math>-140 GeV</li> </ul>
<b>More speculative observables</b>		
What is the trace anomaly contribution to the pion mass?	Elastic $J/\Psi$ production at low $W$ off the pion.	<ul style="list-style-type: none"> <li>• Need to uniquely determine exclusive process <math>e + p \rightarrow e' + J/\Psi + \pi^+ + n</math> (low <math>-t</math>)</li> <li>• High luminosity (<math>10^{34}</math> cm<math>^{-2}</math> sec<math>^{-1}</math>)</li> <li>• CM energy <math>\sim 70</math> GeV</li> </ul>
Can we obtain tomographic snapshots of the pion in the transverse plane? What is the pressure distribution in a pion?	Measurement of DVCS off pion target as defined with Sullivan process	<ul style="list-style-type: none"> <li>• Need to uniquely determine exclusive process <math>e + p \rightarrow e' + \gamma + \pi^+ + n</math> (low <math>-t</math>)</li> <li>• High luminosity (<math>10^{34}</math> cm<math>^{-2}</math> sec<math>^{-1}</math>)</li> <li>• CM energy <math>\sim 10</math>-100 GeV</li> </ul>
Are transverse momentum distributions universal in pions and protons?	Hadron multiplicities in SIDIS off a pion target as defined with Sullivan process	<ul style="list-style-type: none"> <li>• Need to uniquely determine SIDIS off pion <math>e + p \rightarrow e' + h + X + n</math> (low <math>-t</math>)</li> <li>• High luminosity (<math>10^{34}</math> cm<math>^{-2}</math> sec<math>^{-1}</math>)</li> <li>• <math>e + p</math> and <math>e + D</math> at similar energies desirable</li> <li>• CM energy <math>\sim 10</math>-100 GeV</li> </ul>

**Table 7.1:** Science questions related to pion and kaon structure and understanding of the EHM mechanism accessible at an EIC, with the key measurement and some key requirements listed. Further requirements are addressed in the text.

understanding demands that tight links be drawn between dynamics in QCD's gauge sector and pion and kaon light-front wave functions, and from there to observables, such as pion and kaon elastic form factors and distribution amplitudes and functions.

### Sullivan Process

In specific kinematic regions, the observation of recoil nucleons ( $N$ ) or hyperons ( $Y$ ) in the tagged inclusive reaction  $e + p \rightarrow e' + X + (N \text{ or } Y)$  (see Fig. 7.23) can reveal features associated with correlated quark-antiquark pairs in the nucleon, referred to as the "meson cloud" or "five-quark component" of the nucleon. At low values of  $-t$  (with  $t$  the four-momentum transfer squared from the initial proton to the final nucleon or hyperon, see Fig. 7.23), the cross section displays behavior characteristic of meson pole dominance. The process in which the electron scatters off the meson cloud of a nucleon target is called the Sullivan process [83]. For elastic scattering, this process carries information on the meson

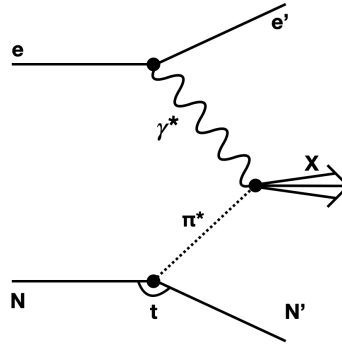


Figure 7.23: Diagram for the Sullivan process used to probe pion structure.

(pion or kaon) form factor. For DIS, the typical interpretation is that the nucleon parton distributions contain a mesonic parton content. To access the pion or kaon partonic content via such a structure function measurement requires scattering from a meson target. An important development in establishing a formal link between the Sullivan process and QCD came with the realization that the moments of PDFs could be expanded in chiral effective field theory in terms of power series in the pion mass. The leading nonanalytic (LNA) contributions were found to depend on the (model-independent) long-range structure of the pion cloud, with a characteristic  $m_\pi^2 \log m_\pi^2$  dependence [84–86]. While the total pion cloud contribution contains also short-distance contributions, which are model dependent and must be fitted to data, the infra-red behavior is model independent and can only arise from a pionic component in QCD.

The Sullivan process can provide reliable access to a meson target in the space-like  $t$  region, if the pole associated with the ground-state meson remains the dominant feature of the process and the structure of the related correlation evolves slowly and smoothly with virtuality. To check whether these conditions are satisfied empirically, one can take data covering a range in  $t$ , particularly low ( $-t$ ), and compare with phenomenological and theoretical expectations. A recent calculation [87] explored the circumstances under which these conditions should be satisfied. For the pion (kaon) Sullivan process, low ( $-t$ ) equates to  $-t < 0.6$  (0.9)  $\text{GeV}^2$  to be able to cleanly extract the pion (kaon) structure, and data over a range of  $-t$  down to the lowest accessible are needed to verify pion (kaon) structure extraction.

### Theoretical Backgrounds in Extracting the Data

The extraction of the mesonic structure of the nucleon from the tagged DIS cross section is inherently model dependent. It will, therefore, be necessary to examine all reasonable models that are available (such as Regge models of baryon production and Dyson-Schwinger equation inspired models), or that may be available in the future, to evaluate the theoretical uncertainty associated with extracting meson structure functions from the tagged deep inelastic data. The measured cross-section can be integrated over the proton

momentum (which is effectively an integration over  $t$  [88]) to obtain the leading proton structure function  $F_2^{LP(3)}$ . The pion structure function  $F_2^\pi$  can then be extracted from  $F_2^{LP(3)}$  using models, such as the Regge model of baryon production. In the Regge model the contribution of a specific exchange  $i$  is defined by the product of its flux  $f_i(y, t)$  and its structure function  $F_2^i$  evaluated at  $(x_i, Q^2)$ . Thus,

$$F_2^{LP(3)} = \sum_i \left[ \int_{t_0}^{t_{min}} f_i(z, t) dt \right] F_2^i(x_i, Q^2), \quad (7.4)$$

where  $i$  is the pion,  $\rho$ -meson etc, and the  $t$  corresponds to the range of  $p_T$  analyzed.

The extraction of the pion structure function will have to be corrected for a number of complications to the simple Sullivan picture. These include non-pion pole contributions,  $\Delta$  and other  $N^*$  resonances, absorptive effects, and uncertainties in the pion flux. For example, the cross section of leading charged pion production from the neutron is about twice reduced by absorptive corrections from other mesons. While these corrections can be large and one cannot extract the pion structure function without inclusion of them, detailed calculations do exist [89]. Moreover, these corrections are minimized by measuring at the lowest  $-t$ . Having data from *both* protons and deuterons will provide essential cross checks for the models used in the extraction of the pion structure function, with different trajectories leading in the proton and neutron case, or the isospin 0 or 1 exchange [89–91].

The measured tagged cross sections and extracted tagged structure functions can be analyzed within a Regge framework where, assuming the dominance of a single Regge exchange. As pion exchange results in a different  $z$  dependence of the cross section, it should be possible to determine the dominant exchange mechanism(s) by comparing the  $z$  dependence from proton and neutron (deuteron) scattering.<sup>1</sup> Further, if the predictions for pion exchange are found to describe the data, the pion flux from the Regge model fits to hadron-hadron data may be safely used to extract the pion structure function.

The largest uncertainty in extracting the pion structure function, however, likely will arise from the (lack of) knowledge of the pion flux in the framework of the pion cloud model. One of the main issues is whether to use the  $\pi NN$  form factor or the Reggeized form factor. The difference between these two methods can be as much as 20% [92]. From the N-N data the  $\pi NN$  coupling constant is known to 5% [93]. If we assume that all corrections can be performed with a 50% uncertainty, and we assume a 20% uncertainty in the pion flux factor, the overall theoretical, systematic uncertainty could approach 25%. The superior approach is to have a direct measurement of the pion flux factor by comparing to pionic Drell-Yan data. For example the pion structure function at  $x = 0.5$  has been measured from the pionic Drell-Yan data to an accuracy of 5% (see, for example [94, 95]). New data from COMPASS should allow us to further leverage this possibility and likely reduce our projected uncertainty even further. On the other hand, we know that there must be a region at small  $|t|$  and large  $x_L$  where the cross section should be dominated by soft pions and hence the dependence on the pion flux is minimal. In the context of a global QCD analysis (see

<sup>1</sup>The differential cross section at fixed  $t$  should be proportional to  $z - n$ , with  $n \approx -1$  for the pion while other Reggeons have  $n > -1$ .

below), one can fit the pion structure function at the same time as determining empirically the boundaries of the region of  $|t|$  and  $x_L$  over which the pion exchange mechanism is the dominant one [96,97].

### Kinematics of interest to address specific theory questions

The science questions of interest of Table 7.1 require a range of physics processes, spanning from tagged inclusive structure function measurements to tagged exclusive measurements such as required for a form factor determination or pion femtography (See Sec. 7.2.1). In general, a large range of CM energies is required to access a wide range in  $x$  and  $Q^2$ , as relevant for pion (kaon) structure function measurements or hadron multiplicity measurements for a transverse-momentum dependent parton distribution program. This has to be balanced against the requirement to uniquely determine the remnant neutron (or  $\Lambda$  or  $\Sigma^0$ ) to ensure the scattering process occurs off a pion (kaon). The latter favors not-too-high CM energies to be able to uniquely determine the remnant  $\Lambda$  (or  $\Sigma^0$ ), both for missing-mass determination and to ensure their decays occur before detection. In addition, there is need for both  $e + p$  and  $e + D$  measurements at similar CM energies to validate the reaction mechanism and understanding. This drives the “typical” CM energy range for pion and kaon structure function measurements to a  $\sim 10$ -100 GeV range. On the other hand, to access the largest- $x$  region to determine the behavior of the valence quarks in pions (or kaons), the lowest CM energy to reach a (sufficiently high and “clean”)  $Q^2$  level has the highest Figure-Of-Merit folding in all kinematic effects. Higher CM energies will increase the range in  $Q^2$ .

For the pion (kaon) fragmentation processes, the collider (as opposed to fixed-target) kinematics greatly facilitate transverse-momentum dependent measurements at low transverse-momentum scales ( $< 1$  GeV), and the largest range in CM energy is required. For some processes the exact CM energy is not that essential, as long as one obtains sufficient phase space to produce the electro-produced particles, to boost the experimental cross section. This is for example true for the (deep) exclusive  $J/\Psi$  measurements to possibly constrain the QCD trace anomaly, and also for access to charged-current cross sections.

### Meson structure function projections

The generator calls various quantities such as CTEQ6 PDF tables, nucleon structure functions, and the tagged  $\pi$  and  $K$  structure functions and splitting functions. The  $\pi$  structure function can be parameterized in a multitude of ways. Here, the parameterization outlined in [98] was used. This parameterization is a scaled version of the proton structure function ( $F_2^\pi = 0.361 * F_2$ ) which allowed an easy comparison to the available DESY-HERA-H1 data in addition to the Glück, Reya, and Vogt (GRV) theoretical fit (shown on the left in figure 7.24). The parameterization also agrees well with the GRV fit at higher  $x$ . Agreement in this regime is beneficial as higher  $x$  data is required for comparisons between the pion and kaon.

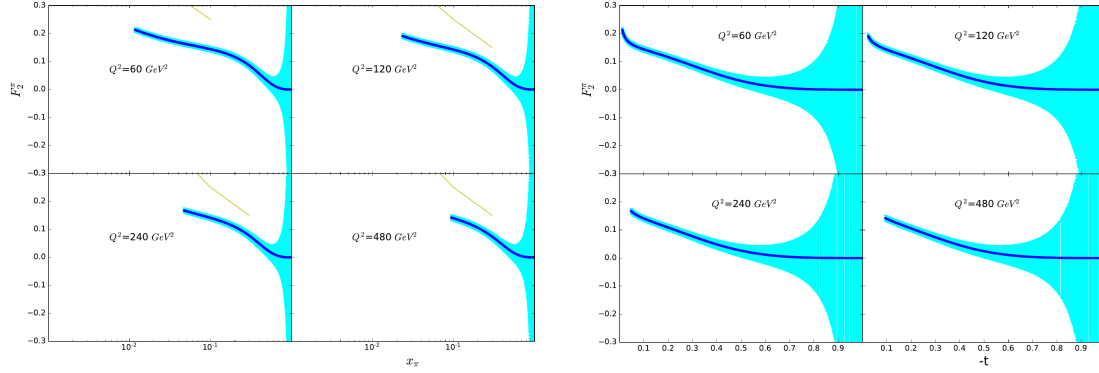


**Figure 7.24:** The Monte Carlo projections of the pion structure function vs  $x$  (left) and  $t$  (right) for a beam energy of  $10 \times 135$ . The blue points are the Monte Carlo projections for  $Q^2$  values of 60, 120, 240, 480  $\text{GeV}^2/c$ . The blue error bars are the statistical uncertainties for a luminosity of  $100 \text{ fb}^{-1}$ . The brown line in the left figure is a GRV fit for similar pion structure function projections [98].

The left plot in figure 7.24 shows the reach in  $x$  for four  $Q^2$  bins. Statistical uncertainties with the addition of the leading neutron detection fraction were incorporated to the overall uncertainty using a luminosity of  $\mathcal{L} = 100 \text{ fb}^{-1}$ . The range of  $x$  coverage is immediately apparent as the plot shows a reach from mid to high  $x$ . The uncertainties are reasonable in the mid to mid-high  $x$  region but, as expected, increase rapidly as  $x \rightarrow 1$ . Even with these restrictions the coverage in mid to high  $x$  is unprecedented and should allow for a detailed comparison between the pion and kaon structure.

As discussed above, theoretical calculations predict that the Sullivan process should provide clean access to the meson structure below a minimum value of  $-t$ . For the pion, this is  $-t \leq 0.6 \text{ GeV}^2$ . The right plot of figure 7.24 shows the accessible range in  $-t$  at the EIC for 10 on 135 GeV with reasonable uncertainties which would allow for an order-of-magnitude gain in statistics compared to HERA. The resulting access to a significant range of  $Q^2$  and  $-t$  values, including small  $-t$ , as well as significant access to a range of  $x$ , will allow for insights into the gluonic content of the pion. A fast Monte Carlo was used for feasibility studies for  $\pi$  and  $K$  structure function measurements.

### Impact on global QCD analysis

The potential impact of EIC neutron production data is illustrated in Fig. 7.25, which shows the valence, sea quark and gluon PDFs in the pion from the JAM global QCD analysis at the input scale  $Q^2 = m_c^2$  [97], with current uncertainties compared with those expected with the addition of EIC data [99]. The analysis of the existing data includes pion-nucleus Drell-Yan cross sections, both  $p_T$ -differential and  $p_T$ -integrated, and the leading neutron structure functions from HERA [100]. The analysis assumes a c.m. energy  $\sqrt{s} = 63.25 \text{ GeV}$  for an integrated luminosity of  $\mathcal{L} = 100 \text{ fb}^{-1}$  and a 1.2% systematic uncertainty across all kinematics. For both the sea quark and gluon distributions, the PDF uncertainties reduce

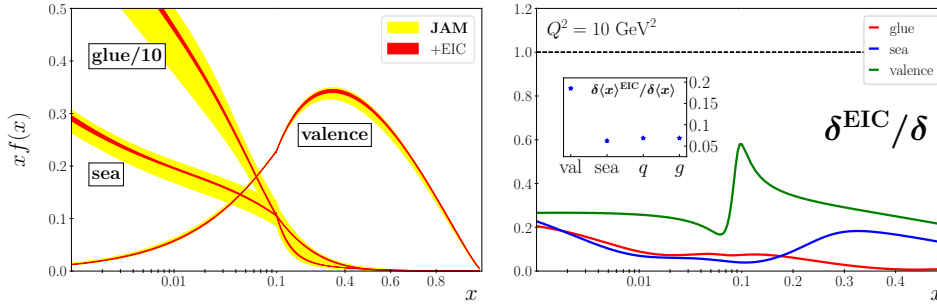


**Figure 7.25:** (Left): Comparison of uncertainties on the pion’s valence, sea quark and gluon PDFs before (yellow bands) and after (red) bands inclusion of EIC data. (Right): Ratio of uncertainties with EIC data to without,  $\delta^{\text{EIC}}/\delta$ , for the valence (green line), sea quark (blue) and gluon (red) PDFs, assuming 1.2% systematic uncertainty, and (inset) the corresponding ratios of the momentum fraction uncertainties,  $\delta\langle x \rangle^{\text{EIC}}/\delta\langle x \rangle$ , for valence, sea, total quark and gluon PDFs [99], at a scale  $Q^2 = 10 \text{ GeV}^2$ .

by a factor  $\sim 5 - 10$  for  $x \lesssim 0.1$ , with a smaller, factor  $\sim 3$  reduction in the valence sector. For the decomposition of the pion mass [101], written in terms of QCD stress-energy tensor matrix elements, the first moments,  $\langle x \rangle_{q,g}$ , are relevant, see Sec. 7.1.4. For these quantities, the reduction in uncertainties is by a factor  $\approx 15$  for both the total quark and gluon contributions, as can be seen in the inset of Fig. 7.25 (right). Note, however, that the errors do not include uncertainties associated with the model dependence of the “pion flux,” which may be of the order 10% – 20% [98, 102], and would reduce the impact of the projected data on the pion PDF uncertainties by several-fold. A similar analysis may be performed for the PDFs in the kaon, which can be obtained from leading hyperon production in the forward region. In this case, the near-absence of empirical information on the parton structure of kaons will mean an even more striking impact of new EIC data.

### Complementarity with other facilities

The unique role of EIC is its access to pion and kaon structure over a versatile large CM energy range,  $\sim 20\text{-}140 \text{ GeV}$ . Jefferson Lab will provide, at its CM energy  $\sim 5 \text{ GeV}$ , tantalizing data for the pion (kaon) form factor up to  $Q^2 \sim 10$  (5)  $\text{GeV}^2$ , and measurements of the pion (kaon) structure functions at large- $x$  ( $> 0.5$ ) through the Sullivan process.

COMPASS++/AMBER will play a crucial role as they can uniquely provide pion (kaon) Drell-Yan measurements in the CM energy region  $\sim 10\text{-}20 \text{ GeV}$ . Some older pion and kaon Drell-Yan measurements exist, but for the kaon this is limited to less than 10 data points worldwide, so these measurements are absolutely important for a global effort of the pion structure function measurements (allowing a handle on determination of the so-called “pion flux” for the EIC Sullivan process measurements) and a *sinequanon* for any kaon structure function data map. The COMPASS++/AMBER data in themselves will already give new fundamental insights in the emergent-hadron mass mechanism.

Lastly, an Electron-Ion Collider in China (EicC) is under consideration with a similar CM energy range as COMPASS++/AMBER of  $\sim 10\text{-}20$  GeV and bridging the energy range from Jefferson Lab to EIC. EicC on its own, and even more in combination with COMPASS++/AMBER, can provide good access to the region of  $x \gtrsim 0.01$  for pion, and especially kaon, structure function determination and the impact on emergent-hadron mass mechanisms on valence quark and gluon structure. In addition, EicC can extend the Rosenbluth L/T-separated cross section technique beyond Jefferson Lab and access pion and kaon form factors to higher  $Q^2$  values, roughly by a factor of 2-4.

Obviously, in the end the EIC, with its larger CM energy range, will have the final word on the contributions of gluons in pions and kaons as compared to protons, settle how many gluons persist in pions and kaons as viewed with highest resolution, and vastly extend the  $x$  and  $Q^2$  range of pion and kaon charts, and meson structure knowledge.

### Synergy with continuum and lattice QCD

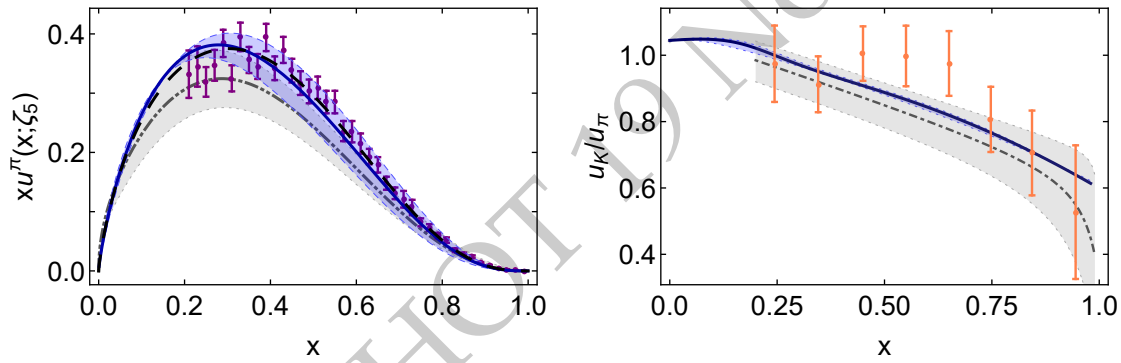


**Figure 7.26:** *Left panel.* Pion valence-quark momentum distribution function,  $xq_\pi(x; \zeta_5 = 5.2 \text{ GeV})$ : solid blue curve – modern continuum calculation [103]; long-dashed black curve – early continuum analysis [104]; and dot-dot-dashed grey curve – lQCD result [105]. Data (purple) from Ref. [94], rescaled according to the analysis in Ref. [106]. *Right panel.*  $u_K(x; \zeta_5)/u_\pi(x; \zeta_5)$ . Solid blue curve – prediction from Ref. [103]. Dot-dashed grey curve within grey band – lQCD result [107]. Data (orange) from Ref. [108].

Pion and kaon structure extracted from EIC data will be confronted with continuum and lattice QCD calculations. The continuum Schwinger function method (CSM) computation [103] for  $u_\pi(x; \zeta_5)$  is depicted in the left panel of Fig. 7.26. It agrees with the predicted large- $x$  behaviour [109–113] for such physical quantity and, moreover, its pointwise form matches that determined in Ref. [106], which included the next-to-leading-logarithm resummation using the “cosine method”. Significantly, lattice-regularized QCD is now beginning to yield results for the pointwise behaviour of the pion’s valence-quark distribution [105, 114], with that delivered by the approach in Ref. [105] being in fair agreement with the CSM prediction. Ref. [103] also provides parameter-free predictions for glue and sea pion DFs, in addition to all kaon DFs. Concerning the kaon valence-quark distributions from Ref. [103], there are qualitative similarities between  $u_K(x)$ ,  $\bar{s}_K(x)$  and

$u_\pi(x)$ , e.g. all three DFs are consistent with the above mentioned large- $x$  prediction, so that  $\bar{s}_K(x)$  is much softer than the first lattice-QCD result [107]. There are also quantitative differences, as highlighted by the prediction for  $u_K(x)/u_\pi(x)$  drawn in Fig. 7.26 – right and compared with the result determined from a measurement of the  $K^-/\pi^-$  structure function ratio [108].

#### 7.1.4 Origin of the hadron mass

99% of the mass of the visible universe come from all the nucleons that constitute it. The Higgs mechanism, which provides mass to the fundamental constituents of matter, can only explain a small fraction of the nucleon mass. The remaining finds its origin in the strong force that tightly binds quarks and gluons together. Understanding how the hadron mass emerges in QCD is therefore of utmost importance.

One way to address the question is to determine how current quarks and gluons contribute to the hadron mass. There exist essentially two types of mass decomposition: one consists in a decomposition of the trace of the energy-momentum tensor (EMT) [115–120], and the other corresponds to an energy decomposition in the system rest frame [121–126]. In QCD, the EMT is given by the following rather simple-looking expression

$$T^{\mu\nu} = \bar{\psi}\gamma^\mu \overleftrightarrow{D}^\nu \psi - G^{a\mu\lambda} G^{a\nu}_\lambda + \frac{1}{4} g^{\mu\nu} G^2, \quad (7.5)$$

and an essential feature related to the emergence of a mass scale is that its trace receives anomalous contributions

$$T^\mu_\mu = \frac{\beta(g)}{2g} G^2 + (1 + \gamma_m) \bar{\psi} m \psi. \quad (7.6)$$

Any mass decomposition starts with a particular split of the EMT into quark and gluon contributions  $T^{\mu\nu} = T_q^{\mu\nu} + T_G^{\mu\nu}$ , which is necessarily renormalization scheme and scale dependent. For a spin-0 or spin- $\frac{1}{2}$  system, the forward matrix elements of these contributions can simply be parametrized in terms of two EMT form factors evaluated at vanishing momentum transfer [69, 121, 122], i.e.

$$\langle P | T_{q,G}^{\mu\nu}(0) | P \rangle = 2P^\mu P^\nu A_{q,G}(0) + 2M^2 g^{\mu\nu} \bar{C}_{q,G}(0) \quad (7.7)$$

while additional spin-dependent contributions are required for higher-spin systems [127, 128]. The trace decomposition takes the form  $M = I_q + I_G$  with

$$I_{q,G} \equiv g_{\mu\nu} \langle T_{q,G}^{\mu\nu} \rangle = [A_{q,G}(0) + 4\bar{C}_{q,G}(0)] M, \quad (7.8)$$

and the energy decomposition reads  $M = U_q + U_G$  with

$$U_{q,G} \equiv \langle T_{q,G}^{00} \rangle = [A_{q,G}(0) + \bar{C}_{q,G}(0)] M, \quad (7.9)$$

where  $\langle T_{q,G}^{\mu\nu} \rangle \equiv \frac{1}{2M} \langle P | T_{q,G}^{\mu\nu}(0) | P \rangle|_{P=0}$  denotes the expectation value in the rest frame of the

system. These two decompositions are consistent with each other since four-momentum conservation implies the constraints  $A_q(0) + A_G(0) = 1$  and  $\bar{C}_q(0) + \bar{C}_G(0) = 0$ . Further decompositions of the quark and gluon energy contributions have also been discussed in the literature [121–123, 125, 126], along with the case of massless systems [123]. They do not however require additional experimental input beside the  $A_{q,G}$  and  $\bar{C}_{q,G}$  EMT form factors.

The various mass decompositions mentioned above become physically more meaningful if each component can be extracted from experimental observables. The first quark EMT form factor can be obtained as the second moment of the unpolarized PDF, i.e.  $A_q(0) = \int dx x f_1^q(x)$  and similarly for gluons. The other form factors  $\bar{C}_i(0)$  are related to the hadron sigma term  $\sigma = \langle \bar{\psi} m \psi \rangle$  and the trace anomaly  $\langle \frac{\beta}{2g} G^2 + \gamma_m \bar{\psi} m \psi \rangle$ . In the case of the nucleon, the former is accessible through low-energy  $\pi N$  phenomenology, like experimental information on  $\pi N$  scattering or  $\pi$ -atom spectroscopy measurements [129–132]. The missing term to directly test the proton-mass sum rule is then the gluon contribution to the trace anomaly, i.e. the gluon condensate  $\langle P | G^2 | P \rangle$ . To probe this in experiments, the best way is to use heavy quarkonia such as  $J/\psi$  and  $Y$  because they interact with hadrons primarily via gluon exchanges. Besides, in order to maximize the sensitivity to the twist-four operator  $G^2$ , the center-of-mass energy must be as low as possible. These considerations have led to propose the near-threshold photo- or lepto-production of  $J/\psi$  or  $Y$  in lepton-proton scattering [117, 133, 134] (see, also, [135–137]). Recent studies have shown that this process is also sensitive to the so-called gluon D-term (or the gluonic ‘pressure’ inside the nucleon) [133, 134, 138] which gives complementary information to the quark D-term measurable in DVCS (see, Sec. 7.2.2). It is thus a unique process that can simultaneously address two important questions of the nucleon structure (mass, pressure), and is worth pursuing at the EIC.

Currently, experiments are ongoing at the Jefferson laboratory, and the first results for near-threshold  $J/\psi$  exclusive photoproduction have been reported recently [139]. However, the JLab energy is not enough to create an  $Y$ . Besides, lepto-production at large photon virtualities  $Q^2$  [134] has certain advantages over photo-production despite smaller cross sections, but the available region in  $Q^2$  is rather limited at JLab ( $Q^2 < 10 \text{ GeV}^2$ ). These problems can be easily overcome at the EIC. On the other hand, studying a low-energy process at a high-energy collider inevitably entails new technical challenges. For example, one has to achieve high luminosity in lowest energy runs. [It is important to distinguish the  $ep$  center-of-mass energy from the  $\gamma^{(*)}p$  energy. The latter is constrained to be close to the threshold.] Moreover, the produced quarkonia and their decay products (lepton pairs) are typically in the very forward region, and this may require special detectors. Section 8.4.4 reports the result of detailed simulations to partly address these questions and indicate directions for future improvements.

Another way to address the question of the origin of the hadron mass is through chiral symmetry. In the chiral limit of vanishing quark masses, the trace anomaly vanishes for the pion owing to cancellations between competing effects associated with different interaction mechanisms, which are exact in the pion channel because of dynamical chiral symmetry breaking (DCSB). The mechanisms responsible for the emergent hadronic mass should manifest themselves in observables that probe the shape and size of the hadron wave func-

tion [140]. Five key measurements at the EIC expected to deliver far-reaching insights into the dynamical generation of mass have been highlighted in Ref. [141]. Among them, there are measurements of the pion electromagnetic form factor as reported in Secs. ??.

While the  $\pi^+$  mass is barely influenced by the Higgs and is almost entirely generated by DCSB, roughly 1/3 of the  $K^+$  mass comes from the Higgs mechanism, due to its strange quark content. Thus, the comparison of the charged pion and charged kaon form factors over a wide  $Q^2$  range would provide unique information relevant to understanding the generation of hadronic mass. Planned simulation work for 2021-23 include extensions of the pion form factor measurements to the case of the charged kaon, assuming that measurements at the 12-GeV JLab on exclusive  $K^+$  electroproduction beyond the resonance region confirm the feasibility of this technique (see Sec. 7.2.1).

### 7.1.5 Multi-parton correlations

#### Introduction

Multiparton correlations can be accessed through higher-twist observables with the underlying twist-classification: “an observable is twist- $t$  if its effect is effectively suppressed by  $(M/Q)^{t-2}$ ” [142]. Despite kinematical suppression, twist-3 observables are in principle not small and can dominate certain kinematics at moderate  $Q^2$ . This is illustrated by the fact that the first single spin asymmetries (SSAs) in SIDIS,  $A_{UL}^{\sin\phi}$  and  $A_{LU}^{\sin\phi}$ , observed at HERMES [143–147] and CLAS [148–150] are twist-3. Observations of large SSAs in single-inclusive hadron production ( $pp \rightarrow hX$ ) [151–156] dating back to the 1970s are further evidence of the importance of twist-3 effects.

Higher-twist distributions reflect the physics of the largely unexplored quark-gluon correlations which provide direct and unique insights into the dynamics inside hadrons including effects such as vacuum fluctuations, see, *e.g.*, [157]. They describe multiparton distributions [158] corresponding to the interference of higher Fock components in the hadron wave functions, and as such have no probabilistic partonic interpretations. Yet they offer fascinating insights into the nucleon structure. A prominent example is the DIS structure function  $g_2(x)$  [159] related to the twist-3 PDF  $g_T^a(x)$  which consists of a Wandzura-Wilczek (WW) part related to the twist-2 PDF  $g_1^a(x)$  [160] and the genuine twist-3 piece  $\tilde{g}_T^a(x)$ . The Mellin moment  $\int dx x^2 \tilde{g}_T^a(x)$  describes the transverse impulse the active quark acquires after being struck by the virtual photon due to the color Lorentz force [161]. The Mellin moment  $\int dx x^2 \tilde{e}^a(x)$  of the pure twist-3 piece in  $e^a(x)$  describes the average transverse force acting on a transversely polarized quark in an unpolarized target after interaction with the virtual photon [161].

The theoretical description of twist-3 SIDIS observables, like  $A_{UL}^{\sin\phi}$  or  $A_{LU}^{\sin\phi}$ , is challenging due to open questions in the TMD factorization at twist-3 level [162]. Under the assumption of factorization, twist-3 observables receive contributions from several unknown twist-3 TMDs or fragmentation functions [163], requiring ad-hoc assumptions in the analyses of the pertinent data, *e.g.*, [164,165]. An example is the WW(-type) approximation [166],

where contributions of genuine  $\bar{q}gq$ -correlators are neglected. The obvious disadvantage of such approximations is the neglect exactly of the new dynamics that enters at twist-3. The situation simplifies in semi-inclusive jet production, a promising process at EIC energies, which could provide valuable complementary information on twist-3 TMDs [167]. The collinear twist-3 distributions  $e^a(x)$ ,  $g_T^a(x)$ ,  $h_L^a(x)$  are accessible in collinear di-hadron production [168–174] where a reduced number of terms contributes to the cross-sections.

Important connections between twist-3 and twist-2 TMDs appear, *e.g.*, in derivations of the evolution equations for transverse moments of TMDs [175–179], calculations of processes at high transverse momentum [180], or calculations of the high transverse momentum tails of TMDs [181, 182]. Ultimately, through global studies of all of these observables, one will simultaneously obtain better knowledge of twist-3 collinear functions and twist-2 TMDs, and at the same time test the validity of the formalism. Gathering as much information as one can on the quark-gluon-quark correlator is essential to reach this goal. One example of such a study is the global fit to twist-2 and twist-3 observables used to extract transversity and the tensor charge described in Sec. 7.2.3 [183]. In this respect, not only will SIDIS experiments play an important role at an EIC but also measurements of  $A_N$  in  $eN^\uparrow \rightarrow hX$  [184]. This is the analogue of the  $A_N$  measurements in  $pp$  collisions at RHIC, which are sensitive to multi-parton correlators connected to the Sivers and Collins functions [185–189].

The EIC spanning a large  $Q$ -range will be an ideal tool to identify higher-twist effects. The possibilities of extracting twist-3 observables represent important doorways to study hadron structure in QCD. Here, we will describe two exemplary measurements that will be highly interesting at the EIC: The double spin asymmetry  $A_{LT}$  in inclusive DIS sensitive to  $g_T^a(x)$  and the longitudinal beam spin asymmetries in SIDIS to access  $e^a(x)$ . Higher twist in hadronization is discussed in Sec. ??

### $g_T^a(x)$ from inclusive DIS.

The clearest example of higher-twist, that is defined in a collinear framework and accessible in inclusive DIS, is the inclusive cross section  $\vec{e}p^\uparrow \rightarrow e'X$ . Factorization theorems imply the collinear PDF, twist-3 PDF  $g_T^a(x)$  [159, 190]. Recent work on higher twist contributions to the spin-dependent structure functions  $g_1$  and  $g_2$  was carried out by the JAM Collaboration [46], which in turn enables an extraction of  $g_T^a(x)$  from  $A_\perp \sim (g_1 + g_2) = g_T$ . Moreover, the derivation of the inclusive cross section in the collinear twist-3 factorization framework [158, 187],  $\sigma_{LT} \rightarrow A_{LT} \sim A_\perp^{\text{DIS}}$ , leading to the “DIS” inclusive result, was carried out by Pitonyak [191], establishing the connection of the DIS and collinear twist-3 factorization frameworks as it pertains to multi-parton correlations. This establishes  $g_T$  and the double spin asymmetry as the most prominent observable to study multi-parton correlations at the EIC. Figure 7.27 shows the projected impact of the EIC data on  $g_T$ . The cyan band gives the error under the WW approximation [160], and the yellow band from DIS world data on  $A_{LL}$  and  $A_{LT}$  within the JAM [46] framework assuming DGLAP evolution for the  $Q^2$  dependence. The impact from EIC pseudo-data is reflected by the red band and indicates the feasibility of measuring the genuine twist-3

effect. Therefore EIC data will give entirely new insights on the interactions of the struck quark with the partons around it.

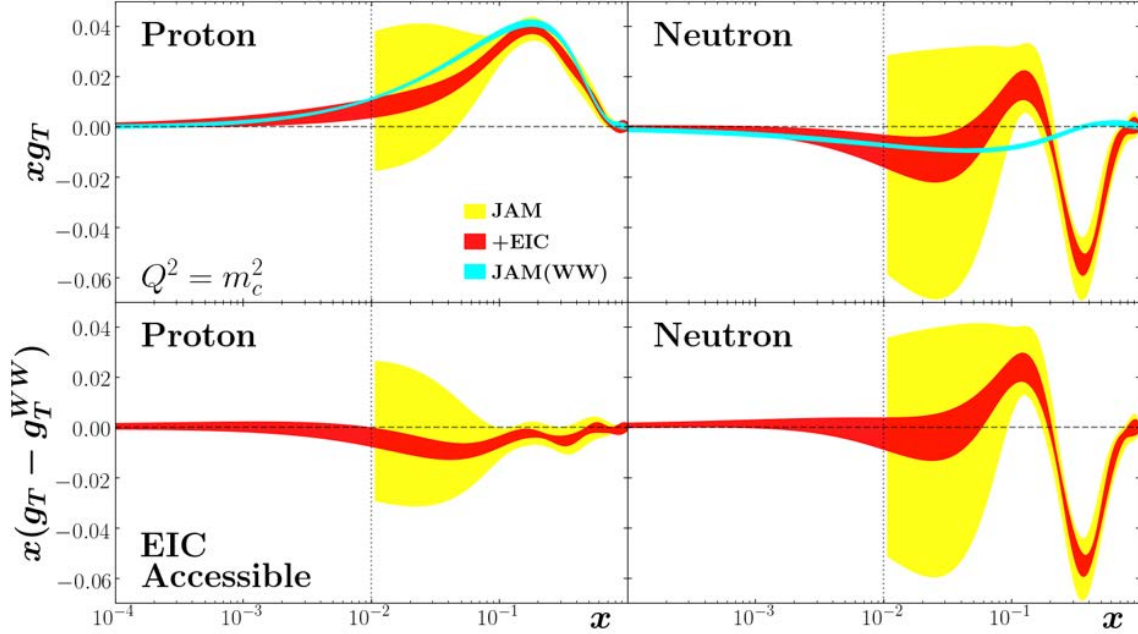


**Figure 7.27:** Impact of  $A_{\perp}$  on  $g_T$  at the EIC with proton, deuteron, and helium targets at  $\mathcal{L} = 100 \text{ fb}^{-1}$  with 1.6% point-by-point uncorrelated systematic uncertainties. The baseline  $g_1$  and  $g_T$  are extracted from the existing world  $A_{LL}$  and  $A_{LT}$  data within the JAM framework. The extraction of  $g_T$  was done using a suitable parametrization for the  $x_{bj}$  dependence at the input scale and assuming DGLAP for the  $Q^2$  dependence. The WW approximation at the structure function is shown to illustrate the feasibility to access genuine higher twist effects in  $g_T$  at the EIC.

### $e^a(x)$ from semi-inclusive DIS.

The PDF  $e^a(x)$  can be decomposed into three contributions [192] through QCD equations of motion. The first term is a  $\delta(x)$ -singularity related to the pion-nucleon sigma-term and the non-trivial QCD vacuum structure [157, 193–197]. The second term  $\tilde{e}^a(x)$  is related to a genuine  $\bar{q}gq$  contribution with the aforementioned force interpretation [161]. The third term is proportional to the quark mass and the unpolarized PDF. In the bag model  $e^q(x)$  is due to the bag boundary [198, 199] while constituent quark models feature the mass term as being dominant [192, 200–205]. Phenomenologically, the chiral-odd PDF must be paired to another chiral-odd object, associated with fragmentation for Deep Inelastic processes similarly to the transversity PDF. This is analogue to the extraction of transversity described in Sec. 7.2.3. In Fig. 7.28 the theoretical predictions are shown for the contribution of  $e^a(x)$  to the beam spin asymmetry in semi-inclusive di-hadron production in the collinear framework. This asymmetry receives a contribution not only from  $e^q(x)$  but also from a term involving a twist-3 di-hadron fragmentation function together with  $f_1^q(x)$ . The

latter has not been considered here [165]. The uncertainties in Fig. 7.28 come from the interference fragmentation function [206] and two models for  $e^a(x)$ , the light-front constituent quark model [205] and model of the mass-term contribution to  $e^q(x)$  with an assumed constituent quark mass of 300 MeV and the unpolarized PDF from MSTW08LO. All PDFs and fragmentation functions are taken at  $Q^2 = 1 \text{ GeV}^2$  and the projected uncertainties for the EIC are shown only for  $Q^2$  values smaller than  $10 \text{ GeV}^2$ . A similar observable can be studied for single-hadron SIDIS in TMD framework [164], but is much more complex as it involves 4 unknown contributions with one of them being due to the TMD  $e^q(x, k_T)$ . The evolution of the genuine twist-3 contribution  $\tilde{e}^a(x)$  has been studied [207–209] but never implemented in the PDF extractions. The EIC kinematics will allow to complement the low- $x$  region, of extremely high relevance for the study of the mass term as well as the scalar charge/non-trivial vacuum.

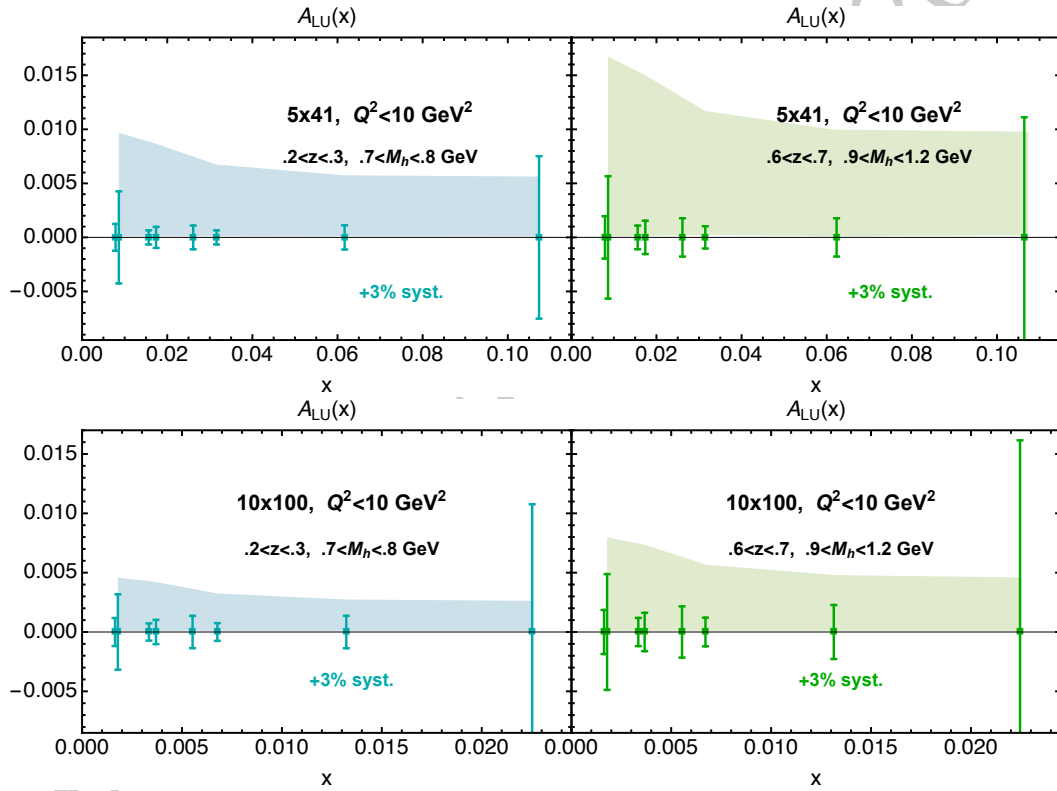


**Figure 7.28:** Beam Spin Asymmetry in semi-inclusive di-hadron production. Predictions corresponding to  $Q^2 = 1 \text{ GeV}^2$  based on the di-hadron fragmentation functions of Ref. [206], low-energy models for the twist-3 PDF  $e(x)$  (see text) and MSTW08 for the unpolarized PDF at LO. The twist-3 fragmentation is neglected. The upper and lower pannel show two different energy configuration ; the left (blue) and right (green) plots correspond, respectively, to the fragmentation kinematics of  $(0.2 < z < 0.3, 0.7 < M_h < 0.8 \text{ GeV})$  and  $(0.6 < z < 0.7, 0.9 < M_h < 1.2 \text{ GeV})$ .

### 7.1.6 Inclusive and hard diffraction

#### Inclusive diffraction

Inclusive diffraction has been extensively studied at HERA collider [210,211]. The diffractive events in Deep inelastic Scattering  $ep \rightarrow eXY$  are distinguished by the presence of the large rapidity gap between the diffractive system, characterized by the invariant mass  $M_X$  and the final proton (or its low-mass excitation)  $Y$  with four momentum  $p'$ . In addition to the standard DIS variables  $(x, Q^2)$ , diffractive events are also characterized by set of variables, specific to diffraction, defined as  $t = (p - p')^2$ ,  $\xi = \frac{Q^2 + M_X^2 - t}{Q^2 + W^2}$ ,  $\beta = \frac{Q^2}{Q^2 + M_X^2 - t}$ . Here,  $t$  is the squared four-momentum transfer at the proton vertex,  $\xi$  (alternatively denoted by  $x_{IP}$ ) can be interpreted as the momentum fraction of the 'diffractive exchange' with respect to the hadron, and  $\beta$  is the momentum fraction of the parton with respect to the diffractive exchange. The two momentum fractions combine to give Bjorken- $x$ ,  $x = \beta\xi$ .

In analogy with the unpolarized, non-diffractive inclusive DIS, the inclusive diffraction cross sections can be expressed in terms of the reduced cross sections and the corresponding structure functions, which however depend on additional variables specific to diffraction

$$\sigma_{\text{red}}^{D(3)} = F_2^{D(3)}(\beta, \xi, Q^2) - \frac{y^2}{Y_+} F_L^{D(3)}(\beta, \xi, Q^2), \quad (7.10)$$

and without integration over  $t$  dependence

$$\sigma_{\text{red}}^{D(4)} = F_2^{D(4)}(\beta, \xi, Q^2, t) - \frac{y^2}{Y_+} F_L^{D(4)}(\beta, \xi, Q^2, t), \quad (7.11)$$

where  $Y_+ = 1 + (1 - y)^2$ .

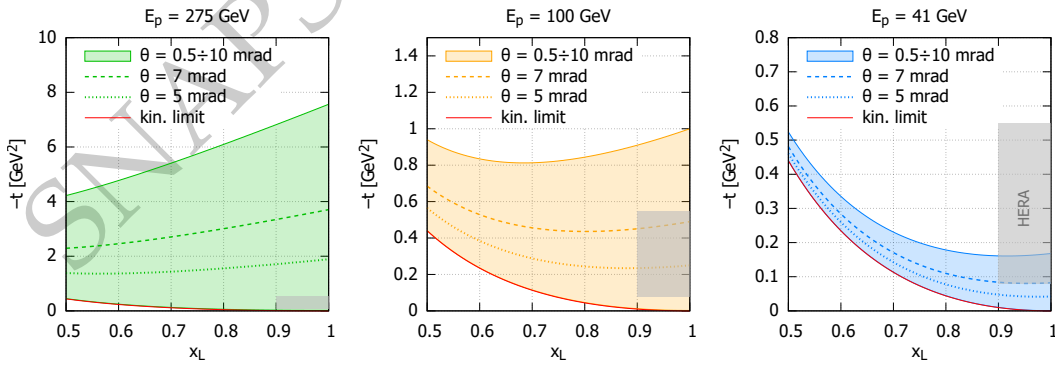


**Figure 7.29:** Accessible kinematic range in  $t$  and  $x_L$  for different small angle acceptance of the final leading proton in three EIC scenarios:  $E_p = 275, 100, 41$  GeV. Red line is the kinematic limit, grey area is the HERA range.

The standard perturbative QCD approach to inclusive diffraction is based on the collinear

factorization [212–214]. The cross section is computed by the convolution of the perturbative hard scattering partonic cross section and the diffractive parton distribution functions (DPDFs). The DPDFs are evolved using the DGLAP evolution equations with appropriately chosen initial conditions at some low scale. At HERA fits to the diffractive structure functions were performed by H1 [215] and ZEUS [216]. They both parametrize the diffractive PDFs in a two component model, which is a sum of two contributions, Pomeron and Reggeon. In both cases the proton vertex factorization is assumed, meaning that the diffractive exchange can be interpreted as colourless objects called a ‘Pomeron’ or a ‘Reggeon’ with an appropriate parton distributions  $f_i^{IP,IR}(\beta, Q^2)$  and factorized flux factor  $f_p^{IP,IR}(\xi, t)$ .

There are number of areas where EIC can significantly expand our knowledge of QCD diffraction. First, thanks to the instrumentation in the forward region the EIC will be able to measure leading protons in a much wider kinematics range of  $t$  and  $x_L$ , the fraction of the longitudinal plus component of the momentum of the initial proton carried by the final proton, than at HERA. This is illustrated in Fig. 7.29 for different proton energies of the EIC. Red curve indicates the kinematic limit, and different curves indicate various an-

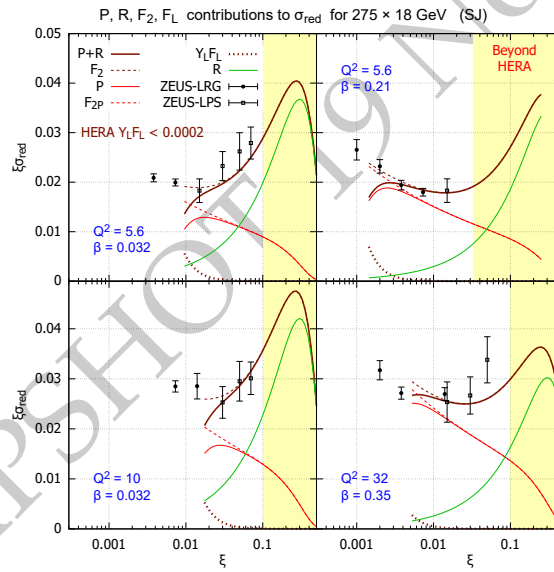


**Figure 7.30:** Reduced cross section as a function of  $\xi$  in bins of  $\beta$  and  $Q^2$  for the energy scenario of  $275 \text{ GeV} \times 18 \text{ GeV}$ . Red solid line: Pomeron contribution, green solid line: Reggeon contribution, brown solid line: sum of Pomeron and Reggeon contributions. Dashed red line:  $F_2^D$  Pomeron contribution, dotted brown:  $Y_L F_L$  contribution, dashed brown:  $F_2$ . The data are from HERA, yellow region was not accessible at HERA. Variable  $Y_L$  is defined as  $Y_L = y^2/Y_+$ .

gular cuts on the final proton. We see that for the case of the angular acceptance which would extend to about 7 mrad, this translates into the range in  $-t$  well up to  $2 \text{ GeV}^2$  for the highest energy range. This is well beyond the HERA range which is indicated in grey on the plots. The second area where EIC could provide valuable information are the Pomeron and Reggeon contributions. At HERA the  $t$  dependence of Reggeon contribution could

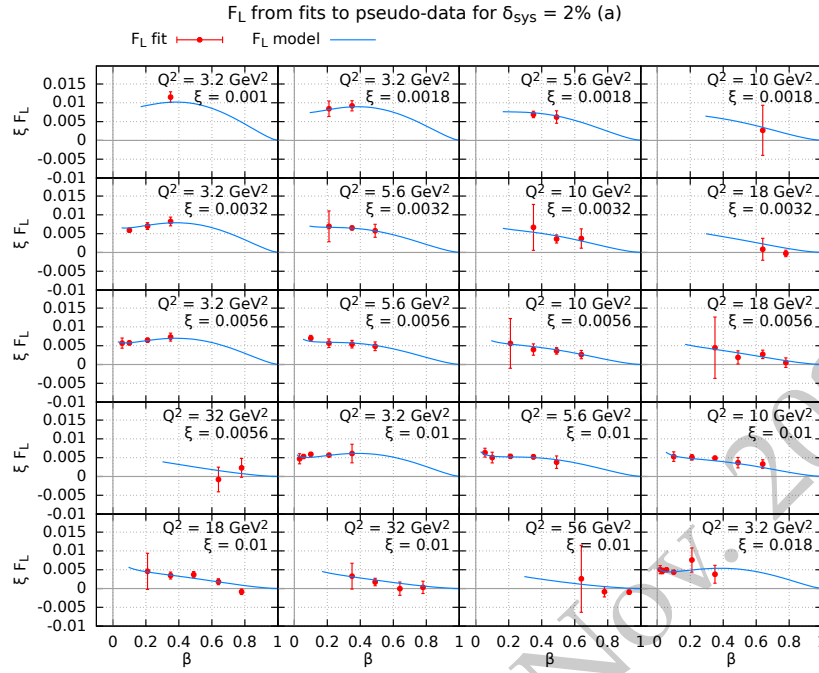


**Figure 7.31:** Longitudinal diffractive structure function  $F_L^{D(3)}$  extracted from fits to the pseudo-data as a function of  $\beta$  in bins of  $Q^2$  and  $\xi$ . Red points indicate the data extracted from the analysis and the curve indicates the prediction.

not be tested at all, as the range in  $\xi$  was not sufficient to probe in detail the region where the Reggeon contribution is dominant. This is illustrated in Fig. 7.30. Here we show the reduced cross section as a function of  $\xi$  in bins of  $Q^2, \beta$  for the highest energy scenario at an EIC. The solid curves (red, green, brown) indicate the Pomeron, Reggeon contributions and their sum. It is clear that the region above  $\xi > 0.1$  is where the Reggeon contribution starts to be dominant, and it was not accessible by HERA. EIC has the potential to explore that region to disentangle the two components. The same plot also illustrates the importance of the  $F_L^D$  in the kinematic region of low  $\xi$ , indicated by the brown dotted line. The superimposed data are from HERA, and they clearly follow the  $F_2^D$  contribution only, since at HERA in this regime the contribution from the longitudinal structure function was extremely small. On the contrary at the EIC, the contribution from  $F_L^D$  for the same values of  $Q^2, \beta, \xi$  is not negligible, as illustrated by the dotted brown curve in Fig. 7.10. With high luminosity and possibility of various centre of mass energies, EIC is in excellent position to perform precise measurements of longitudinal diffractive structure function.

In Fig. 7.31 this possibility of  $F_L^D$  extraction is further explored. For this analysis 18 beam setups were considered  $(5, 10, 18) \times (41, 100, 120, 165, 180, 275)$  GeV. There were 469 bins selected such that they are common to at least four beam setups, with cuts  $Q^2 > 3 \text{ GeV}^2, M_X > 2 \text{ GeV}$ . The measurement of this quantity is dominated by systematic error, which for this analysis was assumed to be equal to 2%. The Fig. 7.31 indicates that EIC has a very good potential for measurement of  $F_L^D$  in wide range of kinematics.

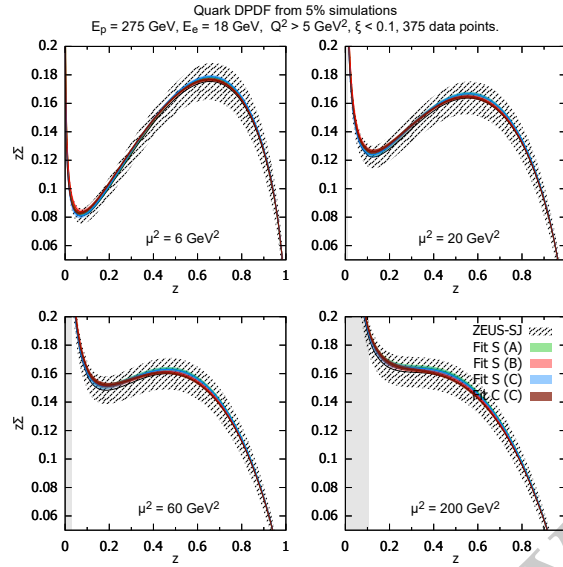


**Figure 7.32:** Diffractive quark distribution as a function of the longitudinal momentum fraction in bins of  $Q^2$ . Hatched bands indicate HERA uncertainty bands. Solid bands indicate the projected uncertainty in extracted DPDFs after fitting to the EIC data.

Finally, given the EIC could potentially improve the extraction of the diffractive parton distribution functions. The DPDFs were for the first time extracted at HERA collider, and success of the DGLAP fits to inclusive diffraction confirmed applicability of the collinear factorization theorem to diffraction. Nevertheless, many open questions remained, since the fits were only valid for the relatively large value of  $Q^2$ , i.e.  $Q^2 > 8 \text{ GeV}^2$  for H1 and  $Q^2 > 5 \text{ GeV}^2$  for ZEUS, below which they failed, indicating perhaps the need of additional corrections. Some studies indicated possible improvement of the description based on the saturation models, which would incorporate higher twists in the fits [217]. In addition, the DPDFs at HERA were not very well constrained at large values of  $\beta$ , the longitudinal momentum fraction of the parton with respect to the diffractive exchange. EIC has unique potential to improve the extraction of the DPDFs at large values of  $\beta$ . In Fig. 7.32 we show an example of an extraction of the diffractive quark distribution function in bins of  $Q^2$  as a function of  $\beta$ . We see from the plot that the projected uncertainty on the DPDF extracted from EIC is reduced significantly with respect to HERA, particularly at large values of the longitudinal momentum fraction.

### Diffractive dijets

Studies of diffraction in high-energy electron-proton scattering is one of highlights of the HERA heritage, which discovered that diffractive processes  $ep \rightarrow eXY$  account for a substantial, 10 – 15% fraction of all events. In deep inelastic scattering (DIS), taking advantage of the QCD factorization theorem [212], diffractive parton distribution functions (PDFs) of the proton have been determined [215, 216] and their universality in diffractive dijet and

open charm production has been shown. At the same time in diffractive dijet photoproduction, next-to-leading order (NLO) perturbative QCD calculations [218] indicated that factorization is broken: the theory agrees with the H1 [219] and ZEUS [220] data after assuming that either the resolved-photon contribution is suppressed by a factor of 0.34 or the entire pQCD cross section is suppressed by a global factor of 0.4 – 0.7 (the exact values depend on the jet transverse momentum and large theoretical uncertainties from scale variations and hadronization corrections).

To explore the EIC potential for diffractive dijet photoproduction, we performed detailed studies of this process in NLO QCD in  $ep$  and  $eA$  scattering in the EIC kinematics [221]. Using the framework developed in Refs. [218], the cross section for the reaction  $e + p \rightarrow e + 2 \text{ jets} + X' + Y$  can be written as follows

$$d\sigma = \sum_{a,b} \int dy \int dx_\gamma \int dt \int dx_P \int dz_P f_{\gamma/e}(y) f_{a/\gamma}(x_\gamma, M_\gamma^2) f_{P/p}(x_P, t) f_{b/P}(z_P, M_P^2) d\hat{\sigma}_{ab}^{(n)}. \quad (7.12)$$

In Eq. (7.12),  $f_{\gamma/e}(y)$  is the photon flux calculated in the improved Weizsäcker-Williams approximation and  $y$  is the photon longitudinal momentum fraction;  $f_{a/\gamma}(x_\gamma, M_\gamma^2)$  is the PDF of the photon (for the resolved-photon contribution) and  $x_\gamma$  is the corresponding momentum fraction; the diffractive PDF of the proton is written in the usually assumed form of Regge factorization as the product of the flux factor  $f_{P/p}(x_P, t)$ , where  $t$  is the invariant momentum transfer squared, and the PDFs of the pomeron  $f_{b/P}(z_P, M_P^2)$ ; finally,  $d\hat{\sigma}_{ab}^{(n)}$  is the cross section for the production of an  $n$ -parton final state from two initial partons  $a$  and  $b$ . In our analysis, we identified the factorization scales  $M_\gamma$ ,  $M_P$  and the renormalization scale  $\mu$  with the average transverse momentum  $\bar{p}_T = (p_{T1} + p_{T2})/2$ . The longitudinal momentum fractions  $x_\gamma$  and  $z_P$  can be experimentally determined from the two observed leading jets through

$$x_\gamma^{\text{obs}} = \frac{p_{T1} e^{-\eta_1} + p_{T2} e^{-\eta_2}}{2yE_e} \quad \text{and} \quad z_P^{\text{obs}} = \frac{p_{T1} e^{\eta_1} + p_{T2} e^{\eta_2}}{2x_P E_p}, \quad (7.13)$$

where  $p_T$  and  $\eta$  is the transverse momentum and rapidity of jet 1 or 2;  $E_e$  and  $E_p$  is the electron and proton beam energy, respectively.

Given experience from HERA, we defined jets with the anti- $k_T$  algorithm with the distance parameter  $R = 1$  and assumed that the detectors can identify jets above relatively low transverse energies of  $p_{T1} > 5$  GeV (leading jet) and  $p_{T2} > 4.5$  GeV (subleading jet).

Using the formalism outlined above, we made predictions for diffractive dijet photoproduction at the EIC as a function of the jet average transverse momentum  $\bar{p}_T$ , the observed longitudinal momentum fractions  $x_\gamma^{\text{obs}}$  and  $z_P^{\text{obs}}$ , the proton longitudinal momentum transfer  $x_P$ , and the jet rapidity difference  $\Delta\eta$ . Several features of the obtained results are important to emphasize. The distribution in the jet average transverse momentum extends only to 8 GeV (it was 15 GeV at HERA) and, hence, the cross section is dominated by contributions from direct photons. The  $K$ -factor giving the ratio of the NLO and leading-order (LO) cross section was found to be approximately constant  $K \approx 2$  and independent on kinematic variables. To address conclusively the mechanism of factorization breaking

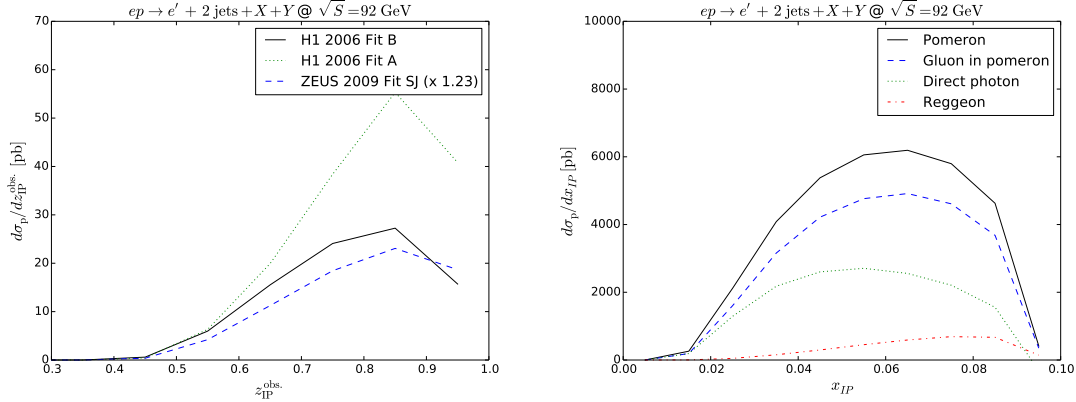


**Figure 7.33:** (Left) NLO QCD predictions for  $z_P^{\text{obs}}$  dependence using three different sets of diffractive PDFs: H1 2006 Fit B (full black), Fit A (dotted green), and ZEUS 2009 Fit SJ (dashed blue curves). (Right) Different contributions to the dijet cross section as a function of  $x_P$ .

requires a high proton beam energy and wide ranges in  $x_P$  (where the subleading contribution at high  $x_P$  becomes important) and  $x_\gamma^{\text{obs}}$ . Replacing the proton by a heavy nucleus and using predictions for nuclear diffractive PDFs [222], we also obtained predictions for these distributions in coherent diffractive dijet photoproduction on nuclei in the reaction  $e + A \rightarrow e + 2 \text{ jets} + X + A$ .

An example of our predictions is presented in Fig. 7.33, where the left panel shows the dijet cross section as a function of  $z_P^{\text{obs}}$  for three different sets of diffractive PDFs and the right panel shows different contributions to the dijet cross section as a function of  $x_P$ .

### Large $|t|$ diffractive production of vector mesons

Among the diffractive processes, particularly interesting are the diffractive production of the heavy vector mesons. The diffractive production of vector mesons is a great testing ground for details of the QCD dynamics, and in particular the soft and hard phenomena. Within QCD, the VM diffractive production is usually described in terms of a colorless exchange, with quantum numbers of a vacuum, which at lowest order is given by an exchange of two gluons. At higher orders this process is described by an exchange, in a  $t$ -channel, by a gluon ladder which is often referred to as Perturbative Pomeron [223, 224]. At high energies, the exchange of the perturbative Pomeron leads to a significantly faster increase with energy of the scattering amplitude than in the soft regime.

Hence, one of the most pressing questions in the high energy QCD is the energy dependence of the Pomeron on the size of the rapidity gap and dependence on the momentum transfer  $t$ .

The exclusive channel, which dominates the region of  $-t \leq 1 \text{ GeV}^2$  is considered in detail in the separate sections of this report. Here, we focus on the diffractive production of

vector mesons at high momentum transfer  $|t|$ . In this case the proton usually does not stay intact but rather dissociates into a low mass excitation (which is however much larger than in the low  $|t|$  diffraction). Such process can be identified by the presence of a large rapidity gap between the heavy meson and the system produced in the fragmentation of parton knocked out of the target. An advantage of this class of processes is that there are two perturbative scales, of the same order, which are present at both ends of the Pomeron, thus largely suppressing the diffusion of transverse momenta along the gluon ladder into the non-perturbative, infrared regime.

This is an excellent setup to investigate the energy dependence of the vacuum exchange amplitude. In fact in this case the rapidity gap dependence of the cross section is directly converted into the intercept of the Pomeron exchange at a given  $t$ . Roughly speaking the dependence on the rapidity gap of the cross section should scale as  $2(\alpha_p(t) - 1)$  which in this case should be about  $0.4 - 0.5$  for the BFKL Pomeron as compared to  $0.2$  for the soft regime.

The HERA detectors had a rather limited acceptance in rapidity and could not measure directly the dependence on the rapidity gap of the cross section of this process. As a result determination of the energy dependence of the Pomeron amplitude was sensitive to details of the  $t$ -dependence of the amplitude and also masked by the convolution with the  $x$  dependence of the parton density in the target which was integrated over.

EIC, with suitable detector, will have the potential to measure directly the rapidity gap, and thus energy dependence of the cross section as a function of the rapidity gap size.

There are two different strategies that can be considered. In the first case, one can require the direct observation of the size of the rapidity gap. In this case one would require an activity in the central detector up to a certain angle. Detailed studies [225] show that angle of about  $4^\circ$ , corresponding roughly to rapidity  $3.3$  would already allow for a range of rapidity gaps. In the second scenario, the size of the gap is unknown since there is no activity in the forward part of the detector. In that scenario lower limit on the gap size can be imposed.

Detailed estimates [225] found that a much higher luminosity of the EIC than of HERA compensates to some extent a lower energy of the EIC. As a result one can test at the EIC dependence of the cross section on rapidity gap interval predicted by the BFKL model for rapidity gaps up four units in rapidity. Importance of a good detector acceptance in the nucleon fragmentation region for such studies is crucial. It was found [225] that the acceptance up to rapidity  $\eta = 3.5$  is sufficient for this process, although acceptance up to higher rapidity, i.e.  $\eta = 4.5$  would allow for a longer lever arm and more stringent tests of the small  $x$  dynamics and the Pomeron. Apart from the  $J/\psi$  production, a rapidity gap production of  $\rho$ -mesons maybe also very promising, perhaps even in a broader range of  $t$ .

### 7.1.7 Global event shapes and the strong coupling constant

#### Introduction

Event shapes [226] are global measures of the momentum distribution of hadrons in the final state of a collision, using a single number to characterize how well collimated or not the hadrons are along certain axes. This simple and global nature makes them highly amenable to high-precision theoretical calculations and convenient for experimental measurement. They then become powerful probes of QCD predictions, the strong coupling  $\alpha_s$ , hadronization effects, etc.

The classic example, for  $e^+e^-$  collisions, is *thrust* [227]:

$$\tau = 1 - T, \quad \text{where} \quad T = \frac{1}{Q} \max_{\hat{\mathbf{t}}} \sum_{i \in X} |\hat{\mathbf{t}} \cdot \mathbf{p}_i| = \frac{2p_z^A}{Q}, \quad (7.14)$$

at a center-of-mass collision energy  $Q$ , where the sum is over all hadrons  $i$  in the final state  $X$ , whose three-momenta  $\mathbf{p}_i$  are dotted into the *thrust axis*  $\hat{\mathbf{t}}$ , which is varied until the sum defining  $T$  is maximized. It is customary to use  $\tau = 1 - T$ , an example of a *two-jet* event shape in  $e^+e^-$  collisions, which goes to the limit  $\tau \rightarrow 0$  as the final-state goes to a pencil-like back-to-back two-jet event, and grows as the jets broaden, up to the limit  $\tau = 1/2$  for a spherically symmetric final state. Other examples of two-jet event shapes are broadening  $B$  [228],  $C$ -parameter [229], and angularities [230, 231].

The thrust axis  $\hat{\mathbf{t}}$  determines two hemispheres  $A$  and  $B$ , in terms of which we have expressed the thrust  $T$  in the last equality of Eq. (7.14) where we have defined the  $+z$  direction to be along  $\hat{\mathbf{t}}$ , and  $p_z^A$  the total  $z$  momentum in the  $+z$  hemisphere. In DIS, a natural division of the final state into hemispheres occurs in the Breit frame, with the incoming current defining the  $z$  direction. Accordingly, the DIS thrust  $\tau_Q$  has been defined [232]

$$\tau_Q \stackrel{\text{Breit}}{=} 1 - \frac{2}{Q} \sum_{i \in \mathcal{H}_C} p_z^i, \quad (7.15)$$

where  $Q$  is now the DIS variable  $Q$ , and  $\mathcal{H}_C$  is the “current” hemisphere in the Breit frame. This  $\tau_Q$  does in fact have a Lorentz-invariant definition, in terms of the class of “ $N$ -jettiness” observables [233]:

$$\tau_N = \frac{2}{Q^2} \sum_{i \in X} \min\{q_B \cdot p_i, q_1 \cdot p_i, \dots, q_N \cdot p_i\}, \quad (7.16)$$

where  $q_B$  is a four-momentum vector in the proton beam direction (for DIS) and  $q_{1, \dots, N}$  are four-momenta in  $N$  “jet” directions in the final state along which one wishes to measure collimation of hadrons. The final-state hadrons are all grouped into regions according to which reference vector  $q_i$  they are “closest” to, in the sense of minimizing the dot products. One will find  $\tau_N \rightarrow 0$  for events with hadrons perfectly collimated along the beam direction and these  $N$  jet directions. For DIS, there is just one beam direction, whereas for

$pp$  collisions one would have two beam directions, and for  $e^+e^-$  collisions, zero.

We will focus on the simplest case for DIS, 1-jettiness [234, 235]. There is a freedom to choose exactly what the reference vectors  $q_B$  in the beam direction and  $q_J$  (which we will call  $q_J$ ) are. Different choices of directions and normalizations give different measures of 1-jettiness. The choice:

$$q_B^b = xP, \quad q_J^b = q + xP, \quad (7.17)$$

where  $P$  is the incoming proton momentum,  $x$  is Bjorken  $x$ , and  $q$  is the current momentum, actually gives the same thing as  $\tau_Q$ :

$$\tau_1^b \equiv \frac{2}{Q^2} \sum_{i \in X} \min\{q_B^b \cdot p_i, q_J^b \cdot p_i\} = \tau_Q. \quad (7.18)$$

The label  $b$  comes from notation used in [235]. It is a simple exercise using momentum conservation to show the last equality with  $\tau_Q$  in Eq. (7.15). Note that  $q_J^b = q + xP$  is the momentum the outgoing jet (quark) would have at Born (tree) level. Nonzero  $\tau_1^b$  measures the deviations and broadening of the jet momentum and structure away from this Born limit. Another version of DIS 1-jettiness we will consider uses a  $q_J$  that is adjusted to align with the physical jet momentum:

$$q_B^a = xP, \quad q_J^a = \text{jet momentum } P_J, \quad (7.19)$$

where  $P_J$  may be found by a suitable algorithm, such as anti- $k_t$ , or minimization over axes such as in  $e^+e^-$  thrust. For small  $\tau_1^a$ , the differences in  $\tau_1^a$  measured using different IRC-safe algorithms will be power-suppressed. The difference between the true and Born-level jet axes used in  $\tau_1^{a,b}$ , however, is a leading-order effect [235]. Computing or measuring  $\tau_1^a$  requires measuring particles in both beam and current hemispheres. Computing or measuring  $\tau_1^b$ , by contrast, according to Eq. (7.15) only requires a measurement of particles in the current hemisphere, with no jet algorithm.  $\tau_1^a$ , however, has a slightly simpler factorization theorem for its theoretical prediction, as we will review below.<sup>2</sup>

## Theoretical Methods

The global nature of event shapes such as those introduced above means that all collinear and soft radiation is probed with a single parameter. For example, the thrust distribution is sensitive to physics at three scales, hard  $\mu_H = Q$ , collinear  $\mu_J = Q\sqrt{\tau}$ , and soft  $\mu_S = Q\tau$ . In fixed-order perturbative expansions of the thrust distribution in QCD, logs of ratios of these scales appear at every order in  $\alpha_s$ . For small values of  $\tau$ , these logs blow up at any fixed order in  $\alpha_s$ , and must be resummed to all orders. This is accomplished by factorization of the logs into pieces that depend on only one of the physical scales (hard,

<sup>2</sup>In [235], a third version of DIS 1-jettiness  $\tau_1^c$  was considered, with  $q_B^c = P$ ,  $q_J^c = k$ , where  $k$  is the incoming electron momentum. This gives a version of 1-jettiness where particles are divided into back-to-back hemispheres in the CM frame. It has some interesting predicted properties, but a more complicated factorization theorem, and to date, fewer theoretical computations, so we do not consider it further in this Report. Yet another version of 1-jettiness, similar to  $\tau_1^a$ , was defined in [234, 236] and computed to NNLL+ $\mathcal{O}(\alpha_s)$  accuracy.

collinear, soft) at a time, and resummation through renormalization group (RG) evolution of each set of factorized contributions. A regularization scale  $\mu$  separates hard, collinear, and soft momentum regions from one another, and RG evolution occurs as this arbitrary scale  $\mu$  is varied.

Traditional methods in perturbative QCD (“direct” QCD) have been used successfully to resum logs in event shapes (e.g. [237–239]), but more recent methods use the technology of effective field theory to do so, namely, soft collinear effective theory (SCET) [240–244]. SCET has successfully been used to resum certain event shapes to  $N^3\text{LL}$  accuracy (e.g. [245, 246]), including DIS 1-jettiness  $\tau_1^a$  and  $\tau_1^b$  (i.e. DIS thrust  $\tau_Q$ ) [247]. For these observables, SCET predicts the factorized cross sections:

$$\begin{aligned} \frac{d\sigma}{dx dQ^2 d\tau_1^a} &= \frac{d\sigma_0}{dx dQ^2} \int dt_J dt_B dk_S \delta\left(\tau_1^a - \frac{t_J + t_B}{Q^2} - \frac{k_S}{Q}\right) J_q(t_J, \mu) S(k_S, \mu) \\ &\times \sum_q H_q(y, Q^2, \mu) B_q(t_B, x, \mu) + \sigma_{\text{ns}}(x, Q^2, \tau_1^a), \end{aligned} \quad (7.20)$$

$$\begin{aligned} \frac{d\sigma}{dx dQ^2 d\tau_1^b} &= \frac{d\sigma_0}{dx dQ^2} \int dt_J dt_B dk_S d^2\mathbf{p}_\perp \delta\left(\tau_1^b - \frac{t_J + t_B}{Q^2} - \frac{k_S}{Q}\right) S(k_S, \mu) \\ &\times J_q(t_J - \mathbf{p}_\perp^2) \sum_q H_q(y, Q^2, \mu) \mathcal{B}_q(t_B, x, \mathbf{p}_\perp^2, \mu) + \sigma_{\text{ns}}(x, Q^2, \tau_1^b), \end{aligned} \quad (7.21)$$

where

$$\frac{d\sigma_0}{dx dQ^2} = \frac{2\pi\alpha_{\text{em}}^2}{Q^4} [(1-y)^2 + 1] \quad (7.22)$$

is the Born-level cross section, with  $xys = Q^2$ , and the sum is over quark and antiquark flavors  $q$ . The factorized part of Eq. (7.20) predicts the singular part of the  $\tau_1^a$  distribution and will resum all the singular logs, and  $\sigma_{\text{ns}}$  is the nonsingular part of the distribution to which the resummed prediction must be matched for large  $\tau_1^a$ . It is predicted in fixed-order perturbation theory. The factors  $H_q, J_q, B_q(\mathcal{B}_q), S$  are universal factors that appear in predictions of many different observables.  $H_q$  is the hard function coming from integrating out hard virtual fluctuations from QCD to match onto SCET and contains logs of  $\mu/Q$ .  $J_q$  describes the collinear final-state radiation in the outgoing (current) jet giving it an invariant mass  $t_J$  [and is independent of (light) quark flavor], and  $B_q$  or  $\mathcal{B}_q$  the collinear radiation from the incoming proton beam with virtuality  $t_B$ . Both sum logs of  $\mu/(Q\sqrt{\tau})$ . The soft function  $S$  sums the wide-angle radiation carrying momentum  $k_S$  between the beam and jet, and depends on the smallest perturbative physical scale, summing logs of  $\mu/(Q\tau)$ .

The  $\tau_1^b$  cross section depends on the transverse-momentum dependent beam function, accounting for the transverse momentum between the actual jet momentum and the Born-level jet axis  $q + xP$  (and also the transverse momentum of ISR from the proton beam). This convolution does not appear in Eq. (7.20) since the alignment of  $q_J^a$  along the jet axis removes this dependence. The two beam functions appearing in Eqs. (7.20) and (7.21) are related through integration over  $\mathbf{p}_\perp$ , and satisfy a matching condition onto ordinary PDFs with a perturbatively calculable matching coefficient [248–253].

The factorization of the singular parts of the  $\tau_1$  cross sections in Eqs. (7.20) and (7.21)

allows for resummation of the the large logs of  $\tau_1$ . The accuracy to which this resummation is achieved can be defined in terms of the integrated distributions  $\sigma_c(\tau_1) = (1/\sigma_0) \int_0^{\tau_1} d\tau d\sigma/d\tau$ , which can be organized in the form

$$\sigma_c(\tau_1) = C(\alpha_s) e^{[Lg_{\text{LL}}(\alpha_s L) + g_{\text{NLL}}(\alpha_s L) + \alpha_s g_{\text{NNLL}}(\alpha_s L) + \dots]} + D(\alpha_s, \tau_1), \quad (7.23)$$

where  $C$  is a constant coefficient with no logs and  $D$  contains the nonsingular terms. Resummation schemes systematically compute the functions  $g_{\text{N}^k\text{LL}}$  order by order, each summing an infinite tower of logs in the fixed-order expansion of  $\sigma_c$  in  $\alpha_s$ .

The resummation of logs in the cross section into the exponential form given in Eq. (7.23) is achieved by solving the RG evolution equations for each piece of the factorized cross sections, each obeying

$$\mu \frac{d}{d\mu} F(x, \mu) = \gamma_F(\mu) F(x, \mu) \quad \Rightarrow \quad F(x, \mu) = F(x, \mu_0) \exp \left[ \int_{\mu_0}^{\mu} \frac{d\mu'}{\mu'} \gamma_F(\mu') \right], \quad (7.24)$$

where  $F = H, B(\mathcal{B}), J, S$  (or, in this form, their Laplace/Fourier transforms),  $x$  is the natural variable for each function, and  $\gamma_F$  is the anomalous dimension. The solution for  $F$  allows one to evaluate each function  $F$  at a scale  $\mu_0$  where the perturbative logs within each are minimized, and the large logs of  $\mu/\mu_0$  at any other scale  $\mu$  are summed into the exponential. The order to which these logs are resummed (the number of towers in Eq. (7.23)) is determined by the accuracy to which the anomalous dimensions are known, each of which takes the form:

$$\gamma_F(\mu) = -\kappa_F \Gamma_{\text{cusp}}[\alpha_s] \ln \frac{\mu}{Q_F} + \gamma_F[\alpha_s], \quad (7.25)$$

where  $\kappa_F$  is a constant,  $\Gamma_{\text{cusp}}$  is a universal ‘‘cusp’’ anomalous dimension,  $Q_F$  is the natural physical scale for the function  $F$  [e.g.  $Q_H = Q, Q_{J,B} = Q/(e^{\gamma_E \nu})^{1/2}, Q_S = Q/(e^{\gamma_E \nu})$ , where  $\nu$  is the Laplace transform variable for  $\tau_1$ ], and  $\gamma_F[\alpha_s]$  is the ‘‘non-cusp’’ part of the anomalous dimension. Because the cusp piece is enhanced by a log, it needs to be known to one higher order in  $\alpha_s$  than the non-cusp piece to achieve a given order of logarithmic accuracy. The order to which each piece is needed at a given resummed logarithmic accuracy is summarized in, e.g., [239].

To date, the cusp anomalous dimension is known to four-loop ( $\alpha_s^4$ ) accuracy [254–257], and the non-cusp anomalous dimensions for the  $\tau_1$  beam, jet, and soft functions to three-loop ( $\alpha_s^3$ ) accuracy. The hard and jet functions themselves are known to  $\alpha_s^3$  [], and the beam and soft functions to  $\alpha_s^2$  accuracy []. This makes it possible to compute DIS 1-jettiness  $\tau_1^{a,b}$  distributions currently to N<sup>3</sup>LL resummed accuracy (see, e.g., [247]). Furthermore the non-singular part of the  $\tau_1^b$  distribution has been computed to first nontrivial order  $\mathcal{O}(\alpha_s)$  in [258].

In addition to the resummation of perturbative logs, the 1-jettiness distributions receive nonperturbative corrections due to hadronization in the final state, growing more important for smaller  $\tau_1$ . These can be accounted for in the soft function, which can be taken to

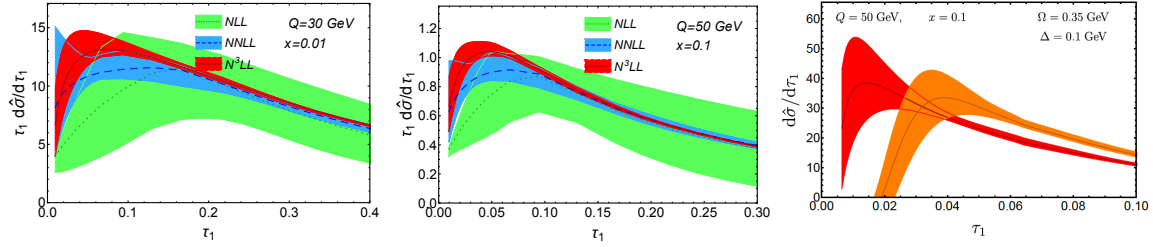


**Figure 7.34:** Theoretical predictions for 1-jettiness (or DIS thrust)  $\tau_1^b$  distributions, from LL to  $N^3$ LL accuracy at  $Q = 30$  GeV,  $x = 0.01$  (left) and  $Q = 50$  GeV,  $x = 0.1$  (center). The right-most panel shows the distribution before (red) and after (orange) convolution with a nonperturbative shape function, which for sufficiently large values of  $\tau_1$  has the primary effect of shift the perturbative distribution to the right, controlled by a universal shift (first moment) parameter  $\Omega_1$ , taken here to be  $0.35$  GeV. A robust determination of  $\alpha_s$  from event shape measurements will also fit for  $\Omega_1$  at the same time.

have the form [259–261]:

$$S(k, \mu) = \int dk' S_{\text{PT}}(k - k', \mu) f_{\text{NP}}(k'), \quad (7.26)$$

for a model function  $f_{\text{NP}}$ . For  $k \sim \Lambda_{\text{QCD}}$  (i.e.  $\tau_1 \sim \Lambda_{\text{QCD}}/Q$ ), the full shape function  $f_{\text{NP}}$  is needed to describe the distribution. Above these values  $\tau_1 \gg \Lambda_{\text{QCD}}/Q$ , an OPE can be performed. For sufficiently large  $\tau_1$ , it can be shown that the first moment of the shape function is given by universal quantity,

$$\int_{-\infty}^{\infty} dk k f_{\text{NP}}(k) = \frac{2\Omega_1}{Q}, \quad (7.27)$$

where  $\Omega_1$  is given by a universal vacuum matrix element of soft Wilson lines [259,262], and is the same for all three versions of  $\tau_1^{a,b,c}$  we have considered [235]. It can be considered, for sufficiently large  $\tau_1$ , to simply cause a shift of the distribution  $d\sigma/d\tau_1$  to the right by  $2\Omega_1/Q$ , and the value of  $\Omega_1$  can be determined by a simultaneous fit for it and for  $\alpha_s$  to the data.

Further refinements can be made to these theoretical predictions, such as accounting for the effect of finite hadron masses on the nonperturbative corrections [263,264], subtracting renormalon ambiguities between the perturbative and nonperturbative contributions [261, 265], and, of course, computing the nonsingular corrections to higher order in  $\alpha_s$ . For direct comparison to experimental results, accounting for cuts on jet/hadron energies, rapidities, jet radii  $R$ , etc. will also be necessary. Track-based observables may also be considered, for which theoretical technology has been developed [266,267] and ought to be explored at EIC. All of of these are tasks that should be carried out to enable the highest precision determination of  $\alpha_s$  and  $\Omega_1$  possible from DIS event shapes.

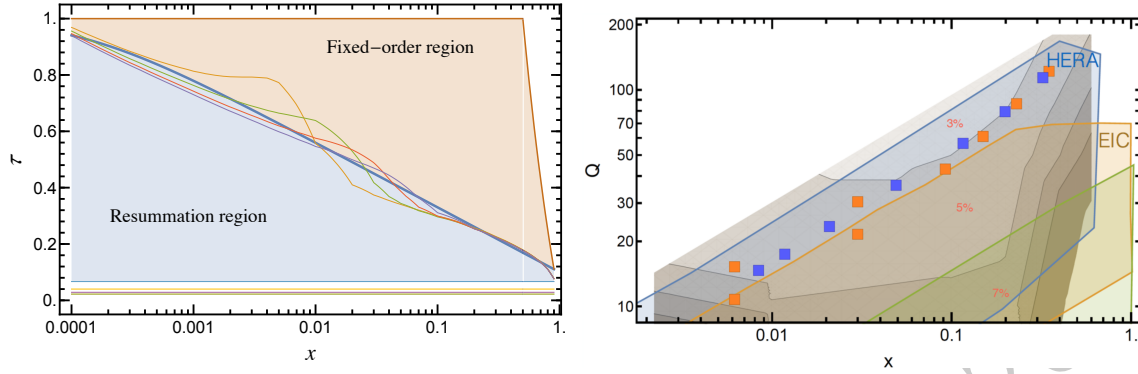


**Figure 7.35:** *Left:* region in  $\tau = \tau_1^b$  over which resummed perturbation theory is expected to be more reliable than fixed-order perturbation theory, based on the value of  $\tau$  at which singular logs and nonsingular terms become of comparable size [258]. *Right:* Contours of theoretical uncertainty in  $x, Q$  space, with coverage at HERA and (expected) EIC. Squares are values of  $x, Q$  for actual previous HERA analyses.

## Predictions

In Fig. 7.34 we show some of our predictions for  $\tau_1^b$  distributions to  $N^3LL + \mathcal{O}(\alpha_s)$  accuracy. The uncertainties are estimated by varying the scales  $\mu_{H,J,B,S}$  between which the RG evolution is performed to resum the large logs, as well as the scale  $\mu_{ns}$  at which the non-singular fixed-order piece is evaluated. The predictions also include the effect of a simple shape function, whose first moment is given by  $2\Omega_1$ , with  $\Omega_1$  set to 0.35 GeV. One observes the good convergence in the perturbative region from one order to the next. In general, the theoretical uncertainties improve for larger  $Q$  (due to better behaved perturbative series), and, somewhat surprisingly, for smaller  $x$ . The resummation is turned off smoothly as  $\tau_1$  grows large, and fixed-order predictions become more reliable than resummed. This occurs around a value  $\tau_1$  where the total contribution of the singular logs at fixed order in  $\alpha_s$  becomes numerically comparable to the non-singular function, and based on  $\mathcal{O}(\alpha_s)$  predictions [258], this transition value turns out to be a function of  $x$ , see Fig. 7.35. This appears to be due to relative contributions of quark and gluon PDFs to the  $\tau_1^b$  distribution as a function of  $x$ . This observation, however, is based on studies that do not yet include any resummation of logs of  $x$  for very small  $x$ .

In Fig. 7.35 we also plot contours of theoretical uncertainty in current  $N^3LL$  predictions for  $\tau_1^b$  in  $Q, x$  space, compared to (projected) coverages at HERA and EIC, serving as a preliminary guide for where the best precision phenomenology might be expected. At present the best theoretical precision is achieved in a central region of  $Q, x$  reflecting values that balance better perturbative behavior with smaller uncertainties from PDFs, as alluded to above.

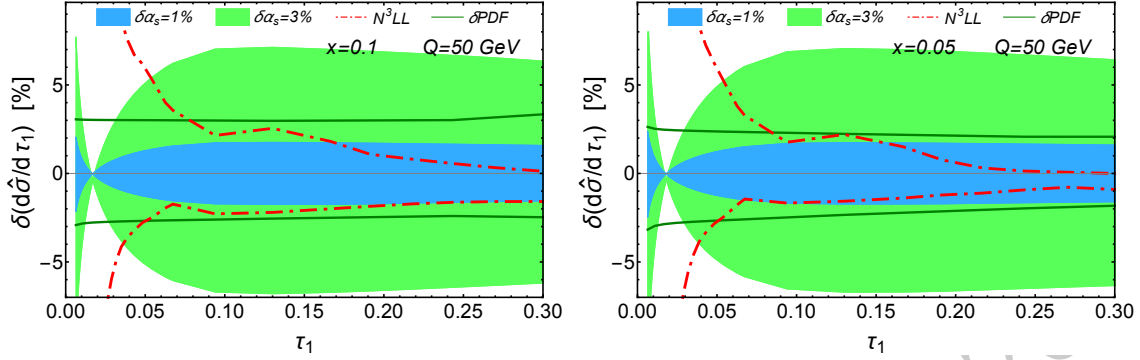


**Figure 7.36:** Current theoretical uncertainties in  $N^3LL$  predictions for  $\tau_1$  (red dot-dashed) vs. the variations in the cross section from 1% (blue) or 3% (green) variations of  $\alpha_s(M_Z)$  itself, along with the uncertainties in the PDF set used in these predictions (grey), at  $Q = 50$  GeV and  $x = 0.1$  (left) and  $x = .05$  (right). [change values?]

### Fitting for $\alpha_s$

In Fig. 7.36 we illustrate the current theoretical uncertainties in our  $N^3LL$  predictions for  $\tau_1$  (red dot-dashed) vs. the variations in the cross section from 1% (blue) or 3% (green) variations of  $\alpha_s(M_Z)$  itself, along with the uncertainties in the PDF set used in these predictions (grey). These indicate that a single prediction and measurement of a  $\tau_1$  distribution could yield a determination of  $\alpha_s(M_Z)$  at the few percent level, with the prospect of using data from many  $x, Q$  values only improving the ultimate sensitivity.

The theoretical predictions depend sensitively on the values of  $\alpha_s$  and, depending on region of  $\tau_1$ , on nonperturbative corrections. As reviewed above, for large enough  $\tau_1$ , the dominant nonperturbative effect is a shift by  $2\Omega_1/Q$ . Thus many recent event-shape-based extractions [268–271] of the strong coupling involve a two-parameter,  $\{\alpha_s(Q_0), \Omega_1\}$ , fitting procedure, using measurements in the relevant region of the event shape distributions. The resulting analysis yields a correlation matrix that describes the degeneracy between the two parameters. Sampling a wide range in  $x - Q^2$  is expected to play an important role in breaking this degeneracy.

In practice, the theoretical predictions are integrated over a region of  $x - Q^2$  and then binned in the event shape,  $\tau$ .<sup>3</sup> This way theoretical and experimental distributions are directly comparable. The fit can be performed within a single range of  $x - Q^2$  or simultaneously for all or a sample of ranges. This freedom is helpful for controlling the various systematics that may enter the theoretical distributions, such as PDF uncertainties and non-perturbative effects.

Finally one needs to decide which region of the event shape spectrum (i.e., which bins in  $\tau$ ) should be included in the analysis. This determination depends on many aspects and the

<sup>3</sup>The computational heavy task of integrating over the  $x - Q^2$  ranges might be a limiting factor and how various non-perturbative effects are incorporated (simple shift vs. shape function, renormalon subtraction, etc.)

dependence of the fitting results on this choice is a manifestation of the degeneracy of the two fitting parameters. Some deciding factors will be: i) the range of  $x - Q^2$  which changes the location of the boundary between the resummation and fixed order QCD regions (see Fig. 7.35 left panel), ii) the treatment of non-perturbative corrections will play an important part in which bins are incorporated in the small  $\tau$  region. It is therefore important to have sufficiently fine binning in the observable to allow for carefully choosing the region for which a more reliable extraction can be performed.

### Experimental projections

This section assesses the experimental issues in the measurement of 1-jettiness at the EIC, for a high-precision determination of the strong coupling  $\alpha_s$ . In this first assessment of experimental capabilities we focus on the measurement of  $\tau_1^a$  (Eq. 7.19) in kinematic region  $Q > 30$  GeV, where the calculational precision is expected to be greatest (Sect. 7.1.7).

For this study, DIS events for  $E_e=18$  GeV and  $E_p=275$  GeV are generated using the PYTHIA8 4C tune [272]. The Truth distributions for  $\tau_1^a$  are determined using these events at the particle level. Instrumentation effects are modeled using the DELPHES framework [273], with detector parameters as specified by the EIC Detector Working Group [274]. The tracking and calorimetry efficiency and resolution maps are based on the EIC detector handbook 1.2 [275], and on the detector matrix provided by the EIC detector working group [274] and collected in the DELPHES card [276].

We classify experimental and instrumentation effects in the measurement of  $\tau_1^a$  as follows, from the more general to the more specific:

1. **Integrated luminosity:** We assume integrated luminosity of  $10 \text{ fb}^{-1}$  ( $E_e+E_p=18+275$  GeV). We scale the differential cross section for the  $\tau_1^a$  distribution generated by PYTHIA with this value to obtain the projected statistical precision in the chosen binning;
2. **Experimental acceptance:**  $|\eta| < 3.5$  for both tracking and calorimetry;
3.  **$Q^2$  resolution:**  $Q^2$  is calculated as the invariant square of the 4-momentum difference between the hardest final-state electron (detector-level) and the incoming electron. We assume that the energy of the incoming electron of 18 GeV is known precisely and only tracking efficiency and tracking momentum resolution of the scattered electron contribute to the  $Q^2$  resolution.
4. **Particle identification:** We explore the effects of limited and no PID over the phase space of the measurement. In the case of no PID, we use the assumptions that all particles have zero mass or the pion mass;
5. **Tracking efficiency:** Charged particles with transverse momentum  $p_T > 0.1$  GeV only are reconstructed. The tracking efficiency is taken to be greater 95% over the full acceptance range, with  $p_T$  and  $\eta$  dependence as parametrized in [276].

6. **Track  $p_T$  resolution:** At  $\eta = 1.5$ , the  $p_T$ -resolution is taken to be 1% at  $p_T = 1 \text{ GeV}/c$  and 1.2% at  $p_T = 10 \text{ GeV}/c$ , with  $p_T$  and  $\eta$  dependence as parametrized in [276].
7. **ECal calorimeter resolution:** 12% stochastic term and 2% linear term, corresponding to a W/ScFi calorimeter with granularity  $2.5 \times 2.5 \text{ cm}$ ;
8. **HCal calorimeter resolution;** 10% linear term and a 50% stochastic term. The resolution in the endcaps is based on EIC detector handbook 1.2, while the resolution at mid-rapidity is based on the sPHENIX HCal [276].

### Jet measurement performance

The axes used for minimization in  $\tau_1^q$  are the beam direction and the jet centroid axis (Eqs. 7.16 and 7.19). The jet is determined using the anti- $k_T$  algorithm [277] with  $R = 1$ , and we assume the pion mass for all tracks and clusters. The jet centroid is defined using the  $p_T$ -weighted average of jet constituents. In each event we utilize the highest- $p_T$  jet whose centroid lies within  $|\eta| < 2.5$ .

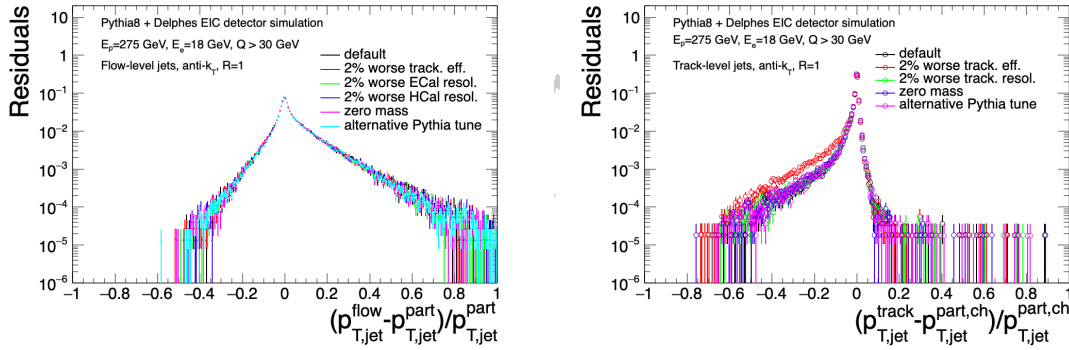


**Figure 7.37:** Residuals distribution for  $R = 1$  for fully-reconstructed (left) and track-level jets (right), for various choices of detector parameters.

In order to show the impact of detector effects on the jet measurement, we calculate the relative difference in jet  $p_T$  at detector and particle-level. Figure 7.37 shows such difference for the default detector parameters and for a set of systematic variation of those parameters, for both fully-reconstructed jets (“flow-level”, which uses Delphes particle-flow information as input) and track-level jets. The Delphes algorithm combines the information from the tracking and calorimetry systems and produces an exclusive set of tracks, photons and neutral hadrons. By track-level jets we denote those jet found using solely tracks as input. The residuals distributions are significantly non-Gaussian, especially for track-level jets, with RMS of 11% and 4% for full and track-level respectively.

Figure 7.37 shows the relative difference for variations in track  $p_T$ -resolution and efficiency, PID assumption, calorimeter resolution, and PYTHIA tune. The width and the tails of the

distributions are largely robust against these variations, with the exception of tracking efficiency for track-level jets. The next step in this assessment is to revisit Fig. 7.37 with performance parameters and systematic uncertainties in them corresponding to specific proposed designs for EIC detectors.

### $\tau_1^a$ measurement performance

Once the hardest jet in the event is found, we loop over all particles in the acceptance and compute the scalar product of each particle four-vector and the jet four-vector as well as the product of the particle four-vector and that of the beam, according to Eqs. 7.16 and 7.19. The minimum of the two products is chosen and accumulated in a loop to obtain  $\tau_1^a$  after normalization by  $Q^2$ .

We then calculate  $\tau_1^a$  at both particle and detector-level. At detector level we again consider two cases: the observable is computed using only tracks as input and the observable is computed using the particle-flow components as input.

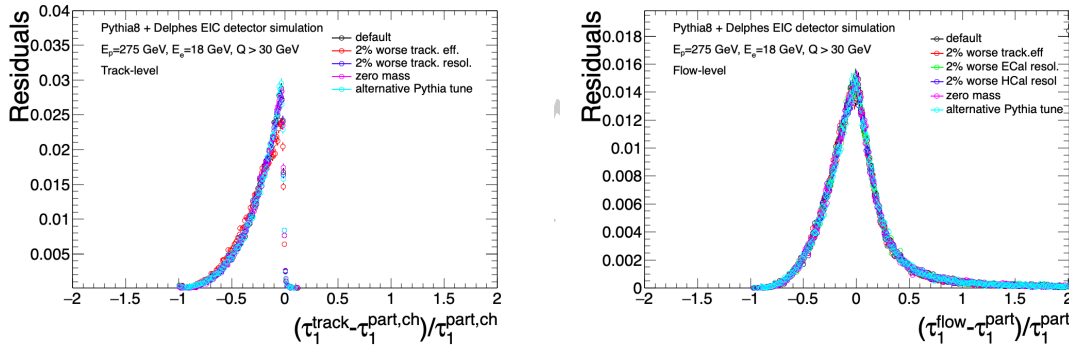


**Figure 7.38:** Residual distributions of  $\tau_1^a$  at particle and detector-levels, for variations choices of detector performance.

Figure 7.38 shows the relative difference of  $\tau_1^a$  at detector and particle level, at both track-level and particle-flow level, and with the same variations in detector performance considered in Fig. 7.37. The residuals distributions are again significantly non-Gaussian, especially at track-level, with RMS of 18% and 36% for track and flow-level respectively. In this case, however, the residuals distribution is largely insensitive to the variations in detector performance considered here.

Figure 7.39 shows directly the distributions of  $\tau_1^a$  at flow and track-level, again for various choices of detector performance. The most notable feature of the figure is the significant change in the distribution from flow (all particles) to track-level (charged tracks only). The systematic shift to lower value of  $\tau_1^a$  for the track-level measurement is due to both lower jet  $p_T$  and fewer terms in the sum in the numerator of Eq. 7.16. Variations in detector

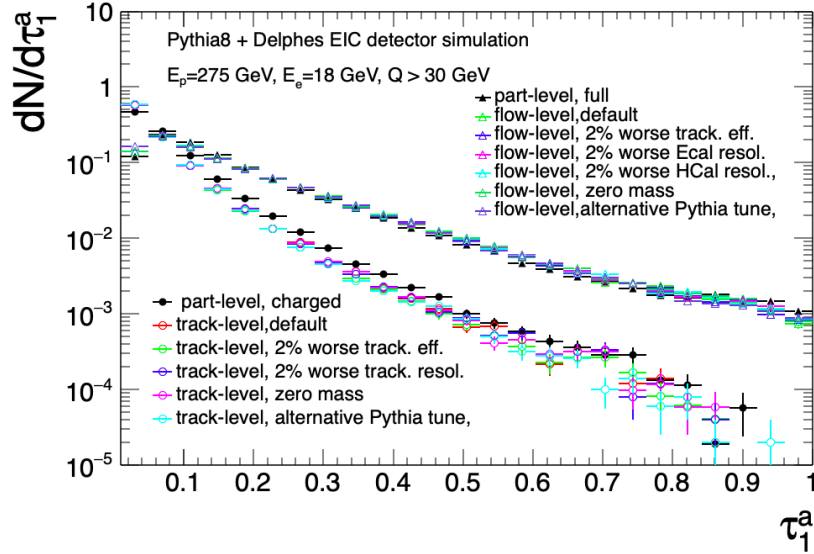


**Figure 7.39:** Distribution of  $\tau_1^a$  at particle and detector-levels, for variations choices of detector performance.

performance give much smaller variation in the  $\tau_1^a$  distribution than the shift in the overall distribution from flow to track-level.

### Systematic Uncertainties and Unfolding

The goal of this analysis is a high-precision measurement of  $\tau_1^a$ . Sect. 7.1.7 outlines the main instrumentation effects for this measurement. If the instrumental response due to these effects is known quantitatively, this information can be utilized to correct such effects and maximize the precision of the measurement, using the approach of regularized unfolding. In this section we estimate the precision achievable for measuring  $\tau_1^a$  at EIC, using unfolding.

The precision of an unfolding procedure is dependent upon the statistical precision of the raw data. As noted above, we utilize the differential cross section for  $\tau_1^a$  given by PYTHIA, scaled by the assumed integrated luminosity of  $10 \text{ fb}^{-1}$ , to calculate the statistical uncertainty in the “raw”  $\tau_1^a$  distributions. We then vary the content of each bin using a Poisson distribution with mean of the number of projected counts.

The unfolding procedure uses the Bayesian approach, as implemented in RooUnfold [278]. The response matrix is constructed by calculating  $\tau_1^a$  at the particle and detector level for each event.

We consider the following contributions to the systematic uncertainty of the  $\tau_1^a$  measurement:

1. Tracking efficiency is degraded by (absolute) 2%. A few percent uncertainty is motivated by the magnitude of the discrepancy between the MC and data in describing the tracking efficiency in LHCb [279] and ALICE [].
2. 2% poorer energy resolution of the ECal and the HCal calorimeters.
3. Variation in Pythia8 tune: Monash tune. Further studies will utilize Herwig.
4. Mass assumption: compare assumption of pion mass for all tracks (default) and perfect PID at detector level.

For each systematic variation, a new response matrix is constructed and the unfolding procedure is repeated.

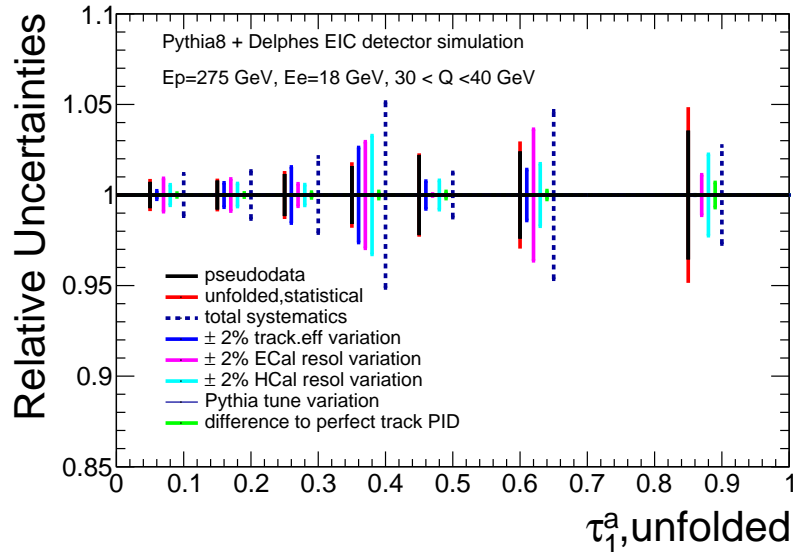


**Figure 7.40:** Relative statistical and systematic uncertainties of the unfolded  $\tau_1^a$  distribution (flow-level) for events with  $30 < Q < 40$  GeV

Figure 7.40 shows the results of this unfolding procedure for  $\tau_1^a$  at the flow level, for events with  $30 < Q < 40$  GeV. Statistical uncertainties of the raw distribution and the unfolded solution in the range  $0.1 < \tau_1^a < 0.7$  are within 2%. The systematic variations in detector performance, described above, give systematic uncertainty in that region on the order of 4%, as indicated by the dashed lines.

## Discussion

Figure 7.40 indicates that statistical and systematic uncertainties of flow-level  $\tau_1^a$   $30 < Q < 40$  GeV are expected to be of the order of 2 to 4 % over the full range of the distribution, for this specific choice of binning in virtuality  $Q$ . Assessing the correlation between the statistical and systematic uncertainties is beyond the scope of this report.

Note that the largest contributions to the systematic uncertainties in Fig. 7.40 are due to the calorimeter performance. As the next step in this analysis, calorimeter performance based upon specific EIC designs should be considered, include the projected effects and uncertainties due to calorimeter non-linearity.

In addition, Fig. 7.40 indicates that track-level measurements may have greater relative precision experimentally. As noted in Sect. 7.1.7, theoretical calculations of track-level event shape observables with controlled and improvable precision may be possible, though such an approach still requires development in both theory and experiment. We will continue to consider the measurement of  $\tau_1^a$  and other event shape observables at both the flow and track-levels.

As discussed in Sect. 7.1.7, fundamental parameters of QCD will be extracted by comparing analytic calculations to the EIC data in bins of  $Q$  and  $x$ .

In this section, we have performed a first evaluation of the expected measurement precision of  $\tau_1^a$ . Uncertainties of few percent are to be compared to systematic uncertainties of typically 10% in  $\alpha_s$  extractions at HERA using inclusive jet cross sections [280] for instance. Further investigation requires with MC pseudo-data based on specific EIC detector designs, together with the application of Bayesian Inference tools [281].

## 7.2 Multi-dimensional Imaging of Nucleons, Nuclei, and Mesons

**Imaging in position space — form factors and GPDs:** The electromagnetic form factors are among the most basic and fundamental quantities containing information about the structure of strongly interacting systems like the nucleon, nuclei and mesons. They are measured through elastic electron scattering, and they depend on the momentum transfer to the target,  $t = -Q^2$ . For the spin- $\frac{1}{2}$  nucleon two such form factors exist, where one considers either the Dirac form factor  $F_1$  and Pauli form factor  $F_2$ , or the electric and magnetic form factor  $G_E$  and  $G_M$ , which are linear combinations of  $F_1$  and  $F_2$ . For a heavy target, the Fourier transforms of  $G_E$  and  $G_M$  can be interpreted as the 3D distribution of charge and magnetization, respectively. But for the nucleon, and especially for the even lighter pions or kaons, such 3D distributions have no clean interpretation due to relativistic corrections. This problem does not arise for 2D distributions when the two dimensions are perpendicular to the (average) momentum of the incoming and outgoing nucleon. For instance, the

2D electric charge distribution of the nucleon is given by the Dirac form factor through

$$\rho(b_T) = \int \frac{d^2\vec{q}_T}{(2\pi)^2} F_1(Q^2 = q_T^2) e^{i\vec{q}_T \cdot \vec{b}_T}, \quad (7.28)$$

with  $\vec{q}_T$  denoting the total transverse momentum transfer to the target and  $\vec{b}_T$  the transverse position (impact parameter). In Sec. 7.2.1 the prospects for measuring electromagnetic form factors at the EIC for the proton, the deuteron and light mesons are outlined in detail. Information about the electromagnetic neutron form factors can be extracted from electron-deuteron scattering. The 2D charge distribution in Eq. (7.28) are related to the momentum-fraction-dependent ( $x$ -dependent) impact parameter distribution for individual quarks  $q(x, b_T) = f_1^q(x, b_T)$  according to

$$\rho(b_T) = \sum_q e_q \int dx q(x, b_T), \quad (7.29)$$

where  $e_q$  is the quark charge in units of the elementary charge. It is very interesting that  $q(x, b_T)$  can actually be measured because of its relation to a generalized parton distribution (GPD),

$$q(x, b_T) = \int \frac{d^2\vec{q}_T}{(2\pi)^2} H_q(x, \xi = 0, q_T^2) e^{i\vec{q}_T \cdot \vec{b}_T}, \quad (7.30)$$

with  $\xi$  indicating the longitudinal momentum transfer to the target. GPDs enter the QCD description of hard exclusive processes like deep-virtual Compton scattering and meson production [Excl. sidebar ?]. The kinematic coverage of the EIC for the DVCS process is shown in Fig. 7.41. Because of the spin degree of freedom, several quark (and gluon) impact parameter distributions can be defined for the nucleon, similar to the PDFs discussed above. The information encoded in GPDs is extraordinary rich since they also allow one to address the parton orbital angular momentum, as well as the distribution of pressure and shear forces inside a hadron. The EIC will be able to move this important field to the next level, where the corresponding discussion can be found in Sec. 7.2.2.

**Imaging in momentum space — TMDs:** Ordinary PDFs provide a 1D image of hadrons in momentum space. Put differently, we “only” learn about the longitudinal motion of partons in a fast-moving hadron, that is, about their momentum distributions along the direction singled out by the hard momentum flow in the process. However, because of confinement and the uncertainty principle, the partons also have a nonzero transverse momentum relative to that direction. (In this context, people often talk about “confined motion.”) It therefore makes sense to define transverse momentum dependent parton distributions (TMDs), where for an unpolarized target and unpolarized quark one typically uses the notation

$$q(x, k_T) = f_1^q(x, k_T). \quad (7.31)$$

Once transverse parton momenta are taken into account, 8 leading-twist quark TMDs can be identified — see table [TMD-SIDIS sidebar?] for a complete list of quark TMDs. TMDs thus provide 3D images of hadrons in momentum space and as such are complementary to GPDs. In inclusive DIS the information about the transverse parton motion is integrated

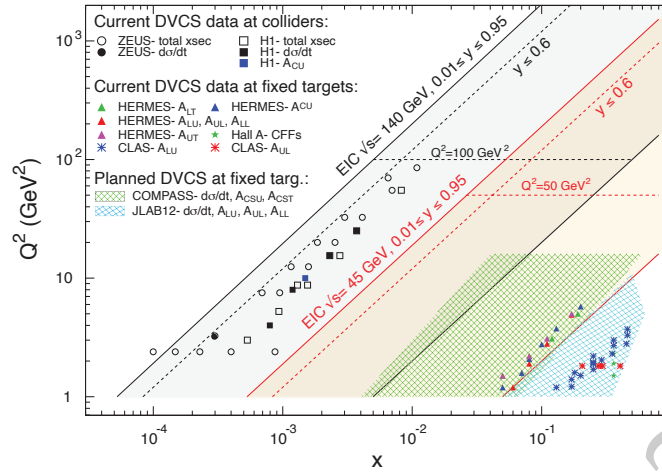


**Figure 7.41:** The kinematic coverage of the EIC for DVCS compared to that of previous experiments.

out, which means that other reactions must be considered to address TMDs. A flagship process for measuring TMDs is semi-inclusive DIS where, in addition to the lepton, one hadron is detected [TMD-SIDIS sidebar?]. In Fig. 7.42 we display the kinematic coverage of the EIC for two important TMD observables. It must be stressed that TMDs can also be studied via different final states in electron-nucleon collisions and, for instance, in reactions that are not lepton-induced such as the Drell-Yan process. The fact that TMDs can be measured through a large number of scattering processes adds to their significance. Like in the case of GPDs and imaging in position space, there is no doubt that the EIC will tremendously enhance our knowledge about the momentum space imaging of the nucleon as discussed in Sec. 7.2.3.

**Wigner functions:** Wigner functions can be considered the quantum-mechanical counterpart of classical phase space distributions. In non-relativistic quantum mechanics they contain the same information as the wave function of a system. Interestingly, Wigner functions can also be defined for partons in quantum field theory. A generic partonic Wigner function  $W(x, k_T, b_T)$  depends on the longitudinal and transverse parton momenta as well as the impact parameter. Therefore, Wigner functions not only contain all the physics encoded in TMDs and GPDs but also additional information [figure similar to WP?]. For instance, they allow one to study spin-orbit correlations that are similar to the ones known from systems like the hydrogen atom. The relation of the parton orbital angular momentum to a specific Wigner function is one example in that regard. For some time it was unclear if, even as a matter of principle, partonic Wigner functions can be measured. But in the meantime some processes have been identified which are directly sensitive to those objects in a model-independent manner. In relation to the EIC, at present the diffractive exclusive di-jet production is of particular interest, which holds promise to give access to Wigner functions for gluons. More details about partonic Wigner functions and how the EIC can make significant contributions to this field are given in Sec. 7.2.4.

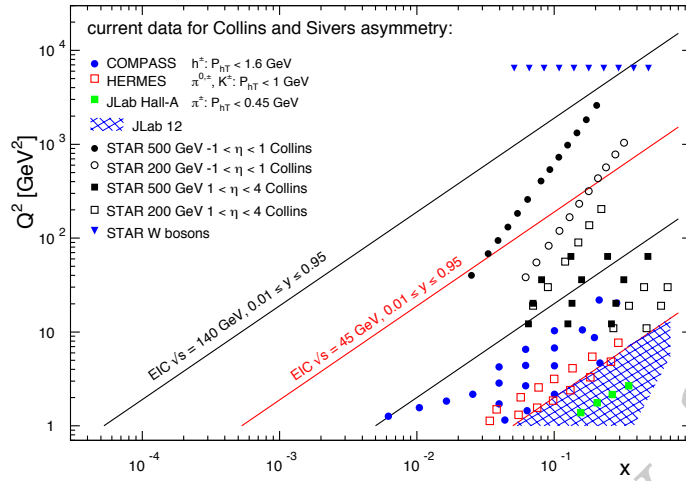


**Figure 7.42:** The kinematic coverage of the EIC for the Sivers and Collins effects compared to that of previous experiments.

**Light (polarized) nuclei:** High-energy lepton scattering off light nuclei ( $d$ ,  ${}^3\text{He}$ ,  ${}^4\text{He}$ ) typically serves a dual purpose. First, both deuteron and  ${}^3\text{He}$  targets can be used to study the neutron, which is important for a complete picture of the nucleon. This not only applies to PDFs, but also to GPDs and TMDs. Nuclear corrections complicate the extraction of information about the neutron from light nuclei, but there exists decade-long expertise in this field to build on. Second, obtaining information about the light nuclei is very interesting in its own right. Topics include the investigation of the EMC effect in position space, exploring the pressure distributions in light nuclei, and exploiting the very unique opportunities which the spin-1 deuteron target offers through its possible tensor polarization. The prospects of this field at the EIC are summarized in Sec. 7.2.5.

## 7.2.1 Nucleon and Meson form factors

### Nucleon Form Factors

Measurements of the unpolarized electron-proton ( $ep$ ) elastic scattering cross section – the cross section for the process where the final state consists of only an electron and proton with soft real photon radiation – at the future EIC will allow us to probe the proton magnetic form factor up to the highest-ever  $Q^2$ . As shown on the left side of Fig. 7.44, with the form factors parameterized by the form given in Ref. [282] and using the fit parameters in Ref. [283], the EIC can potentially make measurements of the  $ep$  elastic cross section up to  $Q^2 \approx 45 \text{ GeV}^2$ . Though unlike fixed target experiments, in collider kinematics, the data collected will be at  $\epsilon \sim 1$ .

If the central arm acceptance on the electron side extends down to  $\eta = -3.5$ , then the electron

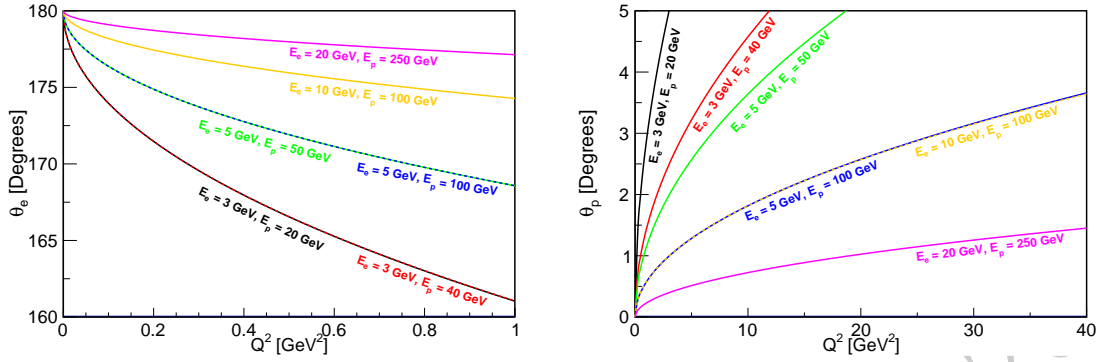


**Figure 7.43:** Left figure shows the electron scattering angle and the right figure the proton scattering angle for different values of  $Q^2$  and for different beam energy combinations.

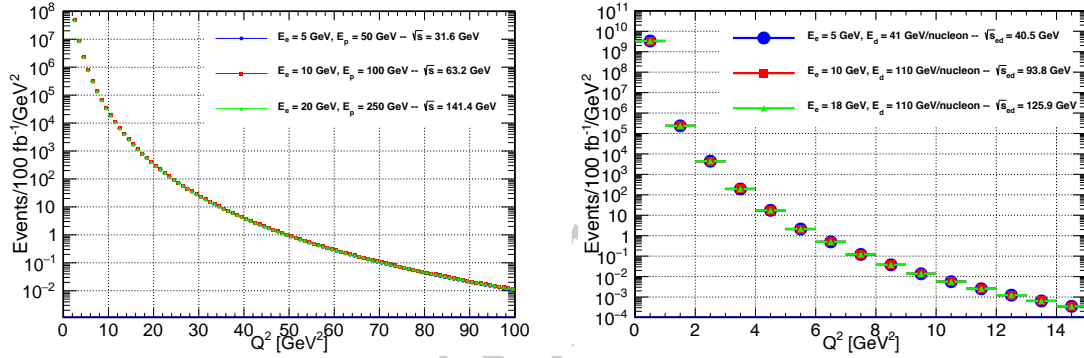


**Figure 7.44:** The left panel shows the expected counts from elastic  $ep$  scattering in an EIC. The right panel shows the expected counts from elastic  $ed$  scattering. Both panels show how the rates change with the beam energies.

will enter the central acceptance at  $Q^2$  below  $1 \text{ GeV}^2$  (except for the highest  $\sqrt{s}$  setting). In order to suppress inelastic backgrounds, it is necessary to detect the proton as well, and far forward detectors will be needed for lower  $Q^2$ , see Fig. 7.43.

Determination of the proton form-factor ratio at high  $Q^2$  via double-spin asymmetry measurements will most likely not be possible due to the small expected asymmetry. However, the addition of a positron beam at the EIC would allow for the study of hard two-photon exchange effects at high  $Q^2$  [284].

Measurements of the unpolarized electron-deuteron cross section are possible at the EIC up to  $Q^2 \approx 5 \text{ GeV}^2$  (see right side of Fig. 7.44), and measurements of the tensor-polarized asymmetry can be made up to  $Q^2 \approx 2.5 \text{ GeV}^2$ , see Fig. 7.46. Here the deuteron form factors for the cross section calculation come from a refit of the Abbott experimental data [285–288]. At low  $Q^2$ , this asymmetry is experimentally well known [289, 290] and can be used to help determine the polarization of a stored tensor polarized deuteron beam.

Because only lower- $Q^2$  measurements are possible here, it is preferable to extend the elec-

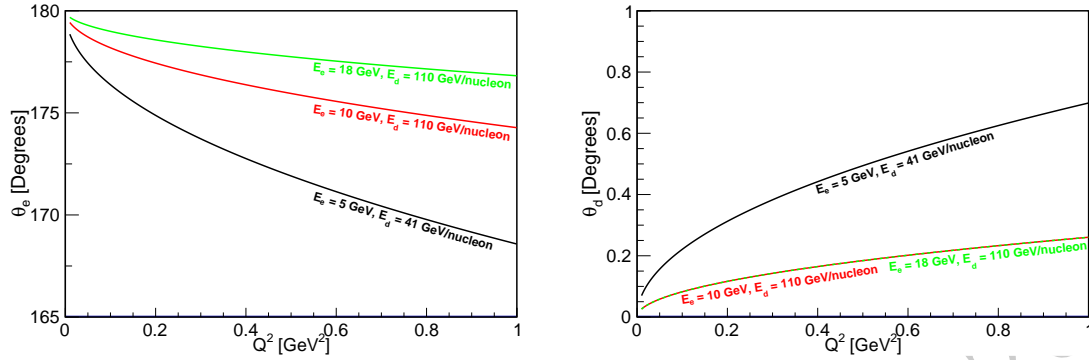


**Figure 7.45:** Left figure shows the electron scattering angle and the right figure the deuteron scattering angle for different values of  $Q^2$  and for different beam energy combinations.

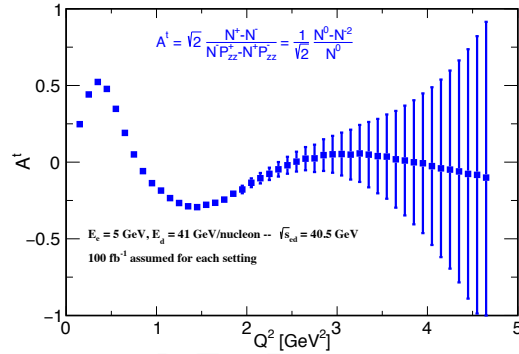


**Figure 7.46:** Shown is the tensor polarized deuteron asymmetry for elastic scattering.

tron acceptance down to  $\eta = 4$ , see Fig. 7.45. It is also necessary to detect the scattered deuteron in order to suppress inelastic background, and far-forward detectors will be required for this.

A positive tensor polarization for the deuterium beam along the beam direction can be achieved using high polarization in the  $m = +1$  or  $m = -1$  state. If the EIC is unable to create deuterons in the  $m = 0$  state (which has a negative tensor polarization), a possible way of creating a negative tensor polarization along the beam direction is shown in the right side of Fig. 7.46. Here, *ed* elastic data is simulated first assuming a negative tensor polarization along the beam direction (blue points); then the simulation is repeated with a polarization perpendicular (positive vector, positive tensor) to the beam direction. Cross sections for these two cases are equivalent.

### Meson Form Factors

Measuring meson form factors can help elucidate the interplay between emergent hadronic mass and the Higgs-mass mechanism, see Sec. 7.1.4 and Table 7.1. The exper-

imental determination of the  $\pi^+$  electric form factor ( $F_\pi$ ) is challenging. The best way to determine  $F_\pi$  would be elastic  $e\pi$  scattering. However, the lifetime of the  $\pi^+$  is only 26.0 ns. Since  $\pi^+$  targets are not possible, and  $\pi^+$  beams with the required properties are not yet available, one must employ high-energy exclusive electroproduction,  $p(e, e'\pi^+)n$ . This is best described as quasi-elastic ( $t$ -channel) scattering of the electron from the virtual  $\pi^+$  cloud of the proton, where  $t$  is the Mandelstam momentum transfer squared  $t = (p_p - p_n)^2$  to the target nucleon. As discussed in Sec. 7.1.3, scattering from the  $\pi^+$  cloud dominates the longitudinal photon cross section ( $d\sigma_L/dt$ ) at sufficiently small  $-t$ .

To reduce background contributions, normally one separates the components of the cross section due to longitudinal (L) and transverse (T) virtual photons (and the LT, TT interference contributions), via a Rosenbluth separation. However, L/T separations are impractical at the EIC, due to the impossibility of acquiring low  $\epsilon$  data. Below, we propose an alternate technique to access  $\sigma_L$  via a model, validated with exclusive  $\pi^-/\pi^+$  ratios from deuterium. Once  $d\sigma_L/dt$  has been determined over a range of  $-t$ , from  $-t_{min}$  to  $-t \sim 0.6 \text{ GeV}^2$ , the value of  $F_\pi(Q^2)$  is determined by comparing the observed  $d\sigma_L/dt$  values to the best available electroproduction model, incorporating off-shell pion and recoil nucleon effects. The obtained  $F_\pi$  values are in principle dependent upon the model used, but one anticipates this dependence to be reduced at sufficiently small  $-t$ . Measurements over a range of  $-t$  are essential as part of the model validation process. JLab 6 GeV experiments were instrumental in establishing the reliability of this technique up to  $Q^2 = 2.45 \text{ GeV}^2$  [291], and extensive further tests are planned as part of JLab E12-19-006.

**Requirements for Separating Exclusive and SIDIS Events** The exclusive  $\pi^+$  channel cross section is several orders of magnitude smaller than neighboring SIDIS background, but is distributed over a much narrower range of kinematics, and this is essential for the separation of the exclusive events from the background. The exclusive  $p(e, e'\pi^+)n$  reaction is isolated by detecting the forward-going high-momentum neutron, i.e.  $e - \pi^+ - n$  triple coincidences. Since the neutron energy resolution is not very good, the neutron hit is used as a tag for exclusive events, and the neutron momentum is otherwise not used in the event reconstruction. Thus, missing momentum is calculated as  $p_{miss} = |\vec{p}_e + \vec{p}_p - \vec{p}_{e'} - \vec{p}_\pi|$

The effectiveness of kinematic cuts to isolate the exclusive  $\pi^+$  channel was evaluated by comparison to a simulation of  $p(e, e'\pi^+)X$  SIDIS events, including both detector acceptance and resolution smearing effects. The most effective cuts are on the detected neutron angle ( $\pm 0.7^\circ$  from the outgoing proton beam), a cut on reconstructed  $-t < 0.5 \text{ GeV}^2$ , and the missing momentum ( $Q^2$ -bin dependent cut. After application of these cuts, the exclusive  $p(e, e'\pi^+)n$  events are cleanly separated from the simulated SIDIS events.

**Determining the Longitudinal Cross Section  $d\sigma_L/dt$**  After the exclusive  $\pi^+$  event sample is identified, the next step is to separate the longitudinal cross section  $d\sigma_L/dt$  from  $d\sigma_T/dt$ , needed for the extraction of the pion form factor. However, a conventional Rosenbluth separation is impractical at the EIC due to the very low proton beam energy required to access  $\epsilon < 0.8$ . Fortunately, at the high  $Q^2$ ,  $W$  accessible at the EIC, phenomenological

models predict  $\sigma_L \gg \sigma_T$  at small  $-t$ . For example, the Vrancx and Ryckebusch Regge-based model [292] predicts  $R = \sigma_L/\sigma_T > 10$  for  $Q^2 > 10 \text{ GeV}^2$  and  $-t < 0.06 \text{ GeV}^2$ , and  $R > 25$  for  $Q^2 > 25 \text{ GeV}^2$  and  $-t < 0.10 \text{ GeV}^2$ . Thus, transverse cross section contributions are expected to be 1.3–14%. The most practical choice appears to be to use a model to isolate the dominant  $d\sigma_L/dt$  from the measured  $d\sigma_{\text{uns}}/dt$ .

To control the systematic uncertainty associated with the theoretical correction to estimate  $\sigma_L$  from the un-separated  $\sigma_{\text{uns}}$ , it is very important to confirm the validity of the model used. This can also be done with EIC data, using exclusive  $^2\text{H}(e, e'\pi^+n)n$  and  $^2\text{H}(e, e'\pi^-p)p$  data in the same kinematics as the primary  $p(e, e'\pi^+n)$  measurement. The ratio of these cross sections is  $R = \frac{\sigma[n(e, e'\pi^-p)]}{\sigma[p(e, e'\pi^+n)]} = \frac{|A_V - A_S|^2}{|A_V + A_S|^2}$  where  $A_V$  is the isovector amplitude, and  $A_S$  is the isoscalar amplitude. Since the pion pole  $t$ -channel process used for the determination of the pion form factor is purely isovector (due to  $G$ -parity conservation), the above ratio will be diluted if  $\sigma_T$  is not small, or if there are significant non-pole contributions to  $\sigma_L$ . The comparison of the measured  $\pi^-/\pi^+$  ratio to model expectations, therefore, provides an effective means of validating the model used to determine  $\sigma_L$ . The same model, now validated, can likely also be used to extract the pion form factor from the  $\sigma_{\text{uns}}$  data.

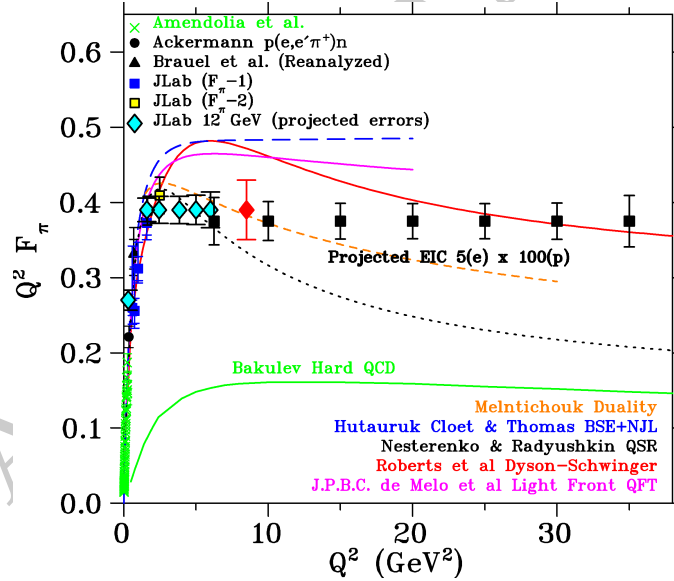


**Figure 7.47:** Existing data (blue, black, yellow, green) and projected uncertainties for future data on the pion form factor from JLab (cyan, red) and EIC (black), in comparison to a variety of hadronic structure models. The EIC projections clearly cover a much larger  $Q^2$  range than the JLab measurements.

**Conclusions** The EIC can allow a pion form factor measurement up to  $Q^2=35 \text{ GeV}^2$ , as shown in Fig. 7.47. The error bars are based on the following assumptions: integrated luminosity of  $20 \text{ fb}^{-1}$  for  $5 \times 100 \text{ GeV}$  measurement, clean identification of exclusive  $p(e, e'\pi^+n)$  events by tagging the forward neutron, cross section systematic uncertainty of 2.5% point-

to-point, and 12% scale,  $R = \sigma_L/\sigma_T = 0.013 - 0.14$  at  $-t_{min}$ ,  $\delta R = R$  systematic uncertainty in the model subtraction to isolate  $\sigma_L$ , pion pole channel dominance at small  $-t$  confirmed in  ${}^2\text{H } \pi^-/\pi^+$  ratios.

**$K^+$  Form Factor** The reliability of the electroproduction method to determine the  $K^+$  form factor is not yet established. JLab E12-09-011 has acquired data for the  $p(e, e'K^+)\Lambda$ ,  $p(e, e'K^+)\Sigma^0$  reactions at hadronic invariant mass  $W = \sqrt{(p_K + p_{\Lambda, \Sigma})^2} > 2.5$  GeV, to search for evidence of scattering from the proton's "kaon cloud". The data are still being analyzed, with L/T-separated cross sections expected in the next  $\sim 2$  years. If they confirm that the scattering from the virtual  $K^+$  in the nucleon dominates at low four-momentum transfer to the target  $|t| \ll m_p^2$ , the experiment will yield the world's first quality data for  $F_K$  above  $Q^2 > 0.2$  GeV<sup>2</sup>. This would then open up the possibility of using exclusive reactions to determine the  $K^+$  form factor over a wide range of  $Q^2$  at higher energies. Studies are planned. While the general technique will remain the same, the  $\pi^-/\pi^+$  validation technique to confirm the  $\sigma_L$  extraction cannot be used for the  $K^+$ . We are optimistic that  $\Lambda/\Sigma^0$  ratios can play a similar role, however, conditions under which the clean separation of these two channels may be possible at the EIC requires further study and would only be possible at CM energies of  $\sim 10$ -50 GeV.

## 7.2.2 Imaging of quarks and gluons in impact-parameter space

A key challenge of nuclear physics is the tomographic imaging of the nucleon, encoded in the Generalized Parton Distribution functions (GPDs). They provide a connection between ordinary parton distribution functions and form factors and hence can describe the correlations between the longitudinal momentum of quarks and gluons and their position in the transverse spatial plane in a nucleon [68, 293].

In the nucleon case, depending on the target and active-parton polarization, one can define four chiral-even GPDs ( $H$ ,  $E$ ,  $\tilde{H}$  and  $\tilde{E}$ ) and four chiral-odd GPDs ( $H_T$ ,  $E_T$ ,  $\tilde{H}_T$  and  $\tilde{E}_T$ ). They depend on three variables (considering the dependence on the factorization scale  $Q^2$  to be known):  $x$ , that is the average longitudinal momentum of the active quark as a fraction of the average target momentum;  $\xi$  and  $t$ , that are, respectively, half the change in the fraction of longitudinal momentum carried by the struck parton and the squared four-momentum transferred to the hadron target. However, one does not have direct experimental access to this multidimensional structure, since the dependence on the three variables enters observables in nontrivial convolutions with coefficient functions.

Since no single process is sufficient to determine GPDs fully, measurement of a variety of processes and observables is necessary to maximally constrain them. Fits of GPDs require educated assumptions for the choice of the fitting functions to incorporate the known theoretical constraints of GPDs, i.e. polynomiality, sum rules, and positivity (see, e.g., Refs. [68, 293–298] for a detailed preface to the GPD formalism and properties). Owing to the factorization property of QCD, a number of related processes are complementary to disentangle the various GPDs and their flavor dependence (see, e.g., Refs. [299–301] for

recent works on the GPD phenomenology).

### Phenomenology of GPDs

The cleanest way to probe GPDs is via deeply virtual Compton scattering (DVCS), i.e.  $\gamma^*N \rightarrow \gamma N'$ , at high photon virtuality ( $Q^2 > 1 \text{ GeV}^2$ ) and low momentum transfer ( $t \ll Q^2$ ), where the scattering happens from a single parton [302]. Experimentally, we access DVCS by measuring the exclusive electroproduction of a real photon (see diagram (a) in Fig. 7.48). In this process the DVCS amplitude interferes with the so-called Bethe-Heitler (BH) process, that corresponds to the emission of the photon by the incoming or the outgoing electron and is exactly calculable in QED once the nucleon electromagnetic form factors are known. DVCS is well described theoretically, including higher orders in  $\alpha_s$ , higher-twist and target mass corrections (for a comprehensive review see e.g Ref. [299]).

The DVCS cross-section is parametrized in terms of Compton form factors (CFFs), through which the full range of  $x$  is not directly accessible. CFFs are complex functions whose real and imaginary parts are convolutions over  $x$  of the GPDs with a hard kernel, systematically computable in perturbative QCD. At leading order, the imaginary part of the CFF gives the GPDs along the diagonals  $x = \pm \xi$ , while the real part of the CFF probes a convoluted integral of GPDs over the initial longitudinal momentum of the partons. The interference between BH and DVCS provides a way to independently access the real and imaginary parts of CFFs. Beam and target single spin asymmetries are proportional to the imaginary part of the DVCS-BH interference amplitude. All three terms (pure BH, pure DVCS, and interference amplitudes) contribute to the unpolarized cross section. The DVCS and interference terms can be separated by exploiting their dependencies on the incident beam energy, a generalized Rosenbluth separation. The real part also appears in double spin asymmetries, but these can receive significant direct contribution from the BH process itself, making the extraction of the real part of the amplitude challenging. Beam-charge asymmetries (from measurements with both electron and positron beams), on the other hand, receive no direct contribution from the pure BH process and are also sensitive to the real part of the DVCS amplitude. Therefore, an experimental program with positron beams can have a significant impact in accessing this crucial observable [284].

Timelike Compton scattering (TCS) is a related process in which a real photon scatters off a parton to produce a virtual photon, detected through its lepton-pair decay (see diagram (b) in Fig. 7.48) [303–309]. As such, this is an inverse process to DVCS, sensitive to the same set of GPDs. The complementarity of DVCS and TCS processes [306] relies mostly on consequences of the analyticity of the  $Q^2$  behaviour of amplitudes, as discussed in [306, 307]. Confronting DVCS and TCS results together is a mandatory goal of the EIC to prove the consistency of the collinear QCD factorization framework and test the universality of GPDs. The differences in the two processes additionally give experimental advantages in the extraction of CFFs – for example the asymmetries associated with the lepton decay in TCS provide a more direct access to the real part of the dominant CFF [136].

Additional information on GPDs can be obtained from hard exclusive meson electropro-

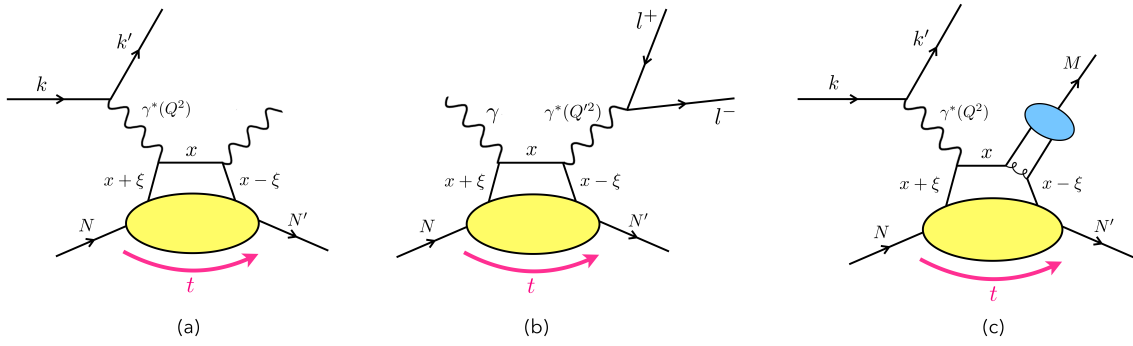


**Figure 7.48:** Illustrations of three main processes which carry sensitivity to GPDs: a) DVCS, b) TCS and c) one of the possible DVMP diagrams.

duction, where a meson, instead of the photon, is produced as a result of the scattering (see diagram (c) in Fig. 7.48) [300]. These processes include:

1. test1
2. test2

Hard exclusive production of  $\pi^0$  mesons has a final state similar to that of DVCS. It consists of one scattered lepton in DIS regime ( $Q^2 > 1 \text{ GeV}^2$ ), one scattered nucleon in a coherent state (i.e., no break of target particle in the interaction), and either one or two photons, for DVCS and DVMP  $\pi^0$ -decay, respectively. This similarity suggests that a common analysis of the detector requirements for both processes can be performed, as discussed in Sec. 8.4.1.

The information that can be extracted from a handful of DVCS measurements at low  $x_B$  by HERA collider experiments, almost entirely consisting of cross sections in loose  $Q^2 - t$  bins, is very limited. GPD-based experiments at larger values of  $x_B$  have been carried out at HERMES and COMPASS. Dedicated fixed target experiments at the upgraded CEBAF 12 GeV facility at JLab are addressing GPDs in the kinematical region dominated by valence-quarks. More precise data mapping, with high granularity and a wider phase-space, is required to fully constrain the entire set of GPDs for gluons and sea quarks. This will be provided by the EIC, which connects the domain typical of fixed target experiments with that of collider measurements. With its wide range in energy and high luminosity, EIC will thus offer an unprecedented opportunity for a precise determination of GPDs.

Simulation studies proved that the EIC can perform accurate measurements of DVCS cross sections and asymmetries in a very fine binning and with a very low statistical uncertainty [310]. This pioneering assessment of the capability of the EIC to constrain GPDs solely relies on global fits of DVCS measurements. Figure 7.49 shows the uncertainties of GPDs extracted from current data (blue bands) and how they are constrained after including the EIC pseudo-data into the fits (orange bands).

This study demonstrated that the EIC can largely improve on our current knowledge of GPD  $H$  for gluons, as shown in Fig. 7.49. Moreover, a precise measurement of the trans-

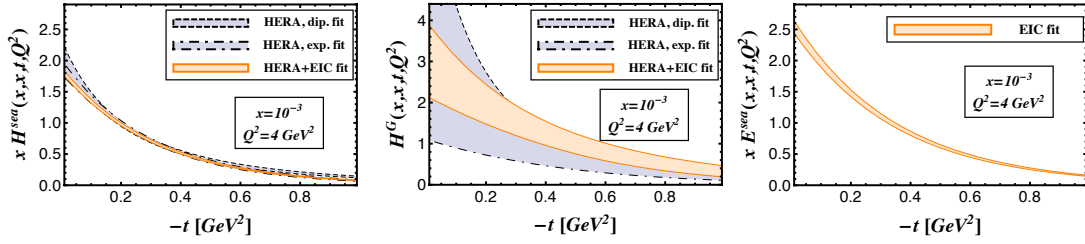


**Figure 7.49:** Extraction of GPD  $H$  for sea quarks (*left*) and gluons (*center*) and GPD  $E$  for sea quarks (*right*) at a particular  $x$  and  $Q^2$ . The violet band is the uncertainty obtained excluding the EIC pseudo-data from the global fit procedure [310].

versely polarized target spin asymmetry  $A_{UT}$ , which allows for a decomposition of GPD  $H$  and  $E$  contributions, leads to the accurate extraction of GPD  $E$  for the sea quarks, which at the moment remains almost unconstrained [310].

Diffractive events are known to constitute a large part of the cross section in high-energy scattering. In Refs. [311–313], access to GPDs is suggested in a diffractive process where a GPD driven subprocess ( $\mathcal{P}N \rightarrow \gamma^*(Q^2)N'$  or  $\mathcal{P}N \rightarrow MN'$ , where  $\mathcal{P}$  is a hard Pomeron and  $M$  a meson) is triggered by a diffractive  $\gamma^*(Q^2) \rightarrow \rho\mathcal{P}$  process, as shown in Fig. 7.50. The kinematical domain is defined with a large rapidity gap separating the  $\rho$  from the  $\gamma^*N'$  or  $MN'$  final state and a small momentum transfer between the initial and final nucleons.

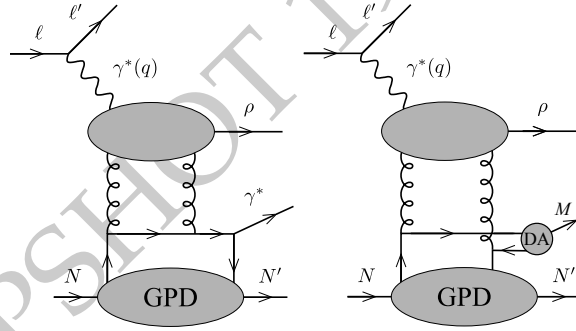


**Figure 7.50:** Leading order diagram for diffractive DVCS (*left panel*) and diffractive two-meson (*right panel*) production, with a large rapidity gap between the forward  $\rho$  and the remaining  $\gamma^*N'$  or  $MN'$  final state.

Contrary to the usual DVCS and TCS processes, the integration over the quark momentum fraction in the amplitudes is restricted to a smaller domain ( $-\xi < x < \xi$ ), with gluons not entering due to C-parity conservation. The skewness parameter  $\xi$  is not related to  $x_B$  as in DVCS, giving access to large  $\xi$  values even for large energy processes [311,312]. In the meson production process, as in DVMP, the nature of the meson and its polarization select particular types of GPDs (vector, axial vector, transversity). The amplitudes are energy independent at leading order, and would acquire a mild energy dependence when large energy evolution is turned on. Cross section projections for the  $\rho M$ -production process at EIC kinematics were studied in Ref. [313]. Detailed EIC simulations for both processes are in progress [314].

In [315–318], a new class of processes is proposed to access GPDs through  $\gamma + N \rightarrow \gamma + M + N'$  and  $\gamma + N \rightarrow \gamma + \gamma + N'$ , focusing on the regime where  $M_{\gamma M}^2$  or  $M_{\gamma\gamma}^2$  provides a hard scale. The connection with GPDs relies on the fact that the fixed angle subprocess  $\gamma(q\bar{q}) \rightarrow \gamma + M$  or  $\gamma(q\bar{q}) \rightarrow \gamma + \gamma$  factorizes from GPDs.

In the photoproduction of  $\gamma\gamma$ , the hard sub-process gives access to GPDs at the special point  $x = \pm\zeta$  [316]. The photoproduction of a photon-meson pair, for example  $\gamma\rho$  [315], is on the other hand sensitive to chiral-odd (transversity) GPDs. Charge chirality constraints dictate that, for  $\gamma\rho$  photoproduction, only chiral-odd GPDs contribute at leading twist (i.e. up to  $1/Q^2$  corrections) to the production of a transversely-polarised  $\rho$ , while chiral-even GPDs contribute to the meson's longitudinal polarization. Separating out the polarisation states via measurements of the  $\rho$  decay products enables separation of the chiral-even and transverse GPDs. This process additionally benefits from a suppression of gluon GPDs in the amplitude, which typically introduce large NLO corrections. Simulations of the process at EIC kinematics are underway [319]. The chiral-even sector ( $M = \pi$  or  $\rho_L$ ) can yield a very large new set of observables, complementing measurements of DVCS, TCS and DVMP which involve the same GPDs. In addition, the case where  $M = \pi^0$  provides a new way to access GPDs of gluons.

A novel method to extract GPDs has recently been proposed [320], which is based on comparison of  $\rho$ - and  $\pi$ -meson production cross sections in charged current processes. These processes are numerically suppressed compared to photoproduction and pose significant experimental challenges, yet are within the reach of the Electron Ion Collider, as described in Sect. 8.4.8.

### Impact parameter distributions

Impact parameter distributions can be reconstructed by taking a Fourier transform of the GPDs in the variable  $t$  at  $\zeta = 0$ . These distributions represent densities of partons with a given momentum fraction of  $x$  as a function of the position  $\mathbf{b}_\perp$  from the center of momentum of the nucleon in the transverse plane [321]. A first attempt to obtain this information directly from photon electroproduction measurements was illustrated in Refs. [322, 323], using a model-dependent extrapolation to the point  $\zeta = 0$  that is not accessible experimentally. Recently, dispersion-relation techniques have been used in Ref. [324] to constrain the GPDs at  $\zeta = 0$  from data. Both these analyses confirm that the width of the impact-parameter distribution for unpolarized quarks in unpolarized protons has a very peaked transverse profile in the limit of  $x \rightarrow 1$ . This behaviour comes from the fact that, in this limit, the active quark is always very close to the transverse center of momentum [321, 325]. It suggests that the higher- $x$  valence quarks are localised closer to the centre of the nucleon than the lower- $x$  sea quarks, which have a wider distribution in the transverse plane.

The DVCS-based EIC impact study of Ref. [310] showed how Fourier-transforming the GPDs constrained at the EIC, it is possible to extract the densities of quarks and gluons in the impact-parameter space, as shown in Fig. 7.51.

While this study is based only on measurements of DVCS, simulation studies have also

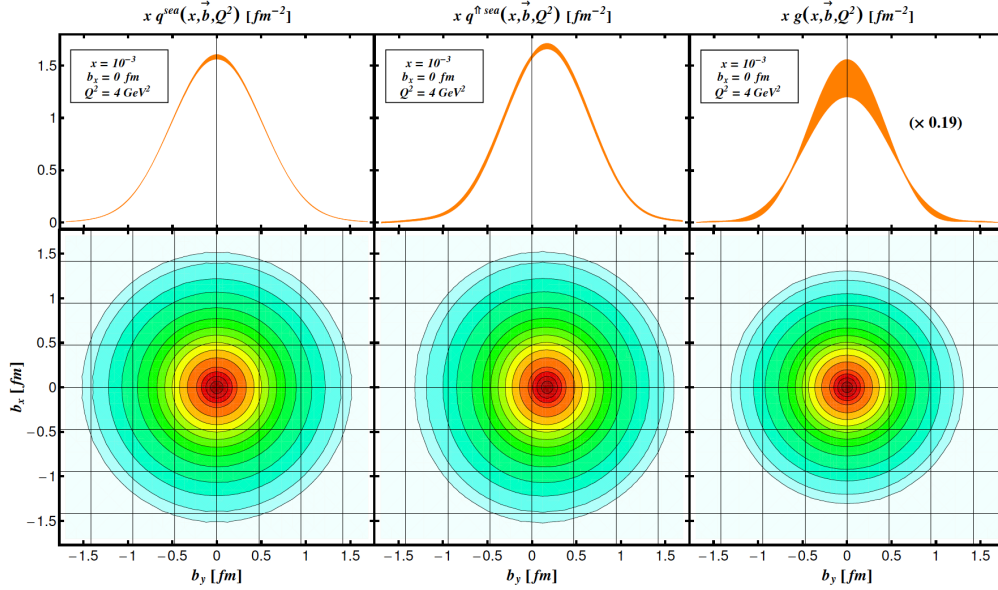


**Figure 7.51:** IPDs at  $x = 0.001$  and  $Q^2 = 4$  GeV<sup>2</sup> for unpolarized sea quarks in an unpolarized proton (left), a transversely polarized proton (middle) and for unpolarized gluons in an unpolarized proton (right), obtained from a combined fit to the HERA collider and EIC pseudo-data. Top row: IPDs at fixed  $b_x = 0$  as function of  $b = b_y$ . Bottom row: density plots of IPDs in the  $(b_y, b_x)$  plane.

shown how EIC can provide high precision measurements of the  $|t|$ -differential cross section of heavy vector mesons [326, 327]. More studies of measurements of light and heavy mesons, performed in the context of this yellow report, are discussed in Sec. 8.4.4. A

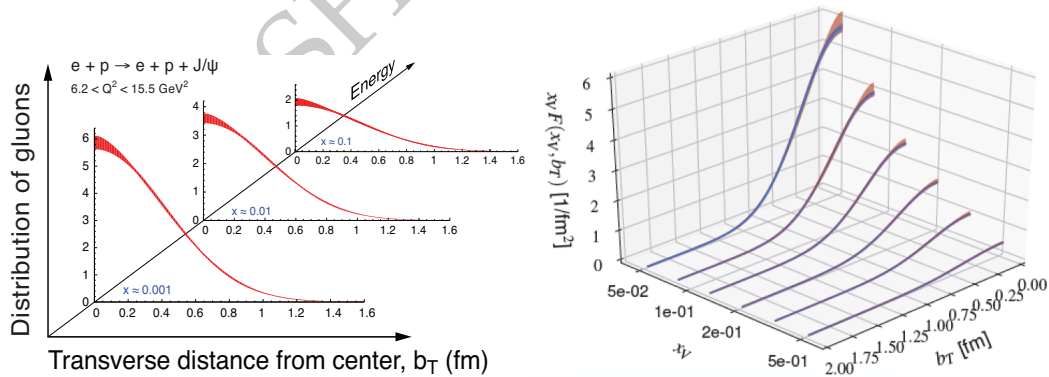


**Figure 7.52:** Projected EIC uncertainties on the measurement of the distribution of the gluon density versus the transverse distance from the center of the nucleon, resulting from differential cross section measurements of  $J/\Psi$  (left) and  $Y$  (right). The gluon distribution uncertainty bands are plotted for a fixed  $Q^2$  bin and three different values of  $x$ .

Fourier-transform of the  $|t|$ -differential cross section for the production of heavy vector mesons can help to visualize the uncertainty achievable on the gluon distributions in the

impact parameter space, though it still contains a contribution from the small but finite size of the meson, which needs to be disentangled in a full GPD analysis. Figure 7.52 shows the projected impact-parameter-dependent distributions of the gluon measurable at the EIC, enabling us to accurately probe the spatial distribution of gluons over two orders of magnitude in  $x$ , up to the region where the dominant partons are valence quarks.

Impact studies in Ref. [310] assume a measurement of the proton four-momentum transfer,  $|t|$ , in a very wide range, starting with the physical minimum  $|t|_{min} \sim 0.03 \text{ GeV}^2$  up to  $|t| = 1.6 \text{ GeV}^2$  which, in a Fourier transform, corresponds to large values of the impact parameter. Studies by the same authors show that limiting the measured  $|t|$ -range would severely impact the precision of the extracted partonic densities, as shown in Fig. 7.53. The bands represent the uncertainty from different extrapolations to the regions of unmeasured (very low and very high) values of  $|t|$ .

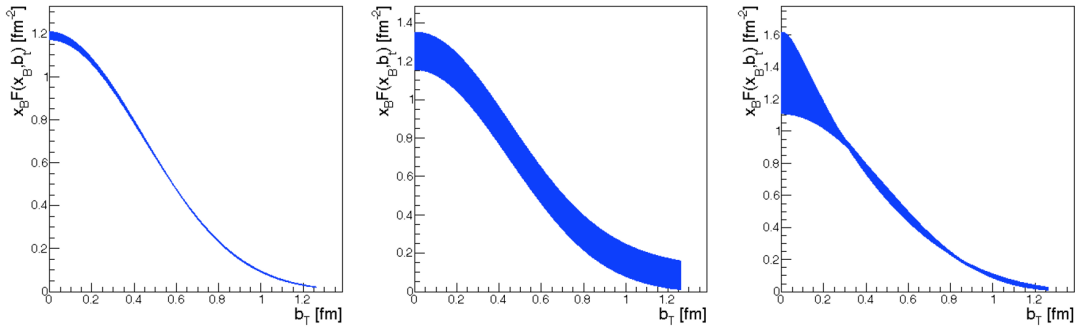


**Figure 7.53:** The combined average impact-parameter dependent partonic density obtained from a Fourier transform of the DVCS cross section measured at the EIC assuming different  $|t|$  acceptances. The bands represent the parametric errors in the fit and the uncertainty from different extrapolations to the regions of unmeasured (very low and very high)  $|t|$  of the scattered protons. Left:  $0.03 < |t| \text{ (GeV}^2) < 1.6$ , middle:  $0.2 < |t| \text{ (GeV}^2) < 1.6$ , right:  $0.03 < |t| \text{ (GeV}^2) < 0.65$ .

### Form factors of the energy-momentum tensor

GPDs also offer the unique and practical opportunity to access the energy-momentum tensor (EMT) form factors, which are canonically probed through gravity. For a symmetric (Belinfante-improved) EMT, there are four independent EMT form factors, usually referred as  $A(t)$ ,  $J(t)$ ,  $D(t)$  and  $\bar{C}(t)$ , for each type of parton. The first three form factors can be related to  $x$ -moments of the GPDs and, at  $t = 0$ , the corresponding “charges” for quarks and gluons give, respectively, the fraction of nucleon momentum carried by the partons, Ji’s relation [69] for the quark and gluon contribution to the total angular momentum of the nucleon (see Sect. 7.1.2), and the  $D$ -term, which is sometimes referred to as the “last unknown global property” of the nucleon [328]. Furthermore, the  $\bar{C}(t)$  form factor is related to the EMT trace anomaly and plays a relevant role in the generation of the nucleon mass (see Sect. 7.1.4). The information encoded in the EMT form factors is revealed in the so-called Breit frame [328, 329] and has been discussed recently in other frames in

Refs. [124, 330]. Working in the Breit frame, the  $D$ -term form factor can be related to the spatial distribution of shear forces  $s(r)$  and pressure  $p(r)$ .

The relation for the shear forces holds also for quarks and gluons separately, while it is defined only for the total system in the case of pressure. In this way, the form factor  $D(t)$  provides the key to mechanical properties of the nucleon and reflects the internal dynamics of the system through the distribution of forces. Requiring mechanical stability of the system, the corresponding force must be directed outwards so that one expects the local criterion  $2s(r) + p(r) > 0$  to hold, which implies that the  $D$ -term for any stable system must be negative,  $D < 0$ , as confirmed for the nucleon in models [331–333], calculations from dispersion relations [334] and lattice QCD [335, 336]. Another consequence of the EMT conservation is the condition  $\int_0^\infty p(r)r^2 dr = 0$ , which shows how the internal forces balance inside a composite particle. This relation implies that the pressure must have at least one node. All models studied up to now show that the pressure is positive in the inner region and negative in the outer region, with the positive sign meaning repulsion towards the outside and the negative sign meaning attraction directed towards the centre. Recently, an analysis of the published JLab data measured at 6 GeV [337, 338] has provided the first experimental information on the quark contribution to the  $D$ -term form factor [339]. The  $D$ -term parameters fitted to the JLab data, with the assumption of a negligible gluon contribution, were used to obtain the radial pressure distribution. Within the uncertainties of the analysis, the distribution satisfies the stability condition, with a zero crossing near  $r = 0.6$  fm. This analysis has been repeated in Ref. [340] using more flexible parametrization by neural networks to improve the analysis of the uncertainties. The obtained results show that presently available beam-spin asymmetry and cross-section measurements alone do not allow to draw reliable conclusions. An independent study relying on neural-network based global fits to existing DVCS measurements [341] also confirms that a reliable extraction of pressure forces from current experimental data is not achievable [342]. The method itself, however, appears valid and may provide a conclusive extraction of the quark distribution in the future, when used in combination with other observables, more sensitive to the real part of Compton form factors and to the  $D$ -term (such as the DVCS beam-charge asymmetry or the production of lepton pairs) and with forthcoming data from present facilities (JLab, COMPASS at CERN) and the EIC. Similarly, exploratory studies for the extraction of the other EMT form factors at the EIC are in progress. Measuring beam-charge asymmetries, the most sensitive probe to the  $D$ -term, requires a positron beam, which can be unpolarized. While this is not envisioned in the EIC baseline, there are no technical obstacles to this upgrade in the future.

### Transition distribution amplitudes

New information on the parton composition of the nucleon can be accessed by studying the  $u$ -crossed channel of hard exclusive meson production. In the kinematics of  $t \sim t_{\max}$  and  $u \sim u_{\min}$ , this process is characterized by a non-zero baryon number exchange in the cross channel and can be studied in terms of non-perturbative objects known as nucleon-to-meson Transition Distribution Amplitudes (TDAs) [343–346]. TDAs describe the underlying physics mechanism of how the target proton makes a transition into a  $\pi$  meson in

the final state. One fundamental difference between GPDs and TDAs is that the TDAs require three parton exchanges between the TDA and the hard part. At leading-twist, there are 8 independent TDAs that can be classified in terms of the light-cone helicity of the exchanged quarks [347]. This opens the way to specific and detailed analysis of the helicity content of correlated quarks in the nucleon. Similarly to GPDs, after the Fourier transform in the transverse plane, TDAs also carry valuable information on the transverse location of hadron constituents and allow one in particular to quantify the effect of diquark clustering in nucleons [348]. In order to advance in the exploration and development of the TDA physics, the EIC, along with the measurements planned at other existing facilities, can play a crucial role (see Sect. 8.4.7 for kinematic studies).

### 7.2.3 Imaging of quarks and gluons in momentum space

Transverse momentum dependent distribution and fragmentation functions (TMDs) describe not only the partons' longitudinal momentum given by the variables  $x$  and  $z$  for distribution and fragmentation functions, respectively, but also the transverse momentum. Initially suggested as potential mechanisms for creating the unexpectedly large single transverse spin asymmetries in hadronic collisions [349, 350], they are now a staple for describing the three-dimensional spin and momentum structure of the nucleon and provide access to quantities that could previously not be studied [351]. At an electron-ion collider the main access to TMDs comes over semi-inclusive DIS where in addition to the general DIS quantities  $x$ ,  $Q^2$ , and  $y$ , one also identifies final state hadrons with a fractional energy  $z$  and transverse momentum  $p_T$  relative to the virtual photon direction. In several cases also azimuthal angles of incoming hadron spin and fragmenting hadron momentum relative to the lepton scattering axis are measured. Accounting for the transverse momentum degrees of freedom allows the extraction of non-perturbative TMDs and, ultimately, reconstructs the three-dimensional picture of hadrons in momentum space. The general description of semi-inclusive DIS can be found in [163, 352] and later additions for single hadron observables. Additional details of the momentum space image, such as flavor substructure, distribution of gluon transverse motion, and others, can be received from different other semi-inclusive processes, primarily di-hadron production and jet-based measurements.

The main theoretical tool for probing TMDs is the TMD factorization theorem and its extensions. Within the TMD factorization theorem one defines universal TMD distributions [353, 354] that are non-perturbative functions of two variables  $x(z)$  and  $k_T$ , which parametrize longitudinal and transverse components of the parton's momentum. The theoretical framework of TMD factorization has been intensively developed during the last decades, and it has led to discoveries of new applicable domains and deeper connections with fundamental properties of QCD. Within the TMD factorization, structure functions have the following generic form (here for example  $F_{UT}^{\sin(\phi-\phi_s)}$  is shown)

$$F_{UT}^{\sin(\phi-\phi_s)} = \sum_q e_q^2 |C_V(Q)|^2 [R(Q, \mu_0) \otimes f_{1T,q}^\perp(x; \mu_0) \otimes D_{1,q}(z; \mu_0)](p_T), \quad (7.32)$$

where  $\otimes$  stands for the convolution in transverse momenta,  $|C_V|^2$  is the perturbative co-

efficient function,  $R(Q, \mu_0)$  represents the evolution factor,  $f_{1T,q}^\perp$  and  $D_{1,q}$  are Siverts TMD PDF and unpolarized TMD FF, respectively. The reference scale  $\mu_0$  depends on the details of the evolution implementation [355, 356]. This factorization formula (7.32) can be cast into a simplified form in the coordinate space representation, and it reads

$$F_{UT}^{\sin(\phi-\phi_s)} = \sum_q e_q^2 |C_V(Q)|^2 \int \frac{d^2b}{(2\pi)^2} e^{i(bp_T)/z} R(Q, b, \mu_0) f_{1T,q}^\perp(x, b; \mu_0) D_{1,q}(z, b; \mu_0) \quad (7.33)$$

Here, the parameter  $b$  is defined in the coordinate space, and it is the Fourier conjugate to  $k_T$ . In  $b$ -space, TMDs have a multiplicative evolution, and simpler theoretical properties, and therefore they are often used in practice.

The central feature of equations (7.32, 7.33) is the presence of three non-perturbative functions: two TMD PDFs/FFs and one non-perturbative part of the evolution kernel, with the so-called Collins-Soper-kernel (CS-kernel) hidden in  $R$ . Each of them contains dependence on  $Q$ ,  $x$ , or  $z$ , and altogether they share  $p_T$ -dependence. To clearly separate these three functions, measurements that are differential in  $(Q, x, z)$  with large kinematic coverage are needed. Considering the corrections to the factorization formula (7.32) which enter in terms of powers of  $\delta \sim p_T/z/Q$ , the applicable domain of the TMD factorization is  $\delta < 0.25$  [357–359]. These restrictions reduce the significance of a large number of existing measurements. The EIC will provide measurements in an unprecedentedly large domain, which ultimately helps to pin down TMD distributions precisely. However, it also complicates the impact studies for such measurements since many quantities are entirely unconstrained by current measurements (especially for  $Q > 5 - 10$  GeV).

### Unpolarized TMDs and TMD evolution

Nowadays, the unpolarized case is the best-studied subject due to lots of measurements in many different kinematic ranges, starting from fixed-target experiments [360–365] at low energy scales up to collider measurements at higher energy scales [366–381]. The precision and large span in  $Q$  make unpolarized measurements ideal for the determination of the CS-kernel. The latest global analyses performed at NNLO perturbative accuracy with  $N^3$ LL TMD evolution, demonstrate an excellent agreement between the theory and experiments, and provide extracted values of unpolarized TMDs with a good precision [357–359] (named as SV17, SV19, Pavia19 for brevity). Nonetheless, the current overall status of the data (which includes extremely precise LHC measurements at  $Q \sim M_Z$ ) does not allow an accurate reconstruction of TMDs in the  $b > 1 - 2 \text{ GeV}^{-1}$  region due to insufficient  $p_T$ -coverage. In this region extractions accomplished by different groups drastically diverge, see for example the comparison in [382]. The measurement at EIC energies will be able to fill in the gap between the low-energy fixed-target experiments and those at the LHC, and this will help pin down these functions at higher values of  $b$ , i.e., lower values of  $k_T$ . Additionally, unpolarized structure functions and unpolarized TMDs enter the definitions of other structure functions and spin-asymmetries, and thus significantly influence the accuracy of polarized TMDs as well.

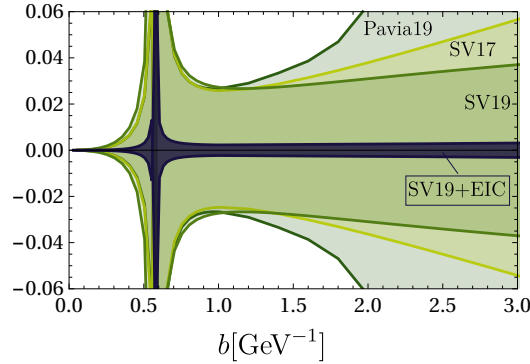


**Figure 7.54:** Comparison of relative uncertainty bands for CS-kernel at  $\mu = 2$  GeV.

To estimate the impact on the non-perturbative part of the CS-kernel and unpolarized TMDs, we have rerun the SV19 fit with the inclusion of EIC pseudo data (in  $5 \times 41$ ,  $5 \times 100$ ,  $10 \times 100$ ,  $18 \times 100$  and  $18 \times 275$  beam energy configurations). The pseudo data, based on PYTHIA [26] simulations, includes expected statistical and estimated systematic uncertainties, obtained for a hand-book detector design with moderate PID. The estimates for expected uncertainty bands in comparison to existing ones are shown in figures 7.54 and 7.55. Clearly, the main impact on the unpolarized sector occurs in the CS kernel, for which the uncertainty reduces by a factor  $\sim 10$ . This is due to the unprecedented and homogeneous coverage of the  $(Q, x, z)$  domain, which can efficiently decorrelate the effects of soft gluon evolution and internal transverse motion. Importantly, the current estimate is based on one-parametric models, which are sufficient to describe current data. Given the preci-

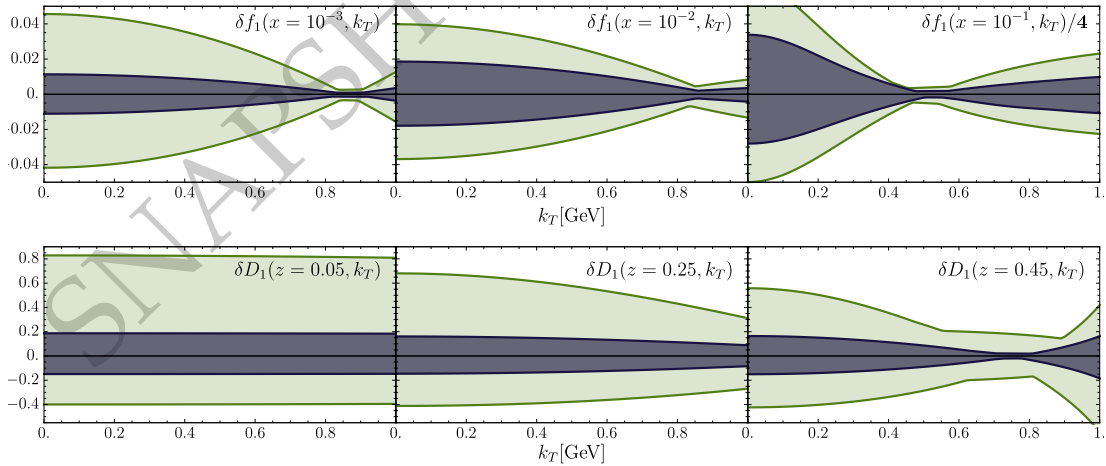


**Figure 7.55:** Comparison of relative uncertainty bands for up quark unpolarized TMD PDFs (upper panel) and up quark to positive pion TMD FFs (lower panel), at different values of  $x$  and  $z$  as a function of  $k_T$ . Lighter band is SV19 extraction, darker is SV19 with EIC pseudo data.

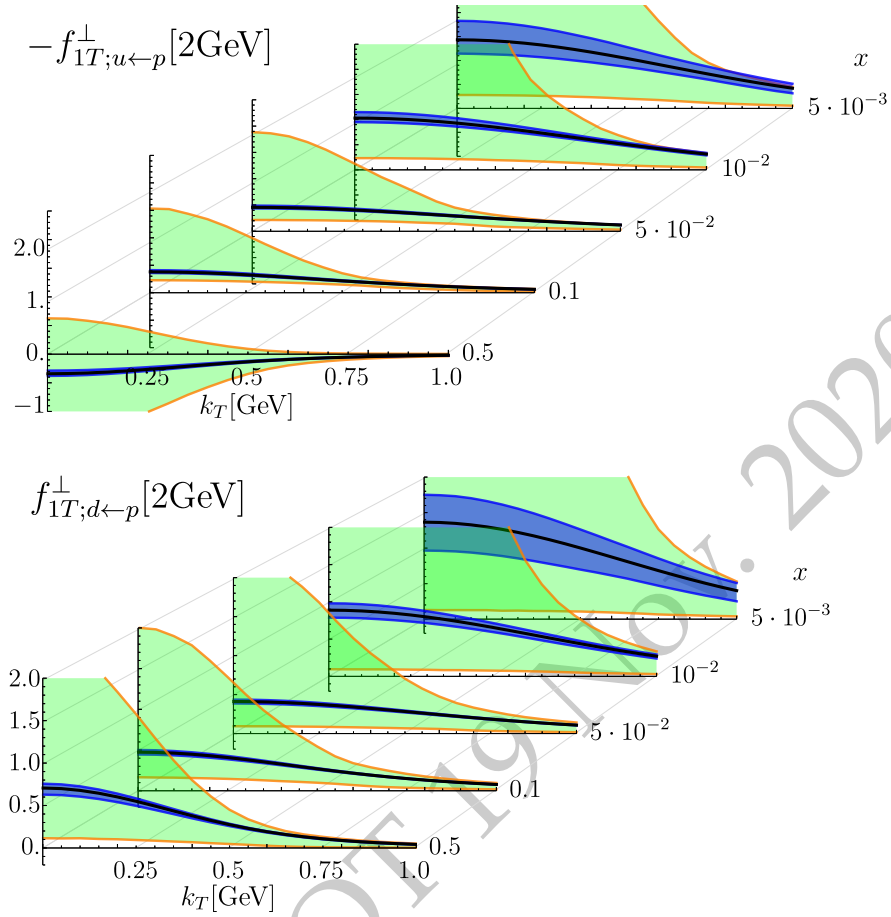


**Figure 7.56:** Expected impact on up and down quark Sivers functions as a function of intrinsic transverse momentum  $k_T$  for slices of  $x$  as obtained from semi-inclusive pion and kaon EIC pseudo-data.

sion of the EIC measurements, one can expect to obtain a fine structure of CS kernel, which will help to explore properties of the QCD vacuum [382]. The unpolarized TMDs are also greatly affected by the EIC. The biggest impact takes place in the regions that are not covered by present data, i.e. the low- $z$  and low- $x$  regions, where the size of the uncertainty bands can be reduced by a factor  $\sim 4$ . In other regions, the reduction of uncertainties is smaller, and typically of the factor  $\sim 2$ . The EIC measurement will also play a key role in the study of sea-quark TMDs, which are currently almost unconstrained, and thus its impact on them could not be estimated.

### Quark Sivers and Collins measurements

**Sivers function measurements:** The determination of the quark Sivers functions,  $f_{1T}^q(x, k_T)$ , is one of the major interests for TMD physics. It can be extracted most directly from the single transverse-spin asymmetries proportional to the  $\sin(\phi_h - \phi_s)$  modulation,

which is expressed through the structure function  $F_{UT}^{\sin(\phi-\phi_s)}$  (7.32). The Siverson function is a P-odd TMD distribution [383], that turns into the Qiu-Sterman matrix element [158,384] in the regime of small- $b$  [385]. Currently, the global pool of Siverson asymmetry data has only a small number of data points that satisfy the TMD factorization criterion. Consequently, the error bands on the Siverson function are enormous. To determine the impact of EIC measurements on the Siverson function we used the pseudo data generated by PYTHIA 6 [26] with a successive reweighing by a phenomenological model for the Siverson and unpolarized structure functions from [386]. For the present impact analysis we used the pseudo data made for  $\pi^\pm$  and  $K^\pm$  production in  $e+p$  and  $e+n$  collisions at the highest ( $18 \times 275$ ) and the lowest ( $5 \times 41$ ) beam-energy configurations. The systematic uncertainties were estimated as in the unpolarized case. The resulting pseudo data set will have about two orders of magnitude more points than current data. Performing the fit of pseudo-data with the initial setup of the Siverson function from the global analysis made in [387] based on SIDIS [388–392] and DY [393,394] data, we observe a crucial reduction of uncertainties, as shown in Fig. 7.56. The uncertainty bands are reduced by order of magnitudes, for all flavors. Via measuring the explicit  $p_T$  dependence for a given  $(x, z, Q)$  bin allows the determination of the shape in  $k_T$  of the Siverson function, which is currently almost unrestricted.

**Collins function based transversity measurements:** Using the framework of the QCD global analysis of single transverse-spin asymmetries (SSAs) developed in Ref. [183] (JAM20), the impact of the EIC single hadron Collins effect SIDIS data on the transversity distributions and the tensor charges was determined (see Fig. 7.57). Both proton and helium-3 beams were considered that were again produced using PYTHIA 6 and reweighted using structure functions based on the extraction by [386]. The Collins asymmetries are expressed by the  $\sin(\phi + \phi_s)$  moment. The JAM20 fit utilizes the connection between TMDs and twist-3 multi-parton correlators to simultaneously fit data from SIDIS [395,396], electron-positron annihilation [397–402], Drell-Yan [393,394], and proton-proton  $A_N$  [154,155]. The significant reduction in the uncertainties is clear. In particular, in going from JAM20 to JAM20+EIC( $ep$ ) to JAM20+EIC( $ep+eHe^3$ ) the results for the tensor charges are  $\delta u = 0.72(19) \rightarrow 0.72(3) \rightarrow 0.719(9)$ ,  $\delta d = -0.15(16) \rightarrow -0.15(6) \rightarrow -0.149(2)$ ,  $g_T = 0.87(11) \rightarrow 0.87(4) \rightarrow 0.87(1)$ . The importance of the polarized  $He^3$  data is also manifest, especially for the down quark transversity. With the EIC data, uncertainties for phenomenological extractions of the tensor charges will become comparable to, and possibly smaller than, current lattice QCD calculations (see, e.g., Ref. [403]). As such, potential discrepancies may become indications of other contributions that are not included in lattice QCD simulations and thus, the Standard Model [404,405].

### Gluon TMD measurements

Gluon TMDs encode different correlations between the momentum and spin of the gluon and its parent nucleon. First classified in [406], they follow a TMD evolution analogous to that of quark TMDs [407]. Apart from the unpolarized and linearly polarized gluon TMDs inside an unpolarized nucleon,  $f_1^g$  and  $h_1^{\perp g}$ , respectively, of special interest for spin asym-

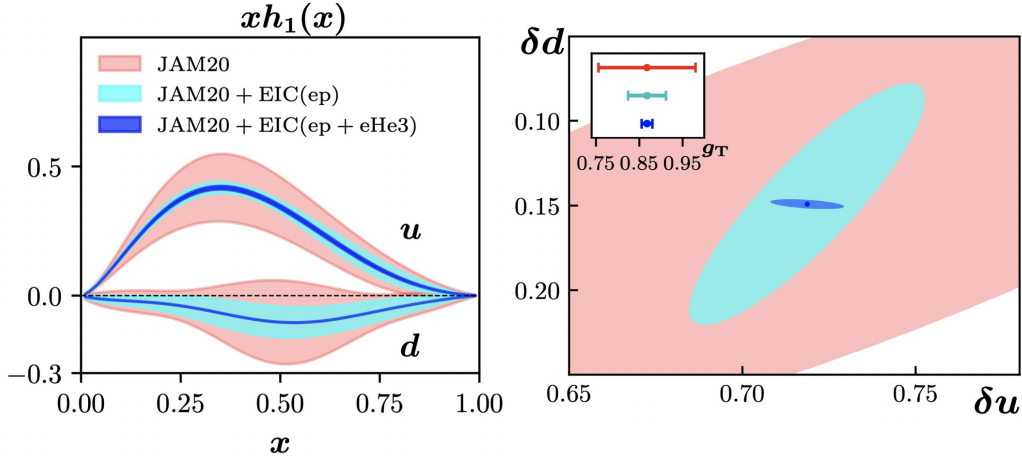


**Figure 7.57:** Left: Expected impact on the up and down quark transversity distributions as a function of  $x$  when including EIC Collins effect SIDIS pseudo-data from  $e+p$  and  $e+\text{He3}$  collisions. Right: The impact on the up quark ( $\delta u$ ), down quark ( $\delta d$ ), and isovector ( $g_T$ ) tensor charges using those transversity functions.

metry measurements are the three naive  $T$ -odd gluon TMDs for a transversely polarized nucleon: the gluon Sivers function  $f_{1T}^{\perp g}$  and the two chiral-even distributions of linearly polarized gluons  $h_1^g$  and  $h_{1T}^g$ .

The operator structure of gluon TMDs is more involved as compared to quark TMDs. Indeed, among the eight leading-twist gluon TMDs, four are naive  $T$ -odd, and thus expected to be process dependent. The underlying interpretation is that the gauge-link structures involved in the definition of gluon TMDs are essentially different in DIS and hadronic collisions. As a result, it is predicted that these  $T$ -odd gluon TMDs accessed in  $ep^\dagger \rightarrow e'q\bar{q}X$  can be related by an overall sign change to those in  $p^\dagger p \rightarrow \gamma\gamma X$  (or any other color-singlet final state, such as  $di-J/\psi$  or  $J/\psi\gamma$ ). Moreover,  $T$ -odd gluon TMDs can be cast into two types, namely the Weizsäcker-Williams (WW) type, also known as  $f$ -type, and the dipole type, also known as  $d$ -type, depending on the gauge link structure involved in the scattering processes [408–414]. Recent progress in TMD and small- $x$  physics reveals that there are two different types of fundamental gluon distributions, namely the WW gluon distribution and the dipole gluon distribution. This issue and its impact on EIC physics are discussed in detail in Sec. 7.3.1. The WW gluon TMDs appear exclusively in the  $\gamma^*g \rightarrow q\bar{q}$  process in DIS and they are generally difficult to be extracted in other hadronic collisions [412]. The process  $ep^\dagger \rightarrow e'q\bar{q}X$  probes the WW type gluon TMDs. Therefore, through the measurement of WW gluon TMDs, the EIC can provide a unique test of the non-universality of gluon TMDs, complementary to the proposed observables at hadron colliders [415–417].

Currently, almost nothing is experimentally known about unpolarized or polarized gluon TMDs. Open charm production is an ideal probe to study gluon TMDs [418–420], but it is statistically challenging [421]. Alternatively, one can measure (single, double or associated) quarkonium production [418, 419, 422–438]. In this case, recent theoretical developments [434, 435] point to the need of new hadronic quantities, the TMD shape functions,

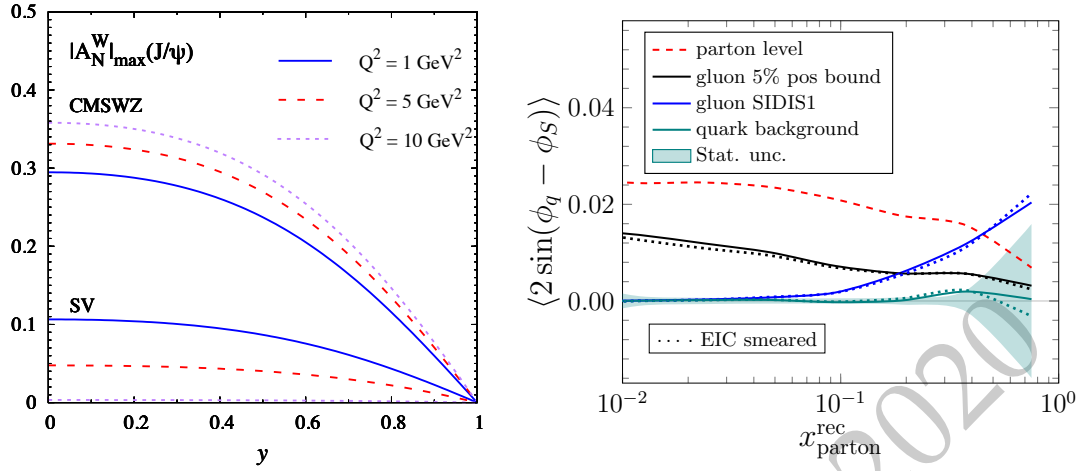


**Figure 7.58:** Left: Maximal  $A_N^W$  asymmetries with  $W = \cos 2\phi_T, \sin(\phi_S + \phi_T), \sin(\phi_S - 3\phi_T)$ , for  $J/\psi$  production in SIDIS. Labels SV and CMSWZ refer to the implemented LDME sets [439, 440] [figure from [432]]. Right: projection of SSA modulation in the dijet channel as a function of the reconstructed parton momentum fraction  $x_{\text{parton}}^{\text{rec}}$ . The following kinematic cuts are used in the selection of events generated in the simulation at  $\sqrt{s} = 141$  GeV with an integrated luminosity of  $10 \text{ fb}^{-1}$ : inelasticity  $0.01 < y < 0.95$  and virtuality  $1 \text{ GeV}^2 < Q^2 < 20 \text{ GeV}^2$ , trigger jet  $p_T^{\text{jet1}} > 4.5 \text{ GeV}$  and associated jet  $p_T^{\text{jet2}} > 4 \text{ GeV}$ .

which have not been yet experimentally constrained.

In order to single out different azimuthal modulations of a measurement, which are related to different gluon TMDs, we introduce the following azimuthal moments:

$$A^{W(\phi_S, \phi_T)} \equiv 2 \frac{\int d\phi_S d\phi_T W(\phi_S, \phi_T) d\sigma(\phi_S, \phi_T)}{\int d\phi_S d\phi_T d\sigma(\phi_S, \phi_T)}, \quad (7.34)$$

where  $\phi_S$  and  $\phi_T$  denote the azimuthal angles of the transverse spin vector and the measured transverse momentum, respectively. For instance, by taking  $W = \cos 2\phi_T$  we define  $A^{\cos 2\phi_T} \equiv 2\langle \cos 2\phi_T \rangle$ . The maximum values of such asymmetries in  $ep^\uparrow \rightarrow eJ/\psi X$  [432], obtained from the positivity bounds of the TMDs, are presented in Fig. 7.58(left) in a kinematic region accessible at the EIC. They turn out to be measurable, but depend very strongly on the specific set of the adopted LDMEs. Similar predictions are obtained for  $Y$  production, and also for  $J/\psi + jet$  production [433], which by varying the mass of the final state also allows to test gluon TMD evolution.

On the other hand, dijet or high  $p_T$  charged dihadron productions [441] have also been recently proposed to access gluon TMDs. In Fig. 7.58(right), the projection [421] of the single-spin asymmetry (SSA)  $\langle 2 \sin(\phi_q - \phi_S) \rangle$  via dijet production is shown as function of  $x_{\text{parton}}^{\text{rec}} = (p_T^{\text{jet1}} e^{-\eta^{\text{jet1}}} + p_T^{\text{jet2}} e^{-\eta^{\text{jet2}}}) / \sqrt{s}$  for  $e + p^\uparrow$  collisions at  $\sqrt{s} = 141$  GeV. By defining  $\vec{q}_T$  as the dijet momentum imbalance, we can compute the angle difference  $\phi_{q_T} - \phi_S$  between  $\vec{q}_T$  and the transverse spin  $\vec{S}$ . Using the anti- $k_T$  jet algorithm and the cone size  $R = 0.8$ , the jets are reconstructed from both charged and neutral particles with a mini-

imum transverse momentum  $p_T^h > 0.25 \text{ GeV}/c$  within the pseudorapidity range  $|\eta| < 3.5$ . First of all, since the gluon Sivers function is largely unconstrained, the  $x_{parton}^{rec}$  dependence of the resulting SSA strongly relies on the model inputs. Two different parametrizations of the gluon Sivers function are used as inputs in this projection. One is the SIDIS1 set extracted from the RHIC  $A_N$  data fit of  $\pi^0$  [442], and the other is an assumption based on 5% of the positivity bound of the gluon Sivers function. The results of these two sets of parametrizations of the gluon Sivers function are shown in terms of the blue and black lines in Fig. 7.58(right), respectively. In contrast, the background asymmetry arising from the quark Sivers function is labeled with the line in teal. Second, the projected statistical uncertainty band as shown in Fig. 7.58(right) is sufficient to resolve the signal of the gluon Sivers function down to 5% of the positivity bound for a wide range of  $x$ . Last but not least, the red dashed line represents the gluon Sivers asymmetry at the parton level. As expected, the jet level SSAs inherit similar shapes as the parton level ones with a smaller magnitude. The dotted lines stand for the SSAs with the EIC detector response and smearing effects taken into account. The impact of detector responses becomes significant only in the large  $x$  region due to the limited statistics.

In summary, gluon Sivers function can be probed at the EIC down to 5% of the positivity bound, which allows to explore the little-known correlation between the spin of the proton and the transverse orbital motion of the gluon inside. To measure the gluon Sivers effects (and also the gluon saturation as discussed in Sec. 7.3.1) via the dijet/dihadron process, a hermetic detector with good tracking (momentum and angular) resolutions will be required, since dijets are produced in the back-to-back azimuthal angle plane across a large range of rapidity, and their momentum imbalance is measured from the vector sum of the reconstructed jet momenta.

### Chiral-odd distribution functions via di-hadron measurements

Di-hadron correlations are sensitive to parton distribution functions via their coupling to di-hadron fragmentation functions (DiFFs) [168–170,173]. Due to the extra degrees of freedom, they allow a more targeted access to the nucleon structure. One well known example is the existence of transverse polarization sensitive FFs in the collinear framework. They have already been described in this report in their role to extract the twist-3 function  $e(x)$  in Sec. 7.1.5 with only one extra contributing term instead of three for the single hadron case. The partial wave decomposition of DiFFs is addressed in Sec. 7.4.1. Here, we focus on the access to transversity via the di-hadron FF  $H_1^{\triangleleft}$  and to the Boer-Mulders function via the TMD di-hadron FF  $\tilde{H}^{\triangleleft}$ . Note that we follow the notation in [170] here, a notation that unifies the di-hadron and single-hadron FFs was proposed in [443].

In SIDIS, transversity can be extracted from the  $A^{\sin\phi_R+\phi_S} \propto h_1 * H_1^{\triangleleft}$  asymmetries, where  $\phi_R$  is the azimuthal angle of the difference of the two hadron momentum vectors (see again Refs. [170,443]). The FF  $H_1^{\triangleleft}$  has been extracted from  $e^+e^-$  data [444] by looking at correlations between the azimuthal orientations of two hadron pairs in back-to-back jets [445–448], and it has been used with SIDIS data [449–452] to extract the valence components of transversity [206,453–455]. Because of the collinear framework, the combina-

tion  $h_1 * H_1^\triangleleft$  was predicted to be accessible also in  $pp$  collisions [456]. Using the STAR data [457], transversity was recently extracted from a global analysis (Pavia18) including both SIDIS and  $pp$  collision data [458]. Similarly to the case of single-hadron Collins effect, the impact of EIC di-hadron SIDIS data on transversity and the related tensor charges has been estimated by producing proton and  $^3\text{He}$  beams using PYTHIA 8 + DIRE MC data and re-weighting it with structure functions based on the Pavia18 extraction, including a conservative estimate of the scaling of the  $H_1^\triangleleft$  error as  $2/\sqrt{N_{\text{EIC}}}$ , with  $N_{\text{EIC}}$  the number of EIC pseudo-data points. In this analysis, the error on  $H_1^\triangleleft$  is a major source of uncertainty; however, a significant reduction is expected beyond the current conservative estimate with future BELLE  $e^+e^-$  data and JLAB12 SIDIS data.

Fig. 7.59 shows the impact of EIC pseudo-data when using electron/ion beam energies in GeV of  $10 \times 100$  and with an integrated luminosity of  $10 \text{ fb}^{-1}$ . Although with only one energy configuration and with the conservative cut  $0.1 \leq y \leq 0.85$ , the impact is quite evident with an average increase of precision by a factor 2. The polarized  $^3\text{He}$  data are particularly important for the down quark transversity. They cause a reduction of the uncertainty width by almost an order of magnitude for  $x \lesssim 0.01$  with respect to the Pavia18 extraction, as shown in the lower left panel. Moreover, they shift up the minimum to higher values of  $x$ , as shown in the upper left panel. In going from Pavia18 to Pavia18+EIC( $ep$ ) to Pavia18+EIC( $ep+e^3\text{He}$ ), the isovector tensor charge changes as  $g_T = 0.53(25) \rightarrow 0.63(9) \rightarrow 0.54(2)$ , respectively. The lower right panel of Fig. 7.59 clearly shows that with the EIC data the uncertainties for phenomenological extractions of the tensor charges can become comparable to, and very likely smaller than, current lattice QCD calculations. The vertical dashed lines in the left plot indicate the  $x$  range covered by current experimental data, with the minimum  $x = 0.0065$  attained by COMPASS [452]. It is important to note that no other data existing or planned covers the range  $x < 0.0065$  whose impact on the full integral giving the tensor charge should not be neglected. Persisting potential discrepancies between phenomenology and lattice QCD simulations would then become an indication that other contributions beyond Standard Model are missing [404, 405]. As systematic effects are difficult to estimate from a fast simulation, consistent with experience from previous SIDIS measurements, a 3% relative uncertainty and a 3% scale uncertainty from the beam polarization were summed in quadrature to the statistical uncertainties.

Not shown here are projections for  $\pi^\pm - \pi^0$  and  $\pi - K$  pairs which will allow improved flavor separation. The EIC will be able to make precision measurements also in these channels due to its excellent PID and EMC capabilities. In the kinematic region where a three  $\sigma$  separation between pion and kaons is possible, the background contribution to the  $\pi - K$  sample will be less than 5%. The complementarity of extracting the tensor charges via two distinct methods (single and di-hadron FFs) will reduce the overall systematic uncertainties, both experimental as well as theoretical, significantly.

The Boer-Mulders function,  $h_1^\perp$ , is chiral odd and naive T-odd [466]. As such it allows the study of similar aspects of QCD as the Sivers function, however it cannot be accessed in spin-asymmetries and is therefore less well determined from data than  $f_{1T}^\perp$ . In addition to complementarity, extracting  $h_1^\perp$  from di-hadron correlations, where the PDF couples

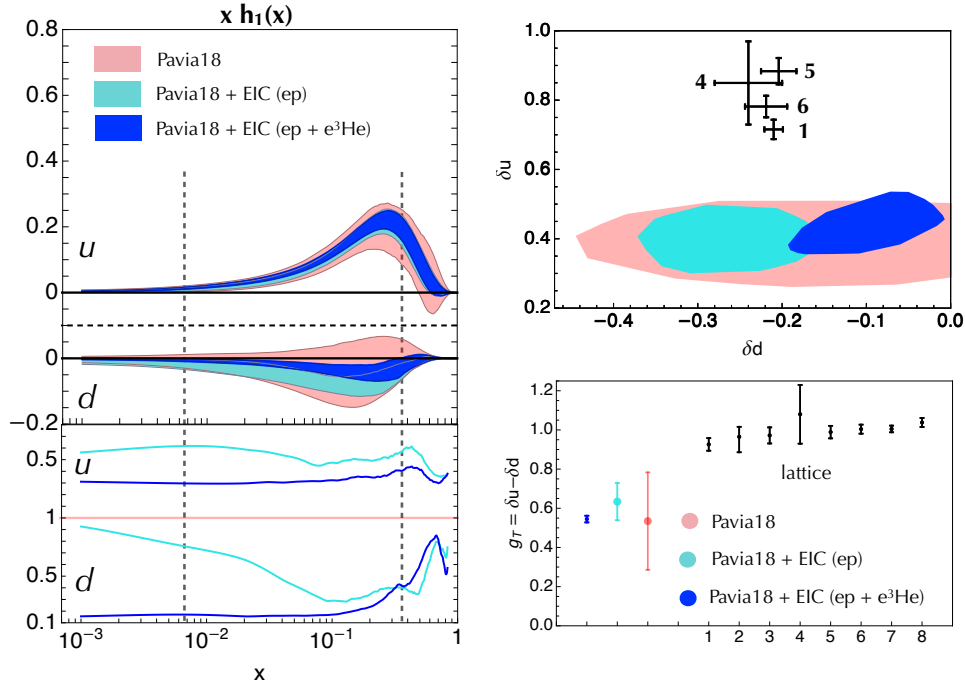


**Figure 7.59:** Left panel: Expected impact on the up and down transversity distribution as a function of  $x$  at  $Q^2 = 2.4 \text{ GeV}^2$  when including EIC SIDIS di-hadron pseudo-data from  $ep$  and  $e^3He$  collisions with electron/ion beam energy  $10 \times 100 \text{ GeV}$ ; vertical dashed lines indicate the  $x$  range covered by existing data; lower panel shows the ratio of uncertainty widths with respect to the Pavia18 extraction. Right panel: impact on the corresponding up quark ( $\delta u$ ), down quark ( $\delta d$ ), and isovector ( $g_T$ ) tensor charges, in comparison with some recent lattice calculations: 1) Ref. [403], 2) Ref. [459], 3) Ref. [460], 4) Ref. [461], 5) Ref. [462], 6) Ref. [463], 7) Ref. [464], 8) Ref. [465].

to the TMD DiFF  $\bar{H}_1^{\leftarrow}$ , has the advantage that contributions from the Cahn or twist-3 effects are not present and thus higher-order corrections are significantly reduced. Another less tangible advantage of using di-hadron asymmetries to extract modulations of the unpolarized cross-section is that acceptance effects are averaged between the hadrons in the pair, contributing to the complementarity of the measurement and ideally leading to lower overall systematics. Di-hadron FFs can also be measured in jets, allowing, *e.g.*, access to the Boer-Mulders function with a collinear FF and a separation of the intrinsic transverse momenta of initial and final states in the measurement of TMD DiFFs. There is some analogy between DiFFs and in-jet fragmentation, since both introduce an additional momentum vector, increasing the number of degrees of freedom. It will be interesting to explore opportunities that are given by the combination of these approaches.

### Jet-based TMD studies: electron-jet Sivers, hadron-in-jet Collins, and TMD evolution with substructure

Over the last few years, various studies [79,427,467–485] showed that jets offer a novel way to probe quark TMDs and TMD evolution at the EIC—this possibility was not discussed in the INT White Paper. Jets are excellent proxies for partons, cleanly separate current from target fragmentation [79,467,468], and can deconvolve TMD PDFs from FFs [468–476]. Moreover, jet substructure observables can probe TMD-evolution effects [427,477–485]. Jet physics flourished during the LHC era [486] and transformed the heavy-ion field [487], so is likely that the development of tailored jet techniques will also advance the field of 3D imaging at the EIC in synergy with traditional SIDIS studies.

Studies of quark TMDs require jets close to Born kinematics ( $\gamma^*q \rightarrow q$ )<sup>4</sup>; see Fig. 7.60. There are two frameworks to access TMD PDFs with jets: one uses the Breit frame, which requires suitable jet algorithms [468], and defines the jet’s energy fraction,  $z$ , and transverse momentum,  $q_T$ , in analogy to SIDIS [469,471,472]. Figure 7.60 shows a jet  $q_T$  prediction, which probes TMD PDFs independently of TMD FFs. The second possibility is to cluster jets with high  $p_T$  in the lab frame, which provides another hard scale, in analogy to RHIC studies [494–497]. The imbalance between the electron and jet probes TMD PDFs independently of TMD FFs [470,474–476]. Figure 7.61 shows a prediction for the electron-jet Sivers asymmetry in transversely-polarized scattering. Flavor sensitivity can be achieved by tagging  $u, d$  or strange-jets using the jet charge [473,498], identified leading hadrons inside the jet [473,499], or with neutrino-jet correlations in charged-current DIS.

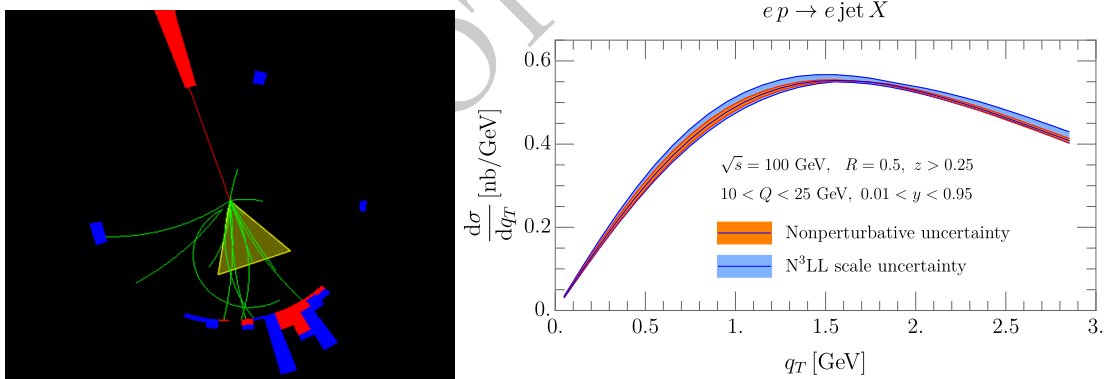


**Figure 7.60:** Left: Lepton-jet production close to the Born configuration in the laboratory frame. Right: predicted jet  $q_T$  spectrum in the Breit frame, adapted from Ref. [469,471]

TMD fragmentation can be studied through jet substructure measurements [427,476,477,479,481]. For example, in the transversely polarized case, hadron-in-jet measurements probe the quark transversity PDF and the Collins FF, see Fig. 7.61. Furthermore, novel techniques such as the winner-take-all scheme [500] and jet grooming [501,502] can boost the study of TMD evolution [478,480,482–485]. Future jet substructure studies will likely

<sup>4</sup>This process was a background for most HERA studies [488], which focused on higher-order DIS; such multi-jet configurations can probe gluon TMDs and GPDs [79,418,441,489–493], as discussed in Sections X,Y.

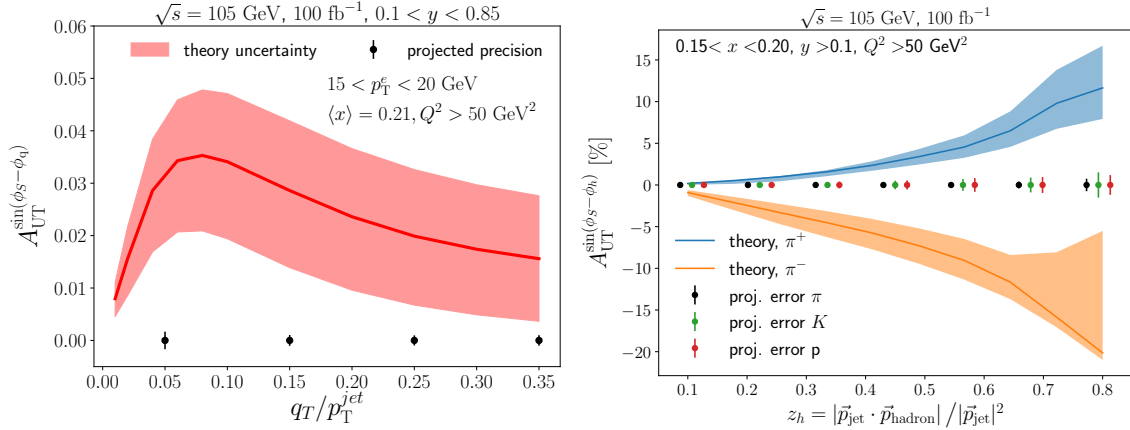


**Figure 7.61:** Left: Electron-jet Siverts asymmetry. Right: Hadron-in-jet Collins asymmetry. The error bars represent the expected precision, whereas the bands represent current uncertainties of the Siverts, transversity and Collins TMDs. Figures adapted from Ref. [470,474,475].

exploit the unprecedented combination of tracking, PID, and full calorimetry of the EIC detectors.

**Event shapes** Event shape observables have been widely used for precision QCD studies at various lepton and hadron colliders. Transverse-energy-energy correlators (TEEC) have recently been calculated to high precision in hadronic collisions using soft-collinear effective theory techniques [503]. In DIS, TEEC can be generalized by considering the transverse-energy and transverse-energy correlation between the lepton and hadrons in the final state,

$$\begin{aligned}
 \text{TEEC} &= \sum_a \int d\sigma_{l p \rightarrow l+a+X} \frac{E_{T,l} E_{T,a}}{E_{T,l} \sum_i E_{T,i}} \delta(\cos \phi_{la} - \cos \phi) \\
 &= \sum_a \int d\sigma_{l p \rightarrow l+a+X} \frac{E_{T,a}}{\sum_i E_{T,i}} \delta(\cos \phi_{la} - \cos \phi), \quad (7.35)
 \end{aligned}$$

where the sum runs over all the hadrons in the final states and  $\phi_{la}$  is the azimuthal angle between final state lepton  $l$  and hadron  $a$ . Recently, this observable has been evaluated to the highest resummed accuracy in DIS [504] - N<sup>3</sup>LL matched with the NLO cross section for the production of a lepton and two jets. Figure 7.62 shows the precision of successive orders in the nearly back-to-back TEEC limit for EIC and HERA center-of-mass energies.

The TEEC cross section can be factorized as the convolution of the hard function, beam function, jet function and soft function in the back-to-back limit. A close connection to TMD factorization is established, as the beam function when combined with part of the soft function is identical to the conventional TMD parton distribution function, and the jet function is the second moment of the TMD fragmentation function matching coefficient. As such, the generalization of TEEC to DIS [504] provides a new way to precisely study

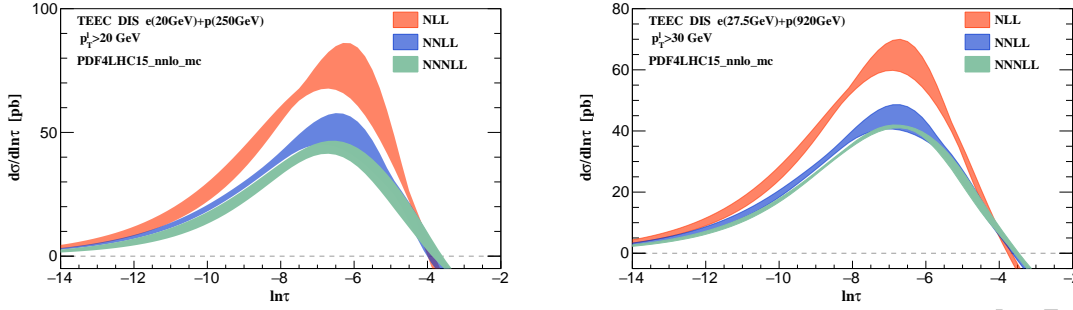


**Figure 7.62:** Resummed TEEC distributions in the back-to-back limit. The orange, blue, and green bands are the predictions with scale uncertainties at NLL, NNLL and  $N^3$ LL, respectively. Left and right panels are for EIC and HERA energies, respectively.

TMD physics and non-perturbative effects at the future Electron-Ion Collider.

**Opportunities with heavy quarks** Charm anti-charm hadron pair production in lepton-nucleon DIS proceeds at Born level via the photon-gluon-fusion process and thus offers attractive opportunities to study gluon TMD distributions [418–420, 489, 505]. The gluon Sivers TMD, for example, and TMDs of linearly polarized gluons can be linked to azimuthal anisotropies of the produced charm anti-charm hadron pair. The Sivers asymmetry can be extracted from measurements of the transverse single spin asymmetry,  $A_{UT}$ , as a function of the azimuthal angle of the  $c\bar{c}$  hadron pair relative to the direction of proton spin.  $A_{UT}(p_T)$  is defined as  $= [\sigma_L(p_T) - \sigma_R(p_T)] / [\sigma_L(p_T) + \sigma_R(p_T)]$ , where  $\sigma_{L(R)}$  are the cross-sections for particle of interest production with spin polarized in the direction opposite to (same as) the spin of the proton, and  $p_T$  is the transverse momentum of the heavy hadron pair. The  $A_{UT}$  is directly related to the Sivers asymmetry,  $A_{UT}(p_T) \propto \Delta f_g(x_g, k_T) / f_g(x_g, k_T)$ , where  $x_g$  is the gluon momentum fraction,  $k_T$  is the transverse momentum of the gluon and  $\Delta f_g$  and  $f_g$  are the gluon Sivers asymmetry and the unpolarized gluon TMD respectively.

The correlation between the azimuthal angle directions of the  $c\bar{c}$  pair momentum and that of the corresponding hadron pair momentum in the case of  $D^0\bar{D}^0$  production was studied in PYTHIA 6.4 simulations and was found to be well-preserved during hadronization. The signal strength,  $A_{UT}$  at the partonic level, can be reduced by up to 30% in the heavy quark production and subsequent hadronization in these simulations. The effects of detector response were investigated using fast simulations that smeared the particle tracks. The analysis included topological selections including cuts on the secondary vertex fitted from the  $D^0$  and  $\bar{D}^0$  decay daughters to assess signal significance and backgrounds. Figure 7.63 shows uncertainty projections for  $A_{UT}$  for different  $Q^2$  and  $x_B$  values in comparison with the possible signal size [489] of this thus far poorly constrained quantity.

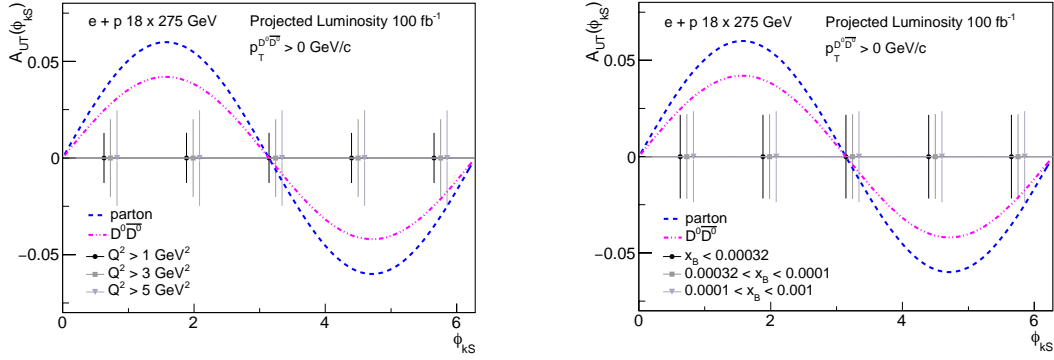


**Figure 7.63:** (left) Statistical uncertainty projections for  $A_{UT}$  in bins of azimuthal angle of the pair momentum of the  $D^0\bar{D}^0$  pair relative to the spin of the proton ( $\phi_{kS}$ ), for different  $Q^2$  (left) and  $x_B$  (right) selections. The two curves indicate the signal strength at parton and  $D^0\bar{D}^0$  levels [489].

### 7.2.4 Wigner Functions

Generalized transverse momentum dependent parton distributions (GTMDs)  $G(x, \mathbf{k}_\perp, \Delta_\perp, \mathcal{W})$  provide the most complete one-body information on the partons inside hadrons [506–509]. They can be thought of as the mother distribution of TMDs and GPDs, since they reduce to these lower-dimensional distributions via appropriate projections. GTMDs contain richer physics than TMDs and GPDs combined, as they can describe nontrivial correlations between  $\mathbf{b}_\perp$  and  $\mathbf{k}_\perp$  which are inaccessible from the studies of TMDs and GPDs separately [510,511]. This is directly evident when considering Wigner distributions  $W(x, \mathbf{k}_\perp, \mathbf{b}_\perp, \mathcal{W})$ , which represent the counterpart of GTMDs in the phase-space of momentum ( $k^+, \mathbf{k}_\perp$ ) and position ( $\mathbf{b}_\perp$ ) coordinates [512, 513]. GTMDs and Wigner distributions are mutually related by a Fourier in  $\Delta_\perp \leftrightarrow \mathbf{b}_\perp$ , at vanishing longitudinal momentum transfer  $\Delta^+ = 0$  [510].

Originally introduced in the context of nucleon structure in 2003 [512, 513], the Wigner distributions have long been thought of as purely theoretical constructs without experimental relevance. In the EIC white paper published in 2012, there was very little account of the Wigner distribution, let alone experimental probes of it. However, the situation has changed dramatically over the past several years. One of the remarkable findings is that the Wigner distribution for unpolarized ( $U$ ) partons in a longitudinally ( $L$ ) polarized nucleon provides an intuitive, but rigorous and gauge invariant, definition of the orbital angular momentum (OAM) of quarks and gluons [510, 514, 515]

$$L_{q,g}^z = \int dx \int d^2\mathbf{k}_\perp d^2\mathbf{b}_\perp (\mathbf{b}_\perp \times \mathbf{k}_\perp)^z W_{LU}^{q,g}(x, \mathbf{k}_\perp, \mathbf{b}_\perp, \mathcal{W}). \quad (7.36)$$

Depending on the path along which the Wilson line  $\mathcal{W}$  is running, the relation (7.36) pertains to the two commonly used definitions of the quark OAM [514, 516], i.e., the (canonical) one by Jaffe and Manohar ( $L_{JM}$ ) [517], and the (kinetic) one by Ji ( $L_{ji}$ ) [69], and allows for an intuitive interpretation of the difference  $L_{JM} - L_{ji}$  [518]. Therefore, an experimental

program to extract the Wigner distributions will give the opportunity to gain information on the kinetic OAM that is complementary to the study through Ji's relation from GPDs. More remarkably, it will open the way to experimentally access the canonical OAM, for which we can obtain only indirect information from TMDs. While this is an unprecedented challenge, we believe that with sufficient theory efforts and experimental planning, one may pursue such measurements at the EIC. The first theoretical ideas for observables can be found in [519–523], but their experimental feasibility is yet to be tested.

Another important development is the recognition that the gluon Wigner distribution  $W^g$  at small- $x$  is proportional to the so-called dipole S-matrix which is a fundamental object in the physics of gluon saturation [490]. Almost all observables calculated in the Color Glass Condensate (CGC) framework involve the dipole S-matrix in one way or another. Moreover, the phase space distribution of gluons and their correlation have long been discussed in the small- $x$  literature, without calling it a Wigner distribution. One can now put these efforts in a fresh context and integrate them into the general goal of studying multi-dimensional tomography at the EIC. This may also be a good starting point to explore the use of the quark and gluon Wigner distributions at large- $x$ .

In this Yellow Report, we consider using exclusive dijet production in  $ep$  collisions to access the gluon GTMD (Wigner) distribution at small- $x$ , as suggested in Refs. [490, 524], see also [525]. This is possible because of the presence of two external momentum vectors, the proton recoil momentum  $\Delta_\perp$ , which is approximately the negative total dijet momentum  $-(\mathbf{p}_{\perp 1} + \mathbf{p}_{\perp 2})$ , and the dijet relative transverse momentum  $\mathbf{P}_\perp = \frac{\mathbf{p}_{\perp 1} - \mathbf{p}_{\perp 2}}{2}$  which is related to  $\mathbf{k}_\perp$  in the GTMD. The angular correlations between  $\mathbf{b}_\perp$  and  $\mathbf{k}_\perp$  are translated into the azimuthal modulations of the dijet cross section in the angle  $\phi$  between  $\Delta_\perp$  and  $\mathbf{P}_\perp$ , which is measurable. First theoretical estimates in the CGC effective field theory suggest that the modulations are at a few percent level, or maximally some tens of percent, depending on the dijet kinematics [491, 526]. It is important to check whether such modulations survive after including the higher order corrections. The complete NLO calculation for this process in the CGC framework has been performed [527], but its numerical implementation is still in progress [528]. In addition, the resummation of soft gluons in the final state should also be considered as it can strongly affect the dijet total momentum  $\mathbf{p}_{\perp 1} + \mathbf{p}_{\perp 2}$  [493]. The connection between the dijet production cross section and the gluon Wigner distribution is established in the so called correlation limit where  $|\mathbf{P}_\perp| \gg |\Delta_\perp|$  [490]. It is also interesting to study dijet production away from this limit, where detailed information on multi gluon correlations at small  $x$  can be accessed [529].

First exploratory simulations of exclusive dijet production at EIC are presented in Sec. 8.4.10. However, we emphasize that, despite the enormous progress in recent years, the study of the GTMD/Wigner distribution is still at an early stage. Therefore, it is important to keep investigating whether additional interesting physics is (exclusively) encoded in GTMDs, and whether it can be probed in processes other than diffractive dijet production. A single process has been identified so far to access information on the *quark* GTMDs, i.e., the exclusive pion-nucleon double Drell-Yan process  $\pi N \rightarrow (l_1^- l_1^+)(l_2^- l_2^+) N'$  [522]. This process is in principle sensitive to all leading-twist quark GTMDs by making use of suitable polarization observables. However, the count rate for the double Drell-Yan re-

action is small since its cross section is proportional to  $\alpha_{em}^4$ . A pressing question is then whether one can identify a process that is sensitive to quark GTMDs, but which has a larger cross section than the double Drell-Yan at the EIC kinematics.

GTMDs also play an important role in exclusive  $\pi^0$  production  $ep \rightarrow e'\pi^0 p'$  [530]. At lower energies, this process is sensitive to chiral-odd GPDs as studied in Sec. 7.2.2. At the top EIC energy, the cross section will be dominated by a particular gluon GTMD called  $F_{12}$  [506, 509] whose forward limit  $\Delta_\perp \rightarrow 0$  is the gluon Sivers function. The latter is in fact equivalent to the QCD odderon at small- $x$  [531]. It is thus a very attractive process which can access the Sivers function in a completely unpolarized setting, and at the same time shed light on the odderon which has evaded experimental detection for decades [532].

### 7.2.5 Light (polarized) nuclei

#### Coherent DVCS on light nuclei

In hard photon electroproduction off nuclear targets (DVCS), two different channels are usually investigated: the full exclusive coherent one, with detection of the recoiling nucleus, and the incoherent one, with detection of the struck proton. An important recent achievement has been the first separation of the two channels in DVCS off  $^4\text{He}$ , [533, 534], which opens the way to a new series of measurements. The ones planned at the EIC, due to the advantages offered by the collider setup in detecting recoiling systems with respect to a fixed target experiment, look very promising. We deal here mainly with the coherent channel, whose interest is described, for example, in [535]. Here the main arguments are just listed, emphasizing the possible role of the EIC: i) nuclear tomography, along the lines of [536], to obtain a pictorial representation of the realization of the EMC effect in the transverse plane, could be realized. This requires measurements at low  $x_B$  in a wide range of  $t$ , a regime which seems at hand at the EIC; ii) the comparison with impulse approximation (IA) realistic calculations, possible for few body nuclei, could expose non nucleonic d.o.f., according to an idea initially proposed in [537]. Indeed, IA predicts a narrow light-cone momentum distribution for light systems; if measurements were performed in a wide enough range of  $t$ , which seems doable at the collider, one could look for longitudinal momenta transferred to the struck nucleon in the target larger than such a width, in a region forbidden by IA conventional description, pointing to possible contributions of non nucleonic d.o.f., among other exotic effects; iii) access to information on the nuclear energy momentum tensor and the distribution of pressure and forces inside the nucleus, and the  $d$ -term (initial idea in [329], a report in [328]); the necessity of accessing the real part of the nuclear Compton form factor makes it easier with an  $e^+$  beam, whose use at the EIC is under study [284]; iv) gluon GPDs in nuclei, exposing possible gluon d.o.f. in nuclei, planned already at JLab [538], will be easier to study at the EIC, due to the very low reachable  $x_B$ ; the same holds for all the low- $x$  phenomena, such as nuclear shadowing, for which a peculiar behavior has been predicted [539]; v) a specific access to the information for the free neutron, possible using specific nuclei and specific polarization setups in the experiments [540].

Light nuclei play a very important role in general: their conventional structure is realistically known so that exotic effects in DVCS processes can be exposed; at the EIC, where they will be used as beams, their importance is evident. In the following, the specific role of deuteron,  $^3\text{He}$  and  $^4\text{He}$  is summarized.

The Deuterium nucleus is a spin one system with a rich spin structure and many GPDs at leading twist [537]. Being a two-body system, its relativistic description is affordable and the GPDs have been evaluated in a light front framework in Ref [541] and, for the transversity sector, in Ref. [542]. Theoretically well studied, the measurements of coherent DVCS would allow the test of several predictions, concerning the EMT [127, 543] and the parton spin content, for which a specific sum rule has been proposed [544]. Nuclear effects are expected to be small and the deuteron is the obvious candidate to extract the neutron information, mainly in the unpolarized setup and in the incoherent channel, where final state interactions can be relevant but can be in principle evaluated realistically.

Being a spin  $1/2$  system, the amplitude of DVCS off  $^3\text{He}$  has the same GPDs decomposition of that of the nucleon, which has been thoroughly studied. The CFFs can be extracted measuring the same asymmetries defined for the proton target, and GPDs can be obtained by performing the same analysis. Its binding energy is in between that of the deuteron and that of  $^4\text{He}$ , making it the ideal target for studying the onset of nuclear effects through the periodic table. Among the light nuclei, it is the only one with non zero isospin, so that it is unique to study isospin-flavor dependence of nuclear effects [545, 546], more easily seen through  $^3\text{H}$  beams, whose use at EIC is presently under discussion [284]. Realistic conventional effects have been studied in IA calculations in terms of (spin-dependent) spectral functions [540, 545–548] and are under control, so that possible effects due to an exotic nuclear parton structure can be safely exposed in forthcoming data; even the evaluation of relativistic effects in a Light-Front framework, although challenging, are under investigation along the lines of [549]. The specific spin structure of  $^3\text{He}$  has been used extensively to extract the information for the polarized neutron. Also in this exclusive process specific CFFs in (polarized) coherent DVCS, where FSI should be negligible with respect to the incoherent case, appear dominated by the neutron contribution [540, 547, 548], so that the extraction of the neutron information, complementary to that to be obtained from the deuteron, looks promising. The possible use of (polarized)  $^3\text{He}$  ( $^3\text{H}$ ) beams, to be detected far from the interaction region, makes the EIC the ideal machine for completely new studies.

The  $^4\text{He}$  nucleus is a spin 0 system and therefore the DVCS amplitude is described in terms of one leading-twist GPD in the chiral even sector, so that only one CFF has to be extracted in the experimental analysis, which is much easier than, for example, that for the nucleon target. From the point of view of nuclear dynamics, it is a deeply bound, "real" nucleus and the nuclear effects are similar to those expected for heavier nuclei. For  $^4\text{He}$ , realistic (non relativistic) descriptions are challenging but possible, making it the ideal target to disentangle exotic medium effects. As already said, it is the only nucleus for which data for the coherent channel have been released [533]. Some calculations are also available since a long time [551, 552]. In the most recent IA theoretical analysis, given in Ref. [550], a semi-realistic nuclear description based on the Av18 interaction [553] and the

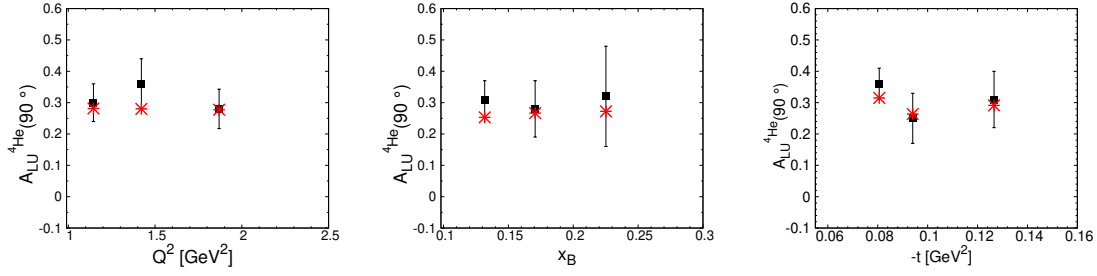


**Figure 7.64:**  $^4\text{He}$  azimuthal beam-spin asymmetry  $A_{LU}(\phi)$ , for  $\phi = 90^\circ$ : results of Ref. [550] (red stars) compared with data (black squares) [533].

UIX three-body forces [554] is used, with the GK model to parametrize the nucleon GPDs, later extended to the incoherent channel [555, 556], successful in reproducing the data for the beam-spin asymmetry  $A_{LU}$ , as shown in Fig. 7.64, and for the real and imaginary parts of the CFFs. This model is currently used in the TOPEG event generator and applied to simulate DVCS at the EIC kinematics. The region of low  $x_B$ , naturally accessible at the EIC and very important to study gluons in nuclei and expose exotic effects, is presently under investigation, for both DVCS and for the exclusive production of vector mesons. As for any coherent exclusive process, in DVCS off  $^4\text{He}$  the collider setup makes the detection of the recoiling intact nucleus easy, which is very slow in a fixed target experiment. This is even more important in the incoherent channel, for which the detection of other nuclear fragments could allow to control FSI effects.

### Tensor polarized deuteron

Rewrite still coming over the weekend Oct 24

The deuteron, being a spin-1 particle, has additional spin degrees of freedom compared to the nucleon. These can be probed using deuteron beams prepared in a spin ensemble with tensor polarization. In inclusive DIS with a tensor polarized target, this gives rise to 4 additional structure functions  $b_{1-4}$ , two of which are leading twist ( $b_1, b_2$ ) [557]. The  $b_1$  structure function has a partonic density interpretation, which is also explicitly dependent on the nuclear magnetic state of the surrounding deuteron. This makes the observable unique because it directly probes nuclear interactions at the parton level. As such, it provides possibilities to unravel novel information about nuclear structure, quark angular momentum, gluon transversity and the polarization of the quark sea that is not accessible in spin-1/2 targets [544, 558–562].

The  $b_1$  structure function is experimentally extracted from the tensor asymmetry

$$A_{zz} = 2 \left( \frac{\sigma^+ - \sigma^-}{|P_{zz}^+| \sigma^- + |P_{zz}^-| \sigma^+} \right), \quad (7.37)$$

where  $P_{zz}$  is the amount of tensor polarization that ranges from  $-2 \leq P_{zz} \leq 1$ , and  $\sigma^{+(-)}$

is the cross-section when the target is polarized along (opposite) the beam momentum.

Tensor polarized deuteron is little explored in electron scattering, elastic measurements are discussed in Sec. 7.2.1, quasi-elastic measurements were carried out at NIKHEF [563] and MIT Bates [564] and an inclusive DIS measurement at HERMES [565]; two measurements are planned at JLAB [566,567]. The Jefferson Lab measurements can be extended to probe QCD effects at much higher energies and lower  $x_{Bj}$  at the EIC.

Measurements of  $A_{zz}$  in the quasi-elastic region illuminate QCD effects at short-range and high-momentum that are dependent on whether the deuteron wavefunction is hard or soft [52]. The discovery of short-range correlations (SRCs) in the quasi-elastic high- $x$  region, where all nuclear cross-sections scale similarly to that of the deuteron, has led to a renewed interest in understanding these effects, see Sec. 7.3.7. The tensor asymmetry  $A_{zz}$  provides a unique tool to experimentally constrain the ratio of the  $S$  and  $D$  wave functions at large momentum, which has been an ongoing theoretical issue for decades.

Conventional nuclear physics models predict  $b_1$  and  $A_{zz}$  in inclusive DIS to be very small. This is due to the averaging over initial deuteron configurations inherent to inclusive measurements and  $b_1$  being proportional to the (small) deuteron  $D$  wave. In combination with tagging of a spectator nucleon (see Sec. xxx), however, maximal  $A_{zz}$  asymmetry values of -2 and +1 can be reached. The tagged DIS cross section also has several tensor polarized structure functions which are zero in the impulse approximation and hence offer an opportunity to study spin-orbit effects specific to tensor polarization.

Preliminary EIC rate estimates for the tensor polarized asymmetry  $A_{zz}$  are shown in Fig. 7.65, assuming a maximum positive and negative tensor polarizations of  $P_{zz}^+ = 0.85$  and  $P_{zz}^- = -1.70$  for approximately two weeks of running. This corresponds to  $1 \text{ fb}^{-1}$  for a 3 GeV electron beam and 38 GeV/nucleon deuteron beam. Similar rates can also be achieved at higher beam energies corresponding to  $10 \text{ fb}^{-1}$  for a 10 GeV electron beam and 60 GeV/nucleon deuteron beam, which would further extend new results to the high  $Q^2 \approx 100 \text{ GeV}^2/c^2$  region. [needs updating for current EIC design]

### Medium modification of azimuthal modulations in nuclear SIDIS

Rewrite still expected

Measurements of medium modifications of spin dependent and independent azimuthal asymmetries in SIDIS provide access to medium modified parton distributions, and to relative magnitude of the transverse momentum width of the nucleon TMDs. Orbital motion of quarks is modified in the medium [568]. That makes the variety of physics observables sensitive to orbital motion, in particular various spin and azimuthal asymmetries, good candidates to provide important information on partonic distributions in bound nucleons. Measurements of medium modifications of various spin and azimuthal asymmetries using unpolarized and longitudinally polarized leptons and nucleons will provide important information on the relative size of the transverse momentum in the proton, allowing to use nuclear targets as a microscope to study the proton.

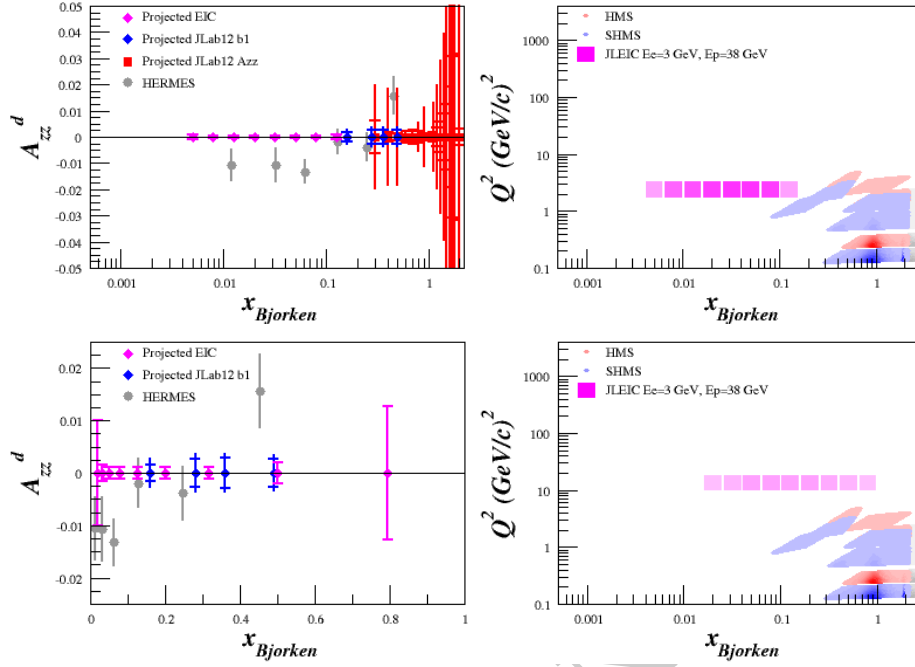


**Figure 7.65:** [Placeholder] Preliminary rate estimates and kinematic coverage for tensor measurements at the EIC (magenta) for  $1 \text{ fb}^{-1}$  for a 3 GeV electron beam and 38 GeV/nucleon deuteron beam are shown alongside rate estimates for the upcoming Jefferson Lab experiments to measure  $A_{zz}$  at small (blue) and large (red) Bjorken  $x$ .

For reactions with nuclear targets  $e+A \rightarrow e+h+X$ , the TMD quark distributions in a nucleus  $A$  can be expressed as a product of nucleon TMDs and some functions depending on the total transverse broadening  $\Delta_{2F}$ , which itself depends on the quark transport parameter  $\hat{q}$  [569,570]:

$$f_1^A(x, k_\perp) \approx \frac{A}{\pi \Delta_{2F}} \int d^2 \ell_\perp e^{-(\vec{k}_\perp - \vec{\ell}_\perp)^2 / \Delta_{2F}} f_1^N(x, \ell_\perp), \quad (7.38)$$

$$|\vec{k}_\perp|^2 g^{\perp A}(x, k_\perp) \approx \frac{A}{\pi \Delta_{2F}} \int d^2 \ell_\perp e^{-(\vec{k}_\perp - \vec{\ell}_\perp)^2 / \Delta_{2F}} (\vec{k}_\perp \vec{\ell}_\perp) g^{\perp N}(x, \ell_\perp). \quad (7.39)$$

Using a Gaussian ansatz [569,570] for TMD quark distributions in a nucleon, the integrations in the leading twist contributions can be carried out analytically:

$$f_1^A(x, k_\perp) \approx \frac{A}{\pi \alpha} f_1^N(x) e^{-\vec{k}_\perp^2 / \alpha}, \quad (7.40)$$

$$g^{\perp A}(x, k_\perp) \approx \frac{A}{\pi \gamma_A} \frac{\gamma}{\gamma_A} g^{\perp N}(x) e^{-\vec{k}_\perp^2 / \gamma}, \quad (7.41)$$

where  $\alpha = \langle k_\perp^2 \rangle + \Delta_{2F}$  and  $\gamma = \langle k_\perp^2 \rangle_\gamma + \Delta_{2F}$  and  $A$  is the atomic number.

Measurement of higher twist SSAs in medium will provide access to medium modifica-

tions of spin-orbit correlations, involving several higher twist TMDs which are sensitive to final state interactions ( $f^\perp$ ,  $g^\perp$ , and  $f_L^\perp$ ) which are essential components of the 3D structure of the nucleons. Detection of jets with EIC would allow studies of medium modified TMDs, with completely different, compared to hadrons, systematics, *viz.* without involvement of unknown fragmentation functions, and their modification in medium. Medium modification of  $A_{LU}^{\sin\phi}$ , for example could be determined by the TMD parton correlation  $g^\perp$ , modified in medium [569].

$$\frac{\langle \sin\phi \rangle_{LU}^{eA}}{\langle \sin\phi \rangle_{LU}^{eN}} \approx \frac{\langle k_\perp^2 \rangle_A}{\langle k_\perp^2 \rangle} \left( \frac{\langle k_\perp^2 \rangle^{g^\perp}}{\langle k_\perp^2 \rangle_A^{g^\perp}} \right)^2 \exp \left[ \left( \frac{1}{\langle k_\perp^2 \rangle_A} - \frac{1}{\langle k_\perp^2 \rangle} - \frac{1}{\langle k_\perp^2 \rangle_A^{g^\perp}} + \frac{1}{\langle k_\perp^2 \rangle^{g^\perp}} \right) \bar{k}_\perp^2 \right]. \quad (7.42)$$

where  $\langle k_\perp^2 \rangle^{g^\perp}$  and  $\langle k_\perp^2 \rangle_A^{g^\perp}$  are widths of  $g^\perp$  distribution in free and bound nucleons. Nuclear modifications of beam SSA, for example, appear to be very sensitive to the relative widths of involved *nucleon* TMDs, and change significantly with transverse momentum (see Fig.7.66). It is worthwhile noticing that the overall magnitude of the effect is governed by the same transport parameter  $\hat{q}$ , or equivalently the transverse momentum broadening  $\Delta_{2F}$ , that controls nuclear suppression of hadron production in unpolarized and polarized electron-nucleus scattering.

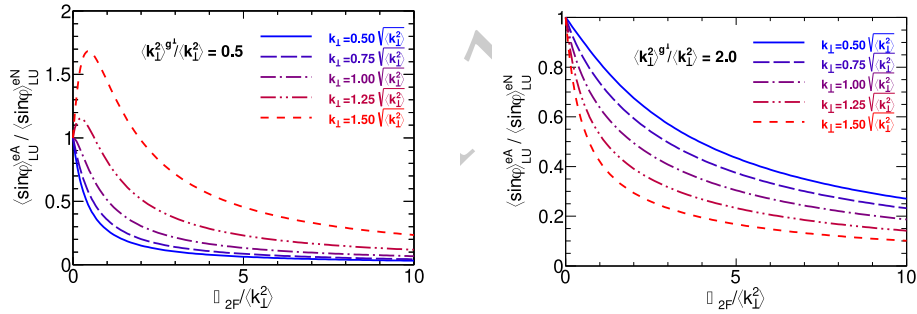


**Figure 7.66:** Ratio of  $\langle \sin\phi \rangle_{LU}^{eA} / \langle \sin\phi \rangle_{LU}^{eN}$  as a function of  $\Delta_{2F}$  for different  $k_\perp$  and  $\langle k_\perp^2 \rangle^{g^\perp} / \langle k_\perp^2 \rangle$  ratios.

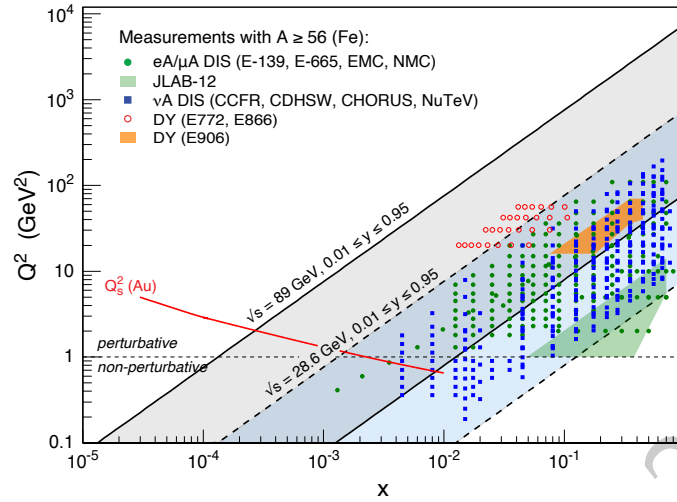


**Figure 7.67:** The kinematic coverage of the EIC for DIS on nuclei compared to that of previous experiments. The expected "saturation scale"  $Q_s^2(x)$  for non-linear gluon dynamics is indicated by a red line.

### 7.3 The Nucleus: A Laboratory for QCD

This section is devoted to an overview of the fundamental physics with light and heavy nuclei that will be performed at the EIC. Of course, nuclei are made of nucleons, which in turn, are bound states of the fundamental constituents probed at short distances, namely quarks and gluons. The EIC will be the world's first dedicated electron-nucleus  $e+A$  collider. It will explore the effect of the binding of nucleons on the momentum distribution of quarks and gluons, but also, for the first time, determine their spatial distribution in a nucleus via diffractive or exclusive processes. In addition, the wealth of semi-inclusive probes at the EIC provides direct and clean access to fluctuations of the density of quarks and gluons in nuclei.

#### Physics of non-linear color fields:

Due to the rapid rise with energy of the gluon density in hadrons, gluons play a key role in our understanding of DIS and hadronic collisions at high energies. Gluons are responsible for much of particle production in such collisions as well as for the rise of total cross sections, related to the saturation of scattering amplitudes with energy as the unitarity limit is approached. This is a fundamental limit of Nature on the maximal strength of color fields in hadrons and nuclei. In particular, the scrutiny of nonlinear gluon dynamics will improve our insight into the strong interaction rather profoundly, and help us to more deeply understand this fundamental pillar of the standard model.

DIS experiments on heavy nuclei at high energies are ideally suited for the study of non-linear gluon dynamics. The projectile interacts coherently with a large number of stacked nucleons. This probes very strong color fields at high energy, which is expected to lead to the phenomenon of gluon saturation, described by an effective theory known as the

Color Glass Condensate (CGC). In particular, the squared transverse momentum (or inverse distance) scale where QCD becomes nonlinear is expected to grow in proportion to the average thickness of the target nucleus, and as a power  $\lambda = 0.2 - 0.3$  of energy:

$$Q_s^2 \sim \frac{A^{1/3}}{x^\lambda}. \quad (7.43)$$

Here,  $x$  denotes the momentum fraction of gluons in the target which is probed in a particular process; it is inversely proportional to the energy.

One of the main goals of the physics program to be pursued at the EIC is to obtain evidence for nonlinear QCD dynamics at a perturbative scale  $Q_s > 1$  GeV from the energy dependence of DIS cross-sections, structure functions, and other observables. This is predicted by the theory in form of nonlinear evolution equations. Discovery of saturation requires unambiguous experimental evidence for these specific nonlinear equations. The high-energy aspects of DIS on nuclei have been presented more extensively in the White Paper [1], and are addressed here in secs. 7.3.1, 7.3.2. The latter section also discusses the unique opportunity at the EIC to measure **nuclear diffractive PDFs** and to understand their connection to shadowing. Section 7.3.9 covers **coherent and incoherent photoproduction** on heavy ion targets.

### Nuclear PDFs

The nuclear parton distribution functions (nPDF) describe the behavior of bound partons in the nucleus. Like their free-proton counterparts, nPDFs are assumed to be universal and are essential tools for understanding experimental data in collider experiments. To date, there is no compelling evidence for violation of the QCD factorization theorem [571] or violation of universality. Thus, precise knowledge of PDFs in general, and nPDF in particular, becomes most relevant for interpreting results from collider experiments and advancing our understanding of strong interactions on nuclear medium. A precise knowledge of nPDFs is crucial for understanding the transition between linear and non-linear scale evolution of the parton densities. Of particular interest is the regime known as "saturation," where the recombination of gluons at low  $x$  becomes increasingly important, and the growth of the gluon density is suppressed. The nPDFs lay an essential foundation for understanding hot Quark-Gluon Plasma (QGP) medium produced in the Heavy Ion Collisions at RHIC and LHC, particularly for experimental measurements initiated by early-state hard scatterings. Proper characterization of the QGP dynamics also relies on the adequate separation of the initial and final state effects, the former encoded in the corresponding nPDFs. The deep-inelastic scattering experiments with nuclear targets are also in critical need of precise nPDFs for the neutrino DIS data making in turn impact on the global analysis of proton PDFs.

Experimentally, the differences between the PDF and nPDF has been firmly established by the deep-inelastic lepton-nucleus scattering data. Significant nuclear effects observed have ruled out a naive model of a nucleus as a superposition of quasi-free nucleons and forced us to factor in modifications due to the nuclear environment. The nuclear modifications are commonly described as shadowing, anti-shadowing, and the EMC effect [572–575]. These

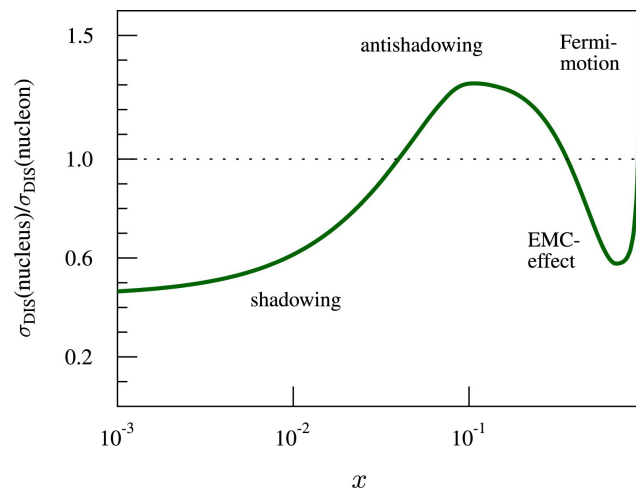


**Figure 7.68:** Typical nuclear effects seen in the DIS measurements. The figure is from [576].

modifications are usually expressed with the help of ratio to the free-nucleon PDFs, with  $R < 1$  indicating suppression of probability distribution compared with the free proton reference, and  $R > 1$  – an enhancement. The approximate domains for these experimentally observed modifications illustrated in Fig. 7.68 are as follows: the shadowing regime ( $R < 1$ ) is affecting the  $x < 0.1$  region; the anti-shadowing ( $R > 1$ ) effect is said to act in  $0.1 < x < 0.3$ , and the EMC effect refers to the slope of  $R$  in the valance-dominant  $0.3 < x < 0.7$ .

Understanding how parton dynamics is modified in the nuclear medium and the exact nature of the mechanisms that generate the shadowing, anti-shadowing, and EMC effects is the field of active pursuit for both the theory and experiment. It is commonly accepted that different physics processes contribute to different  $x$ -regions; however, there is no consensus on these contributions' exact nature. The dependencies on nuclear size and  $x$  for these nuclear effects could not be derived from first-principles calculations but are instead inferred from fits to the existing data experimental. However, in contrast to the free-proton PDFs, the determination of nPDFs is severely limited by the kinematic coverage and the available data precision. The EIC realization with its intended versatility regarding available ion beam species and afforded phase space coverage will profoundly impact nPDF determination. Recent nPDF-related developments are discussed in sec. 7.3.3.

### Particle propagation through matter and transport properties of nuclei

In parallel with the qualitatively new constraints on nPDF, the EIC physics program will allow new advances in the related but intrinsically different modifications induced by the cold nuclear matter – the energy loss of the partons traversing the QCD medium. The energy loss is expected in both hot (QGP) and cold QCD matter through gluon radiation and collisional scattering losses. The quantitative assessments of the related processes in both types of media are central to relativistic heavy ion collisions and the nuclear physics field in general. The cold nuclear matter has specific scales for gluon radiation that are different from the QGP medium. Specifically, the (partially coherent) Landau-Pomeranchuk-

Migdal (LPM) regime, with the gluon formation times of the order of the medium length, and a fully coherent (or factorization) regime, dominating for significantly longer time frames [577]. While the fully coherent part could be evaluated via quarkonic measurements in hadronic collisions [578], the final-state energy loss in nuclei in the LPM regime will be probed at the EIC most directly by hadron production measurements in semi-inclusive deep inelastic scattering events.

The emerging EIC detector concepts suggest excellent capabilities for jet reconstruction and jet studies; relying on jets for extracting cold nuclear matter transport properties gives significant advantages over inclusive and semi-inclusive hadron measurements, as it allows to effectively reduce the role of nPDF modifications (with respect to the free-nucleon PDF) and enhance the effects due to final state interactions. Medium-induced radiation resulting in broadening of the transverse profile of jet shower will be discerning measurement to quantify the final state gluon radiation and its angular dependence with the EIC data. The details of related studies are presented in sec. 7.3.4.

### Collective effects

Until recently, "collective phenomena" were associated exclusively with large fireballs formed in nuclear collisions. These event-wised multiparticle azimuthal correlations, particularly a long-range pseudorapidity feature termed "ridge" [579], were neither expected nor present in any modeling of "small" systems such as p+p or p+A collisions. This paradigm was shattered with the discovery of ridge "ridge"-correlation in (high multiplicity) proton-proton and proton-nucleus collisions [580–590]. These long-range correlations have two compelling theoretical explanations based on orthogonal premises: one interprets the observed effect in the small system data as a final-state phenomenon. The other is the initial state effect. At the EIC, the selection of DIS-events at small- $x$  will provides us with a unique testing ground to test and understand in detail the physics mechanism behind the formation of these collective interactions, see sec. 7.3.5.

### Special opportunities with jets and heavy quarks

The technical capabilities of the EIC machine and detector concept under developments provide an excellent ground for extending jet and heavy quark measurements beyond the inclusive cross-sections and simple semi-inclusive correlations. There is a palpable shift in the research efforts towards the jet substructure studies, including such studies with a required in-jet heavy flavor hadron presence, or "tagging." While the methods for exploring the jet constituent distributions began to develop in the 1990 [591] and possibly earlier, this direction has exploded in recent years in the HEP community [592]. At the same time, the jet substructure methods have been successfully adopted for studies of medium-induced jet modifications in the QGP by the nuclear physics community.

Jet substructure observables are indispensable tools for flavor-tagging, i.e., for statistical identification of the parton originating the jet. Flavor-tagging enables another dimension to explore the nuclear modification effects, of both initial and final state origin, for different hard-scattered partons. At the EIC, the jet substructure observables, specifically jet angularity, can image the nucleon/nuclei 3D structure and map out the hadronization process in a vacuum and nuclear medium. Another substructure tool that has been studied

in the connects of the future EIC data is the jet charge, which showed promise to discern the contributions of quark and anti-quark jets and to, again, pinpoint their original parton flavor. A high precision jet charge measurements at the EIC will provide an excellent way to constrain isospin effects and the up/down quark PDFs in the nucleus. The details are supplied in sec. 7.3.6.

### Short range correlations and the structure of light nuclei:

The EIC will also provide novel insight into the physics of short range correlations (SRC) in nuclei and how they relate to the mechanism by which QCD generates the nuclear force. The modification of the structure of bound nucleons as manifest, for example, in the EMC effect could be caused by short-range correlated nucleon pairs with high internal nucleon momentum. The new collider will investigate the underlying physics of SRC in kinematic regions that so far could not be reached. A more detailed discussion is presented in sec. 7.3.7.

Also, the EIC will provide polarized  $^3\text{He}$  and  $^3\text{H}$  beams, possibly deuteron ( $^2\text{H}$ ) beams and more. This allows to probe the spin structure of the neutron, the tensor polarized deuteron, and measurements of the polarized EMC effect, in order to understand the interplay between partonic QCD phenomena and nuclear interactions; c.f. sec. 7.3.8.

#### 7.3.1 High parton densities and saturation

The study of emergent properties of the ultra-dense gluonic matter is an important pillar of EIC physics. Since the emission of soft gluons is favored in QCD, a large number of low-momentum gluons exist inside high energy nucleons and heavy nuclei. These low momentum gluons are usually referred to as the low- $x$  gluons, where  $x$  is the longitudinal momentum fraction of the gluon with respect to the parent hadron. As a consequence, one observes a rapid increase in the gluon density towards smaller  $x$  and a corresponding increase in the quark density coming from sea quarks via the  $g \rightarrow q\bar{q}$  splitting process. On the other hand, the density of quarks and gluons in the small- $x$  limit will not become infinitely large due to the gluon saturation effect. When the gluon density is sufficiently high, the recombination of gluons via the  $gg \rightarrow g$  process becomes important. Eventually, gluon density is expected to saturate, as a balance is reached between gluon radiation and recombination.

The theoretical framework [593–596], which describes the saturation of the densely populated gluonic system inside nucleons and heavy nuclei, is known as the saturation physics or the Color Glass Condensate (CGC) formalism. This framework can be viewed as an effective theory of high energy QCD in the low- $x$  limit. In the small- $x$  formalism, the emission of soft gluons is captured in the famous Balitsky-Fadin-Kuraev-Lipatov (BFKL) equation [223, 224], while the gluon recombination manifests itself as the additional non-linear term in the extended evolution equations, which are known as the Balitsky-Kovchegov (BK) equation [597, 598] and the Jalilian-Marian-Iancu-McLerran-Weigert-Leonidov-Kovner (JIMWLK) equation [599–602]. These non-linear QCD evolution equations encode the gluon saturation, which emerges as the universal stable fixed

point independent of initial conditions of color sources [603]. In practice, one often defines the so-called saturation momentum  $Q_s^2(x)$  to separate the nonlinear saturated dense regime at low transverse momentum (or virtuality) from the linear dilute regime, and to characterize the strength of the saturation effects. Comparing to the saturation momentum in the proton, the saturation momentum  $Q_s^2$  for a large nucleus target with the nuclear mass number  $A$  is enhanced by a factor of  $\sim A^{1/3}$  due to the overlap of nucleons at a given impact parameter [604]. This nuclear enhancement factor is also known as the “oomph” factor, which indicates that the saturation effect in  $e+A$  collisions is much stronger than that in  $e+p$  collisions.

### Inclusive cross sections at small $x$

At HERA, an extremely interesting phenomenon, which is known as the geometrical scaling [605], has been discovered in the low- $x$  inclusive DIS data in  $e+p$  collisions. In general, the inclusive cross section is the function of independent variables  $x$  and  $Q^2$ . However, in the small- $x$  regime, the inclusive cross section can be cast into a single variable function which only depends on  $\tau \equiv Q^2/Q_s^2(x)$  with  $Q_s^2(x) = Q_0^2 \left(\frac{x}{x_0}\right)^\lambda$ . Using  $Q_0 = 1 \text{ GeV}$  and  $x_0 = 3.04 \times 10^{-3}$  and  $\lambda = 0.288$ , one can show that all the inclusive data points within the range of  $x < 0.01$  and  $Q^2 < 450 \text{ GeV}^2$  fall on a single curve. Later, it was demonstrated in Refs. [603] that this remarkable geometrical scaling phenomenon can be elegantly derived from the traveling wave type solution of the non-linear BK equation. This has been reckoned as one of the striking pieces of evidence for the saturation formalism. At EIC, the inclusive cross section in  $e+A$  collisions in the low- $x$  regime will provide important information about the nuclear shadowing effect and the saturation phenomenon.

A systematic way of calculating inclusive cross sections in the CGC formalism is provided by the dipole factorization picture. Here one separates the process into an impact factor describing the fluctuation of the virtual photon into a partonic state, at leading order a dipole and at NLO also a  $q\bar{q}g$  state, and the scattering amplitude of this state with the target. This dipole scattering amplitude generalizes the concept of a gluon distribution to include the possibility of nonlinear interactions with the target gluon field. Its dependence on  $x$  (or the collision energy  $W$ ) is described by the BK or JIMWLK equations. Depending on the polarization state of the  $\gamma^*$  one must consider separately transversally and longitudinally polarized photons. Measuring both cross sections will be a central part of the physics program at the EIC. In particular, the total virtual photon-target cross section for both protons and heavy nuclei are important “day one” measurements.

In a set of major theoretical advances in recent years both the BK [606] and the JIMWLK equations [607, 608] are now known at NLO accuracy in the QCD coupling constant. An additional resummation of transverse (“collinear”) logarithms is required to stabilize the NLO equations, but by now robust practical methods to achieve this resummation have been achieved [609–611]. Also, the impact factor required for calculating the cross section is now known, both in momentum space [612, 613] and, in a more practical form for use with the BK equation, in mixed transverse coordinate-longitudinal momentum space [614–616].

Using this theoretical machinery, a very good description of existing HERA small- $x$  inclusive cross section data has been achieved using the collinearly resummed BK evolution equations both with LO [617] and NLO impact factors [618]. An extension of the NLO calculation to heavy quarks is expected to appear soon. These calculations are straightforwardly generalizable from protons to nuclei without any other parameters than the Woods-Saxon nuclear density [619]. Together with EIC measurements of the total and longitudinal  $\gamma^*p$  and  $\gamma^*A$  cross sections, they will allow for a clear and precise window into the physics of gluon saturation.

### Accessing low $x$ gluon via di-jets/di-hadrons

At EIC, by going beyond the inclusive measurements and studying the SIDIS observables in the low- $x$  regime, we can obtain more vital information about the gluon distributions. For many years, we have known that there are two gluon distributions in the CGC formalism. On one hand, the dipole unintegrated gluon distribution (UGD), which is defined as the Fourier transform of dipole-target cross section [620], often appears in the calculation for various inclusive processes. On the other hand, the so-called Weizsäcker-Williams (WW) gluon distribution [621,622] has also been derived as the genuine number density of gluon inside a target hadron by applying the well-known WW method of virtual quanta in QCD. In the McLerran-Venugopalan model [595] for a large nucleus, these two UGDs are found to have distinct  $p_T$  behaviors. The small- $x$  evolution of these two gluon distributions can be taken care of by applying the JIMWLK evolution equation to the corresponding correlators in the coordinate space [623,624]. Based on the gauge link structure of the WW gluon distribution and calculation in CGC formalism, it is proposed [412,625] that the DIS back-to-back dijet/dihadron production at the EIC can be used to directly probe the WW distribution, which has not been measured before.

To directly probe the WW gluon distribution and gluon saturation effects at low  $x$ , we can measure the azimuthal angle difference ( $\Delta\phi$ ) between two back-to-back charged hadrons in  $e+A$  collisions ( $e+A \rightarrow e'h_1h_2X$ ). This azimuthal angle distribution can help us map the transverse momentum dependence of the incoming gluon distribution. The away-side peak of the dihadron azimuthal angle correlation is dominated by the back-to-back dijets produced in hard scatterings. Due to the saturation effect, the WW gluon TMD can provide the extra transverse momentum broadening to the back-to-back correlation and cause the disappearance of the away-side peak when the saturation effect is overwhelming [412,626]. A comparison of the heights and widths of the coincidence probability  $C(\Delta\phi) = \frac{N_{pair}(\Delta\phi)}{N_{trig}}$  in  $e+p$  and  $e+A$  collisions will be a clear experimental signature for the onset of the saturation effect.

Furthermore, following the prescriptions in Ref. [627], a Monte Carlo simulation has been carried out for the azimuthal angle correlations of two charged hadrons at  $\sqrt{s} = 90$  GeV in  $e+p$  and  $e+Au$  collisions. The results of the simulation are also compared with the prediction from the saturation formalism. To focus on the low- $x$  region, the events within the range of the virtuality  $1 < Q^2 < 2$  GeV<sup>2</sup> and inelasticity  $0.6 < y < 0.8$  are selected. The events of the nearby  $Q^2$  and  $y$  bins are expected to yield similar results. The hadron pairs

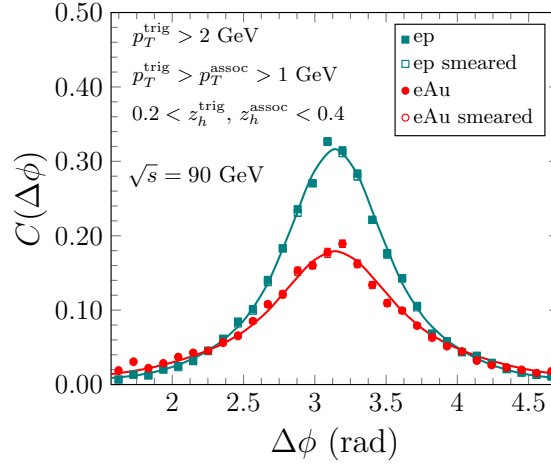


**Figure 7.69:** Comparison between the dihadron azimuthal angle correlation in  $e+Au$  collisions (labeled with filled red circles) and that in  $e+p$  collisions (labeled with filled teal squares). The results with the detector smearing are shown in open markers. The solid lines represent the results obtained from the theoretical model calculations in the CGC formalism.

are required to have the energy fraction  $0.2 < z_h^{trig}, z_h^{assoc} < 0.4$  within the pseudorapidity range  $|\eta| < 3.5$  with  $p_T^{trig} > 2 \text{ GeV}/c$  and  $1 \text{ GeV}/c < p_T^{assoc} < p_T^{trig}$ . The away-side peak of  $C(\Delta\phi)$  distribution is shown in Fig. 7.69. The  $e+p$  reference is displayed by the squares in teal, while the results in  $e+A$  collisions are shown in red. The results which include the detector response to this measurement are represented by the open markers. Based on the current EIC tracking resolution design, the impact of the detector smearing effect on this measurement is negligible. The theoretical results plotted in solid curves include the saturation effects together with the Sudakov resummation in the CGC formalism [628–630]. A significant suppression of the away-side peak in  $e+Au$  collisions compared to the  $e+p$  reference can be observed given the projected statistical uncertainty corresponding to an integrated luminosity of  $10 \text{ fb}^{-1}/A$ .

At last, it should be pointed out that the productions of di-jets/di-hadrons and the heavy quark pair also allow one to probe the linearly polarized gluon distribution described by the TMD  $h_1^{\perp g}$  [631]. At the low- $x$  regime, the WW type of  $h_1^{\perp g}$  [492, 632, 633] can also be important, and generate sizable asymmetries of in azimuthal angle distributions. Detailed numerical studies of the corresponding asymmetries at the EIC can be found in Ref. [634].

### Recent Progress in Probing Gluon Saturation with Jet Observables

Jet observables provide an unprecedented opportunity to probe proton and nuclear structure at small Bjorken  $x$  in a more differential fashion as compared to more inclusive observables. Several theoretical results have been obtained recently for inclusive dijet production in the forward direction, leading in particular to the introduction of new types of TMD distributions in the small  $x$  regime that are sensitive to saturation effects [529, 635, 636].

Moreover, with  $e+A$  collisions at EIC, one will be able to probe partonic content of dense nuclear targets. In particular production of jets at moderate and low values of  $x$  will offer a possibility to study the interplay of the Sudakov effects related to hard scales present in the perturbative description, and the nonlinear effects due to gluon saturation phenomenon predicted in QCD. Also, a variety of nuclear targets offer a chance to explore the so-called small- $x$  Improved TMD factorization framework (ITMD) [635, 637–639].

In addition, semi-inclusive photon+di-jet production is a highly differential measure of the many-body dynamics of gluon saturation in  $e+A$  DIS at small  $x$ . This process can be computed systematically in the CGC effective field theory. At leading order, the cross-section is sensitive to both dipole and quadrupole correlators of lightlike Wilson lines [640], and agrees with prior computations of the LO di-jet cross-section in the soft photon limit [412]. This computation also allows one to extract the LO photon+jet/hadron cross-section; this channel has been shown recently [641] to have a clean and unique sensitivity to the saturation scale that is complementary to that of di-jet/di-hadron correlations. In [642, 643], the  $e+A$  photon+dijet cross-section was computed to next-to-leading-order. This result is sufficiently differential to encompass NLO computations of inclusive photon production, photon+jet correlations, dijet, and single jet production, as well as the fully inclusive cross-section. When combined with the next-to-leading-log JIMWLK evolution [607, 608] for the dipole and quadrupole correlators, these NLO cross-sections can be computed to  $O(\alpha_s^3 \ln(1/x))$  accuracy. Extracting concrete predictions for the semi-inclusive channels in EIC kinematics will be crucial for the discovery and characterization of gluon saturation.

### Helicity TMDs and PDFs at small $x$

In recent years much progress has also been made in extending the discussion of quark and anti-quark helicity TMDs, PDFs, etc. (see sec. 7.1.2) to the high-energy limit of small  $x$ . This is a very interesting topic where the EIC is expected to provide fundamental new insight. Evolution equations for these functions have been derived [42, 43, 644] which resum powers of  $\alpha_s \log^2(1/x)$  in the polarization-dependent evolution, and powers of  $\alpha_s \log(1/x)$  in the unpolarized evolution. In the ladder approximation they reduce to the BER evolution equations [645] for the  $g_1$  structure function. Initial conditions for these evolution equations analogous to the McLerran-Venugopalan model for an unpolarized large nucleus, have also been constructed [646].

## 7.3.2 Diffraction

### Inclusive diffraction with nuclei

Diffraction in  $e+A$  is a poorly studied subject, in particular inclusive diffraction that has never been measured. Similar considerations apply to diffraction in  $e+A$  as to  $e+p$  collisions, Subsection 7.1.6, the main difference being that for incoherent processes one must separately discuss processes where the nucleus breaks up into smaller nuclei, and nucleon-dissociative processes where an individual nucleon in the target dissociates. In terms of

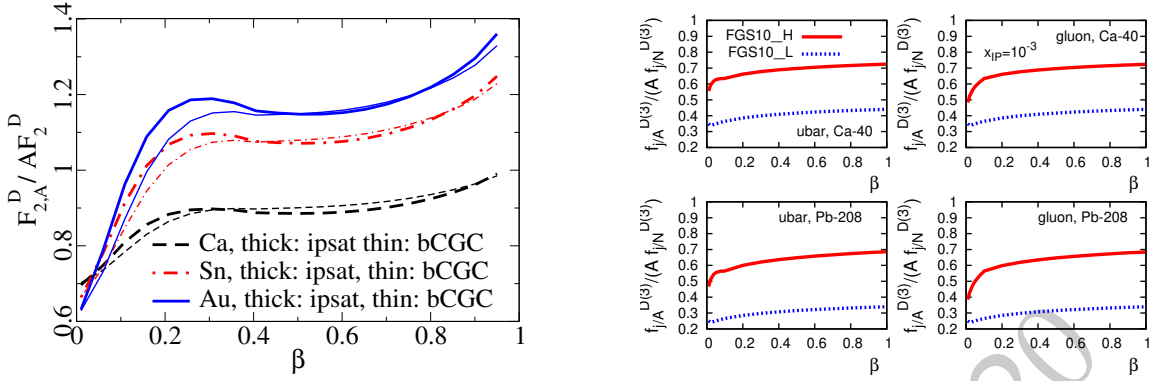


**Figure 7.70:** Left: Ratio of nuclear to proton diffractive structure functions, scaled by  $A$ , at  $\xi = 10^{-3}$  (also referred to as  $x_{\mathbb{P}}$ ) as a function of  $\beta$  from dipole model calculations (Fig. 7 from Ref. [649]). Right: ratios of nuclear to proton diffractive parton distributions, scaled by  $A$ , for sea quarks and gluons at the same  $\xi$  (i.e.  $x_{\mathbb{P}}$ ) from the LTS model (Fig. 72 from Ref. [222]).

the typical  $t$ -dependence, the former is similar to coherent diffraction in  $e+p$ , and the latter to proton dissociation in  $e+p$ . Coherent diffraction is mostly sensitive to the nuclear radius and global nuclear profile and structure, while incoherent diffraction is sensitive to nucleon degrees of freedom, specifically to nucleon and subnucleon fluctuations, see e.g. [647] and [648] for a review and Subsection 7.3.9. All of these cases are characterized by a rapidity gap between the target fragments and the photon fragment system. While detecting experimentally whether the nucleus has disintegrated or not might be challenging, the overall rapidity gap cross section that includes both coherent and incoherent processes should be more easily measurable. In spite of the presence of more physically different sources of fluctuations in nuclei than in protons (fluctuating positions of the nucleons in the nucleus in addition to subnucleonic fluctuations), coherent diffraction is a larger part of the diffractive cross section in  $e+A$  than in  $e+p$ . This is due both to the fact that coherent diffraction grows parametrically as  $A^{4/3}$  with the atomic mass number, and to the fact that nuclei are closer to the black disk limit, where there are no fluctuations and thus no incoherent processes.

Diffraction is generically more sensitive to gluon saturation than inclusive cross sections, since the diffractive cross section is proportional to the square of the gluon density. The ratio of the (coherent) diffractive cross section integrated over  $t$  and some range  $M_X < M_{\max}$  to the inclusive cross section is, in the dipole picture, very generically enhanced in nuclei compared to protons, since in nuclei the dipole-target scattering amplitude at a fixed impact parameter is larger than in the proton [1, 649, 650]. In non-saturation parametrizations of nuclear diffractive parton distribution functions, on the other hand, one observes a nuclear suppression rather than an enhancement, because of the interplay between multiple scattering and gap survival probability. This leads to a very striking difference in the predictions from dipole models vs. leading twist shadowing, as illustrated in Fig. 7.70.

In the dipole or CGC picture, the virtual photon interacts coherently with all nucleons at the same transverse coordinate. Parametrically at large  $A$ , the amplitude for a fixed impact parameter is proportional to the number of overlapping nucleons  $\sim A^{1/3}$ . With a nuclear transverse area  $\sim A^{2/3}$  this leads to a diffractive (or elastic) cross section that parametrically depends on the mass number as  $\sigma^D \sim A^{4/3}$ , compared to  $\sigma^{\text{tot}} \sim A$ . This growth saturates at the black disk limit, where the diffractive cross section is half of the total cross section. At small  $\beta$ , i.e. large masses of the diffractive system, this saturation sets in much earlier because the partonic system is not a simple  $q\bar{q}$  dipole, but a many-particle Fock state.

In the leading twist shadowing picture of Ref. [222], a diffractive interaction also takes place coherently on all the overlapping nucleons of the nuclear target. In contrast to the CGC dipole picture, one separates the interaction into a primary interaction with one nucleon and reinteractions with the other  $A - 1$  nucleons. The reinteractions with target nucleons are treated in the Gribov-Glauber approach to nuclear shadowing by including all possible diffractive intermediate states, which results in a strong nuclear suppression (shadowing) of nuclear diffractive structure functions and parton distributions compared to the proton case. In a different language, this suppression can be identified with the flavor-specific rapidity gap survival probability calculated in the leading twist nuclear shadowing model. Thus the question of nuclear suppression vs enhancement in the diffractive/total cross section ratio is very sensitive probe of the role of coherence and saturation at a specific  $x$  and  $Q^2$ .

In the following we report on a more detailed study [651] of coherent inclusive diffraction in the leading twist shadowing framework [222]. Here we assume that coherent events have been distinguished from the incoherent case using forward detectors, see Section 8.5.

Assuming the same framework (collinear factorization for hard diffraction and Regge factorization) described for  $ep$  in Subsection 7.1.6 to hold for  $eA$ , nuclear diffractive PDFs (nDPDFs) can be extracted from the diffractive reduced cross sections, Eq. (7.10). It should be noted that such nDPDFs have never been measured. The kinematic coverage in  $eA$  at the EIC will be very similar to that shown for  $ep$  in Fig. 3 in Ref. [651].

Due to the lack of previous measurements, there are no parametrizations for nDPDFs but models exist for the nuclear effects on parton densities defined through the nuclear modification factor

$$R_k^A(\beta, \zeta, Q^2) = \frac{f_{k/A}^{D(3)}(\beta, \zeta, Q^2)}{A f_{k/p}^{D(3)}(\beta, \zeta, Q^2)}, \quad (7.44)$$

with diffractive parton densities in nucleus  $A$ ,  $f_{k/A}^{D(3)}(\beta, \zeta, Q^2)$ . We use the model proposed in [222], where parametrizations for nuclear modification factors are provided at the scale  $Q^2 = 4 \text{ GeV}^2$ . Then DGLAP evolution is employed to evolve the ZEUS-SJ proton diffractive PDFs multiplied by  $R_k^A$  from [222] to obtain the nuclear diffractive PDFs, at any  $Q^2$ . The structure functions and reduced cross sections are then calculated in the same way as in the proton case, and these results are used to obtain the modification factors, analogous to Eq. (7.44), for these quantities. We have also repeated the calculation in the Zero-Mass

VFNS in order to check that the resulting modification factors do not depend on the applied scheme.

The model in [222] employs Gribov inelastic shadowing [652] which relates diffraction in  $ep$  to nuclear shadowing for total and diffractive  $eA$  cross sections. It assumes that the nuclear wave function squared can be approximated by the product of one-nucleon densities, neglects the  $t$ -dependence of the diffractive  $\gamma^*$ -nucleon amplitude compared to the nuclear form factor, introduces a real part in the amplitudes [653], and considers the colour fluctuation formalism for the inelastic intermediate nucleon states [654]. There are two variants of the model, named H and L, corresponding to different strengths of the colour fluctuations, giving rise to larger and smaller probabilities for diffraction in nuclei with respect to that in proton, respectively. The corresponding nuclear modification factors, Eq. (7.44), for  $F_2^{D(3)}$  and  $F_L^{D(3)}$  in  $^{208}\text{Pb}$ , are shown in Fig. 13 in Ref. [651].

Pseudodata were generated for  $e\text{Au}$  collisions at the EIC using the same method, and taking the uncorrelated systematic error to be 5%, as described for  $ep$  in [651]. We assumed  $E_e = 21$  GeV,  $E_N = 100$  GeV/nucleon and an integrated luminosity of  $2 \text{ fb}^{-1}$ . The results are shown in Fig. 7.71. Studies performed for  $ep$  at those energies show that the expected accuracy for the extraction of DPDFs at the EIC is comparable to that in existing DPDFs for the proton at HERA, with some improvements at large  $\beta$ , see Subsection 7.1.6. Assuming a similar experimental uncertainty, integrated luminosity and kinematic coverage, the accuracy in the extraction of nDPDFs at the EIC would then be similar to that of existing HERA fits, see Subsection 7.1.6. Improvements would crucially depend on a decrease of the systematic uncertainty, including the separation of coherent from incoherent diffraction.

Finally, the relation between diffraction and nuclear shadowing [652] could be tested at the EIC. The relation is a rigorous theoretical result for the deuteron case, while its extension to larger nuclei becomes model dependent [222, 655]. The possibility of colliding electrons with different nuclear species, including deuterons, will therefore be very important.

### Diffractive dijets

Generally: more differential than inclusive diffraction, since also access to the angle of the dijet with respect to the photon, something that is integrated over in inclusive diffraction. In proton, this angular information is used to extract the Wigner distribution

DPDF-based cross section predictions in [221]

CGC calculations: what is new since the white paper is the proliferation of NLO calculations, for diffractive dijets [656, 657]

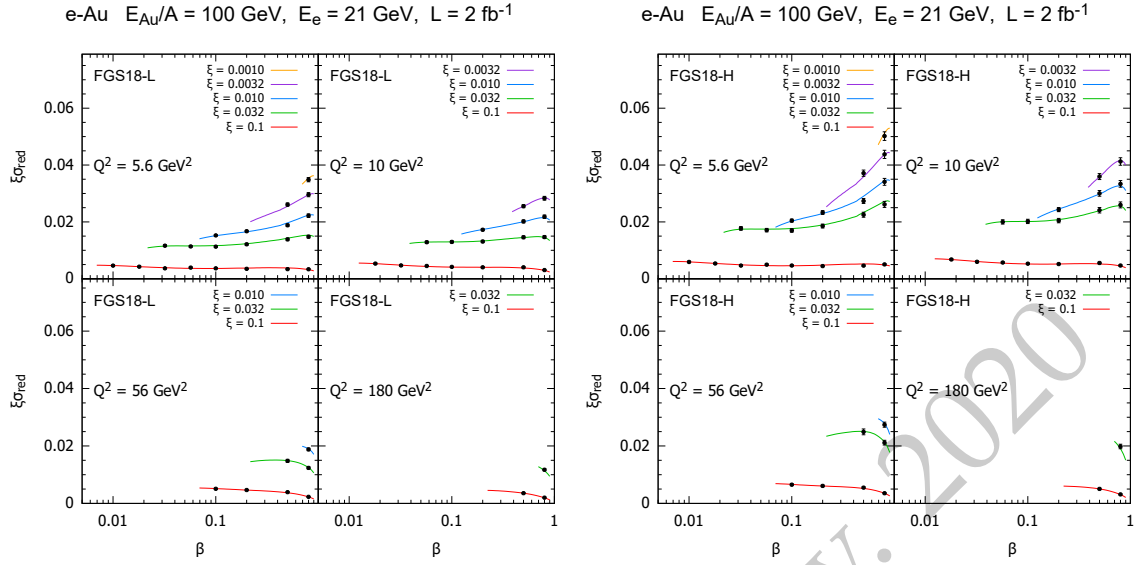


**Figure 7.71:** Simulated data for the diffractive reduced cross section as a function of  $\beta$  in bins of  $\zeta$  and  $Q^2$  for  $e^{197}\text{Au}$  collisions at the EIC, in the models L (left plot) and H (right plot) in [222]. The curves for  $\zeta = 0.032, 0.01, 0.0032, 0.001$  are shifted up by 0.005, 0.01, 0.015, 0.02, respectively. Taken from [651].

### 7.3.3 Nuclear PDFs

Nuclear parton distribution functions (nPDFs) describe the behaviour of bound partons in the nuclear medium. Like free-proton PDFs they are assumed to be universal and are extracted through fits to existing data. To date, there is no compelling evidence of factorization breaking or violation of universality.

A precise knowledge of nPDFs is crucial for understanding the transition between linear and non-linear scale evolution of the parton densities. Of particular interest is the regime known as “saturation”, where the recombination of gluons at low  $x$  becomes increasingly important and the growth of the gluon density is suppressed. The theoretical interpretation of  $A + A$  and  $p + A$  data from the LHC and RHIC also relies on precise knowledge of nPDFs. However, in contrast to the free-proton PDFs, the determination of nPDFs is severely limited by both the kinematic coverage and the precision of the available data.

The realization of the EIC will provide key constraints on nPDFs. Fig. 7.72 shows the significant broadening of the kinematic coverage for all nuclear species at the EIC. Note that nPDFs sets make different selections and apply extra kinematic cuts that further reduce the explored space. In contrast with previous experiments, the systematic uncertainties of the  $e + A$  inclusive DIS cross section measurements at the EIC will be at most a few %, as depicted in Fig. 7.73. Additionally, the statistical uncertainties will be negligible for almost the whole  $x$  coverage, gaining predominance only at the largest values of  $x$ . This broad kinematic coverage, almost doubling the one from existing data, will revolutionize

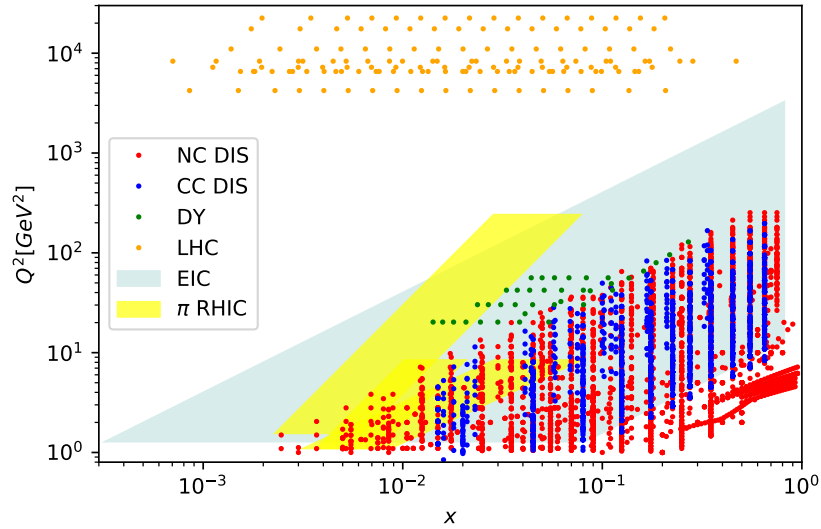


**Figure 7.72:** Kinematic coverage of experimental data and EIC pseudo data used in nPDFs fits. The coverage corresponds to all measured nuclei together. Each nPDFs set has extra cuts that further reduce the explored space.

our current understanding of partonic distributions inside the nuclei.

### nPDFs via inclusive DIS

The DIS cross section can be expressed in terms of the structure functions  $F_2$  and  $F_L$

$$\sigma \propto F_2(x, Q^2) - \frac{y^2}{1 + (1 - y)^2} F_L(x, Q^2). \quad (7.45)$$

The former is mainly sensitive to the (anti-)quark content of the nucleon and dominates the cross-section at high values of  $x$ . The latter, relevant in the unexplored low  $x$  region, has a direct contribution from the gluon density [658]. The large  $Q^2$  lever arm of the EIC will allow us to precisely extract  $F_L$  and further determine the nuclear gluon PDF.

The precision of the inclusive cross section measurements at the EIC at low values of  $x$  ( $x < 10^{-2}$ ) and  $Q^2$  will significantly reduce the current theoretical uncertainties. This is demonstrated in Fig. 7.74 which shows a comparison of the relative uncertainties of three modern sets of nPDFs [659–661] in a gold nucleus (blue bands) and their modification when including EIC DIS pseudodata in the fits (orange bands). The overall effect is a significant reduction of the uncertainties in the low- $x$  region, where data is scarce or non-existent. The high- $x$ , low  $Q^2$  region is covered by fixed target experiments and will be further explored at CLAS.

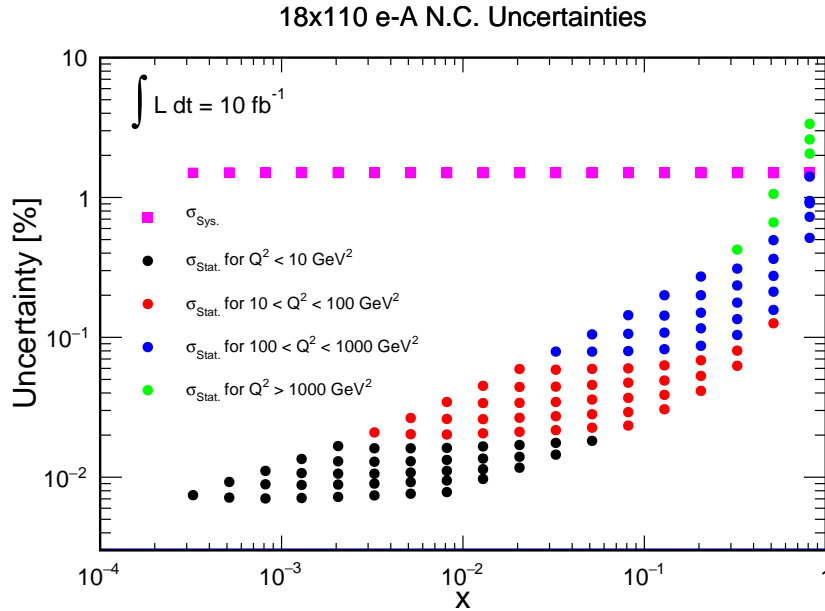


**Figure 7.73:** Relative statistical and uncorrelated systematic uncertainties for inclusive cross section measurements in 18x110 GeV  $e + A$  collisions expected at the EIC. Details of the systematic error estimate may be found in Section 8.1.

### Probing nuclear gluons with heavy flavor production

Heavy flavor (HF) production is a powerful observable that will complement inclusive DIS measurements in determining nuclear modifications of the PDFs, in particular for the gluon distribution. Recent results from ultraperipheral  $A + A$  collisions [662–664] as well as HF and dijet production in  $p + Pb$  [665–667] at the LHC support nuclear suppression with respect to the proton gluon at  $x \ll 0.1$  (shadowing). However, almost nothing is known about gluon enhancement (antishadowing) at  $x \sim 0.1$  or a possible suppression at  $x > 0.3$  (“gluonic EMC effect”). At the EIC it will be possible to obtain a direct constraint of the gluon density by measuring HF pairs which at LO are produced through the photon–gluon fusion process. This channel probes the gluon PDFs for  $x > ax_B$ , where  $a = 1 + 4m_h^2/Q^2$  and  $m_h$  is the heavy quark mass. This measurement will also permit the study of different heavy quark mass schemes and constrain the intrinsic HF components in the nPDFs [668].

The feasibility and impact of nuclear gluon measurements with HF production at the EIC has been studied in dedicated efforts [659, 669, 670] by tagging, from the simulated DIS sample, the  $K$  and/or  $\pi$  decay products from the  $D$  mesons produced in the charm fragmentation. The reconstruction methods used in this analysis [669] demonstrate the key role that particle identification (PID) will play. It was shown that the charm reconstruction is significantly increased [671] when PID capabilities are included.

In Ref. [659] a full fit using the EIC pseudodata for the inclusive ( $\sigma$ ) and the charm cross-section ( $\sigma^{charm}$ ) has found a significant impact on the reduction of the gluon uncertainty

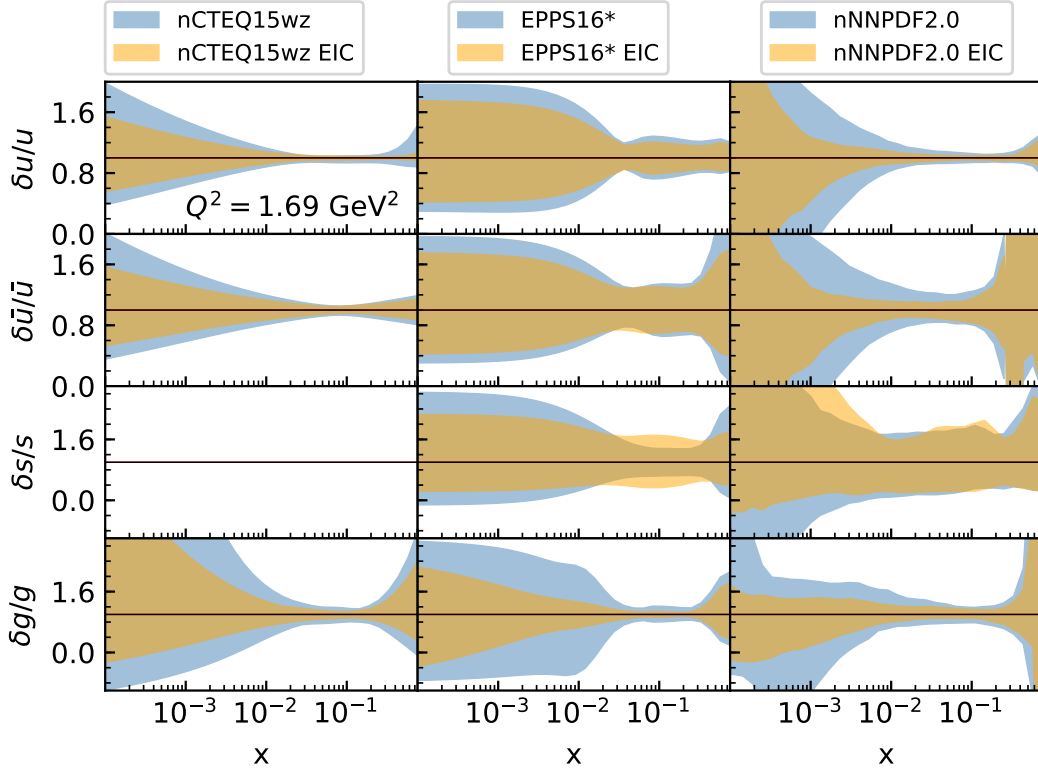


**Figure 7.74:** Relative uncertainty bands for  $Au$  at  $Q^2 = 1.69 \text{ GeV}^2$  for  $u$  (first row),  $\bar{u}$  (second row),  $s$  (third row) and gluon (lower row) for three different sets of nPDFs. The blue and orange bands correspond to before and after including the EIC pseudodata in the fit, respectively.

band at high- $x$ . This is illustrated in the left panel of Fig. 7.75, where the blue band is the original EPPS16\* fit, the green band incorporates  $\sigma$  pseudodata and the orange one adds also  $\sigma^{charm}$ . A similar dedicated study using PDF reweighting with structure function  $F_{2A}^{charm}$  was done in [46]. In the right panel of Fig. 7.75 the impact of Fe pseudodata on the EPPS16 NLO gluon density [672] is shown by the red band. The charm pseudodata substantially reduces the uncertainty at  $x > 0.1$ , providing sensitivity to the presence of a gluonic EMC effect. Comparing the red band (only charm pseudodata) with the results of Fig. 7.74 one can see that the high- $x$  region can be equally studied considering inclusive or charm pseudodata. It is by combining both observables that a striking reduction is achieved (orange band, left panel of Fig.7.75). Moreover, the measurement will be complemented by jet studies that have already shown promising constraining power for gluons in  $p + Pb$  collisions [667].

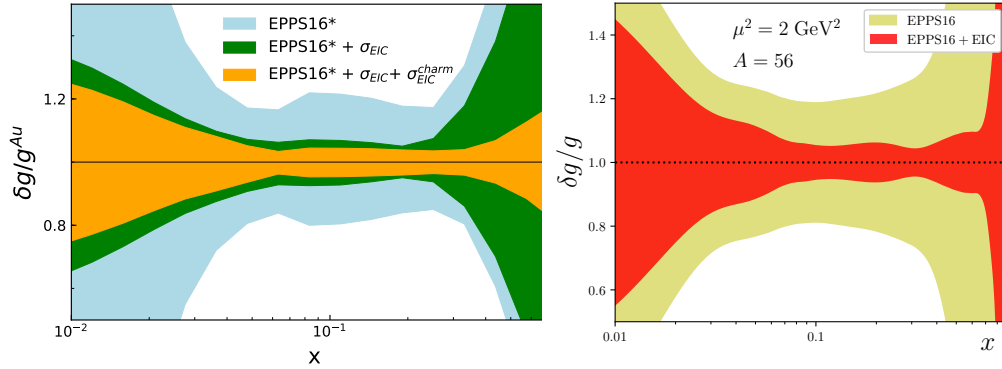


**Figure 7.75:** Left: Relative uncertainty bands of the gluon for  $Au$  at  $Q^2 = 1.69 \text{ GeV}^2$  for EPPS16\* (light blue), EPPS16\*+EIC  $\sigma$  (green) and EPPS16\*+EIC  $\sigma^{charm}$  (orange). Right: same as left panel but for  $Fe$  at  $Q^2 = 2 \text{ GeV}^2$  for EPPS16 (yellow) and EPPS16+EIC  $\sigma^{charm}$  (red).

### Investigating the $A$ dependence of nPDFs

The different nuclei used in the nPDFs fits are usually connected through parameters for which an  $A$  dependence is assumed. This allows one to use the whole set of available nuclei in a single fit instead of individually fitting nuclei, a task that, given the current data, would be difficult if not impossible. The EIC, by effectively being a *nuclear* HERA will provide the opportunity to perform a full scan of the kinematic space for each nucleus individually, permitting a robust extraction of the  $A$  dependence a posteriori. Studies have shown that the impact demonstrated in Fig. 7.74 is representative of the impact for all nuclei.

Finally, an EIC would allow, for the first time, a combined determination of proton, deuteron, and nuclear PDFs within an integrated global QCD analysis. This is a unique and invaluable benefit of this new facility, as it eliminates many of the biases and assumptions that plague current PDF determinations.

### 7.3.4 Particle propagation through matter and transport properties of nuclei

#### Parton showers and energy loss in cold nuclear matter

Understanding particle propagation in matter and nuclear transport properties remain defining questions in the field. Theoretical efforts in the past decades have been focused on understanding the energy loss of partons as they propagate in strongly interacting environments [673–679]. More recently a much more complete understanding of parton showers in matter, beyond the soft gluon approximation, has emerged [680–684]. This allows techniques that bridge the gap between nuclear and particle physics, such as evolution and semi-inclusive jet functions to be applied to reactions with nuclei [?,685–687], see Fig. 7.76. While theoretical approaches differ in the way they treat final-state interactions, a univer-

sal feature is the fractional parton energy loss  $\Delta E/E$ , or more generally the contribution of medium-induced parton showers, becomes negligible for very high parton energies  $\nu$  in the rest frame of the nucleus owing to the non-abelian Landau-Pomeranchuk-Migdal effect. It is thus advantageous to minimize the rapidity gap between the measured jet and the target nucleus  $\delta\eta = |\eta_{p/A} - \eta^{\text{jet}}|$  and focus on the forward proton/nucleus going direction.

### Formation of hadrons in matter

A paragraph will be added soon.

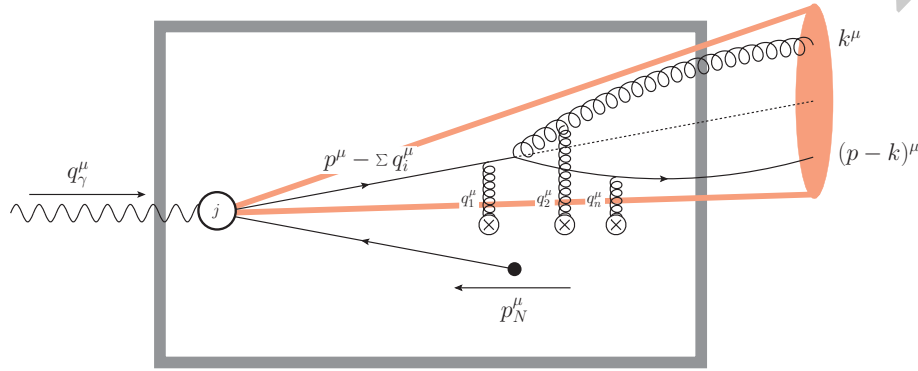


**Figure 7.76:** Illustration of the indicated jet kinematics for SIDIS in the Breit frame. The dark box represents the medium (nucleus) and the red cone represents the jet.

### Jet production and modification in $eA$ collisions

Nuclear effects on reconstructed jets in electron-nucleus collisions can be studied through the ratio

$$R_{eA}(R) = \frac{1}{A} \frac{\int_{\eta_1}^{\eta_2} d\sigma/d\eta dp_T|_{e+A}}{\int_{\eta_1}^{\eta_2} d\sigma/d\eta dp_T|_{e+p}}. \quad (7.46)$$

Predictions for jet modification are taken from Ref. [688]. In the left panel of Fig. ?? for  $R = 0.5$  bands correspond to scale uncertainties from varying the factorization scale and the jet scale by a factor of two independently. For the chosen kinematics the Bjorken- $x$  values corresponding to the so-called anti-shadowing and EMC regions of nuclear PDFs. As a result, there is an enhancement for small  $p_T$  due to anti-shadowing and an suppression for large  $p_T$  due to the EMC effect, which is shown by the blue band. The green band represents the final-state effects, which give rise to 10 - 20% suppression when  $p_T \sim 5$  GeV. They are smaller for larger jet energy as expected, and going to backward rapidities further reduces the effect of medium-induced parton showers. The predicted full  $R_{eA}(R = 0.5)$

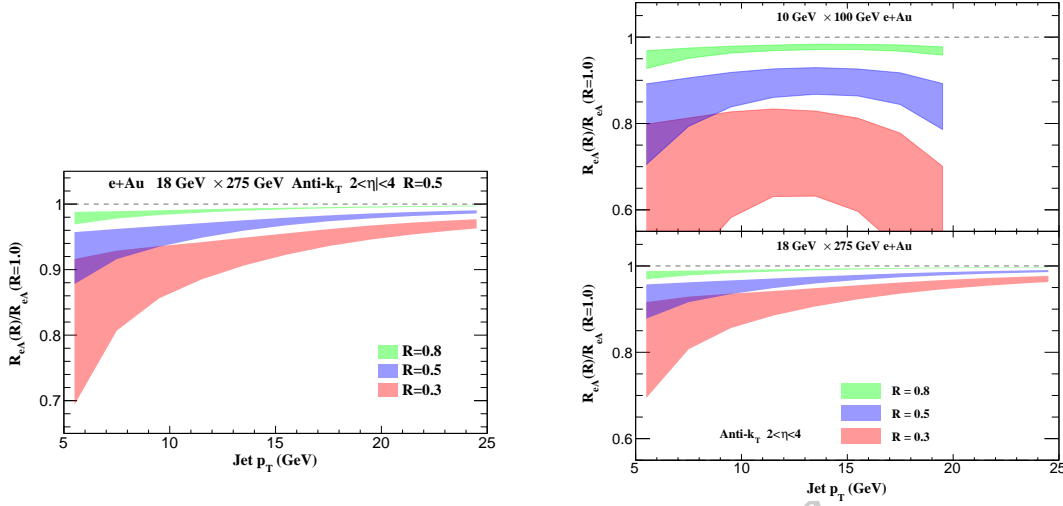


**Figure 7.77:** Left: modifications of the inclusive jet cross section in  $18 \times 275$  GeV  $e+Au$  collisions for the rapidity interval  $2 < \eta < 4$ . The blue and green bands represent contributions from initial-state PDFs and final-state interaction between the jet and cold nuclear matter, while the red band is the full result. Right: ratio of jet cross section modifications for different radii  $R_{eA}(R)/R_{eA}(R = 1.0)$  in  $10 \times 100$  GeV (upper) and  $18 \times 275$  GeV (lower)  $e+Au$  collisions, where the smaller jet radius is  $R=0.3, 0.5$ , and  $0.8$ , and the jet rapidity interval is  $2 < \eta < 4$ .

for  $18 \text{ GeV } (e) \times 275 \text{ GeV } (A)$  collisions is given the red band. The measurements of jet modification in future will improve our understanding of strong interactions inside nuclei and nuclear PDFs at moderate and large  $x$ .

To study cold nuclear matter transport properties with jets at the EIC, it is essential reduce the role of nPDFs and enhance the effects due to final-state interactions. An efficient strategy is to measure the ratio of the modifications with different jet radii,  $R_{eA}(R)/R_{eA}(R = 1)$ , which is also an observable very sensitive to the details of in-medium branching processes [689] and greatly discriminating with respect to theoretical models [690]. Furthermore, it is very beneficial to explore smaller center-of-mass energies. Our predictions for the ratio of jet cross section suppressions for different radii at the EIC is presented in the right panel of Fig. 7.77, where the upper and lower panels correspond to results for  $10 \text{ GeV } (e) \times 100 \text{ GeV } (A)$  and  $18 \text{ GeV } (e) \times 275 \text{ GeV } (A)$  collisions, respectively. The plot in the upper panel is truncated around  $p_T \sim 20$  GeV because of phase space constraints in the lower energy collisions. By comparing the  $18 \text{ GeV } \times 275 \text{ GeV } e+Au$  collision results to the ones in Fig. ?? we see that  $R_{eA}(R)/R_{eA}(R = 1)$  indeed eliminates initial-state effects. The red, blue, and green bands denote ratios with  $R = 0.3, 0.5, 0.8$ , respectively. Since medium-induced parton showers are broader than the ones in the vacuum, for smaller jet radii the suppression from final-state interactions is more significant. Even though the scale uncertainties also grow, the nuclear effect is clear as its magnitude is further enhanced by the steeper  $p_T$  spectra at lower  $\sqrt{s}$ .

### 7.3.5 Collective effects

For a long time it was considered that the collective multiparticle interactions in “small” collision systems (collisions of protons and electrons) are qualitatively different from those in “large” systems, i.e. collisions of heavy nuclei. One of the most important discoveries in nuclear physics during the last decade has been that this is not necessarily the case. In stead, the kind of multiparticle correlations associated with hydrodynamical flow (see Sec. 7.5.4) of bulk, low  $p_T$  particle in nucleus-nucleus collisions have been observed in various systems where they were not anticipated. Some of the first indications of this were the azimuthally near-side structure elongated in the rapidity direction in the  $\Delta\phi, \Delta\eta$ -distribution of particles associated with a high- $p_T$  hadron, which became to be called the “ridge” [579], or a similar correlation on the away-side once known as the “Mach cone” [579, 691]. These correlations were surprising since they involved high- $p_T$  particles that were not expected to form a part of the thermal medium. These discoveries were followed by the observation of the “ridge”-correlation in (high multiplicity) proton-proton collisions at the LHC [580–583], followed soon by similar correlations in proton-nucleus collisions [584–590], which were surprising because a collectively interacting medium was not expected to be present at all.

Such multiparticle correlations are now typically analyzed in terms of Fourier harmonic coefficients of two, four, or higher multiparticle correlation functions, typically involving particles with a large rapidity separation to eliminate correlations from resonance decays. These coefficients are referred to in the field of heavy ion physics as “flow coefficients,” often even when they are calculated in models where they do not originate from any hydrodynamical interactions. Indeed, these correlations have 2 competing, “final state” and “initial state” explanations, that are in fact not mutually exclusive and may both contribute in varying degrees to the observed signals in different small collision systems.

The explanation in terms of final state interactions assumes that the correlations result from interactions after the primary collision translating transverse coordinate space structures into momentum space correlations (see Sec. 7.5.4). The interactions can be modeled by either hydrodynamics [692] or by kinetic theory [693–695]. Many recent results, such as the “geometry scan” of collisions of proton, deuteron- and helium with gold ions reported by PHENIX [696] seem to favor this interpretation.

On the other hand, it is clear that there are also momentum correlations already present among the small- $x$  gluons in the colliding systems [697–699]. Such correlations can naturally manifest themselves in the particles produced in the collision. The initial stage effects can be expected to be stronger in smaller collision systems [700, 701] where they are not diluted by a large number of uncorrelated domains elsewhere in the transverse plane. This is the opposite of the behavior of final state effects that would generically become smaller in smaller systems due to the shorter lifetime of the system. They could naturally explain e.g. observations of flow-like correlations for even heavy flavor hadrons [702, 703].

A DIS-event at small- $x$  provides us with an unique system to test and understand in detail the physics of these collective interactions. The virtual photon interacts as a hadronic system, whose size and lifetime can be tuned by varying  $x$  and  $Q^2$ . Recently, the ATLAS col-

laboration reported collective phenomenon in the photo-nuclear ultra-peripheral  $AA$  (this is equivalent to the  $\gamma^*A$  collision with almost real photons) collisions as well [704]. There is an interesting and strong physical resemblance between the high multiplicity events in photo-nuclear collisions and those in  $pA$  collision. On the other hand, in a reanalysis of HERA data a ridge-like signal was not found [705].

The wave function of a low-virtuality photon can in some event contain many active partons due to the rare QCD fluctuation and the dominant contribution to the high multiplicity events comes from such a partonic structure. Therefore, one can argue that the collective phenomenon could also be observed [706] in certain kinematic region of the EIC where the incoming virtual photon has a sufficiently long lifetime. EIC can offer both  $ep$  and  $eA$  collisions with different values of virtuality  $Q^2$ , which allows one to change initial conditions for the target and the system size  $\sim 1/Q$  of the collisional system. At the EIC one also expects a higher luminosity than at HERA, which increases the possibilities to trigger on rare high multiplicity event, which has already been a condition to observe these correlations in proton-proton collisions. The future efforts in the era of the EIC can help us unravel the origin of the collectivity in high multiplicity events in small systems.

### 7.3.6 Special opportunities with jets and heavy quarks

#### Flavor-tagged jets and the jet charge

Different from inclusive jet cross sections, jet substructure measures the radiation pattern inside a given jet and is governed by a smaller intrinsic scale. At EIC energies, the phase space for radiation inside the jet cone can be restricted, which makes it more challenging to study final-state cold nuclear effects. Even though the differences between the substructure of jets in  $ep$  and  $eA$  are expected to be smaller than in the case of heavy ion physics, the example of the jet charge [707] shows that nuclear effects can indeed be identified. The average jet charge is defined as the transverse momentum  $p_T^i$  weighted sum of the charges  $Q_i$  of the jet constituents

$$Q_{\kappa,\text{jet}} = \frac{1}{(p_T^{\text{jet}})^{\kappa}} \sum_{i \in \text{jet}} Q_i (p_T^i)^{\kappa}, \quad \kappa > 0. \quad (7.47)$$

Studies in proton and heavy-ion collisions [498, 708–710] have found that the jet charge is strongly correlated with the electric charge of the parent parton and can be used to separate quark jets from anti-quark jets and to pinpoint their flavor origin.

Fig. 7.78 presents jet charge results at the EIC in  $18 \text{ GeV} \times 275 \text{ GeV } eAu$  collision and for radius parameter  $R = 0.5$ . The red, blue and green bands correspond to the jet charge parameter  $\kappa = 0.3, 1.0, 2.0$ , see Eq. (7.47), respectively. The upper panel shows the modification for the average charge of up-quark initiated jets, where the rapidity is fixed to be  $\eta = 3$ . It is defined as  $\langle Q_{q,\kappa}^{eA} \rangle / \langle Q_{q,\kappa}^{ep} \rangle$ , which is independent of the jet flavor and originates purely from final-state interactions. Flavor separation for jets has been accomplished at the LHC [711] and should be pursued at the EIC. For a larger  $\kappa$ , the  $(\kappa + 1)$ -th Mellin moment

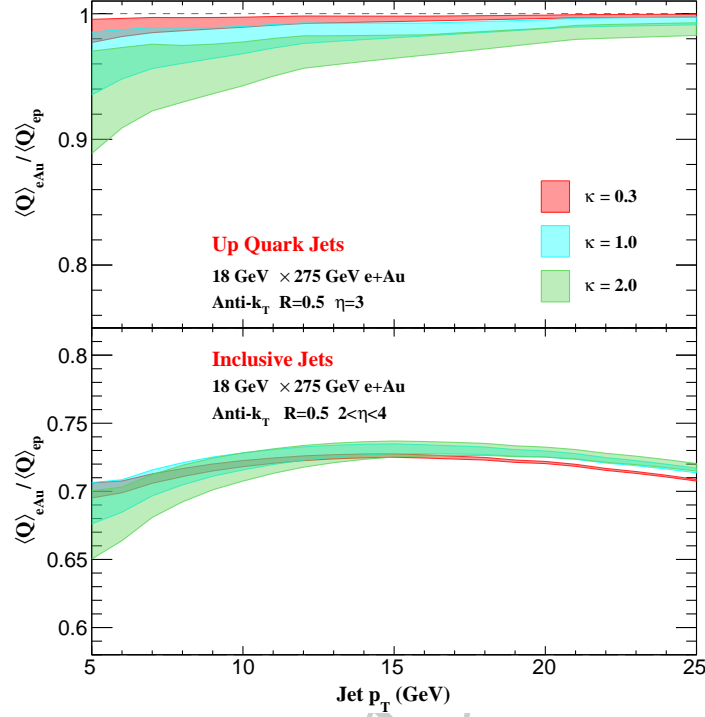


**Figure 7.78:** Modifications of the jet charge in  $eAu$  collisions. The upper panel is the modification for up-quark jet with  $\eta = 3$  in the lab frame. The lower panel is the results for inclusive jet with  $2 < \eta < 4$  in  $18 \times 275$  GeV  $e+Au$  collisions.

of the splitting function is more sensitive to soft-gluon emission, this is the  $z \sim 1$  region in the splitting function where medium enhancement for soft-gluon radiation is the largest. As shown in the upper panel of Fig. 7.78, the modification is more significant for larger  $\kappa$ . The modification of the average charge for inclusive jets behaves very differently because there is a cancellation between contributions from jets initiated by different flavor partons, in particular from up quarks and down quarks. The lower panel of Fig. 7.78 shows the ratio of average charges for inclusive jets with  $R = 0.5$  and  $2 < \eta < 4$  for  $e+A$  and  $e+p$  collisions. The modification is about 30% and the  $\kappa$  dependence is small due to the large difference between up/down quark density between proton and gold PDFs. Precision measurement of the charge for inclusive jets will be an excellent way to constrain isospin effects and the up/down quark PDFs in the nucleus.

### Light and heavy-flavor tagged jet angularities

In the clean EIC environment jet substructure studies can be extended to heavy flavor. In experimental simulations, initial jet reconstruction has been achieved based on true particle information. Inclusive jets are reconstructed with the anti- $k_T$  jet algorithm with cone radius at 1.0. Then jets are tagged with fully reconstructed heavy flavor

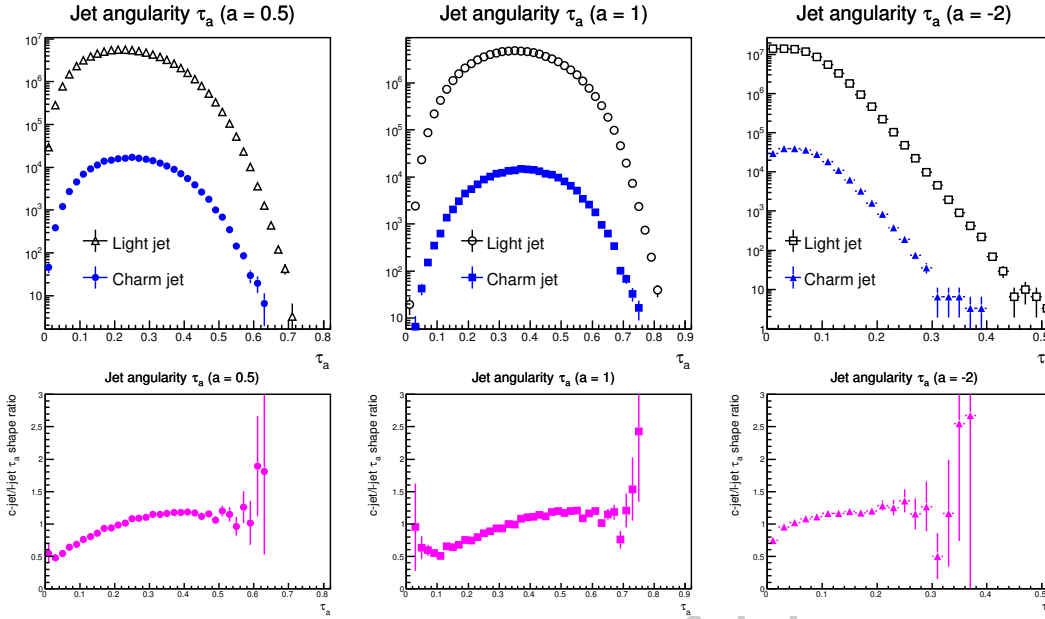


**Figure 7.79:** Jet angularity distributions for light flavor jets (black open points) and charm tagged jets (blue closed points) with different power order  $a$  value selections are shown in the top panel. Distributions with  $a = 0.5$  are shown in the left, with  $a = 1$  are shown in the middle and  $a = -2$  are shown in the right. Bottom panel shows the ratio of normalized charm jet angularity distribution over normalized light flavor jet angularity distributions in the top panel with the corresponding  $a$  value selection. The statistical uncertainties are projected with  $10 fb^{-1} e + p$  at  $\sqrt{s} = 63$  GeV.

meson by requiring these reconstructed heavy flavor hadrons be within the associated jet cone [?]. If there is not a reconstructed heavy flavor hadron can be found within the jet cone, this jet is labeled as light flavor jet.

Jet substructure observable can image the nucleon/nuclei 3D structure and help map out the hadronization process in vacuum and nuclear medium. Recent theoretical developments suggest the jet angularity observable has discriminating power to distinguish quark or gluon initiated jets. We have studied the jet angularity for light flavor jets and charm tagged jets with different power order  $a$  value selections [712,713]. Figure 7.79 shows the jet angularity distributions of light flavor jets and charm tagged jets and ratio distributions of their shapes in  $10 fb^{-1} e + p$  at  $\sqrt{s} = 63$  GeV. Charm jets have a broader jet shape which causes a increasing trends in the jet angularity ratio distributions presented in the bottom panels of Figure 7.79. Nuclear modification effects for different flavor jets are under study.

### Energy flow and quantum number correlations in jets

An interesting opportunity is to study the correlations between energy flow and quantum numbers such as flavor, spin, electric and color charges. The deconstruction of energy-energy correlations at a fixed angle into the contributions of specifically identified particles

builds on classic observables such as jet charge. We have performed exploratory studies on samples generated from Pythia (in future we plan to extend our studies to other event generators with different fragmentation assumptions). The observable we investigate focuses on leading and sub leading jet particles (for example, pion-pion) and the relative cross sections when their electric charges are of the same sign ( $N_{CC}$ ) or opposite sign ( $N_{C\bar{C}}$ ). Specifically, we consider the asymmetry observable  $r$  defined as:

$$r = (N_{CC} - N_{C\bar{C}}) / (N_{CC} + N_{C\bar{C}})$$

We observe that in Pythia, opposite sign cross sections dominate. It is even more pronounced for kaon pairs and proton-antiproton pairs. Its dependence on particle kinematic phase space is being studied. We also propose to study the correlation between jet and forward particles which were conventionally hidden in the beam remnants. This direction will provide a new and essential window toward understanding hadronization through target fragmentation, global color neutralization and enhancing the precision for event tagging.

### 7.3.7 Short-range correlations, origin of nuclear force

#### Diffraction J/psi production in electron-deuteron scattering at the EIC and its implication to short-range correlations

Understanding the role of Quantum Chromodynamics in generating nuclear forces is important for uncovering the mechanism of short-ranged nuclear interactions and their manifestation in short range correlations (SRC). In recent years, experimental data from Jefferson Lab suggested a strong link between the SRC and the EMC effect [714–718]. Specifically, they suggest that the underlying mechanism of nucleon modifications could be caused by short-range correlated nucleon pairs with high internal nucleon momentum, for instance, a quasi-deuteron inside the nucleus. However there are alternative phenomenological models that can explain the EMC effect without involving SRCs; see Ref. [715] for a recent review.

The difficulty in drawing a definitive conclusion based on available experimental data is primarily due to the complexity of the nuclear environment. Given the differing structure and reaction dynamics of different nuclei, the nuclear mass ( $A$ ) dependence could in principle be attributed to other underlying physical mechanisms. Nuclear effects that are driven by SRCs should be similar in light nuclei at extreme high internal nucleon momentum and in medium and heavy nuclei in a similar kinematic range. Therefore the observation of universal properties across a wide range of nuclei would suggest that the effect may be independent of the specifics of nuclear structure and reactions. A confirmation of such universal behavior would then provide a definitive explanation for the EMC puzzle. It may also provide insight into similarly universal dynamics, independent of microscopic details, in physical systems across varying energy scales.

Besides the modifications in the valence quark region in the bounded nucleon, there are a number of other outstanding questions:

- What role do gluons play in the short-range correlations of nucleon pairs?
- Are gluon modifications linked to the SRC, similar to that for valence quarks?
- What is the relation of SRCs to gluon shadowing ? Can this be related to the phenomenon of gluon saturation?
- What are the spatial and momentum distributions of partons in such high nucleon momentum configurations ?

With regard to the last item, nucleon-nucleon elastic scattering experiments at high momentum transfer showed that the energy dependence of such reactions is quite sensitive to differing models of the internal spatial and momentum distributions of partons [719].

The EIC will provide an unprecedented opportunity to systematically investigate the underlying physics of SRC for energies and kinematic regions that are otherwise impossible to reach. In this study, we propose to study the impact on gluon distributions inside of nucleons that are associated with a SRC pair in electron-deuteron ( $ed$ ) scattering. Using the Monte Carlo event generator BeAGLE, we investigate the sensitivity of observables to high internal nucleon momentum in incoherent diffractive  $J/\psi$  vector meson production. In a plane wave impulse approximation, the initial state deuteron wave function can be accessed directly from the four-momentum of the spectator nucleon (See Fig. 7.80 for the Feynman diagram). We use realistic physics estimates and a conceptual far-forward detector simulations of the EIC to fully reveal the potential of this exclusive process. In particular, we provide the luminosity and detector requirements necessary to study SRCs in the deuteron at an EIC.

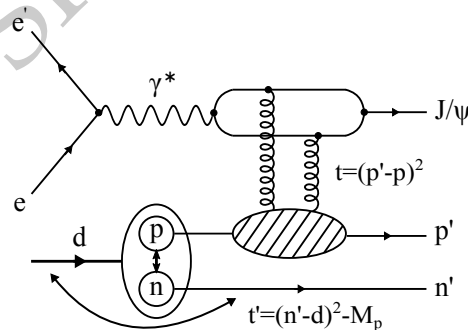


**Figure 7.80:** Diagram of incoherent diffractive  $J/\psi$  productions in electron-deuteron scattering

In Fig. 7.80, kinematic variables are defined in the figure. In particular, the kinematic variable  $t$  is defined between the four-momentum of the incoming and outgoing leading nucleon, while the incoming nucleon momentum inside of the deuteron is not known directly due to the internal nucleon momentum distribution. This is different from the process of

electron-proton ( $ep$ ) scattering where the incoming proton has the beam momentum. In an  $ep$  collider experiment, the paradigmatic example thus far being the H1 and ZEUS experiments at HERA, the  $t$  variable can in principle be reconstructed using different methods [720], including a new method proposed in this study based on purely the spectator and the leading nucleon. The conclusion based on this study is that the best resolution of reconstruction of momentum transfer might come from a combination of different methods, i.e., the spectator tagging technique can be used for identifying the process while the method 3 in Ref. [720] can be used for the values of  $t$ .

In BeAGLE simulations of incoherent diffractive  $J/\psi$  meson production in  $ed$  scattering, both cases where the spectator nucleon can be either a proton or a neutron are considered. In the simulations, the two cases are treated identically at the generator level, while in the reconstruction of the final state particles in the detector simulations, the spectator proton or neutron would experience different acceptances and detector smearing. In Fig. 7.81, the three-momentum distributions of the spectator,  $p_m$ , associated with incoherent diffractive  $J/\psi$  production in  $ed$  collisions, are shown for neutron (left) and proton (right) spectator, respectively. In each panel, the truth level simulation from BeAGLE is shown by solid star markers, where the open circles represent the results after the realistic simulation of the detector acceptance and forward instrumentation. The results of the full simulations (open square markers,) include acceptances, smearing effects coming from intrinsic detector resolutions, and beam-related effects. With the capability of forward detectors, the access of high momentum configuration of the deuteron is experimentally possible.

For the detector and beam-related effect simulations, one sees that the measurements at low momentum would have a larger impact from detector resolutions but with almost 100% acceptance, however for the high momentum range, the impact is found to be opposite.

Note even that at the generator level, proton and neutron spectator cases are identical, reflecting the assumptions on the deuteron wave function. However after acceptance effects and detector smearing are applied in the reconstruction, the resulting distributions are different. In the neutron spectator case, most of neutrons reconstructed by the ZDC are within a  $\pm 4 - 6$  mrad cone varying with the azimuthal angle. The non-uniformity of the azimuthal acceptance is due to the aperture of magnets and the other forward instrumentation. The neutron spectator acceptance is almost 100% up to 600 MeV/c, while about 80% for  $p_m \approx 1$  GeV/c. The momentum smearing effect is noticeable for momenta up to 300 MeV/c. For a nominal beam momentum particle, e.g., 110 GeV/c, the resolution is typically 5%, dominated by the constant energy resolution term of the ZDC.

For the proton spectator case on the other hand, the  $p_m$  distributions are found to be different from the neutron. Since the proton has better overall resolution, the  $p_m$  distribution at low-momentum exhibits less bin migration in the tagged proton case, and a better acceptance for high nucleon momenta. Most of the proton spectators end up within the acceptance of the OMD instead of the RP due to the protons having less magnetic rigidity ( $\sim 50\%$ ) compared to the deuteron beam.

In addition, by selecting different momentum range of the proton-neutron pair, the gluon

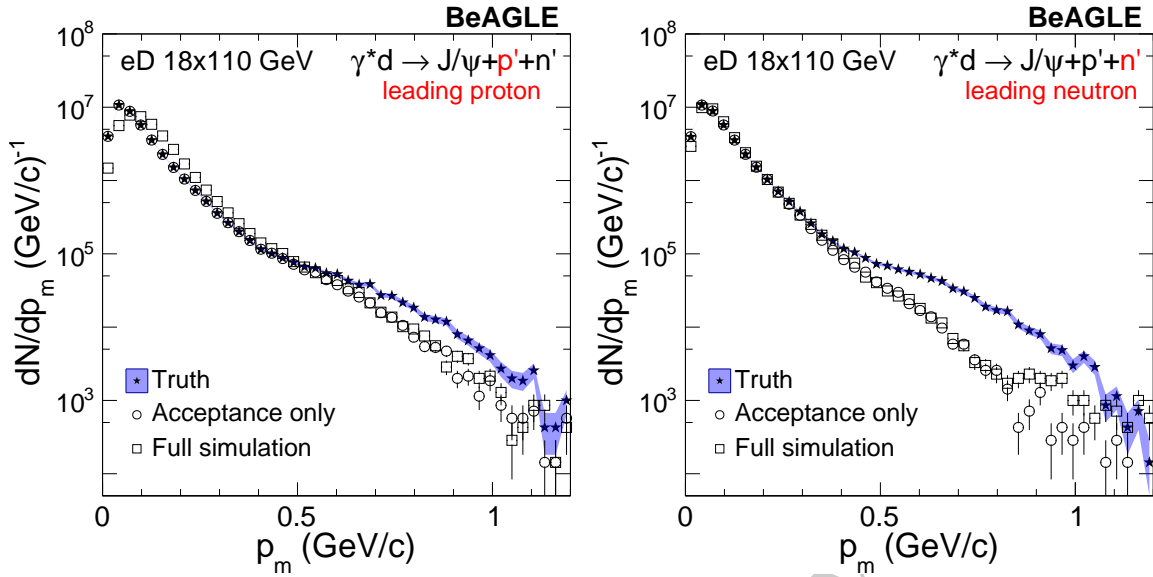


**Figure 7.81:** Distribution of the three-momentum of the spectator nucleon in events associated with incoherent diffractive  $J/\psi$  vector meson production in  $ed$  collisions are shown for the BeAGLE event generator. The left panel is for the neutron spectator case, where the right panel is for the proton spectators. The simulations at the generator level, with acceptance effects only, and for the full simulations, are shown with solid, open circles, and open squared markers, respectively.

density distributions can be compared. Based on Ref. [720], a 10% different size of proton in terms of gluon density is studied and is shown in Fig. 7.82. The impact parameter distribution of the gluon density is based on the Fourier transformation on the momentum transfer  $-t$  distributions, which can be measured up to high precision at the EIC. For details, see Ref. [720]. With the assumption of a similar statistical precision as obtained by the H1 result [721], the 10% difference in the slope parameter of  $-t$  will result in a  $3\sigma$  significant different source distribution. This difference will be mostly dominated by the statistical uncertainty, while the systematic uncertainty will be largely, if not fully, canceled. Overall, the significance of the results depends on the signal strength and the statistical uncertainty. For a quantitative prediction, rigorous theoretical calculations are needed.

In order to achieve a similar statistical precision for  $p_m > 0.6$  GeV/c in photoproduction, the integrated luminosity is estimated to be  $30 \text{ fb}^{-1}$ . For electroproduction of  $Q^2 \sim 10 \text{ GeV}^2$ ,  $100\text{--}500 \text{ fb}^{-1}$  are required depending on the statistical uncertainty of the last measured  $t$  bin.

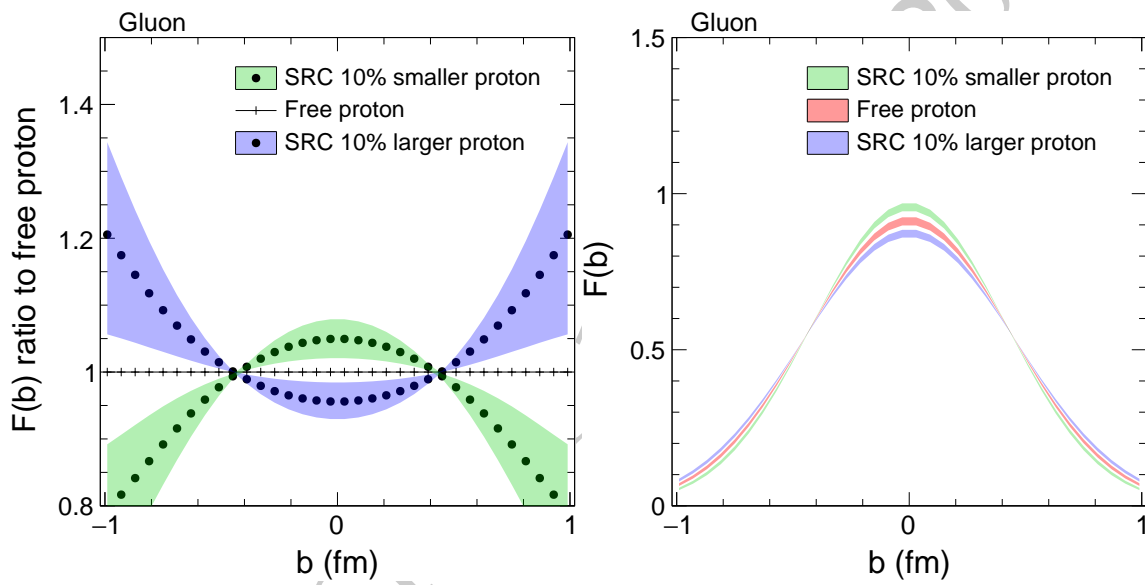


**Figure 7.82:** The gluon source distributions  $F(b)$  (right) and their ratio between SRC protons and the free proton as a function of impact parameter  $b$  (left), based on a Fourier transformation of the  $t$  distributions of elastic  $J/\psi$  production in  $\gamma p$  collisions. The color band indicates a  $1\sigma$  statistical uncertainty.

### Studying Short-Range Correlations with an EIC

Understanding the modification of quarks in nucleons within nuclei (EMC effect) is a long-standing open question in nuclear physics [722]. Recent experimental results from electron scattering at Jefferson Lab strengthen the correlation between the EMC effect and nucleon-nucleon short-range correlated pairs (SRC) within nuclei [714–716]. That means that the EMC effect is probably driven by the high-momentum highly-virtual nucleons of the SRC pairs. This connection can be tested experimentally by measuring electron deep inelastic scattering (DIS) from a nucleon and detecting its correlated SRC partner nucleon (tagging).

The Electron-Ion-Collider (EIC) is an ideal machine for tagging measurements due to the unique capability of measuring recoil nucleons in a collider compared to fixed-target experiments. Furthermore, it will reach much higher  $Q^2$  values obtained in previous DIS measurements. The current design of the EIC detectors allows for a full acceptance for forward-going proton, neutrons and nuclear fragments besides the scattered electron. Ideally, it should be possible to measure the struck nucleon or its target-remnant jet, the SRC-partner, any spectators that were involved in final state interactions, and the nuclear remnant.

In the following figures 7.83 and 7.84 will show missing momentum distributions of the recoil nucleons determined by the electron and leading nucleon with the current IR design. These results were generated using the generalized contract formalism and then passed through EICROOT. Presently head-to-head comparisons are being made between EICROOT and ESCalate's g4e codes.

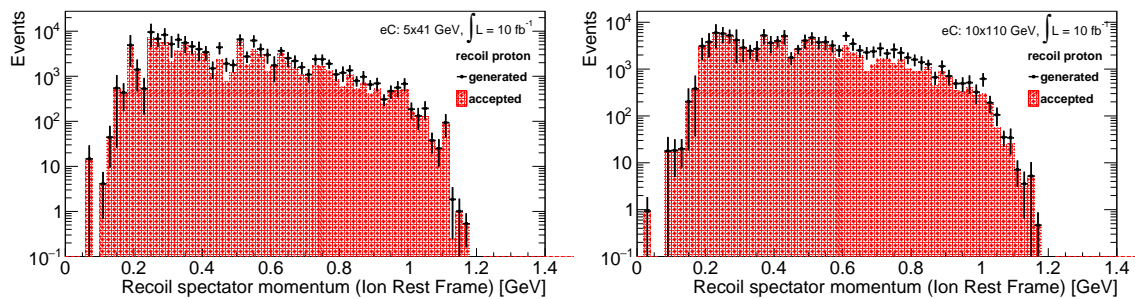


Figure 7.83

The results clearly show very good acceptance for recoil spectator momentum over a very large range of momentum. For neutron the results are not as good for the lower energy setting though nearly complete at the highest energy. This is simply the geometric effect of the size of the zero degree calorimeter along with kinematic focusing provided by the energy energy.

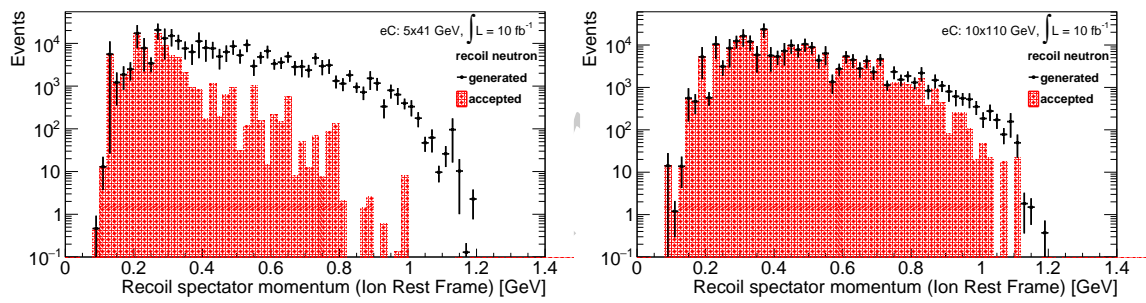


Figure 7.84

### 7.3.8 Structure of light nuclei

The EIC, with its far forward detectors, provides a unique facility for studying light ions at high center of mass energies. Light ions have several unique features that can be used to study the interplay between partonic QCD phenomena and nuclear interactions.

1. Light ions can be polarized. The EIC would allow for polarized  $^3\text{He}$  and  $^3\text{H}$  beams, possibly deuteron ( $^2\text{H}$ ) beams and beyond. This allows to probe neutron spin structure (see Sec. 7.1.2), tensor polarized deuteron (see Sec. 7.2.5) and measurements of the polarized EMC effect.
2. The far forward detectors in the hadron going direction allow for the detection of specific nuclear breakup channels. In inclusive scattering scattering can take place on protons and neutrons, partonic structure can be modified by nuclear interactions and non-nucleonic d.o.f. play a role. These effects can all be controlled by selecting particular break-up channels. Particularly effective breakup channels are the measurement of so-called spectator nucleons, where one or more nucleons are detected in the target fragmentation region of the nucleus, see Fig. 7.17 for the deuteron. This allows to select the active nucleon in the reaction, suppress the contribution of non-nucleonic d.o.f. and select specific intra-nucleon distance scales in the initial nucleus.
3. For light ions well-developed techniques exist to compute nonrelativistic nuclear wave functions from first principles, starting from microscopic  $NN$  interactions. This makes it possible to describe the initial nuclear state and breakup into specific channels with high theoretical precision.

In this subsections the focus is on the use of light ions in the study of nuclear interactions and their influence on medium modifications of parton distribution functions. For free neutron structure, see Sec. 7.1.2, for 3D imaging of nuclear bound states, see Sec. 7.2.5.

Nuclear interactions are effective interactions arising from QCD and describing the low-energy structure of nuclei using interacting nucleons has proven to be highly successful. Several questions remain however. How exactly do the effective  $NN$  forces arise from QCD?; What are the short-distance properties of the nuclear interactions?; Where do non-nucleonic degrees of freedom become manifest in nuclei? Reactions where these questions can be addressed are quasi-elastic or diffractive knockout from nuclei (discussed in Sec. 7.3.7 in the context of nuclear short-range correlations) and DIS in the scaling regime.

In the context of the influence of nuclear interactions on medium modifications, the wide  $Q^2$ -range available at the EIC means the  $Q^2$ -dependence of the EMC effect can be investigated. DIS on polarized light ions results in measurements of the spin-dependent EMC effect, the size of which is unknown so far. In combination with spectator tagging the relevant distances in  $NN$  interactions that cause the EMC effect can be studied. Accurate descriptions of the reaction mechanisms are needed to disentangle the medium modification effects from nuclear final-state interactions [19, 65, 723]. This is especially important for spectators with momenta of a few  $\sim 100$  MeV (relative to the ion rest frame).

In this way DIS on  $d$  with neutron tagging,  ${}^3\text{He}$  with  $d$  or  $pn$  tagging and  ${}^3\text{H}$  with  $nn$  tagging, in combination with free proton data can be used to study proton medium modifications and help to constrain reaction mechanism frameworks. This in turn then will help in the disentanglement of medium modifications and final-state reactions for tagged DIS reactions on light nuclei accessing neutron structure ( $d$  with proton tagging,  ${}^3\text{He}$  with  $pp$  tagging and  ${}^3\text{H}$  with  $d$  or  $pn$  tagging).

For DIS at smaller values of Bjorken  $x$ , nuclear anti-shadowing and shadowing effects in light nuclei are of interest. For the latter, light ions offer the advantage that the multiple scattering series is limited and thus controlled, see below for  ${}^4\text{He}$ .

### Studying nucleon structure in $A=3$ nuclei using double spectator tagging

While there are highly accurate data for proton structure function, it is very hard to measure the neutron structure function due to the fact there is no free neutron target. Neutron structure functions are determined using nuclear targets (deuterium or  ${}^3\text{He}$ ) and often inferred using different theoretical models, see Secs. 7.1.1 and 7.1.2. Modern experiments, such as the Jefferson Lab BONuS experiment tag the recoil proton from deuteron [724,725], but no such tagging experiment has been done with  ${}^3\text{He}$ , see Fig. 7.85 for a diagram.

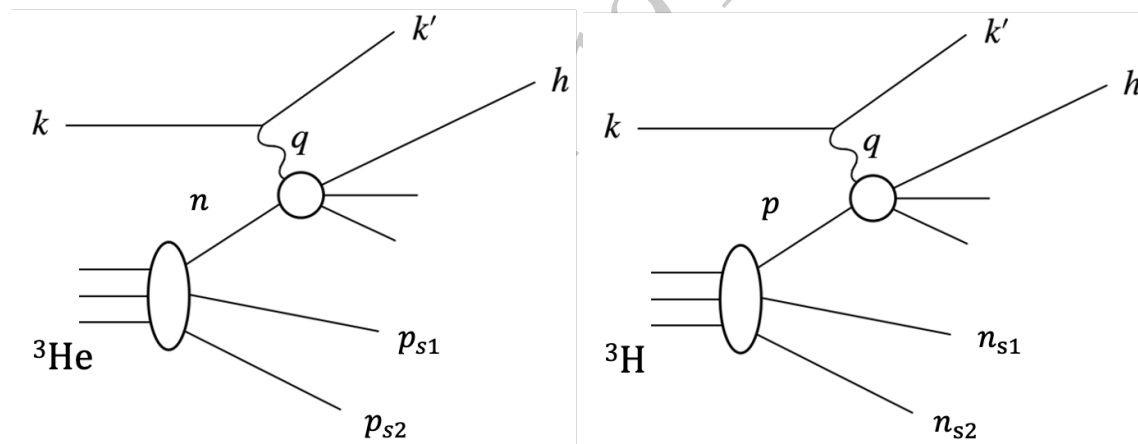


**Figure 7.85:** Shown are Feynman diagrams for double spectator nucleons tagging from  ${}^3\text{He}$  on the left and from  ${}^3\text{H}$  on the right.

Simulations of DIS and SIDIS scattering from  ${}^3\text{He}$  show that both spectator protons can be detected in the far forward region of the EIC. By ensuring that in the ion rest frame the two spectator protons have a low momentum, the initial momentum of neutron can be constrained, which can provide an effective “free neutron” target with minimal model dependence, see Sec. 7.1.2. Taking this idea one step further, by using a tritium beam one can tag two spectator neutrons. Since in this case, the free proton’s structure function is well known, one directly tests how well reaction mechanisms are understood (including final-state interactions with the detected spectators) and a unique way to test the validity of the  ${}^3\text{He}$  extractions of the neutron structure functions as well as offering a window

onto nuclear medium modifications of proton partonic structure. At higher spectator momenta spectator tagging yields information on the influence of nuclear interactions on DIS cross sections, both through medium modifications of partonic distributions (EMC effect, (anti)shadowing) and nuclear final-state interactions.

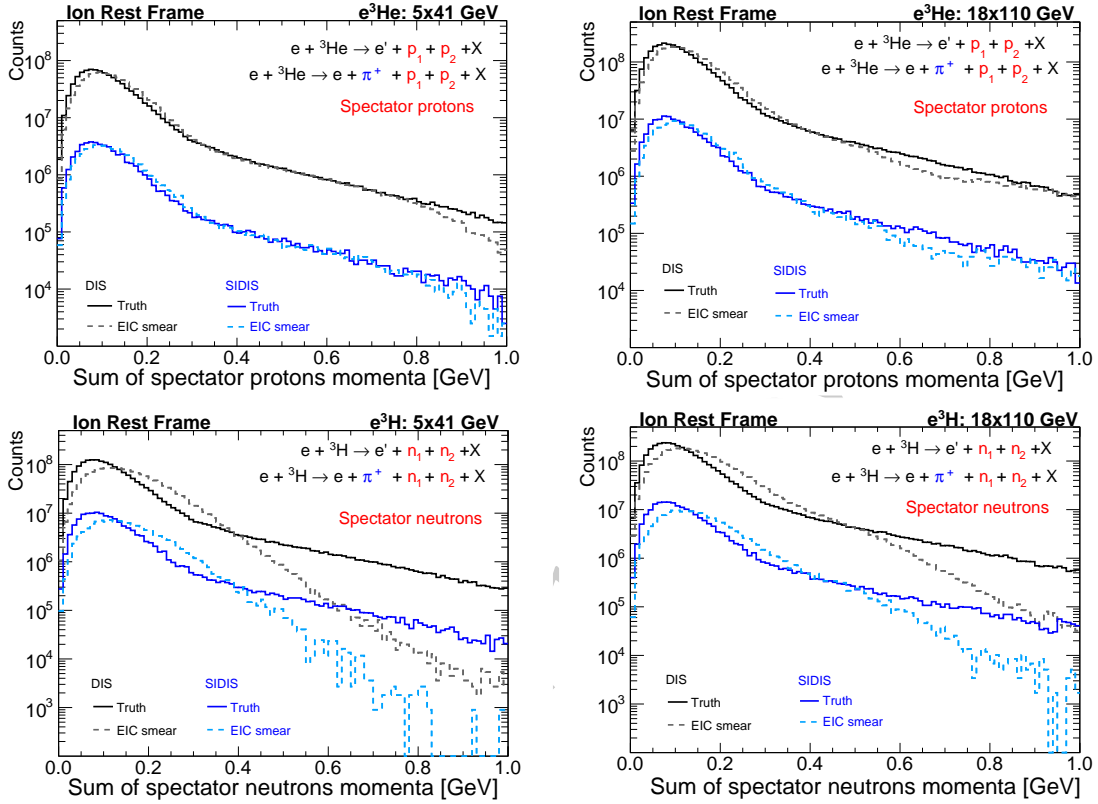


**Figure 7.86:** CLASDIS simulations for DIS and  $\pi^+$  sidis on  $^3\text{He}$  with double proton spectator tagging (top) and on  $^3\text{H}$  with double neutron spectator tagging (bottom) at 5x41 GeV (left) and 10x100 GeV (right).

The DIS and SIDIS process for both  $^3\text{He}$  and  $^3\text{H}$  targets was generated using the CLASDIS generator, a CLAS version of the PEPSI [726] generator, which is based on LEPTO version 6.5 and JETSET version 7.410. CLASDIS was originally intended to be used for the fixed target event generation but has been extended for EIC kinematics. Results are shown in Fig. 7.86 and made use of a version of EICSMPEAR which includes an approximation of the far forward region developed with EICROOT and g4e. The results show that with the EIC one will be able to uniquely determine that the initial-state neutron was nearly at rest; minimizing model dependence for the extraction of quantities such as  $F_2^N$  from unpolarized  $^3\text{He}$  and  $A_1^N$  from polarized  $^3\text{He}$ .

Tagging of spectator nucleons in these reactions means final state interactions between the detected hadrons in the final state should be considered. In Ref. [65], polarized DIS on  $^3\text{He}$  with deuteron tagging was considered. This process would allow to study the onset of the spin-dependent EMC effect in three-body systems and can help to constrain FSI mech-

anisms in the deuteron tagged reaction on  ${}^3\text{H}$ , used to probe neutron structure. Proper kinematical regions where the FSI effect is minimized were identified in Ref. [65]. For spin dependent SIDIS off  ${}^3\text{He}$  and  ${}^3\text{H}$  (important for the extraction of the neutron Sivers and Collins SSA), a recent paper [727] has shown that both at fixed target and the EIC, the FSI described within a generalized eikonal approximation using AV18 wave functions are theoretically under control in the experimental observables. Neutron information can be safely extracted using the same straightforward procedure proposed in a plane-wave impulse approximation analysis [728].

### Coherent scattering off the lightest nuclei

The leading twist theory of the gluon shadowing predicts shadowing both for the pdfs and for coherent production of heavy mesons like  $J/\Psi$ . The theory predictions for coherent  $J/\Psi$  production off lead were tested in ultraperipheral collisions at the LHC for  $x$  down to  $10^{-3}$ . For the most recent comparison of the leading twist theory of nuclear shadowing with the LHC data on coherent  $J/\Psi$  production of Pb and reference to the previous studies see Ref. [664]. So far the gluon shadowing was studied only in the case of heavy nuclei. At EIC studies of the coherent diffraction off heavy nuclei and parallel measurements of the gluon pdfs in the inclusive hard processes would provide further stringent tests of the gluon shadowing dynamics. A complementary set of measurements is possible at the EIC using the beams of the lightest nuclei. In this case one can probe separately shadowing for scattering off two and of three nucleons. Note here that the average number of nucleons involved in the gluon shadowing at  $Q_0^2 \sim \text{few GeV}^2, x = 10^{-3}$  is around two, so the measurements with heavy and light nuclei would nicely complement each other.

An important advantage of the lightest nuclei is that their wave functions are well known and so the impulse approximation term can be reliably calculated. Also it would be possible to test the calculation of the wave function by studying the cross section at  $x \geq 0.03$  where rescattering effects are small and impulse approximation dominates at all  $t$ . An important advantage of  ${}^4\text{He}$ ,  ${}^3\text{He}$  is that the single scattering term (which is proportional to the nucleus form factor nucleus form factor) goes through zero at moderate  $t$  ( $-t = 0.3 \text{ GeV}^2$  for  ${}^4\text{He}$ ; see green line in Fig. 7.87). This provides an opportunity to separate the combination of double and triple scattering amplitudes (interaction with all four nucleons is negligible) in a wide  $t$  range. Moreover combination of measurements off  ${}^3\text{He}$  and  ${}^4\text{He}$  would allow to separate double and triple scattering amplitudes in a practically model independent way due to difference of the strengths of double and triple contributions in these two cases.

One can see from the result of calculation at  $x = 10^{-3}$  the shift of the position of the minimum is very significant and hence would be easy to measure provided the detector has an acceptance in the discussed  $t$ -range ( $-t \leq 0.5 \text{ GeV}^2$ )

In the case of the deuteron beams the rescattering effects are pretty small due to a large contribution of the quadrupole form factor. However, if the polarized deuteron beams would become available, one would be able to separate single and double rescattering

contribution and consequently further improve extraction of the amplitudes of scattering off two and three nucleons.

Obviously there are many other interesting coherent reactions with  ${}^4\text{He}$ . For example, photo and electroproduction of  $\rho$ -mesons. In the soft regime screening should be stronger than for  $J/\Psi$  so the minimum of the differential cross section would be at smaller  $-t$ , to  $Q^2 \sim 10 \div 15 \text{ GeV}^2$  where the  $t$ -dependence of  $\rho$ -meson should approach that of  $J/\Psi$ .

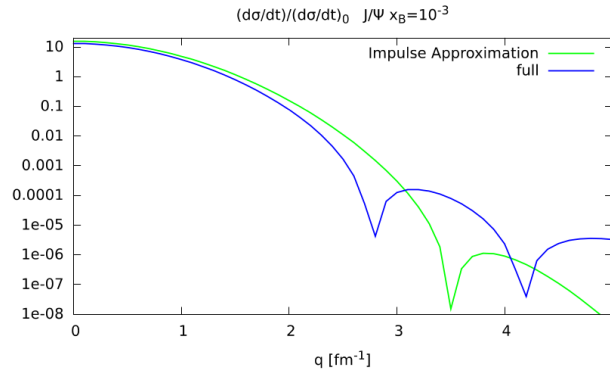


Figure 7.87: Placeholder Figure.

### 7.3.9 Coherent and incoherent photoproduction on heavy targets

Photoproduction and electroproduction are sensitive to the gluon content of the target nucleus, and can provide information on how dipoles interact in nuclei, as is discussed in Section 7.3.2. This section will discuss the additional physics that can be probed by studying coherent and incoherent production separately.

Exclusive production is an excellent probe of the gluon distributions in the nucleus, providing information on the overall gluon content through the overall cross-section, the spatial distribution of the gluons (through  $d\sigma/dt$  for coherent production) and on event-by-event fluctuations in distributions, including gluon hot spots through inelastic production [729].

High-energy photoproduction and electroproduction cross-sections on proton targets were first studied extensively at HERA, where the cross-sections for a variety of mesons, from the  $\rho$  up to the  $Y$  [488, 730]. The photoproduction studies were extended to include heavy nuclear targets at RHIC [731] and the LHC [732]. The LHC data also had a larger energy reach than HERA. The LHC studies found a moderate suppression of the  $J\psi$  cross-section, consistent with moderate gluon shadowing - roughly as predicted by leading order twist calculations [733]. The EIC will allow us to extend these measurements to large  $Q^2$ , and also, through vastly improved statistics, probe the production kinematics in detail, exploring the photon energy and  $Q^2$  evolution of the nuclear targets, as is shown in Fig. 7.88.

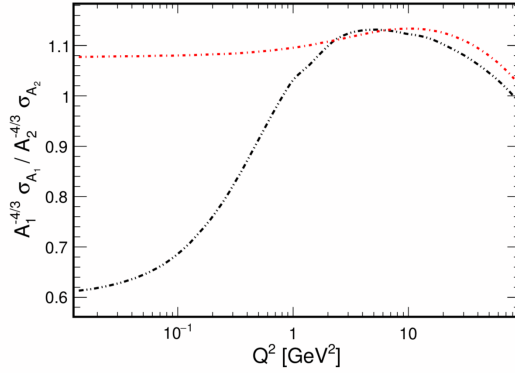


**Figure 7.88:** The scaled (by  $A^{-4/3}$  ratio of the  $\rho$  (black) and  $J/\psi$  (red) coherent production cross-sections on lead and iron targets respectively, as a function of  $Q^2$ . In the absence of nuclear effects, this ratio should be 1. This ratio is roughly reached at high  $Q^2$ , when the nucleus is largely transparent, but, as the  $Q^2$  drops, shadowing reduces the relative cross-section. The drop is much larger for the  $\rho$  than the  $J/\psi$  because the  $\rho$  is much lighter, with a larger dipole. The  $J/\psi$  is heavier, with a much smaller dipole that interacts less. This plot shows why it is important to study shadowing with light mesons. From Ref. [734], but a very similar plot appears in Ref. [735]

### Coherent photoproduction

At high energies, it occurs primarily via photon-Pomeron fusion. The Pomeron represents the absorptive part of the nuclear potential, so it has the same quantum numbers as the vacuum. So, the final state particles predominantly have the same quantum number as the photon,  $J^{PC} = 1^{--}$ , leading to vector meson dominance. In lowest order pQCD, the Pomeron is treated as two-gluon exchange, so the forward scattering cross-section for a vector meson with mass  $M_V$  is [736]

$$\left. \frac{d\sigma}{dt} \right|_{t=0} = \frac{\Gamma_{ll} M_V^3 \pi^3}{48\alpha} \left[ \frac{\alpha_S(\bar{Q}^2)}{\bar{Q}^4} x g(x, \bar{Q}^2)^2 \left( \frac{1+Q^2}{M_V^2} \right) \right], \quad (7.48)$$

where  $\Gamma_{ll}$  is the vector meson width to decay to two leptons,  $g(x, Q^2)$  is the gluon distribution and  $\bar{Q}^2 = (Q^2 + M_V^2)/4$ . Because the vector meson mass provides a hard scale, for heavy quarkonium pQCD should hold, even for nearly real photons. There are several issues with the lowest order treatment: the assumption of two gluons each carrying half the virtuality, the different  $x$  values for the two gluons ( $x_1 \gg x_2$  is preferred) and the choice of the mass scale [737, 738]. Unfortunately, there is not yet a complete NLO calculation. A partial NLO calculation was presented in Ref. [739]. This calculation has its own difficulties, but, with careful choice of scale, the accuracy seems good enough ( $\pm 15\%$  to  $\pm 25\%$ ), good enough for use in determining gluon distributions [740]. There has been relatively recent progress in this area, and, by the time the EIC turns on, these theoretical issues should be under good control. The EIC should get large samples of the  $J/\psi$  and  $\psi'$ ,

over a wide range of  $Q^2$  and significant samples of photoproduction the three  $Y$  states (at small  $Q^2$ . The rapidity of the final state vector meson provides information on the photon energy  $k$  and Bjorken- $x$  of the struck quark. In the lab frame, for low  $Q^2$  [741]

$$k = \frac{M_V}{2} \exp(y) \quad (7.49)$$

and

$$x = \frac{M_V}{4\gamma m_p} \exp(-y). \quad (7.50)$$

Large  $Q^2$  will shift these reactions slightly [734]. These equations can be used to determine the Bjorken  $x$  of the struck gluons accurately, subject to the issues that come from the second gluon.

More sophisticated calculations use a dipole approach to determine the cross-section and  $d\sigma/dt$  **need references**

The rates for vector meson production are very high - 40-50 billion  $\rho^0$  for  $10 \text{ fb}^{-1}/A$  luminosity, for both  $ep$  and  $eA$  [734]. The rates for the  $\phi$  are smaller, about 2.5 billion per  $10 \text{ fb}^{-1}/A$  luminosity, while the  $J/\psi$  rates are about 100 million events/year. Even the  $Y$  states are accessible, with about 140,000/60,000 events expected for  $ep$  and  $eA$  respectively. The rates for electoproduction  $Q^2 > 1 \text{ GeV}^2$  are lower, but, even for the  $J/\psi$ , about 5 million events events with  $Q^2 > 1$  are expected per  $10 \text{ fb}^{-1}/A$ . With these statistics, detailed multi-dimensional studies are possible, including studying the nuclear shape and fluctuations in fairly narrow bins of Bjorken- $x$ .

### Walker-Good and coherent photoproduction

Further information can be extracted from vector meson production using the Walker-Good paradigm [742], which relates the coherent cross-section to the average wave function of the target, while the incoherent cross-section probes its fluctuations [743]. The Walker-Good approach separates vector meson production reactions into two classes: those where the nucleus remains in the ground state, and those where it is excited. The total cross-section considers all possible final states:

$$\frac{d\sigma_{\text{tot}}}{dt} = \frac{1}{16\pi} \langle |A(\Omega)|^2 \rangle \quad (7.51)$$

The coherent cross-section is the subset of the total cross-section where, the final states are the same as the initial. The cross-section is determined by summing the amplitudes for interacting on each nucleon. Schematically Here,  $\Omega$  is the nuclear configuration (nucleon positions, subnucleonic fluctuations etc.). This leads to an  $A^2$  enhancement in  $d\sigma/dt|_{t=0}$ .

The incoherent cross-section is just the difference between the total and coherent cross-sections. The incoherent cross section is then the difference between equations (7.51) and

(??)

$$\frac{d\sigma_{\text{inc}}}{dt} = \frac{1}{16\pi} \left( \langle |\mathcal{A}(K, \Omega)|^2 \rangle - |\langle \mathcal{A}(K, \Omega) \rangle|^2 \right) \quad (7.52)$$

Because of the switched ordering of the squaring and averaging, the incoherent process is sensitive to fluctuations in the nuclear configuration. A more formal treatment of this approach is given in Ref. [647].

### Coherent Photoproduction

Measurements of  $d\sigma/dt$  for coherent photoproduction can be used to image the nucleus; this is the gluonic nuclear equivalent of a GPD, albeit with some complications due to the likelihood of multiple scattering. To be conservative, we can say that this maps out the transverse positions of photoproduction interactions within the target nucleus. As was discussed in the EIC White Paper, this may be determined from the two-dimensional Fourier transform of  $d\sigma/dt$  [744]

$$F(b) \propto \int_0^\infty p_T dp_T J_0(bp_T) \sqrt{\frac{d\sigma}{dt}} \quad (7.53)$$

where  $J_0$  is a Bessel function. The  $\sqrt{\quad}$  is to go from a cross-section to an amplitude. This introduces a sign ambiguity, since the amplitude flips signs at each diffractive minimum. This sign flip needs to be added in 'by-hand' when analyzing the data.

The STAR Collaboration has applied this approach to  $\rho$  and direct  $\pi^+\pi^-$  photoproduction in ultra-peripheral collisions [745, 746], and found some limitations in the method, as have continuing EIC studies.

First, the  $p_T$  integral runs from 0 to  $\infty$ , but the data is limited to a maximum  $p_T$ . Unless the  $p_T$  range encompasses several diffractive minima (up to  $p_T \approx 15\hbar/R_A$ ),  $F(b)$  will not fully capture the shape of the nucleus. This is not easy, because it requires being able to accurately separate coherent and incoherent production up to these large momenta. At the high end of the momentum range, incoherent production dominates, and good rejection is required. This will be discussed in more detail later.

Second, the measured  $d\sigma/dt$  includes contributions from the photon  $p_T$  and the experimental resolution. Naively, one might expect to remove the photon  $p_T$  by measuring it via the outgoing lepton. However, this only works for large  $Q^2$ , where the scattered electron is detected, and, in any case, the momentum spread of the electron beam limits the accuracy with which it can be determined. The experimental resolution and remaining photon  $p_T$  can be removed by an unfolding, but this will be problematic near the diffractive minima; there will be a limit to how well these can be resolved. This will in turn limit how well the location of the minima can be found; this is problematic because of the need to flip signs in Eq. 7.53.

Finally,  $p_T$  is two-dimensional, but  $\sqrt{t}$  is three-dimensional. This is not important for lighter mesons, where the longitudinal component is negligible, but may be a factor for

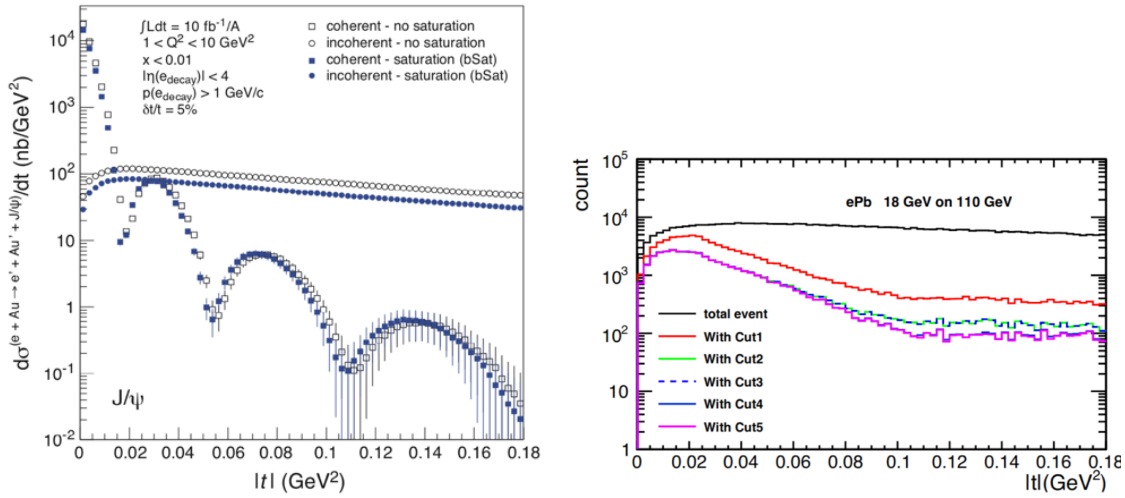


**Figure 7.89:** (left)  $d\sigma/dt$  for coherent and incoherent  $J/\psi$  photoproduction with and without saturation. From the EIC White Paper (and therefore placeholder?) [1] (right)  $d\sigma/dt$  for incoherent  $J/\psi$  photoproduction in the BeAGLE Monte Carlo (black). The other lines show the effect of successive cuts that there are no neutrons (red), no photons with energy above 50 MeV (green), no protons in the draft Roman pot detector or off-energy detector, and no protons in the B0 detector. The main purpose of this figure is not to evaluate detector designs, but to compare the suppression of incoherent production that is achievable in an optimistic detector design with what is required to remove it as a background to coherent production.

heavier mesons like the  $Y$

More study is needed to understand the severity of all of these issues.

### Incoherent Photoproduction

The incoherent component of photoproduction is sensitive to event-by-event fluctuations in the target configuration, as is shown in Eq. 7.52. This equation can be used to test models of nucleon parton fluctuations, with small  $t$  corresponding to long distance scales, and larger  $t$  probing shorter range fluctuations. However,  $d\sigma/dt$  for incoherent production cannot be used to directly extract fluctuation measures.

This approach has mostly been used to probe the proton using  $J/\psi$  production data at HERA. Those studies found that the incoherent cross-section was compatible with a proton model where there were large event-by-event fluctuations in proton configuration, *i. e.* large variations in parton densities [747]. These fluctuations are expected to remain visible with ion targets. A study by the same authors of UPCs at the LHC found that the fluctuations should increase the incoherent cross-section by a factor of about 2 [748]. Although the EIC has a smaller energy reach than HERA or LHC UPCs, it should be able to study these fluctuations for a range of nuclear targets.

### Separating Coherent and Incoherent Production

One key problem for pursuing this physics involves separating coherent and incoherent production. Although most incoherent interactions involve neutron (or sometimes proton) emission, this is not always the case, and nuclear excitations which decay via emission of MeV photons (in the nuclear rest frame) are not easy to detect. The situation is further complicated because models of nuclear excitation in photoproduction are subject to large uncertainties; in most cases, there is no relevant data to constrain the models.

Figure 7.89 shows the magnitude of the problem. The left-hand panel compares  $d\sigma/dt$  for coherent and incoherent  $J/\psi$  production, while the right-hand panel shows the incoherent  $J/\psi$  production as modelled in the BeAGLE Monte Carlo. The black curve is the total  $d\sigma/dt$ , while the colored curves show the  $d\sigma/dt$  after various cuts to remove events with traces of nuclear excitation that would be visible in a model EIC detector.

At the position of the third diffractive minimum, the incoherent cross-section is about 400 times larger than the coherent one, so, to determine the coherent cross-section, a rejection factor for incoherent photoproduction better than 400:1 must be achievable; this factor must also be known accurately. As the right panel shows, BeAGLE simulations show that, by vetoing on neutrons, protons and higher energy photons only leads to a 100:1 rejection factor in that  $|t|$  range.

For  $|t| < 0.01 \text{ GeV}^2$ , the situation is reversed, with the coherent cross-section up to 100 times larger than the incoherent one. Here, the major mis-identification danger is the presence of random (uncorrelated) neutrons, forward protons or photons accompanying a coherent reaction. This probability is not small. In full-energy  $eAu$  collisions at an  $eA$  luminosity of  $8 \times 10^{31} \text{ cm}^{-2} \text{ s}^{-1}$ , the rate for one background reaction, photo-excitation of a gold nucleus, followed by Giant Dipole Resonance (GDR) decay, usually leading to a single neutron is about 2.5 MHz [749] - a significant rate of background neutrons. Other sources will further increase the rate. These rates can be measured using other beam crossings, and statistically subtracted but, because of the large coherent:incoherent ratio, this will significantly increase the measurement uncertainty.

In Chapter 8, we will discuss how experimental constraints in separating coherent and incoherent production will limit how well we can use exclusive production to probe nuclear targets.

## 7.4 Understanding Hadronization

Intimately related to the prominent question of confinement is the one of hadron formation. How do the degrees of freedom of QCD, quarks and gluons, relate to the hadronic degrees of freedom we observe in nature? The EIC will not only address the many outstanding questions about hadron structure, as described in the previous sections, but also will make substantial progress in our understanding of hadron formation.

The theoretical description of hadron formation usually involves factorization theorems,

where part of the production cross section can be calculated perturbatively, and the non-perturbative nature of hadronization is encoded in the so-called fragmentation function (FF). FFs describe how a parton transforms into the color-neutral hadrons that we observe.

The unprecedented luminosity and the polarized beams of EIC will have a strong impact in the measurements of fragmentation functions of light mesons, but also of polarized fragmentation functions, such as  $\Lambda$  hyperons. Much richer information can even be obtained by measuring di-hadron FFs that appear in the description of semi-inclusive processes with two identified hadrons in the final state.

With the combination of different beam species, the EIC will also be able to address how hadronization occurs in the nuclear medium. The possibility to probe the nuclear medium with an electromagnetic probe will provide the cleanest understanding of the effects of the nuclear environment on hadronization.

The study of the production mechanism for quarkonia, heavy quark-antiquark bound states, will provide a unique view on hadronization. Due to the large mass of the quarks, their production involves both perturbative and non-perturbative processes. Its production will be studied in  $e + p$  collisions, but also in  $e+A$  collisions, where quarkonia will hadronize inside the nucleus.

This section also describes the impact that the EIC will have on the study of hadron spectroscopy, in particular in the heavy quark sector. The high projected luminosity of EIC will allow to study in detail rare states that have recently been observed in other facilities.

A complementary way to get insight into hadronization is through the study of target fragmentation through the measurement of fracture functions that describe the hadronization of the target after a parton with a given momentum fraction  $x$  is removed from it. Factorization theorems apply and fracture functions are universal quantities independent of hard process.

### 7.4.1 Hadronization in the vacuum

#### Light meson fragmentation functions and flavor sensitivity

Fragmentation functions, FFs, describe the formation of final-state hadrons off high-energetic, asymptotically free partons [750]. As such, FFs directly connect to the confinement of the strong interaction. While data from electron-positron annihilation mostly constrain the singlet combination of the FFs and proton-proton collisions primarily constrain gluon FFs, the production of light mesons in semi-inclusive DIS is the primary channel for the differentiation between the fragmentation of light quarks and anti-quarks. In addition, semi-inclusive DIS data have a high sensitivity to the separation of quark flavours. Recent determination of spin averaged single hadron fragmentation functions from electron-positron annihilation data can be found in Refs. [751, 752] and global analyses based on the combination of data from electron-positron annihilation [753–762], proton-proton collisions [763–768] and semi-inclusive DIS [363, 769], can be found in Refs. [770, 771]. The

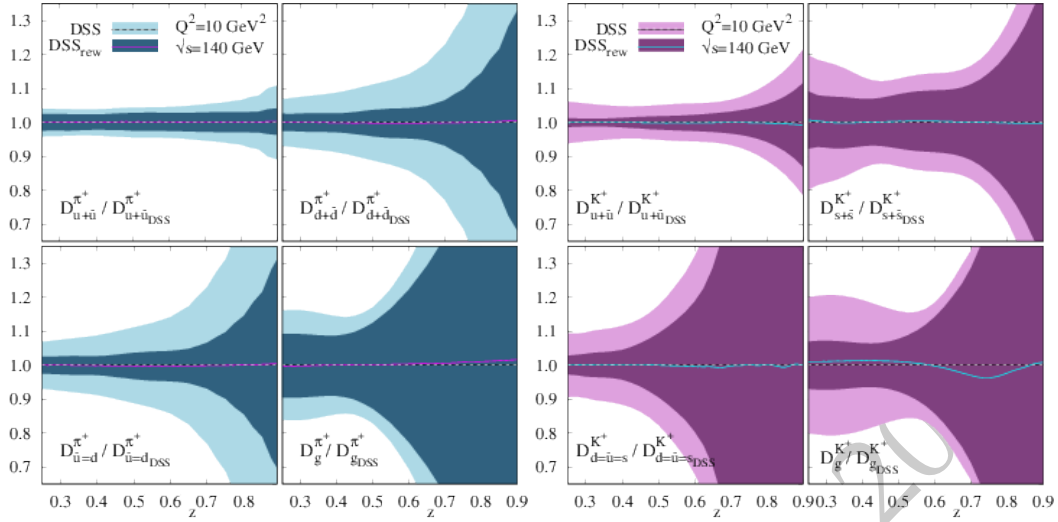


**Figure 7.90:** Pion (left) and kaon (right) FFs obtained from the global DSS analyses [770,771] (dashed line with light uncertainty bands) and obtained from the global DSS analyses with the inclusion of EIC pseudo-data, at a c.m.s. energy  $\sqrt{s} = 140$  GeV, (continuous line with dark uncertainty bands) [25], both normalized to the DSS best fit. The uncertainties reflect the statistical uncertainties from the pseudo-data (evaluated at a luminosity of  $10 \text{ fb}^{-1}$ ) and the uncertainties from the PDFs. The upper (lower) row corresponds to the (un)favored fragmentation.

latter find their origin in Ref. [772].

The impact of EIC pseudo-data can be seen in Fig. 7.90 [25], which shows the pion (left) and kaon (right) FFs obtained from the global analysis (DSS) and those obtained by including the EIC pseudo-data, at a c.m.s. energy  $\sqrt{s} = 140$  GeV, to the DSS global analysis ( $DSS_{rew}$ ), both normalised to the DSS best fit. The uncertainties reflect the statistical uncertainties from the pseudo-data as well as those from the PDF set used. It can be seen that the EIC has a strong potential to improve the determination of the light-meson FFs, both for favored (upper row) and for unfavored (lower row) fragmentation. The improvement is especially pronounced for the unfavored pion FFs and for the favored kaon FFs, while the results for the unfavored kaon FFs should be evaluated with some caution because of the more rigid functional form assumed. Based on the results for the single hadron, spin averaged FFs it is reasonable to expect that EIC data will have also a significant effect on the extraction of di-hadron FFs and polarized FFs. In particular, the EIC will for the first time enable the measurement of spin-averaged and polarization dependent FFs in jets. This allows a separation of the dependence of the FF on the intrinsic transverse momentum generated in the final and initial state. See Sec. 7.2.3 for more details on jet measurements at the EIC.

### Fragmentation into polarized $\Lambda$ hyperons

The detection of self-analyzing  $\Lambda$  hyperons makes it possible to study the dependence of the hadronization process on polarization degrees of freedom in the final state. Here we

will discuss polarized fragmentation functions that can be seen as the FF analogue to the polarized PDFs  $g_1$  and  $h_1$  as well as polarizing FFs that can be seen as the analogue to the Sivers TMD FF or, in the twist-3 framework, the Qiu-Sterman matrix elements.

Polarized Fragmentation Functions (PFFs) describes the hadronization process of a polarized parton with a final state polarized hadron like  $\Lambda$ . The PFF of  $\Lambda$  and  $\bar{\Lambda}$  have been widely studied in experiments including polarized lepton-nucleon DIS process [773–775] and polarized hadron-hadron collisions [776–779]. The first global analysis of longitudinally polarized fragmentation function  $\Delta D$  [780] has been performed with LEP data, but is not well constrained yet. The polarized jet fragmentation function of  $\Lambda$  within a fully reconstructed jet is also studied recently [476]. The spin transfer of  $\Lambda$  and  $\bar{\Lambda}$  from proton beam either longitudinally or transversely polarized in lepton-nucleon DIS process, may also provide valuable information on strange quark helicity or transversity distributions [781–787] if the corresponding PFFs are reasonably determined. The unprecedented high precision data on hyperon spin transfer measurements at EIC will shed new lights into the PFFs and the strange quark distributions. Fig. 7.91 shows a projection of longitudinal spin transfer for  $\Lambda$  and  $\bar{\Lambda}$  from polarized proton beam at EIC energy of  $18 \times 275$  GeV.

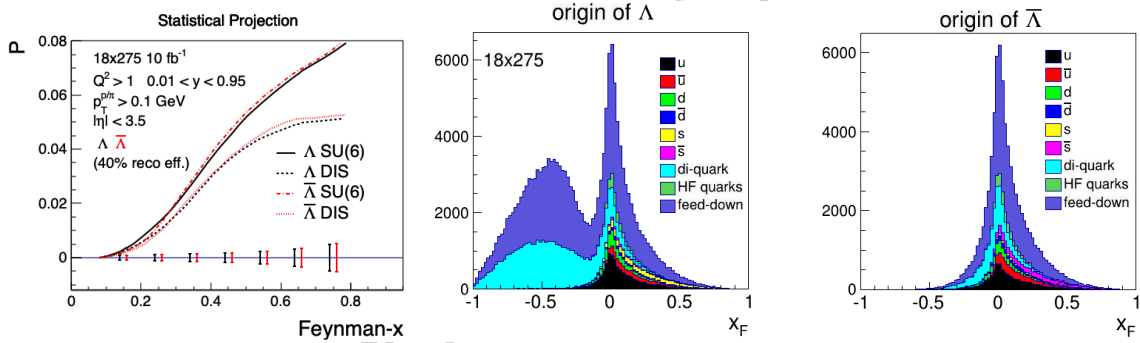


**Figure 7.91:** Left panel: Projection of longitudinal spin transfer for  $\Lambda$  and  $\bar{\Lambda}$  from proton beam at  $18 \times 275$  GeV at EIC. The curves are from model predictions [787]. The two right hand panels show the origin of the reconstructed  $\Lambda/\bar{\Lambda}$ . In the current fragmentation region a significant fraction originates from feed-down. A dominant part of the feed-down component is contributed by  $\Sigma^0 \rightarrow \Lambda\gamma$ .

In the case, where the initial quark is not polarized, the final state  $\Lambda$  can still carry polarization. In fact, it has been a long standing challenge to describe the transverse polarization of  $\Lambda$  hyperons in unpolarized deep inelastic high energy reactions from a factorized framework in perturbative QCD. Initiated by the strikingly large transverse polarization asymmetries of  $\Lambda$  hyperons observed in early experiments at Fermi-Lab (along with follow-up experiments) in  $pA \rightarrow \Lambda X$  fixed target processes already 40 years ago [788–795], experimental and theoretical investigations [796–803] have spanned decades. More recently, polarization of  $\Lambda$  baryons were investigated at the LHC by the ATLAS collaboration [804]. While a small polarization was found in the ATLAS measurements-essentially consistent with zero-in the mid-rapidity region, such experiments demonstrate that the polarization of  $\Lambda$  baryons can be studied at the highest LHC energies and may be larger in different

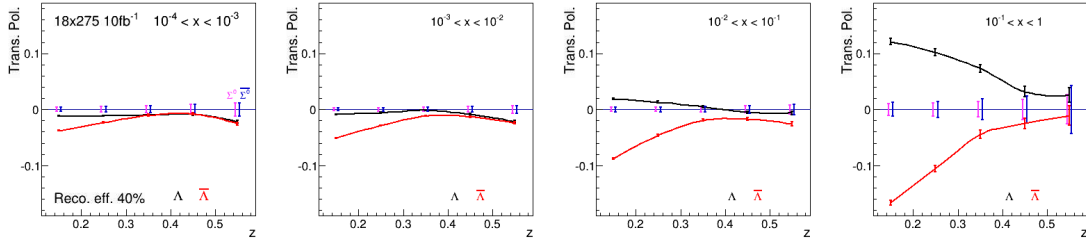


**Figure 7.92:** Projected  $\Lambda$  polarization using the extraction in Ref. [810] for the highest energy configuration. The projected uncertainty on  $\Sigma^0$  polarization is also shown which is important by itself and to estimate the polarization of the feed-down component. A 40% reconstruction efficiency is assumed but not the effect from feed-down which most likely reduces the magnitude of the asymmetries.

kinematical regions at forward rapidities. Experimentally, data on polarized  $\Lambda$  fragmentation has been provided by the OPAL collaboration [805] at LEP. This measurement was performed on the Z-pole, i.e., at a center of mass energy equal to the mass of the Z-boson. While a substantial *longitudinal* polarization of the  $\Lambda$ s was detected by OPAL, the *transverse* polarization was found to be zero within error bars. Recently the BELLE collaboration measured the production of transverse polarization of  $\Lambda$ -hyperons [806] in  $e^+e^-$  - annihilation, where the hadron cross section is studied as a function of the event-shape variable called thrust  $T$ , fractional energy  $z_\Lambda$ , and the transverse momentum  $j_\perp$  with respect to the thrust axis. They find a significant non-zero effect for the process  $e^+e^- \rightarrow \Lambda^\uparrow(\text{Thrust})X$  as well as for back to back production of  $\Lambda + h$ . In the TMD factorization framework [807,808] for back to back production of  $\Lambda + h$ , a chiral even, naively  $T$ -odd fragmentation function, the so-called polarization fragmentation function  $D_{1T}^\perp$  is predicted to be non-zero and universal [350,801]. Recent extractions of  $D_{1T}^\perp$  from the  $e^+e^-$  data can be found in Refs. [809,810]. The FF  $D_{1T}^\perp$  can be seen as the fragmentation analogue to the Sivers function therefore a test of its universality compared to an extraction from SIDIS data is very interesting [801]. As with other FF measurements, SIDIS data is needed to achieve better flavor separation. The EIC will be the first SIDIS facility where a high statistics sample of  $\Lambda$ 's in the current fragmentation region can be collected which will revolutionize the study of FFs with polarization degrees of freedom in the final state. Figure 7.92 shows the projected transverse  $\Lambda$  polarization.

### Partial wave decomposition of polarized and unpolarized di-hadron FFs including TMDs

As discussed in Sec. 7.2.3, di-hadron FFs are more powerful than single-hadron FFs, due to the additional degrees of freedom. This allows FFs to exist that do not have a single-hadron analog. One example that has been attracting recent interest is the helicity dependent FF  $G_1^\perp$  [170,811]. Recent models, similar to the ones for  $H_1^\perp$  [171,812], make projections for the magnitude of  $G_1^\perp$  based on string fragmentation models [813] or on the interference of partial waves (PWs) [814]. However, another consequence is that the di-hadron cross-section contains an infinite series of modulations. In the context of a PW decomposition,

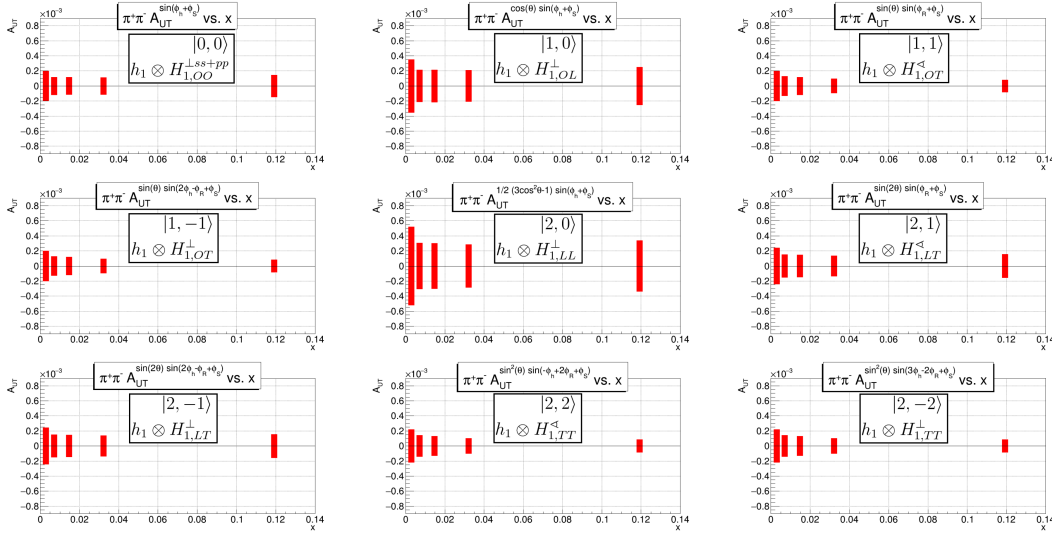


**Figure 7.93:** Projections nine partial waves contributing at twist-2 to  $A_{UT}$  using  $\mathcal{L} = 10 \text{ fb}^{-1}$  of data at  $5 \times 41$ . The labels on the figure indicate the  $m, l$  state and which PDF and FF the PW is sensitive to.

this consequence can be interpreted as originating from the interference of waves with different quantum numbers. We use here the usual notation with the total angular momentum named  $L$  and each PW characterized by angular momentum eigenvalues  $L, M$ . Already in the spin averaged cross-section one encounters 12 terms up to  $L=2$  at leading twist, which is a limit motivated by angular momentum conservation [170,443].

The measurement of these structure functions will provide additional insight into hadronization mechanisms. Since these additional terms are essentially unknown and can interfere with the extraction of the asymmetries of interest, they are a dominant systematic effect for any di-hadron extraction (see, *e.g.*, discussion in Ref [449]), which is another strong motivation for their measurement. For a separation of the PWs, a fit not only in the azimuthal angles but also in the decay angle  $\theta$  is necessary. A large acceptance in  $\theta$  can only be achieved by low minimum momentum cutoff and this has been incorporated into the requirements for an EIC detector. Figure 7.93 shows projections for the PWs that are contained in the azimuthal modulations of  $A_{UT}$  sensitive to transversity coupled the chiral-odd, transverse polarization dependent, DiFF up to  $L = 2$ , *i.e.*, taking only  $s$ - and  $p$ -waves into account. For more details, see the discussion around eq. (52) in Ref. [443]. The projections are for  $\mathcal{L} = 10 \text{ fb}^{-1}$  of data at the low CME configuration of  $5 \times 41$ , where the effect of the  $p_T$  restriction is more severe. A reasonable precision can be achieved for all PWs. The larger uncertainties at low  $x$  are due to the smaller depolarization factor  $D(y)$  at these kinematics.

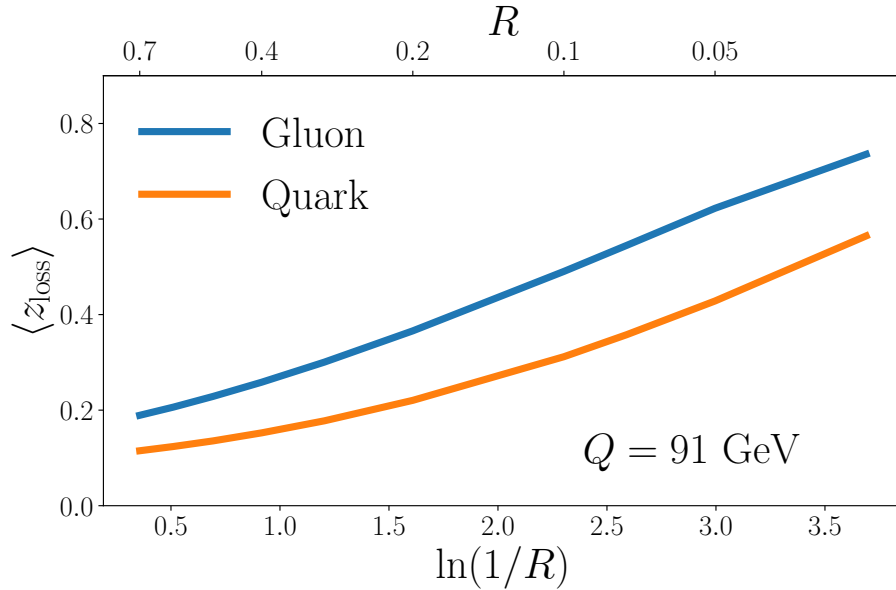


**Figure 7.94:** The average energy loss of leading quark and gluon jets as a function of the jet radius  $R$  at NLL'.

### Leding Jets

Different than inclusive measurements, the reconstruction of leading jets or hadrons allows for a well defined notion of energy loss which can be directly measured at the EIC [499]. By identifying in addition a hard reference scale  $Q$ , the average radiation outside the leading jet  $\langle z_{\text{loss}} \rangle$  can be calculated from first principles in QCD which can be directly identified with parton energy loss. Semi-inclusive cross sections measurements with a suitable jet reconstruction algorithm in the Breit frame [468], allow for a unique opportunity to study the entire energy loss probability distribution as well as the average energy loss, see Fig. 7.94. In  $ep$  collisions leading hadrons and jets probe non-linear QCD dynamics [499, 815, 816]. Additionally, in  $eA$  collisions this provides a unique opportunity to quantify the interaction of energetic quarks and gluons with the cold nuclear matter environment which also allows for a connection to corresponding measurements in  $pA$  and  $AA$  collisions.

### Jet Substructure

Jets and their substructure will be an important tool for understanding hadronization. Since jets are closely related to scattered partons, they can be used to relate final-state hadrons to their parent parton. In particular, jet substructure offers the opportunity to study both the process of fragmentation, or parton radiation patterns, and hadronization, or the formation of the parton shower into bound state hadrons. Single hadrons-in-jets will be used to study a variety of (un)polarized transverse-momentum-dependent fragmentation functions. Fragmentation functions can also be measured for different parton

flavors by, for example, tagging heavy quark mesons such as the  $D^0$ . Additionally, novel jet substructure techniques will be used to study parton radiation patterns in the theoretically clean environment of DIS that allows for better separation of the target and current fragmentation regions. Soft drop declustering techniques can also be used to suppress or enhance nonperturbative effects, which will be essential for better understanding the interplay between the perturbative and nonperturbative roles in the process of hadronization.

One set of substructure observables that have been explored in some detail for the EIC are the one-parameter family of constructs known as jet angularities. For jets with a given transverse momentum  $p_T$ , the observable is defined as [230,817–820]

$$\tau_a = \frac{1}{p_T} \sum_{i \in J} p_{Ti} \Delta R_{ij}^{2-a}. \quad (7.54)$$

Here  $p_{Ti}$ ,  $\Delta R_{ij}$  are the transverse momentum of each particle in the jet and their distance to the jet axis, respectively. Fig. 7.95 shows numerical results for the EIC [821] for two different values of  $a$  and representative jet kinematics. Jet angularities and other jet substructure observables are of great interest at the EIC to study various physics aspects: Test of perturbative methods at low energies and particle multiplicities, universality aspects of nonperturbative shape functions which model hadronization effects, study power corrections, extractions of the QCD strong coupling constant, cold nuclear matter effects, and the tuning of parton showers.

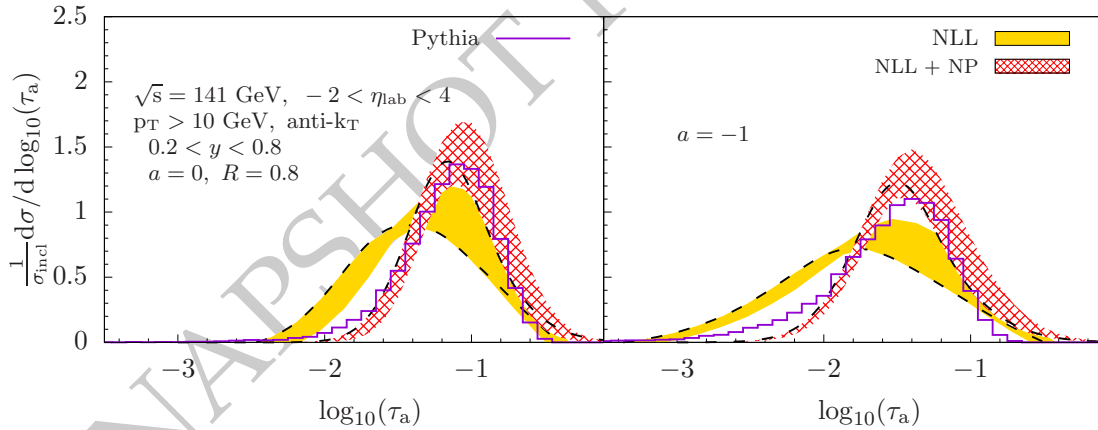


**Figure 7.95:** Predictions for jet angularities at the EIC: Purely perturbative results (yellow band) and with a nonperturbative shape function (red band) compared to simulations from PYTHIA 6 [26].

## Target fragmentation

### 7.4.2 Hadronization in the nuclear environment

#### Collinear Nuclear Fragmentation functions for light hadrons

The modification of the final state in the presence of a nuclear medium is a well known but little understood phenomena in cold nuclear matter physics, with different approaches proposed to describe the measured data [822–828]. In nucleus-light hadron collisions from both RHIC and the LHC the observables depend on nPDFs and in medium FFs simultaneously which leave very little sensitivity to the in medium modification of the FFs or jet functions in the global fits. Thus the cleanest way of exploring the final state effects is through SIDIS, pioneered by the HERMES collaboration [829]. In this case the use of multiplicities increases the sensitivity to the fragmentation functions. The first model independent extraction of nuclear fragmentation functions (nFFs) used the HERMES [829] and RHIC [830, 831] data [832]. Unfortunately the former had a restricted kinematic coverage and no further exploration has been performed since.

Assuming nuclear effects in SIDIS at the EIC will be similar to those seen at HERMES, the incredible precision expected will allow us to fully characterize the nFFs (as well as the nPDFs, see section 7.3.3). Using the latest pion FFs in vacuum from DEHSS [770, 771], a new extraction of nFFs (LIKEn20) from the HERMES data was performed [?].

With these novel nFFs performed an impact study for the EIC using a re-weighting technique. Pseudo data was created using LIKEN20, with appropriate Gaussian noise from the estimated uncertainties that were obtained by PYTHIA simulations reweighted with the nuclear modification of [832] for an accumulated luminosity of  $10 \text{ fb}^{-1}$  for both collision species. Fig. 7.96 shows the distributions for  $u + \bar{u}$ ,  $\bar{u}$  and gluon densities at the initial scales. The corresponding ratios to DEHSS vacuum FFs can be seen in Fig. 7.97. The blue band corresponds to the 90% CL of LIKEN20 and the (very narrow) light cyan band is the one resulting after re-weighting  $pi^\pm$  pseudo data using so far only the lowest collision energy of  $\sqrt{s} \sim 30 \text{ GeV}$ . Given the high precision expected at the EIC, about 10% of the replicas remain. Higher values of  $\sqrt{s}$  produce similar results.

The  $z \leq 0.2$  region is not covered by the data and therefore the shape of the modification should not be considered as anything other than an artificial outcome of the fit at this point. The EIC will definitely explore SIDIS in a much broader kinematic space, opening the way to a full characterization of the FFs and nFFs including flavour separation. Eventually SIDIS data could become an asset in the extraction of nPDFs as shown for the proton case in 7.4.1 for fragmentation functions in the vacuum.

Studies that address the nuclear dependence of transverse momentum for final state hadrons either on the initial state or final state have been discussed in 7.2.5. Further aspects of light hadron fragmentation, such as transverse momentum broadening, a possible  $\nu$  dependence in the suppression of nFFs and other topics can also be studied in detail using the high precision of the EIC data.

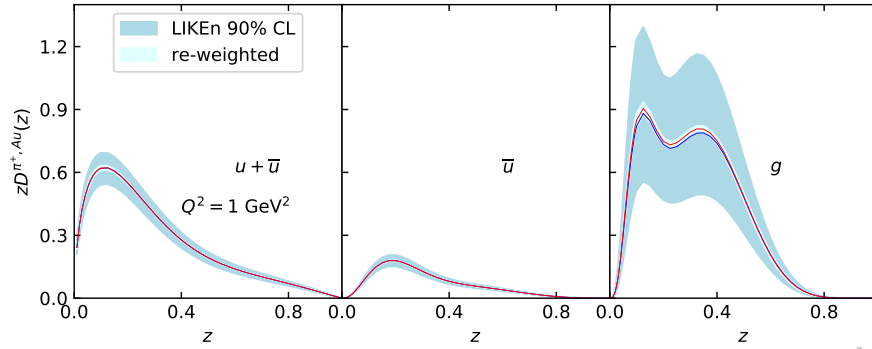


**Figure 7.96:** Nuclear FFs LIKEEn20 for  $Au$  and impact of EIC pseudodata at  $\sqrt{s} \sim 30 \text{ GeV}$  for  $u + \bar{u}$  (left),  $\bar{u}$  (center) and gluon (right). Similar results are found for higher  $\sqrt{s}$ .

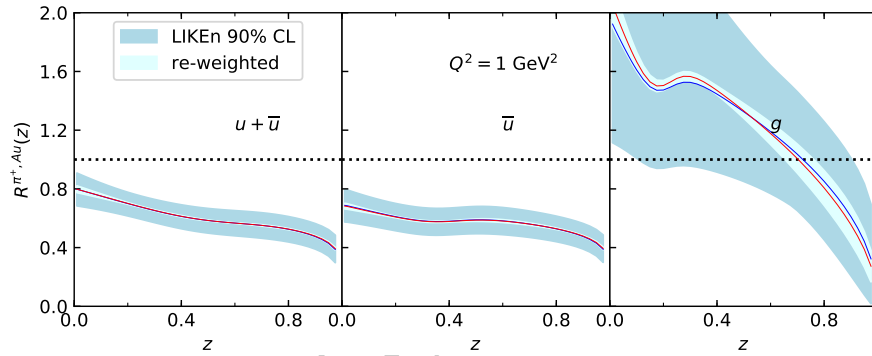


**Figure 7.97:** Ratio of the distributions in Fig.7.96 to vacuum FFs from DEHSS [770, 771].

### In medium evolution for light and heavy flavor mesons

The effect of nuclear environment on hadronization is one of the key questions that the EIC will investigate. Fixed-target HERMES measurements electron beam of energy  $E_{\text{beam}} = 27.6 \text{ GeV}$  [829, 833] have clearly established attenuation of light particle production. Different theoretical approaches have been proposed to explain the data that differ in the underlying assumptions and in the extracted transport properties of large nuclei [685, 834–839]. In addition to precision light flavor studies, the higher enter-of-mass energies at the EIC provide new probes of hadronization - open heavy meson cross sections in  $e+p$  and  $e+A$  collisions [840].

In contrast to light hadrons, the modification of open heavy flavor in DIS reactions with nuclei, such as the one for  $D^0$  mesons and  $B^0$  mesons shown in Fig. 7.98, is much more closely related to the details of hadronization. The observed  $R_{eA}(z)$  is qualitatively consistent with the effective modification of fragmentation functions even after their convolution with the PDFs and the perturbative hard part. There is a significant suppression for large values of  $z$ , but it quickly evolves to enhancement for  $z < 0.65$  and  $z < 0.8$  for  $D$ -mesons and

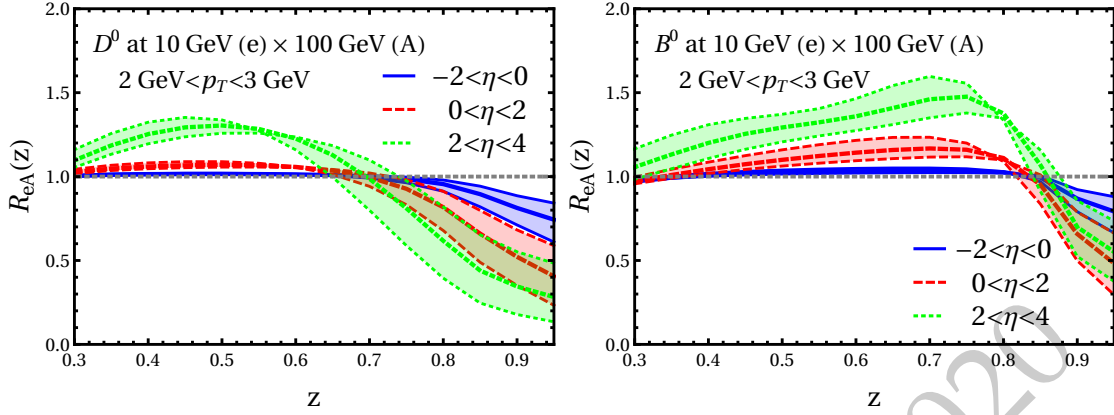


**Figure 7.98:** In-medium corrections for  $D^0$  (left) and  $B^0$  cross sections (right) as a function of the momentum fraction  $z$  at the EIC in three rapidity regions. Top panels are for  $D$ -mesons and bottom panels are for  $B$ -mesons. The electron and proton/nucleus beam energies are 10 GeV  $\times$  100 GeV.

$B$ -mesons, respectively. The effect is most pronounced at forward rapidities and one finds that  $R_{eA}^h$  as a function of  $z$  is a more suitable observable for cold nuclear matter tomography at the EIC than the transverse momentum distributions' modification for hadrons in the laboratory frame alone.

### Heavy meson reconstruction and physics projections

Due to the asymmetric nature of the collisions at the EIC, most of the final state hadrons are produced in the nucleon/nucleus beam going (forward) direction. A silicon vertex/tracking is critical to precisely measure these forward hadrons at the EIC. A LANL experimental team has produced conceptual designs of a Forward Silicon Tracker (FST) coupled to tracking in the central region to enable jet and heavy flavor physics at the EIC [712,713,841]. EIC Fun4all simulation were performed with both the Babar and BeAST magnets. A 95% detection hit efficiency is used in both track and vertex reconstructions. In track reconstruction, the Kalman Filter algorithm is used and a  $20 \mu\text{m}$  vertex Gaussian smearing is applied to both  $x$  and  $y$  directions. The full simulation results, including momentum resolution and distance of closest approach resolution are applied to heavy meson reconstruction in physics simulation that are presented here.

Figure 7.99 shows the mass spectrum of fully reconstructed  $D^\pm$ ,  $D^0$  ( $\bar{D}^0$ ),  $D_s^\pm$ ,  $B^\pm$ ,  $B^0$  ( $\bar{B}^0$ ) and  $B_s^0$  ( $\bar{B}_s^0$ ). For these heavy flavor hadron reconstructions charged tracks are required to have pseudorapidity within  $-2$  to  $4$ . Clear  $D$ -meson and  $B$ -meson signals have been obtained on top of the combinatorial backgrounds. The signal over background ratios and the reconstruction efficiency are listed in the associated panels. An integrated luminosity of  $10 \text{ fb}^{-1}$  is assumed. In addition to heavy flavor meson reconstruction, we also looked for the heavy flavor hadron reconstruction (e.g.  $\Lambda_c$ ). Although the combinatorial background is significantly higher than the  $D$ -meson mass spectrum, clear  $\Lambda_c$  signal can be obtained.

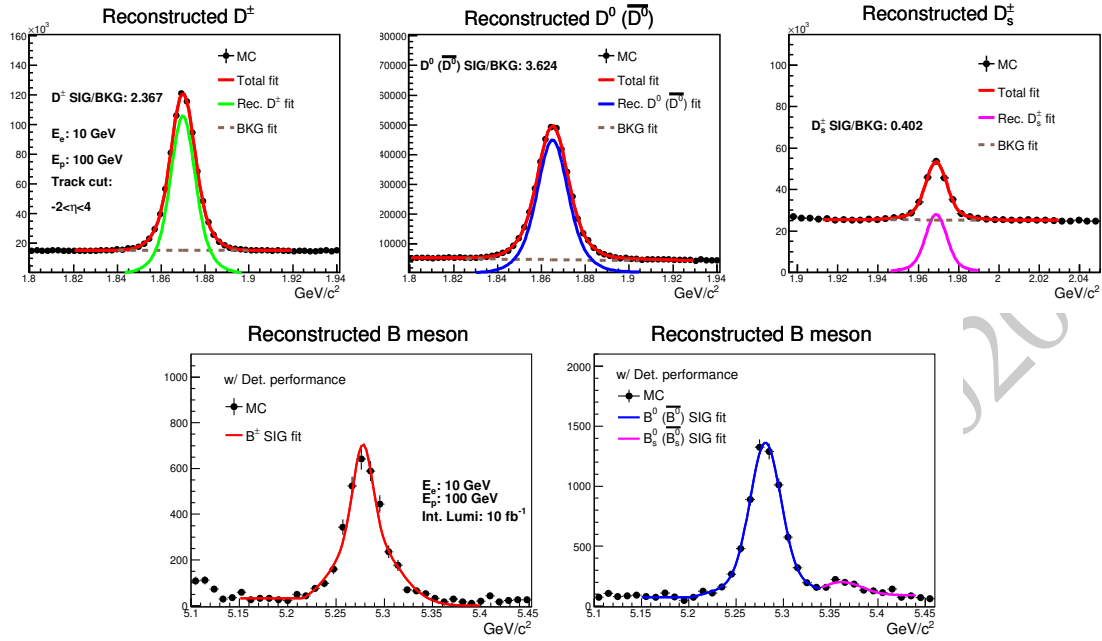


**Figure 7.99:** Reconstructed D-meson and B-meson mass spectrum using the FST with the Beast magnetic field. Pixel pitch for both barrel layers and forward planes are selected at  $20 \mu\text{m}$ . The integrated luminosity of  $e + p$  collisions at  $\sqrt{s} = 63 \text{ GeV}$  is  $10 \text{ fb}^{-1}$ .

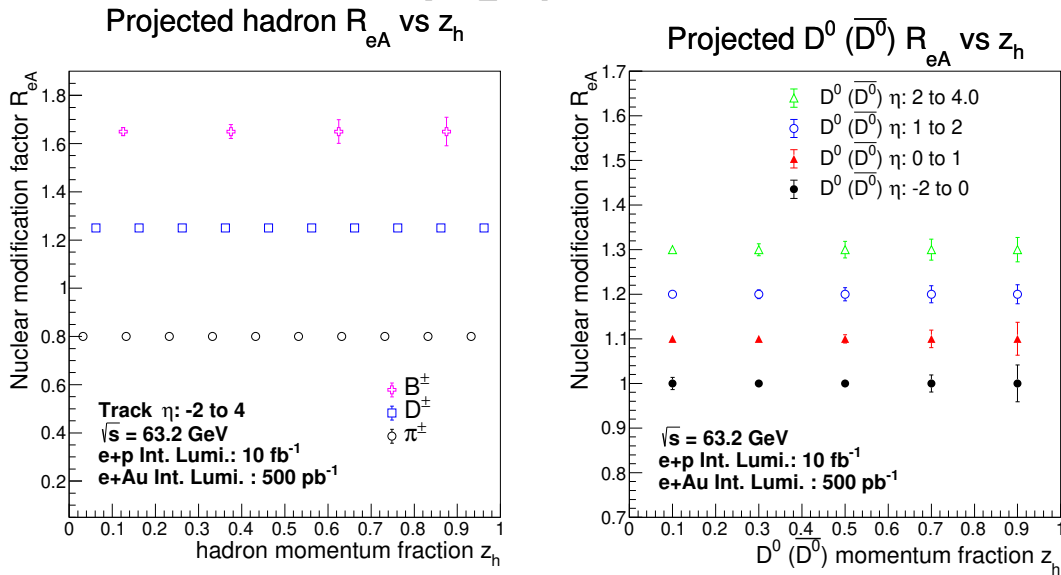


**Figure 7.100:** Projections for nuclear modification factor  $R_{eAu}$  for reconstructed flavor dependent hadron versus the hadron momentum fraction  $z_h$  (left panel).  $R_{eAu}$  projections of reconstructed  $D^0$  ( $\bar{D}^0$ ) in different pseudorapidity bins are shown in the right panel.

The nuclear modification factor  $R_{eA}$  measurements for different flavor hadrons at the future EIC will not only explore both initial and final state effects on hadron production in nuclear medium, but also provide further information on hadronization process and its flavor dependence [840]. Figure 7.100 gives the projected flavor-dependent nuclear modification factor for reconstructed flavor dependent hadron versus the hadron momentum fraction  $z_h$  with detector performance derived from the FST design. The left panel shows that precise and differential measurements can be made for different hadron flavors. Even for B-mesons the modification due to final-state interactions can be clearly identified. The left panel shows the reconstructed  $D^0(\bar{D}^0) R_{eAu}$  in different pseudorapidity intervals which is essential to understand detector requirements as a function of  $\eta$ . Extensive studies with different magnetic field options, technology options and tracker designs have been performed [712,713,841] to ensure that the physics can be delivered. It forms the basis of the reported tracking requirements.

### Heavy flavor-tagged jet substructure at the EIC

Jet substructure will also be an essential probe for studying a wide variety of QCD processes. Beyond the jet charge [688], observables such as jet shapes and jet fragmentation functions can be used to study parton propagation through a nuclear environment and could be sensitive to both fragmentation and hadronization modification in a medium. The relatively low transverse momenta of reconstructed jets will enhance the role of the heavy quark mass in measurements of jet splitting functions [842]. Even though parton multiplicities at the EIC will be low, hadronization models, such as parton recombination, can also be tested by comparing jet substructure measurements in  $e + p$  and  $e + A$  collisions. This can be extended to a variety of mesons and baryons in jets, such as heavy flavor mesons or  $\Lambda$  baryons. Studying the modification of hadronization and fragmentation with both light and heavy quark jets will further our understanding of mass dependent partonic interactions and energy loss with the medium. Techniques such as jet grooming can be used to tease out signals that are weaker than the ones observed in heavy-ion collisions.

#### 7.4.3 Particle production for identified hadron species

#### 7.4.4 Production mechanism for quarkonia and exotic states

Quarkonia,  $Q$ , are the bound states of a heavy quark and the corresponding antiquark. Due to the large mass of heavy quarks, quarkonium production entangles perturbative and non-perturbative QCD in a unique way. Quarkonium is assumed to be produced in two steps. First, the perturbative generation of a heavy quark-antiquark pair with total momentum-squared near the bound state mass-squared, then the pair hadronize into the quarkonium state non-perturbatively. Since their discovery, three main production formalisms have been proposed: i) the color evaporation model (CEM) [843, 844], ii) color singlet model (CSM) [845], and iii) the effective theory of non-relativistic-QCD (NRQCD) [846]. While all three approaches assume quarkonia are produced from the

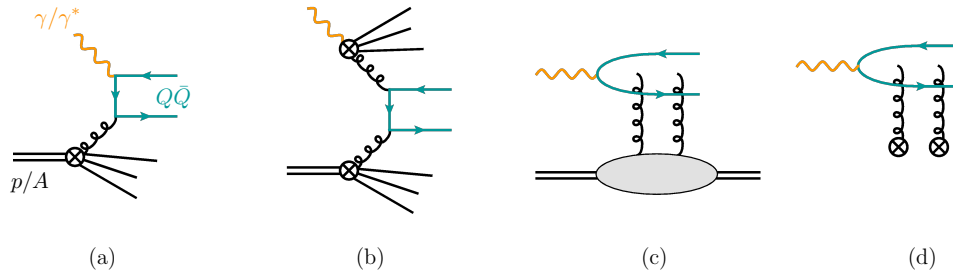


**Figure 7.101:** Illustrative examples of quarkonium production mechanism in  $ep$  and  $eA$  colliders: (a) Direct photo/lepto-production, (b) resolved-photon quarkonium production, (c) exclusive quarkonium production, and (d) heavy quark pair production and subsequent Glauber/Coulomb gluon exchanges with nuclear matter.

hadronization of heavy quark-antiquark pair, they differ on how the probability of this happening depends on other quantum numbers. In the CEM one assumes uniform probability for all other quantum numbers, where in NRQCD assumes probability that depends on the angular momentum and color configuration of the pair. In CSM the only non-zero probability is assigned to the leading color singlet combination. While all these frameworks enjoyed partial success, the theory of quarkonium production still remains an open question.

### Precision quarkonium physics at the EIC

Lepton-nucleon/nucleus collisions constitute an excellent laboratory for the studies of quarkonium production since, it is simplified and cleaner environment compared to hadronic collisions, yet far richer than in the electron-positron annihilation. Quarkonia can be produced either through photo-production ( $Q^2 \simeq 0$ ) or lepto-production ( $Q^2 > 1$  GeV) processes. In these two cases the resolved, diffractive/exclusive, and inclusive productions (see fig. 7.101( a), (b), and (c) respectively) can be relevant depending on the kinematic regimes considered. At HERA both photo-production [847–853] and lepto-production [849, 854–856] have been studied and some of variables typically used in these studies are: the inelasticity,  $z = P \cdot p_Q / P \cdot q$ , the quarkonia transverse momenta  $p_T$  and  $p_T^*$  in the laboratory and the  $\gamma/\gamma^*$ -proton c.o.m. frame respectively, as well as the rapidities  $y$  and  $y^*$ . Although the data collected at HERA had a major impact on our current view of quarkonium production, the interpretation of the these data remain a subject of debate until this day [857–860]. At the EIC the hadronization of quarkonia can be studied in both the laboratory frame and the  $\gamma/\gamma^*$ -proton c.o.m. frame and in various kinematic regimes. We thus foresee that with as high luminosities as estimated at the EIC, we could also provide multi-differential distributions, which would help establish a global picture of quarkonium hadronization.

The various production channels can be disentangled by considering different kinematic regimes, establishing this way DIS as a prime framework for the study quarkonium pro-

duction channels. While at small values of inelasticity ( $z \lesssim 0.3$ ) the resolved process dominates, at mid and large values, the direct production is paramount. At the same time, the diffractive processes are expected to be enhanced at the kinematic endpoint  $z \simeq 1$ , but drop quickly toward smaller  $z$ . The quarkonium photo-production near threshold is also related to the trace anomaly and the origin of the proton mass [117, 136, 861–863], one of the fundamental questions hoping to be answered at the EIC. At small transverse momentum,  $p_T^*$ , quarkonium production can be approached from the TMD factorization perspective and to this end there have been several studies considering both polarized and unpolarized proton beams [432, 433, 438, 864, 865]. Recent theoretical developments in NRQCD [434, 435, 860, 866–869] incorporate the leading perturbative effects from soft radiation in all orders in the strong coupling expansion—allowing us this way to safely study the non-perturbative effects, which can be accessed in the semi-inclusive process at  $z \rightarrow 1$  and/or  $p_T^* \rightarrow 0$  limits. While the  $z \rightarrow 1$  limit involves the quarkonium fragmentation shape functions, the  $p_T^* \rightarrow 0$  limit involves the recently introduced TMD shape functions. There has been no phenomenological extraction of the TMD shape functions. Meanwhile, it has been proposed that exclusive quarkonium production can be understood through the formalism of GPDs and the Wigner functions [870, 871]. Exclusive photoproduction of exotic states, such as the so-called XYZ mesons, is described in Section 7.4.6.

### Production of quarkonia and exotics at in $eA$ collisions

The EIC will also offer the opportunity to observe quarkonium production in  $eA$  collisions where one can study the interactions with nuclear matter and the formation of quarkonia in a nuclear medium. The study of nuclear effects in quarkonium production is an emerging field of nuclear physics where EIC measurements are expected to play a major role in our understanding of these effects. Most of the recent field-theoretic developments rely on the effective theory of NRQCD. In a recent formulation of NRQCD [872, 873] the Glauber/Coulomb gluon interactions with heavy quarks—Fig. 7.101 (d)—in the non-relativistic limit, are incorporated into the effective theory providing this way a systematic and formal approach to the inclusion of nuclear effects on quarkonium propagation [440, 874]. A similar approach has been applied successfully to the propagation of jets through nuclear medium [875, 876]. In a different direction, recently the formalism of open quantum systems has been gaining a significant attention [877–881]. Although primarily formulated in the context of quark-gluon plasma, these formalisms can also be applied to cold nuclear matter effects.

Quarkonia produced in  $eA$  collisions at the EIC will hadronize inside the nucleus. As the heavy  $Q\bar{Q}$  pairs propagate through cold nuclear matter, they will be subject to disruption via interactions with partons inside the nucleus, which can lead to suppression with respect to  $ep$  collisions. These effects are distinctly different from those measured in  $pA$  collisions at RHIC and the LHC, since at those colliders the crossing time is shorter than the charmonium formation time. Charmonium production inside the nucleus has been previously studied in fixed-target  $pA$  collisions, where the crossing time is sufficiently long that hadronization also occurs inside the nucleus. These measurements showed that the relatively weakly bound  $\psi(2S)$  is suppressed more than the  $J/\psi(1S)$  state [882, 883]. This

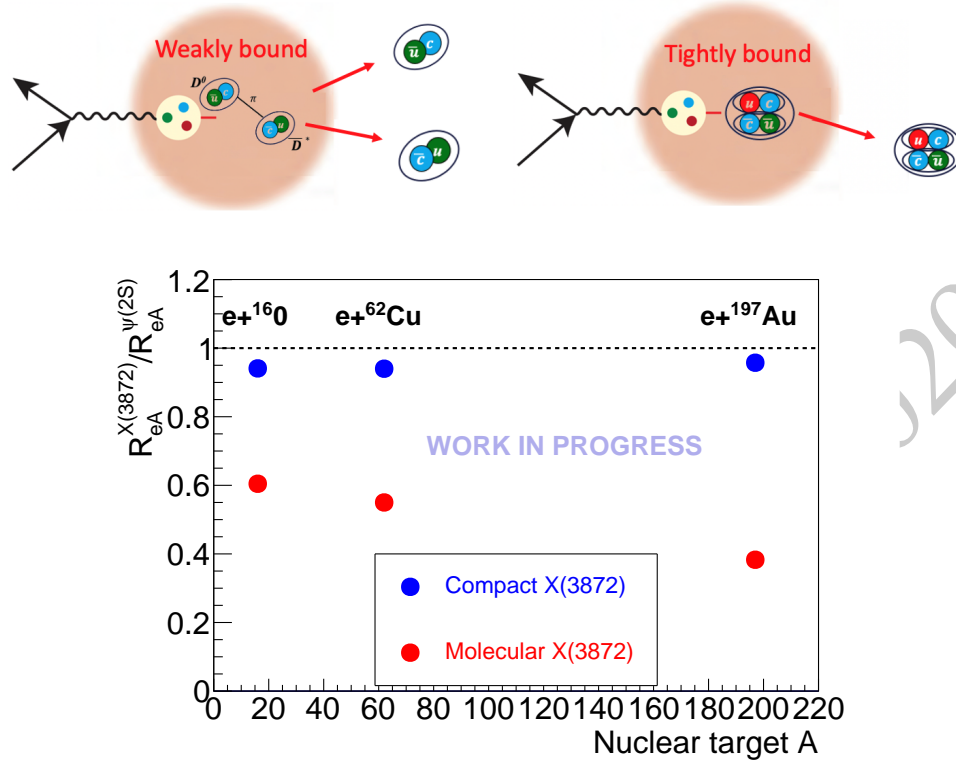


**Figure 7.102:** Top panel: illustration of weakly and tightly bound tetraquark state propagation in a large nucleus. Bottom panel: the ratio of nuclear modification factors  $R_{eA}$  for  $X(3872)$  to  $\psi(2S)$ , for two different assumptions of the  $X(3872)$  structure.

is understood phenomenologically in terms of the size of the state: weakly bound charmonia with a larger radius will effectively sample a larger volume of the nucleus as they propagate outwards, and therefore have a higher probability of interacting and being disrupted [884]. The low backgrounds at the EIC will allow these models to be tested on higher charmonium states which are difficult to reconstruct in hadron-hadron colliders.

These effects can also be used to discriminate between models of exotic hadron structure. Multiple candidates for tetra- and pentaquark states have been identified, such as the  $X(3872)$  and the  $P_c^+$  states, but there is no consensus on whether these states are hadronic molecules or compact multi-quark states [885]. Embedding these resonances in the nuclear medium provides a new environment to study their properties. From the previous experience with conventional charmonium states, one would expect that large, weakly bound hadronic molecules would undergo significantly more disruption which traversing the nucleus than a compact state, as shown in Fig. 7.102.

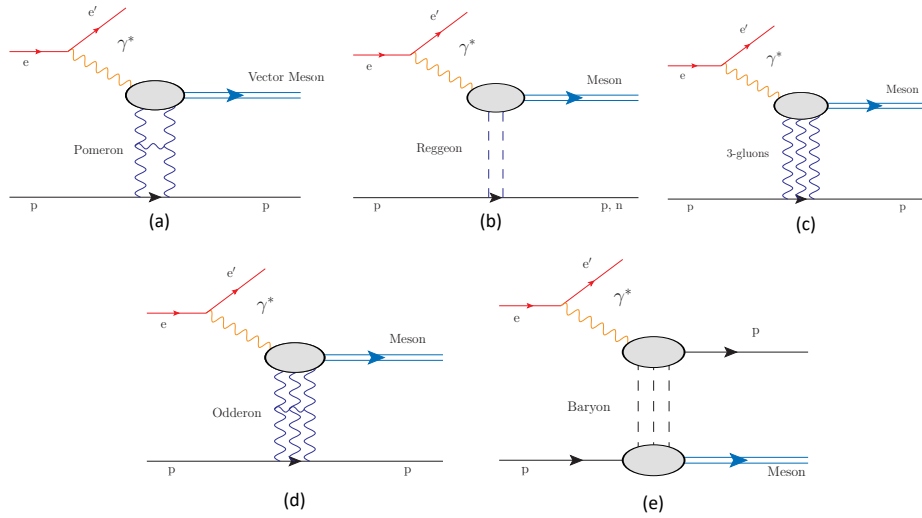


**Figure 7.103:** The exclusive photoproduction mechanisms discussed in this section. They include (a) Pomeron exchange, (b) Reggeon exchange, (c) 3-gluon exchange, (d) Odderon exchange and (e) baryon exchange.

### 7.4.5 New particle production mechanisms

Exclusive vector meson production is usually modelled as occurring via the exchange of a Reggeized particle, either a Pomeron or a Reggeon. Pomeron and Reggeon exchange models have provided excellent fits to a wide range of fixed target and HERA data [886]. However, other types of exchange are possible; this section will explore some of the possibilities, which are shown in Fig. 7.103.

Pomeron exchange represents the absorptive part of the cross-section, so the Pomeron has the same quantum numbers as the vacuum,  $J^{PC} = 0^{++}$ . This naturally explains why vector mesons are predominantly produced; the final state has the same quantum numbers as the incident photon. In pQCD Pomerons can be treated as a gluonic ladder built on two gluon exchange, and obeying the BFKL evolution equations [223, 224]. Almost uniquely, the cross-section for Pomeron-mediated reactions rises slowly with increasing energy.

Reggeons normally represent summed meson trajectories (baryon trajectories will be discussed below), so carry a wider range of quantum numbers, including charge. So, they can lead to a wide range of final states; this makes photon-Reggeon fusion an attractive venue for meson spectroscopy. The cross-section for Reggeon-mediated reactions drops with increasing energy, so these reactions are best studied at energies that are not too high.

This section will explore alternate exchange mechanisms for particle production, involving the Odderon (the three-gluon analog of the Pomeron) and backward production involving baryon trajectories. It will also consider some unique facets of near-threshold production.

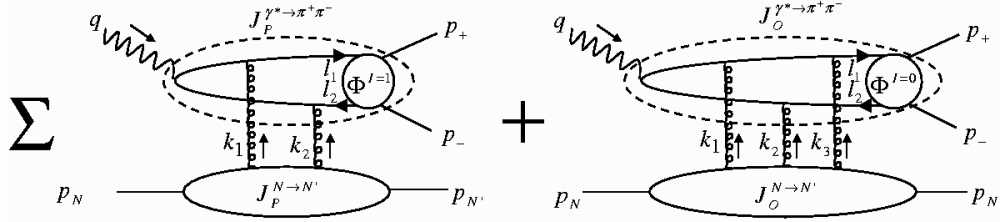


**Figure 7.104:**  $\pi^+\pi^-$  pairs may be diffractively produced through Pomeron and Odderon exchange. The interference of the two amplitudes leads to a characteristic signature of a charge asymmetric observable.

### Odderon exchange

Hadronic reactions at low momentum transfer and high energies for charge-odd exchange are described in Regge language in terms of Odderon exchange, Fig. 7.103(d), which is in QCD and at Born level a three gluon color singlet. Although mandatory to explain the difference between  $pp$  and  $\bar{p}p$  scattering, and a natural object in QCD, its properties remain quite elusive. Exclusive  $\pi^0$  electroproduction data at HERA indicate a small magnitude of the Odderon - exchange cross-section. At an EIC, the Odderon might manifest itself via the production of the  $f_2(1270)$  via photon-Odderon fusion (the same state may also be produced in two-photon interactions).

The study of observables where Odderon effects are present at the amplitude level is thus mandatory to get sensitivity to a rather small normalization of this contribution. One such observable involves charge asymmetries in open charm production [887] or two-pion electroproduction with the exchange of a soft Odderon [888, 889] (shown in Fig. 7.104) or a hard Odderon [890, 891]. In this latter process

$$eN \rightarrow e\pi^+\pi^-N \quad (7.55)$$

at large energy, large  $Q^2$ , modest pion pair invariant mass  $M_{\pi\pi}^2 = O(1\text{GeV}^2)$  and large rapidity gap between the pion pair and the final nucleon, one may factorize the Pomeron-Odderon proton impact factor from a perturbatively calculable hard subprocess where the  $\pi^+\pi^-$  pair is described by a generalized distribution amplitude (GDA) [892–894]. The interference of the C-even and C-odd amplitudes leads to measurable charge asymmetries with a characteristic  $M_{\pi\pi}$  dependence, with a magnitude large enough to be detected if the relative strength of the Odderon to Pomeron couplings is not unexpectedly small.

### Exclusive backward ( $u$ -channel) production

In usual Reggeon exchange events, the cross-section is largest at small  $|t|$ , with, usually  $d\sigma/dt \propto \exp(-b|t|)$ , where  $b$  is related to the square of the transverse interaction radius. In the 1970s fixed-target experiments made a surprising discovery that, at very large  $|t|$ , there is an increase in cross-section near the maximum possible  $|t|$ , corresponding to the region

of small  $u$ , as is shown in the lower-left part of Fig. 7.105. This is known as backward production, because, in the center of mass frame, the produce meson recoils, while the struck nucleon recoils. In very high energy collisions, such as at the EIC, the produced meson will have a rapidity near that of the incident ion beam, while the final state nucleon will be more central.

This can be easily accommodated in a Reggeon framework by allowing the exchange of baryon number, *i. e.* baryon trajectories. This effectively swaps  $u$  and  $t$ , and may explain the photoproduction data on backward production. A comprehensive review article on the Regge model and its success in describing photoproduction of mesons can be found in Ref. [895].

In this paradigm, it is relatively easy to extrapolate fixed-target data on backward photoproduction upward to EIC energies. This is easiest for the  $\omega$  meson, for which there is data at enough different photon energies to be able to fit for the energy dependence. The photon-Reggeon component for  $\omega$  production (with the photon-Pomeron contribution removed) can be parameterized as [741,886]:

$$\frac{d\sigma}{dt} = A(s/1\text{GeV})^B \exp(-Ct) \quad (7.56)$$

where  $A \approx 18 \mu\text{b}/\text{GeV}^2$  and  $B = -1.92$  for the  $\omega$  and, from HERA data [896]  $C \approx 10 \text{ GeV}^{-2}$ . In contrast, the backward-production data can be parametrized [897]:

$$\frac{d\sigma}{du} = A(s/1\text{GeV})^B \exp(-Cu) \quad (7.57)$$

where  $A \approx 4.4 \mu\text{b}/\text{GeV}^2$ ,  $B = -2.7$  and  $C = -21 \text{ GeV}^{-2}$ . Compared to forward photoproduction by Regge exchange, this formula has a constant about four times smaller, a faster drop-off with energy, and a somewhat larger  $C$ . The  $C$  values may not be directly comparable, because the fixed-target backward-production experiments were at much lower photon energies, so  $t_{\min}$  was much larger; this could have led to a larger  $C$  than would be seen at larger beam energies.

The relative  $A$ ,  $B$  and  $C$  all lead to smaller backward:forward cross-section ratios at EIC energies. However, the cross-sections are large enough for backward production to be easily observable.

The final state consists of a proton at mid-rapidity, and an  $\omega$  that is typically near the beam rapidity. The decay  $\omega \rightarrow \pi^0\gamma$  could be studied with far-forward calorimetry. At lower proton beam energies, the  $\omega$  moves further away from the beam, so may be easier to detect. More importantly, if one choose interactions where the proton is produced closer to the incident hadron direction, the  $\omega$  is shifted further from the beam. In all cases, backward production studies require good far-forward instrumentation.

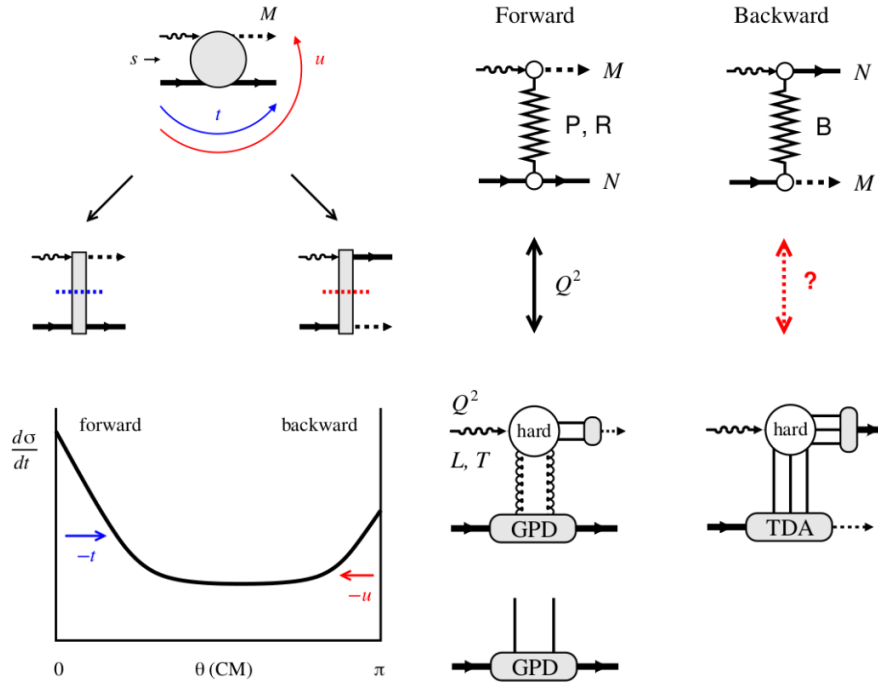


**Figure 7.105:** (left) Soft-hard-soft structure transition. (right) Forward-backward Factorization scheme.

### $u$ -Channel Exclusive Meson Electroproduction

Exclusive electroproduction of mesons from the photoproduction to a large  $Q^2$  above the resonance region, is another good handle to study the Regge exchange reactions. The pioneer experimental and phenomenological effort from JLab [898,899] raise further questions: what are forward-backward cross section ratios in other  $u$ -channel electroproduction interactions such as  $\pi^0, \pi^\pm, \rho, \eta, \eta'$  and  $\phi$ ? Could the  $t$ -channel phenomenology recipe for mapping out the  $W$  and  $x$  dependence, be applied to the  $u$ -channel interactions? How would the  $u$ -channel interactions factorize? These important questions form the core bases for the future studies.

The large acceptance, wide kinematics (in  $Q^2$  and  $W$ ) and forward tagging capability at the EIC provide a great opportunity to study the near-forward and near-backward electroproduction of all mesons simultaneously.

Combining the data collected at JLab 12 GeV and EIC, we aim to accomplish the following objectives to unveil the complete physics meaning of  $u$ -channel interactions:

- At low  $Q^2$  limit:  $Q^2 < 2 \text{ GeV}^2$ , mapping out the  $W$  dependence for electroproduction of all mesons at near-backward kinematics.
- Extracting the  $u$ -dependence ( $\sigma \propto e^{-b \cdot u}$ ) as a function of  $Q^2$ . This could be used to

study the transition from a “soft” Regge-exchange type picture (transverse size of interaction is of order of the hadronic size) to the “hard” QCD regime.

- Studying the model effectiveness between the hadronic Regge based (exchanges of mesons and baryons) and the partonic description through Transition Distribution Amplitudes (exchanges of quarks and gluons), is equivalent to studying the non-perturbative to perturbative QCD transition.

### Three-gluon exchange and near-threshold production

Near threshold, other production mechanisms may visibly contribute. One involves three-gluon exchange, as in Fig. 7.103(c) It is also possible for a target to exchange three gluons with a targets. This mechanism was predicted quite some time ago. It is expected to be subdominant at high energies, but might be visible near threshold. The GlueX experiment at JLab has studied  $J/\psi$  production in near the energy threshold, and found that the cross-section was above that expected in a two-gluon exchange model, but consistent with the sum of two-gluon plus three-gluon exchange [139]. GlueX also searched for narrow peaks in the  $J/\psi p$  cross-section with increasing photon energy, and found none. From this, they set limits on pentaquark production, eliminating some (not all) pentaquark models.

Near-threshold production of heavy quarkonia is sensitive to the quarkonium-nucleon potential [900]. The quarkonium may be treated as a dipole, with length inversely proportional to mass. The potential is itself sensitive to the internal structure of the nucleon target. The potential is often quantified in terms of the meson-nucleon scattering length. This scattering length should decrease with increasing vector meson mass, if, as expected, the potential decreases for small dipoles.

Unfortunately, JLab does not have the energy reach to explore the  $\psi'$  or  $Y$  states, so this should be new territory for the EIC. The EIC will be able to study electroproduction in addition to photoproduction. The threshold region involves relatively low-energy, so good detector acceptance in the hadron-going direction is required to study it.

### 7.4.6 Spectroscopy

Considerable progress in hadron spectroscopy has been made in recent years through many unexpected observations in the heavy quark sector including the proliferation of so-called XYZ states, charmed pentaquark  $P_c$  candidates and more (see reviews Ref. [885, 901–903]). Relatively early in the XYZ discoveries in  $e^+e^-$  colliders and  $b$ -hadron decays it was recognized that they could be studied in alternative processes, such as photoproduction, with many calculations for individual reactions over the years, for example Refs. [904–907]. Photoproduction can also be used to study conventional mesons as well as exotica [907].

Fixed target experiments using the Jefferson Lab 12 GeV electron beam, such as GlueX [908] or CLAS12 [909], provide access to the light-quark regime and  $s$ -channel pro-

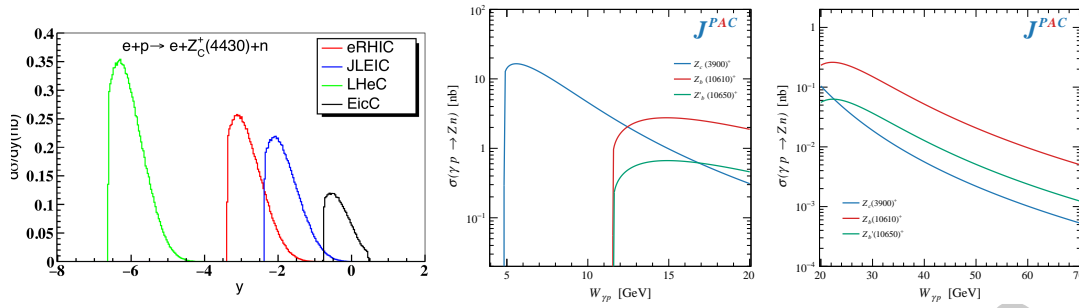


**Figure 7.106:**  $Z^+$  photoproduction rapidity distributions from [907] and integrated cross section predictions [915] for fixed-spin exchange, valid at low energies (center), and for Regge exchange, valid at high energies (right).

duction of  $P_c$  states discovered by LHCb [139], however they do not have sufficient energies to produce  $XYZ$  states *via*  $t$ -channel exchange. Previous measurements in  $ep$  collisions at HERA, however, have demonstrated the ability to study heavy quarkonia through photoproduction, particularly the well known vector  $c\bar{c}$  and  $b\bar{b}$  states [721, 910–912]. The COMPASS collaboration has studied muonproduction of the  $J/\psi\pi^+\pi^-p$  final state finding an indication of a new state  $\tilde{X}(3872)$  [913] and also set limits on  $Z_c$  photoproduction in the  $J/\psi\pi^+n$  final state [914]. The integrated luminosities expected for the EIC, provide the opportunity to study rare exclusive processes not accessible at HERA.

Photoproduction through photon-Pomeron fusion lead predominantly to  $J^{PC} = 1^{--}$  states like the  $J/\psi$ , etc., so is only sensitive to exotic with those quantum numbers. Photon-Reggeon fusion leads to states with a wider range of spin, parity and even charge, so can be used to search for a much wider range of both conventional mesons and exotica. Since the photon-Reggeon fusion cross-sections are typically peaked at low photon-nucleon center of mass energies (a few times the threshold energy) (Fig. 7.106 center-right) these reaction products are typically produced in the forward direction, requiring good detector acceptance in that region. The left panel of Fig. 7.106 shows the predictions for a typical exotica model, where the  $Z_c^+$  is a spin-1 tetraquark candidate. The different curves correspond to different EIC models, with the eRHIC curves very close to the current design. It can be seen that lower-energy collisions (JLEIC or EicC) lead to more central production; lower beam energies may be beneficial for studying exotica.

Recent predictions from the JPAC Collaboration [915] provide a comprehensive assessment of the exclusive cross sections for several  $XYZ$  states. Figure 7.106 shows the predicted photoproduction cross section as a function of the center-of-mass energy for three  $Z$  states:  $Z_c(3900)^+$ ,  $Z_b(10610)^+$  and  $Z_c(10610)^+$  all previously observed in produced in  $e^+e^-$  collisions. In the low energy region near threshold (left) fixed-spin charge exchange is expected to provide a valid description, while high energies are described by Regge exchange. With expected cross sections at the  $\sim 1$ -10 nb level the statistics available for some of these reactions are comparable to current measurements of similar states in  $e^+e^-$  machines and heavy flavor decays. More details on the simulation and detector requirements

are provide in Sec. 8.2.6<sup>5</sup>

### 7.4.7 Target Fragmentation

Target fragmentation in  $ep/eA$  DIS (hadron production in the target rapidity region) offers new ways of exploring hadronization dynamics and nucleon structure in QCD. The QCD factorization theorem for single-inclusive hadron production  $e + p \rightarrow e' + X + h(x_F, p_T)$  permits separation of hard and soft contributions, including QCD radiation, and enables a description of target fragmentation in close analogy to the total DIS cross section [212, 214]. The fracture functions (or conditional PDFs) depend on  $x$  and  $Q^2$  as well as on the hadronic variables  $x_F$  and  $p_T$  and combine aspects of parton distribution and fragmentation functions. They obey standard DGLAP evolution and are independent of the hard process (universal). Physically, the fracture functions describe the hadronization of the target after removal of a parton (quark, gluon) with given  $x$  at the scale  $Q^2$ . As such they contain rich information about hadronization dynamics (confinement, chiral vacuum structure) and nucleon structure (multiparton correlations).

Present experimental knowledge of target fragmentation in DIS is very limited; see [916–922] for fixed-target results. The HERA experiments measured  $p$  production in the diffractive peak  $x_F \approx 1$ , and  $p$  and  $n$  production in the region  $x_F \gtrsim 0.3$  [102, 923–926]. The results indicate strong baryon number flow in DIS at small  $x$  (up to 50% is moved to  $x_F < 0.3$ ), which raises interesting questions about multiparton dynamics that cannot be answered with the HERA data alone.

EIC could transform the knowledge of target fragmentation and open this area up to systematic study [927]. Measurements should focus on the following features connected with specific questions of dynamics and structure:

(a) *x-dependence of target fragmentation*: Theoretical arguments predict qualitative changes of the  $x_F$  distributions of  $p$  and  $n$  depending on the  $x$  of the removed parton:  $\propto (1 - x_F)$  at  $x > 0.2$ ; constant in  $x_F$  at  $x \sim 0.2$ ;  $\propto 1/x_F$  at  $x \ll 0.1$  [928]. Observing these changes would provide direct evidence of the nucleon's multiparton structure and enable quantitative understanding.

(b) *Spin dependence and polarization transfer*: Polarized  $ep$  DIS removes a parton with definite spin from the nucleon wave function. Measuring the spin dependence of the  $x_F$  distributions in target fragmentation provides insight into the role of spin-dependent forces in fragmentation, a major open question with broad implications (string fragmentation, chiral vacuum structure, spin-orbit effects). Fragmentation into self-analyzing  $\Lambda$  baryons [929] or use of the Collins variable [350] would allow one to study the polarization transfer to the produced system.

(c) *Quark vs. gluon fracture functions*: Another interesting question is how the hadronization process changes depending on whether a quark or gluon is removed from the nu-

<sup>5</sup>The relative normalization of the signal and PYTHIA background requires further study and validation of the current XYZ models with data from light mesons may provide some important benchmarks.

cleon wave function. This could be studied by measuring target fragmentation induced by quark- or gluon-sensitive hard processes (e.g. heavy flavor production). At  $x \ll 0.1$ , this comparison will probe the multiparton structure of configurations building up small- $x$  parton densities. At  $x > 0.1$ , it will reveal the coupling of large- $x$  gluons to valence quarks (e.g., if the leading Fock component in the nucleon dominates, gluon fracture functions should be strongly suppressed).

(d) *Correlations of target and current fragmentation:* Measurements of hadron correlations between the current and target fragmentation regions could directly probe the multiparton structure of the nucleon. Correlations between sea quarks are induced by the short-range non-perturbative forces causing the dynamical breaking of chiral symmetry – the phenomenon responsible for hadron mass generation in QCD; these correlations could be revealed in back-to-back pion correlations with  $p_T \approx 0.5$  GeV and moderate rapidity separations  $\Delta\eta \approx 4$  [930]. Generally, such measurements could elucidate the dynamical origin of intrinsic transverse momentum in the nucleon.

The target fragmentation measurements described here could largely be performed with the baseline EIC detector design. An important requirement is continuous coverage in  $x_F$  from  $\sim 1$  down to  $\sim 0.1$ , without gaps between the central ( $\eta < 4$ ) and forward detectors. Fig. 7.107 shows the detector coverage in terms of the target fragmentation variable  $x_F$  at various  $x$ ,  $Q^2$  and beam energies. Simulations are in progress.

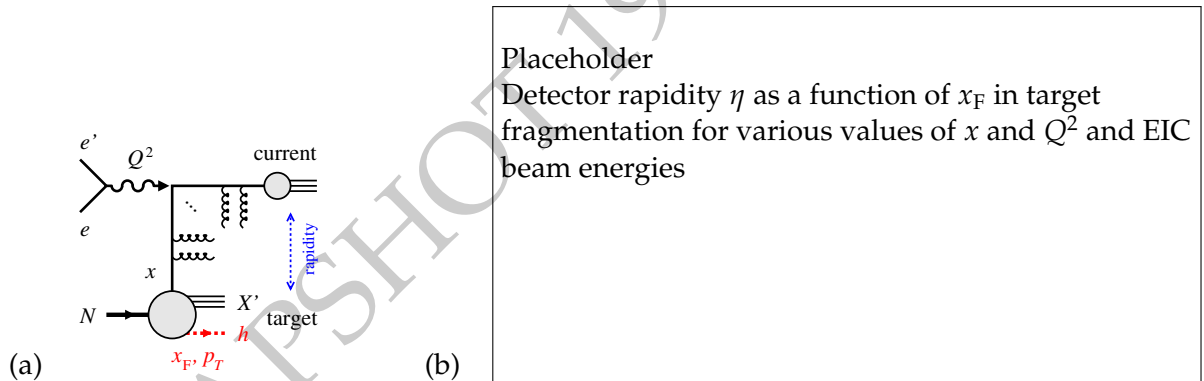


**Figure 7.107:** (a) QCD factorization of target fragmentation in DIS. (b) Detector rapidity ranges covered in target fragmentation measurements at EIC at various values of  $x$  and  $Q^2$ .

## 7.5 Connections with Other Fields

While the principal focus of the physics program at the EIC is QCD there are nevertheless important and unique points of contact with other fields. This is mainly due to the high luminosity, the availability of polarized lepton and hadron beams, and the wide kinematic coverage of the EIC. Section 7.5.1 presents the main opportunities for **electroweak (EW)** and **beyond the standard model (BSM)** physics. Precision measurements at the EIC can provide new limits on various BSM couplings. For example, a polarized positron beam would provide access to the parity-conserving but lepton charge-conjugation-violating couplings  $C_{3q}$  via a measurement of the charge conjugation asymmetry of cross sections of polarized leptons and anti-leptons scattering off a nuclear target. Precision measurements of the  $C_{iq}$  couplings at the EIC over a wide range of  $Q^2$  can also test the running of Weinberg's weak mixing angle. Furthermore, the availability of polarized electron or positron beams with proton or deuteron targets, over a wide range of kinematics, can scrutinize lepton flavor violation mechanisms in the charged lepton sector. The high energy and luminosity at the EIC in principle offers opportunities for new particle searches such as a heavy photon or a heavy neutral lepton. The ability to polarize both electron and proton beams at an EIC may lead to much stronger constraints on heavy new physics operators in the standard model effective field theory (SMEFT) than exist today.

There is considerable overlap between the EIC science program and **neutrino physics**, as outlined in some detail in Sec. 7.5.2. In fact, those two research areas are of mutual benefit. Measurements at the EIC could provide important input for future experiments in neutrino physics, such as a more accurate estimate of nuclear effects. In return, neutrino scattering can help to better understand the parton structure of both nucleons and nuclei, where the nucleon strangeness content is one example.

Measurements at the EIC are also expected to deliver important input for several areas of astro-particle physics. Fields such as **cosmic-ray air showers and neutrino astrophysics** will benefit from better constrained models of hadronic interactions, see discussion in sec. 7.5.3.

Deeply-inelastic scattering and photo-nuclear processes of course have close ties with the physics of hadronic collisions. Sec. 7.5.4 focuses on a few particular aspects which have not been addressed in other parts of this YR. These relate to the issue of **small- $x$  gluons and factorization** in DIS vs.  $p+p$  and  $p+A$ , to the implications of the determination of PDFs for  $p+p$  and  $p+A$  collisions, to **initial conditions for hydrodynamics** of heavy-ion collisions, and to **parton interactions in nuclear matter**.

### 7.5.1 Electro-weak and BSM physics

#### Introduction

The high luminosity, polarized lepton and hadron beams, variety of nuclear targets, and wide kinematic range at the EIC open the door to searches that go beyond the typical

nuclear physics “boundaries”. While the electroweak interaction, through charged current interactions, can be used as a clean probe to separate quark flavors [931], it can also be used to access new observables such as  $\gamma - Z$  interference structure functions [932] through neutral current interactions. Further details on spin structure observables can be found in section 7.1.2. This section will explore the how the EIC will contribute to searches of physics Beyond the Standard Model and where possible will compare to the expected reach of other experimental efforts.

### Weak Neutral Current Measurements

For electron-hadron scattering, in the region where the virtuality of the exchanged boson satisfies  $Q^2 \ll M_Z^2$ , the weak neutral current can be parameterized in terms of contact interactions

$$\mathcal{L} = \frac{G_F}{\sqrt{2}} \sum_{\ell, q} \left[ C_{1q} \bar{\ell} \gamma^\mu \gamma_5 \ell \bar{q} \gamma_\mu q + C_{2q} \bar{\ell} \gamma^\mu \ell \bar{q} \gamma_\mu \gamma_5 q + C_{3q} \bar{\ell} \gamma^\mu \gamma_5 \ell \bar{q} \gamma_\mu \gamma_5 q \right], \quad (7.58)$$

where the  $C_{iq}$  are perturbatively calculable coefficients that depend on the weak mixing angle,  $\theta_W$ . A comparison of the experimentally extracted values of the  $C_{iq}$  couplings with the SM predictions can be used to set limits of the scale  $\Lambda$  at which new interactions may arise. At low energies, well below the scale  $\Lambda$ , these new interactions can be parametrized by the effective Lagrangian:

$$\begin{aligned} \delta \mathcal{L} = & \frac{g^2}{\Lambda^2} \sum_{\ell, q} \left\{ \eta_{LL}^{\ell q} \bar{\ell}_L \gamma_\mu \ell_L \bar{q}_L \gamma_\mu q_L + \eta_{LR}^{\ell q} \bar{\ell}_L \gamma_\mu \ell_L \bar{q}_R \gamma_\mu q_R \right. \\ & \left. + \eta_{RL}^{\ell q} \bar{\ell}_R \gamma_\mu \ell_R \bar{q}_L \gamma_\mu q_L + \eta_{RR}^{\ell q} \bar{\ell}_R \gamma_\mu \ell_R \bar{q}_R \gamma_\mu q_R \right\}, \quad (7.59) \end{aligned}$$

where the mass limit for  $\Lambda$  is defined with the convention  $g^2 = 4\pi$ . The coefficients  $\eta_{ij}^{\ell q}$  take on the values of +1, 0, or -1, allowing for the possibility of constructive or destructive interference with the SM contributions. The  $C_{iq}$  coefficients can now be written as  $C_{iq} = C_{iq}(\text{SM}) + \Delta C_{iq}$ , corresponding to the sum of the SM and new physics contributions. For example, the new physics contribution to the  $C_{2q}$  couplings takes the form  $\Delta C_{2q} = [g^2 / (2\sqrt{2}G_F\Lambda^2)] (\eta_{LL}^{\ell q} - \eta_{LR}^{\ell q} + \eta_{RL}^{\ell q} - \eta_{RR}^{\ell q})$ , depending on a specific combination of chiral structures. Similar expressions can be obtained for the  $C_{1q}$  and  $C_{3q}$  couplings. A new physics scenario with chiral structure  $\eta_{LL}^{\ell q} = 1$  and  $\eta_{RR}^{\ell q} = \eta_{RL}^{\ell q} = \eta_{LR}^{\ell q} = 0$ , results in a specific pattern of shifts  $\Delta C_{1q} = \Delta C_{2q} = -\Delta C_{3q} = g^2 / (2\sqrt{2}\Lambda^2 G_F)$  relative to the SM values which can be used to set limits on  $\Lambda$ .

Different flavor combinations of the  $C_{1q}$  coefficients have best been measured through atomic parity violation [933] and elastic parity violating electron scattering [934]. The  $C_{2q}$  couplings are more challenging due to their relatively small values in the SM. They can be accessed through parity violating deep inelastic scattering on a deuteron target by

measuring the cross section asymmetry between left-handed and right-handed electrons

$$A_{PV}^e = \frac{d\sigma_L - d\sigma_R}{d\sigma_L + d\sigma_R}. \quad (7.60)$$

Recently [935] at JLAB, 6 GeV polarized electrons incident on a unpolarized deuteron target were used to extract the combination  $2C_{2u} - C_{2d} = -0.145 \pm 0.068$  at  $Q^2 = 0$ , showing for the first time that this combination is non-zero at the 95% confidence level. The SoLID [936] spectrometer as part of the JLAB 12 GeV program is expected to further improve the precision of this measurement. The EIC can provide further improvement due to its high luminosity and wide kinematic range, allowing for enhanced sensitivity to the combination  $2C_{2u} - C_{2d}$  over a wide range of  $Q^2$ .

On the other hand, experimental data on the  $C_{3q}$  couplings are quite sparse. They are parity-conserving but charge-conjugation-violating (charge conjugation of the lepton charge). The availability of a polarized positron beam will provide a unique opportunity to access these couplings via a measurement of the charge conjugation asymmetry [937, 938]:

$$A^{e_L^- - e_R^+} = \frac{d\sigma(e_L^- N) - d\sigma(e_R^+ N)}{d\sigma(e_L^- N) + d\sigma(e_R^+ N)}, \quad (7.61)$$

through a comparison of cross sections of polarized leptons and anti-leptons scattering off a nuclear target. Such a measurement has been carried out only once before at CERN [939], using polarized muon and anti-muon beams scattering off a Carbon target, resulting in the extraction  $0.81(2C_{2u} - C_{2d}) + 2C_{3u} - C_{3d} = 1.53 \pm 0.45$ . Using the current experimental value [935] of  $2C_{2u} - C_{2d}$ , yields the result  $2C_{3u} - C_{3d} = 1.65 \pm 0.453$ . A polarized positron beam at the EIC can improve upon this measurement [940]. The isoscalar deuteron nuclear target is preferred over the proton target since it provides access to the combination  $2C_{3u} - C_{3d}$  and minimizes the uncertainty from the d/u ratio of parton distribution functions. However, both the proton and deuteron targets can be used in order in a complementary manner to extract the  $C_{3q}$  couplings.

The importance of precision measurements at the EIC of the  $C_{iq}$  couplings is well illustrated by BSM scenarios that involve heavy Leptophobic  $Z'$ -bosons [941, 942]. Since they couple very weakly to leptons, their primary signature at hadron colliders corresponds to dijets with invariant mass,  $m_{j_1 j_2} \sim M_{Z'}$ . The large dijet background at hadron colliders makes it difficult to constrain such a scenario. However, at the EIC, the existence of a Leptophobic  $Z'$ -boson could introduce a deviation from the SM values in the  $C_{2q}$  couplings without affecting the  $C_{1q}$  couplings. This occurs via a vacuum polarization quark loop that connects a photon vector coupling to the electron current and the  $Z'$  axial-vector coupling to the quark current, leading to a shift only in the  $C_{2q}$  couplings.

Precision measurements of the  $C_{iq}$  couplings at the EIC for a wide range of  $Q^2$  values can also test the running [932] of  $\sin^2 \theta(\mu)$  in the previously unexplored range of 10 GeV  $\mu < 70$  GeV. We denote the  $\overline{MS}$ -scheme value by  $\sin^2 \theta_W(\mu)_{\overline{MS}}$ . Note that in the region  $Q^2 < M_Z^2$ , close to the Z-pole, the effective contact interaction parameterization in Eq. (7.58) is no longer applicable and the full  $Q^2$  dependence in the Z-boson propagator must be included

for a proper interpretation of tests of the running of the weak mixing angle. It is useful to define an effective running weak mixing angle effective [943–947] by  $\sin^2 \theta_W(Q^2) = \kappa(Q^2) \sin^2 \theta_W(m_Z)_{\overline{MS}}$ , where  $\kappa(Q^2)$  incorporates  $\gamma - Z$  vacuum polarization mixing and other universal corrections that appear in the low energy parity-violating observables.

The parity violating electron scattering asymmetry in Eq. (7.60), for the extraction of the weak mixing angle  $\sin^2 \theta_W(Q^2)$  below the Z-pole, is typically seriously considered only for the isoscalar deuteron target where structure function effects largely cancel at leading twist facilitating improved precision and sensitivity to the weak mixing angle. However, the high precision of the PDF data obtained by the EIC may also allow for extractions to be made using a proton target. Fig. 7.108 shows the impact of the observable  $A_{PV}^e$  on  $\sin^2 \theta_W(Q^2)$ , assuming a proton and deuteron target with  $100 \text{ fb}^{-1}$  and  $10 \text{ fb}^{-1}$  luminosity respectively and an uncorrelated systematic uncertainty of 1% from the pion background (for statistics details as a function of Bjorken- $x$  see left part of figure 7.7). Within the JAM MC framework, the normalization of  $\sin^2 \theta_W(Q^2)$  along with the spin-averaged PDFs were simultaneously fit to obtain the result. The functional form of  $\sin^2 \theta_W(Q^2)$  was fixed in this study and the anticipated EIC statistics were used only to constrain the overall normalization. The band in Fig. 7.108 shows the overall constraint using all the parity violating asymmetry data one expects from the EIC. The EIC will span a wide intermediate kinematic region where very little data exist and provide significant constraints on this fundamental parameter of the Standard Model.

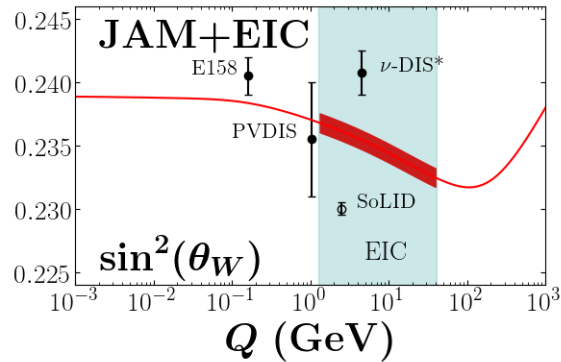


**Figure 7.108:** Impact of entire electron proton and electron deuteron EIC data on  $\sin^2(\theta_W)$ . The red band shows the overall constraint from all the data over the accessible  $x, Q^2$  range (highlighted in gray) at the EIC. For SoLID, only the error bars are shown. For  $\nu$ -DIS the error bars are underestimated.

Such precision tests of the  $Q^2$ -dependence of  $\sin^2 \theta_W(Q^2)$  at the EIC, can also be an effective probe of physics associated with new light degrees freedom that cannot be parameterized as contact interactions. One such scenario, dark parity violation [948, 949], arises through a light dark boson  $Z_d$  corresponding to a spontaneously broken  $U(1)_d$  gauge symmetry in the dark sector. The dark-Z boson is a generalization of the standard dark photon which only couples to the electromagnetic current by mixing with the photon, a result of kinetic mixing with the  $U(1)_Y$  hypercharge sector of the SM before electroweak symmetry breaking. The dark photon is phenomenologically motivated to explain the observed gamma

ray [950] and positron [951–954] excesses through dark matter annihilation near the galactic center. An extended Higgs sector can generalize the dark photon to the dark-Z boson which couples to the SM via both kinetic and mass mixing with the photon and the Z-boson, with couplings  $\epsilon$  and  $\epsilon_Z = m_{Z_d}/M_Z\delta$  respectively. Here  $\delta$  is a model-dependent parameter arising from the extended Higgs sector. The dark-Z gives rise to an additional source of parity violation through its coupling to the weak neutral current by mixing with the Z-boson. In PVDIS, its effects can be absorbed into a shift in the measured weak mixing angle:

$$\Delta \sin^2 \theta_W(Q^2) \simeq -0.42 \epsilon \delta \frac{M_Z}{m_{Z_d}} \frac{m_{Z_d}^2}{Q^2 + m_{Z_d}^2} \quad (7.62)$$

For  $m_{Z_d} \ll M_Z$ , this shift is negligible near the Z-pole  $Q^2 \sim M_Z^2$ . However, at low  $Q^2$ , below the Z-pole, the shift can be significant. In the region explored by the EIC,  $10 < \text{GeV} < Q < 70 \text{ GeV}$ , the mass range  $m_{Z_d} \sim 10\text{-}30 \text{ GeV}$  could result in deviations in the running of the weak mixing angle, large enough to be within reach of the projected EIC sensitivities.

### Charged Lepton Flavor Violation

The discovery of neutrino oscillations have now firmly established lepton flavor violation (LFV) in the neutrino sector, confirming that neutrinos have non-zero mass, pointing to new physics beyond the SM. By contrast, there has been no experimental observation of flavor violation in the charged lepton sector. LFV in the neutrino sector implies charged lepton flavor violation (CLFV) in processes such as  $\mu \rightarrow e\gamma$ . However, it is mediated at one loop and suppressed by the smallness of the neutrino masses, yielding  $\text{Br}(\mu \rightarrow e\gamma) < 10^{-54}$ , well beyond the reach of any current or planned experiments.

However, many beyond the Standard Model (BSM) scenarios [955] predict significantly higher CLFV rates that are within reach of current or future planned experiments. A variety of experiments [956–963] across the energy spectrum have searched for and set limits on CLFV processes that involve transitions between the electron and the muon.

By contrast, the limits on CLFV involving the  $e \leftrightarrow \tau$  transition are worse by several orders of magnitude. Extensive searches for this CLFV transition  $e^\pm p \rightarrow \tau^\pm + X$  were conducted at HERA [963, 964]. Theoretical and simulation studies [419, 965] have been performed for the EIC and indicate that with  $1000 \text{ fb}^{-1}$  of integrated luminosity, the EIC can improve upon the HERA limits by a factor between 10 and 200. A polarized positron beam would complement these planned studies at the EIC, providing an independent probe that can help distinguish between different CLFV mechanisms.

It is convenient to study CLFV within the Leptoquark (LQ) framework. LQs are color triplet particles that couple to leptons and quarks and mediate CLFV processes at tree-level allowing for larger cross sections. The Buchmüller-Rückl-Wyler (BRW) parameterization classifies the LQs into 14 different types according to their spin (scalar or vector), fermion number  $F=3B+L$  (0 or  $\pm 2$ ), chiral couplings to leptons (left-handed or right-handed),  $SU(2)_L$  representation (singlet, doublet, or triplet), and  $U(1)_Y$  hypercharge.

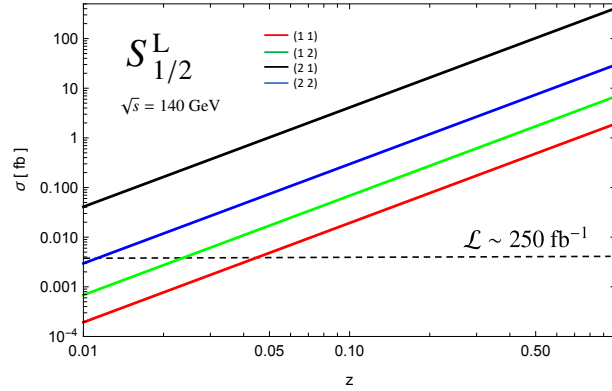


**Figure 7.109:** Improvement over limits set by HERA on CLFV. The different color lines indicate different leptoquark states, while the dashed line indicates the expected reach of the EIC with  $250 \text{ fb}^{-1}$

In the region of LQ mass  $M_{LQ} \gg \sqrt{s}$ , the CLFV process is mediated via a contact interaction and the cross section for  $e^- + N \rightarrow \tau^- + X$  is proportional to the combination  $\kappa_{\alpha\beta} \equiv \lambda_{1\alpha}\lambda_{3\beta}/M_{LQ}^2$ . Here  $\lambda_{1\alpha}$  denotes the coupling of the LQ to the electron and quark of generation  $\alpha$ ,  $\lambda_{3\beta}$  denotes the coupling of the LQ to the  $\tau$ -lepton and quark of generation  $\beta$ , and  $M_{LQ}$  is the LQ mass. Limits on  $\kappa_{\alpha\beta}$  have been set at HERA and through low energy experiments [963,964]. In Fig. 7.109, we plot the cross section ( $\sqrt{s} = 140 \text{ GeV}$ ) for the production of the  $F = 0$  scalar LQ state,  $S_{1/2}^L$ , as a function the variable  $z \equiv \kappa_{\alpha\beta}/\kappa_{\alpha\beta}^{\text{limit}}$ , where  $\kappa_{\alpha\beta}^{\text{limit}}$  denotes maximum value that saturates the existing limit. Thus,  $z = 1$  corresponds to current limit  $\kappa_{\alpha\beta} = \kappa_{\alpha\beta}^{\text{limit}}$ , corresponding to the largest allowed cross section. The factor of  $10^2 - 10^3$  increase in luminosity of the EIC compared to HERA, will allow sensitivity to smaller cross sections and correspondingly smaller values of  $z < 1$ . As seen in Fig. 7.109, an integrated luminosity of  $\mathcal{L} \sim 250 \text{ fb}^{-1}$ , the EIC can improve the bound on  $z$  by one to two orders of magnitude depending on the specific LQ state considered.

Simulation studies are ongoing to evaluate the discovery sensitivity to  $e-\tau$  conversion given the conceptual design of the EIC detector. The challenge is to identify the  $\tau$  lepton amidst the hadron remnants of the DIS event. The goal is to reach a sensitivity to an  $e-\tau$  appearance cross-section at the level of  $0.1 \text{ fb}$ . Beyond increased luminosity the EIC will take advantage of the improvements to detector technology. In particular improved reconstruction of jets, better tracking resolution and most importantly a vertex detector will be hugely beneficial for this search. Early studies indicate that the potential exists, though this must be confirmed with many detailed studies, to achieve an efficiency approaching 10% while being background free for a luminosity of  $100 \text{ fb}^{-1}$ .

The use of different combinations of polarized electron or positron beams with proton or deuteron targets, over a wide range of kinematics, can allow for distinguishing between specific LQ states or CLFV mechanisms. The positron and electron beams can be used to separate the contributions of the  $F=0$  and  $|F|=2$  LQ states. The lepton beam polarization can be used to distinguish between left-handed and right-handed LQ states. A wide kinematic range allows distinguishing between scalar and vector LQs through the difference

in the  $y$ -dependence of the corresponding cross sections. Finally, proton vs deuteron targets can be used to distinguish between “eu” and “ed” LQs, corresponding to LQs with different electroweak quantum numbers [966].

### Charged Current Chiral Structure

The chiral structure of electro-weak interactions allows only left-handed electrons and right-handed positrons to couple to the  $W$ -boson. Thus, the SM predicts a linear dependence on the lepton beam polarization for the charged current processes  $e^\pm + p \rightarrow \begin{smallmatrix} (-) \\ \nu \end{smallmatrix} e + X$ .

Precision measurements of this polarization dependence can test the chiral structure of the charged current interactions. A right-handed  $W$ -boson ( $W_R$ ), arising in Left-Right Symmetric models with spontaneous symmetry breaking  $SU(2)_L \otimes SU(2)_R \otimes U(1)_{B-L} \rightarrow SU(2)_L \otimes U(1)_Y$ , could lead to a deviation from a linear lepton beam polarization dependence. The higher luminosity and degree of lepton beam polarization at the EIC can allow for modest improvements [940] over the HERA [967] limits on the  $W_R$ -boson mass,  $M_R$ . While the Tevatron and the LHC have already set more stringent limits on  $M_R$ , in the TeV range, by looking for deviations in the transverse mass distribution of the Drell-Yan process  $pp \rightarrow W \rightarrow l\nu_l$ , the observed distribution is sensitive to a time-like charged boson and in general can be affected by physics involving different chiral and flavor structures. In this way, the EIC measurements will complement the limits that will be set by the LHC.

### Heavy Photon and Neutral-Lepton Searches

The high energy and luminosity at the EIC offers interesting opportunities for new particle searches such as heavy photon searches as well as heavy neutral lepton (HNL) searches. At the EIC, these searches could take advantage of the accelerator’s unique kinematics, which make it equivalent to a multi-TeV lepton beam on a fixed proton or heavier target. In the nuclear rest frame, radiative production prefers to give a substantial fraction of the beam energy to the radiated particle, producing highly boosted final states. Compared to that hypothetical fixed-target experiment, however, electron-going final states in the EIC have significantly lower boost and hence wider opening angles in the laboratory frame, allowing access to kinematics that are otherwise difficult to capture.

For the heavy photon searches, current limits beyond 1 GeV are set primarily by BaBar, LHCb, and CMS [968, 969]. The CM energy of the EIC reaches above the  $Z^0$  threshold, competitive with the CMS dimuon result [970], the highest mass range currently probed by a collider experiment. In particular, the presence of an initial state lepton with large CM energy may also make it possible to substantially expand probing of the parameter space in models with new force mediators with leptonic couplings.

Dilepton searches for radiative production of a dark photon via  $e + p \rightarrow e + p + A' \rightarrow e + p + l^+ + l^-$  would directly test electronic and muon couplings to a new mediator with minimal model dependence, and could also be performed in  $e + A$  collisions, where ad-

dition charge in the nucleus is expected to enhance radiative production. While, detailed studies of the impact of these model-independent searches are still in its early stages, they have the potential to provide a significant contribution to the field.

The HNL searches [971] are motivated by models suggesting they could contribute to the neutrino mass generation through the Type-I Seesaw mechanism [972–977] as well as the matter-antimatter asymmetry in the universe [978,979]. At the EIC the primary search will focus on the  $e + p \rightarrow N + X$  production channel with a particular focus on the events with a displaced vertex. Preliminary studies suggest that searches at the EIC for such particles would offer sensitivities beyond existing limits at for mass ranges around 5GeV. This mass range can also be probed by other proposed experiments [980].

### General BSM Searches

**SMEFT:** The SM effective field theory (SMEFT) provides a convenient theoretical framework for investigating indirect signatures of heavy new physics without associated new particles at low energies. Considerable effort has been devoted to performing global analyses of the available data within the SMEFT and other frameworks. An issue that arises in such global fits is the appearance of flat directions that occur when the available experimental measurements cannot disentangle the contributions from different EFT operators.

The flat directions that appear when studying 2-lepton, 2-quark four-fermion operators can be resolved with the inclusion of high precision polarized beam measurements. Although the naive expectation is that these operators are well-probed by high invariant-mass Drell-Yan distributions at the LHC, only a very limited number of combinations of Wilson coefficients can be probed by such measurements. The ability to polarize both electron and proton beams at an EIC allows for probes of Wilson coefficient combinations not accessible at the LHC [981]. Combined fits of LHC and projected EIC data lead to much stronger constraints than either experiment alone. Moreover, the addition of polarized positrons to the EIC will provide constraints on additional flat directions in the SMEFT framework leading us closer to a fully constrained system.

**Lorentz- and CPT-violating effects:** Lorentz and CPT symmetry are among the most well established symmetries in physics. However, many BSM theories admit regimes where one or both of these symmetries can be spontaneously broken. Low-energy tests of Lorentz and CPT symmetry can be performed using the effective field theory framework known as the Standard-Model Extension (SME) [982–984]. To date, SME operators describing Lorentz- and CPT-violating effects on QCD degrees of freedom have been largely unconstrained.

Recent studies suggest differential cross section measurements at the EIC will allow for precision tests of Lorentz and CPT symmetry in the quark sector [985–987]. Data for unpolarized inclusive deep inelastic scattering at  $100 \text{ fb}^{-1}$  luminosity can increase bounds on quark sector coefficients by two orders of magnitude over data taken at HERA. Symmetry violations would be visible as variations in the cross section as a function of sidereal time.

Additional processes, including those with polarization effects, charged-current exchange, and QCD corrections, have the ability with the EIC to place first constraints on a number of completely unexplored effects stemming from Lorentz and CPT violation.

### 7.5.2 Neutrino physics

The accurate characterization of the structure of nucleons and nuclei provided by the EIC program can directly benefit neutrino physics. Massive nuclear targets are typically required in neutrino experiments to collect sizable statistics, but they also introduce uncertainties related to nuclear effects [988]. Since the energy of the incoming neutrino is unknown on an event-by-event basis, it must be inferred from the detected final state particles originated in the interactions, which are affected by a substantial nuclear smearing. The latter is present even for an ideal detector since the initial momentum of the bound nucleon is not known and hadrons produced in the primary interactions can be absorbed or re-interact within the nucleus. Target nuclei commonly used in neutrino experiments include C, O, Ar, Fe, Pb. Understanding the impact of nuclear effects on the measured cross-sections and event distributions is particularly critical for the next-generation long-baseline neutrino oscillation experiments like DUNE [989] and Hyper-Kamiokande [990], which are looking for CP violation via tiny differences between neutrino and antineutrino interactions off Ar and H<sub>2</sub>O targets, respectively. The kinematic coverage of the EIC has a significant overlap with the DUNE program since this latter is dominated by inelastic interactions, with more than 54% of the events having  $W > 1.4$  GeV.

Neutrinos and antineutrinos have many desirable properties for a probe of the structure of nucleons and nuclei, including a complete flavor separation ( $d/u, s/\bar{s}, \bar{d}/\bar{u}$ , valence/sea) through the charged current (CC) process, the presence of an axial-vector component of the weak current, and the natural spin polarization. The possibility to address the main limitations of (anti)neutrino experiments at future facilities, allowing the collection of high statistics samples combined with an accurate control of the targets and fluxes [991], can provide valuable information complementary to the EIC program. In particular, precision measurements of  $\nu(\bar{\nu})$  interactions on both hydrogen and various nuclear targets with the high intensity and the energy spectra of the planned Long-Baseline Neutrino Facility (LBNF) beams can offer a broad mixture of measurements of electroweak parameters, parton and hadron structure of nucleons and nuclei, nuclear physics, form factors, structure functions and cross-sections, as well as searches for new physics or verification of existing outstanding inconsistencies [992, 993]. Exploring possible synergies and complementarities between the EIC and future neutrino programs could potentially further enhance their physics reach by combining the unique features of the electron and (anti)neutrino probes [994]. In the following, we review the neutrino-nucleon cross section and the various kinematical regions in scattering with nuclei, and we list a few topics of particular interest.

### Cross sections and kinematical regions

The CC neutrino- or antineutrino-proton scattering cross section is given by three structure functions  $F_1$ ,  $F_2$ , and  $F_3$  as [995–998]

$$\frac{d\sigma_{CC}^{v/\bar{v}}}{dx dy} = \frac{G_F^2 s}{2\pi (1 + Q^2/M_W^2)^2} \left[ F_1^{CC} x y^2 + F_2^{CC} \left( 1 - y - \frac{Mxy}{2E} \right) \pm F_3^{CC} xy \left( 1 - \frac{y}{2} \right) \right], \quad (7.63)$$

where  $\pm$  indicates  $+$  and  $-$  for neutrino and antineutrino, respectively,  $G_F$  is the Fermi coupling constant, and  $M_W$  is the  $W$  boson mass. The structure function  $F_1$  is related to  $F_2$  by the Callan-Gross relation  $2xF_1 = F_2$  in the parton model, and the structure functions are expressed by the PDFs for the proton as

$$\begin{aligned} F_2^{vp(CC)} &= 2x (d + s + \bar{u} + \bar{c}), & xF_3^{vp(CC)} &= 2x (d + s - \bar{u} - \bar{c}), \\ F_2^{\bar{v}p(CC)} &= 2x (u + c + \bar{d} + \bar{s}), & xF_3^{\bar{v}p(CC)} &= 2x (u + c - \bar{d} - \bar{s}), \end{aligned} \quad (7.64)$$

in the leading order of  $\alpha_s$ . The neutral-current (NC) cross section is given in the same way by the replacements,  $M_W \rightarrow M_Z$ ,  $G_F^2 \rightarrow \rho G_F^2$  where  $\rho = M_W^2/(M_Z^2 \cos^2 \theta_W)$  with the weak-mixing angle  $\theta_W$ , and  $F_{1,2,3}^{(CC)} \rightarrow F_{1,2,3}^{(NC)}$ . The NC structure functions are expressed by the PDFs defined by  $q^\pm = q \pm \bar{q}$  as

$$\begin{aligned} F_2^{v/\bar{v}p(NC)} &= 2x [(u_L^2 + u_R^2)(u^+ + c^+) + (d_L^2 + d_R^2)(d^+ + s^+)], \\ xF_3^{v/\bar{v}p(NC)} &= 2x [(u_L^2 - u_R^2)(u^- + c^-) + (d_L^2 - d_R^2)(d^- + s^-)]. \end{aligned} \quad (7.65)$$

The left- and right-hand couplings for a quark are expressed by the third component of isospin  $T_a^3$ , charge  $e_q$ , and the weak-mixing angle  $\theta_W$  as  $q_L = T_q^3 - e_q \sin^2 \theta_W$ ,  $q_R = -e_q \sin^2 \theta_W$ . with  $T_q^3, e_q = +1/2, +2/3$  ( $-1/2, -1/3$ ) for  $q = u, c$  ( $d, s$ ).

In the lepton-nucleus scattering, the kinematical regions of quasi-elastic (QE), resonance (RES), deep inelastic scattering (DIS), and Regge (REG) are shown in Fig.7.110 as the functions of the energy transfer  $\nu$  and  $Q^2$ . For the current neutrino oscillation experiments with neutrino energies from a few hundred MeV to a few GeV, all of these kinematical regions should be understood accurately [999]. At low energies, the lepton interacts with nucleons almost elastically, and nucleon resonances appear as the lepton energy increases. In the DIS region  $W^2 \geq 4 \text{ GeV}^2$  and  $Q^2 \geq 1 \text{ GeV}^2$ , the nucleon is broken up into hadron pieces. The region with  $W^2 \geq 4 \text{ GeV}^2$  and  $Q^2 < 1 \text{ GeV}^2$  is described by the Regge theory with Reggeons and Pomerons. For calculating neutrino cross sections in all of these regions, theoretical descriptions should be tested by charged-lepton data, then

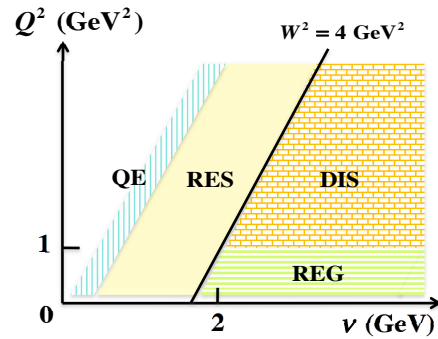


Figure 7.110: Kinematical regions of neutrino-nucleus scattering.

axial-vector components should be added, so that EIC measurements are valuable.

### Studies of (Anti)Neutrino-Nucleus Interactions

The EIC program will provide important information on the nuclear modifications of the nucleon properties which are relevant to understand (anti)neutrino-nucleus interactions [988]. As a result of the structure of the weak current significant differences are expected for nuclear effects in charged leptons and (anti)neutrino DIS. In general, nuclear modifications of structure functions and parton distributions depend on the isospin of the target and on the C-parity and can therefore differ for neutrino and antineutrino interactions [1000]. It is also worth noting that at the typical  $Q^2$  values accessible in  $\nu(\bar{\nu})$  inelastic scattering, high twist contributions play an important role, both at the nucleon and at the nuclear level. Using both neutrino and antineutrino DIS we can access the different structure functions  $F_2, xF_3, F_T$ , as well as  $R = F_L/F_T$ , which is expected to have a different behavior at small  $Q^2$  with respect to electromagnetic interactions [1000].

The flavor separation of the weak current and the availability of precision (anti)neutrino measurements off different nuclear targets would allow to explore the flavor dependence of nuclear effects on parton distributions, structure functions, and form factors [672, 1001–1005]. To this end, a comparison between interactions on hydrogen [1006–1008] and on nuclear targets is particularly relevant. The isospin symmetry can provide a determination of the free neutron structure function and hence the one of the average isoscalar nucleon  $F_{2,3}^{vN} \equiv (F_{2,3}^{vp} + F_{2,3}^{v\bar{p}})/2$ . We can then obtain a direct measurement of the nuclear ratios  $R_A \equiv F_{2,3}^{vA}/F_{2,3}^{vN}$ . An interesting issue to study, in addition to the flavor dependence of nuclear effects, is the role of the axial-vector current and the corresponding differences with electromagnetic interactions. All of these nuclear physics measurements offer complementary information to the EIC program.

### Measurements of the Strangeness Content of the Nucleon

Sensitivity to the strange quark content of the nucleon can be achieved at the EIC from measurements of identified hadrons in semi-inclusive DIS (SIDIS) [25] or from inclusive CC DIS [36]. Neutrino and antineutrino scattering provide a direct access to the strangeness of the nucleon via charm production. The intensity of LBNF beams will allow precision measurements of exclusive decay modes of charmed hadrons (e.g.,  $D^{*+}, D_s, \Lambda_c$ ) and of charm fragmentation and production parameters. In addition, the strange sea quark distributions  $s(x)$  and  $\bar{s}(x)$  can be probed with both the  $\mu\mu$  and  $\mu e$  inclusive semi-leptonic charm decay channels with a statistics more than one order of magnitude higher than the largest samples currently available [1009, 1010]. The analysis of both neutrino and antineutrino induced charm production, in combination with the EIC measurements, can provide an accurate determination of the strange quark content of the nucleon and of the corresponding  $s - \bar{s}$  asymmetry [1011–1013].

While the strange quark vector elastic form factors have been measured with good ac-

curacy in parity-violating electron scattering (PVES) measurements [1014], the strange axial-vector form factors are still poorly determined. Neutrino and antineutrino measurements can accurately determine the latter from NC elastic scattering off protons  $\nu_\mu(\bar{\nu}_\mu)p \rightarrow \nu_\mu(\bar{\nu}_\mu)p$  [1015–1018]. In the limit  $Q^2 \rightarrow 0$  the NC differential cross-section is proportional to the axial-vector form factor  $d\sigma/dQ^2 \propto G_1^2 = (-G_A/2 + G_A^s/2)^2$ , where  $G_A$  is the known axial form factor and  $G_A^s$  is the strange form factor. This process provides a direct measurement of the strange quark contribution to the nucleon spin,  $\Delta s$ , by extrapolating the NC differential cross-section to  $Q^2 = 0$  since in this limit  $G_A^s \rightarrow \Delta s$ . A combined analysis with PVES data would allow an accurate determination of all three strange form factors  $G_E^s, G_M^s, G_A^s$  [1019, 1020].

### Isospin Physics and Sum Rules

Isospin physics is a compelling topic for future neutrino experiments looking for differences between neutrino and antineutrino interactions. The EIC can provide accurate measurements of the  $d/u$  content of the nucleons with p and D data, as well as the corresponding nuclear modifications in nuclei. Complementary measurements can be obtained using both  $\nu$  and  $\bar{\nu}$  interactions on hydrogen [1006–1008]. In particular, the isospin symmetry allows a direct measurement of the free neutron structure functions  $F_{2,3}^{\nu n} \equiv F_{2,3}^{\bar{\nu} p}$  and  $F_{2,3}^{\bar{\nu} n} \equiv F_{2,3}^{\nu p}$ . This measurement provides, in turn, a precise determination of the  $d/u$  quark ratio up to values of Bjorken  $x$  close to 1 [15, 21].

The Adler sum rule [1021, 1022],  $S_A = 0.5 \int_0^1 dx/x (F_2^{\bar{\nu} p} - F_2^{\nu p}) = I_p$ , gives the isospin of the target and can be measured as a function of the momentum transfer  $Q^2$  using  $\nu(\bar{\nu})$  interactions on H and nuclear targets [1000]. The value of  $S_A$  is sensitive to possible violations of the isospin (charge) symmetry, heavy quark (charm) production, and strange sea asymmetries  $s - \bar{s}$ . The Gross-Llewellyn-Smith (GLS) sum rule [1023, 1024],  $S_{GLS} = 0.5 \int_0^1 dx/x (xF_3^{\bar{\nu} p} + xF_3^{\nu p})$ , can also be measured in  $\nu$  and  $\bar{\nu}$  interactions. The value of  $S_{GLS}$  receives both perturbative and non-perturbative QCD corrections and its  $Q^2$  dependence can be used to extract the strong coupling constant  $\alpha_s$  [1025, 1026]. Measurements with both H and various nuclear targets [1000] would allow an investigation of the isovector and nuclear corrections. The EIC measurements can constrain the small  $x$  behavior of the structure functions reducing the uncertainties on both the Adler and GLS sum rules.

The isospin symmetry implies that  $F_{2,3}^{\bar{\nu} p} = F_{2,3}^{\nu n}$  and that for an isoscalar target  $F_{2,3}^{\bar{\nu}} = F_{2,3}^{\nu}$ . These relations as a function of  $x$  and  $Q^2$  can be used for precision tests of isospin (charge) symmetry using a combination of H and isoscalar nuclear targets. The EIC data can provide valuable constraints to improve the accuracy of such measurements.

### Electroweak measurements and the NuTeV anomaly

Neutral currents contain not only isospin currents, which act on left-hand components, but also electromagnetic currents which act on both left- and right-handed ones. The mixing

fraction of these currents is called the weak-mixing angle  $\theta_W$ . This angle was accurately measured by collider experiments; however, the NuTeV collaboration reported anomalously large weak mixing angle [1027],  $\sin^2 \theta_W = 0.2277 \pm 0.0013$  (stat)  $\pm 0.0009$  (syst). It is different from a global analysis of other data,  $\sin^2 \theta_W = 0.2227 \pm 0.0004$  at the stage of 2002. This is called the NuTeV anomaly, which has not been solved yet until now. Since it is one of fundamental physics quantities, it is important to find a reason for the difference. Neutrino and antineutrino charged- and neutral-current events were analyzed for extracting  $\sin^2 \theta_W$  in the NuTeV experiment. The Paschos-Wolfenstein relation  $R^- = (\sigma_{NC}^{\nu N} - \sigma_{NC}^{\bar{\nu} N}) / (\sigma_{CC}^{\nu N} - \sigma_{CC}^{\bar{\nu} N}) = 1/2 - \sin^2 \theta_W$ , which is supposed to be for the isoscalar nucleon, was used for its determination.

Since the NuTeV target was the iron instead of the isoscalar nucleon, various correction factors needed to be considered to this Paschos-Wolfenstein relation. In addition, this relation was obtained by assuming the isospin symmetry in the PDFs of the neutron to relate them to the PDFs of the proton. There are correction terms to the Paschos-Wolfenstein relation from isospin breaking in the PDFs, nuclear correction difference between  $u_v$  and  $d_v$ , finite distributions of  $s(x) - \bar{s}(x)$  and  $c(x) - \bar{c}(x)$ , and neutron-excess effects [1028–1032]. These factors can be measured from the  $\gamma$ - $Z$  interference at EIC via parity-violating asymmetries in polarized electron scattering, providing an independent check of the NuTeV anomaly [932]. It must be emphasized that  $\nu$  and  $\bar{\nu}$ , contrary to charged leptons, give a direct access to both the weak mixing angle  $\theta_W$  and the  $Z^0$  coupling to (anti)neutrinos. Therefore, combined electroweak measurements using electrons and (anti)neutrinos are required. Precision measurements of electroweak parameters can be performed at LBNF using various independent channels including DIS,  $\nu e^-$  elastic scattering, elastic scattering off protons, coherent  $\rho$  production, etc. These processes are characterized by different scales of momentum transfer, providing a tool to test the running of  $\sin^2 \theta_W$  in addition to the EIC measurements.

### Possible GPD measurements in neutrino scattering

Understanding the GPDs [68] is one of major purposes of EIC. It is intended to clarify the origin of the nucleon spin, including the partonic orbital-angular-momentum contribution. However, there is another important purpose to determine gravitational form factors to find the origin of hadron masses and their internal pressures in terms of quark and gluon degrees of freedom, as obtained in the timelike GPDs (or generalized distribution amplitudes) [1033]. The LBNF can supply neutrino beam in the energy 5–10 GeV region, so that it is possible to measure the GPDs, for example, in the pion-production reaction  $\nu_\mu + N \rightarrow \mu + \pi + X$  as shown in Fig. 7.111 [998, 1034]. Since the neutrino reactions are sensitive to the quark flavor, their measurements are complementary to the EIC project and the flavor separation of the quark GPDs will become possible from both measurements at EIC and LBNF.

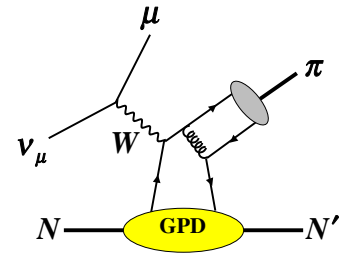


**Figure 7.111:** GPD measurement in the neutrino reaction  $\nu_\mu + N \rightarrow \mu + \pi + X$ .

### 7.5.3 Cosmic ray/astro-particle physics

Measurements at the EIC will be an important input into several areas of astro-particle physics. These areas require more precise models of hadronic interactions to be able to interpret astrophysical data. These areas include cosmic-ray air showers and neutrino astrophysics.

#### Cosmic ray air showers

##### add a figure?

Cosmic-ray air showers occur when a high-energy proton or heavier nucleus strikes the atmosphere, producing a shower of millions to trillions of particles. Cosmic rays with energies above about  $10^{15}$  eV are rare enough so that they can only be studied with ground-based detectors. These detectors sample the shower particles that reach the ground, measuring their density and lateral spread. Cosmic-ray physicists use these indirect data to determine the energy spectrum and nuclear composition of cosmic-rays. The energy can be determined largely from the overall particle density. The composition is often inferred from the muonic content of the shower. The muons are mostly from the decays of charged pions and kaons and neutral kaons, while photons and electrons come from photons from  $\pi^0$  decays. Strangeness production models thus play a large role in inferring the composition from muon data. Very few hadrons reach the ground, so they are only a useful observable below about 1 PeV, where showers are more copious.

Air fluorescence detectors image the shower as it develops in the atmosphere to find the shower-maximum,  $X_{\max}$ , the point in the shower development containing the most particles. Heavier particles, like iron, produce more muons and also reach  $X_{\max}$  at a higher altitude. A hadronic interaction model is required to quantify this relationship, and to infer event energies and composition. Cosmic-ray physicists use a number of different models, for this, with SIBYLL, QGSJet and EPOS being the most common. These models use pQCD to model hard interactions, with a Pomeron inspired phenomenology to simulate the soft interactions that account for most of the produced particles. They are tied, to varying degrees, to RHIC and LHC data, but still vary significantly in their predictions [1035].

Since cosmic-rays essentially follow a fixed-target geometry, measurements in the far forward region are critical to track energy flow downward through the atmosphere. This phase space has not been well studied at RHIC and the LHC. However, the EIC will have excellent forward and far-forward instrumentation, allowing for accurate studies in the target fragmentation region. This far-forward data is essential for tracking energy flow downward through the atmosphere. In particular, a knowledge of the inelasticity of struck protons in hadronic collisions is a vital input to hadronic models.  $ep$  collisions are not the same as  $pp$ , but they will help constrain the models.

These models are receiving attention because the energy spectra measured by the two very large (area more than  $1,000 \text{ km}^2$ ) experiments, Auger [1036] and Telescope Array (TA) [1037] are in tension. A joint working group could not resolve this disagreement [1038].

The difference may be due to physically different cosmic-ray spectra in the Northern and Southern hemispheres [1039]. This would be a very important discovery, pointing to the existence of a few local cosmic-ray sources. However, before reaching that conclusion, we need to exclude other possibilities. The two experiments use somewhat different detection techniques - water Cherenkov detectors for Auger, scintillator for TA, so inaccuracies in hadronic models could lead to differences in energy calibration.

Unfortunately, there is considerable tension between different composition measurements, both between the two experiments, and, for Auger, between composition measurements using air fluorescence and that using muon detectors. Composition is often quantified using the log of the mean atomic number,  $\langle \ln(A) \rangle$ , although this misses the intricacies of the nuclear mass spectrum.

The Auger  $X_{\max}$  analysis finds a significant composition shift with increasing energy, from an apparent mostly-proton composition, with  $\langle \ln(A) \rangle \approx 0.3$  at  $10^{18.5}$  eV to a mixed composition at  $10^{19.5}$  eV, with  $\langle \ln(A) \rangle \approx 1.3$  [1040]. This is with the QGSJET-II-04 hadronic model; with EPOS-LHC,  $\langle \ln(A) \rangle$  is about 0.5 larger - a very significant shift. As was discussed in the EIC White Paper, this inflection point in  $dX_{\max}/dE$  could also come from a change in the character of the hadronic interaction, such as the onset of saturation. In contrast, the TA  $X_{\max}$  study finds a rather small change in  $\langle \ln(A) \rangle$  with increasing energy [1041]. For QGSJET-II-04, their data is consistent with mostly protons, while other hadronic models imply somewhat heavier compositions.

Other Auger analyses, using muons, have found somewhat different results. A study using detector rise time as an indicator of muon content found a somewhat larger composition shift with energy, with the composition at  $10^{19.5}$  eV consistent with pure iron (for the EPOS-LHC model) [1042]. A newer, still preliminary measurement using dedicated muon counters, found an even larger muon excess, pointing to, if naively interpreted, a composition heavier than iron [1043]. The muon content is 40-50% higher than is expected with a lighter (consistent with the  $X_{\max}$  analysis) composition. These muon mismatches are a rather clear sign that there is an issue with the air shower simulations, likely in the hadronic model.

At medium energies ( $10^{15}$  -  $10^{17.5}$  eV), the situation appears somewhat better, in that there are fewer obvious inconsistencies. However, recent studies, such as a new IceCube measurement [1044] show that uncertainties to hadronic models are a major contributor to systematic uncertainty on the cosmic-ray composition. Complementary studies, using high  $p_T$  muons in air shower, should allow for composition extraction in a pQCD framework, are less advanced [1045, 1046].

EIC data could significantly help to reduce these uncertainties, by providing high-accuracy measurements of hadronic particle production to tune the models, especially in the forward region, and, for high  $p_T$  muon analyses, by pinning down parton distributions at low Bjorken- $x$ . If it is observed, saturation could also explain some of the inflection points seen in the composition distributions. Data from oxygen and/or nitrogen targets is of particular value, to match the air-shower targets.

### Astrophysical Neutrinos

The discovery of high-energy (up to at least  $10^{16}$  eV) cosmic neutrinos [1047] is one of the most exciting recent developments in high-energy astrophysics. EIC data can offer important information for future astrophysical neutrino studies, by helping constrain the background from atmospheric neutrinos, and by better predicting the absorption of high-energy neutrinos in the Earth.

Atmospheric neutrinos from cosmic-ray air showers are a significant background to astrophysical neutrinos. A better understanding of atmospheric neutrinos would lead to smaller systematic uncertainties on cosmic neutrino fluxes, especially at lower energies, where atmospheric neutrinos are dominant. One important question is how often downward-going atmospheric neutrinos are self-vetoed' by being accompanied by high-energy muons [1048], either by a muon produced in the same weak decay as the neutrino, or elsewhere in the hadronic interaction or elsewhere in the air shower.

Prompt neutrinos are of particular interest, since they have a harder energy spectrum than neutrinos from pions/kaons, so they are closer to astrophysical neutrinos. A standard calculation [1049] has large uncertainties, due to uncertainties on the cosmic-ray flux and composition, on the pQCD cross-sections, and on the low- $x$  gluon distributions in nitrogen and oxygen. Currently, the only measurements of gluon distributions in medium nuclei come from fixed target experiments, which can only probe the region  $x > \approx 10^{-2}$  (and that at low  $Q^2$ ). EIC data will extend these results downward in  $x$  and cover a wide range in  $Q^2$ , reducing the uncertainties on prompt neutrino production. Beyond this, it will be another place to compare charm production cross-sections with theoretical calculations; this comparison should lead to more accurate treatments of charm production in air showers.

Looking ahead, future detectors, like IceCube Gen2 will instrument much larger areas (order  $100 \text{ km}^3$ ) with radio-detection stations and thereby study astrophysical neutrinos at higher energies, up to  $10^{20}$  eV [1050]. It is necessary to know the interaction cross-section to measure the flux accurately. At  $10^{20}$  eV, neutrino interactions probe quark distributions with a typical  $x \approx 10^{-7}$ , at  $Q^2 \approx M_W^2$ . One recent calculations, using NLO pQCD with DGLAP evolution found roughly 15% [996] uncertainty in the DIS cross-sections at  $10^{20}$  eV, while another calculation, with different assumptions about parton evolution, found a considerably larger, 50% uncertainty at the same energy [1051]. A newer calculation used data from LHCb on D meson production to constrain the low- $x$  parton distributions, with a consequent decrease in uncertainty [?]. This study used a NNLO calculation found a cross-section about 10% below the previous calculations, except at neutrino energies above  $10^{19}$  eV. The stated uncertainties were under 10%.

These results were for isoscalar targets, without nuclear effects. Nuclear effects, because water has more protons than neutrons, and due to nuclear modifications of the parton distributions, can be significant in some kinematic regions. Ref. [?] finds that nuclear corrections are small at low energies, but increase to up to 10% (with large uncertainties) at energies above  $10^{20}$  eV. Ref. [1052] finds smaller overall changes, but finds that anti-shadowing can increase the cross-section in some ranges; furthermore, in the region where large- $x$  parton distributions are significant, the proton excess in water can have a very

large effect, with large uncertainties. This change is particularly visible in the  $\nu$  inelasticity distribution. Since, for most analyses, acceptance varies with inelasticity [1053], assuming the correct inelasticity distribution is critical in determining the neutrino flux. The inelasticity distribution is also important for determining the  $\nu/\bar{\nu}$  ratio on the basis of the overall inelasticity distribution.

Knowing the cross-section is critical for estimating interaction rates and zenith angle distribution in a detector [1054,1055]. A larger cross-section increases the number of downward-going neutrinos that interact, but, because neutrinos interact in the Earth, reduces the number of upward-going events. Neutrino absorption in the Earth has been observed for energies above 6.3 TeV, at a level consistent with the standard model [1056]. The inelasticity distribution is important because, for charged-current  $\nu_\mu$  and most  $\nu_\tau$  interactions, only the energy transferred to the struck target is visible in radio-based detectors [1053].

Beyond rate estimates, a good understanding of the standard-model cross-section is critical in searching for BSM contributions to the total cross-section. A variety of BSM models predict an increase in the neutrino-nucleon cross-section, including those positing sphalerons, leptoquarks, and extra rolled-up dimensions [1055]. EIC measurements of quark distributions in nuclei should reduce the uncertainties on the cross-section and inelasticity distributions significantly. Although EIC measurements cannot cover the full range of Bjorken- $x$  needed for neutrino astrophysics, EIC data should be able to significantly constrain the non-linear evolution to lower  $x$  values, reducing the uncertainties at all energies.

Finally, some recent studies have applied pQCD to calculations of prompt neutrino production in astrophysical accelerators [1057]. Improved measurements of gluon distributions in protons would reduce the uncertainties on the predicted neutrino flux and energy spectrum. The spectra are of particular importance because different spectra can be characteristic of different source classes.

#### 7.5.4 Other connections to pp, pA, AA

##### Low- $x$ gluons and factorization in $eA$ ( $ep$ ) vs $pA$ and $AA$

	Inclusive DIS	SIDIS	DIS dijet	Inclusive in pA	$\gamma$ +jet in pA	dijet in pA
$xG_{WW}$	–	–	+	–	–	+
$xG_{DP}$	+	+	–	+	+	+

**Table 7.2:** The process dependence of gluon distributions in  $eA$  ( $ep$ ) and  $pA$  collisions.

Recently, an interesting connection between the CGC formalism and the TMD factorization has been established, and a lot of progress in both fields is made [1058]. In particular, this has led to a fundamental understanding of two different gluon distributions, namely the Weizsäcker-Williams (WW) gluon distribution and the dipole gluon distribution, from the perspective of the operator definition in the CGC formalism [411,412]. This progress and

its impact on EIC physics are discussed in detail in Sec. 7.3.1. This part is devoted to the small- $x$  gluon and its factorization in  $eA$  vs  $pA$  and  $AA$  collisions.

First, based on the small- $x$  factorization in DIS and  $pA$  collisions, the WW and dipole gluon distributions can be viewed as the fundamental building blocks of all gluon distributions in the CGC formalism, and they can be used to construct other more complicated gluon distributions appearing in the dijet production in  $pA$  collisions in the large  $N_c$  limit. Since the gauge links associated with the gluon distributions depends on the details of the scattering process, the low- $x$  gluons are then process-dependent as shown in Table 7.2, where the + and - signs indicate that the corresponding gluon distributions appear and do not appear in certain processes, respectively. The table also shows that many processes are sensitive to the dipole gluon distribution, while the back-to-back dijet production in DIS can provide the direct measurement of the WW gluon distribution. In the meantime,  $pA$  collisions can serve as a gateway to the EIC as far as saturation physics is concerned, and it also plays an important and complementary role in the study of these two fundamental gluon distributions. Furthermore, in this factorization at the low- $x$  limit, the virtual photon and the proton are treated as dilute probes for the dense gluons in the target. The corresponding cross section for a certain process in DIS and  $pA$  collisions can still be expressed in terms of the convolution of the relevant gluon distributions and the short distance hard part. The small- $x$  factorization in DIS and  $pA$  collisions is expected to hold at higher order [1059], since the higher-order corrections do not generate genuine new correlators in the large  $N_c$  limit. Last but not least, the production of color-neutral particles in hadron-hadron collisions, such as the Higgs production [629, 1060, 1061] in  $pA$  and  $AA$ , are also sensitive to the WW gluon distribution in heavy nuclei. However, for the productions of hadronic final states in  $AA$  collisions, the issue of the factorization [1062, 1063] becomes more complicated due to the color entanglement of initial and final state interactions, and one needs to use a more complicated form [1064–1066] of small- $x$  factorization in the CGC formalism and resort to numerical methods to obtain results in this case.

### Implications of PDF determinations for proton-proton collisions

The realization of ultimate precision at hadron colliders like the (HL-)LHC remains limited by uncertainties in the unpolarized proton PDFs. Achieving heightened sensitivity to various BSM scenarios requires a variety of improvements, including next-generation theoretical accuracy (such as N<sup>3</sup>LO hard cross sections) and additional constraints to the PDFs themselves. By recording copious high-precision DIS data, the EIC has the potential to impose important constraints to the PDFs as illustrated in Sec. 7.1.1 with implications for observables in  $pp$  scattering at the LHC and precision QCD and EW theory. We highlight several representative examples, concentrating on potential EIC impacts in the Higgs sector in Fig. 7.112 and precision QCD and EW physics in Fig. 7.113.

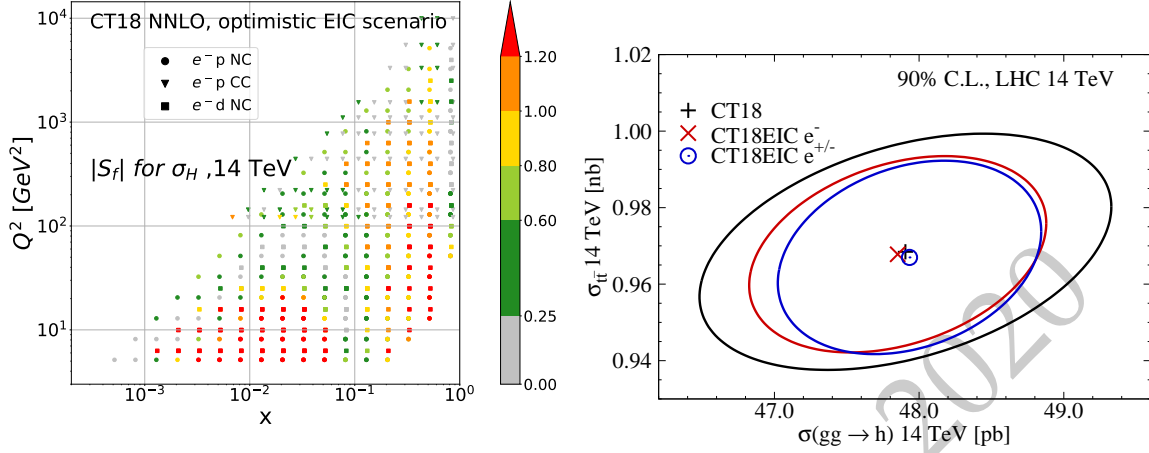


**Figure 7.112:** (Left) The PDF sensitivity,  $|S_f|$ , of the main EIC  $e^-$  pseudodata of Sec. 7.1.1 to  $\sigma_H(14 \text{ TeV})$ , the total  $gg \rightarrow H$  cross section for Higgs production at 14 TeV. The pseudodata assume an integrated luminosity of  $\mathcal{L} = 100 \text{ fb}^{-1}$  and correspond to the optimistic scenario for detector performance and systematic uncertainties. Redder points indicate points with stronger pull as described in Refs. [11–13], implying significant impact of the  $e^-$  information on  $\sigma_H(14 \text{ TeV})$ . (Right) Significant per-point sensitivities translate into a pronounced total impact on the computed 14 TeV cross sections as seen by comparing the Higgs- $t\bar{t}$  uncertainty ellipses for the calculations based on the CT18 NNLO [14] baseline (outer black) and post- $e^-$  (inner red) and post- $e^-/e^+$  (inner blue) fits.

### Implications of PDF determinations for proton-nucleus collisions

It has been demonstrated [659, 1067] that measurements at EIC are bound to significantly improve our knowledge of the nuclear PDFs. In particular, it should be possible to tightly constrain the gluon distribution at  $x \gtrsim 10^{-2}$  at scales comparable to the charm-quark mass,  $Q \sim m_{\text{charm}}$ . Due to DGLAP dynamics, this translates to well constrained gluons even at  $x \ll 10^{-2}$  at higher interaction scales

Such an improved description will lead to more precise predictions for pA collisions at the LHC and thereby allow for stringent tests of factorization. For example, the forward D-meson production measured by LHCb [1068] can probe the nuclear structure down to  $x \sim 10^{-6}$  at perturbative scales. It thus serves as an ideal place to search e.g. for non-linear dynamics beyond DGLAP for which the  $x$  reach at EIC is possibly too restricted. At the moment the nuclear PDFs are not particularly well constrained at small  $x$  and can be easily fitted to reproduce the LHCb D-meson data without conflicts with the other existing data [665, 666]. However, after constraining nuclear PDFs with EIC data, there should be significantly less room for additional tuning which then increases the chances for discovering e.g. the onset of non-linear evolution at the LHC. Similar conclusions hold in the case of other observables such as the direct photon production at forward direction [1069] possibly to be measured by ALICE [1070]. In fact, even the inclusive Z and W production at the CMS and ATLAS acceptances carry a significant sensitivity on the gluon PDFs [1071]

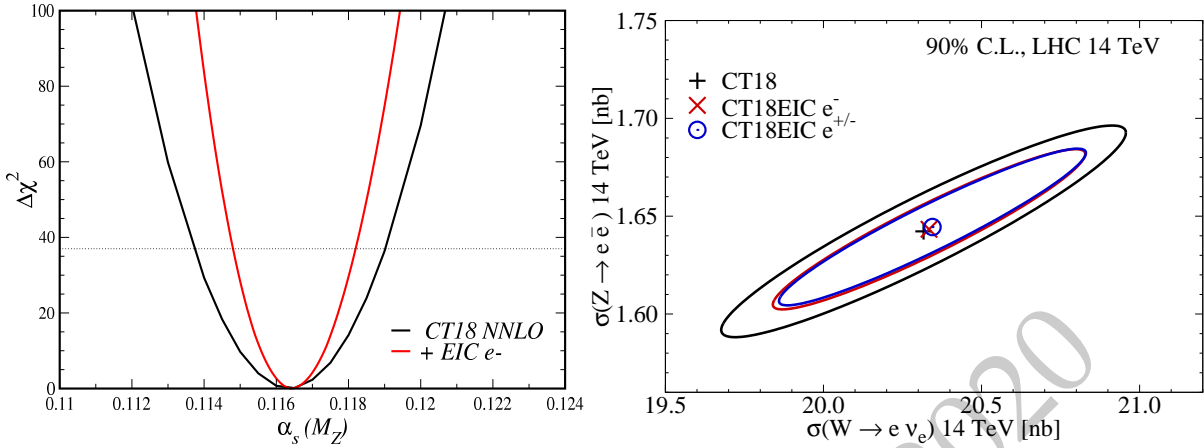


**Figure 7.113:** Precise DIS data over a wide range of  $x$  and  $Q^2$  are expected to impose significant constraints to QCD-sector Standard Model inputs, including  $\alpha_s$  and heavy-quark masses. Inclusion of the main EIC  $e^-$  optimistic scenario pseudodata results in an improved constraint to  $\alpha_s$  (left) in the CT18 NNLO global analysis. This can be seen by the more rapid growth of the likelihood function,  $\chi^2$ , in the fit with the EIC  $e^-$  data (red) relative to the CT18 baseline (black) as  $\alpha_s$  varies away from the value preferred by the global analysis. This narrowing corresponds to a  $\sim 40\%$  reduction of the 68% C.L. uncertainty of the strong coupling. Improved precision extends to  $pp$  observables in the electroweak sector (right), as seen in the tightening of the uncertainty ellipses for total  $W$  vs.  $Z$  production at 14 TeV once the EIC  $e^-$  (inner red ellipse) or combined  $e^-/e^+$  (inner blue) pseudodata are included on top of the baseline CT18 prediction (outer black).

(Sect. 10.4.2) as the gluons at low  $Q$  dictate the behaviour of sea quarks at the electroweak interaction scale. On the other hand, phenomenological studies of  $J/\Psi$  production in ultra-peripheral PbPb collisions will profit from precise nuclear PDFs when modeling the generalized nuclear PDFs. In this sense an extraction of nuclear PDFs in a clean environment such as EIC will allow for precision searches of new phenomena in a broad range of observables in pA collisions.

### Initial conditions for hydrodynamics in AA collisions

Heavy ion collision experiments at RHIC and LHC aim to produce deconfined quark-gluon matter and study its properties [1072]. The standard model of the “little bang” of a heavy ion collision consists of several stages. The initial particle production is followed by a phase of thermalization and equilibration leading to the creation of a droplet of quark-gluon plasma. The plasma then cools and expands in a process that is usually modeled by relativistic hydrodynamics, before undergoing a phase transition to ordinary hadronic matter which then decouples into the hadronic final states that are observed by the detectors. Extracting properties of the quark gluon plasma from measurements requires a simultaneous analysis of different experimental observables in a common theoretical framework. Recent years have seen significant progress performing such analyses in a systematical statistical framework (see e.g. [1073]).

The standard little bang framework is able to predict heavy ion collision observables starting from a given initial condition at the time of equilibration, and from a given set of transport coefficients describing the evolving matter. Inverting this process to infer both the matter properties and the initial conditions is a daunting task, and can in many cases be an ill-posed problem. This is where the physics program of the EIC is relevant in several ways. Firstly, exclusive and diffractive measurements of protons and nuclei at the EIC, discussed e.g. in Secs. 7.2.2, 7.2.4 and 7.3.9, will provide accurate information on the spatial distribution (and its fluctuations) of quarks and gluons in protons and nuclei [648]. This spatial structure is one of the most important inputs into hydrodynamical calculations of the quark-gluon plasma, because collective interactions can transform spatial structures in the initial condition into momentum space correlations among produced particles, i.e. hydrodynamical flow generated as a response to pressure gradients in the matter.

As discussed in Sec. 7.3.5, multiparticle correlations that are present in the wavefunctions of the colliding systems can have effects that are very similar to ones resulting from hydrodynamical flow [1074,1075]. Especially in what are referred in the heavy ion context to as “small systems”, i.e. proton-proton and proton-nucleus collisions, it can be difficult to disentangle the effects of hydrodynamical correlations (i.e. “flow”) from such multigluon “initial state” correlations. The “initial state” correlations can be studied very precisely at the EIC, and analyzed in terms of concepts like linear gluon polarization [492, 1076], or Wigner functions. A precise understanding of the CGC wavefunction from the EIC will also help constrain our understanding of the pre-equilibrium thermalization stage of the heavy ion collision.

### Parton interactions in matter

The importance of understanding parton and particle propagation and parton energy loss in DIS has been well articulated in Secs. 7.4.2, 7.4.4, 7.3.4. Advances in this direction will facilitate the interpretation of the data from  $pA$  and  $AA$  reactions. In proton-nucleus collisions, final-state effects associated with the quark-gluon plasma (QGP) are expected to be absent/suppressed. However, experimental results on the centrality dependence of high energy jet cross sections in  $pPb$  collisions at LHC [1077] and in  $dAu$  collisions at RHIC [1078] show highly nontrivial and large nuclear effects from different centrality selections. These are observed at all transverse momenta  $p_T$  at forward (in the direction of the proton beam) rapidities and for large  $p_T$  at mid-rapidity, and they are manifest as suppression of the jet yield in central events and enhancement in peripheral collisions [1077], see Fig. 7.114. Theoretical work on hadron, jet, Drell-Yan, and  $J/\psi$  production in  $pA$  reactions has emphasized the importance of cold nuclear matter (CNM) energy loss [679,1079–1081]. Calculations that incorporate this physics are qualitatively consistent with the central to peripheral cross section ratio denoted  $R_{cp}$  in Fig. 7.114 [1082]. Away from kinematic bounds, CNM energy loss effects are small but can still contribute to the observed quenching in  $AA$  [1083]. The impact on cross sections and particle correlation is amplified at smaller center-of-mass energies [1084,1085].

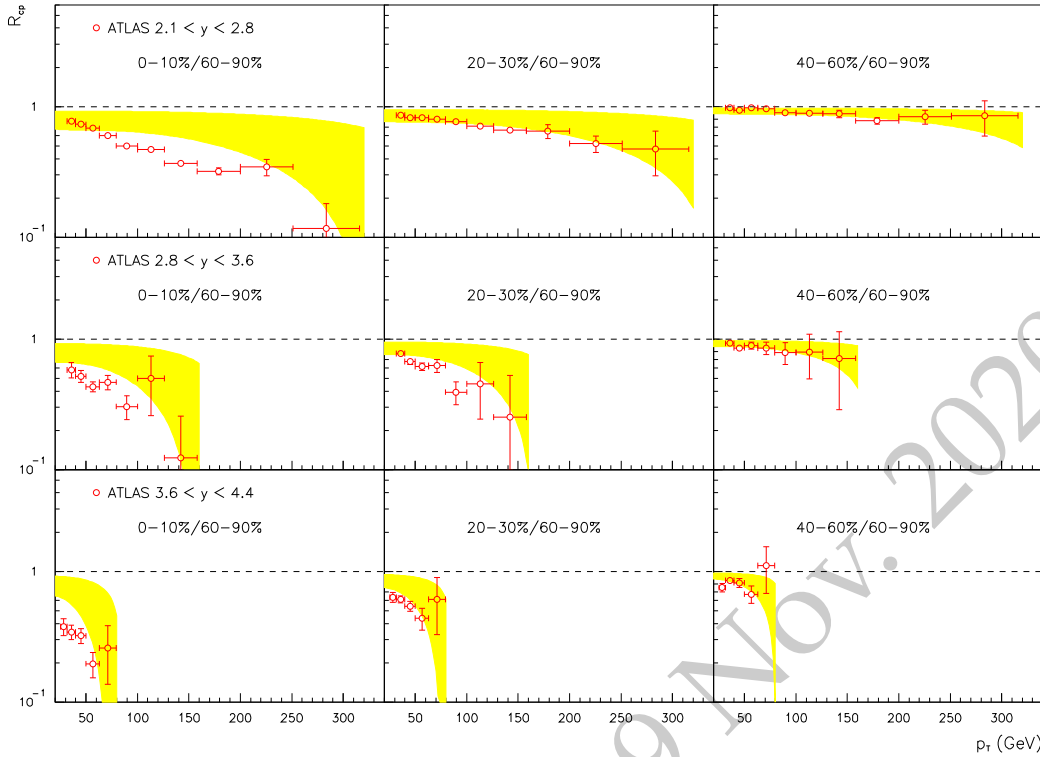


**Figure 7.114:**  $R_{cp}$  for inclusive jet production in p+Pb collisions at  $\sqrt{s} = 5.02$  TeV in central (left), mid-central (middle) and mid-peripheral (right) events. Four different rapidity intervals ( $2.1 < y < 2.8$ ,  $2.8 < y < 3.6$  and  $3.6 < y < 4.4$ ) are presented. Data are from the ATLAS collaboration at the LHC [1077].

### 7.5.5 The EIC and nuclear structure physics

Even though the EIC is a high energy collider with typical energy scales in the tens-to-hundred GeV range, there are key measurements that are of relevance to nuclear physics at much lower energies in the tens to hundreds of MeV range. This section outlines measurements and studies at the EIC that have the potential to provide insight into certain aspects of nuclear structure physics. Conversely, guidance and insight from nuclear structure physics are also important in realizing key aspects of the EIC program.

Short-range nucleon-nucleon correlations (SRCs) [715, 1086, 1087], dominate the high-momentum tails of the many-body nuclear wave function and show signs of universal behavior in nuclei from deuterium to the heavy nuclei [1088–1095]. Experimental data from JLab indicate that SRCs may provide novel insight into the EMC effect and one expects that Jlab data in this decade will help distinguish between competing explanations [715, 1096, 1097]. The dynamics of these SRCs can also be studied at EIC using quasi-elastic two-nucleon knockout, see Sec. 7.3.7 for more details.

A key related question is the role of gluons in SRCs, and by extension, in the EMC effect. At small  $x$ , gluon shadowing is expected to play an important role in nucleon modification in

nuclei, as confirmed now in ultraperipheral heavy-ion collisions [1098, 1099]; what is their role at large  $x$ ? At the EIC, the higher energies and the large lever arm in  $Q^2$  will allow one to probe the role of gluon degrees of freedom in short-range forces.

A novel way to explore the role of gluon degrees of freedom in the nucleon-nucleon potential is to look at exclusive heavy quarkonium (“Onium”) production in coincidence with knock-out reactions of protons and neutrons. The simplest example to consider is that of exclusive scattering off the deuteron<sup>6</sup>. There are two interesting possibilities here. The first is when there is a color singlet gluon exchange between the Onium and a “leading” proton or neutron with a spectator counterpart. In this case, at large relative momentum transfer between the two knock-out nucleons, the scattering is sensitive to color singlet SRCs in the deuteron wave function [19]. The second case also corresponds to color singlet exchange between the Onium and the deuteron; however in this instance one gluon from the color singlet attaches itself to the proton and another to the neutron. The color singlet structure of the interaction is then necessarily sensitive to color octet SRCs in the deuteron wave function [1100].

The first of these gluon dominated SRCs has been simulated recently using the Monte Carlo event generator BeAGLE [1101] using a novel idea for extracting the  $t$ -dependence of the knock-out reaction by simultaneous tagging the leading and spectator nucleons [720]. This study suggests that deuteron configurations with typical internal momenta of up to 1 GeV are accessible, see Sec. 7.3.7 for more details.

An important challenge for both the outlined processes and nuclear breakup channels in general is to identify and isolate final state interactions (FSIs). In exclusive measurements with nuclear breakup the dominant FSI will be between the slow moving (relative to the nucleus center of mass) breakup products. In nuclear DIS with tagging, reinteractions of slow hadrons in the DIS target fragmentation region with the spectator fragments also contribute [19]. Given the low relative momenta in these FSIs, the dynamics have a lot of common ground with low- and medium-energy nuclear breakup reactions [19, 1102–1108].

Because of the collider environment of the EIC, its potential for clean measurements of nuclear fragments with its far forward detectors, and the high projected luminosities, the EIC can provide novel insight into low energy nuclear reactions and correlations. The most relevant measurements are diffractive observables corresponding to a low momentum transfer color singlet exchange (of momenta larger than the nuclear Fermi momentum) and a large rapidity gap separating nuclear fragments from the current fragments of a wide range of invariant masses  $M_X$ . At high energies, there is a very clean separation of time scales between the hard QCD physics of the current fragmentation region and the soft physics of nuclear fragments. In the other direction, accurate nuclear structure input is needed in coherent exclusive channels with light ions (enabling the study of nuclear tomography in partonic degrees of freedom) and in reactions with spectator tagging, which result in additional control over the initial nuclear configuration. The latter is important in studies of free neutron structure, the short-range nature of the nuclear force and medium modifications of partonic structure.

---

<sup>6</sup>Other light nuclei (such as  $^3\text{He}$ ) will also be interesting to consider but will require the reconstruction of more non-trivial kinematics.

Since the nuclei are strongly boosted, the light-front framework for nuclear structure and correlations is appropriate. Because the nucleus is probed at fixed light-front time in the high energy reaction, boost invariant wave functions can be constructed and off-shell effects remain finite. In the reaction frameworks these enter as light-front momentum distributions and spectral functions [19,48,52,65,67,1109,1110]. High-precision phenomenological or EFT derived potentials [553,1111–1113] enter in this description or can be reformulated starting from light-front quantization [1110,1114]. The similarity between light front approaches such as “basis light-front quantization” [1115] and many-body approaches to nuclear structure and correlations such the no-core shell model [1116] has been noted previously. For a review of such *ab initio* approaches, see [1117].

In particular, considerable insight can be gained into understanding how the high momentum tails of nuclear wavefunctions that we noted in the context of SRCs scale with nuclear size [1118]; further, similarity renormalization group methods [1119] (pioneered originally in the light-front framework [1120]) allow one to extend the study of such ultraviolet correlations in nuclei to lower momenta [1121].

Polarized light ion beams will be available at the EIC. Measurements with the deuteron’s tensor polarization allow one to probe the interplay between high energy QCD dynamics and low energy nuclear interactions—see Sec. 7.2.5 for more details. Tensor polarized observables are proportional to the deuteron’s radial D-wave ( $L = 2$ ) component and therefore place constraints on the size and momentum dependence of the D-wave [66]. This is important in the context of the universality of SRCs. Spin 1 nuclei such as the deuteron also allow to probe the gluon transversity pdf in inclusive DIS [559]; this is impossible in the nucleon and arises purely from nuclear interactions.

Precision nuclear structure input is essential to extract the full potential of the high-luminosity EIC for many of the channels considered in this report. For inclusive DIS, the dominant neutron structure uncertainty in the high- $x$  region arises from nuclear structure corrections. Pinning down the link between medium modifications and nuclear interactions or inferring the size of non-nucleonic components in nuclei (such as Delta isobars) cannot be done without a baseline nuclear structure calculation. Observables such as the deuteron tensor  $b_1$  structure function encode the difference of the unpolarized quark pdf between a deuteron in polarization state  $M = \pm 1$  (“dumbbell”) and  $M = 0$  (“donut”) and are thus inherently sensitive to nuclear interactions.

Another aspect of the EIC program where nuclear structure input can play a decisive role, is in the experimental separation of the coherent and incoherent part of the cross section in diffractive and exclusive processes on heavy nuclei. This is critical for nuclear imaging and studies of gluonic fluctuations. In the incoherent signal, the reaction can involve nuclear excitations that decay with the emission of MeV photons in the nucleus rest frame. Detecting these photons with the EIC detectors would be very hard, and is further complicated because of large uncertainties (due to lack of data) in the models of nuclear excitation and differences in level structure between different heavy nuclei (spectra, decay times) which have an impact on detection. Other contributions to the incoherent signal have nucleons evaporating from the nucleus. The models for nucleon evaporation in heavy nuclei used in  $eA$  Monte Carlo generators for EIC (such as BeAGLE) can be better constrained. All this

complicates the vetoing of incoherent events at larger momentum transfer (direct detection of a coherent scattering event with a heavy nucleus being impossible), see Secs. 7.3.9 and 8.5 for more details. Further input from the nuclear structure community will help resolve these outstanding issues.

### 7.5.6 Interface to High-Energy Physics efforts

The Particle Physics Community Planning Exercise (“Snowmass’2021”) [?] is a study organized by the Division of Particles and Fields (DPF) of the American Physical Society to consider all options of interest to the US particle physics community and to identify a path forward. The Snowmass’2021 study is taking place concurrently with the EIC Yellow Report study. It will inform the Particle Physics Project Prioritization Panel (P5) and High Energy Physics Advisory Panel (HEPAP) with recommendations and research priorities for the US Department of Energy and the US National Science Foundation to pursue.

The EIC will be a unique facility for several reasons: a) it will be the first electron-hadron/nucleus collider with polarized beams; b) it will have high luminosity – about 100-1000 times larger than that achieved by HERA; c) it will operate in a broad range of center-of-mass energies  $\sqrt{s} = 20 - 140$  GeV, without significant loss of luminosity; and d) its scientific program, as described in the EIC White Paper [1] and this Yellow Report, requires unprecedented integration of detector components and machine elements to facilitate maximal (arguably, full) acceptance and particle identification over a broad range of particle momenta.

The versatility of the machine performance, required by the EIC science, pushes the frontiers of accelerator science on many fronts [2]. It is hence natural that the EIC Yellow Report and the Snowmass’2021 process cooperatively explore the opportunities that the EIC and its integrated detector will provide to the HEP community and the broader scientific community. It is fortuitous that both the European and the US particle physics communities are engaged in their future planning activities exactly at the time when the US EIC crossed a major milestone of a formal approval (CD0) by the US DoE. The European Particle Physics Strategy Update (EPPSU) [?] concluded in Spring of 2020, and the US particle physics community is conducting the Snowmass study as this report goes into print. Both studies proactively engage the high-energy physics communities in exploring opportunities for their own interests at the EIC. Community inputs pertinent to the EIC studies are submitted to the Snowmass process in the form of Letters Of Interest [1122], Snowmass Proceedings [1123], and Snowmass Frontier reports.

**Hadron tomography.** The EIC is expected to have a significant impact on the reach in precision of hadron scattering experiments at future hadron colliders. The program of the High-Luminosity LHC (HL-LHC) is premised on achieving the next-generation sensitivity to a wide variety of standard model (SM) and beyond standard model (BSM) processes. The success of this program in testing the SM and performing impact measurements at the TeV scale is critically dependent upon advancements in knowledge of the internal structure of hadrons within the standard theory of strong interactions, QCD. As developed in

this Yellow Report, the EIC will undertake a dedicated tomography program to measure the 2+1-dimensional (dependent on two transverse and one longitudinal direction) structure of the nucleons and a broad range of nuclei [1124]. This program envisions measurement of observables sensitive to various parton distributions in the proton and other QCD bound states, including Transverse Momentum Dependent distributions (TMDs) and Generalized Parton Distributions (GPDs), in addition to (un)polarized collinear (longitudinal) parton distribution functions (PDFs). By facilitating controlled extractions of these various parton distributions and testing relations among them predicted by QCD, the EIC will provide unique observational data that will clarify detailed mechanisms of formation of QCD bound states. The EIC measurements will be confronted with advanced predictions from multi-loop QCD and lattice-QCD theory.

**Semi-inclusive DIS, hadron fragmentation, and jet formation.** The significant range of beam energies available at the EIC, combined with the fine resolution and particle identification of the EIC detector, opens a unique venue for exploring formation of hadronic jets, especially the interplay of perturbative QCD radiation and nonperturbative hadronization. The process of semi-inclusive production of hadronic states in deep inelastic scattering (SIDIS) will measure in detail the flavor composition of the initial hadronic states as a function of the parton's momentum fraction  $x$  and fragmentation of partons into various hadrons as a function of the momentum fraction  $z$ . At the EIC, it will be possible to study the multiplicity and angular distributions of final hadronic states as a function of the variable center-of-mass energy of lepton-hadron scattering events [1125]. These observations will offer unique insights about formation of final-state jets, jet substructure and jet angularity, and they will test universality of underlying perturbative and nonperturbative QCD mechanisms. In turn, production of hadronic jets accompanied by the relevant theoretical advancements will offer novel channels to probe the flavor and spin composition of the EIC initial states ranging from nucleons to heavy nuclei.

**Heavy-flavor production** at the EIC will play an important role and will elucidate QCD factorization formalisms ("factorization schemes") for processes with massive quarks, as well as the nonperturbative aspects of heavy-quark scattering dynamics [1126]. Advanced capabilities for detection of jets containing charmed particles will open avenues for unique measurements, such as determination of the strangeness content of the (polarized) nucleons and nuclei at momentum fractions  $x > 0.1$  [36]. Hypothetical dynamical mechanisms for massive quark scattering such as "intrinsic charm" [30] will be constrained.

**Electroweak precision and BSM physics.** The unique combination of high luminosity, a range of accessible energies, and beam polarization at the EIC opens unique opportunities for precision tests of the Standard Model and searches for new physics beyond the Standard Model [1127]. A whole series of observables will be extracted from the measurement of the parity-violating asymmetry  $A_{PV}$  in the deep inelastic scattering, the unique EIC process that can be studied using a combination of initial beams and spin polarizations. By tagging on either a final-state electron or missing transverse energy, the EIC will distinguish between DIS events mediated by neutral ( $\gamma^*$ ,  $Z$ ) and charged ( $W^\pm$ ) vector bosons. In neutral-current DIS, the EIC will measure the less constrained parity-violating structure function  $F_3^{\gamma^*, Z}$  that would access the EW coupling constants  $g_{1,5}^{\gamma, Z}$  of the fundamental SM

Lagrangian. The difference between neutral-current weak couplings of leptons to up- and down-type quarks can be measured in the previously unexplored region of boson virtualities  $Q = 10 - 70$  GeV, providing information about the energy dependence of the weak mixing angle  $\theta_w$ . These measurements will impose constraints on BSM models based on "dark parity violation" and a leptophobic  $Z'$  boson.

The ability to register various leptonic final states –  $e, \tau$ , missing transverse energy – in deep inelastic scattering with either electron or positron beams will be used to look for evidence of heavy elementary particles such dark photons, extra  $Z'$  bosons, new fermionic states. A search for charged-lepton flavor violation in the  $e + N \rightarrow \tau + X$  channel at the EIC will surpass the HERA  $ep$  collider in searches for massive leptoquarks (LQ) generically predicted by grand unified theories. The extended kinematic reach of the EIC will allow to distinguish between scalar and vector leptoquarks. The polarization of the EIC beams, alternations between electron and positron beams, and between initial-state hadronic targets will enable versatile tests of LQ electroweak couplings as a function of spin and flavor.

We expect synergy between the EIC and HL-LHC programs of new physics searches, especially if periods of operation of two colliders overlap. The EIC has the potential to significantly constrain the PDFs and their flavor composition in the region of large partonic momentum fractions,  $x > 0.1$ , where the main constraints on the nucleon structure are currently provided by the fixed-target experiments. The measurements of the PDFs at the EIC will not be affected by possible new physics contributions that may be present in the relevant kinematic region at the LHC. In addition, dedicated EIC searches for indirect signatures of new physics in the framework of the Standard Model Effective Field Theory (SMEFT) will be complementary to the LHC. The EIC, with its polarizable beams, will likely constrain dimension-6 SMEFT operators from new physics that cannot be easily accessed at the LHC. "Combined fits of LHC and projected EIC data can lead to much stronger constraints than either experiment alone." [1127]

**Saturation and diffractive effects.** The intermediate energy of the EIC will allow to examine power-suppressed hadronic contributions and their dependence on the nuclear target. A large part of the EIC program will be dedicated to the structure of nuclei probing in high-energy collisions, including shadowing or saturation effects predicted by QCD for scattering of high-density partonic systems.

To summarize, the numerous instances in which the studies of precision QCD and hadronic structure at the EIC will impact activities at the Snowmass Energy Frontier include, but are not limited to

- high-energy QCD measurements with accompanying improvements in PDF precision; measurements of the QCD charge and heavy-quark masses;
- new knowledge on the gluonic structure of the proton affecting Higgs phenomenology at the HL-LHC;
- studies of QED interactions of the partons and the photon parton density;
- TMDs for precision electroweak physics, including indirect determination of  $W$  bo-

son mass;

- in-depth studies of formation and structure of hadronic jets, and of scattering processes with heavy-quark states;
- improved resolution of nuclear structure and nuclear-medium effects, with connections to phenomena like ultra-peripheral photonuclear collisions at hadron colliders;
- accurate measurements of unpolarized and polarized parton distributions with large momentum fractions that can be confronted by predictions from lattice QCD.

These developments will depend on various technical and methodological advances, including

- next-generation perturbative QCD developments, such as multi-loop QCD computations, explorations of QCD factorization theorems and resummation formalisms;
- phenomenological studies of TMDs/GPDs, including QCD fits and model-based calculations;
- novel insights from lattice QCD; and
- application of AI and machine-learning techniques to proton tomography.

## 7.6 Connected Theory Efforts

In order to maximize the output of the EIC program, dedicated theory efforts in various directions are of utmost importance. One example is the calculation of **higher-order QCD corrections**, including the resummation of large logarithmic corrections. The status of this field depends on the final state under consideration. It is also important that data analyses include higher-order corrections as much as possible. For a number of reasons, also **non-perturbative approaches/models** will keep being essential in the EIC era. They can reveal general, model-independent results, where the “re-surrection” of the Sivers function, based on a model calculation [1128], is just one striking example. Such approaches can as well provide intuition about non-perturbative quantities and, in particular, allow one to compute (new) observables which can help to guide the experiments. Also the synergy with **lattice QCD** will be absolutely critical. This field has become remarkably mature by now, thanks to improvements in algorithms, increased computer power and new conceptual breakthroughs. An example for the latter are new space-like parton correlators through which, for the first time, the  $x$ -dependence of PDFs and related quantities can be computed directly in lattice QCD. Lattice calculations can be used to interpret data from the EIC. Moreover, combining information from lattice QCD with EIC data will (considerably) increase our knowledge about the structure of strongly interacting systems. An overview of this field in relation to the EIC science is given in Sec. [LQCD]. Another very important area is **QED radiative corrections**, as discussed in more detail in Sec. [RadCorr]. Extraction of precision information about nucleons, nuclei and mesons will be impossible without having a very good understanding of such perturbative effects.

### 7.6.1 Lattice QCD

Understanding the internal quark-gluon structure of hadrons from *first principles* remains a long-term goal of Nuclear Physics, and has been emphasized, e.g., in the Nuclear Science Advisory Committee’s Long Range Plan [?]. At the typical energy scales associated with hadron physics, QCD is not amenable to perturbative techniques. The only known approach that captures the full non-perturbative QCD dynamics involves a discretization of the continuum theory on a 4-dimensional Euclidean lattice as an intermediate step, which allows to study QCD via numerical simulations. This approach, known as lattice QCD, provides a rigorous framework for understanding the non-perturbative aspects of QCD directly from the underlying fundamental theory. Lattice QCD has advanced significantly since the first numerical explorations about 4 decades ago, and has successfully reproduced many measurable quantities, such as hadron masses. The progress has enabled lattice calculations to predict new excited and exotic states, some yet to be discovered experimentally. Lattice QCD also enables many studies of the structure of hadrons, for example elucidating the decomposition of the proton’s spin among its constituents. Dedicated efforts within lattice QCD thermodynamics are also emerging, providing key insights for the exploration of the phases of QCD. The lattice formulation of QCD is also used for high precision calculations of standard-model parameters, studies of confinement, and weak decays. In many of these areas, lattice QCD follows a scientific program that strongly aligns with EIC physics. Moreover the synergy between perturbative and lattice QCD will help the EIC program reach its full potential and highest impact.

Lattice QCD calculations currently provide the most precise determination of the strong coupling constant  $\alpha_s$ . Both phenomenological and lattice calculations have systematic uncertainties associated with perturbative series truncation. In lattice calculations, however, it is possible to follow the evolution of  $\alpha_s(\mu)$  to high scales where the perturbative expansion becomes more precise and nonperturbative corrections are negligible<sup>7</sup>. The only experimental input needed in the lattice QCD determinations are the quark masses and the overall scale which are determined from matching to hadron spectrum and have negligible impact on precision. The other important lattice QCD uncertainty is due to discretization effects, and it can be progressively improved with more computing. The most recent lattice average value [1129] has 30% improved precision compared to the 2016 value, and already more precise than non-lattice determinations [1130]. Non-lattice determinations combine multiple experimental inputs, in particular  $\ell N$  deep-inelastic scattering data, which will be improved with the increased luminosity at the EIC. Since lattice calculations provide an entirely independent determination, they will continue to provide an excellent check for the theory, phenomenology and experiments combined to determine  $\alpha_s$ .

As discussed extensively above, one can obtain information on the partonic structure of hadrons through the PDFs and their generalizations (GPDs and TMD PDFs). These distribution functions are defined around the light-cone, which is inaccessible from lattice QCD as it is formulated in euclidean space. Limited information on the distribution func-

<sup>7</sup>Current lattice determination of  $\alpha(5)_{\overline{\text{MS}}}$  NOTATION? is done in lattice QCD from nonperturbative calculations with up to  $N_f = 4$  dynamical flavors, with perturbative matching at the quark mass thresholds.

tions may be accessed, through the Mellin moments, which have been extensively studied within lattice QCD for the PDFs and GPDs. However, systematic study of moments beyond the third nontrivial moment is obstructed due to the decaying signal and power-law mixing between operators. A new field has emerged in recent years, with most notable the so-called quasi-PDFs approach [1131], which connects lattice-calculable matrix elements to light-cone PDFs via a perturbative matching procedure in Large Momentum Effective Theory (LaMET) [1132, 1133]. Other approaches to extract the  $x$ -dependence of distributions functions have been proposed earlier that are based on the hadronic tensor [1134–1136], as well as auxiliary quark field approaches [1137, 1138]. Following the work on the quasi-PDFs approach, a number of other methods have been developed, such as the current-current correlators approach [1139–1141], the pseudo-PDFs [1142], and a method based on OPE [1143]. These approaches are now widely applied in lattice QCD, for the study of proton PDFs, GPDs and more recently TMDs. They have also been extended for the pion and kaon distribution amplitudes and the PDFs of the  $\Delta$  baryon. For recent reviews of the aforementioned approaches and their implementation in lattice QCD, see Refs. [1133, 1144–1146].

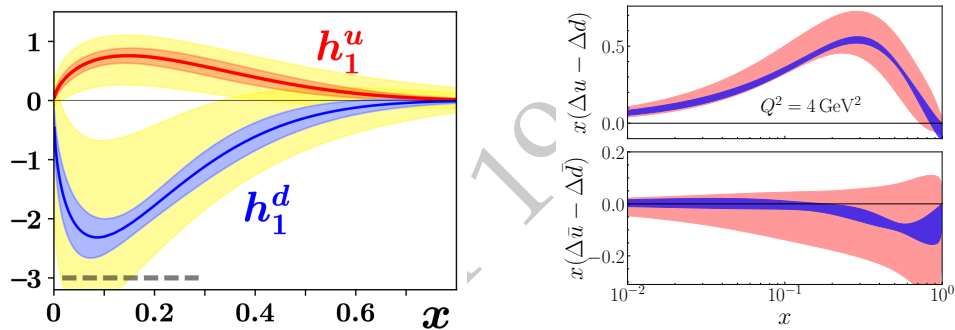


**Figure 7.115:** Left: The transversity PDF from the JAM global analysis without constraints from lattice QCD (yellow band) and with constraints using the lattice estimate for the tensor charge (red band for the up quark and blue for the down quark) [1147]. Right: The helicity PDF from the JAM global analysis obtained from experimental data sets only (red bands), or combined with lattice data (blue bands) [1148].

The progress of lattice calculations in obtaining Mellin moments of PDFs and  $x$ -dependent distribution functions, is of interest to the phenomenological community analyzing experimental data sets to extract the distribution functions. In particular, lattice data are now beginning to be incorporated into global analyses on similar footing as the experimental data sets. This leads to improved estimates of PDFs, particularly in regions where the experimental data are either sparse, imprecise, or non-existing. Synergy between phenomenology and lattice lead to better estimates of the transversity PDFs [1147], using lattice results on the tensor charge. The left panel of Fig. 7.115 shows how the lattice data constrain the JAM Collaboration global fits on SIDIS data, to extract the up- and down-quark contributions to the transversity PDFs. As can be seen, the accuracy of the PDFs is improved by a factor of 3–4, demonstrating the constraining power of lattice QCD results. Lattice data on the helicity PDF were also included within the JAM global analysis framework, and the combined helicity PDFs is shown in the left panel of Fig. 7.115 [1148]. Here,

compared to experiment alone, the combined analysis leads to reduction of uncertainties by a factor of 3–6 depending on the  $x$  region. This holds for both the quark and antiquark contributions. These determinations open up new possibilities for synergy between lattice QCD and global QCD fits, to improve, e.g., the small- $x$  region, which is difficult to constrain in experiment. Currently, the small- $x$  region, as well as the large- $x$  region, cannot be accessed from lattice QCD calculations, as extremely fine lattice discretizations and large lattice volumes are required. Nevertheless, combining the lattice data with the experimental data sets helps to constrain a wide range of the kinematic regions, including small  $x$ . It is expected that, within the next few years, more combined analysis will be available, utilizing lattice results from the various approaches mentioned above.

The EIC provides a unique tool with which to probe the modification of the partonic structure of the nucleon in nuclei. Along with precise studies of nuclear modification of the unpolarized PDFs through the  $F_2$  structure function, the famous EMC effect [53,573,718,1149], it will also provide access to a polarized analog [1118, 1150–1152]. LQCD calculations of moments of parton distributions in light nuclei are just beginning [1153] and in the coming years will improve significantly. It is expected that LQCD predictions for the spin and flavor dependence of EMC-like effects will be available before EIC begins taking data. Additionally, the EIC will enable studies of double helicity flip structure functions of nuclei with spin  $J > 1/2$ ; these distributions isolate contributions of exotic nuclear gluons that cannot be localized to the individual constituent nucleons. First attempts to access moments of this distribution for the deuteron have been made [1154] and will be improved upon in the coming years.

LQCD can also play an important role in tests of electroweak and beyond-Standard-Model physics at the EIC. As one example, the polarization asymmetry in  $eD$  scattering provides a method for extracting the weak mixing angle,  $\theta_W$  [932], as discussed in Section XXXX. In the limit that charge symmetry violation is neglected (up quarks in the proton are the same as down quarks in the neutron) and sea-quark effects are negligible ( $\bar{s} - s = 0$ ), the asymmetry is independent of hadron structure for  $Q^2 \rightarrow \infty$  [1155]. However, in reality these approximations limit the precision with which  $\theta_W$  can be extracted and even rudimentary LQCD calculations of  $u_p - d_n$  or  $\bar{s} - s$  or their moments will enable better determinations.

## 7.6.2 Radiative corrections

In many nuclear physics experiments, radiative effects quickly become a dominant source of systematics and indeed the uncertainty on the correction might be the dominant source for high-statistics experiments. It is therefore important to have a good handle, both experimentally and theoretically, on this important issue. The following discussion mainly focuses on QED radiative corrections.

### *Introduction*

Radiative processes can roughly be divided into several groups, in Fig. 7.116 shown as an example for deep inelastic scattering. The first-order radiative diagrams relative to the

base process a) include an additional photon. The effect of self-energy diagrams of type b) and vertex corrections (c), where the photon is emitted and absorbed by the same incoming or outgoing particle, can be combined, using the QED Ward identity, and are absorbed in the electron wave function renormalization. The dominant QED contribution to vacuum polarization (d) can be calculated exactly in QED. Hadronic vacuum polarization can best be extracted from measurements, see e.g. [1156] for a recent analysis. Corrections described by Feynman diagrams with photons attached on the hadron side are harder to handle. In the easiest case, elastic scattering, they depend on the hadronic substructure. In the case of DIS, photons can be radiated by one of the quarks in the hard scattering process.

Two-photon exchange, very topical currently in the discussion of the proton form factor ratio puzzle, requires additional information about the hadron structure, and so far eludes accurate theoretical treatment even in the simple case of elastic electron-proton scattering, see e.g. Refs. [1157–1159].

Correction terms described by Feynman diagrams with loops of the type (b) to (e) do not change the observed kinematics. In the lowest order, they contribute via the interference term of (a) with the sum of (b) to (e), and are naturally suppressed by a factor of  $\alpha$ , the finestructure constant, from the two additional photon vertices. However, the loop integrals can enhance the contribution of the graph beyond this level. These graphs contain ultraviolet and infrared divergences. The former can be handled via various schemes, for example dimensional regularization, and are absorbed in renormalization constants. The latter remain and cancel on the cross section level with the graphs of type (f) and (g), where an additional photon exists in the final state. These real radiation corrections have to be taken into account since scattering accompanied by soft photons cannot be distinguished experimentally from the elastic scattering without photons. The cancellation between virtual and real photonic corrections is proven to be correct to all orders. [1160].

Since the final state is different, diagrams (f) and (g) do not interfere with those of types (b) to (e). In contrast to those, for finite photon momenta, they change the observable final state kinematics. This makes corrections dependent on the experimental acceptance. The cross section drops typically inversely proportional to the photon energy. However, for radiation from the lepton line (f) and (g), there is an additional enhancement. Since the photon carries away energy, reducing  $Q^2$  for the same electron scattering angle, the cross section is enhanced. In extreme cases, where the photon carries away close to all of the energy, the radiative cross section can be much larger than the (semi-)elastic one.

#### *Peaking approximation*

Photon radiation is dominated by emission (almost) collinear with the emitting particle, but with a tail extending to large angles. Assuming strictly collinear radiation leads to the common peaking approximation [1161], where the particle scattering angles are unmodified. However, this is not exact, and for high-precision predictions for cross sections one has to take into account non-collinear photon radiation.

#### *Expected size, higher orders and uncertainty*

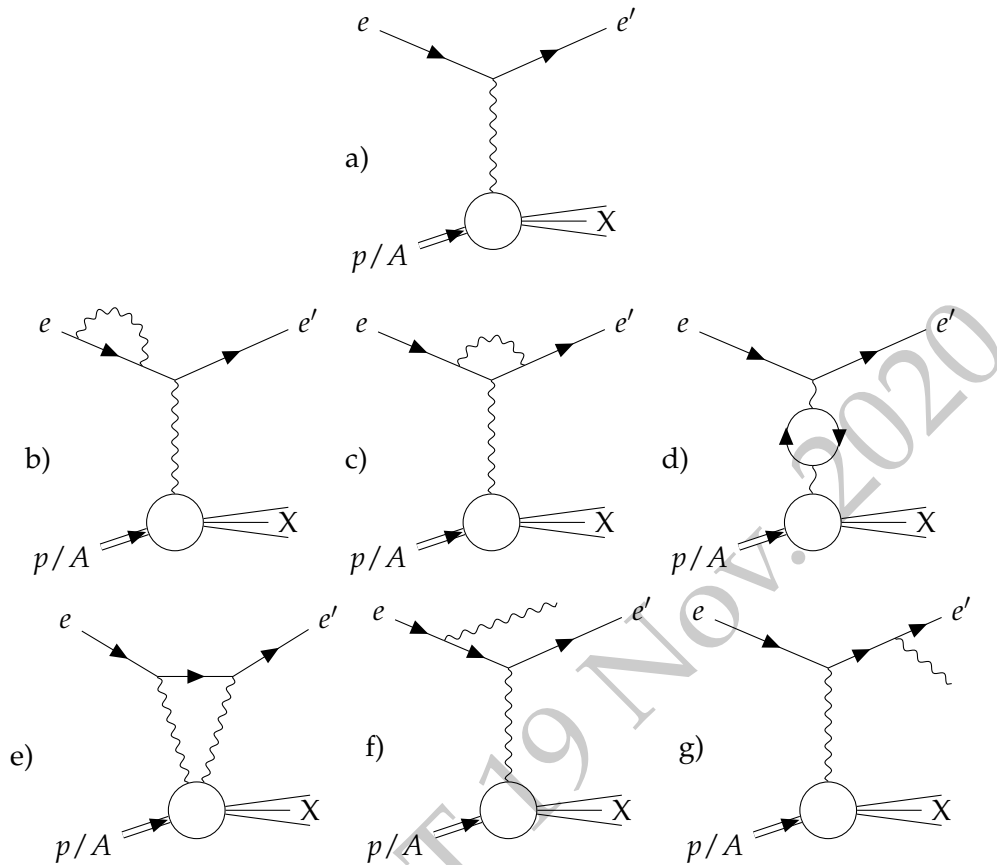


**Figure 7.116:** Selection of typical Feynman diagrams describing first-order radiative corrections, here for inelastic scattering,  $ep \rightarrow eX$ .

Because of the acceptance and resolution dependence of radiative corrections, absolute numbers for the scale of the effect and, more importantly, the uncertainty, are strongly dependent on the details of the experimental conditions. Radiative effects in the size of a couple of tens of percent are easily possible. Calculations for DIS [1162], specifically, show that radiative corrections can be very large, in particular at small Bjorken- $x$  and at large inelasticity  $y$ , with a strong sensitivity on the exact radiative correction prescription.

When first-order corrections are large, one should ask whether unknown higher-order corrections will induce large uncertainties for the cross section predictions. In the soft-photon approximation, one can estimate higher-order corrections since they are known to exponentiate to all orders [1160, 1163]. In practice, this exponentiation is often used even for non-vanishing photon momenta, but this approach does not capture all important higher-order corrections. In particular, there are logarithmically enhanced contributions due to hard collinear photons. These can also be estimated [1164, 1165] and recent work provides a practical approach to include them based on an approach which factorizes leading logarithms into structure functions [1162]. A proper estimate of the error requires an accurate calculation of the second order, which recently became available [1166, 1167]. Results so

far show that second order corrections are comparatively small.

While classically, radiative corrections were applied post-hoc as a correction factor, this approach quickly reaches uncertainty limits, especially when complicated acceptances come into play. Most modern experiments therefore use Monte Carlo integration with generators including radiative effects [1168, 1169] to extract physics in their analysis, as has been done in the HERA experiments H1 and ZEUS.

It is important to note here that, generally, the size of the corrections and the size of its uncertainty are somewhat unrelated. In principle, also large corrections can be calculated reliably, and vice-versa, numerically small corrections can have similarly large (absolute) uncertainties as large corrections. Particularly relevant are acceptance-dependent contributions to the corrections since they depend on experimental conditions which may not be known with good precision. It may be possible that acceptance cuts, for example on the accepted energy deficit, can be chosen in such a way that the total radiative corrections are small, but uncertainties from neglected higher orders are large, while a different cut would produce larger corrections, but minimize the influence of neglected terms. Additionally, an uncertainty on the acceptance cut may induce uncertainties on the corrections which may be difficult to estimate.

#### *Polarization degrees of freedom*

For measurements using polarized degrees of freedom, the situation is even more complex. On one side, Two-Photon-Exchange corrections on extractions of the proton form factor ratio from experiments using polarization are generally expected to be small compared to the effect on Rosenbluth-type measurements—similar to common normalization uncertainties, they are suppressed in asymmetries. On the other hand, measurements of polarization transfer observables exhibit so far theoretical unexplained deviations from their Born prediction [1170]. For SIDIS, calculations for arbitrary polarization of the initial nucleon can be found in [1171].

#### *Monte Carlo methods*

The structure of initial- and final-state radiation makes the development of efficient Monte Carlo generators a particularly hard problem. In convenient parametrizations of the scattering kinematics, cross sections vary by many orders of magnitude. A Monte Carlo generation with weighted events is then very inefficient. This also defeats naive rejection sampling methods to un-weight events, as the ratio of accepted events is then approaching zero. Automatic volume reweighting approaches are challenged by the high derivatives near the peak cross section.

Therefore, the algebraic structure has to be exploited to generate events suitably and efficiently. For the fixed-target elastic case, multiple generators for first-order (partly including soft-photon exponentiation) exist (e.g. [1158, 1172–1174]). They implement different ways to keep event weights constant or low-variance, improving MC efficiency. Recently, higher-order generators became available [1166, 1167]. It should be straightforward to port these generators to the situation at a collider, however, extra work is

needed to validate the calculation since numerical precision and efficiencies strongly depend on the kinematic conditions.

#### *QCD radiation and new directions*

Treating radiative effects as corrections to some Born-level base process becomes increasingly difficult for reactions beyond DIS. On the other hand, QCD higher-order graphs bear a close resemblance to these QED diagrams, and a unified approach handling both QCD and QED effects is possible. Based on the factorization theorem, it is possible to describe resummed leading logarithmic higher-order corrections with the help of distribution and fragmentation functions [1162]. Partons and photons can be treated democratically in the event generation, allowing resummation of higher-order corrections in the form of parton showers [1175]. In this way, hadronic radiation can be described, at least in the perturbative regime. This approach is currently implemented in the main HEP generators [1176].

#### *The way forward*

While the theoretical treatment of QED radiative corrections is well established, some questions remain, especially when hadronic effects come into play. Experimental validation is then required, and allows us to extract new information about these processes, transforming radiative corrections from a nuisance in the extraction of physics to a physics goal. For example, an exclusive measurement, i.e., one where the photon is detected, can give additional important information about the internal structure of the target. Deeply virtual Compton scattering is an example.

The ability to change the lepton charge, i.e., the ability to collide positron as well as electron beams with nucleons and ions, offers a powerful degree of freedom in the control of radiative corrections [1177]. Most importantly, the next term beyond the leading single photon exchange, is directly accessed via the ratio of positron to electron scattering, as has been pursued in experiments at DESY [1158], Jefferson Lab [1178] and VEPP-3 [1179]. Positron beams also offer unique scientific opportunities to access flavor separation of parton distributions and new electroweak structure functions, using the charged current electroweak interaction, as well as access to beam charge asymmetries to determine new Generalized Parton Distributions in the important Deeply Virtual Compton Scattering process. A possible program for the energy regime of JLAB-12 is describe in [284], similar physics opportunities would exist for an EIC. Realization of a positron beam at Jefferson Lab in advance of EIC would be very desirable in terms of achieving a better understanding of the radiative corrections to electron scattering.

Experiment design can be instrumental in reducing uncertainties. Here, progress thus far has been limited by the availability of suitable generators that apply in collider kinematics, a deficit which is currently being addressed. In parallel, it seems prudent to consider a systematic experimental test of radiative correction procedures once the EIC becomes operational. This will likely require a dedicated detector/beam configuration to enhance sensitivity to particular kinematics, where such corrections are large. It seems reasonable to organize a dedicated effort focused on radiative correction generator development and experimental validation in the EIC era.

*Summary*

Radiative corrections are an important uncertainty, and experiment design should take them into account, not only to minimize their effect, but also as a physics goal itself. While progress on the theoretical treatment, there is still some way to go, especially for the theory for  $e+A$ . On generators, more work must be done to either include radiative generators, or extend existing generators with radiative effects. There appear to be no real fundamental problems, but the amount of work required is still substantial, and corresponding efforts must be supported by the EIC community. A more detailed snapshot of the current state is reflected by the contributions to a recent ad-hoc workshop at the Center for Frontiers in Nuclear science [1180], the first in a series of meetings on this topic, with the next meeting planned for the end of 2020.

SNAPSHOT 19 Nov. 2020

## Chapter 8

# Detector Requirements

### 8.1 Inclusive Measurements

Inclusive reactions may be divided into two types of interactions – those that proceed via the exchange of a virtual photon or Z boson, referred to as neutral current (NC) events, and those that proceed via the exchange of a charged W boson, referred to as charged current (CC) events. By definition, inclusive reactions do not place any constraints on the flavor of the interaction that occurs at the boson-quark vertex or the type of particles produced in the final state. As a result, inclusive channels are sensitive to a range of QCD, electroweak and beyond-the-standard-model (BSM) processes and provide a wealth of physics opportunities. Examples include spin-averaged and spin-dependent nucleon and nuclear parton distributions functions, non-linear QCD and higher twist effects as well as CPT and Lorentz violating measurements.

#### 8.1.1 Reconstruction of kinematic variables

For inclusive reactions the kinematics of the interaction are reconstructed by either detecting the scattered beam electron, or by reconstructing the hadronic recoil. In the case of electron reconstruction the following definitions for  $x$ ,  $Q^2$  and  $y$  are used:

$$Q^2 = 4EE' \cos^2(\theta_p^{e'}/2) \quad y = 1 - \frac{E'(1 - \cos\theta_p^{e'})}{2E} \quad x = \frac{Q^2}{sy} \quad (8.1)$$

where  $s$  is the center-of-mass energy,  $E$  and  $E'$  are the energy of the incoming and scattered electron and  $\theta_p^{e'}$  is the angle of the scattered beam electron measured with respect to the incoming proton axis (+z). If the hadronic recoil is used to reconstruct the event kinematics, then the Jacquet-Blondel definitions are used instead:

$$Q_{JB}^2 = \frac{p_T^2}{1 - y_{JB}} \quad y_{JB} = \frac{(E - p^z)}{2E} \quad x_{JB} = \frac{Q_{JB}^2}{s y_{JB}} \quad (8.2)$$

where  $p_T^2 = (\sum_h P_h^x)^2 + (\sum_h P_h^y)^2$  and  $(E - p^z) = \sum_h (E_h - p_h^z)$  are summed over the all of the final state hadrons in the event. For CC channels, JB reconstruction is the only option, while for NC channels it is possible to use electron, JB or a mixture of electron and hadronic reconstruction techniques. Typically, JB reconstruction is used for events with small  $y$ , as the  $x$  and  $y$  resolutions decrease rapidly in this region for the electron reconstruction variables.

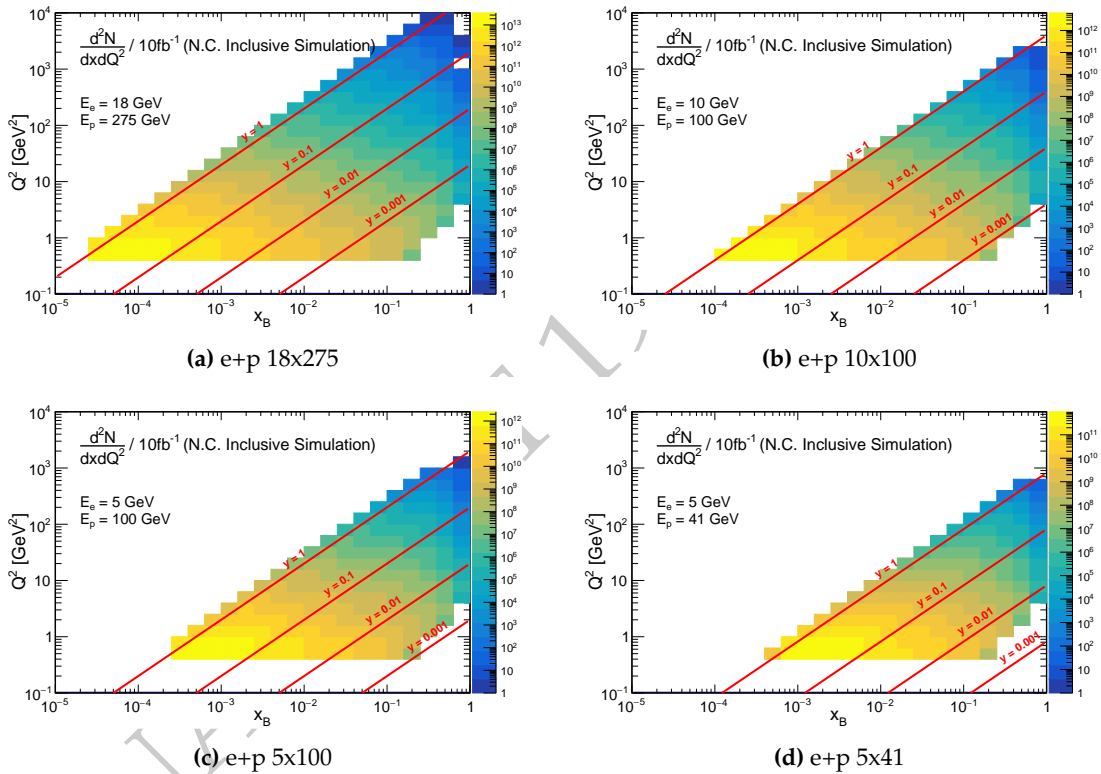


**Figure 8.1:** Differential yields for neutral-current interactions binned in  $x$  and  $Q^2$  for four proposed center-of-mass energies. These plots were created using the Pythia event generator with cuts of  $Q^2 > 0.5 \text{ GeV}^2/c^2$  applied at the vertex level. Radiative effects are not included.

The  $x$  vs  $Q^2$  coverage for NC electron reconstruction for four e+p beam configurations, 18x275, 10x100, 5x100, 5x41 GeV is shown in Figures 8.1a - 8.1d.

### 8.1.2 Kinematic phase space

The first step in defining detector requirements for the inclusive channels is to identify the kinematic regions in scattering angle  $\theta_p^{e'}$  and momentum  $p^{e'}$  for the final state electrons, photons and hadrons. Figures 8.2a-8.2d show the momentum- $\theta_p^{e'}$  distributions of the scattered beam electron for four beam e+p beam configurations, 18x275, 10x100, 5x100, 5x41 GeV. As expected, the electron typically scatters in the backward direction, between  $-3.5 < \eta < 1$ . The average momentum of the scattered electron increases with  $\sqrt{s}$  and  $Q^2$ , peaking at mid-to-forward rapidities.

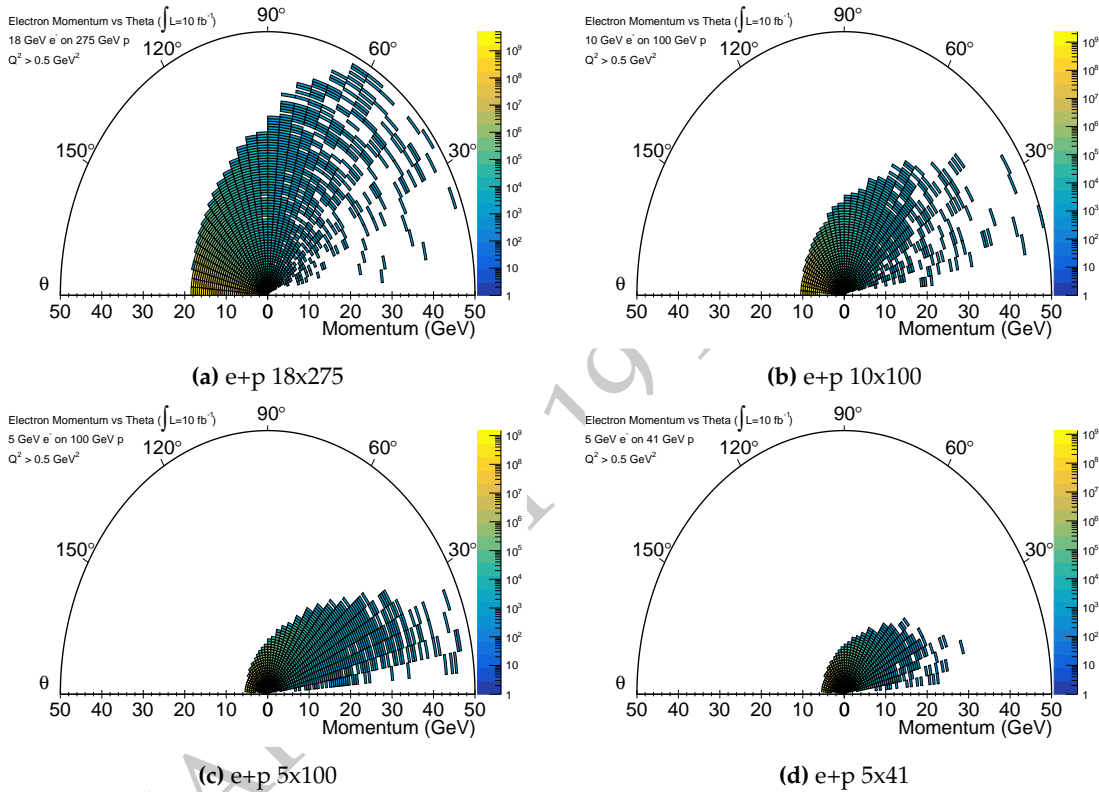


**Figure 8.2:** Polar plots of yields for scattered electrons in NC interactions binned in  $\theta_p^{e'}$  and  $p$  for four proposed center-of-mass energies. These plots were created using the Pythia6 event generator with cuts of  $Q^2 > 0.5 \text{ GeV}^2/c^2$  applied at the vertex level. Radiative effects are not included.

The distributions in 8.2a-8.2d only show the kinematics of the scattered beam electron with a minimal cut of  $Q^2 > 0.5 \text{ GeV}^2/c^2$ . Figure 8.3a shows the enhanced electron yield in the far forward regions, due largely to hadronic and leptonic decays. Figure 8.3b shows the same distribution for the scattered electron with  $(10 < Q^2 < 100) \text{ GeV}^2/c^2$  cuts applied.

Figures 8.4a - 8.4d show the momentum- $\theta_p^h$  distributions of the hadronic recoil in NC events for the four canonical beam configurations. The yield and average momentum are highly peaked in the proton beam direction. The accuracy of the JB reconstruction method

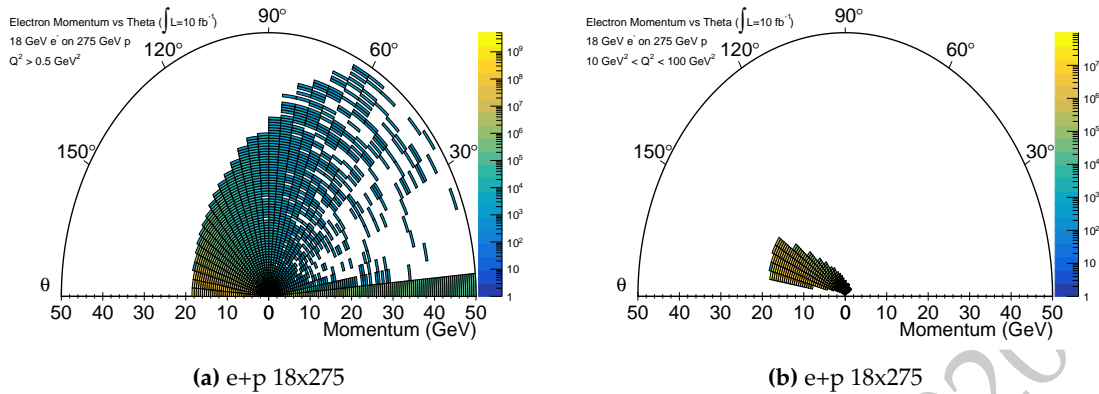


**Figure 8.3:** Polar plots of yields for detected electrons in NC interactions binned in  $\theta_p^{e'}$  and  $p$  for 18x275 beam configuration. The left plot includes scattered and decay electrons. The right plot is the scattered electron distribution but with a  $10 < Q^2 < 100 \text{ GeV}^2/c^2$  cut applied.

relies on detecting as much of this hadronic recoil as possible, motivating forward coverage for both electromagnetic (for photons) and hadronic calorimeters. Distributions for neutrons, protons and photons may be found in the inclusive reactions wiki [Can we add a link/reference?](#). The same distributions produced by the DJANGO event generator were found to be nearly identical to those generated by Pythia6 and may be found on the inclusive reactions wiki as well.

Charged Current events also rely on the JB reconstruction method so it critical to investigate the electromagnetic and hadronic recoil in CC events. Similar to the NC case, Figures 8.5a and 8.5b show a highly peaked distribution in the far forward region. However, in contrast to NC events, there is a much larger, higher momentum tail extending into the mid-forward rapidity region. The photon distributions are very similar to the hadron distributions, reinforcing the need for continuous electromagnetic and hadronic calorimeter coverage through the mid-rapidity region and as far possible into the forward region.

### 8.1.3 Electron Acceptance and Particle Identification

The detection and identification of the scattered electron is critical for nearly all inclusive reaction channels. The exception is the CC channel, where the resulting neutrino escapes undetected, and the kinematic reconstruction relies completely on the detection of the hadronic recoil. In those cases no particle identification (PID) is necessary, only energy and momentum reconstruction.

The minimum electron momentum that can be detected is set by the proposed acceptance of  $-3.5 < \eta < 3.5$  and the magnetic field of the detector. Figure 8.6 shows the limits placed on  $Q^2$ ,  $x$  and  $y$  due to the detector acceptance for 18x275 GeV NC events. The vast majority of the inclusive channels require a  $Q^2 > 1 \text{ GeV}^2/c^2$  and  $W^2 > 4 \text{ GeV}^2/c^4$  cut for interpretation within a pQCD framework. These requirements alone exclude nearly

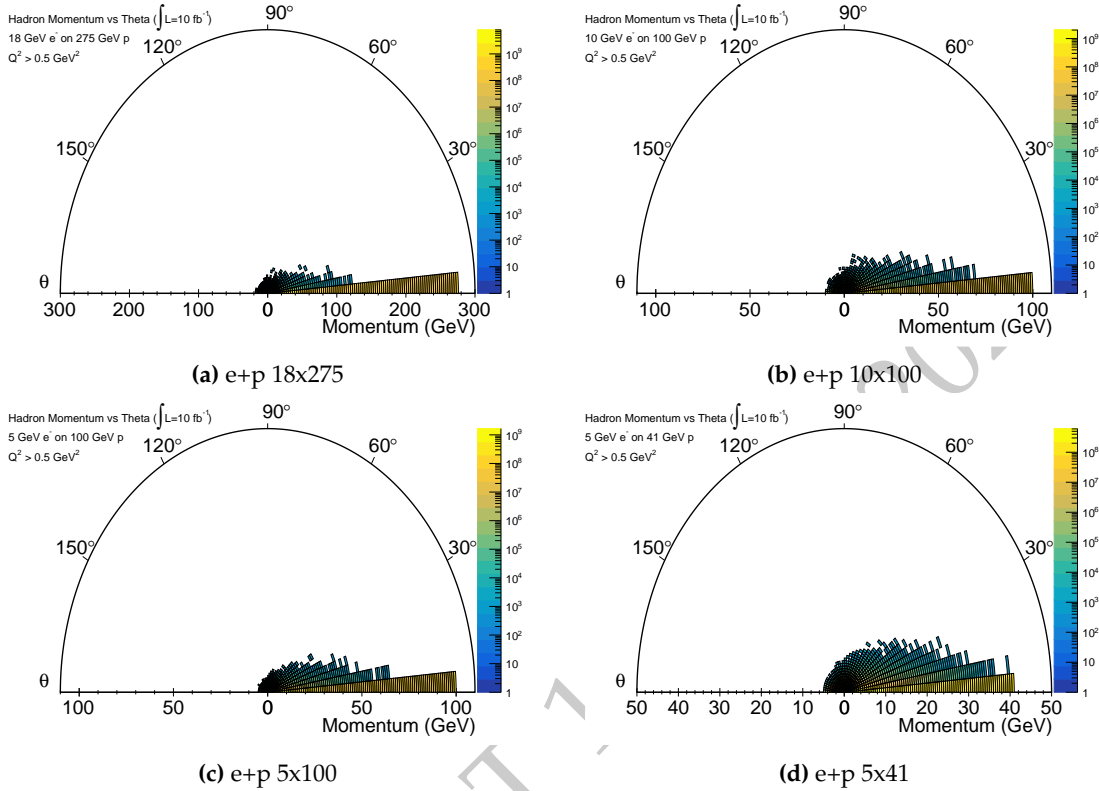


**Figure 8.4:** Polar plots of yields for scattered hadrons in NC interactions binned in  $\theta_p^{e'}$  and  $p$  for four proposed center-of-mass energies. These plots were created using the Pythia6 event generator with a cut cut of  $Q^2 > 0.5 \text{ GeV}^2/c^2$  applied at the vertex level.

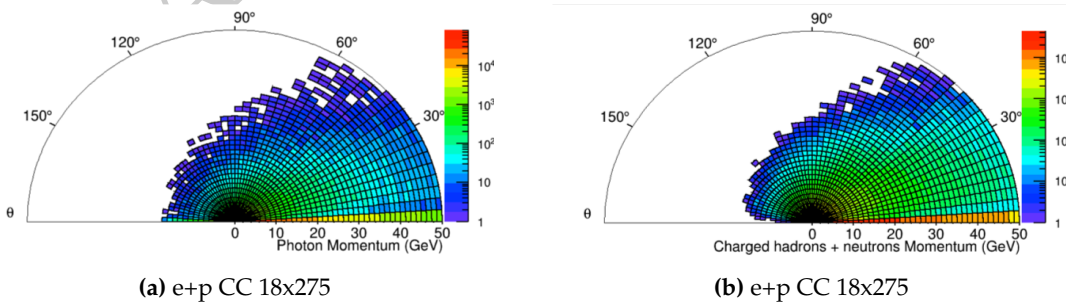


**Figure 8.5:** Polar plots of yields for photons (left) and hadrons (right) in CC interactions binned in  $\theta_p^{h/\gamma}$  and  $p$  for 18x275 GeV beam configuration.

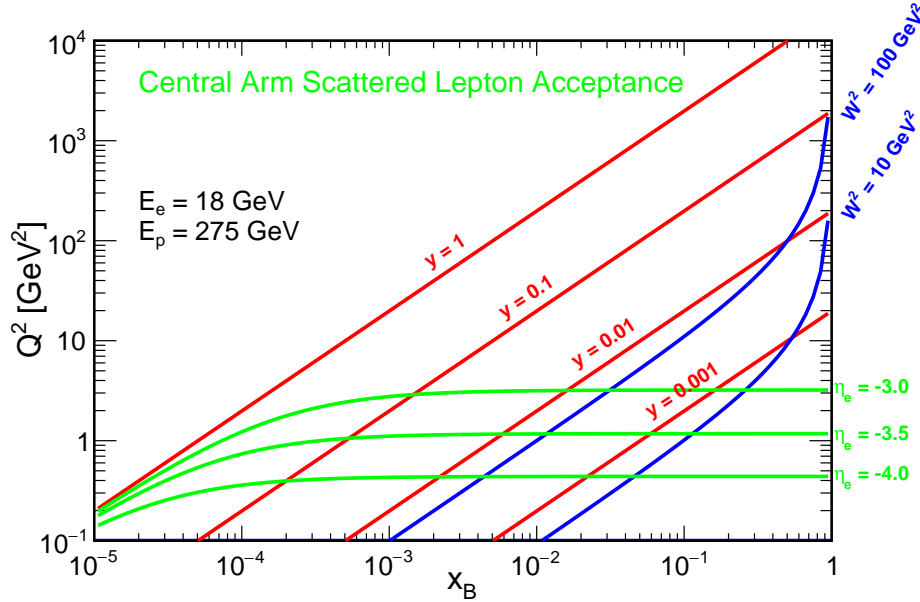


**Figure 8.6:** Scattered lepton acceptance as a function of  $x_B$  and  $Q^2$  for 18x275 GeV beam collisions. Green lines denote possible fiducial edges of the proposed central arm detector. Red and blue lines indicate the lines of constant  $y$  and  $W^2$ .

the entire available phase space for  $\eta < -3.5$ . The conclusion is that inclusive reactions with these kinematic cuts do not require detection capabilities beyond  $\eta = -3.5$ . By their nature, gluon saturation, color glass condensate and low  $Q^2$  photo-production studies do not have these requirements and would likely utilize detectors in the far backward region.

In addition to the minimum  $Q^2$  requirement, a  $y < 0.95$  cut is typically applied in order to maintain a reasonable  $Q^2$  resolution. Figure 8.7 shows the minimum momentum of the detected electron as a function of detector  $\eta$ . Note that this figure does not account for any acceptance losses at low momentum due to curvature in the magnetic field. Once included, the minimum momentum is likely to be  $\sim 500$  MeV/c.

Electron PID is required to suppress two types of backgrounds. The largest background comes from the significant rate of same-sign charged pion production. Figures 8.9a-8.9d show the scattered  $e^-$  and  $\pi^-$  yields, for each center-of-mass configuration, as a function of particle momentum for six bins in the range  $-3.5 < \eta < 3.5$ . The dashed grey lines mark the minimum momentum of the detected electron for the given  $\eta$  bin. Table 8.1 documents the maximum  $\pi^-/e^-$  for each beam

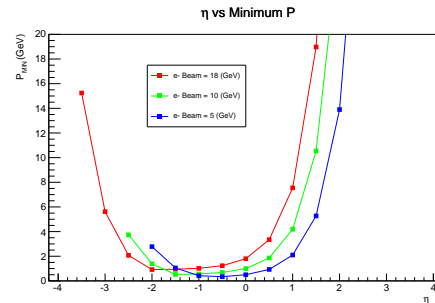


**Figure 8.7:** The  $p_{MIN}$  of the scattered  $e^-$  vs detector  $\eta$ . In the central, central-backward region, the scattered  $e^-$  momenta extend down to 0.3-0.5 GeV/c. These calculations do not include magnetic field effects.

configuration and  $\eta$  bin. Note, bins with negligible  $e^-$  rates above the minimum detectable momentum are omitted from the table.

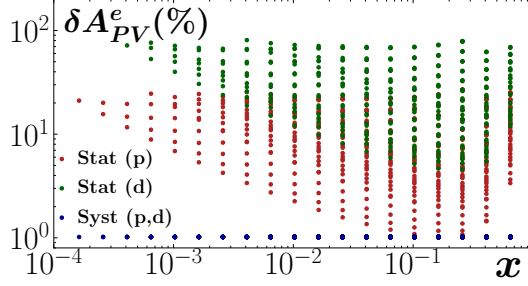


**Figure 8.8:** The % statistical and systematic errors for the electron parity violating asymmetry  $A_{PV}^e$  from  $10fb^{-1}$  of  $e^- + p$  and  $e^- + d$  running.

shown in Fig. 8.8 and the systematic error formulation outlined in Eq. 3.12.2 in [1181]. In contrast, the  $A_{LL}$  asymmetries tolerate contaminations on the order of  $\sim 0.01 \pi^- / e^-$ .

The most stringent constraints on the detector electron PID capabilities come from the longitudinal double spin and parity violating asymmetries,  $A_{LL}$  and  $A_{PV}^e$ . The pion contamination has two effects; it inflates the statistical errors because it typically acts as a dilution on the electron asymmetry and it incurs a  $\sim 1\%$  systematic error on the correction. In the case of  $A_{PV}^e$ , requiring the pion contamination systematic error to be  $\sim 10\%$  of the statistical error translates into the strict limit of  $1 \times 10^{-3} \pi^- / e^-$  contamination. This estimate is based on the statistical errors

$E_{beam}^{e^-}$ (GeV)	$\eta$ bin	$p_{min}^{e^-}$ (GeV)	Max $\pi^- / e^-$	final $\pi^- / e^-$ ratio
18	(-3.5,-2)	0.9	200	0.02
18	(-2,-1)	0.9	800	0.08
18	(-1, 0)	1.0	1000	0.1
18	(0, 1)	1.8	100	0.01
10	(-3.5,-2)	1.4	10	0.001
10	(-2,-1)	0.5	400	0.04
10	(-1, 0)	0.6	800	0.08
10	(0, 1)	1.0	1000	0.1
5	(-3.5,-2)	2.8	0.1	0.00001
5	(-2,-1)	0.4	100	0.01
5	(-1, 0)	0.3	500	0.05
5	(0, 1)	0.5	1000	0.1

**Table 8.1:** The minimum detected  $e^-$  momentum, the maximum  $\pi^- / e^-$  ratio and detector level  $\pi^-$  suppression for each beam energy and scattered  $e^-$   $\eta$  bin. The calculation of  $p_{min}^{e^-}$  includes a  $Q^2 > 1$  and  $y < 0.95$  requirement.

The current estimate of  $\pi^-$  suppression, at the detector level, is  $10^{-4}$ . Applying this factor to the current estimates of  $\pi^- / e^-$  rates results in the suppression indicated in column 4 of Table 8.1. For the highest beam energies the requirement for  $A_{LL}$  is only met for the  $0 < \eta < 1$  bin. The situation improves for lower energy beams but is still not met for  $\eta > -2$  for

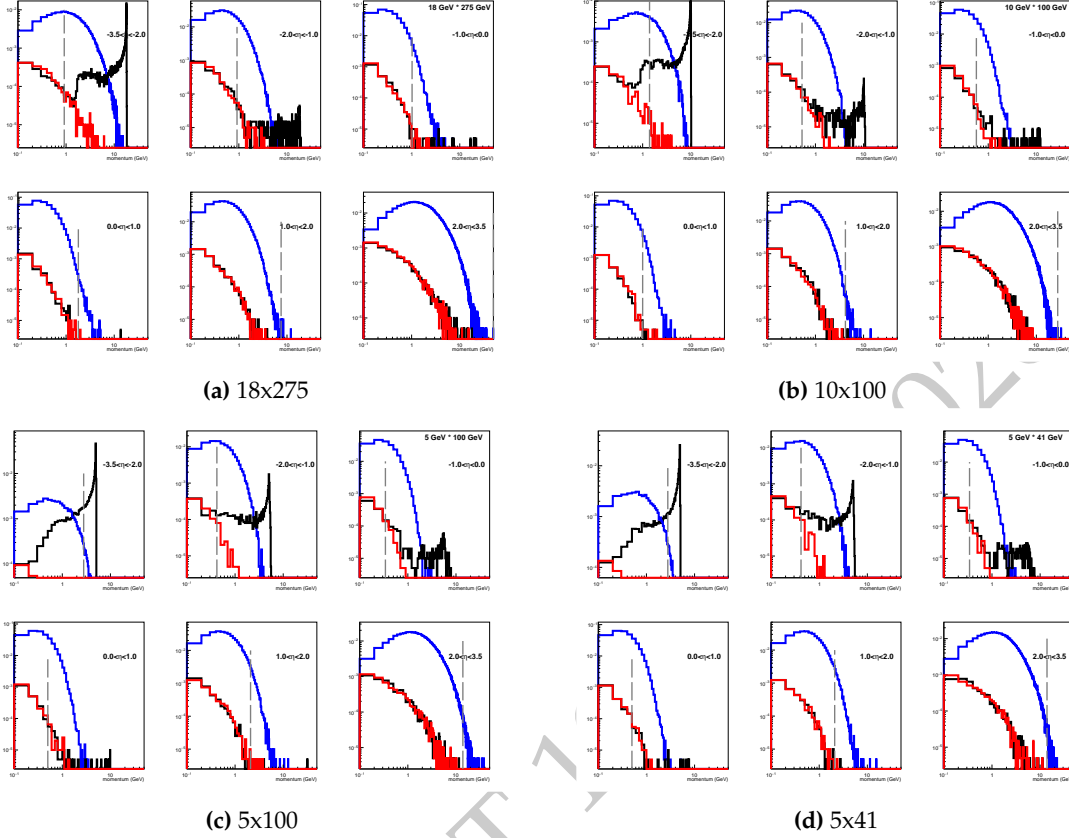


**Figure 8.9:** Electron (black), positron (red) and negatively charged pion (blue) yields for the four canonical beam configurations and six pseudorapidity bins. The dashed line indicates the minimum scattered electron momentum within the detector acceptance.

$E_{beam}^{e^-} = 10$  GeV and  $\eta > -1$  for  $E_{beam}^{e^-} = 5$  GeV. It is worth noting that  $\pi^-$  suppression may be enhanced through software pion ID algorithms that were not included in these studies and are expected to increase pion suppression by factors of 2-4. Studies that incorporate realistic detector materials and response to hadronic interactions are necessary to robustly evaluate  $\pi^-$  suppression capabilities.

Pair-symmetric production of  $e^-$  constitutes the second most significant background contribution to inclusive channels. These electrons are the result of pair-production via interactions of the scattered electron with detector material and Dalitz decays. The pair-symmetric contribution to the total  $e^-$  yield is represented by the red  $e^+$  distribution in Figures 8.9a-8.9d. Robust evaluations of the size of the pair-symmetric background require simulation of the full material budget. Corrections are typically based on a combination of dedicated systematic runs (with a reversed magnetic field for example) and analysis level-algorithms that discriminate between the scattered electron and pair-symmetric backgrounds.

### 8.1.4 Resolution and bin migration effects in electron reconstruction.

The resolution on the reconstruction of  $x$ ,  $Q^2$  and  $y$  via electron detection in NC events was evaluated by passing  $10 fb^{-1}$  of  $18 \times 275$ ,  $10 \times 100$  and  $5 \times 100$  GeV neutral current pseudo-data through the EICSmear fast simulation package. The pseudo-data was produced using the DJANGO event generator with full radiative effects turned on. The EICSmear package implements a one mRad smearing in  $\theta$  and  $\phi$  and an energy resolution of  $2\% \oplus 1\%$ ,  $7\% \oplus 1\%$ ,  $12\% \oplus 2\%$  for the backward, mid and forward electromagnetic calorimeters.

The resolution  $\Delta x/x$  and  $\Delta y/y$  can be shown from Eqs.8.2 to diverge as  $y \rightarrow 0$ . Indeed the plots in Figure 8.11 show that  $\Delta y/y$  and  $\Delta x/x$  diverge at small  $y$ . The resolution on the reconstruction of  $x$  also develops a systematic offset with a subset of high  $x$  events being reconstructed with very low  $x$ . This offset originates from the large positive fluctuations of  $y$ , due to the increasing poor resolution at low  $y$ , which then lead to the suppression in  $x$ . The plots in figure 8.12 show that this offset effect is mitigated once a  $y > 0.01$  cut is applied. Similarly, as  $y \rightarrow 1$  the scattered electron energy and  $\theta_p^{e'}$  become small. Figure 8.10 shows that the resolution on the reconstructed energy degrades as the scattering goes more forward, motivating a  $y < 0.95$  cut as well.

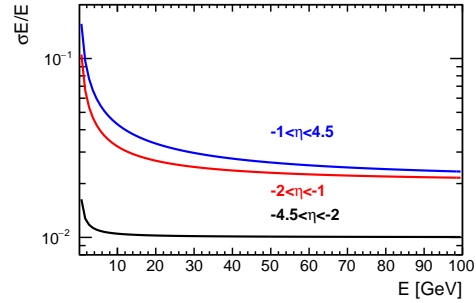


**Figure 8.10:** Energy resolution as a function of  $e^-$  energy for the backward, central and forward electromagnetic calorimeters.

With the appropriate inelasticity cuts established it is important to evaluate the purity and stability for the detector resolutions proposed in the detector matrix. The purity is defined as the fraction of events reconstructed in a given bin that were generated in the same bin. It reflects the bin migration into a reconstructed kinematic bin  $(x_R, y_R, Q_R^2)$ . The stability is defined as the fraction of events generated in a given bin that were reconstructed in the same bin. It reflects the migration of events outside of a generated kinematic bin  $(x_G, y_G, Q_G^2)$ . For a given detector configuration, the  $x$  and  $Q^2$  binning should be optimized in order to maximize both purity and stability and therefore minimize the size and systematic errors associated with kinematic corrections. In an effort to test the proposed calorimeter resolutions the process was reversed, with the binning first chosen to be five bins in  $x$  and 4 bins in  $Q^2$  per decade. Figures 8.13a - 8.13b show that the purity and stability are both well above 30% for all bins, the typical lower limit deemed acceptable in HERA analyses. The conclusion is that, with the  $y > 0.01$  cut applied, the current detector resolutions are sufficient.

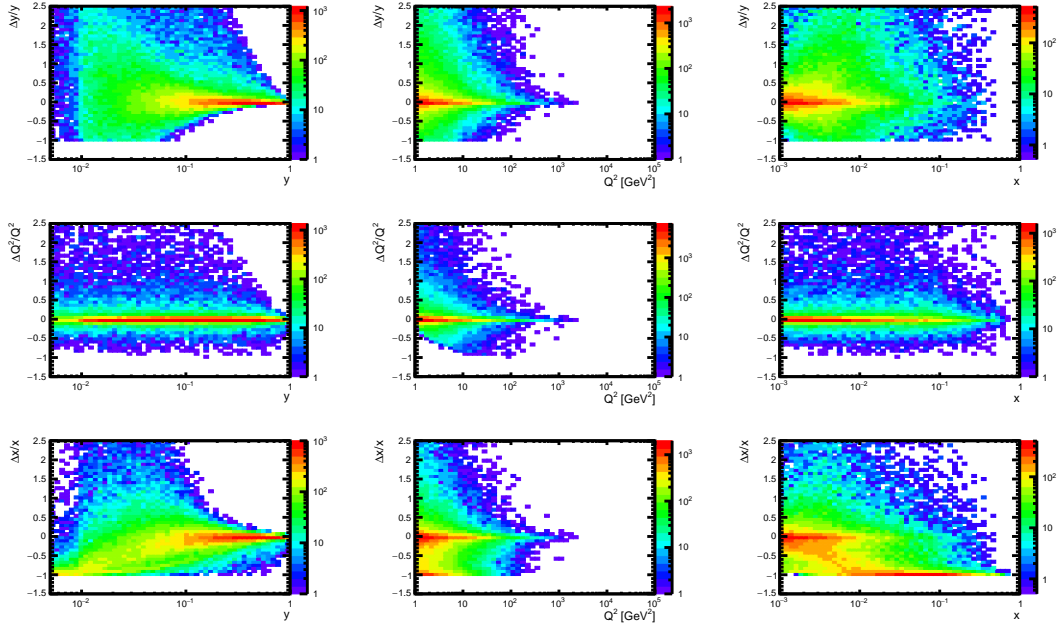


**Figure 8.11:** Resolutions, defined as (reconstructed - true)/true, for kinematic variables in NC 18x275 events. The inelasticity is required to be  $\gamma < 0.95$

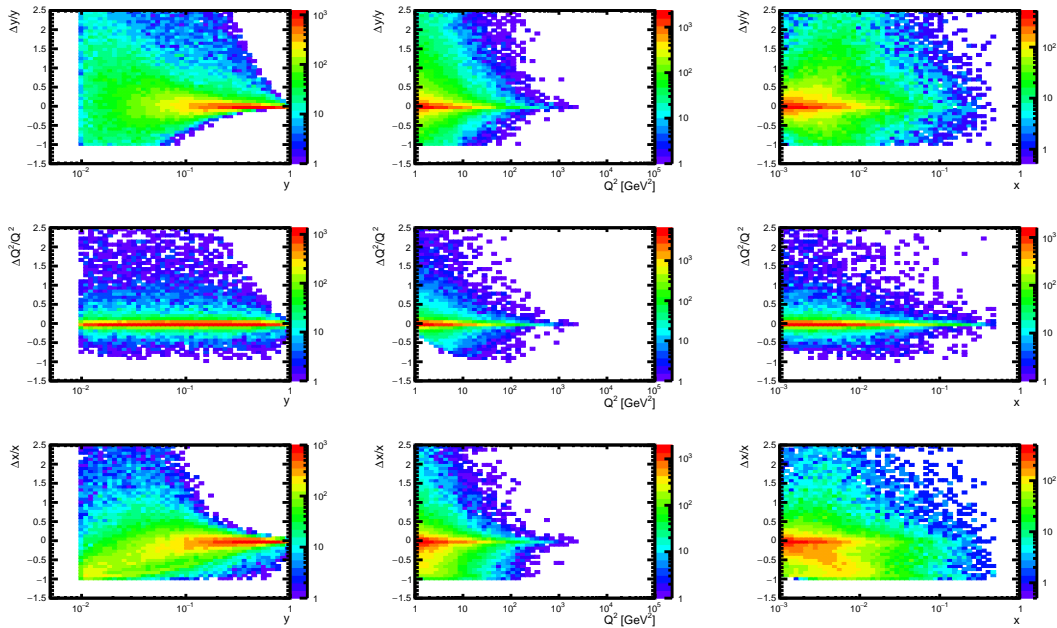


**Figure 8.12:** Resolutions, defined as (reconstructed - true)/true, for kinematic variables in NC 18x275 events. The inelasticity is required to be  $0.01 < \gamma < 0.95$

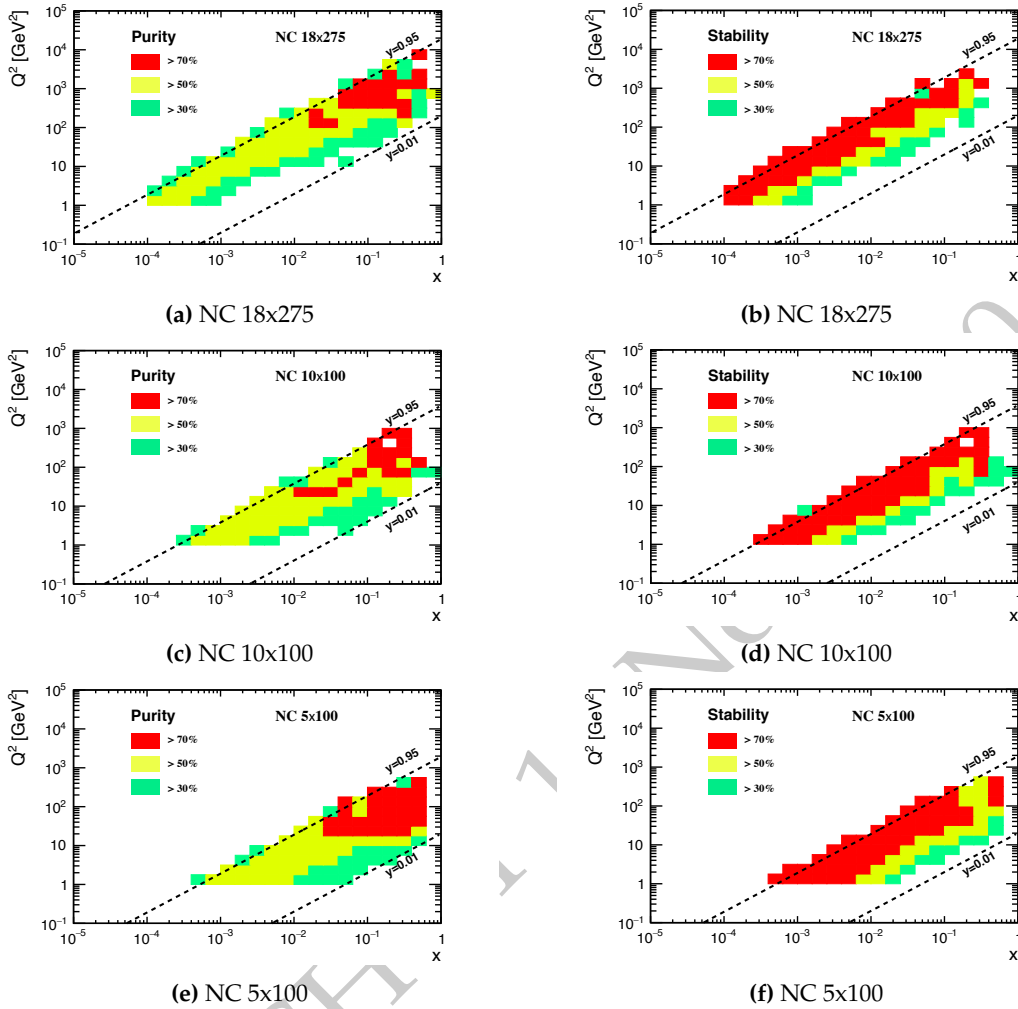


**Figure 8.13:** The purity (left) and stability (right) for 18x275 GeV (top), 10x100 GeV (middle) and 5x100 GeV (bottom) beam configurations.

### 8.1.5 Acceptance, resolution, and bin migration effects in Jacquet-Blondel reconstruction

The resolution on the reconstruction of  $x$ ,  $Q^2$  and  $y$  via hadronic reconstruction in either CC or NC events was evaluated by passing  $10 \text{ fb}^{-1}$  of 18x275 GeV NC and CC pseudo-data through the EICSmear fast simulation package. The pseudo-data was produced using the DJANGO event generator with full radiative effects turned on. In addition to the EICSmear settings described in the previous section, the barrel hadronic calorimeter resolution was set at  $85\% \oplus 7\%$  and the back/forward hadronic calorimeters at  $45\% \oplus 6\%$ .

As demonstrated in Figures 8.5a and 8.5b the hadronic recoil of CC and NC events extends past the proposed nominal coverage of  $-3.5 < \eta < 3.5$ . The accuracy of the JB reconstruction method relies, in part, on the fraction of particles that are reconstructed in the detector

acceptance. The blue and black curves in Figure 8.14 show the distribution of the final state kaons, pions, neutrons, protons and photons, with and without the acceptance cut applied. Approximately 30% of all final state particles fall outside the  $-3.5 < \eta < 3.5$  acceptance. Despite losing nearly a third of the final state particles in the CC event, the changes in the reconstructed  $x$ ,  $y$ , and  $Q^2$  are minimal. Figure 8.15 shows the kinematic variables reconstructed at the true, or vertex level, compared with the reconstructed variables with nominal ( $-3.5 < \eta < 3.5$ ) or expanded ( $-4.0 < \eta < 4.0$ ) acceptance. The difference between the nominal and expanded reconstruction is negligible for  $x$ ,  $y$  and  $Q^2$ .

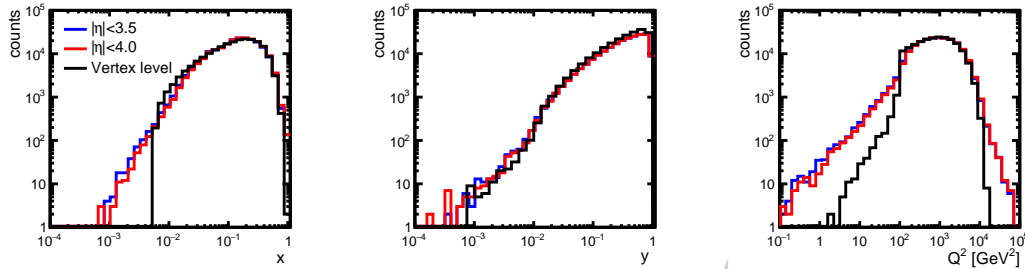


**Figure 8.15:** JB reconstruction of  $x$ ,  $y$  and  $Q^2$  for the vertex level (black), nominal (blue) and expanded (red) reconstruction.

As in the case of the electron reconstruction, it is important to investigate bin migration effects in JB reconstruction. Specifically, the detector group requested an investigation into several resolution performances for the hadronic calorimeter in the forward region. Figures 8.16a - 8.16f show the purity and stability for  $40\% \oplus 5\%$ ,  $45\% \oplus 6\%$  and  $50\% \oplus 10\%$  resolution. In all cases the stability and purity are worse than in the electron reconstruction case, but the differences are not large, suggesting the bin migration effects not driven by differences in hadronic calorimeter resolution at this level.

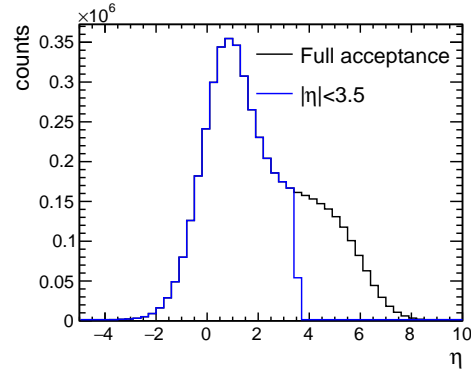


**Figure 8.14:** The  $\eta$  distribution of all final state hadrons and photons with (blue) and without (black) the nominal acceptance cut.

### 8.1.6 Generator Verification

The *Pythia6* and *Djangoh* monte-carlo event generators were used extensively to determine the above detector requirements, as well as provide estimates of the statistical and systematic uncertainties used in the inclusive pseudo-data. For these reasons, it was necessary to validate that the monte-carlo generators give reasonable results when compared to data and theory calculations.

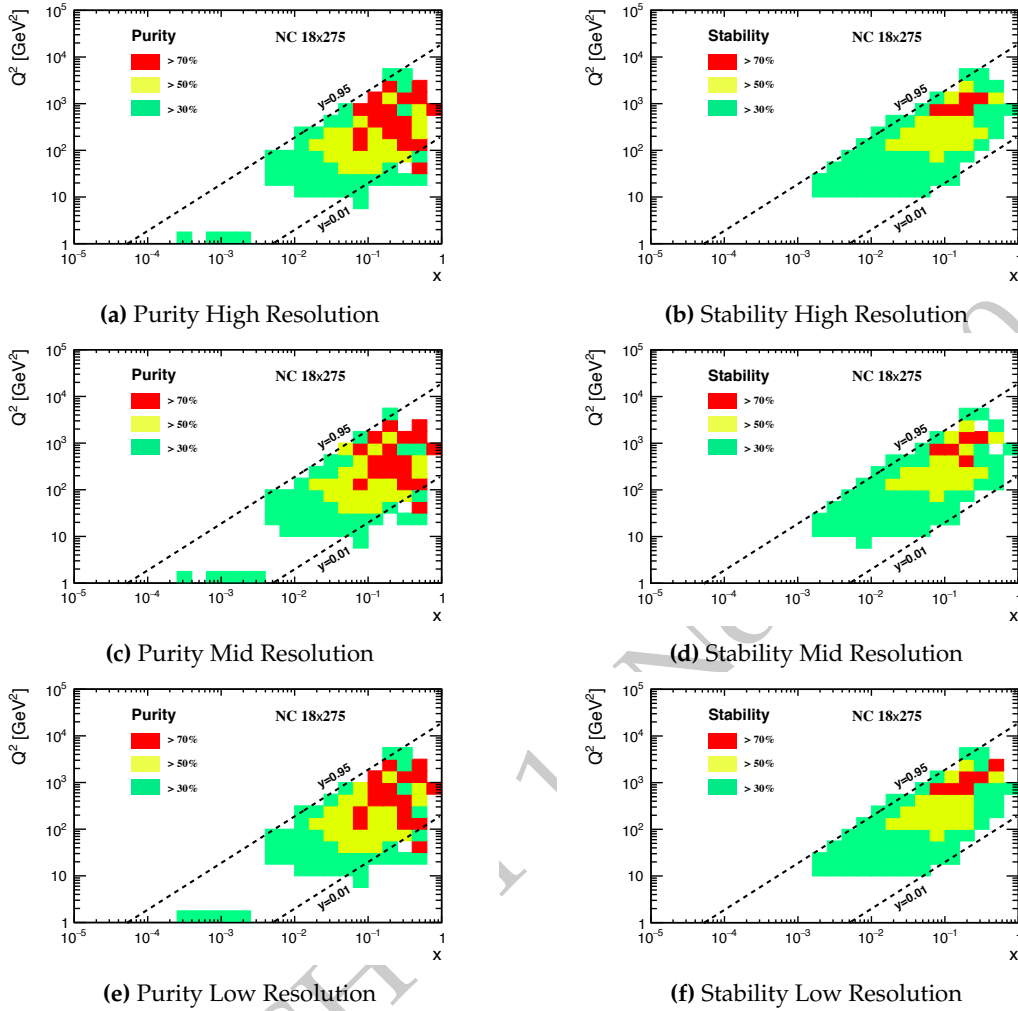


**Figure 8.16:** The purity (left) and stability (right) for JB reconstruction of NC events in 18x275 GeV collisions. The resolution of the back/forward hadronic calorimeter is varied from  $40\% \oplus 5\%$  (top),  $45\% \oplus 6\%$  (middle) to  $50\% \oplus 10\%$  (bottom). The resolution of the barrel hadronic calorimeter is fixed at  $85\% \oplus 6\%$ .

Comparisons of the reduced inclusive positron-proton NC cross section for both event generators to *HERA* data are shown in figure 8.17. The *Djangoh* simulation was performed using the cteq61.LHgrid (10150) LHAPDF5 grid as a PDF input, while the *Pythia6* simulation was performed using the cteq6ll.LHpdf (10042) LHAPDF5 grid. As can be seen in the figure, the *Djangoh* simulation agrees better with the *HERA* data at lower  $Q^2$ , and both simulation programs agree well with the data at higher  $Q^2$ . In addition, modern PDF fits at LO, NLO, and NNLO are compared to the *HERA* data in figure 8.18. These theory calculations then served as the baseline for validating the monte-carlo simulations at *EIC* energies.

Comparisons of the electron-proton NC reduced cross sections at the *EIC* energy setting of

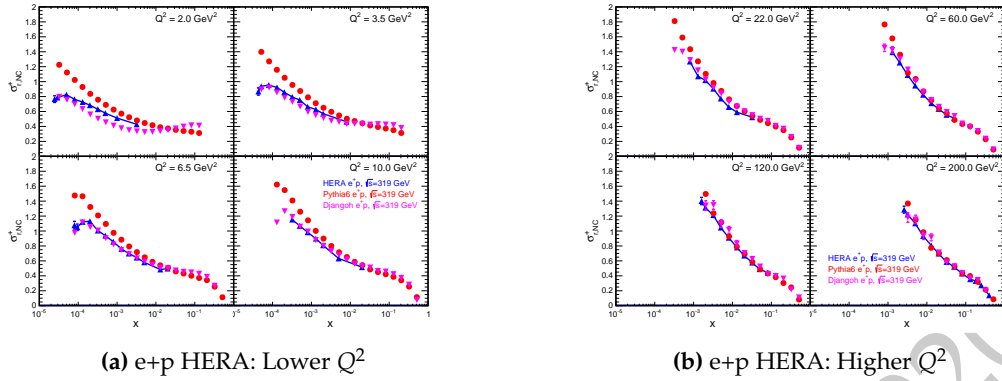


**Figure 8.17:** Comparison of *Pythia6* and *Djangoh* monte-carlo event generators at *HERA* energy with the EIC tune to *HERA* NC inclusive cross section measurements. The simulation cross sections are calculated from the generators at the vertex level with QED Radiative effects turned OFF.

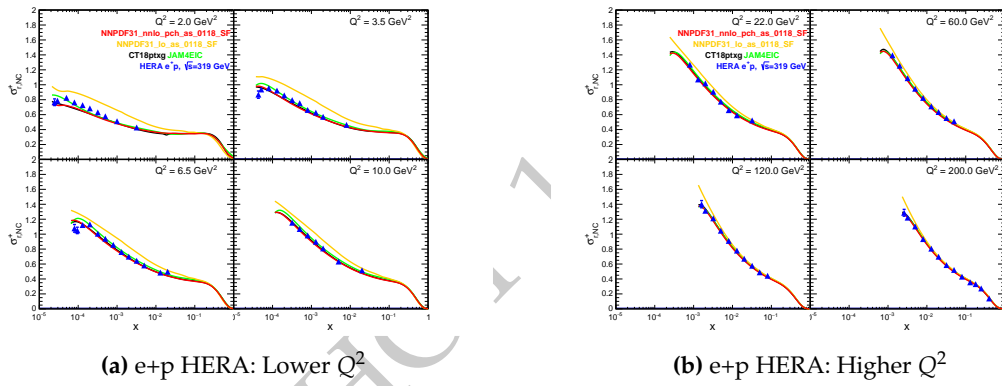


**Figure 8.18:** Comparison of modern PDF fit results to *HERA* NC inclusive cross section measurements. The cross section is calculated at LO for the orange curve; at NLO for the green curve; and NNLO for the red and black curves.

$18 \times 275$  GeV extracted from the monte-carlo simulations to those calculated from the PDF fits are shown in figure 8.19. (Results are similar for the other studied beam energy configurations –  $5 \times 41$  GeV,  $5 \times 100$  GeV, and  $10 \times 100$  GeV.) The binning chosen is equivalent to the one shown in figure 8.1a. The simulation events have been corrected for bin-centering effects (which are on the order of 5-8% for the chosen binning) using a cross section model in order to quote the reduced cross sections at the center of each  $x$ - $Q^2$  bin.

In figures 8.19a and 8.19b, the *Pythia6* simulation was performed using the *cteq6ll* PDF set; while in figures 8.19c and 8.19d, the *Pythia6* simulation was run using the *cteq6l* PDF set. In all cases, the *Djangoh* simulation was run using the *cteq6l* PDF set. As can be seen, the simulation performed using the *cteq6l* PDF set more accurately reproduces the low  $x$ , low  $Q^2$  fit cross sections results; and the simulation performed using the *cteq6ll* PDF set more accurately reproduces the higher  $x$ , higher  $Q^2$  fit cross sections results. The simulation

results agree with the fit results to the 10% level over most of the kinematic phase space.

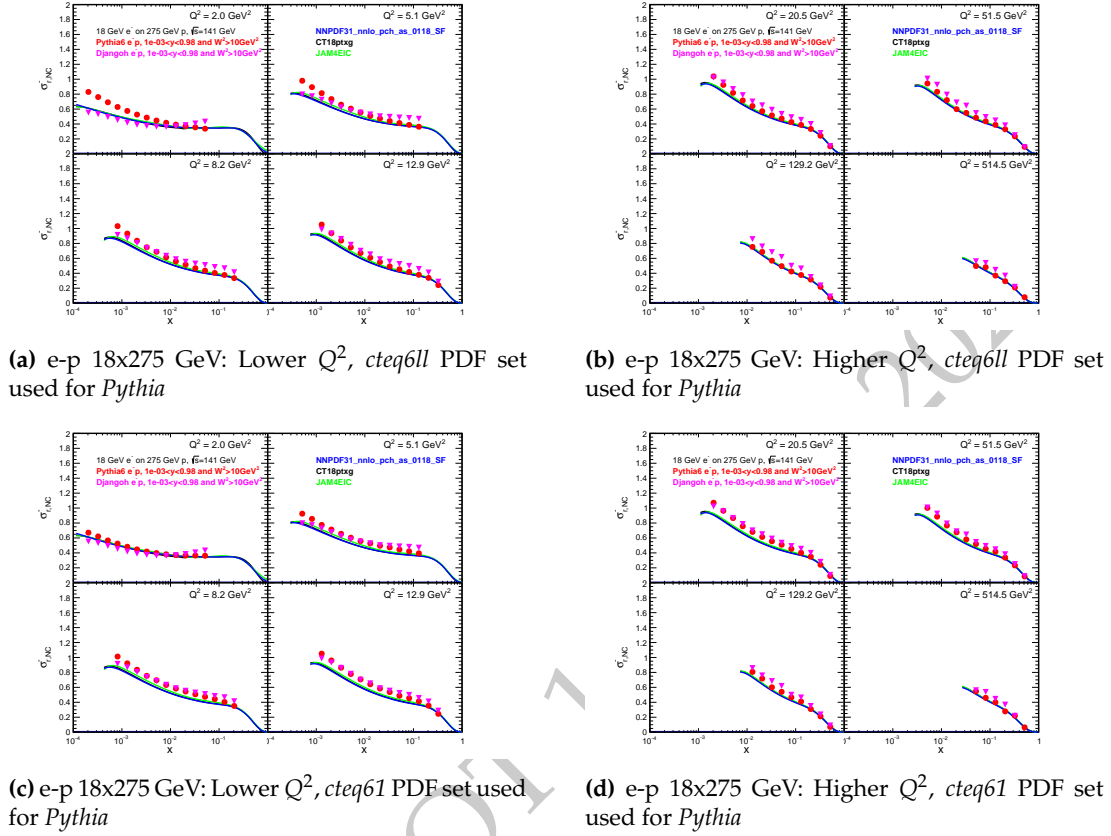


**Figure 8.19:** Comparison of *Pythia6* (red) and *Djangoh* (pink) reduced cross-sections for  $e^- + p$  scattering at 18x275 to NNPDF [7] [9], CT18 [14] and JAM [16] global fits. The top row uses *cteq6ll* PDFs for *Pythia6*, while the bottom row uses *cteq61*. The *cteq61* PDFs were used for all *Djangoh* simulations.

Figure 8.20 shows excellent agreement, for  $Q^2$  of 110, 130, 200 and 400  $GeV^2$ , between the differential charged current cross-sections reconstructed at the vertex level with NLO theory curves produced with xFitter. The 10  $fb^{-1}$  of CC pseudo data was simulated with the DJANGO generator.

### Systematic Uncertainties for the Inclusive Pseudo-data

As the uncertainties on the NC inclusive cross section measurements at the EIC will be dominated by systematic errors for much of the probed kinematic phase space, it is necessary to make estimates of those errors for the generated pseudo-data. For the CC inclusive cross section and the single-spin and double-spin asymmetry measurements, the systematic uncertainty will most likely be at a similar level as the statistical uncertainty for much of the measured kinematic phase space. Although it is very difficult to determine systematic uncertainties for an accelerator and detector which have not yet been constructed,

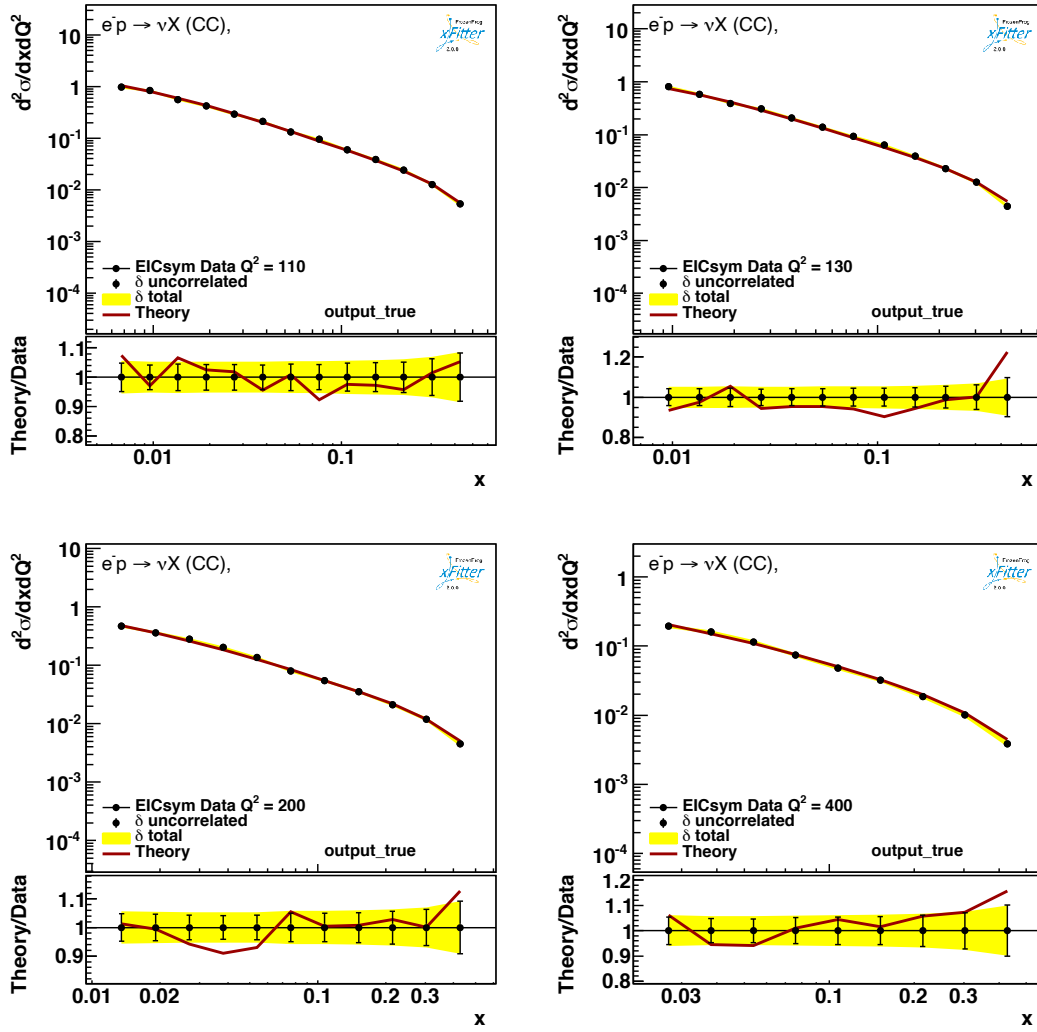


**Figure 8.20:** Comparison of CC differential cross-sections reconstructed from  $10 \text{ fb}^{-1}$  of pseudo-data created with DJANGO and NLO theory curves from xFitter [1182].

estimates of these uncertainties can be made based on the experience of previous experiments (primarily those at *HERA*) as well as simulation studies using the EIC Handbook detector and the current EIC detector matrix.

The systematic uncertainties on the pseudo-data were divided into uncorrelated uncertainties (i.e. point-to-point or bin-by-bin uncertainties) and scale uncertainties (i.e. normalization uncertainties). No attempt was made to estimate partially correlated systematic uncertainties. Two sets of systematic uncertainties were constructed: an optimistic set and a pessimistic set.

For the unpolarized NC electron(positron)-proton cross section measurements, the esti-

mate of the uncorrelated uncertainty was 1.5% (2.3%) in the optimistic (pessimistic) scenario. These uncertainties came from a 1% uncertainty on the Radiative corrections; and a 1-2% uncertainty due to detector effects. An additional uncertainty of 2% was added for the pseudo-data with  $y < 0.01$ , as hadronic reconstruction methods are required in that kinematic region. The normalization uncertainty was set at 2.5% (4.3%) in the optimistic (pessimistic) scenario. This included a 1% uncertainty on the integrated luminosity; and 2-4% uncertainty due to detector effects. During the fits of the pseudo-data, the normalization uncertainty was treated as fully correlated between different beam energy settings.

The same uncertainties were used the unpolarized NC electron-nucleus cross section measurements, with the exception that data at  $y < 0.01$  was not included for the e-A pseudo-data sets.

For the unpolarized CC electron(positron)-proton cross section measurements, a uncorrelated uncertainty of 2% and a normalization uncertainty of 2.3/5.8% was used for the optimistic/pessimistic scenarios of the pseudo-data. The point-to-point uncertainties came from a 2% on the background subtraction and a 0.5% uncertainty on acceptance and bin-centering effects. The normalization uncertainties include optimistic/pessimistic contributions from luminosity, radiative corrections and simulation errors.

## 8.2 Semi-Inclusive Measurements

### 8.2.1 General SIDIS kinematics and requirements

Semi-inclusive DIS (SIDIS) uses the information of the hadronic final state to obtain additional information about the nucleon or nuclei with the help of fragmentation functions. Fragmentation functions can inform about the spin, momentum (transverse and longitudinal) and, in particular, flavor of an outgoing parton. As such, in addition to the main DIS kinematics as obtained by the scattered lepton or the total hadronic final state one or several final-state hadrons have to be detected as well. The applicability of perturbative QCD for the hard processes and factorization into non-perturbative distribution and fragmentation functions to be valid, the DIS kinematics require a  $Q^2$  larger than  $1 \text{ GeV}^2$ . Together with a selection of  $0.01 < y < 0.95$  and  $W^2 > 10 \text{ GeV}^2$  they will be referred to as DIS cuts in the following. For the final state hadrons the fractional momentum  $z = \frac{P_{in} \cdot P_h}{P_{in} \cdot q}$ , where  $P_{in}$  is the incoming nucleon 4-momentum,  $q$  is the momentum transfer and  $P_h$  is the 4-momentum of the outgoing hadron, ranges typically between 0.1 and 1. Particularly higher  $z$  are of interest, since the correlation with the fragmenting partons flavor, spin, etc is higher. Typically, hadrons that are part of the outgoing nucleon remnant (so-called target fragmentation) are found at low  $z$ . Such hadrons are not as important for the main SIDIS measurements. In addition to the  $z$  of the hadron, also the type of detected hadron needs to be reconstructed as it is strongly correlated with the fragmenting flavor. These characteristics define the general range of scattered lepton and detected hadrons in terms of energy and rapidity. They are summarized in Fig. 8.21 for the highest collision energies. As can be seen, the scattered lepton rapidity and momentum moves with increasing  $Q^2$

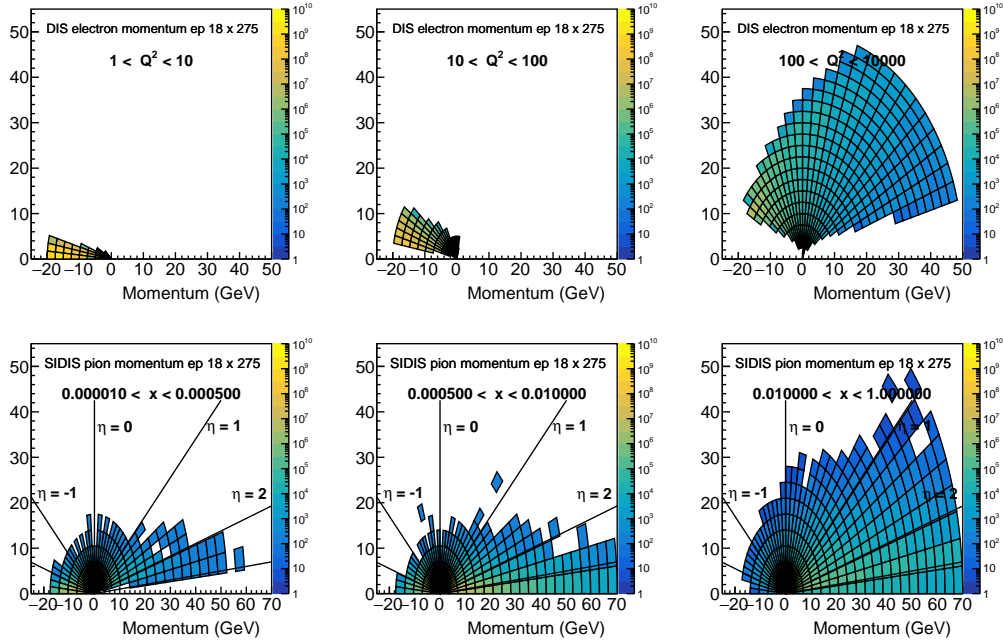


**Figure 8.21:** Top panel: Polar figures of the scattered DIS lepton momentum distributions for the highest collision energies for small to high momentum transfers from left to right. Bottom panel: Polar figures of SIDIS hadron momentum distributions for the highest collision energies for small to high  $x$  from left to right. All yields are extrapolated to  $10 \text{ fb}^{-1}$  of accumulated luminosity.

from backward rapidities and being bounded by the electron beam energy to forward rapidities and energies that are governed by the hadron beam energy. In contrast, the hadron kinematics are more closely correlated with the  $x$  of the event. At low  $x$  the hadron gets predominantly emitted into the backward region and the momentum follows that of the electron beam. With increasing  $x$  the fragmenting hadrons move into the forward region and can take up substantial fractions of the hadron beam momentum.

Within these rapidity and momentum ranges, a good tracking resolution is required not only for the hadrons but even more so for the scattered leptons. The reason for this lies in the fact that hadron transverse momenta and azimuthal angles, that are generally necessary for all TMD related measurements, are typically defined relative to the virtual photon axis in the frame where the incoming nucleon is at rest. The scattered lepton momenta provide the boost into that frame and can substantially distort those distributions.

### 8.2.2 Hadron PID impact on 4D TMD measurements

As described in the previous part, the hadron momenta can reach up to  $18 \text{ GeV}/c$  in the backward region ( $-4 < \eta < -1$ ), occasionally more than  $10 \text{ GeV}/c$  at central rapidities ( $-1 < \eta < 1$ ), and more than  $50 \text{ GeV}/c$  at forward rapidities ( $1 < \eta < 4$ ). For all SIDIS

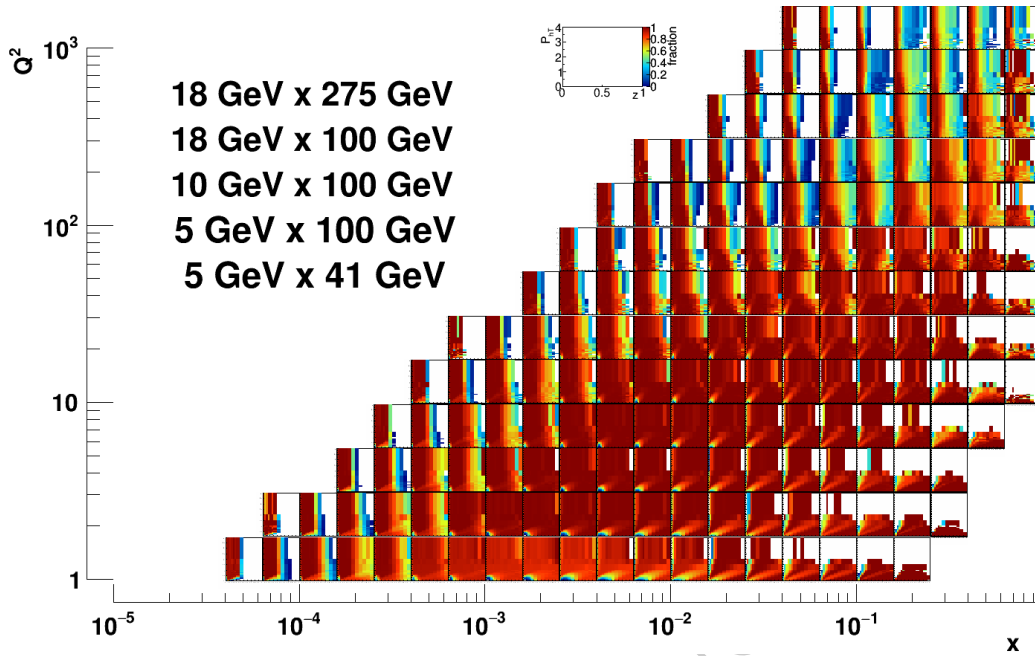


**Figure 8.22:** PID acceptance fractions as a function of pion fractional energy  $z$  and transverse momentum  $P_{hT}$  in bins of  $x$  and  $Q^2$ , taking into account all collision energies. The fractions are evaluated by calculating the yield of accepted pions within the PID momentum ranges described in the text normalized by all pions. The standard DIS event selection criteria are applied.

measurements that is also the maximum momentum for which the hadron type needs to be well identified. The lowest momenta of interest in all rapidities are of several hundred MeV/ $c$ .

As the high momenta are usually also related to high fractional momenta  $z$  where the correlation to the fragmenting parton flavor and spin is largest, the high momentum hadron PID requirements are most important. To illustrate the relevance of the PID requirements, the impact of PID ranges are displayed as a function of  $x$ ,  $Q^2$ ,  $z$  and  $P_T$  assuming perfect tracking using a realistic PID range normalized by the hadron yields in these variables with perfect tracking and PID information. Some regions, particularly at intermediate  $x$  and  $Q^2$  can be compensated between different beam energy combinations, but particularly high  $x$  at low and high  $Q^2$  can only be obtained by the lowest and highest beam energy combinations, respectively. It is however important to also keep in mind that in addition to the bins in the DIS kinematics the coverage of SIDIS variables  $z$  and  $P_T$  is important. The coverage is displayed in Fig. 8.22 assuming PID coverage of up to 7 GeV/ $c$  from  $-3.5 < \eta < -1$ , 6 GeV/ $c$  from  $-1 < \eta < 1$  and 50 GeV/ $c$  from  $1 < \eta < 3.5$  for pions after combining all beam energy options. For the most part this PID selection covers most kinematic regions, but the rather low maximum momentum in the barrel part of the detector significantly cuts into the intermediate- $x$ , high- $Q^2$  and higher- $z$  range that would be particularly important for any TMD evolution studies.

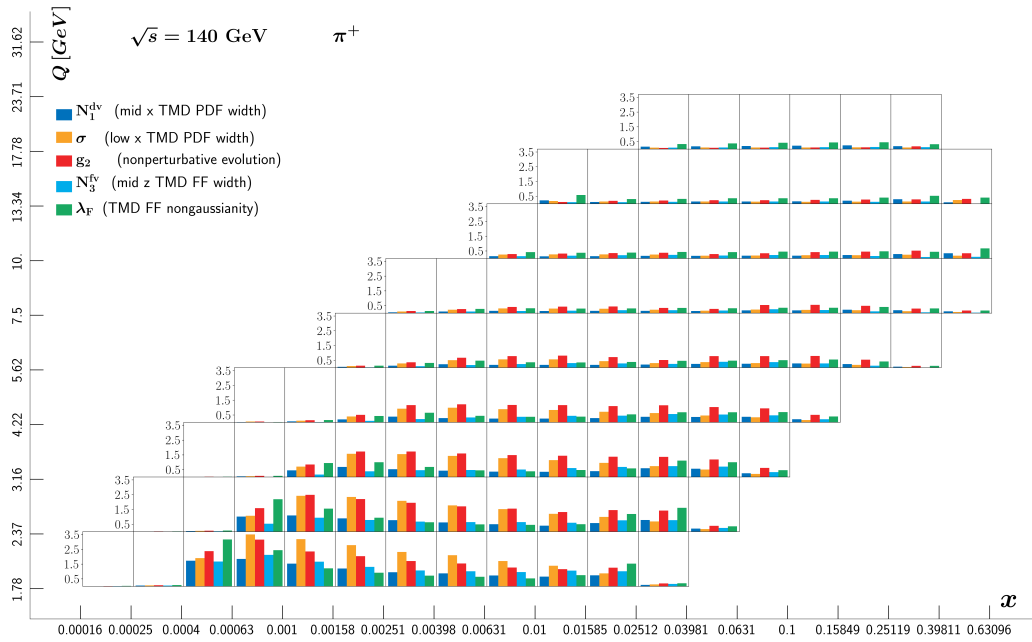


**Figure 8.23:** Expected sensitivities to various TMD PDF and FF parameters, as well as the TMD evolution as shown for the highest collision energy option and for detected final-state positive pions. The impact has been averaged of finals transverse momentum and fractional energy for better visibility.

In order to see why all kinematic regions in the previous figure are relevant, a simplified version of the expected sensitivities from the EIC data to the unpolarized TMDs are shown in Fig. 8.23 based on the [359]. The bars represent the overall impact to a set of TMD PDF and FF parameters, as well as the TMD evolution itself. Naturally at lower  $x$  the sensitivity for the low- $x$  dependence of transverse momentum width of the PDFs is largest. For the TMD evolution both low and high  $Q^2$  data are important although the fact that for unpolarized TMDs some LHC data is available somewhat reduces the need for very high  $Q^2$ , at least at intermediate  $x$ . It is interesting to see, that the non-Gaussian tails of the transverse momentum dependent fragmentation functions are very relevant at both low- $x$  and higher- $x$  and  $Q^2$ . Not shown in this figure is that at lower collision energies naturally the higher  $x$  regions become more relevant as well as the fragmentation-related parameters are getting better constrained at those  $x$ .

### 8.2.3 Using the hadronic final state to reconstruct SIDIS variables

The JB method discussed in Sec. 8.1 can also be used to reconstruct  $x$  and  $Q^2$  in SIDIS. When considering neutral current events with a reconstructed electron, one can also use methods that use information from both, the scattered electron and the hadronic final state to increase the precision of the reconstructed kinematic variables. Two of those methods are the so-called "mixed" method and the double-angle method [1183]. In the mixed method,

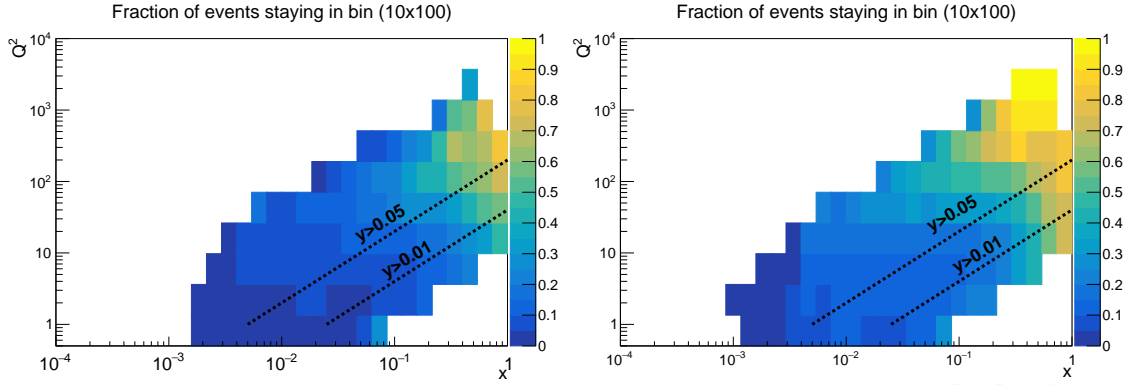


**Figure 8.24:** Fraction of events staying in the respective  $x/Q^2$  bin for the  $10 \times 100$  configuration. JB method is shown on the left, whereas the double angle method is shown on the right. The double angle method improves on the JB method at high  $x$  and moderate  $Q^2$ .

the exchanged 4-momentum  $q$  is calculated from the electron, and the energy transfer  $y$  is calculated from the hadronic final state, whereas the double angle method uses only information about the angles of the scattered lepton and hadronic final state. This method is therefore less affected by the loss of relative energy resolution of the scattered lepton which make measurements at low values of  $y$  unfeasible.

We studied JB, mixed and double-angle method in a simulation using pythia8+DIRE and Delphes. Consistent with the finding in Sec 8.1 the JB method increases the resolution of  $x-Q^2$  reconstruction at high  $x$  and  $Q^2$ . We also observed that the methods that include the final state perform better than the JB method as shown in Fig. 8.24. While the reconstruction of the DIS variables from the hadronic final state is well known, to our knowledge the reconstruction of the SIDIS variable, in particular  $z$ ,  $p_T$  and azimuthal angles in the Breit frame from the hadronic final state has not been studied so far. Similar to the reconstruction of the DIS variables, the importance of the extension of these methods to SIDIS variables lies in the loss of resolution in the measurement of Breit frame variables due to the poorly reconstructed 4-vector  $q$ . The transverse component of  $q$  can be calculated from the transverse momentum of the hadronic final state which only leaves two components that can be determined by solving two equations

$$Q^2 = -q^\mu q_\mu \quad (8.3)$$

$$y = \frac{P^\mu q_\mu}{P_\mu l_\mu}. \quad (8.4)$$

Here  $P$  is the four-vector of the nucleon,  $l$  the four-vector of the lepton. The values for  $Q^2$  and  $y$  are determined consistently with the method used (JB, mixed or double-angle). A complication arises, since the quadratic equation has two solutions. From simulations it is determined that the smaller solution is most often the correct one, but more studies can be done to improve this criterion. In our simulation studies, we observed a similar improvement for the SIDIS variables as for the DIS variables. Fig. 8.25 shows the comparison between the reconstruction of  $z$  using just the scattered electron or the double-angle

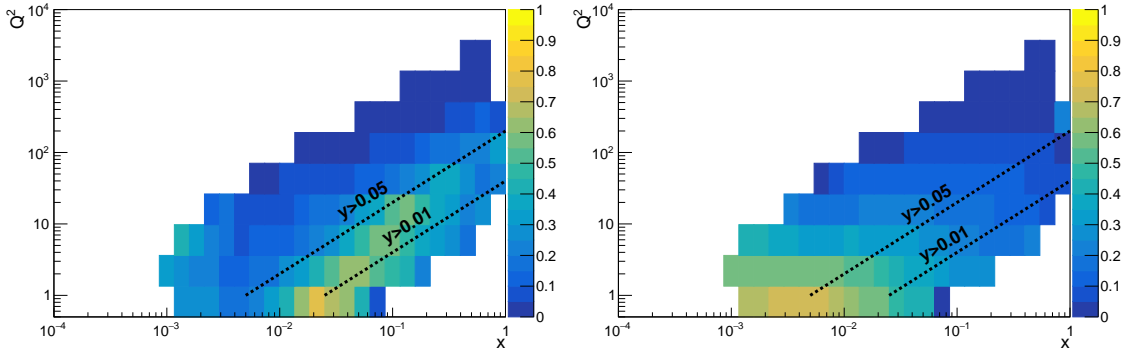


**Figure 8.25:** Mean relative error in reconstructing  $z$  using just the scattered electron (left) and the double-angle method (right). The double-angle method shows improved resolution at low  $y$ . The  $10 \times 100$  configuration was simulated for these results.

method. The improvement at low  $y$  is evident. It is worth emphasizing that using these methods also allows the reconstruction of jets in the Breit frame. We studied this as well using the recent Centauro algorithm [468] and found that at low  $y$  and low  $p_{T,\text{jet}}$  the hadronic methods perform better than using just the electron for the reconstruction of the particle momenta in the Breit frame.

**Requirements for the detector** The requirements on the detector to be able to reconstruct the final state are obviously similar to the requirements for the JB methods described in Sec. 8.1. In particular it is observed that expanding the coverage from  $\eta = 3.5$  to  $\eta = 4.0$  on the hadron going side extends the region where DIS/SIDIS variables can be reconstructed in the highest  $x$  region at low  $y$ . We note that, unlike for the JB method, a hadronic calorimeter does not lead to a significant improvement of the mixed or double angle methods.

#### 8.2.4 Requirements for di-hadron measurements

The di-hadron channels naturally share most requirements with the single hadron TMD requirements discussed above. There are two additional aspects though, which need special consideration. The first is the dependence of the acceptance on the decay angle  $\theta$  and the second the PID performance for hadron pairs. We will first discuss these requirements in order. As discussed in Sec. 7.4.1, one physics objective is the decomposition of the di-hadron cross-section in terms of partial waves (PWs). The different PWs can be distinguished by their dependence on azimuthal angles in the Breit-frame and the decay angle  $\theta$  defined in the di-hadron CMS as the angle between one hadron and the direction of the pair in the lab system [170]. While the azimuthal coverage requirement is similar to the single-hadrons and therefore has been on criterion of optimization for the EIC detector design, the coverage in  $\theta$  is not that obvious. Small values of  $\theta$  are correlated with an asymmetric distribution of the energy between the hadrons and thus with one hadron

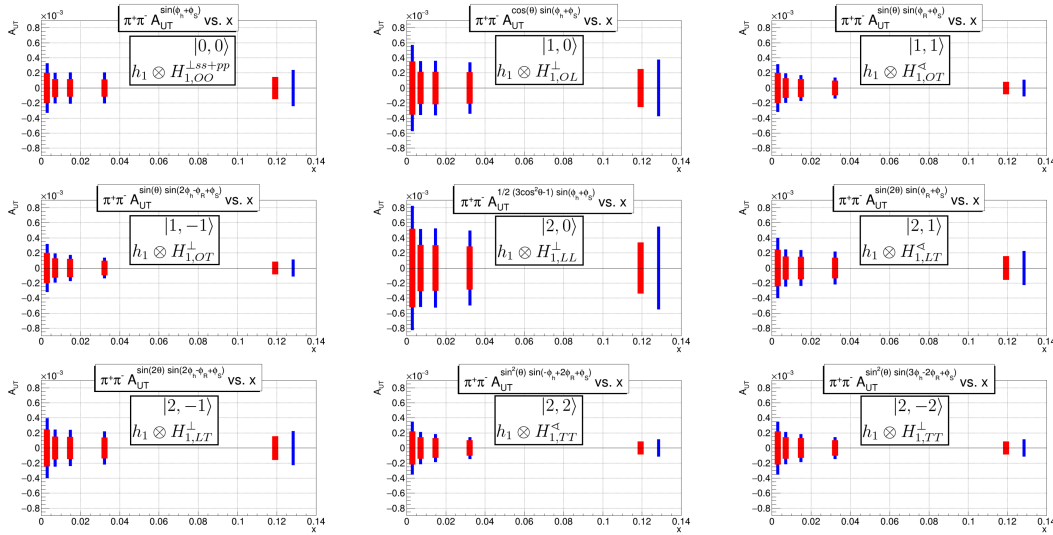


**Figure 8.26:** Statistical uncertainties estimated for the PW decomposition up to  $L=2$  for  $H_1^<$  for  $10 \text{ fb}^{-1}$  at  $5 \text{ GeV} \times 41 \text{ GeV}$ . Narrow blue bands correspond to a requirement of  $p_T > 300 \text{ MeV}$  and wide, red bands to a requirement of  $p_T > 100 \text{ MeV}$  on the pion tracks. The labels on the figure indicate the  $m, l$  state and which PDF and FF the PW is sensitive to.

having a small momentum relative to the other. Therefore, restrictions on the minimum accepted hadron momentum, mainly due to the curling up of low  $p_T$  tracks, lead to restrictions on the accessible  $\theta$  range and thus on our ability to do a PW separation of the cross-section. We investigated the impact of several minimum  $p_T$  values corresponding to several proposed detector layouts on the projected statistical uncertainties of the PW separation. Fig. 8.26 shows the statistical uncertainties for  $p_T > 100$  and  $300 \text{ MeV}$ . It is observed that lowering the limit below  $100 \text{ MeV}$ , which corresponds to the requirement imposed by the  $\Lambda$  reconstruction discussed in Sec. 8.2.5, does not improve the uncertainties significantly..

Concerning PID requirements, again, the di-hadron requirements are similar to the single hadron requirements discussed above. However, since two hadrons are required, the dilution of the samples for a given significance in separation can be more severe. A study was performed to assess the impact of two and three  $\sigma$  separation between pions and kaons. This is mainly motivated by the PID in the central region for which three  $\sigma$  separation at high momenta is more difficult to achieve. For di-hadrons, the  $p_T$  dependence of the dilution is flat. As expected, with two  $\sigma$  separation, the  $\pi\pi$  samples are still very pure, above 95%. However,  $\pi K$  samples drop to below 70% and  $KK$  pairs to about 75%. With three  $\sigma$  separation, the purity of the samples is above 95% for all cases. Therefore having  $\pi - K$  separation at three  $\sigma$  is very important for precision measurements involving kaons.

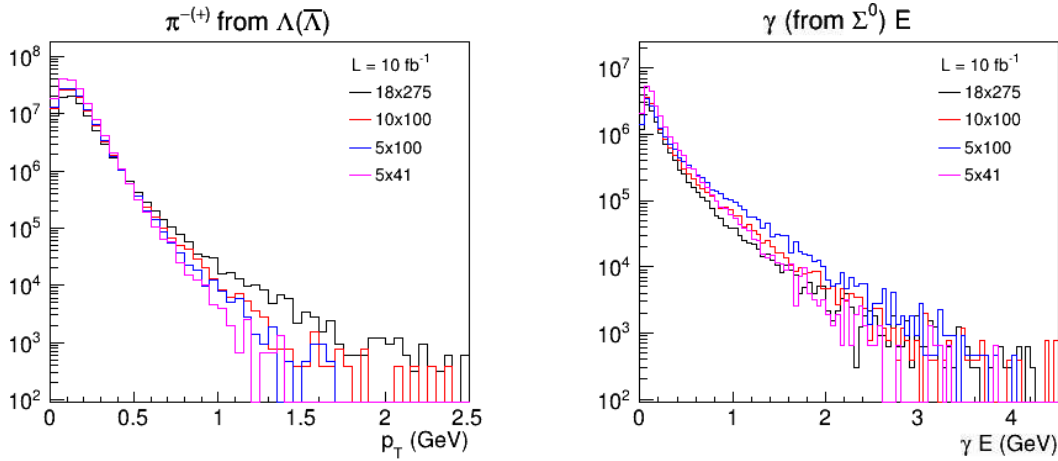


**Figure 8.27:** Transverse momentum and energy spectrum of pions from  $\Lambda \rightarrow p\pi$  and  $\Sigma^0 \rightarrow \Lambda\gamma$  respectively.

### 8.2.5 Requirements for $\Lambda$ measurements

The efficient detection of  $\Lambda$  hyperons poses specific requirements to a potential detector. Experimentally the channels  $\Lambda \rightarrow p\pi^- / \bar{\Lambda} \rightarrow \bar{p}\pi^+$  are the most promising. In these channels the  $p/\bar{p}$  carries the majority of the momentum of the parent  $\Lambda$ , leading to a very soft spectrum of the decay pions. Fig 8.28 shows the kinematics of the produced  $\Lambda$  and its decay product. The left panel in fig. 8.27 shows the projected spectrum for the decay pion for a representative energy and  $x_F > 0$ . It is evident that any minimum  $p_T$  restriction will cut significantly into the  $\Lambda$  spectrum. For example, requiring  $p_T > 300$  MeV leaves less than 5% of  $\Lambda$ 's even at the highest energies. From these studies we deduced a requirement of  $p_{T\pi} > 100$  MeV.

The  $\Lambda$  measurements discussed in this report are assuming that the hyperon is promptly produced by the fragmenting quark. However, a significant fraction of  $\Lambda$ 's are coming from non-strong decays and thus have to be corrected for. The right panel in fig. 8.27 shows the spectrum for the decay photons. For  $\Sigma^0$  boosted in the forward direction the spectrum is somewhat harder but additional material in that region is still a concern. We concluded that a requirement of  $\gamma$  detection with the nominal resolution in that region for  $\gamma_E > 200$  MeV up to  $\eta = 3.0$  and  $\gamma_E > 400$  MeV for  $3.0 < \eta < 4.0$  is sufficient to maintain a reasonable acceptance for  $\Sigma^0$ 's.

### 8.2.6 Spectroscopy requirements for forward electron identification

The spectroscopy of XYZ mesons in photoproduction relies on the efficient detection of all the meson decay products and adequate resolution to identify and study the produced resonances. One particular reaction of interest  $\gamma p \rightarrow Z_c(3900)^+ n$  was introduced in Sec. 7.4.6, which provides useful insight to the detector requirements. Here we'll focus on the  $Z_c(3900)^+ \rightarrow J/\psi\pi^+$  decay mode with  $J/\psi \rightarrow e^+e^-$ , however the  $Z_c^+$  has been

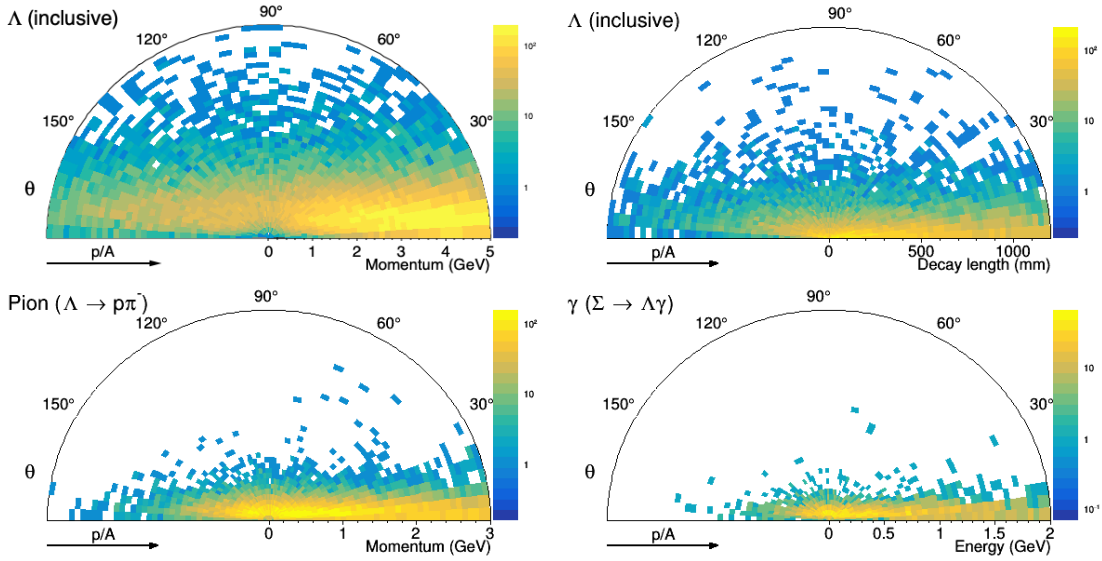


**Figure 8.28:** From top left to bottom right: kinematics of  $\Lambda$ , decay length of  $\Lambda$ , kinematics of decay  $\pi^-$  and kinematics of decay  $\gamma$  from the non-prompt  $\Lambda$  production chain  $\Sigma^0 \rightarrow \Lambda + \gamma$ . All plots from fast simulation of the  $18 \times 275$  configuration.

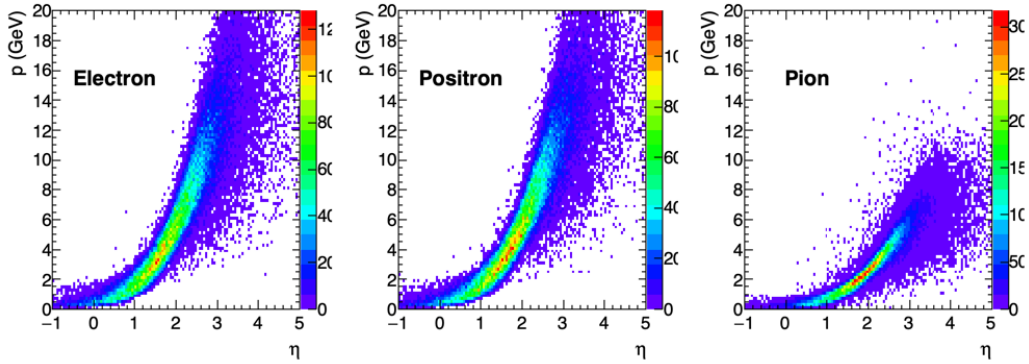


**Figure 8.29:** Simulated kinematics  $p$  vs  $\eta$  for  $Z_c^+ \rightarrow J/\psi\pi^+$ ,  $J/\psi \rightarrow e^+e^-$  decay products for  $5 \times 41$  GeV beam energies

observed in open charm decay modes as well. This reaction (and other XYZ final states) are simulated using the amplitudes provided by the JPAC Collaboration [915] integrated into the ELSPECTRO event generator [1184].

The lab frame kinematics ( $p$  vs.  $\eta$ ) of the meson decay particles  $e^-$ ,  $e^+$  and  $\pi^+$  are shown in Fig. 8.29 and 8.30 for  $5 \times 41$  and  $18 \times 275$  GeV beam energies, respectively. Due to the large kinematic boost from the proton beam, the decay particles populate most of the forward hadron acceptance. In particular, for the highest proton beam energies many of the tracks have  $\eta > 3.5$  which will limit the acceptance for these reactions. Therefore, we expect the low beam energy (high acceptance) and high beam energy (high luminosity) to

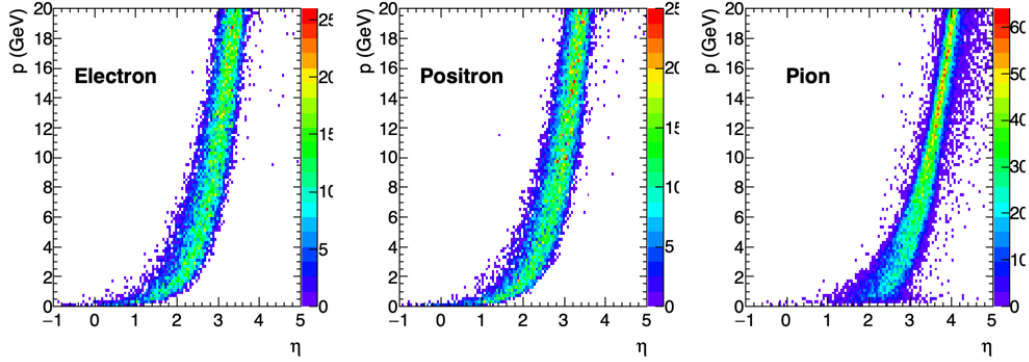


**Figure 8.30:** Simulated kinematics  $p$  vs  $\eta$  for  $Z_c^+ \rightarrow J/\psi\pi^+, J/\psi \rightarrow e^+e^-$  decay products for  $18 \times 275$  GeV beam energies

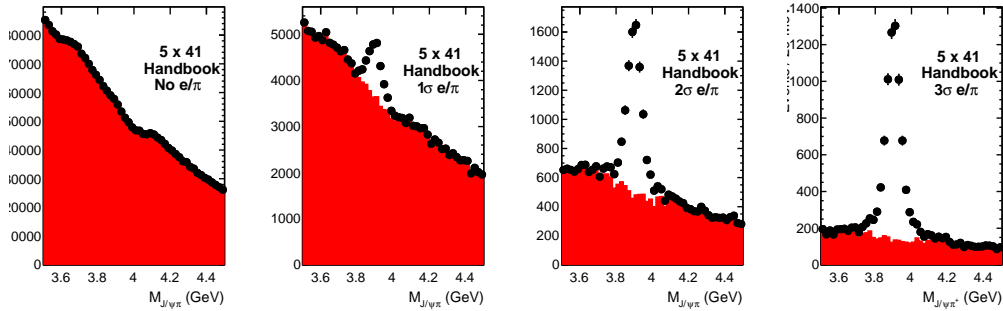


**Figure 8.31:** Simulated  $Z_c^+ \rightarrow J/\psi\pi^+$  mass distribution from smeared simulation for  $5 \times 41$  GeV beam energies with increasing (left-to-right)  $e/\pi$  separation. The PYTHIA background (red) is significantly reduced by addition  $e/\pi$  separation relative the signal.

be complementary in studying the photoproduction of the XYZ spectrum.

Additional requirements on the particle identification are also necessary to identify the  $J/\psi \rightarrow e^+e^-$  decay particles in this forward region of the detector. Background from inclusive hadron production was studied using PYTHIA minimum bias events, where charged hadrons were nominally assumed to be mis-identified as  $e^\pm$  candidates. The  $J\psi\pi^+$  mass distribution in Fig. 8.31 illustrates the level of background (red) and expected  $Z_c(3900)^+$  signal (black) for electron-pion separations from none to  $3\sigma$ . For an  $e/\pi$  separation of  $3\sigma$ , a purity of  $\sim 90\%$  is achieved which would allow further study of the observed resonance, including the decay angular distributions, etc.

### 8.3 Jets and Heavy Quarks

!!!!

Note to readers: The text below is a rough draft of the bulk of the material we plan to present. All figures should be taken as placeholders to be updated/beautified in due course. Citations have not yet been included. Some further editing should be expected over the next week.

!!!!

An impressive amount of information on the partonic structure of the nucleon can be extracted from inclusive DIS reactions, where only the scattered lepton is measured. However, including information from the hadronic final state as in a semi-inclusive DIS (SIDIS) measurement can provide further insight that is not possible with purely inclusive analyses. The observables evaluated by the Jets and Heavy Quark working group (JHQ WG) characterize more fully the total final state by taking into account correlations between the produced particles or by identifying specific final states and provide complimentary, and often times unique, information compared to standard SIDIS measurements. Jets cluster many of the final state particles arising from a hadronizing parton into a single object, which gives a better representation of the kinematics of that parton than a single hadron measurement could. In addition, many well defined techniques exist to systematically explore the distribution of energy within a jet, providing a unique way to study the hadronization process. Heavy quark production at the EIC will provide a clean probe of gluon dynamics in the nucleon/nucleus while the large mass of charm and bottom mesons will provide many advantages in the study of hadronization and cold nuclear matter effects. Finally, global event shapes aim to classify the energy flow of the entire final state and can yield very high precision measurements of fundamental quantities such as the strong coupling constant.

The precision reconstruction of jets, heavy quark states, and global event shapes places performance constraints on tracking, calorimetry, and particle identification in the central detector region. Specific requirements for each of these components, along with the driving physics considerations, will be enumerated in the sections below.

### 8.3.1 Simulation and Detector Modeling

The detector performance requirements listed in the sections below were derived from the analysis of a number of representative jet, heavy flavor, and event shape observables. For each relevant observable, the appropriate process was simulated using a Monte Carlo event generator and the output was run through a smearing framework or a more detailed detector simulator to evaluate the effects of finite resolutions and acceptances and determine the detector qualities needed to measure the observable with the necessary precision to extract the desired physics.

All studies carried out by the JHQ WG utilized either the Pythia6 or Pythia8 event generator. Pythia6 was implemented within the pythiaeRHIC program which has been tuned to reproduce ep data from HERA. The pythiaeRHIC Monte Carlo has been used in numerous EIC studies and has been shown to reproduce HERA (di)jet cross sections and jet profiles in both the photoproduction and electroproduction regions []. The Pythia8 gener-

ator was used primarily for simulations of jet production in neutral and charged current DIS at moderate to large  $Q^2$  values as well as heavy flavor production. As Pythia8 has not been specifically tuned to reproduce ep jet data (beyond the development and setting of default parameters by the Pythia authors), several checks were made to ensure the Monte Carlo was giving reasonable output. Figure 8.32a compares  $d\sigma/dp_T$  for lab frame jets as measured by the ZEUS experiment to that obtained from Pythia8. A comparison is also made between Pythia8 and a theoretical calculation of the jet cross section as a function of  $Q^2$  for kinematics relevant for the EIC in Fig. 8.32b. In both cases, the agreement with the simulation is seen to be excellent, giving confidence that at least for the relevant kinematic regions, Pythia8 produces reasonable results.

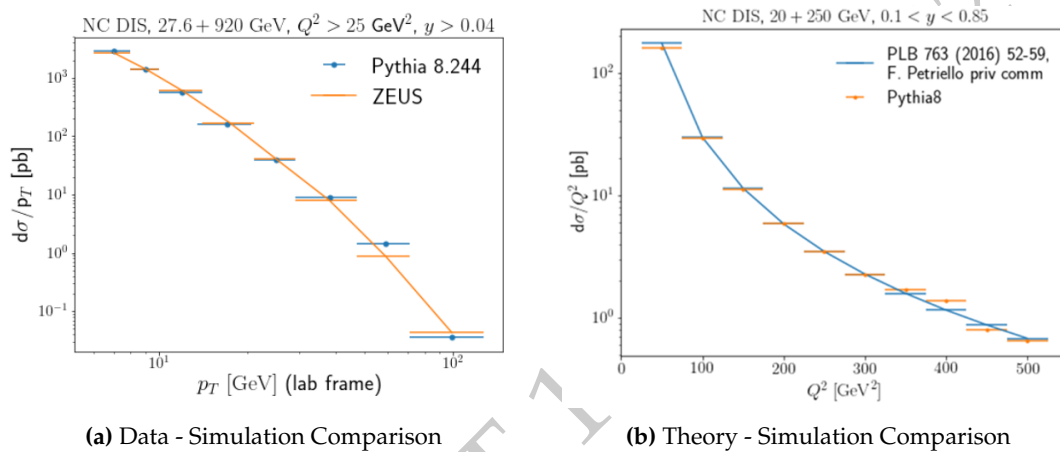


**Figure 8.32:** [PLACEHOLDER](a) Comparison of jet cross section as a function of  $p_T$  for inclusive lab frame jets from ZEUS data and PYTHIA8. (b) Comparison of the lab frame inclusive jet cross section as a function of  $Q^2$  between PYTHIA8 and theory.

The second step in the evaluation of detector requirements involves distorting the output from the event generators to mimic the effects of finite detector resolutions and acceptances. For jet observables, this was done using a fast smearing framework, either eic-smear or DELPHES [1]. Eic-smear is a relatively light-weight framework which allows for the definition of different ‘detector volumes’ which will smear either the momentum or energy of particles which traverse these regions. The energy or momentum is smeared according to a Gaussian distribution whose sigma is set by the user and should correspond to the proposed energy or momentum resolution of a given subsystem. DELPHES is a more sophisticated tool that takes into account the bending of charged particles in a solenoidal magnetic field and gives access to higher level observables such as particle flow objects and missing transverse energy. As with eic-smear, the resolutions of the detector components are supplied in parameterized form and incident particles are smeared according to a log-normal distribution. Because of the event generator / smearing frameworks in place during most of the Yellow Report exercise, eic-smear was used with pythiaRHIC and DELPHES was used with Pythia8 for all analyses.

While fast smearing based on parameterized descriptions of tracker and calorimeter responses are largely adequate for jet observables, a more detailed accounting of detector

characteristics is needed to evaluate requirements for heavy flavor reconstruction. Because of this, many of the heavy flavor analyses utilized more complete detector geometries implemented in the eic-root and Fun4All frameworks.

### 8.3.2 Kinematics Summary

Plots of relevant kinematic quantities for jets and heavy flavor states are presented below for several beam energy combinations and  $Q^2$  ranges.

For jets, both the transverse momentum (Fig. 8.33) and energy (Fig. 8.34) are plotted as a function of pseudorapidity. Diffractive jet production is not considered here. Jets were found in the laboratory frame using the Anti- $k_T$  algorithm with a radius parameter of 0.4. The radius used here is somewhat smaller than the  $\mathcal{O}(1.0)$  radius jets that were used in most analyses in order to show more of the behavior at large pseudorapidity while keeping the jet fully contained in the range  $|\eta| < 3.5$ . The counts have been scaled to the equivalent of  $10 \text{ fb}^{-1}$ . Note that the actual generated statistics for the  $10^{-5} < Q^2 < 1.0$  samples amount to only  $0.02 \text{ fb}^{-1}$  and so the available phase space is not fully populated. Further jet kinematic distributions can be found in []

The momentum vs pseudorapidity distributions for pions and kaons emitted in  $D^0$  decays can be found in Fig. 8.35 for beam energies of  $10 \times 100 \text{ GeV}$ ,  $18 \times 100 \text{ GeV}$ , and  $18 \times 275 \text{ GeV}$ . As with the jet plots, the counts have been scaled to the equivalent of  $10 \text{ fb}^{-1}$ . Further heavy flavor kinematic distributions can be found in [].

### 8.3.3 Tracking

Charged particle tracking is an essential component of all analyses considered by the JHQ WG, including jet and heavy meson reconstruction and event shape measurements. Due to the generally low energies of produced hadrons at the EIC, the tracking system will provide better resolution than hadron calorimetry at all but the most forward rapidities, where particle energies can be large and tracking resolution is expected to degrade. It is therefore anticipated that charged tracks (which comprise roughly two-thirds of the energy contained in an average jet) will be the dominant input to jet-finding algorithms. The superior pointing resolution for tracks compared to calorimeter clusters will also be critical for jet substructure and event shape measurements where the spatial distribution of energy is an explicit aspect of the observable. Charged tracks are also indispensable to the study of heavy flavor states, where the invariant mass of (identified) track combinations is used to select heavy hadrons. The ability to accurately reconstruct track trajectories also allows for the identification of the secondary vertex associated with the decaying heavy particle which aids in background suppression.

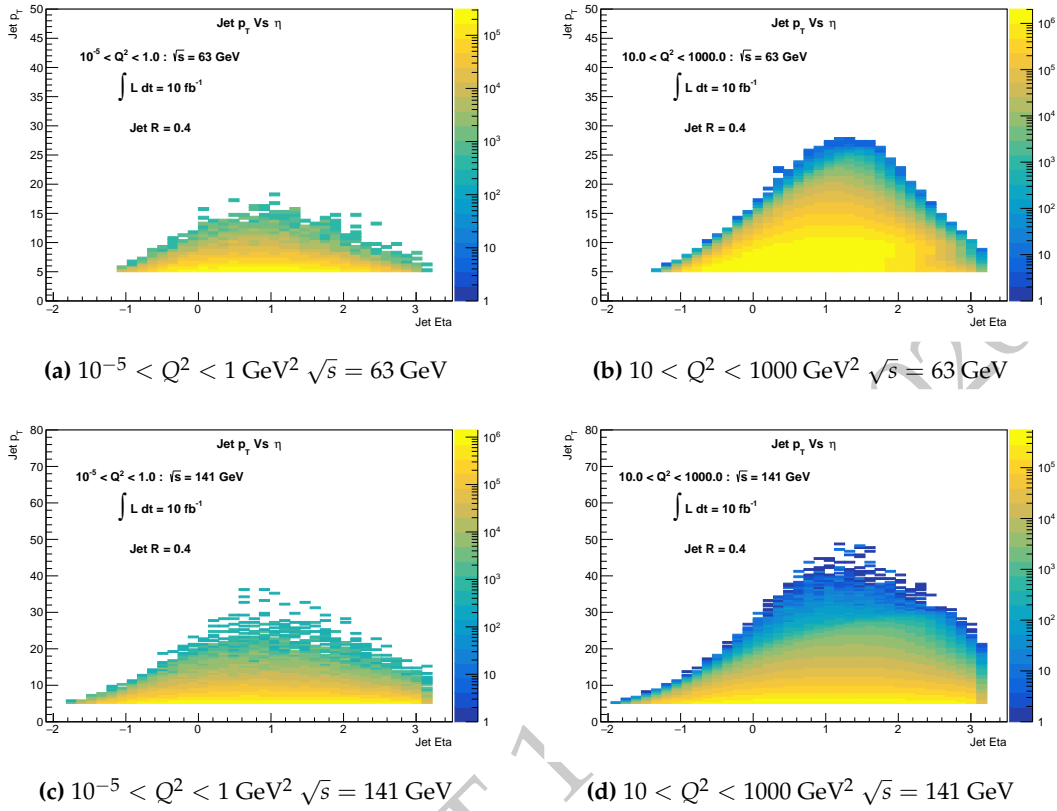


**Figure 8.33:** Jet  $p_T$  vs pseudorapidity for beam energies of 10x100 GeV (top row) and 18x275 GeV (bottom row) and  $10^{-5} < Q^2 < 1.0 \text{ GeV}^2$  (left column) and  $10 < Q^2 < 1000 \text{ GeV}^2$  (right column). Counts have been scaled to correspond to  $10 \text{ fb}^{-1}$ .

### Momentum Resolution

For the purposes of the Yellow Report effort, a baseline set of track momentum resolutions, which represented reasonable assessments of potential tracker performance, were supplied. These resolutions were parameterized in the form  $A\% \times P \oplus B\%$ , where  $P$  is the track 3-momentum, in six pseudorapidity intervals between  $\pm 3.5$  and can be found in Tab. 8.2. These resolutions (or similar) were used in a number of jet analyses, including studies of neutral and charged current jet production for TMD extractions, (groomed) jet substructure, and jet angularity [1]. The primary metric used to evaluate the suitability of the supplied track resolutions was the size of the observed jet energy resolution (JER), which can be seen as a function of jet energy in Fig. 8.36 from both the eic-smear and DELPHES smearing frameworks. Experience from other experiments suggests that JER values on the order of 10% lead to reasonable unfolding performance, while the desire to perform measurements of, for example, the lepton-jet Siverts asymmetry differentially in  $q_T = \vec{p}_T^{\text{Lepton}} + \vec{p}_T^{\text{Jet}}$  implies the need for JER slightly less than 10%. While the JER shown here also include effects from the calorimeter resolutions, we can still conclude that the momentum resolutions listed in Tab. 8.2 are sufficient for our needs and put them forward

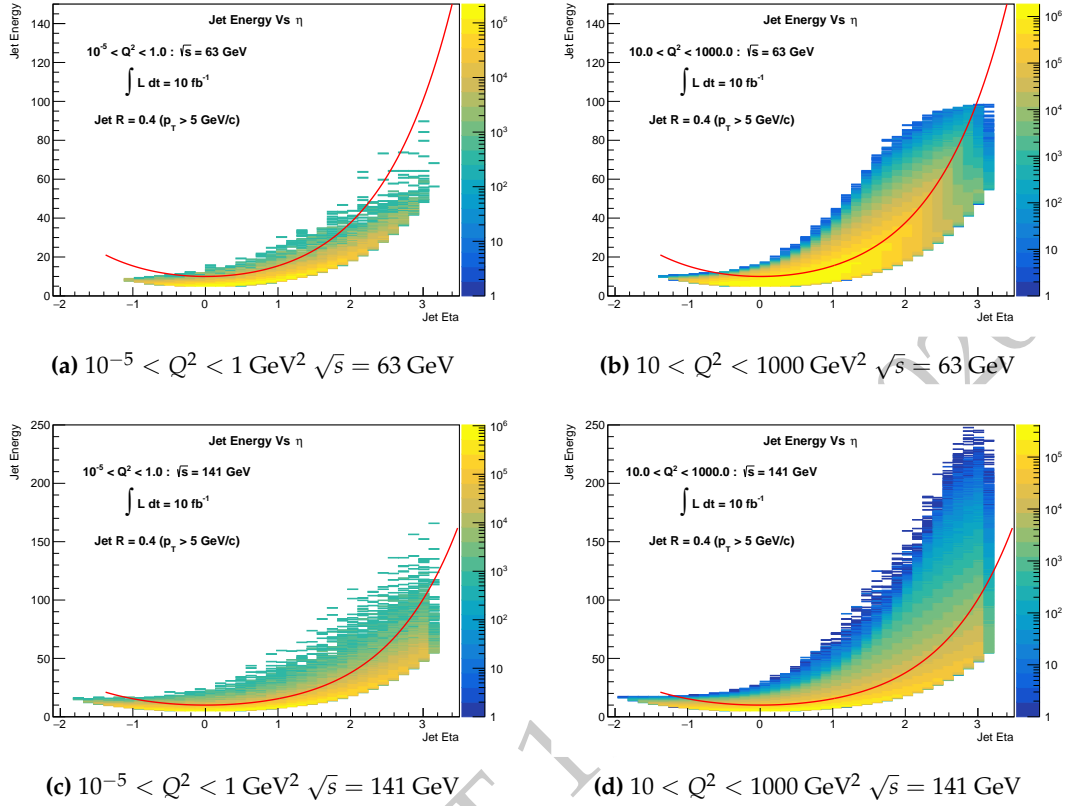


**Figure 8.34:** Jet energy vs pseudorapidity for beam energies of 10x100 GeV (top row) and 18x275 GeV (bottom row) and  $10^{-5} < Q^2 < 1.0 \text{ GeV}^2$  (left column) and  $10 < Q^2 < 1000 \text{ GeV}^2$  (right column). Counts have been scaled to correspond to  $10 \text{ fb}^{-1}$ . The distributions are shown with a minimum jet  $p_T$  of 5 GeV and the red line shows the lower limit of the distribution assuming a minimum jet  $p_T$  of 10 GeV.

as the requirements from the JHQ WG.

Pseudorapidity Range	Resolution ( $\sigma P/P\%$ )
$-3.5 < \eta < -2.5$	$0.1\% * P \oplus 0.5\%$
$-2.5 < \eta < -2.0$	$0.1\% * P \oplus 0.5\%$
$-2.0 < \eta < -1.0$	$0.05\% * P \oplus 0.5\%$
$-1.0 < \eta < 1.0$	$0.05\% * P \oplus 0.5\%$
$1.0 < \eta < 2.5$	$0.05\% * P \oplus 1.0\%$
$2.5 < \eta < 3.5$	$0.1\% * P \oplus 2.0\%$

**Table 8.2:** Requested track momentum resolution.

While the above momentum resolutions are adequate for our needs, there is some worry that the parameterization gives a better resolution than can realistically be expected for

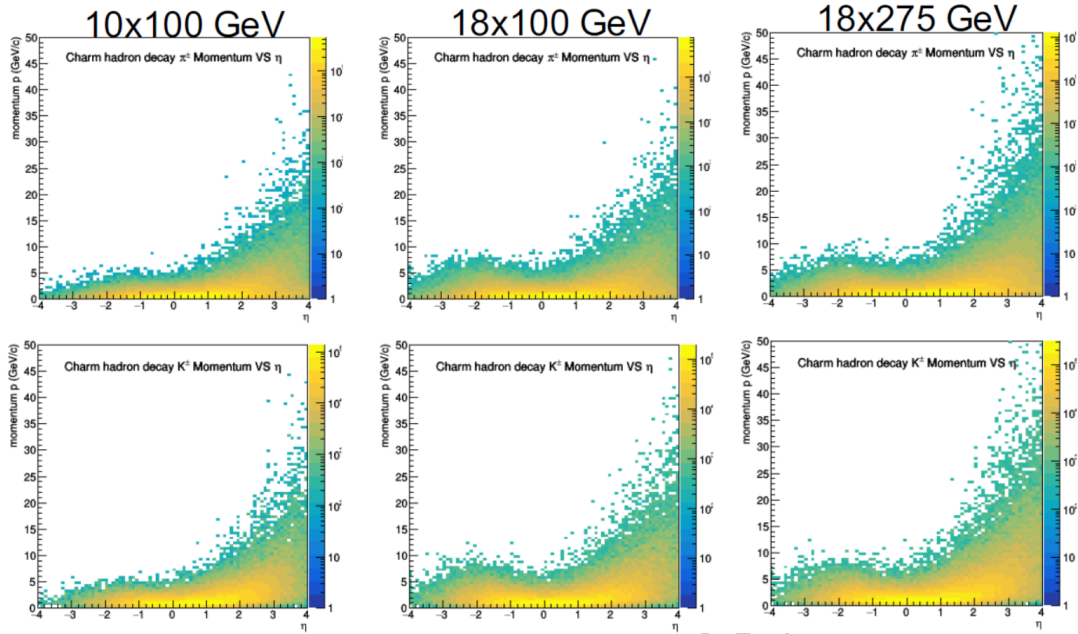


**Figure 8.35:** Momentum vs pseudorapidity for the decay products of  $D^0$  mesons. Charged pions are on the top row and charged kaons are on the bottom. The columns display different center of mass energies:  $\sqrt{s} = 63$  GeV (left),  $\sqrt{s} = 85$  GeV (middle), and  $\sqrt{s} = 141$  GeV (right).

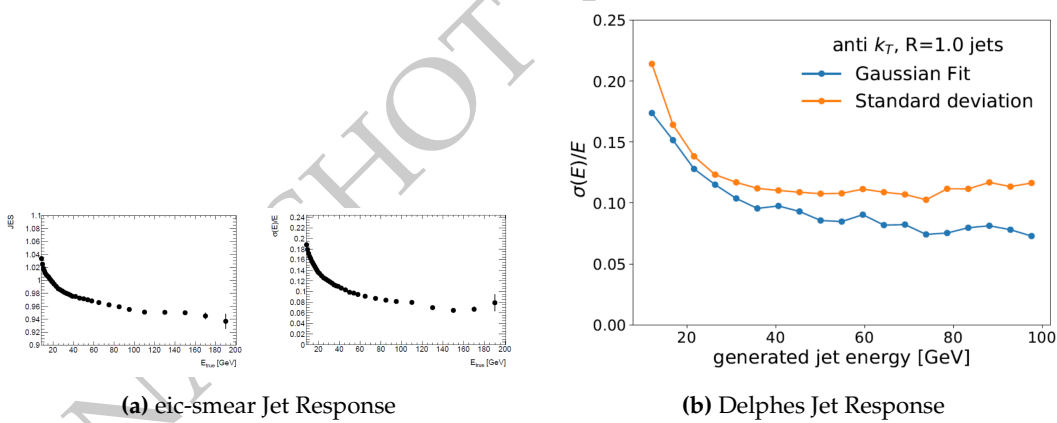


**Figure 8.36:** (a) Jet energy scale (left) and jet energy resolution (right) as a function of jet energy for jets smeared using the eic-smear framework and track momentum resolutions listed in Tab. ?. (b) Jet energy resolution from the DELPHES smearing framework as a function of jet energy.

tracks with the highest momenta at the most forward (positive) pseudorapidities. It will be important to understand in detail the momentum resolution in this region as it is an area where hadron calorimetry could be competitive (see ?? for further discussion).

### Vertex Resolution

When considering heavy flavor reconstruction, there are two vertices of interest: the primary collision vertex where the initial scattering occurs, and a secondary vertex which is the origin of tracks arising from the decaying heavy meson. The reduction of background associated with the heavy meson reconstruction can benefit greatly from cuts on a number of topological relationships between the two vertices, such as the decay length (distance between vertices) and the distance of closest approach (DCA) between the primary vertex and reconstructed meson trajectory []. One of the most relevant parameters for determining the vertices and the relationships between them is the transverse DCA and its resolution,  $\sigma_{xy}$ . This resolution is parameterized for different pseudorapidity ranges in the form  $A/p_T \oplus B$  where  $A$  and  $B$  are in microns and  $p_T$  is the track transverse momentum in GeV/ $c$ . The requirements on  $\sigma_{xy}$  requested by the JHQ WG can be seen in Tab. 8.3. We currently do not request independent limits on the longitudinal DCA or primary vertex resolution.

Pseudorapidity Range	Resolution
$-3.5 < \eta < -3.0$	N/A
$-3.0 < \eta < -2.5$	$\sigma_{xy} \sim 30/p_T \oplus 40 \mu\text{m}$
$-2.5 < \eta < -1.0$	$\sigma_{xy} \sim 30/p_T \oplus 20 \mu\text{m}$
$-1.0 < \eta < 1.0$	$\sigma_{xy} \sim 20/p_T \oplus 5 \mu\text{m}$
$1.0 < \eta < 2.5$	$\sigma_{xy} \sim 30/p_T \oplus 20 \mu\text{m}$
$2.5 < \eta < 3.0$	$\sigma_{xy} \sim 30/p_T \oplus 40 \mu\text{m}$
$3.0 < \eta < 3.5$	$\sigma_{xy} \sim 30/p_T \oplus 60 \mu\text{m}$

**Table 8.3:** Requested vertex position resolution.

The requirements listed in Tab. 8.3 were largely derived from studies performed by the Los Alamos group on using open charm and bottom mesons in high precision measurements of the nuclear modification factor  $R_{eA}$  over a wide pseudorapidity range in order to discriminate between different models of parton energy loss and hadronization. Further details on the models and required precision on  $R_{eA}$  can be found in []. The requested  $\sigma_{xy}$  resolutions lead to the reconstructed  $D^0$  and  $B^0$  seen in Fig. 8.37 which in turn lead to the precision extractions of  $R_{eA}$  in Fig. 8.37. A detailed technical note describing designs of a silicon vertex detector and forward tracking system leading to the performance listed above can be found here: [].

While the parameters above have been shown to be sufficient for measurements of  $R_{eA}$ , it should be noted that more differential measurements may benefit from higher vertex resolutions. The advantage would come in the form of better signal to noise ratios which would lead to higher significance measurements for a given sampled luminosity. The LBNL group has done several studies [] based on an all Silicon tracking system which aim to quantify the potential significance improvement for increased vertex resolution. It was seen that an improvement in  $\sigma_{xy}$  from  $20 \mu\text{m}$  to  $10 \mu\text{m}$  at a track  $p_T$  of 1 GeV/ $c$  can

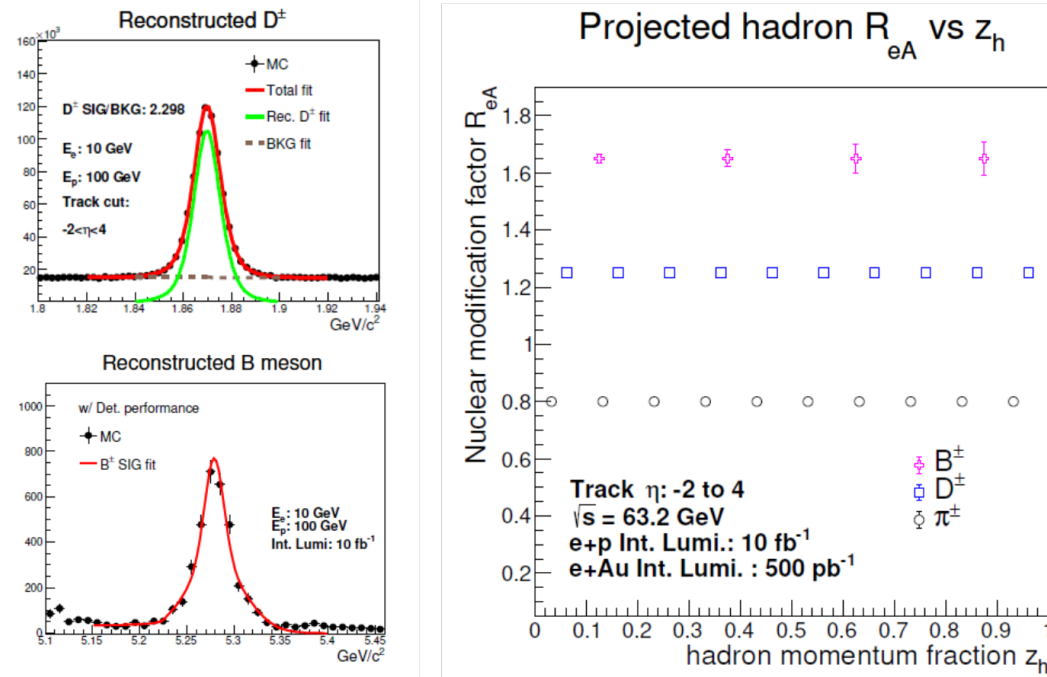
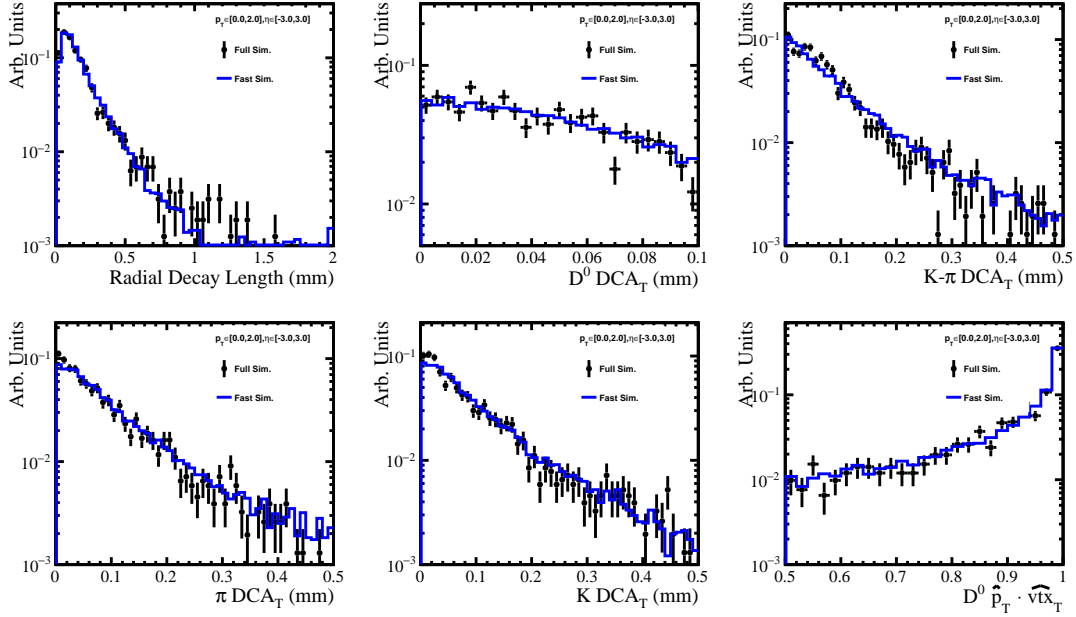


Figure 8.37: [PLACEHOLDER] plot of charm / bottom reconstruction and  $R_{eA}$

increase  $D^0$  significance by 20%. In addition, other heavy mesons of interest, such as the  $\Lambda_c^+$  have transverse displacements from the primary vertex of on the order 20 microns, making tighter resolutions advantageous.

The effects of vertex resolution have also been studied in the context of charm jet tagging via (among other parameters) the presence of a certain number of ‘high impact parameter’ tracks []. Here, the (unsigned) impact parameter is defined as  $\sqrt{(d_0/\sigma_{d_0})^2 + (z_0/\sigma_{z_0})^2}$  where  $d_0$  and  $z_0$  are the distances of closest approach of a track in the transverse and longitudinal direction, respectively and  $\sigma_{d_0}$  and  $\sigma_{z_0}$  are the corresponding uncertainties. The tagging procedure was optimized assuming  $\sigma_{d_0} = \sigma_{z_0} = 20$  microns. To test the impact of vertexing performance, both DCA resolutions were set to 100 microns and the tagging procedure re-optimized. The degraded resolutions led to a 60% loss in charm jet efficiency. A more optimistic scenario was also tested with both resolutions being improved to 10 microns leading to a 30% increase in charm yield for the same light jet contamination. While it is clear that better  $\sigma_{xy}$  resolution will benefit this measurement, it has not been demonstrated that the requested resolutions are inadequate. Therefore, we did not elevate these considerations to the level of requirements.

It should be noted that EICsmear incorporates fast simulation of track parameters, but does not incorporate vertex fitting. This presents a conundrum for several heavy-quark studies in this report where they rely on displaced vertex techniques. An extensive set of GEANT4-based simulations have been performed to extend fast simulations of the detector response for topological observables by the Berkeley group. This response has been propagated in the studies of gluon polarization and the gluon Sivers’ TMD using heavy quark probes



**Figure 8.38:** Comparison of the reconstructed  $D^0$  topological variables in the GEANT4-based all silicon simulation (data points) and the fast simulation (blue histograms). All distributions are normalized to have unit area. The  $D^0$  candidates shown here are required to have a  $|\eta| < 3$  and  $p_T < 2$  GeV/ $c$ .

discussed in the preceding chapter. Figure 8.38

### Additional Considerations

In addition to the requirements on momentum resolution and vertex position resolution, the JHQ WG has identified two further track related performance parameters which should be considered: minimum transverse momentum threshold for detection, and  $p_T$  dependent tracking efficiency.

One driver of the minimum tracking threshold for the JHQ WG is the reconstruction of  $D^*$  mesons via the tagging of the soft pion in the decay  $D^{*\pm} \rightarrow D^0 \pi^\pm$ . GEANT simulation utilizing an all silicon tracker concept show that for a minimum  $p_T$  threshold of roughly 200 MeV/ $c$ , the soft pion acceptance efficiency is 60% at mid-rapidity and drops to a low of 20% at  $|\eta| = 3$ . However, decreasing the tracking threshold to 100 MeV/ $c$  increases the acceptance efficiency to 90% at mid-rapidity with a falloff to 70% at  $|\eta| = 3$ . Lower tracking thresholds are also more desirable for jet analyses as it will allow more of the energy associated with the hadronizing parton to be included in the jet.

The second topic which needs to be discussed is the  $p_T$  dependent tracking efficiency. In the absence of a recommended tracking efficiency function, many analyses assumed an efficiency of 100%. The 1-jettiness [ ] analysis did look at a number of tracking efficiency models with efficiencies ranging between 30 and 70% at  $p_T$  of 200 MeV/ $c$  and saturating

between 93 and 97%. It was seen that the reconstructed 1-jettiness value was not strongly dependent on the efficiency model used []. However, as (low momentum) tracks will comprise a large fraction of the energy budget of a jet, losses in track finding efficiency could have non-negligible effects on jet finding.

### 8.3.4 Particle Identification

The ability to positively identify charged hadron species (topics such as electron and heavy meson identification are not covered here) will enable a suite of measurements which are sensitive to flavor dependencies in the final state. Chief among these will be analyses of the unpolarized identified hadron-in-jet fragmentation functions and the related polarized Collins asymmetry []. It is also expected that certain grooming and substructure techniques will be utilized with PID to trace the flavor evolution through the jet shower. PID will also be an asset to heavy flavor tagging as charm and bottom mesons will often contain a kaon in their decay chain, while lambda particles will emit a proton, so being able to tag these particles will help reduce combinatoric background.

When evaluating the PID needs for an analysis, there are two aspects to consider: how well the charged hadron can be identified and the momentum range over which a given identification power is needed. The requirements on momentum range are informed simply by the momentum spectrum of charged hadrons within reconstructed jets and the desire to measure as much of the  $z = p^{\text{had}} / p^{\text{jet}}$  spectrum as possible. The pseudorapidity vs momentum for charged hadrons inside of jets at moderate to large  $Q^2$  can be seen in Fig. 8.39 for beam energy combinations of 10x100 GeV and 18x275 GeV. As expected, the maximum particle momentum increases with pseudorapidity until roughly  $\eta = 2.2$ , where the particle momentum begins to drop due to an interplay between fiducial volume cuts and the jet radius.

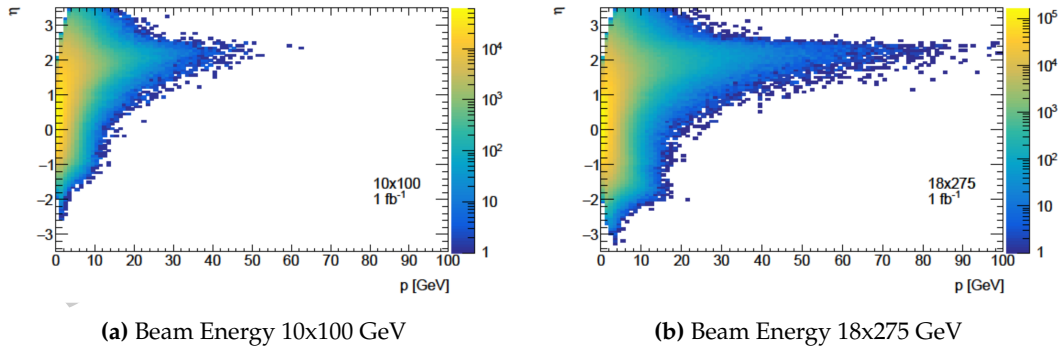


**Figure 8.39:** [PLACEHOLDER]Pseudorapidity vs momentum for charged hadrons found inside jets with a radius ?? at beam energies of 10x100 GeV (a) and 18x275 GeV (b).

The hadron momenta spectra shown in Fig. 8.39 inform our requested PID momentum coverage presented in Tab. 8.4, where the momentum limit represents the particle momentum up to which at least  $3\sigma$  separation between pions and kaons would be possible. This request is more ambitious in terms of momentum reach than the initially proposed values

of 5 GeV/ $c$  in the barrel and between 8 GeV/ $c$  and 45 GeV/ $c$  over the hadronic endcap. The barrel request in particular will necessitate additional research and development to realize a technical path to separation at momenta above 5 GeV/ $c$ . Despite this, the requested PID capabilities will enable a host of measurements which would not be possible otherwise. For example, measurements with light and Heavy Ions, which have maximum beam energies of 100-110 GeV, will see significant fraction of jets produced in the barrel, and the phase space which is not covered due to low PID limits will not be recoverable by moving to different detector regions or center-of-mass energies.

Pseudorapidity Range	Momentum Range
$-3.5 < \eta < -1.0$	$\leq 7$ GeV/ $c$
$-1.0 < \eta < 0.5$	$\leq 10$ GeV/ $c$
$0.5 < \eta < 1.0$	$\leq 15$ GeV/ $c$
$1.0 < \eta < 1.5$	$\leq 30$ GeV/ $c$
$1.5 < \eta < 2.5$	$\leq 50$ GeV/ $c$
$2.5 < \eta < 3.0$	$\leq 30$ GeV/ $c$
$3.0 < \eta < 3.5$	$\leq 20$ GeV/ $c$

**Table 8.4:** Requested PID momentum coverage for  $3\sigma$  pion/kaon separation.

One way of characterizing the kinematic distribution of hadrons within a jet is via the particle  $j_T$  and  $z$ , which are the transverse momentum of the particle with respect to the jet axis and the ratio of the total particle momentum over the jet momentum, respectively. Figure 8.40 demonstrates the loss in  $j_T$  and  $z$  coverage for identified particles which would result from lowering the PID momentum reach with respect to what we have requested. Figure 8.40a shows the available phase space for identified hadrons assuming the PID momentum ranges in Tab. 8.4 while Fig. 8.40b shows the ratio of the restricted momentum coverage phase space to the requested momentum coverage phase space. The restricted momentum coverage values were taken as  $\leq 5$  GeV/ $c$  for  $-1.0 < \eta < 1.0$ ,  $\leq 8$  GeV/ $c$  for  $1.0 < \eta < 2.0$ ,  $\leq 20$  GeV/ $c$  for  $2.0 < \eta < 3.0$ , and  $\leq 45$  GeV/ $c$  for  $3.0 < \eta < 3.5$ . It is readily apparent that a large fraction of  $j_T$  coverage is lost with the more restrictive PID reach and  $z$  values above 0.5 become inaccessible.

The impact of this phase space loss on the Collins asymmetry measurement [] can be seen in Fig. 8.41, which shows the statistical precision of the extracted Collins asymmetry for identified particles as a function of  $z$  for three  $x$  ranges assuming perfect PID (8.41a), the restricted PID momentum ranges listed above (8.41b), and the requested PID momentum ranges listed in Tab. 8.4 (8.41c). It is evident that restricting the PID coverage below our requested values, especially in the region  $1.0 < \eta < 2.5$ , will severely restrict the ability to measure the Collins asymmetry in the high  $z$  region where both the expected asymmetry and theoretical uncertainties are largest.

!!!! NEED TO ADD SECTION ON SIGMA SEPARATION STUDY !!!!

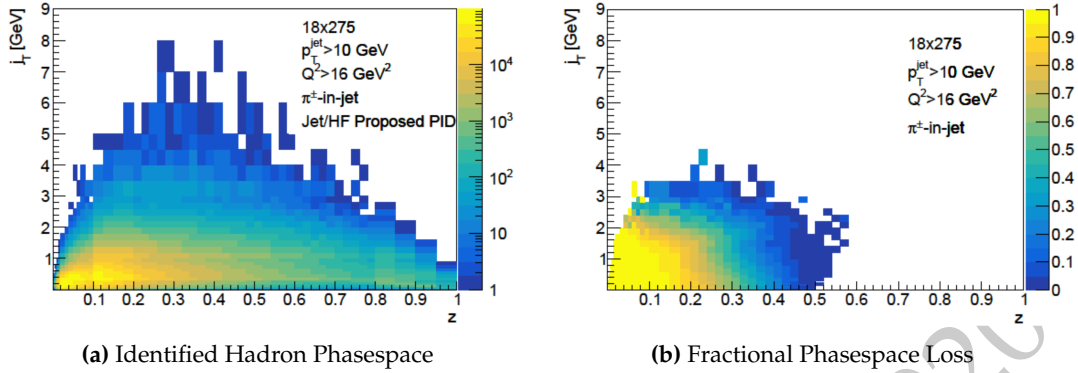


**Figure 8.40:** [PLACEHOLDER](a)  $j_T$  vs  $z$  distribution for identified hadrons inside jets assuming the PID capability listed in Tab. ?? . (b) Ratio of identified hadron  $j_T$  vs  $z$  phasespace assuming the originally proposed PID momentum limits enumerated above to the  $j_T$  vs  $z$  phasespace assuming the momentum limits in Tab. ?? .

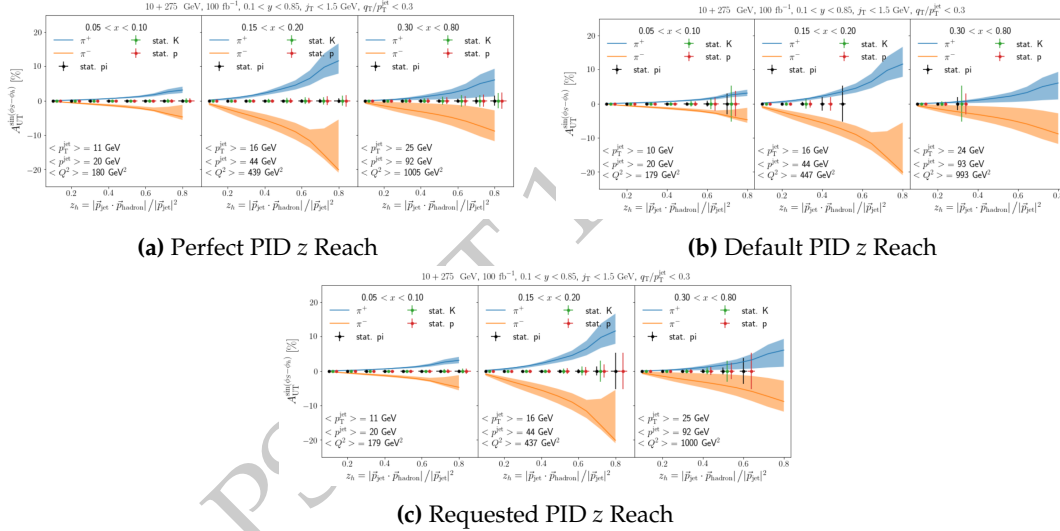


**Figure 8.41:** [PLACEHOLDER]Expected precision of Collins asymmetry measurement for identified hadrons as a function of  $z$  in three  $x$  bins assuming (a) perfect PID, (b) PID with the restricted momentum reach, and (c) PID with the requested momentum reach.

### 8.3.5 Calorimetry

For analyses considered by the JHQ WG, electromagnetic and hadron calorimetry will be utilized primarily in jet and event shape reconstruction where it will compliment information from the tracking detector to measure the full energy of the event. The calorimeters will provide the only means of measuring neutral energy, such as photons from (predominantly)  $\pi^0$  decay or long-lived neutral hadrons such as neutrons and  $K_L^0$ s. The electromagnetic and neutral hadron energy fractions in a typical jet are roughly 25% and 10%, respectively. As discussed in Sec. 8.3.3, the superior momentum resolution of the track-

ing system will make it the primary subsystem for detecting charged hadrons, yet at the most forward rapidities, jet energies are expected to be large enough for the calorimeter resolution to be competitive or superior to that of the tracker.

### Electromagnetic Calorimetry

The primary performance metric for the electromagnetic calorimeters (ECals) will be energy resolution, which directly effects the jet energy resolution as well as the accuracy of the reconstructed event shape. The resolution of the ECals, especially in the lepton-going direction, are primarily driven by the need to accurately reconstruct the scattered beam electron in order to reconstruct the event kinematics. As with the tracking momentum resolution, a set of baseline resolution values were provided based on appraisals of what performance could realistically be achieved with proven technology. These energy resolution values are parameterized in the form  $A\%/\sqrt{E} \oplus B\%$  and can be found in Tab. 8.5 for several pseudorapidity intervals. These resolutions were utilized in a number of jet analyses and, as shown in Fig. 8.36, resulted in acceptable JER values. The JHQ WG therefore puts forward these baseline resolutions as our requested ECal performance. Note that the baseline ECal energy resolutions did not include constant terms so many of the analyses included values between 1 and 3% depending on pseudorapidity range and the specific analysis.

Pseudorapidity Range	Energy Resolution ( $\sigma E/E\%$ )
$-3.5 < \eta < -2.5$	$2\%/\sqrt{E} \oplus 1 - 3\%$
$-2.5 < \eta < -2.0$	$2\%/\sqrt{E} \oplus 1 - 3\%$
$-2.0 < \eta < -1.5$	$7\%/\sqrt{E} \oplus 1 - 3\%$
$-1.5 < \eta < -1.0$	$7\%/\sqrt{E} \oplus 1 - 3\%$
$-1.0 < \eta < 3.5$	$10 - 12\%/\sqrt{E} \oplus 1 - 3\%$

**Table 8.5:** Requested electromagnetic calorimeter energy resolutions.

In addition to the energy resolution, there are several other performance aspects of the ECals which should be considered, such as detection thresholds and cluster separation and position resolutions. The threshold for detection of a ‘hit’ in the ECal will influence how much of the energy from a hadronizing parton is included in a jet, or accounted for in event shape and missing energy measurements. Several analyses have assumed minimum energy thresholds of between 100 MeV/ $c$  and 200 MeV/ $c$  and see good jet energy scales and missing transverse energy resolutions. While the JES and MET responses were not systematically explored as a function of ECal energy threshold, values in the vicinity of 100 to 200 MeV/ $c$  seem reasonable. The ability to isolate and accurately determine the position of clusters in the ECals will be important for analyses which consider the spatial distribution of energy such as (groomed) jet substructure and event shape measurements. The impact of ECal cluster position resolution was not studied in detail, but it is our expectation that resolutions arising from tower segmentation on the order of the Molière radius

would be adequate.

### Hadron Calorimetry

As with the electromagnetic calorimeters, the main performance criteria for the hadron calorimeters (HCals) will be energy resolution. Unlike with tracking or the ECals, however, the combination of low particle energies and poor resolution will make the relationship between HCal resolution and JER/JES non-trivial. For low energy jets, primarily at mid to negative rapidity, the poor HCal resolution can introduce large biases in the detector level jet sample due to the misreconstruction of low energy hadrons to much higher energies. Thus, in some regions, the capability of the HCal to identify and isolate neutral hadrons could have just as much impact on jet reconstruction as the intrinsic energy resolution. The studies below assume an energy detection threshold of between 400 and 500 MeV/c.

The JHQ WG requests hadron calorimeter coverage over nearly the full extent of the central detector ( $-3.5 < \eta < 3.5$ ) with the energy resolutions specified in Tab. 8.6. The baseline performance guidance indicated that a energy dependent resolution term of  $50\%/\sqrt{E}$  was realistic for the endcaps and it was determined that this, plus a 10% constant term, gave adequate jet energy resolutions in the lepton endcap ( $\eta < -1.0$ ) and so was kept as our official request. Likewise, a resolution of  $50\%/\sqrt{E} \oplus 10\%$  was found to lead to acceptable jet energy resolutions in the forward region ( $1.0 < \eta < 3.0$ ) where tracking resolutions are still relatively good. For very forward jets ( $\eta > 3.0$ ), a reduction of the HCal constant term (which dominates the energy resolution at high jet energy [1]) from 10% to 5% can appreciably improve JER (see presentation here [2]). This will benefit measurements such as the electron-jet Sivers asymmetry, where having an overall JER of around 8% will allow for differential measurements as a function of the vector sum of the lepton and jet transverse momenta (see [3] for more details). We note however, that the most forward resolution requirements could be compensated by lowering the hadron beam energy, which will shift jets at a given  $x - Q^2$  point to lower pseudorapidity as seen in Fig. 8.42. We thus keep our constant term request at 10% over the full hadron endcap range. The ability to shift jet pseudorapidities to lower values by reducing the beam energy also relieves the requirement that the calorimeter resolution performance extend beyond  $\eta > 3.5$ .

The resolution requirements in the barrel region ( $|\eta| < 1.0$ ) were explored in detail in two analyses: charged current DIS tagging and photoproduction jet reconstruction. One signature of charged current events is a large missing transverse energy ( $E_T^{\text{miss}}$ ), which is defined as the magnitude of the vector sum of all energy deposits in the detector. A study of charged current tagging was carried out in the Delphes framework and good resolution in ( $E_T^{\text{miss}}$ ) was seen even assuming a relatively poor barrel HCal resolution of  $100\%/\sqrt{E} \oplus 10\%$  [4]. However, the absence of a hadron calorimeter in the barrel led to large asymmetric tails in the ( $E_T^{\text{miss}}$ ) distribution that would complicate unfolding procedures and reduce photoproduction and NC DIS background rejection ability.

A somewhat higher resolution barrel HCal ( $85\%/\sqrt{E} \oplus 7\%$ ) was also studied in the eic-smear framework for photoproduction ( $Q^2 < 1.0 \text{ GeV}^2$ ) jet reconstruction (the findings

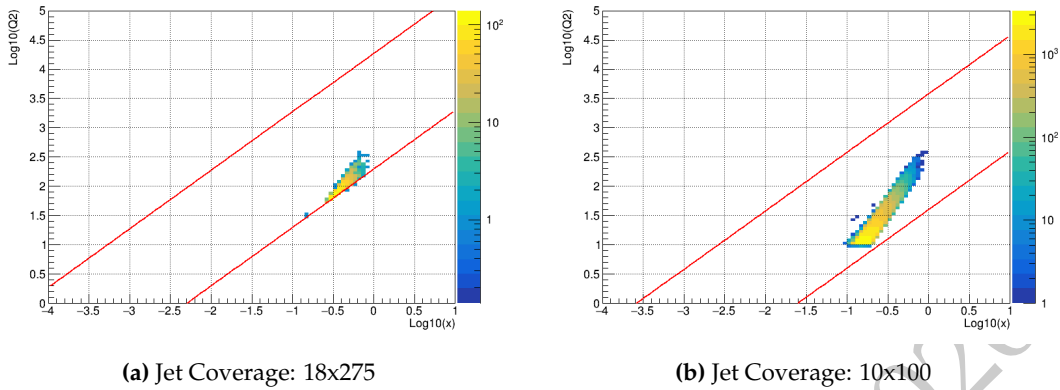


**Figure 8.42:** [PLACEHOLDER] $x - Q^2$  phase space covered by the struck quark (jet) from LO DIS at an energy combination of  $18 \times 275$  in the pseudorapidity range 3.0 to 3.5 (a) and at an energy combination of  $10 \times 100$  in the pseudorapidity range 2.0 to 2.5 (b). The  $x - Q^2$  range covered by high eta jets at the largest beam energy is also covered by lower rapidity jets at the lower beam energy.

Pseudorapidity Range	Energy Resolution ( $\sigma E/E\%$ )
$-3.5 < \eta < -1.0$	$50\%/\sqrt{E} \oplus 10\%$
$-1.0 < \eta < 1.0$	$85\%/\sqrt{E} \oplus 10\%$
$1.0 < \eta < 3.5$	$50\%/\sqrt{E} \oplus 10\%$

**Table 8.6:** Requested hadron calorimeter energy resolution.

below also manifest in the electroproduction region as well). When selecting smeared jets and comparing them to their matched particle level counterparts, a large bias in average transverse momentum / energy difference is seen for jets at lower pseudorapidities, while no such bias is seen if the HCal information is not used in the jet reconstruction as shown in the left hand panel in Fig. 8.43a. This effect arises because a certain fraction of the jets in a smeared  $p_T$  or energy bin actually arose from a particle level jet with much lower  $p_T$  or energy which contained a neutral hadron whose energy was smeared to a much higher value, and because of the steeply falling spectra, even small smearing at low  $p_T$  or energy can contribute to higher smeared bins. This effect becomes more pronounced at lower eta where jets have smaller energies. This bias can be reduced by improving the resolution of the barrel HCal as shown in Fig. 8.43b. However, a more effective method would be to select only those jets which do not contain a neutral hadron, and thus do not suffer from the large energy distortion, by using the HCal as a neutral hadron veto. This is illustrated in Fig.8.43c where the red curve, which is for jets which do not contain a neutral hadron, shows no bias and much better resolution. This neutral hadron veto capability depends critically on the ability to physically isolate individual showers within the calorimeter and match them to a charged particle track to select clusters arising from long-lived neutral hadrons. The feasibility of this method will need to be studied in more detail using full detector models, especially in the forward region where individual showers will

be physically close to one another. Despite the bias seen in Fig., we request a barrel HCal resolution of  $85\%/\sqrt{E} \oplus 10\%$  with the expectation that the total resolution will be somewhat improved when information from the HCal and ECal are used in concert and/or veto methods can be implemented.

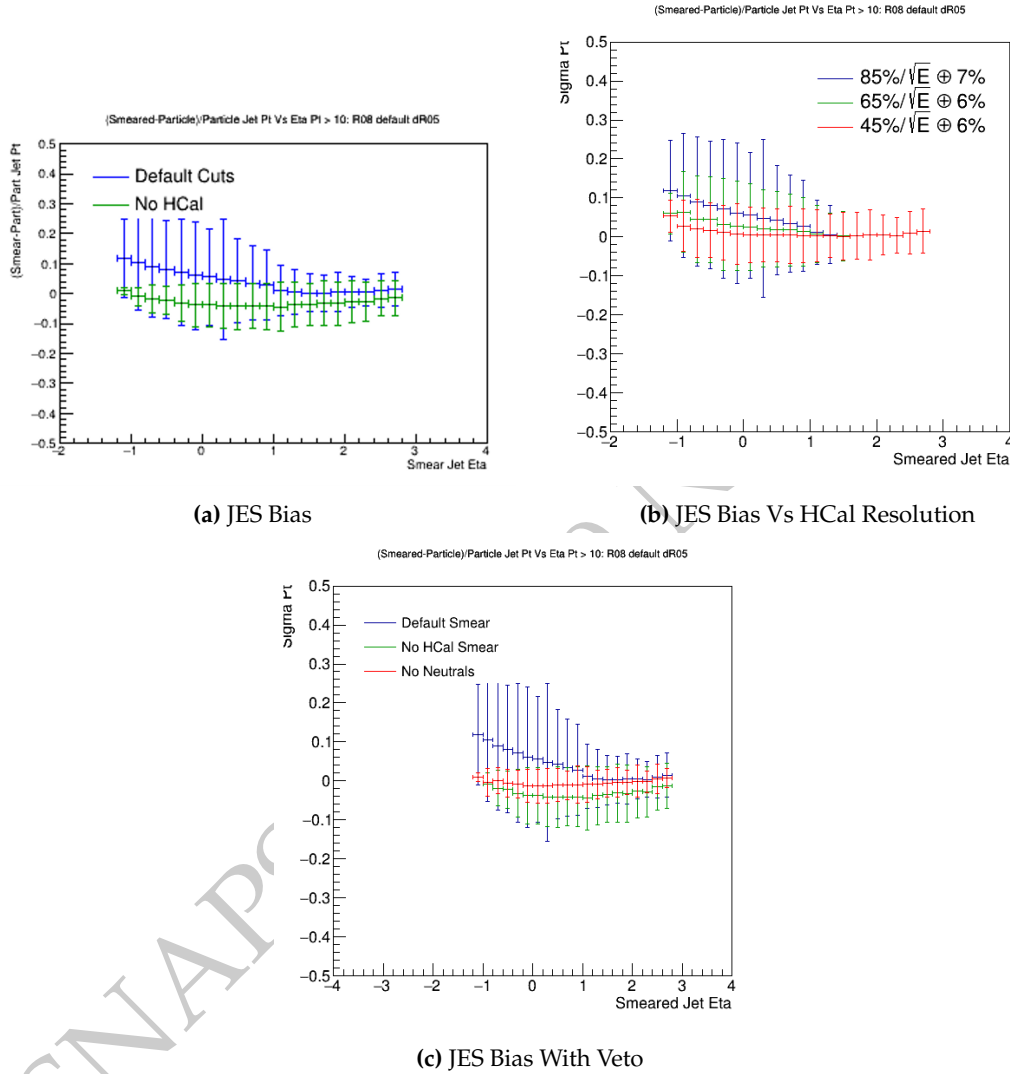


**Figure 8.43:** [PLACEHOLDER](a) Relative difference between matched particle and smeared jet  $p_T$  as a function of jet pseudorapidity when selecting smeared jets with  $p_T \geq 10$  GeV/ $c$  when reconstructing jets with (blue) and without (green) HCal information. (b) Same as blue curve in (a) for three different barrel HCal energy resolutions. (c) Blue and green curves are the same as in (a) and red curve shows relative difference for those smeared jets which do not contain a neutral hadron.

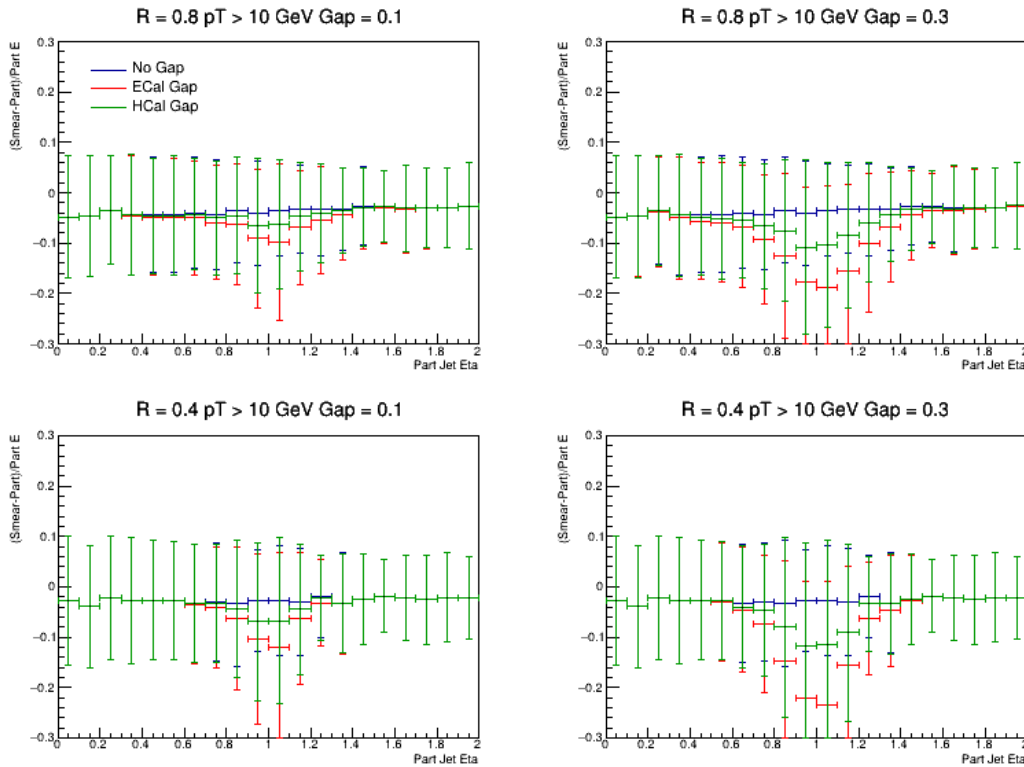


**Figure 8.44:** [PLACEHOLDER] Effect of electromagnetic and hadron calorimeter coverage gaps of 0.1 (left column) and 0.3 (right column) units of pseudorapidity on particle level jets of  $R = 0.8$  (upper row) and  $R = 0.4$  (lower row) and  $pT \gtrsim 10 \text{ GeV}/c$ . The gap is centered at  $\eta = 1$ .

### Coverage Continuity

All analyses carried out by the JHQ WG assumed uninterrupted calorimeter coverage over the full range of the central detector. In a real detector, however, there is the possibility of a coverage gap(s) (likely near the barrel-endcap interface) to accommodate services to/from the inner detectors or due to interference between barrel and endcap detector components. Without a full detector model, it is impossible to know the exact size and location of any gap(s) and determine the effect one would have on our observables. However, a qualitative assessment of the impact of a gap can be achieved in fast simulation simply by zeroing out the calorimeter response in the desired region.

Figure 8.44 shows the effect of a gap in calorimeter coverage on the smearing of particle level jets. As should be expected, greater deviations are seen for the larger gap size, while jets with larger radii show a less pronounced dip than their smaller radii counterparts due to the fact that they always cover more of the pseudorapidity range unaffected by the coverage gap. It is also seen that a gap in electromagnetic calorimetry will have a larger effect than a break in hadron calorimetry.

While the simple analysis above does not set a requirement on the tolerable size of a gap for any given analysis, it should give a qualitative picture as to what the effects on a jet would be. Given that jets are extended objects and event shape analyses aim to characterize the energy distribution of the entire event, the JHQ WG requests that any calorimeter gap in the main detector volume be kept as small as possible.

### 8.3.6 Summary

The detector performance requirements as determined by the JHQ WG are summarized in Tab. 8.7 below.

$\eta$	Tracking			PID		ECal		HCal	
	Momentum Resolution	Vertex Resolution	Min pT	Momentum Range	Separation	Energy Resolution	Min Energy	Energy Resolution	Min Energy
$-3.5 < \eta < -3.0$	$0.1\% \times P \oplus 0.5\%$	N/A	100 MeV/c	$\leq 7$ GeV/c	$3\sigma$	$2\%/\sqrt{E} \oplus 1 - 3\%$	200 MeV/c <sup>2</sup>	$50\%/\sqrt{E} \oplus 10\%$	400 – 500 MeV/c <sup>2</sup>
$-3.0 < \eta < -2.5$	"	$30/p_T \oplus 40 \mu\text{m}$	"	"	"	"	"	"	"
$-2.5 < \eta < -2.0$	"	$30/p_T \oplus 20 \mu\text{m}$	"	"	"	"	"	"	"
$-2.0 < \eta < -1.5$	$0.05\% \times P \oplus 0.5\%$	"	"	"	"	$7\%/\sqrt{E} \oplus 1 - 3\%$	"	"	"
$-1.5 < \eta < -1.0$	"	"	"	"	"	"	"	"	"
$-1.0 < \eta < -0.5$	"	$20/p_T \oplus 5 \mu\text{m}$	"	$\leq 10$ GeV/c	"	$10 - 12\%/\sqrt{E} \oplus 1 - 3\%$	"	$85\%/\sqrt{E} \oplus 10\%$	"
$-0.5 < \eta < 0.0$	"	"	"	"	"	"	"	"	"
$0.0 < \eta < 0.5$	"	"	"	"	"	"	"	"	"
$0.5 < \eta < 1.0$	"	"	"	$\leq 15$ GeV/c	"	"	"	"	"
$1.0 < \eta < 1.5$	$0.05\% \times P \oplus 1.0\%$	$30/p_T \oplus 20 \mu\text{m}$	"	$\leq 30$ GeV/c	"	"	"	$50\%/\sqrt{E} \oplus 10\%$	"
$1.5 < \eta < 2.0$	"	"	"	$\leq 50$ GeV/c	"	"	"	"	"
$2.0 < \eta < 2.5$	"	"	"	"	"	"	"	"	"
$2.5 < \eta < 3.0$	$0.1\% \times P \oplus 2.0\%$	$30/p_T \oplus 40 \mu\text{m}$	"	$\leq 30$ GeV/c	"	"	"	"	"
$3.0 < \eta < 3.5$	"	$30/p_T \oplus 60 \mu\text{m}$	"	$\leq 20$ GeV/c	"	"	"	"	"

Table 8.7: Summary of requirements

## 8.4 Exclusive Measurements

### 8.4.1 Deeply virtual Compton scattering and exclusive production of $\pi^0$ in $ep$

Deeply virtual Compton scattering (DVCS) and the hard exclusive production of  $\pi^0$  mesons off a nucleon play a prominent role in the studies of GPDs. DVCS gives access to chiral-even GPDs, which are important for the extraction of information on both the nucleon tomography and the energy-momentum tensor (EMT), including access to the total angular momentum of partons, as discussed in Sec. 7.2.2.

Hard exclusive production of  $\pi^0$  mesons, on the other hand, gives access to chiral-odd GPDs, some of which are related to transversity distributions, which are extensively studied in SIDIS and Drell-Yan processes.

The similarity between the final states of DVCS and hard exclusive production of  $\pi^0$ , see Sec. 7.2.2, suggests that the detectability of both processes in an apparatus equipped with electromagnetic calorimeters (ECALs) can be studied together. Another reason for a joined study of this type is that DVMP  $\pi^0$  may become a background to DVCS. This happens when one low-energy photon coming from  $\pi^0$  decay misses ECALs, its energy is too low

for a detection, or if two electromagnetic cascades induced by photons can not be distinguished from each other. A common analysis of DVCS and DVMP  $\pi^0$  therefore allows to stress three main aspects of ECALs design: geometrical acceptance, energy thresholds and granularity.

The study presented in this subsection is based on two Monte Carlo generators. The first one is MILOU 3D, a recently updated version of MILOU [1185], used to generate DVCS events. The original version of MILOU is supplied with two-dimensional  $(x_{\text{Bj}}, Q^2)$  lookup tables of DVCS sub-amplitudes, referred to as Compton form factors (CFFs), while  $t$ -dependance of those factors is factorised out and modelled with either exponential or dipole Ansatz. This way of modeling of CFFs has been modified for the purpose of this study. Namely, MILOU 3D can now be supplied with three-dimensional  $(x_{\text{Bj}}, Q^2, t)$  tables, allowing one to take into account an interplay between all three variables, which is important to describe data at energies lower than those available at HERA [1186]. This modification allowed us to use two realistic GPD models to generate the lookup tables: KM [1187–1190] implemented in GeParD and GK [1191–1193] implemented in PARTONS [1194]. These two models significantly differ by the construction, i.e. they are based on different schemes of GPD modelling, and they are constrained by different experimental data. The second generator is toyMC, which was developed for the purpose of this study. It assigns a weight to each generated event, which corresponds to either DVCS or DVMP  $\pi^0$  cross-section. For this generator the lookup tables of cross-sections were generated with GK model, which includes chiral-odd GPDs crucial for the description of exclusive  $\pi^0$  production. The amplitudes for DVMP  $\pi^0$  were evaluated using GK formalism [1191], which is based on the modified perturbative approach [1195], allowing one to overcome the problem of infrared divergences that appear for transversely polarised virtual photons. Among many available versions of chiral-odd GK GPDs we have chosen the one that successfully describes cross-sections measured by COMPASS [1196]. The kinematic domain covered by this measurement significantly overlaps that of EIC, particularly at its lowest beam energy configuration:  $5 \text{ GeV} \times 41 \text{ GeV}$ . Both generators can be interfaced with eic-smearer.

Figure 8.45, realized simulating 500k events with MILOU 3D, compares the DVCS kinematics generated according to KM20 [1190] (blue) and GK [1193] (red) for the lowest and highest beam energy configurations. The following cuts have been applied at generation level:  $Q^2 > 1 \text{ GeV}^2$ ,  $0.01 < y < 0.95$ , and  $0.01 < |t| \text{ GeV}^2 < 1.6$ . Both models predict a significant drop of the cross section with  $Q^2$ . The different  $|t|$  distributions for GK (exponential) and KM20 (dipole) are also evident.

Using the same sample of generated DVCS events, we have also simulated the energy and pseudo-rapidity distributions of scattered electron and produced real photon in a DVCS process. Figure 8.46 visualizes these spectra for the lowest and highest beam energy configuration. At lower energies the electron is predicted to be scattered within the nominal combined EMCAL+Tracker acceptance of  $|\eta| < 3.5$ . At the top electron-beam energy, the peak in the scattered electron distribution is predicted to be at  $\eta = -3.6$ . This is expected to be valid for other exclusive processes, making a slightly extended acceptance at backwards pseudo-rapidities beneficial for detection efficiency. Both models predict that the nominal  $|\eta| < 3.5$  acceptance should be enough for detecting most of the produced photons, with a

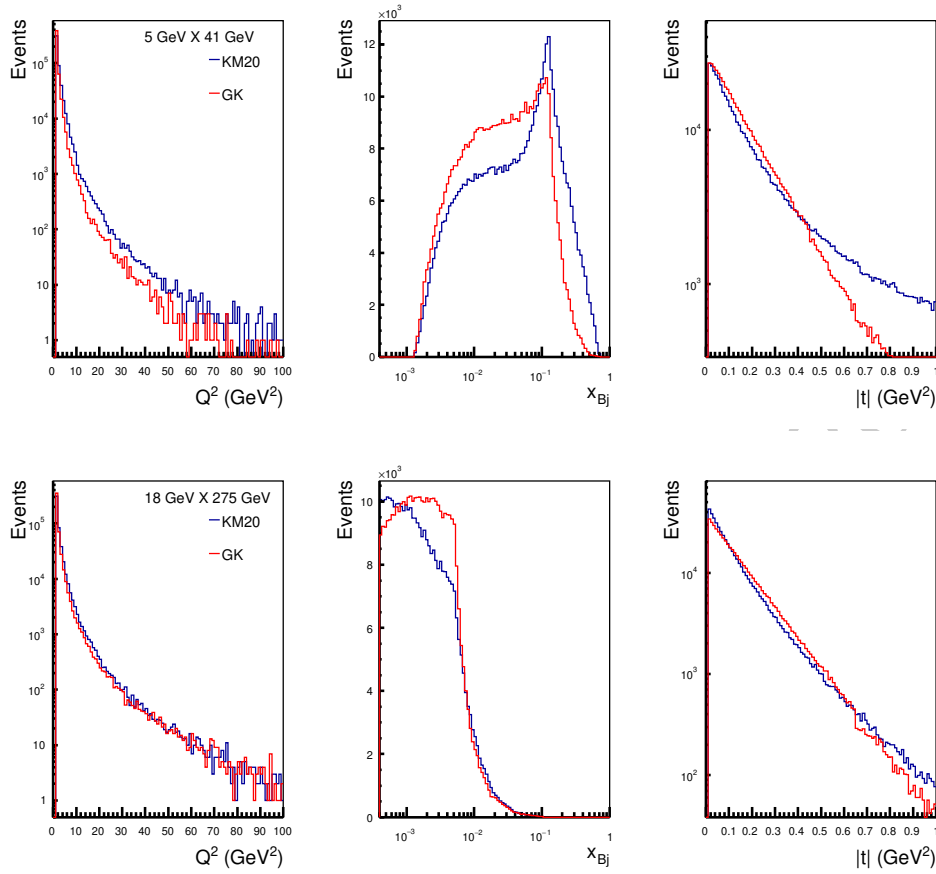


**Figure 8.45:** Kinematic distributions of DVCS events generated according to KM20 (blue) and GK (red) models.

nearly perfect situation at smaller beam energies and a slight loss in efficiency at top beam energy, notably at very low values of  $x_B$ .

In order to assess the significance of  $\pi^0$  background, the pseudo-rapidity distribution of photons from DVCS and exclusive  $\pi^0$  production before applying the smearing is compared in Fig. 8.47. These histograms represent the sample of events generated with toyMC for the four beam energy configurations considered in this report and assume an integrated luminosity of  $\mathcal{L} = 10 \text{ fb}^{-1}$  per each configuration. Two cuts were applied to the sample before making the histograms:  $Q^2 > 1 \text{ GeV}^2$  and  $0.01 < y < 0.95$ . The validity of  $y$ -cut was checked with a sample of events after applying the smearing. This study shows that at  $y = 0.01$  one may expect the resolution of this variable at the order of  $dy/y \approx 0.5$  for  $5 \text{ GeV} \times 41 \text{ GeV}$  and  $dy/y \approx 1$  for  $18 \text{ GeV} \times 275 \text{ GeV}$  beam energy configuration. We conclude that for  $18 \text{ GeV} \times 275 \text{ GeV}$  and the assumed acceptance of  $|\eta| < 3.5$  for both electrons and photons one may expect to lose 14%/17% of DVCS events and 11%/12% of exclusive  $\pi^0$  events, where the first number is due to the acceptance on electrons, while

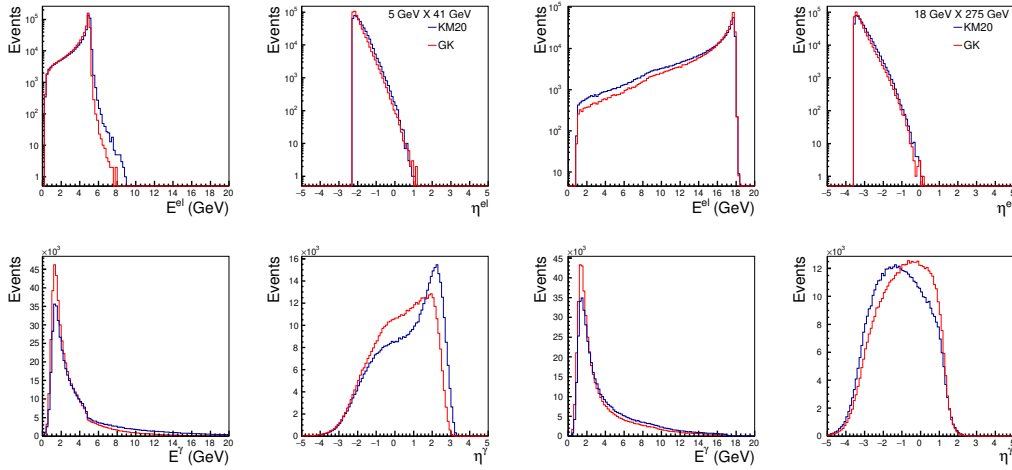


**Figure 8.46:** Energy and pseudo-rapidity spectra of DVCS events generated according to KM20 (blue) and GK (red) models.

the second one is due to the acceptance on both electrons and photons. The loss is mainly seen for  $Q^2 \approx 1 \text{ GeV}^2$  events. The loss of DVCS events can be almost entirely recovered by slightly extending coverage in backwards pseudo-rapidity to  $\eta < -3.7$  from the currently assumed value of  $\eta < -3.5$ . For lower beam energies the loss is smaller, in particular for  $5 \text{ GeV} \times 41 \text{ GeV}$  it is at the order of 1%.

The contamination of DVCS sample by misinterpreted exclusive  $\pi^0$  events is demonstrated with Fig. 8.48, where the ratio of events in bins of  $(x_{Bj}, Q^2)$  is shown for  $5 \text{ GeV} \times 41 \text{ GeV}$  beam energies. This energy configuration is chosen because of the relative event yield (cf. Fig. 8.47) being the largest one comparing to other configurations. The plot is made for the sample of events generated with toyMC after applying  $Q^2 > 1 \text{ GeV}^2$  and  $0.01 < y < 0.95$  cuts, requiring both electrons and photons to be reconstructed assuming  $|\eta| < 3.5$  acceptance. With no additional cuts on energy thresholds for the detection of photons in ECALs and cuts on the spacial separation of  $\pi^0$  decay photons, we may estimate that in the domain of high- $x_{Bj}$  one may expect a significant yield of DVMP  $\pi^0$  events with respect to DVCS. The effect of such cuts can be deduced from plots like those show in Fig. 8.49, where spectra of energy and opening angles of photons are shown.

### 8.4.2 Neutron target

Neutron GPDs can also be studied at the EIC, where the unique collider experiment at high energy with fully reconstructed final-state particles can provide insights into the neutron substructure. Since there is no easy source of a free neutron target at collider facilities, one of the experimental challenges of constraining the neutron GPDs is to separate the background from nucleus-induced effect when colliding with nuclei. Hereby, the newly proposed experimental technique of spectator tagging in light nuclei [19], e.g. deuteron,

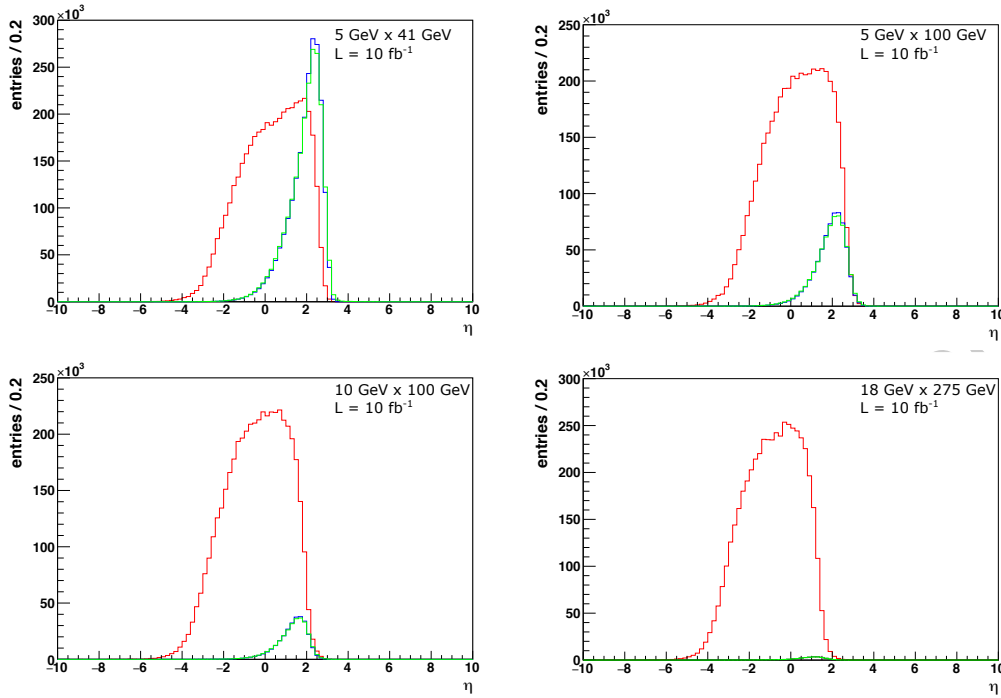


**Figure 8.47:** Distributions of pseudo-rapidity for DVCS photons (red), exclusive  $\pi^0$  mesons (blue) and photons coming from decays of  $\pi^0 \rightarrow \gamma\gamma$  (green, histogram scaled by  $\frac{1}{2}$ ) for four beam energy configurations (see the insert labels) and  $10 \text{ fb}^{-1}$  of integrated luminosity.

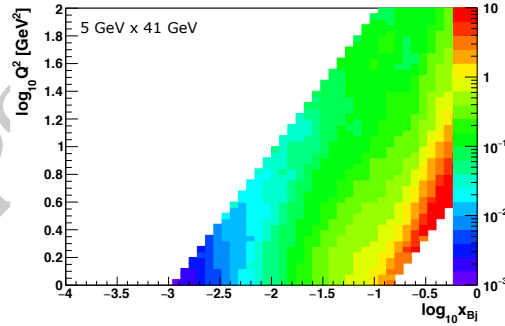


**Figure 8.48:** Ratio of DVMP  $\pi^0$  to DVCS event yields in phase-space of  $(x_{Bj}, Q^2)$  for  $5 \text{ GeV} \times 41 \text{ GeV}$  beam energies. For more details see the text.

will provide a clean and unambiguous way to measure the neutron GPD. The idea is to measure an exclusive reaction, e.g. DVCS, on the deuteron, where the final-state particles are exclusively identified, including the real photon and the spectator nucleon. Generally the real photon goes into the main detector at mid-rapidity, while the spectator nucleon has a rapidity close to the deuteron beam that goes to the far-forward region. For the

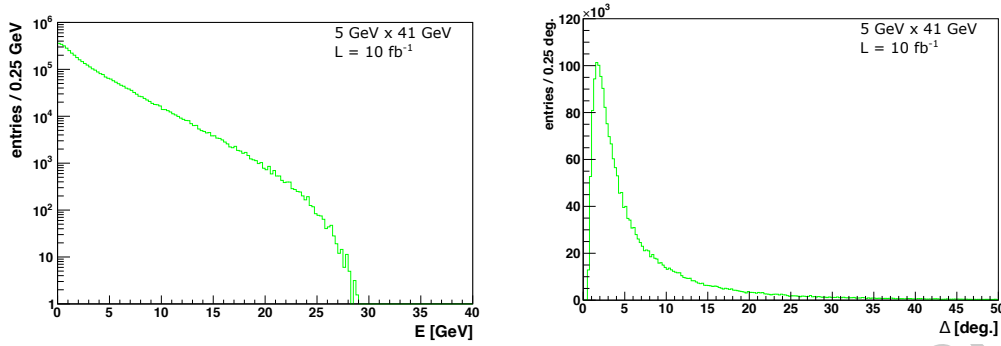


**Figure 8.49:** energy distribution of photons coming from decays of exclusively produced  $\pi^0 \rightarrow \gamma\gamma$  (left) and distribution of opening angle between those photons (right). Plots are for  $5 \text{ GeV} \times 41 \text{ GeV}$  beam energies and  $10 \text{ fb}^{-1}$  of integrated luminosity

case of studying the neutron GPDs, the spectator nucleon would be a proton such that the exclusive process can be unambiguously measured on the neutron. This will be almost no different than the DVCS measurement on a free proton because the deuteron is very loosely bound. For the detector requirements on the DVCS on neutron, they are in fact very similar to the study of the diffractive  $J/\psi$  measurement in electron-deuteron scattering at the EIC, which can be found in Ref. [720] and also discussed in Sec. 8.5.5 of this Yellow Report. The conclusion based on these detail studies is that, a reasonable design of forward proton and neutron detectors at the EIC, the momentum transfer distributions  $t$  of the DVCS process can be measured very precisely for a wide range of  $t$  range. This can be achieved by combining two different methods described in Sec. 8.4.6 for  $t$  reconstruction and with spectator tagging method to identify the events. The spectator proton acceptance is almost 100% for the general case of deuteron breakups. In addition, different methods of reconstructing the  $t$  distribution can provide a better handle of systematic uncertainty on the measurement, including sources arising from beam momentum spread and angular divergence.

### 8.4.3 Deeply virtual Compton scattering off helium

To evaluate the feasibility of the physics of exclusive reactions on light nuclei described in section ???. The expected main limitation is the detection range in  $t$ , for which the most challenging situation is helium, thus we will concentrate here on these nuclei. Many processes are of great interest, but here we will focus on coherent DVCS. For reactions such as tagged DVCS or DVMP, the detector needs combine the ones we identify in this section, in addition to the ones identified from the similar processes tagged DIS and DVMP on the proton.

### The Orsay-Perugia Event Generator (TOPEG)

For this study, a new Monte Carlo event generator for the coherent DVCS off the  $^4\text{He}$  nucleus has been developed. This tool, called the Orsay-Perugia event generator (TOPEG), is based on the Foam ROOT library [1197]. The generated cross section exploits at LO the model for the chiral even GPD describing the  $^4\text{He}$  parton structure presented in Ref. [550]. Checks at the JLab kinematics with an electron beam energy of 6 GeV have been successfully performed. TOPEG works in two stages: the exploration and the generation. During the exploration, a *foam* of cells is generated and filled with an approximated cross section constant in each cell. The weight, i.e. the ratio between the true distribution and the approximated one, is calculated. The generation is then based on the approximated distribution. For each generated event, a call of the function is done to check that the cross section has a reasonable value at the exact generated kinematic. In the model calculation, the real part of the Compton form factor, involving a principal value integral, is most time consuming. Besides, since this term affects the magnitude of the cross-section only with a little impact at the kinematics considered, we neglected this term in the generation of the event presented in the following.

For the three scenarios of EIC, we generated 1 million events with  $Q^2 > 4 \text{ GeV}^2$  and  $t_{min} < |t| < t_{min} + 0.5 \text{ GeV}^2$ . The corresponding luminosity ranges between [100-250]  $\text{nb}^{-1}$  going from the high energy configuration to the lower ones. The obtained total cross section ranges between [4-11]  $\mu\text{b}$  and grows with the beam energies since it is dominated by the form factor of the  $^4\text{He}$  strongly dependent on  $t$ . This value, however, is significantly reduced (around 95% or more) when accounting for the  $t$  acceptance of the helium nuclei in the far forward detectors.

### Central detector

From these events, we evaluated the acceptance of electrons and photons to be detected in the central detector. The DVCS photons are shown in Fig. ?? for all energy configurations. We observe that they are mostly in easily accessible kinematics within the acceptance described by the detector matrix. The limit is reached only for some low angle photons in the highest energy configuration. This concerns mostly the lowest  $x_B$  events and thus the highest energy settings for  $\phi_h \approx 0$  kinematics. This is not too concerning as this kinematic region concentrates mostly the BH contribution to the process and has little importance for the extraction of the CFF and the physics goals in general. However, the proportion of lost events raises to 20% for the highest energy setting, which shows that the pseudorapidity limit of 3.5 is critical and starts to significantly affect the data collected. If this limit was to be modified, it could affect strongly the physics reach at low  $x_B$  and reduce the interest to run light nuclei at the highest energy settings.

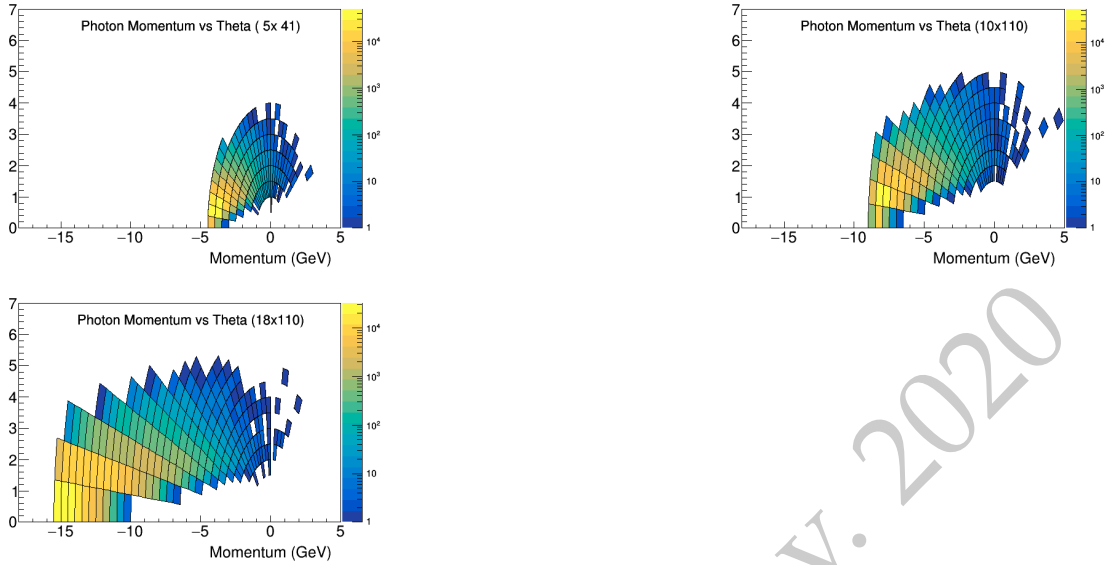


**Figure 8.50:** Kinematic distribution of the photons produced in coherent DVCS on helium-4 as generated with TOPEG for the three energy configurations envisioned for the EIC.

### Forward detector

In the far forward region, where the scattered helium nuclei is detected, the situation is more complicated. At low  $x_B$ ,  $t_{min}$  becomes very small leading to kinematics impossible to access. Effectively, the minimum  $t$  will be the one set by the detector capabilities. While on the high  $t$  the limitation will be the luminosity. These two values are the critical limits that need to be evaluated for the light nuclei coherent processes.

In the detector matrix, the limit at low  $t$  is given by the Roman pot capabilities. It is expected to detect recoil nuclei at transverse momenta as low as 0.2 GeV. This corresponds to  $-t \approx 0.04 \text{ GeV}^2$ . In a similar fashion to the photon acceptance, this appears to leave plenty of room to study the  $t$  dependence between  $t_{min}$  and the first minimum (at  $-t \approx 0.7, 0.42, 0.48 \text{ GeV}^2$  for  $d, {}^3\text{He}, {}^4\text{He}$ , respectively). However, we have  $t \sim p_{\perp}^2$  such that a degradation of the reach proposed would rapidly affect our capability to study  ${}^3\text{He}$  and  ${}^4\text{He}$  coherent DVCS.

### Overall performance

Overall, it appears that the detector capabilities proposed in this report have a wide enough kinematical range to study the tomography and other possible elusive nuclear parton dynamics around the critical first diffraction minimum of the electromagnetic form factor. We identify two key points as critical for these studies, in the sense that a degradation would directly affect the physics accessible. These are the minimum angle of photon detection in the backward detector and the minimum transverse momentum accessible in

the Roman pots for recoil nuclei.

**R. Dupré:** To be included soon a figure illustrating the degradation of the figure of merit for different detection ranges.

#### 8.4.4 Exclusive vector meson production in $ep$

We used the lAger event generator [1198] to obtain samples of  $J/\psi$  and  $Y$  events, where the  $J/\psi$  and  $Y$  photoproduction cross sections are those from fits in a vector-meson dominance model to the world data from Refs. [136, 1199]. This photoproduction cross section is then used to obtain the electroproduction cross section as described in Ref. [1199] Appendix A. For the decay into  $e^\pm$  and  $\mu^\pm$  we assumed s-channel helicity conservation. We used the PHOTOS [1200] package to account for the radiative effects on the vector meson decay. Finally, we used the GRAPE-DILEPTON [1201] program to simulate the dilepton background to the detected exclusive final state. To simulate detector effects, we used eic-smear with matrix detector [1202], including far-forward elements. Finally, for our studies, we evaluated the nominal beam configurations: 5 GeV electrons on 41 GeV protons, 5 GeV electrons on 100 GeV protons, 10 GeV electrons on 100 GeV protons, and 18 GeV electrons on 275 GeV protons. For brevity, we only include results for the lowest and highest energy configuration in this document, as they form a realistic envelope for the other configurations.

#### Detector requirements

To fully detect the exclusive reaction, we need to detect the scattered lepton, recoil proton, and both decay leptons. Note that the event geometry concerning the scattered lepton and recoil proton is very similar to that of DVCS. A summary of the polar distributions of the leptons in DVMP for the lowest and highest collision energies are shown in Figure 8.51.

The recoil proton detection occurs through a combination of forward and far-forward detector elements. For increasing collision energy, the recoil becomes increasingly forward. Figure 8.52 shows recoil  $p_T$  as a function of the recoil polar angle  $\theta$ . The dashed line shows a nominal  $p_T$  cutoff below 200 MeV, which does not majorly impact the detector's physics reach. Comparing the lower and higher beam setting in this figure, we will need a smooth transition between a forward B0-style detector into a Roman Pot-like system.

Fig. 8.53 shows  $Q^2$  as a function of pseudorapidity  $\eta$ . The orange box corresponds to a nominal central detector covering  $|\eta| < 3.5$ , while the magenta box corresponds to a nominal low- $Q^2$  tagger accepting  $-6.9 < \eta < -5.8$ . The central detector acceptance is sufficient for all configurations to accept events from  $Q^2 > 0.1$  to large values of  $Q^2$ . The lower limit of  $Q^2 > -3.5$  is restrictive for photoproduction events in the main detector, especially for higher collision energies. The photoproduction of DVMP at higher energies will completely depend on the low- $Q^2$  tagger unless a significant enhancement of the backward region's electron acceptance is possible. More acceptance in the low  $Q^2$  tagger would directly translate into more measured photoproduction events. A better acceptance

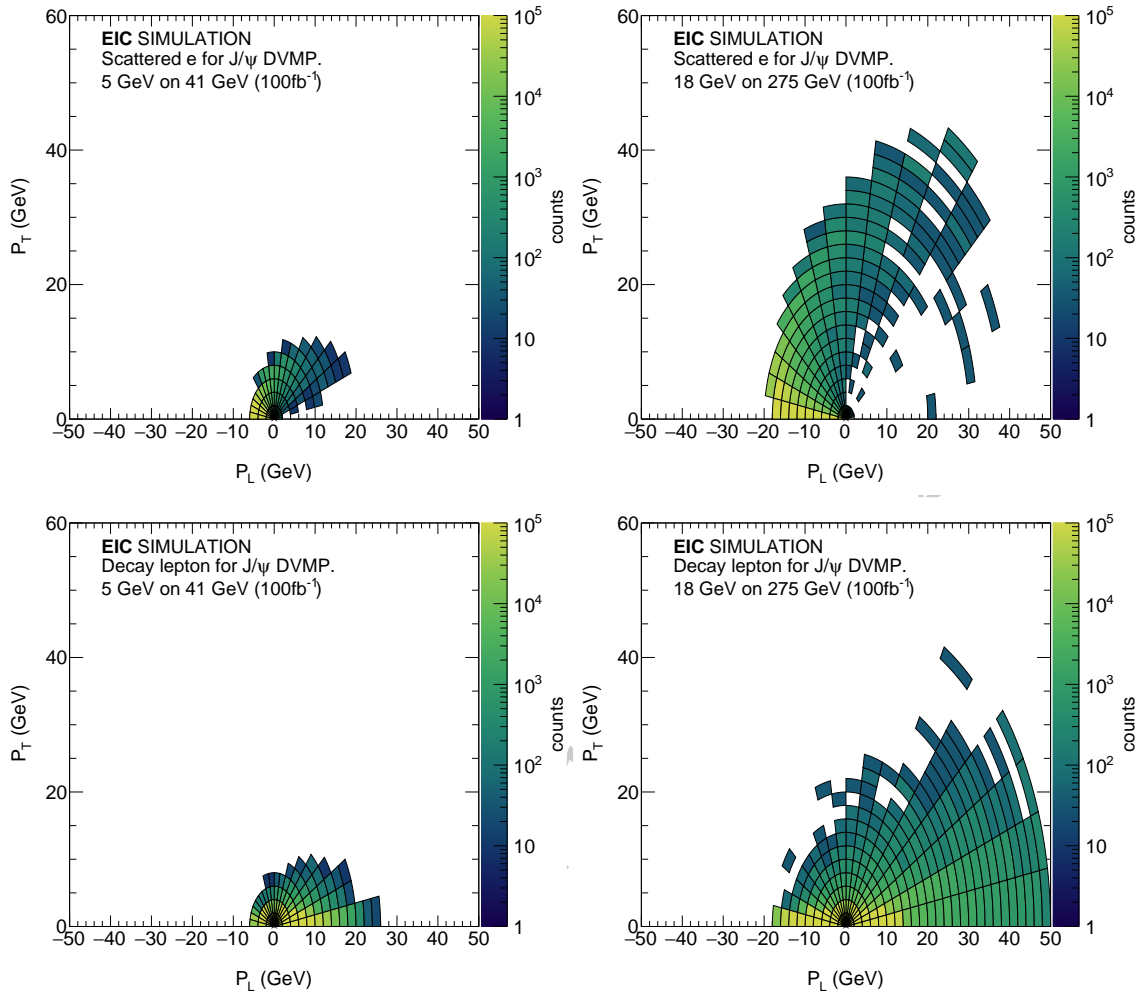


**Figure 8.51:** Polar figures of the momentum distribution for the scattered electron (top panels) and decay leptons (bottom panels) for  $J/\psi$  DVMP at the lowest and highest energy configurations.

for low  $Q^2$  events would benefit Upsilon photoproduction near threshold, where the projected statistical precision is particularly low (cf. Fig. 8.57). For a summary graph of the polar distributions for the scattered electron, see Figure 8.51 (top panels).

The main detector will measure the  $e^\pm$  and  $\mu^\pm$  pair from  $J/\psi$  and  $Y$  decay. Figure 8.54 shows  $Q^2$  (top) and  $W$  (bottom) versus decay lepton rapidity. The nominal central detector range of  $|\eta| < 3.5$  envelopes the majority of events. The bottom panels show a slight  $W$  dependence of the decay particle eta, but the loss of acceptance at lower  $W$  is relatively minor. The top panels show a discontinuity between the higher and lower  $Q^2$  points, caused by the rapidity gap between the electron endcap and the low- $Q^2$  tagger. From a detector point of view, the limiting factor for DVMP is the low  $Q^2$  acceptance, limiting the event count in the  $Y$  threshold region important for the physics of mass. Expanding the accep-

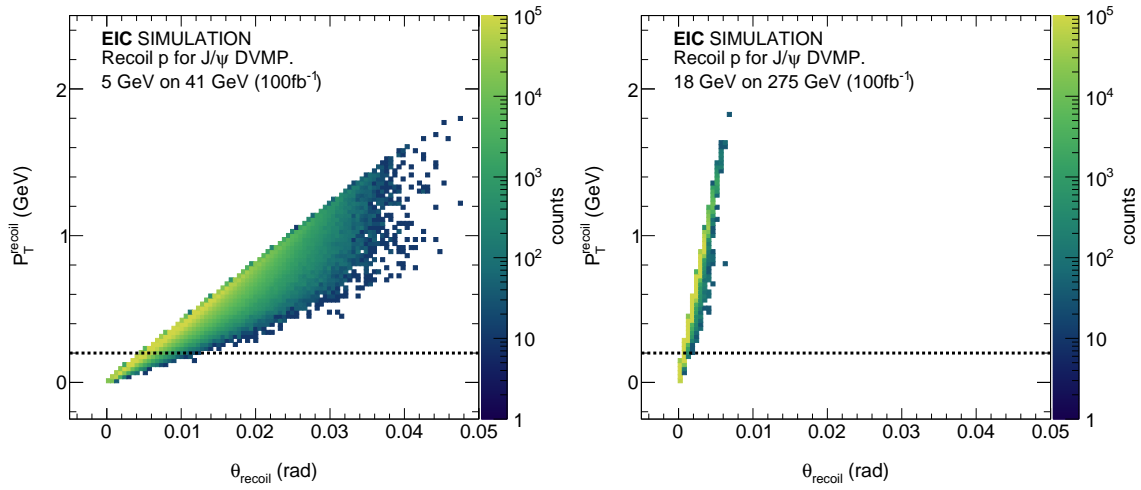


**Figure 8.52:** Transverse momentum  $p_T$  versus polar angle  $\theta$  for recoil protons in exclusive  $J/\psi$  DVMP for the lowest and highest energy configurations. The dashed line corresponds to a lower  $p_T$  cut of 200 MeV.

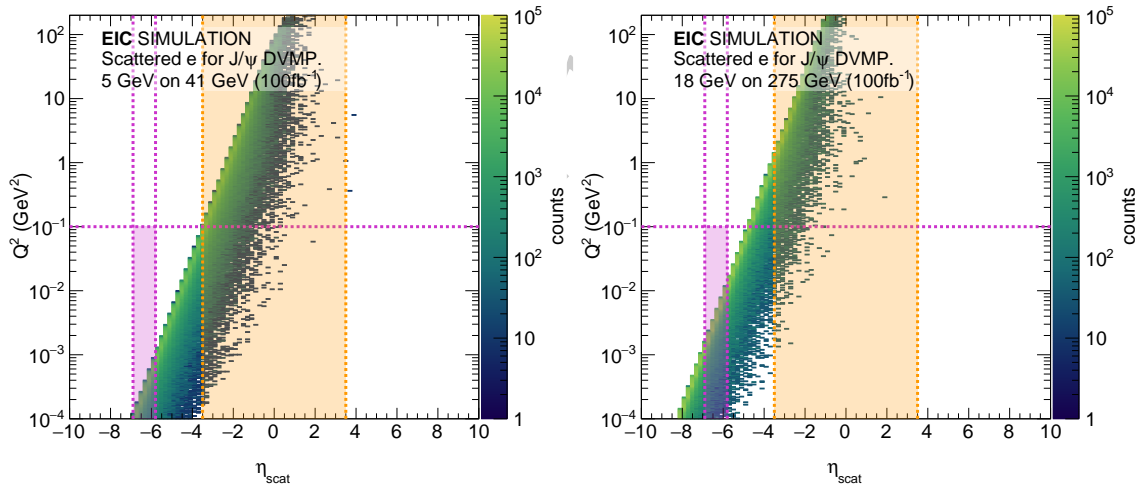


**Figure 8.53:**  $Q^2$  as a function of the scattered electron pseudo-rapidity for exclusive  $J/\psi$  DVMP with the lowest and highest energy configurations. The orange box indicates scattered electrons detected in the nominal central detector, while the magenta box corresponds to events detected with the low- $Q^2$  tagger.

tance in the low- $Q^2$  tagger would dramatically improve the statistics in these regions. For a summary graph of the polar distributions for the decay leptons, see Figure 8.51 (bottom panels).

The impact of the nominal fiducial volume of  $|\eta| < 3.5$  in the main detector on the  $x_V$  coverage at the highest collision energy for  $J/\psi$  DVMP is explored in Figure 8.55 for elec-

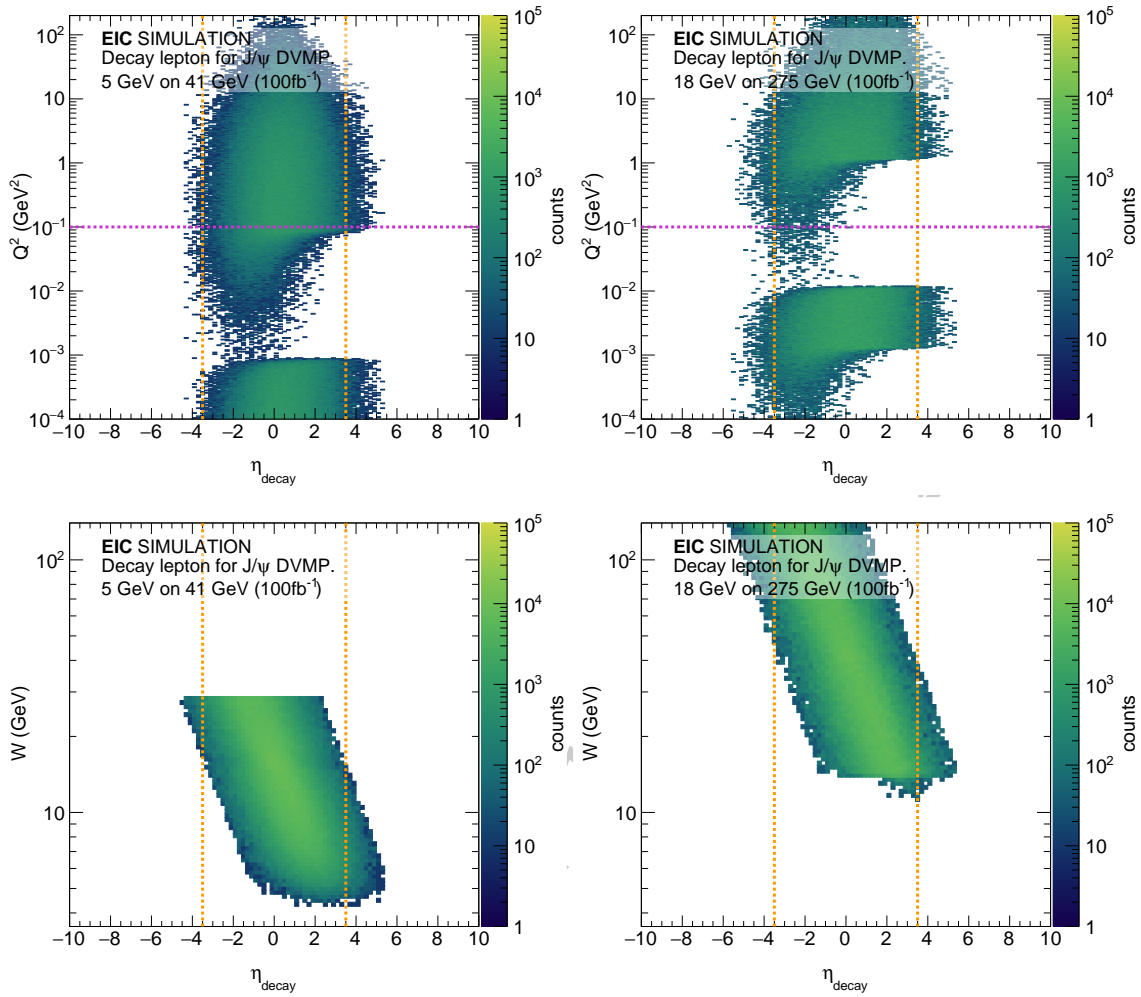


**Figure 8.54:**  $Q^2$  (top) and  $W$  (bottom) versus decay lepton rapidity for exclusive  $J/\psi$  DVMP for the lowest and highest energy configurations (left and right). The two structure on the top graphs are due to the discontinuity between scattered electrons detected in the main detector and those detected in a nominal low- $Q^2$  tagger. The orange lines on both graphs show a nominal main detector acceptance for  $|\eta| < 3.5$ , and the magenta line on the top graph shows a upper limit for photoproduction events for  $Q^2 < 0.1\text{GeV}^2$ .

troproduction and photoproduction. The top panels show  $x_V$  versus the scattered electron  $\eta$  without detector cuts. Here too, it is clear that for photoproduction we are fully dependent on the low- $Q^2$  tagger. For electroproduction, we have good coverage of the full  $x_V$  range within the main detector. Note that the lower bound of  $Q^2 > 1$  coincides almost exactly with the  $\eta > -3.5$  cutoff in the backward region. The case for the  $J/\psi$  decay leptons is shown in the bottom panels. While there is a clear relation between  $\eta_{\text{decay}}$  and  $x_V$ , we do not loose access to any kinematic region due to the main detector acceptance. This is similar to what we concluded for  $W$  (cf. Figure 8.54).

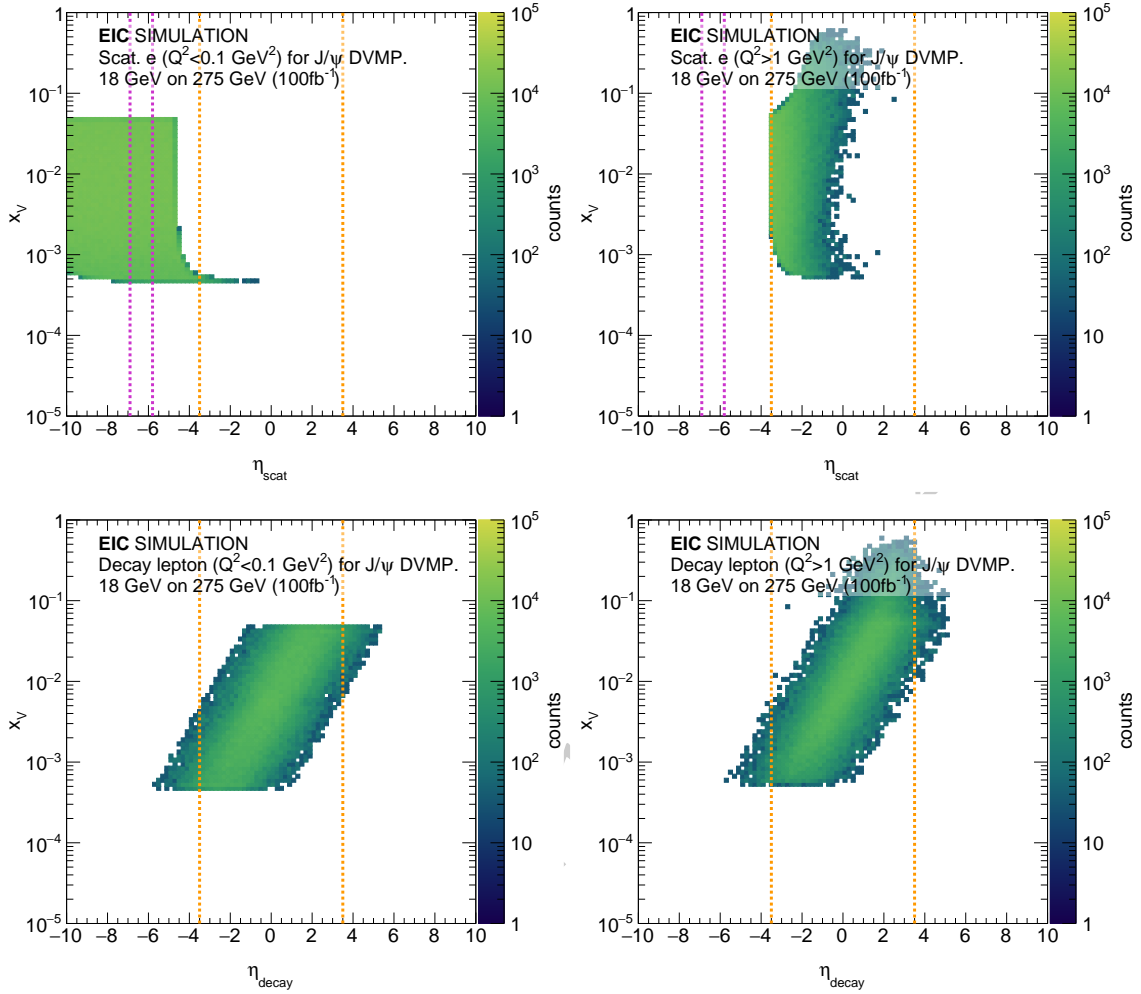


**Figure 8.55:**  $x_V$  versus the pseudo-rapidity of the scattered electron (top panels) and decay lepton (bottom panels) in photoproduction (left) and electroproduction (right) for  $J/\psi$  DVMP at the highest energy configuration. The dashed orange lines show the nominal central detector range of  $|\eta| < 3.5$ , and the dashed magenta line shows a nominal low- $Q^2$  tagger at  $-6.9 < \eta < -5.8$ . There are no detector cuts in the top figures, while the bottom figures have a nominal acceptance applied to only the scattered electron and recoil proton. The straight edge in the top right figure is caused by the  $Q^2 > 1\text{GeV}^2$  requirement for electroproduction.

Figure 8.56 makes the case for muon PID for exclusive DVMP. The left panel compares the  $J/\psi \rightarrow e^\pm$  projected count rate with the dilepton background count for  $J/\psi$  photoproduction events for an intermediate energy configuration. The background becomes non-negligible for events with decay leptons in the backward region. While this background issue is only significant for certain kinematic corners for DVMP, it will be much more severe for TCS. Muon PID will be important to control for this.

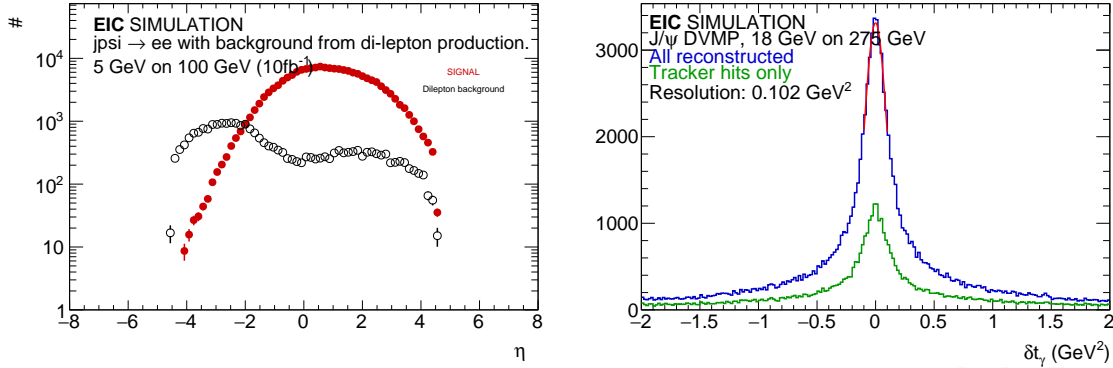


**Figure 8.56:** Left: for some kinematics, in particular in photo-production, there is a non-negligible dilepton background. Right: There are potentially large resolution effects on the reconstructed VM kinematics. Both of these issues, as well as the need for statistics near threshold, make a strong case for muon PID.

The right panel in 8.56 shows the difference  $\delta t$  between generated and measured  $t$  based on the reconstructed scattered electron and vector meson kinematics. Note that beam divergence effects and beam energy spread, which will further complicate this reconstruction, are not accounted for in this study. The long tails on this resolution originate from limited resolution effects and radiative effects in the vector meson decay. These heavy tails are present in all reconstructed kinematics, particular at lower  $W$ . More sophisticated tracking reconstruction algorithms should make this situation a bit better. The improved resolution for muon events and the smaller impact of radiative effects will make this channel crucial to study and control for these resolution effects.

Finally, the muon channel's availability will double the available statistics, vital for threshold physics where a typical bin in  $W$  and  $t$  may have single-digit counts, illustrated in Figure 8.57.

### Kinematic coverage

Figure 8.58 shows the phase space in  $Q^2 + M_V^2$  versus  $x_V$  for  $J/\psi$  (top) and  $Y$  (bottom) DVMP at EIC. Varying the collision energy will provide for sensitivity to the gluon GPD from the valence region to the sea region. Due to its much larger mass,  $Y$  DVMP will access this gluonic structure at a much larger scale than  $J/\psi$  production, providing for an important handle on the evolution and factorization of the formalisms used to extract the GPDs. A nominal luminosity of  $100\text{fb}^{-1}$  will allow for a precise determination of the  $Q^2$  dependence of  $J/\psi$  production, while being sufficient to study  $Y$  production in several bins of  $Q^2 + M_V^2$ .

Figure 8.57 shows  $|t|$  as a function of  $W$  for  $Y$  DVMP for all detected events (left), and photoproduction events where  $Q^2 < 0.1\text{GeV}^2$ . Measuring DVMP near the threshold is challenging due to the steeply dropping cross-section as the production phase space closes.

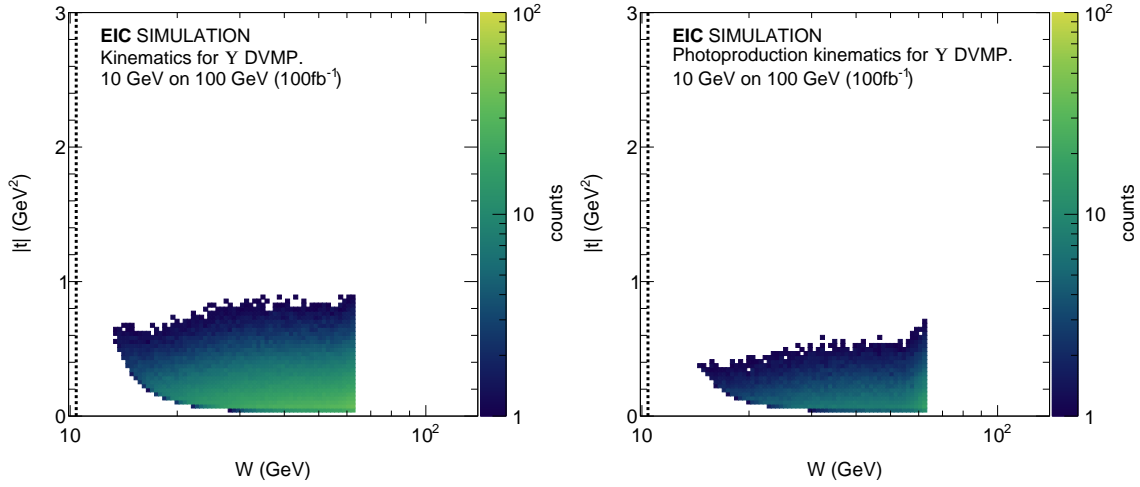


**Figure 8.57:** Coverage in  $W$  and  $t$  for  $Y$  DVMP for an intermediate energy configuration. The left panel shows all events, and the right panel shows photoproduction events only. Note that the photoproduction events is relatively low statistics. They would directly benefit from either more acceptance in the backward region of the main detector, or an expanded  $\eta$ -coverage for the low- $Q^2$  tagger.

Furthermore, going to the threshold region is intrinsically limited due to finite detector resolution. The nominal lower limit of  $y > 0.01$  driven by resolution effects translates to a lower limit on  $W$ . The measurement of the  $Y$  photo-production cross-section near-threshold would greatly benefit from increased statistics, achievable through either an extension of the acceptance in the backward region or through an increased acceptance in the low- $Q^2$  tagger. The situation is better for electroproduction, and in both cases a nominal luminosity of  $100 \text{ fb}^{-1}$  is sufficient as long as the low- $Q^2$  can be improved from the nominal values used for this study.

### 8.4.5 Timelike Compton Scattering

Timelike Compton Scattering (TCS) is an inverse process to DVCS, where a real photon scatters from a nucleon to produce a large  $Q^2$  virtual photon which decays into a pair of leptons. As such, TCS has a final state identical to the exclusive production of  $J/\Psi$ , but without the advantage of a well-defined invariant mass for the lepton pair. Exclusive reconstruction of TCS is, therefore, experimentally more challenging. We have simulated TCS using a toy Monte Carlo which generates a spectrum of quasi-real photons in a head-on collision of electrons and protons and interpolates through tables of CFFs to calculate TCS cross-sections, which are applied as weights to each event [1203]. The CFF tables were produced with the PARTONS framework and used the Goloskokov-Kroll parametrization – the same CFFs were also employed in the DVCS simulations in section 8.4.1. Similarly to DVCS, the TCS amplitude interferes with the Bethe-Heitler (BH) process, which can produce the same final state. Both the pure TCS and the pure BH distributions were sim-

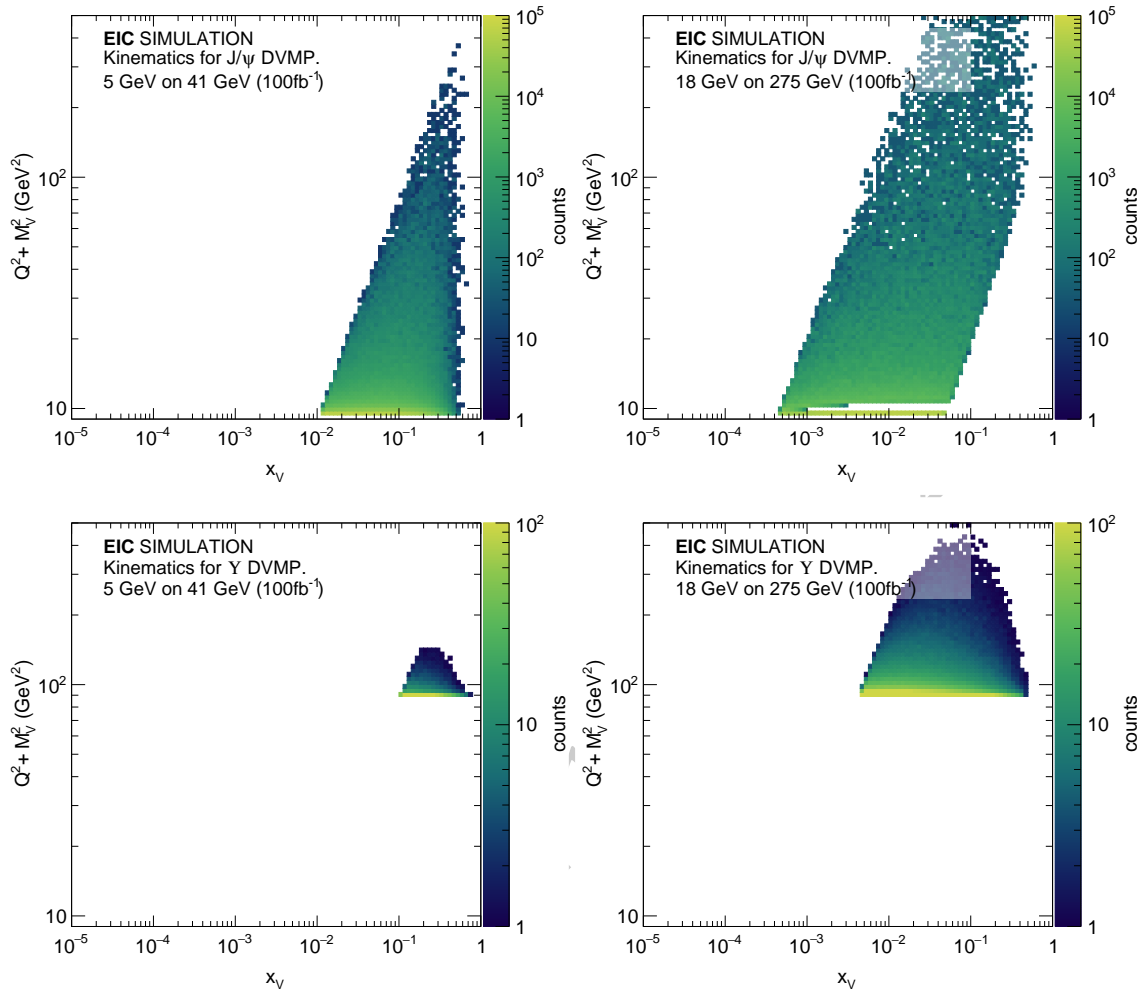


**Figure 8.58:**  $Q^2 + M_V^2$  versus  $x_V$  for DVMP of  $J/\psi$  (top) and  $Y$  (bottom). The left panels show the lowest energy configuration, and the right panels show the highest energy configuration. The discontinuity at lower  $Q^2 + M_V^2$  in the top right graph is due to events with scattered electrons in either the low  $Q^2$  tagger or the main detector.

ulated, each for  $e^+e^-$  and  $\mu^+\mu^-$  decay leptons. To suppress the BH contribution where it particularly dominates the kinematics, a cut was applied on  $\pi/4 < \theta < 3\pi/4$ , which is the angle between the positive lepton momentum and scattered proton in the lepton centre of mass frame. An additional cut on the virtuality of the produced photon,  $Q^2 > 2 \text{ GeV}^2$ , ensured a hard scale in the scattering, while requiring  $Q^2 < M_{J/\psi}^2$  suppressed the resonant background. All quasi-real photon virtualities up to  $Q^2 = 0.1 \text{ GeV}^2$  were included. The integrated kinematics of the simulation, for both the BH and the TCS signal, are shown in Fig.8.59. The resulting distributions of the decay leptons, for TCS and BH separately and for the lowest and highest collision energy settings, are shown in Fig. 8.60 - 8.61.

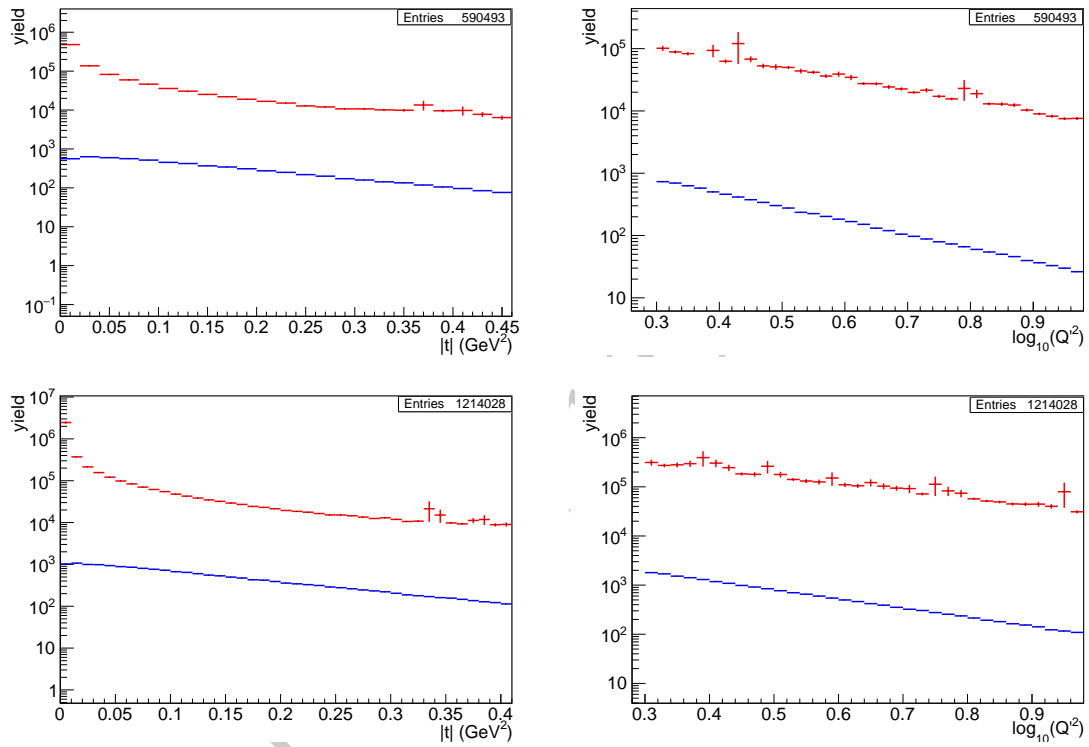


**Figure 8.59:** Comparison of the kinematics between simulated pure BH (red) and pure TCS (blue) at two collision energies: 5 GeV × 41 GeV (top) and 18 GeV × 275 GeV (bottom). Left column:  $|t|$  distribution, right column:  $Q^2$ . The yield is quoted for integrated luminosity of  $10 \text{ fm}^{-1}$ .

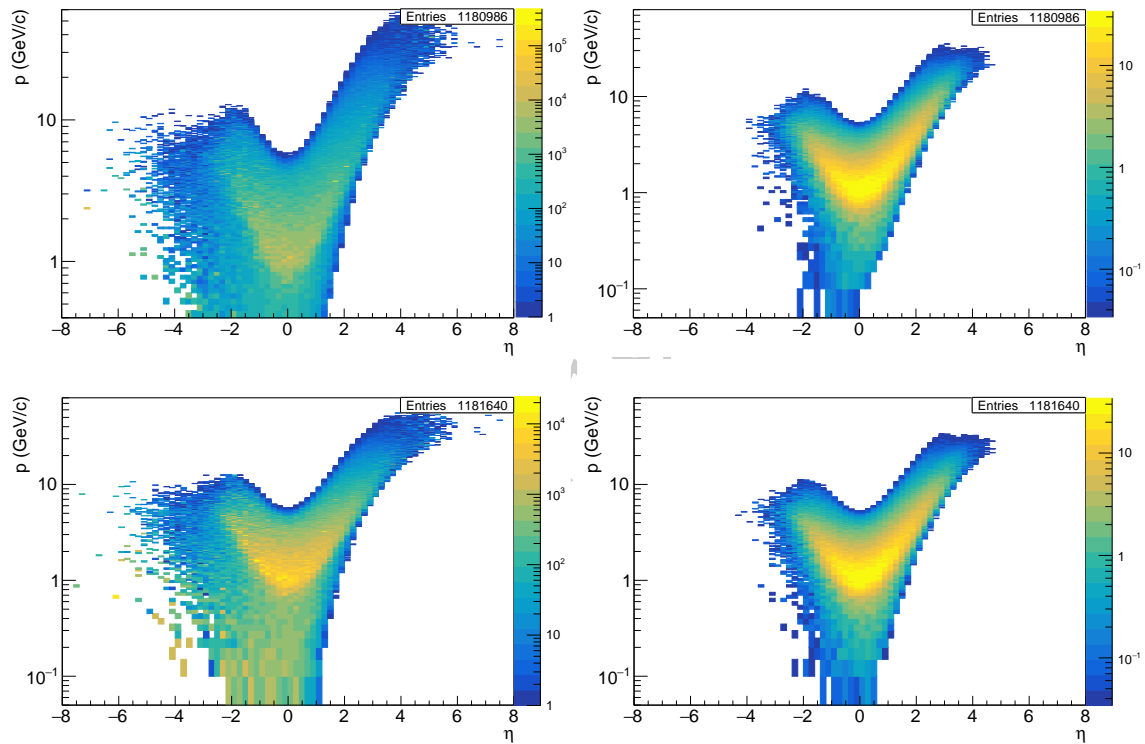


**Figure 8.60:** Momentum vs pseudorapidity for  $e^+e^-$  (top) and  $\mu^+\mu^-$  (bottom) at the  $5 \text{ GeV} \times 41 \text{ GeV}$  collision energy. Left: BH, right: TCS.

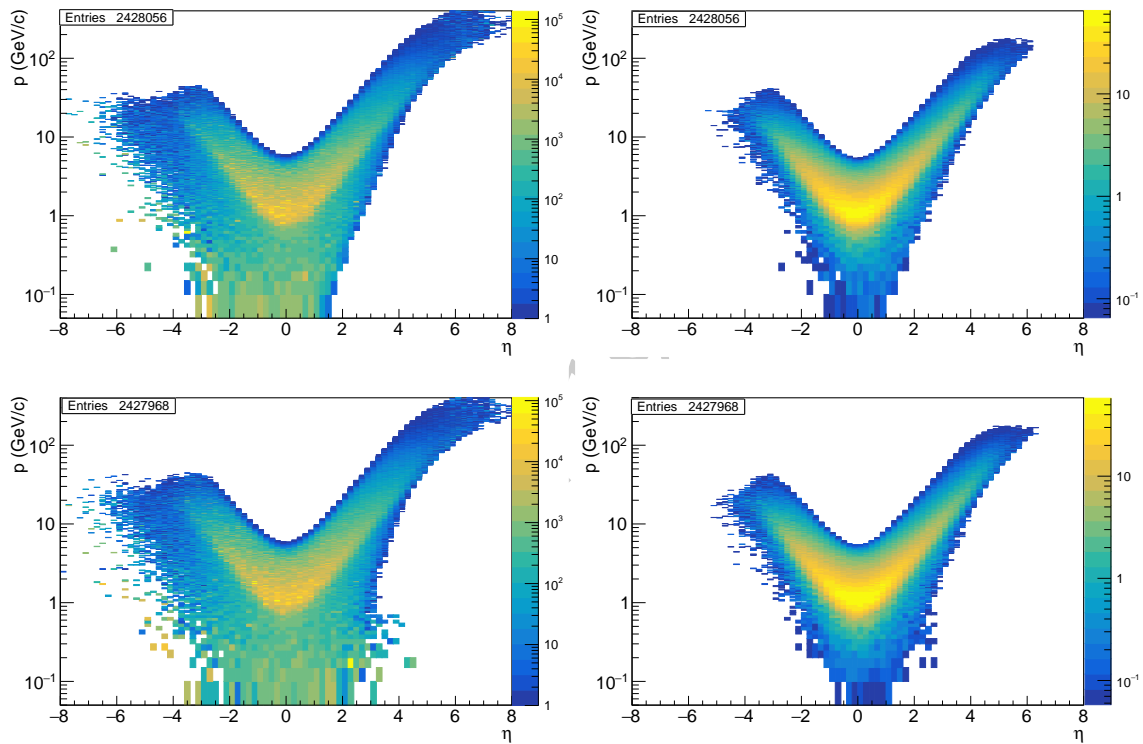


**Figure 8.61:** Momentum vs pseudorapidity for  $e^+e^-$  (top) and  $\mu^+\mu^-$  (bottom) at the  $18 \text{ GeV} \times 275 \text{ GeV}$  collision energy. Left: BH, right: TCS.

The BH contribution dominates over the TCS cross-section by approximately two orders of magnitude. Similarly to DVCS, access to the TCS amplitude is usually obtained via the BH-TCS interference term in the overall cross-section. This is expected to provide a boost to the TCS signal on the order of 10-15%.

While the electron-positron final state may be the obvious experimental choice, measurement through muon decays has two advantages: it avoids any combinatorial background from  $e^+e^-$  pairs where the  $e^-$  is the scattered electron, and muons provide a considerably better mass resolution due to the absence of bremsstrahlung, and thus a better signal-to-background ratio. The cross-sections for both decay channels are equal and the kinematic distributions of the leptons are very similar. A measurement of both channels would therefore allow for systematic cross-checks and a doubling of statistics. The scattered electron follows the same distribution as for all quasi-real photoproduction processes – detection of the electron in a low- $Q^2$  tagger would further help to suppress the background and ensure exclusivity.

#### 8.4.6 Exclusive vector meson production in $e+A$

Measuring exclusive cross sections for vector mesons in heavy nucleus targets,  $e + A \rightarrow e' + A' + V$ , where  $V = \rho, \phi, J/\psi, Y$ , was prominently discussed in the EIC White Paper [1] and is considered as one of the key measurements of the  $e+A$  program at the EIC. The cross-section for these exclusive processes, especially for lighter mesons [744] is generically more sensitive to saturation (or shadowing) than inclusive cross sections.

In addition to the integrated cross section, one is particularly interested in the  $t$ -distribution  $d\sigma/dt$  and the separation of coherent from incoherent events, where the target proton or nucleus stays intact or breaks up into color neutral fragments, respectively. These give access to the transverse spatial structure and fluctuations of the gluons in the target, see Sec. 7.3.9. For typical values of  $t$  for coherent and incoherent processes see the discussion in Sec. 7.3.9 and Fig. 8.68 below. For coherent events with heavy nuclei, unlike for proton targets, the nucleus does not leave the beam pipe, and  $t$  must be reconstructed within the central detector. This is the procedure discussed in this section. Here we discuss specifically production of  $\rho, \phi$ , and  $J/\psi$  in coherent  $e+A$  events, but the ability to reconstruct  $t$  in the central detector will also be useful for light ions, incoherent events with either protons or nuclei, and also as a cross check for events using the far forward spectrometers. However coherent  $eA$  processes typically involve the smallest values of  $|t|$  and thus pose the most stringent requirements.

Here we follow earlier studies by [647] and focus on the  $p_T$ -resolution as the dominating factor that determines the precision with which we can measure the momentum transfer  $t$ . The resolution is parametrized as  $\sigma_{p_T}/p_T = (\sigma_{p_T}/p_T)_{\text{meas}} \oplus (\sigma_{p_T}/p_T)_{\text{MS}}$ , and use as start values the ones listed in the EIC Detector Requirements and R&D Handbook [1204] for the respective pseudorapidity interval.

### Event Generation and decay channels

Simulations were carried out with the Sartre event generator [744, 1205, 1206] version 1.34, based on the bSat [1207] dipole model. The generator describes vector meson production at HERA ( $e+p$ ) and data from ultra-peripheral collisions at the LHC in  $p+Pb$  and  $Pb+Pb$  [1206] quite well. To speed up simulations, skewedness corrections as well as corrections of the real part of the amplitude were not applied. This affects the magnitude of the cross-section but has little impact on the kinematics, which is the focus of this study.

Data sets for photoproduction, defined here as  $Q^2 < 0.01 \text{ GeV}^2$  and moderate  $Q^2$ ,  $1 < Q^2 < 10 \text{ GeV}^2$  were generated for  $\rho$ ,  $\phi$ , and  $J/\psi$  mesons at maximum energy, i.e.,  $E_e = 18 \text{ GeV}$  and  $E_{Au} = 110 \text{ GeV}$ . For each meson we generated between 160 and 430 million events. Decays of the vector mesons were conducted with tools from the Sartre library taking the polarization of the virtual photon into account. We assume that the particle identification will be sufficient to reconstruct the vector mesons via the invariant mass of the respective state. A continuous background from the Bethe-Heitler process  $e + Au \rightarrow e' + Au' + e^+ + e^- (\mu^+ + \mu^-)$  will have to be handled in the analysis of the data. Since most event generators assume colliding beams with a zero crossing angle, one cannot directly generate events in the detector frame from beams that have a momentum spread and divergence. Instead, we generate events from nominal head-on beams and only after this smear the incoming electron and ion 4-momenta.

For the  $J/\psi$  we use here the  $e^+e^-$  decay channel. The muon decay channel would have similar kinematics, with two main advantages: (i) avoiding combinatorial background from the scattered electron and (ii) the absence of bremsstrahlung. For the  $\phi$  we use here the decay  $\phi \rightarrow K^+K^-$ , with a branching ratio of 49.2%. The decay into kaons has a serious disadvantage that since  $m_\phi - 2m_K = 32.107 \text{ MeV}$  at low  $Q^2$  as the  $p_T$  of the decay kaons can remain below the cut-off values of any EIC detector. A possible remedy would be tracking of curled tracks in the vertex detectors tolerating the absence of particle identification, or runs with a small magnetic field settings. The  $\rho$  is measured through  $\rho \rightarrow \pi^+\pi^-$ . Since  $m_\rho - 2m_\pi = 496.35 \text{ MeV}$  the measurement at low  $Q^2$  is feasible, but also requires a low  $p_T$  threshold for tracking.

### Kinematic coverage

Figures 8.62 and 8.63 show the kinematics in  $p_T$  and pseudorapidity for  $J/\psi$ ,  $\phi$ , and  $\rho$ , respectively. From these figures we can determine the pseudorapidity range we want to focus our studies on. For  $1 < Q^2 < 10 \text{ GeV}^2$  the decay daughters of the vector meson are spread over a wide range with the bulk sitting at midrapidity for the  $J/\psi$ , at  $\eta \sim -1$  for the  $\phi$  and at  $\eta \sim -2$  for the  $\rho$ . In all cases, measurements in the barrel region of  $-1 < \eta < 1$  would yield sufficient statistics for a successful measurement. For all vector mesons the scattered electron falls dominantly in the backward range of  $-3.5 < \eta \sim -2.5$ . For photoproduction ( $Q^2 < 0.01 \text{ GeV}^2$ ) the vector meson decay products tend to drift further backward peaking at  $\eta \sim -1.5$  for the  $J/\psi$ , at  $\eta \sim -3$  for the  $\phi$  and  $\eta \sim -4$  for the  $\rho$ . The scattered electron is pushed into the far backward region,  $\eta < -5$  and can only be

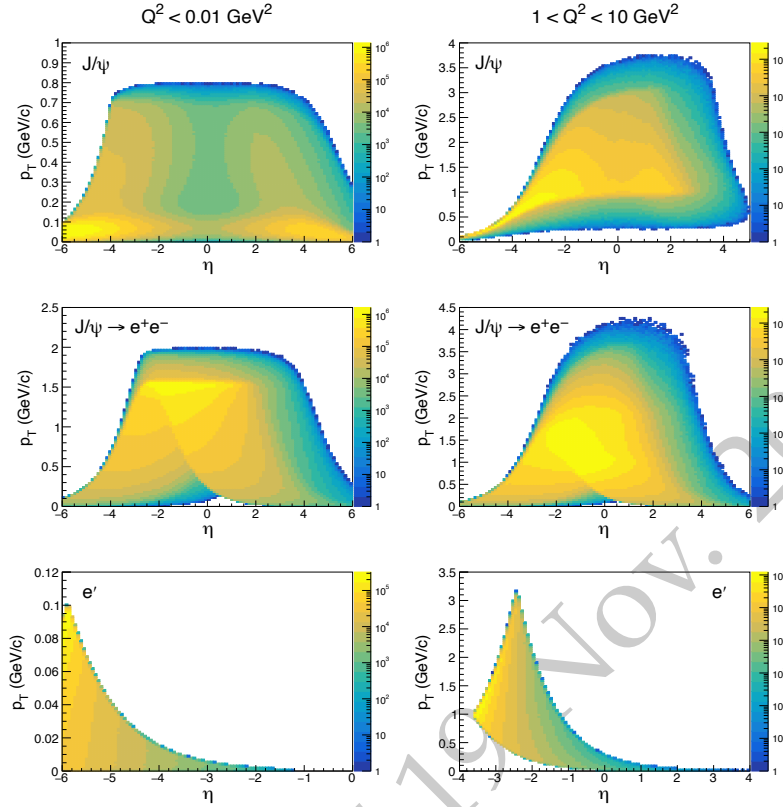


**Figure 8.62:** Kinematics for diffractive  $e + \text{Au} \rightarrow e' + \text{Au}' + J/\psi$  with  $J/\psi$  decaying into  $e^+e^-$ . The left column is for photoproduction and the right for  $1 < Q^2 < 10 \text{ GeV}^2$ . Shown, from top to bottom are  $p_T$  versus pseudorapidity ( $\eta$ ) for  $J/\psi$ , electrons from the  $J/\psi$  decay, and the scattered electron.

detected with a low- $Q^2$  tagger.

The  $p_T$  range of the vector meson decay particles is ranging from the tracking threshold (few hundred  $\text{MeV}/c$ ) to 2-3  $\text{GeV}/c$ . From this we can already conclude that the multiple-scattering term in the  $p_T$  resolution will play a dominant role. In our simulations we use a lower  $p_T$  cut of 300  $\text{MeV}/c$  unless otherwise noted.

### Beam effects

There are two beam effects that potentially can affect the  $t$  resolution, the spread of the beam momentum  $dp/p$  and the horizontal and vertical beam divergence  $\sigma_h$  and  $\sigma_v$ . None of these effects can be corrected on an event-by-event basis. Note that this is different from the effect of a finite crossing angle that is well defined. In this study we neglect therefore crossing-angle effects assuming that they can be fully corrected for. We assume the values in Table 8.8.

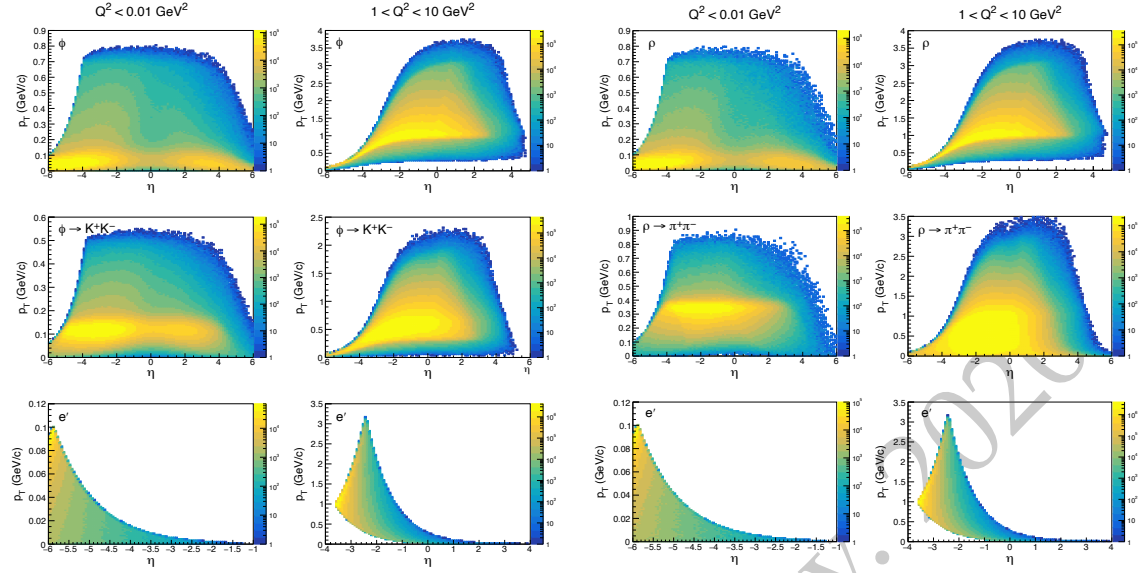


**Figure 8.63:** **Left:** Kinematics for diffractive  $e + \text{Au} \rightarrow e' + \text{Au}' + \phi$  with  $\phi$  decaying into  $K^+ K^-$ . The left column is for photoproduction and the right for  $1 < Q^2 < 10 \text{ GeV}^2$ . Shown, from top to bottom are  $p_T$  versus pseudorapidity ( $\eta$ ) for  $\phi$ , kaons from the  $\phi$  decay, and the scattered electron. **Right:** Same for  $e + \text{Au} \rightarrow e' + \text{Au}' + \rho$  with  $\rho$  decaying into  $\pi^+ \pi^-$ . Note the different scale on the vertical axis for photoproduction and electroproduction.

Species	Au	e	Au	e	Au	e	Au	e
Energy (GeV)	110	18	110	10	110	5	41	5
Strong hadron cooling:								
RMS $\Delta\theta, h/v$ ( $\mu\text{rad}$ )	218/379	101/37	216/274	102/92	215/275	102/185	275/377	81/136
RMS $\Delta p/p$ ( $10^{-4}$ )	6.2	10.9	6.2	5.8	6.2	6.8	10	6.8
Stochastic Cooling:								
RMS $\Delta\theta, h/v$ ( $\mu\text{rad}$ )	77/380	109/38	136/376	161/116	108/380	127/144	174/302	77/77
RMS $\Delta p/p$ ( $10^{-4}$ )	10	10.9	10	5.8	10	6.8	13	6.8

**Table 8.8:** Horizontal and vertical beam divergence and beam momentum spread and for various energies for e+Au running used in this study. The values vary depending on the beam cooling option.

The default method for reconstructing  $t$  based on using only the transverse momenta of the vector meson and the scattered electron ignoring all longitudinal momenta. This method was extensively used at HERA in diffractive vector meson studies. We take

$$t = [\vec{p}_T(e') + \vec{p}_T(V)]^2, \quad (8.5)$$

which we refer to as method A here. We compared this method with the actual  $t$  in our generated events without any smearing due to beam and detector effects and made the following observations:

method	effect	$t$ -range (GeV <sup>2</sup> )					
		0-0.1	0.1-0.4	0.04 - 0.07	0.07 - 0.10	0.10 - 0.13	0.13 - 0.18
E	beam divergence	0.061	0.015	0.008	0.007	0.006	0.005
E	beam mom. spread	149.61	10.36	3.03	1.86	1.37	1.03
L	divergence & mom. spread	0.048	0.016	0.009	0.007	0.006	0.005

**Table 8.9:** Effect of beam momentum spread and beam divergence on  $t$ -resolution,  $\sigma_t/t$ , with method E and L for  $J/\psi$  production in  $1 < Q^2 < 10$  GeV<sup>2</sup>. Shown is the relative difference between smeared and actual  $t$  for 6 ranges in  $t$ . The quoted  $\sigma_t/t$  is the r.m.s of the respective distribution calculated in the full range.

- In  $J/\psi$  production method A is underestimating the actual  $t$ . The offset is largest at  $Q^2 = 1-2$  GeV<sup>2</sup> with around 2% and decreases towards larger  $Q^2$  to 1% at  $Q^2 = 9-10$  GeV<sup>2</sup>. The offset is absent for photoproduction ( $Q^2 < 0.01$  GeV<sup>2</sup>). For  $1 < Q^2 < 10$  GeV<sup>2</sup> and including the offset we obtain  $\sigma_t$  resolutions (r.m.s.) of 10% for  $t < 0.01$  GeV<sup>2</sup>, 1.8% at  $t = 0.10$  GeV<sup>2</sup>, and 1.6% at  $t = 0.16$  GeV<sup>2</sup>. In photoproduction we observe no  $t$  smearing except at the lowest  $t$  ( $t < 0.01$  GeV<sup>2</sup>) of 1.3%.
- In  $\phi$  production method A shows similar issues as for the  $J/\psi$  but to a lesser degree. Except at the lowest  $t$ , the offset is  $\sim 0.5\%$ . The  $\sigma_t/t$  resolutions (r.m.s.) is 6.3% for  $t < 0.01$  GeV<sup>2</sup> and 0.45% for  $t > 0.10$  GeV<sup>2</sup>, both for  $1 < Q^2 < 10$  GeV<sup>2</sup>.
- The trend continues in  $\rho$  production. Including a minimal offset in the range of  $1 < Q^2 < 10$  GeV<sup>2</sup> we find a  $\sigma_t/t$  resolutions (r.m.s.) is 6.3% for  $t < 0.01$  GeV<sup>2</sup> and 0.3% for  $t > 0.10$  GeV<sup>2</sup>.

In general the approximation of method A leads to small to negligible  $t$  resolution effects due to the beam divergence and momentum spread, except for very small  $t$  (close to  $t_{\min.}$ ), where the longitudinal component of the momentum exchange dominates. At small  $t$  one can improve the resolution by using the full measured 4-momenta. In principle one would use the conservation of 4-momentum to calculate the momentum transfer as  $t = (p_V + p_{e'} - p_e)^2$ , which we call here method E. Calculating this inner product involves the accurate subtraction of two large numbers: the incoming and outgoing electron longitudinal momenta. This makes it very sensitive to the momentum spread in the electron beam, rendering this exact reconstruction impractical.

The poor resolution at small  $t$  can be significantly improved with the very nontrivial assumption that it is possible to assure that the reaction is inclusive by vetoing all decay products of the target nucleus. In this case one can use one additional constraint, namely that the invariant mass of the outgoing nucleus must be  $M_A^2$ , to determine the actual longitudinal momentum of the incoming electron, instead of assuming the nominal electron beam momentum. We refer to this procedure as method L. As an additional check in method L (that has not been performed here) one could verify that the inferred  $e$  energy is within the expected spread of electron energies in the beam. The impact of beam effects on the  $t$  resolution is summarized in table 8.9.

### Impact of momentum resolution

In order to study the impact of momentum resolution effects on the  $t$ -resolution, we look at processes with  $1 < Q^2 < 10 \text{ GeV}^2$  since the resolution of the scattered electron plays a more important role than is the case in photoproduction. We focus on the region discussed in Sec. 8.4.6 where the vector meson is detected in the barrel ( $|\eta| < 1$ ) and the scattered electron at  $-3.5 < \eta < -2.5$ ).

Tables 8.10, 8.11, and 8.12 show our results for  $\sigma_t/t$  for  $J/\psi$ ,  $\phi$ , and  $\rho$  mesons, respectively, in 6  $t$  bins between 0 and  $0.18 \text{ GeV}^2$ . The first line in each table is the Detector and R&D Handbook [1204] value, and the subsequent lines show the effect of an improved resolution. The lowest  $t$  bin has a poor resolution, but as discussed above in Sec. 8.4.6 for low  $t$  a different analysis method is needed that takes into account the longitudinal component of the momentum exchange.

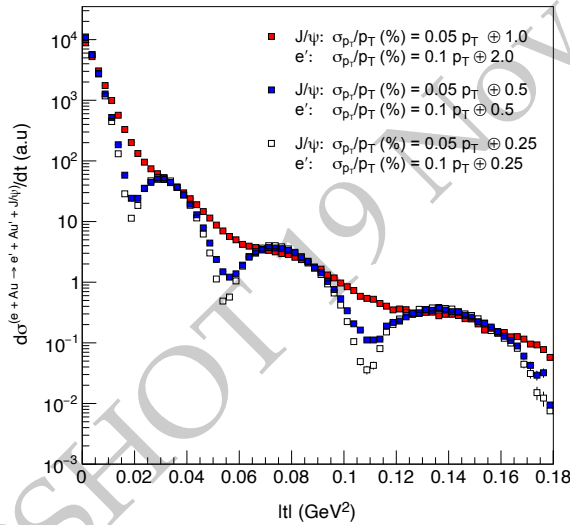


**Figure 8.64:** Illustration of the impact of different  $p_T$  resolutions on the coherent  $J/\psi$  production cross-section,  $d\sigma/dt$ , for  $1 < Q^2 < 10 \text{ GeV}^2$ .

The most important finding is that the measurement precision term in  $\sigma_{p_T}/p_T$  has little impact on the overall  $t$  resolution in the barrel as can be seen in columns 1-3. This holds for all studies vector mesons. We conclude that a precision term of 0.05% for the barrel and 0.1% for the backward region seems adequate. The case is different for the MS term, especially in the backward region, which appears to have a substantial impact on  $\sigma_t/t$  as seen in columns 4-8. Figure 8.64 illustrates this effect, demonstrating that the Handbook settings completely wash out the diffractive structure of the distribution. Note that unfolding procedures will not improve the situation as the position of the minima is a priori unknown. The  $t$  resolution for the  $\phi$  and the  $\rho$  appears to be better than that of the  $J/\psi$  at lower  $t$  due to the different  $p_T$  range of the decay particles.

The evaluation of the  $t$ -resolution on photoproduction is more involved since much will depend on the performance of a low- $Q^2$  tagger and its potential  $p_T$  resolution, which is

measurement precision term for barrel (backward) (%)	MS term for barrel (backward) (%)	$t$ -range (GeV <sup>2</sup> )					
		0-0.1	0.1-0.4	0.04 - 0.07	0.07 0.10	0.10 - 0.13	0.13 - 0.18
0.05 (0.1)	1.0 (2.0)	4.58	0.45	0.25	0.19	0.16	0.14
0.1 (0.2)	1.0 (2.0)	4.71	0.46	0.25	0.20	0.17	0.14
0.025 (0.05)	1.0 (2.0)	4.54	0.45	0.24	0.19	0.16	0.14
0.05 (0.1)	0.5 (2.0)	3.53	0.38	0.21	0.17	0.14	0.12
0.05 (0.1)	0.5 (1.0)	1.29	0.22	0.12	0.10	0.08	0.07
0.05 (0.1)	0.5 (0.5)	0.78	0.16	0.09	0.07	0.06	0.05
0.05 (0.1)	0.25 (0.5)	0.49	0.12	0.07	0.05	0.05	0.04
0.05 (0.1)	0.25 (0.25)	0.36	0.09	0.05	0.04	0.04	0.03

**Table 8.10:**  $\sigma_t/t$  for  $J/\psi$  production in  $1 < Q^2 < 10$  GeV<sup>2</sup> in 6 different  $t$  bins. Each row shows the  $t$  resolution for the two different terms that make up the  $p_T$  resolution of the  $J/\psi$  decay particles. The measurement precision term and the MS term are shown for the two different regions studies, the barrel region for the  $J/\psi$  detection and the backward region for the measurement if the scattered electron. See text for details.

measurement precision term for barrel (backward) (%)	MS term for barrel (backward) (%)	$t$ -range (GeV <sup>2</sup> )					
		0-0.1	0.1-0.4	0.04 - 0.07	0.07 - 0.10	0.10 - 0.18	
0.05 (0.1)	1.0 (2.0)	5.91	0.31	0.18	0.14	0.12	0.11
0.1 (0.2)	1.0 (2.0)	6.00	0.32	0.18	0.14	0.13	0.11
0.025 (0.05)	1.0 (2.0)	5.88	0.31	0.18	0.14	0.12	0.11
0.05 (0.1)	0.5 (2.0)	5.41	0.30	0.17	0.14	0.12	0.10
0.05 (0.1)	0.5 (1.0)	1.59	0.15	0.09	0.07	0.06	0.05
0.05 (0.1)	0.5 (0.5)	0.63	0.09	0.05	0.04	0.04	0.03
0.05 (0.1)	0.25 (0.5)	0.51	0.08	0.05	0.04	0.03	0.03
0.05 (0.1)	0.25 (0.25)	0.26	0.05	0.03	0.02	0.02	0.02

**Table 8.11:**  $\sigma_t/t$  for  $\phi$  production in  $1 < Q^2 < 10$  GeV<sup>2</sup> in 6 different  $t$  bins. Each row shows the  $t$  resolution for the two different terms that make up the  $p_T$  resolution of the  $\phi$  decay kaons. The measurement precision term and the MS term are shown for the two different regions studies, the barrel region for the  $\phi$  detection and the backward region for the measurement if the scattered electron. See text for details.

currently unknown. However,  $t$  can also be calculated in photoproduction by ignoring the scattered electron  $p_T$  in method A, taking  $t \approx -p_T^2$ , with an error less than  $Q^2$  [1208], which is acceptable e.g. for a selection of events with  $Q^2 \lesssim 10^{-4}$ . For  $\phi$  meson photoproduction one needs to detect decay kaons have momenta of 100-150 MeV/ $c$  (see Fig. 8.63), that can only be captured in either low-field runs or with the inner layer of a vertex tracker. The situation is only slightly better for the  $\rho$  where the decay pions have  $p_T$  around 300-400 MeV/ $c$  and optimal for the  $J/\psi$  with decay electrons of 1-1.5 GeV/ $c$ .

measurement precision term for barrel (backward) (%)	MS term for barrel (backward) (%)	$t$ -range (GeV <sup>2</sup> )					
		0-0.1	0.1-0.4	0.04 - 0.07	0.07 - 0.10	0.10 - 0.18	
0.05 (0.1)	1.0 (2.0)	6.87	0.33	0.19	0.15	0.13	0.11
0.1 (0.2)	1.0 (2.0)	6.99	0.33	0.19	0.15	0.13	0.11
0.025 (0.05)	1.0 (2.0)	6.99	0.33	0.19	0.15	0.13	0.11
0.05 (0.1)	0.5 (2.0)	6.17	0.31	0.18	0.14	0.12	0.10
0.05 (0.1)	0.5 (1.0)	1.83	0.16	0.09	0.07	0.06	0.06
0.05 (0.1)	0.5 (0.5)	0.74	0.10	0.06	0.05	0.04	0.04
0.05 (0.1)	0.25 (0.5)	0.57	0.08	0.05	0.04	0.03	0.03
0.05 (0.1)	0.25 (0.25)	0.29	0.05	0.03	0.03	0.02	0.02

**Table 8.12:**  $\sigma_t/t$  for  $\rho$  production in  $1 < Q^2 < 10$  GeV<sup>2</sup> in 6 different  $t$  bins. Each row shows the  $t$  resolution for the two different terms that make up the  $p_T$  resolution of the  $\rho$  decay pions. The measurement precision term and the MS term are shown for the two different regions studies, the barrel region for the  $\rho$  detection and the backward region for the measurement if the scattered electron. See text for details.

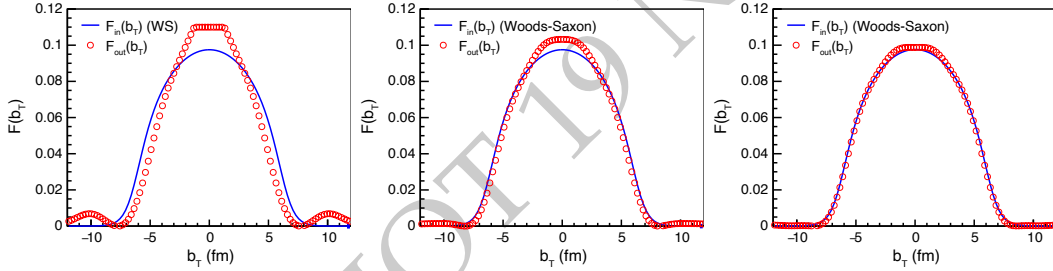


**Figure 8.65:** Extracted  $F(b_T)$  (red circles) compared to the Wood-Saxons input distribution (blue line). Left: handbook detector, with  $\sigma_{p_T}/p_T = 0.05p_T \oplus 1.0\%$  for  $J/\Psi$  and  $\sigma_{p_T}/p_T = 0.1p_T \oplus 2.0$  for  $e'$ . Center: a MS-term resolution improved by a factor 2:  $\sigma_{p_T}/p_T = 0.05p_T \oplus 0.5\%$  for  $J/\Psi$  and  $\sigma_{p_T}/p_T = 0.1p_T \oplus 1.0$  for  $e'$ . Right: resolution on the scattered electron improved by a further factor 2:  $\sigma_{p_T}/p_T = 0.05p_T \oplus 0.5\%$  for  $J/\Psi$  and  $\sigma_{p_T}/p_T = 0.1p_T \oplus 0.5$  for  $e'$ , corresponding to our “nominal” resolution.

The coherent distribution  $d\sigma/dt$  allows, as discussed in Secs. 7.2.2 and 7.3.9, one to obtain information about the gluon distribution in impact-parameter space through a Fourier transform [744]. This is regarded as one of the key studies in the  $e+A$  program. Successfully extracting the source distribution is essential and will be used in the following to establish the requirements on  $\sigma_t/t$  and thus on  $\sigma_{p_T}/p_T$ .

Assuming here for simplicity that a complex phase of the amplitude does not depend on  $t$  or  $b$ , we can regain the impact-parameter dependent amplitude  $F(b)$  as a Fourier transform of the square root of the cross-section. In order to maintain the oscillatory structure of the amplitude we have to switch its sign in every second minimum.

The Sartre generator starts from an explicit transverse density function  $T_A(b)$ . Gluon saturation results in a deviation of the  $b$ -dependence of the amplitude from the input density.

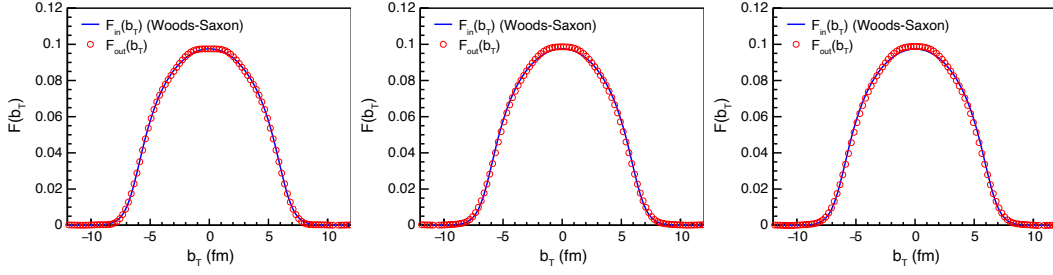


**Figure 8.66:** Extracted  $F(b_T)$  (red circles) compared to the Wood-Saxon input distribution (blue line). Left:  $J/\Psi$  source extraction with a further improvement compared to the nominal resolution of Fig 8.65 (right), with  $\sigma_{p_T}/p_T = 0.05p_T \oplus 0.25\%$  for  $J/\Psi$  and  $\sigma_{p_T}/p_T = 0.1p_T \oplus 0.25$  for  $e'$ . Center and right:  $\phi$  and  $\rho$  production with the nominal resolution of  $\sigma_{p_T}/p_T = 0.05p_T \oplus 0.5\%$  for  $J/\Psi$  and  $\sigma_{p_T}/p_T = 0.1p_T \oplus 0.5$  for  $e'$ .

Here we investigate the accuracy of extracting  $F(b)$  as the difference ( $F_{\text{out}}(b) - F_{\text{in}}(b)$ ) between the input and extracted amplitudes. Figure 8.65 shows a comparison between the input and extracted source densities. This figure uses the bNonSat model, where the amplitude is exactly proportional to the input distributions, and thus ( $F_{\text{out}}(b)$  would be equal to  $F_{\text{in}}(b)$ ) for an ideal detector and in the absence of beam effects, and including the longitudinal component of the momentum transfer. We see that a reduction of the MS term to 0.5GeV for both the meson decay products and the scattered electron is required for a reconstruction of the impact parameter profile, representing a factor 2 improvement with respect to the handbook detector for the barrel and a factor 4 for the scattered electron. *This is our nominal detector requirement resulting from this study.* Figure 8.66 (left) shows the result of an even further improvement by a factor 2. A closer look at the Fourier-transforms reveals that what is crucial is to resolve the minima up to the third one, as discussed in the next subsection.

From studies discussed in Sec.8.4.6 we already observed that the  $\sigma_t/t$  resolution for a given  $p_T$ -resolution is smaller for the  $\rho$  and  $\phi$  than for the  $J/\psi$ . Figure 8.66 (center, right) shows the source extraction accuracy for  $\phi$  and  $\rho$  with the nominal resolution  $\sigma_{p_T}/p_T = 0.05p_T \oplus 0.5\%$  in the barrel and  $\sigma_{p_T}/p_T = 0.1p_T \oplus 0.5$  for  $e'$

### Separating coherent and incoherent processes

Experimentally, the measured spectra in diffractive vector meson production contain the sum of coherent and incoherent processes (see Fig. 8.67). At low  $t$ , coherent production dominates the cross-section while already at around  $|t| > 0.02 \text{ GeV}^2$  the incoherent process start to take over. Both processes are of substantial interest in their own rights as discussed in Sec. 7.3.9. While it is relatively easy to select a clean sample of incoherent events by requiring a breakup neutron in the ZDC or a charged fragment in the Roman Pots, the inverse is not true. The coherent spectra will thus be contaminated by a fraction of incoherent events that passed all cuts. Our purpose here is to assess the degree of suppression of the incoherent background required for the physics. Here we should emphasize, that the

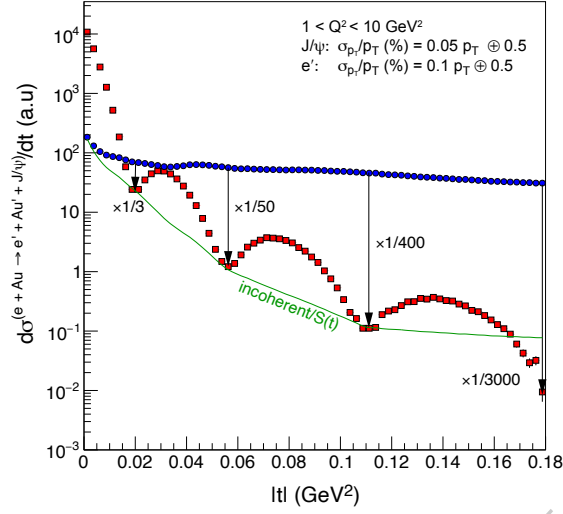


**Figure 8.67:** Coherent (red) and incoherent (blue) cross-section  $d\sigma/dt$  for diffractive  $J/\psi$  production in  $1 < Q^2 < 10 \text{ GeV}^2$ .

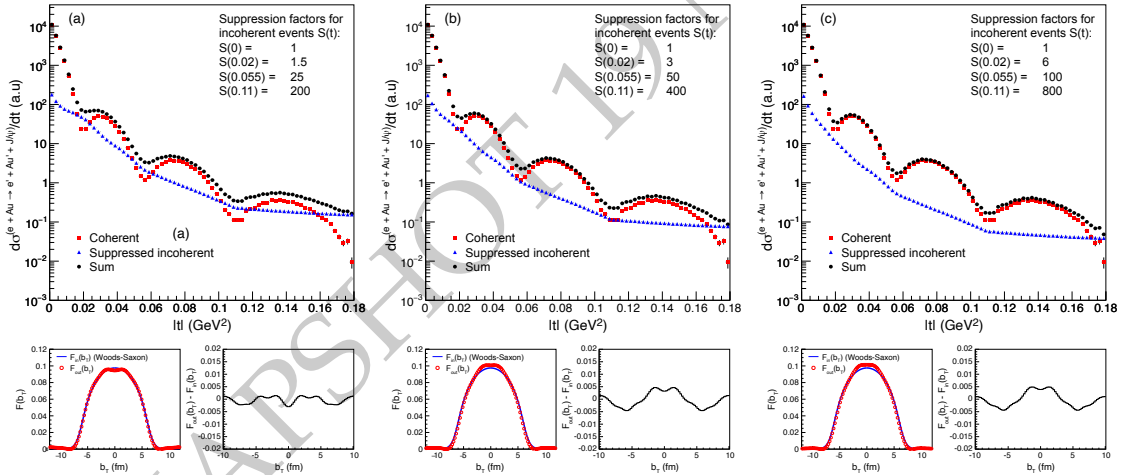


**Figure 8.68:** Each panel depicts  $d\sigma/dt$  for coherent, suppressed (detected and rejected) incoherent events and their sum. The sum is used to extract the source  $F(b_T)$  which is shown in the bottom left of each panel and compared to the input Woods-Saxon distribution. The plot on the bottom right illustrates the difference between extracted and true  $F(b_T)$ . The suppression of the incoherent background increases from the left to right panel in steps of a factor 2.

ratio  $\sigma_{\text{incoh}}/\sigma_{\text{coh}}(t)$  is strongly model dependent, and while it is kinematically accessible in UPC events at the LHC, models are currently not calibrated to LHC experimental data.

Figure 8.67 depicts the coherent (red) and incoherent (blue) cross-section with the nominal resolution defined above in Sec. 8.4.6. In order to vary the level of suppression to

define reliable requirements we construct first a template suppression curve  $S(t)$  (green in Fig. 8.67), by linear interpolation in the logarithm of the suppression factor, between fix points at the minima and leveling at larger  $t$ . With this template at hand, we now can vary the suppression values (except at  $t = 0$ ) by a common factor,  $c_s$ , to study the effects of different background levels on the extraction.

Figures 8.68(a)-(c) depict 3 scenarios with (from left to right) increasing levels of suppression of the incoherent contribution. The extraction of  $F(b_T)$  is surprisingly robust in a considerable range around the nominal scenario shown in Fig. 8.67 and 8.68(b). Further studies, not displayed here, show that significant distortions start to affect  $F(b_T)$  for suppressions that are a factor 4 less than the nominal values and that they are fully negligible for suppression level of 4 times larger than nominal. Conducting the same studies for  $\phi$  and  $\rho$  production yields the same conclusions as for the  $J/\psi$ , in fact even slightly better.

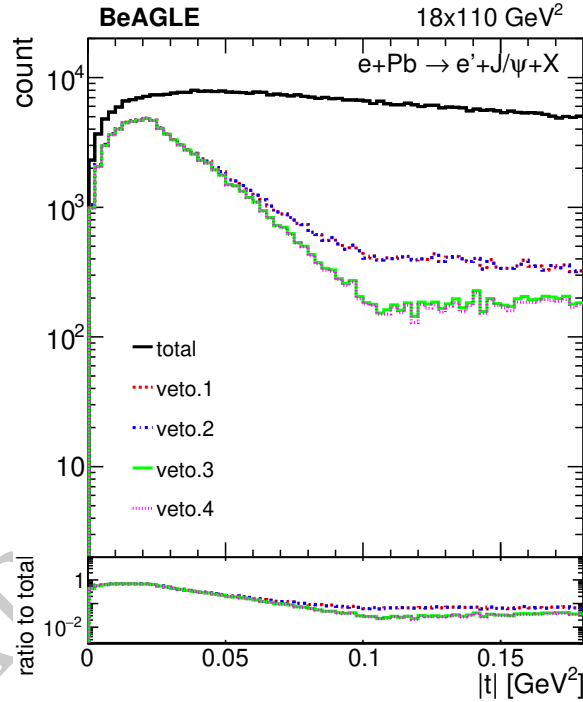


**Figure 8.69:** Suppression of incoherent background events by successive cuts: see text for explanation.

A separate study using the BeAGLE generator has been initiated to assess the veto inefficiency for incoherent events. Preliminary studies use the following combination of cuts:

**Veto 1** no neutrons in the ZDC

**Veto 2** Veto 1 and no protons in the Roman Pots

**Veto 3** Veto 2 and no proton in the off-energy detector

**Veto 4** Veto 3 and no proton in the B0.

These cuts alone, as shown in Fig. 8.69, are not yet enough to suppress the incoherent contribution to measure the diffractive pattern of the coherent contribution down to the required level. There is an additional prospect of improving the vetoing efficiency by detecting decay photons from the nuclear  $\gamma$ -decay, ideally in both the ZDC and the B0. This additional rejection factor is, however, still in the process of being quantified.

### 8.4.7 $u$ -channel exclusive electroproduction of $\pi^0$

The EIC is anticipated to play a significant role in the extraction of TDAs through the backward ( $u \sim u_{\min}$ ) exclusive  $\pi^0$  process  $e + p \rightarrow e' + p' + \pi^0$  at kinematics beyond the reach of existing facilities. The Fig. ?? illustrates the perspective of  $Q^2$  evolution from 2 to 10  $\text{GeV}^2$  from the combination of planned measurements at JLAB [1209], PANDA [1210] and EIC, at fixed  $s = 10 \text{ GeV}^2$ .

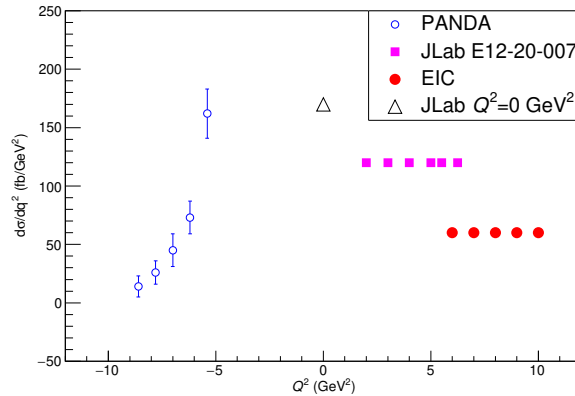


**Figure 8.70:** The anticipated global data set of  $d\sigma/dq^2(\gamma^* p \rightarrow p\pi^0)$  vs  $Q^2$  at fixed  $s = 10 \text{ GeV}^2$ . The projected data points are: open blue circles, results from PANDA (FAIR); magenta squares, results from the JLab E12-20-007 experiment; red full circles, results at EIC. A potential JLab 12 measurement at real-photon point  $Q^2 = 0 \text{ GeV}^2$  is indicated by the open triangle.

All the detection parameters required for the measurement at EIC with a 5 GeV electron beam colliding with a 100 GeV proton beam and in the range from  $Q^2 = 6.2$  to  $10.5 \text{ GeV}^2$  are summarized in Table. 8.13 and Fig. 8.71. For the experimental setup, we intend to use the Zero Degree Calorimeter (ZDC) to detect the decayed photons from  $\pi^0$  with momentum from 40 to 60 GeV. Exploring also different collision energies, we found that a lower proton energy would produce a lower momentum  $\pi^0$ , and the the decayed photon will not reach the ZDC due to acceptance.

In summary, the pseudorapidity and momentum are, respectively,  $|\eta| \sim 4.1$  and  $P_{p'} \sim 50 \text{ GeV}$  for the recoiled proton and  $|\eta| < 1.5$  and  $P_{e'} \sim 5.4 \text{ GeV}$  for the scattered electron, while the  $\pi^0$  momentum is  $P_{\pi^0} \sim 50 \text{ GeV}$ .

According to the latest detector study, there may be problems to reach the pseudorapidity values  $|\eta| \geq 4$  at the Hadron End Cap. In this case, a dedicated detector is required to tag

the recoiled proton at  $\eta \sim 4.1$ . Otherwise, we should apply the missing mass reconstruction technique to resolve the proton.

**Table 8.13:** The nominal values for the particle momentum and  $\eta$  of scattered electrons, recoiled protons and produced  $\pi^0$ .

$Q^2$ (GeV <sup>2</sup> )	$\eta_{e'}$	$P_{e'}$ (GeV)	$\eta_{p'}$	$P_{p'}$ (GeV)	$\eta_{\pi^0}$	$P_{\pi^0}$ (GeV)	$P_\gamma$ (GeV)
6.2	-1.39	5.31	4.13	43.40	4.38	56.29	28.24
7.0	-1.32	5.35	4.09	45.50	4.38	54.12	27.06
8.2	-1.24	5.40	4.12	49.74	4.38	49.84	24.72
9.3	-1.19	5.46	4.09	51.90	4.38	47.60	23.80
10.5	-1.12	5.52	4.07	54.96	4.38	44.50	22.25

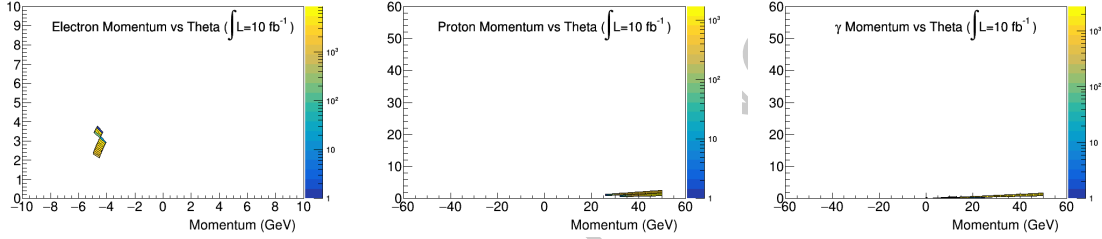


**Figure 8.71:** Angular momentum distributions for scattered electrons (left), recoiled proton (middle) and decayed photons (right).

### 8.4.8 Exclusive meson production by charged currents

The Charged Current (CC) DVMP processes are numerically suppressed compared to photoproduction, yet are within the reach of the Electron Ion Collider. Fig. 8.72 shows the results for the cross-section of exclusive  $\pi^-$  production in CCDVMP process  $ep \rightarrow \nu_e \pi^- p$  in the framework of [320, 1211], as function of the Bjorken variable  $x_B = Q^2 / (2p \cdot q)$ , with  $Q^2 = -q^2$  the virtuality of the charged boson and  $p$  the incoming proton momentum. The details of the evaluation of the cross-section and its relation to proton GPDs can be found in [320]. For the sake of convenience, we rescaled the right vertical bar of the figure to show the values of the product

$$\frac{d^2 N}{dx_B dQ^2} = \frac{d^2 \sigma}{dx_B dQ^2} \times \int dt \mathcal{L} \quad (8.6)$$

which facilitates estimates of the expected number of events per bin (we used the integrated luminosity  $\int dt \mathcal{L} = 100 \text{ fb}^{-1}$  for estimates). For other channels (like exclusive CC production of strangeness or charm) we expect that the cross-section is of the same order of magnitude. For nuclei we expect that the exclusive cross-section should scale with atomic number as  $\sim Z^4$  (modulo a factor of 2 effect due to model-dependent nuclear corrections).

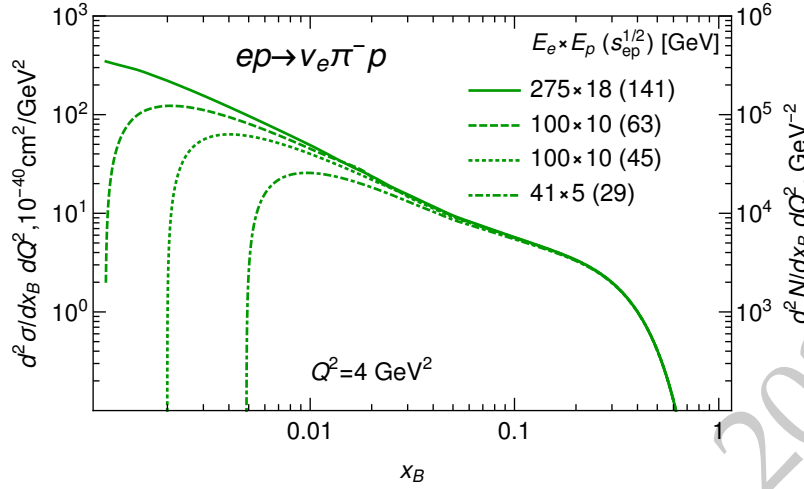


**Figure 8.72:** The cross-section of charged current pion production in EIC kinematics evaluated in the framework of [320]. The right vertical axis is rescaled by the integrated luminosity  $\int dt \mathcal{L} = 100 \text{ fb}^{-1}$  to give the expected number of events per bin as in Eq. (8.6).

However, there are certain challenges which must be addressed in order to make possible measurements of charged current exclusive processes, ensure their exclusiveness, as well as suppress backgrounds from quasi-real photoproduction. For nuclei additional backgrounds stem from the subprocess on neutrons. In the following, we will focus on the  $ep \rightarrow \nu_e \pi^- p$  channel, yet many challenges are common to all other final states.

### Kinematics reconstruction

The CCDVMP processes contain undetected neutrino in the final state, and no recoil electron which is conventionally used as a trigger in experimental setup. For this reason, there are certain challenges for reconstruction of the kinematics of such processes. As in the  $ep \rightarrow \nu_e \pi^- p$  channel both the final state hadrons ( $\pi^-$  and  $p$ ) are charged, their kinematics might be reconstructed with good precision. From energy-momentum conservation, we have for the neutrino momentum

$$p_{\nu_e} = p_e + p_i - p_f - p_\pi, \quad (8.7)$$

where  $p_i \equiv (E_i, \mathbf{p}_i)$  and  $p_f \equiv (E_f, \mathbf{p}_f)$  are, respectively, the initial and final four-momenta of the nucleon,  $p_e$  is the four-momentum of the incident electron, and  $p_\pi$  is the four-momentum of the produced pion. If we detect the four-momenta of recoil proton and produced pion, we may reconstruct the kinematics of the process. For the Bjorken variables  $Q^2$ ,  $x_B$  and  $t$ , in the massless limit ( $m_N \approx m_\pi \approx 0$ ) valid in high energy kinematics,

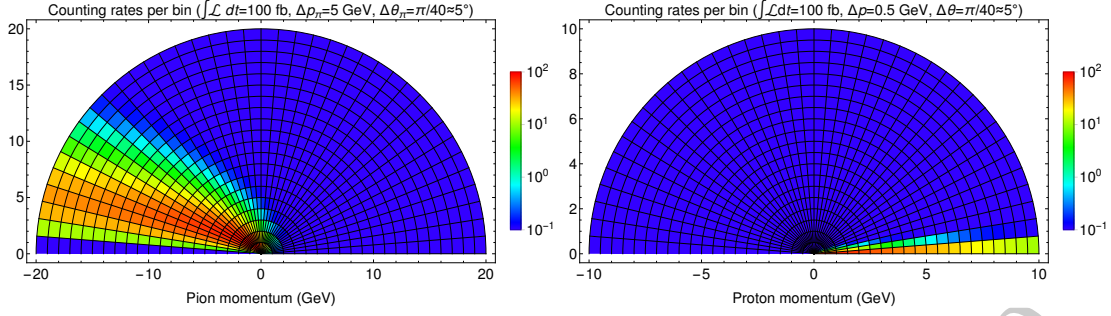


**Figure 8.73:** Left plot: Angular distributions of produced pions (integrated over the proton momentum in the kinematically allowed domain). Right plot: Angular distributions of recoil protons (integrated over the pion momentum in the kinematically allowed domain). The number of events was estimated assuming integrated luminosity  $\int \mathcal{L} dt = 100 \text{ fb}$  and the size of the bins  $\Delta p_i \times \Delta \theta_i$  given in the title of each Figure. In both cases, the angle  $\theta$  is measured with respect to direction of incident proton beam.

we have

$$Q^2 \approx 4E_e \left( E_p - p_f \cos^2 \left( \frac{\theta_f}{2} \right) - p_\pi \cos^2 \left( \frac{\theta_\pi}{2} \right) \right), \quad (8.8)$$

$$x_B \approx \frac{2E_e}{E_p} \left( 1 + \frac{E_p - p_f - p_\pi}{p_f \sin^2 \left( \frac{\theta_f}{2} \right) + p_\pi \sin^2 \left( \frac{\theta_\pi}{2} \right)} \right),$$

$$t \approx -4E_p p_f \sin^2 \left( \frac{\theta_f}{2} \right), \quad (8.9)$$

where we used the notation  $(p_i, \theta_i)$ , with  $i \equiv \pi, f$ , for the absolute value of the three-momentum and polar angle (w.r.t. incident proton) of the pion and recoil proton. Since the cross-section is exponentially suppressed as a function of  $t$ , from (8.9) we may expect that the dominant contribution comes from configurations with small scattering angle  $\theta_f$  of recoil proton and small momenta  $p_f$ .

In Figure 8.73 we show the angular distributions of  $\pi^-$  and recoil proton (integrated over the momenta of the spectator particles in the kinematically allowed domain). As expected, the recoil protons predominantly scatter in the forward direction, whereas pions are produced mostly in the backward direction. It is expected that the dominant contribution will come from the pions with momenta  $\lesssim 20 \text{ GeV}$  and protons with momenta  $\lesssim 10 \text{ GeV}$ .

The distributions shown in the Fig. 8.73 do not reflect the kinematic constraints which impose limits on possible mutual variations of the momenta of the particles. In order to illustrate such constraints, in Fig. 8.74 we show that the three-momentum of the recoil proton may change in a very limited range when the momentum of the produced pion is fixed.

In summary, it is possible to reconstruct the kinematics of the process using only the mo-

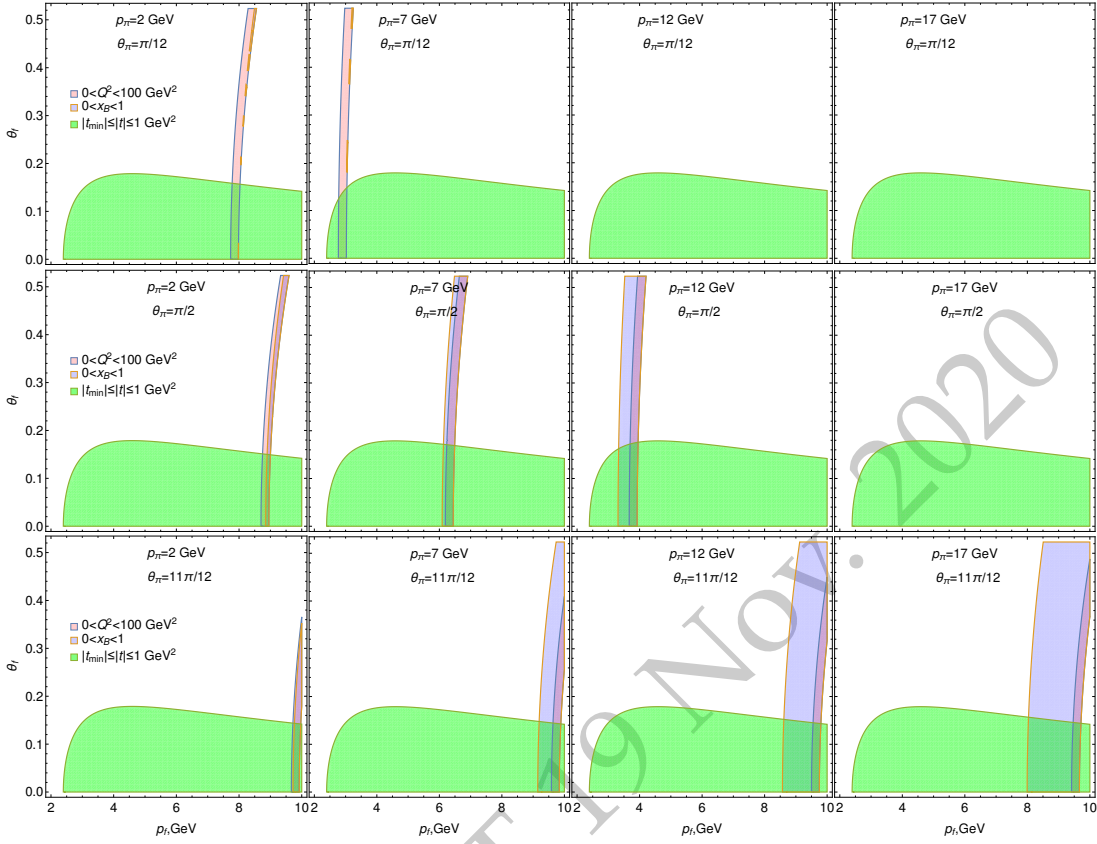


**Figure 8.74:** Kinematic restrictions on the momentum  $p_f$  and scattering angle  $\theta_f$  of the recoil proton in the case when the three-momentum of the pion is fixed. The blue band corresponds to the physical region  $0 < x_B < 1$ . The intersection of the subdomains  $0 < Q^2 \lesssim 100 \text{ GeV}^2$  (pink band) and  $|t| \lesssim 1 \text{ GeV}^2$  (green area) gives the dominant contribution to the DVMP cross-section, then limiting significantly the momentum of the proton. The angles  $\theta_f, \theta_\pi$  are measured w.r.t. direction of the incident proton beam (the first, second and third rows correspond to a pion produced in forward, central and backward directions, respectively).

menta of the pion and recoil proton.

### Photoproduction backgrounds

We expect that sizeable backgrounds to the charged current processes might come from the processes mediated by virtual photon,  $ep \rightarrow e\pi^- p X$ , where the scattered electron and some remnants remain undetected. The cross-sections of photon-mediated processes are enhanced by the kinematic factor  $\sim (Q^2 + M_W^2)^2/Q^4$  compared to the charged current channel, and for the values of  $Q^2$  available at EIC the quasi-real photoproduction will exceed by several orders of magnitude the contributions of charged current exclusive

processes. For this reason, the possibility to measure the charged current processes will depend crucially on the possibility to reject events which contain anything except  $\pi^-$  and  $p$  in the final state. The detectors with  $4\pi$  coverage are needed for this purpose. Since this is experimentally very challenging, we suggest some additional checks (“cutoffs”) which might be used in order to ensure there is no undetected remnants of the photoproduction processes.

- From charge conservation, we desume that the photoproduction of  $\pi^- p$  should include at least a charged pion, *e.g.*, via the subprocess the  $ep \rightarrow e\pi^-\pi^+p$ . In order to ensure that such backgrounds are missing, we suggest to check that the value of the missing mass of a pion (the mass of the undetected neutrino) is below a threshold, *i.e.*

$$m_{\nu_e}^2 \equiv p_v^2 = (p_e + p_i - p_f - p_\pi)^2 < m_\pi^2. \quad (8.10)$$

Such a cutoff is sufficient to exclude contributions of any process with photoproduction of additional (undetected) hadrons. However, the strict implementation of the cut (8.10) is experimentally challenging: the quantities in the l.h.s. of (8.10) are of order of dozens of GeV, for this reason the cut requires measurements of the momenta of the scattered particles with outstanding precision (with a relative error  $\lesssim 10^{-5}$ ). Yet we still believe that even a relaxed cut (8.10), with higher upper limit, might be useful to improve signal/noise ratio.

- Another important background comes from quasi-elastic scattering  $ep \rightarrow ep$ , which might give an important contribution due to the misidentification of electrons as pions in the EIC detectors. For this reason, we suggest to use an additional missing energy cutoff

$$\Delta E = E_e + E_i - E_{(\pi/e')} - E_f \gtrsim 0.5 \text{ GeV}, \quad (8.11)$$

where  $E_{(\pi/e')}$  is the energy of the final pion or misidentified electron produced in the collision. Imposing this cut, it will completely eliminate the quasi-elastic background.

- In case of nuclear targets, there are additional contributions from photoproduction processes on neutrons, *e.g.*, the  $en \rightarrow e\pi^-p$  subprocess which will give the dominant contribution, both for inclusive and exclusive production<sup>1</sup>. For this reason, we believe that nuclear targets cannot be used for CCDVMP studies.

To summarize, we believe that the CCDVMP processes have sufficiently large cross-sections to be measured at EIC kinematics. However, there are huge backgrounds from photoproduction processes. The ability to exclude these backgrounds will be crucial to finally determine the possibility to study if charged current exclusive processes at the EIC. We checked that a combination of the cuts (8.10) and (8.11) allows us to get rid of different photon-induced background processes, though the cut (8.10) might be difficult to implement.

<sup>1</sup>In case of exclusive production on heavy nuclei we expect that CCDVMP will be overshadowed by photoproduction of long-living nuclides via  $en \rightarrow e\pi^-p$  subprocess, *e.g.*  $e^{63}\text{Cu} \rightarrow e\pi^-^{63}\text{Zn}$ . Experimentally it is very challenging to distinguish its final state from that of CCDVMP process  $eA \rightarrow \nu\pi^-A$ .

### 8.4.9 Deep Exclusive $\pi^+$ production

Studies during the last decade, based on JLab 6-GeV measurements, have generated confidence in the reliability of  $\pi^+$  electroproduction as a tool for pion form factor extractions. Forthcoming measurements at the 12-GeV JLab will deliver pion form factor data that are anticipated to bridge the region where QCD transitions from the strong (color confinement, long-distance) to perturbative (asymptotic freedom, short-distance) domains.

At the EIC, pion form factor measurements can be extended to still larger  $Q^2$ , by measuring ratios of positively- and negatively-charged pions in quasi-elastic electron-pion (off-shell) scattering via the  $p(e, e' \pi^+)n$  and  $n(e, e' \pi^-)p$  reactions, accessed with proton and deuterium beams. The measurements would be over a range of small  $-t = -(p_p - p_n)^2$ , and gauged with theoretical and phenomenological expectations, to again verify the reliability of the pion form factor extraction at EIC kinematics.

#### Kinematics

Simulations demonstrating the feasibility of pion electric form factor measurements at the EIC have been performed using a Deep Exclusive Meson Production (DEMP)  $p(e, e' \pi^+ n)$  event generator based upon the Regge model of Ref. [1212]. This model provides an excellent description of the existing JLab data up to  $-t=4.3 \text{ GeV}^2$  [1213] and is well-behaved over a wide kinematic range. DEMP event kinematic distributions are shown in Fig. 8.75. The neutrons take nearly all of the proton beam momentum and are detected at very forward angles (ZDC). The scattered electrons and pions have similar momenta, except that the electrons are distributed over a wider range of angles, e.g. for  $5 \times 100$  beam energies, the 5-6 GeV/c electrons are primarily scattered  $25\text{-}45^\circ$  from the electron beam, while the 5-12 GeV/c  $\pi^+$  are  $7\text{-}30^\circ$  from the proton beam.

### 8.4.10 Diffractive dijets

In this section we focus on the photo-produced diffractive dijets in ep collisions. A typical event display is shown in Fig. 8.76, showing a back-to-back dijet separated by a rapidity gap from the beam. The initial state consists of an electron and a proton, with the former radiating off a (virtual) photon. If the photon is highly virtual, we are in the range of deep inelastic scattering (DIS) while a photon with low enough virtuality can be considered (quasi-)real. This is the photoproduction regime. No clear distinction between the two regimes exists, however, and photons of intermediate virtuality require careful consideration to avoid double-counting. A special feature in the photoproduction regime is that the process can be separated into different “resolved” and “unresolved” contributions [1214] depending on whether the partonic structure of the photon is resolved or whether it directly participates in the hard subprocess, see Fig. 8.77. These resolved photons open up for all possible hadron-hadron processes, including diffractive ones [1214].

Several complementary experimental methods have been developed to identify diffrac-

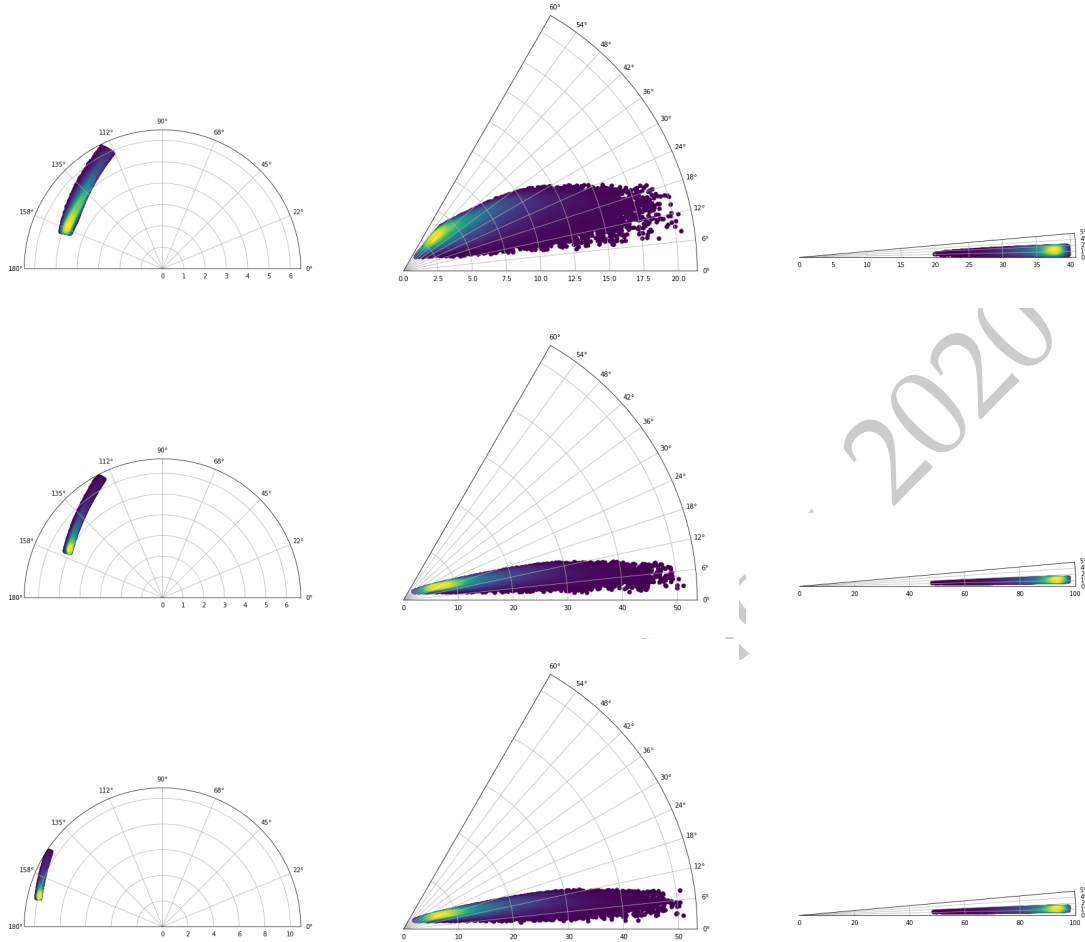


**Figure 8.75:** Exclusive  $p(e, e' \pi^+ n)$  kinematic distributions for  $e'$  (left),  $\pi^+$  (center),  $n$  (right) at  $5 \times 41$  (top),  $5 \times 100$  (middle) and  $10 \times 100$  (bottom) GeV beam energy combinations. The radial component is momentum, and the polar coordinate is the scattering angle with the proton beam direction to the right and the electron beam direction to the left.

tive events in  $e+p$  collisions. Each method exploits a specific signature characteristic of diffraction. The diffractive events can be directly detected by means of a forward spectrometer [88, 1215]. Because of the low  $t$  of the process, the outgoing  $p$  or nucleus is scattered at very low angles with respect to the initial direction and one needs to place the spectrometer very far from the interaction point and very close to the beam axis. The other common technique to tag on diffraction is to require a "rapidity gap" in the detector. This means that there is a region in the detector from the hadron beam towards the center of the detector in which there is no activity from the hadronic final state [215, 1215–1217]. The efficiency for detecting, and the purity of, diffractive events therefore depends strongly on the rapidity coverage of the detector.

Experimentally one measures the pseudorapidity of the most forward particle in the de-

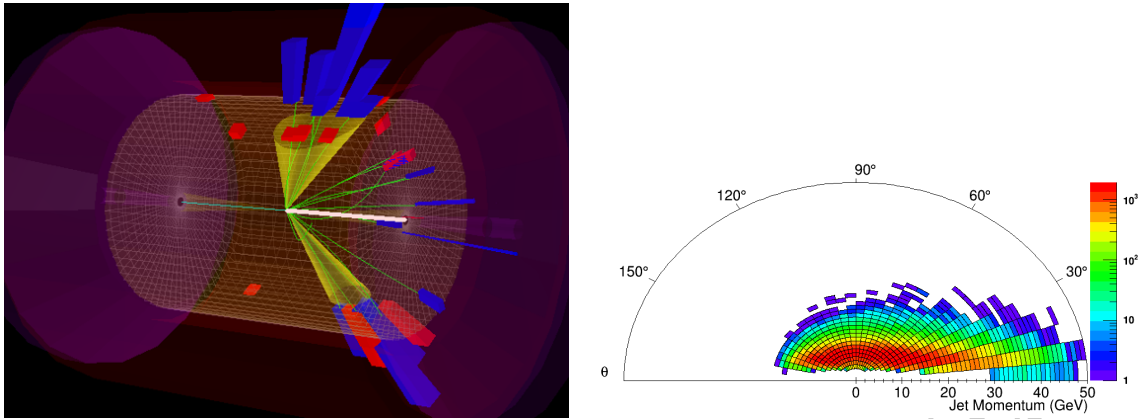


**Figure 8.76:** Left: event display of diffractive dijet event at 140 center-of-mass energy. Pythia 8.244 simulation with 18 GeV on 275 GeV. Right: Distribution of jets in angle and momentum.

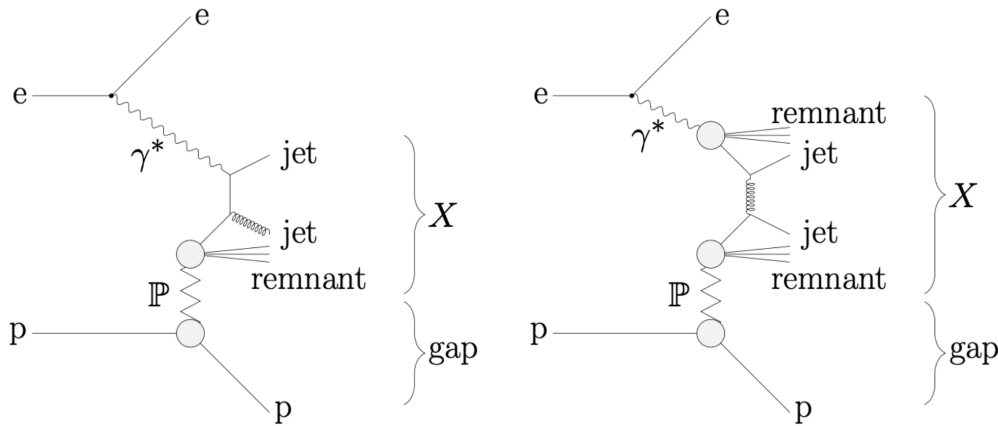


**Figure 8.77:** Leading order Feynman diagrams for diffractive dijet photoproduction in ep collisions. In the left part, the photon participates directly in the hard scattering matrix element. In the right part, a parton from the resolved photon participates.

tector ( $\eta_{max}$ ) and requires that the  $\eta$  range between it and the edge of the forward detector instrumentation is large enough. The diffractive events concentrate therefore at low values of  $\eta_{max}$ , corresponding to large values of  $\Delta\eta$  (The eta gap between the most forward particle of the event and the edge of the forward detector instrumentation). The large rapidity gap method has the advantage of a much higher statistics compared to the forward spectrometer method. The model for photoproduced diffractive dijets for  $18\text{GeV} \times 275\text{GeV}$  beam energy presented here is based on the general-purpose event generator Pythia 8. And the DIS events are simulated by Pythia6. We select  $Q^2 < 1\text{GeV}^2$  events. The  $p_T$  cut for the leading jet is  $5\text{GeV}$  and for the associated jet is  $4\text{GeV}$ . The jet kinematic distribution in diffractive events is shown in Fig. 8.76 (right). We assume the ratio of inclusive DIS events and diffractive events is 7:1. In the left figure in Fig. 8.78, we show the eta distribution of the most forward particle (MFP) in the event, for both inclusive DIS and diffractive event samples. So we can obtain the purity and efficiency distribution as shown in Fig. 8.78. The

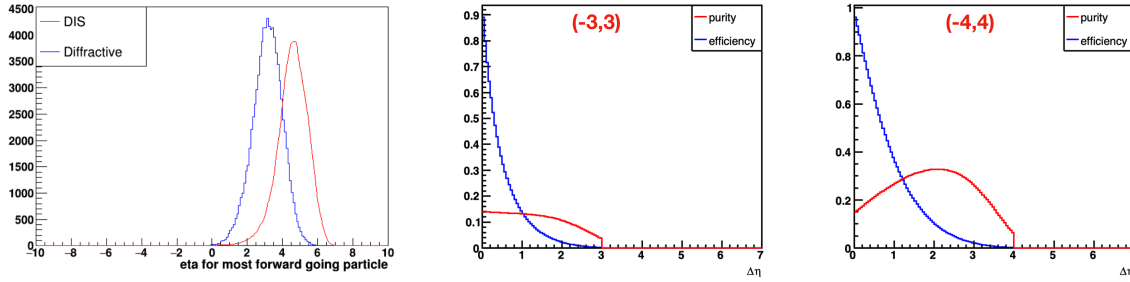


**Figure 8.78:** Left figure: The eta distribution of the most forward particle (MFP) in the event, for both inclusive DIS and diffractive event samples; The right two figures: the efficiency and purity distribution in ep collisions for different eta coverage (-3,3) and (-4,4). Here we assume the inclusive DIS to diffractive cross section ratio is 7:1.

larger eta coverage would give us better purity of diffractive events.

## 8.5 Diffractive Measurements and Tagging

### 8.5.1 Requirements for exclusive vector meson production

Although exclusive vector meson production,  $e + p/A \rightarrow eVX$  is a simple reaction, with a final state that is typically the scattered electron, two charged mesons or leptons from a vector meson decay, and, for incoherent photoproduction, the products of nuclear breakup, it does impose some significant requirements on the detector. Here, we discuss requirements related to pseudorapidity coverage of tracking detectors, ability to track soft kaons, momentum resolution and detecting nuclear breakup.

The simulations that are shown were done with the eSTARlight Monte Carlo generator [734] which accurately reproduces the essential features of the vector meson production and decay. eSTARlight is based on parameterized HERA data, and has been benchmarked against many HERA reactions. The ratio of longitudinal to transverse production as a function of  $Q^2$  is also based on HERA data, with judicious extrapolations where needed. The vector meson decays depend on the vector meson polarization and on the Clebsch-Gordon coefficients related the vector meson to its daughters, as is shown in Fig. 8.79.

#### Pseudorapidity acceptance

Since, per Eq. 7.50, it should be immediately clear that a detector with broad acceptance in pseudorapidity is required. Figure 8.80 shows the rapidity distribution for photoproduced  $\rho$  for both ep and eA collisions, along with the pseudorapidity distribution for the daughter pions. The ep collision cover a wider range in rapidity, for a couple of reasons. First, the ion Lorentz boost is larger, allowing collisions down to lower Bjorken-x values. Second, the coherent requirement for photoproduction on an ion is roughly  $x < \hbar/m_p R_A$ ;

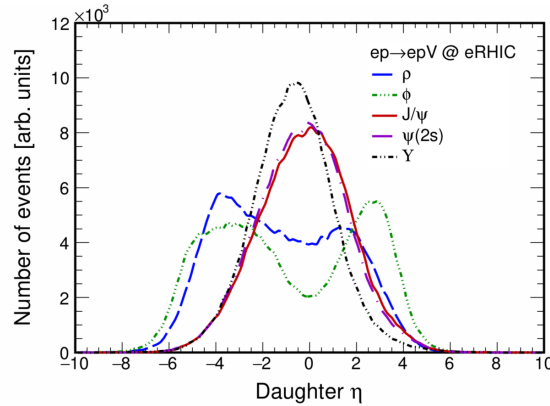


**Figure 8.79:** The pseudorapidity distribution for the daughter particles from the decay of different vector mesons at the EIC:  $\rho \rightarrow \pi^+\pi^-$ ,  $\phi \rightarrow K^+K^-$ ,  $J/\psi \rightarrow e^+e^-$ ,  $\psi(2s) \rightarrow e^+e^-$ ,  $Upsilon(1S) \rightarrow e^+e^-$ . The lighter mesons have a broader pseudorapidity distribution because the Clebsch-Gordan coefficients for a spin 1 particle decaying to two spin-0 particles is very different than from a decay to two spin-1/2 particles. From Ref. ??.

for heavy ions, coherence is only possible for roughly  $x < 0.03$ . Incoherent photoproduction is possible for all  $x$  values, so incoherent  $eA$  photoproduction looks more like the  $ep$  coherent distribution. It is important to note that, for ions, Fermi motion allows interactions to occur with  $x > 1$ . That is not included in these simulations, but could lead to final states with an even larger rapidity.

Very roughly, the decay of a  $\rho$  with rapidity  $y$  leads to pions in the pseudorapidity range  $x - 1$  to  $x + 1$ . It is important to have good acceptance in at least this broad a range around the  $\rho$  rapidity to be able to reconstruct the spin-density matrix of the  $\rho$ , and, from that, determine the mixture of longitudinal to transverse polarization.

If the rapidity is cut off at too high a negative rapidity, sensitivity to partons with the lowest Bjorken- $x$  will be lost. This region is also critical for probing backward production of mesons, as discussed in Sec. 7.4.5. Per Eq. 7.50, each unit of rapidity in Fig. 8.80 that is lost is roughly equivalent to raising the minimum accessible Bjorken- $x$  by a factor of  $e$ .

Similarly, if acceptance is cut off in the other side of the detector, sensitivity to near-threshold production will be lost. This may be a particular issue for nuclear targets, where the study of partons with  $x > 1$  (possible because of Fermi motion) is important to understand nuclear correlations [1218]. This region is also important for studying the production of exotics like pentaquarks, discussed in Sec. 7.4.6.

### Soft kaons from $\phi$ decays

Exclusive production of the  $\phi$  was one of the featured reactions in the EIC White Paper [1]. The White Paper considered only electroproduction, but it is very important to study the  $Q^2$  evolution of exclusive production, to see how saturation turns on as the  $Q^2$  is reduced

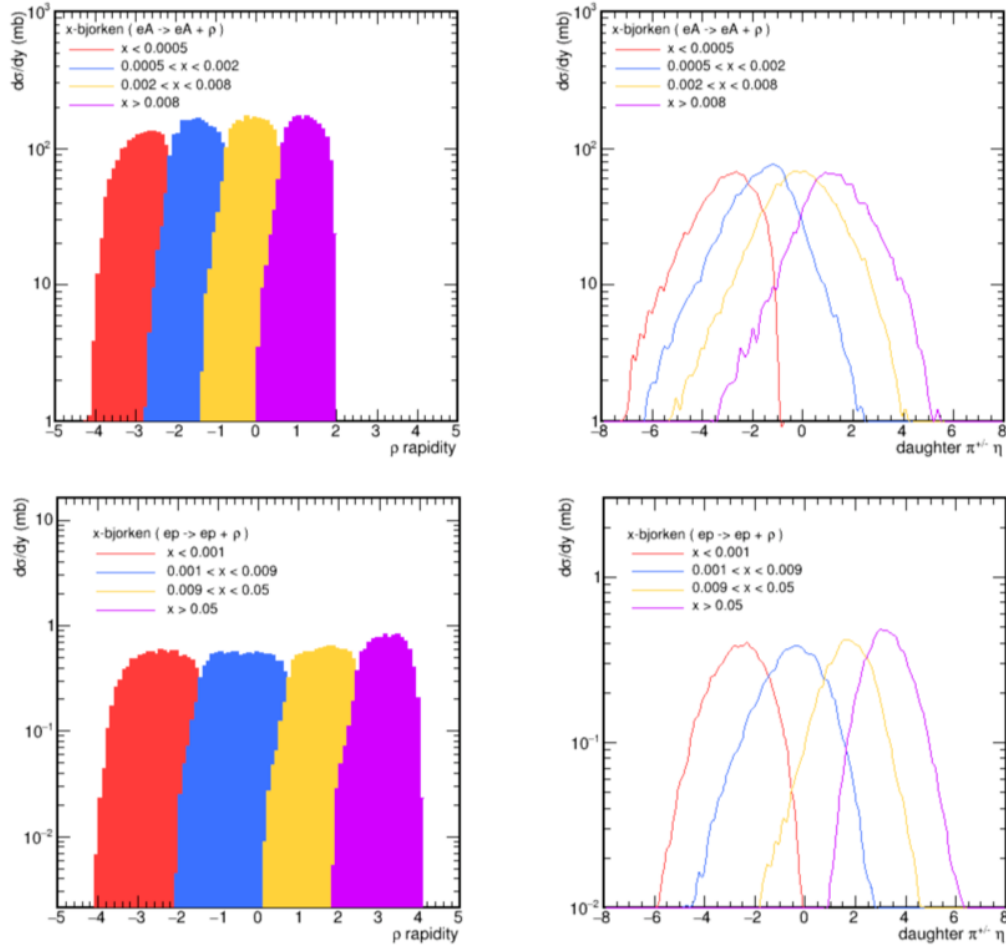


**Figure 8.80:** (left)  $d\sigma/dy$  for coherent  $\rho$  photoproduction using the eSTARlight Monte Carlo [734]. The top plots are for 18 GeV electrons colliding with 100 GeV ions, while the bottom plots are for 18 GeV electrons on 275 GeV protons. The total production is divided up in terms of Bjorken- $x$  of the struck gluon; rapidity increases smoothly with  $x$ . (right) Daughter pion pseudorapidity for coherent  $\rho$  photoproduction under the same conditions, also divided up by  $x$ .

[734, 735]. Among the different  $\phi$  final states, only  $K^+K^-$  seems feasible. The  $K_S K_L$  final state is problematic because of the long  $K_L$  lifetime; it is too soft to be easily reconstructible in hadronic calorimeters. The dilepton final states would be easy to reconstruct, but the branching ratios are too low to allow for adequate statistics; their small signals would also challenge particle identification systems.

$\phi \rightarrow K^+K^-$  is a challenge because the kaons are so soft. In the  $\phi$  rest frame, the kaon momenta are only 135 MeV/c, or  $v/c \approx 0.2$ . Besides the low velocity, they are heavily ionizing, so are easily stopped in detector elements.

Figure 8.81 shows the rapidity distribution for coherently produced  $\phi$ , along with the pseudorapidity distribution of its charged kaon decay products. In addition to showing all gen-

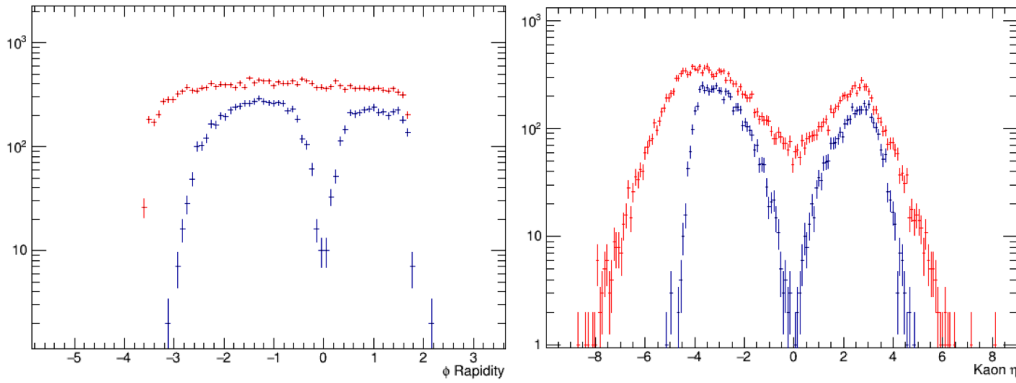


**Figure 8.81:** (left)  $d\sigma/dy$  for coherent  $\phi$  production using the eSTARlight Monte Carlo [734] for 18 GeV electrons on 275 GeV protons. The red curve shows the total production while the blue shows the acceptance in an all-silicon tracker with a 1.5 T solenoidal field. The drop-off around  $y = 0$  is because the tracker cannot reconstruct the low-momentum tracks from kaons that decay nearly at rest. (right) pseudorapidity distribution for charged kaons from coherent  $\phi$  production under the same conditions, with the same red and blue curves. The gaps around  $y = 0$  and  $\eta = 0$  are because the tracker cannot reconstruct the soft kaons from  $\phi$  decays near rest.

erated  $\phi$  and daughters, it also shows the  $\phi$  and kaons that are reconstructed in a model of an all-silicon detector in a 1.5 T solenoidal magnetic field. There is a large drop-off for kaons with pseudorapidity near zero, and a corresponding fall for  $\phi$  with rapidity near zero. The reason is that this detector cannot reconstruct soft kaons from  $\phi$  decays near rest. Although this is only one example detector, it has thinned silicon MAPS sensors in a precision vertex chamber, and it would not be easy to do significantly better than this. Away from  $y = 0$ , the kaons are Lorentz boosted; the higher velocity kaons are more penetrating, and the  $\phi$  can be reconstructed. Likewise, at higher  $Q^2$  the  $\phi$  should have a significant transverse momentum, leading to increased acceptance. The acceptance limitations near  $y = 0$  and  $p_T = 0$  will create a hole in acceptance at  $Q^2 = 0$  will preclude  $\phi$  measurements around  $x = 1/2\gamma$  ( $x = 0.005$  for ions). The importance of this hole will depend on its size; this should be studied in future detector designs.

### Momentum Resolution

The need to be able to separate  $Y(1S) \rightarrow ll$ ,  $Y(2S) \rightarrow ll$  and  $Y(3S) \rightarrow ll$  requires a detector with good momentum resolution; separating the  $J/\psi$  and  $\psi'$  is much easier. The mass difference between the  $Y(2S)$  and  $Y(3S)$  is only 334 MeV, or 3% of their mass. This separation is a signature requirement for the sPHENIX collaboration; their analysis found that a mass resolution of 100 MeV, giving a bit over  $3\sigma$  separation. A recent sPHENIX simulation found  $\sigma = 87$  MeV [1219].

A simple case, an  $Y$  at  $y = 0$ ,  $p_T = 0$ , has two back-to-back tracks each with energy  $M_{ll}/2$  and momentum close to that value. Then, neglecting the small lepton masses,  $M_{ll}^2 = 4p_1p_2$ . Assuming that the two track momenta and resolutions are roughly equal, then

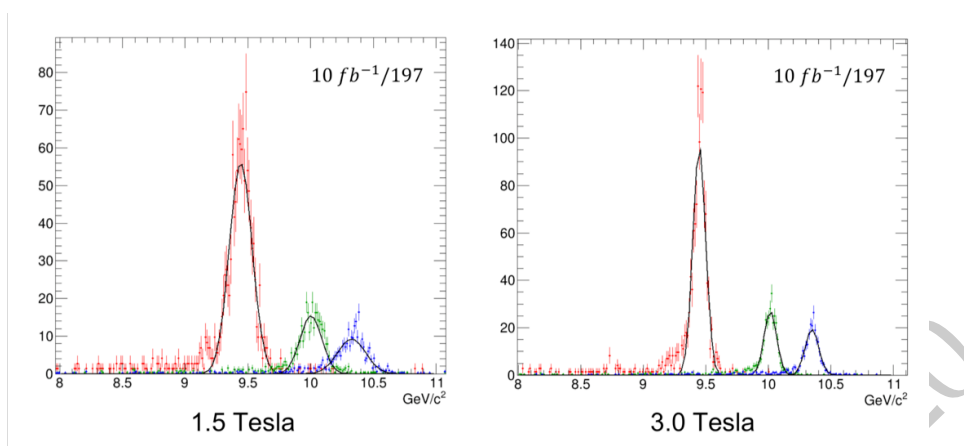


**Figure 8.82:** Dielectron mass spectra for combined  $Y(1S)$  plus  $Y(2S)$  plus  $Y(1S)$  production in an all-silicon detector in (left) a 1.5 T magnetic field and (right) a 3.0 T magnetic field.

$\sigma_M/M = 2\sigma_p/p$ . So, for tracks with momentum around 5 GeV/c, the required momentum resolution is about 0.5%. Away from  $y = 0$ ,  $p_T = 0$ , an analytic analysis is more difficult, but it seems that the Lorentz boosts lead to slightly looser requirements, when expressed in terms of  $\sigma p/p$ . Going further requires simulations; Fig. 8.82 shows the dielectron mass spectrum for a simulation combining the three  $Y$  states in an all-silicon detector in 1.5 and 3.0 T magnetic fields. Adequate separation is seen at 1.5 T, while at 3.0 T the separation is almost complete.

### Separating coherent and incoherent interactions

As was discussed in Section 7.3.9, separating coherent and incoherent production is critical for using vector meson production for nuclear imaging and studies of gluonic fluctuations. For moderate/large  $|t|$ , rejection factors of more than 400:1 are required. This poses extreme requirements on the forward detection elements at an EIC detector. The nuclear excitation typically occurs via neutron, proton or photon emission. Neutrons and protons can be detected with zero degree calorimeters and forward proton spectrometers respectively, but it is critical that these both have excellent acceptance out to transverse momenta of several times the Fermi momentum. Photon detectors must be able to detect photons with MeV energies in the nuclear rest frame, corresponding to 100 MeV in the lab frame. Here, it is important to point out that different nuclei will impose different requirements.

Lead is doubly magic, so its lowest energy excited state is at 2.6 MeV [1220], leading to lab-frame photon energies of hundreds of MeV. These photons are likely isotropic in the nuclear frame. So, in going to the lab frame, half of them are Lorentz boosted, and half are Lorentz downshifted. The downshifted ones will be undetectable. Allowance must be made for these missed photon.

In contrast, gold has an excitation with an energy of 77 keV, and a lifetime of 1.9 nsec [1220]. The long lifetime means that the excited gold nucleus may travel tens of meters

before decaying, making the decay products essentially impossible to observe. There are additional low-lying states with energies of 269 and 279 keV, which translate to maximum detector-frame energies below 60 MeV. Although we do not have good models to predict which levels are excited in exclusive vector meson production, it seems unlikely that the required separation can be achieved with gold nuclei.

In short, some nuclear deexcitations will involve very soft photons; for gold, some of these photons are emitted after the excited nucleus has left the interaction region. These photons are probably undetectable. Separating coherent and incoherent production is likely to be considerably easier with lead beams, but more study is required to determine what rejection factor is achievable, and how it will impact the physics.

### 8.5.2 Overview of Far Forward Region

From a requirements standpoint, the diffractive and tagging working group focused mainly on the region of the EIC beyond the main detector, a region known as the far-forward area. This unique area allows particles that have extremely small scattering angles to be detected. In the hadron going direction, this area includes Roman Pots (RP), off-momentum detectors (OMD), a B0 tracker, and a Zero Degree Calorimeter (ZDC), see Sec. 11.6 for more details. In Fig. 8.83, the geometric layout of the far-forward region of the IR is shown, together with a tentative conceptual design of the far-forward particle detectors, see caption for details.

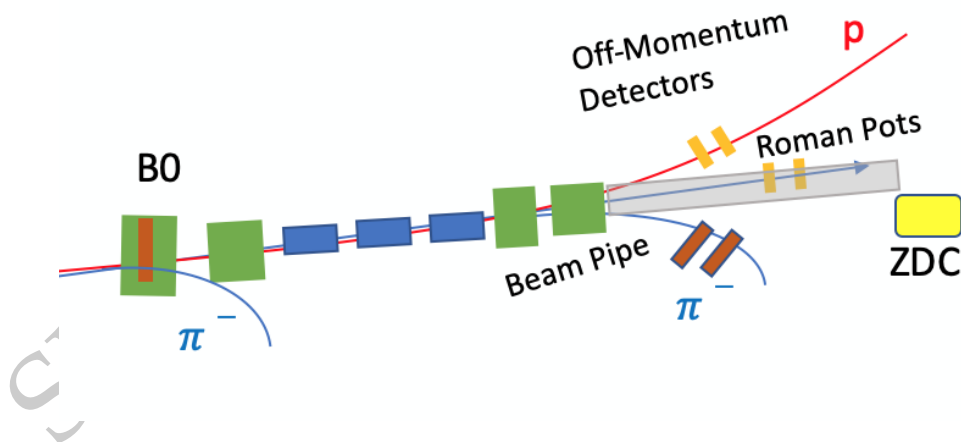


**Figure 8.83:** Geometric layout of the far-forward area setup in the hadron going direction. The green boxes denote the dipole magnets; the blue rectangles denote the quadrupole focusing magnets; the gray tube is a simple representation of the beam pipe in the drift region where many of the far-forward protons and neutrons are detected. A detailed engineering design of the beam pipe is currently in progress. Blue  $\pi^-$  and red proton tracks originating from  $\Lambda$  decays are shown, of importance to the meson structure studies, see Sec. 8.5.3.

### 8.5.3 Meson structure

For the detection of particles of relevance to meson structure studies all sub-components of the far-forward area play an important role, the detection in the B0 area, detection of decay products with the off-momentum detectors, and detection of forward-going protons and neutrons with the Roman Pots and ZDC.

**Sullivan process for pion structure:  $e + p \rightarrow e' + X + n$**

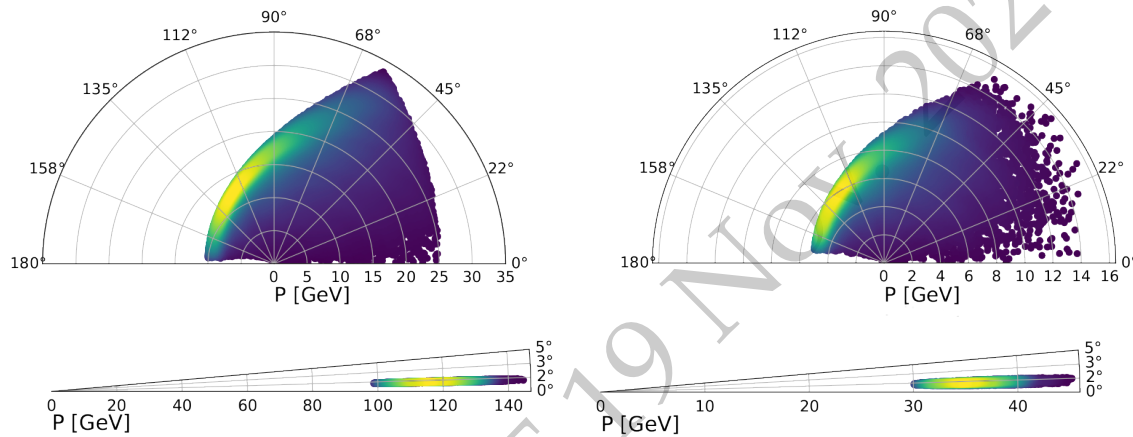


**Figure 8.84:** A comparison of the scattered electron (top) and leading neutron (bottom) kinematics for two energy settings -  $10 \times 135$  (left) and  $5 \times 41$  (right). The momentum,  $P$  and angle,  $\theta$  are defined in the lab frame. The scattered electrons, in both cases, are within the acceptance of the central detector and the leading neutrons are at small forward angles and carry most of the proton beam energy after the scattering process.

The initial pion structure studies were conducted at the highest energy of  $18 \times 275$  (corresponding to the electron and proton beam energy, respectively, both in GeV) to maximize the kinematics coverage. However, to improve access to the high  $x_\pi$  region (see Sec. 7.1.3), alternate lower beam energies  $10 \times 135$  and  $5 \times 41$  were also selected. These lower beam energies allow access to this high  $x_\pi$  regime over a wider range of  $Q^2$ . For a comparison, the  $18 \times 275$  energies allow access to high  $x_\pi$  data over a  $Q^2$  range of  $\sim 200$ - $1000$   $\text{GeV}^2$ , while with the  $10 \times 135$  energies that range was increased to  $\sim 30$ - $1000$   $\text{GeV}^2$ , and with the  $5 \times 41$  energies to  $\sim 5$ - $1000$   $\text{GeV}^2$ . The lower-energy combination of  $5 \times 41$  is even more beneficial to tag kaon structure by allowing detection of the leading  $\Lambda$  events (see below).

The kinematics for the more advantageous lower energy settings,  $10 \times 135$  and  $5 \times 41$ , are shown in Fig. 8.84. While the scattered electrons are within the acceptance of the central detector, the leading neutrons for these two energy settings are at a very small forward angle while carrying nearly all of the proton beam momentum. These leading neutrons will be detected by the ZDC.

Figs. 8.85 shows the acceptance plots for neutrons in the ZDC for different beam energy

settings. As one can see, the spatial resolution of ZDC plays an important role for the higher beam energy setting ( $18 \times 275$ ), since it is directly related to the measurements of  $p_T$  or  $t$ . For the lower beam energy setting ( $5 \times 41$ ), the total acceptance coverage of the ZDC is important. This sets a requirement for the total size of ZDC to be a minimum of  $60 \times 60 \text{ cm}^2$ . Such a configuration of the ZDC allows to achieve close to 100% neutron detection efficiency for this channel.

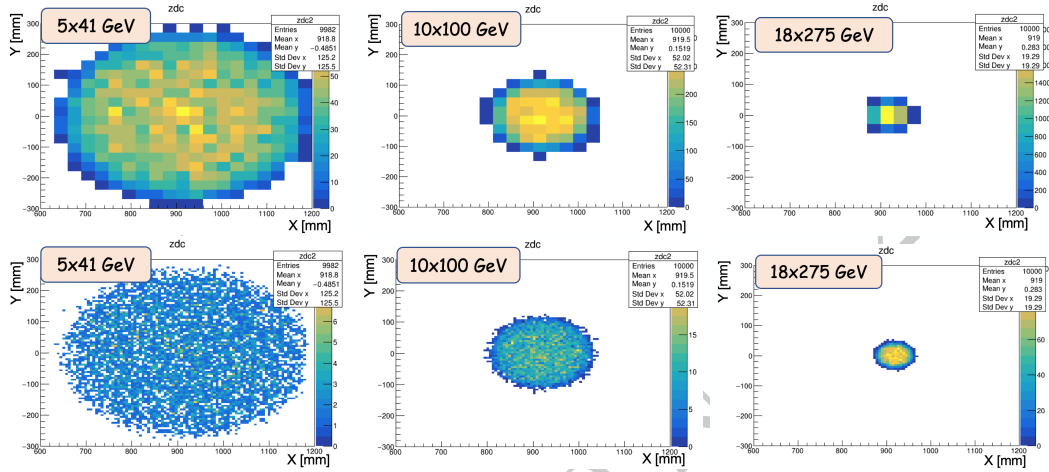


**Figure 8.85:** Acceptance plot for neutrons in  $60 \times 60 \text{ cm}^2$  ZDC, with a low spatial resolution of 3 cm (upper panels) and with a high spatial resolution of 0.6 cm (lower panels), for different beam energy settings, from left to right  $5 \times 41$ ,  $10 \times 100$ , and  $18 \times 275$ . The acceptance plot for  $5 \times 100$  would be similar as shown for  $10 \times 100$ . The lower proton (ion) energies set the requirement for the size of the ZDC, whereas the higher proton (ion) energies drive the spatial resolution requirement.

### Sullivan process for kaon structure: $e + p \rightarrow e' + X + \Lambda$

For the case of a leading  $\Lambda$  event, to tag the DIS process on a kaon, both its decay products are detected at small forward angles due to the nature of two-body decay kinematics. The detection of these  $\Lambda$  decay products requires additional high-resolution and granularity due to the small angle of separation of decay products.

Detection of the decay channel  $\Lambda \rightarrow n + \pi^0$  is feasible but will require a means for EM Calorimetry before the ZDC, in order to distinguish the neutron and the two photons coming from  $\pi^0$  decay. Detection of the other decay channel,  $\Lambda \rightarrow p + \pi^-$ , poses a more challenging measurement due to its requirement of additional charged-particle trackers or a veto trigger on the path to ZDC.

The reconstruction of the  $\Lambda$  event in the far-forward detection area is one of the most challenging tasks. This comes mainly from the fact that these leading  $\Lambda$ 's have energy close to the initial beam energy, and thus their decay lengths can be tens of meters along the Z-axis (or beam-line). This complicates detection of the decay products, and thus the final  $\Lambda$  mass reconstruction.

Fig. 8.86 illustrates this further, and shows the Z-coordinate of where the  $\Lambda$ -decay occurs for different beam energies. For the lower beam energy settings ( $5 \times 41$ ) most  $\Lambda$  decays are within the central detector region, but at the higher proton (ion) beam energies the  $\Lambda$  decays happen more in the forward-detection area, with tails of the decay process to near the ZDC location. Table 8.14 shows the percentage of decayed  $\Lambda$  for different energies and different Z ranges.

$E_{\text{beams}}$	$Z_{\text{vtx}} < 5 \text{ m}$	$5 \text{ m} < Z_{\text{vtx}} < 30 \text{ m}$	$Z_{\text{vtx}} > 30 \text{ m}$
$5 \times 41$	83.0%	16.6%	0.4%
$5 \times 100$	52.1%	46.7%	1.2%
$10 \times 130$	41.8%	54.2%	4%

**Table 8.14:** Percentage of decayed  $\Lambda$ 's in different detection ranges.

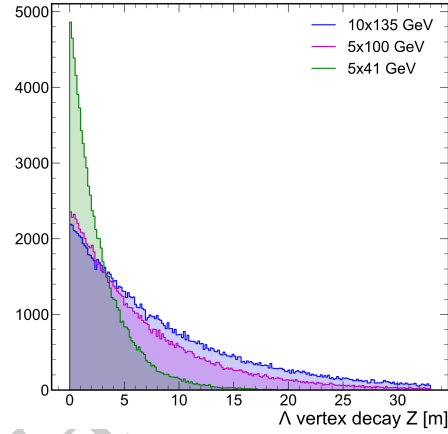


**Figure 8.86:** The  $\Lambda$ -decay spectrum along the beam line for different beam energies.

To study the possibility of  $\Lambda$  mass reconstruction further, both main decay modes were looked into:  $\Lambda \rightarrow p + \pi^-$  with a branching ratio of 63.9%, and  $\Lambda \rightarrow n + \pi^0$  with a branching ratio of 35.8%. Both channels can be clearly separated by the different charge of the final-state particles, and thus the different detector components which will play a role for their detection.

$\Lambda \rightarrow p + \pi^-$  For this process we only have charged particles in the final state. Therefore, for detection, we have to rely on sub-components along the far-forward area such as the B0 tracker, the Off-Momentum trackers, and Roman Pots.

As an example, occupancy plots for the beam energy setting of  $5 \times 41$  are shown in Fig. 8.87. Since this is the lowest beam energy setting, most of the lambdas would decay in the first meter (before the B0 magnet), and the decay products of lambda are expected to have low momenta. Therefore, as expected, protons coming from the  $\Lambda$  decays will mostly be detected, due to their lower rigidity, in the off-momentum detectors (c) and partially in a

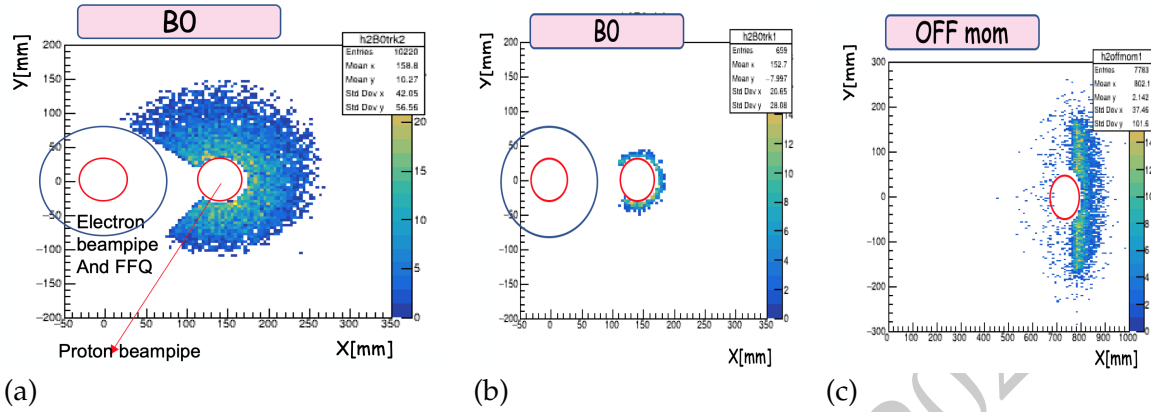


**Figure 8.87:** Occupancy plots for energy setting  $5 \times 41$  (a) for  $\pi^-$  in the B0 tracker, (b) for protons in the B0 tracker and (c) in Off-Momentum detectors. The red circle shows the beam pipe position and the blue circle shows the electron Final-Focus Quadrupole (FFQ) aperture inside the B0 dipole.

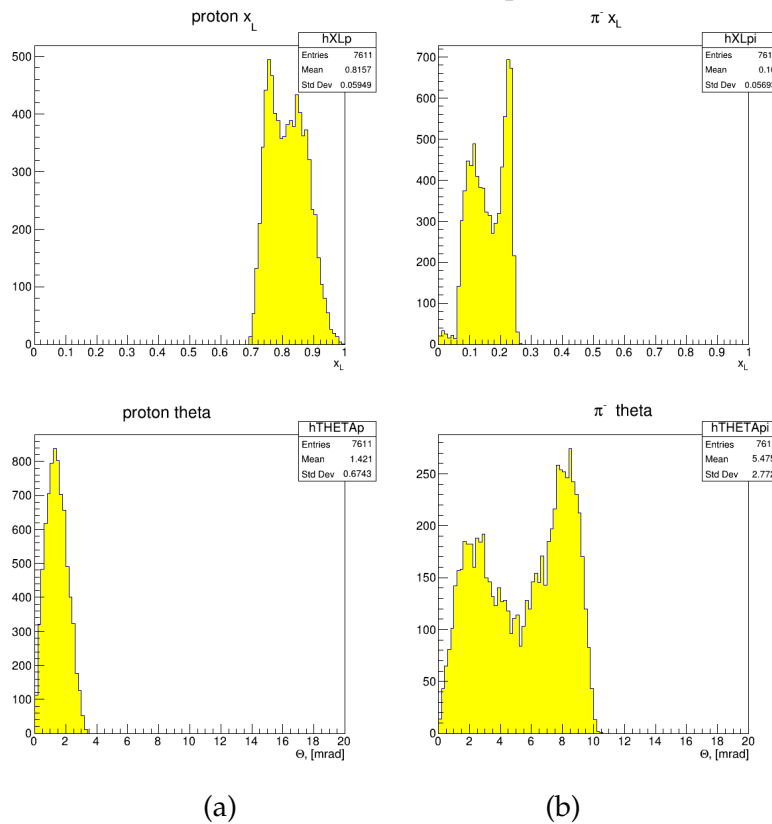


**Figure 8.88:**  $x_L$  and theta distributions for detected decay products of  $\Lambda$  particles for the  $5 \times 41$  beam energy combination: protons (left panels) and pions (right panels).

B0 tracker (b). While for pions, the tracker inside the B0 dipole will be the only detecting element (a). As one can also see from this Figure, the proton-beam-pipe aperture inside the B0-dipole plays an important role and sets the detection efficiency for pions, as well as the azimuthal angle  $\phi$ -coverage of the detecting elements around the proton beam-pipe. Further information on the distributions for detected decay products at these lower beam energies of  $5 \times 41$  are given in Fig. 8.88.

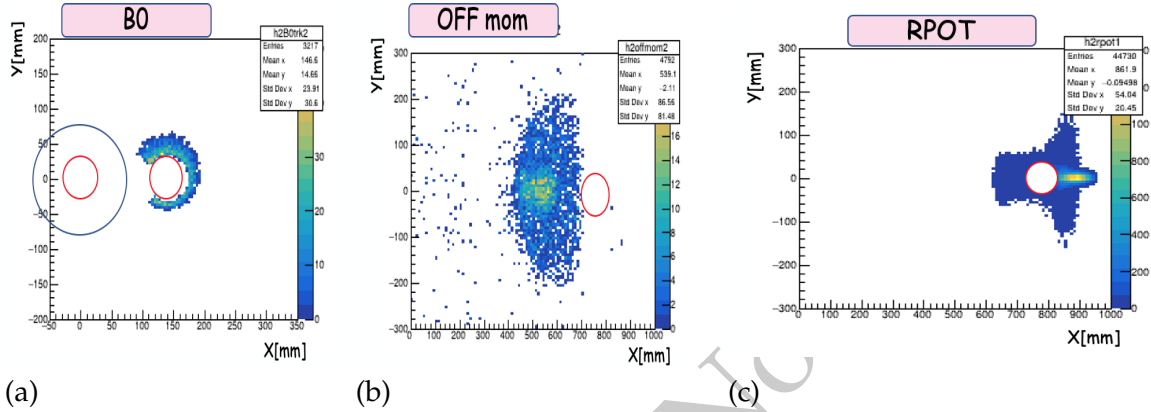


**Figure 8.89:** Occupancy plots for energy setting  $10 \times 100$  (a) for  $\pi^-$  in the B0 tracker and (b) the Off-Momentum tracker, and (c) for protons in the Roman Pots detectors. The red circle shows the beam pipe position and the blue circle shows the electron FFQ aperture inside the B0 dipole.

For the higher beam-energy settings, for example  $10 \times 100$ , the protons are to be detected in the roman-pots (and partially in Off-Momentum) detectors, see Fig. 8.89. Pions originating from a  $\Lambda$ -decay with  $Z_{vxt} < 4 m$  will only partially be detected in the B0-area, while most of them will go undetected through the proton beam pipe. Pions with higher momentum and lower angles ( $p_t$  or theta) can pass through the bores of the Final-Focusing Quadrupole magnets (FFQs) and be detected in the Off-Momentum detectors. Their detection represents the denser (light) area of detection in the Off-Momentum detectors (Fig. 8.89(b)). Note that due to the negative charge of the pions, they will experience an opposite bending in dipoles, as compared to protons (compare with the protons in the Off-Momentum detectors on Fig. 8.87(b)). Therefore, in order to detect the  $\Lambda$ -decays in this channel the Off-Momentum detectors need to provide a full azimuthal coverage, to establish a proper detection for the negatively-charged particles.

For the  $5 \times 41$  beam energy combination, Fig. 11.97 shows the momentum (top panels) and angular (bottom panels) distributions of protons (left panels) and pions (right panels) from  $\Lambda$ -decay as a function of distance of the  $\Lambda$ -decay point, as detected in one of the beam line sub-detectors. This then in turn illustrates which of the sub-detectors along the beam line detect the decay products. The protons carry most of the initial proton beam momentum and extend over the far-forward direction, with angles less than 8 mrad. On the other hand, as one can clearly see from the high density of hits, the  $\Lambda$ -reconstruction efficiency will mainly depend on the efficiency for the detection of pions in the B0 area, with angles in the 5-25 mrad range.

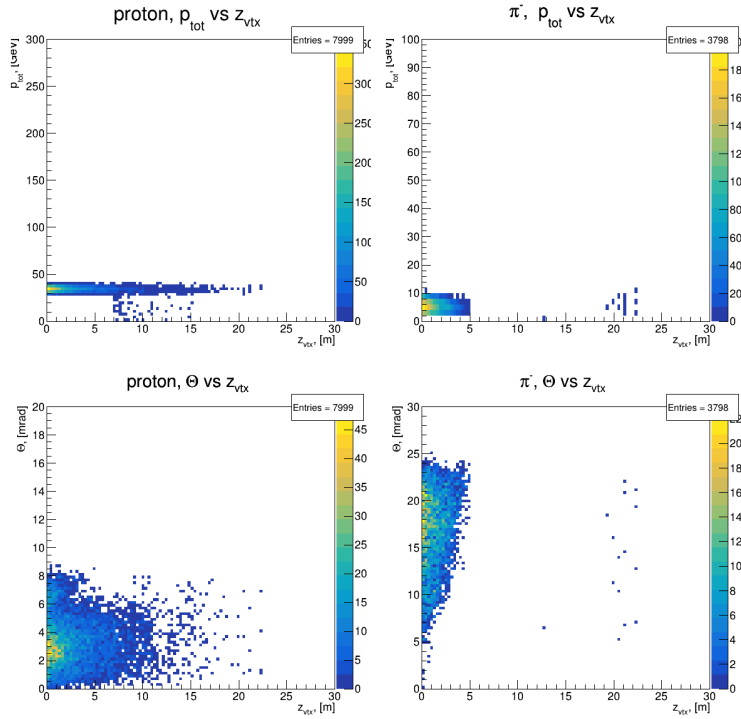


**Figure 8.90:** Momentum (top) and angular (bottom) distributions of protons (left) and  $\pi^-$  (right) from the  $\Lambda \rightarrow p + \pi^-$  decay at beam energy setting  $5 \times 41$ , as registered in the far-forward detectors as a function of their origination (the decay vertex).

For the higher beam energy combination, for example  $10 \times 100$ , the situation will be much different. Fig. 8.91 shows the momentum and angular distributions for protons and  $\pi^-$ . For the latter, one can clearly see a “dead” area appear along the beam line, where the FFQ beam elements are located, prohibiting placement of detectors and thus  $\pi^-$  detection. This comes from the fact that these pions have significantly low momentum, and the beam magnet optics settings does not allow them to pass through this area, they get swept into the magnets and beam line. Those  $\Lambda$ 's which decay after the set of FFQs will be tagged by the off-momentum detector, but since the  $Z_{vtx}$  is unknown, it will be hard (or impossible) to make a one-to-one correlation between the tagged position and the particle's momentum or angle. Therefore, for the final reconstruction of the  $\Lambda$  invariant mass, one has to use only events with  $Z_{vtx} < 3 - 5$  meters, to make this correlation possible. That this indeed remains possible is shown in Fig 8.92 (right panel), which shows the invariant mass spectra of the  $\Lambda(p, \pi^-)$  channel for this  $10 \times 100$  beam energy setting. The corresponding  $p_T$  spectrum of the  $\Lambda$  particles is shown on the left panel of Fig 8.92.

We summarize this result in Table 8.15, which shows the expected  $\Lambda$  detection efficiency for the decay  $\Lambda \rightarrow p + \pi^-$ . A cut on decay within 4 meters,  $Z_{vtx} < 4m$  has been applied for this selection. The decrease in detection efficiency for the higher-energy settings comes mainly from this  $Z_{vtx}$  cut, but is necessary to ensure  $\Lambda$  mass reconstruction.

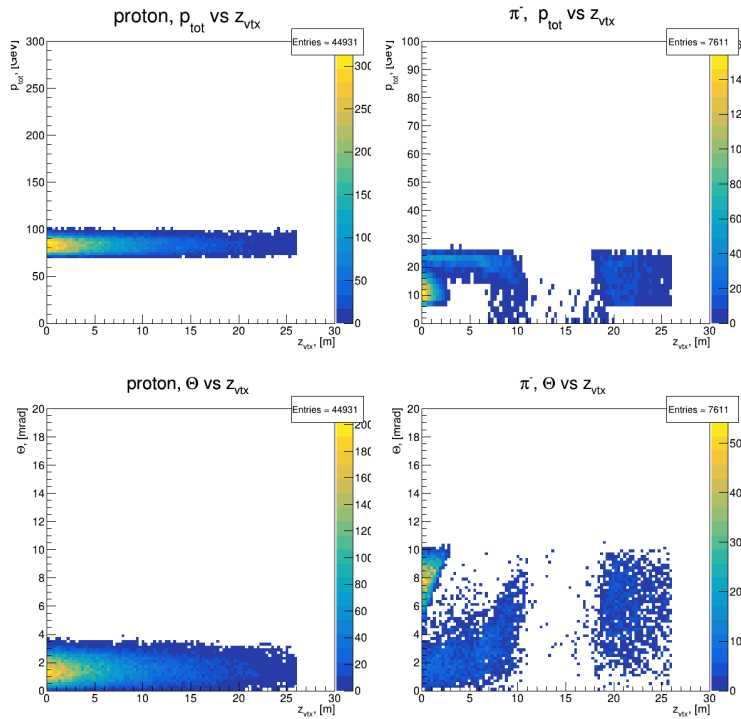


**Figure 8.91:** Momentum (top) and angular (bottom) distributions of protons (left) and  $\pi^-$  (right) from the  $\Lambda \rightarrow p + \pi^-$  decay at beam energy setting  $10 \times 100$ , as registered in the far-forward detectors as a function of their origination (the decay vertex). For the  $\pi^-$ , the “dead” area in the Final-Focusing Quadrupole magnet region where placement of detectors is impossible is apparent.

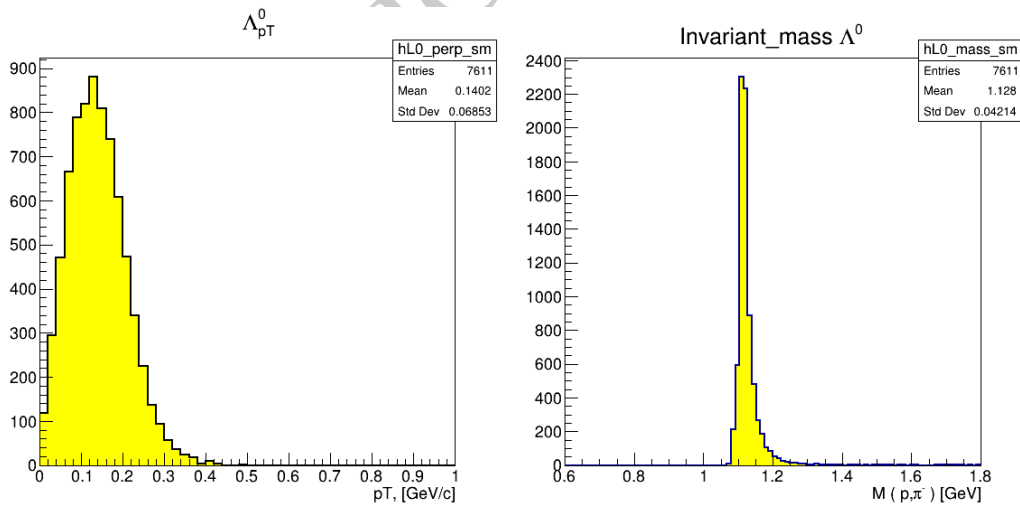


**Figure 8.92:** The  $p_T$  (left) and invariant mass (right) of the reconstructed  $\Lambda$  particles for the beam energy settings of  $10 \times 100$ .

Beam energies	5×41	10×100	18×275
Lambda Efficiency	20%	15%	1%

**Table 8.15:** The number of detected particles for 10k events, or final  $\Lambda$  detection efficiency, as a function of beam energy combinations, for  $\Lambda$  detection with a cut on decay applied of  $Z_{vtx} < 4$  m to ensure  $\Lambda$ -mass reconstruction.

$\Lambda \rightarrow n + \pi^0$  For this process we only have neutral particles in the final state. The main scheme of detection for these particles will be the ZDC and/or some kind of electromagnetic calorimeter/photon detector in the B0 area. Similar as for the  $p + \pi^-$  decay mode, with lower beam energies more particles can be detected in the central detector region. Fig. 8.93 shows the angular ( $\Theta$ ) distributions for  $n$  and  $\pi^0$  for different beam energies. It is furthermore assumed that the  $\pi^0$  is reconstructed from  $\pi^0 \rightarrow \gamma\gamma$ , where the photons are deposited in one of the corresponding detectors.

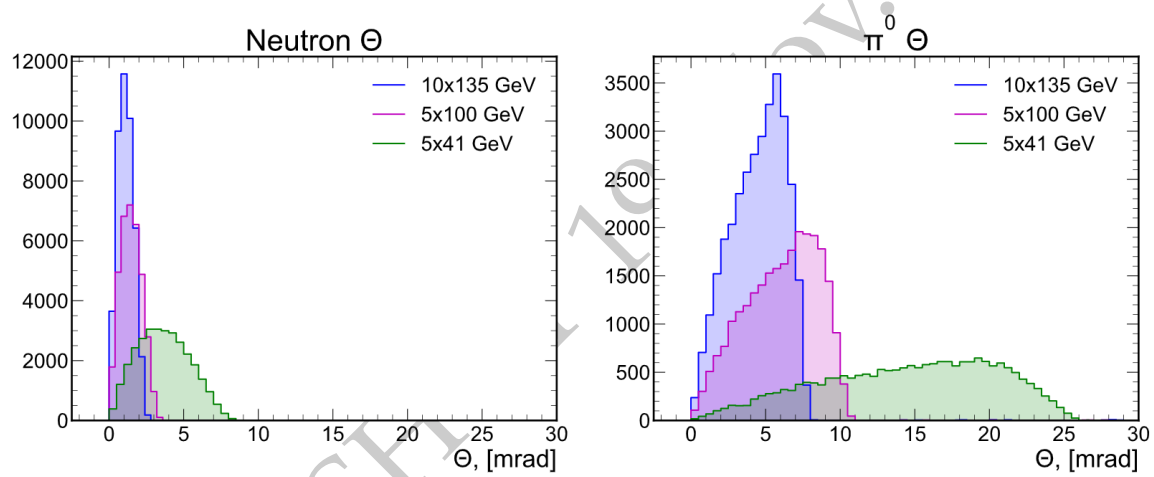


**Figure 8.93:** Angular distributions for detected decay products of  $\Lambda \rightarrow n + \pi^0$ : neutrons (a) and  $\pi^0$  (b), for beam energy settings 10×135, 5×100, and 5×41.

The energy and angular distributions of the two photons from the  $\pi^0$  decay are shown in Fig. 8.94, for various beam energy settings. At lower beam energy settings, like 5×41, some measurement to detect the larger-angle photons in the B0 area is required to recapture efficiency. As the beam energy increases, the ZDC starts playing the main role for detection of both neutrons and neutral-pions. Fig. 8.95 shows occupancy plots of  $n$  and  $\gamma\gamma$  used for  $\pi^0$  reconstruction for different energy settings.

#### Exclusive $p(e, e' \pi^+ n)$ events

WC: from here also prob appears in exclusive summary, text on exclusive pion prod. + our fig 8.96, so could be cut.

The kinematic distributions for exclusive  $p(e, e' \pi^+ n)$  events are shown in Fig. 8.96. As

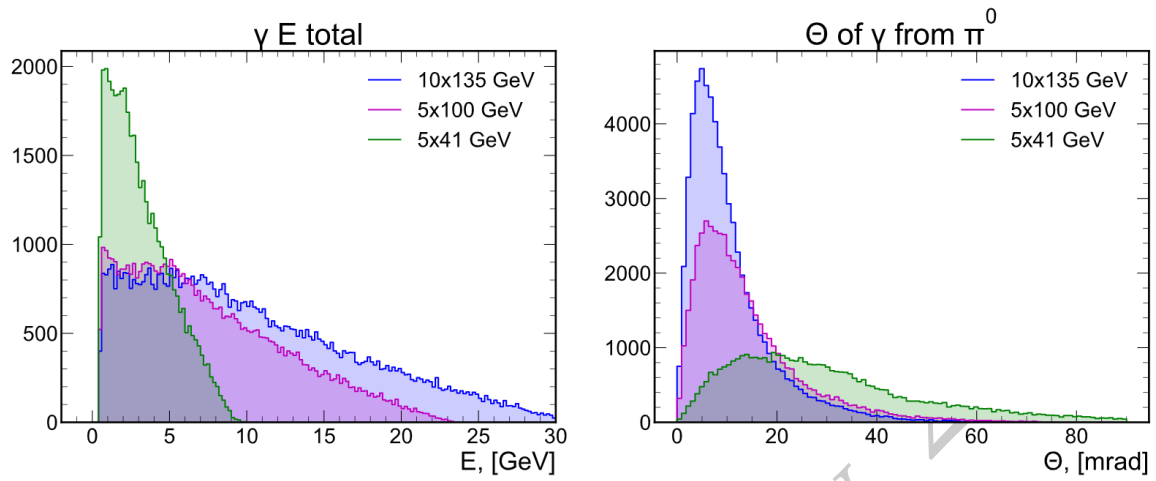


Figure 8.94: Energy and angular  $\Theta$  distributions for detected  $\gamma\gamma$  from  $\pi^0$  of  $\Lambda$  decay

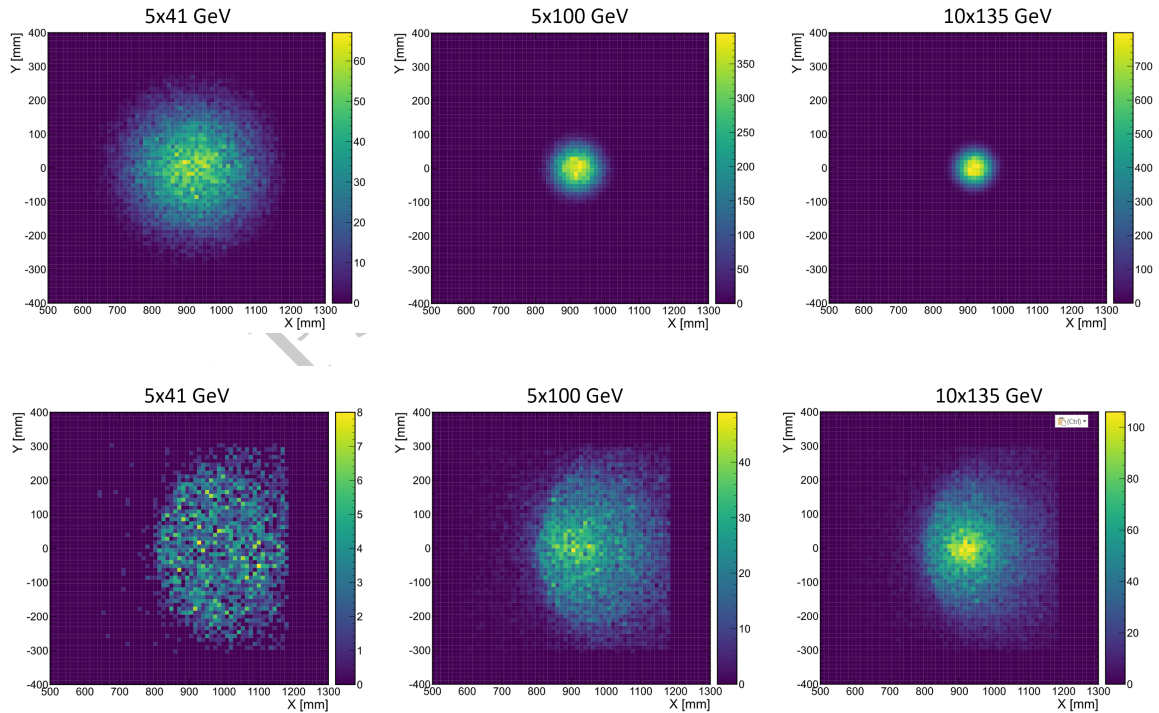
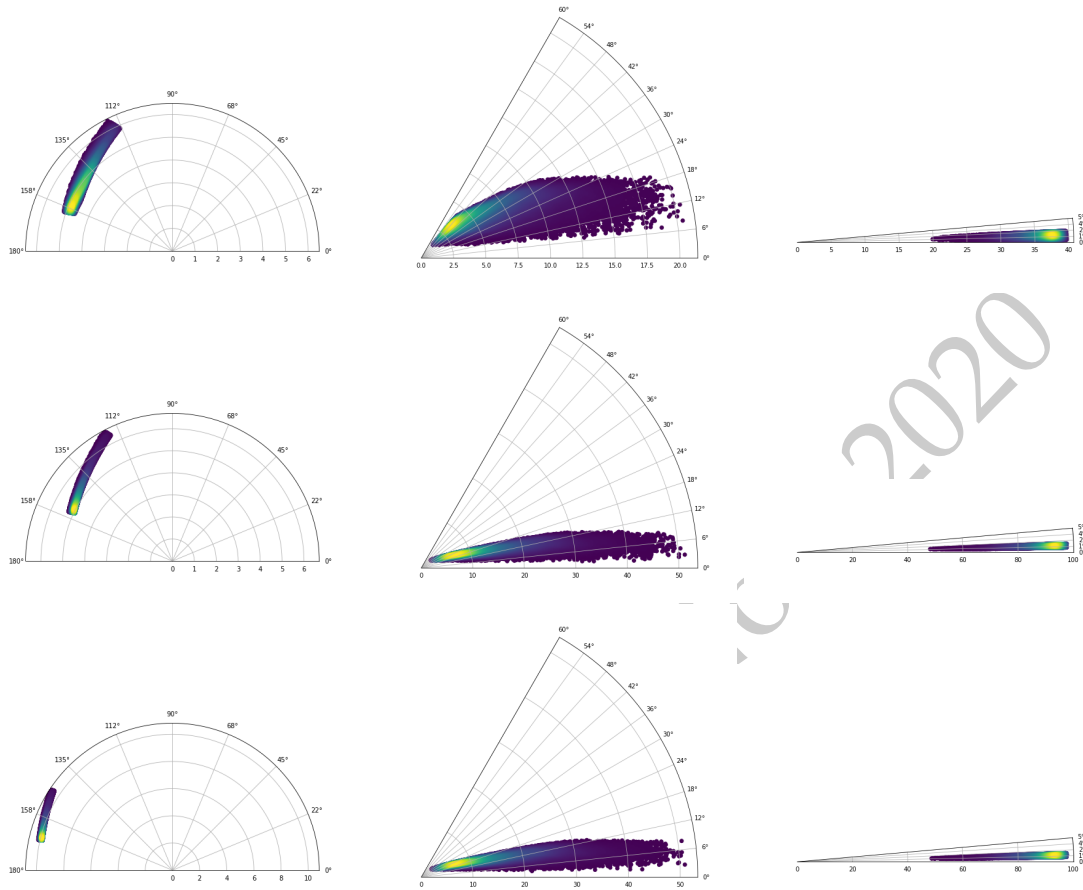


Figure 8.95: Occupancy distribution for neutrons (top panels) and  $\gamma\gamma$  from  $\pi^0$  decay (bottom panels) as detected in the ZDC for different beam energy settings.



**Figure 8.96:** Kinematic distributions for exclusive  $p(e, e' \pi^+ n)$  events for  $e'$  (left),  $\pi^+$  (center), and  $n$  (right), at beam energies of  $5 \times 41$  (top),  $5 \times 100$  (middle), and  $10 \times 100$  (bottom). The radial component is momentum, and the polar coordinate is the scattering angle, with the proton (electron) beam direction pointing to the right (left).

for tagged DIS events, the neutrons assume nearly all of the proton beam momentum, and need to be detected at very forward angles in the ZDC. The scattered electrons and pions have also similar momenta as in the tagged DIS case, except that here the electrons are distributed over a wider range of angles. E.g., for the  $5 \times 100$  beam energy setting, the 5-6 GeV/c electrons are primarily scattered  $25^\circ$ - $45^\circ$  from the electron beam, while the 5-12 GeV/c  $\pi^+$  are at  $7^\circ$ - $30^\circ$  from the proton beam.

### Accelerator and Instrumentation requirements

As one can see from the detector simulation examples shown, access to meson structure physics greatly benefits from EIC operations at the lower center-of-mass energies. Apart from that there is need for both  $ep$  and  $ed$  measurements at similar center-of-mass energies, lower energies enhance the range of  $Q^2$  at large  $x_\pi$ , and the detection needs to uniquely tag

kaon structure requires lower energies to enhance  $\Lambda$  decay probability at short distances and allow  $\Lambda$ -mass reconstruction to work from detected decay products. To tag the pion and kaon structure, proper instrumentation of B0 tracking detectors is needed, requiring full azimuthal coverage and perhaps pushing a smaller proton-beam pipe diameter. Off-momentum detectors have to also provide this full azimuthal coverage for detection of negatively-charged decay particles.

#### 8.5.4 Deuteron DIS with spectator tagging: Free neutron structure and nuclear modifications

DIS on the deuteron with detection of the spectator nucleon (“spectator tagging”),

$$e + d \rightarrow e' + X + N, \quad N = p \text{ or } n \quad (8.12)$$

offers a unique method for extracting the free neutron structure functions and studying the nuclear modifications of proton and neutron structure (EMC effect, antishadowing, shadowing). Detection of the spectator nucleon identifies the active nucleon in the DIS process and eliminates dilution. Measurement of the spectator nucleon momentum (typically  $p_N \lesssim 300 \text{ MeV}/c$  in the deuteron rest frame) controls the nuclear configuration in the deuteron initial state and permits a differential analysis of nuclear effects, enhancing the experimental reach and theoretical accuracy of the analysis. In DIS with proton tagging, pole extrapolation in the spectator proton momentum selects large-size  $pn$  configurations in the deuteron where nuclear interactions are absent and provides a model-independent method for extracting the free neutron structure functions [18]. In DIS with proton or neutron tagging, measurements with spectator momenta  $p \sim 200\text{--}600 \text{ MeV}/c$  (rest frame) select small-size  $pn$  configurations where the EMC effect is enhanced and can be studied systematically as a function of the size of the  $pn$  configuration (tagged EMC effect). Measurements of bound proton structure in deuteron DIS with neutron tagging can be compared with free proton structure measured in proton DIS, transforming the analysis of nuclear modifications (independent normalization, size of modifications). The theoretical framework for tagged DIS on the deuteron is being developed, including final-state interactions and polarization [19,47,48,66,1221].

In tagged DIS at EIC, the spectator nucleon moves in the forward ion direction with  $\approx 1/2$  the deuteron beam momentum, with an offset that is determined by its boosted rest-frame momentum (its light-cone momentum fraction is conserved):  $p_{\parallel,N}[\text{collider}] = x_L p_{\parallel,d}$  with  $x_L \approx \frac{1}{2}(1 + p_{\parallel,N}[\text{restframe}]/m) = 0.35\text{--}0.65$ ,  $p_{\perp,N}[\text{collider}] = p_{\perp,N}[\text{restframe}] \lesssim 300 \text{ MeV}/c$ . Proton spectators are detected with the forward spectrometer; neutron spectators are detected with the ZDC. Generic detector requirements are: (a) Acceptance for proton and neutron spectators in the given  $x_L$  and  $p_{\perp}$  range; (b) Proton longitudinal momentum resolution  $\delta x_L/x_L \ll 10^{-2}$  and transverse momentum resolution  $\delta p_{\perp}/p_{\perp} \approx 20\text{--}30 \text{ MeV}/c$ ; (c) neutron momentum resolution of  $9\text{--}11 \text{ GeV}/c$  for  $p > 110 \text{ GeV}/c$  and  $p_T$ -resolution of  $40\text{--}80 \text{ MeV}/c$ , assuming a ZDC with energy resolution  $\sigma_E < 50\%/\sqrt{E}$  for hadrons, and an angular resolution of  $3 \text{ mrad}/\sqrt{E}$  as assumed for other e+d studies in this report (see Sec. 11.6.6 for details).

Simulations have been performed of neutron structure extraction with deuteron DIS with spectator proton tagging and pole extrapolation in the proton momentum (see Fig. 8.98); see Ref. [1221] for earlier studies. The kinematic variables and theoretical method are described in Refs. [19,48]. The spectator proton momentum is specified by the light-cone fraction  $\alpha_p = 2p_p^+ / p_d^+$  and transverse momentum  $p_T$  in the deuteron-photon collinear frame. Electron-deuteron DIS events are generated with BeAGLE [1101]. The top plots in Fig. 8.98 show the kinematic distribution of events in  $p_T^2$  in two bins of  $\alpha_p$ , as determined by the strong momentum dependence of the deuteron spectral function. The bottom plots show the kinematic distributions after removal of the deuteron pole factor  $(p_T^2 + a_T^2)^2 / [2(2\pi)^3 R]$ , which removes most of the momentum dependence, and the pole extrapolation to unphysical  $p_T^2 \rightarrow -a_T^2$ , which gives the free neutron structure function  $F_{2n}$  [48]. The plots show the procedure in a typical  $(x, Q^2)$  bin in EIC kinematics; similar results are obtained in other bins. The procedure has been verified by comparing the extrapolation results with the free nucleon structure functions in the physics model. The study of detector and beam smearing effects is in progress.

### 8.5.5 Diffractive $J/\Psi$ production on the deuteron with spectator tagging

Diffractive  $J/\Psi$  production on the deuteron with the goal of probing short-range correlations requires that the spectator nucleon is tagged, see Sec. 7.3.7. In the EIC, these spectators are moving with the hadron beam will end up in the far-forward region of the EIC. Some general considerations used to establish baseline particle acceptance and detector resolutions via full simulations in Geant4 [1222] are presented here and further details can be found online [720].

Four different forward detectors are considered in the current study: the  $B0$  silicon tracker, off-momentum detectors, Roman pots and ZDC. The location, size, resolution of transverse and total momentum, energy, and scattering angle of these four detectors used in the simulation are summarized in Ref. [720]. In addition to the intrinsic detector related effects, the beam related effects, smearing of the three-momentum components of the nominal

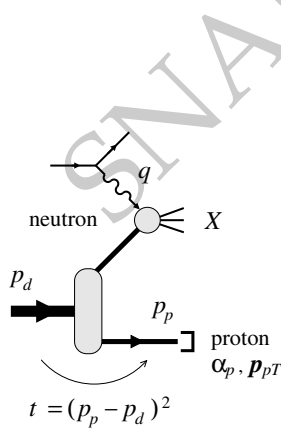


**Figure 8.97:** Deuteron DIS with spectator proton tagging,  $e + d \rightarrow e' + X + p$ . The measured proton momentum is described by the light-cone fraction  $\alpha_p = 2p_p^+ / p_d^+$  and transverse momentum  $p_T$  in the deuteron-photon collinear frame. The proton controls the neutron virtuality  $t - m^2$  in the deuteron (off-shellness). The on-shell point can be reached by extrapolation to  $p_T^2 \rightarrow -a_T^2$ , where  $a_T^2(\alpha_p)$  is the pole position in the deuteron light-cone wave function and is of the order  $\sim \epsilon_d m$  ( $\epsilon_d = 2.2$  MeV is the deuteron binding energy,  $m$  is the nucleon mass). The graph shows the cross section in the impulse approximation; final-state interactions and polarization effects are discussed in Refs. [19,47,48,66].

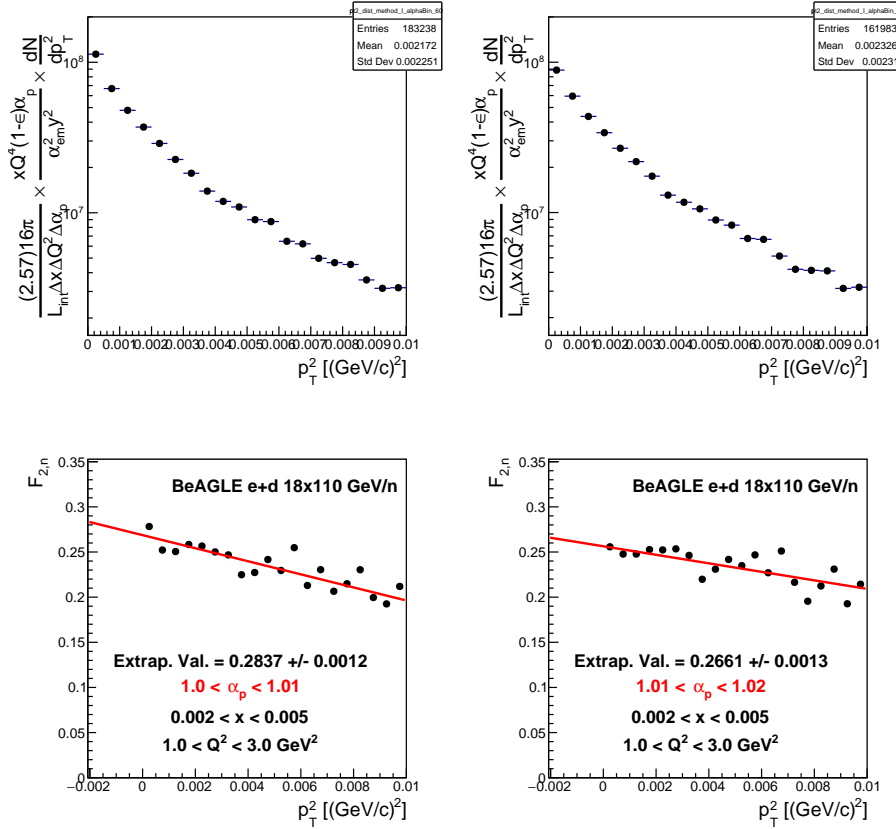


**Figure 8.98:** Top row:  $p_T^2$  distributions for two proton spectator  $\alpha_p$  bins in the same  $x$  and  $Q^2$  bins (cuts are shown in the text on the bottom row of plots). The distributions in the top row include the bin-weighting by the flux factor, as well as all constants included to achieve the final, scaled histograms. Bottom row: The same distribution multiplied by the inverse spectral function pole factor  $(p_T^2 + a_T^2)^2 / [2(2\pi)^3 R]$  [48]. The resulting dependence is then used to perform the on-shell extrapolation to calculate the neutron structure functions. The red line shows the first-degree polynomial used to fit the data and perform the extrapolation to  $p_T^2 \rightarrow -a_T^2$ .

deuteron beam are carried out using Gaussian smearing with a width proportional to the values of angular divergence and beam energy spread. The modified deuteron beam four-vector is used to calculate a Lorentz boost vector. The final state protons and neutrons are then boosted from the lab-frame to the deuteron rest frame using the original, unsmearred deuteron boost vector, and then boosted back to the lab-frame using the smeared boost.

With the current baseline design of the far-forward detectors and the consideration of beam-related effects, the measurement of diffractive  $J/\Psi$  production in electron-deuteron collision is experimentally possible with good precision up to 800 MeV in internal nucleon momentum. The gluon density distributions can be obtained via measurement of the momentum transfer distributions in different bins of nucleon momentum, where the

underlying mechanism of gluon dynamics can be directly studied in terms of short-range nuclear correlations. Depending on the  $Q^2$  and nucleon momentum range, the required integrated luminosity is between 30 to 500  $\text{fb}^{-1}$ .

### 8.5.6 Double Tagging In The Far Forward Region

As discussed in section 7.3.7, one can do very interesting and unique physics with the  $A=3$  nuclei if it is possible to tag the spectator protons from  $^3\text{He}$  or the spectator neutrons from  $^3\text{H}$ .

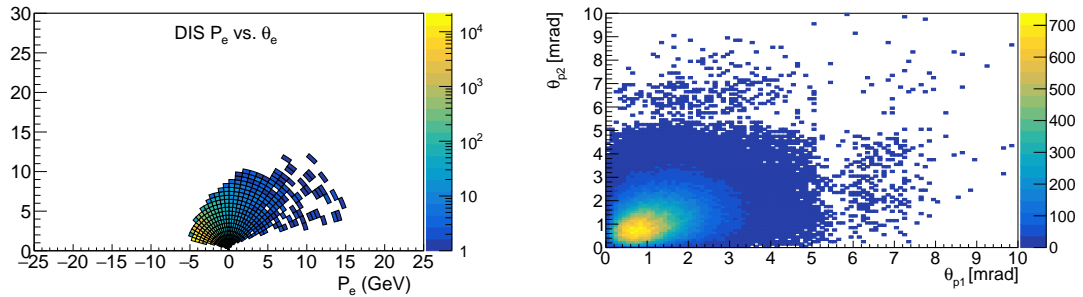


**Figure 8.99:** DIS kinematics for the  $^3\text{He}(e,e'pp)$  reaction at  $5 \times 41$  GeV with the protons detected in the far forward region.

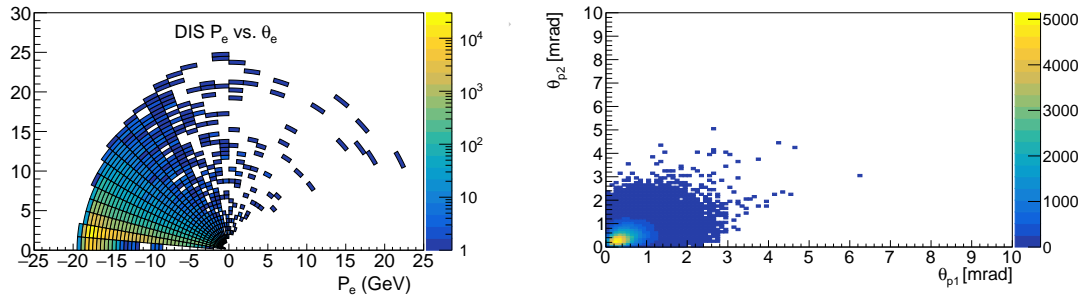


**Figure 8.100:** DIS kinematics for the  $^3\text{He}(e,e'pp)X$  reaction at  $110 \times 18$  GeV. Here the protons are more kinematically focused than in the lower energy case and will be better detected in the Roman pots.

Thus following the requirements as detailed in the Meson production section of the far forward region, one will be able to do double spectator tagging from  $A=3$  nuclei, opening new ways to extract nucleon information as well as study reaction mechanism effects.

### 8.5.7 Short-Range Correlations and EMC Effect Studies

Going beyond just using nuclei as an effective free nucleon target by tagging spectator particles, one can also make use of tagging to determine when the system was in a highly

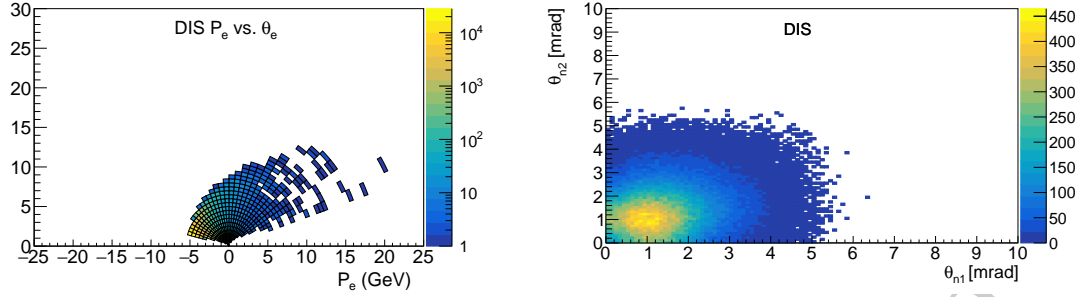


**Figure 8.101:** DIS kinematics for the  $3\text{H}(e,e'nn)\text{X}$  reaction at  $5\times 41$  GeV with the neutrons detected in the far forward region.

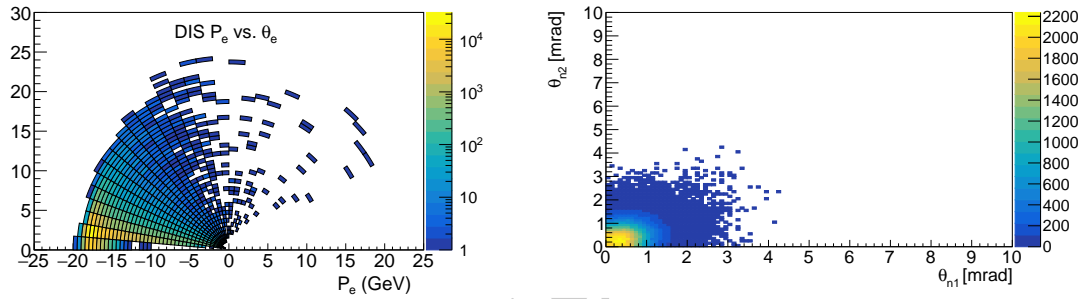


**Figure 8.102:** DIS kinematics for the  $3\text{H}(e,e'nn)\text{X}$  reaction at  $18\times 110$  GeV with the neutrons detected in the far forward region.

offset state. This is critical for studying short-range nucleon-nucleon correlation and could be the key to finally fully understanding the EMC effect.

To model the effect of initial-state corrections, the generalized contact formalization was used and study preformed with EICROOT, g4e as well as EICSMEAR. All the studies show a significant fraction of the highly-correlated nucleons from pairing can be detected in the far forward region. As a representative example, in Fig. 8.103 and Fig. 8.104 are shown the angles where a proton-proton SRC pair from  ${}^3\text{He}$  and a neutron-neutron SRC pair from  ${}^3\text{H}$  go. This is an extreme example, nevertheless, a significant fraction of the events would be detected, especially at the highest center-of-mass energies.

### 8.5.8 Inclusive diffraction

The studies of inclusive diffractive DIS ( $ep \rightarrow eXp$ ) presented in sections 7.1.6 and 7.3.2 by default assume that diffractive final states can be identified with perfect efficiency. In this section, we discuss methods of selecting diffractive processes in which the proton remains intact and summarise the challenges in achieving a high level of experimental performance.

At HERA, the inclusive diffraction process was studied successfully using a 'rapidity gap'

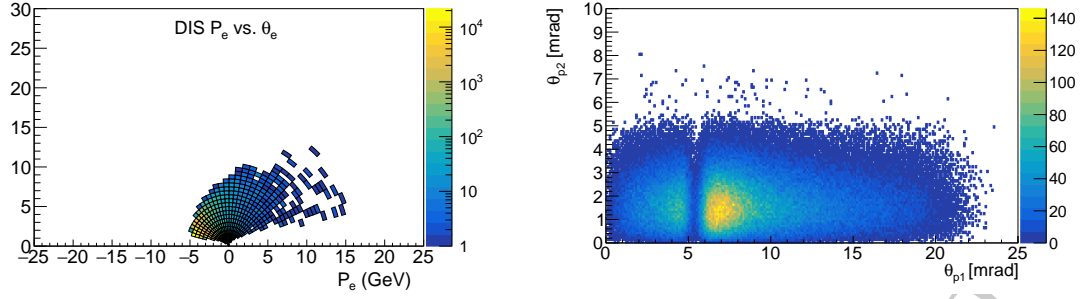


**Figure 8.103:** DIS kinematics for the  $3\text{He}(e,e'pp)$  reaction at  $5 \times 41$  GeV but now for initial-state SRC proton pairs with the protons detected in the far forward region.

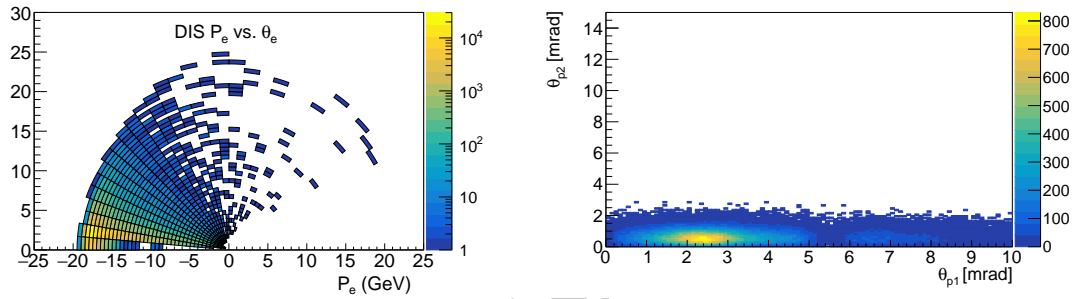


**Figure 8.104:** DIS kinematics for the  $3\text{He}(e,e'pp)$  reaction at  $18 \times 110$  GeV but now for initial-state SRC proton pairs with the protons detected in the far forward region.

method [211, 215, 488] in which events were identified on the basis of an absence of activity in a large forward region of pseudorapidity extending as close to the outgoing proton direction as possible. The gap size is strongly correlated with the fractional energy loss of the proton, with an approximate dependence of the form  $\Delta\eta \sim -\ln \zeta$ . Events in which the proton did not remain intact were vetoed on the basis of particles observed in ‘forward detectors’, either directly from the primary interaction, or as a result of secondary interactions with the beam-pipe or collimators. For the example of H1 [215], the most forward acceptance for veto detectors was obtained using scintillators surrounding the beam pipe 26 m downstream, which were able to detect charged particles in the range  $6.0 < \eta < 7.5$ . Whilst it led to high acceptance at sufficiently small  $\zeta$ , this method suffered from a number of drawbacks. Most importantly, the non-observation of the scattered proton leads to contamination from proton dissociation sources ( $ep \rightarrow eXY$  where  $Y$  is a low mass proton excitation) and even from non-diffractive processes with naturally occurring fluctuations in the hadronisation process, generating rapidity gaps that are exponentially suppressed as a function of gap size. These unobserved backgrounds were ultimately the largest source of systematic uncertainty. Furthermore, the use of the most forward part of the calorimeter as part of the veto (using an ‘ $\eta_{\text{max}}$ ’ cut) limited the range in  $\zeta$  and  $\beta$  that could be accessed. The reduced centre of mass energy at EIC leads to smaller gap sizes for fixed dissociation system mass  $M_X$ , implying that a gap based selection would at best be applicable only at small  $M_X$ . Nonetheless, rapidity gap identification remains a powerful tool, even if it is

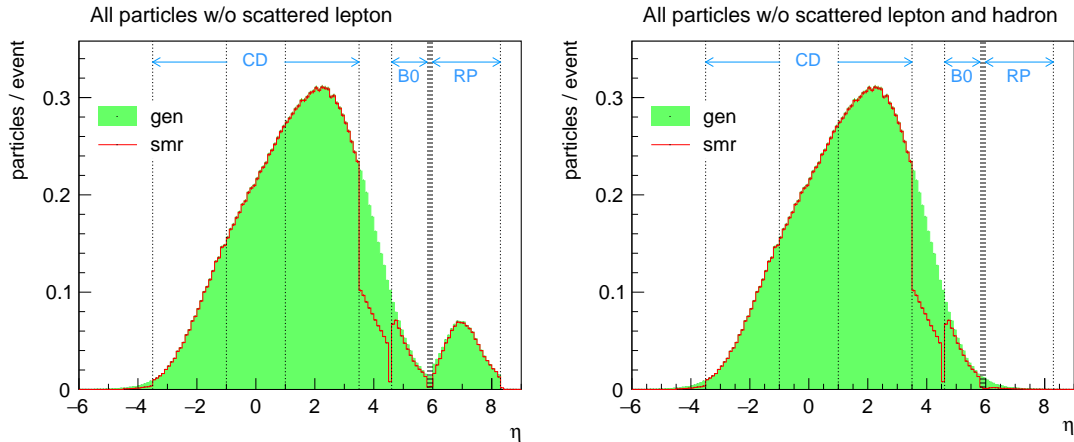


**Figure 8.105:** Pseudorapidity distribution of stable final state particles in a RAPGAP simulation of diffractive DIS with  $x_L > 0.6$  at the EIC (electrons with energy 18 GeV and protons of 275 GeV). The left panel corresponds to all final state particles whilst the right excludes the final state proton. The full set of generated particles is shown in green ('gen'). Those remaining after passing through an EIC detector simulation incorporating losses due to incomplete acceptance and migration due to imperfect detector resolution are shown with the red line ('smr'). The vertical lines delineate the central detector region with full coverage (CD), the region in which only electromagnetic calorimetry is currently envisaged and the regions covered by the B0 and Roman Pot ('RP') detectors. The normalisation is to the average number of particles per bin per event.

only used as a veto against background contamination. It is correspondingly advisable to ensure the fullest possible acceptance for forward-going particles.

Figure 8.105 illustrates final state particle flow in a sample of diffractive events simulated using the RAPGAP Monte Carlo model [1223]. The potential for vetoing forward activity is clear from the comparison between the distribution at the generator level ('gen') and that after accounting for experimental effects ('smr'). Most interesting from this point of view is the most forward part of the central detector, where there is almost full acceptance for both electromagnetic and hadronic calorimetry up to  $\eta = 3.5$  and continued electromagnetic calorimetry up to  $\eta = 4.5$  (hence approximately half of final state particles are considered to be observed in the region  $3.5 < \eta < 4.5$  according to the simple simulation). The use of the B0 detectors (integrated into the beampipe around 6 m downstream and covering an angular region  $5.5 < \theta < 20$  mrad) or the addition of dedicated veto detectors using for example scintillating tiles (the 'off-momentum' detectors envisaged in the current EIC design may be useful in this context) could extend this considerably. Nonetheless, the rapidity gap method doesn't reach the level of precision to which we aspire for diffractive studies at EIC and limits the acceptance in  $\xi$  and  $\beta$ .

The second method of studying diffractive processes with intact protons is through the direct observation and measurement of the scattered proton. This has been achieved at various colliders is using 'Roman pot' insertions to the beampipe which house sensitive

detectors that are able to approach the beam to within a few mm without compromising the vacuum. Roman pot technologies have come of age at the LHC, with the TOTEM experiment for example operating 14 separate stations. Detection and tracking have benefited from the use of radiation-hard silicon pixel detectors, whilst Time-of-Flight techniques have been introduced in the case where both protons are detected, using either multiple layers of ‘ultra-fast’ silicon or diamond- or quartz-based Cerenkov radiators to achieve precisions approaching 20 ps per proton.

The current version of the EIC design incorporates Roman pot detectors at 26 m and 28 m, with an angular acceptance extending up to 5 mrad. Full coverage in azimuthal angle may be possible, exploiting the spectroscopic effects of the machine magnets to ensure that all protons scattered with lower energy than the beam pass inside the arc of the main beam. As can be seen from a comparison between the left and right panels of figure 8.105, the Roman pot detector acceptance is well-matched to the detection of scattered protons over a wide range of kinematic phase space. The B0 silicon detectors incorporated in the current EIC design add acceptance at larger scattering angles. This angular acceptance range can be mapped directly onto a kinematic plane in  $\zeta$  and  $t$ . As illustrated in figure 7.29, the upper limit of the Roman pot angular coverage is adequate for the study of diffractive DIS across the full region of interest in  $\zeta$  and also across a wide range in  $t$  for high energy EIC configurations. The addition of the kinematic range covered by the B0 further improves matters at very large  $|t|$  such that there is almost full coverage at least to  $|t| = 1 \text{ GeV}^2$  at  $E_p = 275 \text{ GeV}$  and  $E_p = 100 \text{ GeV}$ . Whilst the situation is more challenging at  $E_p = 41 \text{ GeV}$ , highly interesting measurements could still be made.

It should be noted that the choice of lower limit of scattering angle  $\theta = 0.5 \text{ mrad}$  in figure 7.29 is somewhat ad hoc. In practice this limit is determined by the proximity to the beam-line that can be tolerated without causing disruption to the beam. Experience at previous colliders suggests that this lower limit is likely to be decreased slowly and steadily over time and is a matter for constant discussion between experiments and machine experts. A natural way to decrease the lower limit in  $\theta$  is to locate the Roman Pots further from the interaction point. However, it is not possible to instrument the beampipe further downstream than around 30 m in the current EIC design due to the crab cavities.

One final consideration in proton tagging is to avoid a large gap in acceptance between the B0 and Roman pot detectors. The current design achieves this for the most part, as illustrated in figure 8.106(top), where protons from the RAPGAP simulation are shown in the plane of  $\eta$  versus  $x_L = 1 - \zeta$ . The plot after passing through a simple simulation of EIC instrumental effects exhibits a small band in which acceptance is lost around  $\eta = 6$ , corresponding to the gap between the B0 and the Roman pot acceptances. Mapping these distributions onto the plane in  $x_L$  and  $t$ , as shown in figure 8.106(bottom), shows that, at least for the highest  $\sqrt{s}$ , the ‘dead zone’ band of lost acceptance is at relatively large  $|t|$  values and is unlikely to seriously compromise measurements. On the other hand, the band migrates to smaller  $|t|$  values at lower  $\sqrt{s}$ . It may be possible to mitigate this if there are two EIC detectors, by adjusting the design of the forward detectors in the second interaction region such that the gap falls at a different angle.

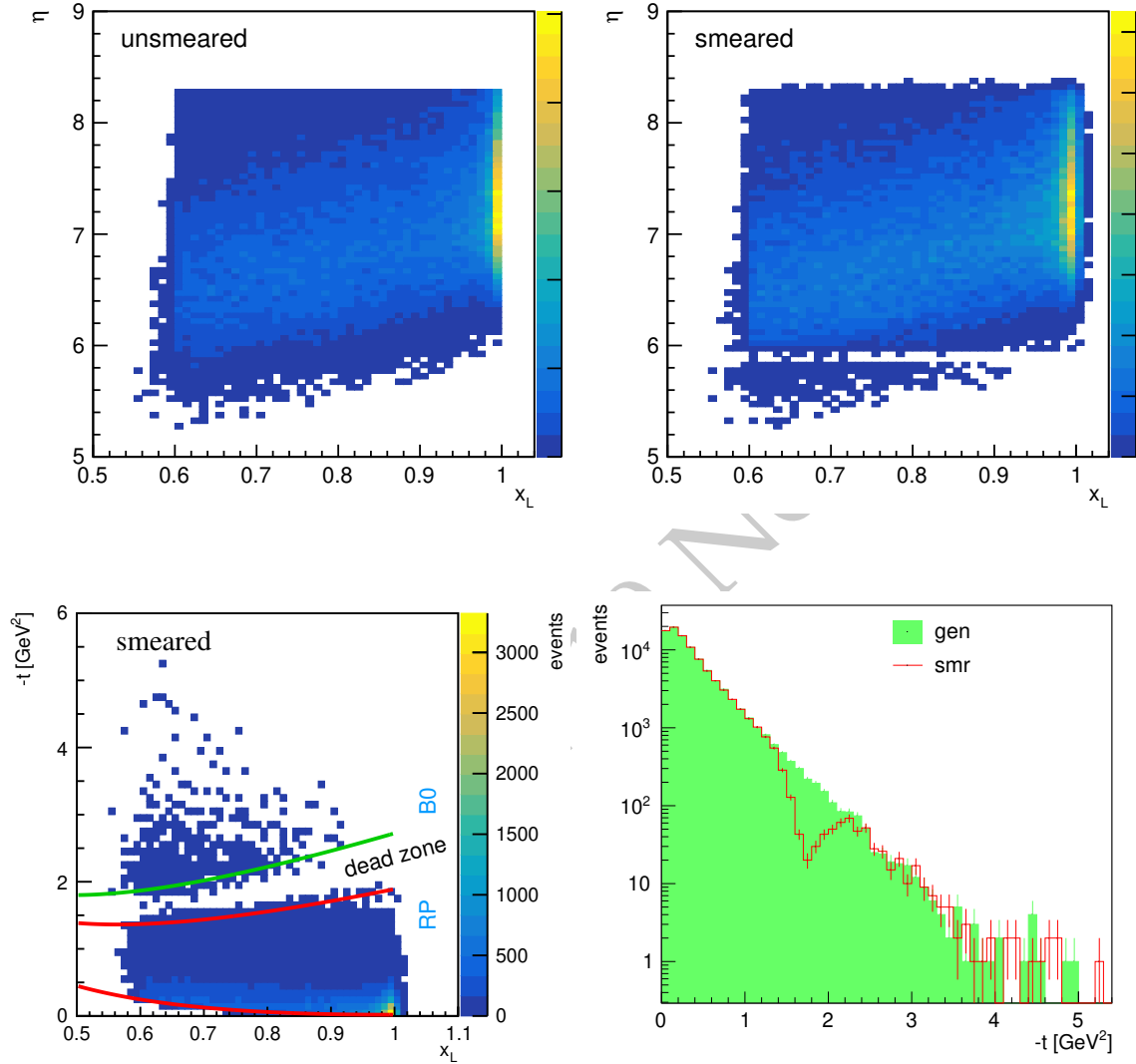


**Figure 8.106:** Distribution of final state protons in the RAPGAP simulation of diffractive DIS at the EIC (electrons with energy 18 GeV and protons of 275 GeV). Top left: generator level distribution in the plane of  $\eta$  versus  $x_L = 1 - \zeta$ . Top right: similar distribution after passing through a simple model of instrumental effects (migrations and acceptance). Bottom left: distribution mapped onto the plane of  $x_L$  versus  $t$  after passing through the simulation of migration and acceptance effects. Bottom right: one dimensional projection onto the  $t$  axis after passing through the simulation of migration and acceptance effects. No lower limit on the acceptance in  $\theta$  is applied in these figures.

### 8.5.9 Summary of Far Forward Region Physics Requirements

For the far forward region, we have seen that numerous physics channels can be studied with the current design and layout of the various detectors. For the B0 sensors, 3.4 cm inner radius and 20 cm outer radius with a  $50 \times 50 \mu\text{m}^2$  pixel is needed. For the off momentum tracker an 10 cm inner radius is assumed along with a  $10 \times 30 \text{ cm}^2$  sensor with a  $500 \times 500 \mu\text{m}^2$  pixel pitch. For the roman pots, it is assume that they will be  $10 \sigma$  from the beam halo size with a  $20 \times 10 \text{ cm}^2$  sensor with  $500 \times 500 \mu\text{m}^2$  pixel pitch.

For the zero degree calorimeter, it is assumed the device will be at least  $60 \times 60 \text{ cm}^2$  made up of low and high granularity electromagnetic calorimeter as well as a  $10 \times 10 \text{ cm}^2$  hadronic calorimeter. Ideally, the calorimeter would have an energy resolution of  $35\%/\sqrt{E}$ , but less then  $50\%/\sqrt{E}$  is acceptable for carrying out the physics goals that have been laid out by the diffractive and tagging physics working group.

In addition to these detector requirements, for the spin physics studies with the light nuclei require that the accelerator be able to store polarized spin-1/2 and spin-1 particles (e.g. polarized  $^3\text{He}$  and Deuterium). It is understood that persevering the polarization of polarized deuterons in a circular storage ring is particularly challenging and at a glance would seem to be beyond the scope of the planned spin rotation capabilities of the EIC. A clever solution to this problem is to use natural preserving deuteron energies, as known as magic energies, where only a limited amount of spin rotator and/or Siberian snakes are required to maintain the polarization. At per nucleon momentum of 104.9, 111.5, 124.6 and 131.2 GeV/c, full polarization can be provided at one interaction region while at 39.3 GeV/c or 118.0 GeV/c full polarization could be provided at both of the planned interaction regions.

Finally, the measurement of the inclusive, diffraction puts additional requirements on the forward and far-forward detectors. The rapidity gap method for inclusive diffraction requires vetoing forward activity, thus hermiticity of the detector setup is crucial. The B0 detectors are very useful for this measurement, but it would be also necessary to have additional detectors to veto the activity. The method of the tagged proton puts another requirements on the far forward detectors. While the current setup is already very well suited for this measurement there exists a gap in the proton acceptance between B0 and Roman pot detectors. While it would be difficult to completely close the gap within the current detector setup, perhaps the complementary detector design could be modified in such a way that the gap would appear in the different regime of angles and thus at different values of momentum transfer for the extracted cross section.

## 8.6 Summary of Requirements

**Part III**  
**Detectors**

SNAPSHOT 19 Nov. 2020

## **Chapter 9**

### **Introduction**

*SNAPSHOT 19 Nov. 2020*

## Chapter 10

# Detector Challenges and Performance Requirements

### 10.1 Beam Energies, Polarization, Versatility, Luminosities

#### 10.1.1 Integration with accelerator

##### Beam parameters and lattice

The integration of Far-forward detector components with accelerator plays an important role for emerging EIC physic program. It is important to start at it at the earliest stage of the design, since it could have an impact on both parties: it could affect accelerator impedance, or, on the other hand, incorrect placement of accelerator elements could have an impact on the detector acceptance by blocking or obscuring incident particles. The current studies were done with the accelerator lattices described in the Table( 10.1 for an ion beam and Table( 10.2 for an electron beam. Note, that sets of the quadrupoles will be placed in the common cryostat volume, therefore there will be no possibility to place any detecting elements there.

##### Beam pipe, vacuum, background

At this point we do not have a mature engineering design of the beampipe in the far-forward area. In this section we just formulate some requirements for it.

One of the important areas to pay attention an the material budget while designing the beampipe is the B0-dipole location. First of all we have to minimize amount of material at the exit window - this will be the area where common conical shape of the beampipe transfer to the two separate beampipes for the incoming electron and outgoing ion beams. Vacuum pumps, in front of the B0 dipole will be the sources of the background, where incident particles could start to develop showers, increasing an occupancy in the B0-tracker.

Name	Type	L [m]	$R_{in}$ [m]	$R_{out}$ [m]	Dipole [T]	Quadrupole [T/m]	$X_c$ [m]	$Y_c$ [m]	$Z_c$ [m]	$\Theta_{c}$ [rad]
Rear elements										
iYI6_HB2	SBEND	5.69	0.05	0.3	0 / -4.64	0	-1.18	0	-48.96	0.011
iYI6_HQ3	QUAD	1.2	0.05	0.3	0 / 0	47.8	-0.52	0	-20.7	0.025
iYI6_HQ2	QUAD	2.57	0.05	0.3	0 / 0	47.1	-0.323	0	-12.9	0.025
iYI6_HQ1	QUAD	3.42	0.05	0.3	0 / 0	-67.45	-0.2046	0	-8.18	0.025
Forward elements										
iB0PF	SBEND	1.2	0.2	0.5	0/-1.3	0	0.148	0	5.9	0.0259
iB0APF	SBEND	0.6	0.043	0.256	0/-3.47	0	0.2	0	7.7	0.0278
iQ1APF	QUAD	1.46	0.056	0.28	0/0	-72.61	0.24	0	9.23	0.0289
iQ1BPF	QUAD	1.61	0.078	0.34	0/0	-66.18	0.293	0	11.06	0.0289
iQ2PF	QUAD	3.8	0.131	0.58	0/0	39.45	0.383	0	14.16	0.0289
iB1PF	SBEND	2.99	0.135	0.5	0/-3.79	0	0.505	0	18.06	0.035
iB1APF	SBEND	1.5	0.168	0.4	0 / -2.70	0	0.6113	0	20.81	0.0436
iB2APF	SBEND	5.7	0.05	0.3	0 / 6.00	0	1.5221	0	41.890	0.02713

Table 10.1: Ion beam lattice for 275 GeV

Also shower-tails from the central detector HCAL or cryo-module around the B0- dipole could potentially give an additional source of background for the B0-tracker.

The exit window of the beampipe for Zero Degree Calorimeter needs to be properly designed, due to impact on the detection efficiency for low- energy photons in the forward direction.

Also the beampipe material around the off-momentum detectors needs to be minimized in order to minimize impact on the momentum resolution due to the multiple scattering.

The second vacuum chamber for the movable Roman-Pot sensors needs to be developed and impact on the accelerator impedance needs to be evaluated and minimized. In order to protect sensors from incident beam losses, a proper collimation scheme needs to be designed together with a beam-loss monitor system.

At the backward direction a proper collimating scheme against the synchrotron radiation needs further development to protect low-Q2 tagger. The beampipe material needs to be optimized to minimize impact on the multiple scattering in this area.

An exit window for the bremsstrahlung photons is needed for the luminosity monitor.

Name	Type	L [m]	$R_{in}$ [m]	$R_{out}$ [m]	Dipole [T]	Quadrupole [T/m]	$X_c$ [m]	$Y_c$ [m]	$Z_c$ [m]	$\Theta_{c_c}$ [rad]
Rear elements										
eQ5ER	QUAD	1.2	0.05	0.3	0/0	7.481	0.4131	0	-46.8267	0
eQ4ER	QUAD	0.6	0.05	0.3	0/0	8.85796	0.4131	0	-37.99667	0
eDB3ER	RBEND	5.199	0.05	0.3	0/0.2115 0		0.39525	0	-34.79671	-0.00916
eQ3ER	QUAD	0.6	0.05	0.3	0/0	-22.7971	0.354	0	-31.597	-0.01832
eDB2ER	RBEND	5.5	0.05	0.3	0/-0.1999	0	0.01889	0	-12.249	-0.00916
eQ2ER	QUAD	1.4	0.05	0.3	0/0	14.1466	0	0	-8.3	0
eQ1ER	QUAD	1.8	0.05	0.3	0/0	-14.478	0	0	-6.2	0
Forward elements										
eQ0EF	QUAD	1.2	0.0031	0.007	0/0	-13.54	0	0	5.9	0
eQ1EF	QUAD	1.61	0.05	0.3	0/0	7.4612	0	0	11.065	0
eQ2EF	QUAD	3.8	0.05	0.3	0/0	0	0	0	14.17	0
eQ3EF	QUAD	1.2	0.05	0.3	0/0	-5.5461	0	0	20.82	0
eQ4EF	QUAD	1.2	0.05	0.3	0/0	5.85445	0	0	29.95	0

Table 10.2: Electron beam lattice for 18 GeV

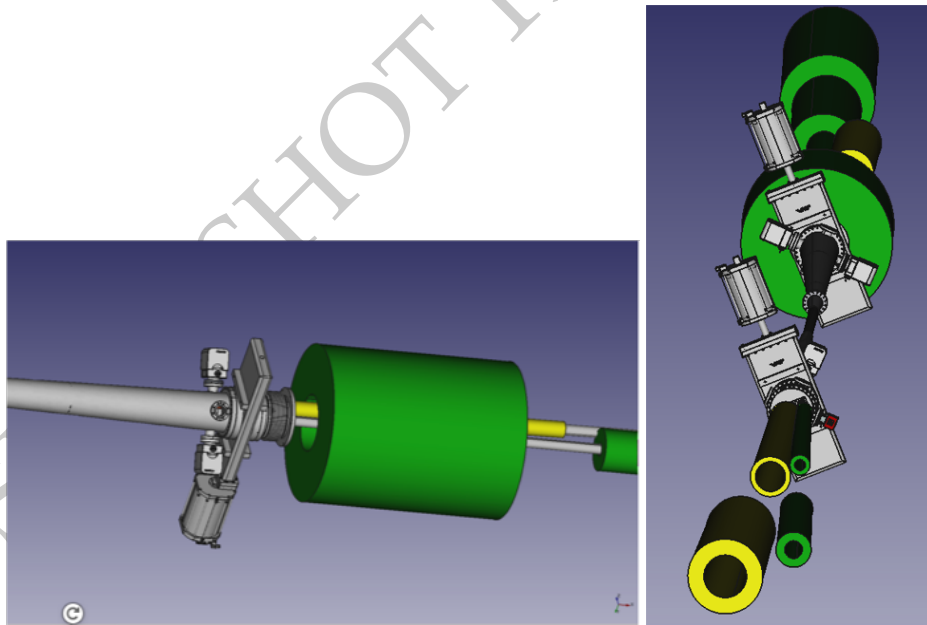


Figure 10.1: Beampipe at the B0 location

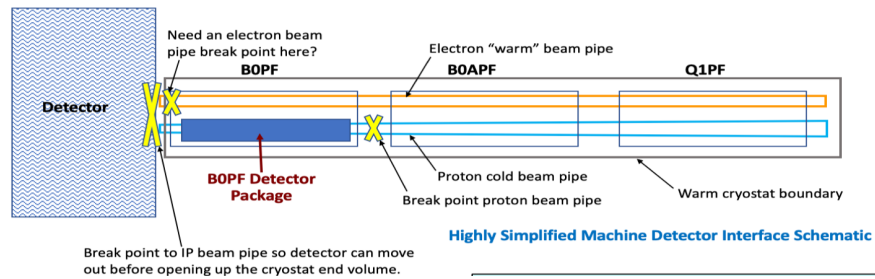


Figure 10.2: The integration of B0-dipole

## 10.2 Rate and Multiplicities

## 10.3 Integrated Detector and Interaction Region

## 10.4 Backgrounds

## 10.5 Systematics and Ancillary Detectors

### 10.5.1 Luminosity

### 10.5.2 Polarimetry

## 10.6 Physics Requirements

# Chapter 11

## Detector Aspects

### 11.1 Magnet

The EIC detector is built around a central solenoid magnet with optional correction trim coils required to meet the solenoid field specification. Tracking resolutions in the central pseudo-rapidity range suggest the nominal field of 1.5 T, but a range between 1.5 T and 3 T makes physics measurements accessible. A central field as high as 3 T is needed to maximize the effective  $|B| \cdot dl$  integral for particles scattered at small polar angles, both in forward and backward directions. High magnetic fields come at the cost of reducing the low-pT acceptance of charged tracks. The acceptance for low-pT particles down to the momenta  $\sim 100$  MeV/c requires that a fraction of physics data are taken at a substantially lower field. Field polarity flip is a standard measure to address systematic effects due to a different acceptance for the positively and negatively charged particles, hence a bipolar magnet operation with a polarity switch is one of the magnet requirements.

Physics studies available to date suggest a solenoid with a bore diameter 2.5-3.5 m in a traditional composition of an EIC detector. Specifications on coil length, presently assumed to be able to provide a  $\sim 3.0$  m magnetic length as a reference figure, cryostat radial space, and coil configuration require an optimization integrated with the overall detector design. The solenoid design is characterized by three regions, the barrel and backward endcap with the field parallel to the magnet axis and the RICH detector in the forward direction, which extends from +100 cm to +240 cm with respect to the magnet centre, where the field lines should be projective with respect to the nominal IP location. A flux return path could be provided through the hadronic calorimeter assemblies in the forward and backward directions. Correction coils in the hadron end-cap may be required to meet the RICH detector readout on field projectivity. The need for these coils should be avoided as they will adversely affect the hadron calorimeter performance, but if needed, should be allowed to occupy a maximum of 10 cm of the available linear space.

Alternative detector integrated designs, where a dipole or toroidal field are superimposed with the solenoid field in the central region of the detector, have been considered to im-

prove the  $|B| \cdot dl$  integral at small scattering angles. These integrated designs could be an option if an acceptance that meets the physics requirements can be demonstrated.

Re-use of the existing BABAR/sPHENIX magnet is an alternative to the realization of a new solenoid with optimized design. Whereas the new solenoid main specifications are an up-to 3T magnetic field, a 2.5-3.5 m diameter bore, and a magnetic length of  $\sim 3$  m, the BABAR/sPHENIX magnet provides an up-to 1.5 T field, a 2.8 m diameter bore, and similar magnetic length. The magnet for the BABAR experiment at PEP-II at SLAC, CA was manufactured by Ansaldo, Italy in 1997 and was commissioned in 1998. It was then transferred to BNL, NY in 2015 for use in the sPHENIX experiment where it still resides today. It received a high-field test (up to 1.3 T) in 2018. The prolonged use of the BABAR/sPHENIX magnet requires the implementation of several maintenance and improvement modifications, including new protection circuits such as voltage taps, inspection of and as needed reinforcement of the internal mechanical support, including new strain gauges, and replacement of control instrumentation sensors. Several of these implementations involve the delicate operation of disassembly of the magnet. To repair an existing small leak in the valve box for the cryogenic cooling system requires a replacement of the valve box or disassembly to inspect cooling pipework and to repair leaks. Moreover, additional changes are required for re-using the magnet, for example those needed to match the requirements of projective field lines in the RICH region.

The main parameters of both a new superconducting solenoid magnet, at the present stage of magnet optimization integrated with the overall detector design, and the existing BABAR/sPHENIX magnet are shown in Table 11.1. For a new magnet, a slightly larger bore of 3.2 meter is chosen as compromise between, on one hand, magnet complexity and mechanical Hall space considerations, and on the other hand providing some much-needed space in the bore to ensure more detector technology choices to ensure functionality of tracking, hermetic electromagnetic calorimetry and particle identification (both  $e/\pi$  and  $\pi/K/p$ ) over a large range of particle momenta. The choice of NbTi conductor in a Cu matrix for the new magnet is driven by that for EIC no detection beyond hadronic calorimetry is foreseen beyond the bore, alleviating a material requirement on small radiation lengths and allowing use of Cu facilitating the magnet mechanical design.

The coil length is driven by the present definition of the barrel region as between pseudorapidity of -1 and 1. This corresponds to an angle of  $\sim 40$  degrees. This means that for a certain bore size, the space for the mechanical length of the magnet cryostat is roughly 20% larger, or 3.84 meter for a 3.2-meter bore. Folding in an approximate need of 12 cm additional need on each side of the magnet coil for inner vacuum and helium vessels, and multi-layer isolation, determines the coil length requirement to be 3.6 meter. A somewhat larger coil length of 3.8 meter would not be a major issue, but likely not much more as the edge of the cryostat is one of the regions where detector infrastructure (support, cabling, etc.) will reside, and deliberations between the need for equal coverage of tracking and electromagnetic calorimeter as trade-off with particle identification detector readout will occur.

The main advantage of accessibility of low central solenoid fields (down to  $\sim 0.5$  T) is towards the low-PT acceptance of charged-particle tracks. A central field of 0.5 T roughly

Parameter	New Magnet	BABAR/sPHENIX Magnet
Maximum Central Field (T)	3	1.5
Coil length (mm)	3600	3512
Warm bore diameter (m)	3.2	2.8
Uniformity in tracking region ( $z = 0, r < 80$ cm) (%)	3	3
Conductor	NbTi in Cu Matrix	Al stabilized NbTi
Operating Temperature (K)	4.5	4.5

**Table 11.1:** Summary of some of the main requirements of the EIC detector solenoid magnet.

equates to a detection capability of charged particles down to transverse momenta of below  $\sim 0.1$  GeV/c. This is for example relevant for mapping the decay products of heavy-flavor mesons. The main advantage of a 3 T versus a 1.5 T central solenoid field is for the momentum resolution of charged particles as function of pseudo-rapidity. Doubling the magnetic field can lead to a reduction of the momentum resolution by a factor of  $\approx 2$  from a leading order  $\sim 1/B$  dependence. This is relevant in the central region, but even more so in the forward pseudo-rapidity regions,  $\eta > 2$ , where the momentum resolutions rapidly worsen. For example, for  $\eta \sim 3$ , a momentum resolution of  $\sim 2$ -3% is achievable for pions with momenta up to about 30 GeV/c with a 3 T central field, and only double that resolution for a 1.5 T central field.

## 11.2 Tracking

### 11.2.1 Introduction

This section represents an attempt to combine the requirements from the physics working groups and tracking technologies and detector design into viable detector concepts that can meet these requirements. These concepts contain assessments of the current state of the art in both the technologies, services, mechanical support and other components to deliver a design that is deemed to be consistent with what can reasonably be expected to be deployed at the EIC in the needed timescales. In order to reduce risk and ensure that the needed development proceeds apace with the construction schedule, a set of areas of targeted R&D have also been generated and are presented in Chapter 14.

### 11.2.2 Main requirements and acceptance coverage

The requirements for the tracking in an EIC detector are derived from the physics simulations and are represented by the detector requirements table. This is shown in table 11.1: The ranges in pseudorapidity are accompanied with requirements for momentum resolu-

$\eta$	$\theta$	Nomenclature	Tracking																															
			Resolution	Relative Momentum	Allowed $X/X_0$	Minimum-pT	Transverse Pointing Res.	Longitudinal Pointing Res.																										
< -4.6		Far Backward Detectors	low-Q2 trigger																															
-4.6 to -4.0	pA	Central Detector	Backward Detector	$\sigma_{pT}/p \sim 0.2\% \oplus 5\%$	70-150 MeV/c (R=1.5 T)	dca(ry) ~ 40/pT um. #. 10 um	dca(z) ~ 100/pT um. #. 20 um																											
-4.0 to -3.5				$\sigma_{pT}/p \sim 0.04\% \oplus 2\%$																														
-3.5 to -3.0				-5% or less X				200 MeV/c	dca(ry) ~ 30/pT um. #. 5 um	dca(z) ~ 30/pT um. #. 5 um																								
-3.0 to -2.5											$\sigma_{pT}/p \sim 0.04\% \oplus 2\%$																							
-2.5 to -2.0											70 - 150 MeV/c (R = 1.5 T)	dca(ry) ~ 40/pT um. #. 10 um	dca(z) ~ 100/pT um. #. 20 um																					
-2.0 to -1.5														$\sigma_{pT}/p \sim 0.04\% \oplus 2\%$																				
-1.5 to -1.0														Forward Detectors																				
-1.0 to -0.5																		$\sigma_{pT}/p \sim 0.04\% \oplus 1\%$																
-0.5 to 0.0																		Instrumentation to separate charged particles from photons																
0.0 to 0.5																						$\sigma_{pT}/p \sim 0.04\% \oplus 2\%$												
0.5 to 1.0																						Proton Spectrometer												
1.0 to 1.5																										$\sigma_{pT}/p \sim 0.04\% \oplus 2\%$								
1.5 to 2.0																										Zero Degree Neutral Detection								
2.0 to 2.5																														$\sigma_{pT}/p \sim 0.2\% \oplus 5\%$				
2.5 to 3.0																														Far Forward Detectors				
3.0 to 3.5																																		$\sigma_{pT}/p \sim 0.2\% \oplus 5\%$
3.5 to 4.0																																		
4.0 to 4.5																																		
> 4.6																																		

Figure 11.1: Requirements Table

tion, allowed radiation length, minimum pT cutoff and transverse and longitudinal pointing resolution. These requirements form the basis of the designs that are presented.

### 11.2.3 Technology survey

#### Silicon Detector Technologies for EIC

[TEXT BY LAURA GONELLA - 16 NOVEMBER 2020]

To satisfy the requirements detailed above, the EIC silicon vertex and tracking (SVT) detector needs to have high granularity and very low material budget. Performance simulations of the detector concepts presented in 11.2.6, 11.2.5 highlight the need for: - a spatial resolution  $\leq 5 \mu\text{m}$  in tracking layers and disks, and around  $3 \mu\text{m}$  in the vertex layers; - a material budget  $\leq 0.1\% X_0$  in the vertex layers,  $\leq 0.8\% X_0$  in the tracking layers and  $\leq 0.3\% X_0$  in the disks.

The stringent requirements for the vertex layers are driven by the rather large beam pipe radius and are necessary to obtain the required vertex reconstruction performance. This is shown in Figure 11.2. Pre-CD0 simulations assumed a beam pipe radius of 18 mm and an ALICE ITS2 derived SVT detector where vertexing layers and disks had a material budget of  $0.3\% X/X_0$  per layer, and the tracking layers had a material budget of  $0.8\% X/X_0$  per layer. The pixel size was  $20 \times 20 \mu\text{m}^2$ . This configuration gives the transverse pointing resolution described by the green curve in Figure 11.2. With the updated beam pipe radius of 31 mm, this configuration would lead to a severe decrease in tracking performance (blue curve). The transverse pointing resolution can be recovered, and even improved, with higher granularity and lower material budget. The result in the red curve assumes a configuration based on the ALICE ITS3 technology explained below, where the vertexing layers have a material budget of  $0.05\% X/X_0$  per layer, the tracking layers  $0.55\% X/X_0$  per layer, and the disks each have a material budget of  $0.24\% X/X_0$ . The pixel size is  $10 \times 10 \mu\text{m}^2$ .

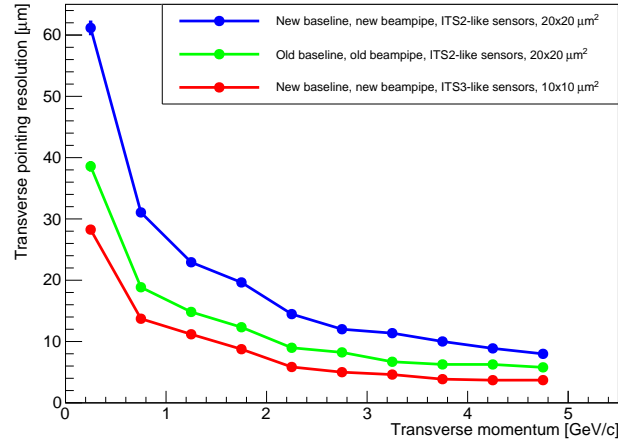


**Figure 11.2:** Transverse pointing resolution versus transverse momentum, comparing the ALICE ITS2 based detector configuration with old (green) and new (blue) beam pipe, and the ALICE ITS3 based detector configuration with new beam pipe (red).

In addition to these requirements, an EIC SVT detector needs to be designed with an integration time below to  $2 \mu\text{s}$  to cope with the interaction frequency expected at the highest luminosity, i.e.  $500 \text{ kHz}$  at  $10^{34} \text{ cm}^{-2} \text{ s}^{-1}$ . These requirements drive the choice of the silicon detector technology.

A broad survey of silicon detector technologies has been presented and discussed at the first EIC Yellow Report Workshop in March 2020 [1224] covering hybrid pixel detectors, strip detectors, Low Gain Avalanche Detectors (LGAD), the DEPFET sensor, and Monolithic Active Pixel Sensors (MAPS). The survey has considered existing examples of these detectors as well as the silicon technologies used for their development to understand their potential for application at the EIC. MAPS have been identified as the best detector technology to satisfy the requirements of the EIC SVT and are discussed below. These detectors provide the highest granularity, lower power consumption and consequently lower material budget, as well as the required readout speed in one device. Recent development of these devices are the only option to satisfy the requirements of the EIC vertex layers 11.2.3. The integration of charge collection and readout capabilities into one silicon substrate is well suited for the required level of integration and acceptance coverage of the EIC SVT. Silicon technologies such as LGAD and SOI whose developments in the next few year could produce a viable alternative for the EIC SVT are presented in [reference to chapter 14].

## MAPS

[TEXT BY LAURA GONELLA - 16 NOVEMBER 2020]

MAPS are currently used as vertex detectors in the STAR Heavy Flavour Tracker [1225]

and in the upgraded ALICE Inner Tracker (ITS2) [1226]. The latter deploys the ALPIDE sensor [1227]. This sensor represents a breakthrough with respect to traditional MAPS such as the MIMOSA used by the STAR experiment. ALPIDE is fabricated in a commercial 180 nm CMOS imaging process provided by Tower Jazz (TJ). The main novelty of this device is the possibility to partially deplete the substrate and thus collect part of the charge by drift, and to integrate both PMOS and NMOS transistors. These features have improved MAPS charge collection properties, radiation hardness, and signal processing capabilities. Figure 11.3 shows the cross-section of an ALPIDE pixel. This design retains as in previous MAPS generations a small collection electrode and thus a small sensor capacitance of a few fF that is key to low power, low noise, fast sensor readout, and compact front-end electronics design for small pixel pitch.

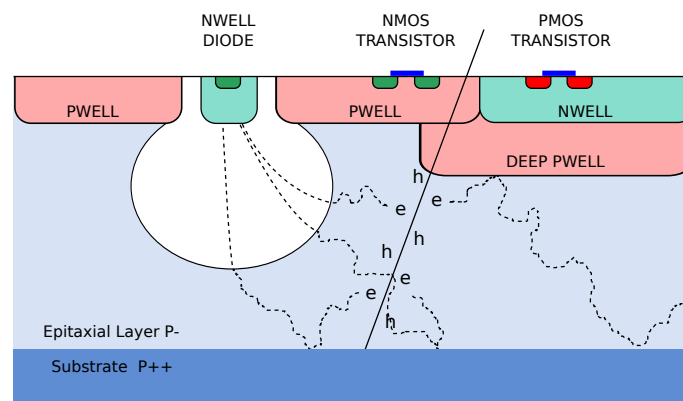


**Figure 11.3:** Cross-section of an ALPIDE pixel, showing the small n-type collection electrode and the p-wells containing the electronics in a p-type epitaxial layer. A small depletion region develops around the collection electrode for an applied reverse bias voltage of a few volts [1226].

Following on from the ALPIDE, a new generation of MAPS sensors has been developed in the past ten years with the goal of reaching the rate and radiation tolerance capability typically required by high luminosity particle physics experiments. These so-called Depleted MAPS (DMAPS) are fabricated in High Voltage or High Resistivity commercial 150/180 nm CMOS imaging technologies and can be fully depleted. A number of prototypes have been fabricated targeting the upgrades of the ATLAS pixel detector for the HL-LHC in different CMOS technologies. The ATLASPix sensor in the AMS/TSI technology [1228] and the LF-MONOPIX in the LFoudry technology [1229] feature a large collection electrode that contains the electronics. This results in a uniform electric field in the sensor substrate needed to achieve the required speed and radiation hardness but comes at the price of high sensor capacitance. The MALTA and TJ-MONOPIX prototypes in the TJ 180 nm technology [1229–1231] keep the small collection electrode and achieve full depletion with a modification of the process by adding a deep n-implant so that the depletion region grows from below the collection electrode and electronics implant [1232, 1233]. These sensors have demonstrated to fulfil the requirements of operation at the HL-LHC, but use at the EIC SVT would have to be demonstrated as they have been designed to match very different requirements. An application of the MALTA sensor for tracking at large  $z$  is described

in 11.2.5.

It is however important to note that the CMOS imaging technologies in which existing DMAPS prototypes have been fabricated could be used to design a dedicated MAPS sensor for the EIC SVT. In particular, the TJ 180 nm modified CMOS imaging process is very interesting because of the benefit of the small sensor capacitance towards low power and fine pitch. This technology has been positively evaluated for use at the EIC by the eRD18 project, a collaboration between the University of Birmingham and the RAL CMOS Sensor Design group (CSDG), in the framework of the EIC Generic Detector R&D programme [1234].

Recently, an effort is emerging to develop a third generation MAPS in a 65 nm CMOS imaging technology. A large community is gathering to develop this process for future experiments through the ALICE ITS3 project and the CERN EP R&D programme. This path is more attractive for the development of an EIC MAPS as the 65 nm technology offers improved performance in terms of granularity and power consumption that are key for precision measurements at the EIC, as well as process availability on the EIC project timescale. The drawbacks with respect to older technology nodes are higher non recurring engineering (NRE) costs and complexity.

A joint EIC SVT sensor development has started with the ALICE ITS3 group [1235]. The ALICE ITS3 project aims at developing a new generation MAPS sensor at the 65 nm node to build an extremely low mass detector for the HL-LHC. The ITS3 sensor specifications and development timescale are largely compatible with those of the EIC. Furthermore, non-ALICE members are welcome to contribute to the R&D to develop and use the technology for other applications. Having joined the ITS3 collaboration, the EIC can leverage on a large effort at CERN, sharing development costs, to design an innovative sensor solution at the 65 nm node, suited for an experiment starting in approximately 10 years and demonstrating the capabilities of this technology for future proposed collider experiments.

### **65 nm MAPS SVT detector**

[TEXT BY LAURA GONELLA - 16 NOVEMBER 2020]

An EIC SVT concept is being developed based on the proposed 65 nm MAPS sensor and ITS3 detector concept [1236]. Both baseline configurations presented under investigation (11.2.5, 11.2.6) assume the use of this technology to define pixel pitch and realistic estimates of material budget for services and support structure [1237], and configuration of the vertex layers. In addition to the advantages discussed in 11.2.3, joining the ITS3 development has additional benefits.

Figure 11.4 compares the specifications for the proposed ITS3 sensor to the ones of the existing ALPIDE. Figure 11.5 shows preliminary specifications for an EIC sensor. From these it is clear that the ITS3 fully satisfies and even exceeds the requirements of the EIC SVT with higher granularity, lower power consumption, shorter integration time and lower fake hit rate. In particular, the 10  $\mu\text{m}$  pixel pitch is key to the design of the vertex layers

(Figure 11.2).



## Specifications

Parameter	ALPIDE (existing)	Wafer-scale sensor (this proposal)
Technology node	180 nm	65 nm
Silicon thickness	50 $\mu\text{m}$	20-40 $\mu\text{m}$
Pixel size	27 x 29 $\mu\text{m}$	O(10 x 10 $\mu\text{m}$ )
Chip dimensions	1.5 x 3.0 cm	scalable up to 28 x 10 cm
Front-end pulse duration	$\sim 5 \mu\text{s}$	$\sim 200 \text{ ns}$
Time resolution	$\sim 1 \mu\text{s}$	$< 100 \text{ ns}$ (option: $< 10 \text{ ns}$ )
Max particle fluence	100 MHz/cm <sup>2</sup>	100 MHz/cm <sup>2</sup>
Max particle readout rate	10 MHz/cm <sup>2</sup>	100 MHz/cm <sup>2</sup>
Power Consumption	40 mW/cm <sup>2</sup>	$< 20 \text{ mW/cm}^2$ (pixel matrix)
Detection efficiency	$> 99\%$	$> 99\%$
Fake hit rate	$< 10^{-7}$ event/pixel	$< 10^{-7}$ event/pixel
NIEL radiation tolerance	$\sim 3 \times 10^{13}$ 1 MeV n <sub>eq</sub> /cm <sup>2</sup>	$10^{14}$ 1 MeV n <sub>eq</sub> /cm <sup>2</sup>
TID radiation tolerance	3 MRad	10 MRad

M. Mager | ITS3 kickoff | 04.12.2019 | 5

**Figure 11.4:** Specifications for the ALICE ITS2 ALPIDE sensor and the proposed sensor for the ITS3 upgrade.

Parameter	EIC Vertex and Tracking MAPS
Technology	65 nm (Backup: 180 nm)
Substrate Resistivity [kohm.cm]	$\geq 1$
Collection Electrode	Small
Detector Capacitance [fF]	$< 5$
Chip size [cm x cm]	Full reticule or stitched
Spatial resolution [ $\mu\text{m}$ ]	$\leq 5$ 3 for vertex layers
Integration Time [ $\mu\text{s}$ ]	$\leq 2$
Timing Resolution [ns]	$< 9$ (optional)
Particle Rate [kHz/mm <sup>2</sup> ]	<b>TBD</b>
Readout Architecture	Asynchronous
Power [mW/cm <sup>2</sup> ]	$< 20$
NIEL [1MeV neq/cm <sup>2</sup> ]	$10^{10}$
TID [Mrad]	$< 10$
Noise [electrons]	$< 50$
Fake Hit Rate [hits/s]	$< 10^{-5}$ /evt/pix
Interface Requirements	<b>TBD</b>

**Figure 11.5:** Preliminary specifications for an EIC SVT MAPS sensor based on simulations by the eRD18 (Birmingham/RAL CSDG) and eRD16 (LBNL) projects of the EIC Generic Detector R&D programme.

The ITS3 project is taking an integrated approach where design and post-processing techniques are combined to develop a three-layer vertex detector with an extremely low material budget (Figure 11.6). The use of low power design techniques, large area, 2D stitched sensors thinned below 50  $\mu\text{m}$  and bent around the beam pipe minimises cooling, support structure and services in active area allowing to reach a material budget of only 0.05%

$X_0$ . Such detector concept is a very attractive solution for the EIC vertex layers where extremely low material budget coupled with the sensor's high granularity will deliver the required vertex resolution (Figure 11.2). The implementation of the ITS3 detector concept into the EIC vertex layers is currently being worked out by the EIC Silicon Consortium.

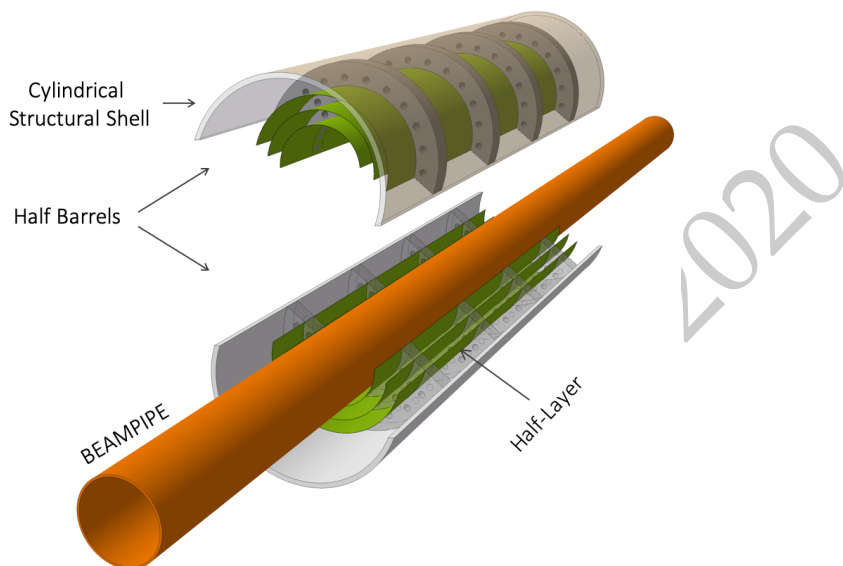


**Figure 11.6:** Layout of the ITS3 Inner Barrel. The figure shows the two half-barrels mounted around the beampipe [1235].

Despite the large overlap, the EIC and ITS3 detectors have some significant differences, most notably the size. The ITS3 is a  $0.12 \text{ m}^2$ , three layers vertex detector. The EIC SVT baseline configurations presented in (11.2.5, 11.2.6) have an area of approximately  $12 \text{ m}^2$  and  $15 \text{ m}^2$ , for hybrid and all-silicon respectively. Cost and yield of stitched wafer-scale sensors will not be compatible with use in the EIC detector outside the vertex layers. For the tracking layers and disks the EIC sensor development will fork off the ITS3 sensor design path to develop a reticule-size version of the ITS3 sensor (no changes in other aspects of the sensor design are foreseen a part from its size) as well as a more conventional design of support structures (classical staves and disks), where dedicated engineering solutions will be deployed to meet the material budget constraints [1237].

### Alternative Silicon Sensors

[Edited by Xuan Li on behalf of the LANL EIC team, on Nov. 3rd]

[COMMENT BY LAURA: as discussed at the last YR working group meeting, MAPS are covered above including the ones mentioned here. I have added explicitly now that MALTA is proposed for the LANL detector concept and put a reference to 15.3. The LGAD, as well as SOI, will be discussed in the write-up that Leo prepared and circulated to us for review, and will be in chapter 14. I would suggest the following, if Xuan and Leo agree:

remove this section as part of the information is covered elsewhere, but add in 15.3 explicitly why you choose MALTA for the disks at high Z. I suppose you might do anyway to justify why MALTA and not MPGDs for instance. I also do not understand the comment on needing ASIC development. MAPS do not need a separate ASIC, the readout is fully integrated in the same substrate which is the attractiveness of this solution. The production line will also not be the same for MALTA and ITS3 sensor. The technology is from TJ for both but one is 180 nm and the other 65nm. These are very different production lines and imaging processes.]

The proposed silicon vertex/tracking detector will be built around the beam pipe and is close to the beam interaction region of the EIC. High beam background such as synchrotron radiation generated by keV electrons and MeV neutron gas could generate dead areas in the silicon detector which significantly impacts on its vertex/tracking capability. To achieve precise measurements in Semi-Inclusive Deeply Inelastic Scattering (SIDIS) processes, event separation from different collisions is required. A radiation hard and fast timing silicon detector, which can survive the accidental beam injection onto the detector and is capable to separate the 1-10ns EIC bunch crossings, will enhance the physics measurement precision and could reduce the correlated systematical uncertainties.

To meet these requirements, various silicon technology options have been considered, which are 1) High-Voltage Monolithic Active Pixel Sensor (HV-MAPS) and 2) the Low Gain Avalanche Detector (LGAD). The HV-MAPS technology process fully depleted charged particle propagation inside the active silicon region. This technology can reach relatively low material budgets ( $< 0.5\%X$  per layer), fine spatial resolution ( $< 10 \mu\text{m}$ ) and fast timing ( $< 5 \text{ ns}$ ). The ongoing R&D will further improve the performance for the next-generation sensor production. Meanwhile, we also consider the LGAD [1238–1241] or AC-LGAD [1242] technology to be placed in the most forward planes, which can provide fast time stamping to separate different bunch crossings. The HV-MAPS technology such as MALTA [1243–1245], ATLASPIX3 [1246] or Mupix [1246] could be implemented for the EIC day-1 detector. The LGAD or AC-LGAD technology could be used for EIC detector upgrade depends its R&D progresses. The performance of the LGAD (AC-LGAD) and MALTA technology has been summarized in Table 11.27.

The advantages of the MALTA technology are: 1) prototype sensor and front-end readout electronics exist; 2) its spatial and temporal resolutions have been demonstrated by previous/ongoing bench/beam tests; 3) this technology with further developments could be in production stage in around 2 to 3 year time scale. The power consumption of the MALTA sensor is relatively higher than the ALPIDE sensor. Although it is in a reasonable scale, additional R&D for the next generation sensor developments and dedicated mechanical structure design are needed. The advantages of the LGAD technology are: 1) prototype sensor and front-end readout electronics exist; 2) fast timing ( $20\text{ps}$ ) provided by the LGAD technology can not only be used for time stamping but also for PID purpose. This technology is in early R&D stage, and the full readout chain needs to be defined.

The required R&D path includes back-end electronics and the readout full chain developments. The most critical (urgent) item is ASIC design and readout developments. The HV-MAPS technology (e.g. MALTA) can use the same production line as the ITS-3 tech-

Parameter	LGAD or AC-LGAD	MALTA
Technique	Low Gain Avalanche Diode	180 nm Tower Jazz DMAPS
Pixel size	current 1.3mm $\times$ 1.3mm towards 100 $\mu\text{m}$ $\times$ 100 $\mu\text{m}$ , $\sim$ 10 $\mu\text{m}$ spatial resolution is achieved with the new design.	36.4 $\mu\text{m}$ $\times$ 36.4 $\mu\text{m}$ , $\sim$ 7 $\mu\text{m}$ spatial resolution.
Integration time	300-500 ps	< 5 ns
Thickness per layer	< 1% $X_0$	< 0.5% $X_0$
Power consumption	under R&D	80 mW/cm <sup>2</sup>
Noise level	under R&D	10 <sup>-5</sup> with low threshold
Radiation tolerance	$\sim 1.5 \times 10^{15}$ n <sub>eq</sub> /cm <sup>2</sup>	> 10 <sup>15</sup> n <sub>eq</sub> /cm <sup>2</sup>

**Table 11.2:** Comparison of the LGAD and MALTA sensor performance

nology. We could share the R&D on sensor developments, readout integration and EIC silicon/vertex detector conceptual design. The approximated timeline for the relevant R&D is: Ongoing detector R&D work which includes the silicon sensor characterization and down selection supported by the LANL LDRD project from 2020 to 2022. Continued R&D efforts which focus on the readout chain developments for the EIC day-1 detector from 2022 to 2025 depend on additional funding availability. This is a rough estimate and may change depends on the schedule.

## Gaseous Tracking Detector Technologies

### Time Projection Chambers (TPC)

A TPC is an option for the central detector in an EIC detector. It will provide required momentum resolution for the physics program at an EIC and is also a detector that can deliver PID by means of  $dE/dx$ .

A TPC is presently under construction for the sPHENIX experiment which is expected to start taking data in IP8 of RHIC, in 2023. The sPHENIX-TPC is a compact detector with a minimum material budget in the central region. It has been also designed with an eye toward the use in an EIC detector. This concerns the minimization of the material budget in the forward region which takes into account not only the front-end electronics but also necessary infrastructure, like mounting structure and cooling.

The TPC design follows the classical cylindrical double-sided TPC layout, with a cathode located at the middle of the interaction region dividing the TPC into two mirror-symmetric volumes. The end-caps of the TPC accommodate gas-amplification modules in a subdivided arrangement; 12 sectors in azimuth and 3 sectors in radial extension. This results in a total of 72 readout modules for both end-caps. An illustration can be seen in Fig. 11.7.

The physics program with the sPHENIX detector requires excellent pattern recognition as

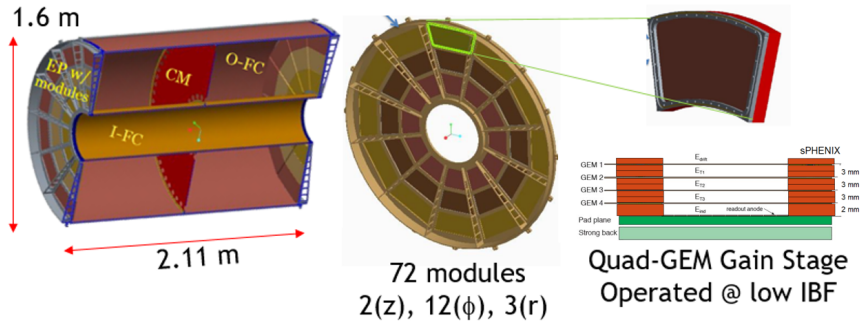


**Figure 11.7:** Pictorial diagram of the sPHENIX TPC. The gas volume and thus the active registration volume for charged particle tracks is between the inner field-cage (I-FC) and the outer field-cage (O-FC). The cathode consist of a thin metallized membrane.

well as excellent momentum resolution. One of the performance parameters to be fulfilled for the sPHENIX program is the separation of the Y-states which requires a momentum resolution from the TPC in the order of  $\Delta p/p \approx 1.2\% \times p(\text{GeV}/c)$ . This translates to a required position resolution  $\sigma_{r\phi} \lesssim 300\mu\text{m}$  with 40 track points in the sPHENIX TPC. This requirement is relaxing with more space points. A test-beam campaign with a TPC prototype verified that this resolution goal more than achievable, see Fig. 11.8,

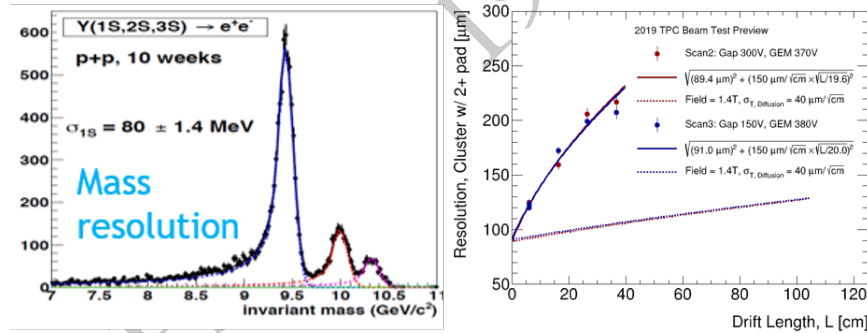


**Figure 11.8:** Left: simulation for the mass resolution sufficient to separate Upsilon states. Right: test-beam results extrapolated to sPHENIX conditions.

The TPC has to be operated in a gate-less configuration such that the readout is not limited due a severe dead-time. This requires in turn the use of Micro Pattern Gas Detectors (MPGDs). For the sPHENIX TPC the choice was made to use a quadruple-GEM avalanche structure, similar to the solution that has been implemented in the ALICE-TPC at the LHC. The operating point of the GEM-stack has been adapted to the sPHENIX environment.

**Gas Amplification** The goal to limit space charge effects requires a low ion-back flow from the amplification device into the main tracker gas volume. A vast R&D program to this extent has been performed by the ALICE collaboration and the experience gained there directly affected the design choices for the sPHENIX TPC. One of the R&D results can be seen in Fig. 11.9, left. For the sPHENIX program the energy resolution does not play a

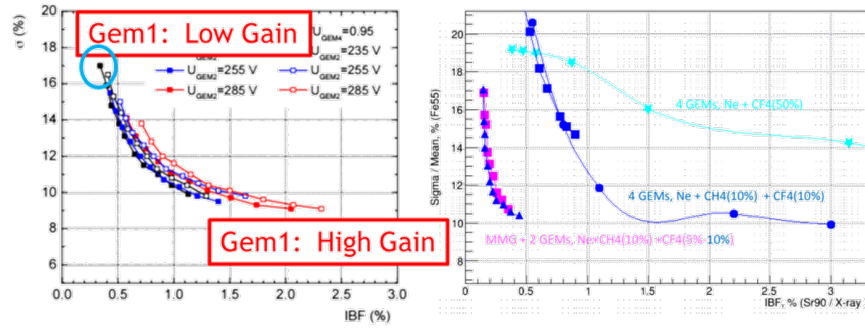


**Figure 11.9:** Left: Operation regime for a quadruple-GEM amplification for a Ne-CO<sub>2</sub> gas mixture. The trend for the behavior of energy resolution vs. IBF can be attributed to the gain of the first GEM. Right: comparison of the operation regime between MM2G and quadruple-GEM amplification with various gas mixtures.

role, hence the operating point for the readout has been chosen around the minimum IBF ( $\sim 0.3\%$ ). For the EIC program this choice can be modified to gain back good energy resolution: the space charge effects in an EIC TPC might be less severe. Studies on the effect of space are ongoing. In principle, there are already solutions in the prototype stage if it turns out that IBF will play a similar role in an EIC environment (see next paragraph). The gas choice for the sPHENIX TPC is based on Ne-CF<sub>4</sub> because of its advantageous properties: 1) high drift velocity, 2) low transverse diffusion and 3) comparatively fast ion drift velocity. The Neon component could be exchanged with Argon which provides a higher ionization yield and therefore improves  $dE/dx$  performance. Other gas components can be added to the gas mixture which is under consideration for optimizing the TPC for EIC purposes. It is worth the mentioning that the sPHENIX configuration has been investigated in a test-beam environment with a modified operating point and promising  $dE/dx$  performance has been measured. An alternative to the quadruple GEM readout option is the MM2G option. It consists of a double-GEM layer on top of a MicroMegas as the main amplification device, hence the term MM2G. The double-GEM structure provides the necessary field ratios to maintain a low IBF and act as pre-amplifier. It has been shown that it is possible to obtain a low IBF while maintaining an energy resolution of better than 12% (Fig. 11.9, right).

**Modifications to the sPHENIX TPC** A major modification of the TPC presently under construction for sPHENIX will be the recovery of about 10 cm vertical track length. The design for sPHENIX was chosen such that the first 10 cm in radial extension will not be read out electronically. This choice has its origin in that space charge distortions, i.e., deflections from the ideal electron trajectory are largest in the vicinity of the field cage. Therefore, the space charge distortions will be still real within the vicinity of the field-cage, however, the track information from this part will not be considered and therefore not electronically read out. This can be easily reverted in the EIC era.

A modified readout pad-geometry with perhaps a modified readout electronics might improve the performance for the TPC in the EIC era. However, these are topics which are

discussed in the Section 14.2.

### Micro Pattern Gaseous Detectors (MPGDs)

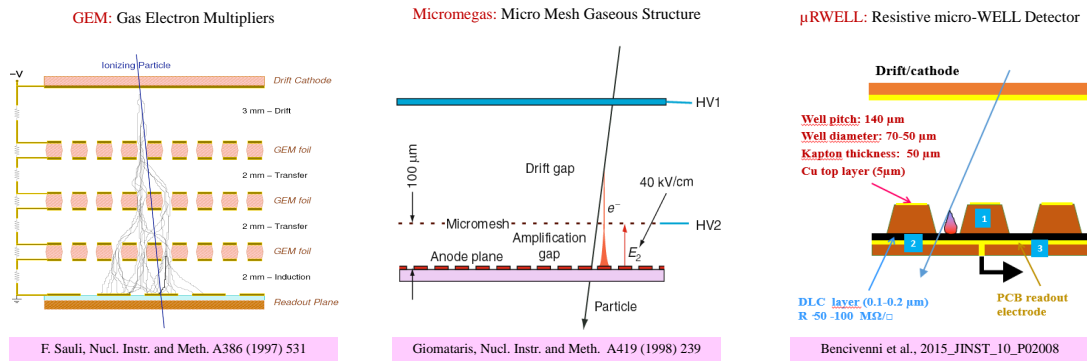


**Figure 11.10:** Cross sectional view of mature MPGD Technologies for tracking: Triple-GEM detector [1247], (left); Micromegas [1248], (center);  $\mu$ -RWELL detector [1249], (right).

MPGD technologies such as Gas Electron Multiplier (GEM) [1247], Micro Mesh Gaseous Structures (Micromegas) [1248], Resistive Micro Well ( $\mu$ -RWELL) [1249] are widely used for tracking in various particle physics experiment across the world such as the COMPASS [1250], LHC main detectors upgrade (ATLAS, CMS ALICE & LHCb) at CERN, SBS [1251], CLAS12 [1252], PRad [1253], MOLLER [1254] and SoLID [1255] at Jefferson Lab, STAR FGT and PHENIX HDB at BNL. These technologies typically combine a gaseous device for electron amplification with high granularity strips or pads anode readout PCB to provide a combined excellent 2D space point resolution ( $\approx 50 \mu\text{m}$ ), fast signal ( $\approx 5\text{ns}$ ), high rate capabilities ( $\approx \text{MHz}/\text{cm}^2$ ), low material budget ( $\approx 0.5\%X_0$ ) per layer, radiation hardness and large area capabilities at a significantly lower cost compared to silicon trackers.

An extensive R&D program conducted by the eRD6 Consortium [1256] within the EIC Generic Detector R&D program is dedicated to the development and optimization of MPGD technologies as main tracker in the central region of a baseline EIC hybrid tracker as described in section 11.2.6. In this hybrid configuration, two options, both of them involving MPGD detectors, are under study for the barrel tracker. The first option has a TPC detector (see section 11.2.3) for the main tracker with a MPGD device or a combination of two MPGD devices for electron amplification and readout in the TPC end cap. The alternative to the TPC in barrel region explores large cylindrical Micromegas or  $\mu$ -RWELL layers for the main tracker. Both TPC and cylindrical MPGDs options are complemented in the hadron end electron end caps by planar MPGD discs. Performances studies for various geometrical configurations of the planar MPGD layers in the end cap regions are reported in section 11.2.6

## Drift Chambers & Straw Tubes (DCs)

Grancagnolo...

### Small-strip Thin Gap Chambers (sTGCs)

Small-strip thin gap chambers (sTGC) detector technology was developed for the ATLAS new small wheel upgrade [1257]. A modified version of the sTGC tracker, based on the ATLAS design, is being used for the STAR forward rapidity upgrade [1258]. The small-strip thin gap chamber detector technology offers a reasonably good space-point resolution ( $\approx 100\mu\text{m}$ ) and low material budget  $\sim 0.5X_0$  per layer, for a relatively low cost compared to various other technologies. The sTGC as designed by ATLAS for the new small wheel upgrade consists of a grid of  $50\mu\text{m}$  diameter gold-plated tungsten wires with a 1.8mm pitch sandwiched between two cathode planes 1.4mm from the wire plane. The sTGC wires operate at 2.9 kV in a gas mixture of 55%  $\text{CO}_2$  and 45% n-pentane. The sTGC modules feature both strip and pad readout. Copper strips with a pitch of 3.2 mm are located on one of the anode planes and run perpendicular to the wires. Large rectangular readout pads, useful for fast triggering, are located on the other anode plane. An illustration of the basic design of an sTGC is shown in Fig. 11.11.

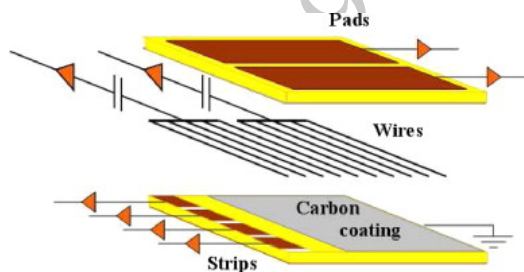


**Figure 11.11:** Schematic diagram of the basic sTGC structure reproduced from [1259].

While position resolution better than  $50\mu\text{m}$  has been achieved in test beam studies [1259], in practice, the sTGC strip readout is expected to provide position resolution on the order of  $100 - 150\mu\text{m}$ , depending on the charged track's incident angle. The ATLAS new small wheel setup employs sTGC modules with strips aligned to provide precise position measurement in the bending coordinate, with measurement of the azimuthal information provided by wire readout. The STAR forward upgrade application employs sandwiches of two layers of sTGC modules with one layer providing precise x-position measurements and the other layer providing precise y-position measurements [1258, 1260]. In addition, the design used by STAR replaces pads on one of the two layers with diagonal strips to help improve space point reconstruction.

Since the sTGC detectors are highly cost-effective with a low material budget and robust up to single hit rates of  $100\text{ kHz}/\text{cm}^2$ , they are a suitable technology choice for large area planar regions of tracking. Specifically, sTGC layers could be employed for tracking in the hadron-going (forward) direction at a  $z \approx 300\text{ cm}$  beyond the Ring Imaging Cherenkov

(RICH) detector. The sTGC may be a good choice for tracking in this region, beyond the central tracking and PID detectors, where the magnitude of the multiple scattering effects will be larger rendering precise space point resolution less important. Similarly, sTGC planes may be a viable cost-effective option for the regions that require large area trackers in the electron-going (backward) direction.

#### 11.2.4 Comparison of Technology Choices

Domenico, Kondo, Leo ...

#### 11.2.5 Detector concepts and performance studies

In this section we present two baseline detector concepts. The first is an all-silicon set of tracking layers and discs. The second concept is a hybrid design that contains silicon tracking layers and discs with a gaseous tracking detector surrounding the silicon based barrel layers. Each of these designs has particular strengths. In the all-silicon case, the full tracking detector can be realized in a comparatively compact form while retaining excellent tracking capabilities. In the hybrid case, the gaseous detector can provide  $dE/dx$  measurements that can add to the PID capabilities while maintaining tracking that meets the EIC requirements. It is hoped that the inclusion of two simulated baseline configurations will aid in the selection of a detector that will contain optimizations based on the full set of overall detector requirements. In addition, these options may aid in the formulation of complimentary detector configurations for the second interaction point. The detector performance for each detector baseline in comparison to the physics derived requirements can be found in summary tables in the concluding Summary section of the tracking chapter.

##### All-Silicon Tracking Option

##### Baseline All-Silicon Tracking Option (Barrel & End Caps)

A pixelated all-silicon tracker prototype for the EIC is shown in Fig. 11.12 (left). The detector is cylindrically symmetric and has three main regions: a 6-layer barrel in the mid-rapidity region, 5 disks in the forward region, and 5 disks in the backward region. The extent of the tracker along the beam axis is identical in both directions, a constraint consistent with the current choice to have the nominal beam collision point coincide with the geometric center of the overall general purpose detector concepts. In the barrel region, the trade-off from pairing layers to gain momentum-resolution performance is primarily with the momentum measurement threshold,  $2p_T \simeq 0.3B \cdot r$  (about 0.2 GeV for a representative  $B = 3$  T and  $r \simeq 0.4$  m). Pairing of layers also reduces the number of stave designs and associated tooling. In the all-silicon concept under consideration, the layers that constitute the barrel are thus paired with the outermost pair at  $\simeq 0.4$  m and the intermediate pair near the mid-point to the beam axes to best capture the sagitta. The transition between the outer

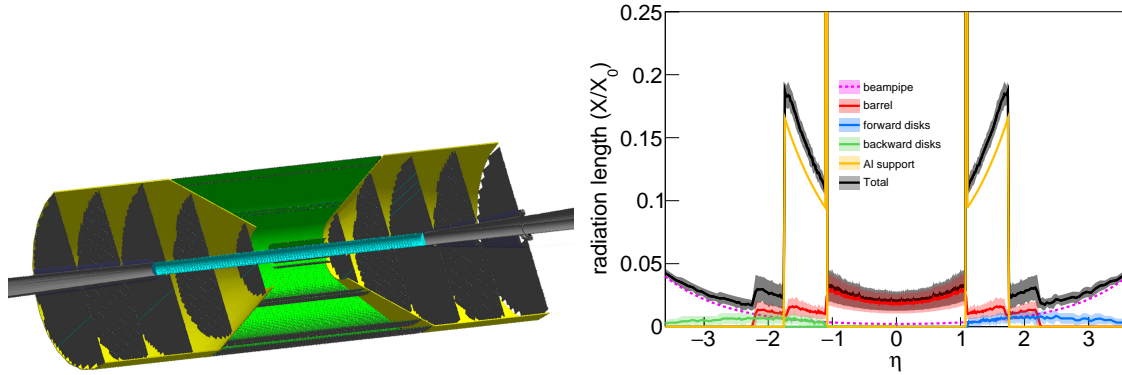


**Figure 11.12:** All-silicon tracker geometry. Left: Geant-4 schematic of the tracker cross section. The barrel, disks, and support structure correspond to the green, dark-gray, and yellow components, respectively. The beryllium section of the beam pipe is shown in cyan. The rest of the beam pipe, which takes into account the expected electron-hadron-beam crossing angle is shown in light-gray. Right: Detector material scan. The dashed line describes the baseline material budget from the beam pipe. The red, blue, and green curves correspond to the barrel, forward, and backward components of the detector, respectively. The uncertainty band defines the minimum and maximum amounts of material found in a given  $\eta$  as the material is scanned around  $\phi$ . The yellow curve describes the aluminum support structure. See text for details.

barrel layers and the disks is near  $|\eta| \simeq 1.1$  to minimize the amount of traversed material. Further details on the barrel and disk geometries are presented in tables 11.3 and 11.4, respectively. In this concept, the innermost barrel layers drive the vertexing performance. Their length (well) exceeds the extent of the  $\simeq 8$  cm beam-collision region and is chosen to accept (displaced) tracks for  $|\eta| \lesssim 2$  without relying on track-pointing with the disks, which will near-inevitably involve tracking across inactive material from services and supports in this region of the detector. The dominant parts of the services and supports are thought to be guided out in a projective way along the transition angle between the barrel and the disks. This is modeled in a simplified form as an effective 5-mm-thick aluminum cone in the performance simulations thus far; engineering evaluations remain to be done. This geometry is wrapped around the EIC beam pipe, which in the region  $-79.8 < z < 66.8$  cm corresponds to a 3.17-cm-radius beryllium cylinder of thickness of  $760 \mu\text{m}$ .

In this configuration, the detector is made up of ALICE-ITS3-like staves, each having an average material budget of  $X/X_0 = 0.3\%$ . These staves, assembled into the detector geometry, contribute the amount of material shown in Fig. 11.12 (right). Since the staves form a periodic but changing material budget, the azimuth ( $\phi$ ) is swept for each pseudorapidity ( $\eta \equiv -\ln(\tan \theta/2)$ , where  $\theta$  is the polar angle) direction, and the minimum and maximum found  $X/X_0$  define the width of the uncertainty band. Overall, the active areas of the detector provide a material budget of  $X/X_0 < 5\%$ . The support structure adds a significant amount of material. The projective design of this structure ensures that most of this material is concentrated in a small pseudorapidity range, at  $|\eta| \approx 1.1$ .

**Table 11.4:** Main disk characteristics.**Table 11.3:** Main barrel-layer characteristics.

Barrel layer	radius [cm]	length along z [cm]
1	3.30	30
2	5.70	30
3	21.00	54
4	22.68	60
5	39.30	105
6	43.23	114

Disk number	z position [cm]	outer radius [cm]	inner radius [cm]
-5	-121	43.23	4.41
-4	-97	43.23	3.70
-3	-73	43.23	3.18
-2	-49	36.26	3.18
-1	-25	18.50	3.18
1	25	18.50	3.18
2	49	36.26	3.18
3	73	43.23	3.50
4	97	43.23	4.70
5	121	43.23	5.91

This configuration was studied and optimized using the Geant-4-based Fun4All framework [1261–1263]. Momentum, pointing, and angular resolutions at the vertex were studied by bombarding the detector over the entire acceptance with single particles (charged pions, electrons, and protons) generated in the momentum range of  $0 < p < 30$  GeV/ $c$  with a fixed vertex at  $(x, y, z) = (0, 0, 0)$ , and reconstructing their tracks with the detector. The simulated silicon-pixel size corresponds to  $10 \mu\text{m}$  (point resolution =  $10/\sqrt{12} \mu\text{m}$ ). The studies were carried out with magnetic-field maps describing the BaBar (1.4 T) [1264] and Beast (3.0 T) [1265, 1266] solenoids.

The fractional momentum resolution is determined as the standard deviation of a normal function fitted to the  $\Delta p/p \equiv (p_{\text{truth}} - p_{\text{reco}})/p_{\text{truth}}$  distribution. Here, the labels ‘truth’ and ‘reco’ represent generated and reconstructed variables, respectively. Momentum-resolution results for pions are shown as a function of pseudorapidity in Fig. 11.13 (left). As expected from the leading-order  $\sim 1/B$  dependence of the momentum resolution, doubling the magnetic field reduces the momentum resolution by a factor of  $\approx 2$ . The resulting distributions were characterized via fits with the functional form

$$dp/p = Ap \oplus B, \quad (11.1)$$

where  $\oplus$  is shorthand notation for sum in quadrature. The  $A$  and  $B$  fit parameters are presented in Table 11.5.

The Distance of Closest Approach (DCA) is defined as the spatial separation between the primary vertex and the reconstructed track projected back to the  $z$  axis ( $\text{DCA}_z$ ) or to the  $x - y$  plane ( $\text{DCA}_T$ ). The DCA resolutions were determined as the standard deviation of normal functions fitted to the  $\text{DCA}_z$  and  $\text{DCA}_T$  distributions. DCA-resolution results as a function of transverse momentum ( $p_T$ ) for pions are shown in Fig. 11.13 (center and right). The resulting distributions were characterized via fits with the functional form

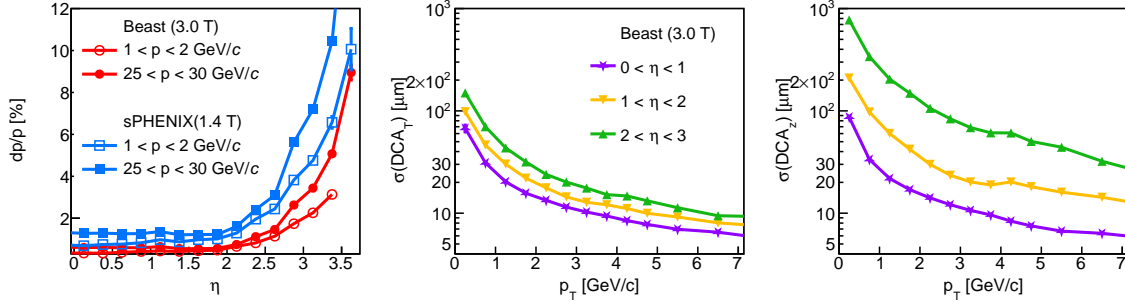


**Figure 11.13:** Detector resolutions. Left: Momentum resolution as a function of pseudorapidity for pions for two magnetic-field configurations for representative momentum bins. Center: Transverse Distance-of-Closest-Approach ( $\text{DCA}_T$ ) resolution as a function of transverse momentum for several pseudorapidity bins. Right: Longitudinal Distance-of-Closest-Approach ( $\text{DCA}_z$ ) resolution as a function of transverse momentum for several pseudorapidity bins.

**Table 11.5:** All-silicon tracker momentum and pointing resolution parametrizations.

		$\delta p/p = Ap \oplus B$		$\text{DCA}_z = A/p_T \oplus B$		$\text{DCA}_T = A/p_T \oplus B$	
		A [%/GeV]	B [%]	A [ $\mu\text{m GeV}$ ]	B [ $\mu\text{m}$ ]	A [ $\mu\text{m GeV}$ ]	B [ $\mu\text{m}$ ]
$0.0 <  \eta  < 0.5$	B = 3.0T	0.018	0.382	27	3.2	25	4.9
	B = 1.4T	0.041	0.773	27	3.3	26	3.9
$0.5 <  \eta  < 1.0$	B = 3.0T	0.016	0.431	37	3.8	28	4.5
	B = 1.4T	0.034	0.906	35	3.8	31	4.0
$1.0 <  \eta  < 1.5$	B = 3.0T	0.016	0.424	56	5.9	33	5.5
	B = 1.4T	0.034	0.922	56	5.4	35	5.1
$1.5 <  \eta  < 2.0$	B = 3.0T	0.012	0.462	111	7.0	40	5.1
	B = 1.4T	0.026	1.000	112	7.1	41	4.9
$2.0 <  \eta  < 2.5$	B = 3.0T	0.018	0.721	213	13.8	47	7.1
	B = 1.4T	0.041	1.551	212	16.0	48	7.7
$2.5 <  \eta  < 3.0$	B = 3.0T	0.039	1.331	347	40.5	52	11.9
	B = 1.4T	0.085	2.853	373	37.9	59	11.2
$3.0 <  \eta  < 3.5$	B = 3.0T	0.103	2.441	719	87.6	59	26.0
	B = 1.4T	0.215	5.254	732	87.7	66	25.3
$3.5 <  \eta  < 4.0$	B = 3.0T	0.281	4.716	1182	206	69	65.9
	B = 1.4T	0.642	9.657	1057	221	69	72.1

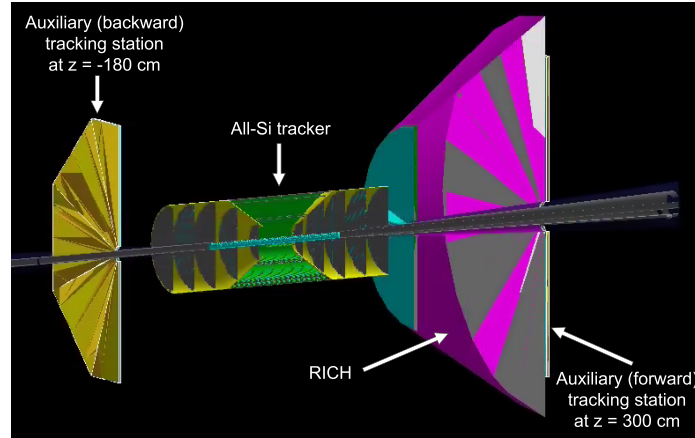


**Figure 11.14:** Event display showing the all-silicon tracker complemented with additional tracking stations in the available space [1267]. In the backward region, the tracking station is installed at  $z = -180$  cm with no significant amount of material expected between the all-silicon tracker and the complementary tracking station. In the forward region, the auxiliary tracking station is installed at  $z = 300$  cm, behind the Ring Imaging Cherenkov (RICH) detector. The RICH material parameters were provided by the PID detector working group [1268].

$$\sigma(\text{DCA}) = A/p_T \oplus B. \quad (11.2)$$

The  $A$  and  $B$  fit parameters are presented in Table 11.5.

As seen in Fig. 11.13 (left), the momentum resolution is overall constant as a function of pseudorapidity up to  $\eta \sim 2$ , and then rapidly worsens. We studied the possibility of recovering the quickly-worsening momentum resolution at forward and backward pseudorapidities by complementing the all-silicon tracker with auxiliary tracking stations, including Gas Electron Multiplier (GEM) detectors with  $50\text{-}\mu\text{m}$  resolution in the radial and azimuthal directions and additional  $10\text{-}\mu\text{m}$ -pixel silicon disks in the available space away from the interaction point [1267]. The available space for such additional detectors is different in the forward and backward directions, as shown in Fig. 11.14. In the electron-going (backward) direction, a complementary tracking station can be installed at  $z \sim -180$  cm, and no significant amount of material is projected to be placed between said detector and the all-silicon tracker. In the hadron-going (forward) direction, the additional station can be installed at  $z \sim 300$  cm, behind the Ring Imaging Cherenkov (RICH) detector.

The effect of complementing the all-silicon tracker in the electron-going direction is shown in Figs. 11.15 and 11.16 for a  $10\ \mu\text{m}$  and  $20\ \mu\text{m}$  all-silicon-tracker pixel sizes, respectively. In the backward region, where the available space is closer to the all-silicon tracker, an auxiliary  $10\text{-}\mu\text{m}$ -pixel detector provides a significantly better momentum resolution, mainly in the higher momentum region.

Results in the forward region are shown in Figs. 11.17 and 11.18 for a  $10\ \mu\text{m}$  and  $20\ \mu\text{m}$  all-silicon-tracker pixel sizes, respectively. The auxiliary station is placed behind the Ring

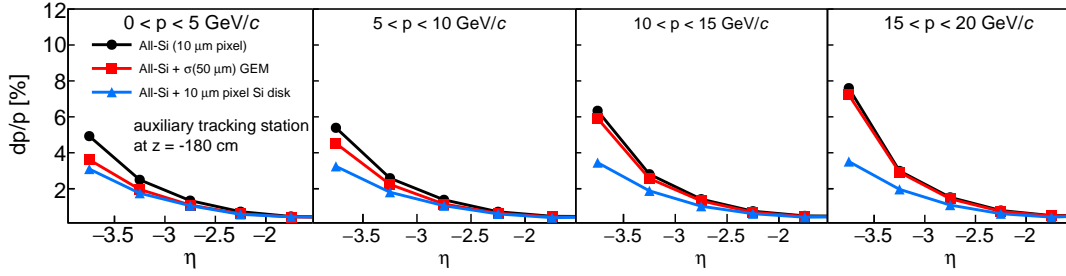


**Figure 11.15:** Momentum resolution as a function of pseudorapidity demonstrating the effect of complementing the all-silicon tracker in the electron-going (backward) direction. Each panel corresponds to a different momentum bin, from 0 to 20 GeV/c. The black circles correspond to the standalone all-silicon tracker (for a  $10\ \mu\text{m} \times 10\ \mu\text{m}$  pixel size). The red squares and blue triangles correspond to the all-silicon tracker complemented with a  $50\text{-}\mu\text{m}$ -resolution GEM detector and a  $10\text{-}\mu\text{m}$ -pixel silicon disk, respectively.

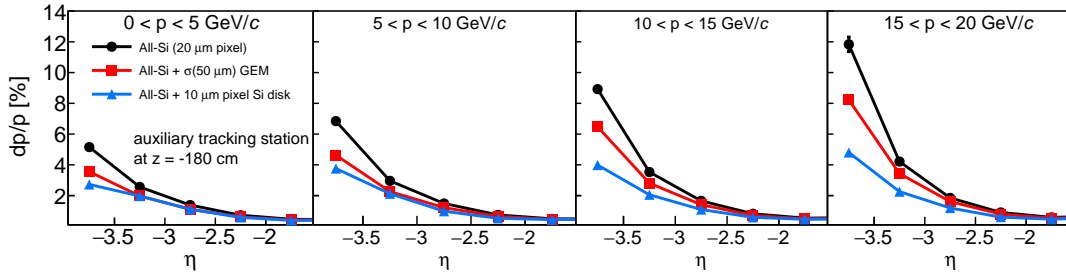


**Figure 11.16:** Same as Fig. 11.15, but for a  $20\ \mu\text{m} \times 20\ \mu\text{m}$  all-silicon-tracker pixel size.

Imaging Cherenkov (RICH) detector. The RICH material parameters were provided by the PID detector working group [1268]. Since in the forward region the available space is farther away from the all-silicon tracker, the path traversed by a charged particle through the magnetic field in the tracking region ( $\int \mathbf{B} \cdot d\mathbf{l}$ ) is larger. As a result, the resolution is less sensitive to the complementary detector resolution, and while the silicon disk provides the best performance, the GEM detectors considered provide a comparable enhancement to the momentum resolution. The effect of these auxiliary tracking stations depends on the EIC magnetic-field details. In these simulations, solenoidal fields were used. Likely, the magnetic field lines will be shaped to minimize bending inside the RICH detector, which will lower the  $\int \mathbf{B} \cdot d\mathbf{l}$ .

While the auxiliary tracking stations in these simulations cover pseudorapidities  $|\eta| > 1.2$ , they have a larger impact at higher pseudorapidities ( $|\eta| \gtrsim 2.5$ ). Consequently, smaller tracking stations can be used to complement the all-silicon tracker.

In closing, we have discussed several of the considerations for an instrument-performance driven integration of barrel tracking and vertexing layers with backward and forward disk arrays into an all-silicon tracking concept based on MAPS technology [1269]. This all-silicon concept offers similar or better momentum and angular performance than the

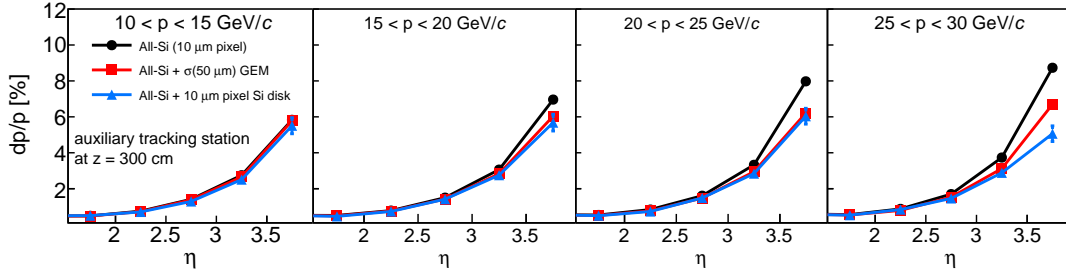


**Figure 11.17:** Momentum resolution as a function of pseudorapidity demonstrating the effect of complementing the all-silicon tracker in the hadron-going (forward) direction. Each panel corresponds to a different momentum bin, from 10 to 30 GeV/c. The black circles correspond to the standalone all-silicon tracker (for a  $10\ \mu\text{m} \times 10\ \mu\text{m}$  pixel size). The red squares and blue triangles correspond to the all-silicon tracker complemented with a  $50\text{-}\mu\text{m}$ -resolution GEM detector and a  $10\text{-}\mu\text{m}$ -pixel silicon disk, respectively.

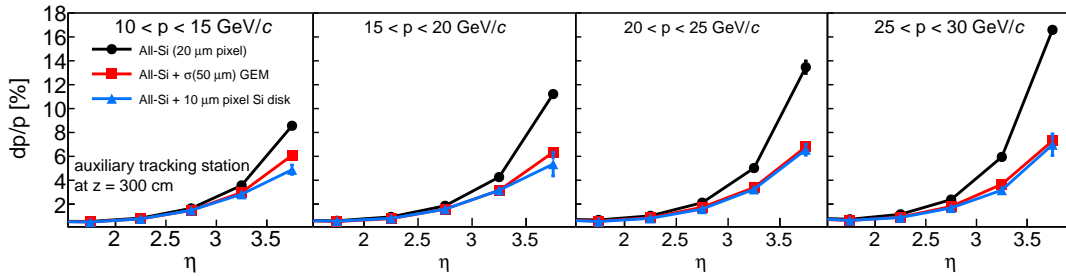


**Figure 11.18:** Same as Fig. 11.17, but for a  $20\ \mu\text{m} \times 20\ \mu\text{m}$  all-silicon-tracker pixel size.

hybrid TPC-silicon concept of BeAST [1270] with identical vertexing performance. It is radially more compact,  $r = 43.23\ \text{cm}$  versus  $r = 80.0\ \text{cm}$ , thereby freeing  $36.77\ \text{cm}$  that could be used for alternate purposes such as PID and offering opportunities for complementary baseline EIC general purpose central detector concepts.

#### Alternative Forward Tracking Option: Hadron End Cap with Si disk + MPGDs

[UPDATED BY CHEUK-PING WONG ON 11/15/2020]

A forward silicon tracker (FST) is designed for heavy flavor and jet measurements in EIC [713,841]. The proposed FST covers pseudorapidity between 1–3.5 and momentum up to 30 GeV. An integrated detector design with the use of both FST and GEM tracker, which will be a cost effective option, are also studied in detector simulation.

**Detector Design** The FST, which is implemented in Fun4All simulation, consists of six planes of silicon sensor as shown in Figure 11.19. The FST detector design parameters are listed in Table 11.6. The FST is placed between 35 cm and 300 cm along the

$z$  axis. The inner radius of each plane changes with the  $z$  position to fit the ion beam pipe geometry. Effects on detector performance from different pixel pitch size and thickness of silicon thickness are studied and documented in ref [713]. In the latest FST detector design, the first three planes (plane 0-2) use a pixel pitch of  $20 \mu\text{m}$  and a silicon thickness of  $50 \mu\text{m}$  that are close to the ALICE ITS-3 type sensor [1235, 1271] while the last three planes (plane 3-5) apply MALTA sensor properties [1243, 1245, 1272]. With both sensor technologies, the FST can provide excellent spatial and timing resolutions.

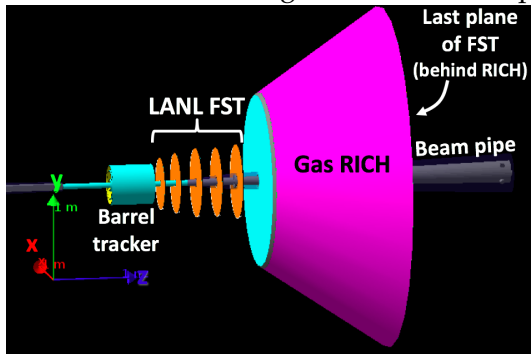


Figure 11.19: FST setup in Fun4All simulation.

Plane	$z$ (cm)	$r_{\text{in}}$ (cm)	$r_{\text{out}}$ (cm)	pixel Pitch ( $\mu\text{m}$ )	silicon thickness ( $\mu\text{m}$ )
0	35	4	25	20	50
1	62.3	4.5	42	20	50
2	90	5.2	43	20	50
3	115	6	44	36.4	100
4	125	6.5	45	36.4	100
5	300	15	45	36.4	100

Table 11.6: FST geometry parameters

**Detector Integration** Integrated detector setups are also implemented in the simulation. The first integrated setup, which is shown in Figure 11.19, includes an additional gas RICH with aerogel and  $\text{C}_2\text{F}_6$  gas as radiator. The second integrated setup is similar to the first integrated setup, but replaces the last plane (plane 5) of FST with a mock up GEM tracker. The GEM tracker, which consists of three planes filled with methane, covers  $1.5 < \eta < 3.5$ . The material budgets of the integrated setups are shown in Figure 11.20. The material budgets of the first and the second integrated setup are  $< 8\% X_0$  and  $< 10\% X_0$  at  $\eta < 3.3$ , respectively.

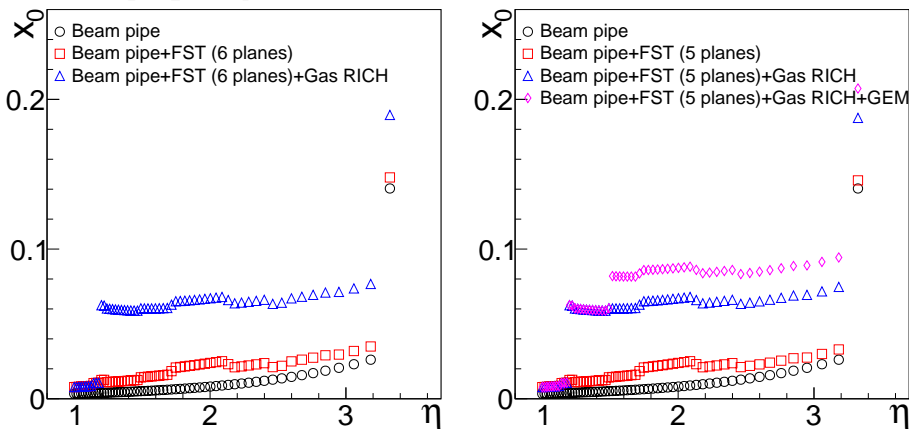
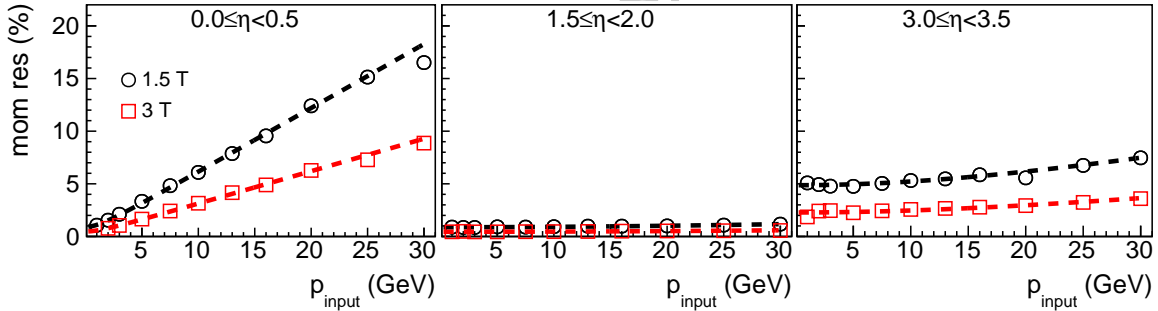


Figure 11.20: Material budgets of different integrated detector setups.

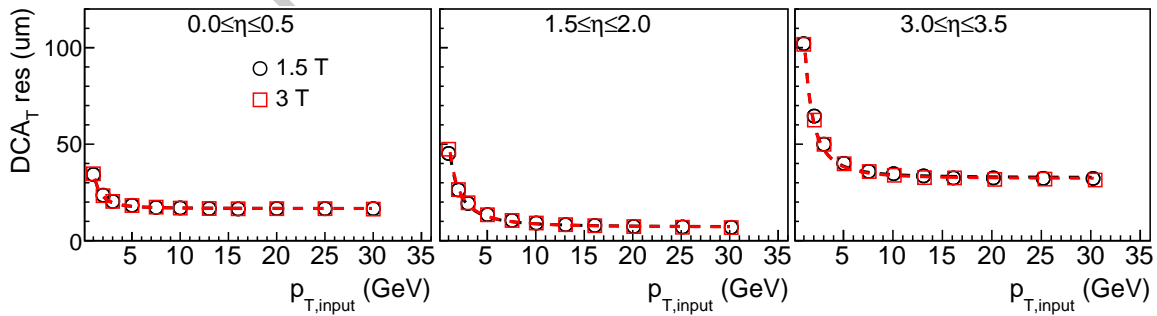
**Detector performance** The momentum resolutions of the integrated detector setup with the GEM track are shown in Figure 11.21. The results are fitted using Equation (11.1). The fitting results of different detector setups are listed in Table 11.7. The momentum resolutions of the integrated detector setups with the 3 T (1.5 T) magnet are  $< 10\%$  ( $18\%$ ) and  $< 4\%$  ( $8\%$ ) at  $\eta < 1$  and  $\eta > 1$ , respectively. Comparing results of different detector setups as shown in Table 11.7, the additional gas RICH worsens the momentum resolutions by about 1% at  $\eta > 2.5$ . Furthermore, Table 11.7 shows that replacing the last plane of FST with a GEM tracker does not give significant changes in momentum resolution. The  $DCA_T$  resolutions of the integrated detector setups with the GEM tracker are shown in Figure 11.22. The  $DCA_T$  resolutions are fitted using Equation (11.2). The fitting results of different detector setups with the use of the 3 T magnetic field are listed in Table 11.8. The fitting results of  $DCA_T$  resolutions with the use of the 1.5 T magnetic fields are not shown in Table 11.8 as the  $DCA_T$  resolutions shows a weak dependence on the magnetic fields. Table 11.8 shows that the  $DCA_T$  resolutions are  $< 50 \mu\text{m}$  and  $< 110 \mu\text{m}$  at  $\eta < 2$  and  $\eta > 2$ , respectively. Furthermore, Table 11.8 shows that the replacement of the last plane of FST with the GEM tracker gives no significant differences in  $DCA_T$  resolution. The results of momentum and  $DCA_T$  resolutions, which show that replacing the last plane of FST by the GEM tracker does not give significant differences in detector performance, make the integrated detector setup with the GEM tracker an attractive option considering the lower cost of a GEM tracker compared to a silicon detector.



**Figure 11.21:** Momentum resolutions as a function of input momentum of the integrated detector setup with the beam pipe, the barrel tracker, the five-plane FST, the gas RICH and the GEM tracker. The dash lines are the fits using Equation (11.1). The fitting results are shown in Table 11.7.

**Table 11.7:** Fitting parameters of the momentum resolutions of different detector integration setups.

$\eta$	B field	FST (6 planes)		FST (6 planes) + RICH		FST (5 planes) + RICH + GEM	
		A (%/GeV)	B (%)	A (%/GeV)	B (%)	A (%/GeV)	B (%)
0.0–0.5	3 T	0.313	0.440	0.310	0.457	0.309	0.475
	1.5 T	0.608	0.880	0.605	0.892	0.608	0.915
0.5–1.0	3 T	0.267	0.510	0.259	0.494	0.263	0.494
	1.5 T	0.520	0.971	0.513	1.035	0.513	1.010
1.0–1.5	3 T	0.039	0.568	0.040	0.551	0.032	0.597
	1.5 T	0.076	1.039	0.077	1.120	0.070	1.088
1.5–2.0	3 T	0.019	0.454	0.018	0.448	0.013	0.445
	1.5 T	0.039	0.839	0.039	0.882	0.026	0.876
2.0–2.5	3 T	0.032	0.687	0.035	0.682	0.028	0.704
	1.5 T	0.068	1.346	0.070	1.374	0.051	1.402
2.5–3.0	3 T	0.037	1.190	0.062	1.306	0.062	1.336
	1.5 T	0.086	2.362	0.127	2.607	0.123	2.629
3.0–3.5	3 T	0.063	1.746	0.095	2.069	0.095	2.278
	1.5 T	0.124	3.378	0.189	4.305	0.189	4.868

**Figure 11.22:**  $DCA_T$  resolutions of the integrated detector setup with the beam pipe, the barrel tracker, the five-plane FST, the gas RICH and the GEM tracker. The dash lines are the fits using Equation (??). The fitting results are shown in Table 11.8.

**Table 11.8:** Fitting parameters of the  $DCA_T$  resolutions of different detector setup with the use of the 3 T magnetic field.

$\eta$	FST (6 planes)		FST (6 planes) + RICH		FST (5 planes) + RICH + GEM	
	A ( $\mu\text{m}\cdot\text{GeV}$ )	B ( $\mu\text{m}$ )	A ( $\mu\text{m}\cdot\text{GeV}$ )	B ( $\mu\text{m}$ )	A ( $\mu\text{m}\cdot\text{GeV}$ )	B ( $\mu\text{m}$ )
0.0–0.5	30.73	16.71	30.17	16.86	30.84	16.78
0.5–1.0	32.80	17.22	32.14	17.37	32.83	17.28
1.0–1.5	41.54	14.19	39.47	14.39	40.73	14.06
1.5–2.0	49.57	8.24	48.49	8.43	51.56	7.36
2.0–2.5	57.87	13.73	54.79	14.16	59.58	11.48
2.5–3.0	76.78	20.42	81.63	21.13	83.90	20.35
3.0–3.5	77.79	29.71	95.90	30.01	104.95	31.55

## 11.2.6 Hybrid Tracking System

### Barrel: Silicon Vertex + TPC

Figure 11.23 shows the simulated layout of this hybrid configuration. The silicon part is made of three layers close to the beampipe (vertexing layers) and two layers at larger radii (tracking layers) in the central region, and seven disks in the forward and backward regions. A TPC surrounds the central region and two TPC endcaps are placed after the silicon disks in both forward and backward regions.

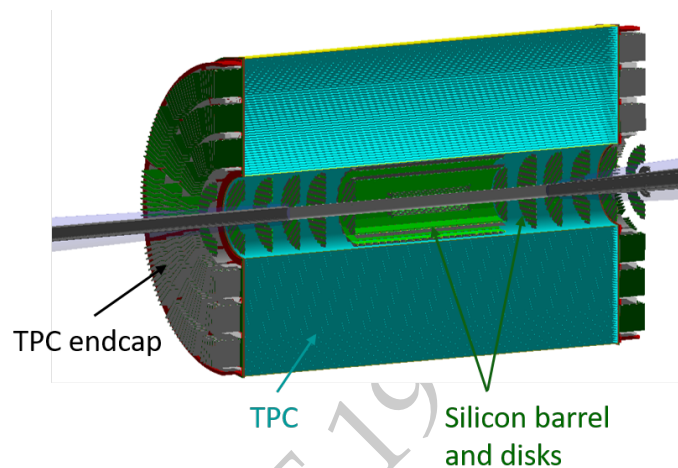


**Figure 11.23:** New hybrid baseline layout. The silicon layers and disks are shown in green, and the TPC in light blue.

The silicon detector parameters are based on the ALICE ITS3 technology. The vertexing layers have a material budget of  $0.05\% X/X_0$  each, the tracking layers  $0.55\% X/X_0$ , and the disks each have a material budget of  $0.24\% X/X_0$ . The pixel size is  $10 \times 10 \mu\text{m}^2$ .

The placements and parameters of barrel layers and disks are described in detail in Tables 11.9a and 11.9b. The table for the disks only shows the forward region, since this detector layout is symmetric in  $z$ . The radial positions for the barrel layers are based on the minimum distance between layers used in the ALICE ITS2 system [1273]. While it may be possible to put layers closer together, using these distances give a detector that is plausible to build with currently existing technologies and structure solutions. Each detector layer is built up of overlapping staves, consisting of several chips along with material representing cables, cooling pipes, and simple support structures.

**Momentum and pointing resolutions;** Studies for the resolutions are made in the following parameter space:

- Transverse momentum range: 0 to 30 GeV/c

Layer	Length	Radial position	Disk	z position	Inner radius	Outer radius
Layer 1	420 mm	36.4 mm	Disk 1	220 mm	36.4 mm	71.3 mm
Layer 2	420 mm	44.5 mm	Disk 2	430 mm	36.4 mm	139.4 mm
Layer 3	420 mm	52.6 mm	Disk 3	586 mm	36.4 mm	190.0 mm
Layer 4	840 mm	133.8 mm	Disk 4	742 mm	49.9 mm	190.0 mm
Layer 5	840 mm	180.0 mm	Disk 5	898 mm	66.7 mm	190.0 mm
TPC start	2110 mm	200.0 mm	Disk 6	1054 mm	83.5 mm	190.0 mm
TPC end	2110 mm	780.0 mm	Disk 7	1210 mm	99.3 mm	190.0 mm

(a) Barrel region

(b) Disk region

**Table 11.9:** Positions and lengths of detector parts in the barrel region and the disk region. In the disk region, the seven disks in the forward region are shown, but this layout is symmetric so it is the same with reversed sign on the  $z$  position in the backward region.

- Pseudorapidity:  $-1.0 \leq \eta \leq 1.0$ ,  $1.0 \leq \eta \leq 2.5$ ,  $2.5 \leq \eta \leq 3.5$
- Magnetic field: 1.5 T and 3.0 T

Since this detector layout is symmetric, negative pseudorapidities will have the same resolutions as the positive ones. Positive pions are used, with 1 000 000 events in each pseudorapidity range.

The formulae for resolution parameterisation are given in Equation 11.3, where  $A$  and  $B$  indicate constants.

$$\frac{\sigma_p}{p} = A \cdot p \oplus B = \sqrt{(A \cdot p)^2 + B^2}, \quad \frac{\sigma_{xy}}{p_T} = \frac{A}{p_T} \oplus B = \sqrt{\left(\frac{A}{p_T}\right)^2 + B^2} \quad (11.3)$$

This parametrisation works well for the pointing resolution, but it has limitations for the relative transverse momentum resolution when using a gas TPC. In this case, as can be seen from Figure 11.24, the parametrisation works well for  $p_T$  between 0 and 4 GeV/c, but the resolution value goes into a less steep linear increase after this point. The figure shows the relative transverse momentum resolution versus transverse momentum for both a 1.5 T field and a 3.0 T field, and the dashed line shown is the parametrisation provided by the Physics Working Group. Fits to these data will be split up in momentum intervals to characterise the two clear regions (above and below 4 GeV/c) separately. The pseudorapidity interval  $1 \leq \eta \leq 2.5$  receives similar treatment. The final results from the relative momentum fits, with parameters taken from Equation 11.3 can be seen in Table 11.10 for a 1.5 T field and a 3.0 T field.

Table 11.11 shows a comparison between the currently listed parameters provided by the Physics Working Group for the transverse pointing resolution, and the fit values for the data from simulations using the silicon plus TPC hybrid baseline detector. Table 11.12 shows the same for the longitudinal pointing resolution.

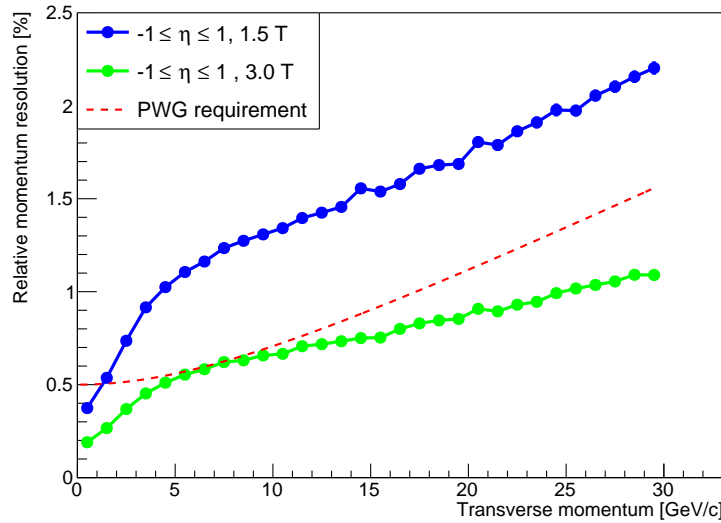


**Figure 11.24:** Relative transverse momentum resolution versus transverse momentum, for the baseline hybrid silicon plus TPC layout. The data are for the central region ( $-1 \leq \eta \leq 1$ ). The blue curve shows the resolution for a 1.5 T field, and the green curve shows the resolution for a 3.0 T field. The red line shows the relative momentum resolution parametrisation requirement as given by the Physics Working Group (see Equation 11.3).

These results show that the requirements on pointing resolutions can be met with this layout and the ITS3-like technology, in all regions. The relative momentum resolution does not meet the requirements however, especially with a 1.5 T magnetic field. With a 3.0 T magnetic field the requirements are met apart from at  $|\eta| \geq 2.5$ .

**Minimum- $p_T$  limit;** The minimum reconstructable  $p_T$  is investigated in the full pseudorapidity range, by sending out low-momentum (0 to 0.5 GeV/c in  $p_T$ ) kaons and pions from the vertex, and seeing what fraction of total tracks in a region can be reconstructed, using a simple fast Kalman filter reconstruction algorithm. Improved reconstruction methods may fare better, but as an approximation of the highest limit of the minimum- $p_T$  that can be reconstructed, this method is deemed feasible. Table 11.13 contains minimum reconstructable  $p_T$  values for different pseudorapidity regions. Results for pions and kaons are similar, and thus only one value is presented, representing the cutoff point where 90% of events are reconstructed. This cutoff point is important to keep in mind; lower  $p_T$  tracks can also be reconstructed up to a point, but less efficiently.

### Barrel: Silicon Vertex + Cylindrical MPGDs

In the barrel, the silicon vertex tracker can be complemented by several layers of MPGDs. Each cylindrical layer of the MPGD tracker consists of curved detector elements of about 50cm width and long enough to cover the range  $|\eta| < 1$ . The spatial resolution both in

Interval	$p_T$ interval	PWG values [%]	Fit 1.5 T [%]
$-3.5 \leq \eta \leq -2.5$	0 to 30 GeV/c	$A = 0.1, B = 0.5$	$A = 0.6 \pm 0.01, B = 4.2 \pm 0.03$
$-2.5 \leq \eta \leq -1.0$	0 to 4 GeV/c	$A = 0.1, B = 0.5$	$A = 0.5 \pm 0.01, B = 0.9 \pm 0.01$
	4 to 30 GeV/c	$A = 0.1, B = 0.5$	$A = 0.1 \pm 0.01, B = 2.2 \pm 0.01$
$-1.0 \leq \eta \leq 1.0$	0 to 4 GeV/c	$A = 0.05, B = 0.5$	$A = 0.2 \pm 0.01, B = 0.4 \pm 0.01$
	4 to 30 GeV/c	$A = 0.05, B = 0.5$	$A = 0.07 \pm 0.001, B = 1.1 \pm 0.01$
$1.0 \leq \eta \leq 2.5$	0 to 4 GeV/c	$A = 0.05, B = 0.5$	$A = 0.5 \pm 0.01, B = 0.9 \pm 0.01$
	4 to 30 GeV/c	$A = 0.05, B = 0.5$	$A = 0.1 \pm 0.01, B = 2.2 \pm 0.01$
$2.5 \leq \eta \leq 3.5$	0 to 30 GeV/c	$A = 0.05, B = 1.0$	$A = 0.6 \pm 0.01, B = 4.2 \pm 0.03$
Interval	$p_T$ interval	PWG values [%]	Fit 3.0 T [%]
$-3.5 \leq \eta \leq -2.5$	0 to 30 GeV/c	$A = 0.1, B = 0.5$	$A = 0.3 \pm 0.01, B = 2.1 \pm 0.01$
$-2.5 \leq \eta \leq -1.0$	0 to 4 GeV/c	$A = 0.1, B = 0.5$	$A = 0.2 \pm 0.01, B = 0.5 \pm 0.01$
	4 to 30 GeV/c	$A = 0.1, B = 0.5$	$A = 0.06 \pm 0.001, B = 1.1 \pm 0.01$
$-1.0 \leq \eta \leq 1.0$	0 to 4 GeV/c	$A = 0.05, B = 0.5$	$A = 0.1 \pm 0.01, B = 0.2 \pm 0.01$
	4 to 30 GeV/c	$A = 0.05, B = 0.5$	$A = 0.03 \pm 0.001, B = 0.5 \pm 0.01$
$1.0 \leq \eta \leq 2.5$	0 to 4 GeV/c	$A = 0.05, B = 0.5$	$A = 0.2 \pm 0.01, B = 0.5 \pm 0.01$
	4 to 30 GeV/c	$A = 0.05, B = 0.5$	$A = 0.06 \pm 0.001, B = 1.1 \pm 0.01$
$2.5 \leq \eta \leq 3.5$	0 to 30 GeV/c	$A = 0.05, B = 1.0$	$A = 0.3 \pm 0.01, B = 2.1 \pm 0.01$

**Table 11.10:** Relative transverse momentum resolution fit parameters for a 1.5 T magnetic field and a 3.0 T magnetic field, using the fit presented in Equation 11.3, and how they compare to the Physics Working Group values provided for the detector matrix.

Interval	PWG values [ $\mu\text{m}$ ]	Fit 1.5 T [ $\mu\text{m}$ ]	Fit 3.0 T [ $\mu\text{m}$ ]
$-3.5 \leq \eta \leq -2.5$	N/A	$A = 49.3 \pm 0.2, B = 9.64 \pm 0.02$	$A = 48.5 \pm 0.2, B = 9.58 \pm 0.02$
$-2.5 \leq \eta \leq -1.0$	$A = 40, B = 10$	$A = 23.3 \pm 0.1, B = 3.32 \pm 0.01$	$A = 23.1 \pm 0.1, B = 3.31 \pm 0.01$
		$A = 14.1 \pm 0.1, B = 2.11 \pm 0.01$	$A = 13.7 \pm 0.1, B = 2.14 \pm 0.01$
$1.0 \leq \eta \leq 2.5$	$A = 40, B = 10$	$A = 23.3 \pm 0.1, B = 3.32 \pm 0.01$	$A = 23.1 \pm 0.1, B = 3.31 \pm 0.01$
		$A = 14.1 \pm 0.1, B = 2.11 \pm 0.01$	$A = 13.7 \pm 0.1, B = 2.14 \pm 0.01$
$2.5 \leq \eta \leq 3.5$	N/A	$A = 49.3 \pm 0.2, B = 9.64 \pm 0.02$	$A = 48.5 \pm 0.2, B = 9.58 \pm 0.02$

**Table 11.11:** Transverse pointing resolution fit parameters, using the fit presented in Equation 11.3, and how they compare to the Physics Working Group values provided for the detector matrix.

the  $z$  and the  $r \cdot \varphi$  directions is assumed to be of  $150 \mu\text{m}$ . The implementation of each tile in simulation is based of the technology developed for the CLAS12 barrel Micromegas tracker [1252]: the material budget in the active area per each detector is about  $0.3\% X/X_0$ .

Figure 11.25 shows a possible configuration of the MPGD tracker where six layers have been grouped in three pairs. Several configurations have been investigated: one configuration with six layers equally spaced at regular radial intervals, one with three pairs of

Interval	PWG values [ $\mu\text{m}$ ]	Fit 1.5 T [ $\mu\text{m}$ ]	Fit 3.0 T [ $\mu\text{m}$ ]
$-3.5 \leq \eta \leq -2.5$	N/A	$A = 596.9 \pm 1.5, B = 41.05 \pm 0.12$	$A = 596.5 \pm 1.5, B = 40.79 \pm 0.12$
$-2.5 \leq \eta \leq -1.0$	$A = 100, B = 20$	$A = 78.3 \pm 0.2, B = 3.11 \pm 0.02$	$A = 78.1 \pm 0.2, B = 3.12 \pm 0.02$
$-1.0 \leq \eta \leq 1.0$	$A = 30, B = 5$	$A = 23.2 \pm 0.1, B = 2.64 \pm 0.01$	$A = 22.9 \pm 0.1, B = 2.64 \pm 0.01$
$1.0 \leq \eta \leq 2.5$	$A = 100, B = 20$	$A = 78.3 \pm 0.2, B = 3.11 \pm 0.02$	$A = 78.1 \pm 0.2, B = 3.12 \pm 0.02$
$2.5 \leq \eta \leq 3.5$	N/A	$A = 596.9 \pm 1.5, B = 41.05 \pm 0.12$	$A = 596.5 \pm 1.5, B = 40.79 \pm 0.12$

**Table 11.12:** Longitudinal pointing resolution fit parameters, using the fit presented in Equation 11.3, and how they compare to the Physics Working Group values provided for the detector matrix.

$\eta$ interval	Min- $p_T$ , 1.5 T	Min- $p_T$ , 3.0 T
$-3.0 \leq \eta \leq -2.5$	100 MeV/c	150 MeV/c
$-2.5 \leq \eta \leq -2.0$	130 MeV/c	220 MeV/c
$-2.0 \leq \eta \leq -1.5$	70 MeV/c	160 MeV/c
$-1.5 \leq \eta \leq -1.0$	150 MeV/c	300 MeV/c
$-1.0 \leq \eta \leq 1.0$	200 MeV/c	400 MeV/c
$1.0 \leq \eta \leq 1.5$	150 MeV/c	300 MeV/c
$1.5 \leq \eta \leq 2.0$	70 MeV/c	160 MeV/c
$2.0 \leq \eta \leq 2.5$	130 MeV/c	220 MeV/c
$2.5 \leq \eta \leq 3.0$	100 MeV/c	150 MeV/c

**Table 11.13:** Minimum reconstructable  $p_T$ , using simple Kalman filter reconstruction algorithm, for different pseudorapidity intervals. This study is done using the silicon plus TPC baseline layout.

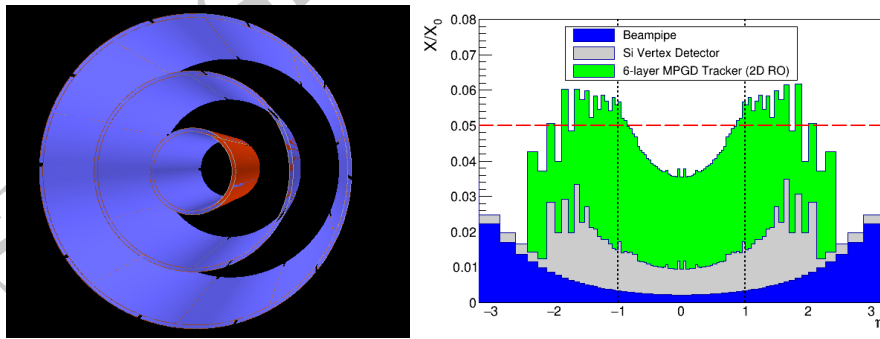


**Figure 11.25:** (left) A possible configuration of the cylindrical MPGD tracker with three pairs of layers. (right) The stack plot of the material budget for the hybrid detector with a six layer MPGD tracker: in blue the contribution of the beam pipe, in gray the silicon vertex detector and in green the MPGD tracker contribution.

layers (inner, middle and outer pairs) and a configuration with two layers in the middle and four layers in the outer part of the barrel. Table 11.14 shows the radial position of the layers for the last two configurations.

Layer	Radial position
0 inner	198 mm
1 inner	217 mm
2 middle	477 mm
3 middle	496 mm
4 outer	719 mm
5 outer	736 mm
6 outer	756 mm
7 outer	775 mm

**Table 11.14:** Radial position of MPGD tracker layers.

Studies of relative momentum resolution have been performed by simulating ten thousand  $\pi^-$  per momentum bin at an angle of  $66^\circ$  with a magnetic field of 1.5 T. The polar and azimuthal angular resolutions have been evaluated at a radius of 81.5 cm, where PID detectors will be placed. The results shown in Figure 11.26 are compared with resolutions obtained with the ideal TPC hybrid detector. Given the equivalent reduced number of measuring position of the MPGD tracker with respect to the TPC, the relative momentum resolution of the former is higher than latter. It is interesting to note, that the configuration “2-middle 4-outer” shows a better momentum resolution likely due to the bigger lever arm relative to the silicon detector and with the reduced material budget closer to the silicon detector. The angular resolutions results show similar behaviors for all the tested configurations.

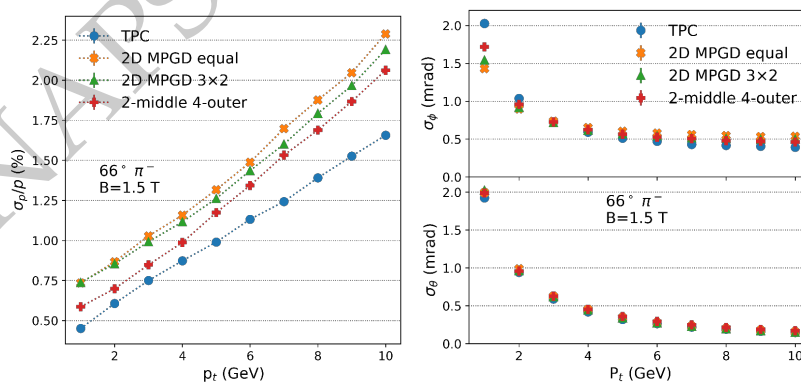


**Figure 11.26:** (left) Relative transverse momentum resolution. (right) Angular resolution at 81.5 cm.

A study has been made combining the baseline hybrid silicon vertex tracker (as described in Section 11.2.6) with a “three pair” MPGD layer layout, as shown in Figure 11.25. The

study is made in the central region ( $-1 \leq \eta \leq 1$ ) with a 1.5 T field, in a transverse momentum range of 0 to 30 GeV/c. Fitting the resulting resolutions with the equations shown in Equation 11.3, the following results are obtained;

- Relative momentum resolution:  $A = 0.1 \pm 0.01$ ,  $B = 0.92 \pm 0.02$
- Transverse pointing resolution:  $A = 18.5 \pm 0.2$ ,  $B = 2.5 \pm 0.01$
- Longitudinal pointing resolution:  $A = 26.5 \pm 0.2$ ,  $B = 2.8 \pm 0.02$

When compared to the PWG requirements, these results echo those presented in Section 11.2.6; the pointing resolutions exceed the requirements, but the relative momentum resolution does not meet the requirements over most of the momentum interval. It does however exceed them at  $p_T \leq 3$  GeV/c.

### Hadron & Electron End Cap: MPGDs

The tracking in the forward region of the hybrid configuration is composed of two large-area GEM stations, the inner forward GEMs and the outer forward GEMs, with each station made of three disks of triple-GEM detectors as shown in a standard BEAST detector geometry in Fig. 11.27 (left). Using the EicRoot simulation framework, we have studied the impact of inner and outer GEMs on the momentum resolution and the number of hits available for track fitting as a function of particle scattering angle and particle momentum. The simulated detector components include the beam pipe, the vertex and forward silicon

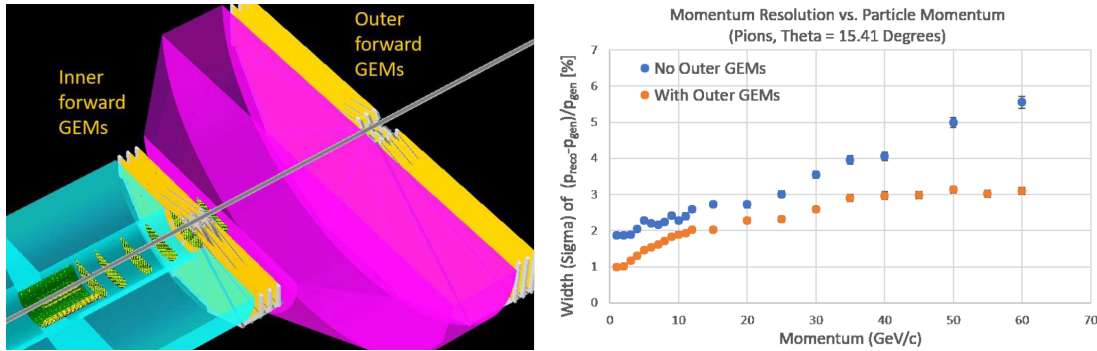


**Figure 11.27:** *Left:* Simulated BeAST geometry with outer forward GEM detectors. *Right:* Momentum resolution vs. momentum for pions at fixed scattering angle  $\theta = 15.41^\circ$  ( $\eta = 2.0$ ) with (orange) and without (blue) outer forward GEMs.

trackers, the time projection chamber (TPC), the inner forward GEM station, the ring imaging Cerenkov (RICH) detector gas volume, and the outer forward GEM station behind the RICH. Specifically, the impact of the outer GEM detector on the tracking performance is

studied by comparing the performance of the BeAST detector in the standard configuration with only the inner GEMs against the configuration including the outer GEMs while varying the particle parameters (scattering angle and momentum). Here, it is assumed that the detector would operate with a 1.5 T B-field. The scattering angle  $\theta$  is varied from  $5^\circ$  to  $75^\circ$ . The outer GEMs impact performance within their angular acceptance of  $5^\circ < \theta < 35^\circ$  ( $3.1 > \eta > 1.15$ ). The dimensions of the outer GEMs in these simulations are chosen to closely match the acceptance of the inner GEMs.

Fig. 11.27 (right) shows the momentum resolution as a function of momentum while keeping the scattering angle fixed at  $\theta = 15.41^\circ$  ( $\eta = 2.00$ ). It demonstrates that the significant improvement from outer GEMs holds over a large momentum range from 1 - 60 GeV/c. From the results shown in Fig. 11.28 (left), it is clear that the outer GEMs significantly improve the momentum resolution, particularly for small scattering angles where the improvement reaches a factor of two. The particular structure of the graph is presumably due to the varying number of hits on the individual detectors. In order to verify this, we plot the average number of hits in each tracking subdetector as a function of  $\theta$  in Fig. 11.28 (right). Over the full  $5^\circ < \theta < 35^\circ$  acceptance region of the outer forward GEM, both inner and outer GEM subdetectors provide a constant number of hits while the number of TPC hits drops rapidly below  $\theta = 15^\circ$  and the number of vertex hits is down to one hit below  $\theta = 18^\circ$ . In this angular range, the number of forward Si hits is comparable to the number of hits in each GEM subdetector. The design of the two GEM subdetector is very similar, so adding the outer forward GEM doubles the total number of GEM hits in this region. The forward Si detector, inner GEMs, and outer GEMs each contribute roughly a third to the total number of track hits in this region. This explains the significant impact of the outer forward GEM in the angular range below  $\theta = 15^\circ$  ( $\eta > 2$ ).

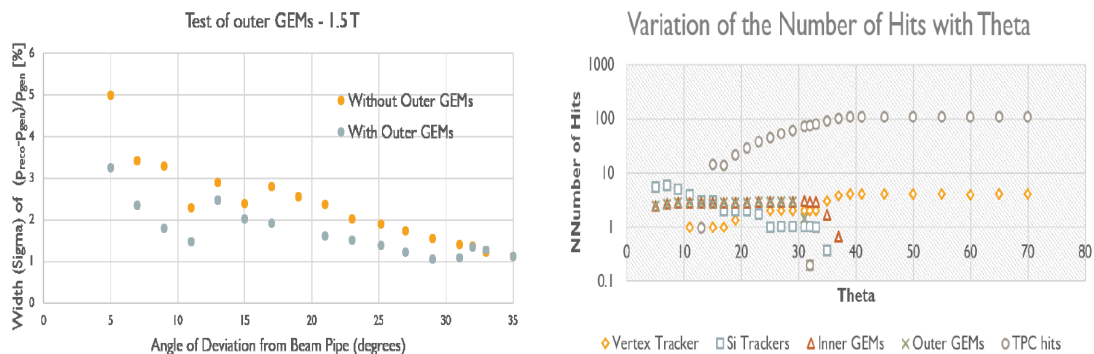


**Figure 11.28:** *Left:* Momentum resolution vs. scattering angle  $\theta$  for 10 GeV/c pion tracks from simulation of the standard BeAST detector with (gray) and without (orange) outer forward GEMs added. *Right:* Average number of hits in each tracking subdetector vs. scattering angle Theta.

## 11.2.7 Fast tracking Layers & Additional PID detectors

### Fast Signal & High Resolution MPGDs for DIRC in the Barrel Region

For the scenario where a TPC is chosen as the central tracker option for the EIC detector and MAPS technology is adopted as the vertex tracker, we have identified three strong motivations for the need of a high-precision and fast-signal tracking detector to complement the inherent limitations of the TPC + MAPS as main tracking detectors in the barrel region.

**High angular resolution tracking layer for the barrel PID detector:** Particle identification at an EIC is going to be critical. High angular tracking resolution will improve the effectiveness of the PID detectors, in particular the DIRC and RICH detectors. We have studied the impact that our fast cylindrical  $\mu$ RWELL trackers would have on the angular tracking resolution in the central region.

We simulated a detector setup within the EicRoot framework, which implemented a silicon vertex tracker, TPC, and cylindrical  $\mu$ RWELL trackers [1274]. The study was performed with  $\pi^-$  particles in a 1.5 T magnetic field for scattering angles of  $43^\circ$ ,  $66^\circ$ , and  $89^\circ$  over a momentum range of 1 to 7 GeV. We find an improvement in the angular resolution of tracks entering and exiting the DIRC when cylindrical  $\mu$ RWELL layers are located in front and behind the DIRC [1274]. The simulation studies demonstrate that the two layers configuration surrounding the DIRC detector will improve the PID detector performances, and help aid in achieving the required  $3\sigma$   $\pi/K$  separation at 6 GeV.

**High space point resolution tracking layer for TPC field distortions correction/calibration:** In addition to providing the angular resolution information to the DIRC detector, cylindrical  $\mu$ RWELL layers will also provide precision tracking to calibrate the TPC tracks and help correct for well known "scale distortions" of TPC tracks. For this case, the optimal configuration will be two cylindrical  $\mu$ RWELL layers, the first inside the TPC inner field cage and the second outside. We are performing simulation studies for the two-layers configurations to evaluate the performances.

**Fast tracking layer to complement slow TPC and MAPS detector** Both TPC and MAPS technologies are slow detectors and having an additional fast tracker with a timing resolution of a few ns will be required to provide the bunch crossing timing information to the reconstructed vertex as well as central tracks.  $\mu$ RWELL detector technologies provides the timing resolution needed to satisfy these requirements

### MPGD-based-TRDs for Electron PID and Tracking in the End Caps

Identification of secondary electrons plays a very important role for physics at the Electron-Ion Collider (EIC).  $J/\psi$  has a significant branching ratio for decays into leptons (the branching ratio into electrons ( $e^+e^-$  pair) is 6%). The branching ratio of D-mesons is  $\text{Br}(D^+ \rightarrow e + X) \sim 16\%$  and the branching ratio of B-mesons is  $\text{Br}(B^\pm \rightarrow e + \nu + X_c) \sim 10\%$ . Electron identification is also important for many other physics topics, such as

spectroscopy, beyond the standard model physics, etc. By using more sophisticated electron identification an efficiency of those channels could be increased. A high granularity tracker combined with a transition radiation option for particle identification could provide additional information necessary for electron identification or hadron suppression. Due to asymmetric beam energies and boosted kinematics, it is important to provide such additional instrumentation in the hadron endcap. The basic concept of GEM-based TRD is

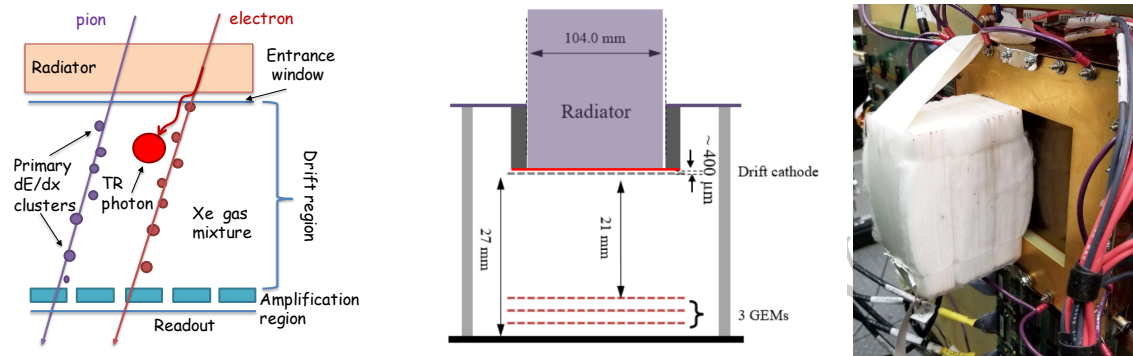


**Figure 11.29:** The concept of GEM-based TRD (left), the prototype scheme (middle), prototype in testbeam setup (right)

shown on the Fig. 11.61. A standard triple-GEM detector [1247] with high granularity strip pitch ( $400\ \mu\text{m}$ ) capable of providing high resolution space point position information was converted into a transition radiation detector and tracker (GEM-TRD/T) [1275]. This was achieved by making several modifications to the standard GEM tracker. First, since heavy gases are required for efficient absorption of X-rays, the operational gas mixture has been changed from an Argon based mixture to a Xenon based mixture. Secondly, the drift region also needed to be increased from  $\sim 3\ \text{mm}$  to 20-30 mm in order to detect more energetic TR photons. Then to produce the TR photons, a TR radiator was installed in front of the GEM entrance window. Finally, the standard APV25 GEM readout electronics was replaced with faster electronics based on flash ADC (FADC) [1276] and developed for JLab HallD GlueX Drift Chambers. A GEANT4 simulation and optimized the radiator and detector thicknesses for a single chamber (Fig. 11.61) has been performed. G4XTRGammaRadModel model was used for a fleece radiator, which could be simulated in GEANT4 as an irregular type of radiator with a certain density and two parameters ( $\alpha_1, \alpha_2$ ), which define a spread of materials and air-gaps within a radiator. Due to the self-absorbing property of the radiator, soft photons (3-6 keV) generated within first few centimeters of the TR-radiator will be absorbed, leading to an increase in the hard X-ray photon spectrum at the exit from a radiator. A thin layer of gas in Xe-based detector will not be effective at detecting hard X-ray photons. As one could see in Fig. 11.63 (left), rejection power is saturated after 22cm of radiator for our GEM detector with 21mm gas thickness, including  $400\ \mu\text{m}$  of dead gas layer in front. Experimental data points (stars) shows a good agreement with MC projections. A TRD needs information about the ionization along the track, to discriminate TR photons from the ionization of the charged particle. The GEM-TRD/T prototype used a precise (125 MHz, 12 bit) FADC [1276] coupled with fast shaper pre-amplifiers, developed

at JLAB, with a VME-based readout. The FADCs have a pipeline readout window of up to  $8 \mu\text{s}$ , which covers the entire drift time (500ns) of the GEM-TRD/T prototype and gives a room for HV scan. The pre-amplifiers used GAS-II ASIC chips to provide  $2.6 \text{ mV/fC}$  amplification with a peaking time of 10 ns. For the  $e/\pi$  rejection factor the amplitude and

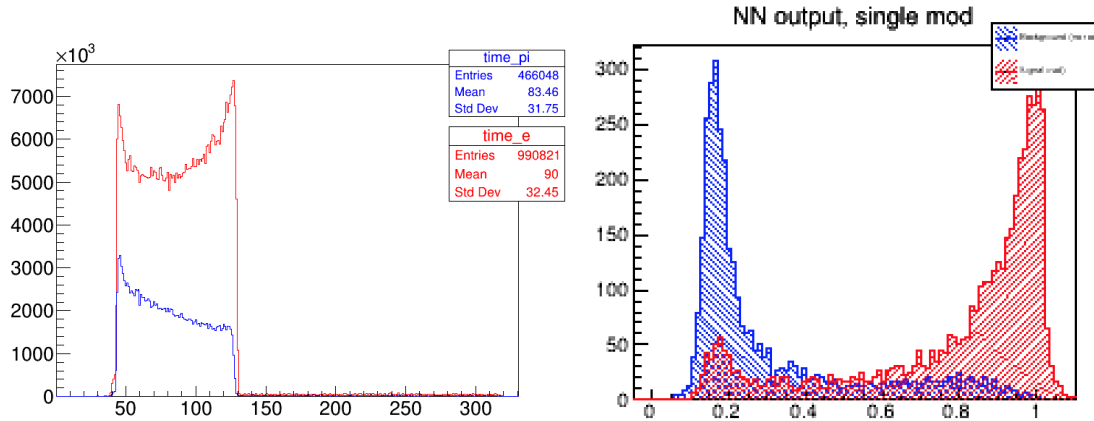


**Figure 11.30:** Left plot shows average energy deposition along the drift time (x-axis in fADC time-bins). Right plot is output from Neural Network, showing the separation between electrons and pions.

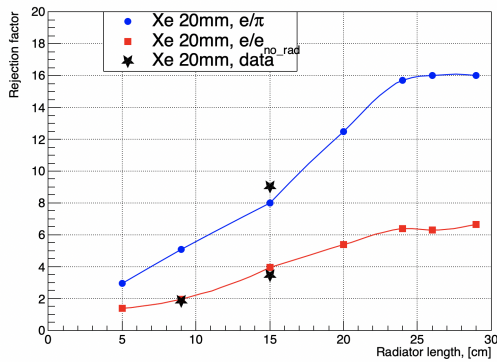


**Figure 11.31:** Rejection vs. TR-radiator thickness.

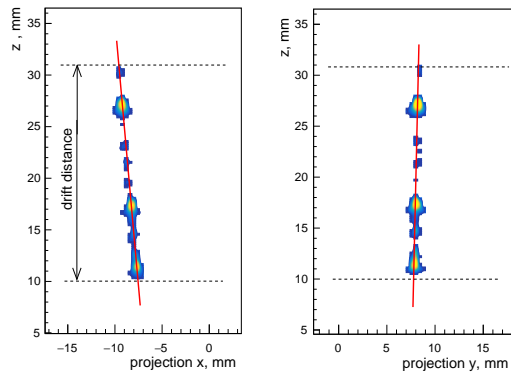


**Figure 11.32:** Single track reconstruction.

arrival time of each individual cluster along the drift time were analyzed. All this information (up to 20 variables) was used as input for likelihood and artificial neural network (ANN) programs, such as JETNET or ROOT-based (Multi-layer Perceptron). The ANN system was trained with MC or data samples of incident electron and pions. Then an independent sample was used to evaluate the performance. An example of such a training procedure is shown in Fig. 11.62. A 90% efficiency for our electron identification was required. The neural network output for  $e/\pi$  rejection is shown Fig 11.63. As one could see, with a 15cm radiator rejection factor ca. 9 could be achieved.

As for tracking aspects, a standard GEM plane can only provide the 2D X-Y position of a track, while the GEM-TRD/T with increased drift volume and with Flash ADC readout allows for 3D track segments to be reconstructed as in  $\mu$ -TPC configuration. In the hadron end cap region, in addition to the  $e/\pi$  rejection capabilities, GEM-TRD track segment behind dRICH could be used to:

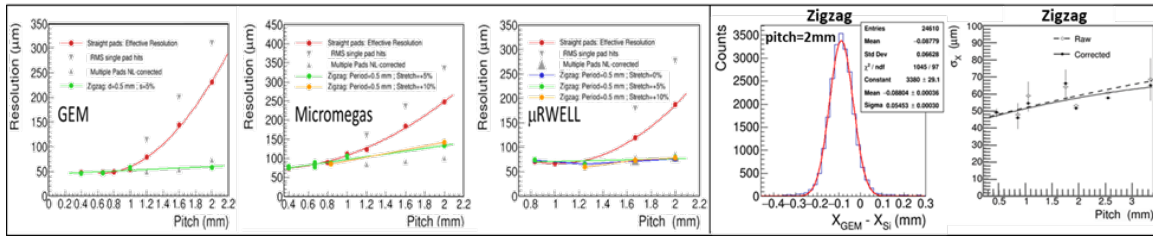
- measure a track angular resolution and therefore help to improve dRICH performance;
- correct for a multiple scattering before EMCAL and improve tracking performance for charged particles.
- improve pointing track resolution and cluster-seed position measurements for EMCAL
- could be used as a seed-element for a track finding algorithms.

Figure 11.64 shows projections of a typical 3D reconstructed track from the GEM-TRD/T prototype. The left panel shows the track projection in XZ plane with Z the drift time as a function of the cluster position in the X direction. The right panel shows corresponding projection in YZ plane.

### Readout structures for MPGDs

#### Zigzag Shaped Charge Collection Anodes

The segmentation of the readout plane for MPGDs can play a critical role for the detector performance, especially for the spatial and angular resolution and should be seriously considered for future experiments. To improve the resolution, a typical strategy is to simply reduce the pitch of the anodes, but this comes at the cost of greater instrumentation. As an alternative, highly interleaved anode patterns, such as zigzags offer relatively coarse segmentation, while preserving performance [1277] [1278]. By optimizing the three main operant geometric parameters of the zigzag (including the pitch, the periodicity of the zigzag, and the degree of interleaving, here referred to as the “stretch” parameter), charge sharing among neighboring pads or strips may be finely tuned for specific avalanche schemes. The left panel of Fig. 11.33 compares the resolution as a function of the pitch for standard straight strips and various zigzag parameters for GEM, Micromegas, and  $\mu$ RWELL detectors. In all cases, the position resolution is comparable below a pitch of 1mm, but the resolution quickly degrades for straight strips at larger pitch. This is mainly due to poor charge sharing, where the majority of charge is collected by a single pad. An equally beneficial feature of zigzags is the ability to maintain a highly uniform and linear response across the full detector acceptance. The “out of the box” detector response of optimized zigzag anodes is shown in the right panel of the figure, which includes a purely Gaussian raw residual distribution, without the need for pad response functions, as in the case of straight strips. Ultimately, in situations where the detector occupancy is fairly low and a



**Figure 11.33:** Left panel: Position resolution vs. pitch for straight strip and zigzag shaped anodes in GEM, Micromegas and  $\mu$ RWELL detectors respectively. The resolution for straight strips is corrected using pad response functions, however the raw resolutions are quoted for the zigzags. The resolution for the straight strips is broken down into regions of the readout dominated by single and multi-pad clusters (grey points), where the red points denote the weighted average. Right panel: Residual distribution for zigzag anodes with pitch = 2 mm, period = 0.4 mm, and stretch = 0 % and a plot of the position resolution vs. pitch in the case of a 4-GEM detector, respectively.

relatively coarse readout segmentation is acceptable, zigzag shaped charge collection anodes provide a very efficient means of encoding high resolution positional information, with values remaining below  $65 \mu\text{m}$  for a pitch as large as 3.3 mm as indicated in the right-hand plot.

## 11.2.8 Integration issues

## 11.2.9 Material Budget Considerations

As is clear from the requirements, the silicon tracking layers require a very low material budget per layer/disc and this need for low mass material budget in the acceptance extends to the surrounding detectors. In order to assess the balance of mass that contributes to the overall load, one needs to make an estimate of the additional material in the fiducial volume that is associated with the tracking detectors. The material budget for the tracking detector is dependent on the parameters of the silicon sensors used, the architecture of the services (powering, readout, cooling, monitoring, safety interlocks, etc.) employed in the deployed detector design and the design and composition of the mechanical support structures used for precisely locating the tracking detector in the main detector volume. A reasonable starting point for estimating the services load is to start with existing technology and powering/readout architectures and project what could be expected should we adopt what has been accomplished. The current state of the art tracking detector of similar characteristics (MAPS sensors,  $10/m^2$  of silicon area) is the recently upgraded ALICE ITS. As part of the EIC User Group Yellow Report activities, the service loads have been estimated and parameterized [1237]. These estimates have been scaled for what can be expected for a detector system based on the ITS3 sensor which is currently under development [1235]. These parameterizations are currently being added to the simulation efforts for the EIC silicon detector baseline detector configurations so that the effects of these mass loads on the physics measurements can be assessed. The largest mass in the

services, by far, is the power supply and return cabling. This can be addressed in multiple ways. The most obvious avenue to explore is reducing the power required by the sensors. This is under investigation. An EIC sensor based on the ITS3 type development is expected to reduce the power needed by half to a dissipation of  $20 \text{ mW/cm}^2$ . This helps, but as the voltage supplied to the sensors is also reduced from 1.8V to 1.2V, to maintain the cable voltage drops to manageable levels, a significant fraction of the conductor is still required. It is possible to reduce the radiation length of the power cabling by moving to copper clad aluminum conductors. This can help significantly since the  $X_0$  of copper is a factor of  $\tilde{6}$  lower than the  $X_0$  of aluminum. Using aluminum conductors unfortunately comes at a cost in space required by the services since the conductivity of aluminum is 65% that of copper. Other options would include significantly reducing the number of required conductors to power the detector. This could be addressed by either serial powering of detector staves, or the integration of radiation tolerant DC-DC converters at the staff ends [1279]. Both of these options require exploration and R&D to become viable. The readout cabling is also a significant load. It could be possible to combine staff outputs and multiplex the data from multiple staves on detector for readout over high speed fiber optical connections. The multiplexing circuitry and fiber optic drivers would need to be radiation tolerant. In addition, this reduction in the readout granularity would lead to larger portions of the detector becoming inactive in the case of single point failures in the multiplexing and fiber circuits. Clearly an optimization using these factors will need to be carried out. This is also an area for targeted R&D. The reduction in the sensor power dissipation using ITS3 like sensors would significantly help the cooling requirements so smaller and possibly fewer lines could be used. Air cooling is also a possibility, but the envisioned detector is very compact and arranging proper flow and ducting would require careful study. For the detector safety system sensors and environmental monitors, it is likely that the level of services would be similar to what is seen in the ALICE ITS.

### 11.3 Particle Identification

All multi-purpose detectors, for example as illustrated in Figure 11.34, contain systems that work symbiotically toward achieving the physics goals. Among these detector systems is the subset that identifies the species of collision ejectiles commonly known as Particle Identification Detectors or PID. Typically, the tracking systems provide a momentum measurement ( $\vec{p} = m\gamma\vec{\beta}$ ) which when combined with information on velocity ( $\vec{\beta}$ ) is sufficient to distinguish the various particle species. Most often "PID" refers to the separation of  $\pi$ ,  $K$ , and *proton* whereas eID refers to the identification of electrons. This section discusses each of these two topics, the requirements for EIC, and possible technological implementations necessary to achieve the physics goals.

The two basic approaches to PID are the direct measurement of the particle's velocity (known as Time-of-Flight or "TOF") and the measurement of velocity dependent interactions of the particle with the detector. Four common velocity-dependent detector interactions are:

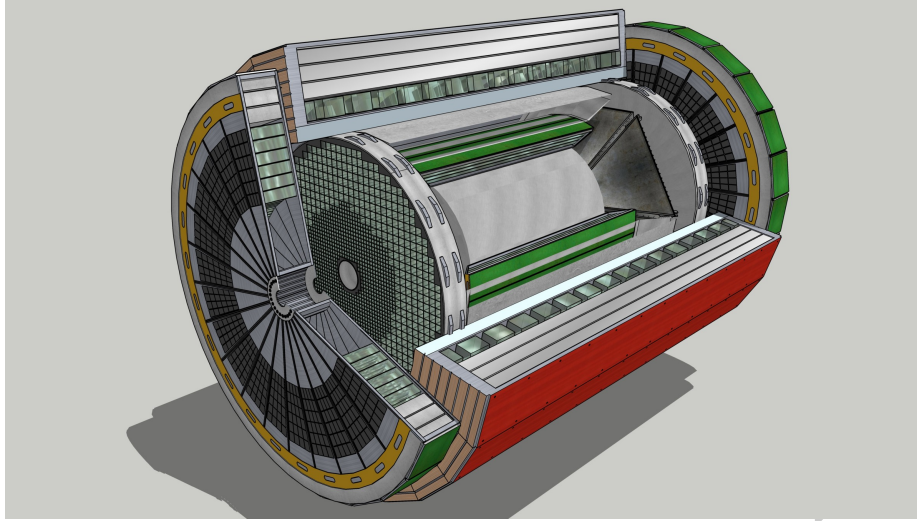


Figure 11.34: Conceptual detector cutaway figure.

- Specific Ionization (aka  $\frac{dE}{dx}$ ), wherein the rate of energy deposit (typically left in a gaseous medium) is measured precisely.
- Cerenkov Radiation, wherein the angle of Cerenkov photon production depends upon velocity as  $\cos(\theta_C) = \frac{1}{n\beta}$ .
- Bremsstrahlung, wherein the power dissipated to braking radiation goes as  $P = \frac{q^2\gamma^4}{6\pi\epsilon_0c} \left( \dot{\beta} + \frac{(\vec{\beta} \cdot \ddot{\beta})^2}{1-\beta^2} \right)$
- Transition Radiation (TR), wherein the intensity of transition radiation goes as  $I = \frac{Z^2e^2\gamma\omega_p}{3c}$ .

Bremsstrahlung is the effect by which eID is accomplished in an electromagnetic calorimeter. The calorimetry requirements for EIC are discussed in Section 11.4 and will not be additionally discussed here. The velocity necessary to produce sufficient transition radiation is high enough that at EIC a Transition Radiation Detector (TRD) should be considered specifically as an eID device. The velocity dependence of  $\frac{dE}{dx}$  and the Cerenkov Effect are highlighted in Figure 11.35 are suitable for PID and eID applications.

### 11.3.1 Physics Requirements

As described in part 2 in this report, simulations of collisions for an extensive list of physics processes, each spanning the  $\sqrt{s}$  anticipated at EIC have been performed. As an example, Figure 11.36 displays an overview of electron and hadron production as a function of particle lab momentum and polar production angle. The full suite of such calculations were considered and used to formulate the so-called "Requirements Matrix" that specifies

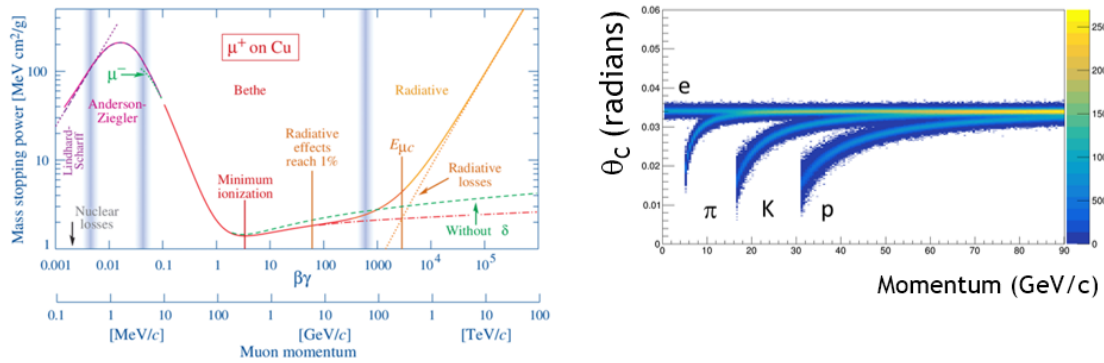


Figure 11.35: Physics of PID devices.

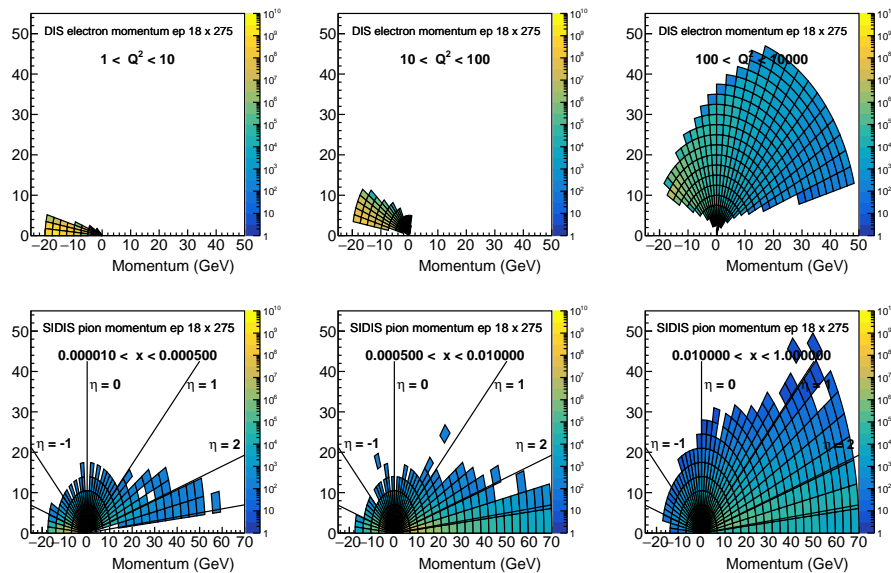


Figure 11.36: SIDIS electron and pion kinematics. This calculation and others were used to establish the detector requirements.

relevant detector performance parameters as a function of  $\eta$ . A successful detector design is any that satisfies the detector performance requirements. The PID-relevant subset of the detector matrix is shown in Figure 11.37.

In the following sections we discuss the performance characteristics of multiple suitable detector technologies for the final EIC detector. Following that we discuss how these technologies can be arrayed to best address the requirements matrix.

$\eta$	$\theta$ (mrad)	Nomenclature	Electrons and Photons			$\pi/K/p$		
			Resolution $\sigma_r/E$	PID	min E photon	p-Range (GeV/c)	Separation	
-4.0 to -3.5			not accessible					
-3.5 to -3.0								
-3.0 to -2.5								
-2.5 to -2.0								
-2.0 to -1.5								
-1.5 to -1.0		Backward Detector	1%/E $\oplus$ 2.5%/√E $\oplus$ 1% (for 40 cm space)	$\pi$ suppression up to 1.1E-4	20 MeV	≤ 10 GeV/c	≥ 3 $\sigma$	
-1.0 to -0.5								
-0.5 to 0.0								
0.0 to 0.5								
0.5 to 1.0		Barrel	2%/E $\oplus$ (12-14)%/√E $\oplus$ (2-3)% for 30 cm space A better stochastic term can be achieved with more space: 2.5% with crystals 35cm 10% sampling 40cm 4% SciGlass 65cm *Better resolution requires ~65 cm space allocated )	$\pi$ suppression up to 1.1E-2	100 MeV (50 MeV if higher resolution)			
1.0 to 1.5								
1.5 to 2.0								
2.0 to 2.5								
2.5 to 3.0								
3.0 to 3.5								
		Forward Detector	2%/E $\oplus$ (4-12)%/√E $\oplus$ 2% Upper limit achievable with 40cm space *Better resolution requires ~65 cm space allocated	3 $\sigma$ e/ $\pi$ up to 15 GeV/c	50 MeV	≤ 50 GeV/c (worse approaching 3.5)		

Figure 11.37: Detector performance matrix only for PID.

### 11.3.2 $\frac{dE}{dx}$

Although many tracking detector configurations are possible (as described in section 11.2), Figure 11.38 captures well two of the leading options. The left panel “hybrid” option includes a Time Projection Chamber (TPC) as its outer layer, which may provide PID information via  $\frac{dE}{dx}$ . It is thus important to understand the limits of such devices.

At EIC, available space is at a premium, partly due to the longitudinal limit of  $\pm 4.5$  meters in Zed. This limit propagates naturally into a radial restriction in the barrel if one chooses the most natural interface between barrel and endcap devices at roughly  $45^\circ$  or  $\eta \sim \pm 1.0$ . Given available space, tracking is generally limited to a radii extend of roughly 1 meter, which is significantly smaller than common TPCs such as STAR (2m) and ALICE (2.5m). It is thus, important to work to achieve excellent  $\frac{dE}{dx}$  performance in a small distance.

The primary challenge in any  $\frac{dE}{dx}$  measurement comes from the process of energy loss being two steps. Each locus of ionization is independent of its neighbors and therefore the rate of primary ionization follows Poisson statistics. This rate is typically captured by the parameter  $N_p$  which counts the primary ionization sites per unit length (usually expressed as  $\frac{\text{primary}}{\text{cm}}$ ). Unfortunately, primary electrons are often released with sufficient energy to generate several secondaries making a so-called “cluster” of ionization. The total ionization is characterized by  $N_t \frac{\text{total}}{\text{cm}}$  and follows a probability distribution with a long “Landau tail”. Battling the resolution loss due to the Landau tail is the primary challenge for any PID detector.

The traditional method of addressing the Landau is to make many independent samples

of the ionization and perform either a fit to the  $\frac{dE}{dx}$  probability distribution or via a so-called "truncated mean" calculation. An improvement recently suggested and tested by sPHENIX for EIC applications is to use a gas that has an intrinsically small ratio of  $\frac{N_t}{N_p}$  so that the fundamental ionization statistics are closer to Poisson. The left panel of Figure 11.39 shows a comparison of STAR  $\frac{dE}{dx}$  (72 samples, 150 cm,  $\frac{N_t}{N_p} = 3.9$ ) to a small sPHENIX prototype (48 samples, 60 cm,  $\frac{N_t}{N_p} = 2.3$ ) as measured in test beam. By clever gas choice, similar performance is indeed achieved in a much smaller device. The right panel shows a simulation of performance assuming that one can count explicitly the individual clusters of ionization and thereby approach the limit of Poisson statistics. Such a device might be rather attractive for EIC, but requires further R&D to demonstrate its efficacy in sort length applications such as required for EIC.

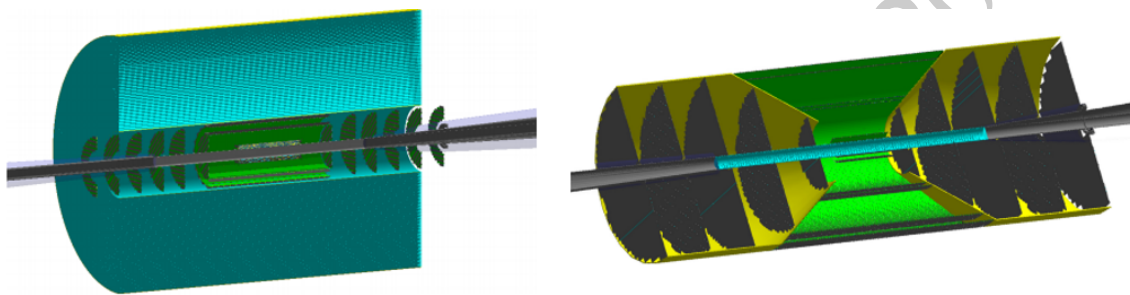


**Figure 11.38:** Two tracking options. The left panel denotes the "hybrid" option of a silicon tracker to small radius with accompanying TPC, while the right panel denotes an all-silicon tracking option.

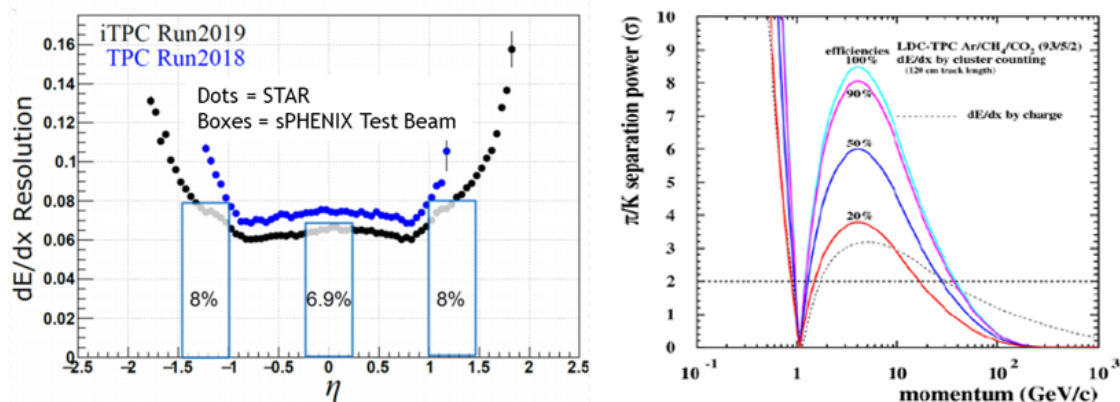


**Figure 11.39:** Comparison of STAR  $\frac{dE}{dx}$  resolution with sPHENIX Test Beam and simulation of a "cluster-counting" detector.

### 11.3.3 Cerenkov

The measurement of the emission angle of Cerenkov photons is a powerful PID technique with a tunable dynamic range. Because the Cerenkov angle depends upon velocity as  $\cos(\theta_C) = \frac{1}{n\beta}$ , one is able to accomplish PID at the highest momentum using the lowest index of refraction,  $n$ . There are two penalties for choosing low  $n$ . First, with lower index, the Cerenkov threshold  $\beta > \frac{1}{n}$  goes up, resulting in non-detection of low momentum particles. Second, with lower index, the photon yield per unit length  $\frac{dN_\gamma}{dL} = 2\pi\alpha \sin^2(\theta_C) \int \frac{d\lambda}{\lambda^2}$ , goes down resulting in long radiators. As a result, Cerenkov detectors must be carefully tuned to the required physics. Because the momentum range needs at EIC (Figure 11.37) vary significantly with  $\eta$  it is necessary to tune the radiator index differently in three regions called "electron endcap", "barrel", and "hadron endcap".

A subtle coupling between Cerenkov measurement and tracking resolution is illustrated in Figure 11.40. Because a Cerenkov detector rarely measures the trajectory of the track it is reliant upon the tracker to provide a direction vector of the track itself while the track passes through the radiator. The effect of a mistake is demonstrated by a simple Monte Carlo that assumes a certain track direction error  $\alpha$  as well as a certain photon yield. This simple calculation demonstrates that there is an effect of mismeasurement on the apparent Cerenkov angle and also that the magnitude of the effect depends upon the photon yield of the detector. It is therefore difficult to understand the requirements imposed by the PID device upon the tracker without a detailed Monte Carlo simulation. Detailed simulations have been performed for a number of configurations under consideration and are discussed below.

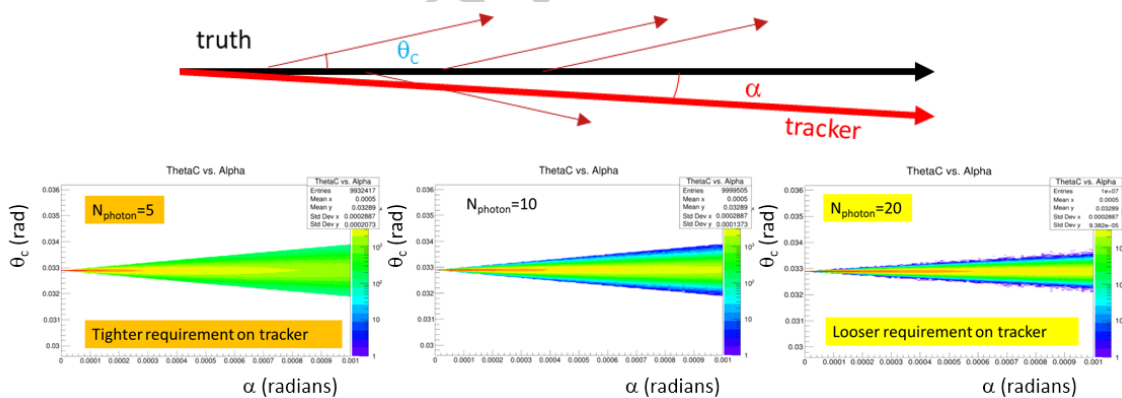


Figure 11.40: Affect of tracking resolution on apparent Cerenkov angle.

A variety of effects limit the precision of measurement of Cerenkov angle in any realistic device. These are listed and discussed here:

- **Chromaticity**

All materials suffer from an index of refraction that varies with wavelength ( $n(\lambda)$ ) thereby creating a photon-by-photon chromatic smearing of the Cerenkov angle. This effect is particularly acute near the transmission cutoff of the radiating medium.

- **Optical Aberration (aka "Emission Point Error")**

Even at normal particle-to-mirror incidence, a spherical mirror is just an approximation to a parabolic reflector. Furthermore, as the angle of incidence strays from the normal, optical aberrations increase. This effectively means that the location at which a photon is detected picks up a dependence on the place within the radiator at which the photon was emitted. It is therefore most often termed as an "Emission Point" Error.

- **Pixelation**

Cerenkov photons are detected individually and the finite pixel density of the focal plane readout detector thereby generates an uncertainty in the initial emission angle.

- **Magnetic Field**

Ideally the radiator medium for a Cerenkov radiator is free of magnetic field so that the particle direction is not changing as it propagates through the radiator medium. In a compact application like EIC this is often difficult to arrange and is sometimes approximated by attempting to minimize  $\vec{v} \times \vec{B}$  through careful adjustment of the magnetic field orientation. Imperfections necessarily generate uncertainty in the Cerenkov angle.

- **Tracking**

Finally, the Cerenkov angle resolution can be limited by the knowledge of the track direction as it traverses the radiator medium.

In the following sections, we'll discuss in detail several options for Cerenkov detector configurations that have been studied in the EIC context.

### Hadron Blind Detector (HBD)

An HBD device collects unfocused Cerenkov light and makes no attempt to focus the light so as to determine the Cerenkov angle. It is instead operated in a "Threshold Mode" wherein the fastest particles will radiate, making it suitable only for eID and not for PID. The PHENIX experiment was the first implementation of such a device. That implementation is shown in Figure 11.41. Pure  $CF_4$  gas ( $n=1.00056$ ) is used as a radiator. The transparency at low wavelength is leveraged to take advantage of the  $\frac{1}{\lambda^2}$  photon yield. As measured by the " $N_0$ " parameter (325), this is the brightest Cerenkov detector ever built.

A CsI photocathode is evaporated onto Gas Electron Multipliers (GEMs) and provides sensitivity to  $\lambda < 200nm$  and has a yield of 20 photon-electrons in 50 cm. In PHENIX, the device was optimized for distinguishing closed Dalitz pairs (40 p.e.) from isolated electrons (20 p.e.). It was not optimized for  $e/\pi$  separation and suffers from an ionization signal generated by any charged particle passing through the focal plane.

Simulations have been done on an alternative HBD implementation (HBD++) as is shown in Figure 11.42. Here the later GEM gain stages are replaced by  $\mu$ MEGAS detector(s) thereby minimizing the ionization signal from the charged particles. This results in a near

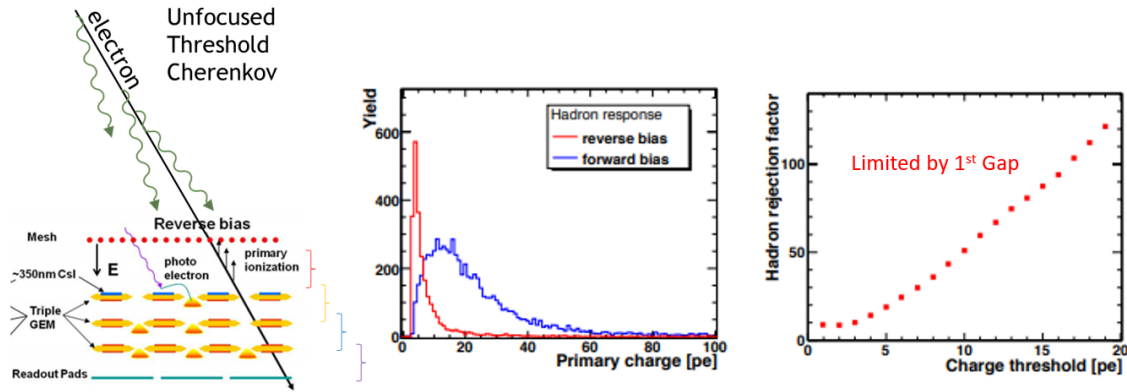


Figure 11.41: Configuration and performance of an HBD Detector in PHENIX.

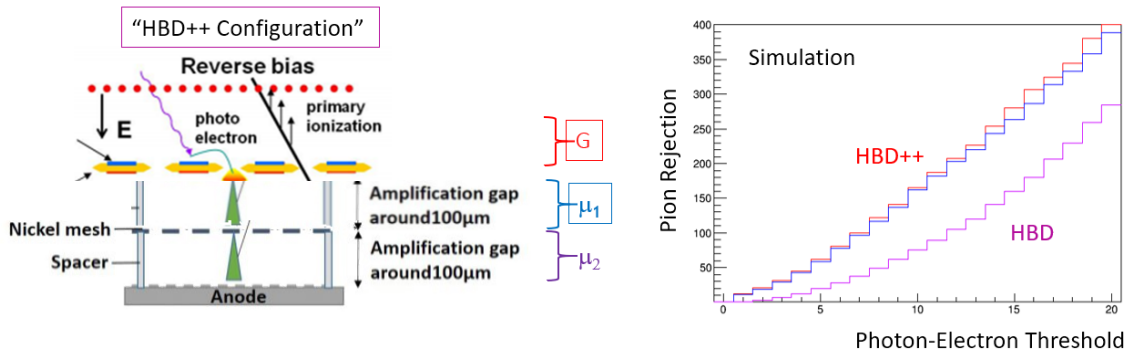


Figure 11.42: Simulated performance of a new HBD Configuration (HBD++).

doubling of the pion rejection provided by the device, but has never been proven in an actual implementation.

### CsI RICH

A corollary to the HBD design can be achieved by focusing the Cherenkov light into the focal plane and thereby enabling a measurement of the Cherenkov angle. This configuration mostly retains the brightness of the original HBD although there is additional light loss due to both the increased gas path length (round trip including the mirror). The concept benefits from the fact that the low material budget of the photon detector (GEMs) can be placed directly in the path of the particles at the entrance of the device. The design suffers, in two critical aspects:

- The low index results in a rather high threshold for pion and Kaon radiation. It must therefore be supplemented by an additional PID device to match the physics requirements.

- Use of the radiation gas down to the transparency cutoff results in a high distortion due to chromaticity.

A detector concept called "ePHENIX" (Figure 11.43) is what results from maximal reuse of sPHENIX detectors and accompanying devices placed in both end caps. The default configuration of this device uses a Cerenkov radiator with  $CF_4$  gas as described above. A prototype of this device was tested at Fermilab (Figure 11.44) with excellent  $\pi$ -K separation measured at 32 GeV/c and extrapolated 3- $\sigma$  performance to 60 GeV/c.

Figure 11.45 shows the result of a simulation in which the measured detector performance is parameterized and subjected to varying errors in track direction. Because the device is severely limited by "chromaticity" (wavelength-dependent index), this device has comparatively lax requirements on the tracking and is unaffected by track pointing errors of roughly 2 mrad or less.

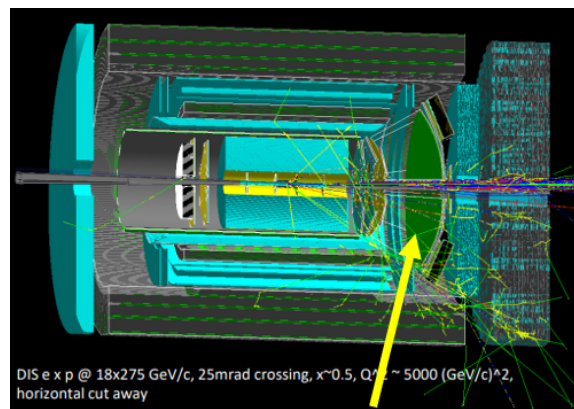


Figure 11.43: ePHENIX configuration of a gas Cerenkov.

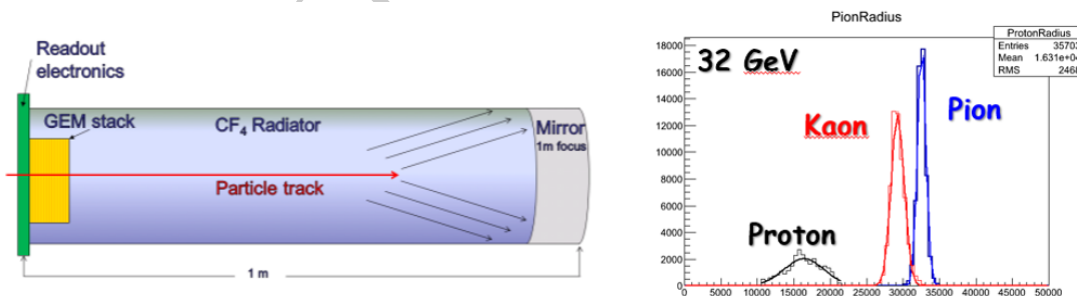


Figure 11.44: Test beam results for the GEM RICH.

In the ePHENIX implementation, the CsI RICH is complemented by mRICH detectors (see below) that compensate for the high Cerenkov threshold over some of the aperture. While somewhat effective, this design is not the most optimal for EIC at the highest momenta.

An alternative to the GEM-based photon detector, is represented by the hybrid MPGD photon detector in use since 2016 in COMPASS RICH [1]: two THick GEM (THGEM) multipli-

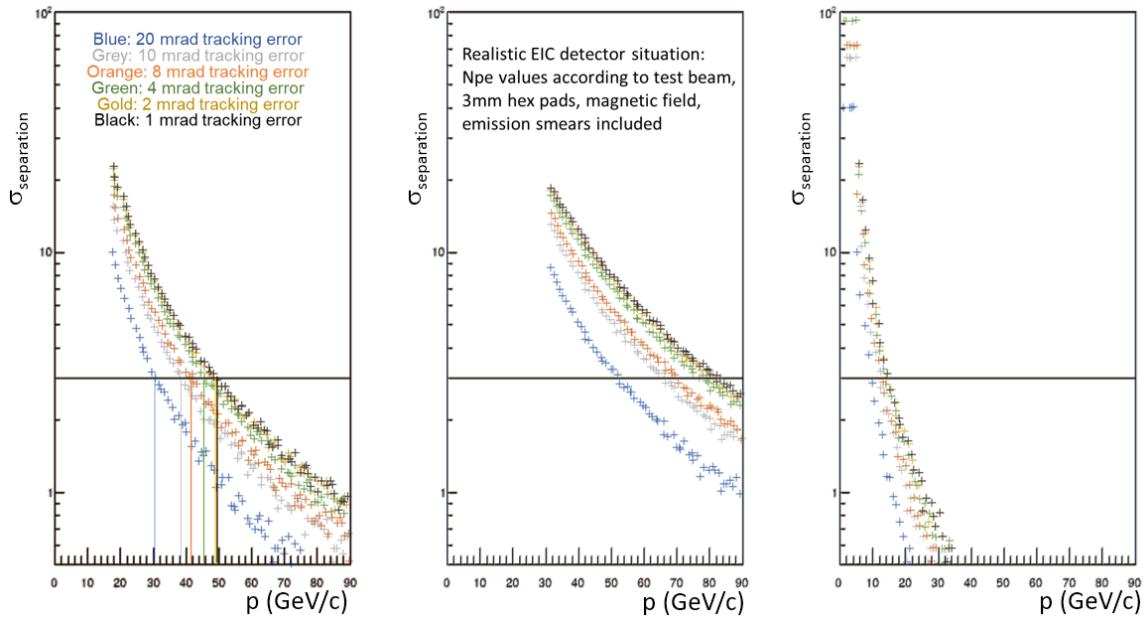


Figure 11.45: Simulation results for the GEM RICH.

cation layers, the first one coated with a CsI film and acting as photocathode are followed by a resistive MICROME GAS stage (Fig. 11.46). A reduced pad size is needed to match the compact configuration at EIC, where the gaseous RICH focal length is of the order of 1 m. A prototype with reduced pad-size from 8 mm to 3 mm has been designed, built and successfully beam tested (Fig. 11.47). Its operation in a window less configuration as the ePHENIX one has to be confirmed.

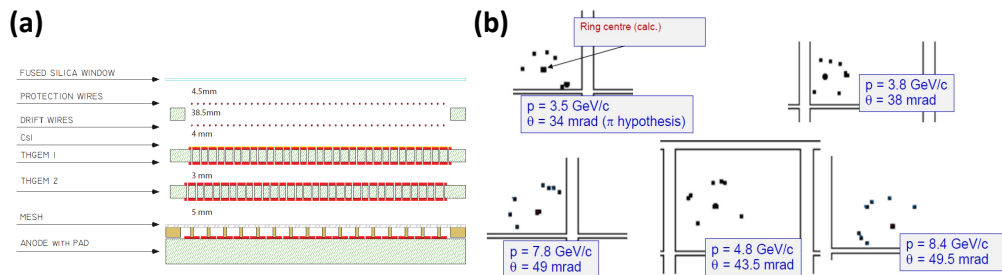
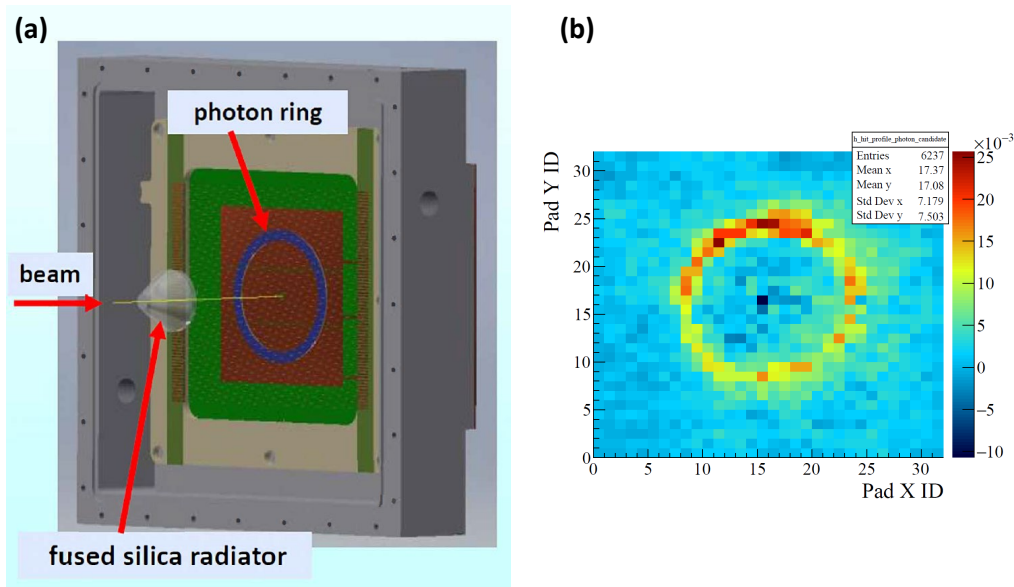


Figure 11.46: (a) Sketch of the hybrid single photon detector: two staggered THGEM layers are coupled to a resistive bulk MM; image not to scale. (b) Ring images detected with the hybrid single photon detector of COMPASS RICH; ring centres calculated from the reconstructed trajectory; no image filtering applied.

So far, CsI is the only photoconverter that has been successfully used in gaseous detectors, although its usage is affected by some difficulties and limitations. In fact, its quantum efficiency is destroyed by the bombardment due to ions produced in the multiplication process when the integrated charge overcome a level of  $1 \text{ mC/cm}^2$ . Therefore, the detectors



**Figure 11.47:** (a) The formation of the ring image on the photon detector prototype by Cherenkov photons generated in a quartz radiator crossed by beam particles (principle). (b) 2-D histogram of the hits produced by the Cherenkov photons in the small pad-size prototype

have to be used at limited gain that affects their overall efficiency. CsI is chemically fragile, in particular if exposed to water vapour and this feature imposes tedious manipulation always in dry inert atmosphere. A novel, more robust option is offered by Hydrogenated Nano Diamond (HND) powder. It has sizeable quantum efficiency in the same UV domain as CsI with analogous values. Hydrogenation has to take place at high temperature. The powder hydrogenation before forming the converting coating makes this approach compatible with the components of gaseous detectors. HND exhibits good chemical stability and the coating layer is mechanically robust. The performance of THGEMs with HND coating is unchanged, when an appropriate post-coating heating protocol is applied (Fig. 11.48, (a)). The preservation of the quantum efficiency when the protocol is applied is under study (Fig. 11.48, (b)); presently, the protocol is being optimized to obtain a complete preservation. The goal of these R&D is to obtain a valid alternative to CsI in order to empower the potentialities of single photon detection by gaseous detectors.

### Dual RICH (dRICH)

A so-called "Dual RICH" utilizes two different radiator indices and thereby is able to cover the full momentum range without penalty owing to the Cerenkov threshold of the gas section. The design optimized for EIC is shown in Figure 11.49 and uses both an aerogel radiator and a gas radiator ( $C_2F_6$ ) to cover the full momentum range in a single device. In the current design, it is assumed that the photon readout would use conventional technology (e.g. multi-anode phototubes) and therefore is inappropriate to locate the focal

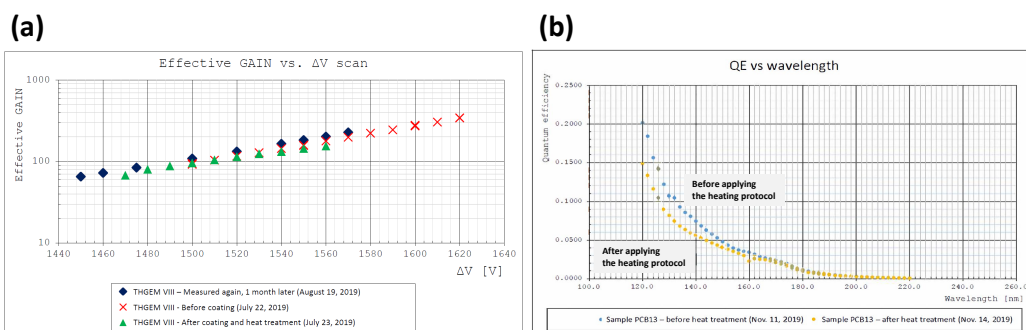


**Figure 11.48:** (a) Effective gain versus applied biasing voltage for a same THGEM measured with the bare device and with HND coating after applying the heating protocol; the measurement has also been repeated a month later. (b) QE versus wavelength of a NHD-coated sample measured before and after the heating protocol.

plane directly in the path of the particles. This has multiple effects that drive the device performance:

- The optics is less ideal and therefore the emission term becomes dominant in the resolution.
- The focal plane is moved to a lower radiation zone. This helps not only in the level of background hits that can interfere with the photon ring, but also may allow the use of emerging technology such as SiPM detectors to be used for the readout.

Shifting the focal plane to one side widens and complicates the parameter space for detector design, making optimization a daunting task. The present design of the detector was optimized using neural network techniques to investigate a wide space of detector configurations. The design shown here is the result of that exhaustive investigation.

Figure 11.50 shows the converged solution for the detector performance optimization in both the aerogel and the gas sections. Each term in the final resolution is isolated by its contribution of the Cerenkov angle resolution. The aerogel performance is dominated by the natural chromaticity of the radiator medium itself. All other contributing factors to the aerogel performance are negligible as compared to chromaticity which represents a fully optimal performance.

The angular resolution of the gas section is more complex. As referenced previously, emission terms (aberration) are dominant and peak at the edges of the segmented RICH mirrors. The optimization of this factor is evident by the fact that the Emission resolution term is of equal height at the two extremes of the polar angle acceptance.

Figure 11.51 indicates the calculated performance of the dRICH detector for  $e-\pi$ ,  $\pi-K$ , and  $K-p$  separation. Several features are worth noting. First, the dRICH is not merely limited to PID application, but also provides excellent eID out to roughly 20 GeV/c momentum. Second, the dRICH does not have "holes" in the performance either at low momentum

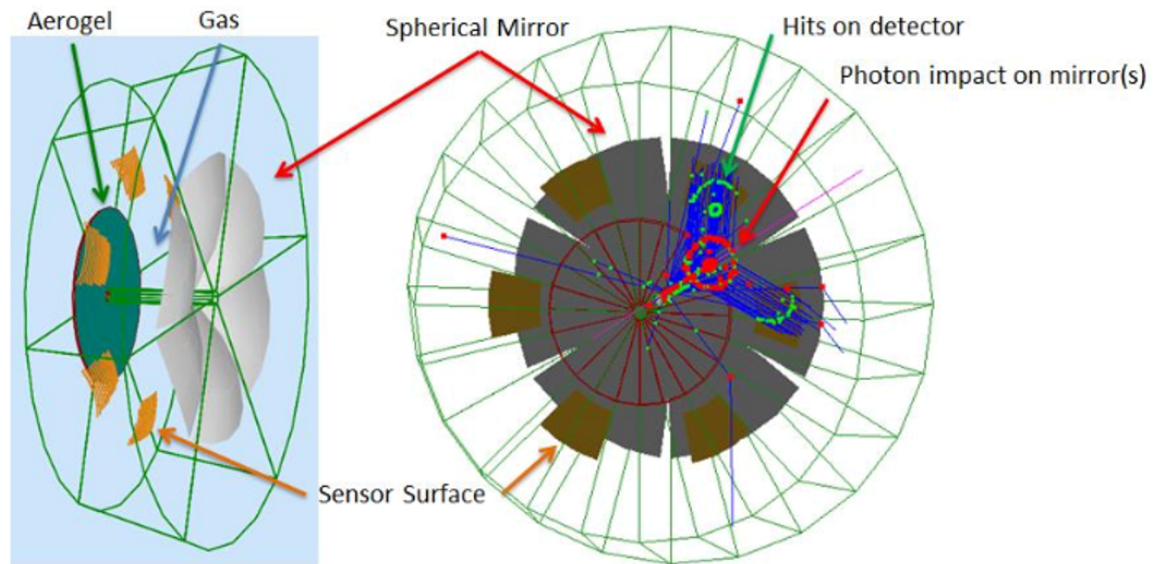


Figure 11.49: Dual RICH detector configuration.

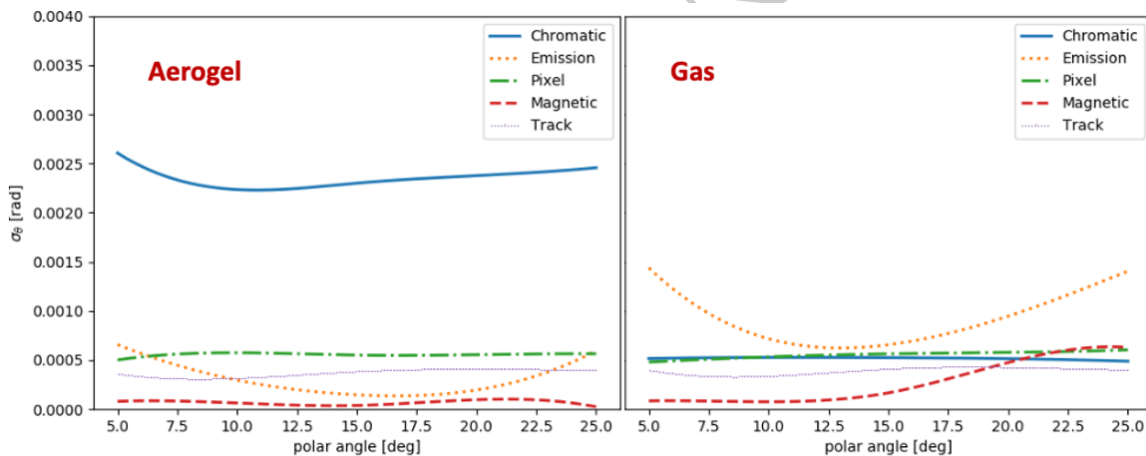


Figure 11.50: Resolution contributions for the Dual RICH.

(due to aerogel) nor at intermediate momentum due to the index match of the aerogel and gas radiator performance. Finally, the  $\pi$ -K performance achieves the full goals of the requirements matrix.

As is true for most modern gas Cerenkov detectors, the dRICH design utilizes the superior performance of perfluorocarbon radiator gas ( $C_2F_6$ ). Future environmental concerns can have two kinds of impact:

Current calculations demonstrate that these issues could be avoided by running an environmentally friendly gas at high pressure. Indeed, current calculations indicate that the dRICH performance would be insignificantly affected by a switch to Ar gas at 3 atm. This

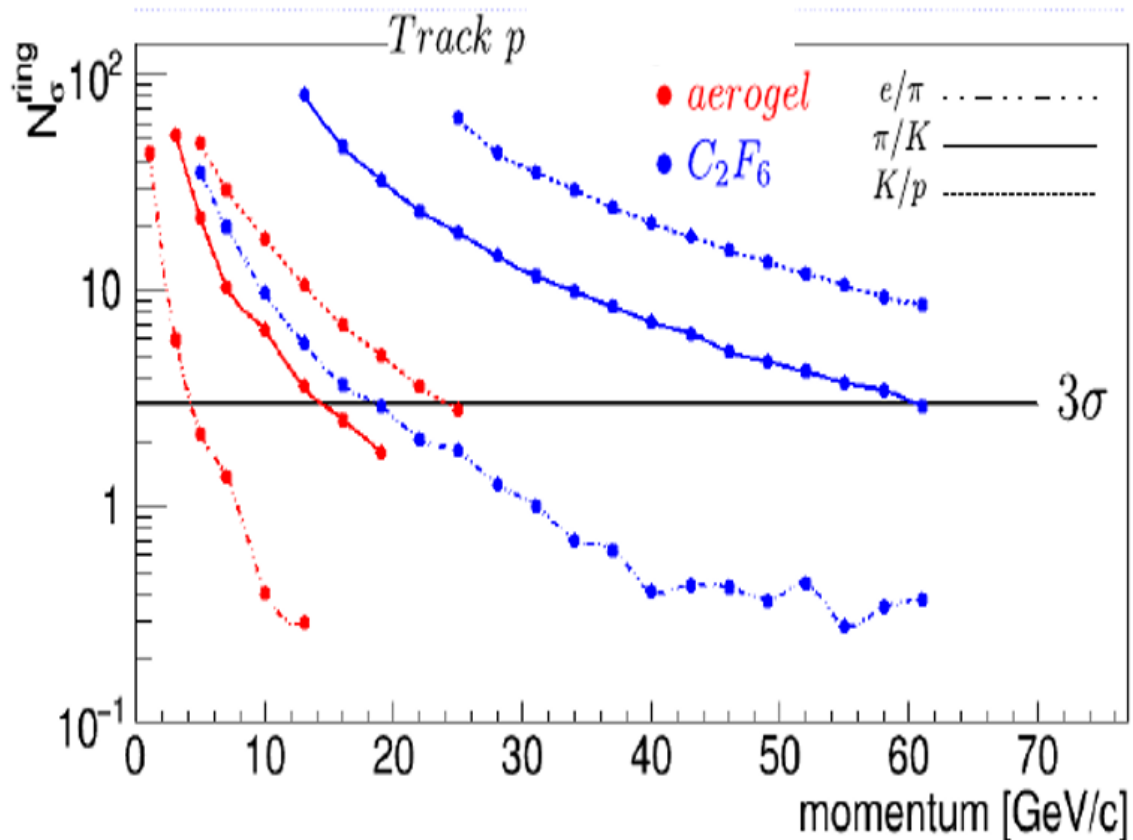


Figure 11.51: Performance of the Dual RICH.

will nonetheless impose an engineering challenge to maintain a low material budget.

One final note is that the external requirement on the tracking systems was modeled to be a limiting resolution of 1 mrad on track inclination while the track passes through the whole length of the gas radiator. Due to the large lever arm (1.5 meters) and possible scattering internal to the detector itself (entrance window in the high pressure version), it is likely wise to supplement the tracking prior to the dRICH with a detector that provides an additional space point beyond the radiation volume. This latter point can be rather low resolution as compared to the rest of the tracking while still providing the necessary 1 mrad uncertainty in track direction.

- It may be required to recover and purify the radiator gas to avoid release to the environment, which is a significant cost and complexity.
- Environmental concerns in the worst case could drive the cost and availability of the gas beyond tolerable levels.

At the time of this writing, the dRICH is the best known approach to EIC particle at the

highest possible momenta due to its full coverage of the dynamic range in momenta desired for the hadron arm.

### Modular RICH (mRICH)

A so-called "Modular RICH" is an aerogel-based RICH. A unique feature of this device is the use of a Fresnel lens to make a focused ring, thereby significantly improving the performance as compared to a "proximity focused" detector which is more common in aerogel applications. As shown in Figure 11.52, mirrors along the sides of the device allow it to collect light which is not initially directed to the photocathode found at the detector exit. Several aspects of the design of this device allow it to outperform conventional aerogel-based RICH detectors:

- The fresnel lens acts to generate a lens-focused rather than a proximity-focused ring.
- The fresnel lens imposes a wavelength cutoff on the transmitted light limiting the chromaticity effect.
- The focusing aspect somewhat relaxes the mechanical tolerances on the exit surface of the aerogel.
- The mRICH can possibly be configured with a photodetector that exhibits precision timing.

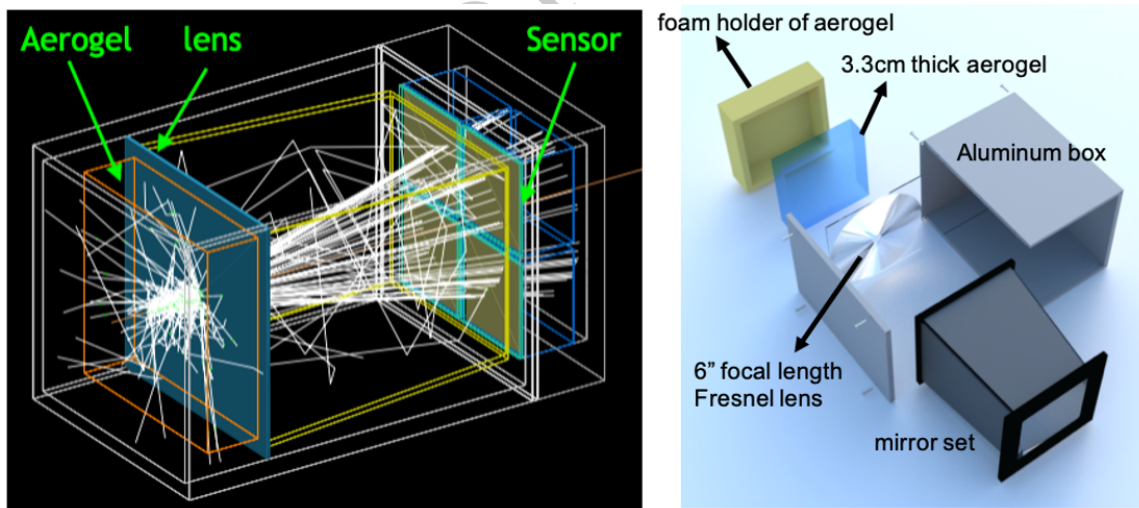


Figure 11.52: Configuration of the Modular RICH.

This device is useful both in the electron arm performing both eID and PID functions and also in the hadron arm (under the presumption of a gas RICH instead of a Dual RICH).

The limit to the resolution of the mRICH detector is the chromaticity term (as was true for the aerogel section of the dRICH), indicating the the design is presently optimal. The

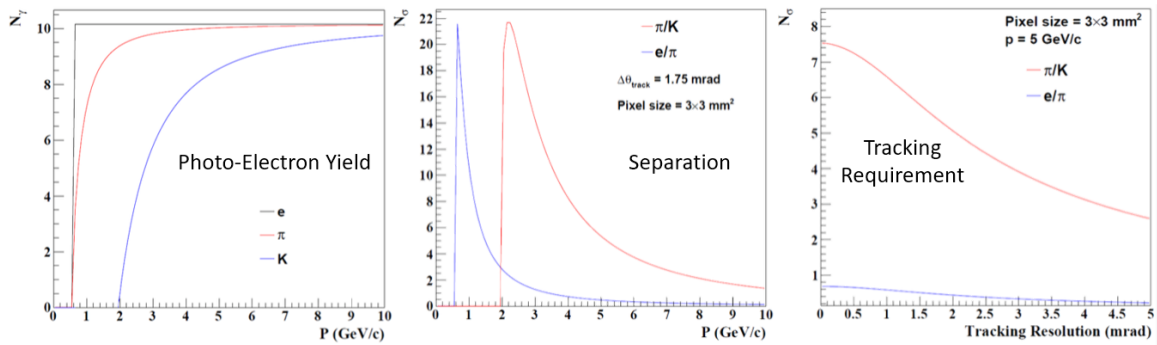


Figure 11.53: Performance of the Modular RICH.

simulated performance of the mRICH is shown in Figure 11.53. The saturation yield of Cerenkov photons is 10 per ring and is shown as a function of momentum for  $\pi$  and K. The center panel shows that the  $e$ - $\pi$  rejection extends until roughly 2 GeV/c and  $\pi$ -K until roughly 6-7 GeV/c. These are well, but not perfectly matched to the requirements matrix in the electron arm. Finally, as with all precision Cerenkov devices, the mRICH has strict requirements on the tracking resolution provided. The third panel shows the degradation in separation as the tracking resolution worsens indicating a tolerance of roughly 1 mrad as supplied by the external system.

Finally, Figure 11.54 shows an option for configuring the output detection stage of the mRICH with a high precision timing detector so that it can additionally serve as a TOF tag, thereby improving its PID capability.

### Detection of Internally Reflected Cerenkov (DIRC)

An interesting aspect of Cerenkov detectors emerges at high index. Since both the saturation Cerenkov angle ( $\beta = 1$ ) and the angle for total internal reflection are solely dependent upon refractive index, one finds that at normal incidence, Cerenkov light will be totally internally reflected by any material whose index satisfies the condition  $n > \sqrt{2}$ . This technique offers the unique advantage that, so long as the sides and corners of the radiator are made with high precision, the light can be propagated to the end of the radiator while preserving the Cerenkov angle. The result is a geometrically thin device that allows light detector detection only at the end(s). Furthermore, due to the in-medium light propagation length depending upon the Cerenkov angle, timing can also be used to aid the refining the Cerenkov angle determination.

The original application of DIRC was in the BaBar experiment at SLAC wherein the barrel section of the detector was surrounded by a series of quartz bars. Rings were imaged by a so-called "expansion volume" that effectively made for a "proximity focus". In the years that followed many advances of DIRC technology have been accomplished to effectively replace the proximity focus with an actual focus. The result is that it is conservatively anticipated that an EIC application of DIRC technology can be made that far outperforms

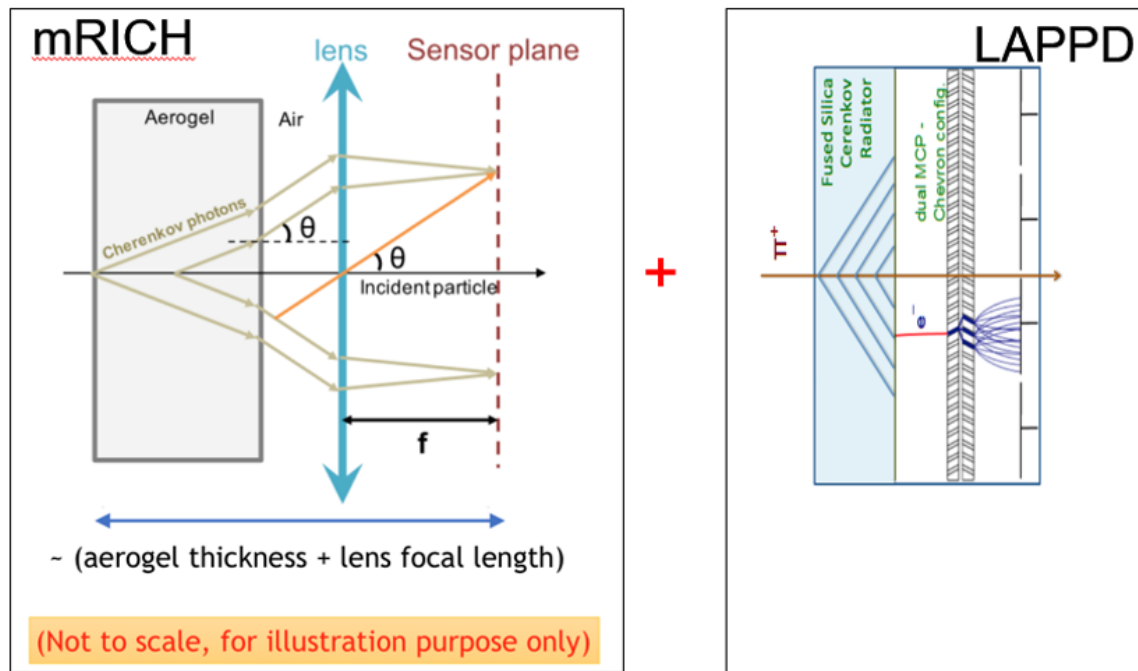


Figure 11.54: Timing Option for the Modular RICH.

the Babar application while dramatically reducing the size of the expansion volume. A picture of this High Performance or hpDIRC is shown in Figure 11.55. The left panel shows the quartz bars and the expansion volume isolated from the rest of the EIC detector. The right panel shows one possible geometry by which the DIRC could be realized in an EIC detector. Here the expansion volume is terminated with the photon detectors as indicated in red. Because the photon detectors prefer to be normal to the spectrometer's magnetic field, their explicit locations will be tightly coupled to the edge field orientation. It has been demonstrated that all plausible magnetic field orientations can be accommodated with little or no degradation in overall performance.

The DIRC application in many ways represents exquisite precision in all the geometric aspects of Cerenkov. As a result, the DIRC's precision must be similarly reflected in the tracking. The contribution of tracking resolution falls into the category of "correlated terms" in the analysis of the DIRC performance. It is determined through detailed simulation that the full contribution of all correlated terms must not exceed 0.8 mrad and that the tracking terms must not exceed 0.5 mrad. Fortunately, these strict requirements are able to be achieved with technologies discussed elsewhere in this report.

Figure 11.56 summarizes the anticipated DIRC performance in the so-called "hpDIRC" configuration and also compares the performance to the Babar and PANDA applications of this technology. The improvement in performance improvement is close to a factor of two in particle momentum for successful  $\pi$ -K separation and reaches 6 GeV/c. It is important to note that as with all PID detector technologies, various assumptions about the performance of other detector systems is vital to estimate the efficacy of the device.

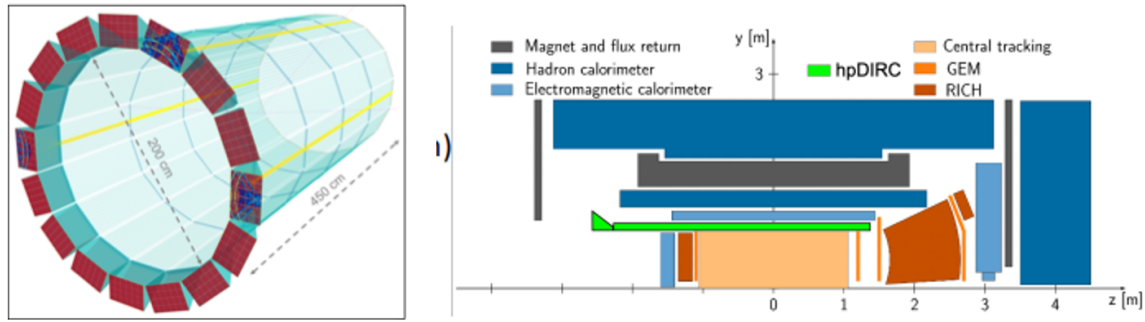


Figure 11.55: Configuration of the DIRC.

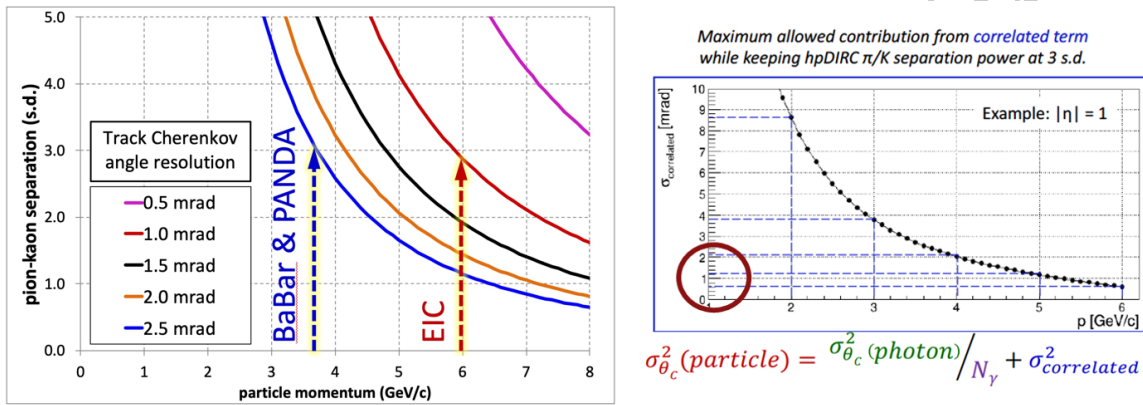


Figure 11.56: Performance of the DIRC in simulation.

These factors can be combined into a single so-called “correlated term”, the effect of which is indicated by the right half of Figure 11.56. In particular, this figure denotes the limit applied to the convolution of all sources of correlated term as a function of desired  $3\text{-}\sigma$   $\pi$ -K separation goal. To reach the required performance for EIC, it is clear that the correlated term must not exceed 0.8 mrad and this places a restriction on the tracking performance at the level of 0.5 rad.

### 11.3.4 Time Of Flight (TOF)

Recent years have seen major advancements in the precision by which detector devices can measure the time of passage of a particle. Such time, whether compared to a reference time for the collision as a whole (aka “Start time”) or whether measured at multiple points along the trajectory of a particle as it passes through the spectrometer allow for a direct measurement of the particle’s velocity and hence are useful forms of particle identification. An intrinsic advantage of measurements is that they contain no limiting threshold in performance (*e.g.* Cerenkov radiation is only produced for  $\beta > \frac{1}{n}$ ) and are thereby produce signals for charged particle of any momentum. These detectors are most often rather thin measured both by radiation length and by physical dimension.

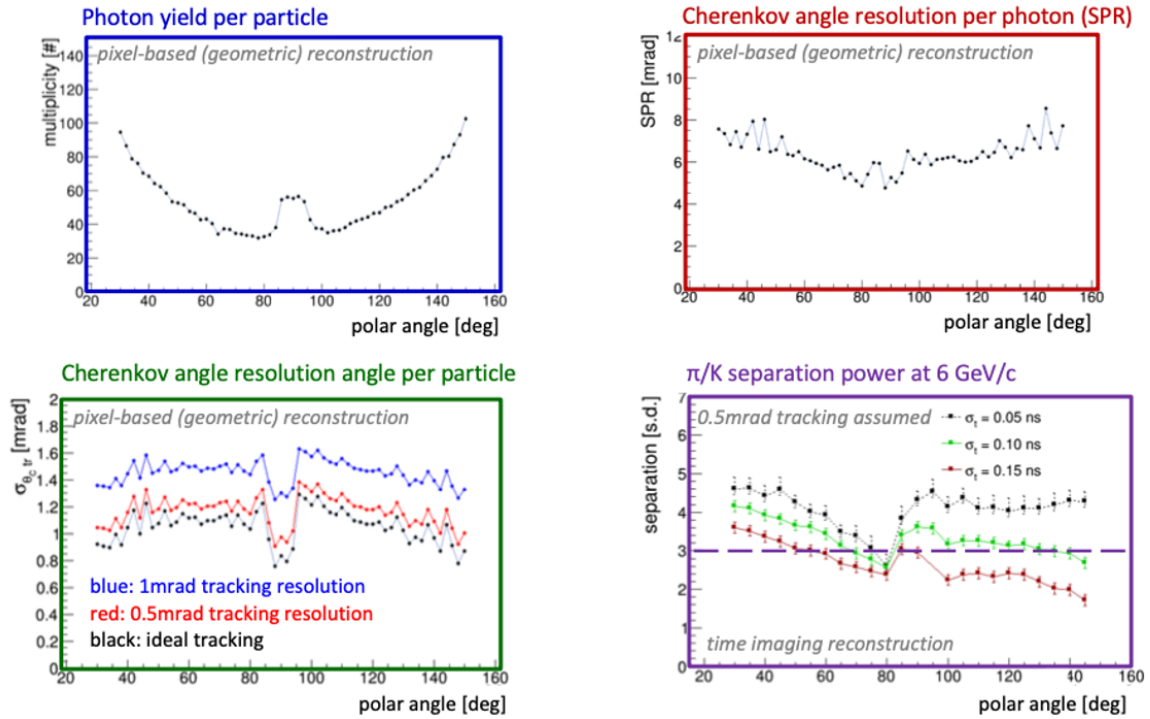


Figure 11.57: Dependence of the DIRC performance on  $\eta$ .

One can divide modern TOF technologies into two categories depending upon whether the technology converts light into photo-electrons (which subsequently avalanche) or whether they produce and detect ionization directly. The former case (as discussed in more detail in Section 11.3.5) is most often sensitive both to the strength and orientation of the external magnetic field.

Figure 11.59 displays one possible configuration of TOF detectors as arrayed into the typical EIC detector geometry. This particular geometry makes the assumption that the ToF measurements would be achieved with a silicon-based technology such as LGAD that is intrinsically insensitive to magnetic fields. The technology is layered in each direction so that several measurements of time are performed on every track and that these measurements additionally contribute to the tracking system by virtue of providing precision space points as well as precision timing ("4D" tracking).

The performance of the all-silicon TOF system shown previously is summarized in the left two panels of Figure 11.60. We note several aspects of this calculation. First, the calculation assumes that the overall time measurement scales with the number of measurements as  $\frac{1}{\sqrt{N_{meas}}}$ . This requires that common issues such as clock jitter are small compared to the intrinsic detector resolution. Appropriate R&D is ongoing to ensure that this will be the case by the time of EIC. Second, the calculation assumes the absence of HCAL detectors in the endcaps so that the flight path of the particles can be maximized. The existence or not of HCAL is thus one of the issues that can be addressed in the design of complementary EIC designs.

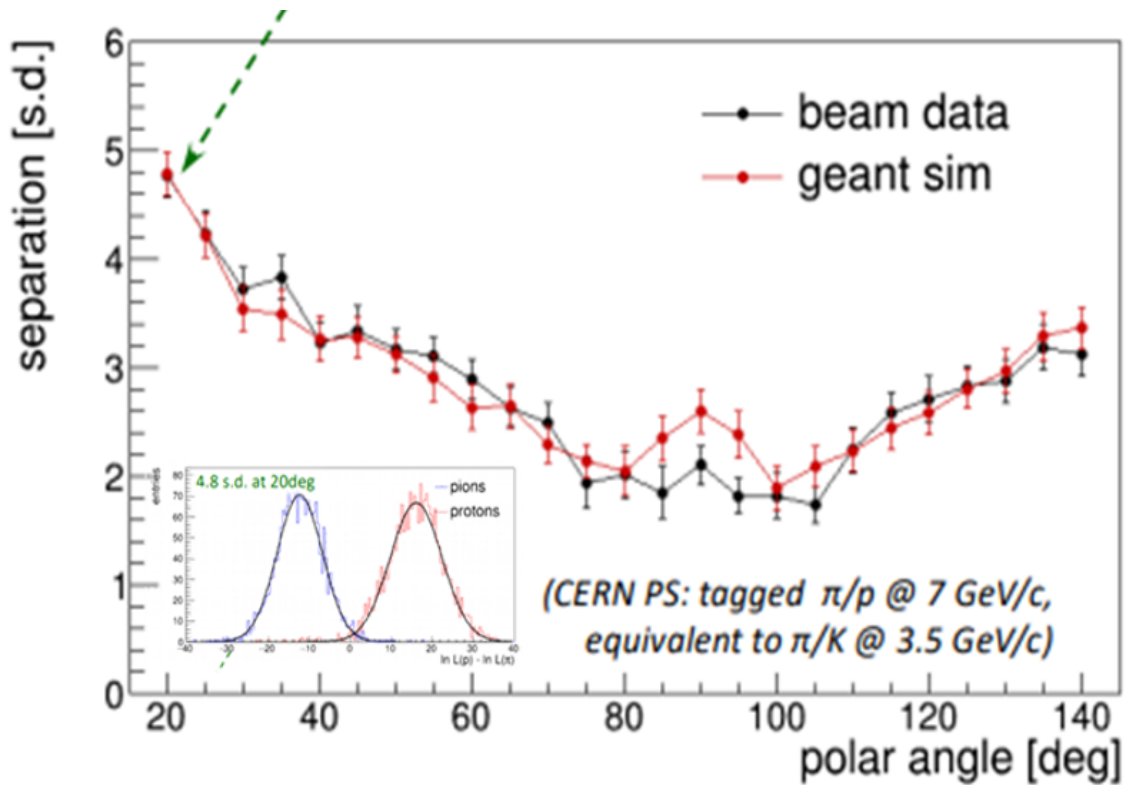


Figure 11.58: Comparison of the DIRC performance to test beam measurements.

At the time of this writing, the best TOF performance is supplied by LAPPD (Large Area Picosecond Photon Detector) devices at roughly 5 psec  $\sigma$ . The performance of that detector is summarized in the right-most panel of Figure 11.60. Because these devices utilize the avalanche of photo-electrons to generate their signal they are sensitive to the magnetic field. The current implementations of the technology are therefore limited to end cap implementations.

### MPGD-based-TRDs for Electron PID and Tracking in the End Caps

Identification of secondary electrons plays a very important role for physics at the Electron-Ion Collider (EIC).  $J/\psi$  has a significant branching ratio for decays into leptons (the branching ratio into electrons ( $e^+e^-$  pair) is 6%). The branching ratio of D-mesons is  $\text{Br}(D^+ \rightarrow e + X) \sim 16\%$  and the branching ratio of B-mesons is  $\text{Br}(B^\pm \rightarrow e + \nu + X_c) \sim 10\%$ . Electron identification is also important for many other physics topics, such as spectroscopy, beyond the standard model physics, etc. By using more sophisticated electron identification an efficiency of those channels could be increased. A high granularity tracker combined with a transition radiation option for particle identification could provide additional information necessary for electron identification or hadron suppression. Due to asymmetric beam energies and boosted kinematics, it is important to provide such

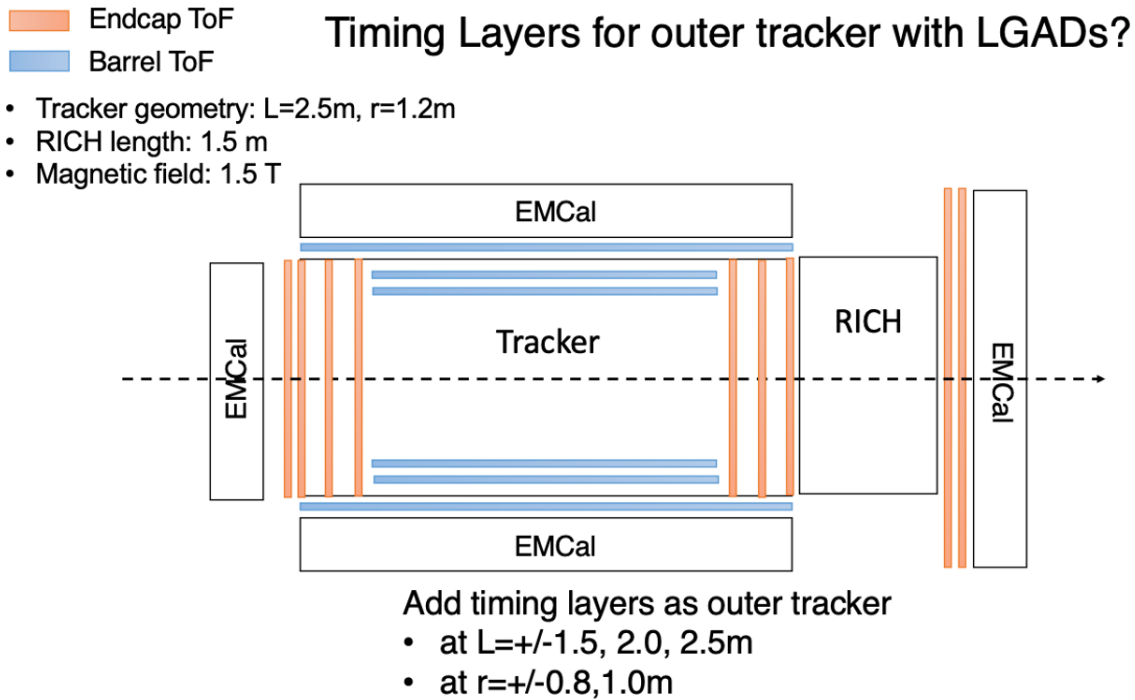


Figure 11.59: Configuration of Time of Flight for EIC.

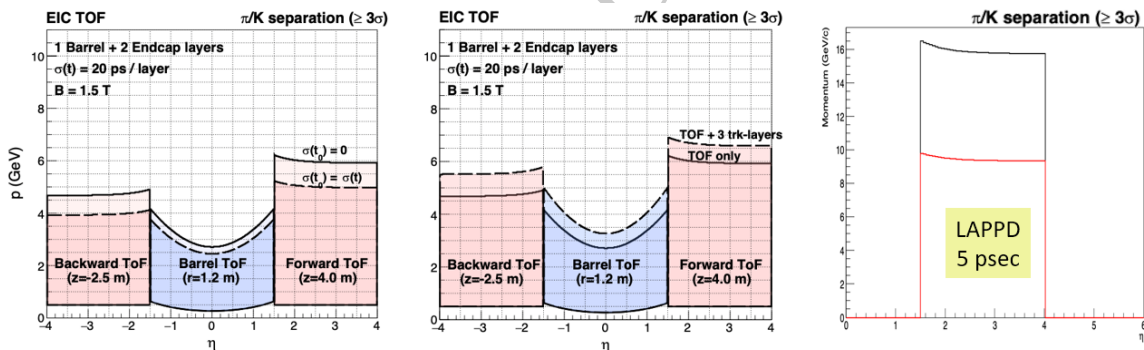
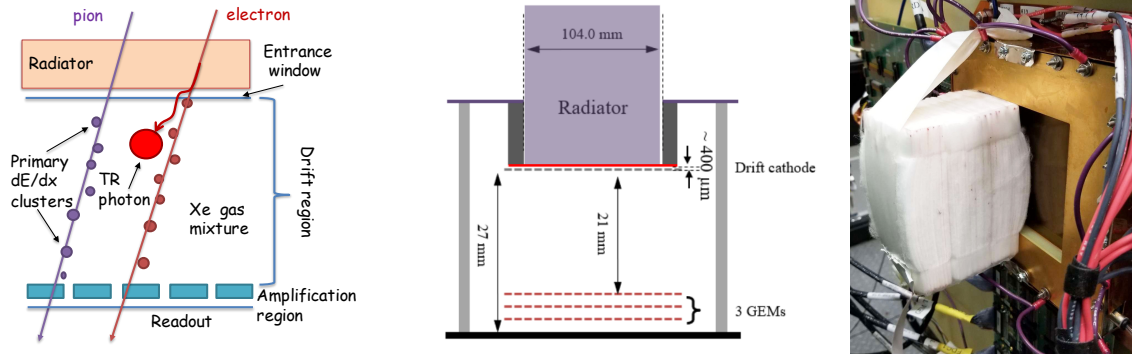


Figure 11.60: Performance of Time of Flight for EIC.

additional instrumentation in the hadron endcap. The basic concept of GEM-based TRD is shown on the Fig. 11.61. A standard triple-GEM detector [1247] with high granularity strip pitch ( $400\ \mu\text{m}$ ) capable of providing high resolution space point position information was converted into a transition radiation detector and tracker (GEM-TRD/T) [1275]. This was achieved by making several modifications to the standard GEM tracker. First, since heavy gases are required for efficient absorption of X-rays, the operational gas mixture has been changed from an Argon based mixture to a Xenon based mixture. Secondly, the drift region also needed to be increased from  $\sim 3\ \text{mm}$  to 20-30 mm in order to detect more energetic TR photons. Then to produce the TR photons, a TR radiator was installed in front of the GEM entrance window. Finally, the standard APV25 GEM readout electronics was replaced with



**Figure 11.61:** The concept of GEM-based TRD (left), the prototype scheme (middle), prototype in testbeam setup (right)

faster electronics based on flash ADC (FADC) [1276] and developed for JLab HallD GlueX Drift Chambers. A GEANT4 simulation and optimized the radiator and detector thicknesses for a single chamber (Fig. 11.61) has been performed. G4XTRGammaRadModel model was used for a fleece radiator, which could be simulated in GEANT4 as an irregular type of radiator with a certain density and two parameters ( $\alpha_1, \alpha_2$ ), which define a spread of materials and air-gaps within a radiator. Due to the self-absorbing property of the radiator, soft photons (3-6 keV) generated within first few centimeters of the TR-radiator will be absorbed, leading to an increase in the hard X-ray photon spectrum at the exit from a radiator. A thin layer of gas in Xe-based detector will not be effective at detecting hard X-ray photons. As one could see in Fig. 11.63 (left), rejection power is saturated after 22cm of radiator for our GEM detector with 21mm gas thickness, including 400 $\mu$ m of dead gas layer in front. Experimental data points (stars) shows a good agreement with MC projections. A TRD needs information about the ionization along the track, to discriminate TR photons from the ionization of the charged particle. The GEM-TRD/T prototype used a precise (125 MHz, 12 bit) FADC [1276] coupled with fast shaper pre-amplifiers, developed at JLAB, with a VME-based readout. The FADCs have a pipeline readout window of up to 8  $\mu$ s, which covers the entire drift time (500ns) of the GEM-TRD/T prototype and gives a room for HV scan. The pre-amplifiers used GAS-II ASIC chips to provide 2.6 mV/fC amplification with a peaking time of 10 ns. For the  $e/\pi$  rejection factor the amplitude and arrival time of each individual cluster along the drift time were analyzed. All this information (up to 20 variables) was used as input for likelihood and artificial neural network (ANN) programs, such as JETNET or ROOT-based (Multi-layer Perceptron). The ANN system was trained with MC or data samples of incident electron and pions. Then an independent sample was used to evaluate the performance. An example of such a training procedure is shown in Fig. 11.62. A 90% efficiency for our electron identification was required. The neural network output for  $e/\pi$  rejection is shown Fig 11.63. As one could see, with a 15cm radiator rejection factor ca. 9 could be achieved.

As for tracking aspects, a standard GEM plane can only provide the 2D X-Y position of a track, while the GEM-TRD/T with increased drift volume and with Flash ADC readout allows for 3D track segments to be reconstructed as in  $\mu$ -TPC configuration. In the hadron

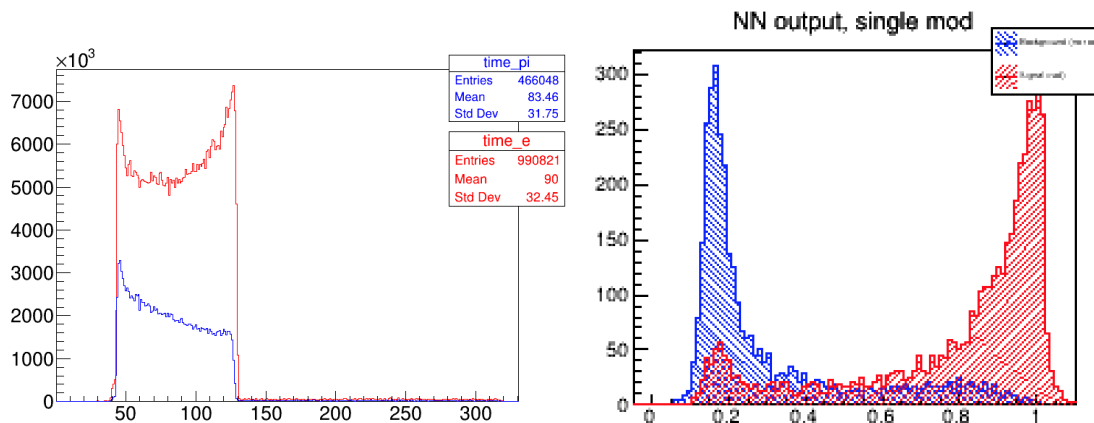


**Figure 11.62:** Left plot shows average energy deposition along the drift time (x-axis in fADC time-bins). Right plot is output from Neural Network, showing the separation between electrons and pions.

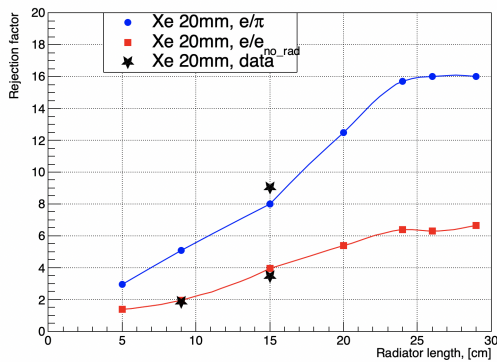


**Figure 11.63:** Rejection vs. TR-radiator thickness.

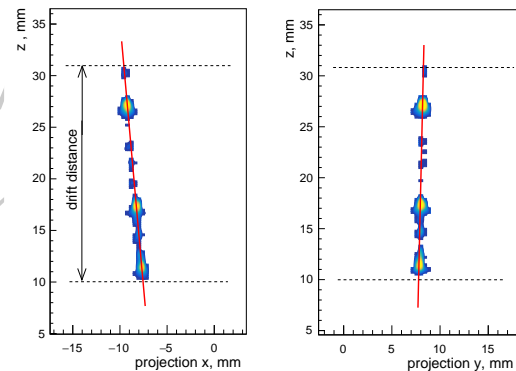


**Figure 11.64:** Single track reconstruction.

end cap region, in addition to the  $e/\pi$  rejection capabilities, GEM-TRD track segment behind dRICH could be used to:

- measure a track angular resolution and therefore help to improve dRICH performance;
- correct for a multiple scattering before EMCAL and improve tracking performance for charged particles.
- improve pointing track resolution and cluster-seed position measurements for EMCAL
- could be used as a seed-element for a track finding algorithms.

Figure 11.64 shows projections of a typical 3D reconstructed track from the GEM-TRD/T prototype. The left panel shows the track projection in XZ plane with Z the drift time as a function of the cluster position in the X direction. The right panel shows corresponding projection in YZ plane.

### 11.3.5 Photon Detection Technology Options

Many of the devices discussed previously involve the detection of visible and/or UV photons, frequently with an accompanying requirement of being able to discriminate between noise the signal resulting from a single photo-electron. Furthermore, the detection must maintain its quantum efficiency and much of its gain while immersed in the magnetic field of the spectrometer. Many traditional devices for single photo-electron detector fail the final criterion of operation when immersed in a magnetic field. Several suitable technologies exist or under development and have been studied in the context of EIC applicability.

The MCP PMT uses micro channel plate technology to replace the traditional dynode structure for achieving gain in a photomultiplier tube. These devices are intrinsically more tolerant to an external field, but are not entirely immune. Several options have been studied, one of which is summarized in Figure 11.65. Here the 10  $\mu\text{m}$  Planacon device's performance is summarized in both quantum efficiency (dashed lines) and gain (solid lines) as a function of external magnetic field. At normal field incidence, and up to 1 Tesla, the device maintains sufficient gain (particularly at higher bias) and quantum efficiency to be suitable for use in a RICH detector. Further study is required to extend these studies to higher field since tracking considerations imagine central values of the field as high as 3 Tesla. At such a field it seems difficult to position photon detectors of the various Cerenkov detector devices (dRICH, mRICH, DIRC) in a manner such that they experience 1 Tesla or below. Conversely, it has been shown that for a 3 T central field, 1 T in the region of photon detection is plausible, but requires careful design. It should also be noted that the incident angle of the field to the PCM PMT is a critical parameter. By an incident angle of  $20^\circ$ , the quantum efficiency of the device drops into the 20-40% range by roughly 1/2 Tesla. Typically a loss of 2X in photon statistics damages the performance of a Cerenkov device significantly and would require major changes in the device design.

Another developing photon detection technology is that of LAPPD. These devices also use micro channel plates as their basic of avalanche. These can be used both for Cerenkov readout (*e.g.* in an mRICH configuration to add timing) or directly as a TOF detector. As shown in Figure 11.66, these devices also suffer a significant loss in signal strength which is a combination of gain loss (somewhat tolerable) and quantum efficiency loss. The QE loss is a second order impact when the LAPPD is used as a TOF detector since the primary signal already consists of multiple photoelectrons. However, this loss is critical to the use of LAPPD as a Cerenkov detector readout.

Finally, we note the developments in recent years of silicon photo-multipliers or SiPMs. Initially, these devices (which operate on a Geiger avalanche mode in each pixel) were highly susceptible to radiation damage. Much work has been done to improve this per-

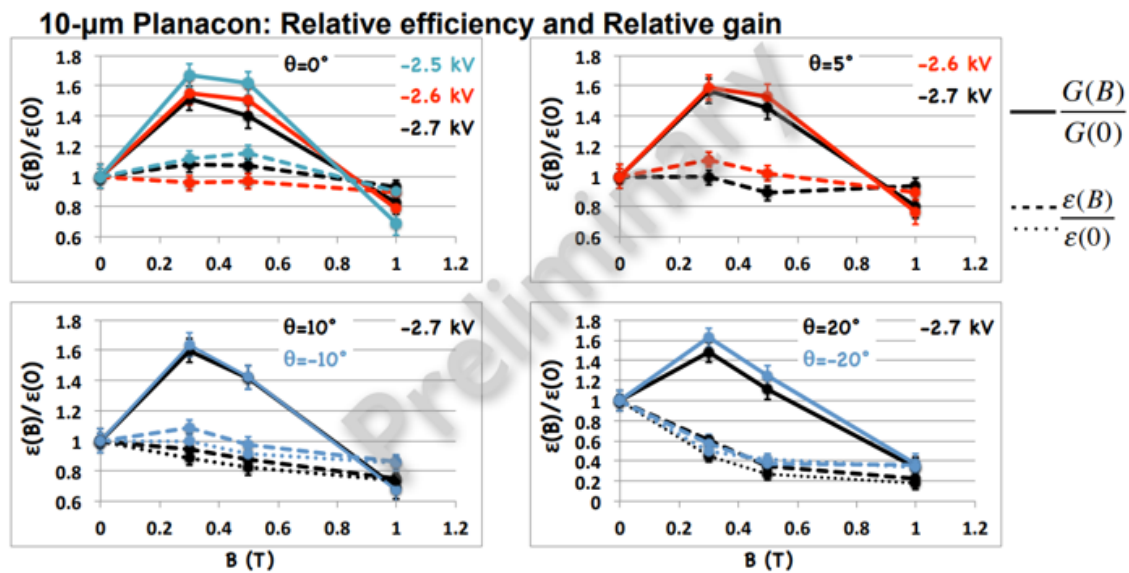


Figure 11.65: Magnetic Field Effects on MCP PMT Devices.

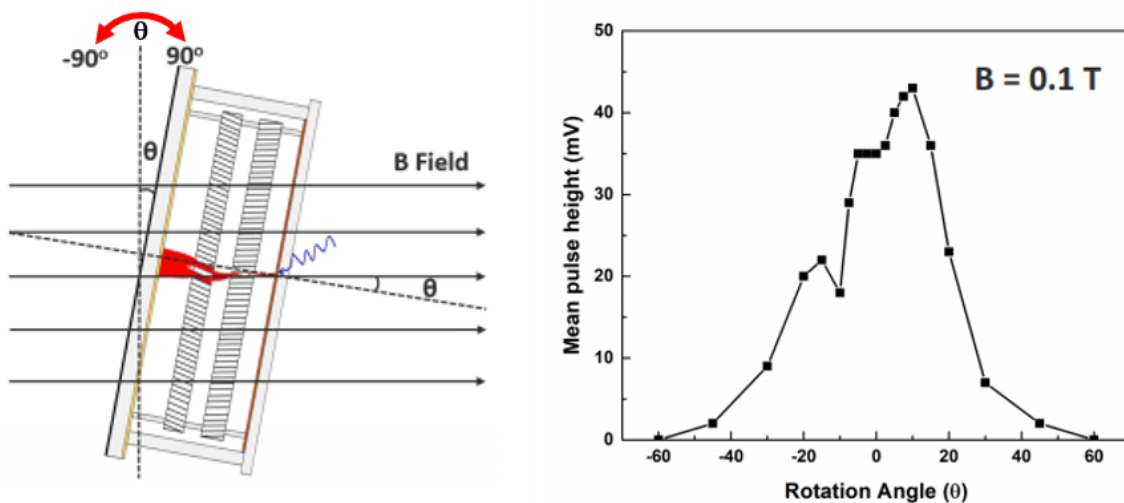


Figure 11.66: Magnetic Field Effects on LAPPD Devices.

formance intrinsically and it is now known as well that operation at cold temperatures and post-annealing processes have been effective means to maintain and restore operation. For this reason, SiPM technology seems a leading choice for readout of light signals from calorimeter devices at the EIC. That said, more work is required to demonstrate the efficacy and long term viability of SiPM technology for use in a Cerenkov detector. The basic distinction is signal size. A well designed and high performance calorimeter will deposit many photons into a single pixel, making the presence or absence of "several" photoelectrons a mere shift and widening of the pedestal. RICH detectors, on the other hand,

must distinguish zero from one photo-electron and thereby are much more vulnerable to radiation damage of an SiPM. It is therefore a clear priority to continually develop and evaluate the performance of SiPM detectors for RICH applications in the coming years.

### 11.3.6 Configuration for EIC

Based upon the characteristics of known detector technologies as described above, it is possible to assert solutions for the detector performance matrix in each of the pseudo-rapidity regions. These possibilities are outlined in the table below and discussed in more detail in the sections that follow.

Arm	eID-only Technologies	PID Technologies
Electron	HBD, TRD	mRICH, LAPPD, LGAD
Central	-	dE/dx, DIRC, LGAD
Hadron	TRD	dRICH, gRICH/LAPPD

Before we continue, it is necessary to establish simple criteria for what can be considered as acceptable performance and in particular the definition of dynamic range. The PID/eID task can be simplified to the identification of four particle species which in mass order are the electron, pion, kaon, and proton. For Cerenkov technologies, both the threshold and "imaged" mode of operation can be utilized as part of the ID process. Positive ID is defined as follows:

- Positive eID for a threshold device is valid up to the momentum at which the pion begins to radiate.
- Positive PID for an imaging device begins at the momentum where the kaon starts to radiate.

While careful analysis shifts these limits somewhat, they are nonetheless useful in comparison across detector technology comparisons. To this end, we list the Cerenkov thresholds for each radiator considered in any of our detector systems in Table 11.15.

These thresholds along with the detailed calculations shown in the prior sections can be summarized to form the following table of dynamic range summaries of each detector system discussed above:

#### Hadron Arm

The PID requirements in the hadron-going direction are naturally the most stringent in the spectrometer owing to the broad momentum range required for hadron identification. The various technologies considered have been accumulated into a table distinguishing their range in  $e-\pi$  separation and also in  $\pi$ -K separation. For Cerenkov devices, the lowest

radiator	index	Threshold (GeV/c)			
		e	$\pi$	K	p
quartz (DIRC)	1.458	0.00048	0.13	0.47	0.88
aerogel (mRICH)	1.03	0.00207	0.57	2.00	3.80
aerogel (dRICH)	1.02	0.00245	0.69	2.46	4.67
C <sub>2</sub> F <sub>6</sub> (dRICH)	1.0008	0.01277	3.49	12.34	23.45
CF <sub>4</sub> (gRICH)	1.00056	0.01527	4.17	14.75	28.03

**Table 11.15:** Table of Cerenkov thresholds for various media.

momentum for  $e-\pi$  is put at the Cerenkov threshold and the lowest momentum for  $\pi-K$  is placed at the kaon threshold. The results are summarized in Table 11.16.

Hadron Arm Technology	Range (GeV/c)	
	$e - \pi$	$\pi - K$
CsI RICH	0.0150 - 20	14.75 - 50
dRICH (aerogel)	0.0025 - 5	2.46 - 16
dRICH (gas)	0.0127 - 18	12.34 - 60
dRICH (overall)	0.0025 - 18	2.46 - 60
TOF (LGAD)	0 - 1	0.00 - 5
TOF (LAPPD 4m 5psec)	0 - 2.5	0.00 - 16
TRD	1.0 - $\infty$	-

**Table 11.16:** Performance ranges for possible hadron arm detector technologies.

Among the various options it becomes immediately clear that there is a clear need for gas-based Cerenkov to reach the high end momentum requirements of the EIC. It is also immediately clear that owing to the high threshold imposed by a low-index radiator choice necessary to reach the high momentum range, there must be an additional technology. The dRICH presents an elegant solution to the issue by incorporating aerogel. The gRICH option must be augmented by the addition of technology like aerogel-base mRICH or by high resolution TOF in order to cover the full dynamic range.

### Central Arm

The principle challenge of the central arm is the lack of space provided therein. As a result the DIRC technology and TOF technology become leading options in most designs. There exist, however, two significant issues with a DIRC-only solution. These are:

- The DIRC provides a threshold for kaon radiation at 0.47 GeV/c.
- There is a need for eID ( $e-\pi$ ) that may not be fully met.

Central Arm Technology	Range (GeV/c)	
	e - $\pi$	$\pi$ - K
$\frac{dE}{dx}$	0 - 2	0 - 3
$\frac{dE}{dx}$ (Cluster Count)	0 - 10 ??	0 - 15
DIRC	0.00048 - 1	0.47 - 6
TOF (LGAD)	0 - 1	0.00 - 5
HBD	0.0150 - 4.17	N/A

**Table 11.17:** Performance ranges for possible central barrel detector technologies.

It is therefore likely that a complementary technology in addition to the DIRC is required for the central barrel. The use of  $dE/dx$  follows naturally when one assumes that the tracking system would contain a hybrid of silicon and TPC. However, one must be cautious. Because of the so-called "band crossings" in any  $dE/dx$  measurement, it is absolutely necessary to have a "tag" of low velocity particles to eliminate these from any eID system (wherein the electron is well into the high beta plateau). TOF provided either by the DIRC system or by the inclusion of timing layers in the silicon tracker will be a must for such systems.

In a non-hybrid tracking system (internal silicon layers to 50 cm radius), one can imagine utilizing the additional space for a new PID device to complement the DIRC and TOF options. In this case, one can even imagine exceeding the TPC  $dE/dx$  performance by a significant factor utilizing cluster counting rather than merely energy loss measurements. Cluster counting devices require further R&D in the coming time to demonstrate that this capability can be reached. RICH systems modeled similar to the Delphi Barrel RICH can also be imagined, however the viability of SiPM devices as readouts for RICH detectors long term in the face of a high radiation environment must be demonstrated.

### Electron Arm

In the direction of the electron arm, several possibilities exist. One of these possibilities is that despite the asymmetry of the collision itself, one could choose to place a device such as dRICH in the electron arm direction as well. This creates a challenge since the dRICH technology requires significant space. Nonetheless, dRICH in the electron arm would overperform all the requirements of the electron ion collider and provide a singular solution for both endcaps.

More conventional thinking would attempt to fulfill the less stringent needs in the electron arm by instead using one or several layers of a more compact PID technology. The ideal requirement of 4 GeV/c eID capability is well matched to the HBD-style technology. In the sPHENIX application, a 50 cm radiation of gas with a 4.17 GeV/c pion threshold. A limitation of this technology is that its original design is optimized for separation of 2e from 1e and not for  $e-\pi$ . Calculations exist as shown above for a new avalanche stage that

promises to produce a pion rejection of roughly 100X. An alternative, is to split the HBD volume into two halves and square a lesser pion rejection factor. Both these concepts are unproven at the time of the Yellow Report and would require further R&D to prove their validity.

Electron Arm Technology	Range (GeV/c)	
	e - $\pi$	$\pi$ - K
dRICH (aerogel)	0.0025 - 5	2.46 - 16
dRICH (gas)	0.0127 - 18	12.34 - 60
dRICH (overall)	0.0025 - 18	2.46 - 60
HBD	0.0150 - 4.17	-
mRICH	0.0025 - 2	2.00 - 6
TOF (LAPPD 4m, 5psec)	0 - 3	0.00 - 16
TOF (LAPPD 3m, 10psec)	0 - 1.8	0.00 - 10
TRD	1.0 - $\infty$	-

**Table 11.18:** Performance ranges for possible electron arm detector technologies.

A more conventional approach is to use one or more compact PID technologies. The mRICH is reasonably well suited to the task for providing additional eID and also PID. An option is being considered for augmenting the readout of mRICH with LAPPD which adds high resolution TOF to the mix. Two improvements occur. First, the TOF tag does not need to exceed the Cerenkov threshold for aerogel (instead it need to exceed the threshold in the LAPPD window). This enhances the capability at the lowest momenta. Second, the TOF information will augment the performance so long as the mRICH would be placed with a long enough flight path (not a restriction for the ring-based mRICH mode of operation).

TRD is also a possibility in the electron arm. TRD, like HBD, can be thought of as a threshold technology in that only the electrons radiate while the pions do not. The threshold is at roughly 1 GeV which makes the TRD technology an excellent complement to the mRICH in providing the necessary eID in the electron arm.

## 11.4 Electromagnetic Calorimetry

### 11.4.1 Requirements and Overview

In EIC experiments the electromagnetic calorimeters (ECAL) are needed for their usual tasks:

- Detect the scattered electrons in order to separate them from pions and also improve the energy / momentum resolution at large  $|\eta|$ .
- Detect neutral particles - photons, and measure the energy and the coordinates of the impact.
- PID: separate secondary electrons and positrons from charged hadrons.
- Provide a spacial resolution of two photons sufficient to identify decays  $\pi^0 \rightarrow \gamma\gamma$  at high energies.

The physics requirements for the EIC detector system including the calorimeters are specified in Chapter 8.6. The kinematic range and the requirements for the electron detection in ECAL was discussed at length in presentations [?, ?, ?, ?, ?] (see Fig.11.67). The background to DIS electrons is shown in Fig.11.68.

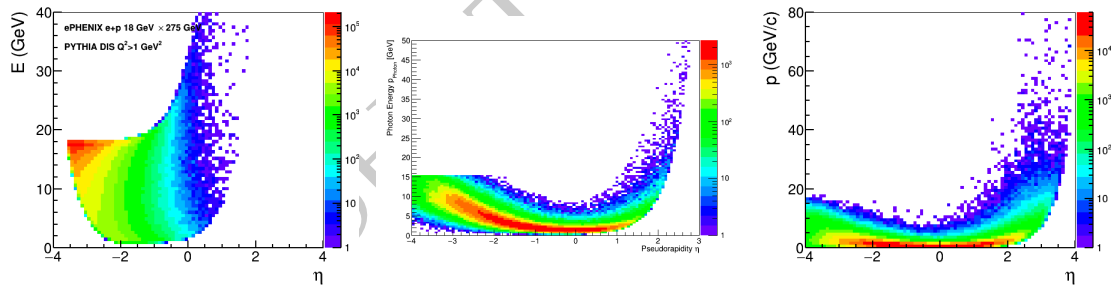


**Figure 11.67:** Calculated momentum spectra of particles in  $e + p 18 \times 275$  GeV collisions [?]. Left: DIS  $e^-$  from PYTHIA [272]; Middle: DVCS  $\gamma$  from MILOU [1185]; Right:  $\pi^0$  from PYTHIA.

$\eta$	-4 to -2	-2 to -1	-1 to 1	1 to 4
$\sigma_E / E \cdot \sqrt{E} / 1 \text{ GeV}$	2%	7%	10-12%	10-12%

**Table 11.19:** The initial requirements for the ECAL energy resolution [?, p. 25].

The initial requirements for ECAL are summarized in Table 11.19. The highest energy resolution is required at  $\eta < -2$ . Such a resolution can be achieved with heavy scintillating

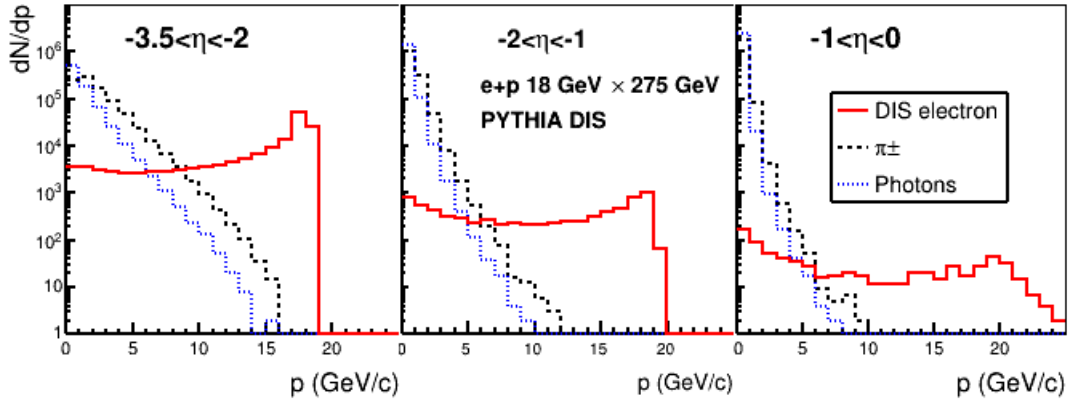


**Figure 11.68:** Calculated momentum spectra of DIS electrons, photons and pions in  $e + p 18 \times 275$  GeV collisions [?].

crystals. The best two-photon resolution is required at  $\eta > 2$ , which can be achieved with a fine granularity of a detector made of heavy materials, or by using a preshower detector with a fine granularity. The physics goals favor a reasonably hermetic detector, covering a range of about  $-4 < \eta < 4$ .

A practical limitation on possible choices of technologies comes from the space allocated for the EIC calorimeters. The tightness of the space in the endcaps is driven by the luminosity requirements. The barrel calorimeter depends on the magnet design. For the BaBar magnet the outer diameter of ECAL can go up to 140 cm, while the minimal radial thickness of ECAL is about 30 cm (based on the sPHENIX experience). The space in the magnet barrel is valuable for the momentum measurements, the PID etc. The tentative layout allocates:

- $\Delta Z < 50$  cm in the electron endcap;
- $\Delta R < 30$  cm in the barrel;
- $\Delta Z < 40$  cm in the hadron endcap;

Such a short space would favor calorimeter materials with a short radiation length ( $X_0$ ).

The radiation environment at EIC is considered to be moderate at  $|\eta| < 3$ .

Only light-collecting calorimeters for the EIC have been considered in this report<sup>1</sup>. ECAL will be located in a strong magnetic field - in the bore of the solenoid, or in the stray field of  $> 0.1$  T. Therefore, regular PMTs can not be used. Silicon photomultipliers (SiPM) are considered the most promising photosensor for ECAL. Compared to PMTs, SiPMs take much less longitudinal space, mostly for the readout electronics, which is an advantage at

<sup>1</sup>An alternative approach to the EIC spectrometer - *TOPSiDE* [1280] would require a separate consideration

EIC. Based on the current experience the SiPM readout and the services (cables, cooling pipes etc) may take about 15 cm of the longitudinal space.

### 11.4.2 ECAL: Requirements, Options and Features

The important parameters of calorimeters are:

- **Energy resolution.** The commonly used approximation for a particle of energy  $E$  is:

$$\sigma/E = \alpha \oplus \beta/\sqrt{E} \oplus \gamma/E. \quad (11.4)$$

The term  $\gamma$  depends on the noise level and is typically small for photosensors with high gains. The constant term  $\alpha$  depends on a number of factors, including the calorimeter thickness (on the leakage of showers outside of the calorimeter active area), and also on the quality of the detector calibration. For ECALs with hundreds of channels or more, typically  $\alpha > 1\%$  [1281,1282]. The stochastic term  $\beta$  depends on the technology used (the sampling ratio, the size of the signal observed etc.).

- **Position resolution** of the particle impact. An approximation is used:

$$\sigma_X = \delta \oplus \epsilon/\sqrt{E} \oplus \Delta \cdot \sin \theta_I. \quad (11.5)$$

The resolution depends on the granularity (for ECAL limited by the Molière radius) and the energy resolution. The coefficients  $\delta$  and  $\epsilon$  are approximately proportional to the cell size. The third term describes the dependence on the angle  $\theta_I$  between the incoming particle direction and the longitudinal axis of the calorimeter cell. The coefficient  $\Delta$  is  $d \approx X_0$ , where  $X_0$  is the average radiation length of the calorimeter material [1283, p. 527].

- **Lowest detectable energy** depends on the signal size versus the noise and low-energy background.
- **Electron/pion separation** Mostly depends on the energy resolution and the longitudinal segmentation (if any).
- **Two-photon separation.** Two photon not hitting adjacent cells can be separated at the clustering level. An analysis of the shower profile allows to separate photons hitting adjacent cells, provided the hits are at least one cell-size apart.
- **Detector longitudinal size.** A denser material allows to make the detector shorter for the given thickness in radiation lengths. The resolution may depend on the thickness.
- **Signal timing.** A long signal may affect the signal/noise ratio and the pattern recognition.

The energy resolution of any calorimeter depends on:

- Uniformity of the measured response across the volume of the detector. The effect may be important both in high-resolution homogeneous calorimeters, in particular of a trapezoidal shape [1284, 1285], and in medium-resolution sampling calorimeters [?, 1286].
- Shower containment. In a shorter calorimeter the fluctuations of the shower leakage lead to a higher constant term  $\alpha$  and a worse resolution at high energies. The dependence of the energy resolution of the calorimeter on its depth in radiation length was calculated in Ref. [?]. For the expected energy range of  $E < 20$  GeV the impact of the downstream leakage would not significantly change the resolution, for a thickness:

$\beta$	2.5%	7%	12%
thickness in $X_0$	>22	>20	>18

The dependence of the constant term of a sampling calorimeter with a  $0.25X_0$  layer thickness on the overall thickness  $x = X/X_0$  has been calculated [?, p. 12] in a range of 18-24. The result is well fit using a polynomial  $\alpha \approx 12.1 + 0.826x + 0.0144x^2$  and can be extrapolated to a wider range as 14-28.

- Signal size. More photoelectrons/GeV lead to smaller relative fluctuations and a lower impact of noise. A typical yield of a classic lead glass calorimeter is about 1000 p.e./GeV providing fluctuations of RMS=3% at 1 GeV, to be compared with the factor  $\beta$ . For high resolution calorimeters of  $\beta < 3\%$  the yield should be higher.
- The readout threshold may be important since a shower splits between several cells. It is selected depending on the noise and background.

Numerous ECAL technologies have been developed for the field and the development is still ongoing. A number of technologies have been studied and developed in the framework of the EIC R&D, project eRD1 [?]. The results have been used in this report. The technologies considered are discussed in more details in in Section 11.4.3.

### Homogeneous Calorimeters

Typically, the best energy resolution is obtained with homogeneous detectors not affected by the sampling fluctuations. Heavy scintillating materials produce large signals per MeV absorbed, leading to a good resolution. The best results have been achieved so far with scintillating crystals. Detectors using the Cherenkov light in heavy glass provide a medium resolution.

- **PbWO<sub>4</sub>**. A combination of the requirements for the resolution, compactness, radiation hardness, the signal length, as well as the cost and availability considerations led to one candidate among the scintillating crystals: lead tungstate PbWO<sub>4</sub> (see Sec. 11.4.3) - a mature technology used in many experiments (Tab. 11.23). It typically provides  $\beta \approx 2.5\%$ .

- **Scintillating glass.** A search for a new, cheaper material - scintillating glass (see Sec. 11.4.3) - is being pursued in the framework of eRD1 [?]. Such a material may provide a resolution comparable with the lead tungstate. The material is less dense than lead tungstate and would require more space for the same thickness in  $X_0$ . A potential advantage with respect to lead tungstate would be a lower cost and higher availability.
- **Lead glass.** This technology uses the Cherenkov light produced in glass containing lead oxide (see Sec. 11.4.3) and provides a medium resolution of  $\beta \approx 6\%$ . Lead glass is less dense than lead tungstate and would require more space. It has been widely used in experiments since the 1960-s, and some of those detectors may become available for re-use at EIC.

### Sampling Calorimeters

The resolution of sampling detectors may vary  $\beta \sim 5 - 15\%$  depending on the sampling fraction and the granularity of the active and passive material:

- Sampling fraction  $f_{\text{samp}}$  is the fraction of the total energy released in the active material, evaluated typically for MIPs. For a better resolution one needs a larger sampling fraction, which typically increases the detector length for the same thickness in  $X_0$ .
- Sampling frequency is related to the thickness of one "layer" of the absorber and the active material (scintillator). This parameter is well defined for the "sandwich"-type geometry.

It has been argued [1287, p. 119] that the stochastic coefficient is approximately proportional to  $\sqrt{d[\text{mm}] / f_{\text{samp}}}$ , where  $d$  is the thickness of the active material layer (or the fiber's diameter). This subject is discussed in Section 11.4.3 (*shashlyk* subsection), Figure 11.74 and Equation 11.6.

The requirements for the resolution and radiation hardness favor the absorber-scintillator combination. The popular technologies are:

- **Absorber/Scintillating Fibers: Pb/ScFi or W/ScFi.** The fibers are embedded into a heavy material as lead or tungsten (see Sec. 11.4.3). In one implementation the fibers are glued between lead sheets. Such *SPACAL-type* detectors have been used in a number of experiments [1288–1290]. In another implementation tungsten powder is used for the absorber. This technology [1286] has been developed for the sPHENIX experiment. The resolution depends of the fiber density and the absorber material and may vary in a range of  $\beta = 6 - 15\%$ . A better resolution is provided by a less dense detector.
- **Shashlyk** - a stack of absorber and scintillator plates (see Sec. 11.4.3). The light is collected with the help of WLS fibers passing through the plates. For the absorber lead

or tungsten are used. The technology is widely used and allows detectors of various resolutions and sizes (see Tab. 11.24). The resolution depends on the thickness of the plates and may vary between  $\beta = 5 - 15\%$ . Tungsten for the absorber material provides a high density and a short length of the calorimeter.

### ECAL technologies considered for EIC

Technologies which may fit the EIC requirements are listed in Table 11.20.

#	Type	samping, mm	$f_{samp}$	$X_0$ mm	$R_M$ mm	$\lambda_I$ mm	cell mm <sup>2</sup>	$\frac{X}{X_0}$	$\Delta Z$ cm	$\sigma_E/E, \%$	
										$\alpha$	$\beta$
1	W/ScFi**	∅0.47 ScFi W powd.	2%	7.0	19	200	25 <sup>2</sup>	20	30	2.5	13
2	PbWO <sub>4</sub> ***	-	-	8.9	19.6	203	20 <sup>2</sup>	22.5	35	1.0	2.5
3	Shashlyk***	0.75 W/Cu <sup>a</sup> 1.5 Sc	16%	12.4	26	250	25 <sup>2</sup>	20	40	1.6	6.3
4	W/ScFi** with PMT	0.59 <sup>2</sup> ScFi W powd.	12%	13	28	280	25 <sup>2</sup>	20	43	1.7	7.1
5	Shashlyk***	0.8 Pb 1.55 Sc	20%	16.4	35	520	40 <sup>2</sup>	20	48	1.5	6
6	TF1 Pb glass***	-	-	28	37	380	40 <sup>2</sup>	20	71	1.0	5-6
7	Sc. glass <sup>*b</sup>	-	-	26	35	400	40 <sup>2</sup>	20	67	1.0	3-4

\*\*\* Mature technology, well understood. used in several experiments

\*\* New technology, proven in test beams, in production for experiments

\* Technology under development, not fully proven in test beams

a Material 80% W + 20% Cu by volume,  $X_0=4.1$  mm

b The parameters of scintillating glass are tentative, see Section 11.4.3.

**Table 11.20:** The technologies promising for ECAL, ordered by the radiation length of the material. The Molière radius  $R_M$  is defined as  $R_M = X_0 \cdot 21 \text{ MeV}/E_{crit}$  and calculated for mixtures according to Ref. [1130] (Eq. 34.37–34.38).  $X/X_0$  is the thickness of the active area measured in radiation lengths, selected to provide the resolution presented in the table. A shorter active area would increase the constant term  $\alpha$ .  $\Delta Z$  denotes the full length of the module calculated as  $X + 15$  cm, where 15 cm is reserved for everything but the active area and includes the photosensors, the readout electronics, the cables and services, and the support structure. The resolution is parametrized using Equation 11.4. The “noise” factor  $\gamma$  depends on the type of the photosensor, for SiPM  $\gamma \approx 0.01$  GeV is expected.

Comments to Table 11.20:

1. Such a W/ScFi detector is being built for sPHENIX [1286]. The properties have been measured in test beams.

2.  $\text{PbWO}_4$  crystals have been used in a number of experiments (Tab. 11.23) and typically provide such properties.
3. Such a  $20X_0$  calorimeter would fit into 40 cm space. The W/Sc sampling is similar to the Pb/Sc sampling of #5. The resolution coefficients  $\alpha$  and  $\beta$  have been evaluated using Eq. 11.6. In order to account for calibration uncertainties 1% was added to the constant term:  $\alpha \rightarrow \alpha \oplus 0.01$ .
4. Such a W/ScFi prototype has been built and the properties measured in a test beam [?]. It used a long light guide and a PMT. The sampling can be adjusted to fit into a shorter space, as 40 cm.
5. Such a Pb/Sc *shashlyk* calorimeter (but  $23X_0$ ) is used in the COMPASS experiment [1291]. The constant term  $\alpha$  is scaled to a shorter calorimeter of  $20X_0$ . See also Table 11.23.
6. TF1 glass has been used in many experiments (see Ref. [1283, 1291] for example). Cherenkov light is detected. For details see Section 11.4.3.
7. Several types of Scintillating glass are being tested [?]. For details see Section 11.4.3.

The technologies listed can provide the energy resolution close to the initial requirements (Table 11.19). The  $\text{PbWO}_4$  crystals nearly fit the requirements for the  $-4 < \eta < -2$  area. The costs and manufacturing constraints will likely prevent its use in larger areas. The  $1 < \eta < 4$  area requires a medium resolution, and a high granularity, which implies a dense material. The choice of the technologies for the  $-2 < \eta < 4$  areas will depend on the geometrical constraints of the spectrometer and the space allocated.

All the described technologies are considered radiation hard for the radiation levels expected at the EIC.

### Impact of the material in front of ECAL

A certain amount of material will be distributed along the path of particles from the interaction point to the face of ECAL. The electrons radiate and the photons convert to pairs. Because of the magnetic field the radiated photons may hit the calorimeter at a distance from the impact of the electron. Simulated signals are shown in Figure 11.69. The detected energy distribution has a tail to lower energies. A typical identification criteria for electrons  $E/p > 1 - 2\sigma_E$  may lead to losses of 5-30%, in particular at low momenta (Fig. 11.69). The losses can be partly recovered, since the material is expected to be concentrated at certain places, allowing to predict the impact position of radiated photons for a given particle trajectory. Still losses of 10-20% are expected for certain areas at  $p < 10$  GeV.

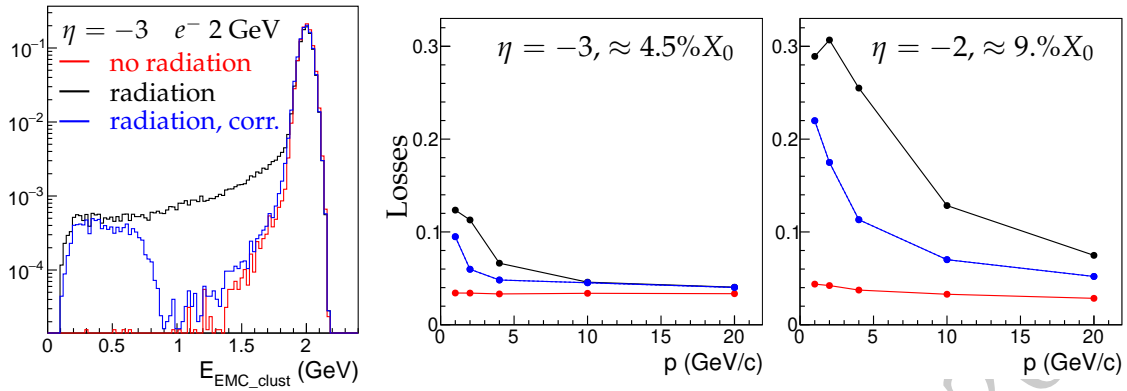


**Figure 11.69:** Simulated impact of material in front of ECAL on detection of 2 GeV electrons [?]. The amount of material depends on  $\eta$ . Three cases are considered: a) electron does not radiate in the material; b) electron radiates and only the cluster associated with electron track is considered; c) attempt made to recover the photons radiated in the thick objects upstream, whose positions can be predicted. Practically all the energy has been recovered up to a loss of a half of the initial energy, which was an arbitrary cutoff. The real cutoff will depend on the background, the tracking quality etc.

**Left:** The energy spectrum of the cluster in ECAL from GEANT4 [1222] simulation.

**Middle and Right:** the losses of electrons, selected using  $E/p > 1 - 2\sigma_E$ .

### Impact of the Cell Size and the Projective Geometry

In order to have the best coordinate resolution while minimizing the number of the read-out channels the cell transverse size is usually selected close to the Molière radius of the calorimeter material. The coordinate resolution depends on the position of the hit and is the best at the boundary between two cell. The average resolution depends on the particle energy and the incident angle (see Equation 11.5). Based on experience (see Table 11.21) we may expect a resolution for the normal incident angle  $\theta_I$  of about  $(1 \oplus 3/\sqrt{E/1\text{GeV}})$  mm for the cell size 20-25 mm, and  $(1 \oplus 6/\sqrt{E/1\text{GeV}})$  mm for the cell size of about 40 mm. Let us consider a dense detector with  $X_0 \approx 10$  mm and the cell size of 25 mm. In the non-projective geometry, at  $\theta_I = 45^\circ$ , the additional term  $X_0 \sin \theta_I \approx 7$  mm will dominate the coordinate resolution. The relative deterioration of the resolution does not depend strongly on the density of the material.

Another important characteristics of ECAL is the ability to discriminate a single photon from a merged photon pair from a high momentum  $\pi^0$  meson decay. For high momentum  $\pi^0$  the minimal angle between two photons in the Lab frame is  $\approx 2m_{\pi^0}/p_{\pi^0}$  and most of the decays produce two photons at angles close to the minimal angle. At high enough momentum two photons appear in the ECAL in a close proximity to each other, so that the ECAL response to a pair of decay photons becomes indistinguishable from the response to a single photon with the energy equal to a sum of decay photon energies. ECAL granularity defines the highest momentum at which ECAL can discriminate single photon from merged photons from  $\pi^0$  meson decay. Usually, two photons are easily distinguishable in the ECAL when they are separated at least by a distance equal to twice of cell size. In this

Type	$R_M$ , mm	cell size, mm	$\sigma_E/E$ at 1 GeV	$\delta$ mm	$\epsilon$ , mm GeV <sup>0.5</sup>	Ref
PbWO <sub>4</sub>	20	20	2.9%	0.4	2.6	[1292]
PbWO <sub>4</sub>	20	22	3.9%	0.3	2.6	[1293]
TF1	37	38	5.7%	0.5	6.0	[1294]
Shashlyk	41	55	8.4%	1.6	5.7	[1283]
Shashlyk	59	110	4.7%	3.3	15.4	[1295]

**Table 11.21:** The coordinate resolutions observed with several detectors for the normal incident angle  $\theta_I$ . The resolution is parametrized using Equation 11.5. The stochastic factor  $\epsilon$  appears to be approximately proportional to the cell size.

case two photons produce two clusters in ECAL, or a single cluster with two distinct local maxima. With smaller distance between two photons, they produce a single cluster with one local maximum. Even in this case, different mathematical techniques to analyze the energy distribution among the cluster cells still can discriminate a single photon cluster from a merged photon cluster, down to a distance between two photons equal to the cell size, or even down to a half of the cell size, though with limited efficiency. Figure 11.70 illustrates such a capability for the hadron endcap ECAL with the cell transverse size of 2.5 cm, located at 3 m from the collision point. The performance deteriorates for a non-orthogonal impact (here at lower  $\eta$ ), due to a wider shower profile and its larger fluctuations in the ECAL transverse plane. For a transverse size  $d$  and the distance to the collision point  $Z_{ECAL}$ , the momentum reach for  $\pi^0/\gamma$  discrimination scales roughly as  $Z_{ECAL}/d$ .

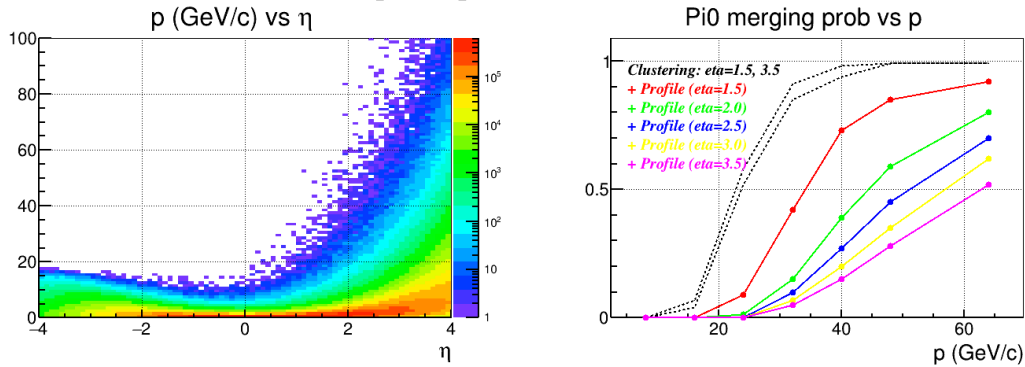


**Figure 11.70:** **Left:** The calculated  $\pi^0$  momentum spectrum for SiDIS at  $e + p$   $18 \times 275$  GeV collisions, using PYTHIA [272]. **Right:** The probability of two photons to merge, calculated [?] using GEANT4 [1222] for the cell size of  $25 \times 25$  mm<sup>2</sup> located at 3 m from the interaction point, for the non-projective geometry. For the projective geometry the results for  $\eta > 3.5$  would be close to the non-projective curve at for  $\eta=3.5$ .

The requirements to the hadron endcap strongly favor a calorimeter material with a short radiation length and a small Molière radius, allowing a fine segmentation of  $\leq 25$  mm.

Using the projective geometry for ECAL in the barrel is standard for solenoid-based spectrometers. For the endcaps it is geometrically more complex. The projective geometry would provide a significantly better coordinate resolution at large radii.

### Electron/pion separation

The DIS momentum spectra of the DIS electrons and pions are shown in Fig. 11.68. At lower momenta the pion flux dominates the flux of scattered electrons by orders of magnitudes. ECAL is expected to be the main tool for the electron identification. Pions produce smaller signals in ECAL than electrons of the same momentum (Fig. 11.71, left). Using the measured momentum of the charged track  $p$  and the energy deposited by this track in ECAL one can select electrons requiring  $E/p > 1 - \Delta$ . The fluctuations of the  $E/p$  value are characterized by  $\sigma(E/p) = E/p(\sigma_E/E \oplus \sigma_p/p)$ , where  $\sigma_p/p$  are expected to be significant at  $|\eta| > 2$ . In this review we use typically  $\Delta = 1.6\sigma_E/E$ , using only the Gaussian width of the calorimeter signal. For the Gaussian calorimeter response the efficiency to electrons would be 95%. However, the response typically has a tail to lower energies, increased by material in front (Fig. 11.69), which reduces the efficiency for electrons. Larger  $\sigma_E$  and  $\sigma_p$  lead to a lower efficiency for electrons and a smaller rejection factor for pions for a given  $\Delta$ .

In general, one expects a better electron-PID performance for a better energy resolution of the calorimeter and the momentum resolution of the spectrometer. Analysis of the shower profile can provide an additional pion suppression. However, the effect depends on the impact angles, and therefore, on the geometry of the calorimeter (projective or not).

The pion suppression performance of calorimeters has been measured in test beams and also evaluated using simulation. One should note that it is challenging to measure or calculate large rejection factors  $R_\pi > 1000$  because of beam contamination, or uncertainties in simulation of hadronic processes. The pion rejection factor may be limited by charge exchange processes as  $\pi^- + p \rightarrow \pi^0 + n$  that would produce signals similar to electrons at the same energy (noted in Ref. [1296] for example). The cross section for such processes typically falls with energy.

Several examples of the measured pion suppression in various calorimeters are shown in Table 11.22. For the sampling calorimeters the largest reported rejection factor of  $R_\pi=2000$ , at the measured  $\varepsilon_e = 90\%$ , was obtained at 100 GeV, where the energy resolution was about 2%. A rejection of  $R_\pi = 500$  was measured for a  $\text{PbWO}_4$  calorimeter at 2.5 GeV, where the energy resolution was 2%. In this test a cut  $\Delta > 2 \cdot \sigma_E$  was applied (98% "Gaussian" efficiency), which may translate to a  $\varepsilon_e \approx 90\%$  of the real efficiency.

Figure 11.71 shows the calculated suppression dependence on energy, the calorimeter resolution and the track momentum resolution. The simulated pion-produced signals in  $\text{PbWO}_4$  and in sampling detectors are compared - the former have a shorter tail to high values. A stronger response to neutrons by the plastic scintillator than by an inorganic one may contribute to the effect. While the results of calculations for sampling calorimeters are consistent with the measurements, the calculated  $R_\pi$  for  $\text{PbWO}_4$  is more than an

Type	Experiment	$\sigma_E/E, \%$			E, GeV	$\varepsilon_e$		particle	$R_\pi$	Ref
		$\alpha$	$\beta$	$\gamma$		meas.	calc.			
PbWO <sub>4</sub>	-	0.1	3.1		1.0-2.5		98%	$\pi^-$	500	[1297]
PbWO <sub>4</sub>	-	0.5	4.0		80.		90%	$\pi^-$	6000	[1298]
TF1	PHENIX	0.8	6.0	1.5-4.0		80%	98%	$\pi^-$	250	[1283]
						90%			160	
						95%			100	
					1.0	80%	98%		80	
					0.75	80%	98%		45	
					0.50	80%	98%		7	
TF1	Hall C	1.0	6.0		3.2	95%		$\pi^-$	*200	[1299]
Pb/Sc	PHENIX	2.1	8.1	40		77%	84%	$\pi^+$	430	[1300]
						88%	95%		350	
						92%	98%		300	
						95%	100%		200	
					4		95%		100	unpub
					3		95%		80	unpub
					2		95%		43	unpub
					1		95%		12	unpub
0.5		95%		3.4	unpub					
Pb/Sc	ALICE	1.7	11.1	5.0	100	90%		$\pi^-$	2000	[1296]
					100	95%			1100	
					40	90%			700	
					40	95%			400	
W/ScFi	sPHENIX	2.8	15.5	8			50%	$\pi^-$	710	[1301]
									330	
									210	
									160	
									90	

\* The longitudinal segmentation not used

**Table 11.22:** The measured pion suppression factor  $R_\pi$  and the associated efficiency  $\varepsilon_e$  to electrons. The shower shape has not been taken into account, except for Ref. [1298] (PbWO<sub>4</sub>). In several studies the  $\varepsilon_e$  was measured and from the data reported it was possible to calculate the “Gaussian” efficiency, that is considerably higher than the measured one, as expected. For other studies only the calculated “Gaussian” efficiency is available. The measurements marked “unpub” come from the authors of the paper, but have not been included into the paper.

order of magnitude higher than a measurement at 2.5 GeV. It may be caused by systematic uncertainties of both the measurement and simulation. At this time we can not claim that a rejection power higher than 1000 is achievable at moderate energies even with the relatively high-resolution PbWO<sub>4</sub> detector.

Figure 11.71 (right) demonstrates how the momentum resolution affects the performance at small angles  $|\eta| > 3$ .

Calculations also show that taking the shower shape into account can improve the pion rejection by a factor of 2 even in non-projective geometry, or by a factor of 3-4 at small incident angles and in projective geometry.

In summary, in the energy range 4-20 GeV sampling calorimeters and lead glass calorimeters can provide a pion rejection factor from a hundred to a thousand.  $\text{PbWO}_4$  crystals may be able to provide factors 3-5 higher, but factors  $> 1000$  need to be confirmed by measurements.

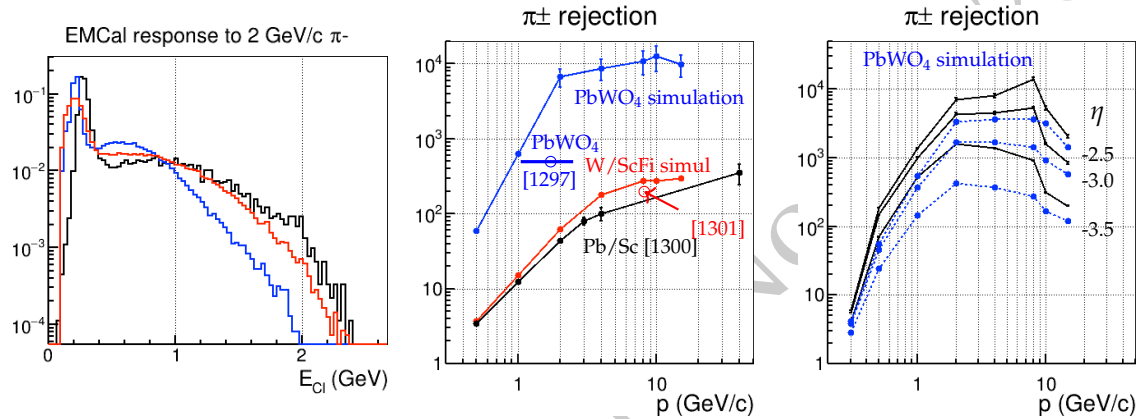


**Figure 11.71:** Measured and simulated (GEANT4 [1222]) pion suppression [?, ?], evaluated with a  $\Delta = 1.6 \cdot \sigma_E$  cut ("Gaussian"  $\varepsilon_e = 95\%$ ).

**Left:** the response to 2 GeV pions for: black - measured for Pb/Sc  $8\%/\sqrt{E} \oplus 2\%$  (PHENIX); red - simulated for W/ScFi  $13\%/\sqrt{E} \oplus 3\%$ ; blue - simulated for PbWO<sub>4</sub>  $2.5\%/\sqrt{E} \oplus 1\%$ .

**Middle:** pion suppression, momentum resolution neglected;  $E/p$  cut only;

black - measured for Pb/Sc  $8.1\%/\sqrt{E} \oplus 2.1\%$  (PHENIX [1300], see also Table 11.22);

red - simulation for W/ScFi  $12\%/\sqrt{E} \oplus 3\%$ , calculation compared with a measurement at 8 GeV (Ref. [1301] and Tab. 11.22);

blue - simulation for PbWO<sub>4</sub>  $2.5\%/\sqrt{E} \oplus 1\%$ . The calculation, exceeds a measurement at 1-2.5 GeV (Table. 11.22) by a factor of  $< 10$ .

**Right:** simulated pion suppression for PbWO<sub>4</sub>  $2.5\%/\sqrt{E} \oplus 1\%$ , at  $\eta = -3.5, -3.0, -2.5$ , the momentum resolution taken into account. The dependence on  $\eta$  is caused by the momentum resolution.

blue -  $E/p$  cut,  $\varepsilon_e = 95\%$ ;

black -  $E/p$  and shape cuts,  $\varepsilon_e = 92\%$ .

Figure 11.72 shows the calculated purity of electrons in the DIS sample, in 3 areas of  $\eta$ , each equipped with ECAL of a different resolution, close to the specifications in Table 11.19. The levels of the pion background are also different in these areas (Fig. 11.68). In all areas a  $>95\%$  purity is reached at  $p > 4$  GeV. The  $-3.5 < \eta < 2$  area is supposed to be covered with a high-resolution ECAL ( $\beta = 2.5\%$ ), and the purity  $>90\%$  is reached at  $E > 2$  GeV. The other areas are supposed to be covered with  $\beta = 7\%$  and  $\beta = 12\%$ -resolution calorimeters and at  $p < 4$  GeV the pion contamination remains high.

Pion rejection can be improved by using a “preshower” detector. Also, the calorimeter itself may be equipped with a second readout from the front part of the modules, which does not require an extra space for another detector. A factor of 2 improvement in  $e/\pi$  separation was achieved equipping a *shashlyk* detector with scintillator plates with different emission times [1302].

Since  $X_0/\lambda_I$  is smaller for heavier materials, they should provide a better pion suppression. One should note that the material passed by the electron track in front of the calorimeter will reduce the energy reaching the calorimeter, affecting the  $E/p$  ratio and the  $e/\pi$  PID. For the same pion rejection factor the efficiency to electrons will be reduced. A lower efficiency typically causes a higher uncertainty of the measurement.

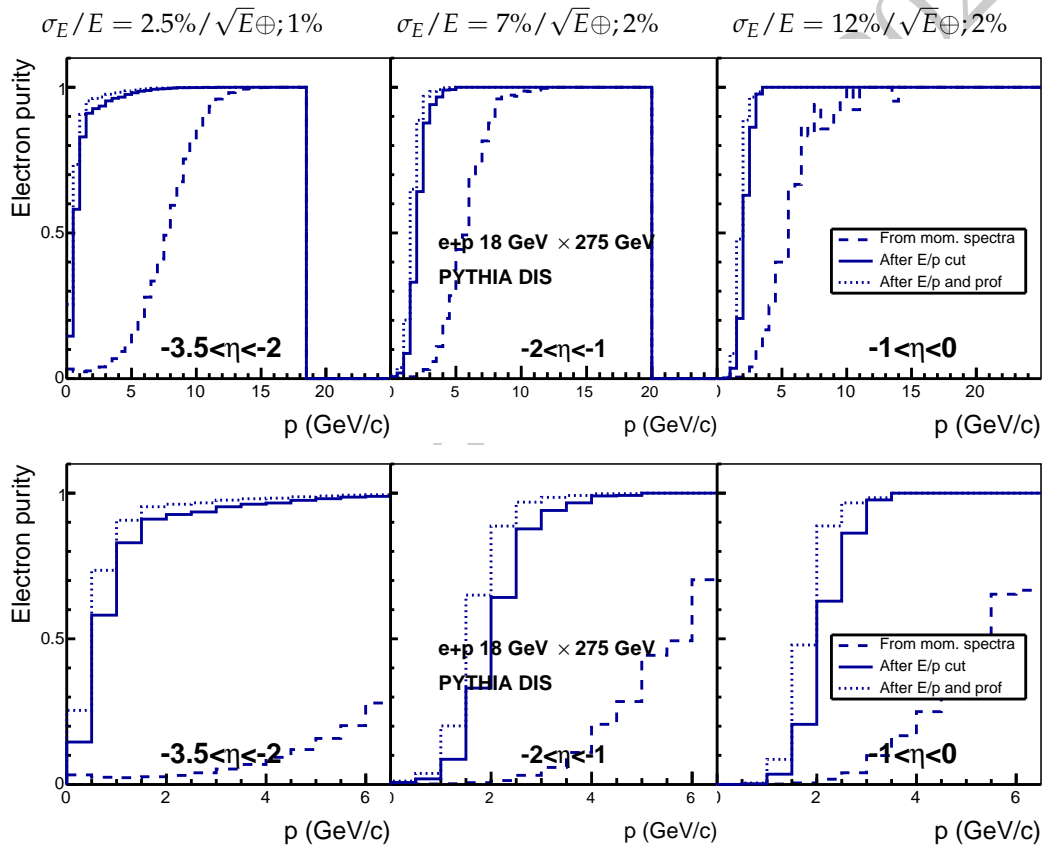


**Figure 11.72:** Calculated purity of the DIS electron sample and the effect of the pion suppression [?] for  $e+p 18 \times 275$  GeV. The pion suppression was evaluated using a  $\Delta = 1.6 \cdot \sigma_E$  cut (“Gaussian”  $\varepsilon_e = 95\%$ ). The columns present three areas of  $\eta$  with the assigned  $\sigma_E/E$  for each area. The bottom panel presents the zoomed in plots of the top panel. Dashed lines - no cuts, solid lines -  $E/p$  cut, dotted lines -  $E/p$  and shower shape cuts. A cap of 1000 on the calculated pion rejection was set in order to address the existing uncertainties.

### Lowest detectable energy

The lowest detectable energy depends on the amount of light detected versus noise of various origin and low-energy background. With  $\text{PbWO}_4$  as low as 20 MeV photons can be detected, provided low-noise sensors and electronics, although with a 30-50% energy resolution. For sampling detectors one may expect the lowest detectable energy of 50-100 MeV.

### Readout Considerations

Only detectors with optical readout have been considered. In the current scenarios the endcap ECAL photosensors will be located in a magnetic field of  $>0.1$  T, which precludes the usage of regular PMTs. The barrel ECAL is located in a  $>1$  T field. At the moment the sensor of choice is SiPM, which provides a high gain (about  $10^6$ ) and a medium photodetection efficiency of about 20%. The drawbacks are small surface, noise, susceptibility to radiation, in particular to neutron/proton radiation [1303,1304], sensitivity to temperature, a small dynamic range, and the intrinsic nonlinearity [1305]. Radiation leads to a higher noise. Additionally, the performance degrades with the current flown [?]. For the same amount of light a SiPM can fire a number of pixels comparable to a PMT photoelectron count [1306]. However, a fraction of the pixels fire due to the cross talk, not improving the statistical fluctuations. While a SiPM readout is natural for the fiber technologies as *Shashlyk*, it does not look optimal for a large-surface -  $16 \text{ cm}^2$  - glass blocks. Such a readout has not been tested yet with  $4 \text{ cm}^2$  crystals.

The effect of non-linearity for SiPMs depends on the desired dynamic range and the calorimeter resolution. Let us consider the requirements of a 2% energy resolution at 1 GeV and the maximum energy of 20 GeV (at the center of the electron endcap), and find the total number of pixels needed for one calorimeter cell. With the optimal cell size about 80% of a shower energy on average goes to one cell, but with considerable fluctuations. The p.e. (or pixel) count at 1 GeV should be  $\gtrsim 10\text{k}$  (1% statistical fluctuations). Then, at 20 GeV the pixel count with no saturation would be about 200k. The saturation effects for MPPC S12572-010P 90k-pixel,  $3 \times 3 \text{ mm}^2$  device have been shown to be as large [1305] as would be expected for a 30k-pixel device. The correction to nonlinearity has to be calibrated rather than calculated, and may contain large uncertainties. This may require to limit the number of fired pixels to  $<20\%$  of the total. Therefore, per one crystal one would need a device(s) with about 1M pixels in total. The technology of SiPM is still developing and the linearity might be improved in the future. Another factors to consider is the density of light coming from the crystal's face per GeV compared with the PDE and the density of pixels.

A *shashlyk* module made for MPD [?] has been tested with a Hamamatsu MPPC S13360-6025 which contains 57k pixels  $25 \times 25 \mu\text{m}^2$ . With the yield of about 5000 pxs/GeV the loss to non-linearity at 2 GeV was about 10%.

It is expected that for the electronics readout special ASIC chips will be developed (see Section ??), which will provide the bias voltage to the SiPM, read out the signals using fADC,

and process the signals producing the timing and the integral and/or maximum amplitude. Since both the detectors considered and the SiPM sensors are fast, one may expect a timing resolution of  $<1$  ns. At least 12-bit fADCs are needed. It will be also important to be able to send out not only the processed, but also the raw signals as waveforms. Without an ASIC chip the power consumption of the on-detector electronics will be considerably higher and its functions may be limited.

ECAL must be equipped with a monitoring system, which distributes light flashes to the photosensors. The on-board electronics, additionally to the readout, must also operate the monitoring system.

### Discussion

The EIC resolution requirements to the electromagnetic calorimetry system can be met or nearly met by using developed technologies. For the area  $\eta < -2$  the  $\text{PbWO}_4$  crystals appear to be the only practical choice providing a performance close to the required, and also being compact enough to meet the expected geometrical constraints. For the other areas several options exist. The choice strongly depends on the geometrical constraints. A better performance may be achieved with more space, which is a subject for a global optimization of the experiment. Other considerations to be mentioned:

- The area  $\eta > 1$  requires a high granularity of ECAL in order to resolve photons from  $\pi^0$  decays. It favors a small cell size and high- $A$  materials, which would also allow a shorter space.
- The projective geometry allows a better coordinate resolution and  $e/\pi$  separation. The barrel part is supposed to be projective. A decision has to be made about the endcaps.
- The  $e/\pi$  separation provided by the “basic” ECAL with the required resolution will be sufficient to study the  $e+p$   $18 \times 275$  GeV DIS at  $p > 4$  GeV. At  $\eta < -2$  the high-resolution ECAL will extend the coverage to about 2 GeV. With the electron beam energy of 10 GeV the signal to background ratio is different and a similar purity can be reached at momenta of about 1 GeV lower. The ePD can be improved either by using calorimeters with a much better resolution, or by providing a “preshower” capability, or by using different detectors as a Cherenkov or TRD.
- At this time a SiPM is the photosensor of choice. However, such a sensor may bring limitations to the performance of high-resolution detectors, as  $\text{PbWO}_4$ , that have to cover a relatively large dynamic range. Large-surface sensors with a high pixel density are needed for this application.

The eRD1 “EIC Calorimeter R&D Consortium” [?] is expected to continue the development of a number of technologies, including  $\text{PbWO}_4$  crystals, scintillating glass, W/ScFi and *shashlyk* detectors.

### 11.4.3 ECAL: Appendix

#### PbWO<sub>4</sub> crystals

The EIC high-resolution EM Calorimeters have the following basic requirements:

- Interaction rate capability up to  $0.5 \times 10^6$  Hz requiring reasonably fast scintillation kinetics
- Sufficient energy resolution and efficiency over a large dynamic range of photon energies, typically from order 50 MeV to 50 GeV
- Adapted geometrical dimensions to contain the major part of the EM shower
- Moderate radiation hardness up to 3 krad/year (30 Gy/year) electromagnetic and  $10^{10} n/cm^2$  hadronic at the top luminosity.

This rules out most of the well-known scintillator materials. Finally, even a compact geometrical design requires, due to a minimum granularity, a large quantity of crystal modules, which rely on existing technology for mass production to guarantee the necessary homogeneity of the whole calorimeter. For hadron physics measurements with electromagnetic reactions, such as at multiple setups at Jefferson Lab and also at PANDA/GSI, the most common precision calorimeter of choice has been lead tungstate, PbWO<sub>4</sub> (PWO). This is mostly driven by the requirement of good energy resolution and high granularity to detect and identify electrons, photons and pions. Good energy resolution aids in electron-pion separation and to determine the electron scattering kinematics, compactness and high granularity is driven by need for position resolution and separation of single-photons from neutral-pion decays. PWO meets the requirements of an extremely fast, compact, and radiation hard scintillator material providing sufficient luminescence yield to achieve good energy resolution. PWO is available from two commercial vendors with established mass production capability.

Parameters of PbWO<sub>4</sub> calorimeters used in various experiments and results of beam tests are summarized in Table 11.23.

#### Scintillating glass

A bridge between PWO and less stringent resolution requirements could be provided by SciGlass. Over the last year Scintilex, LLC has made tremendous improvements and progress in the formulation and production of transparent barium-silicate-based glass scintillators (SciGlass) using new formulation approaches that improve properties and solve the issue of macro defects that becomes even more acute upon scale-up. The properties of SciGlass in comparison to PbWO<sub>4</sub> are shown in Table 1. SciGlass has excellent radiation resistance - no damage up to 1000 Gy electromagnetic and  $10^{15} n/cm^2$  hadron irradiation, the highest doses tested to date. The SciGlass insensitivity to temperature is

Experiment	Ref	#	cell size mm <sup>3</sup>	$\frac{X}{X_0}$	Photo-sensor mm <sup>2</sup>	Temperature °C	Test beam GeV	matrix E <sub>min</sub> , MeV	p.e./MeV	$\sigma_E/E[\text{GeV}],\%$		
										$\alpha$	$\beta$ GeV <sup>0.5</sup>	$\gamma$ GeV <sup>-1</sup>
GAMS 1995	[1307]	35	20 <sup>2</sup> ×180	20	XP1911 <sup>b</sup> 176 mm <sup>2</sup>	14 ±0.2	10 70	5×5	6 p.e.	0.47 ±0.06	2.8 ±0.2	
KEK 2000	[1292]	9	20 <sup>2</sup> ×200	22.5	R4125 <sup>b</sup> 25 mm <sup>2</sup>	13	0.2 1.0	3×3		0.0 ±2.7	2.5 ±0.1	1.4 ±0.1
ALICE 2005	[1308]	18k <sup>N</sup>	22 <sup>2</sup> ×180	20	S8148 <sup>a</sup> 25 mm <sup>2</sup>	-25 ±0.1	0.6 150	3×3	7.5 p.e.	1.1 ±0.3	3.6 ±0.2	1.1 ±0.3
CMS 2006	[1309]	76k <sup>B</sup>	22 <sup>2</sup> –27 <sup>2</sup> ×230	26	S8148 <sup>a</sup> 2×25 mm <sup>2</sup>	18 ±0.1	25 100	3×3	10 p.e. <sup>f</sup>	0.4 ±0.3	2.9 ±0.2	12.9 ±0.2
PRIMEX 2006	[1310]	1k <sup>S</sup>	20.5 <sup>2</sup> ×180	20	R4125A <sup>b</sup> 176 mm <sup>2</sup>	14 ±0.1	25 100	5×5		0.9	2.5	1.0
PANDA 2011	[1311] [1312]	11k <sup>C</sup> 5k <sup>B</sup>	21 <sup>2</sup> –27 <sup>2</sup> ×200	22.5	LAAPD <sup>ac</sup> 190 mm <sup>2</sup>	-25	0.05 0.75	3×3	16 p.e.	0.5	2.3	0.27
HPS 2017	[1313]	442 <sup>B</sup>	13.3 <sup>2</sup> –16 <sup>2</sup> ×160	18	S8664-1010 <sup>a</sup> 100 mm <sup>2</sup>	-17 ±0.3	0.35 2.35	3×3		2.5	2.87	1.62
CLAS12 FT 2020	[1314]	332 <sup>S</sup>	15 <sup>2</sup> ×200	22.5	S8664-1010 <sup>a</sup> 100 mm <sup>2</sup>	0.0 ±0.1	2.2	3×3	230 p.e. <sup>e</sup>	3.3 <sup>d</sup>		
NPS 2019	[1315]	670 <sup>S</sup> 350 <sup>C</sup>	20.5 <sup>2</sup> ×200	22.5	R4125 <sup>b</sup> 176 mm <sup>2</sup>	18.0	4.7	3×3	14 p.e.	1.6 <sup>d</sup>		
CCAL-NPSprot 2019	[?]	140 <sup>S</sup>	20.5 <sup>2</sup> ×200	22.5	R4125 <sup>b</sup> 176 mm <sup>2</sup>	17.0	4.7	3×3	14 p.e.	0.4	2.6	1.9

Manufacturer: **B** BTCP; **N** NCC-RSS; **S** SICCAS; **C** CRYTUR.

**a** - APD; **b** - PMT; **c** - Signal shaping 1  $\mu$ s. **d** - The full resolution at the given energy

**e** It is unclear why the yield is much higher than the yield from PANDA. **f** from Ref. [1315].

**Table 11.23:** A list of parameters of PbWO<sub>4</sub> EM calorimeters.

a clear advantage over PbWO<sub>4</sub>, which has a dependence of about 2-3%/°C and has to be continuously monitored. Scintilex has demonstrated a successful scaleup method and can now reliably produce glass samples of sizes up to 10 radiation lengths. Initial beam test results with particle energies of 4-5 GeV suggest that Scintilex glass samples have an energy resolution comparable to PbWO<sub>4</sub> crystals, if comparable radiation lengths are used, for higher light yield, which is important for low energy particle detection. Scale up to  $\approx 15 - 20X_0$  long blocks is planned for late 2020. Additional beam tests are anticipated for 2021.

## Lead glass

The lead-glass electromagnetic calorimeters for EIC can be analogous to VENUS at Tristhan [1316], OPAL at LEP [1317], JLab GlueX forward calorimeter [?]. Several types of lead glass, of different parameters have been used as radiator. The light generation mechanism for the lead-glass is dominantly Cherenkov radiation (scintillation is below 1-2%). The

fraction of PbO in chemical composition may vary from 45% to 75% by weight, and density from  $3.6 \text{ g/cm}^3$  to  $5.5 \text{ g/cm}^3$  [?,1299,1317]. The radiation length is within 1.5 cm to 3.1 cm. The Moliere radius is 3.3 –3.7 cm, typically. In practice, homogeneous calorimeters must be 20 radiation length deep to contain electromagnetic shower. For the lead glass radiator this implies 30 – 50 cm length. For a hodoscopic construction, the optimal granularity size is  $\approx 4 \text{ cm}$ , which is conditioned by the Moliere radius. The refractive index ranges from 1.62 to 1.85 (1.65 typically) [?, 1299, 1317]. The transparency window starts from 350 nm, except for the Ce doped radiation resistant lead glass for which it starts from 400 nm [1299]. PMT-s with bialkali photocathode (sensitivity range from 300 nm to 600 nm, peak quantum efficiency 20% at 400 nm) are well suited for Cherenkov light detection from electromagnetic showers in lead glasses. The lead glass calorimeters have modular construction. The glass blocks are wrapped in thin reflector (usually aluminized Mylar), then by light tight Tedlar film. It is important to have a thin layer of air between the block and Mylar, for full internal reflection of light at oblique incident angles. The PMT-s are optically coupled to the blocks by means of optical glue or grease of suitable refractive index. In the moderate magnetic field the PMT-s can be shielded by layers of  $\mu$ -metal. In stronger fields (10 – 100 G) additional shielding of photocathode by soft iron can be implemented. A light guide between the block and PMT, no shorter than diameter of photocathode shall be placed between the block and PMT. Such design of modules was effectively used in many lead glass calorimeters [?, 1316–1318]. Radiation hardness of lead-glass crystals is  $\sim 10$  krad integral dose for TF-1, and 50 krad for F-101 type radiation hard crystals. The crystals recover from damage on their own within 1 to 3 months [1299]. They can be cured in situ by exposing to UV radiation. A 30% reduction in transparency of 4 cm glass thickness can be recovered within 8 hours. Alternatively, off-line gradual heating, up to  $260^\circ \text{C}$  and cooling may be implemented. Resolution of lead-glass calorimeters strongly depends on optical quality and light-yield of the crystals, light detection efficiency and electronic noise, and may vary from  $\approx 5\%/\sqrt{E} + 1\%$  [1318] to  $\approx 8\%/\sqrt{E} + 3\%$  [1299, 1318, 1319]. A coordinate resolution  $6.4/\sqrt{E}(\text{GeV})\text{mm}$  for incoming photons was obtained in a hodoscopic construction of  $4 \times 4 \text{ cm}^2$  granularity [?].

#### Scintillating fibers embedded in absorber

Scintillating fiber calorimeters (*SPACALs*) have been built and used in many experiments in both High Energy and Nuclear Physics and have been used for both electromagnetic and hadronic calorimeters [1288–1290, 1320, 1321]. They consist of many scintillating fibers embedded in an absorber material which are then gathered at the front or the back (or both) and read out with photosensors. The sampling fraction and sampling frequency can be adjusted by changing the number of fibers and their spacing to provide a range of energy resolutions and other properties. In addition, the absorber material can be selected for a specific application in order to achieve a variety of requirements.

One of the requirements for any ECAL at EIC is that it be compact, i.e., that it has a short radiation length and small Molière radius so that the total length of the calorimeter can be minimized and that the lateral extent of the shower can be contained to provide good separation of neighboring showers. This can best be achieved with a high Z absorber such as

tungsten. The sPHENIX barrel ECAL utilizes a tungsten *SPACAL* (W/SciFi) design where an array of scintillating fibers is embedded in a matrix of tungsten powder and epoxy. Some of the properties of this design are listed in Table 11.20. This design was originally developed at UCLA [1322] and then later adopted by the sPHENIX Experiment [1301] which then further developed the technology into an industrialized process to produce more than 6000 2D projective absorber blocks. These blocks are read out using SiPMs that are coupled to the blocks using short light guides, which keeps the total radial length of the calorimeter to 26 cm inside the BaBar solenoid magnet, including the readout and supporting structure. This calorimeter is currently under construction and is expected to be completed by the end of 2021.

One of the issues with the W/SciFi design is that the boundaries between the blocks and the light guides introduce certain non-uniformities in the energy response. These can be measured using the position information provided by the calorimeter itself and/or the tracking system and used to correct the energy response. For the sPHENIX design, this leads to an energy resolution  $\sim 13\%/\sqrt{E} \oplus 2.5\%$ .

For any future W/SciFi calorimeter for EIC, it would be advantageous to minimize the number of boundaries produced by the blocks and the light guides, which is possible by greatly reducing the length of the light guides to just a few mm (which is necessary to act as mixer for the light coming out of the fibers) and then covering nearly all of the readout area with SiPMs. This is now also possible with the availability of large area ( $6 \times 6 \text{ mm}^2$ ) SiPMs at an affordable cost.

### **Shashlyk**

*Shashlik* calorimeters have been used in many High Energy and Nuclear Physics experiments (Table 11.24). The light produced in an alternating stack of absorber plates and scintillating tiles is collected with the help of wavelength shifting (WLS) fibers passed through the stack and is detected on one or both of the fiber's ends. The outgoing light is concentrated on a surface much smaller than the cell size - an advantage for using the relatively small semiconductor photosensors.

The plate thickness can be selected in order to obtain the required sampling fraction and the sampling frequency. It should be noted that, as with other sampling calorimeters, a larger sampling fraction leads to a larger radiation length and the Molière radius, which then increases the length of the total stack and allows the shower to spread out more laterally.

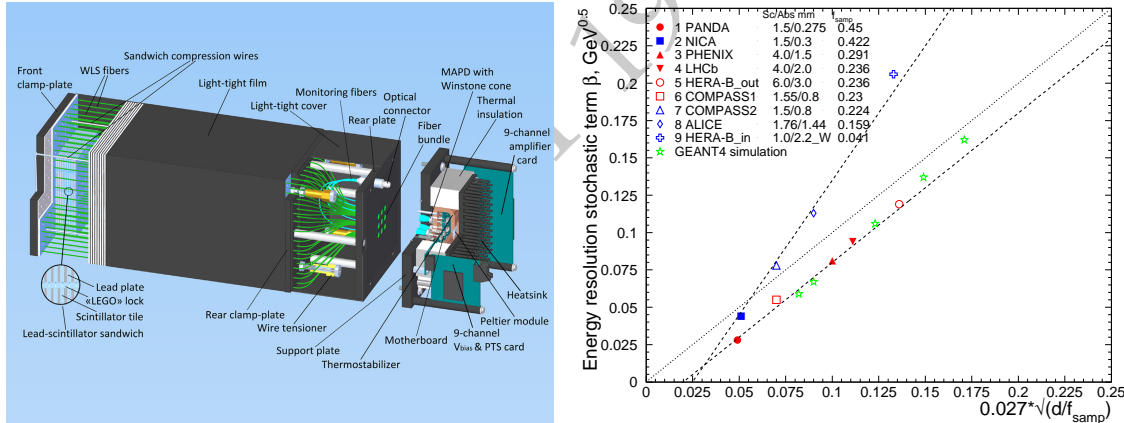
Most of the *shashlyk* calorimeters to date have used lead for the absorber plates. Using tungsten helps to reduce the lateral overlap of showers (Table 11.24: HERA-B inner calorimeter), and to reduce the total length of the calorimeter.

Figure 11.73 shows several examples of the *shashlyk* detector. Typically, the WLS fibers are 1 cm apart. In most *shashlyk* calorimeters, the WLS fibers are bundled at the back of the detector and read out with a single photosensor. In a new eRD1 W/Sc prototype



**Figure 11.73:** Left: COMPASS Pb/Sc “spiral”  $4 \times 4$  cm<sup>2</sup> modules [1291]; Middle: LHC-B Pb/Sc 3 module types, with a single  $12 \times 12$  cm<sup>2</sup> cell, with four  $6 \times 6$  cm<sup>2</sup> cells, and with nine  $4 \times 4$  cm<sup>2</sup> cells [1323]; Right: eRD1 W/Sc prototype  $4 \times 4$  cm<sup>2</sup> cell, readout: 16 small SiPM per cell [?,?].

(Fig. 11.73, right) each fiber is readout by a small SiPM. One module is often split into several readout cells in order to reduce the effect of the edges between cells (Fig. 11.73, middle). The grid of fibers leads to variations of the response across the cell surface. The best uniformity has been achieved with a “spiral” geometry of the fibers (Fig. 11.73, left). An example of a  $3 \times 3$  module design is shown in Figure 11.74 (left).



**Figure 11.74:** Left: A  $3 \times 3$  module design [1324] with a SiPM readout.

Right: The measured stochastic term  $\beta$  of the resolution of *shashlyk* calorimeters (Tab. 11.24) against a predicted value of  $\beta = 0.027\sqrt{d/f_{smp}}$  [1287, p. 119], where  $d$  is the thickness of the scintillator tile in mm. The “scaling variable”  $\sqrt{d/f_{smp}}$  at the first order does not depend on the thickness of the scintillator tile. The plot indicates that the data can be split in two groups. In each group the dependence on the “scaling variable” is nearly linear:  $\beta \approx 0.027(\sqrt{d/f_{smp}} - 0.74)$  and  $\beta \approx 0.049(\sqrt{d/f_{smp}} - 0.92)$ . The origin of the difference between the groups is unclear at this moment. The results of GEANT4 simulation (Fig. 11.75) match the lower curve well at moderate layer thickness.

The scintillator and WLS fibers are selected in order to match their spectral properties.

Table 11.24 shows the parameters of several large-scale *shashlyk* detectors as well as two prototypes. These detectors are built both in rectangular and trapezoidal shapes, the lat-

Experi- ment # ch	Ref	sampling mm # layers	$f_{samp}$ %	$\rho$ $\frac{g}{cm^3}$	$X_0$ mm	$R_M$ mm	$\frac{X}{X_0}$	cell read- out mm mm <sup>2</sup>	Yield/ MeV	Beam GeV	$\sigma_E/E[\text{GeV}]$	
											$\alpha$ %	$\beta$ %
KOPIO few	[1325]	Pb/Sc 0.275/1.5 ×300	2.75 45.	35. 2.60	60. 35.	16. 57.	110. 144	APD 200.	50 p.e.	0.2-0.4	2.0	2.74
PANDA ~ 2000	[1295]	Pb/Sc 0.275/1.5 ×380	45.	2.60	35.	57.	110. 144	PMT 200.	5 p.e.	1-19	1.3	2.8 3.5
MPD NICA 38000	[1326]	Pb/Sc 0.3/1.5 ×220	43.	2.70	32.	55.	110. 144	SiPM 36.		0.5-3.0	1.0	4.4
PHENIX 15500	[1283]	Pb/Sc 1.5/4.0 ×66	29.	3.81	20.	42.	55. 36	PMT 200.	1.5 p.e.	5-80	2.1	8.1
LHCb 6000	[1323]	Pb/Sc 2.0/4.0 ×66	24.	4.44	17.	35.	24. 16	PMT	3.0 p.e.	5-100	0.8	9.4 14.
HERA-B 4000	[1327]	Pb/Sc 3.0/6.0 ×37	24.	4.45	17.	42.	56. 36	PMT 490.	0.8 p.e.	5-28	1.4	11.9
COMPASS 888	[1291]	Pb/Sc 0.8/1.55 spiral ×156	23.	4.50	16.	37.	23. 16	PMT 490.		1-7		5.5
COMPASS ≈2000	[1328] [1329]	Pb/Sc 0.8/1.5 ×109	22.	4.60	16.	36.	40. 16	SiPM 9.		1-7	2.3	7.8
ALICE 12288	[1296]	Pb/Sc 1.44/1.76 ×77	9.5 16.	5.68 5.63	12.3 12.4	32. 30.	20. 60.	APD 25.	4.4 p.e.	0.5-100	1.7	11.3 5.
HERA-B 2100	[1327]	W <sup>a</sup> /Sc 2.2/1.0 ×37	4.1	12.5	5.7	13.9	23. 9	PMT 490.	0.13 p.e.	5-28	1.2	20.6
eRD1	[?]	W <sup>b</sup> /Sc 1.58/1.63 ×79	9	8.9	8.4	19.	31. 16	SiPM			1.	7.7 <sup>c</sup>

a - W/Fe alloy 90/10 % by volume;

b - W/Cu alloy 80/20 % by volume

c - Results of GEANT simulation;

**Table 11.24:** A list of parameters of *shashlyk* EM calorimeters used in experiments. The values of the average properties of the calorimeter material ( $f_{samp}$ ,  $\rho$ ,  $X_0$ , and  $R_M$ ), if published, are presented in the top lines of the proper cells. The values calculated using the published sampling structure are presented in the bottom line. The calculation is simplified, but done in a standard way for all the entries facilitating the comparison between the entries. The results of the calculations are usually close to the published values, except the only one published value of  $f_{samp}$ . The resolution is parametrized using Equation 11.4. The resolution was measured in test beams in the energy range specified. The size of the readout cell is shown, along with the number of WLS fibers per cell.

ter provides the projective geometry (ALICE [1296] and MPD [1326] for example). Various photosensors have been used: conventional PMTs, avalanche photodiodes (APD), and SiPMs.

It has been argued [1287, p. 119] that the stochastic coefficient is approximately proportional to  $\sqrt{d/f_{samp}}$ , where  $d$  is the thickness of the active material layer (or the fiber's diameter). For a number of sampling calorimeters of various types (LAR, LKr, Pb/Sc *shashlyk*, SPACAL etc) it was found that  $\beta \approx 2.7\% \sqrt{(d/1 \text{ mm})/f_{samp}}$ . The data from Tab. 11.24

is shown in Fig. 11.74 (right). It is not clear what causes the data to split in two groups with different slopes. The lower group is described by the predicted slope of 0.027, while the higher group is described by a larger slope of 0.049. The offsets of the linear functions are not physical ( $\beta$  can not be negative at any layer thickness) but indicate that at a smaller layer thickness some other processes must dominate the resolution. Results of GEANT4 simulation of *shashlyk* calorimeters are shown in Fig. 11.75. The stochastic term describes the data well (Fig. 11.74). The constant term simulated for  $0.25 \cdot X_0$  is well described by a parabolic function. In summary, the resolution of a *shashlyk* calorimeter can be approximated by:

$$\beta \approx 2.7 \cdot (\sqrt{d/f_{\text{samp}}} - 0.74)\% \quad (11.6)$$

$$\alpha \approx (1.31 - 0.251(x - 20) + 0.144(x - 20)^2)\%,$$

where  $d$  is the thickness of the scintillator tile in mm,  $f_{\text{samp}}$  is the sampling ratio;  $x = X/X_0$  is the full thickness of the calorimeter. The constant term depends on the layer thickness as well. In a real experiment it also depends on the calibration quality and other factors.

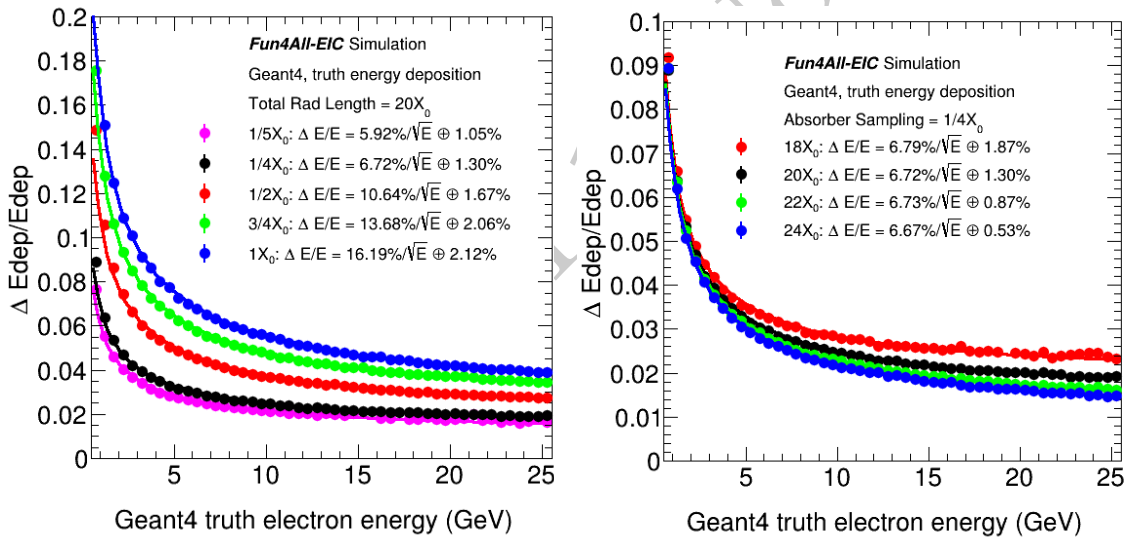


**Figure 11.75:** GEANT4 calculation of the *shashlyk* W/Sc detector resolution [?]. The scintillator tile is 1.5 mm (?) thick. Left: Dependence on the absorber plate thickness for  $20X_0$  total thickness. The results are compared with data in Fig. 11.74. Right: Dependence on the total thickness  $x = X/X_0$  for a  $0.2X_0$  thick layer. The constant term is described by a polynomial:  $\alpha = (1.31 - 0.251(x - 20) + 0.144(x - 20)^2)\%$ .

The expected spatial constraints of the EIC favor the use of tungsten alloys for the absorber. One can select the sampling structure in order to be able to fit the detector into 40 cm of space (see Tab. 11.20). Assuming the approximation of Eq. 11.6 one may expect that such a structure of W/Sc 0.75/1.5 mm would provide a stochastic term of  $6.3\% \text{ GeV}^{0.5}$ .

The eRD1 Consortium is planning to study in a test beam a  $3 \times 3$  W/Sc detector prototype [?,?] (see Fig. 11.73, right and Tab. 11.24). Instrumenting each individual fiber with its

own small SiPM may provide more detailed information about the position of the shower inside the stack, thus providing better position resolution, and also allowing this information to be used to correct for any non-uniformity in either the light collection or energy response. One may also consider adding the signals from several of those SiPMs electrically, reducing the number of readout channels. Such a design reduces the length of the module, saving a few cm of space needed for bundling of the fibers.

## 11.5 Hadronic Calorimetry

### 11.5.1 General consideration for Hadron Calorimeters

The major point for the design of hadron calorimeters (HCAL) at the EIC is the capability of the whole detector to provide precise reconstruction of the jet energy. At EIC a particle flow-style approach is envisioned for jet reconstruction, unlike pure calorimetric methods used in the past. The calorimetry based jet reconstruction at HERA required very high resolution hadronic calorimetry systems [1330]. Meanwhile at EIC tracker and EmCal will measure about 95% of jet energy with precision much higher than any hadron calorimeters built in the past, except may be for very forward region in the hadron endcap, where tracking performance starts to deteriorate (depends on magnet design). Particle flow-style methods rely on precision measurement of charged fragments of jets using the tracker instead of the calorimeters (ECal + HCal). However, calorimeter information is still needed to account for contributions from neutral particles for which a sufficient high granularity may be important to disentangle the different contributions, i.e. proper assignment of signal to the neutral components of the jet. These considerations lead to the set of parameters for hadron calorimeters of the EIC detectors shown in Table XX Energy resolution in the table is referred to a single particle resolution rather than jet.

At EIC all envisioned calorimetry systems are binary, i.e. EmCal followed by HCal. This is driven by the relatively high EM energy resolution requirement which will be difficult to achieve with a single device serving simultaneously as EmCal and HCal. A possible exception may be the very forward hadron endcap where the stochastic term for EM energy resolution might be relaxed due to the higher energy of incoming particles. Achieving high resolution for both EM particles and hadrons is a very difficult task, and there are no precedents from past experiments. For instance, the ZEUS collaboration at HERA operated a very high resolution hadron calorimeter, but paid a price in the form of rather mediocre performance for EM shower detection  $18\%/\sqrt{E}$  while the situation was vice versa for the H1 detector (ref H1). A common scenario is if one focuses on excellent EM resolution, one pays a heavy price when it comes to hadronic shower detection. As an example, as the pointed out in Ref. [1331] once the choice is made for a crystal EM section, it essentially does not matter what one installs behind it. The hadronic energy resolution will be poor. It will be completely determined by fluctuations in the energy sharing between the EM and hadronic calorimeter sections, which in this case have very different e/h values. This results in a typical hadronic resolution of approximately  $100\%/\sqrt{E}$ . Even the most sophisticated compensating hadronic sections cannot alter this conclusion. The chal-

length of balancing EM and hadronic calorimeter performance is a common problem for any calorimetry system, independent of other, detector/collider specific limitations such as available space, dead material between EM and hadronic sections, choice of readout and etc. These degrade the hadronic resolution of any system even more and will be discussed later in this section. To conclude this introduction, we will list some of the parameters of existing high-resolution hadronic calorimeters which will be referred to in subsequent subsections.

The total hadronic resolution of three high-resolution calorimeters (approximately compensated) and the various factors contributing to it are listed in the table below (where are  $\sigma_p$ ,  $\sigma_s$ ,  $\sigma_i$  the fluctuations in the number of signal quanta, sampling fluctuations and intrinsic fluctuations, respectively).

	ZEUS $U^{238}$	ZEUS Pb	SPACAL
$\sigma_p$	6%/ $\sqrt{E}$	10%/ $\sqrt{E}$	5%/ $\sqrt{E}$
$\sigma_s$	31%/ $\sqrt{E}$	42%/ $\sqrt{E}$	27%/ $\sqrt{E}$
$\sigma_i$	19%/ $\sqrt{E}$	11%/ $\sqrt{E}$	11%/ $\sqrt{E}$
$\sigma_h$	37%/ $\sqrt{E}$	44%/ $\sqrt{E}$	30%/ $\sqrt{E}$

**Table 11.25:** Hadronic energy resolution of different calorimeters. Data taken from [1330, 1332–1334]

In all three detectors, the hadronic resolution is dominated by sampling fluctuations. This is a direct consequence of compensation ( $e/h=1$ ), which requires small sampling fractions, for example, 2.3% for lead/plastic detectors and 5.1% for uranium/plastic devices.

Much effort went into understanding the mechanism of compensation in the past [1335], upon which the high-resolution ZEUS calorimetry system was built. However, one aspect of compensation was not immediately clear at that time, namely, the energy dependence which affects the precision of jet reconstruction. Data from ZEUS, showed that, for particles below 10 GeV, the  $e/h$  ratio of the ZEUS calorimeter gradually decreases by 30% with decreasing energy (ref ZEUS, compensation). There is no known solution to this problem. For the EIC central detector, with exception of the very forward region in the hadron endcap (at  $\eta > 2.5$ ), most hadrons will have energies below 10 GeV, and thus there is little value to pursue compensation (such as using depleted uranium) for the hadronic calorimeter section in these regions. In the very forward region of the hadron endcap the hadron energy will be above 10 GeV and the compensation technique is very relevant.

### 11.5.2 Central detector consideration

Precise measurements of the hadron energy with calorimeters requires sufficient containment of hadronic showers. Unlike the compact electromagnetic showers hadronic showers are very broad. The longitudinal and radial containment  $L_95\%$  and  $R_95\%$ , the required length and radius of the calorimeter for 95% hadronic energy deposition containment as

given in [1336], scales as:

$$L_{95\%} \approx t_{max} + 2.5\lambda_a, R_{95\%} \approx 1\lambda_{int} \quad (11.7)$$

, where  $t_{max} \approx 0.2 \log[e]E(\text{GeV}) + 0.7$  is the shower maximum depth, and  $\lambda_a$  (in units of  $\lambda_{int}$ ) describes the exponential decay of the cascade beyond  $t_{max}$  and varies with hadron energy as  $\lambda_a = [E(\text{GeV})]^{0.13}$ . For the EIC central detector a calorimeter system of approximately  $5 \lambda_{int}$  depth seems sufficient for most regions, except for the forward region of the hadron endcap where it should be of order 6-7  $\lambda_{int}$ . Table 11.25 lists absorber materials typically used for HCals for 95% containment. (Absorber material - 95% containment). The choice of absorber material is often driven (apart from energy resolution) by cost, engineering constraints, magnet design, desire for a compensated calorimeter system, and, in case of readout with SiPM's, acceptable levels of neutron fluences. Low Z absorbers generates less neutron flux and in this regard steel absorbers are preferable.

### 11.5.3 HCal Energy resolution

Precise measurements of hadron energy with sampling calorimeters require sufficiently high sampling fraction and sampling frequency to keep sampling fluctuations and number of signal quanta fluctuations below the acceptable threshold (see Table 11.25). Increasing the sampling fraction leads to significant reduction of the final calorimeter density. In addition, calorimeters with large sampling fraction require significant additional space for mechanical stability, as they are usually not self supporting. For example,  $\lambda_{abs}$  for DU is 10.5 cm. However, the effective  $\lambda_{abs}$  of the ZEUS calorimeter is 24 cm, about a factor of two larger. Collider central detectors are generally large-volume detectors, and thus cost plays a non-negligible role in calorimeter, and in particular hadron calorimeter, design. As a consequence, compromises are usually necessary. As an example, the ZEUS and SPACAL HCAL systems listed in Table 11.25 can give an idea of the space requirement for high resolution calorimeters. The ZEUS calorimeter system (hadron endcap) extended over almost 4 meters, of which about half the space was occupied by the high resolution DU/Sc calorimeter. The remaining space was occupied by the backing calorimeter whose purpose was to control longitudinal leakages. The SPACAL system required about 2 meters for the Pb/ScFi structure and additional 0.7 meters for the readout, which is similar for the E864 calorimeter based on the SPACAL design).

The space available for all EIC detectors including the calorimeter systems is finite. Desired properties for the EIC calorimeters, beyond the requirement on energy resolution, are thus: compactness and mechanical sturdiness, which allow for building self-supporting structures and minimizing the space required for passive mechanical support structures. This for example, makes lead as a non-ideal choice for the HCAL absorber as it would require significant passive reinforcement to keep mechanical stability of detector plus additional space to support the Emcal section. Ideally, it would be preferable if the HCal structure serve as a support for the Emcal. This is possible to achieve with a steel absorber. This choice of material would also eliminate dead material between Emcal and HCal sec-

tions which degrades the overall system performance as the dead material sits almost in the shower maximum position. To control longitudinal leakage one usually employs tail catchers, or backing calorimeters, as in case of ZEUS. At the EIC a tail catcher would have to be integrated with the main calorimeter due to the lack of space for a separate device. Such an approach is described in Ref. XX, where the last few layers of the HCal section would have additional independent readout. The information from the tail catcher allows for clean identification of showers without longitudinal leakage. There is a desire to have a higher resolution (better than  $\approx 40\%/\sqrt{E}$  with a constant term of  $\approx 5\%$ ) calorimeter in the forward hadron endcap ( $\eta > 2.5$ ), i.e. the region where the calorimeter performance is anticipated to exceed that of the tracker. This interplay of calorimeter and tracker performance is similar to that in the electron endcap, where the inner part requires the highest resolution and the outer part has more relaxed requirements (see Table XXX). In the hadron endcap taking into account the limited available space, a very dense calorimeter that minimizes leakage and ideally serves as both Ecal and Hcal with a single readout would be preferable. Such a calorimeter should have a small sampling fraction and sufficiently high sampling frequency (to keep the Em energy resolution at an acceptable level), which is currently only possible with a fiber calorimeter technology.

#### 11.5.4 eRD1 EIC R&D and STAR forward developments

To date R&D efforts towards high-resolution hadron calorimetry at the EIC have been limited as existing technologies have been considered sufficient. The very first eRD1 calorimetry consortium proposal aimed to develop new W powder ScFi technology for both EM and HCal sections to help balance the requirements of EM and hadron energy resolutions. In particular, the technique was aimed at simplifying the construction of EM calorimeters with high sampling frequency and small sampling fraction (approximately being compensated) and targeting about  $12\%/\sqrt{E}$  resolution. With support from STAR Forward upgrade project the eRD1 consortium built a small prototype of a compensated calorimeter system with the new W/ScFi technology in the EM section and an HCal section copying the ZEUS Pb/Sc prototype, listed in 11.25. This system was tested at FNAL in 2014 and was modeled in the BEAST EIC detector model model as a hadron endcap. Such a compensated system can meet the requirements for EIC hadron calorimeters listed in Table XX. However the non-compensated variant was considered as well. This originated from a budgetary constraint for the STAR forward upgrade that eventually led to the development of a non-compensated calorimetry system consisting of Pb/Sc shashlik for the EM section (utilizing existing EM blocks from PHENIX experiment) and Fe/Sc for the hadronic section. A small prototype of this system was built and tested at FNAL in 2019. As expected, the compensated prototype had approximately 30% better hadronic energy resolution compare to the non-compensated one. Additional R&D efforts have been carried out to demonstrate a similar system with W/ScFi for the EmCal section that can meet the EIC physics requirements. [?].

### 11.5.5 Alternative methods for high resolution HCal

Over the past two decades there were attempts to significantly improve the energy resolution of hadron calorimeters using the dual readout method. This method uses an observable which correlates with the number of neutrons released in the hadronic shower, which correlates with "invisible" energy ( $\approx 40\%$  in the hadronic shower). By comparing the signals produced by Scintillation light and Cherenkov light in the same detector, including timing and spatial characteristics of the showers, the EM shower fraction, whose fluctuations are the main culprit for problems encountered with hadronic calorimetry, can be determined for individual events. The validity of this principle has been demonstrated with the DREAM fiber calorimeter. [1337]. A realization of dual readout at EIC would have to take into account the relatively low energy of hadrons and the limit of available space. eRD1 took an opportunity to look at timing characteristic of showers using STAR Forward calorimeter prototype with steel absorber during the 2019 test run at FNAL and observed no meaningful correlations of fast component of hadronic shower with total energy, i.e. accounting for em fraction of the shower on event by event basis with this method did not look promising (at least with steel absorber).

At the end of this section we should also mention alternative concepts of designing the whole detector in which the role of calorimeters is quite different compared to what has been traditionally used. These concepts were initially driven by the HEP community for future linear collider development which require extremely high energy resolution for jets. Hadron calorimeters in these concepts are essentially digital devices with hundreds of millions of channels to track every single particle in hadronic showers, as required by particle flow algorithms. This approach requires significant space for the detector, appropriate design of the magnet, and perfect tracking performance over the entire rapidity. The TOP-SIDE concept of the EIC detector is an example of such approach.

In summary, the set of parameters listed in Table XX should be achievable with existing technologies as demonstrated by the eRD1 consortium and STAR Forward upgrade with some additional R&D efforts to improve on the performance of a STAR-like forward calorimeter system. High resolution hadron calorimetry will require additional R&D efforts, e.g. to develop a high density fiber calorimeter with SiPM readout or another suitable technology.

## 11.6 Far-Forward Detectors

### 11.6.1 Introduction

The EIC physics program includes a very broad need for diffractive physics measurements. Experimentally, this means that robust far-forward ( $\eta > 4.5$ ) hadron and photon detection, and far-rear electron detection ( $\eta < -4.5$ ) is required. These regions of the IR require multiple detector concepts to meet the needs of the physics program, including calorimetry for electrons, neutrons, and photons, silicon sensors for charged particle tracking, and detec-

tor concepts such as Roman Pots for detecting protons or nuclear remnants that are very close to the central beam. The subsequent sections will introduce the various detectors and technologies, and discuss the results of simulations (including realistic acceptance, beam effects, and detector resolutions) and the associated impact on the physics.

### General Layout of Far-Forward IR Region

The far-forward region of the interaction region at the baseline EIC detector is complex and requires novel ideas for covering a broad acceptance for charged and neutral particles from a long list of interactions. Fig. 11.76 shows a top-down sketch of the full baseline EIC IR region. Fig. 11.77 shows the layout of the far-forward region used in the GEANT4 simulations. The image shows the various magnets for the hadron beam that create a unique engineering problem for placement of particle detectors and for allowing passage of particles scattered away from the beam.

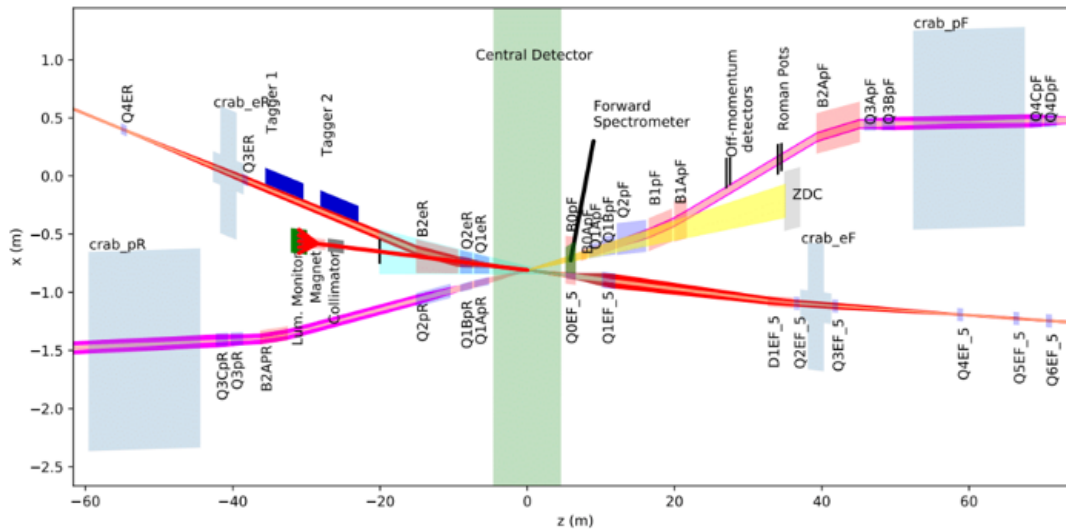
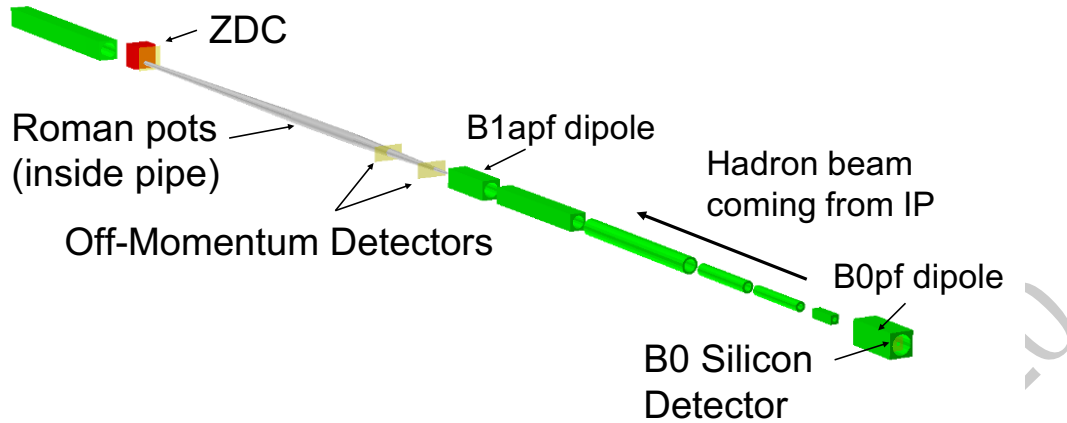


Figure 11.76: Image of the full EIC baseline IR layout.

The various subsystems involved in the far-forward region are summarized in Table 11.26 and depict the challenge of building a suite of detectors to cover the full acceptance for the various interaction channels.

#### 11.6.2 Roman Pots

Roman Pots (RP) are vessels with a thin window in which silicon detectors are placed. The pot vessel is inserted into the beam pipe vacuum, allowing detection of scattered charged particles that are very close to the beam. These detectors can measure scattered protons or light nuclei which are separated from the hadron beam by up to 5 mrad. The windows



**Figure 11.77:** Image of the Far-Forward IR and the associated detector components. Image generated using Geant4+EicRoot.

Detector	(x,z) Position [m]	Dimensions	$\theta$ [mrad]	Notes
ZDC	(0.96, 37.5)	(60cm, 60cm, 2m)	$\theta < 5.5$	$\sim 4.0$ mrad at $\phi = 0$
Roman Pots (2 stations)	(0.85, 26.0) (0.94, 28.0)	(25cm, 10cm, n/a)	$0.0 < \theta < 5.5$	$10\sigma$ cut.
Off-Momentum Detector	(0.8, 22.5), (0.85, 24.5)	(30cm, 30cm, n/a)	$0.0 < \theta < 5.0$	$0.4 < x_L < 0.6$
B0 Spectrometer	(x = 0.19, 5.4 < z < 6.4)	(26cm, 27cm, n/a)	$5.5 < \theta < 13.0$	$\sim 20$ mrad at $\phi = 0$

**Table 11.26:** Summary of far-forward detector locations and angular acceptances for charged hadrons, neutrons, photons, and light nuclei or nuclear fragments. In some cases, the angular acceptance is not uniform in  $\phi$ , as noted in the table. For the three silicon detectors (Roman Pots, Off-Momentum Detectors, and B0 spectrometer) a depth is not given, just the 2D size of the silicon plane. For the Roman Pots and Off-Momentum Detectors, the simulations have two silicon planes spaced 2m apart, while the B0 detectors have four silicon planes evenly spaced along the 1.2m length of the B0pf dipole magnet bore. The planes have a "hole" for the passage of the hadron beam pipe that has a radius of 3.2cm.

on the pots through which protons or light nuclei can enter to be measured by the silicon are generally placed within 1 mm or so of the beam (depending on the beam optics and transverse beam size at the RP location), with safe distance being defined as the " $10\sigma_{x,y}$ " region, where  $\sigma_{x,y}$  is the transverse size of the beam in x and y. Fig. 11.78 shows a cartoon sketch of the basic concept being considered, but note that the stainless steel pots themselves are not shown in the cartoon. In this section, basic requirements for the sensors will be discussed first, and technology appropriate for use in the EIC diffractive physics program will be discussed at the end.

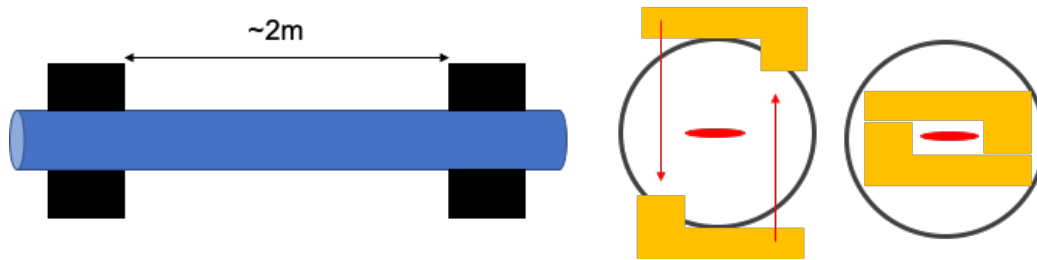


**Figure 11.78:** Cartoon sketch of the Roman Pots concept, without the stainless steel pots shown. This Yellow Report study assumes two Roman Pots stations, separated by 2 meters, for all of the simulations. The right side of the cartoon shows a potential shape of the sensors and how the pots could be inserted into the beam line. Given the small amount of space between the hadron and electron beams at this spot in the IR, horizontal movement of the pots could be challenging.

### Basic Requirements for Roman Pots

In general, the Roman Pots need to have both the necessary acceptance and resolution to carry out the diffractive physics program at the EIC. The acceptance is driven by the machine optics (i.e. transverse beam size at RP location) and active sensitive region of the detector (sensor size). From studies of Deeply Virtual Compton Scattering in e+p collisions, the sensitive area of the sensors needs to be about 25cm x 10cm to capture the majority of the protons within the 5 mrad acceptance required. Protons at larger scattering angles can be measured with the B0 detector (see Sec. 11.6.4). At the highest proton beam energy (275 GeV), the protons are within the 5 mrad acceptance, with the lower cutoff of scattering angle acceptance being driven by the size of the beam at the RP. For protons at the lower beam energies (100 GeV and 41 GeV), the B0 and RP detectors are both required to cover the full acceptance range. Fig. 11.87, discussed in the physics impact from DVCS in Sec. 11.6.6 shows the  $p_T$ -acceptance of protons at various energies, and with two beam configurations.

The  $p_T$  resolution of the RP is dictated by both beam effects and detector effects. The effects are listed below in general order of the size of the effect, with the first being the largest contribution.

- Beam angular divergence
- Crab cavity rotation
- Silicon pixel pitch
- Transfer matrix uncertainty

The beam angular divergence sets the lower bound of the achievable resolution, so the goal is to mitigate the other effects such that they are less than the angular divergence contribution. The contribution from the crab cavity rotation manifests itself as an effective

vertex smearing, since the crab cavity rotates the bunch horizontally such that the electron and hadron bunches arrive at the IP head-on. The effective vertex smearing is approximately  $(.5 * \theta_{crossing} * L_{bunch})$ . This contribution can be mitigated with fast timing ( $\sim 35$ ps), allowing for precise measurement of the location of the collision within the bunch. Table 11.28 summarizes the smearing contributions with reference to the study that generated the quantitative assessment these values and relative impact.

### Silicon Sensors for Roman Pots

The development of high spatial resolution pixel detectors with high per-pixel time resolution has been one of the major technological drivers in collider physics in recent years in order to meet some of the challenges posed by future collider experiments. Current particle trackers in collider experiments are based on silicon technology with a spatial resolution of few tens of microns, while novel silicon technologies have recently allowed timing resolution of few tens of ps, for instance with the Low Gain Avalanche Diodes (LGADs) [1338, 1339]. For example, the ATLAS and CMS experiments [1340, 1341] at the High Luminosity LHC (HL-LHC) [1342, 1343] have developed fast-timing detectors based on LGAD sensors.

The LGAD is based on a simple  $p$ - $n$  diode concept, where the diode is fabricated on a thin high-resistivity  $p$ -type silicon substrate. A highly-doped  $p$ -layer (the “gain” layer) is implanted under the  $n^+$ : application of a reverse bias voltage creates an intense electric field in this superficial region of the sensor, able to start an avalanche multiplication for the electrons. The gain is limited to a factor of typically 10-100, such that the noise low compared to the case of avalanche photodiodes. The drift of the multiplied carriers through the thin substrate generates a fast signal with a time resolution of few tens of ps. However, there is a severe limit at the spatial resolution this detector can achieve. Important dead areas exist at the edges of the pixels and in-between the pixels, so that large-pitch pixel only are possible lest a low fill-factor is introduced. For example, the LGAD sensors developed for the ATLAS and the CMS timing-detectors have relatively large pads of about  $1.3 \times 1.3 \text{ mm}^2$  size.

Recent research has studied how to segment LGAD sensors [1344], e.g. with pixels or strips with pitches in the tens of microns, in order to achieve fine spatial resolution while maintaining the fine LGAD time resolution. It was demonstrated [1345, 1346] that the new technology of AC-coupled LGADs (AC-LGADs [1344]) is a good candidate for a 4-dimensional (4-D) silicon detector to provide time resolution in the few tens of ps and segmentation of few tens of microns. Figure 11.79 shows a schematic section of a segmented AC-LGAD sensor.

Differently from a standard DC-coupled LGAD, see Ref. [1338], the  $n^+$  layer is more resistive than in the standard LGAD. Above the active area, a thin dielectric layer is deposited and, on top of it, metal pads are placed to define the AC-couple electrodes of the structure. Signals are induced on these pads, which are connected to the read-out electronics. If the pads are close enough, there is an important cross-talk between them that can be used for

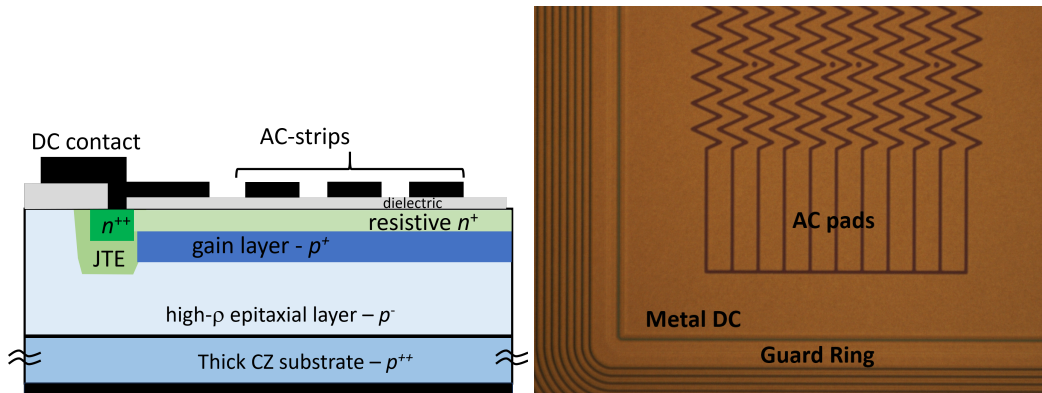


**Figure 11.79:** Left. sketch of the cross section of a segmented AC-LGAD (not to scale). For simplicity, only three AC electrodes are shown. Right: microscope image of an AC-LGAD, fabricated at BNL.

interpolation. Since the geometry of these pads can be arbitrary, by patterning the pads as zigzag (Figure 11.79) it is possible to use the cross-talk among strips to enhance the spatial resolution and, at the same time, to keep the number of the read-out channels low.

Since they are fabricated on thin substrates, the LGAD sensors, intrinsically have a very limited dead area external to the active region. One floating guard ring is sufficient to sustain the high voltage and scribelines at a distance smaller than  $100 \mu\text{m}$  are possible.

Another sensor option for the Roman Pots is the 3D pixel technology that has been used, for example, in the ATLAS IBL. 3D sensors are intrinsically fast and are lacking of the "landau" noise, which constitutes the ultimate limit of the timing resolution of the LGAD. On the other hand, 3D sensors do not have intrinsic gain and have a capacitance which is 4-5 times higher than that of an LGAD of the same area. Their fast timing properties cannot therefore be exploited by a power budget-limited readout electronics.

In fact, a critical aspect for the development of a Roman Pot pixel detector with fast-timing capabilities is the readout. The front-end electronics must have timing and feature size compatible with those of the sensor. Current ASICs for ATLAS (ALTIROC) and CMS (ETROC) are designed in the CMOS TSMC 130 nm and CMOS 65 nm technologies respectively, and they use TDCs to measure the Time of Arrival and Time over Threshold, as well as RAM for data buffering. In the ALTIROC, for example, the maximum jitter is of the order of 25 ps for 10 fC charge, and the ALTIROC and ETROC total power consumption per unit area is about  $200\text{-}300 \text{ mW} / \text{cm}^2$ . As a comparison, the RD53 readout chip for pixel detectors for tracking (i.e. no timing) at the HL-LHC with  $50 \times 50 \mu\text{m}^2$  and  $25 \times 100 \mu\text{m}^2$  feature sizes is estimated to have a power density of about  $1 \text{ W} / \text{cm}^2$  or less. Small pixels complicate the design due to limited space to accommodate TDCs and RAM and increased preamp and TDC power density. However, it seems reasonable to reach  $500 \times 500 \mu\text{m}^2$  feature size by rearranging blocks and removing components that are likely unnecessary in a Roman Pot detector (e.g. a large RAM), while maintaining the same timing performance. In addition, by using Time-Over-Threshold (TOT) features in the ASICs, the charge sensed by pixel can be measured and in turn the charge sharing among pixels esti-

mated. Therefore, using the TOT information the spatial resolution may improve beyond the fixed pixel pitch.

### Summary of the Current Design Constraints

Based on the requirements listed above, and the results of the studies detailed in Secs. 11.6.6 and 11.6.6, the overall optimized Roman Pots requirements can be summarized in the following way. In order to fully cover the  $p_t$  range of scattered protons and ions from the various physics channels covered by the Roman Pots, a total active sensor area of 25cm x 10cm will be required. This can be achieved with various different arrangements of the sensors, but the total area covered must be preserved in order to maximize the kinematic coverage.

The studies to date, along with the expected improvement of the proposed silicon sensor technology (AC-LGADs), indicate that a  $500\ \mu\text{m} \times 500\ \mu\text{m}$  pixel size will properly balance the smearing contribution and R&D efforts. The simulations detailed in Secs. 11.6.6 and 11.6.6 assumed two RP stations with one sensor plane each. However, in actual operation, anywhere from 2-5 sensor planes per station would likely be used for redundancy and background rejection. With the assumed active area per plane and pixel size, this leads to 100k channels (pixels) per plane.

Finally, in order to meet the needs of both background rejection and reduction of vertex smearing from the crab cavity rotation, a timing per plane of  $\sim 35\text{ps}$  will be required.

### 11.6.3 Off-Momentum Detectors

#### Basic Design Considerations

In any e+A collision event, protons and other charged particles can appear in the final state with very small scattering angles (e.g. proton spectators in nuclear breakup). In this scenario, the resulting charged particles will be directed toward the far forward (FF) detectors, but will have a significantly different magnetic rigidity compared to the nuclear beam in question. For example, a proton with 100 GeV/c of total momentum arising from an e+d collision where the deuteron beam has 200 GeV/n of energy would mean that the proton has an  $x_L \sim 0.5$ , and half the rigidity of the deuteron beam, causing it to experience more severe magnetic deflections in the lattice. In this case, the protons will not stay in the beam pipe all the way down to the Roman Pots, and will instead be bent out of the beam pipe after the B1apf dipole magnet, as shown in Fig. 11.80. Measuring these so-called “off-momentum” protons (or other charged particles) will require additional sensor planes outside the beam pipe - the so-called “off-momentum detectors” (OMD). These detectors will cover  $0.25 < x_L < 0.6$  for protons, with the azimuthal symmetry of the acceptance degrading at  $x_L < 0.4$  due to losses in the quadrupole magnets.

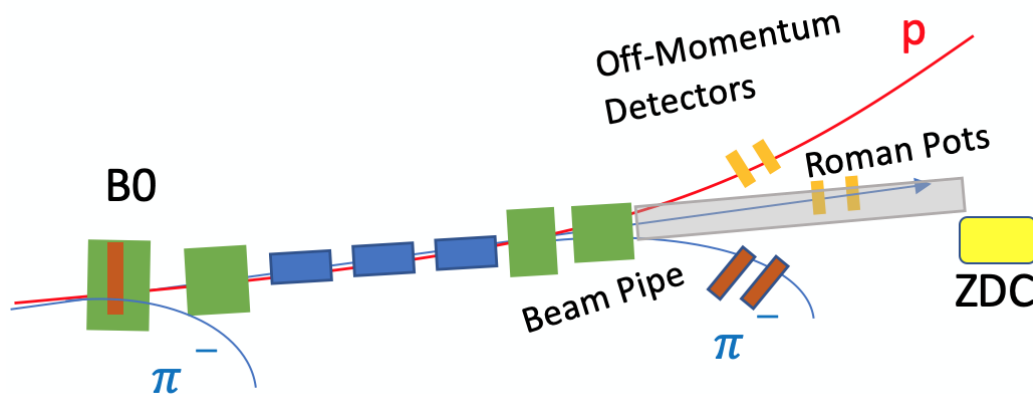


**Figure 11.80:** Cartoon schematic of the operation of the off-momentum detectors. In the schematic a nuclear beam is being used and the final state particles shown are from various potential collision events, such as from nuclear breakup or lambda decay.

The technology employed in these detectors can be the same used for the Roman Pots since the reconstruction approach using a transfer matrix will be similar. The main difference aside from the detection of off-momentum particles is that there will be no need for a  $10\sigma$  cut that limits low- $p_T$  acceptance since the detectors sit outside of the beam pipe.

The simulations using the OMD system are shown in Secs. 11.6.6, 11.6.6.1, and 11.6.6.2. The spectator proton studies included only detectors on one side of the beam pipe, with two stations and the reconstruction approach as with the Roman Pots. The studies of lambda decay indicate the need for detectors on the other side as well for detection of negative

pions, and also a more complicated reconstruction method to account for the highly displaced lambda decay vertex.

### Summary of the Off-Momentum Detector Considerations

The Off-Momentum Detectors will be important for tagging final state charged particles from nuclear breakup and lambda decay. The reconstruction of charged particles with this subsystem will be carried out in the same way as for the Roman Pots, using a lattice transfer matrix to reconstruct the IP coordinates from the hits at the sensor planes. It should be noted, however, that significant non-linear contributions to this transfer matrix approach will need to be considered for the Off-Momentum Detectors compared to the Roman Pots due to the off-momentum particles interactions with the quadrupole fields. More sophisticated reconstruction methods should be considered for future development. In the simulations, the sensors were assumed to be 30cm x 30cm, covering both sides of the beam pipe after the B1apf dipole magnet. This assumption will need to be refined when more up-to-date beam pipe designs are finalized.

### 11.6.4 B0-spectrometer

#### Basic requirements for B0

The B0 tracker can help provide very forward tracking capability for charged tracks. Such capability is important for forward ( $\eta > 3$ ) particle measurements as well as event characterization and separation. Fig. 11.81 shows some conceptual drawings of the B0 bore with the sensors included. There has also been discussion of including electromagnetic calorimetry into the B0pf magnet bore, but simulations have not been carried out at this point.

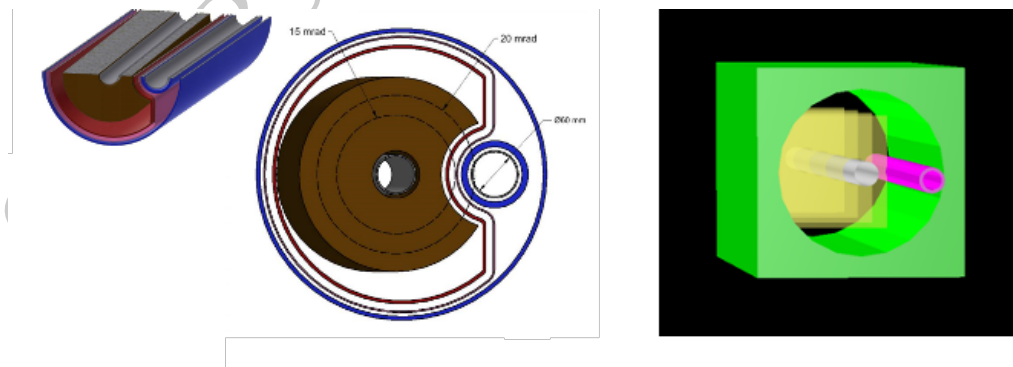


**Figure 11.81:** Conceptual drawings of the B0pf magnet showing the hadron and electron beam pipes going through the B0pf magnet bore (left side) and a basic set of silicon planes implemented in the EicRoot GEANT4 simulations (right side). Some other studies have assumed more conservative placement and shape of sensors, and this is still to be optimized and decided by a more mature design.

### Silicon Sensors for B0-tracker

To meet the radiation tolerance, spatial and timing resolutions in this kinematic region, several silicon sensor candidates are considered.

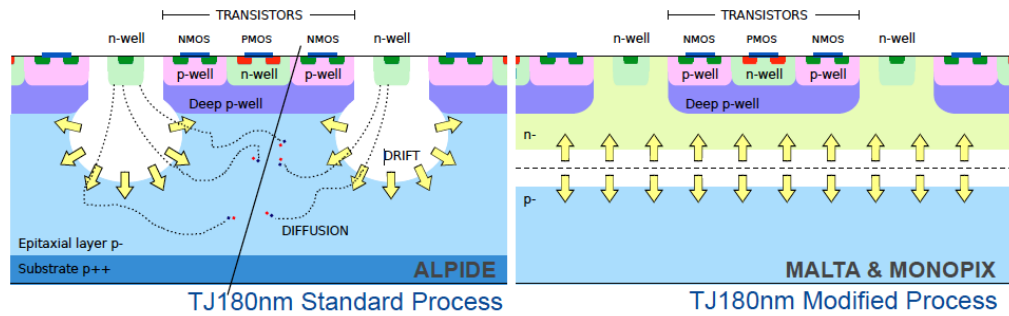


**Figure 11.82:** Comparison on charge ionization process between a normal Tower Jazz 180 nm Monolithic Active Pixel Sensor (left panel) and a depleted Tower Jazz 180 nm Monolithic Active Pixel Sensor (right panel). the Figure from H. Pernegger presentation in the HSTD2019 Hiroshima conference.

One candidate is the Low Gain Avalanche Detector (LGAD) which has better than 30 ps timing resolution. Technical details are described in the previous chapter. Another top candidate is the radiation hard Monolithic Active Pixel Sensor technique: MALTA [1243,1244]. This technique utilize the Depleted Monolithic Active Pixel Sensor (or High Voltage Monolithic Active Pixel Sensor) to meet high granularity, low cost and low material budgets. The existing MALTA sensors based on the Tower Jazz 180 nm design, contain  $36.4\mu\text{m}$  by  $36.4\mu\text{m}$  pixels with the average silicon thickness at around  $300\mu\text{m}$ . Faster readout speed has been achieved for the MALTA sensor due to the charge ionization process is depleted (see Figure 11.82. High radiation tolerance ( $> 10^{15}n_{eq}/\text{cm}^2$ ) has been demonstrated at shaping time at 25 ns [1347]. Please see Table 11.27 for the summarized performance of the LGAD and the MALTA technique. Ongoing R&D for different silicon sensor techniques will improve their radiation tolerance, achieve better timing and finer spatial resolution and get low material budgets.

Parameter	LGAD or AC-LGAD	MALTA
Technique	Low Gain Avalanche Diode	180 nm Tower Jazz HV-MAPS
Pixel size	current $1.3\text{ mm} \times 1.3\text{ mm}$ towards $100\mu\text{m} \times 100\mu\text{m}$	$36.4\mu\text{m} \times 36.4\mu\text{m}$
Integration time	$< 100\text{ ps}$	$< 5\text{ ns}$
Thickness per layer	$< 1\%X_0$	$< 0.5\%X_0$
Radiation tolerance	$\sim 10^{14}n_{eq}/\text{cm}^2$	$> 10^{15}n_{eq}/\text{cm}^2$

**Table 11.27:** Comparison of the LGAD and MALTA sensor performance

Some things that will need to be considered for the future design of the B0 detector system are listed below.

- Radiation background ( in particular a synchrotron radiation and a radiation coming from the primary collisions) in the proposed very forward pseudorapidity region.
- The need for higher resolution sensors for reconstruction compared to the Roman Pots (pixels size  $\sim 50\mu\text{m}$ )
- Available space in bore for sensors, support structure, and cabling.

### **Pre-shower or EMCAL in the B0 spectrometer**

In order to provide a detection of low-energy photons and to provide a coverage in the transition area between central detector and ZDC calorimeters, a pre-shower detector or electro-magnetic calorimeter might be considered in this area. Taking into account a limited amount of available along a Z-axis, and difficulties with integration a pre-shower might be a better option.

### **Summary of the Current Design Constraints**

For the current design,  $26 \times 27 \text{ cm}^2$  planes were used with  $50 \times 50 \mu\text{m}^2$  pitch size. At least 4 layers will be needed, as a combination of high granularity and fast-timing detectors, to provide proper charged particle detection/tracking, momentum reconstruction, and to deal with the high-background expected in this area. Currently, the final layout of the sensors is still under consideration as the design of hadron and electron beam pipes inside the B0pf magnet bore are still being finalized.

### 11.6.5 Zero-Degree Calorimeter (ZDC)

#### Basic requirements for the ZDC

The Zero Degree Calorimeter (ZDC) will serve critical roles for a number of important physics topics at EIC, such as distinguishing between coherent diffractive scattering in which the nucleus remains intact, and incoherent scattering in which the nucleus breaks up; measuring geometry of  $e + A$  collisions, spectator tagging in  $e + d/{}^3\text{He}$ , asymmetries of leading baryons, and spectroscopy. These physics goals require that the ZDCs have high efficiency for neutrons and for low-energy photons, excellent energy,  $p_T$  and position resolutions, large acceptance and sufficient radiation hardness.

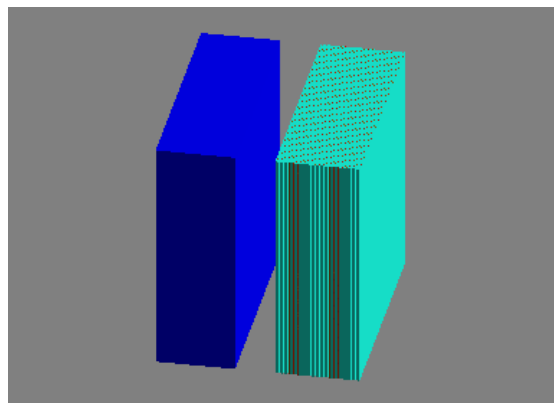
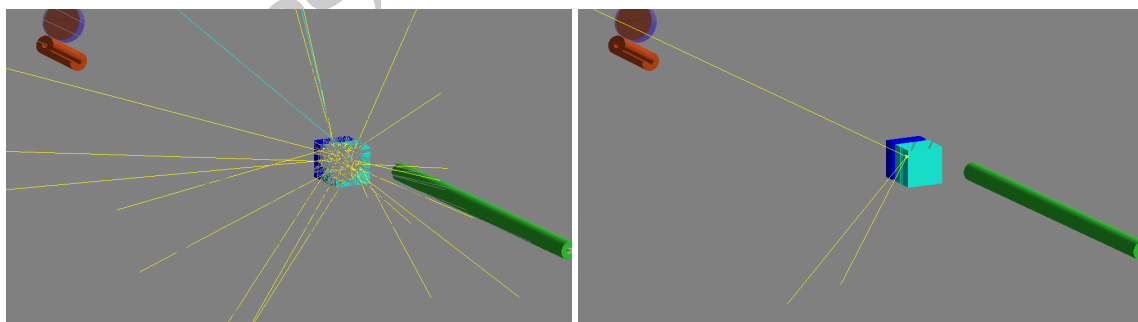


Figure 11.83: The schematic ZDC in Geant4 simulation.

The ZDC schematic plot is shown in Fig. 11.83. A 10 cm lead tungstate absorber is placed in front of 20 layers ALICE FoCal. Figure 11.84 shows event display for a 20 GeV neutron and a 500 MeV photon interacting with the ZDC.



(a) ZDC 20 GeV neutron event display.

(b) ZDC 500 MeV photon event display

Figure 11.84: Event displays for (Left) a 20 GeV neutron and (Right) a 500 MeV photon interacting with the ZDC.

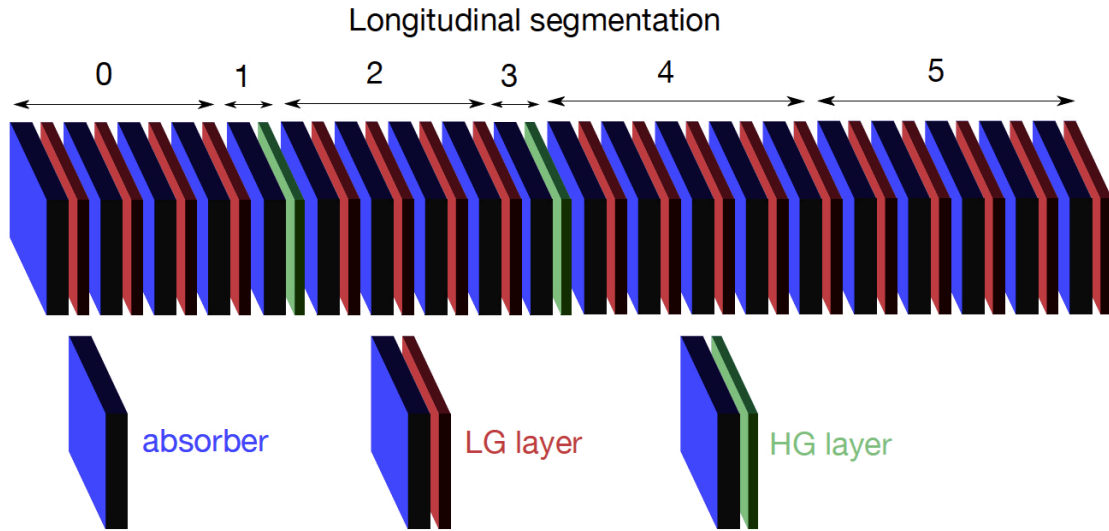


**Figure 11.85:** Schematic of the FoCal electromagnetic calorimeter. The blue absorber is tungsten, the red low granularity silicon layers are used for energy measurement while the green high granularity layers give precise position information [1348].

### EMCAL technologies for ZDC

There are several possible approaches to achieve high energy and position resolution in an electromagnetic calorimeter. As an example, the ALICE FoCal [1348], is silicon-tungsten (Si+W) sampling calorimeter with longitudinal segmentation. Low granularity layers are used for the energy measurement while higher granularity layers provide accurate position information. A schematic of FoCal is shown in Fig. 11.85.

From simulations the photon energy resolution for FoCal is estimated to be  $\sigma_E = 25\%/\sqrt{E} \oplus 2\%$ . This is comparable to that expected for the sPHENIX W/SciFi calorimeter. Other technologies that would provide suitable resolution include crystals ( $\text{PbWO}_4$ , LYSO, GSO, LSO), DSB:Ce glass, and W/SciFi.  $\text{PbWO}_4$  crystals and DSB:Ce glass have been developed and characterized by the eRD1 Consortium and the Neutral Particle Spectrometer project at Jefferson Lab. Tests have shown energy resolutions of  $\sim 2\%/\sqrt{E}$  for photon energies  $\sim 4$  GeV [1349]. The orbiting Fermi Gamma Ray Telescope uses a CsI crystal array and tracker to achieve very high spatial and energy resolution [1350].

### HCAL technologies for ZDC

The hadronic part of the ZDC is needed for neutron identification. An energy resolution of  $\sigma_E < 50\%/\sqrt{E}$  with an angular resolution of at least  $3 \text{ mrad} / \sqrt{E}$  is desired, especially for tagging spectator neutrons from light nuclei. Cerenkov calorimeters, which measure only the high energy component of the showers, give excellent position resolution and tight containment but are non-compensating and so somewhat non-linear. Sampling all charged

particles produced gives better energy resolution at the cost of worse lateral containment. We seek to exploit both techniques to maximize both the energy and position resolution of the ZDC. This could be done by using the quartz fibers developed for the LHC ZDCs, [1351], with traditional scintillators.

### Soft photon detection

In order to detect coherent collisions it is necessary to veto events in which soft photons are emitted from an excited nucleus. In general, the photon decay chain of a heavy nucleus is dominated by photons of energy of the order of 10 KeV. These photons may be indistinguishable from background. However, for a doubly magic nucleus such as  $^{208}\text{Pb}$ , every bound-state decay sequence has at least one photon with an energy of at least 2.6 MeV. After accounting for the boost of the nucleus with momentum  $275 \text{ GeV}/c$ , 20% of these decay photons (with minimum energy 455 MeV) are detectable in the ZDC aperture of  $\sim 4.5 \text{ mrad}$ . In order to detect such photons from nuclear excitation it is important that the ZDC have the largest possible aperture. It is possible that a 2nd IR design will allow a larger ZDC acceptance. Resolving nuclear decay photons from background will require a full absorption EM calorimeter with excellent energy resolution, e.g. made with crystal scintillator (LYSO, PWO, ...).

### Scintillator Tracker Detector

The meson structure research for the EIC has shown the need of a tracker, in combination with the ZDC, to be used as a veto detector for  $\pi^-$  for an efficient measurement of the  $\Lambda \rightarrow n + \pi^0$  channel (Section XXX Meson Structure WG). Besides this main purpose, adding a tracker could improve the reconstruction of charged particles in the ZDC for other different channels. A non-expensive and feasible option is the use of scintillating fibers (SciFi) as a tracker detector.

SciFi trackers combine the fast response of scintillator detectors with the flexibility and granularity that fibers can provide. A high efficiency fiber is made of a core of polystyrene-based scintillator surrounded by a cladding of PMMA, and some fibers by another cladding of fluorinated PMMA. A SciFi tracker can handle high rates and is highly tolerant to radiation [1352], but in the other hand, the photon yield is quite low due to the small photon capture fraction, about 5% for the double cladding fibers<sup>2</sup>. Detection efficiency is increased adding extra fiber layers (Fig.11.86). Scintillating light can be read-out by several pixel devices like Avalanche Photo-diodes, Silicon photo-multipliers or multi-anode photo-multipliers. A SciFi tracker with a layout as figure 11.86 can achieve a spatial resolution of  $\approx 300 \mu\text{m}$  and a time resolution of  $\approx 500 - 220 \text{ ps}$  [1353] [1354], but different fiber diameter and overlap between channels results in similar spatial resolutions [1355].

---

<sup>2</sup>one side output of the fiber

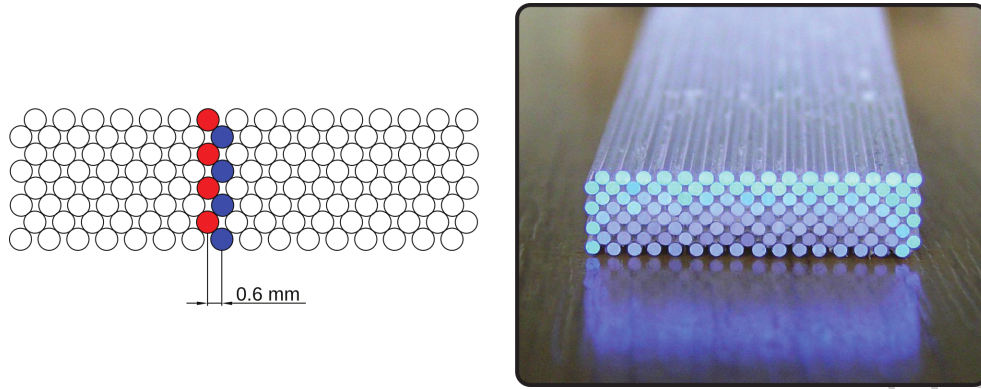


**Figure 11.86:** (Left) Schematic layout of a 4 layers SciFi bundle showing, in red and blue, two corresponding read-out channels for particles coming in the vertical direction. (Right) Picture of an assembled 4 layers, 32 channels SciFi bundle.

### Sumamry of the current design

The number of spectator neutrons is predicted to have somewhat correlation with the collision geometry. The required performance of the detector to identify the coherence of the collision is under development using the BeAGLE simulation [1101]. Some of performance parameters are under ongoing study. The optimization of the performance requirements is included in the scope of the development based on the requirements known as of now as listed below.

**Acceptance** A large acceptance (e.g.  $60 \times 60 \text{ cm}^2$ ) to establish good identification efficiency between coherent and incoherent collisions is necessary for vetoing spectator neutrons from nuclear breakup. This large acceptance is also required to determine the collision geometry [1356]. For studying very forward production and asymmetry of hadrons and photons, a large acceptance is also important. The EIC aperture of  $\pm 4 \text{ mrad}$  gives  $p_T < 1 \text{ GeV}/c$  coverage for 275 GeV hadrons and photons, which covers the transition from elastic/diffraction to incoherent regime; for low-energy hadron beam the acceptance in terms of  $p_T$  is more limited e.g.  $p_T < 0.4 \text{ GeV}/c$  coverage for 100 GeV beam.

**Energy, position, and  $p_T$  resolutions** Due to the strong  $\beta$  squeeze  $< 1$  meter for the high luminosity, a beam spread of  $\sim 20 \text{ MeV}$  and  $\sim 1 \text{ cm}$  of the hadron beam angular divergence is induced. Thus the position resolution of neutron in sub cm won't help. 1 cm position resolution provides  $300 \mu\text{rad}$  angular resolution, which can be translated to transverse momentum resolution  $p_T \sim 30 \text{ MeV}/c$  of 100 GeV spectator neutron.

The minimum energy resolution  $\Delta E/E \sim 50\%/\sqrt{E(\text{GeV})}$  to distinguish number of spectator neutrons from 20 to 30 for collision geometry determination. In order to accommodate a single MIP track to 30 spectator neutrons, wide dynamic energy range in the readout electronics is required.

It is anticipated to be a sampling type calorimeter with a sufficient longitudinal size of  $\sim 10$  interaction length [1356]. It is also required to have a sufficient transverse size of  $\sim 2$  interaction length to avoid transverse leakage of the hadron shower and to achieve good hadron energy resolution.

### 11.6.6 Physics impact

#### Simulation Details

The simulations presented for the far-forward region of the IR were carried out using Geant4 implemented in either EicRoot or ESCalate. The simulations include the most-recently available layout of the IR magnets and engineering components (e.g. beampipe) and additionally include beam effects such as the smearing of the vertex due to rotation of the bunch by the crab cavity and beam angular divergence, unless noted otherwise for a particular study (e.g. studies of acceptance only). The parameters for the various beam effects can be found in the pre-CDR.

#### Deeply Virtual Compton Scattering (DVCS)

The initial proton is scattered by very small angles ( $\sim$  few mrad), and therefore is within the far-forward acceptance - specifically in the Roman Pots or the B0 spectrometer. Using only the tagged final-state proton, one has access to the momentum transfer,  $t$ , in the interaction. The precise measurement of this  $t$ -distribution yields access to the impact parameter distribution related to the gluon GPD.

This simulation study was carried out using the MILOU MC generator to produce the simulated DVCS events, which were then passed through EicRoot and GEANT4 to simulate detector responses. These full simulations were then used to evaluate the DVCS proton acceptance and detector smearing. The study was conducted using three beam energy combinations, and included all of the smearing effects noted in Sec. 11.6.6. Fig. 11.87 shows the  $p_T$ -acceptance for the three different beam energy configurations.

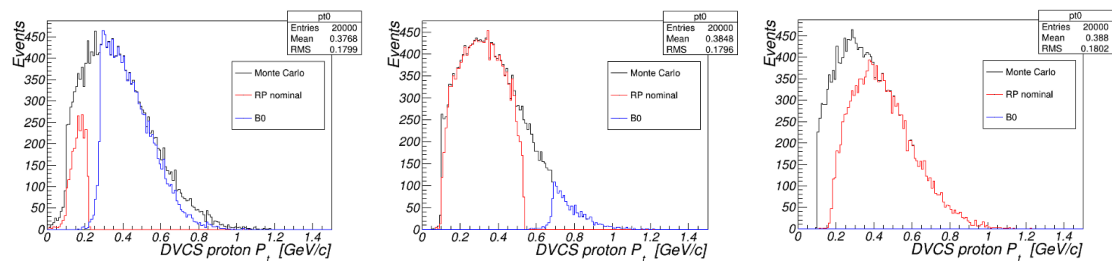


**Figure 11.87:**  $p_T$  acceptance for three different beam energy configurations: 5x41 GeV (left), 10x100 GeV (middle), 18x275 GeV (right). The black data in each figure represent the MC information from MILOU, the red data are the accepted particles in the Roman Pots, and the blue are particle accepted in the B0 sensors.

The acceptance is driven by the aperture size (affected high  $p_T$  acceptance) and the beam optics choice, which determines the transverse beam size at the Roman Pots location, and provides the low  $p_T$  acceptance cutoff. Fig. 11.88 shows the impact of the optics choices for the  $10\sigma$  safe distance for two different beam energies.

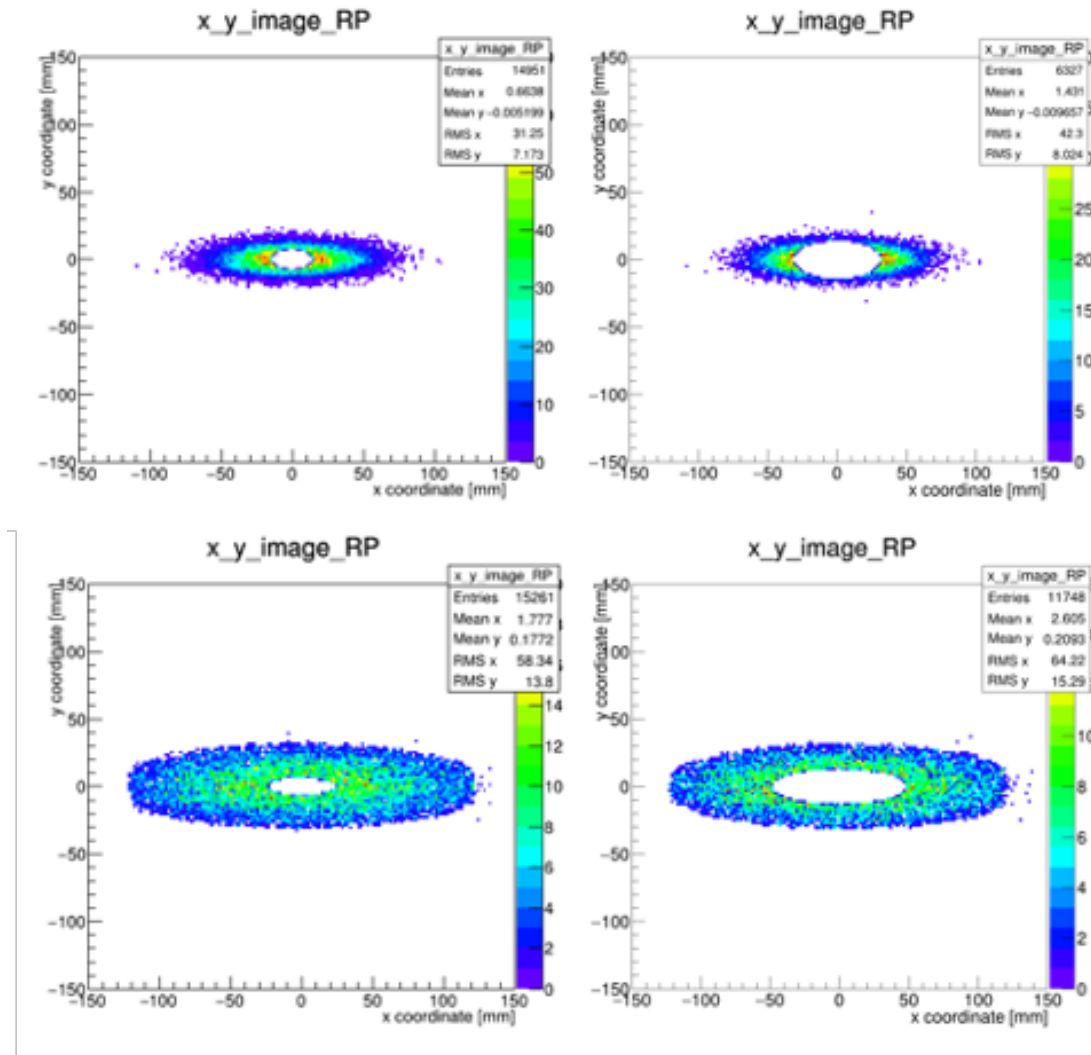


**Figure 11.88:** Acceptance images for protons incident on the first Roman Pots sensor plane. The top row is for the 18x275 GeV beam energy configuration, with the left plot and right plot being the high acceptance and high divergence optics configurations, respectively. The bottom row is for the 10x100 GeV beam energy configuration. Note the decrease in the size of the  $10\sigma$  region (iris in the center of the plots) when we use the high acceptance optics, with left and right plots being the high acceptance and high divergence optics configurations, respectively. As noted previously, the trade off for more acceptance is a drop in luminosity at the IP.

Another important conclusion to be drawn from these acceptance plots is the need for a large active sensor area to maximize the high- $p_T$  acceptance. Fig. 11.88 implies the need

for sensors to cover an active area of approximately  $25\text{cm} \times 10\text{cm}$ .

These simulations also included the effects of angular divergences, crab cavity rotation (which effectively smears the primary vertex), and detector reconstruction smearing. Table 11.28 summarizes the smearing contributions from this study. Based on this study and discussions ongoing in the EIC R&D effort, a  $500\ \mu\text{m} \times 500\ \mu\text{m}$  pixel size gives the necessary resolution while still keeping the cost and design constraints reasonable.

$\Delta p_T$	Ang. Div. (HD)	Ang. Div. (HA)	Crab Cavity	250 $\mu\text{m}$	500 $\mu\text{m}$	1.3 mm
$18 \times 275\ \text{GeV}$	40	28	20	6	11	26
$10 \times 100\ \text{GeV}$	22	11	9	9	11	16
$5 \times 41\ \text{GeV}$	14	-	10	9	10	12

**Table 11.28:** Summary of smearing contributions from angular divergence, crab cavity rotation, various pixel size choices (for the Roman Pots).

### Spectator Tagging in e+D Interactions

In diffractive e+D interactions, either the proton or the neutron acts as a spectator, while the other nucleon is active. For this study, only the p+n final state for each spectator case was considered. The major difference here in proton detection is due to the proton having a different magnetic rigidity compared to the deuteron beam, requiring use of the off-momentum detector system for tagging these breakup protons.

Figs. 11.89 and 11.90 show the kinematic acceptances for the protons in neutrons for their respective spectator/active categories.

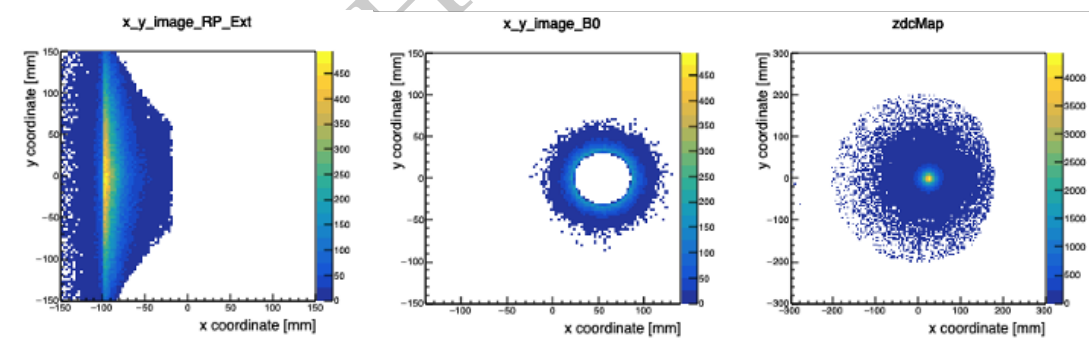


**Figure 11.89:** Acceptance images for protons and neutrons in the case where the neutron acts as a spectator. In this case, the protons have a larger range of scattering angles, and detection requires both the off-momentum detectors and the B0 detector. The plots show the protons incident on the off-momentum detectors (left), the B0 detector (middle), and the neutrons incident on the ZDC (right). All coordinates are local to the sensor plane.

Figs. 11.91 and 11.92 show the kinematic acceptances for the protons in neutrons for their respective spectator/active categories.

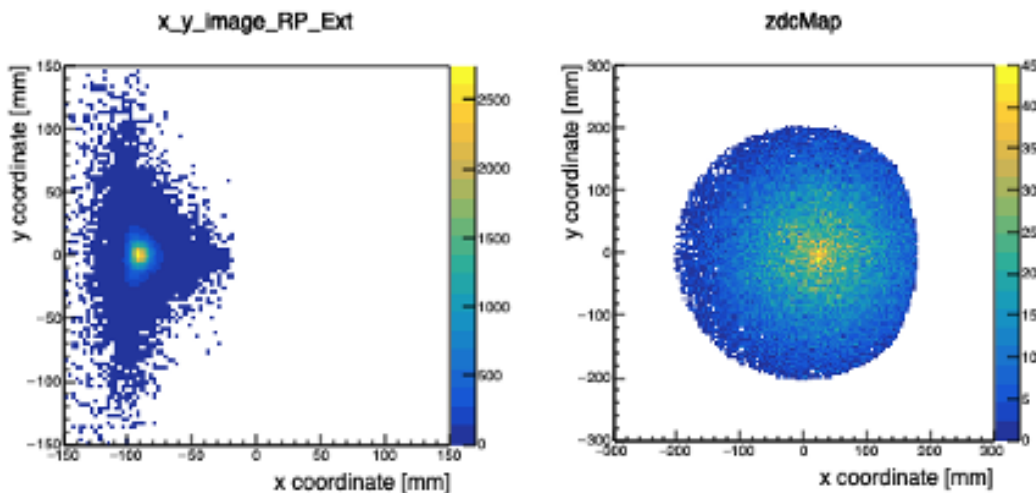


**Figure 11.90:** Acceptance images for protons and neutrons in the case where the proton acts as a spectator. The plots show the protons incident on the off-momentum detectors (left), and the neutrons incident on the ZDC (right). All coordinates are local to the sensor plane.

From these figures it is clear that when a particle acts as a spectator, its acceptance is optimized because its distribution of scattering angles is smaller. For the neutrons, this helps your acceptance because the aperture size limits your neutron acceptance to  $< 5$  mrad. For the protons, larger scattering angles are okay in the case of angles  $> 5$  mrad, since many of these enter the acceptance of the B0 spectrometer. However, the larger spread in momenta imparted to the protons in the neutron spectator cases causes many protons to be lost in the lattice before making it to the off-momentum detectors.

In addition to the acceptances, the resolutions were studied in detail, and their effect on various physics observables evaluated. These results can be found in [1357].

### Spectator Proton and Neutron Tagging in $e+^3\text{He}$ and $e+^3\text{H}$ Collisions

Studying short-range correlations (SRC) and the polarized neutron structure can be accomplished by studying  $e+^3\text{He}$  ( $e+^3\text{H}$ ) collision events in which the neutron (proton) is the active nucleon in the collision and the protons (neutrons) act as spectators. In order to do this type of study, the prospects of tagging both spectator protons or neutrons in the far-forward region needs to be assessed. A full-simulation study was carried out to this end using  $e+^3\text{He}$  DIS events from BeAGLE, as well as SRC events using a spectral function approach. These two paradigms allow for the study of the double-tagging of the final state spectator protons in two very different kinematic regimes. In the DIS case, the two protons end up with very similar final state kinematics, while in the SRC case, one of the protons is in an SRC pair with the active neutron and therefore has a very different initial  $p_T$  distribution than the other spectator proton. Fig. 11.93 shows the occupancy of protons incident on the various detector subsystems. These plots show the repeated need for multiple subsystems to cover the acceptance, as well as the need for a large active area for the

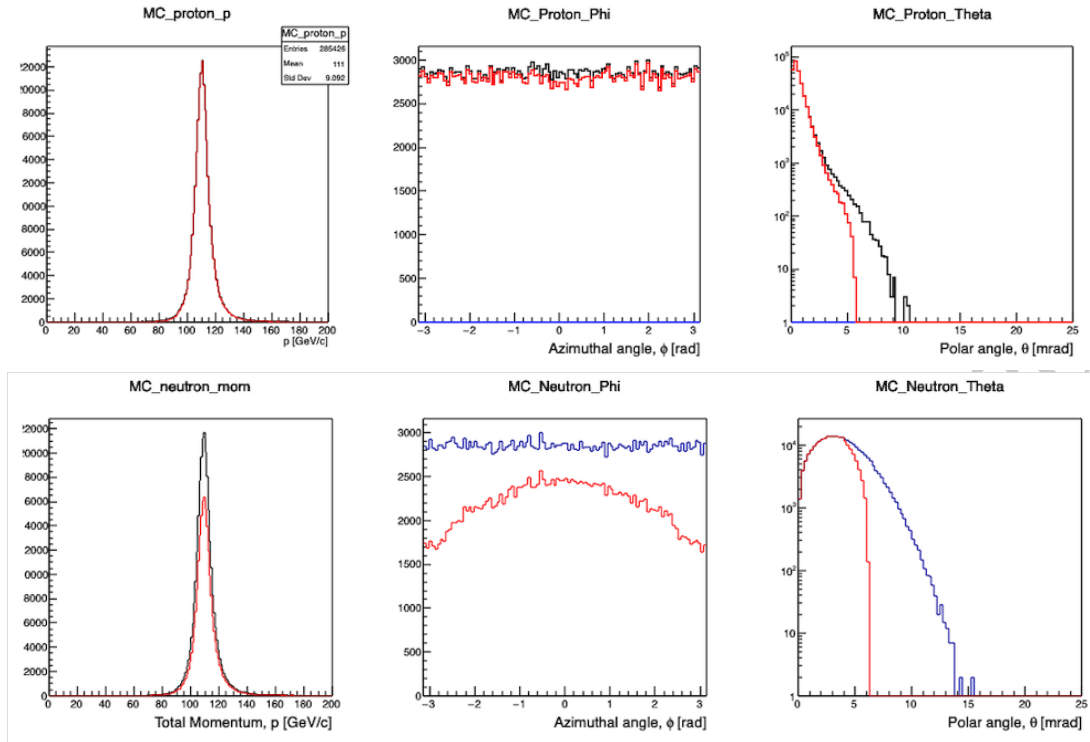


**Figure 11.91:** 3-momentum  $p$ , azimuthal angle ( $\phi$ ), and polar angle ( $\theta$ ) acceptance for protons (top) and neutrons (bottom) for the proton spectator case. The blue lines are from the BeAGLE MC, and the red are the accepted particles.

Roman Pots subsystem. Fig. 11.93 only shows the lowest beam energy configuration since it is the most demanding on the acceptance.

Figs. 11.94 and 11.95 show the results of the study for two different energy configurations. The results indicate that the double-tagging efficiency for the spectator protons look very promising for the baseline interaction region, with most cases having a double-tagging efficiency above 85% (above 90% for the higher energy configuration), except for the lower energy SRC case which has an efficiency above 75%. Most of the losses in the double-tagging efficiency comes from a single proton being lost between the B0 detector and Roman Pots, or between the off-momentum detectors and Roman Pots. These acceptance gaps are to some point unavoidable do to the finite thickness of the beam pipe being the main driver of that gap between the detectors.

A study of the neutron double-tagging efficiency in  $e+^3\text{H}$  events was also carried out using fast simulations in eic-smear. The results indicate that the neutron double-tagging efficiency is also quite good, with most of the acceptance losses being in the SRC case when one of the neutrons has a larger scattering angle that may cause it to be lost in the 4.5 mrad aperture.

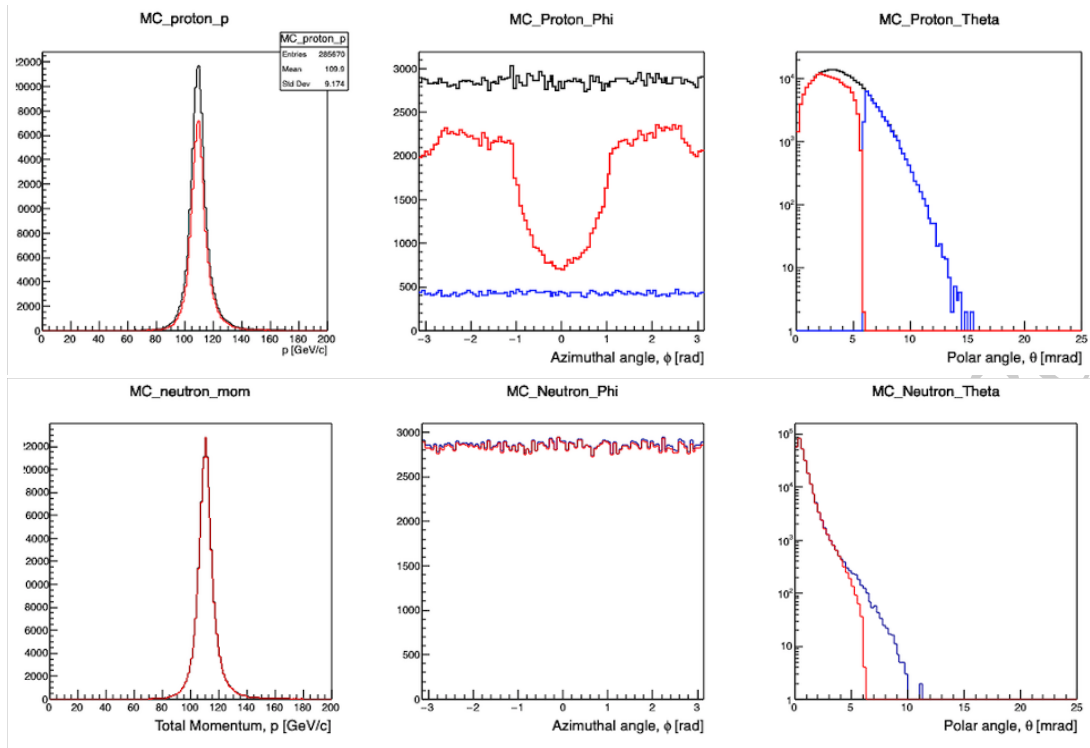


**Figure 11.92:** 3-momentum  $p$ , azimuthal angle ( $\phi$ ), and polar angle ( $\theta$ ) acceptance for protons (top) and neutrons (bottom) for the neutron spectator case. The blue lines are from the BeAGLE MC, and the red are the accepted particles.

### Far-forward tagging ions

At the time of writing this document, no MC samples for light-nuclei tagging in the FF direction were available for validation in our simulation framework. However, based on the numerous other studies, some basic conclusions can be drawn. Light-ion tagging (e.g.  ${}^4\text{He}$ ) should have similar constraints as those seen for the tagging of protons in the FF direction (e.g. proton DVCS). The machine optics can be tuned similarly to maximize the low- $p_T$  acceptance at the Roman Pots. From this, the main limitation will be the shape of the  $p_T$  distribution given by the coherent light nuclear scattering process. If the  $p_T$  distributions are similar as for the e+p case, then the acceptance of these light nuclei at the Roman Pots will also be similar. More studies should be carried out in the future to assess the impact of the various choices of machine optics on the FF light nuclei acceptance.

### Meson Structure and FF Lambda Decay

The reconstruction of Lambda in the target fragmentation area is one of the most challenging tasks in the FF region of the IR. It comes from the fact that the decay vertex of such lambdas is spread by tens of meters along the Z-axis (along the beam-line) which makes

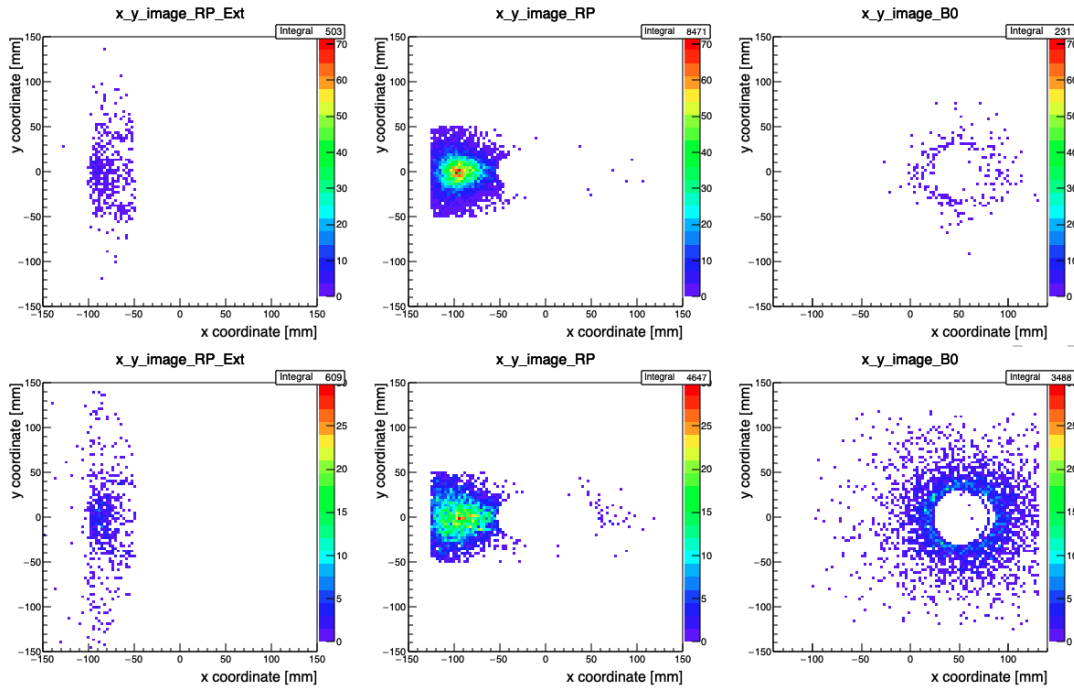


**Figure 11.93:** Occupancy plots of protons incident on the various FF detectors. The top row is 5x41 GeV BeAGLE DIS events, while the bottom row is 5x41 GeV SRC events. The left column is protons incident on the off-momentum detectors, the middle column is the Roman Pots, and the right column is the sum of the 4 individual planes of the B0 detector used in this simulation. All plots show the local coordinate system for the particular detector.

detection of the decay products and mass reconstruction very difficult.

Occupancy plots for the beam energy setting of  $5 \times 41$  GeV for pions and protons from Lambda decays is shown on Fig. 11.96. Since this is the lowest beam energy setting, most of the lambdas would decay in the first meter (before the B0 magnet), and the decay products of lambda are expected to have low momenta and larger theta. Therefore, as expected, protons coming from the  $\Lambda$  decays will mostly be detected, due to their lower rigidity, in the off-momentum detectors and partially in a B0 tracker, while the B0 tracker will be the only detecting element for pions (a). As one can also see from this Figure, the proton-beam-pipe aperture inside the B0-dipole plays an important role and sets the detection efficiency for pions. Also a full azimuthal angle  $\phi$ -coverage of the detecting elements around the proton beam-pipe is important: outer radius of electron FFQ needs to be minimized to provide enough space for tracking detectors.

For another beam energy setting, for example  $10 \text{ GeV} \times 100 \text{ GeV}$  (Fig. 11.97), one could clearly see, for charged pions, the “dead” area along the beamline, where the beam elements (focusing quadrupoles) are located. This comes from the fact that those pions have significantly lower momentum than the beam, and very small  $x_L$ , causing the pions to be lost in the lattice before they can be detected. It is also important to point out that negative charged particles ( pions) will bend into opposite direction, compared to protons, as

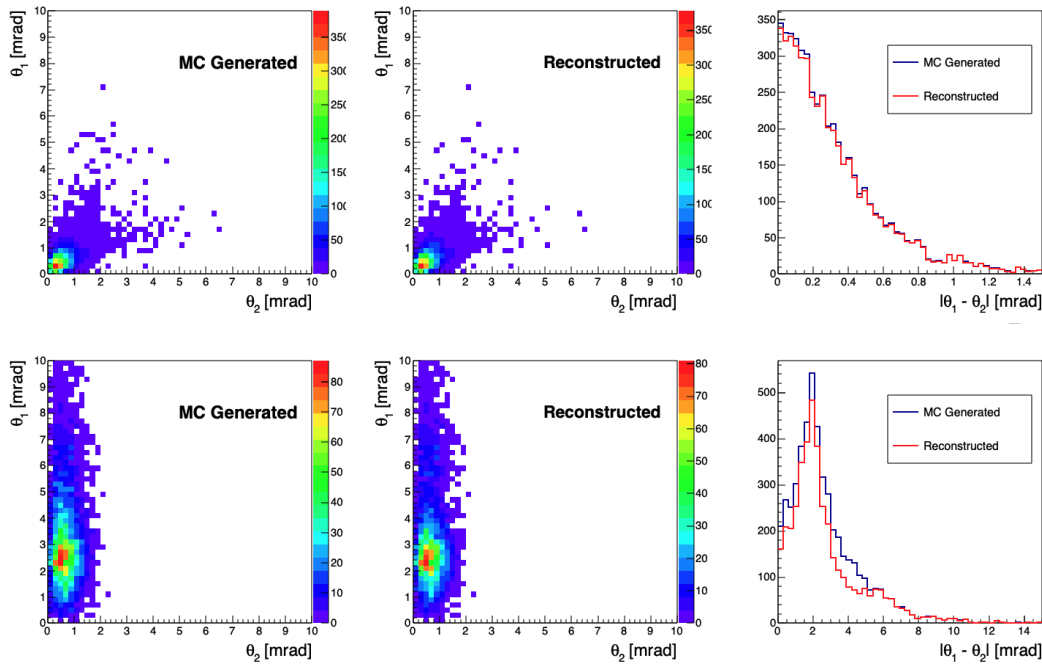


**Figure 11.94:** Scattering angle plots for spectator protons from  $e+^3\text{He}$  collisions using BeA-GLE DIS events at  $10 \times 110$  GeV (top row) and SRC events at  $18 \times 110$  GeV (bottom row). The left panel in both rows shows the scattering angle of proton one vs. proton two from the MC generator, the middle plots shows what is reconstructed in the EicRoot GEANT simulation, and the right panel shows the absolute value of the difference between the angles, which tells us how close together they are when they arrive at the detector.

shown on the Fig. 11.80, therefore a proper coverage of off-momentum detectors would be required to provide an efficient detection for those particles.

### 11.6.7 Conclusions

The far-forward region of the EIC baseline IR has been studied extensively throughout this entire Yellow Report process. The main conclusions from these studies are that several detector subsystems are needed to cover the entire far-forward region including Roman Pots, a high resolution zero-degree calorimeter, a silicon-based spectrometer in the first dipole magnet after the IP, and various planes of silicon on either side of the beam pipe after the B1apf dipole to capture charged particles with  $x_L < 0.6$ , so-called “off-momentum particles”. The technology choices detailed in this chapter reflect the R&D efforts of numerous people and represent our recommendations to meet the needs of the FF physics programs at the EIC. As can be seen throughout the document, the IR design has undergone some revisions (especially the B0 magnet) that have led to different considerations for the detector geometry, as seen in the difference in the B0 coverage between the  $e+D$  study and the  $\lambda$  study. These details are not yet final, and the different assumptions should make

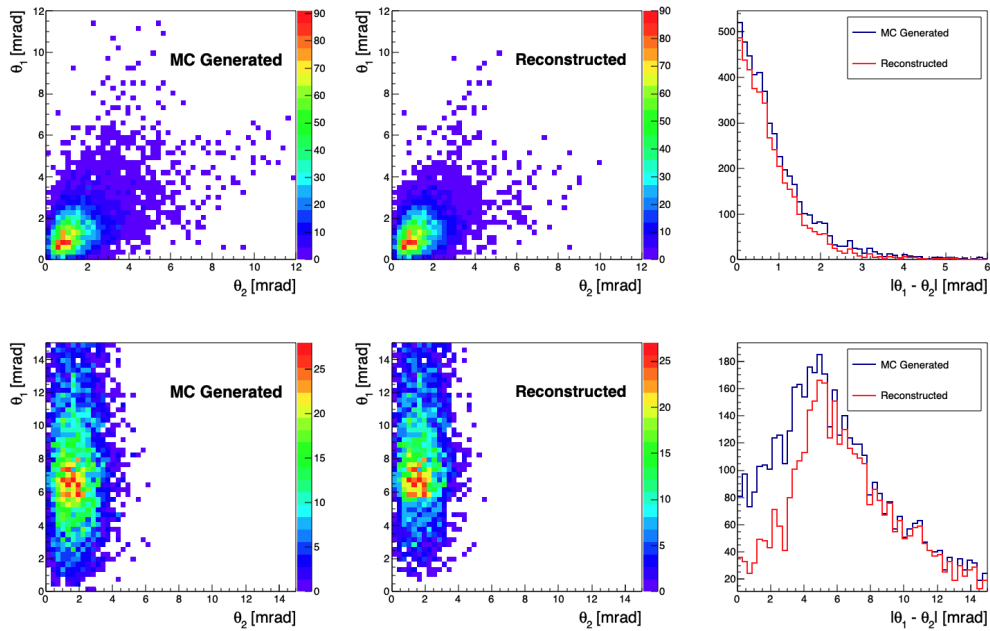


**Figure 11.95:** Scattering angle plots for spectator protons from  $e+{}^3\text{He}$  collisions at  $5\times 41$  GeV using BeAGLE DIS events (top row) and SRC events (bottom row). The left panel in both rows shows the scattering angle of proton one vs. proton two from the MC generator, the middle plots shows what is reconstructed in the EicRoot GEANT simulation, and the right panel shows the absolute value of the difference between the angles, which tells us how close together they are when they arrive at the detector.

it clear what kinds of design difficulties could be faced in the B0 detector planning. As the IR design progresses and the community moves toward the formation of an experimental collaboration, more detailed simulations will need to be carried out in addition to what has been provided by these studies, and we hope these studies provide a strong foundation for validation of the future detector simulation and design efforts.

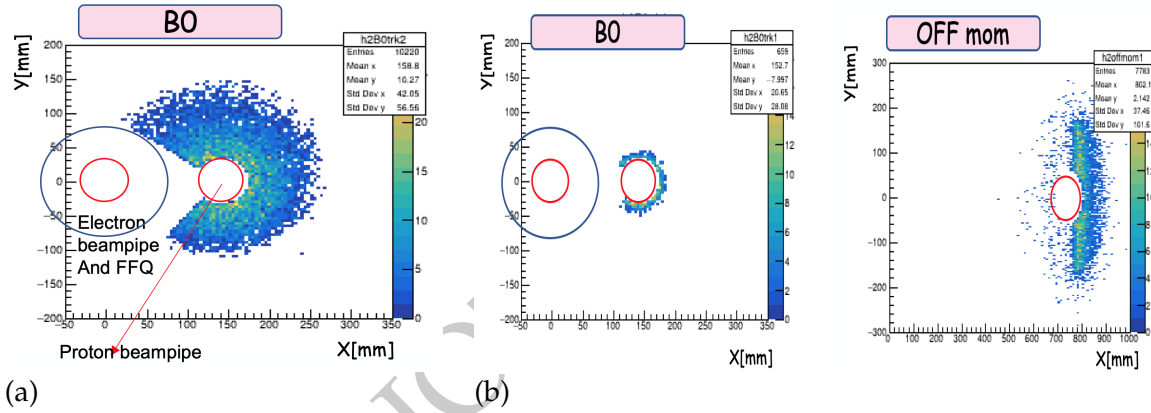


**Figure 11.96:** Occupancy plots for energy setting 5x41 GeV (a) for  $\pi^-$  in B0 tracker (b) for protons in B0 and Off-Momentum detectors. The red circle shows the beampipe position and the blue circle shows electron FFQ aperture inside B0 dipole.

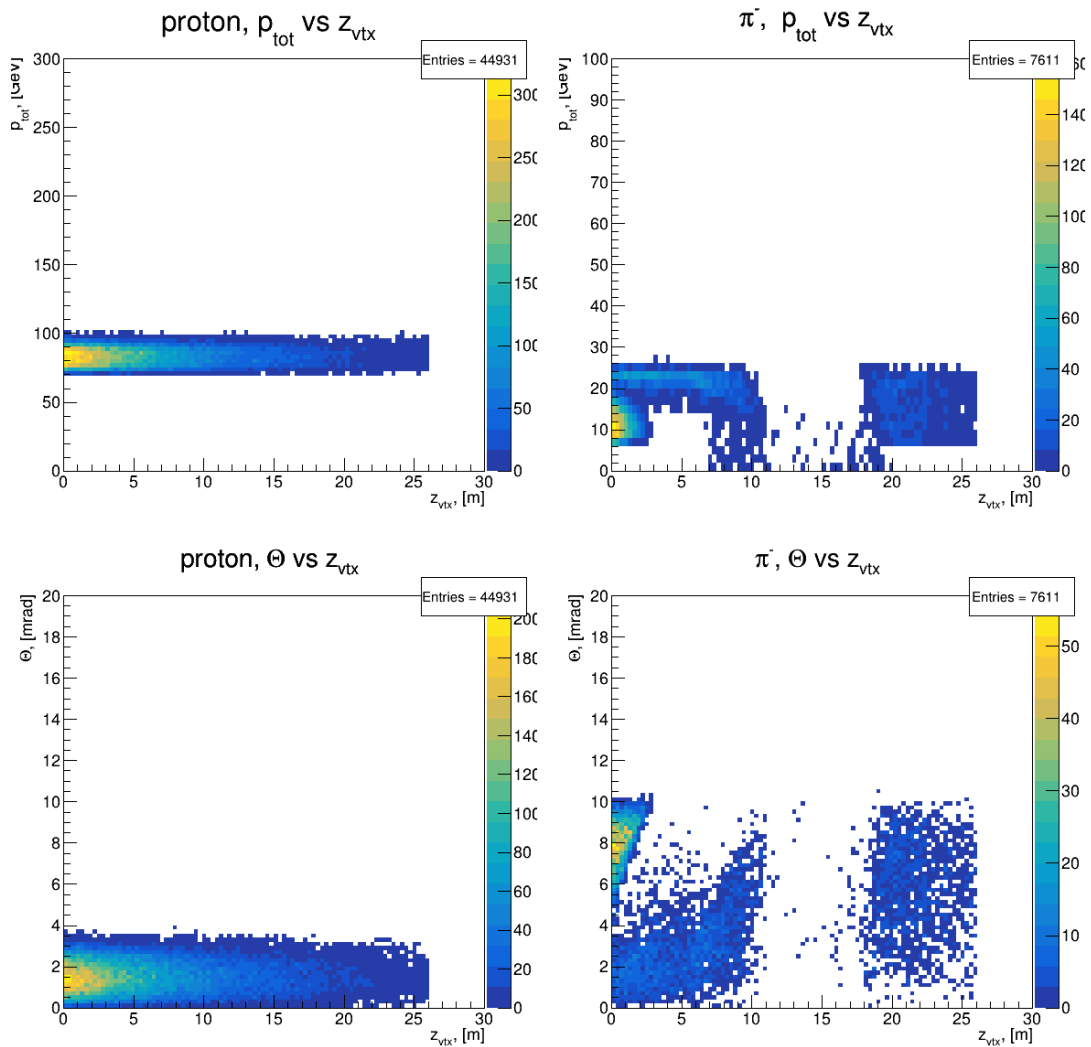


**Figure 11.97:** Beam energy 10x100 GeV. Momentum and Theta distributions for Lambda decay particles, protons (left) and  $\pi^-$  (right), registered in far-forward detectors vs their origination (decay vertex).

**11.6.8 Appendix**

[1358]

SNAPSHOT 19 Nov. 2020

**Table 3.3:** eRHIC beam parameters for different center-of-mass energies  $\sqrt{s}$ , with strong hadron cooling. High divergence configuration.

Species	proton	electron								
Energy [GeV]	275	18	275	10	100	10	100	5	41	5
CM energy [GeV]	140.7		104.9		63.2		44.7		28.6	
Bunch intensity [ $10^{10}$ ]	20.5	6.2	6.9	17.2	6.9	17.2	4.7	17.2	2.6	13.3
No. of bunches	290		1160		1160		1160		1160	
Beam current [A]	0.74	0.227	1	2.5	1	2.5	0.68	2.5	0.38	1.93
RMS norm. emit., h/v [ $\mu\text{m}$ ]	4.6/0.75	845/72	2.8/0.45	391/24	4.0/0.22	391/25	2.7/0.27	196/20	1.9/0.45	196/34
RMS emittance, h/v [nm]	16/2.6	24/2.0	9.6/1.5	20/1.2	37/2.1	20/1.3	25/2.6	20/2.0	44/10	20/3.5
$\beta^*$ , h/v [cm]	90/4.0	59/5.0	90/4.0	43/5.0	90/4.0	167/6.4	90/4.0	113/5.0	90/7.1	196/21.0
IP RMS beam size, h/v [ $\mu\text{m}$ ]	119/10		93/7.8		183/9.1		150/10		198/27	
$K_x$	11.8		11.9		20.0		14.9		7.3	
RMS $\Delta\theta$ , h/v [ $\mu\text{rad}$ ]	132/253	202/202	103/195	215/156	203/227	109/143	167/253	133/202	220/380	101/129
BB parameter, h/v [ $10^{-3}$ ]	3/2	100/100	14/7	73/100	10/9	75/57	15/10	100/66	15/9	53/42
RMS long. emittance [ $10^{-3}$ , eV·sec]	36		36		21		21		11	
RMS bunch length [cm]	6	0.9	6	2	7	2	7	2	7.5	2
RMS $\Delta p/p$ [ $10^{-4}$ ]	6.8	10.9	6.8	5.8	9.7	5.8	9.7	6.8	10.3	6.8
Max. space charge	0.006	neglig.	0.003	neglig.	0.028	neglig.	0.019	neglig.	0.05	neglig.
Piwinski angle [rad]	5.6	0.8	7.1	2.4	4.2	1.2	5.1	1.5	4.2	1.1
Long. IBS time [h]	2.1		3.4		2		2.6		3.8	
Transv. IBS time [h]	2		2		2.3/2.4		2/4.8		3.4/2.1	
Hourglass factor $H$	0.86		0.86		0.85		0.83		0.93	
Luminosity [ $10^{33}\text{cm}^{-2}\text{sec}^{-1}$ ]	1.65		10.05		4.35		3.16		0.44	

**Table 3.4:** eRHIC beam parameters for different center-of-mass energies  $\sqrt{s}$ , with strong hadron cooling. High acceptance configuration.

Species	proton	electron								
Energy [GeV]	275	18	275	10	100	10	100	5	41	5
CM energy [GeV]	140.7		104.9		63.2		44.7		28.6	
Bunch intensity [ $10^{10}$ ]	19.53	6.248	6.9	17.2	6.9	17.2	4.7	17.2	2.6	13.3
No. of bunches	290		1160		1160		1160		1160	
Beam current [A]	0.71	0.227	1	2.5	1	2.5	0.68	2.5	0.38	1.93
RMS norm. emit., h/v [ $\mu\text{m}$ ]	4.9/0.62	845/42.3	2.8/0.45	391/22	3.5/0.25	391/27	2.7/0.27	196/20	1.9/0.45	196/34
RMS emittance, h/v [nm]	16.7/2.1	24.0/1.2	9.6/1.5	20/1.1	33/2.4	20/1.4	25/2.6	20/2.0	44/10	20/3.5
$\beta^*$ , h/v [cm]	395/4.0	274/7.0	227/4.0	109/5.5	102/4.0	169/6.8	90/4.0	113/5.0	90/7.1	196/21
IP RMS beam size, h/v [ $\mu\text{m}$ ]	256/9.2		148/7.8		184/9.7		150/10		198/27	
$K_x$	0.036		18.9		18.9		14.9		7.3	
RMS $\Delta\theta$ , h/v [ $\mu\text{rad}$ ]	65/229	94/131	65/196	135/143	180/243	109/143	167/253	133/202	220/380	101/129
BB parameter, h/v [ $10^{-3}$ ]	3/1	100/71	14/5	75/71	11/8	75/57	15/10	100/66	15/9	53/42
RMS long. emittance [ $10^{-3}$ , eV·sec]	36		36		21		21		11	
RMS bunch length [cm]	6	0.9	6	2	7	2	7	2	7.5	2
RMS $\Delta p/p$ [ $10^{-4}$ ]	6.8	10.9	6.8	5.8	9.7	5.8	9.7	6.8	10.3	6.8
Max. space charge	0.006	neglig.	0.003	neglig.	0.027	neglig.	0.019	neglig.	0.05	neglig.
Piwinski angle [rad]	2.6	0.4	4.5	1.5	4.2	1.2	5.1	1.5	4.2	1.1
Long. IBS time [h]	2		3.4		2		2.6		3.8	
Transv. IBS time [h]	2		2		2.0/3.0		2/4.8		3.4/2.1	
Hourglass factor $H$	0.88		0.87		0.85		0.83		0.93	
Luminosity [ $10^{33}\text{cm}^{-2}\text{sec}^{-1}$ ]	0.83		6.4		4.07		3.16		0.44	

**Figure 11.98:** Parameters for eRHIC, ep operation

**Table 3.5:** eRHIC beam parameters for e-Au operation for different center-of-mass energies  $\sqrt{s}$ , with strong hadron cooling.

Species	Au ion	electron						
Energy [GeV]	110	18	110	10	110	5	41	5
CM energy [GeV]	89.0		66.3		46.9		28.6	
Bunch intensity [ $10^{10}$ ]	0.08	7.29	0.05	17.2	0.05	17.2	0.036	17.2
No. of bunches	290		1160		1160		1160	
Beam current [A]	0.23	0.26	0.57	2.50	0.57	2.50	0.41	2.50
RMS norm. emit., h/v [ $\mu\text{m}$ ]	5.1/0.7	705/20	5.0/0.4	391/20	5.0/0.4	196/20	3.0/0.3	196/20
RMS emittance, h/v [nm]	43.2/5.8	20.0/0.6	42.3/3.0	20.0/1.0	42.3/3.0	20.0/2.0	68.1/5.7	20.0/2.0
$\beta^*$ , h/v [cm]	91/4	196/41	91/4	193/12	91/4	193/6	90/4	307/11
IP RMS beam size, h/v [ $\mu\text{m}$ ]	198/15		196/11		197/11		248/15	
$K_x$	0.077		0.057		0.056		0.061	
RMS $\Delta\theta$ , h/v [ $\mu\text{rad}$ ]	218/379	101/37	216/274	102/92	215/275	102/185	275/377	81/136
BB parameter, h/v [ $10^{-3}$ ]	1/1	37/100	3/3	43/47	3/2	86/47	5/4	61/37
RMS long. emittance [ $10^{-3}$ , eV·sec]	16		16		16		16	
RMS bunch length [cm]	7	0.9	7	2	7	2	11.6	2
RMS $\Delta p/p$ [ $10^{-4}$ ]	6.2	10.9	6.2	5.8	6.2	6.8	10	6.8
Max. space charge	0.007	neglig.	0.008	neglig.	0.008	neglig.	0.038	neglig.
Piwiniski angle [rad]	4.4	1.1	4.5	1.2	4.5	1.5	5.8	1.2
Long. IBS time [h]	0.33		0.36		0.36		0.85	
Transv. IBS time [h]	0.81		0.89		0.89		0.16	
Hourglass factor $H$	0.85		0.85		0.85		0.71	
Luminosity [ $10^{33}\text{cm}^{-2}\text{sec}^{-1}$ ]	0.59		4.76		4.77		1.67	

**Table 3.6:** eRHIC beam parameters for e-Au operation for different center-of-mass energies  $\sqrt{s}$ , with stochastic cooling.

Species	Au ion	electron						
Energy [GeV]	110	18	110	10	110	5	41	5
CM energy [GeV]	89.0		66.3		46.9		28.6	
Bunch intensity [ $10^{10}$ ]	0.10	7.29	0.10	30	0.08	30	0.09	30
No. of bunches	290		580		580		580	
Beam current [A]	0.29	0.26	0.57	2.18	0.44	2.18	0.50	2.18
RMS norm. emit., h/v [ $\mu\text{m}$ ]	2.0/2.0	845/60	2.0/2.0	391/102	2.0/2.0	196/63	2.0/2.0	196/113
RMS emittance, h/v [nm]	16.9/16.9	24.0/1.7	16.9/16.9	20.0/5.2	16.9/16.9	20.0/6.4	45.4/45.4	20.0/11.5
$\beta^*$ , h/v [cm]	288/12	203/116	91/12	77/39	146/12	113/31	149/50	339/196
IP RMS beam size, h/v [ $\mu\text{m}$ ]	221/45		124/45		157/45		261/150	
$K_x$	0.202		0.363		0.284		0.577	
RMS $\Delta\theta$ , h/v [ $\mu\text{rad}$ ]	77/380	109/38	136/376	161/116	108/380	127/144	174/302	77/77
BB parameter, h/v [ $10^{-3}$ ]	3/1	35/100	11/4	66/93	11/3	100/96	9/5	100/100
RMS long. emittance [ $10^{-3}$ , eV·sec]	64		64		64		64	
RMS bunch length [cm]	15	0.9	18	2	18	2	18	2
RMS $\Delta p/p$ [ $10^{-4}$ ]	10	10.9	10	5.8	10	6.8	13	6.8
Max. space charge	0.001	neglig.	0.001	neglig.	0.001	neglig.	0.007	neglig.
Piwiniski angle [rad]	8.5	0.5	18.1	2.0	14.3	1.6	8.6	1.0
Long. IBS time [h]	2.65		2.65		3.39		2.02	
Transv. IBS time [h]	1.02		0.80		1.32		0.93	
Hourglass factor $H$	0.54		0.54		0.54		0.65	
Luminosity [ $10^{33}\text{cm}^{-2}\text{sec}^{-1}$ ]	0.14		2.06		1.27		0.31	

**Figure 11.99:** Parameters for eRHIC, eAu operation**Figure 11.100:** IR

## 11.7 Far-Backward Detectors

The path of the electron beam downstream of the interaction point is shown in Fig. 11.101. Beam magnets are shown in full green, drift space in hatched green and detectors and components in red and yellow. The horizontal axis is aligned with the direction of the beam at the collision point, along which photons from  $e+p$  and  $e+A$  interactions will travel. These photons come predominantly from the bremsstrahlung process used for luminosity determination. The lower left of the figure shows possible instrumentation for the luminosity measurement. Bremsstrahlung and low- $Q^2$  processes also produce electrons with momenta slightly below the beam energy. After being bent out of the beam by lattice dipoles they may be measured by taggers as shown in the top left of the figure. This section will detail studies of a luminosity monitor as well a tagger for electrons from bremsstrahlung and low- $Q^2$  events. The technology considerations and machine-driven acceptances are both addressed as well.

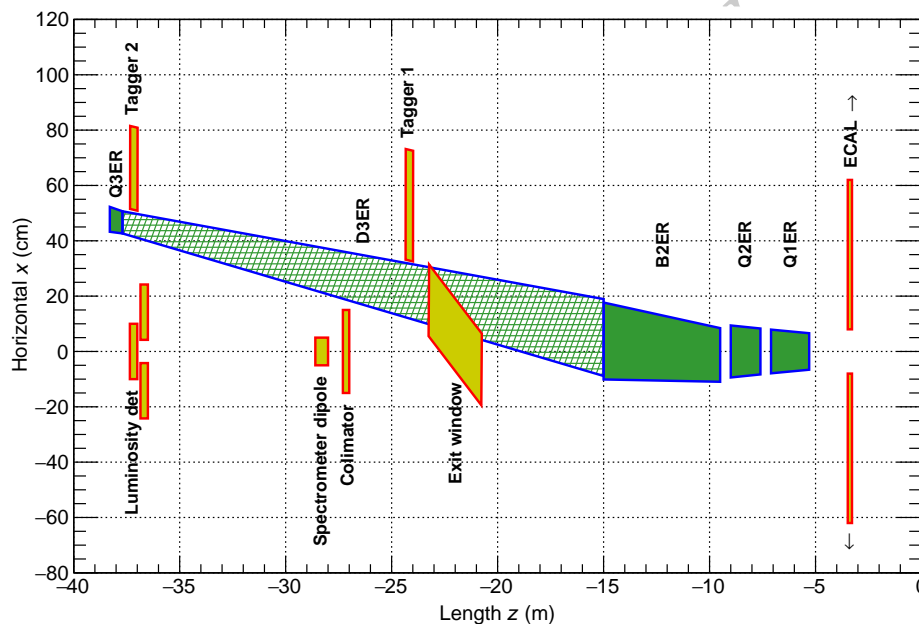


Figure 11.101: The region downstream of the interaction point in the electron direction.

### 11.7.1 Far-Backward Photons

#### Luminosity Measurement

The luminosity measurement provides the required normalization for all physics studies. At the broadest scale it determines absolute cross sections, such as needed for the structure function  $F_2$  and derived PDFs. On an intermediate scale, it is also required to combine different running periods, such as runs with different beam energies needed to measure  $F_L$ , or runs with different beam species to study  $A$  dependencies. Asymmetry measurements

are conducted using beams with bunches of both spin states. On the finest scale, the relative luminosity of the different bunch crossings is needed to normalize the event rates for the different states; the uncertainty on the relative bunch luminosity is a limiting factor for asymmetry measurements.

The bremsstrahlung process  $e + p \rightarrow e + p + \gamma$  was used successfully for the measurement of luminosity by the HERA collider experiments [1359–1362]. It has a precisely known QED cross-section [1363] which is large, minimizing theoretical uncertainty and providing negligible statistical uncertainty. Thus the scale uncertainty of the luminosity is determined by the systematic uncertainties of the counting of bremsstrahlung events. The ZEUS collaboration at HERA measured luminosity with a 1.7% scale uncertainty; further improvements at the EIC should be able to reduce this to  $<1\%$  as required by the physics program.

In contrast to HERA, where only the electron beam was polarized, both the electron and proton/light ion beams will be polarized in the EIC. In this case the bremsstrahlung rate is sensitive to the polarization dependent term  $a(P_e, P_h)$  in the cross section  $\sigma_{\text{brems}} = \sigma_0(1 + a(P_e, P_h))$ . Thus, the polarizations  $P_e, P_h$  and luminosity measurements are coupled, and the precision of the luminosity measurement is limited by the precision of the polarization measurement. This is especially important for relative luminosities for asymmetry measurements, where the bremsstrahlung process used for normalization has different cross sections for different spin states. The precision needed for the relative luminosity measurement is driven by the magnitude of the physics asymmetries which can be as low as  $10^{-4}$ ; the uncertainty on relative bunch luminosities must exceed this level of precision.

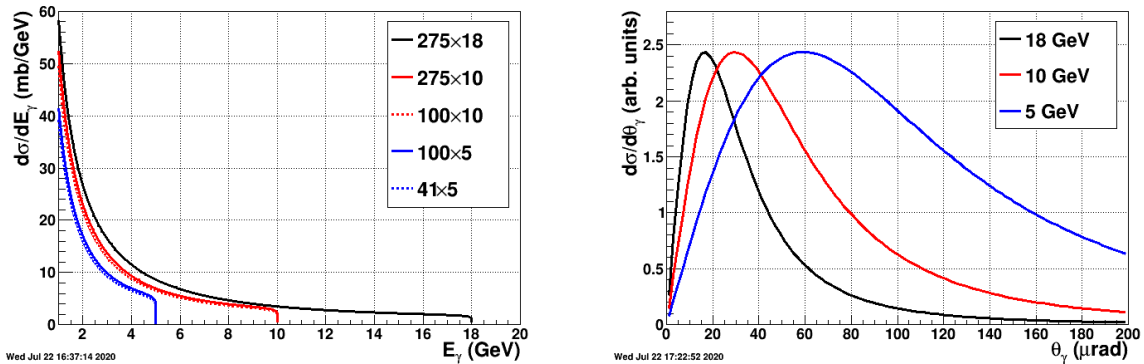


**Figure 11.102:** Bremsstrahlung photon energy (left) and angular (right) distributions for EIC beam energies.

The bremsstrahlung photon energy  $E_\gamma$  distributions for EIC beam energies are shown in left of Fig. 11.102. They diverge as  $E_g \rightarrow 0$  and have sharp cutoffs at the electron beam energies. As shown in the right of Fig. 11.102, the bremsstrahlung photons are strongly peaked in the forward direction with typical values of  $\theta_\gamma \approx m_e/E_e$ , with values of 20–60  $\mu\text{rad}$  at the EIC. The RMS angular divergence of the electron beam is significantly larger than these values and will dominate the angular distribution of bremsstrahlung photons as shown in Fig. 11.103.

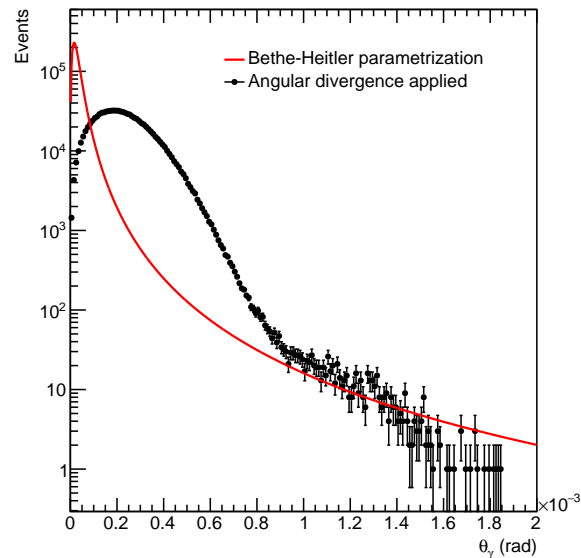


**Figure 11.103:** Angular dependence of bremsstrahlung cross section. The effect of beam angular divergence is shown.

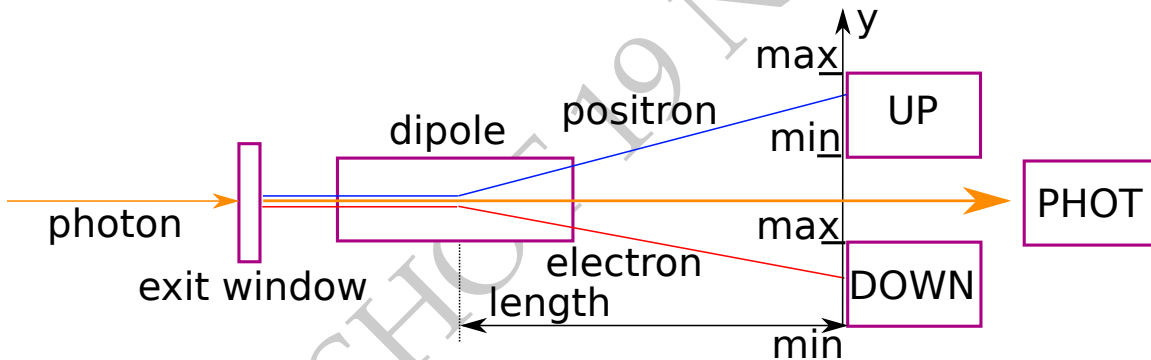


**Figure 11.104:** Principle of the luminosity measurement. Bremsstrahlung photons are incident on an aluminum exit window. Converted electron-positron pairs are split in the spectrometer dipole magnet and detected in the UP and DOWN detectors. Non-converted photons reach the photon calorimeter PHOT.

### Bremsstrahlung Photon Detection Principles and Requirements

Figure 11.104 shows a side view of detector components along the photon zero-degree line in the backward direction. The straightforward method for measuring bremsstrahlung situates a calorimeter at zero degrees in the electron direction counting the resulting photons, PHOT in the figure. The calorimeter is also exposed to the direct synchrotron radiation fan and must be shielded, thus degrading the energy resolution. This also imposes a rough low energy cutoff on photons typically  $\approx 0.1\text{-}1\text{ GeV}$  below which the calorimeter is insensitive. At peak HERA luminosities, the photon calorimeters were sensitive to 1-2 photons per HERA bunch crossing. At an EIC luminosity of  $10^{33}\text{ cm}^{-2}\text{ s}^{-1}$ , the mean number of such photons per bunch crossing is over 20 for electron-proton scattering and

increases with  $Z^2$  of the target for nuclear beams. The per bunch energy distributions are broad, with a mean proportional to the number of photons per bunch crossing. The counting of bremsstrahlung photons thus is effectively an energy measurement in the photon calorimeter with all of the related systematic uncertainties (e.g. gain stability) of such a measurement.

An alternative method to counting bremsstrahlung photons, used effectively by the ZEUS collaboration at HERA [1360], employs a pair spectrometer. A small fraction of photons is converted into  $e^+e^-$  pairs in the vacuum chamber exit window. A dipole magnet splits the pairs vertically and each particle hits a separate calorimeter adjacent to the unconverted photon path, UP and DOWN in Fig. 11.104. This has several advantages over a zero-degree photon calorimeter:

- The calorimeters are outside of the primary synchrotron radiation fan.
- The exit window conversion fraction reduces the overall rate.
- The spectrometer geometry imposes a well defined low energy cutoff in the photon spectrum, which depends on the magnitude of the dipole field and the location of the calorimeters.

The variable parameters of the last two points (conversion fraction, dipole field and calorimeter locations) may be chosen to reduce the rate to less than or of order one  $e^+e^-$  coincidence per bunch crossing even at nominal EIC luminosities. Thus, counting of bremsstrahlung photons is simply counting of  $e^+e^-$  coincidences in a pair spectrometer with only small corrections for pileup effects.

The locations of a zero-degree calorimeter and pair spectrometer are shown in the bottom left of Fig. 11.101. Careful integration into the machine lattice is required, not only to allow for enough space for the detectors, but also to accommodate the angular distribution of the photons. This is dominated by the angular divergence of the electron beam, with RMS values as high 0.2 mrad. Thus a clear aperture up to a few mrad is required to measure the angular distribution and minimize the acceptance correction. The spectrometer rate is directly proportional to the fraction of photons which convert into  $e^+e^-$  pairs, placing stringent requirements on the photon exit window. It must have a precisely known material composition, and a precisely measured and uniform thickness along the photon direction.

Calorimeters are required for both luminosity devices, for triggering and energy measurements. The high rates dictate a radiation hard design, especially for the zero-degree calorimeter, which must also have shielding against synchrotron radiation. The spectrometer must also have precise position detectors to measure the  $e^\pm$ . Combined with the calorimeter energy measurement this allows reconstruction of the converted photon positions. The distribution of photon positions is required to correct for the lost photons falling outside the photon aperture and detector acceptances.

### Bremsstrahlung Photon Detector Implementation

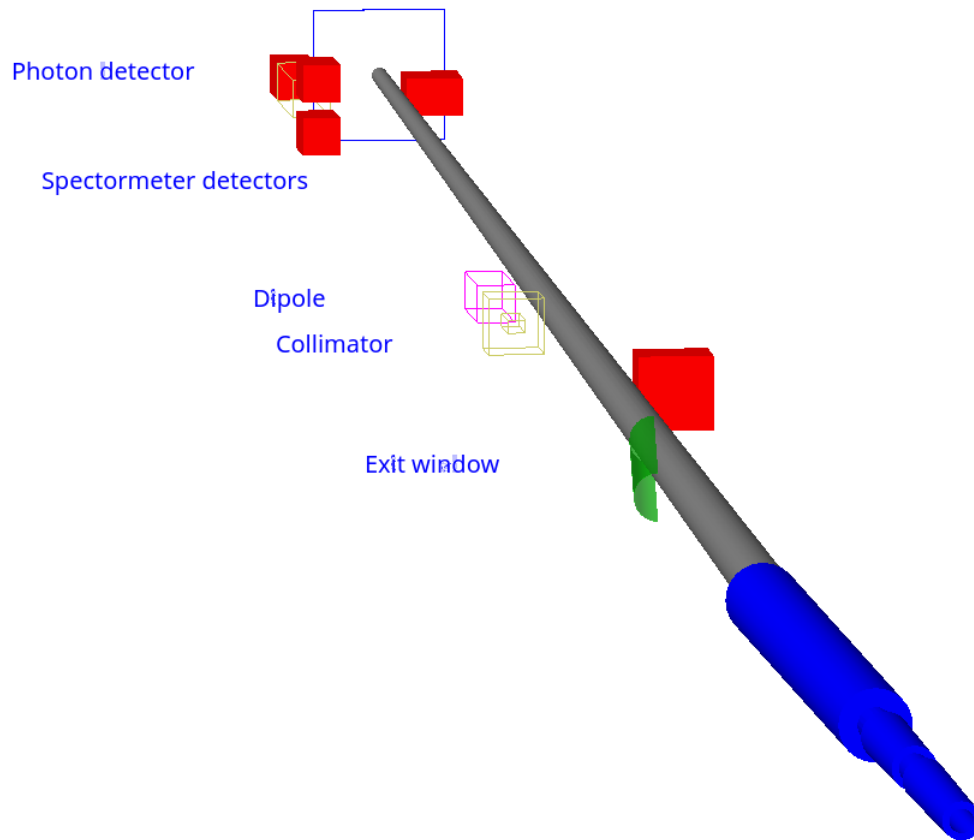


**Figure 11.105:** Geant4 model of luminosity detectors.

The luminosity system is shown in plan view in the bottom left of Fig. 11.101. A Geant4 model of all essential components for the luminosity measurement is shown in Fig. 11.105. A photon exit window is placed at  $z = -20.75$  m. It is tilted by 100 mrad relative to the axis of the electron beam (and of the photons), to achieve an acceptable heat load from synchrotron radiation. A collimator at  $z = -27$  m will prevent synchrotron radiation at larger angles from entering the luminosity system. A dipole spectrometer magnet at  $z = -28$  m will split converted electron-positron pairs into the spectrometer detectors. A direct photon detector is placed at  $z = -37.8$  m, after a graphite filter of  $5 X_0$  length. The pair of spectrometer detectors is at  $z = -36.5$  m. The spectrometer detectors are displaced vertically so their nearest edges are 42 mm above and below  $y = 0$ . The detectors are implemented in the model as boxes which register hits by all incoming particles.

The spectrometer acceptance as a function of bremsstrahlung photon energy depends on its layout as shown in Fig. 11.104. Namely it depends on the distance *length* from the dipole magnet to the spectrometer detectors, the magnetic field of the dipole and the detector positions *min* and *max* of the UP and DOWN detectors along the vertical  $y$  axis.

The acceptance is shown in Fig. 11.106 for the top energy of  $18 \times 275$  GeV beams, as a

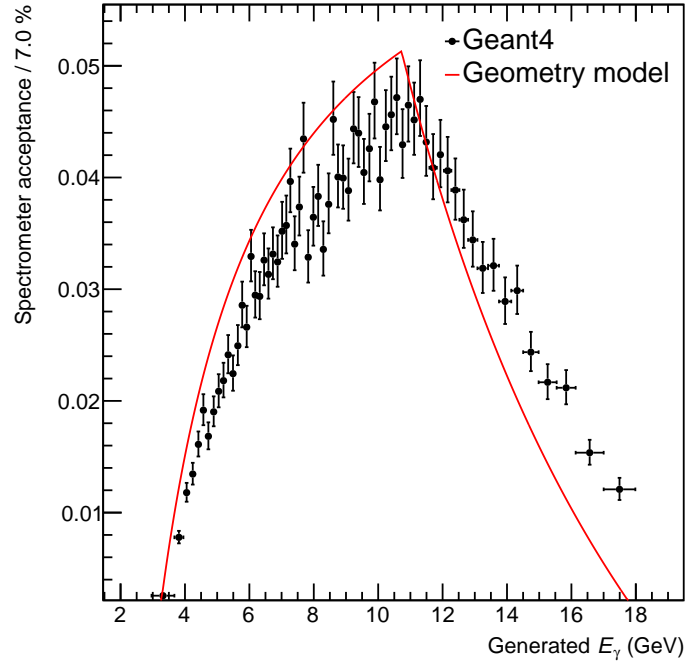


**Figure 11.106:** Luminosity spectrometer acceptance as a function of the bremsstrahlung photon energy  $E_\gamma$ .

function of generated bremsstrahlung photon energy  $E_\gamma$ . The Geant4 distribution is a result of simulation of 1M bremsstrahlung events generated by the eic-lgen event generator [1364] and passed through the layout of Fig 11.105. The acceptance is constructed as a fraction of events with at least 1 GeV of energy hitting both the UP and DOWN detectors.

A geometric model for the acceptance, shown in Fig. 11.106 as a solid line, is based on the formula for deflection of a charged particle in a magnetic field and the coincidence requirement of both pair electrons hitting the detectors. An unit charge particle moving along the  $z$  direction through a magnetic field  $B_x$  oriented along  $x$  axis gets a transverse momentum  $p_T \propto \int B_x dz$  along the vertical  $y$  direction. The position in  $y$  on the UP or DOWN detectors of the arriving electron is given by

$$y = l \frac{p_T}{p}, \quad (11.8)$$

where  $l$  is the length from the magnet center to the detector face, and  $p$  is the momentum of the electron.

If the electron in the pair hitting the upper detector has a fraction of photon energy  $z = p/E_\gamma$ , the other has a fraction  $1 - z$ . The positions of the pair arriving at the UP and DOWN detectors  $y_{\text{up}}$  and  $y_{\text{down}}$ ,  $z$  and  $E_\gamma$  are related by:

$$zE_\gamma = \frac{lp_T}{y_{\text{up}}}, \quad (1 - z)E_\gamma = \frac{lp_T}{y_{\text{down}}}. \quad (11.9)$$

Both spectrometer detectors cover minimal and maximal positions along  $y$ , as indicated in Fig. 11.104. The coincidence requirement then limits the range in  $z$  for which the converted photon would be detected by the spectrometer. The integral of  $\frac{dN}{dz}$  over this range of  $z$  then determines the acceptance at a given  $E_\gamma$ , shown as the solid line in Fig. 11.106. There is reasonable agreement with the full Geant4 simulation.

The geometric model has been used to determine the magnetic field for the spectrometer dipole magnet as  $B_x = 0.26$  T in order to optimize the acceptance for  $18 \times 275$  GeV beams. A unique magnetic field will be required for each electron beam energy.

## 11.7.2 Far-Backward Electrons

### Far-Backward Electron Processes and Measurements

**Bremsstrahlung and Low- $Q^2$  Electron Detectors:** Downstream of the interaction point the electron beam is accompanied by a flux of electrons at small angles with respect to the beam direction and at slightly lower energy. They are predominantly final state electrons from the bremsstrahlung process  $e + p \rightarrow e + p + \gamma$ , with an energy distribution the mirror image of the left of Fig. 11.102 with  $E'_e = E_e - E_\gamma$ . Also, a fraction of the electrons in this region are produced in quasi-real photoproduction with  $Q^2 \approx 0$ .

The final state bremsstrahlung electrons provide a powerful tool for calibrating and verifying the luminosity measurement with photons. Tagging bremsstrahlung electrons and counting corresponding photons in the photon detectors provides a direct measure of the luminosity detector acceptance in the tagged energy range. This is of paramount importance to precisely determine the pair conversion probability for the luminosity spectrometer, which depends on the exit window composition and thickness.

Tagging of low- $Q^2$  processes provides an extension of the kinematic range of DIS processes measured with electrons in the central detector. It crosses the transition from DIS to hadronic reactions with quasi-real photons. An example of acceptance as a function of  $Q^2$  for measurements with the central detector and electron taggers as depicted in Fig. 11.101 is shown in Fig. 11.107. The electrons are generated by a simple model of quasi-real photoproduction [1359] and Pythia. The taggers provide useful acceptance in the range  $10^{-6} < Q^2 < 10^{-2}$  GeV<sup>2</sup>. Application of the electron taggers for low- $Q^2$  physics will face a challenge from the high rate bremsstrahlung electrons, which can be addressed by tagger design and correlation with information from the central detector.

Possible locations of detectors for these electrons are shown in the top left of Fig. 11.101. Electrons with energies slightly below the beam are bent out of the beam by the first lattice dipole after the interaction point. The beam vacuum chamber must include exit windows for these electrons. The windows should be as thin as possible along the electron direction to minimize energy loss and multiple scattering before the detectors.

The taggers should include calorimeters for triggering and energy measurements. They should be finely segmented to disentangle the multiple electron hits per bunch crossing

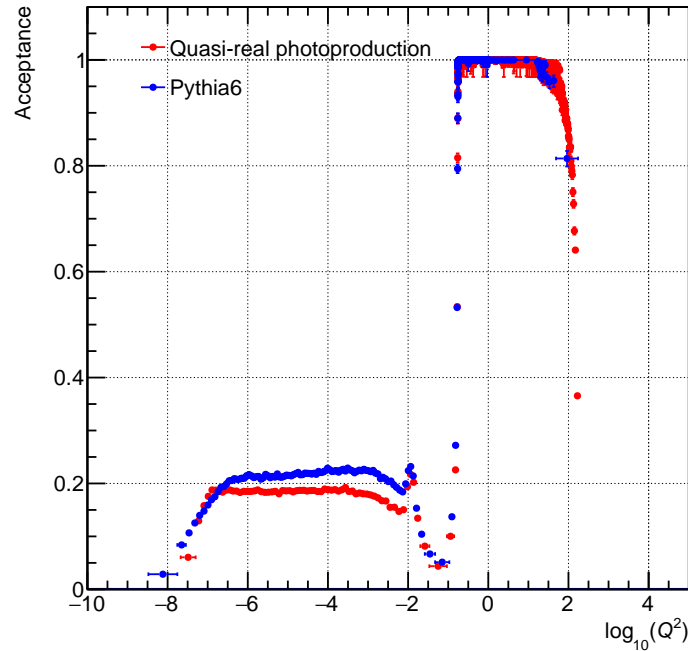


**Figure 11.107:** Acceptance as a function of  $Q^2$  for electrons measured in the central detector (right plateau) and downstream taggers (left plateau). The electrons are generated by a simple model of quasi-real photoproduction and Pythia.

from the high rate bremsstrahlung process. The taggers should also have position sensitive detectors to measure the vertical and horizontal coordinates of electrons. The combined energy and position measurements allow reconstruction of the kinematic variable  $Q^2$  and  $x_{BJ}$ . If the position detectors have multiple layers and are able to reconstruct the electron direction this will overconstrain the variable reconstruction and improve their measurement; this may also provide some measure of background rejection. The beam angular divergence will introduce significant errors on the variable reconstruction. The reconstructed versus generated  $Q^2$  is shown in Fig. 11.108 with smearing from beam divergence. There is reasonable resolution for  $Q^2$  as low as  $10^{-3} \text{ GeV}^2$ ; below  $10^{-4} \text{ GeV}^2$  meaningful reconstruction of  $Q^2$  based on the electron is not possible.

**Start old YR:** The aim of the low- $Q^2$  tagger is to detect electrons scattered at very small angles, beyond coverage of central detector. Layout of backward (electron-outgoing) side of interaction region is shown in Fig. ?? . Beam magnets are shown in full green, drift space in dashed green and detectors and components in red and yellow. Two tagger detectors are proposed, Tagger 1 at  $z = -24 \text{ m}$  and Tagger 2 at  $z = -37 \text{ m}$  respectively. Backward electromagnetic calorimeter ECAL is a part of central detector, located at  $z = -3.28 \text{ m}$ . Rapidity coverage of ECAL as implemented in model for tagger studies is  $-4.4 < \eta < -1.0$ .

Geant4 model of backward side of interaction region is shown in Fig. 11.109. The tagger de-

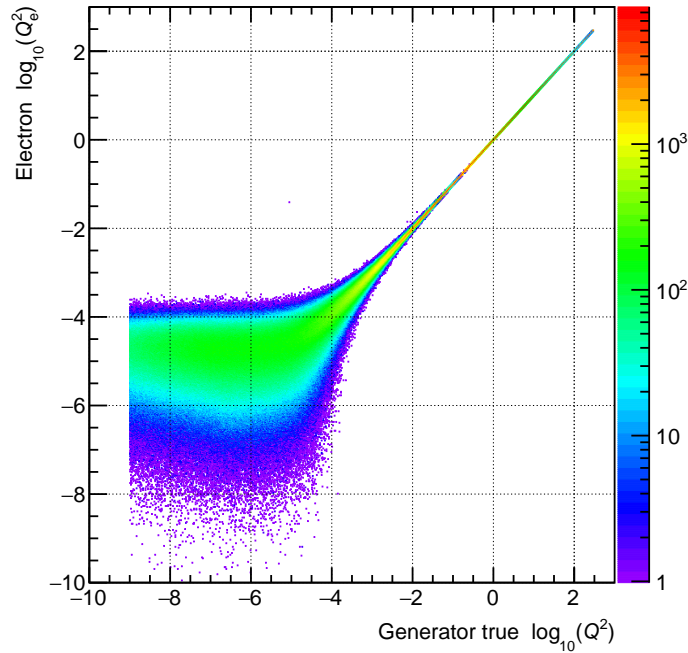


**Figure 11.108:** Comparison of generated and reconstructed electron  $Q_e^2$  with smearing for beam angular divergence.

tectors Tagger 1 and 2 and backward electromagnetic calorimeter ECAL are implemented as boxes which mark hits by all incoming particles. Solenoid field of central detector is based in 3 T BeAST parametrization. Beam magnets eQ1ER, eQ2ER and eB2ER ( 10.2 ) are shown as blue cylinders. Drift spaces in gray are transparent to all particles. The layout ends with marker at position of Q3eR magnet.

Two generated samples, Pythia 6 and quasi-real photoproduction, were used to address acceptance of the taggers, both for the top energy  $18 \times 275$  GeV for electron and proton beam respectively. Total cross section for both samples as a function of event true  $Q^2$  is shown in Fig. 11.110.

Model of quasi-real photoproduction is based on approach used at HERA study [1359] and implemented in eic-lgen event generator [1364].

Angular and energy coverage for both tagger detectors is shown in Fig. 11.111. Energy of scattered electrons  $E_e$  and polar angle  $\theta_e$  is shown for events where the scattered electron is incident on one of the tagger detectors. Energy and mainly angular coverage is complementary for both tagger detectors.

Coverage in  $Q^2$  is shown in Fig. 11.112 for quasi-real photoproduction. Events with a hit in one of the taggers or in ECAL are shown along with all generated quasi-real events. Coverage in  $Q^2$  for both of the taggers follows a similar interval, although as illustrated from Fig. 11.111, the coverage is achieved by different combinations of electron energies and angles. Transition of coverage takes place at lower reach of ECAL and upper reach of

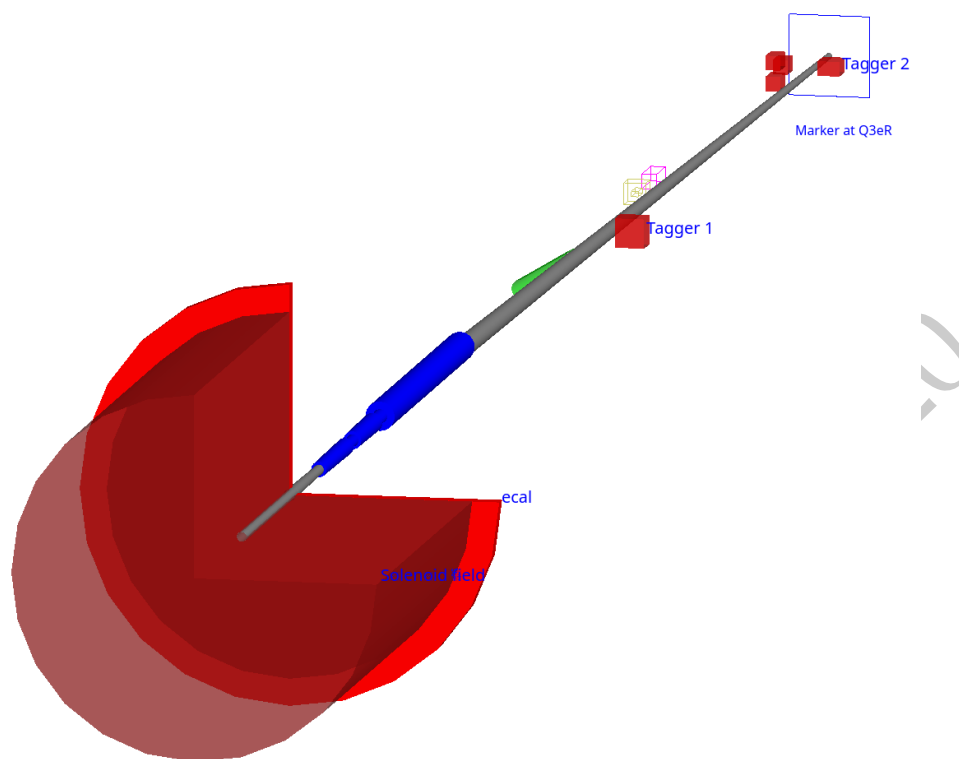


**Figure 11.109:** Geant4 model of backward interaction region, side of electron tagger detectors.

tagger detectors.

Combined acceptance of tagger detectors and ECAL is shown in Fig. 11.113 for both samples of Pythia 6 and quasi-real photoproduction. The acceptance is obtained as a fraction of all generated events with a hit in one of the tagger detectors or in ECAL. A dip takes place at a transition between ECAL and taggers acceptance, at  $Q^2$  about  $0.1 \text{ GeV}^2$ . It was shown that magnitude and width of the dip strongly depends on available inner radius for ECAL. The acceptance is well compatible between the two event generators.

As main kinematics variables include Bjorken- $x$ , inelasticity  $y$  and virtuality  $Q^2$ , coverage of both taggers is given in combinations of  $x$ ,  $y$  and  $Q^2$  in Fig. 11.114. Intervals of all generated events are shown as underlying red bands, box diagrams then give events with a hit in one of the taggers or in ECAL.

## 11.8 Polarimetry

Rapid, precise beam polarization measurements will be crucial for meeting the goals of the EIC physics program as the uncertainty in the polarization propagates directly into the uncertainty for relevant observables (asymmetries, etc.). In addition, polarimetry will play

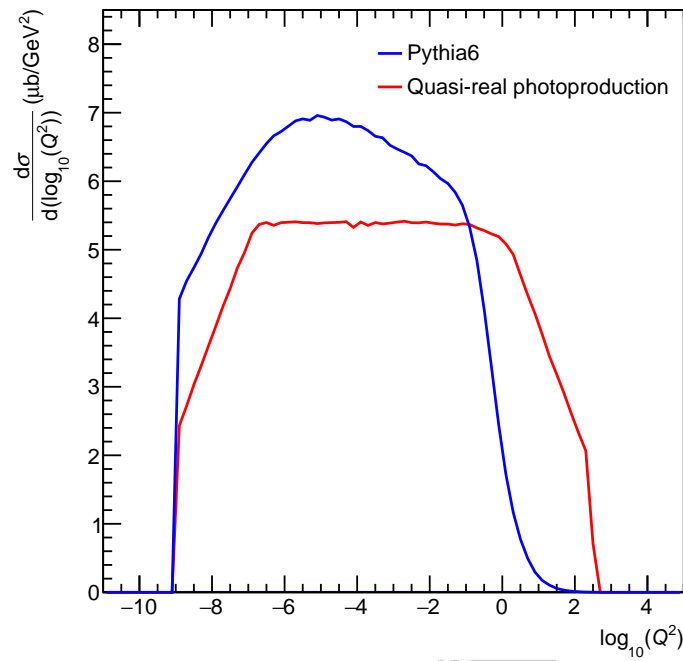
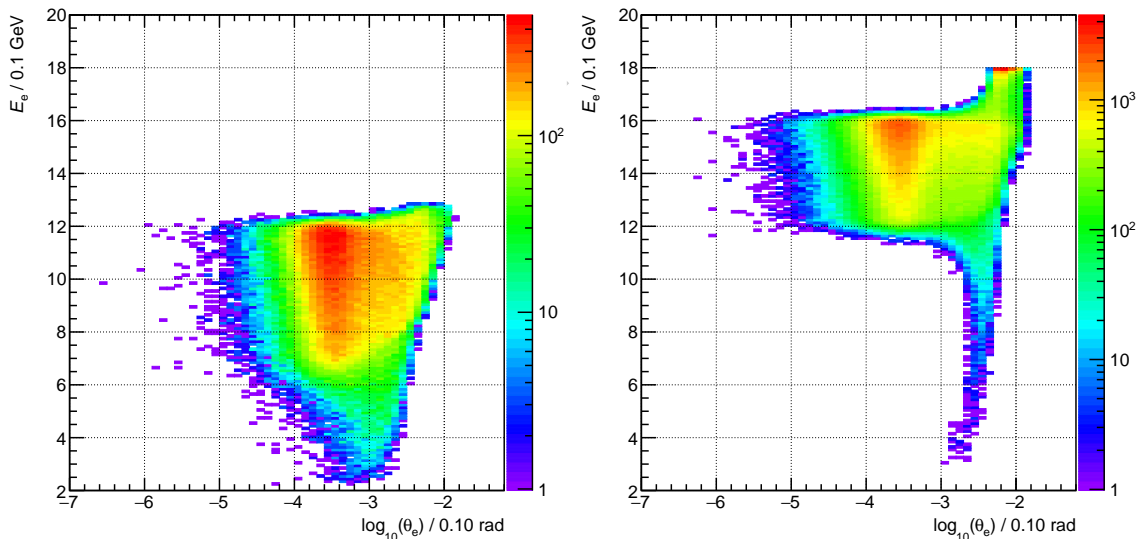


**Figure 11.110:** Total cross section as a function of event true  $Q^2$  for Pythia 6 and quasi-real photoproduction.



(a) Hit in Tagger 1

(b) Hit in Tagger 2

**Figure 11.111:** Scattered electron energy  $E_e$  and polar angle  $\theta_e$  for events of quasi-real photoproduction with a hit in Tagger 1 or 2.

an important role in facilitating the setup of the accelerator.

The basic requirements for beam polarimetry are:

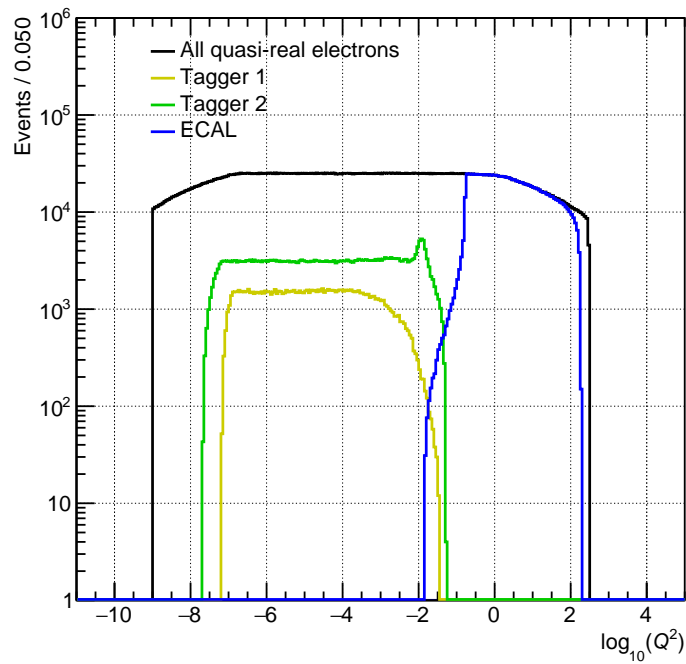


Figure 11.112: Coverage in  $Q^2$  for tagger detectors and ECAL.

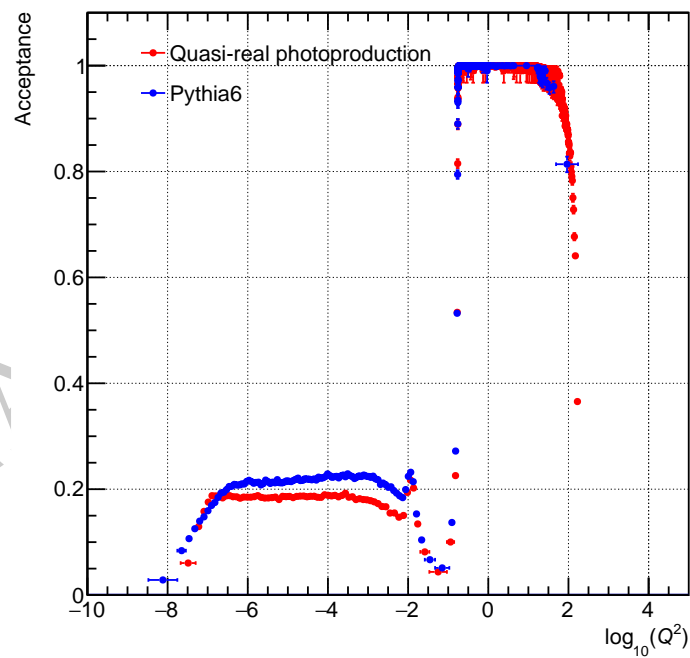
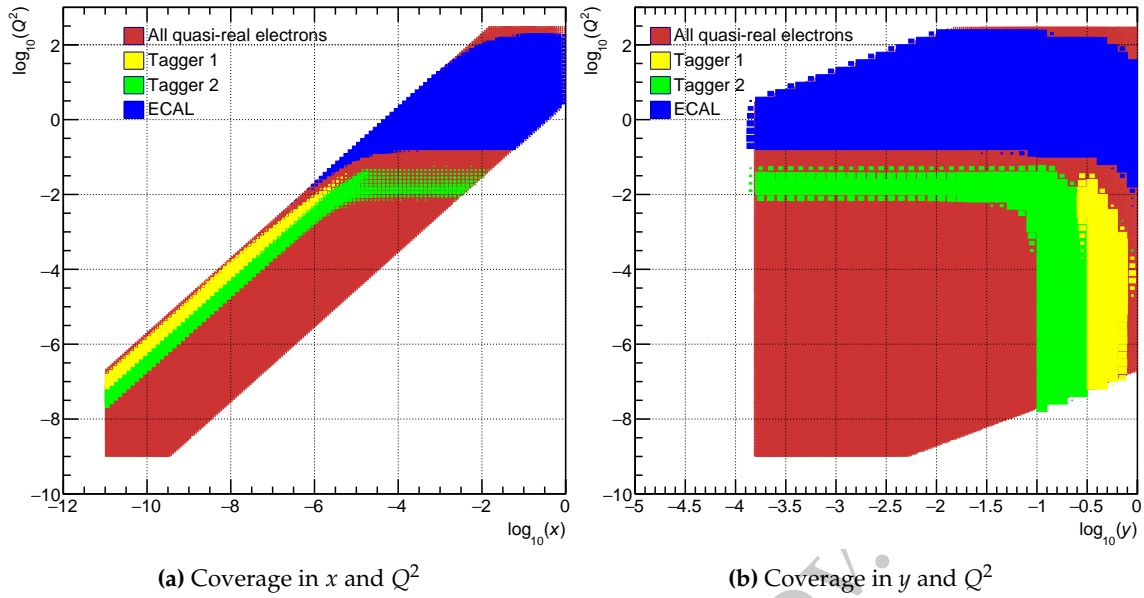


Figure 11.113: Acceptance in  $Q^2$  for tagger detectors and ECAL as a fraction of events with a hit in one of the taggers or in ECAL

- Non-destructive with minimal impact on the beam lifetime



**Figure 11.114:** Coverage in  $x$ ,  $y$  and  $Q^2$  for tagger detectors and ECAL.

- Systematic uncertainty on the order  $\frac{dP}{P} = 1\%$  or better
- Capable of measuring the beam polarization for each bunch in the ring - in particular, the statistical uncertainty of the measurement for a given bunch should be comparable to the systematic uncertainty
- Rapid, quasi-online analysis in order to provide timely feedback for accelerator setup

### 11.8.1 Electron Polarimetry

The most commonly used technique for measuring electron beam polarization in rings and colliders is Compton polarimetry, in which the polarized electrons scatter from 100% circularly polarized laser photons. The asymmetry from this reaction is measured via the scattered electrons or high energy backscattered photons. A brief review and description of several previous Compton polarimeters can be found in [1365]. A particular advantage of Compton polarimetry is that it is sensitive to both longitudinal and transverse polarization.

The longitudinal analyzing power depends only on the backscattered photon energy and is given by,

$$A_{\text{long}} = \frac{2\pi r_o^2 a}{(d\sigma/d\rho)} (1 - \rho(1 + a)) \left[ 1 - \frac{1}{(1 - \rho(1 - a))^2} \right], \quad (11.10)$$

where  $r_o$  is the classical electron radius,  $a = (1 + 4\gamma E_{\text{laser}}/m_e)^{-1}$  (with the Lorentz factor  $\gamma = E_e/m_e$ ),  $\rho$  is the backscattered photon energy divided by its kinematic maximum,  $E_\gamma/E_\gamma^{\text{max}}$ , and  $d\sigma/d\rho$  is the unpolarized Compton cross section. In contrast, the transverse analyzing power depends both on the backscattered photon energy and the azimuthal

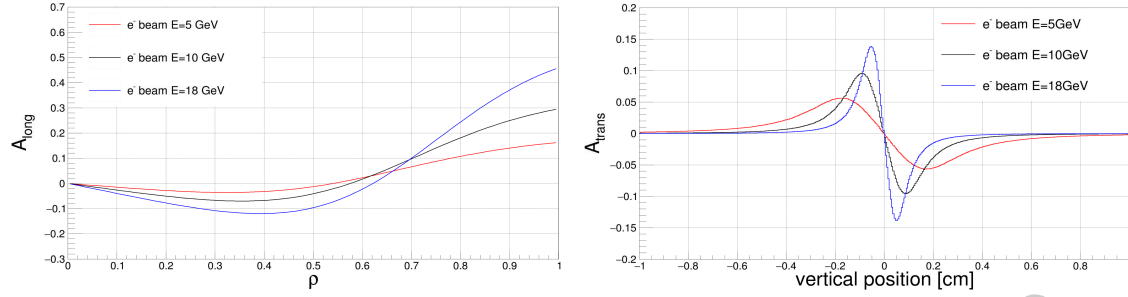


**Figure 11.115:** Longitudinal (left) and transverse (right) analyzing powers assuming a 532 nm wavelength laser colliding with an electron beam at 5 GeV, 10 GeV, and 18 GeV. The transverse analyzing power is shown for photons projected 25 m from the collision point and plotted vs. the vertical position.

angle ( $\phi$ ) of the photon (with respect to the transverse polarization direction);

$$A_{\text{tran}} = \frac{2\pi r_0^2 a}{(d\sigma/d\rho)} \cos \phi \left[ \rho(1-a) \frac{\sqrt{4a\rho(1-\rho)}}{(1-\rho(1-a))} \right]. \quad (11.11)$$

This azimuthal dependence of the asymmetry results in an “up-down” asymmetry (assuming vertically polarized electrons) and requires a detector with spatial sensitivity. Both the longitudinal and transverse analyzing powers are shown in Fig. 11.115.

Plans for electron polarimetry at EIC include a Compton polarimeter at IP 12, where the electron beam is primarily vertically polarized. A Compton polarimeter near the primary detector in the vicinity of IP 6, where the beam will be a mix of longitudinal and transverse polarization, is also under investigation; since that region of the ring is extremely crowded, care must be taken in the assessment of whether a polarimeter can be accommodated. A schematic of the placement of the Compton polarimeter at IP 12 is shown in Fig. 11.116.

As noted above, a key requirement of the Compton polarimeter is the ability to make polarization measurements for an individual bunch. The measurement time to achieve a statistical precision  $dP/P$  is given by a combination of the luminosity, Compton cross section, and analyzing power:

$$t_{\text{meth}} = \left( \mathcal{L} \sigma_{\text{Compton}} P_e^2 P_\gamma^2 \left( \frac{dP_e}{P_e} \right)^2 A_{\text{eff}}^2 \right)^{-1}. \quad (11.12)$$

The effective Compton analyzing power,  $A_{\text{eff}}$ , depends on the measurement technique; in order of increasing effective analyzing power, these are integrated, energy-weighted integrated, and differential. For measurement time estimates here, we will use the smallest analyzing power (i.e., integrated) to be conservative.

Nominal electron beam parameters at IP 12 are provided in Table 11.29. Of particular note is the relatively short bunch lifetime at 18 GeV. Table 11.30 shows the average transverse

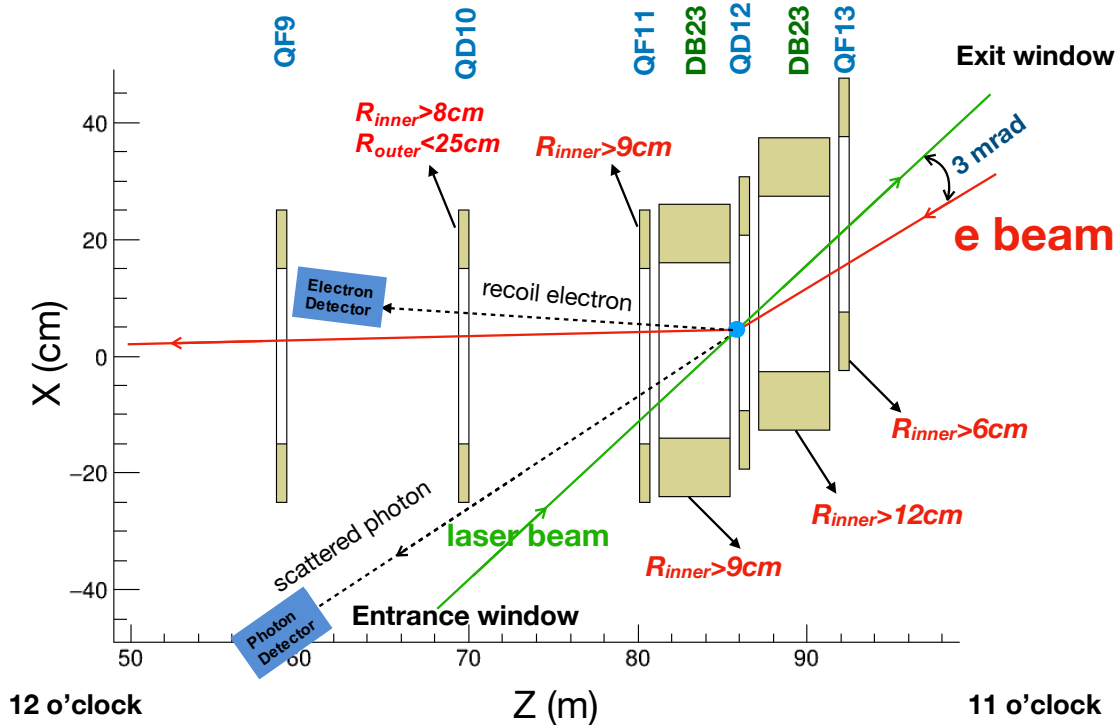


**Figure 11.116:** Layout of the Compton polarimeter at IP 12. In this figure the electron beam travels from right to left - the laser beam collides with the electrons just downstream of QD12. The dipole just downstream of the collision (DB12) steers the unscattered electrons allowing detection of the backscattered photons about 25 m downstream of the collision. DB12 also momentum-analyzes the scattered electrons, facilitating use of a position sensitive electron detector downstream of QD10. Also noted in the figure are constraints on required apertures of the magnets needed to allow transport of the laser beam, backscattered photons, and scattered electrons.

analyzing power, luminosity, and time required to make a 1% (statistics) measurement of the beam polarization for an individual bunch, assuming a single Compton-scattered event per crossing. The constraint of having a single event per crossing is related to the need to make a position sensitive measurement at the photon and electron detectors. Note that even with this constraint, the measurement times are relatively short and, in particular, shorter than the bunch lifetime in the ring.

Even for a single electron bunch (circulating through the ring at a frequency of  $\approx 75$  kHz), the luminosities provided in Table 11.30 can be readily achieved using a single-pass, pulsed laser. Since the electron beam frequency varies with energy, it would be useful to have a laser with variable pulse frequency. A laser system based on the gain-switched diode lasers used in the injector at Jefferson Lab [1366] would provide both the power and flexible pulse frequency desired. Such a system would make use of a gain-switched diode laser

beam property	5 GeV	10 GeV	18 GeV
Bunch frequency	99 MHz	99 MHz	24.75 MHz
Beam size (x)	390 $\mu\text{m}$	470 $\mu\text{m}$	434 $\mu\text{m}$
Beam size (y)	390 $\mu\text{m}$	250 $\mu\text{m}$	332 $\mu\text{m}$
Pulse width (RMS)	63.3 ps	63.3 ps	30 ps
Intensity (avg.)	2.5 A	2.5 A	0.227 A
Bunch lifetime	>30 min	>30 min	6 min

**Table 11.29:** Beam parameters at IP12 for the EIC nominal electron beam energies.

beam energy [GeV]	$\sigma_{unpol}$ [barn]	$\langle A_\gamma \rangle$	$t_\gamma$ [s]	$\langle A_e \rangle$	$t_e$ [s]	$L[1/(\text{barn}\cdot\text{s})]$
5	0.569	0.031	184	0.029	210	1.37E+05
10	0.503	0.051	68	0.050	72	1.55E+05
18	0.432	0.072	34	0.075	31	1.81E+05

**Table 11.30:** Asymmetries, measurement times needed for a 1% statistical measurement for one bunch and needed luminosities for three different beam energies for a 532 nm laser.

at 1064 nm, amplified to high average power (10-20 W) via a fiber amplifier, and then frequency doubled to 532 nm using a PPLN or LBO crystal. The repetition rate is set by the applied RF frequency to the gain-switched seed laser.

A laser system based on the gain-switched diode lasers used in the injector at Jefferson Lab [1366] can provide all of the requirements noted above. The proposed system will make use of a gain-switched diode laser at 1064 nm, amplified to high average power (10-20 W) via a fiber amplifier, and then frequency doubled to 532 nm using a PPLN or LBO crystal. The repetition rate of the laser is dictated by an applied RF signal and can be readily varied. In addition to the laser system itself, a system to set up and measure the laser polarization at the interaction point is required. Determination of the laser polarization in the beamline vacuum is non-trivial due to possible birefringence of the beamline window under mechanical and vacuum stress. We will employ a technique similar to that used at Jefferson Lab [1367, 1368] that makes use of optical reversibility theorems to determine the laser polarization inside the vacuum using light reflected backwards through the incident laser transport system. This polarization monitoring and setup system will require a remotely insertable mirror in the beamline vacuum so will need to be considered in the beamline design. A schematic of the proposed laser system is shown in Fig. 11.117.

The detector requirements for the EIC Compton polarimeters are dictated by the requirement to be able to measure the transverse and longitudinal polarization simultaneously. For longitudinal polarization, this means the detectors will require sensitivity to the backscattered photon and scattered electron energy. The photon detector can make use of a fast calorimeter, while the electron detector can take advantage of the dispersion introduced by the dipole after the collision point to infer the scattered electron energy from a detector with position sensitivity in the horizontal direction.

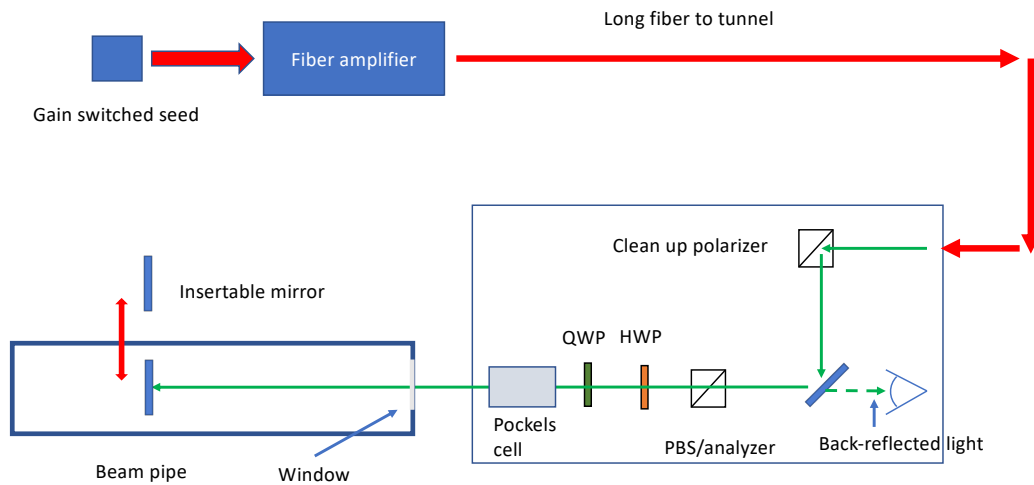


**Figure 11.117:** Layout of the Compton polarimeter laser system, including diagnostics to accurately determine the laser polarization at the interaction point.

To measure transverse polarization, position sensitive detectors are required to measure the up-down asymmetry. This is particularly challenging given the very small backscattered photon cone at the highest EIC beam energy. At HERA, the vertical position of the backscattered photon was inferred via shower-sharing between the optically isolated segments of a calorimeter [1369]. Calibration of the non-linear transformation between the true vertical position and the energy-asymmetry in the calorimeter was a significant source of uncertainty. The proposed detector for the EIC Compton will measure the vertical position directly via segmented strip detectors, avoiding the calibration issues faced at HERA.

The transverse Compton analyzing power vs. position at the detector for the backscattered photons and scattered electrons at 5 and 18 GeV is shown in Fig. 11.118. The backscattered photon cone will be largest at the lowest energy (5 GeV) - this will determine the required size of the detector. The distribution at 18 GeV, where the cone is the smallest, sets the requirements for the detector segmentation. Note that the scattered electrons are significantly more focused than the photons. Monte Carlo studies indicate that the transverse polarization can be reliably extracted at 18 GeV with a vertical detector segmentation of  $100\ \mu\text{m}$  for the photon detector and  $25\ \mu\text{m}$  for the electron detector. The detector size should be at least  $16 \times 16\ \text{mm}^2$  for the photons and  $10\ \text{cm} \times 1\ \text{mm}$  for the scattered electrons. The horizontal segmentation for the electron detector can be much more coarse due to the large horizontal dispersion introduced by the dipole.

Diamond strip detectors are a feasible solution for both the photon and electron detectors. Diamond detectors are extremely radiation hard and are fast enough to have response times sufficient to resolve the minimum bunch spacing (10 ns) at EIC. Tests of CVD diamond with specialized electronics have shown pulse widths on the order of 8 ns [1370]. For the photon detector, about 1 radiation length of lead will be placed in front of the

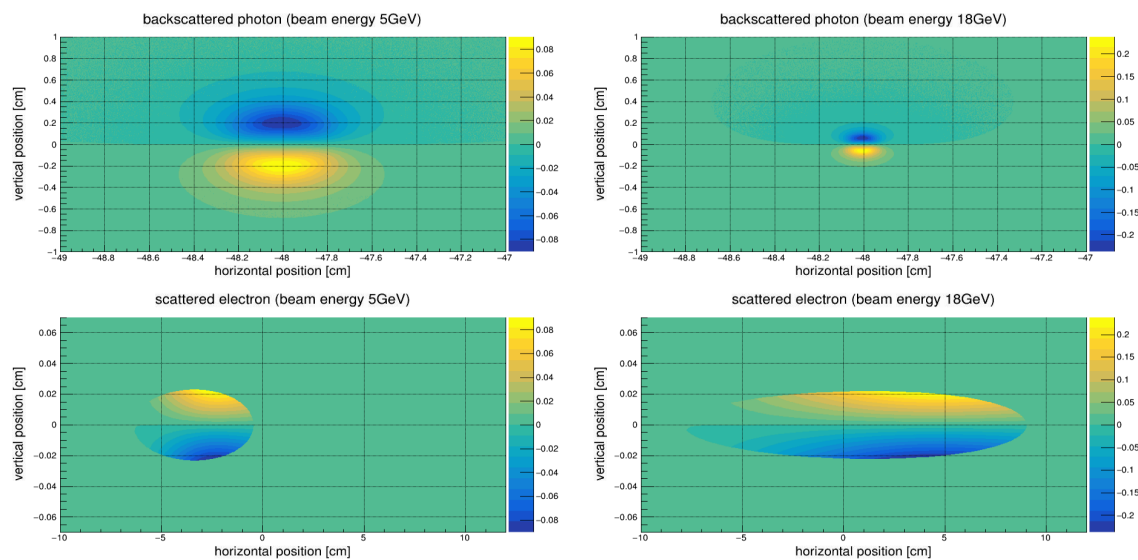


**Figure 11.118:** Compton (transverse) analyzing power at the nominal photon and electron detector positions for the IP 12 polarimeter.

strip detectors to convert the backscattered photons. As an alternative to diamond detectors, HVMAPS detectors are also under consideration. The radiation hardness and time response of HVMAPS will need to be assessed to determine their suitability for this application.

As noted earlier, the photon detector will also require a calorimeter to be sensitive to longitudinal components of the electron polarization. Only modest energy resolution is needed; radiation hardness and time response are more important requirements for this detector - a tungsten powder/scintillating fiber calorimeter would meet these requirements.

Backgrounds are an important consideration for Compton polarimetry as well. The primary processes of interest are Bremsstrahlung and synchrotron radiation. Monte Carlo studies have shown that the contribution from Bremsstrahlung should be small for a beam-line vacuum of  $10^{-9}$  Torr. Synchrotron radiation, on the other hand, will be a significant concern. Careful design of the exit window for the backscattered photons will be required to mitigate backgrounds due to synchrotron. The electron detector is not in the direct synchrotron fan, but significant power can be deposited in the detector from one-bounce photons. This can be mitigated by incorporating tips or a special antechamber in the beampipe between the Compton IP and the detector [1371]. The electron detector will also be subject to power deposited in the planned Roman Pot housing due to the beam Wakefield. Preliminary simulations indicate the Wakefield power should not be large enough to cause problems, but this will need to be considered in the detailed Roman Pot design.

In addition to measurements in the EIC electron ring, it is important to be able to determine the electron beam polarization in or just after the Rapid Cycling Synchrotron (RCS) in order to facilitate machine setup and troubleshoot possible issues with the electron beam polarization. In the RCS, electron bunches of approximately 10 nC are accelerated from

400 MeV to the nominal beam energy (5, 10, or 18 GeV) in about 100 ms. These bunches are then injected into the EIC electron ring at 1 Hz. The short amount of time each bunch spends in the RCS, combined with the large changes in energy (and hence polarimeter analyzing power and/or acceptance) make non-invasive polarization measurements, in which the the RCS operates in a mode completely transparent to beam operations, essentially impossible. However, there are at least two options for making intermittent, invasive polarization measurements.

The first, and perhaps simplest from a polarimetry perspective, would be to operate the RCS in a so-called “flat-top” mode [1372]. In this case, an electron bunch in the RCS is accelerated to its full or some intermediate energy, and then stored in the RCS at that energy while a polarization measurement is made. In this scenario, a Compton polarimeter similar to that described above could be installed in one of the straight sections of the RCS. The measurement times would be equivalent to those noted in Table 11.30 (since those are for a single stored bunch), i.e., on the order of a few minutes.

Another option would be to make polarization measurements in the transfer line from the RCS to the EIC electron ring. In this case, one could only make polarization measurements averaged over several bunches. In addition, the measurement would be much more time consuming due to the low average beam current ( $\approx 10$  nA) since the 10 nC bunches are extracted at 1 Hz.

The measurement time at 10 nA using a Compton polarimeter similar to the one planned for IP12 would take on the order many days. The IP12 Compton limits the number of interactions to an average of one per crossing to be able to count and resolve the position of the backscattered photons. A position sensitive detector that could be operated in integrating mode, would allow more rapid measurements. However, the required position resolution (25-100  $\mu\text{m}$ ) would be very challenging for a detector operating in integrating mode. An alternative to Compton polarimetry would be the use of Møller polarimetry. Møller polarimeters can be used to measure both longitudinal and transverse polarization and can make measurements quickly at relatively low currents. The longitudinal and transverse Møller analyzing powers are shown in Fig. 11.119 and are given by,

$$A_{ZZ} = -\frac{\sin^2 \theta^* (7 + \cos^2 \theta^*)}{(3 + \cos^2 \theta^*)^2}, \quad (11.13)$$

$$A_{XX} = -\frac{\sin^4 \theta^*}{(3 + \cos^2 \theta^*)^2}, \quad (11.14)$$

where  $A_{ZZ}$  is the analyzing power for longitudinally polarized beam and target electrons,  $A_{XX}$  for horizontally polarized beam and target electrons, and  $\theta^*$  is the center-of-mass scattering angle. Note that  $A_{YY} = -A_{XX}$ . The magnitude of the analyzing power is maximized in both cases at  $\theta^* = 90$  degrees, where  $|A_{ZZ}| = 7/9$  and  $|A_{XX}| = 1/9$ .

Møller polarimeters at Jefferson Lab can make (longitudinal) polarization measurements with a statistical precision of 1% at average beam currents of 1  $\mu\text{A}$  with a 4  $\mu\text{m}$  iron foil target in about 15 minutes. Electrons from the RCS will be transversely polarized, and the analyzing power will be a factor of 7 smaller, which implies a factor of 50 increase in mea-

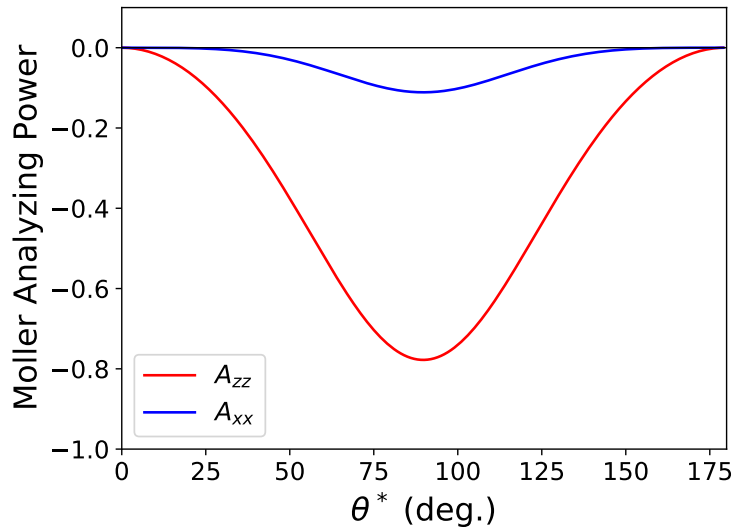


**Figure 11.119:** Analyzing power for longitudinally polarized beam and target electrons ( $A_{zz}$ ) and transversely polarized beam and target electrons ( $A_{xx}$ ) vs. center of mass scattering angle,  $\theta^*$ . The magnitude for both is largest at  $\theta^* = 90$  degrees;  $A_{zz} = -7/9$  and  $A_{xx} = -1/9$ .

surement time for the same precision. This smaller analyzing power combined with the low average beam current results in very long measurement times. These long measurement times can be partially mitigated through the use of thicker target foils. Even then, the measurements still take a significant amount of time - 1.5 hours for a 10% measurement of the polarization using a  $30 \mu\text{m}$  target. While target foil thicknesses of  $10\text{-}30 \mu\text{m}$  have routinely been employed in Møller polarimeters, it is possible that even thicker targets (perhaps a factor of 10 thicker) could also be used, reducing the measurement time further. The maximum useful target thickness would need to be investigated.

A key drawback of Møller polarimetry is that the solid foil targets are destructive to the beam, so cannot be carried out at the same time as normal beam operations. An additional complication is the requirement for a magneto-optical system to steer the Møller electrons to a detector system. In the experimental Hall A at Jefferson Lab, the Møller spectrometer employs several quadrupoles of modest length and aperture, combined with a dipole to deflect the Møller electrons into the detector system (see Fig. 11.120). The whole system occupies about 7 m of space along the beamline, but the space used by the quadrupoles can also be used for beam transport during normal operations (i.e., when Møller measurements are not underway).

The preferred choice for polarimetry at the RCS is a Compton polarimeter in the RCS ring, with measurements taking place during “flat-top” mode operation. However, if this “flat-top” mode is not practical, then a Møller polarimeter in the RCS transfer line could serve as a reasonable fallback, albeit with reduced precision and a larger impact on the beamline design.

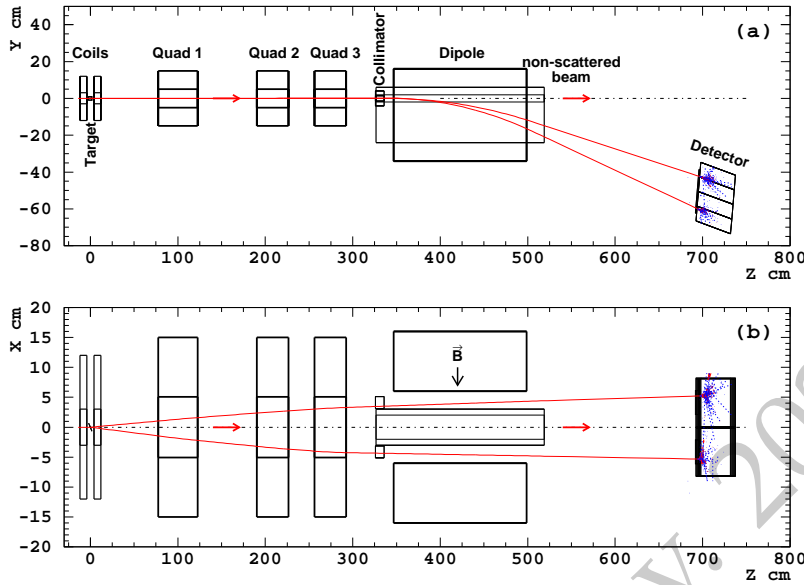


Figure 11.120: Layout of the Møller polarimeter in experimental Hall A at Jefferson Lab.

### 11.8.2 Hadron Polarimetry

Hadron polarimetry has been successfully performed on RHIC polarized proton beams for nearly two decades. Through continual development a systematic uncertainty  $\sigma_p^{\text{synt}}/P < 1.5\%$  [1373] was achieved for the most recent RHIC polarized proton run. After improving data analysis, systematic uncertainties in measurement of the beam profile averaged polarization were reduced to  $\sigma_p^{\text{synt}}/P \lesssim 0.5\%$  [1374]. As the only hadron polarimeter system at a high energy collider it is the natural starting point for hadron polarimetry at the EIC.

Hadron polarization is typically measured via a transverse single spin left right asymmetry:  $\epsilon = A_N P$ . Unlike for polarized leptons, the proportionality constant is not precisely known from theory. The solution at RHIC employs an absolute polarimeter with a polarized atomic hydrogen jet target (HJET) [1375], illustrated in Fig. 11.121. The hydrogen polarization vector is alternated between vertically up and down. The RHIC beam also has bunches with up and down polarization states. By averaging over the beam states the asymmetry with respect to the target polarization may be measured, and vice versa:

$$\epsilon_{\text{target}} = A_N P_{\text{target}} \quad \epsilon_{\text{beam}} = A_N P_{\text{beam}} . \quad (11.15)$$

The target polarization is precisely measured with a Breit-Rabi polarimeter. Combined with the measured asymmetries the beam polarization is determined:

$$P_{\text{beam}} = \frac{\epsilon_{\text{beam}}}{\epsilon_{\text{target}}} P_{\text{target}} . \quad (11.16)$$

The absolute polarization measurement is independent of the details of  $A_N$ .

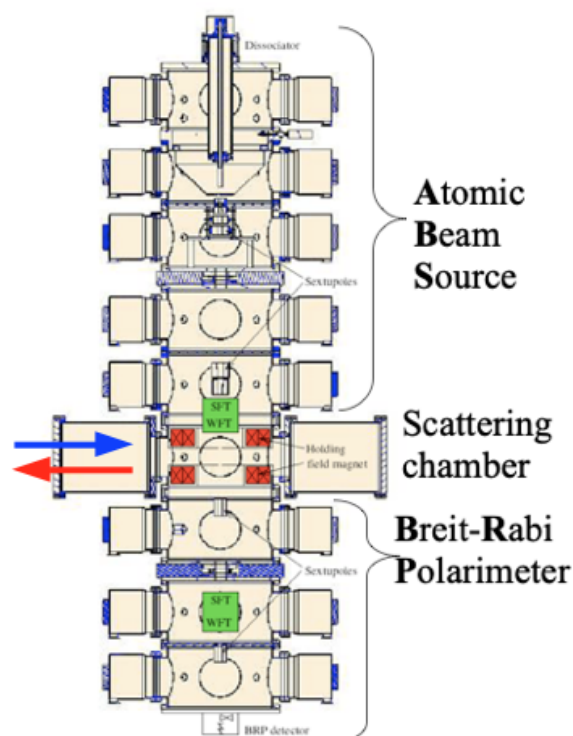


**Figure 11.121:** The RHIC polarized hydrogen jet polarimeter. The atomic beam source at the top passes polarized hydrogen across the beams (blue and red arrows) in the scattering chamber, with detectors left and right of the beams. The atomic hydrogen polarization is measured by the Breit-Rabi polarimeter at bottom.

Even though, the diffuse nature of the polarized jet target provides only a relatively low rate of interactions, continuous operation during the store resulted in statistical precision of the polarization measurement of about  $\sigma_p^{\text{stat}} \sim 2\%$  per 8-hour RHIC fill (in Run 17). These measurements, however, are not sensitive to the inevitable decay of beam polarization throughout a fill. Also, the jet target is wider than the beam and measures only the average polarization across the beam. The beam polarization is larger at the center than the edges transversely; the polarization of colliding beams differs from the average polarization due to this effect [1376]. The polarimeters must measure this transverse polarization profile to provide correct polarizations for use by collider experiments.

At RHIC the required finer grained polarization details are provided by the proton-carbon (pC) relative polarimeter, illustrated in Fig. 11.122. A thin carbon ribbon target is passed across the beam and scattered carbon nuclei are measured in detectors arrayed around the beam. The dense target provides a high interaction rate, allowing an asymmetry measurement with a few per cent statistical precision in less than 30 seconds. Such measurements are made periodically throughout a RHIC fill, providing a measurement of the beam polarization decay. The ribbon target is narrower than the beam; thus it is able to measure asymmetry as a function of position across the beam and determine the transverse polarization profile. The absolute polarization scale of the pC polarimeter is set by normalizing

an ensemble of pC measurements to the results from the Hjet polarimeter for the corresponding RHIC fills.

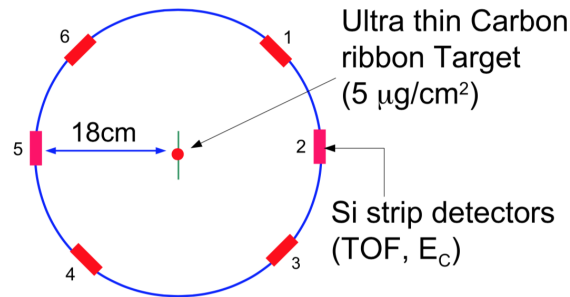


**Figure 11.122:** Cross section of the RHIC proton-carbon polarimeter. A thin carbon ribbon target is passed across the beam (into page) and scattered carbon nuclei are measured in the six detectors.

Both of the RHIC hadron polarimeters can in principle be used for proton polarimetry at the EIC. At present two significant difficulties are foreseen. First, backgrounds in both polarimeters are observed and lie partially beneath the signal events. They are distinguished by timing distributions different from the signal allowing separation or estimation of a subtraction from the signal. At the EIC with higher bunch crossing frequency, the backgrounds will lie under the signal events from adjacent bunches and separation or subtraction based on timing will not be possible. Studies are under way to determine the nature of the background and possibly find a rejection method. Second, materials analysis of the carbon ribbon targets indicates that the higher proton beam currents and bunch crossing frequencies at the EIC will induce heating to temperatures causing the targets to break after only a few seconds in the beam. A search for alternative target materials has been initiated.

A possible alternative to the pC polarimeter has been proposed. It is based on the observation by the PHENIX collaboration of a large azimuthal asymmetry of forward neutrons in the proton direction in  $p+Au$  collisions [1377]. This effect is well described by a process of the high Z Au nucleus emitting a photon, which produces neutrons off of the polarized proton [1378]. A polarimeter based on this process would replace the Au beam with a high Z fixed target as a source of photons; a Xe gas jet may be a suitable target. Such a polarimeter could be tested at RHIC in the final years of operation.

For light ion polarimetry at the EIC, the following methods can be considered:

- Using a polarized light ion jet target. Similarly to the proton beam measurement with hydrogen jet target, the light ion beam polarization is given by Eq. (11.16). Tagging of breakup of beam nuclei may be necessary to isolate the elastic scattering signal required for an absolute polarization measurement. However, a preliminary evaluation, based on deuterium beam scattering at HJET, indicates that the breakup contamination of the elastic data is small, only few percent, and, thus, the correction to Eq. (11.16) is expected to be negligible.
- Using polarized hydrogen jet target to measure light ion, e.g. He-3 (h), beam polariza-

tion. Since the beam and target particles are not identical, Eq. (11.16) should be corrected

$$P_{\text{beam}} = \frac{\epsilon_{\text{beam}}}{\epsilon_{\text{target}}} P_{\text{target}} \times \frac{\kappa_p - 2\text{Im} r_5^p - 2\text{Re} r_5^p T_R/T_c}{\kappa_h - 2\text{Im} r_5^h - 2\text{Re} r_5^h T_R/T_c} \quad (11.17)$$

where,  $\kappa_p = \mu_p - 1 = 1.793$  and  $\kappa_h = \mu_h/2 - 1/3 = -1.398$  are parameters derived from magnetic moments of proton and He-3,  $r_5^p$  and  $r_5^h$  are hadronic spin flip amplitudes [1379] for  $hp^\uparrow$  and  $h^\uparrow p$  scattering, respectively,  $T_R$  is the recoil proton kinetic energy and  $T_c = 4\pi\alpha Z_h/m_p\sigma_{\text{tot}}^{hp} \approx 0.7 \text{ MeV}$ . Since  $|r_5| = \mathcal{O}(1\%)$  are small, such measured absolute He-3 beam polarization will meet the EIC requirement if  $r_5^p$  and  $r_5^h$  can be related, with theoretical uncertainties better than 30–50%, to the proton-proton  $r_5$  experimentally determined at HJET [1380].

– Using low energy technique, e.g. [1381], determine absolute light ion polarization in source and, then, monitor beam polarization decay and profile with beam acceleration control tools. This method is expected to work well if the beam polarization losses will be small at EIC. However, for a precision calibration, alternative measurements of the absolute polarization may be needed.

The pC polarimeter or an alternative developed for protons at the EIC should also provide suitable relative polarimetry for light ions.

The main polarimeters may be situated anywhere in the EIC hadron ring. The Hjet and pC polarimeters each require 1-2 m space along and transverse to the beam. However, one relative polarimeter (pC or alternative) should be placed near the experimental interaction point between the hadron spin rotators. The hadron polarimeters are only sensitive to transverse spin polarization. During longitudinal spin runs asymmetry measurements near the interaction point are required to verify that the transverse component of the spin direction is zero.

## 11.9 Readout Electronics and Data Acquisition

### 11.9.1 Introduction

The Readout Electronics and Data Acquisition system is a key component for the future EIC detectors. The readout electronics is responsible of processing the electric signals from the various detector sensors and converting them into a numerical representation that can be handled by a digital system. The DAQ system, in an other hand, is responsible of collecting, filtering, and storing these data. The overall system must be designed keeping into account the constraints dictated both by the physics program and by the operation environment.

For these reasons, the architecture of the readout system has a very strong impact on the physics program that can be performed at the future EIC experiments. The front-end electronics have to be adapted to the characteristics of the sensors to be equipped, and to the measurements which have to be done with them. And in the same time the DAQ system

must offer performance adapted to the data flow coming from these front-end electronics. Filtering features of the DAQ system could be required, in order to maintain the data flow at acceptable level, taken into account the limitation in term of bandwidth of this system. But such a feature would affect directly the EIC physics outcome, since any data discarded at the online level will be lost irretrievably - a careful design, construction, and validation of this system is thus necessary.

This section aims to review the possible solutions on which the readout and DAQ system for the EIC experiments could be built. Hypothesis in term of detector characteristics and data flux are considered, leading to a reflection on the possible architecture on which the DAQ system could be based. Efforts made to validate the proposed architectures are also described. At last a description of the state of the art of the detector front-end electronics is proposed, with a few hypothesis on what could be the possible evolution in this domain.

### 11.9.2 Glossary

Several terms used in the DAQ and readout electronics domains could be ambiguous or meant differently from one reader to the other. In order to lift up the ambiguities several of these terms are defined below. These definitions are the reference for the whole section.

#### Readout electronics terms

**Front-end electronics (FEE):** The electronics which amplify and put in shape the signals of the detector. After this stage the analog signals are generally digitized using analog-to-digital (ADC), charge-to-digital (QDC), or time-to-digital (TDC) converters<sup>3</sup>. FEE is typically associated to data treatment, data bufferization and logic for data transfer to the downstream element in the read-out and DAQ chain. Digitization and data treatment stages are often directly integrated in some of the existing front-end chips.

**Amplification stage:** groups the preamplifier + amplifier/shaper of the detector raw analog signals

**Embedded amplification stage:** preamplifier + amplifier/shaper directly integrated into the detector hardware

**Digitization stage / Digitizer:** transforms amplified signal into digital values (amplitudes, charges and/or times)

**Bufferization / data concentration stage:** setup which concentrates and stores temporarily digital values from several digitizers before to send them to the DAQ, could do data selection and/or reconstruction

**Peaking time:** time between the beginning of the pulse and its maximum after the amplification/shaping stage

---

<sup>3</sup>TDC: digitizer which measures times of amplified signals going above a given threshold.

**Occupation time:** time between the beginning and the end of the pulse after the amplification/shaping stage

**Analog memory:** temporary storage of samples of analog signals, generally made of capacitor arrays, before digitization. Allow to select the samples which will be digitized

**Amplifier chip:** ASIC which groups the preamplifier and the amplifier/shaper

**Digitizing amplifier chip:** ASIC which groups the amplification and the digitization stages

### Data acquisition system terms

**Triggered readout:** A data acquisition system in which some data from a subset of detectors ("trigger data") is sent to a dedicated subsystem to produce a trigger decision. This is usually a hardware system, generally based on programmable devices such as FPGAs. The trigger decision is based on a partial elaboration of the "trigger data". "Trigger primitives" are reconstructed and analyzed to assess whenever all the data from the detector has to be stored for later analysis. In this case, a proper signal is sent back to all the readout elements to control the conversion of detector signals into the digital domain, or to trigger the read-out of a data-window from a continuously filled buffer. A key aspect of a triggered readout system is the fixed latency between the physical event time (FE → Trigger system) and the trigger time (Trigger system → FE) - in case of systems with multiple trigger levels, this is true for the first-level trigger.

**Pipelined/buffered readout:** A triggered readout system where event data is stored on the front ends and read out asynchronously by the backend when the trigger signal is received.

**Second-level / high-level filtering:** In triggered systems, higher-level triggers are often used to reduce deadtime (via a fast clear) or data amount (by dropping the so-far recorded data for that event). Each level in such a system typically has different time constraints and complexity limits. For example: a certain time frame could not be forwarded to the tracker if certain conditions are not met. In certain, complex, triggered setups, the later stages can resemble a streaming system, where a stream of events flows through a network of analysis nodes, and data selection criteria either accept or drop the event. The main remaining difference for this part is then that the data is organized and tagged by an event number instead of time stamps.

**Streaming readout (SRO):** A data acquisition system characterized by a unidirectional data flow from front-end electronics to the storage system. Each channel, independently, records data over a certain threshold and streams them to a CPU farm for further elaboration. In a streaming readout system there are no dedicated systems to

control the conversion into the digital domain or readout of a buffer. Different implementations of streaming readout are possible, depending on the manipulations and filtering applied online to the data.

**Unfiltered readout:** A streaming data acquisition system without any system dedicated to event filtering / building. Only minimal zero suppression at the front-end level is adopted. Data is streamed directly from the front-end electronics to the storage system. Each detector hit is saved together with its time-stamp.

**Zero suppression:** Removal of data if close to the no-signal level of the detector. For example, in ADC data, removal of the signal digital values below a given threshold.

**Noise suppression:** Removal of data produced by intrinsic or extrinsic detector noise, for example by correlation with neighboring channels or shape analysis.

**Feature extraction:** Calculation of higher-level information. E.g. calculation of hit time and energy from ADC<sup>4</sup> samples, or calculation of track information from hits. Often, but not necessarily, accompanied with the removal of the underlying lower-level data.

**Online Physics analysis:** Analysis of the high-level information provided by the feature extraction steps to produce physics-relevant information (e.g. missing mass).

**Data selection:** In a SRO system, data can be algorithmically selected for further processing and long-term storage. Not selected data is dropped and not further processed. This is equivalent to the function of first and higher-level triggers in triggered systems but can make use of all detector information and results from further analysis steps including feature extraction and online physics analysis.

### 11.9.3 Overview on DAQ Structure

Most of the past and currently running particle-physics experiments adopt a DAQ system based on a triggered setup, usually with a multi-layer architecture. Usually the first data reduction is achieved by using dedicated boards where a significant filtering is applied by selection algorithms implemented on FPGAs, while the subsequent trigger layers are based on software components: a CPU farm reduces the data stream to a manageable size for storing and off-line processing and applies a second, more sophisticated, level of filtering. The main limitations of a FPGA-based trigger, where FPGAs are actively involved in the events-selection, reside in: the difficulty of implementing algorithms over a certain degree of complexity and sophistication; the difficulty of optimizing the selection criteria that requires reprogramming the boards each time a change is implemented; the partial information accessible at front-end level both in the term of quality (usually it incorporates only basic calibration) and quantity (trigger is usually performed using a limited subset of the full detector).

---

<sup>4</sup>ADC: digitizer which measures the amplitude of one or several samples of the amplified signals.

These limitations may directly affect the ultimate detector performances and the quality of recorded data since only partial information is available at trigger level, when the decision whether to write or not an event to tape has to be taken. Another drawback of this approach consists in the difficulty of changing the FPGA-board in case of unexpected experimental configuration changes or upgrades requiring more trigger resources.

At the same time, complicated hardware or firmware implementations of trigger logic are hard to characterize, for example via software simulations aimed to find their efficiencies and their intrinsic dead times. This can lead to significant challenges in controlling systematic uncertainties.

All these issues are largely solved when moving to a full (CPU) software-based system. The FPGA-based system may be replaced by a fully triggerless approach that removes the hardware trigger, performs the full on-line data reconstruction and provides precise selections of (complicated) final states for further high level physics analysis (a similar effort is currently faced at LHC in preparation for the high luminosity upgrade).

In a triggerless data acquisition scheme, each channel over a threshold implemented on the front-end electronics is transferred after being labeled with a time-stamp, disregarding the status of the other channels. A powerful station of CPUs (usually an on-line farm), connected by a fast network link (usually optical fibers) to the front-end electronic, receives all data from the detector, reorganizes the information ordering hits by time, includes calibration constants, and, at the end, applies algorithms to find specific correlations between reconstructed hits (online event reconstruction), eventually keeping and storing only filtered events. Advantages of this scheme rely in: making use of fully reconstructed (and corrected) hits to define a high-level events selection condition; online algorithms implementation in a high-level programming language; easy reprogramming to upgrade the system configuration and accommodate new requirement. Furthermore, the system can be scaled to match different experimental conditions (unexpected or foreseen in a planned upgrade) by simply adding more computing (CPUs) and/or data transfer (network switches) resources. We underline that FPGAs are still used in a streaming-readout DAQ system, not to take decisions concerning events to select, but to make more “low-level” tasks such as adding the time-stamp to the data or canalize the data.

A triggerless option may result in: on-line implementation of calibration parameters, providing a more precise reconstruction of the kinematic quantities; implementation of more sophisticated reconstruction algorithms for a better reconstruction of close-by tracks; improvement in EM/hadron discrimination for a more efficient background rejection.

These considerations directly apply to the EIC. The EIC physics program will be carried out by measuring different reactions with at least one electron in the final state. Electromagnetic calorimeters will thus play a key role in the online events selection and filtering. For these sub-detectors, a triggerless option may result in: on-line implementation of calibration constants to compensate for longitudinal and transverse EM shower leakage and gain variation, providing a more precise reconstruction of the energy deposition (and therefore an improvement in the ultimate energy resolution); implementation of more sophisticated clustering algorithms for a better reconstruction of close-by tracks allowing

to resolve gammas from  $\pi^0$  in a wider kinematics; improvement in EM/hadron shower discrimination for a more efficient pion rejection.

A triggerless scheme will facilitate future extensions of the envisaged EIC physics program. For instance, hadron spectroscopy requires to identify rare exclusive final states difficult to access experimentally (e.g. kaon-rich reactions). This would require to set and add multiple and sophisticated algorithms to select the physics of interest. Same rationale is valid for other physics program that will be considered in the future.

The triggerless scheme is also an opportunity to extend the integrated IR-detector design to analysis to optimize physics reach as described above and to streamline workflows. A seamless data processing from DAQ to analysis would allow for a combined software effort for the triggerless scheme, online and offline analysis and to utilize emerging software technologies, e.g. AI / ML, at all levels of the data processing. A near real-time analysis at the EIC with auto-alignment and auto-calibration of the detectors and automated data-quality monitoring would enable significantly faster access to physics results and accelerate science.

**For these reasons, we propose to design and develop a full streaming-readout DAQ system for the EIC detector, integrating all the sub-detector components.**

#### 11.9.4 Constraints and Environment

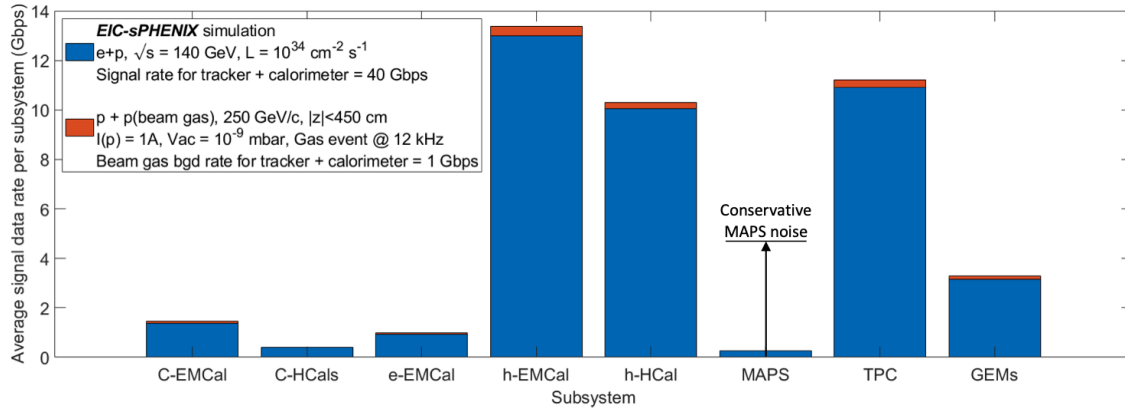


**Figure 11.123:** Collision data rate from each detector subsystem for the EIC sPHENIX detector model, at luminosity  $\mathcal{L} = 10^{34}$  cm<sup>-2</sup>s<sup>-1</sup> [1382, 1383]. The total collision signal is approximately 100 Gbps, including a conservative estimate of the MAPS noise motivated by the recent ALICE ITS2 experience. We note this rate include collision signal only to record down all EIC physics events. In case excessive background rate, e.g. synchrotron photon hits, are observed, further noise and background filtering would be required.

The EIC readout and DAQ system should be designed considering the following constraints, dictated both by the physics program (measurements to be performed) and by the experimental environment. The overall goal for the system, as an integrated compo-

Detector	Sub-system	Type	Sub-type	Channels
<b>Tracking</b>				
	Silicon Vertex Tracker	Si	Pixel	200M
	TPC	GEM	Pads	160K
	GEM	GEM	Strips	217K
	uRWELL	GEM	Strips/Pads	
	Cylindrical Micromegas	GEM	Strips	
	Drift Chambers	DWC	Wires	
	sTGC	GEM	Pad, Strip, Wire	
	Straw Tubes	Straw	Wires	
<b>Calorimetry</b>				
	e-EMCal	Cal	PMT/SiPM	5k
	C-EMCal	Cal	PMT/SiPM	24k
	h-EMCal	Cal	PMT/SiPM	26k
	h-Hcal	Cal	PMT/SiPM	3k
	c-Hcals	Cal	PMT/SiPM	2.8k

Detector	Sub-system	Type	Sub-type	Channels
<b>PID</b>				
	mRICH @ e-endcap	RICH	PMT/SiPM	
	dRICH @ h-endcap	RICH	PMT/SiPM	300k
	GEM RICH	GEM	Strips	220k
	hpDIRC @barrel	DIRC	PMT/SiPM	100k
	psTOF @barrel	TOF	PMT/SiPM	
	LGAD TOF	TOF	PMT/SiPM	
	LAPPD/MCP-PMT TOF	TOF	PMT/SiPM	
<b>Far Forward Detectors</b>				
	ZDC		PMT/SiPM	
	Low Q2 tagger		PMT/SiPM	
	Luminositymonitors		PMT/SiPM	
	Roman Pots	Si Strips	Si	
	Proton Spectrometer		PMT/SiPM	
	Lepton Polarimeter		PMT/SiPM	
	Hadron Polarimeter		PMT/SiPM	

Readout Variant	Channels (actual)	Channels w/+10% Spares	Type
V1	200M	220M	Si
V2	220k+	242k+	Straw/GEM - fADC
V3	377k+	415k+	GEM
V4	461k+	507k+	PMT/SiPM

Figure 11.124: Estimate of the number of different EIC Readout Channels.

ment of the EIC detector, is to make it possible to complete the challenging EIC Science program, providing a seamless integration from the DAQ to the physics analysis.

The EIC detector will be made by many sub-components, based on different technologies and with different requirements concerning the values to be measured by them. This translates into specific constraints on each readout solution, in terms of needs and performances. In general, each sub-detectors will introduce its own requirements on the FEE parameters (shaping time, peaking time, gain, ...). For example, it is anticipated that one of the most realistic options to read out EIC calorimeters will be SiPM (or matrix of SiPM's) photosensors. It is expected that to realize the electronics readout chain a novel FE ASIC chip will be developed: the ADC board would provide the bias voltage to the SiPM and allow for signal amplification, processing and readout, including possibly the recording of the raw waveform. Similarly, each sub-detector will be characterized by different radiation levels, affecting the choice of the readout technology.

The number of channels anticipated for the EIC detector readout is shown in Fig. 11.124; a relatively small number of channels are not included. It is anticipated that three, and possibly four, different readout solutions will address the front-end readout needs of the various types of detectors.

The main constraint on the DAQ system is the total data rate to be processed, including both the signal (i.e. physics reaction of interest for the EIC physics program) and the background. A preliminary estimate of the total collision signal rate from the EIC detector was discussed in [?], assuming  $e + p$  collisions at  $\mathcal{L} = 10^{34} \text{ cm}^{-2}\text{s}^{-1}$  and the sPHENIX-based

detector concept [1382, 1383]. The calculation includes, for each component of this specific EIC detector model, the signal data rate from  $e + p$  collisions and also from  $p - p$  (beam-gas) interaction, and also considers a conservative estimate of the MAPS noise motivated by the recent ALICE ITS2 experience. The result is summarized in Fig. 11.123: a total collision signal rate from the EIC detector of approximately 100 Gb/s is expected.

Further constraints are introduced by the requirement of having, during EIC operations, an immediate online feedback concerning detector performance and data quality. Finally, the engineering requirements related to the concrete EIC detector construction and assembly will introduce further constraints on the readout and DAQ system: available space, rating and standards to be satisfied, cooling power availability.

### 11.9.5 Readout Electronics: Present State of the Art

#### Introduction

The role of the readout electronics for an experiment like EIC is crucial. The quality of the data delivered by the data acquisition system will be directly dependent of the performance of each element of the readout chain. The characteristics of these elements should be in accordance with the characteristics of the detectors which will be read by the electronics, as well as with the constraints which are described in the previous section.

The readout chain for a given detector is formed by electronics cards and chips with different functions: signal pre-amplification, amplification and shaping, digitization, data treatment like common mode noise reduction or zero suppression, data bufferization concentration, and transfer to the DAQ system. Side systems like readout trigger system can be also necessary to reduce the flux of data to be treated by the chain. At last several support systems are necessary in order for the readout electronics to work: clock signal distribution to synchronize all the electronics, slow-control to monitor the electronics behavior, power distribution, etc...

In this section a summary of the state of the art for the different elements of the electronics chain are given, with a few examples. Some of the chips described here regroup several functionalities listed above, for instance amplification and digitization.

#### Front-end electronics

The front-end electronics is there to amplify the signals from the detectors and to put them in a shape compatible with the digitization step. The amplification step is important in particular for detectors which deliver very low amplitude signals, like silicon detectors or gaseous detectors. Other detectors like photomultipliers used in some calorimeters deliver larger signals, so the electronics gain should be lower in order to avoid any saturation. Another important parameter is the shaping applied to the signal, which can be characterized by the "peaking time", which is the time taken by the shaped signal to reach its maximum. A short shaping, for instance a few ns of peaking time, allows to get sharp output signals

well adapted for fast detectors and fitted to time measurements, but may also induce a non-optimal noise figure. In an other hand slower shapes, in the order of a hundred of ns, are more adapted to slow detectors, for instance gaseous detectors, in order to integrate the totality of their signal and thus to get a more accurate amplitude measurement. A larger peaking time also induce a larger occupancy of the signal in the readout chain, which may limit the signal rate which can be read by the electronics.

In the current designs proposed for the future EIC experiments which are described in the sections **XXX** of this document, both silicon and gaseous detectors are considered to measure the trajectory of the secondary particles. However the silicon detectors presently considered, the Monolithic Active Pixel Sensors (MAPS) **to be verified with tracking WG, references**, integrate directly in the silicon die their own front-end electronics, signal processing and zero-suppression with adjustable threshold. These detectors return addresses of the hit pixels, with typically around 3 pixels per charged particle track. The thresholds are adjusted to give 99% efficiency and less than  $10^{-9}$  fake hit rate.

Several existing chips are dedicated to the readout of small signals coming from gaseous detectors. A few examples of chips used in particle physics experiments are presented below. They are all based on pre-amplifier and amplifier/shaper stages. However the treatment of the signals after these stages vary from one chip to the other, depending on the purpose of these chips. Some of them are more focused on the measurement of the signal time, combining then a fast shaping with a TDC stage, while others are measuring the amplitudes with flash ADCs. 32 to 64 channels are usually read by these chips which are 5 to 15 mm large. Peaking times are usually tunable, with values from 25 ns to 1  $\mu$ s. Maximum charges accepted by these chips, also usually tunable, cover a range from 50 fC to a few pC. The internal capacitance of the detector channels also play a role in the behavior of the pre-amplification stage. Depending on the design of this stage, a large capacitance, larger than 100 pF for instance, may alter the gain of the preamplifier and thus, of the whole chip. Some pre-amplification designs prevent this effect, allowing the chip to work with large detector capacitance at the level of several hundreds of pF. At last to keep the power consumption as low as possible is an important aspect for highly integrated detectors like the one foreseen for EIC, in order to limit the need of cooling. Power consumption values are typically around 10 to 30 mW/channel.

### **Digitization and data treatment**

After amplification and shaping, detector signals are meant to be digitized before to be transmitted to the data acquisition system. Depending on the DAQ structure, signals may be continuously digitized, or the digitization can be triggered only when an interesting event happens. From one kind of chip to the other the digitization strategy can be different. Some chips, like the SAMPA chip (cf section **XXX**) are indeed able to continuously digitize the signal at a rate of several MHz and to transmit these data to the DAQ. But depending on the kind of detector to be read and the information to be extracted this may or may not an optimal strategy. That strategy is the most demanding in term of ADC performance and output data link bandwidth. Present ADC integrated in readout chips are able to read

continuously signals with a sampling rate around 10 to 20 MHz, with a ADC dynamics of 10 bits. Data links of a few Gbit/s are also a common performance of the readout chips. Data treatment may be necessary to reduce the data flux to a scale compatible with the DAQ capacity. Several kinds of algorithms can be applied: common mode reduction which compensate the part of the electronic noise which is common to all channels of a chip, zero suppression which discards the sample measurements below a given thresholds, peak finding, correlation with other detectors which conditions the preservation of the data with data from an other detector, etc... Such data treatments can be performed directly in the chip, for instance in an integrated DSP, or later by specific DSP electronics in the acquisition chain.

Another strategy which may be more adapted to detectors which do not require to store the full signal waveform, for instance trackers, would be to digitize only specific values like signal amplitude, using a sample & hold (S&H) circuit like in the VMM chip, or signal time. This strategy produces a much lower data flux. A last strategy is to not include any digitization of the signals in the readout chip, but rather to store them in analog memories which are arrays of capacitances, and to transmit in case of triggers the analog signals to commercial ADCs managed by a FPGA. This strategy is adopted by several chips like the AGET, the DREAM or the AFTER. However this strategy is largely incompatible with the streaming readout structure foreseen for the DAQ.

### Examples of readout chips

Several chips representing the state of the art of the readout electronics are presented here. They concern mostly gaseous detectors and silicon detector front-end readout but their usage may be extended to other cases. The table 11.31 summarizes the characteristics of these chips.

**ATLAS VMM and the CERN SRS Architecture:** Building upon the highly successful APV25 architecture developed for the CMS experiment, VMM was built for the ATLAS experiment upgrades, as part of CERN's implementation of the Scalable Readout System (SRS) for micropattern gaseous detectors developed by the RD51 Collaboration. Introduced in 2010 for ATLAS Micromegas and based on the APV25 chips, the SRS extended a modular architecture to integrate disparate ASIC chips to read-out electronics to select the most suitable front-end for the detector technology employed for a particular experiment. In short, SRS offered a modular and scalable architecture to act as a detector-dependent bridge between front-end and read-out sections of any HEP data acquisition architecture, where users could choose from a variety of front-end chips, readout by a central hub called a Scalable Readout Unit (SRU). The architecture is a bit complex, with ASIC-specific firmware modules residing in the FPGA chips on cards, however a large number of channels (maximum limit of up to 16000 channels) and up to 64 Front-end FPGA cards can be supported by the architecture.

The VMM chip was developed at Brookhaven (BNL) as a 64-channel mixed signal

ASIC for readout from both the ATLAS Micromegas and sTGC detectors, specifically for the ATLAS Muon Spectrometer's New Small Wheel upgrade. Its first version, viz VMM1, was a bit primitive simple architecture chip, but a lot of functionality and features were added in the second version, known as VMM2. Another version, VMM3, and its revision VMM3a were also produced. The new versions were claimed to contain enhanced features such as deep readout buffer logic, longer TAC (Time-to-Amplitude Converted) ramps, SEU mitigation circuitry as well as handling of higher input capacitance of the order of 1.5 nF. The device (version 3) was fabricated at IBM's foundry with a 130nm MOSFET technology (die size 15.3 x 8.3mm), housing approximately 5.2 million transistors (with nearly 160 k MOSFETs per channel), and produced in a 1mm pitch 400-BGA (Ball Grid Array) package. It is indeed a state-of-the-art mixed signal ASIC device which was perhaps created to achieve the System on Chip (SoC) paradigm.

An excellent feature of the chip are having both time and amplitude (peak) detection circuitry on-board. For each of the 64 channels, a signal obtained from the input pads is amplified by a charge amplifier (CA) and after a shaping circuit (Shaper) is passed over to both a peak detector and time detector working in tandem and giving their respective output to a digitization section. The digitization section is comprised of a novel three-ADC chain in a so-called "Domino Architecture". Output from the peak detector is given to both a 6-bit ADC for feed-thru synchronization/threshold and to a 10-bit ADC for precision read-out, whereas the time detector has its output passed over to an 8-bit ADC for TDC functionality. Outputs from both ADCs are read-out through a FIFO buffer, which is designed to accommodate 4 MHz data in 10 $\mu$ s latency windows. In addition, a 12-bit Gray code time-stamp is provided to facilitate time measurements, which incremented by an external clock provides a cumulative 20-bit timing information. The chip tests claim peak detection digitization process to complete in 25 ns. The chip also features a novel third-order filter and shaper architecture with a DDF (Delayed Dissipative Feedback) topology. This architecture results into a higher dynamic range, enabling the measurement to achieve a relatively high resolution at very low input capacitance ( $\ll$ 200 pF). The architecture offers a variable gain in eight values (from 0.5, 1, 3, 4.5, 6, 9, 12, to 16 mV/fC) with four possible shaping time intervals, viz. 25, 50, 100, and 200 ns.

Two VMM chips are soldered on a FEC card in association with a Virtex-6 FPGA for a so far maximum streaming read-out rate of 1G-bit/s. However, theoretically, an ideal 9.7 Gbit/s should be achieved in principle by the ASIC, independent of FPGA and other logic. In short, the VMM chip's latest versions seem to achieve the promised sub-fC and sub-ns resolutions at 200 pF and 25 ns capacitance and time windows, respectively.

**TIGER:** TIGER is an acronym for the Torino Integrated GEM Electronics for Readout, a mixed signal ASIC chip first developed at INFN Torino. It is a general-purpose chip for readout from gaseous detectors with up to 64 channels, fabricated with a 110nm CMOS technology (fabricated on a die area of 5 $\times$ 5 mm<sup>2</sup>). While featuring a low-noise level of less than 2000  $e^-$ , the chip offers a high input dynamic range of 2.0 to 50.0fC and gains of 12.4 mV/fC for time and 11.9 mV/fC for energy measure-

ments, with time intervals of 60ns and 170ns, respectively. There is a provision of an on-chip calibration circuit which allows injected external pulses to calibrate the amplifiers and exploit the full input dynamic range. The signal conditioning circuitry in the time and energy measurement sections comprise both discriminator and pulse shaper in addition to a Time to Amplitude Converter which works in association with the ADC. A "Channel Controller", running at a clock speed of 200MHZ, supervises the operation and synchronization of the charge integration, quantization, and time to amplitude conversion sections. The data is readout from the chip using Low-Voltage Differential Signaling (LVDS) standard links. TIGER is a fine chip, with a simple yet elegant state-of-the-art architecture. Its major advantages include high input dynamic range, two high-resolution (10-bit) Wilkinson ADC's with very low non-linearity at each channel for both time and energy, and fast and a high-speed trigger-less readout, among other features, all offered with a reasonably low-power operation (less than 12 mW per channel while powered with 1.2 V). The limitations or drawbacks include a bit higher ENC noise, limited value of input capacitance range, no digital processing functions, and possible internal analog signal conditioning structure supporting negative polarity signals only.

**SAMPA:** The SAMPA chip has been designed as a 32-channel device with on-board pre-amplification (CSA with AGC), pulse shaping, quantization (digitizing) and DSP sections, including a high-bandwidth digital interface for computer readout. With the help of its eleven e-links with individual data transfer speed of 320 MB/s, it offers a sufficiently fast bandwidth ( 3.4 Gbit/s) to readout all 32 channels, at a sampling rate of 10 MSPS.

The chip is fabricated with 130 nm CMOS technology with a chip area of  $9.6 \times 9.0 \text{ mm}^2$  and offered in a 372 Ball Grid Array (BGA) package. A charge-sensitive amplifier amplifies the measured analog signals, followed by a near-Gaussian pulse shaper, a novel element of the design. The 10-bit Successive Approximation ADC digitizes the amplified and shaped signals at a sampling rate of 10 MS/s (which can be configured to up to 20 MS/s), whereas the on-board DSP circuitry filters and carries out signal processing and compression operations on the digitized data. The chip offers a sufficiently high gain of 20-30 mV/fC with a low-noise performance (less than  $1000 e^-$ ).

SAMPA is a relatively modern chip suitable for high-performance applications. Its superior signal conditioning, digitization and on-board digital signal processing capabilities, as well as fast readout rates, are ideal for applications requiring a high-bandwidth, precision and versatile mixed signal data acquisition architecture.

**AFTER (ASIC For TPC Electronic Readout):** The AFTER chip is manufactured with AMS CMOS  $0.35 \mu\text{m}$  technology. The die area is of  $7.8 \times 7.4 \text{ mm}^2$  (involving 500,000 transistors). The final chip is produced in a 160-pin LQFP package: ( $28 \times 28 \times 1.4 \text{ mm}$ ). It offers 72 channels which can be preset for a negative/positive polarity by resistor arrays, with a counting rate of up to 0.3 Hz/channel. The chip has a power consumption of less than 10 mW/channel while powered at 3.3 V. This chip has a dynamic range of 120 fC-600 fC with an integral non-linearity of less than 2% of LSB.

However, it does not have an on-board ADC and requires an external ADC (with 20-25 MHz sampling rate). The specified peaking time range, as per the chip's technical sheet, is 100 ns to 2  $\mu$ s (in 16 denominations). The sampling frequency range spans from 1 MHz to 50 MHz. Input signals sampled in circular analog memory buffers (in the form of a Switched Capacitor Array, SCA, with a depth of 511 time buckets). However, since the chip does not have an on-board ADC it needs an external one to digitize the SCA matrix signals. The SCA can be frozen by an external trigger. The minimum dead-time for the SCA is fixed at  $79 \times 40 \text{ ns} \times \text{Number\_Of\_Time\_Buckets}$  (out of 511).

As AFTER chips do not include digitization stage, they should be associated to external ADC ASIC. A suitable commercial or custom low-latency 12-bit ADC ASIC can be employed to work with the chip. An hybrid ASIC chip built by Pacific Microchip Corp. PMCC ADC [?] is generally employed, as it presents interesting features like 12-bit digitization for up to 32 channels, a 8 ns latency, a 8 Gigabit/s transfer glue-logic on-chip. The company claims to have a fabrication facility down to 7 ns with both CMOS and BiCMOS processes, and have worked with DOE in recent past.

**AGET (ASIC for General Electronics for TPC, GET system):** The AGET chip is the very front-end of the GET system that performs the first concentration of the data from 64 input channels to one analog output connected to an external ADC. Each channel integrates a charge-sensitive pre-amplifier (CSA) with selectable signal polarity, a configurable shaper, a discriminator for multiplicity building and a 512-cell switch capacitor array (SCA). The gain and peaking times are tunable by slow control from 120 fC to 10 pC (4 values) and from 70 ns to 1  $\mu$ s (16 values) respectively. The filtered signal is sent to an analog memory and discriminator inputs. The SCA for the analog memory is a 512-cell deep circular buffer in which the analog signal from the shaper is continuously sampled and stored. The sampling frequency is adjustable from 1 MHz to 100 MHz depending on the particular requirements of each detector. To process two consecutive events within a time window of 2 ms, such as the implantation of a radioactive ion followed by its decay, the SCA memory can be split into two halves using an adjustable parameter in slow control. The first signal that arrives is sampled and stored in the first half of the SCA memory. This is followed by a switch to the second half of the memory to sample and store the second signal. The system waits for this second signal to arrive for up to 2 ms. The switching from one half of the memory to the other corresponds to 2 sampling times. Sampling is stopped by a trigger decision. In the readout phase, the analog data from the different channels is multiplexed towards a single output and sent to the external 12-bit ADC at a readout frequency of 25 MHz. It is possible to read only a user-defined fraction of the 512 analog cells (1 to 512) beginning from an index defined with a constant offset from the cell corresponding to the trigger arrival. In addition to the 64 input signal channels, the AGET chip has 4 channels that are called fixed-pattern noise (FPN) channels. The inputs of these channels are not connected to the detector but they are treated by the SCA in exactly the same way. The chip is fabricated with 0.35  $\mu$ m AMS CMOS technology and is 8.5 x 7.6 mm<sup>2</sup> large. It is housed in a LQFP 160-pin package.

The placement scheme for the AGET ASIC is that an "AsAd (ASIC Support & Analog-Digital conversion)" card is formed with four AGET's soldered on it supported by four 4-channel 12-bit ADC's, one for each AGET. With the help of a glue-logic the digital outputs from ADCs are finally transmitted via 8 differential lines to a "CoBo (Concentration Board)" board, with a maximum speed of 1.2 Gbit/s. This board is responsible for functions such as applying time stamp, zero suppression and compression algorithms to the data. In addition, it serves as a communication intermediary between the AsAd boards and the outside world. The slow control signals and commands to the AsAds are transmitted via the CoBo (four AsAD per CoBo). MuTanT (Multiplicity Trigger And Time) card issues a three level trigger via the external trigger, multiplicity and the event pattern. It manages also the clock distribution over the whole system.

**SAMPIC:** The SAMPIC chip is a 16-channels low depth high-speed digitizer. Each of its 16 channels associates a DLL-based TDC providing a raw time with an ultra-fast analog memory (5 GHz sampling frequency) allowing fine timing extraction as well as other parameters of the pulse. Each channel also integrates a discriminator that can trigger itself independently or participate to a more complex trigger. After triggering, each sample is digitized by an on-chip ADC and only that corresponding to a region of interest is sent serially to the DAQ. The association of the raw and fine timings permits achieving timing resolutions of a few ps rms.

**ALCOR (A Low power Chip for Optical sensor Readout):** The ALCOR chip prototype is a first test vehicle for a high-rate digitization back-end for SiPM readout in fast timing applications. It is a 32-channel ASIC that features signal amplification, conditioning and digitization. It features low-power TDCs that provide single-photon tagging with time binning down to 50 ps and able to work down to cryogenic temperatures. The design of a system-grade ASIC targeting dRICH detector specifications is now being pursued at INFN. The ALCOR chip is based on a triggerless time-based (time-of-arrival and time-over-threshold) readout and features a SEU-protected logic. A dedicated design of the front-end shall allow for integrated cooling and customized decoupling circuits (high pass filter) for possible signal pre-conditioning and count rates well exceeding 500 kHz per channel. The chip architecture and matrix floor-plan will allow for a future version to be assembled chip-on-board with bump-bonding (the first prototype uses wire-bonding padframes), which will be an enabling factor for the design of very compact and robust front-end electronic board.

## Support system

### 11.9.6 Possible Readout Chip Evolution and Future Technological Constraints

It seems that a mixed-signal multi-channel (greater than  $n=64$ ) high-performance ASIC chip architecture is entailed with at least a 10-bit/12-bit resolution SAR ADC (offering a minimum sampling rate of 25MHz, very low non-linearity, INL  $<2.0\%$ , and a low latency,

	SAMPA	VMM	TIGER	DREAM	AGET	AFTER
Architecture	Front-end + ADC + DSP	Front-end + S&H + discr + 3xADC	Front-end + S&H + discr + TDC + ADC	Front-end + analog memory		
Analog characteristics						
Number of channels	32	64	64	64	64	72
Input dynamic range	66/500 fC	0.1-2.0pC	2.0-50 fC	50-600 fC	120 fC - 10 pC	120-600 fC
Peaking time range	160-300 ns	25, 50, 100 and 200 ns	60 ns (TDC), 170 ns (ADC)	50 ns - 1 $\mu$ s	50 ns - 900 ns	100 ns - 2 $\mu$ s
Full signal occupancy	550 ns					
Polarity	+/-	+/-		+/-	+/-	+/-
Detector capacitance range	18.5 pF/40-80 pF	200pF	up to 100pF	200 pF		30pF
Noise level	600/900 e <sup>-</sup>	300 e <sup>-</sup> at 9 mV/fC	up to 2000 e <sup>-</sup>	610 e <sup>-</sup> + 9 e <sup>-</sup> /pF	580 e <sup>-</sup> + 9 e <sup>-</sup> /pF	370 e <sup>-</sup> + 14.6 e <sup>-</sup> /pF
Sensitivity/Gain	4/20-30 mV/fC		12.4 mV/fC (TDC), 11.9 mV/fC (ADC)			120 fC/mV
Remarks			CR-RC shapers			
Digital characteristics						
Sampling frequencies	10-20 MHz	200 MHz	1-40 MHz	1-50 MHz	1-100 MHz	1-100 MHz
ADC resolution	10-bit	10-bit	10-bit (Wilkinson)	No ADC	No ADC	No ADC
TDC time resolution		8-bit + 12 global	5 ns			
Remarks	10 MS/s			Internal trigger	Internal trigger	
Data treatment functions	On-board DSP	none	none			
Data bandwidth	11x320 Mbit/s	1 Gbit/s (ideal 9.7 Gbit/s)	1.28 Gbit/s (triggerless)			
Streaming readout capacity	3.4G bit/s		Readout on internal trigger, programmable threshold			
Other information						
Die size	9.6x9.0 mm <sup>2</sup>	15.3x8.3 mm <sup>2</sup>	5x5 mm <sup>2</sup>			7.8 x 7.4 mm <sup>2</sup>
Package size	TFBGA 15x15 mm <sup>2</sup>	400BGA				28 x 28 mm
Power consumption	20 mW/ch	10 mW/ch	12 mW/ch @ 3.3V	10 mW/ch	10 mW/ch	10 mW/ch
Technology	130 nm CMOS	130 nm MOSFET	110 nm CMOS			350 nm AMS CMOS
Remarks						

**Table 11.31:** Characteristics of different chips presently available for gaseous detector read-out

<10.0 ns), working in tandem with a high-speed TDC (with excellent time resolution), preferably with buffer and glue-logic on-board, and a complementary FPGA with intelligent firmware designed, in the form of a total solution for readout. Additional features like an on-board DSP module (for baseline correction, zero suppression, anti-aliasing digital filtering etc.) would be added advantages. Other approaches such as companding ADC can also be explored to make a trade-off for low-resolution (6/8-bit ADC), if resources permit and substantial advantage is expected on the cost of chip component overhead.

There are certain other ASIC chips available in the HEP community, suitable for GEM and TPC applications etc., such as ALTRO and ALTRO-16 (CERN) with 12-bit ADC and digital processing etc on-board, and ALICE collaboration SDD chip. However, detailed evaluation is needed. So far, there seem to be not enough material available to evaluate them, or they seem to be in preliminary or unfinished stages. Necessary features and functionality are needed there perhaps, in addition to thorough radiation damage tests commensurate with the expected luminosity at the EIC.

Evaluation of radiation, thermal, and magnetic field effects needs to be carried out for all chips, although some of the chips discussed earlier have been through radiation damage tests and seemed to offer satisfactory performance in general, with very little damage.

So far, unfortunately, one single chip suitable for the prospective experiments at the EIC does not seem to exist. Every chip has some extremely vital feature or necessary bench-

mark missing.

The most promising places for development of future ASIC and mixed signal devices (and the supporting hardware and firmware/software) seem to be the CEA (France), INFN Torino (Italy) and Brookhaven National Laboratory (USA), etc., where excellent chips have been developed in past. However, more refinements are needed in existing chip architectures. A collaborative effort with these institutions could be a viable direction for fostering future front-end and readout technologies necessary for endeavors like the EIC.

### 11.9.7 Existing streaming readout DAQ Systems for particle physics experiments

In the following, we briefly present some existing data acquisition systems for particle physics experiments adopting, completely or in part, a streaming readout approach for data readout. Further examples not reported in this section are the ALICE experiment Online-Offline (O<sup>2</sup>) system [?] and the new Compass data acquisition system [1384].

#### LHCb streaming readout DAQ

The LHCb detector at CERN [1385] is currently ongoing a major upgrade to replace the current trigger-based DAQ system to a fully streaming DAQ system (see [1386] for a complete description). The new system will allow to acquire and select events at the full 30 MHz rate of proton-proton collisions at the interaction point<sup>5</sup>. To reach this goal, all front-end boards in the upgraded LHCb detector will be capable of acquiring signals at the full bunch-crossing frequency. The custom GBT protocol [1387] will be used to transport data via optical fibers from the front-end boards to the readout system, with up to 4.5 Gb/s bandwidth per link. Data is then processed by the upgraded LHCb event builder system, capable of aggregating, analyzing, and filtering the events - considering the full 30 MHz collision rate and with a single event size up to 150 kB, the system was scaled to handle a total data rate up to 40 Tb/s. The main components of the event builder system are the readout units and the builder units. Each readout unit is responsible of collecting data from part of the readout board, using point-to-point links, and sends this to a builder unit. For each event, one builder unit receives all the fragments from all the readout units and aggregates them into the event. Each event is then passed to the online processing farm for reconstruction and filtering. A first level filter (HLT1) performs a fast reconstruction and events selection, reducing the input rate from 30 MHz to approximately 1 MHz. A second, more sophisticated, filtering level (HLT2) performs the final event selection, resulting to an output event rate of approximately 100 kHz to be written to the disk.

---

<sup>5</sup>The nominal bunch-crossing frequency at the LHC is 40 MHz, corresponding to one interaction every 25 ns. At the LHCb interaction point, however, one every four collisions is empty, resulting to a 30 MHz physics events rate.

## sPHENIX Hybrid DAQ

Construction is ongoing for the sPHENIX triggered-streaming Hybrid DAQ, which simultaneously reads out the conventionally triggered calorimeter subsystems and the streaming tracking subsystems [?]. Both the sPHENIX front-end readout and the back-end DAQ will also serve as an exercise of a large-scale streaming system that is applicable to future EIC experiments.

The tracking front-ends consist of the on-detector streaming ASICs for the readout of the MAPS pixel tracker (ALPIDE), a silicon strip tracker (PHFX), and GEM-based TPC read out with a new version (V5) of the ALICE SAMPAs chip [1388]. The streaming data are time-stamped with beam collision clock, aggregated in the front-end FPGAs, and transported to the back-end DAQ via  $O(1000)$  multi-Gbps fiber links providing  $O(10)$  Tbps overall readout bandwidth. A global timing system provides a low jitter collision clock, fixed-latency trigger signal, and time-stamp counter to all front end electronics, which are embedded in the data stream and serves as the basis for the streaming and hybrid synchronizations.

A fleet of  $O(50)$  Front-End Link eXchange (FELIX) [1389] readout cards hosted in commodity Linux PCs is used to read out, buffer, and process these data streams. In the version used by sPHENIX, each FELIX is a PCI-express card carrying a large FPGA (Xilinx Kintex UltraScale KU115). It supports 48 bi-directional 10-Gbps optical links to the front-end and a 100-Gbps PCI-express Gen3 link with the hosting server's CPU. It is initially designed for the ATLAS Phase-I upgrade and continues to be developed to utilizing recent parts with a higher speed for future ATLAS upgrade towards the HL-LHC. The strategy of using PCIe FPGA cards to bridge the custom front-end and commodity computing is also used by the LHCb, ALICE, ATLAS, and CBM experiments. The overall peak disk data rate is designed to accommodate the RHIC Au+Au collision at the top luminosity that is orders of magnitude higher charged particle production rate when compared with the EIC.

While sPHENIX will have a trigger, the overall architecture is streaming-oriented and highly parallel. Individual substreams coming from the detector are written to different files directly, and synchronization will be performed via time stamps, not event numbers. The actual event building is moved to the offline analysis, removing the necessity to build a distributed, fault tolerant, reliable one-shot online event builder.

The FELIX system also provides the flexibility of throttling the recorded streaming data corresponding to the calorimeter triggers (i.e. global zero-suppression) or allows for triggerless recording of a fraction of or all of the tracker data. The streaming tracker data are demonstrated to enable a unique set of heavy flavor measurements that would be otherwise inaccessible, and this streaming DAQ development is recently commended by the RHIC Program Advisory Committee.

## The RCDAQ Data Acquisition System

sPHENIX uses a powerful but lightweight data acquisition system called "RCDAQ" [1390]. It is currently in use for virtually all sPHENIX R&D projects such as test

beams, tests in labs, detector calibrations, and the like. RCDAQ supports all current sPHENIX front-ends and both triggered and streaming readout modes. It also supports, by way of plugins, a large variety of commercial or otherwise available readout electronics, such as the DRS4 Evaluation Board [1391], the CERN SRS system [1392], several CAEN modules such as the V1742 Waveform Digitizer, and many more.

RCDAQ has long been the de-facto standard data acquisition system for several EIC R&D groups, such as eRD1 (calorimetry), eRD6 [1256] (tracking), eRD14 (time-of-flight), and eRD23 (streaming readout technologies). In addition, RCDAQ is used by dozens of external groups not connected to the EIC or RHIC R&D efforts because of the support for those common readout devices, its built-in support for ROOT-based online monitoring, comprehensive controls, and small footprint.

### The ERSAP system

Development is underway for the Environment for Real-time Streaming, Acquisition and Processing (ERSAP) Streaming Data Readout System at JLab. ERSAP is a backend software system that combines components to form a reactive data flow architecture. This combines software originally developed as part of the CODA data acquisition system and then advanced as part of the CLARA reactive microservices framework [?] used by the CLAS12 experiment. The system encapsulates each component into a microservice with well defined inputs and outputs that allow for local or remote communications. This allows both horizontal and vertical scaling to make the system highly configurable. It also supports micro-services written in any language (C,C++, Python, Java, ...). Utilizing such a design helps ensure a level future-proofing since individual services can be easily replaced with ones using new syntax, languages, or technology (e.g. heterogeneous hardware components). A prototype of the system was tested successfully in summer 2020 using beam at the CLAS12 Forward Tagger. Also being developed as part of ERSAP is high performance tiered memory or "Data Lake" system that allows efficient data cooling (i.e. temporary buffering). The system is scalable enough to be used on a single desktop with other DAQ components in benchtop system or in a dedicated node with a large memory+disk. The Data Lake implements automatic fail-over to disk if its allotted memory resource becomes exhausted.

### 11.9.8 A Progressive Approach toward the EIC DAQ System

The final goal of the EIC streaming readout system is to reconstruct online all events, adding to the raw-data banks the high-level information from the reconstruction - ideally, four-vectors and PID assignment for all particles in a given interaction, and store all of them to the disk. Eventually, filtering algorithms can run online to tag events according to a certain condition (for example, events belonging to a certain exclusive channel), to speed-up the offline analysis.

Based on the preliminary estimates discussed before in Sec. 11.9.4, and considering the

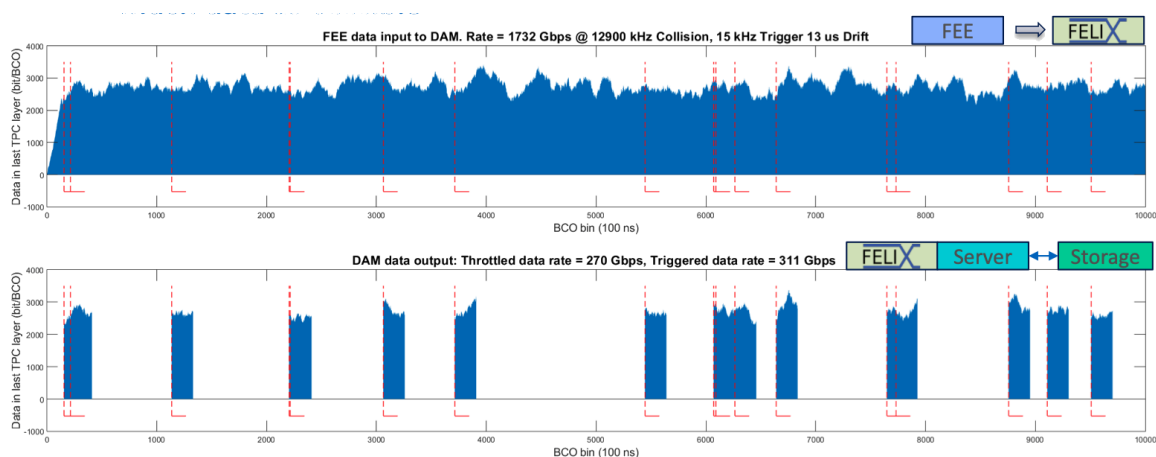


**Figure 11.125:** The sPHENIX hybrid DAQ system cross-detector zero suppression. The sPHENIX streaming tracker can use the calorimeter trigger as a data throttle for loss-less data reduction for triggered events + streaming as much data as possible [?]

technologies that are available already today, the following key arguments concerning the EIC streaming DAQ system can be assessed (see also Fig. 11.125).

- In principle, it will be possible to write all raw data directly to the disk, without further online processing. However, unexpected large noise levels could exceed the system capacity, and the system must be prepared for such an event. This is particularly true during the initial phase of EIC operations, when unexpected backgrounds not predicted by simulations and not observed in the preliminary sub-detectors characterization phase could be present, and the machine still needs to be tuned.
- High-quality calibration constants are necessary for the online events reconstruction, analysis, and filtering. This requires a depth knowledge of the detector behavior, that may not be available at the beginning of the EIC operations.

The solution that we envisage is to design a modular system that will evolve with the experiment. During the first part of the EIC run, a hybrid streaming readout strategy will be adopted, using the so-called “cross-detector zero suppression technique”. In this scheme, all hits from the detector are streamed to the online computing farm and stored to a temporary buffer. Only “interesting” portions of the data stream are further processed, while the others are discarded. Considering that most of the reactions measured to complete the EIC scientific program foresee the measurement of the scattered electron, we think that EIC calorimeter is an excellent candidate to provide the signal to identify the portions of the data stream to be further processed. Technically, this can be achieved both with a parallel hardware system, as in the sPHENIX case, or with a dedicated software component (the sPHENIX hardware-based cross-detector zero suppression system operation is illustrated in Fig. 11.125). Online filtering and online reconstruction will be then gradually introduced when the detector will be more under control.

A possible solution for the EIC readout architecture is shown in Fig. 11.126. Some front-end

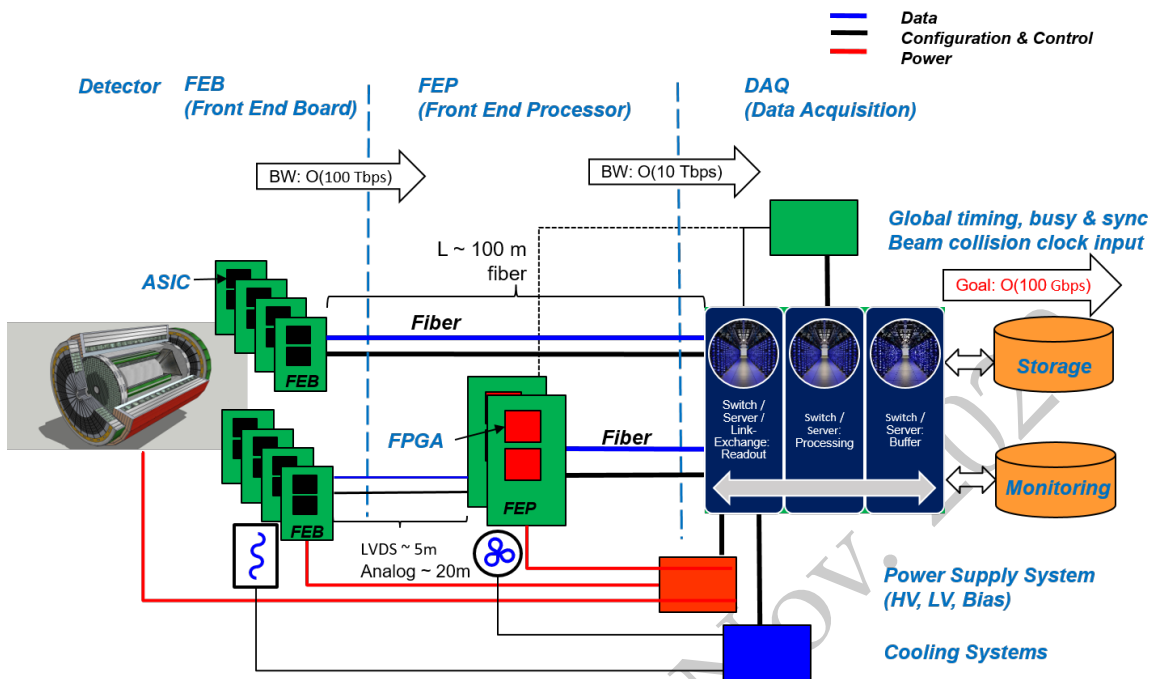


Figure 11.126: A possible scheme for the EIC Readout Architecture

boards (FEB) containing ASICs and specific to different sub-detectors will likely require an intermediate stage of processing via FPGAs for data aggregation and reduction by employing front-end processors (FEP). Data transport to servers or link-exchange cards, such as FELIX, will be made via extensive use of optical fibers. Power supply and cooling systems are planned to be commercial-off-the-shelf (COTS) units.

An intense R&D program has already started to study and design the EIC readout system, covering all the technical aspects involved with it, including the different FE options compatible with a streaming readout system, the data transport system, the synchronization system, the back-end online processing software. **Andrea: how to reference to this part in the Yellow Report document??**

### 11.9.9 Experimental Validation of the Approach

Despite the conceptual simplicity of a triggerless DAQ, a realistic implementation with the specific detector readout is necessary to validate this solution and demonstrate the expected performances. The sophisticated combination of a suitable front-end electronics, network facilities and CPU algorithms requires a significant effort to identify, or develop in case they are not yet available, the best option for each element, set-up and test the whole scheme and compare results with more traditional approaches.

A dedicated test and validation program, with complementary experimental efforts, has already started in view of the EIC detector design and construction. In the following, we

briefly present these efforts.

### Jefferson Laboratory efforts

A first experimental characterization and validation campaign for the new DAQ approach has started at Jefferson Laboratory in 2020, using a streaming readout solution based on FA250+VTP / Waveboard digitizer boards [?, ?] for the front-end readout and on the Tri-DAS software [1393] interfaced with the JANA2 data analysis framework for the back-end online data reconstruction and filtering [1394].

Due to the comparable luminosity and detector complexity, **the CLAS12 detector in Hall B is an ideal study case to characterize and validate the streaming DAQ approach in view of its application for the EIC detector [909]**. A first measurement on beam was carried out using the CLAS12-Forward Tagger Calorimeter and Hodoscope detectors [1314], with the CEBAF 10.6 GeV electron beam impinging on a lead (early 2020 run) / deuterium (summer 2020 run) target.

This represented the first attempt to acquire some CLAS12 sub-detectors using streaming readout: the growing interest for this approach is demonstrated by the plans of the CLAS Collaboration to extend it to the full detector in the near future. During the test, the single  $\pi^0$  quasi-real photoproduction reaction was used as a benchmark to assess the performances of the streaming DAQ system. The  $\pi^0$  was identified measuring the two photons from the decay in the Forward Tagger Calorimeter, whereas the scattered electron was identified by a combination of an electromagnetic cluster in the Forward Tagger Calorimeter and a geometrically matched signal in the Forward Tagger Hodoscope. Preliminary results show a good agreement between the measured data and the predictions from a Monte Carlo numerical estimate, in terms of the energy distribution and total yield of the measured  $\pi^0$ . The data analysis is currently in progress, and final results from the test are expected to be published in early 2021.

A pilot beam study was also conducted to test streaming data processing of the CLAS12 Forward Tagger Calorimeter and Hodoscope using ERSAP software package that includes JLAB data acquisition and data processing frameworks, such as CODA, CLARA and JANA. Specifically CODA VTP stream firmware was used to stream raw data to stream-aggregator, hit-finder, noise-reduction and event-building micro-services, followed by standard, Forward Tagger reconstruction micro-services from the CLAS12 reconstruction application. CLAS12 reconstruction application is based on the CLARA, which is a reactive micro-services orchestration framework for designing, deploying and scaling data stream processing applications [?] [?]. The goal of this study was to optimize (both performance and resource utilization) newly developed data-stream curation micro-services, and to estimate existing CLAS12 reconstruction micro-services scaling levels and resource requirements that will keep up with the VTP data stream. Preliminary results were reported at the 22nd IEEE Real Time Conference.

A complementary test was performed in Hall D, at the pair spectrometer (PS) facility [1395]. The general purpose of the beam tests was to study the light yield and the

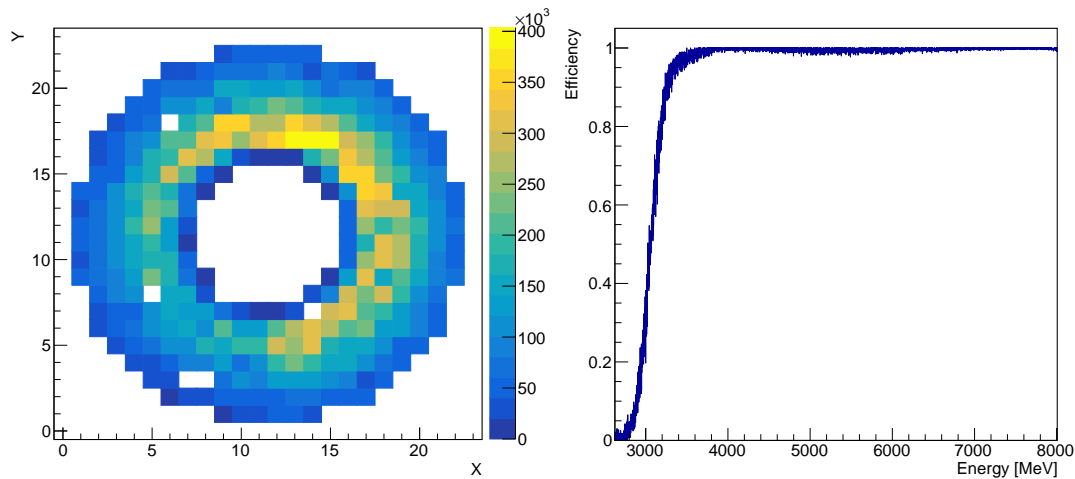


**Figure 11.127:** Left: measured FT-Cal hits during the early 2020 Hall-B streaming readout tests. Right: Efficiency of the online clustering algorithm, with a 3.0 GeV cluster threshold applied.

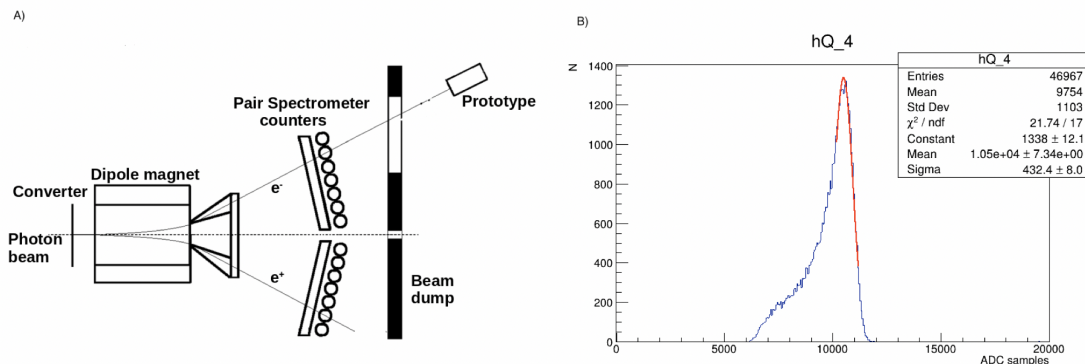


**Figure 11.128:** Left: Hall D PS beam test setup scheme; Right: Calorimeter central response (in arbitrary units) to 4.5 GeV impinging electrons.

energy resolution of glass-ceramic scintillator bars made in VSL/CUA/Scintilex and new produced  $\text{PbWO}_4$  crystals made by CRYTUR/SICCAS. A glass-ceramic and a  $\text{PbWO}_4$  prototype were installed behind the Hall D pair spectrometer and the response to the tagged electrons from the PS was measured. The prototypes were also used to test and optimize the entire readout chain: photosensors (PMT vs SiPM), preamps, fADC or Waveboard digitizers in combination with streaming DAQ system. During the spring run 2020 at Jlab HallD a single prototype, assembled from nine scintillators coupled with R4125-01 Hamamatsu PMTs and active HV dividers with integrated preamplifier, was used. Signals were digitized using a Waveboard device. The SRO tests was performed parasitically during GlueX High Luminosity runs (350nA photon beam). The waveboard read-out nine calorimeter channels plus two scintillator pads mounted in front of the calorimeter, to tag

the impinging electron. The system was operated with a rate up to 1.5kHz per channel. The full SRO chain (Waveboard+TriDAS+JANA2) was successfully tested, with data collected using different combination of software L2 triggers. The offline data analysis is currently ongoing, and final results from the test are expected to be published in early 2021.

### **BNL efforts**

An example of a detector read out in streaming mode is a prototype of the sPHENIX TPC that was tested at the FermiLab Test Beam Facility (FTBF) in 2019. The TPC prototype, shown in Fig. 11.129, was moved perpendicular to the beam and rotated with respect to the beam to get particle tracks at different distances away from the pad plane, resulting in different drift lengths and angles.

At the test beam, we found that our event rate capability could be significantly increased by running the FELIX readout in “streaming mode”. We still triggered the front-end card with signals from the FTBF beamline, however, the FELIX cards are oblivious to how the FEE actually arrived at the decision to send up the data. But by allowing the FELIX card to format the data as streaming data, one does not need to wait for all data from a particular beam event to be fully transmitted. In streaming mode, while data from trigger  $n$  are already arriving from one front-end, other parts can still be transmitting data from trigger  $n - 1$ , or even  $n - 2$ . In streaming mode, there is no need to wait for the completion of the data transmission from a given trigger, as the data parts are later re-assembled by their embedded clock information. That is what led to the increased event rate in streaming mode.

This also validated a running mode that sPHENIX is committed to in production running, combining the streaming data from the tracking system with triggered data from the calorimeters and the Minimum-Bias detector. During the test beam we achieved the simultaneous logging of data from the TPC prototype together with several channels worth of beamline instrumentation channels read out in “classic” triggered mode.

This also served as an early test of our timing system that provides a common clock to the various front-end cards, and can on demand also provide a standard trigger signal to legacy electronics.

## **11.10 Software, Data Analysis and Data Preservation**

This section will describe the computing needs for the reference detector at the EIC and discuss the foreseen software developments.

Aside from possible contribution of machine backgrounds, the reconstruction of events at the EIC will be easier than the same task at present LHC or RHIC hadron machines, and, in perspective, much easier than for the high luminosity LHC (HL-LHC), which will start

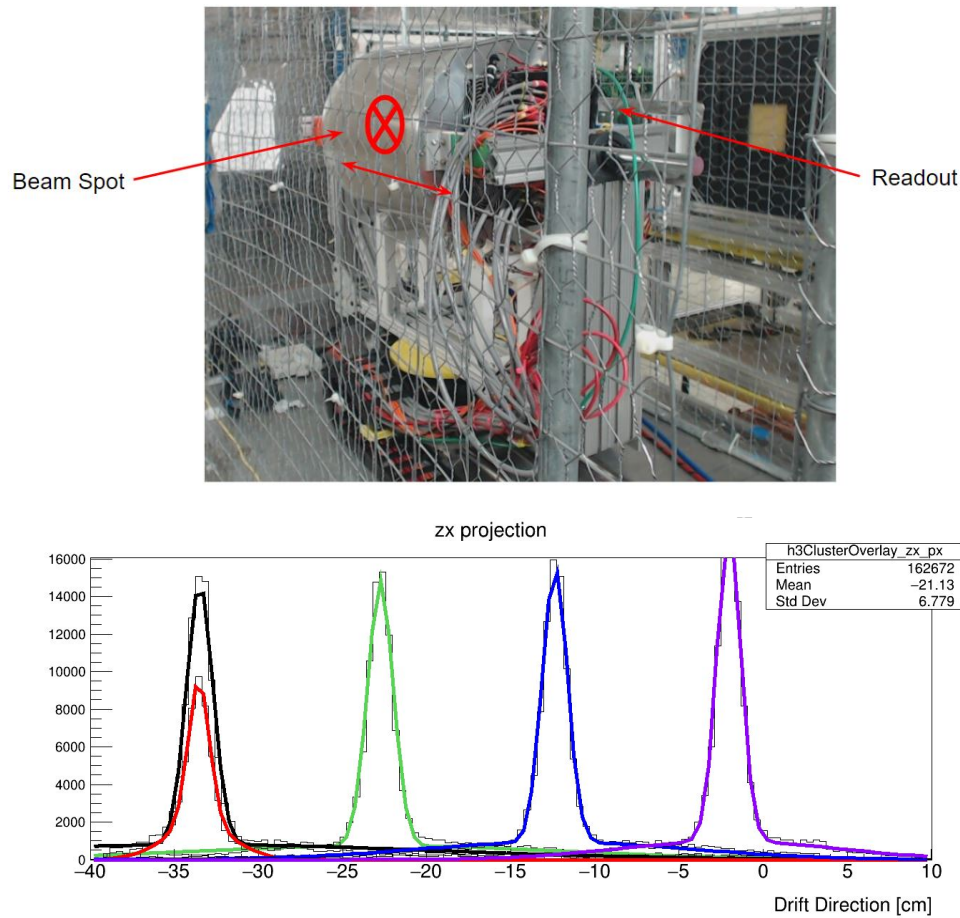


**Figure 11.129:** Left: The TPC prototype shown in the test beam which is read out with FELIX and the RCDAQ. The red cross-hair indicates the approximate beam position. Right: The reconstructed drift distance for 4 different positions of the TPC prototype relative to the beam.

operating two years earlier than the EIC, when we may expect a gain in performance for CPUs of about a factor of 10 with respect to now.

Reconstruction time of DIS events at presently running experiments is around 0.35 s (or  $\sim 5\text{HS06 s}$ ) both at COMPASS and at CLAS12, with event sizes of 0.03 MB and 0.02 MB respectively. Filtering out machine background with high efficiency will allow to keep the reconstruction time at  $5\text{HS06 s}$  also in 2030. Processing events at the same speed of acquisition, or 500 000 events per second, on today nodes will therefore require 200 000 cores or 1500 nodes, a computing farm well in the size of the EIC project. The expected gain in CPU power in the next 10 years, as well as the possible improvement in the reconstruction software from the use of machine learning techniques give a considerable margin to cope with higher event complexity that may come by higher backgrounds rates.

Software design and development will constitute an important ingredient for the future success of the experimental program at the EIC. Moreover, the cost of the IT related components, from software development to storage systems and to distributed complex e-Infrastructures can be raised considerably if a proper understanding and planning is not taken into account from the beginning in the design of the experiment itself.

A growing group dedicated to this effort already exists. An important step in the clustering of a core group focusing on computational aspects at an EIC has been the approval by the EIC Generic R&D program of the eRD20 proposal, creating in 2016 the EIC Software Consortium or ESC. ESC has been the backbone to form in 2018 the Software Working Group within the EICUG. The Software Working Group has supported the Yellow Report initiative and provided the tools for simulations and helped in the creation of the infrastructure for storage and documentation.

The Software Working Group is starting in parallel a greenfield development that will focus on different aspects of future needs:

- Simulations for detector optimization, to cover the more immediate needs of the design and integration of the various sub detectors
- Help in the development of state of the art Monte Carlo event generators for the full spectrum of EIC physics. Validation of these generator will be possible by using data from running experiments.
- Development of a full simulation-reconstruction chain allowing to benchmark the performances of the reconstruction software.
- Development of modern “event reconstruction” schemes both using standard approaches but also exploring novel methods based on artificial intelligence machine learning techniques.

The reconstruction software will have to cope with the streaming read-out scheme adopted and will be design to match the chosen solution.

**Software tools:** While developing the software for simulation and reconstruction of events from a detector which will be up and running in 2030, we need to inquire ourselves about the long term perspective of software used in today HEP experiments and evaluate different options. Leaving aside for the moment both full purpose or dedicated Monte Carlo Event Generator discussed in a separate section, this means that we have to decide on: how to describe the detector; which program to use for particle transportation/interaction; reconstruction tools and the data model.

The choice of LHC experiments for the Run4 and after may guide us in this task.

DD4hep [1396] is a toolkit for detector description developed within the AIDA2020 EU program (Advanced European Infrastructures for Detectors at Accelerators). It can be an interesting option for the EIC since recently the CMS collaboration announced that it plans to use it to provide the structure of the experiment to all their data processing applications.

It is worth considering it for the EIC since it is designed to answer a very common need of experiments, i.e. the development of a coherent set of software tools for the description of high-energy physics detectors from a single source of information. Detector description in general includes not only the geometry and the materials used in the apparatus, but all parameters describing, e.g., the detection techniques, constants required by alignment and calibration, description of the readout structures, conditions data and more.

Given its use withing CMS choice, it is expected that DD4hep will be supported over the entire experiment life-time.

DD4hep reuses existing software components, combines the functionalities and thus optimizes the flexibility, minimizing the efforts required by users to leverage the benefits. Reused components include elements of the ROOT geometry package [1397] and the GEANT4 simulation toolkit [1222].

GEANT4 [1222] is the baseline for detector simulation on all LHC experiment and is a natural choice for the EIC. We have developed strong connections with the core developer team of GEANT4 and the improvements in physic list and in non standard geometries which may be needed for the EIC are being discussed with them. About one year ago, the core team of the Software Working Group organized together with the GEANT4 Collaboration a Technical Forum on the EIC. The Forum allowed to discuss both the information on recent updates on GEANT4, but also the physics list for the EIC as maintained by the EIC Software Consortium. The requested improvements on photo-nuclear and electro-nuclear reactions were included in GEANT4 version 10.6, and this is under test right now. The study of vectorizing this transportation, as done withing the GEANT4, the vector transport R&D collaboration [1398] will offer interesting improving options for GEANT4 itself and we will follow this activity closely.

ROOT [1397] is by nowadays standards a fundamental ingredient of virtually all HEP workflows, being used for data persistency, modeling, graphics, and analysis. It is structured to have excellent, active connections with the experiments including, at least for LHC, direct investment by the experiments. The developing team is investing in future developments for HL-LHC, and is also assuming interesting approaches to machine learning tools. It pushes in fact the HEP community to not develop its own machine learning tools but, maybe in a more efficient way, to collaborate with other sciences on improving and growing tool-sets. For that they offer a Toolkit for Multi Variate Analysis TMVA to bridge between ROOT and external machine learning tools such as scikit-learn, XGBoost, TensorFlow, Keras, mxnet, or PyTorch.

ACTS [1399] (A Common Tracking Software) is an experiment-independent toolkit for (charged) particle track reconstruction in (high energy) physics experiments, implemented in modern MCEG, with 2017 standards. It is being developed for the HL-LHC, but is also targeting sPHENIX. Adopts a highly-templated design allowing to avoid virtual lookup, and it is agnostic of detectors and magnetic fields for high portability. Another important aspects with respect to development is the designed rigorous unit tests, an essential aspect for the future EIC software. All these characteristics made this software an interesting option worth evaluation for the reconstruction software for the EIC reference detector.

Many others codes are under evaluation, like GENFIT [1400], a generic track-fitting toolkit, GAUDI [1401,1402], a software architecture and framework for building HEP data processing applications, JANA2 [1394], a multi-threaded event reconstruction and others.

Finally, following the large worldwide spread, we are moving to the use of tools facilitating collaborative analysis and logbook as presently done at CERN with SWAN [1403], as a Service for Web-based ANalysis, built upon the widely-used Jupyter notebooks.

**Simulations for detector optimization:** The tools developed for the Yellow Report initiative will be expanded and used for extensive full simulations of the reference detector. This is a short term goal for software developers in order to support with detailed simulation studies the finalization of the reference detector, thus allowing to move from the CDR stage toward the full technical design.

**Monte Carlo event generators for the EIC:** The EIC Software Working Group, and before the eRD20 Software Consortium have initiated a project with the Monte Carlo communities in the US and Europe (MCnet) to work on MCEGs for the EIC, requiring MCEG for polarized  $e+p$ ,  $e+D$ , and  $^3\text{He}$  as well as  $e+A$  measurements. The MCEG initiative is connecting the MCEG efforts in NP and HEP and is encouraging a strong interplay between experiment and theory already at an early stage of the EIC. As an initial step, we have started a workshop series on "MCEGs for future  $e+p$  and  $e+A$  facilities" where the third workshop was held in November 2019 at the Erwin Schrödinger International Institute for Mathematics and Physics in Vienna, Austria. During the workshop, we reviewed the theory for physics with light and heavy ions and discussed the modifications needed on the general-purpose MCEGs to simulate unpolarized observables also for  $e+A$  where a precise treatment of the nucleus and its breakup is needed. There were presentations about pioneering MCEG projects for  $e+A$  (BeAGLE, spectator tagging in  $e+D$ , Sartre), as well as on the ongoing development of the  $e+A$  adaptation of JETSCAPE and the Mueller dipole formalism in Pythia8. We also summarized the status of MCEG-data comparisons in HZ-Tool/Rivet that are critical to tune MCEGs to existing DIS and heavy ion data as well on the ongoing work of verifying MCEGs for TMDs with TMD theory/phenomenology. Our current focus is on benchmarks and validation. We are working with the EICUG on benchmark MC productions and the validation of MC results. This will facilitate the adaption of modern MCEGs that have been so far only used by the LHC community.

As a recent development, the DIRE authors [1404,1405] introduced radiative effects in the simulation of the DIS. This is an important step, since a full multidimensional analysis will be needed in the study of TMDs and GPDs, given the dependence of the cross section over many kinematic variables. From the experimental point of view, and without entering to much in detail of the analysis, this means that detectors and RC effects will have to be accounted together at simulation level in order to derive matrices transforming from raw counts in the detector to Born cross sections.

The DIRE parton showers is a modern MCEG, able as a extension of the general purpose event generation frameworks PYTHIA, and will be included as an option from the 8.3 release. This will allow to check the prediction of the Monte Carlo both using the data of running DIS experiments (at JLab and COMPASS at CERN) and with the outcome of the

simulation of DJANGO [931,1406], the reference tool for the study of RC effects at HERA.

## 11.11 Artificial Intelligence for the EIC Detector

In the world of computing there is growing excitement for what is perceived as the revolution of the new millennium: artificial intelligence (AI). In particular the R&D program of the future EIC could be one of the first programs systematically exploiting AI. AI is becoming ubiquitous in nuclear physics [?]. According to a standard taxonomy [?], AI encompasses all the concepts related to the integration of human intelligence into machines; a subset of AI is machine learning (ML), which is usually grouped into supervised, unsupervised and reinforcement learning; deep learning (DL) is a particular subset of ML based on deep (*i.e.*, made by many hidden layers) neural networks, which is often considered the evolution of ML since it typically outperforms other methods when there is a large amount of data and features, provided sufficient computing resources. In the most frequent applications in our field, features are selected and a model is trained for classification or regression using signal and background examples.

Experimental particle and nuclear physics is big data [?]: the gigantic data volumes produced in modern experiments are typically handled with “triggers”—a combination of dedicated hardware and software—to decide near-real-time which data to keep for analysis and which to toss out. In this respect, AI plays already an important role in experiments like LHCb [?], where machine learning algorithms (see, *e.g.*, topological trigger and ghost probability requirements) make almost 70% of these decisions, from triggers to higher level analysis of reconstructed data.

Supported by modern electronics able to continuously convert the analog detector signals, new approaches like Streaming Readout [?] could further the convergence of online and offline analysis: the incorporation of high level AI algorithms in the analysis pipeline can lead to better data quality control during data taking and shorter analysis cycles. Recently the Fast Machine Learning workshop [?] highlighted emerging methods and scientific applications for DL and inference acceleration, with emphasis on ultrafast on-detector inference and real-time systems, hardware platforms, co-processor technologies, and distributed learning. In this context, AI (used here in a broader sense to embrace different approaches) could foster in the next years significant advances in areas like anomaly detection (see, *e.g.*, [?]) and fast calibration/alignment of detectors.

For tracking detectors, particle tracking is always a computationally challenging step. Several approaches have been developed recently for tracking based on deep learning [?], but there are still open questions about the best way to incorporate such techniques. The problem in Nuclear Physics experiments is typically different, being characterized by most of the computing cycles spent in propagating the particles through inhomogeneous magnetic fields and material maps. Here AI can contribute to determine the optimal initial track parameters allowing to decrease the number of iterations needed by Kalman-Filter.

As for particle identification and event classification, we have witnessed in the last years

a growth of applications based on machine learning both for global particle identification (see, *e.g.*, [?]) as well as custom novel solutions which combine different architectures for specific detectors (see, *e.g.*, [?] for imaging Cherenkov detectors).

The search for rare signatures in large acceptance detectors at high intensities necessitates advanced techniques to filter those events. The GlueX experiment at Jefferson Lab for example is searching for exotic hadrons and demonstrated the utility of machine learning techniques based on BDTs [?] to achieve the required performance in filtering events with rare reactions [?].

The utilization of jets at the future EIC can be beneficial for a variety of fundamental topics [?], including the gluon Wigner distribution, the gluon Sivers function, the (un)polarized hadronic structure of the photon, the (un)polarized quark and gluon PDFs at moderate to high momentum fraction ( $x$ ) as well as studies of hadronization and cold nuclear matter properties. Machine Learning is having a major impact in jet physics, empowering powerful taggers for boosted jets as well as flavor tagging, and various deep learning applications like recursive neural network which leverage an analogy to natural language processing [?] have been developed. ML4Jets [?] is a series of workshop dedicated to these topics.

Another area where AI can significantly contribute is that of fast simulations. Simulating the detector response of large scale experiments like EIC is typically slow and requires immense computing power. One of the most computationally expensive step in the simulation pipeline of a typical experiment is the detailed modeling of the high multiplicity physics processes characterizing the evolution of particle showers inside calorimeters. AI, could speed up simulations and potentially complement the traditional approaches. Recent advances with generative networks (see, *e.g.*, GAN, VAE, Flow-based models [?, ?, ?]) look as a compelling alternative to standard methods with orders of magnitude increase in simulation speed [?] but so far usually at the cost of reduced accuracy.

Detector design is another fundamental area of research for EIC. Advanced detector design often implies performing computationally intensive simulations as part of the design optimization process. One of the conclusions from the DOE Town Halls on AI for Science on 2019 [?] was that “*AI techniques that can optimize the design of complex, large-scale experiments have the potential to revolutionize the way experimental nuclear physics is currently done*”. There are at present various AI-based optimization strategies based on, *e.g.*, reinforcement learning or evolutionary algorithm [?, ?]. Among these, Bayesian Optimization (BO) [?, ?] has gained popularity for its ability of performing global optimization of black-box functions that are expensive to evaluate and that can be in addition noisy and non-differentiable. It consists in a surrogate modelling technique where the regression is typically done through Gaussian processes or decision trees depending on the dimensions of the problem, and a cheap acquisition function is used to suggest which design points to query next, overall minimizing the number of evaluations.

Recently, an automated, highly-parallelized, and self-consistent procedure has been developed [?] and tested for the dual-radiator Ring Imaging Cherenkov (dRICH) design, which has been considered as a case study. These studies not only showed a statistically sig-

nificant improvement in performance compared to the existing baseline design but they also provided hints on the relevance of different features of the detector for the overall performance. This procedure can be applied to any detector R&D, provided that realistic simulations are available. One example is the optimization of detector materials, e.g. the optimization of large size aerogel composites for aerogel-based detectors in [?].

Beyond individual subdetectors AI can be also used to efficiently optimize the design of different sub-detectors combined together, taking into account mechanical and geometrical constraints. An interesting approach consists in a multi-objective optimization (see, e.g., [?, ?, ?]), which allows to encode the performance of the detectors as well as other aspects like costs in the design process, to determine the Pareto front [?]. Currently ongoing activities within the EIC R&D program which are leveraging AI for optimization include the EM/Hadronic Calorimetry, e.g., optimizing the glass/crystal material selection in “shared rapidity regions” for best performance of the EM calorimeter.

Even more, AI has the ability to optimize the collection of all subdetectors of a large detector system, using more efficiently the figures of merit we use to evaluate the performance that drive the detector design. Remarkably, the design optimization of multiple subdetectors operating together has not been explored yet. This is a high dimensional combinatorial problem that can be solved with AI.

This is undoubtedly a strategic moment to discuss how to fully take advantage of the new opportunities offered by AI to advance research, design and operation of the future EIC. The interest of the community has been evidenced by the number of contributions and attendance of workshops dedicated to AI in Nuclear Physics, e.g. at the [?, ?], and the 2021 AI4EIC-exp workshop [?], which bring together the communities directly using AI technologies and provide a venue for discussion and identifying the specific needs and priorities for EIC.

## **Chapter 12**

### **The Case for Two Detectors**

SNAPSHOT 19 Nov. 2020

## Chapter 13

# Integrated EIC Detector Concepts

### 13.1 General Purpose Detector Concept

#### 13.1.1 Standard Layout

#### 13.1.2 Detector technology description

#### 13.1.3 Electronics, Data Acquisition and Computing technology description

#### 13.1.4 Detector Integration

The baseline EIC configuration currently includes one fully instrumented Interaction Region (IR) and one general purpose physics detector. For the purposes of this document, it is assumed that the detector will be located in IP-6 (the STAR Hall), and that the available infrastructure will either be re-used or will serve as a reference for the future EIC installation. Complementary information about IP-8 (the PHENIX Hall) is given where appropriate.

#### Hall infrastructure

In addition to the beam line area (the Wide Angle Hall), RHIC complex 1006 has an Assembly Building with adequate floor space for detector maintenance work, as well as a control room, counting house, office space, electronic/mechanical workshops, gas shed, online computing room and other service areas, as shown in Fig. 13.1.

The general specifications for the IP6 and IP8 experimental halls are provided in Tab. 13.1.

The coordinate system of the EIC experiment is oriented as follows. The z-axis is along the beam line toward the outgoing hadron direction, the y-axis points upward, and the x-axis points toward the EIC-accelerator center.

Detector subsystem infrastructure requirements include cooling (HVAC, CW, LCW),

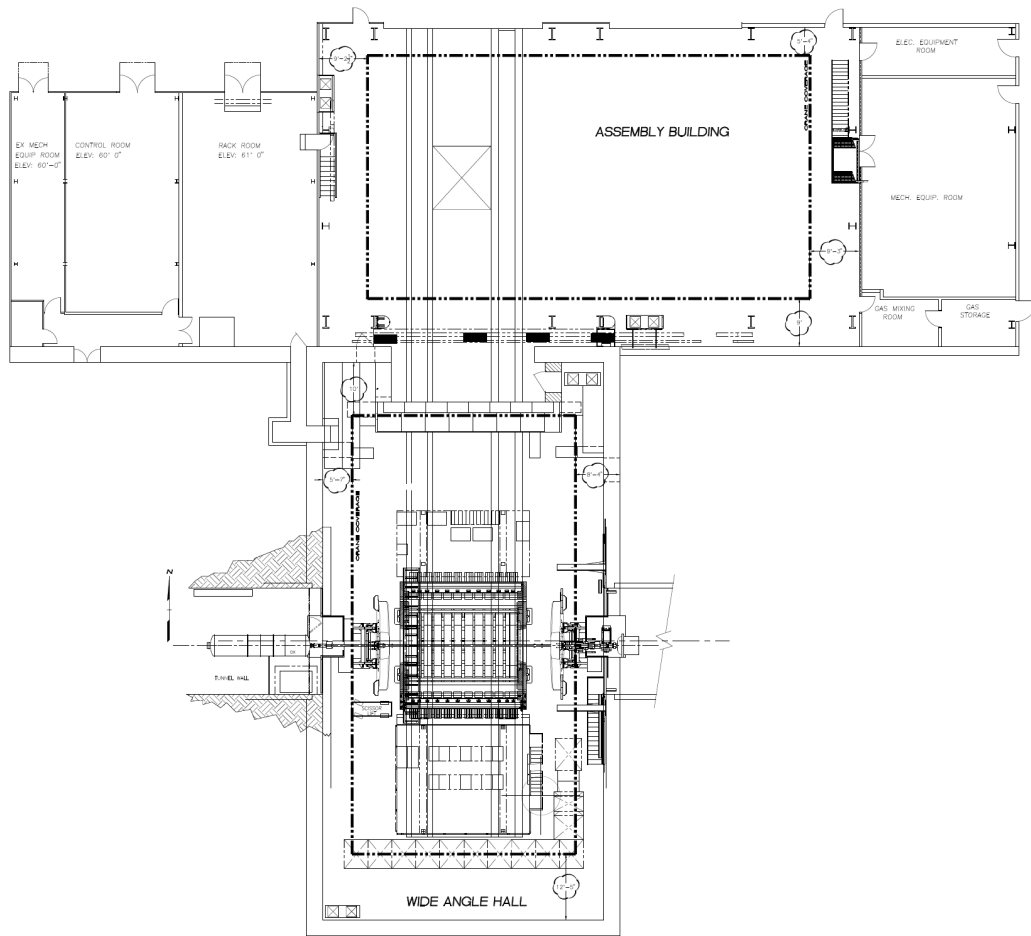


**Figure 13.1:** RHIC IP6 experimental area layout. STAR detector shown schematically in the beam position.

power (clean, utility, generator-backed), cryogenics, cabling, service lines, and gas system specifications for gaseous detectors. These requirements cannot be specifically identified at this stage of planning, but will be developed by the Detector Working Groups for a subset of the EIC detector technologies on the time scale of the Yellow Report. The new requirements will be reported in the next revision of this document, along with a table containing the existing capacities available in the RHIC IP-6 Hall. The following is a list of items which needs to be considered during integration:

- *electronics racks and data cables* The bulk of the electronics cables and service lines for the sub-detectors will be routed through gaps which exist between the barrel and endcap regions. As a result, the installation design for these cables must accommodate the removal/repositioning of the endcaps.
- *Power distribution and grounding*

**Table 13.1:** IP6 and IP8 experimental hall dimensions and related data. Hall width goes parallel to the beam line in this table, see also the Wide Angle Hall boundaries in Fig. 13.1.

	IP6	IP8
Hall length and width	3200 cm x 1615 cm	1737 cm x 1859 cm
Distance from floor to beam line	432 cm	523 cm
Door dimensions (W x H)	823 cm x 823 cm	927 cm x 1017 cm
Floor load capacity	5000 psi	4000 psi
Crane capacity	20 ton	12 ton

- *Cooling and gas installation*
- *Cryogenic capacity*
- *Pressure and temperature control of the experimental hall*
- *Shielding against the penetrating particles from the machine*

### Safety and Environmental Protection

For the purpose of this document, it is assumed that the experimental hall's safety systems (sprinklers, ODH monitors, smoke alarm) are provided as part of the RHIC infrastructure. The design and operation of EIC sub-detector components will follow BNL safety regulation rules.

- *Radiation control*
- *Interlock system*
- *Hazardous materials and systems* (flammable gases, lasers, cryogenic fluids, electric shock hazard, magnetic forces, beam line vacuum, etc.)

### Installation

At this time, the composition of the EIC central detector is not defined to a level of detail that is sufficient to provide a step-by-step installation procedure. However, the overall detector layout, as well as several boundary conditions, are sufficiently understood to make the following assertions:

- In order to maximize luminosity, the beam line final focusing quads must be positioned as close to the IP as possible. The current Interaction Region design provides approximately 9 meters of space for the main physics detector, with accelerator beam

line elements installed in the adjacent areas. It is assumed that these elements (quads on the incoming hadron side and B0 magnet on the incoming electron side) WILL NOT be moved for installation or maintenance of the central detector.

- Having  $4\pi$  coverage in tracking, calorimetry and PID, the general purpose EIC detector is likely to consume 100% of the available space.
- The door connecting the assembly area and the installation area is 823 cm wide. Accordingly, the fully assembled,  $\sim 9$  meter long detector cannot be moved intact between the two areas without making structural modifications. To accommodate this, it is assumed that one or more of the calorimetry endcaps will be placed on independent carriages that allow them to be separated from the main detector before moving.
- The space in the installation area is not sufficient to perform any significant assembly or maintenance on the central detector (see Fig.13.1). Consequently, the bulk of assembly and maintenance must be performed in the assembly hall.

Although the following considerations do not represent hard constraints, they will impact system design and operation:

- In order to maximize luminosity, the beam line final focusing quads must be positioned as close to the IP as possible. The current Interaction Region design provides approximately 9 meters of space for the main physics detector, with accelerator beam line elements installed in the adjacent areas. It is assumed that these elements (quads on the incoming hadron side and B0 magnet on the incoming electron side) WILL NOT be moved for installation or maintenance of the central detector.
- Having  $4\pi$  coverage in tracking, calorimetry and PID, the general purpose EIC detector is likely to consume 100% of the available space.
- The door connecting the assembly area and the installation area is 823 cm wide. Accordingly, the fully assembled,  $\sim 9$  meter long detector cannot be moved intact between the two areas without making structural modifications. To accommodate this, it is assumed that one or more of the calorimetry endcaps will be placed on independent carriages that allow them to be separated from the main detector before moving.
- The space in the installation area is not sufficient to perform any significant assembly or maintenance on the central detector (see Fig.13.1). Consequently, the bulk of assembly and maintenance must be performed in the assembly hall.
- The solenoid cryostat chimney must be designed such that it does not need to be disconnected whenever the detector is relocated from the installation area to the assembly area, and vice versa. The current expectation is that the cryo-can will be mounted to the interior wall of the assembly area and will be connected to solenoid using a flexible cryogenic line. This line will be sufficiently long to remain connected to the solenoid when the central detector is in either room.

- In order to minimize the amount of silicon detector cabling in the electron endcap acceptance, the pre-assembled silicon tracker modules must be inserted into their nominal position from the hadron endcap side, with all cabling attached and routed through the “service gap” between the barrel and the hadron endcaps. This operation cannot be performed with the high-momentum gaseous RICH detector already installed in the hadron endcap, since it will block access to the central area. Additionally, due to space constraints along the beamline, the  $\sim 1.5$  meter long RICH modules cannot easily be installed into the central detector in the beam position. A possible solution is to pre-assemble the entire central part of the main detector (the barrel, the silicon forward / vertex / backward tracker, and all of the endcap acceptance equipment except for the calorimetry), together with the central piece of the beam pipe, in the assembly area.

This set of constraints and supporting considerations provides the foundation for the detector “building block” composition and the installation sequence, described below. A general purpose EIC detector, schematically shown in Figure 13.2, will be used as a reference. Figure 13.3 shows a perspective view of the EIC detector.

As illustrated in these figures, the detector can be naturally subdivided into three parts: the central barrel, which is built around the solenoid magnet yoke, and the two endcaps.

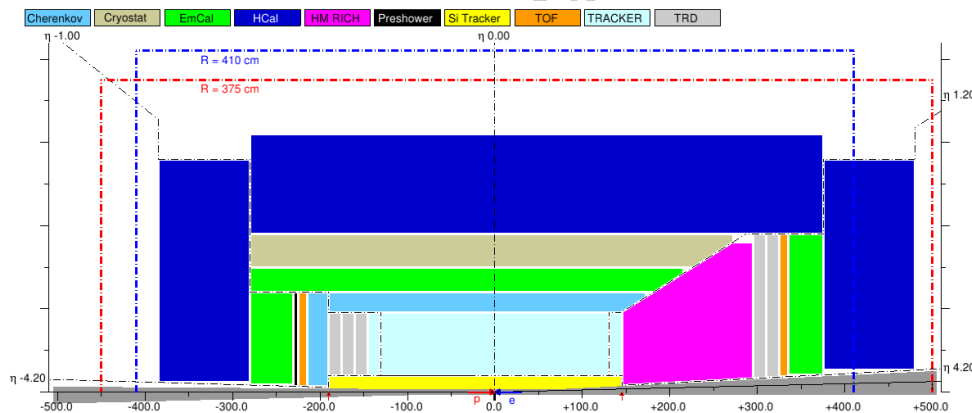


**Figure 13.2:** A 2D sketch of an EIC detector layout, horizontal cross cut. Only one half of the detector is shown, with the other half being mirror-symmetric in this view, up to the crossing angle. Beam pipe footprint (in dark gray) is to scale. Blue dashed line shows the doorway size between the assembly and the installation halls. Red dashed line shows the realistic central detector envelope with the available  $[-4.5 \dots 5.0]$  m space along the beam line.

The endcap hadronic calorimeters are expected to be of an Fe/Sc sandwich type, with the magnetic structural steel used as an absorber. By design, they will be self-supporting, serve as a solenoid flux return, and will be able to provide mechanical support to other subsystems. To optimize construction, as well as the access strategy, it may be beneficial to locate not only the hadronic, but also the electromagnetic calorimetry in the endcap

assemblies, as shown in Figure 13.6 for the hadronic calorimetry. This will certainly be true for the hadron endcap should a spaghetti W/SciFi e/m calorimeter technology be used in a configuration with the photo-sensor electronics installed on the upstream end of the towers. In that case, the hadronic and e/m calorimeter assemblies will likely be physically connected to one another face-to-face, with the barrel hadronic calorimeter to hadron endcap split then also needing to be aligned with the front of the e/m calorimeter. Once the endcap halves are rolled out, one will have access to both the e/m calorimetry front end electronics, and to the electronics and services of a substantial fraction of the central (barrel) part of the detector.

In order to meet space constraints, it is expected that the endcap assemblies can be moved laterally relative to the central part of the main detector. This should be achievable with a few cm of clearance, making it unnecessary to move them a substantial distance outward along the beam line. To accommodate this, it will be required that no part of the central detector is installed in the recess of either of the endcaps, and vice versa.

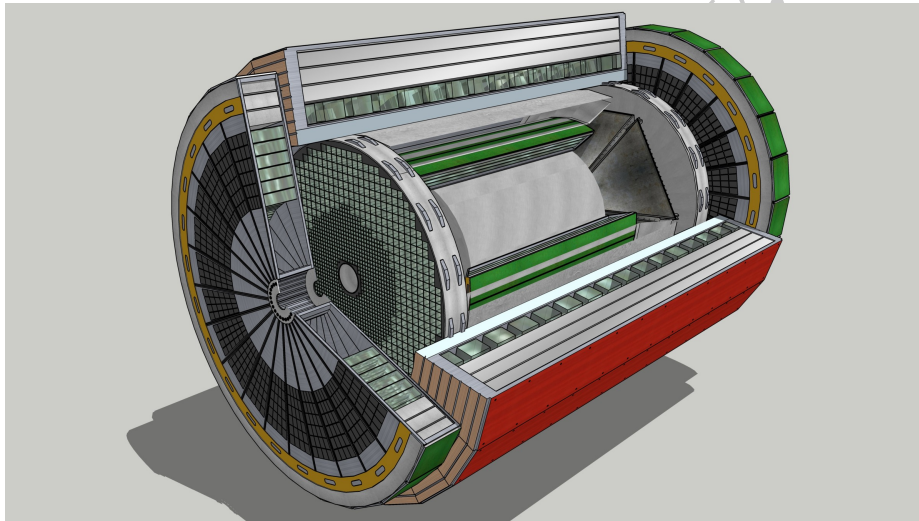


**Figure 13.3:** CAD model of the EIC detector, with the artistic rendering of the calorimetry subsystems.

In this approach the support frame and the carriage system consist of five independent parts (one for the central piece and two more for each of the endcaps (see Figure 13.6), each on their own sets of the heavy duty Hilman rollers. Given the size of the endcap calorimeters, and the expected density of the absorber material, the total weight of each of the four of the endcap halves is estimated to be between 80-100 tons. The weight of the central part of the detector is estimated to be on the order of 500 tons, similar to the fully assembled sPHENIX detector without endcaps.

The beam pipe configuration (as shown in Figure 13.4), is expected to roughly follow the 1.5 m + 6.0 m + 1.5 m breakdown scheme, matching the main physics detector and consists of a  $\sim 6.0$  m long central part and two  $\sim 1.5$  m long endcaps. The central piece may

be composed of more than one part. However, the installation procedure described here may be impacted if bulky, permanent flanges are used to interconnect the parts.

As shown in Figure 13.2, it is assumed that a clear  $\sim 40$  cm diameter "bore" is allocated for the forward / vertex / backward silicon detector assembly installation, and it is not obstructed by any other endcap equipment.

The pre-assembly sequence of the endcaps is straightforward, and does not require a detailed description at this stage.

Starting from the outer parts (the hadronic calorimeter, integrated into the solenoid flux return) the central part of the detector will be assembled on its own support structure. The inner barrel components (the solenoid cryostat, e/m calorimeter modules, PID detectors and the central volume tracker) will be added to the assembly one by one, in sequence, as is typically done for this type of detectors (e.g. BaBar and sPHENIX). Next the central piece of the beam pipe, as well as the two pre-assembled halves of the vertex silicon tracker are installed, with the latter ones connected to provide minimal clearance to the beam pipe. The endcap tracker and PID detector modules will be installed afterwards, starting from the inner modules.

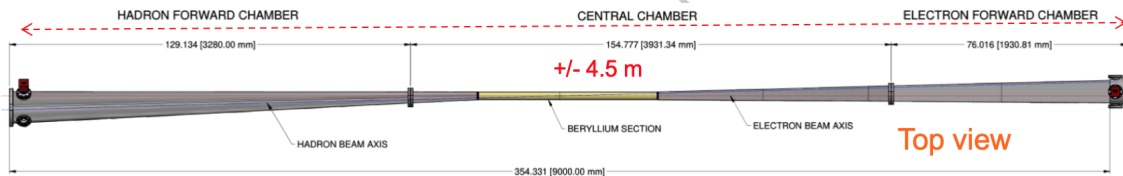


Figure 13.4: Interaction Region vacuum chamber layout.

The installation sequence of the B0 magnet equipment and the pre-assembled main detector blocks can look like this:

- The silicon tracker and the e/m calorimeter of the B0 magnet spectrometer are installed in its warm bore.
- The approximately 6 m long central part of the main detector, built around the solenoid magnet yoke, is rolled into the beam position, together with the electronics trailer and the pre-installed central piece of the beam pipe. Both endcaps are also rolled into the experimental hall, being split into halves, and moved away from the beam line, in order not to block access to the beam pipe installation.
- $\sim 1.5$  m long pieces of the beam pipe are installed, together with the respective pump stands. This operation closes the accelerator UHV volume.
- The endcap halves are rolled towards the beam line and bolted together, as well as connected to the solenoid flux return yoke.

These actions are performed in the reverse sequence to move the detector from the experimental hall to the assembly area for maintenance.

Figure 13.5 shows the final installation of the EIC detector in the IP6 hall.

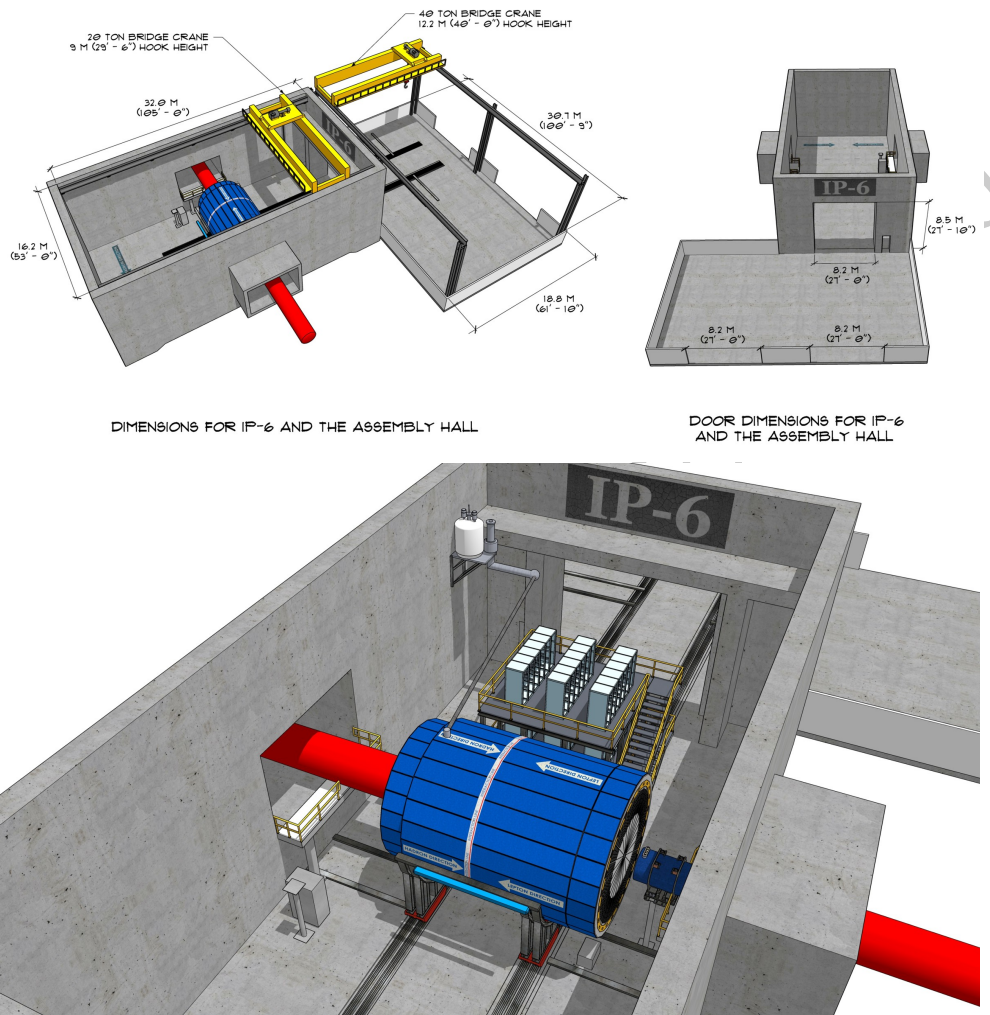


**Figure 13.5:** A model of the current detector system design in the experimental hall with magnets, cryocan, and rear carriage for the electronics.

### Detector Alignment

The internal alignment of the high-precision silicon tracker modules will be done on the bench, prior to installation in the experimental apparatus. It is assumed that the relative alignment of the detector components with respect to one other, to the solenoid magnet and to the beam line elements should be performed to accuracy on the order of  $\sim 100 \mu\text{m}$ . This level of accuracy can be achieved using modern laser tracker survey apparatus,

and by providing a redundant set of alignment marks on the detector frames, which are surveyed together with the network of the permanently mounted 3D points (survey mark nests) in the experimental hall. Maintaining visibility of the detector survey marks within the dense EIC installation environment will be a concern though, particularly for the inner tracker modules. Still, it should be noted that the ultimate alignment on the micron level of accuracy will be performed by software using the real particle tracks.

### Access and Maintenance

Typically three different access and / or maintenance scenarios are expected. A short-term (controlled) access to the detector installation area where there will be no (dis)assembly of the equipment. This scenario would allow access to the electronics trailer, as well as the outer part of the sub-detector components, like FEE of the hadronic calorimeters.

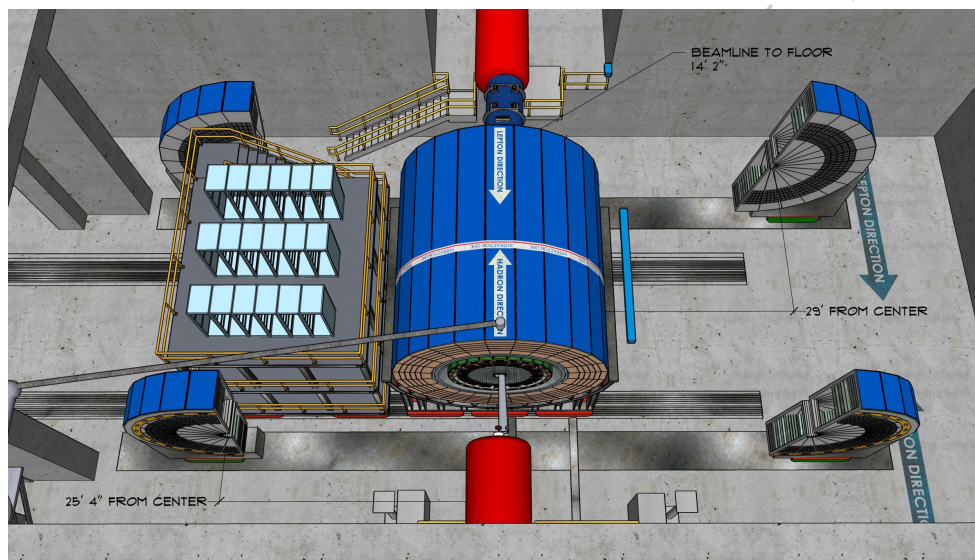


**Figure 13.6:** Barrel part of the main detector shown in the beam position. The endcaps shown rolled out to provide the space to access the inner parts of the barrel detectors.

A short shutdown (typically an emergency event, downtime of  $< 48$  hours) would allow the detector endcaps to be rolled out as indicated in Figure 13.6, providing an access to the endcap e/m calorimeters, outer part of the endcap trackers, beam pipe, as well as to a portion of the barrel part of the detector and the B0 silicon tracker for short maintenance. This procedure will be easier in IP-6 (STAR Hall) than in IP-8 (PHENIX Hall) due to the tighter space constraints in IP-8, see Tab. 13.1, leaving less space to walk or move equipment (Fig 13.7).

During a long shutdown, the barrel part of the EIC detector could be moved out of the hall completely and sub-components could be disassembled safely. Fig. 13.8 shows how the barrel part of the detector together with the rear carriage could be rolled into the mainte-

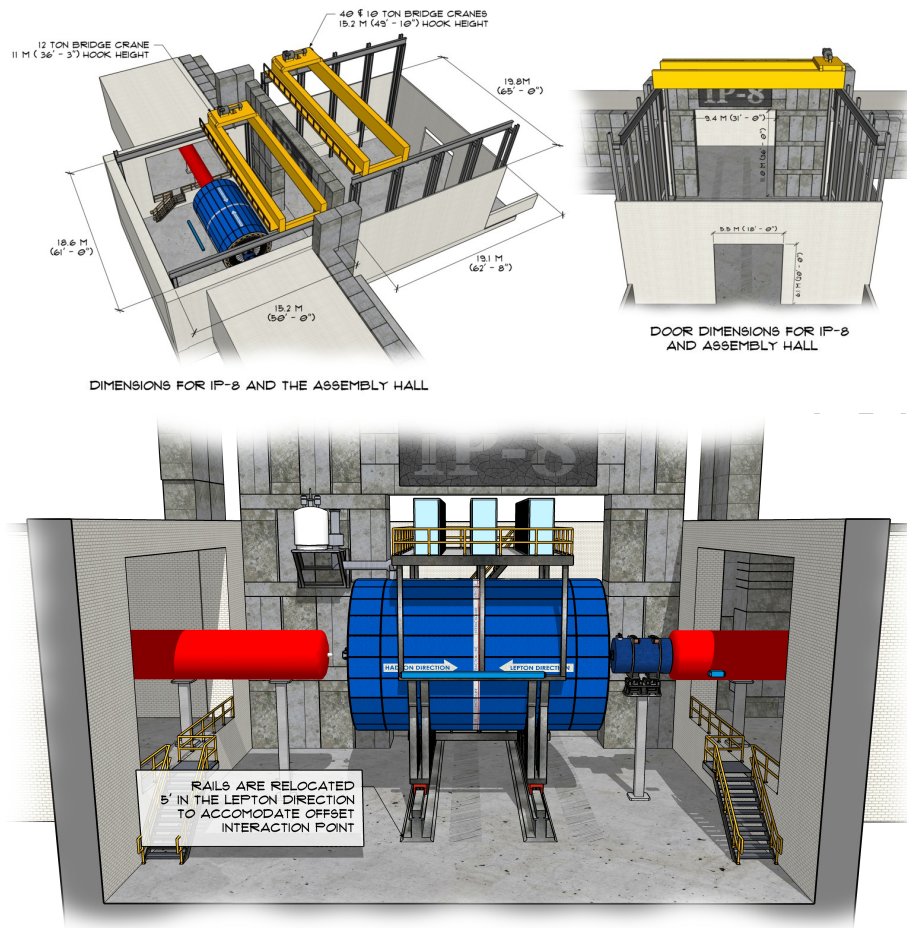
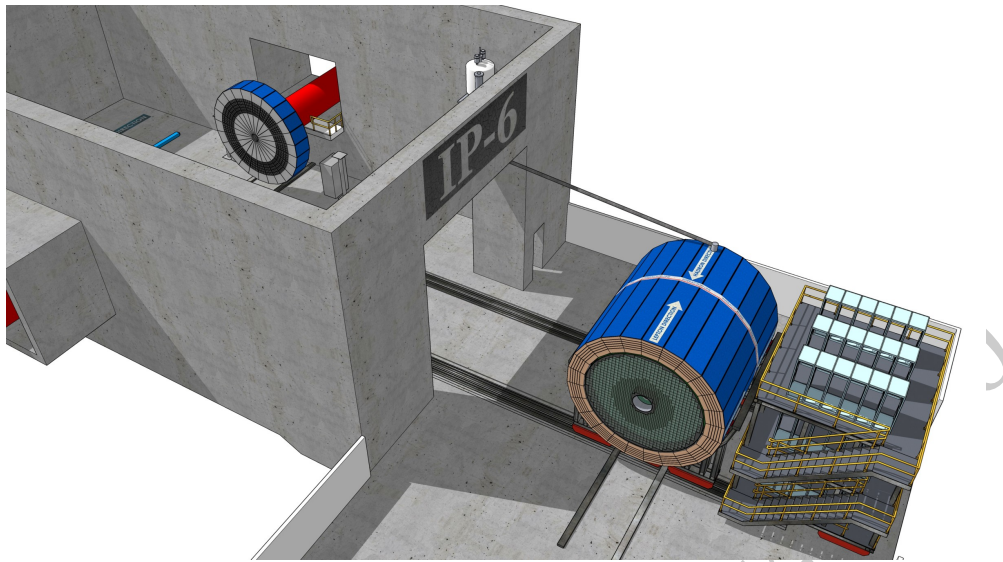


Figure 13.7: IP-8 (PHENIX Hall) installation

nance area outside of the hall. It is important to keep the readout electronics at the rear carriage next to the detector, to provide an easy way to test sub-components during the shutdown. Such a shutdown involves disassembly of the IP beam pipe section, as well as the beam pipes of RCS, dismantling of the shielding wall between the installation and assembly halls, and would require several weeks of downtime.



**Figure 13.8:** The barrel part of the detector and the rear carriage rolled into the maintenance area.

Central Detector

Forward and Backward Detector

13.1.5 Systematics Discussion

## 13.2 Second General Purpose Detector Concept

13.2.1 Standard Layout

13.2.2 Detector technology description

13.2.3 Electronics, Data Acquisition and Computing technology description

13.2.4 Detector Integration

Central Detector

Forward and Backward Detector

13.2.5 Systematics Discussion

## Chapter 14

# Detector Technology

In this report, the EIC community motivates the need for two general-purpose detectors. With this in mind, different specific detector concepts with complementary designs have been developed, studied, and are described in previous chapters. While significant progress has been reached in developing these concepts, work is still needed to ensure that the respective detector technologies reach a viable state of maturity for construction readiness and EIC science.

The need for R&D was realized early by the community and laboratories and in January 2011 Brookhaven National Laboratory, in association with Jefferson Lab and the DOE Office of Nuclear Physics, created a generic detector R&D program to address the scientific requirements for measurements at an EIC. The primary goals of this program were to develop detector concepts and technologies that have particular importance to experiments in an EIC environment, and to help ensure that the techniques and resources for implementing these technologies are well established within the EIC user community. It was also meant to stimulate the formation of user groups and collaborations that will be essential for the ultimate design effort and construction of the EIC experiments.

This program is, at the time of writing of this report, supported through R&D funds provided to BNL by the DOE Office of Nuclear Physics and is open nationally and internationally to the whole EIC community. Funded proposals are selected on the basis of peer review by a standing EIC Detector Advisory Committee consisting of internationally recognized experts in detector technology and collider physics. This committee meets approximately twice per year, to hear and evaluate new proposals, and to monitor progress of ongoing projects<sup>1</sup>. The program is administered by the BNL Physics Department.

Many of the supported projects, ongoing or completed, developed technologies that are now integral parts of existing detector concepts or are regarded as potential alternatives. The vertex detector R&D consortium, eRD25, aims to develop new improved MAPS sensors to meet the requirements demanded by the EIC requirements. Various MPGD tech-

---

<sup>1</sup>The web site of the generic R&D program with a description of the projects and all related documents and presentations is [https://wiki.bnl.gov/conferences/index.php/EIC\\_R%25D](https://wiki.bnl.gov/conferences/index.php/EIC_R%25D).

nologies, such as GEM, Micromegas, and  $\mu$ RWELL, have been pursued by the tracking consortium, eRD6, for low material tracking in barrel and forward regions as well as TPC readouts. New concepts like miniTPCs and integrated Cherenkov-TPCs had been developed and tested. Many options for electromagnetic, and recently, hadronic calorimetry have received R&D effort. From this grew the W-SciFi calorimeter, scintillating fibers embedded in a W-powder composite absorber. In parallel, novel scintillating glasses have been developed with unprecedented quality as an alternative to expensive  $\text{PbWO}_4$  crystals. The particle ID consortium, eRD14, is pursuing various technologies, such as DIRC, dual RICH with gas *and* aerogel radiators, and new coating materials like nano-diamonds to replace CsI for RICH photo sensors are under investigation in eRD1. Time-of-Flight detectors, as well as Roman Pots for forward proton detection, require highly segmented AC-LGAD sensors whose development has just started to get supported by the program.

Besides hardware R&D the program supports various vital projects such as machine background studies and simulation software developments to enable more accurate definition of the physics' requirements. Sartre and Beagle are two examples of Monte-Carlo event generators whose development was substantially boosted by the program. Both were intensively used in the context of this report.

The generic R&D program was and is a vital part of the overall EIC efforts with over 280 participants from 75 institutions. Despite moderate funding, many groups are making excellent progress on many vital technologies needed for an EIC detector. The generic R&D program was not the only source of support for R&D relevant for an EIC detector. Several National Laboratories, among them BNL, JLab, ANL, and LANL, supported EIC detector R&D through Laboratory Directed Research & Development Programs (LDRDs) and many university groups in and outside of the US, active in the many R&D projects received support from their respective department and/or funding agencies. The EIC also benefited substantially from R&D conducted for many HEP and NP experiments such as ALICE and LHCb at CERN, Panda at GSI and Belle-II at KEK.

In the coming years the generic R&D program will be replaced by a targeted program funded out of the EIC project and guided by a Detector Advisory Committee (DAC). However, the community sees also a need for a continuation of a more generic program to support technologies that go beyond the immediate needs of a day-1 detector.

In the following we discuss the remaining R&D needs for technologies that are candidates for being deployed in a multi-purpose EIC detector. Here we do not distinguish areas of targeted R&D, *i.e.*, R&D needed to ensure a functional baseline EIC detector on day-1 and more generic R&D, *i.e.*, more future-looking detector concepts and technologies that have the potential to enhance the scope of EIC science in the outyears. The respective timelines are indicated in the individual section.

## 14.1 Silicon-Vertex Tracking

### 14.1.1 Monolithic Active Pixel Sensors (MAPS)

The EIC requires precision tracking with very low  $X/X_0$ . The goal of MAPS R&D is to develop sensors that meet the stringent EIC requirements for vertexing and tracking. The combination of very high single point spatial resolution ( $< 5 \mu\text{m}$ ) and very low mass detector layers makes MAPS technology the most suitable candidate. More specifically, work is underway at CERN on a 65 nm MAPS detector for the ALICE ITS3 project and it is suggested that joining this development is the most efficient route to an EIC MAPS detector. The advantage of this route is that the design parameters for the ITS3 based sensor technology closely match EIC needs, including  $10 \mu\text{m}^2$  pixels (very precise spatial resolution), low power dissipation (reduced needs for cooling and power delivery leading to reduced infrastructure) and sensors thinned to 30-40  $\mu\text{m}$  (low  $X/X_0$ ). Furthermore, there are significant advantages in joining a well-funded and staffed existing design effort (high likelihood of success). The ITS3 work is already underway, so funds and support would be needed rapidly to enable full exploitation of this opportunity. An additional consideration is that further effort and funds would be needed to adapt the existing ITS3 design goals to an EIC specific sensor for the barrel and disc layers. The needed R&D is to support the development of a MAPS sensor based on the ITS3 effort currently underway at CERN. The work done will follow the path of the eRD-25 effort and the EIC silicon consortium. The goal of this consortium is to develop a MAPS sensor and associated powering, support structures, control and ancillary parts as necessary to produce a detector solution for silicon tracking and vertexing for the central tracking parts of an EIC detector. This will include significant design, testing, prototyping and the groundwork/R&D to lead to a funded construction project. A more detailed description of the current path that leads to an EIC optimized sensor and associated infrastructure can be found in the eRD-25 proposal<sup>2</sup>.

It is critical that this effort be supported immediately and continuously to allow for the integration of the EIC based design and testing team into the ITS3 effort and to allow for the contribution of the EIC consortium members to the developing design. Looking at the schedule for this development to lead to an EIC optimized sensor in the time-frame needed for detector construction, delay would seriously impact the likelihood of success. The product of this effort can be used at either or both interaction points. It is intended as a full silicon based inner tracking and vertexing solution. The overall designs (number of barrel layers and discs, spacing, etc.) may be different for each region, but the need for high precision inner tracking/vertexing is likely to be present at both detectors. The timeline is indicated in detail in the FY21 eRD-25 proposal. This effort is needed for a day-1 detector and would be very applicable to subsequent/parallel efforts for a detector at the second interaction point.

---

<sup>2</sup>See <https://wiki.bnl.gov/conferences/images/6/6d/ERD25-Report-FY21Proposal-Jun20.pdf>

### 14.1.2 Silicon-Sensor Tracking Fallback

The EIC detector requires precision tracking with very low  $X/X_0$ . The goal of sensor tracking fallback R&D is to monitor developments in 180 nm MAPS, Silicon on Insulator (SOI), and LGAD technologies that can be developed into tracking sensor solutions for EIC tracking. It is prudent to keep abreast of developing sensor technologies and to plan for a fallback solution should the 65 nm MAPS development in collaboration with the ALICE ITS3 project prove to be unsuitable for this purpose.

The combination of very high single point spatial resolution ( $< 5 \mu\text{m}$ ) and very low mass detector layers leads to the selection of silicon based sensors for EIC tracking. While a path to meet the EIC requirements using 65 nm MAPS technology has been identified, production of sensors for construction of an EIC tracking detector should begin in the 2026 time frame in order for a detector to be ready for use in the 2030 time frame. During this development time, contingency plans using other technologies should be developed. The most promising existing technology for a fallback path is 180 nm MAPS based on ALPIDE or Depleted MAPS (DMAPS) sensors such as MALTA. The pros are having an alternative path to success should the existing effort be unsuitable due to technology or schedule considerations. The cons are that general silicon R&D can be expensive in both material costs and effort and having two parallel path of MAPS development might be prohibitive. While this is not the primary path, this could become the primary path to having a sensor that meets the EIC requirements available in the needed time frame.

The path involving the least amount of additional development is through the adaptation of existing 180 nm designs. At this point it is still prudent to maintain a close watch on the developing technologies of SOI and LGADs as progress is being made in both technologies. Doing the baseline R&D to develop a fallback path is urgent and increases the chances of having a sensor available that meets EIC requirements in the needed time frame. This should be explored in the 180 nm technologies.

This effort should be done in parallel with the timelines developed for the primary ALICE ITS3 based effort on 65 nm MAPS. This effort is needed for a day-1 detector and would be very applicable to subsequent/parallel efforts for a detector at the second interaction point or future detector upgrades. The LGAD technology offers very high temporal resolution (tens of ps) and is also a candidate for TOF and bunch crossing timing at the EIC. Whilst MAPS technologies have proven low mass, low power dissipation and very high single point spatial resolution to match EIC vertex and tracking requirements, these features are not yet available in current state-of-the-art LGAD sensors. R&D in this direction is however undertaken by a number of HEP and NP groups and progress should be monitored.

A significant effort in simulation has been made to assess the suitability of additional technologies of HV MAPS and LGADs for use in the hadron endcap region and the B0 tracker. While the current specifications of prototypes in these technologies do not meet the requirements for the central barrel and inner-most discs, the technologies can be adapted for tracking in the outermost discs. Current pixel sizes are  $36.4 \mu\text{m}^2$  for MALTA and  $100 \mu\text{m}^2$  for LGADs. This effort is shown in [reference tracking section]. A more developed presentation of the path proposed for this development can be found in [713].

### 14.1.3 Services Reduction – Multiplexing and Serial-Fiber Off Detector Output

The primary goal for this R&D is to reduce services loads by reducing the number and volume of the way that data is taken off of the silicon tracking and vertexing detector. This effort will need to balance the reduction in service loads with the risks of losing communication with larger parts of the detector in the event of single point failures. It is possible that even with redundancy, one would be able to reduce the service loads significantly. While this is primarily geared for the silicon tracking barrel layers and discs, the product of this R&D could apply to other detectors in the main detector volume. The product of this R&D would be envisioned for a day-one EIC detector, but also could be improved for future detector upgrades.

The envisioned EIC requirement is the need for the reduction of the services loads and corresponding space and radiation length reduction. This matches the need for very low radiation length of non-active parts of the detector. Most of these services will exist in the acceptance of the parts of the tracking detectors and most of the acceptance of the surrounding detectors (PID, Calorimetry, etc.) The advantages are what has been described. The risks could be related to single point failures and the hope that redundant paths with higher bandwidth and lower mass connections could ameliorate this yielding net positive results.

R&D would be needed in radiation tolerant multiplexing (probably using radiation tolerant FPGAs) and in high speed (5 GHz and above) fiber or multi-fiber optical transmission components. Both of these technologies are complimentary and urgent. This R&D, while initially envisioned for the silicon tracking/vertexing detector, can be applied to other detector readout systems. In general, the application of this type of R&D benefits most when it is co-developed with the detector technology (MAPS sensors, GEMS, etc.). This research could also compliment and integrate additional efforts in moving some of the early stage analysis onto the detector (providing track candidates, etc.). This R&D could lag the primary sensor R&D by up to 6 months as an estimate, but should be considered as part of the system level approach to developing detector solutions. This is envisioned for a day one detector implementation.

### 14.1.4 Services Reduction - Serial Powering and/or DC-DC Converters for Powering of Detector Components

This R&D aims at reducing the services loads by minimizing the number and volume of the primary service load of the silicon tracking and vertexing detector, the power and return cables. The magnitude of this load in existing architectures has been documented in detail (see section 11.2.11). This effort envisions investigating both possibilities of serial powering, possibly with on chip regulation and the use of on detector radiation tolerant DC-DC converters, either or both of which could significantly reduce the required amount of power cabling. While this is primarily geared for the silicon barrel tracking layers and discs, the product of this R&D could apply to other detectors in the main detector volume. The product of this R&D would be envisioned for a day-one EIC detector, but also could

be improved for future detector upgrades. The envisioned EIC requirement is the need for the reduction of the services loads and corresponding space and radiation length reduction. This matches the need for very low radiation length of non-active parts of the detector. Most of these services will exist in the acceptance of the parts of the tracking detectors and most of the acceptance of the surrounding detectors (PID, Calorimetry, etc.) The advantages are what has been described. The risk could be related to single point failures in the serial powering chains which, depending on the architecture, could cause loss of powering to larger segments of the detector, and limitation in the current scaling factor for integrated DC-DC converters. The architectural aspects would be a significant part of the R&D.

This effort envisions investigating both possibilities of serial powering, possibly with on chip regulation and the use of on detector radiation tolerant DC-DC converters. Both of these technologies are complimentary and urgent. This R&D, while initially envisioned for the silicon tracking detector, can be applied to other detector powering systems with commensurate improvements in the powering services loads. In general, the application of this type of R&D benefits most when it is co-developed with the detector technology (MAPS sensors, GEMS, etc.). This R&D could lag the primary sensor R&D by up to 6 months as an estimate, but should be considered as part of the system level approach to developing detector solutions. This is envisioned for a day one detector implementation.

## 14.2 Tracking

### 14.2.1 Low-Mass Forward/Backward GEM Detectors

Gas Electron Multipliers (GEMs) are a well-established MPGD detector technology that will soon be operational on a large scale in current NP and HEP experiments, *e.g.*, SBS tracker, ALICE TPC upgrade, and CMS muon upgrade. In a day-one EIC detector, they can provide cost-efficient fast tracking with good spatial resolution in the forward and backward regions because they can cover a large area. For the same reason, GEMs could also be employed as muon detectors at the outside of the detector.

The requirements on the momentum resolution are summarized in Sec. ???. Early simulations using EICroot for 10 GeV pions showed that for a detector geometry with vertex tracker, TPC, six forward MAPS disks, and with three GEM detector layers each placed in front and behind a RICH vessel, the momentum resolution with a 1.5 T magnetic field is  $\sigma_p/p \leq 1.5\%$  in the GEM acceptance region  $1.2 < \eta < 1.7$ , which is close to meeting the backwards requirements. In the GEM acceptance region  $1.7 < \eta < 3.1$ , the resolution is above 1.5% rising to about 3% at  $\eta = 3.1$ . Unlike the requirements, it was observed in the simulation that the resolution does not grow exactly linearly with momentum at higher momenta. For example, for a 40 GeV pion at  $\eta = 2.0$ , the resolution is  $\sigma_p/p = 4\%$ , which meets the backwards requirement.

The available material budget is 5% of  $X_0$ . In the active area of one foil-based Triple-GEM detector layer, the material accounts for 0.6% of  $X_0$ . Consequently, up to eight layers could

be installed in an EIC detector, e.g. four in front of a RICH and four behind it.

To bring low-mass GEM tracker technology to a state where it can be implemented in an EIC detector some R&D is still required: Improvements in the simulations and a second beam test.

The simulations need to be repeated and refined in the new fun4all simulation framework. Actually measured spatial resolutions and realistic support materials need to be incorporated properly into the simulation, in particular the materials in the TPC endplates, MAPS support structures, and the GEM support frames. Their impacts on forward/backward tracking performance and RICH seeding need to be fully quantified. This should take six months to a year to complete.

For the glued UVa prototype built at UVa different types of zebra strip connectorizations need to be tested. The mechanically-stretched FIT prototype with carbon fiber frames has been undergoing major refurbishments of its mechanics and its operation needs to be confirmed. If successful, both prototypes will be evaluated in a second beam test at Fermilab planned for Spring 2021 to finalize the spatial resolution studies and the overall performance characterisation of the prototypes.

### 14.2.2 Large Cylindrical $\mu$ RWELL Layer

One significant need for large cylindrical  $\mu$ RWELL layers in the central barrel region is to provide high angular resolution for barrel PID detectors. This additional tracking information can aid in the PID particle seed reconstruction, leading to better particle separation. For the scenario where a TPC is chosen as the central tracker option for the EIC detector and MAPS technology is adopted for the vertex tracker, we have identified two additional motivations for the need of a high-precision and fast-signal tracking detector to complement the inherent limitations of the TPC + MAPS as main tracking detectors in the barrel region. The first is to have the cylindrical  $\mu$ RWELL layer serve as a high space point resolution tracking layer to aid in the TPC field distortion corrections and TPC calibrations. The second need would have the cylindrical  $\mu$ RWELL serve as a fast (a few ns) tracking layer to compliment the relatively slow TPC and MAPS detector suite.

The simple construction of a  $\mu$ RWELL detector relative to a triple-GEM detector makes it an ideal MPGD technology to use in a cylindrical geometry. However there are still several R&D items related to its construction and performance that still need to be investigated. The first is related to the  $\mu$ RWELL technology itself. Efforts are needed to reduce the overall material budget of the current "standard"  $\mu$ RWELL. This involves the development of low mass amplification and readout structures. Ideally the cylindrical  $\mu$ RWELL would consist of one large foil and thus have no dead region in the active area. However, like with GEMs,  $\mu$ RWELL raw material is limited to a width of about 50 cm. To provide proper coverage for a barrel PID detector, several  $\mu$ RWELLS will be needed to form the full cylindrical layer. R&D is needed to determine best way to integrate the  $\mu$ RWELLS into one large cylindrical detector while minimizing dead regions in the active area.

Another area of R&D that is needed is related to the support structure of the cylindrical  $\mu$ RWELL layer. This involves developing large, high strength and lightweight cylindrical  $\mu$ RWELL supports to hold the detector's cylindrical shape. Additionally, end cap structures to hold the cylindrical detector in place need to be designed.

Several performance studies such as rate capabilities,  $dE/dx$ , tracking, and timing resolutions need to be carried out with the detector operating in a  $\mu$ TPC mode. These results will help to determine the proper readout electronics that are needed. The detector's cylindrical uniformity, discharge rate and aging properties will also need to be assessed.

### 14.2.3 Large Micromegas Barrel Tracker

The central region of the EIC detector requires very low material budget sub-detectors. Large area Micro-Pattern Gaseous Detectors are a possible solution to complement the silicon vertex detector. In particular, Micromegas detectors have been already successfully employed for building compact and light trackers, such as the Barrel Micromegas Tracker (BMT) of the CLAS12 experiment at the Jefferson Lab. Studies conducted within the Yellow Report effort showed that a barrel tracker made of MPGD tiles of a similar technology to the CLAS12 BMT one, would fulfill the requirements in terms of material budget and tracking resolutions. The CLAS12 BMT consists of six concentric layers of curved resistive Micromegas detectors where each layer is composed of three tiles of about 120 degrees width. The material budget of on tile in the active area is about 0.3% of  $X_0$ . From the experience of the CLAS12 BMT, the R&D on the EIC tracker will have two main objectives: reducing even more the material budget and simplifying production and integration.

In the CLAS12 BMT, the thickness of the self-supporting curved detector is determined by the ability to maintain the desired curved shape when constrained at both end by the carbon structure. The material thickness is  $\sim 200 \mu\text{m}$  FR4 for a radius of  $\sim 400$  mm. Reducing the thickness further requires R&D, initially of flat stretched detectors using Micromegas made on a Kapton film of  $50 \mu\text{m}$ . A detector will consist of two stretched foils (readout and drift) on a carbon frame with pillars to maintain and control the drift distance. Two additional external thin foils (made of  $10 \mu\text{m}$  polypropylene) will hold the gas pressure instead of the thin electrodes. The R&D should start with the choice of optimal material followed by a full size prototype to demonstrate the integration technique.

Curved detectors impose the use of specific sizes and tools for each curvature radius, thus making the production line more complicated. Excessive large area detector elements require numerous tooling to handle and to control the mechanical uniformity. A modular flat detector that would allow a higher production yield rate and possibly reduce the costs. The necessary R&D will need study a thin support structure to integrate this modular design.

On most MPGDs, copper is the chosen readout material with a thickness of at least  $9 \mu\text{m}$ . The use of lower mass material for the strip readout such as metalized aluminum of about  $0.4 \mu\text{m}$  requires R&D. The aluminum strips will have to be protected by a resistive layer to prevent vaporization of the metalized layer due to sparks.

The standard thinnest mesh used for large surface Micromegas detectors is a stainless-steel woven mesh of  $18\ \mu\text{m}$  wires. The alternative solution is electro-formed meshes (i.e Nickel of  $10\ \mu\text{m}$ ) which are expensive, very fragile and limited in size ( $\sim 30 \times 30\text{cm}^2$ ). Since 2018, in parallel with the use of laser techniques for etching “zigzag” patterns, a proof of concept has been made of laser etching holes on a small surface with different material (Cu, Al, Steel) of varying thicknesses ( $10, 15, 20\ \mu\text{m}$ ). R&D is needed to study this technique on larger surfaces to obtain large thin stretched aluminum foil with millions of holes to be used in the Micromegas bulk process.

Standard connectors made of plastic and brass contacts are quite heavy in term of material budget. If the active area is segmented, the multiplication of connectors can be a problem. Further R&D will test kapton-kapton connections with metal pixels clamped with light materials (carbon or 3D printed plastic).

#### 14.2.4 R&D Needs for Planar $\mu\text{RWELL}$ Detectors

$\mu\text{RWELL}$  is a promising MPGD alternative to the well established GEM or Micromegas detectors for tracking in EIC end cap regions. One significant advantage of  $\mu\text{RWELL}$  is that it combines its electron amplification stage ( $\mu\text{RWELL}$  foil) and the readout plane into a single device, making its fabrication simpler and more cost effective than GEM and Micromegas, specially for large area trackers. In addition,  $\mu\text{RWELL}$  are expected to be easier to operate and more stable under harsh radiation environment. These features makes large planar  $\mu\text{RWELL}$  an ideal option for EIC end cap trackers or as additional tracking layers in the Silicon - Gaseous hybrid configuration.  $\mu\text{RWELL}$  technology is also to be considered as amplification & readout layer option for TPC end cap readout or for transition radiation detectors (TRDs) required for electron identification.

As a relatively new MPGD technology,  $\mu\text{RWELL}$  have not been fully operated in an NP or HEP large scale experiment so far. Therefore, several area of R&D studies both generic and specific to EIC environment are still needed to fully validate this technology. Below is a list of a few identified R&D studies needed for EIC.

##### *Generic R&D: Performances and stabilities of $\mu\text{RWELL}$ technology*

- **Rate capabilities and spatial resolution studies:** The impact of the uniformity of  $\mu\text{RWELL}$  resistive layer (DLC), for large area detector on the rate capabilities and spatial resolution performances required detailed R&D studies. Rate limitation is not expected to be an issue with  $\mu\text{RWELL}$  in EIC environment because  $\mu\text{RWELL}$  can operate at a rate of  $100\ \text{kHz} / \text{cm}^2$ , exceeding by a few order of magnitude the expected rate in the EIC end cap regions. However, these rate and spatial resolution studies performed on small prototypes require validation in beam test for large area detectors.
- **Discharge and aging properties of  $\mu\text{RWELL}$ :** With the introduction of the resistive (DLC layer) as one of the key component of  $\mu\text{RWELL}$ , several studies have demonstrated that  $\mu\text{RWELL}$  is, if not spark-free, a robust spark-resistant detector. Several

studies also demonstrated the technology robustness against ageing in harsh particle environment. Additional R&D is required to study the best gas mixture for operation of the detector in a wide range of gain for applications at the EIC.

#### *EIC specific R&D: Low-mass & large $\mu$ RWELL trackers*

In addition to the generic R&D on  $\mu$ RWELL technology, high performance tracking with radiation length in the EIC end cap region required dedicated R&D studies and prototyping for  $\mu$ RWELL. The required R&D, listed below, have strong synergy with the ones described in section 14.2.2.

- **Development of low-mass & large area  $\mu$ RWELL:** R&D efforts are needed to minimize the material budget of the current standard  $\mu$ RWELL to keep the radiation length around 0.4% per tracking layers. This means the development of a rigid PCB free detector and lightweight and narrow support structure based on high strength-to-weight ratio materials such as carbon fibers rather than standard G10 fiberglass frames.
- **Development of low mass 2D readout plane:** Another important R&D area is the development of high resolution low mass and low channel count flexible 2D readout layers to be coupled with the  $\mu$ RWELL amplification layer. A few new ideas for such readout planes are already being investigated

#### 14.2.5 MPGD Readout for a Time Projection Chamber

In general, the TPC for the sPHENIX experiment can serve as a central tracking device in a Day-1 EIC detector. It has to undergo several upgrades and/or modifications in order to be optimized for the EIC program.

The sPHENIX TPC has been optimized to have a good momentum resolution which requires a good space point resolution for the tracks to be measured. The sPHENIX program does not require PID ( $dE/dx$ ) to be performed with the TPC. Hence, the optimization for the sPHENIX TPC has concentrated on very good IBF suppression which sacrifices good  $dE/dx$  resolution. For the EIC program this feature has to be restored. In the EIC era it is also expected that IBF will not have the same significant impact as during the RHIC program.

For the introduction of a “new” TPC R&D consideration will be in the readout electronics section.

#### **GEM and MicroMegas**

Prospects for R&D are in the restoration of good  $dE/dx$  resolution. This requires the investigation on GEM-properties and different gas choices which find the optimum of relatively good IBF suppression and optimum  $dE/dx$  resolution.

The MicroMegas technology has the best intrinsic IBF suppression and is a good candidate for good  $dE/dx$  resolution. However, stability issues have to be investigated and is an indicator for R&D in the next time for pursuing the MicroMegas option.

### Hybrid and Gating

A very promising candidate for combining very good IBF suppression and good energy resolution is the hybrid option of combining MicroMegas and GEMs into a single amplification stage. The MicroMegas acts as the main amplification stage and reduces the IBF to a minimum. The GEMs act as pre-amplifiers and provide the necessary field ratios to further suppress IBF. The combination of both technologies provide the robustness needed to operate in a high rate environment. First R&D projects have been already established and this amplification structure needs continued detailed investigation.

Gating grids that have been used in TPCs based on MWPC cannot be used in an EIC environment. The readout rate would not allow to cope with the luminosity requirement of the physics program. The requirement is that the TPC will be read out continuously which does not allow a traditional gating grid. Consequently, one has to investigate amplification devices that minimize IBF as described in the previous sections. R&D topics materialize in investigating gating device that work dead-time less. One of the option is to use a passive gating grid which “naturally” allows electrons to pass through the structure whereas ions will be attracted to a high degree and eliminated from the gas volume. The investigation of such structures has started and is ongoing.

### Readout Electronics

An issue present for a TPC in an EIC environment is the material budget in the forward region, in particular the electron direction. One can possibly overcome this problem by introducing alternative readout electronics which presents at this time the major contribution to the material budget, including all its required infrastructure.

Possible candidates for improved readout electronics is the TimePix or similar constructed microscopic readout structured front-end electronics. The options are (a) small sized TPC with microscopically sized readout pads,  $\mathcal{O}(10^{-3} \text{ mm}^2)$  and (b) a regular sized TPC with small sized readout pads,  $\mathcal{O}(0.1 \text{ mm}^2)$ .

Option (a) provides the registration of single electrons from the ionization trail of a track, acting as a form of digital camera. This would allow precise tracking and excellent  $dE/dx$  resolution. The R&D needs on this option are manifold, in particular gas choices and readout capabilities.

Option (b) would provide the registration of single clusters from the ionization trail of a track. This would allow precise tracking and excellent  $dE/dx$  resolution. The R&D needs for this option are in particular toward the adaptation of the microscopic readout structure of the front-end electronics and distribution over larger areas.

A further option for decreasing the material budget in the electron going direction of a TPC would be to investigate a single sided readout structure, i.e, having one readout plane

whereas the other cap of the TPC consists of a thin cathode. This option would require feasibility studies.

All the above mentioned R&D topics should be investigated to a mature level until the final design of a possible central tracker in form of a TPC is established.

## 14.3 Particle Identification

### 14.3.1 A Modular RICH (mRICH) for Particle Identification

The mRICH is designed for providing PID capabilities for EIC experiments for kaon and pion separation in momentum coverage between 3 to 10 GeV/ $c$  and electron and pion separation around 2 GeV/ $c$ .

mRICH detector R&D has been supported within the EIC eRD14 Consortium since 2015. The key components of a mRICH module include a radiator (Aerogel,  $\sim 10 \text{ cm} \times 10 \text{ cm} \times 3 \text{ cm}$ ,  $n = 0.03$ ), a Fresnel lens (with focal length range from 3" to 6"), a mirror set, and a photosensor. The characteristic longitudinal dimension of a mRICH module is from 15 cm to 25 cm depending on the focal length of the lens. A realistic GEANT4-based simulation for mRICH has also been developed and verified with beam test data.

Two rounds of detector prototyping and beam tests were completed with a focus on verifying the detector working principle and performance. The results from the first beam test (in 2016) have been published in NIMA 871,2017. The second beam test was done in 2018 and the data analysis is still ongoing. Two more beam tests with particle tracking capability are under preparation in order to quantify the mRICH PID performance and new photosensors. One is planned at Fermilab in March of 2021 for testing the mRICH with a LAPPD. The groups involved in this test are BNL, ANL, SBU and GSU. The other test is planned at JLab Hall D in summer of 2021 using secondary electrons in momentum range from 1 to 6 GeV/ $c$ . The participating groups for this test include DukeU, INFN, JLab, USC and GSU.

Two key components of a mRICH module are the Aerogel block and a photosensor with single-photon detection capability and fine-segmented pixel size ( $< 3 \text{ mm} \times 3 \text{ mm}$ ). The photosensor also needs to be working properly in high magnetic field.

To meet the needs of EIC experiments, a proper photosensor choice is critical. The planned beam test at Fermilab in March 2021 will help to evaluate the integration and performance with LAPPD. During the second mRICH beam test in 2018, three SiPM matrices were tested with varying cooling temperature range from -30 C degree to room temperature. This effort was led by Marco Contalbrigo at INFN, Ferrara. The radiation damage effects to SiPM performance is currently under study at INFN.

In regarding to the possible kinematic coverage in EIC experiments with mRICH modules, one can envision deployment in (i) the electron endcap, (ii) the hadron endcap in the range  $1 < \eta < 2.5$ , and (iii) the central barrel region assuming available space in radial direction  $\sim 20 \text{ cm}$  is available. The mRICH is considered as a day-1 detector.

Besides the two planned mRICH beam tests in coming year, there is a longer-term R&D effort for mRICH toward engineering design which includes: (a) high quality mirror and mirror assembly; (b) mRICH holder box engineering for reducing total weight, easy assembling, and projective installation; and (c) continued test with available photosensor options.

### 14.3.2 A Dual-Radiator Ring Imaging Cherenkov Detector (dRICH)

The dual-radiator Ring Imaging Cherenkov (dRICH) detector is designed to provide continuous full hadron identification ( $\pi/K/p$  separation better than  $3\sigma$  apart) from  $\sim 3$  GeV/c to  $\sim 60$  GeV/c in the ion-side end cap of the EIC detector. It also offers a remarkable electron and positron identification ( $e/\pi$  separation) from few hundred MeV up to about 15 GeV/c. The baseline geometry covers polar angles from  $\sim 5$  up to  $\sim 25$  degree (pseudorapidity range  $\sim 1.5 - 3$ ). Achieving such a momentum coverage in the forward ion-side region is a key requirement for the EIC physics program. Currently, the dRICH is, by design, the only hadron identification detector in EIC able to provide continuous coverage in RICH mode over the full momentum range required for the forward end-cap.

The dRICH baseline configuration consists of six identical open sectors. Each sector has two radiators (aerogel with refractive index  $n \approx 1.02$  and gas with  $n \approx 1.008$ ) sharing the same outward focusing mirror and instrumented area made of highly segmented photosensors ( $3 \times 3$  mm<sup>2</sup> pixels). The photosensor tiles are arranged on a curved surface in a way that minimises aberrations. The original benchmark configuration assumed  $\sim 160$  cm longitudinally long thickness but even a shorter, down to  $\sim 100$  cm, dRICH preliminary version features a performance that fulfills the above mentioned key physics requirements, indicating a remarkable flexibility of possible dRICH configurations.

To meet the EIC specifications, critical elements are an effective interplay between the two radiators and a proper choice of the photosensor, that should preserve single-photon detection capability inside a strong magnetic field. The dRICH focusing system is designed to keep the detector outside the EIC spectrometer acceptance, in a volume with reduced requests in terms of material budget and radiation levels. This feature makes dRICH a natural candidate for the exploitation of magnetic field tolerant SiPMs with an integrated cooling system to mitigate their significant dark count.

The dRICH design and performance have been studied through various means: a full Geant4 simulation (including an event based particle reconstruction processor) [1407], AI-based learning algorithms with Bayesian optimisation to maximise the hadron separation [1408], analytic parameterisations taking into account the optical properties of each component and the Geant4 simulated resolutions.

A small-scale prototype is being developed to investigate critical aspects of the proposed dRICH detector, in particular related to the interplay and long-term performance of the two radiators and the simultaneous imaging. The prototype vessel is composed by standard vacuum parts to contain the cost and support pressures different from the atmospheric one. This would allow efficient gas exchange and, in principle, adjustment of the

refractive index and consequent flexibility in the gas choice (in the search for alternatives to greenhouse gases). The prototype supports the usage of various type of photosensors, in particular SiPM matrices and MCP-PMTs.

A program has been initiated to study the potential of SiPM sensors for Cherenkov applications, aiming to an assessment of the use of irradiated SiPM in conjunction with the dRICH prototype. Promising SiPM candidates will be irradiated at various integrated doses (up to the reference value of  $10^{11} n_{\text{eq}} \text{ cm}^{-2}$ ) and will undergo controlled annealing cycles at high temperature (up to 180 C). The SiPM response before and after irradiation will be characterised and their imaging potential will be studied with a customised electronics. High-frequency sampling and Time-of-Threshold-based readouts will be compared. Of particular interest, the ALCOR front-end chip designed to work down to cryogenics temperatures, features low-power TDCs that provide single-photon tagging with binning down to 50 ps and potential counting rate well exceeding 500 kHz per channel. The irradiated sensors will be cooled down to the working temperature (down to -40 Celsius) to instrument an area suitable for imaging tests with the dRICH prototype. After an initial survey of the most promising candidates available on the market, a dedicated R&D could be pursued to meet the EIC specifications.

dRICH is considered as a day-1 detector given the EIC physics requirement for PID.

Besides the first SiPM irradiation campaign and the baseline prototype realisation in coming year, there is a longer-term R&D effort for dRICH toward engineering design which includes: (a) light and stiff support structure in composite materials (b) high quality mirror assembly; (c) cost-effective production of high-quality aerogel; (d) alternatives to the greenhouse gases; (e) magnetic field tolerant single-photon sensors; [1407] (f) dedicated readout electronics and cooling.

### 14.3.3 High-Performance DIRC

The high-performance DIRC (hpDIRC) is a proposed hadronic PID system for the barrel region of the central detector, capable of  $\pi/K$  separation with  $3\sigma$  or more up to at least 6 GeV/ $c$  momentum over a wide angular range. It can also contribute to  $e/\pi$  identification at lower momenta and provide a supplemental time-of-flight measurement.

The hpDIRC is a compact system with a radial thickness of less than 8 cm. The design is flexible, the radius and length of the bars can be modified without impact on the PID performance and the shape of the expansion volume prism can be selected for optimum position of the sensors in the magnetic field. It has low demands on the detector infrastructure (no cryogenic cooling, no flammable gases) and is easy to operate. The R&D of the hpDIRC is at an advanced stage. The PID performance estimate is based on test beam results, with excellent agreement between simulation and prototype data.

Several areas still require significant R&D. Optimizing the cost efficient design, matched to the final EIC detector layout, in simulation and validating it with the full system hpDIRC prototype is the most critical item. Another example is developing a procedure to disas-

semble the BaBar DIRC bar boxes and extract high-quality radiator bars for hpDIRC. In addition, the hpDIRC requires “external” R&D by EIC groups working on developing the fast readout electronics for small-pixel MCP-PMTs and on pixelated LAPPD sensors. This R&D is important for several other EIC detectors as well. Significant funding is needed soon to upgrade the PANDA DIRC prototype, which is being transferred from GSI to CUA/SBU, to fully equip it with new sensors and electronics, in order to validate the resolution and PID performance with cosmic muons and/or particle beams. A new Cosmic Ray Telescope (CRT) facility is being developed for the hpDIRC in collaboration between SBU, ODU, and CUA to study the prototype prior to possible tests in particle beams. This CRT will be available for use by other EIC systems.

The feasibility of reusing the BaBar DIRC bars vs ordering new radiator bars, and of using LAPPDs instead of commercially available MCP-PMTs, have to be determined since they have a large impact on the projected cost. The recently discussed potential increase of the PID momentum coverage, required by EIC physics, may require additional design improvements and utilizing possible post-DIRC tracking. Since the discussions about higher magnetic field options for the EIC detector are still ongoing, further investigation of a sensor solution for a possible 3T field is required. If the funding for the continuation of the R&D program is made available, we expect the hpDIRC TDR readiness to be achievable by 2024/2025.

#### 14.3.4 Photosensor: MCP-PMT and LAPPD

The choice of photosensors is essential for reaching the cost and performance goals of all EIC PID subsystems. The best possible photosensor solution for each detector component is driven by the detector’s specific operational parameters, naturally with cost optimization in mind. Ultimately, it would be preferable to use a common photosensor thus reducing development and procurement costs.

Microchannel-plate photomultipliers (MCP-PMTs) from commercial vendors have shown superior good timing and position resolution as well as high magnetic field tolerance but are generally far too expensive for large area coverage. The recently commercialized new type MCP-PMT using the atomic layer deposition technique as a large area picosecond photodetector (LAPPD) provides a promising cost-effective MCP-PMT for the EIC RICH detectors. Efforts have already been devoted to optimizing the LAPPD as photosensor of choice for EIC Cherenkov detectors (e.g. dRICH, mRICH, DIRC) as well as TOF applications.

A list of performance requirements of the photosensors for EIC Cherenkov based detectors is listed in Tab. 14.1.

R&D at Argonne National Laboratory using the Argonne MCP-PMT ( $6 \times 6 \text{ cm}^2$ ), a small format of LAPPD, has demonstrated all the required parameters, especially a magnetic field tolerance over 1.5 Tesla and less than a 1 mm position resolution with a pixel size of  $3 \times 3 \text{ mm}^2$ . To expedite the application of MCP-PMT for EIC Cherenkov detectors, a  $10 \times 10 \text{ cm}^2$  MCP-PMT fabrication facility is under construction to produce larger size, high-

Parameter	gas-RICH, mRICH, dRICH	DIRC
Gain	$\sim 10^6$	$\sim 10^6$
Timing Resolution	$\leq 800$ ps	$\leq 100$ ps
Pixel Size	$\leq 3$ mm	2–3 mm
Dark Noise	$\leq 5$ MHz/cm <sup>2</sup>	$\leq 1$ kHz/cm <sup>2</sup>
Radiation Hardness	Yes	Yes
Single-photon mode operation	Yes	Yes
Magnetic-field tolerance	Yes (1.5–3 T)	Yes (1.5–3 T)
Photon Detection Efficiency	$\geq 20\%$	$\geq 20\%$

**Table 14.1:** Performance requirements of photosensors for EIC Cherenkov based detectors.

performance MCP-PMTs. The commercial available LAPPD module has also achieved almost all the requirements except fine pixel size and magnetic field tolerance. Our industrial partner INCOM has adapted the Argonne MCP-PMT R&D results to develop low-cost pixelated LAPPDs for EIC Cherenkov detectors. Fine pixel size ( $3 \times 3$  mm<sup>2</sup>) is the urgent focus for commercial LAPPDs; bench and beam line tests are required for the LAPPD validation.

The Argonne MCP-PMT/LAPPD R&D is a generic effort. These photosensors can be widely used where large areas, low cost and high performance are needed. The required R&D is aimed at both near-term and future detector designs. Testing and performance results have already been shared with all EIC Cherenkov and TOF detector design efforts.

Rapid progress has been achieved on the Argonne MCP-PMT/LAPPD. Recently, a Gen-II LAPPD from INCOM was successfully tested at Jefferson Lab in a high rate, high background environment. Furthermore, a Fermilab beam line test of a pixelized MCP-PMT performance is planned for Spring 2021. To validate the LAPPD performance and apply this new technology to the EIC-PID subsystems, critical R&D is needed in the next two years. A bench test and multiple beam tests of Cherenkov prototype detectors using the MCP-PMT/LAPPD will need to be performed. For example, an mRICH beam test with LAPPD is mentioned in the mRICH section, and a gaseous RICH detector with Argonne  $10 \times 10$  cm<sup>2</sup> MCP-PMT is under development and planned for a beam line test as well.

### 14.3.5 R&D Needs for GEM-TRD/Tracker in the Forward Direction

Identification of secondary electrons plays a very important role for physics at the Electron-Ion Collider (EIC). A high granularity tracker combined with a transition radiation option for particle identification could provide additional information necessary for electron identification or hadron suppression. The scope of the project is to develop a transition radiation detector/tracker capable of providing additional pion rejection ( $> 10 - 100$ ).

A low mass radiator available for mass production is critical and various materials still need to be tested and optimized. This includes the optimization of a pseudo-regular ra-

diator using thin ( $\sim 12 - 15 \mu\text{m}$ ) Kapton foils and thin net spacers and a detailed test of available fleece/foam materials for TR-yield.

The transition radiation detector readout is based on well established GEM technology. The main difference to a GEM tracker as discussed in Sec. 14.2.1 is the thickness of the drift volume. In order to keep the electric field uniform a special field cage needs to be developed. This includes the mechanical design and construction of the field-/gas-cage to minimize a Xe-filled gas gap between radiator and the drift cathode.

The anode readout PCB layer of the current GEM-TRD prototype is based on a readout developed for the COMPASS experiment that is made of X and Y strips with a pitch size of  $400 \mu\text{m}$ . While this is optimal for a high occupancy environment, the large number of channels does increase the price of the readout electronics. Work is under way to develop a new concept of pad readout more suited for GEM-TRD applications. This novel large-pad readout PCB combines three crucial advantages: large readout pads to reduce the number of readout channels, excellent spatial resolution (despite the large pad size), and improved noise reduction. In this context we also plan to test a zigzag readout option.

The GEM TRD will need 2 HV lines, one for GEM amplification stage and the second to set a uniform drift field. To work in a high occupancy environment, the drift time needs to be minimized, providing fields of  $\sim 2\text{-}3 \text{ kV/cm}$ . For a 2 cm drift distance the HV should be at the level of 4-5 kV. Depending on the chosen grounding scheme, the total voltage including GEM stage, could be up to 8-9 kV. Optimization of HV for large drift distances is ongoing.

In the current tests the GEM TRD uses the readout electronics originally developed for the GlueX wire chambers. It consists of a preamplifier (GAS2 ASIC chip) with shaping times of  $\sim 10\text{-}12 \text{ ns}$ . The flash ADC has a sampling rate of 125 MHz and 12 bit resolution but provides only pipe-lined triggered readout. The total price is about \$ 50 per channel. The collected high resolution data recorded in test beams allow us to estimate the minimum needed shaping times of preamplifier, the FADC sampling rate and corresponding resolution. Development of a new FADC125 will be needed to enable the streaming of zero-suppressed data over fiber links. Another possibility would be to adopt other existing readout chip such as the SAMPA.

Over the past few years, the price of Xe has gone up significantly. Design and Development of a recirculation system to purify, distribute, circulate, and recover the gas, possibly based on a design of ATLAS TRD gas system at CERN will be necessary but will require only moderate R&D.

### 14.3.6 Gaseous Single Photon Detectors Based on MPGD Technologies

Single Photon Detectors (PD) for Cherenkov imaging devices represent a key challenge at EIC where minimum material budget and operation in high magnetic field is required. Gaseous PDs, which have played /are playing a major role in establishing and operating Ring Imaging Cherenkov (RICH) counters, satisfy these requirements and they represent

the most cost-effective solution when equipping large detector areas. So far, the only photon converter successfully coupled to gaseous detector is CsI with Quantum Efficiency (QE) limited to the far UV domain. Optimized detector architecture and operative conditions have to be established to ensure effective photoelectron extraction and control of the Ion BackFlow (IBF) to the photocathode. In particular, Micro Pattern Gaseous Detector (MPGD) technologies offer natural answers to IBF and photon feedback suppression and fast response, as tested by successful applications: the PHENIX HBD with triple GEM PDs [1409], the COMPASS RICH upgrade with Hybrid (THGEMS and resistive MICROMEGAS) PDs [1410], the windowless RICH prototype and test beam with quintuple GEM PDs [1411], the TPC-Cherenkov (TPCC) tracker prototype with quadruple GEM PDs [1412].

In the EIC context, gaseous PDs represent a valid option for the high momentum RICH with gaseous radiator. An R&D program for further developments of the hybrid approach in operation at COMPASS, aiming at making it fully adequate for the high momentum RICH at EIC, is ongoing, where the reduced space availability imposes a compact RICH. The whole program includes:

1. Establishing the hybrid PD for a windowless RICH approach to increase the number of detected Cherenkov photons;
2. Increasing the granularity of the read-out elements for fine resolution with limited lever arm; this item is well advanced;
3. Comparing the detector performance using either THGEM (as in COMPASS) or GEMs for the first multiplication stages;
4. Identification of an adequate front-end chip: studies for coupling the hybrid PD with VMM3 ASIC have been initiated;
5. Coupling of the THGEMs with a novel and more robust photoconverter by Hydrogenated Nano Diamond powder (HND) to overcome the limitation imposed by the use of CsI due to its chemical fragility in contaminated atmosphere or under ion bombardment, that imposes gain limitations and complex handling; very promising initial studies are ongoing.

The R&D will progress along these lines. The action items 1, 2, 3 and 4 are needed to make this technology adequate for its use at EIC and they can be completed within a couple of years. Establishing the novel photoconverter for gaseous PDs will take longer, due to the largely innovative character of the approach. If converging, it can represent an added value to the project. It can be selected for the EIC PDs according to its level of maturity when the detector design is finalized.

#### 14.3.7 Fast Timing Silicon Sensor: LGADs

The Low Gain Avalanche Detector (LGAD) with internal gain [1238,1413–1417] is an ultra-fast silicon sensor technology, which has recently been chosen for constructing a fast-

timing layer in the forward rapidity region of the CMS [1418] and ATLAS [1341] experiments at the high-luminosity (HL) LHC starting in 2027. The new timing layers will help the experiments mitigate significantly larger pileups of proton-proton interactions (up to about 200) by providing 4-D vertex reconstruction, and serve as a time-of-flight system for hadron identification in QCD and heavy-ion physics.

Traditional  $n$ - $p$  silicon sensors with gains provided by external bias voltages can provide a typical time resolution on the order of 150 ps. The LGAD silicon sensors have an intrinsic gain of 10–30 provided by a special implant layer to generate a strong electric field locally and trigger avalanches. This internal gain helps the LGADs to achieve a low-jitter fast-rising pulse edge and overcome many other noise sources that enable high precision timing measurements for MIPs. LGAD sensors of 35–50  $\mu\text{m}$  in active area thickness can achieve a typical time resolution of about 30 ps. The handling wafer has a typical thickness of 150–300  $\mu\text{m}$ .

With excellent timing and position resolutions, the LGADs provide an attractive option for constructing a compact, multi-layer system to simultaneously provide TOF-PID and trajectory reconstruction as part of the tracking system. In addition, the LGADs have several other key advantages of being highly tolerant to strong magnetic fields (up to  $B \sim 4$  T), radiation-hard (up to  $\sim 2 \times 10^{15}$   $n_{\text{eq}}/\text{cm}^2$ , compared to the expected level of radiation of  $\sim 10^{11}$   $n_{\text{eq}}/\text{cm}^2$  at EIC) and compact (flexible for integration). To fulfill the requirements for EIC physics, there are three main areas of R&D needed, which are discussed below:

- **Time resolution:** while LGAD silicon sensors used by CMS and ATLAS can provide a time resolution of 30–50 ps, particle flight distance at EIC detectors is likely to be much shorter due to tight space constraints. Therefore, a total time resolution (including readout electronics) of 20 ps or better per layer is desired to meet the PID requirement at low and intermediate momentum regions. The jitter contribution to the time resolution is directly related to the signal slew rate, which is inversely proportional to the sensor thickness. Reducing the thickness from 50  $\mu\text{m}$  to 35, 25 and even 20  $\mu\text{m}$  will not only improve the jitter but can also suppress the Landau noise. Note that to maintain the total charge collection for a large signal, both internal and external gains applied also need to be optimized. Recent R&D work on 35  $\mu\text{m}$ -thin LGADs shows a time resolution of about 20–25 ps per layer, a promising step toward achieving the PID requirements for EIC [1419].
- **Fill factor and position resolution:** to serve as (part of) a tracking system, a position resolution much better than the 1 mm pixel size has to be accomplished to be competitive to other types of silicon pixel and/or strip sensors that are designated for position measurements. The current limitation lies in the approximately 50  $\mu\text{m}$  width of the intra-pad no-gain region, which is needed to protect against early breakdowns. Smaller pixel sizes would lead to too low fill factors, or loss of acceptance. The CMS and ATLAS timing layers have a fill factor of 85% per disk, with the two-disk system compensating for a 100% acceptance.

To achieve better position resolution (beyond 1 mm pixel size), two viable solutions are present. Trench-isolated (TI) LGADs is capable of reducing the no-gain region

down to a width of only a few  $\mu\text{m}$ , essentially eliminating it to achieve 100% fill factor. All readout schemes can be kept the same as standard LGADs. For AC-coupled LGADs, segmentation is not done on the silicon sensor but at metallic readout contacts sitting on top of a dielectric layer, reading out induced charges. The fill factor is effectively 100%. The signal pulse is shared among several adjacent pads, further improving its position sensitivity. The metallic readout pads can be fabricated into pixels, strips or any shape desired. The AC-coupled LGADs are also considered as an option for a high precision timing Roman Pots, where R&D needs are discussed in Sec. 14.5.1.

- **ASIC readout chips:** The needs for better timing performance and finer granularity also pose significant challenges to the readout electronics and specifically to the ASIC readout chips. Present ASIC chips designed for CMS and ATLAS timing detectors have a jitter on the order of 20–30 ps, and a pixel granularity of  $1.3 \times 1.3 \text{ mm}^2$ . Reduced granularity will make it more difficult to fit all the circuit components within the available space, and is also likely to lead to significantly increased power consumption due to increased total number of channels. Based on architectural designs of CMS and ATLAS timing layers, an ASIC chip with a size of  $0.5 \times 0.5 \text{ mm}^2$  is feasible to achieve and would meet the requirements set by the Roman Pot detector. A finer granularity, likely required for the tracker application, would require dedicated efforts of new architectural designs and adoption of more advanced silicon fabrication processes.

## 14.4 Electromagnetic and Hadronic Calorimetry

### 14.4.1 Tungsten Scintillator Calorimetry

Tungsten scintillator (W/Scint) calorimetry can play a major role in many of the regions of an EIC detector, covering a rapidity range from  $\sim -2.0$  to  $4.0$ . It offers a very compact design in terms of its short radiation length, thus limiting the total length of the calorimeter, as well as providing a small ( $\sim$  few cm) Moliere radius which limits the lateral extent of the shower, therefore allowing good separation between neighboring electromagnetic showers as well as limiting the overlap with hadronic showers. In addition, the energy resolution can be tuned by changing the sampling fraction and sampling frequency to meet the different requirements in the various rapidity regions.

There are primarily two candidates that are being considering for a W/Scint calorimeter for EIC. One is a tungsten scintillating fiber (W/SciFi) SPACAL, which consists of a matrix of tungsten powder and epoxy with embedded scintillating fibers. This technology is used for the sPHENIX barrel EMCAL that consists of more than 6K individual 2D projective absorber blocks. The blocks are read out using SiPMs that are coupled to the blocks using short light guides. This calorimeter is currently under construction and is expected to be completed by the end of 2021.

The technology for producing the blocks, which was originally developed at UCLA [1420],

has now been developed to produce these blocks on an industrial scale at the University of Illinois [1301]. Therefore, no further R&D is required for producing the blocks. However, the method used for reading out the blocks with SiPMs could be improved. This would include the use of large area SiPMs to provide more photocathode coverage and eliminate the boundaries between the light guides which leads to non-uniformities in the energy response. It is planned to refurbish the sPHENIX EMCAL with this type of readout for use as a Day-1 detector at EIC.

The second W/Scint technology that is being considered for EIC is a tungsten shashlik (W/Shashlik) design. Many shashlik calorimeters have been built and used by many experiments. A W/Shashlik design offers some distinct advantages but also poses some significant challenges. In addition to being compact and being able to tune the energy resolution as in the W/SciFi, a W/Shashlik offers the possibility of improving the light collection and providing better uniformity by reading out each individual WLS fiber with its own SiPM. This allows a better determination of the shower position and the possibility of using this information to correct for non-uniformities in the energy response. However, the mechanical properties of tungsten make it difficult to machine and requires using a slightly less dense alloy of tungsten, thereby increasing the radiation length and Moliere radius. Also, making a shashlik calorimeter projective makes the mechanical design and assembly more complicated.

Both calorimeter technologies use SiPMs as photosensors, but it is well known that these devices are subject to radiation damage, particularly neutrons. The development of more radiation hard SiPMs would be of great benefit for calorimetry at EIC, as well as for many other detectors, but developing radiation hard SiPMs would take several years of R&D and require a substantial investment with the manufacturers.

#### 14.4.2 SciGlass for Electromagnetic Calorimetry

Nearly all physics processes require the detection of the scattered electron in the electron endcap (forward rapidities). The requirement of high-precision detection is driven mainly by inclusive DIS where the scattered electron is critical for all processes to determine the event kinematics. Excellent electromagnetic calorimeter resolution of better than  $2\%/\sqrt{E}$  is required at small scattering angles, while very good resolution is acceptable at larger angles. For hadron physics measurements with electromagnetic reactions, the most common precision calorimeter material of choice has been lead tungstate,  $\text{PbWO}_4$  (PWO). However, the production of crystals is slow and expensive.

The technology goal of SciGlass R&D is to develop a scintillating glass for homogeneous electromagnetic calorimetry. SciGlass is a radiation hard material optimized to provide characteristics similar to or better than  $\text{PbWO}_4$ . SciGlass fabrication is expected to be cheaper, faster, and more flexible than  $\text{PbWO}_4$  crystals. SciGlass is being developed by Scintilex, LLC in collaboration with the Vitreous State Laboratory at CUA. Tremendous progress has been made in the formulation and production of SciGlass that improves properties and solves the issue of macro defects. Scintilex has demonstrated a success-

ful scaleup method and can now reliably produce glass samples of sizes up to  $\sim 10$  radiation lengths. Simulations combined with initial beam tests at photon energies of 4-5 GeV suggest that high resolution competitive with  $\text{PbWO}_4$  can be reached for  $> 15X_0$ . SciGlass has excellent radiation resistance (no damage up to 1000 Gy electromagnetic and  $1015 \text{ n/cm}^2$  hadron irradiation, the highest doses tested to date), response time of 20-50 ns, and good transmittance in the near UV domain (74% at 440 nm). The SciGlass insensitivity to temperature is also a clear advantage over  $\text{PbWO}_4$ , which has a dependence of about 2-3%/°C and has to be continuously monitored. The present samples have a density up to  $5.4 \text{ g/cm}^3$ , radiation length ( $X_0$ ) of 2.2-2.8 cm, and a Moliere radius of 2-3 cm.

The areas of needed R&D for SciGlass include the final formulation optimization, scale up to block sizes  $\gtrsim 15X_0$ , and beam tests to establish characteristics like energy resolution. The most critical items are to demonstrate scale up to block sizes  $\gtrsim 15X_0$  and to establish SciGlass characteristics with beam tests. The evaluation of SciGlass as particle detector has been shared in part with activities on  $\text{PbWO}_4$  crystals for the electron endcap calorimeter, *e.g.* simulations, radiator characterization and prototype construction, commissioning, and beam tests. The approximate timeline for completing the SciGlass R&D is about 1 year assuming R&D funds are available. The goal is to be ready for a day-1 detector. SciGlass could also be available for future detector upgrades.

#### 14.4.3 Hadronic Calorimetry

Optimum jet reconstruction will require the use of several detector systems (tracking, EMCAL and HCAL) but is a main driver for hadronic calorimetry. As such, the requirements for the resolution of the hadronic calorimeter are different for the endcaps and the barrel region. The most challenging is the forward region of hadronic endcap where pure calorimetric measurements starts to outperform particle-flow like approaches due to the degradation of tracker performance. For the electron endcap and the barrel region, only modest hadronic energy resolution is required from calorimeter system (ECAL+HCAL). It is believed that these systems can be built using standard construction methods and no additional R&D efforts are needed. For the hadronic endcap, covering the rapidity range from  $\sim 1.0$  to 2.5 where better energy resolution is required, modest R&D efforts will be needed to improve the performance of these systems. For example, the STAR Forward Calorimeter, which is currently being constructed using a new and efficient method developed at UCLA [1322, 1421], would require improvements for a more efficient light collection scheme due to the relatively low energy of hadrons in this region of hadronic endcap at EIC.

At more forward rapidities in the hadron endcap, it is important to have the best possible performance of the calorimeter system. The main constrain at EIC is the lack of space for a high sampling fraction and high sampling frequency calorimetry system, both of which are required to achieve good resolution. Developing a high resolution calorimetry system for this region will require significant R&D efforts. At present we believe that there is only one technology option that may be suitable for this region, which is a very high density, approximately compensated fiber calorimeter, which would serve as both the EMCAL and

HCAL with a common readout.

To date, R&D for hadron calorimetry for EIC has had a low priority and very limited funding. The synergy between the STAR Forward Upgrade and eRD1 R&D activities lead to construction and testing of two prototypes forward calorimeter systems. One was a compensated system with an EMCAL section built with a W/ScFi technique followed by hadronic section made of a lead scintillator sandwich. The other non-compensated version had a lead scintillating shashlyk EMCAL and an iron scintillator sandwich HCAL section behind. A later version was a final design prototype for STAR Forward Calorimetry system. Both versions had SiPM readouts and both were tested at FNAL. The performance of both systems led us to believe that the initial requirements for the EIC calorimetry system can be reached with only the modest improvements mentioned above. However, due to lack of funds, both versions of the prototypes had limited size which lead to significant transverse leakage and required an extrapolation of the test results to larger size detectors. This should be avoided for future EIC targeted R&D.

A common theme for the R&D needs for both an EMCAL and HCAL at EIC is the readout with SiPM sensors covering a large surface area. This may be challenging at the forward rapidities of the hadron endcap due to the relatively low light yield of hadron calorimeters (compared to EM calorimeters), and the high neutron fluences in this region, which will lead to significant degradations in SiPM performance. Operation of the STAR Forward Calorimetry system in the 2022 500 GeV RHIC run will be very valuable because the conditions at STAR will be very close to those in the EIC hadron endcap in terms of neutron fluxes. Future R&D is therefore needed in this direction.

#### 14.4.4 CSGlass for Hadronic Calorimetry

Achieving high-quality science at nuclear physics facilities requires the measurement of particle energy with excellent calorimeter energy resolution. Particles that produce EM showers can be detected with high precision. However, there is a need to improve the energy resolution of hadron calorimetry. The technology goal of CSGlass R&D is to develop a scintillating glass for improving hadronic calorimeter resolution, which is desired for measurements of hadronic jets.

CSGlass is optimized for the dual readout approach, where one compares the signals produced by Cherenkov and Scintillation light in the same detector. This approach has been a promising method to achieve better performance for hadron calorimeters. Homogeneous crystals are an option, but have to be outfitted with optical filters, which results in insufficient Cherenkov light detection. Crystals are also prone to radiation damage, time consuming to manufacture, and relatively expensive. In comparison, radiation-hard glasses can be tuned for favorable Cherenkov/Scintillation signal ratio, eliminating the need for optical filters, and thus offer great potential for both precision hadron calorimetry and significant cost reductions if competitive performance parameters can be achieved. CS-Glass is derived from SciGlass and expected to be similarly resistant to EM and hadron irradiation up to 1000 Gy and  $10^{15}$  n/cm<sup>2</sup>, the highest doses tested so far. The CSGlass

interaction length is comparable to crystals and should allow for small tower size. The anticipated space for the homogeneous calorimeter configuration could be similar to the binary system and may provide better resolution.

The areas of needed R&D for CSGlass include the demonstration of CSGlass with sufficient UV transparency for Cherenkov light collection, clear separation of Cherenkov and Scintillation light of sufficient intensity (slow scintillation,  $> 500$  nm beneficial), low cost, and characterization of CSGlass in the lab and with test beam R&D prototypes. The most critical items are the formulation optimization and production of CSGlass test samples. Some of the CSGlass R&D is shared with SciGlass and  $\text{PbWO}_4$  crystals for EM calorimeters. The approximate timeline for completing the CSGlass R&D is  $\sim 3$  years assuming R&D funds are available. CSGlass could be ready for future detector upgrades.

## 14.5 Auxiliary Detectors

### 14.5.1 Roman Pots and LGAD Technology

A Far forward proton spectrometer, based on the well known technique of Roman Pots, is an integral part of an EIC detector system, essential for the success of its physics program (see Secs. 8.4 and 8.5), and thus is envisioned as a subsystem for a day-one EIC detector. A forward proton spectrometer will provide a critical contribution to the study of inclusive diffractive and exclusive production processes in coherent  $e+p$  and  $e+D$  collisions. Furthermore, it is essential to provide a veto of incoherent background to measurements of exclusive meson production in  $e+A$  collisions, see Sec 8.4.6. An innovative silicon technology, based on *Low Gain Avalanche Diode (LGAD)*, is proposed to instrument the Roman Pots, as well as other EIC detector subsystems, as it has the potential to combine in a single sensor fine spatial resolution and precise timing. More specifically, by AC-coupling the metal layer (that is connected to the readout electronics) to the active silicon layers of an LGAD (*AC-LGAD*), the sensor can be finely pixelated (in the order of few tens of microns) to reach a spatial resolution similar to conventional pixel trackers, and its timing performance can be maintained compatible to the one of standard LGADs, i.e.  $\approx 30$  ps. While the LGAD technology is established and is being used by the ATLAS and CMS experiments at the LHC for their timing subsystems for the High Luminosity phase (HL-LHC), the AC-LGAD technology is instead under intense development in US, Europe and Japan.

Simulations show that  $500 \mu\text{m}$  square pixels and 30–40 ps time resolution are sufficient to achieve the desired physics performance. In more detail, simulations showed that the detector pixels must be at least as small as  $500 \times 500 \mu\text{m}^2$  to make the smearing contribution negligible with respect to the other effects at 275 GeV. Currently available LGAD sensors for the HL-LHC have  $1.3 \times 1.3 \text{ mm}^2$  pixels, which would provide smearing contributions outside of the Roman Pots specifications. The  $500 \times 500 \mu\text{m}^2$  pixelation can be achieved in AC-LGADs, and, with reasonable effort, in the associated readout electronics, i.e. by small modifications of the ASIC developed for the ATLAS timing detector. It must be noted that a space resolution an order of magnitude smaller than the pixel pitch can be

achieved by using the information from the signal sharing between neighboring pixels, with a substantial advantage in power and real estate in the readout electronics. At the same time, in the high acceptance configuration, the impact of the angular divergence on the smearing of the transverse momentum becomes comparable to the contribution from the crab cavity rotation of the beam bunch. To remove the smearing contribution from the crab cavity rotation, in addition to further rejecting the backgrounds, fast timing is required in the range  $\approx 30 - 40$  ps. Such timing performance has been demonstrated by the LGAD sensors developed for the HL-LHC, and it has been recently shown to be achievable by AC-LGAD sensors too. In addition, such sensors must be placed as close as possible to the beam, therefore their inactive area at the edge of the sensor must be minimized, and must be  $\leq 100 \mu\text{m}$ . Laboratory tests showed that the inactive edges of LGADs can be reduced to about  $50 \mu\text{m}$ , i.e. to values compatible with the Roman Pots specifications.

In summary, the novel AC-LGAD sensor technology has recently been shown to meet both spatial and timing performance as well as small edge specifications for its application in Roman Pots. However, further work is needed to fully characterize the AC-LGAD performance, test their robustness and optimize their design for the specific implementation in Roman Pots. For instance, the intrinsic sensor gain and thickness can be optimized to improve the time resolution, finer spatial resolution can be achieved by exploiting the signal sharing properties of neighboring pixels, and larger area prototypes with advanced designs need to be fabricated and tested. Most critical at this point in time is the development of an architecture of the readout electronics, and more urgently the ASIC R&D.

Given the need of fast-timing at EIC and the growing interests in LGAD technology to meet those needs (see time-of-flight detector, 4D tracker, TOPSiDE detector concept,  $4\pi$  hybrid LGAD/SOI tracker, preshower), a collaborative effort will be extremely beneficial. An international consortium is being formed to accomplish the above-mentioned R&D tasks.

In a time-frame of 2 years, thanks to prototyping and laboratory testing, the AC-LGAD can be confirmed as the baseline technology for Roman Pots, while an optimization of the sensor readout can be achieved in a 5 year time scale. In a 2 year timeframe the readout architecture can be developed and its viability demonstrated via simulations as well as laboratory tests based on existing prototypes for the LHC, while in a 5 year time scale a more detailed design of the ASICs and the readout chain, including initial prototyping, can be achieved.

### 14.5.2 Zero Degree Calorimeter

The ZDC will serve critical roles for a number of important physics topics at EIC, such as distinguishing between coherent diffractive scattering in which the nucleus remains intact, and incoherent scattering in which the nucleus breaks up; measuring geometry of  $e + A$  collisions, spectator tagging in  $e + d/{}^3\text{He}$ , asymmetries of leading baryons, and spectroscopy. These physics goals require that the ZDCs have high efficiency for neutrons and for low-energy photons, excellent energy,  $p_T$  and position resolutions, large acceptance

and sufficient radiation hardness.

There are several possible approaches to achieve high energy and position resolution in a calorimeter. For example, the ALICE FoCal [1348], is silicon-tungsten (Si+W) sampling calorimeter with longitudinal segmentation. Low granularity layers are used for the energy measurement while higher granularity layers provide accurate position information.

From simulations the photon energy resolution for FoCal is estimated to be  $\sigma_E = 25\%/\sqrt{E} \oplus 2\%$ . This is comparable to that expected for the sPHENIX W/SciFi calorimeter. Other technologies that would provide suitable resolution include crystals (PbWO<sub>4</sub>, LYSO, GSO, LSO), DSB:Ce glass, and W/SciFi. PbWO<sub>4</sub> crystals and DSB:Ce glass have been developed and characterized by the eRD1 Consortium and the Neutral Particle Spectrometer project at Jefferson Lab. Tests have shown energy resolutions of  $\sim 2\%/\sqrt{E}$  for photon energies  $\sim 4$  GeV [1349].

To identify neutrons, the ZDC needs a hadronic section with a resolution of  $\sigma_E < 50\%/\sqrt{E}$  with an angular resolution of at least  $3 \text{ mrad} / \sqrt{E}$  is desired. Cerenkov calorimeters, which measure only the high energy component of the showers, give excellent position resolution and tight containment but are non-compensating and so somewhat non-linear. Sampling all charged particles produced gives better energy resolution at the cost of worse lateral containment. We seek to exploit both techniques to maximize both the energy and position resolution of the ZDC. This could be done by using the quartz fibers developed for the LHC ZDCs, [1351], with traditional scintillators.

In order to detect coherent collisions it is necessary to veto events in which soft photons are emitted from an excited nucleus. For <sup>208</sup>Pb, every bound-state decay sequence has at least one photon with an energy of at least 2.6 MeV. For a beam momentum of 275 GeV/c, 20% of these decay photons (with minimum energy 455 MeV) are detectable in the ZDC aperture of  $\sim 4.5$  mrad. In order to detect such photons from nuclear excitation it is important that the ZDC have the largest possible aperture. It is possible that a 2nd IR design will allow a larger ZDC acceptance.

The meson structure research for the EIC has shown the need of a tracker, in combination with the ZDC, to be used as a veto detector for  $\pi^-$  for an efficient measurement of the  $\Lambda \rightarrow n + \pi^0$  channel. Besides this main purpose, adding a tracker could improve the reconstruction of charged particles in the ZDC for other different channels. A non-expensive and feasible option is the use of scintillating fibers (SciFi) as a tracker detector.

The number of spectator neutrons is predicted to have somewhat correlation with the collision geometry. The required performance of the detector to identify the coherence of the collision is under development using the BeAGLE simulation [1101]. Some of performance parameters are under ongoing study. The optimization of the performance requirements is included in the scope of the development based on the requirements known as of now as listed below.

A large acceptance (e.g.  $60 \times 60 \text{ cm}^2$ ) to establish good identification efficiency between coherent and incoherent collisions is necessary for vetoing spectator neutrons from nuclear breakup. This large acceptance is also required to determine the collision geometry [1356]

. For studying very forward production and asymmetry of hadrons and photons, a large acceptance is also important. The EIC aperture of  $\pm 4$  mrad gives  $p_T < 1\text{GeV}/c$  coverage for 275 GeV hadrons and photons, which covers the transition from elastic/diffraction to incoherent regime; for low-energy hadron beam the acceptance in terms of  $p_T$  is more limited e.g.  $p_T < 0.4\text{GeV}/c$  coverage for 100 GeV beam.

Due to the strong  $\beta$  squeeze  $< 1$  meter for the high luminosity, a beam spread of  $\sim 20$  MeV and  $\sim 1$  cm of the hadron beam angular divergence is induced. Thus the position resolution of neutron in sub cm won't help. 1 cm position resolution provides  $300 \mu\text{rad}$  angular resolution, which can be translated to transverse momentum resolution  $p_T \sim 30$  MeV/ $c$  of 100 GeV spectator neutron.

The minimum energy resolution  $\Delta E/E \sim 50\%/\sqrt{E(\text{GeV})}$  to distinguish number of spectator neutrons from 20 to 30 for collision geometry determination. In order to accommodate a single MIP track to 30 spectator neutrons, wide dynamic energy range in the readout electronics is required.

It is anticipated to be a sampling type calorimeter with a sufficient longitudinal size of  $\sim 10$  interaction length [1356]. It is also required to have a sufficient transverse size of  $\sim 2$  interaction length to avoid transverse leakage of the hadron shower and to achieve good hadron energy resolution.

### 14.5.3 Superconducting-Nanowire Particle Detectors

Superconducting Nanowire Single-Photon Detectors (SNSPDs) have become the dominant technology in quantum optics due to their unparalleled timing resolution and quantum efficiency. The Argonne National Laboratory group, supported by eRD28, is currently investigating the pathway to transform these sensors into a novel particle detector for the EIC. The sensors can operate in magnetic fields greater than 5 T at a high rate with high efficiency, and with a timing resolution as low as  $\lesssim 20$  ps. The R&D effort aims to produce a small ( $\text{mm}^2$ ) superconducting nanowire pixel array for detecting high energy particles. This first of its kind detector will have the flexibility to be used in multiple far forward detector systems. It can extend the EIC's scientific reach beyond what is possible with contemporary technology for far-forward detection.

Superconducting nanowire detectors have multiple characteristics that make them a uniquely capable detector technology for applications at the EIC. (a) Superconducting nanowire detectors are high-speed detectors and have time resolutions typically on the order of 20 ps scale, with a current record of 3 ps. (b) A meandering wire layout allows for small pixel sizes and allows for  $\mu\text{m}$  position resolution if needed. (c) Single pixels can operate efficiently at high-rates in strong magnetic fields (up to 5 T) [1422]. (d) Edgeless sensor configurations are a possibility, with the sensitive element positioned to within a few 100 nm of the substrate edge, eliminating dead material in between the particle beam and the detector. (e) Wide choice of substrate material – the detectors can be fabricated on membranes as thin as few  $10 \mu\text{m}$ , further cutting down on material thickness. (f) Radiation hardness allows for a longer service cycle of detectors operating near the beam and

interaction regions.

The EIC R&D committee identified four applications at the EIC for future R&D [?]. (1) A Roman pot detector in the forward region about 35 meters or more from the interaction point to tag low momentum transfer recoiling ions. (2) An integrated detector inside the cold bore of superconducting magnets for the forward ion detection would provide tracking in regions of high magnetic fields. This would include placing the detector inside the magnet and integrating it with the magnet's cooling system, eliminating the need for a separate cryogenic system. Further applications include (3) placing the detector in front of the ZDC detector and around the forward ion spectrometer section, filling in the detection gaps where radiation hard detectors with excellent position and timing resolution are needed. Finally, (4) use in an electron detector for a Compton Polarimeter, because the high rate capability, allows the nanowire detectors to handle the 100 MHz beam pulse rate to measure the azimuthal asymmetries needed to extract the beam polarization.

Superconducting nanowire sensors are an entirely new technology for high energy particle detection in nuclear physics [?]. This unique opportunity comes with some R&D needs to leverage the full potential for applications at the EIC. Further R&D includes optimizing the wire parameters or high energy ion detection, developing cryogenic bias and readout ASICs for high channel count tracking detectors, and design integration of superconducting nanowire sensors into the cold bore of superconducting magnets. The required R&D can be completed within the next few years, depending on the specific application.

## 14.6 Data Acquisition

### 14.6.1 Streaming-Capable Front-End Electronics, Data Aggregation, and Timing Distribution

A streaming readout is the likely readout paradigm for the EIC, as it allows easy scaling to the requirements of EIC, enables recording more physics more efficiently, and allows better online monitoring capabilities. The EIC detectors will likely be highly segmented, leading to a large number of readout channels. At the same time, multiplicities and pile-up are likely less demanding than other experiments like sPHENIX. The physics case is very wide, and many analysis will be systematics dominated. It is therefore crucial to minimize systematic effects from the readout, for example trigger biases. Further, minimally biased data recording allows to data-mine for novel physics later in the EIC life-cycle. A streaming readout system further reduces scaling choke-points and critical failure points like online event building.

A working readout system is crucial for any data taking and must be ready at day-1. In fact, ideally, prototypes should be ready for detector tests well ahead of first beam. R&D is required in multiple areas:

Streaming readout requires the distribution of clock information. While crucial for successful data taking, this is a less demanding task than the distribution of triggers, and a

scheme similar to the one at sPHENIX is a likely solution. This approach will be tested by sPHENIX well ahead of EIC completion, and other test beams will likely use other timing systems. Front end electronics need to be read out via some sort of data collection hardware. These will likely be evolutions of already available components like the FELIX cards, and existing hardware can be used during test beams until the final hardware iterations are available. Both of these research topics are rather low risk.

Of higher risk is the development of suitable front-end electronics. Here, possible front-end readout ASICs have to be matched to the detector requirements. While existing ASICs cover many use cases, it is not clear yet if the requirements of the final detector configurations for the EIC are covered by current capabilities. History tells us that timelines for development of completely new ASICs is 6 or more years, while modifications of existing designs might be done in 3+ years. It is therefore paramount that cases where new readout ASICs are required are identified soon, and whether a readout is at all feasible within the given constraints. This puts this research into the high-risk and high priority category. We want to note here that this risk is not unique to a streaming readout—in fact, most high-performance ASICs today fit a streaming readout solution better than a triggered one—and is indeed a risk for the readout in general, independent of chosen paradigm.

The research intrinsically touches upon a wide range of other detector projects. It is very likely that data collection hardware is shared between most detector components. For front-end electronics, designs will be shared as much as possible.

### 14.6.2 Readout Software Architecture, Orchestration and Online Analysis

In addition to readout hardware, it is important to develop and test protocols and software to provide a stable, high-performing readout. This includes a scalable platform, both in channel count and processing capabilities, and the inclusion of analysis into the online system as much as possible. The system must be resilient against errors in the FEE to enable an overall highly efficient data taking. High quality, high level monitoring will secure the recording of high-quality data, reducing time-to-publication. Similar to the hardware, prototype designs should be ready well in advance to support test beam times, and to collect experience necessary to build the online analysis.

The development of software and protocol components must go hand in hand with the hardware. As the highest priority, it is important to define a logical protocol for data exchange. This will enable groups to develop interoperable electronics and software components early in the development cycle. The community is actively working on this issue, but revisions will be likely in the years to come.

To achieve optimal usage of beam times, techniques must be developed to make the readout resilient against FEE errors (e.g. Single Event Upsets) without requiring a full stop and restart of the system. This issue is exacerbated by the high channel count and density. In a similar fashion, it is an open research question how to best address bandwidth restrictions. Since the data rate is governed by a stochastic process, they will have peak rates substantially above the average data rate, with almost no ceiling. While large memory buffers

can mitigate this by smearing out peak rates over time, the system must still be able to handle buffer overflows. For both problems, R&D is required to develop a framework and control algorithms that react in a predictable and reconstructable way, so that overall detector/DAQ efficiencies can be extracted. Such a system must be available essentially at first beam, with improvements later in the life cycle.

The amount of data collected and the changing landscape of compute infrastructure to a federated model makes it necessary to rethink data storage and retrieval to achieve efficient usage of the computing resources. Here, a flexible software layer must be developed to isolate the analysis code from the changing infrastructure. While a first solution is required at first beam, it is likely that this will evolve together with the compute infrastructure during the EIC lifecycle. Connected to this issue is the integration of analysis into the online and near-online processing to maximize data quality. This includes the efficient handling of calibration procedures, and minimization of time delay between analysis and data taking.

The latter points are, to some degree, also required R&D for other projects like sPHENIX and CLAS-12, and an EIC solution would likely be straight-forward iterative development. On the other hand, even with sophisticated simulations and detector tests, the initial conditions at an EIC in the sense of observed background and dark rates, beam quality etc. are hard to predict, and will probably require some time for tuning. The initial rates might overwhelm the readout system and a system to mitigate this risk must be developed. A possible avenue is include a hard data reduction stage early in the readout system, for example controlled by a trigger, or via software cuts at a very early stage. This capability is the equivalent of raising trigger thresholds or disabling trigger sources in a classical triggered system, and would secure the ability to record data required to understand and calibrate detectors and optimize the machine, at the cost of physics reach during this tune-up period. A possible approach based on hardware signals is essentially realized at sPHENIX, and other implementations are straight forward. Research and development has to show if a pure software-based solution can be implemented, which would allow for more flexibility in the transition to normal operation.

## 14.7 Electronics

### 14.7.1 R&D of High Precision Timing Distribution Over Large System

High precision timing distribution is important for sub-detectors like TOF and LGAD based timing detectors. This technology will be used to distribute phase controllable high precision clocks to sub-detectors, and to provide precision timing for the physics events. It should also support online calibration of the clock phase drift caused by fluctuation of the environment, for instance the temperature drift. As a reference, for proposed TOF in sPHENIX and LGAD detectors in HL-LHC, the required resolution for measurements of individual arrival times of particles is about 25 to 50 ps, to mitigate the relatively short flight length, the extreme pile-up and occupancy [1423]. The contribution of the resolution

comes from both detector and electronics. For future HEP experiments, the requirement to the electronics may reach picosecond level. R&D based on phase adjustment and measurement within the back-end FPGA is a candidate solution for it. The R&D will focus on the back-end electronics in the DAQ system and the front-end readout electronics of sub-detectors. It will demonstrate the full path of transmission of signal and data with the system clock embedded. The most critical part of the R&D is to guarantee the phase stability of the low jitter clock in the front-end. Leverage of expertise is available in ongoing R&D at CERN for HL-LHC experiments [1424]. Depending on the detailed requirements of EIC, this R&D may be finished in about 1 year.

### 14.7.2 R&D of FPGA Operation in Radiation Environment

Depending on the design methodology for the sub-detectors readout electronics, FPGAs may be used in the FEB (front-end board) and FEP (front-end processor) board. Both will have to endure radiation, especially for the FEB board. This R&D will mainly focus on the application of commercial FPGAs in the front-end electronics. The purpose is to provide common FPGA based solutions for readout electronics in a radiation environment. Some similar research has been carried out for existing FPGAs, for example the Xilinx 7 series and Ultrascale series FPGAs in sPHENIX and the LHC experiments. This R&D will focus on: selection of the FPGA (SRAM-based or Flash-based FPGA) depending on the detailed requirements to the FPGA functions, radiation dose and radiation types; the measurement of cross section for different types of errors caused by the radiation; and the FPGA firmware design methodology to mitigate the errors like SEU and SEFI, for example the TMR (Triple Modular Redundancy) for the logic firmware, the data coding with error correction for high-speed serial links and the scrubbing for FPGA configuration. Several radiation tests will be needed for this R&D. The whole R&D may last for 1 to 1.5 years and will inform the selection criteria, as well as, implementation mitigating factors.

### 14.7.3 R&D of Micro-electronics, Optop-Electronics and Powering

R&D of Micro-electronics will include survey and evaluation of CMOS technologies such as 65nm, 28nm technologies; facilitate the mitigation of radiation effects on the technology; models, cell libraries and IP blocks development for extreme environments [1423, 1425]. Due to the limited available resources within the EIC community, expertise and experience from HEP should be employed. R&D of specific front-end ASICs will depend on the requirements from the various sub-detectors.

R&D of Opto-electronics: this is mainly about the radiation hard optical link architecture for high speed serial links, including the optical module and common ASIC for data aggregation [1425]. This R&D may need a lot of effort, but the existing designs with 2.5 Gbps, 5 Gbps and 10 Gbps line rate at CERN for LHC and HL-LHC experiments [1426] should be competent for EIC. Small revisions may be needed to match with the EIC machine parameters, for instance different clock frequency and line rate for the data transmission.

R&D of powering may need to cover: research on radiation tolerant DC-DC converters, for instance the development activities at CERN [1427]; low voltage power distribution; serial powering for trackers.

For readout and data acquisition, it would be critical for its R&D to be integrated with the detector technology selection, design and prototyping. The detector groups are encouraged to work closely with the readout and DAQ group in considering readout requirements (e.g. noise performance requirement), using the supported readout chips (e.g. streaming compatible chips), and perform tests with the compatible DAQ software (RC-DAQ, etc.) at the earliest opportunities.

SNAPSHOT 19 Nov. 2020

# Appendix A

## Deep Inelastic Scattering Kinematics

### A.1 Structure functions

In general, the inclusive DIS process can be written as

$$e(l) + N(p) \rightarrow e(l') + X(p_X), \quad (\text{A.1})$$

where  $e$  refers to the electron or positron,  $N$  is the nucleon in the initial state with momentum  $p$ , and a system  $X$  (which is not measured) is produced with momentum  $p_X$ . In case of an unpolarized nucleon, the cross section for this process can be written in terms of the structure functions  $F_2$  and  $F_L$  in the one photon exchange approximation neglecting electroweak effects as

$$\frac{d\sigma}{dx dQ^2} = \frac{4\pi\alpha^2}{xQ^4} \left[ \left(1 - y + \frac{y^2}{2}\right) F_2(x, Q^2) - \frac{y^2}{2} F_L(x, Q^2) \right]. \quad (\text{A.2})$$

Instead of structure functions, the reduced cross section  $\sigma_r$  is often used

$$\sigma_r = \frac{d^2\sigma}{dx dQ^2} \frac{xQ^4}{2\pi\alpha^2[1 + (1-y)^2]} = F_2(x, Q^2) - \frac{y^2}{1 + (1-y)^2} F_L(x, Q^2). \quad (\text{A.3})$$

With longitudinally polarized electron and nucleon beams, it is also possible to extract the structure function  $g_1$

$$\frac{1}{2} \left[ \frac{d\sigma^{\rightarrow\rightarrow}}{dx dQ^2} - \frac{d\sigma^{\rightarrow\leftarrow}}{dx dQ^2} \right] = \frac{4\pi\alpha^2}{Q^4} y(2-y)g_1(x, Q^2). \quad (\text{A.4})$$

Here terms suppressed by  $x^2 m_N^2 / Q^2$  have been neglected, and  $\sigma^{\rightarrow\leftarrow}$  refers to the case where the nucleon and electron spins are opposite (and parallel to the  $z$  axis), and  $\sigma^{\rightarrow\rightarrow}$  to the scattering process in case of aligned spins. The kinematical variables  $x, y$  and  $Q^2$  are introduced below, and  $m_N$  is the nucleon mass and  $\alpha$  is the fine structure constant. At large  $Q^2$  and to leading order in the strong coupling constant  $\alpha_s$  the  $F_2$  structure function is proportional

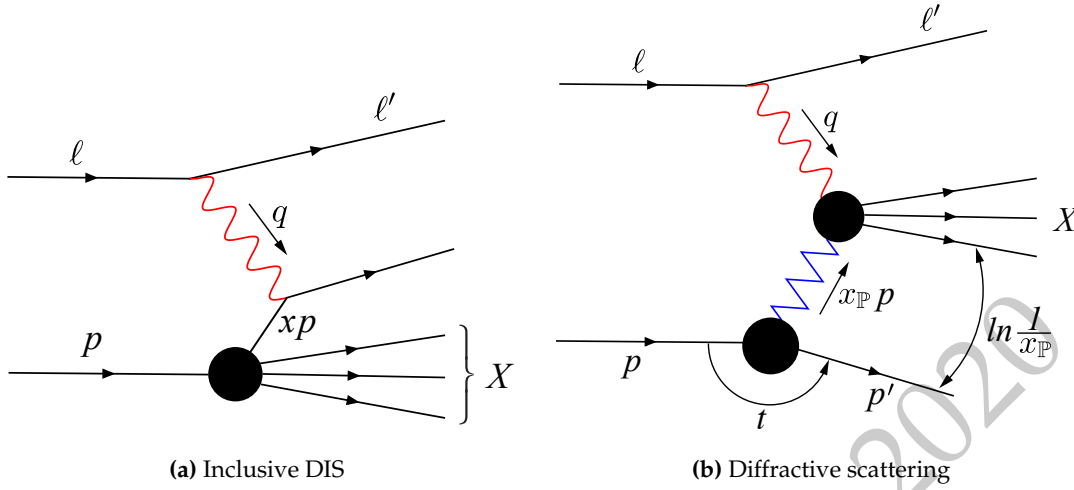


**Figure A.1:** Kinematical variables of inclusive and exclusive DIS. The blobs correspond to interactions.

to the unpolarized quark and antiquark distributions in the nucleon, and  $g_1$  is sensitive to the longitudinally polarized distributions. In this limit  $F_L = 0$ , and it obtains a first contribution at next to leading order in perturbative expansion, and is thus particularly sensitive to the gluon distribution.

In diffractive (and also semi-inclusive) scattering, the process becomes

$$e(l) + N(p) \rightarrow e(l') + N'(p') + X(p_X), \quad (\text{A.5})$$

where  $N'$  refers to the nucleon or the nucleon remnants in the final state with momentum  $p'$  and a specific system  $X$  is produced. The electron mass is neglected in the following discussion, and the nucleon mass  $p^2 = m_N^2$  is kept non-zero unless otherwise stated. In this appendix,  $p$  is a four vector and  $\mathbf{p}$  and  $\mathbf{p}_\perp$  refer to the three-momentum and the transverse momentum, respectively. The momentum vectors are illustrated in Fig. A.1.

## A.2 Invariants

Let us first consider inclusive scattering where the final state  $X$  is not completely determined and the scattered nucleon (nucleon remnants) are not reconstructed. The center-of-mass energy squared for the DIS process can be written using the momenta defined in Eq. (A.1) as

$$s = (l + p)^2 = m_N^2 + 2p \cdot l \approx 2\sqrt{E_e E_n}. \quad (\text{A.6})$$

Here  $E_e$  is the electron energy and  $E_n$  the nucleon energy, and the approximation is valid in the high energy limit where the nucleon mass can be neglected.

As the scattering process is mediated by a virtual photon, the center-of-mass energy  $W$  for

the photon-nucleon system is generically more useful:

$$W^2 = (p + q)^2 = m_N^2 - Q^2 + 2p \cdot q. \quad (\text{A.7})$$

Here the virtual photon momentum is  $q = l - l'$  and its virtuality  $-Q^2 = (l - l')^2$ . The other useful Lorentz invariant quantities describing the DIS process are

$$x \equiv \frac{Q^2}{2p \cdot q} = \frac{Q^2}{2m_N v} = \frac{Q^2}{Q^2 + W^2 - m_N^2} \quad (\text{A.8})$$

$$y \equiv \frac{p \cdot q}{p \cdot \ell} = \frac{W^2 + Q^2 - m_N^2}{s - m_N^2} \quad (\text{A.9})$$

These invariants have intuitive physical interpretations in particular frames. The Bjorken variable  $x$  can be interpreted in the parton model in the infinite momentum frame where the nucleon carries a large longitudinal momentum. In such a frame,  $x$  is the fraction of the nucleon momentum carried by the struck parton if the quark masses are neglected. In electron-nucleon collisions,  $0 < x < 1$ .

The variable  $y$  is called *inelasticity*. When expressed in the nucleon rest frame, one finds  $y = 1 - \frac{E_l'}{E_l}$ , where  $E_l$  and  $E_l'$  are the energies of the incoming and outgoing leptons in this frame, respectively. Consequently,  $0 \leq y \leq 1$ , and in particular, the highest possible photon-nucleon center-of-mass energies are reached at the  $y \rightarrow 1$  limit. A closely related variable  $\nu$  also exists:  $\nu \equiv \frac{p \cdot q}{m_N}$  describes, in the nucleon rest frame, the electron energy carried away by the virtual photon:  $\nu = E_l - E_l'$ .

The invariants presented above are not independent, and in inclusive scattering the collision kinematics is completely determined by three variables, e.g.  $s$ ,  $Q^2$  and  $x$ . This becomes apparent when noticing that the invariants defined above satisfy e.g. the following relations:

$$Q^2 = xy(s - m_N^2), \quad \text{and} \quad (\text{A.10})$$

$$W^2 = \frac{1-x}{x} Q^2 + m_N^2. \quad (\text{A.11})$$

The smallest kinematically allowed virtuality  $Q_{\min}^2$  can be determined if the electron mass  $m_e$  is non-zero:  $Q_{\min}^2 = m_e^2 \frac{y^2}{1-y}$ .

Let us then discuss diffractive production of a system  $X$  with an invariant mass  $M_X^2$ . In the unpolarized case where the cross section is symmetric in azimuthal angle, we can describe the kinematics by introducing the following new invariants:

$$t \equiv -(p' - p)^2 \quad (\text{A.12})$$

$$x_P \equiv \frac{(p - p') \cdot q}{p \cdot q} = \frac{M_X^2 + Q^2 - t}{W^2 + Q^2 - m_N^2} \quad (\text{A.13})$$

$$\beta \equiv \frac{Q^2}{2q \cdot (p - p')} = \frac{Q^2}{M_X^2 + Q^2 - t} \quad (\text{A.14})$$

In the infinite momentum frame,  $x_{\mathbb{P}}$  has the interpretation that in the scattering process an exchange of vacuum quantum numbers (a *pomeron* exchange) takes place, and the pomeron carries a fraction of  $x_{\mathbb{P}}$  of the nucleon longitudinal momentum. Similarly, in the partonic language  $\beta$  is the longitudinal momentum of the struck parton inside the pomeron. These invariants are not independent, and can be related to the invariants of inclusive DIS discussed above via e.g.

$$x = \beta x_{\mathbb{P}}. \quad (\text{A.15})$$

An experimental signature of a diffractive event is the presence of a rapidity gap between the outgoing nucleon (nucleon remnants) and the system  $X$ . This gap size is  $\Delta y \sim \ln 1/x_{\mathbb{P}}$ .

### A.3 Laboratory frame

In the laboratory frame the collisions are asymmetric, and the inclusive DIS invariants can be determined by measuring the energy and the scattering angle of the outgoing electron. In the limit of small nucleon mass, the invariants read

$$s = 4E_e E_n \quad (\text{A.16})$$

$$Q^2 = 2E_e E'_e (1 - \cos \theta_e) \quad (\text{A.17})$$

$$W^2 = 4E_e E_n - 2E'_e [E_n + E_e + (E_n - E_e) \cos \theta_e] \quad (\text{A.18})$$

$$x = \frac{E_e E'_e (1 - \cos \theta_e)}{2E_e E_n - E'_e E_n (1 + \cos \theta_e)} \quad (\text{A.19})$$

$$y = \frac{2E_e E_n - E'_e E_n (1 + \cos \theta_e)}{2E_e E_n}. \quad (\text{A.20})$$

Here  $E_e$  and  $E'_e$  are the incoming and outgoing electron energies, and the electron scattering angle is  $\theta_e$ , with  $\theta_e = 0$  corresponding to the forward scattering, or photoproduction region  $Q^2 \approx 0$ . Similarly the incoming nucleon energy is  $E_n$ .

In exclusive processes it is possible to also measure the momentum of the produced particle and its invariant mass by measuring the decay products. Although the kinematical variables can be reconstructed using the scattered electron only, a common method to determine  $y$  and  $Q^2$  is to express these invariants in terms of the scattering angles of both the electron and the produced particle using the double angle method [1428]:

$$Q^2 = 4E_e^2 \frac{\sin \theta_e (1 - \cos \theta_V)}{\sin \theta_V + \sin \theta_e - \sin(\theta_e + \theta_V)} \quad (\text{A.21})$$

$$y = \frac{\sin \theta_e (1 - \cos \theta_V)}{\sin \theta_V + \sin \theta_e - \sin(\theta_e + \theta_V)}. \quad (\text{A.22})$$

Here  $\theta_V$  is the scattering angle of the produced particle. These expressions are again valid in the limit where the nucleon mass can be neglected, and other similar methods can be found from Ref. [1428]. Note that once  $Q^2$  and  $y$  are determined,  $x$  and  $W^2$  can be obtained using Eqs. (A.10) and (A.11).

The squared momentum transfer  $t$  can be written as

$$t = -\frac{(\mathbf{p}_{X\perp} - \mathbf{l}'_{\perp})^2 + x_{\mathbb{P}}^2 m_N^2}{1 - x_{\mathbb{P}}} \approx -(\mathbf{p}_{X\perp} - \mathbf{l}'_{\perp})^2. \quad (\text{A.23})$$

Here  $\mathbf{p}_{X\perp}$  is the transverse momentum of the produced particle and  $\mathbf{l}'_{\perp}$  the transverse momentum of the scattered electron, and the approximation is valid at high energies where  $x_{\mathbb{P}}$  is small and the momentum transfer is approximatively transverse. Note that the kinematical lower bound for  $t$  reads

$$-t > -t_{\min} = \frac{x_{\mathbb{P}}^2 m_N^2}{1 - x_{\mathbb{P}}}. \quad (\text{A.24})$$

When  $t$ ,  $Q^2$  and  $W^2$  are determined,  $x_{\mathbb{P}}$  can be obtained by using Eq. (A.13).

In exclusive and semi-inclusive processes the particle  $X$  is identified by measuring the invariant mass of the decay products. In inclusive diffraction the invariant mass  $M_X^2$  is determined by measuring the total energy  $E_X$  and the total momentum  $\mathbf{p}_X$  of the produced particles:

$$M_X^2 = E_X^2 - \mathbf{p}_X^2. \quad (\text{A.25})$$

In these events, it is also possible to construct inelasticity using the hadron method

$$y_h = \frac{E_X - \mathbf{p}_{Xz}}{2E_e}. \quad (\text{A.26})$$

The hadron method can also be used to determine inelasticity in exclusive particle production in the photoproduction limit where the scattered electron can not be detected. For a better experimental accuracy, different methods to construct e.g. inelasticity can be combined (see e.g. [210]). Generically in inclusive diffraction  $M_X^2 + Q^2 \gg |t|$ , and consequently  $t$  can be neglected when determining  $x_{\mathbb{P}}$  and  $\beta$  using Eqs. (A.13) and (A.14).

## A.4 Breit frame

A natural frame to describe hard scattering process in DIS is the Breit (or brick wall) frame, where the incoming photon carries no energy, and the parton to which the photon couples to behaves as if it bounced off a brick wall. Let us choose that the ultrarelativistic nucleon moves along the positive  $z$  axis, and the photon propagates to the  $-z$  direction. The nucleon momentum in this frame is  $p_z = \frac{1}{2x}Q$ , and the parton longitudinal momentum  $k_z$  can be written as  $k_z = xp_z = \frac{1}{2}Q$ . Similarly, the photon four-momentum reads  $q = (0, 0, 0, -Q)$ . Now, after the photon absorption  $\mathbf{k}' = -\mathbf{k}$ , where  $\mathbf{k}'$  is the parton mo-

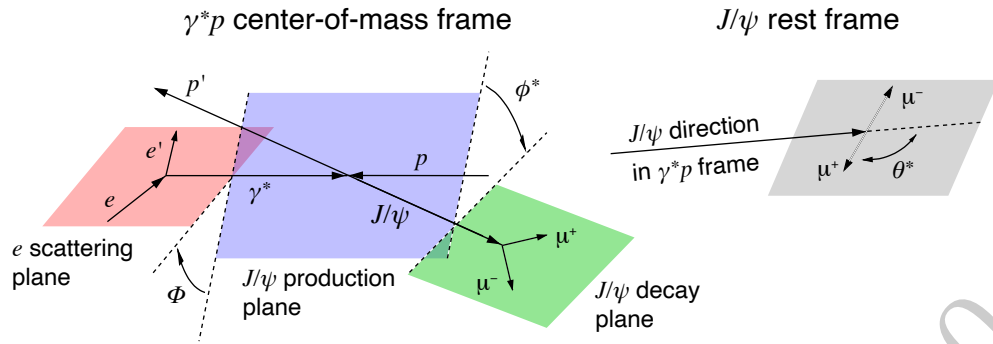


Figure A.2: Planes in exclusive vector meson production.

mentum after the scattering. Note that in this frame there is no energy transfer to the proton.

The Breit frame is not the center-of-mass frame for the parton-photon scattering. This is advantageous when separating the produced particles from the beam remnants. In the Breit frame, the produced particles populate the region of negative  $z$  momentum, while the beam remnants generically have a positive momentum  $z$  component.

## A.5 Helicity studies

Studying the helicity structure of exclusive particle production processes requires one to measure the azimuthal angles  $\phi^*$  and  $\Phi$  defined in Fig. A.2. Note that the angles are defined in the frame where the photon and the nucleon momenta are aligned along the same axis (here  $z$  axis), so this discussion is valid both in the Breit frame and in the  $\gamma$ -nucleon center-of-mass frame.

The production plane is defined as the plane spanned by the  $z$  axis and the momentum of the produced particle. The azimuthal angle between this plane, and the electron scattering plane spanned by the momenta of the incoming and outgoing electron momentum vectors is denoted by  $\Phi$  in Fig. A.2, where the geometry is illustrated in case of  $e^+ + p \rightarrow e^+ + p + J/\psi$  scattering. Similarly, we define the decay plane, which is spanned by the momenta of the decay products of the produced particle, and the azimuthal angle between this plane and the production plane is denoted by  $\phi^*$ .

The third angle required to specify the geometry  $\theta^*$  also shown in Fig. A.2 is required to determine the polarization state of the produced particle. This angle is defined as the polar angle of the decay particle having the same charge as the incoming lepton in the rest frame of the decaying particle. The  $\theta^* = 0$  case corresponds to the direction of the produced particle in the photon-nucleon center-of-mass frame.

# References

- [1] A. Accardi *et al.*, “Electron Ion Collider: The Next QCD Frontier,” *Eur. Phys. J.*, vol. A52, no. 9, p. 268, 2016.
- [2] *An Assessment of U.S.-Based Electron-Ion Collider Science*. The National Academies Press, 2018. <https://doi.org/10.17226/25171>.
- [3] “Eic yellow reports – kick-off meeting,” MIT Laboratory for Nuclear Science, MA, 2019.
- [4] J. Gao, L. Harland-Lang, and J. Rojo, “The Structure of the Proton in the LHC Precision Era,” *Phys. Rept.*, vol. 742, pp. 1–121, 2018.
- [5] J. J. Ethier and E. R. Nocera, “Parton Distributions in Nucleons and Nuclei,” *Ann. Rev. Nucl. Part. Sci.*, no. 70, pp. 1–34, 2020.
- [6] J. Rojo *et al.*, “The PDF4LHC report on PDFs and LHC data: Results from Run I and preparation for Run II,” *J. Phys.*, vol. G42, p. 103103, 2015.
- [7] R. D. Ball *et al.*, “Parton distributions from high-precision collider data,” *Eur. Phys. J. C*, vol. 77, no. 10, p. 663, 2017.
- [8] V. Bertone, S. Carrazza, and J. Rojo, “APFEL: A PDF Evolution Library with QED corrections,” *Comput. Phys. Commun.*, vol. 185, pp. 1647–1668, 2014.
- [9] F. Faura, S. Iranipour, E. R. Nocera, J. Rojo, and M. Ubiali, “The Strangest Proton?,” 8 2020.
- [10] N. Sato, C. Andres, J. Ethier, and W. Melnitchouk, “Strange quark suppression from a simultaneous Monte Carlo analysis of parton distributions and fragmentation functions,” *Phys. Rev. D*, vol. 101, no. 7, p. 074020, 2020.
- [11] B.-T. Wang, T. Hobbs, S. Doyle, J. Gao, T.-J. Hou, P. M. Nadolsky, and F. I. Olness, “Mapping the sensitivity of hadronic experiments to nucleon structure,” *Phys. Rev. D*, vol. 98, no. 9, p. 094030, 2018.
- [12] T. Hobbs, B.-T. Wang, P. M. Nadolsky, and F. I. Olness, “Charting the coming synergy between lattice QCD and high-energy phenomenology,” *Phys. Rev. D*, vol. 100, no. 9, p. 094040, 2019.

- [13] T. Hobbs, B.-T. Wang, P. M. Nadolsky, and F. I. Olness, "Collinear PDFs in the era of HL-LHC, LHeC, and EIC," *PoS*, vol. DIS2019, p. 247, 2019.
- [14] T.-J. Hou *et al.*, "New CTEQ global analysis of quantum chromodynamics with high-precision data from the LHC," 12 2019.
- [15] A. Accardi, L. Brady, W. Melnitchouk, J. Owens, and N. Sato, "Constraints on large- $x$  parton distributions from new weak boson production and deep-inelastic scattering data," *Phys. Rev. D*, vol. 93, no. 11, p. 114017, 2016.
- [16] C. Cocuzza, N. Sato, J. Ethier, W. Melnitchouk, and A. Metz, "Parton distributions functions from JLab to LHC," *in preparation*, 2020.
- [17] T. Hobbs, J. Londergan, D. Murdock, and A. Thomas, "Testing Partonic Charge Symmetry at a High-Energy Electron Collider," *Phys. Lett. B*, vol. 698, pp. 123–127, 2011.
- [18] M. Sargsian and M. Strikman, "Model independent method for determination of the DIS structure of free neutron," *Phys. Lett.*, vol. B639, pp. 223–231, 2006.
- [19] M. Strikman and C. Weiss, "Electron-deuteron deep-inelastic scattering with spectator nucleon tagging and final-state interactions at intermediate  $x$ ," *Phys. Rev.*, vol. C97, no. 3, p. 035209, 2018.
- [20] C. Weiss *et al.*, "JLab LDRD project "Physics potential of polarized light ions with EIC at JLab"." [www.jlab.org/theory/tag/](http://www.jlab.org/theory/tag/), 2015. Accessed: 2020-10-23.
- [21] S. Alekhin, S. Kulagin, and R. Petti, "Nuclear Effects in the Deuteron and Constraints on the d/u Ratio," *Phys. Rev. D*, vol. 96, no. 5, p. 054005, 2017.
- [22] A. Tropiano, J. Ethier, W. Melnitchouk, and N. Sato, "Deep-inelastic and quasielastic electron scattering from  $A = 3$  nuclei," *Phys. Rev. C*, vol. 99, no. 3, p. 035201, 2019.
- [23] K. Griffioen *et al.*, "Measurement of the EMC Effect in the Deuteron," *Phys. Rev. C*, vol. 92, no. 1, p. 015211, 2015.
- [24] S. Malace, D. Gaskell, D. W. Higinbotham, and I. Cloet, "The Challenge of the EMC Effect: existing data and future directions," *Int. J. Mod. Phys. E*, vol. 23, no. 08, p. 1430013, 2014.
- [25] E. C. Aschenauer, I. Borsa, R. Sassot, and C. Van Hulse, "Semi-inclusive Deep-Inelastic Scattering, Parton Distributions and Fragmentation Functions at a Future Electron-Ion Collider," *Phys. Rev. D*, vol. 99, no. 9, p. 094004, 2019.
- [26] T. Sjostrand, S. Mrenna, and P. Z. Skands, "PYTHIA 6.4 Physics and Manual," *JHEP*, vol. 0605, p. 026, 2006.
- [27] R. D. Ball, V. Bertone, F. Cerutti, L. Del Debbio, S. Forte, A. Guffanti, J. I. Latorre, J. Rojo, and M. Ubiali, "Reweighting NNPDFs: the  $W$  lepton asymmetry," *Nucl. Phys. B*, vol. 849, pp. 112–143, 2011. [Erratum: *Nucl.Phys.B* 854, 926–927 (2012), Erratum: *Nucl.Phys.B* 855, 927–928 (2012)].

- [28] R. D. Ball, V. Bertone, F. Cerutti, L. Del Debbio, S. Forte, A. Guffanti, N. P. Hartland, J. I. Latorre, J. Rojo, and M. Ubiali, "Reweighting and Unweighting of Parton Distributions and the LHC W lepton asymmetry data," *Nucl. Phys. B*, vol. 855, pp. 608–638, 2012.
- [29] R. D. Ball *et al.*, "Parton distributions for the LHC Run II," *JHEP*, vol. 04, p. 040, 2015.
- [30] S. Brodsky, P. Hoyer, C. Peterson, and N. Sakai, "The Intrinsic Charm of the Proton," *Phys. Lett. B*, vol. 93, pp. 451–455, 1980.
- [31] P. Jimenez-Delgado, T. Hobbs, J. Londergan, and W. Melnitchouk, "New limits on intrinsic charm in the nucleon from global analysis of parton distributions," *Phys. Rev. Lett.*, vol. 114, no. 8, p. 082002, 2015.
- [32] T.-J. Hou, S. Dulat, J. Gao, M. Guzzi, J. Huston, P. Nadolsky, C. Schmidt, J. Winter, K. Xie, and C. P. Yuan, "CT14 Intrinsic Charm Parton Distribution Functions from CTEQ-TEA Global Analysis," *JHEP*, vol. 02, p. 059, 2018.
- [33] J. Aubert *et al.*, "Production of charmed particles in 250-GeV  $\mu^+$  - iron interactions," *Nucl. Phys. B*, vol. 213, pp. 31–64, 1983.
- [34] T. Hobbs, M. Alberg, and G. A. Miller, "Bayesian analysis of light-front models and the nucleon's charmed sigma term," *Phys. Rev. D*, vol. 96, no. 7, p. 074023, 2017.
- [35] R. D. Ball, V. Bertone, M. Bonvini, S. Carrazza, S. Forte, A. Guffanti, N. P. Hartland, J. Rojo, and L. Rottoli, "A Determination of the Charm Content of the Proton," *Eur. Phys. J. C*, vol. 76, no. 11, p. 647, 2016.
- [36] M. Arratia, Y. Furlitova, T. Hobbs, F. Olness, and S. J. Sekula, "Charm jets as a probe for strangeness at the future Electron-Ion Collider," 6 2020.
- [37] E. C. Aschenauer, I. Borsa, G. Lucero, A. S. Nunes, and R. Sassot, "Revisiting Helicity Parton Distributions at a Future Electron-Ion Collider," 7 2020.
- [38] D. De Florian, G. A. Lucero, R. Sassot, M. Stratmann, and W. Vogelsang, "Monte Carlo sampling variant of the DSSV14 set of helicity parton densities," *Phys. Rev. D*, vol. 100, no. 11, p. 114027, 2019.
- [39] Y. Zhou, N. Sato, J. Ethier, and W. Melnitchouk, "Gluon polarization from a simultaneous analysis of unpolarized and polarized PDFs," *in preparation*, 2020.
- [40] J. Ethier, N. Sato, and W. Melnitchouk, "First simultaneous extraction of spin-dependent parton distributions and fragmentation functions from a global QCD analysis," *Phys. Rev. Lett.*, vol. 119, no. 13, p. 132001, 2017.
- [41] D. Adamiak, D. Pitonyak, Y. V. Kovchegov, W. Melnitchouk, N. Sato, and M. D. Sievert, "Small- $x$  Helicity Evolution Meets the Data: Fits and Predictions," *in preparation*, 2020.

- [42] Y. V. Kovchegov, D. Pitonyak, and M. D. Sievert, "Helicity Evolution at Small- $x$ ," *JHEP*, vol. 01, p. 072, 2016. [Erratum: *JHEP* 10, 148 (2016)].
- [43] Y. V. Kovchegov, D. Pitonyak, and M. D. Sievert, "Helicity Evolution at Small  $x$ : Flavor Singlet and Non-Singlet Observables," *Phys. Rev. D*, vol. 95, no. 1, p. 014033, 2017.
- [44] Y. V. Kovchegov, D. Pitonyak, and M. D. Sievert, "Small- $x$  asymptotics of the quark helicity distribution," *Phys. Rev. Lett.*, vol. 118, no. 5, p. 052001, 2017.
- [45] Y. V. Kovchegov and M. D. Sievert, "Small- $x$  Helicity Evolution: an Operator Treatment," *Phys. Rev. D*, vol. 99, no. 5, p. 054032, 2019.
- [46] N. Sato, W. Melnitchouk, S. Kuhn, J. Ethier, and A. Accardi, "Iterative Monte Carlo analysis of spin-dependent parton distributions," *Phys. Rev. D*, vol. 93, no. 7, p. 074005, 2016.
- [47] W. Cosyn and C. Weiss, "Neutron spin structure from polarized deuteron DIS with proton tagging," *Phys. Lett. B*, vol. 799, p. 135035, 2019.
- [48] W. Cosyn and C. Weiss, "Polarized electron-deuteron deep-inelastic scattering with spectator nucleon tagging," 6 2020.
- [49] M. Anselmino, A. Efremov, and E. Leader, "The Theory and phenomenology of polarized deep inelastic scattering," *Phys. Rept.*, vol. 261, pp. 1–124, 1995. [Erratum: *Phys. Rept.* 281, 399 (1997)].
- [50] S. E. Kuhn, J. P. Chen, and E. Leader, "Spin Structure of the Nucleon - Status and Recent Results," *Prog. Part. Nucl. Phys.*, vol. 63, pp. 1–50, 2009.
- [51] C. A. Aidala, S. D. Bass, D. Hasch, and G. K. Mallot, "The Spin Structure of the Nucleon," *Rev. Mod. Phys.*, vol. 85, pp. 655–691, 2013.
- [52] L. L. Frankfurt and M. I. Strikman, "Hard Nuclear Processes and Microscopic Nuclear Structure," *Phys. Rept.*, vol. 160, pp. 235–427, 1988.
- [53] M. Arneodo, "Nuclear effects in structure functions," *Phys. Rept.*, vol. 240, pp. 301–393, 1994.
- [54] C. Ciofi degli Atti, S. Scopetta, E. Pace, and G. Salme, "Nuclear effects in deep inelastic scattering of polarized electrons off polarized  $^3\text{He}$  and the neutron spin structure functions," *Phys. Rev.*, vol. C48, pp. R968–R972, 1993.
- [55] W. Melnitchouk, G. Piller, and A. W. Thomas, "Deep inelastic scattering from polarized deuterons," *Phys. Lett.*, vol. B346, pp. 165–171, 1995.
- [56] S. A. Kulagin, W. Melnitchouk, G. Piller, and W. Weise, "Spin dependent nuclear structure functions: General approach with application to the deuteron," *Phys. Rev.*, vol. C52, pp. 932–946, 1995.

- [57] G. Piller, W. Melnitchouk, and A. W. Thomas, "Polarized deep inelastic scattering from nuclei: A Relativistic approach," *Phys. Rev.*, vol. C54, pp. 894–903, 1996.
- [58] L. Frankfurt, V. Guzey, and M. Strikman, "The Nuclear effects in  $g_1^{3\text{He}}$  and the Bjorken sum rule for  $A = 3$ ," *Phys. Lett.*, vol. B381, pp. 379–384, 1996.
- [59] F. R. P. Bissey, V. A. Guzey, M. Strikman, and A. W. Thomas, "Complete analysis of spin structure function  $g_1$  of  $^3\text{He}$ ," *Phys. Rev.*, vol. C65, p. 064317, 2002.
- [60] J. J. Ethier and W. Melnitchouk, "Comparative study of nuclear effects in polarized electron scattering from  $^3\text{He}$ ," *Phys. Rev.*, vol. C88, no. 5, p. 054001, 2013.
- [61] J. L. Friar, B. F. Gibson, G. L. Payne, A. M. Bernstein, and T. E. Chupp, "Neutron polarization in polarized He-3 targets," *Phys. Rev.*, vol. C42, pp. 2310–2314, 1990.
- [62] C. Ciofi degli Atti and B. Kopeliovich, "Final state interaction in semiinclusive DIS off nuclei," *Eur. Phys. J. A*, vol. 17, pp. 133–144, 2003.
- [63] C. Ciofi degli Atti, L. Kaptari, and B. Kopeliovich, "Final state interaction effects in semiinclusive DIS off the deuteron," *Eur. Phys. J. A*, vol. 19, pp. 145–151, 2004.
- [64] V. Palli, C. Ciofi degli Atti, L. Kaptari, C. Mezzetti, and M. Alvioli, "Slow Proton Production in Semi-Inclusive Deep Inelastic Scattering off Deuteron and Complex Nuclei: Hadronization and Final State Interaction Effects," *Phys. Rev. C*, vol. 80, p. 054610, 2009.
- [65] L. Kaptari, A. Del Dotto, E. Pace, G. Salme', and S. Scopetta, "Distorted spin-dependent spectral function of an  $A=3$  nucleus and semi-inclusive deep inelastic scattering processes," *Phys. Rev. C*, vol. 89, no. 3, p. 035206, 2014.
- [66] L. L. Frankfurt and M. I. Strikman, "High momentum transfer processes with polarized deuterons," *Nucl. Phys.*, vol. A405, pp. 557–580, 1983.
- [67] L. L. Frankfurt and M. I. Strikman, "High-Energy Phenomena, Short Range Nuclear Structure and QCD," *Phys. Rept.*, vol. 76, pp. 215–347, 1981.
- [68] M. Diehl, "Generalized parton distributions," *Phys. Rept.*, vol. 388, pp. 41–277, 2003.
- [69] X.-D. Ji, "Gauge invariant decomposition of nucleon spin," *Phys. Rev. Lett.*, vol. 78, pp. 610–613, 1997.
- [70] E. Leader and C. Lorcé, "The angular momentum controversy: What's it all about and does it matter?," *Phys. Rept.*, vol. 541, no. 3, pp. 163–248, 2014.
- [71] D. de Florian, R. Sassot, M. Stratmann, and W. Vogelsang, "Extraction of Spin-Dependent Parton Densities and Their Uncertainties," *Phys. Rev.*, vol. D80, p. 034030, 2009.
- [72] D. de Florian, R. Sassot, M. Stratmann, and W. Vogelsang, "Evidence for polarization of gluons in the proton," *Phys. Rev. Lett.*, vol. 113, no. 1, p. 012001, 2014.

- [73] A. Airapetian *et al.*, “Quark helicity distributions in the nucleon for up, down, and strange quarks from semi-inclusive deep-inelastic scattering,” *Phys. Rev.*, vol. D71, p. 012003, 2005.
- [74] M. Alekseev *et al.*, “Quark helicity distributions from longitudinal spin asymmetries in muon-proton and muon-deuteron scattering,” *Phys. Lett.*, vol. B693, pp. 227–235, 2010.
- [75] E. R. Nocera, R. D. Ball, S. Forte, G. Ridolfi, and J. Rojo, “A first unbiased global determination of polarized PDFs and their uncertainties,” *Nucl. Phys. B*, vol. 887, pp. 276–308, 2014.
- [76] E. R. Nocera, “Impact of Recent RHIC Data on Helicity-Dependent Parton Distribution Functions,” in *22nd International Symposium on Spin Physics*, 2 2017.
- [77] J. Desay and J. Zhang, “Kaon impact studies on delta s.” [https://indico.bnl.gov/event/9261/contributions/40809/attachments/30169/47151/Strange\\_Spin\\_Jay.pdf](https://indico.bnl.gov/event/9261/contributions/40809/attachments/30169/47151/Strange_Spin_Jay.pdf), 2020.
- [78] E. C. Aschenauer, R. Sassot, and M. Stratmann, “Unveiling the Proton Spin Decomposition at a Future Electron-Ion Collider,” *Phys. Rev.*, vol. D92, no. 9, p. 094030, 2015.
- [79] B. Page, X. Chu, and E. Aschenauer, “Experimental Aspects of Jet Physics at a Future EIC,” *Phys. Rev. D*, vol. 101, no. 7, p. 072003, 2020.
- [80] X. Chu, E.-C. Aschenauer, J.-H. Lee, and L. Zheng, “Photon structure studied at an Electron Ion Collider,” *arXiv preprint arXiv:1705.08831*, 2017.
- [81] F. Hekhorn and M. Stratmann, “Next-to-Leading Order QCD Corrections to Inclusive Heavy-Flavor Production in Polarized Deep-Inelastic Scattering,” *Phys. Rev. D*, vol. 98, no. 1, p. 014018, 2018.
- [82] C. Adolph *et al.*, “Leading and Next-to-Leading Order Gluon Polarization in the Nucleon and Longitudinal Double Spin Asymmetries from Open Charm Muoproduction,” *Phys. Rev. D*, vol. 87, no. 5, p. 052018, 2013.
- [83] J. Sullivan, “One pion exchange and deep inelastic electron - nucleon scattering,” *Phys. Rev. D*, vol. 5, pp. 1732–1737, 1972.
- [84] A. W. Thomas, W. Melnitchouk, and F. M. Steffens, “Dynamical symmetry breaking in the sea of the nucleon,” *Phys. Rev. Lett.*, vol. 85, pp. 2892–2894, 2000.
- [85] J.-W. Chen and X.-d. Ji, “Constructing parton convolution in effective field theory,” *Phys. Rev. Lett.*, vol. 87, p. 152002, 2001. [Erratum: *Phys.Rev.Lett.* 88, 249901 (2002)].
- [86] W. Detmold, W. Melnitchouk, J. W. Negele, D. B. Renner, and A. W. Thomas, “Chiral extrapolation of lattice moments of proton quark distributions,” *Phys. Rev. Lett.*, vol. 87, p. 172001, 2001.

- [87] S.-X. Qin, C. Chen, C. Mezrag, and C. D. Roberts, "Off-shell persistence of composite pions and kaons," *Phys. Rev. C*, vol. 97, no. 1, p. 015203, 2018.
- [88] C. Adloff *et al.*, "Measurement of leading proton and neutron production in deep inelastic scattering at HERA," *Eur. Phys. J. C*, vol. 6, pp. 587–602, 1999.
- [89] B. Kopeliovich, B. Povh, and I. Potashnikova, "Deep inelastic electroproduction of neutrons in the proton fragmentation region," *Z. Phys. C*, vol. 73, pp. 125–131, 1996.
- [90] K. J. Golec-Biernat, J. Kwiecinski, and A. Szczurek, "Reggeon and pion contributions in semiexclusive diffractive processes at HERA," *Phys. Rev. D*, vol. 56, pp. 3955–3960, 1997.
- [91] Y. Kazarinov, B. Kopeliovich, L. Lapidus, and I. Potashnikova, "Triple Regge Phenomenology in the Reaction  $p + p \rightarrow p + x$ ," *Sov. Phys. JETP*, vol. 43, p. 598, 1976.
- [92] U. D'Alesio and H. Pirner, "Target fragmentation in  $p p$ ,  $e p$  and  $\gamma p$  collisions at high-energies," *Eur. Phys. J. A*, vol. 7, pp. 109–119, 2000.
- [93] V. Stoks and T. Rijken, "Soft core baryon baryon potentials for the complete baryon octet," *Phys. Rev. C*, vol. 59, pp. 3009–3020, 1999.
- [94] J. Conway *et al.*, "Experimental Study of Muon Pairs Produced by 252-GeV Pions on Tungsten," *Phys. Rev. D*, vol. 39, pp. 92–122, 1989.
- [95] S. Drell and T.-M. Yan, "Connection of Elastic Electromagnetic Nucleon Form-Factors at Large  $Q^2$  and Deep Inelastic Structure Functions Near Threshold," *Phys. Rev. Lett.*, vol. 24, pp. 181–185, 1970.
- [96] J. McKenney, N. Sato, W. Melnitchouk, and C.-R. Ji, "Pion structure function from leading neutron electroproduction and SU(2) flavor asymmetry," *Phys. Rev. D*, vol. 93, no. 5, p. 054011, 2016.
- [97] P. Barry, N. Sato, W. Melnitchouk, and C.-R. Ji, "First Monte Carlo Global QCD Analysis of Pion Parton Distributions," *Phys. Rev. Lett.*, vol. 121, no. 15, p. 152001, 2018.
- [98] S. Chekanov *et al.*, "Leading neutron production in  $e + p$  collisions at HERA," *Nucl. Phys. B*, vol. 637, pp. 3–56, 2002.
- [99] P. Barry, C.-R. Ji, W. Melnitchouk, and N. Sato, "Threshold resummation effects on pion PDFs at large  $x$ ." (in preparation).
- [100] N. Cao, P. Barry, N. Sato, and W. Melnitchouk, "Towards the 3-dimensional parton structure of the pion: integrating transverse momentum data into global QCD analysis." (in preparation).
- [101] Y.-B. Yang, Y. Chen, T. Draper, M. Gong, K.-F. Liu, Z. Liu, and J.-P. Ma, "Meson Mass Decomposition from Lattice QCD," *Phys. Rev. D*, vol. 91, no. 7, p. 074516, 2015.

- [102] F. Aaron *et al.*, “Measurement of Leading Neutron Production in Deep-Inelastic Scattering at HERA,” *Eur. Phys. J. C*, vol. 68, pp. 381–399, 2010.
- [103] Z.-F. Cui, M. Ding, F. Gao, K. Raya, D. Binosi, L. Chang, C. D. Roberts, J. Rodríguez-Quintero, and S. M. Schmidt, “Kaon parton distributions: revealing Higgs modulation of emergent mass,” 6 2020.
- [104] M. Hecht, C. D. Roberts, and S. Schmidt, “Valence quark distributions in the pion,” *Phys. Rev. C*, vol. 63, p. 025213, 2001.
- [105] R. S. Sufian, J. Karpie, C. Egerer, K. Orginos, J.-W. Qiu, and D. G. Richards, “Pion Valence Quark Distribution from Matrix Element Calculated in Lattice QCD,” *Phys. Rev. D*, vol. 99, no. 7, p. 074507, 2019.
- [106] M. Aicher, A. Schafer, and W. Vogelsang, “Soft-gluon resummation and the valence parton distribution function of the pion,” *Phys. Rev. Lett.*, vol. 105, p. 252003, 2010.
- [107] H.-W. Lin, J.-W. Chen, Z. Fan, J.-H. Zhang, and R. Zhang, “The Valence-Quark Distribution of the Kaon from Lattice QCD,” 3 2020.
- [108] J. Badier *et al.*, “Measurement of the  $K^- / \pi^-$  Structure Function Ratio Using the Drell-Yan Process,” *Phys. Lett. B*, vol. 93, pp. 354–356, 1980.
- [109] Z. Ezawa, “Wide-Angle Scattering in Softened Field Theory,” *Nuovo Cim. A*, vol. 23, pp. 271–290, 1974.
- [110] G. R. Farrar and D. R. Jackson, “Pion and Nucleon Structure Functions Near  $x=1$ ,” *Phys. Rev. Lett.*, vol. 35, p. 1416, 1975.
- [111] E. L. Berger and S. J. Brodsky, “Quark Structure Functions of Mesons and the Drell-Yan Process,” *Phys. Rev. Lett.*, vol. 42, pp. 940–944, 1979.
- [112] S. J. Brodsky, M. Burkardt, and I. Schmidt, “Perturbative QCD constraints on the shape of polarized quark and gluon distributions,” *Nucl. Phys. B*, vol. 441, pp. 197–214, 1995.
- [113] F. Yuan, “Generalized parton distributions at  $x \rightarrow 1$ ,” *Phys. Rev. D*, vol. 69, p. 051501, 2004.
- [114] J.-H. Zhang, J.-W. Chen, L. Jin, H.-W. Lin, A. Schäfer, and Y. Zhao, “First direct lattice-QCD calculation of the  $x$ -dependence of the pion parton distribution function,” *Phys. Rev. D*, vol. 100, no. 3, p. 034505, 2019.
- [115] M. A. Shifman, A. Vainshtein, and V. I. Zakharov, “Remarks on Higgs Boson Interactions with Nucleons,” *Phys. Lett. B*, vol. 78, pp. 443–446, 1978.
- [116] D. Kharzeev, “Quarkonium interactions in QCD,” *Proc. Int. Sch. Phys. Fermi*, vol. 130, pp. 105–131, 1996.
- [117] D. Kharzeev, H. Satz, A. Syamtomov, and G. Zinovjev, “ $J/\psi$  photoproduction and the gluon structure of the nucleon,” *Eur. Phys. J. C*, vol. 9, pp. 459–462, 1999.

- [118] Y. Hatta, A. Rajan, and K. Tanaka, "Quark and gluon contributions to the QCD trace anomaly," *JHEP*, vol. 12, p. 008, 2018.
- [119] K. Tanaka, "Three-loop formula for quark and gluon contributions to the QCD trace anomaly," *JHEP*, vol. 01, p. 120, 2019.
- [120] C. D. Roberts, "Empirical Consequences of Emergent Mass," *Symmetry*, vol. 12, no. 9, p. 1468, 2020.
- [121] X.-D. Ji, "A QCD analysis of the mass structure of the nucleon," *Phys. Rev. Lett.*, vol. 74, pp. 1071–1074, 1995.
- [122] X.-D. Ji, "Breakup of hadron masses and energy - momentum tensor of QCD," *Phys. Rev. D*, vol. 52, pp. 271–281, 1995.
- [123] C. Lorcé, "On the hadron mass decomposition," *Eur. Phys. J. C*, vol. 78, no. 2, p. 120, 2018.
- [124] C. Lorcé, H. Moutarde, and A. P. Trawiński, "Revisiting the mechanical properties of the nucleon," *Eur. Phys. J. C*, vol. 79, no. 1, p. 89, 2019.
- [125] S. Rodini, A. Metz, and B. Pasquini, "Mass sum rules of the electron in quantum electrodynamics," *JHEP*, vol. 09, p. 067, 2020.
- [126] A. Metz, B. Pasquini, and S. Rodini, "Revisiting the proton mass decomposition," 6 2020.
- [127] W. Cosyn, S. Cotogno, A. Freese, and C. Lorcé, "The energy-momentum tensor of spin-1 hadrons: formalism," *Eur. Phys. J. C*, vol. 79, no. 6, p. 476, 2019.
- [128] S. Cotogno, C. Lorcé, P. Lowdon, and M. Morales, "Covariant multipole expansion of local currents for massive states of any spin," *Phys. Rev. D*, vol. 101, no. 5, p. 056016, 2020.
- [129] J. Alarcon, J. Martin Camalich, and J. Oller, "The chiral representation of the  $\pi N$  scattering amplitude and the pion-nucleon sigma term," *Phys. Rev. D*, vol. 85, p. 051503, 2012.
- [130] J. Alarcon, L. Geng, J. Martin Camalich, and J. Oller, "The strangeness content of the nucleon from effective field theory and phenomenology," *Phys. Lett. B*, vol. 730, pp. 342–346, 2014.
- [131] M. Hoferichter, J. Ruiz de Elvira, B. Kubis, and U.-G. Meißner, "Roy–Steiner-equation analysis of pion–nucleon scattering," *Phys. Rept.*, vol. 625, pp. 1–88, 2016.
- [132] M. Hoferichter, J. Ruiz de Elvira, B. Kubis, and U.-G. Meißner, "High-Precision Determination of the Pion-Nucleon  $\sigma$  Term from Roy-Steiner Equations," *Phys. Rev. Lett.*, vol. 115, p. 092301, 2015.
- [133] Y. Hatta and D.-L. Yang, "Holographic  $J/\psi$  production near threshold and the proton mass problem," *Phys. Rev. D*, vol. 98, no. 7, p. 074003, 2018.

- [134] R. Boussarie and Y. Hatta, "QCD analysis of near-threshold quarkonium lepton production at large photon virtualities," *Phys. Rev. D*, vol. 101, no. 11, p. 114004, 2020.
- [135] S. Brodsky, E. Chudakov, P. Hoyer, and J. Laget, "Photoproduction of charm near threshold," *Phys. Lett. B*, vol. 498, pp. 23–28, 2001.
- [136] O. Gryniuk and M. Vanderhaeghen, "Accessing the real part of the forward  $J/\psi$ - $p$  scattering amplitude from  $J/\psi$  photoproduction on protons around threshold," *Phys. Rev. D*, vol. 94, no. 7, p. 074001, 2016.
- [137] M.-L. Du, V. Baru, F.-K. Guo, C. Hanhart, U.-G. Meißner, A. Nefediev, and I. Strakovsky, "Deciphering the mechanism of near-threshold  $J/\psi$  photoproduction," 9 2020.
- [138] K. A. Mamo and I. Zahed, "Diffractive photoproduction of  $J/\psi$  and  $\Upsilon$  using holographic QCD: gravitational form factors and GPD of gluons in the proton," *Phys. Rev. D*, vol. 101, no. 8, p. 086003, 2020.
- [139] A. Ali *et al.*, "First Measurement of Near-Threshold  $J/\psi$  Exclusive Photoproduction off the Proton," *Phys. Rev. Lett.*, vol. 123, no. 7, p. 072001, 2019.
- [140] J.-L. Zhang, Z.-F. Cui, J. Ping, and C. D. Roberts, "Contact interaction analysis of pion GTMDs," 9 2020.
- [141] A. C. Aguilar *et al.*, "Pion and Kaon Structure at the Electron-Ion Collider," *Eur. Phys. J. A*, vol. 55, no. 10, p. 190, 2019.
- [142] R. L. Jaffe, "Spin, twist and hadron structure in deep inelastic processes," in *Ettore Majorana International School of Nucleon Structure: 1st Course: The Spin Structure of the Nucleon*, pp. 42–129, 1 1996.
- [143] A. Airapetian *et al.*, "Observation of a single spin azimuthal asymmetry in semiinclusive pion electro production," *Phys. Rev. Lett.*, vol. 84, pp. 4047–4051, 2000.
- [144] A. Airapetian *et al.*, "Single spin azimuthal asymmetries in electroproduction of neutral pions in semiinclusive deep inelastic scattering," *Phys. Rev. D*, vol. 64, p. 097101, 2001.
- [145] A. Airapetian *et al.*, "Measurement of single spin azimuthal asymmetries in semiinclusive electroproduction of pions and kaons on a longitudinally polarized deuterium target," *Phys. Lett. B*, vol. 562, pp. 182–192, 2003.
- [146] A. Airapetian *et al.*, "Subleading-twist effects in single-spin asymmetries in semiinclusive deep-inelastic scattering on a longitudinally polarized hydrogen target," *Phys. Lett. B*, vol. 622, pp. 14–22, 2005.
- [147] A. Airapetian *et al.*, "Beam-Spin Asymmetries in the Azimuthal Distribution of Pion Electroproduction," *Phys. Lett. B*, vol. 648, pp. 164–170, 2007.
- [148] W. Gohn *et al.*, "Beam-spin asymmetries from semi-inclusive pion electroproduction," *Phys. Rev. D*, vol. 89, no. 7, p. 072011, 2014.

- [149] H. Avakian *et al.*, "Measurement of beam-spin asymmetries for  $\pi^+$  electroproduction above the baryon resonance region," *Phys. Rev. D*, vol. 69, p. 112004, 2004.
- [150] M. Aghasyan *et al.*, "Precise measurements of beam spin asymmetries in semi-inclusive  $\pi^0$  production," *Phys. Lett. B*, vol. 704, pp. 397–402, 2011.
- [151] D. Adams *et al.*, "Comparison of spin asymmetries and cross-sections in  $\pi^0$  production by 200-GeV polarized anti-protons and protons," *Phys. Lett. B*, vol. 261, pp. 201–206, 1991.
- [152] K. Krueger *et al.*, "Large analyzing power in inclusive  $\pi^{+-}$  production at high  $x(F)$  with a 22-GeV/c polarized proton beam," *Phys. Lett. B*, vol. 459, pp. 412–416, 1999.
- [153] C. Allgower *et al.*, "Measurement of analyzing powers of  $\pi^+$  and  $\pi^-$  produced on a hydrogen and a carbon target with a 22-GeV/c incident polarized proton beam," *Phys. Rev. D*, vol. 65, p. 092008, 2002.
- [154] J. Adams *et al.*, "Cross-sections and transverse single spin asymmetries in forward neutral pion production from proton collisions at  $s^{*(1/2)} = 200$ -GeV," *Phys. Rev. Lett.*, vol. 92, p. 171801, 2004.
- [155] S. Adler *et al.*, "Measurement of transverse single-spin asymmetries for mid-rapidity production of neutral pions and charged hadrons in polarized p+p collisions at  $s^{*(1/2)} = 200$ -GeV," *Phys. Rev. Lett.*, vol. 95, p. 202001, 2005.
- [156] J. Lee and F. Videbaek, "Single spin asymmetries of identified hadrons in polarized p + p at  $s^{*(1/2)} = 62.4$  and 200-GeV," *AIP Conf. Proc.*, vol. 915, no. 1, pp. 533–538, 2007.
- [157] X. Ji, "Fundamental Properties of the Proton in Light-Front Zero Modes," 3 2020.
- [158] J.-w. Qiu and G. F. Sterman, "Single transverse spin asymmetries," *Phys. Rev. Lett.*, vol. 67, pp. 2264–2267, 1991.
- [159] R. Jaffe, " $g_2$ -The Nucleon's Other Spin-Dependent Structure Function," *Comments Nucl. Part. Phys.*, vol. 19, no. 5, pp. 239–257, 1990.
- [160] S. Wandzura and F. Wilczek, "Sum Rules for Spin Dependent Electroproduction: Test of Relativistic Constituent Quarks," *Phys. Lett. B*, vol. 72, pp. 195–198, 1977.
- [161] M. Burkardt, "Transverse force on quarks in deep-inelastic scattering," *Phys. Rev. D*, vol. 88, p. 114502, 2013.
- [162] L. Gamberg, D. Hwang, A. Metz, and M. Schlegel, "Light-cone divergence in twist-3 correlation functions," *Phys. Lett. B*, vol. 639, pp. 508–512, 2006.
- [163] A. Bacchetta, M. Diehl, K. Goeke, A. Metz, P. J. Mulders, and M. Schlegel, "Semi-inclusive deep inelastic scattering at small transverse momentum," *JHEP*, vol. 02, p. 093, 2007.

- [164] A. Efremov, K. Goeke, and P. Schweitzer, "Azimuthal asymmetries at CLAS: extraction of  $e^*a(x)$  and prediction of  $A(UL)$ ," *Phys. Rev. D*, vol. 67, p. 114014, 2003.
- [165] A. Courtoy, "Insights into the higher-twist distribution  $e(x)$  at CLAS," 5 2014.
- [166] S. Bastami *et al.*, "Semi-Inclusive Deep Inelastic Scattering in Wandzura-Wilczek-type approximation," *JHEP*, vol. 06, p. 007, 2019.
- [167] A. Bacchetta, P. J. Mulders, and F. Pijlman, "New observables in longitudinal single-spin asymmetries in semi-inclusive DIS," *Phys. Lett. B*, vol. 595, pp. 309–317, 2004.
- [168] A. Bianconi, S. Boffi, R. Jakob, and M. Radici, "Two hadron interference fragmentation functions. Part 1. General framework," *Phys. Rev. D*, vol. 62, p. 034008, 2000.
- [169] A. Bacchetta and M. Radici, "Two hadron semiinclusive production including sub-leading twist," *Phys. Rev. D*, vol. 69, p. 074026, 2004.
- [170] A. Bacchetta and M. Radici, "Partial wave analysis of two hadron fragmentation functions," *Phys. Rev. D*, vol. 67, p. 094002, 2003.
- [171] A. Bacchetta and M. Radici, "Modeling dihadron fragmentation functions," *Phys. Rev. D*, vol. 74, p. 114007, 2006.
- [172] R. Jaffe, X.-m. Jin, and J. Tang, "Interference fragmentation functions and the nucleon's transversity," *Phys. Rev. Lett.*, vol. 80, pp. 1166–1169, 1998.
- [173] M. Radici, R. Jakob, and A. Bianconi, "Accessing transversity with interference fragmentation functions," *Phys. Rev. D*, vol. 65, p. 074031, 2002.
- [174] F. A. Ceccopieri, M. Radici, and A. Bacchetta, "Evolution equations for extended dihadron fragmentation functions," *Phys. Lett. B*, vol. 650, pp. 81–89, 2007.
- [175] J. Zhou, F. Yuan, and Z.-T. Liang, "QCD Evolution of the Transverse Momentum Dependent Correlations," *Phys. Rev. D*, vol. 79, p. 114022, 2009.
- [176] W. Vogelsang and F. Yuan, "Next-to-leading Order Calculation of the Single Transverse Spin Asymmetry in the Drell-Yan Process," *Phys. Rev. D*, vol. 79, p. 094010, 2009.
- [177] Z.-B. Kang and J.-W. Qiu, "Evolution of twist-3 multi-parton correlation functions relevant to single transverse-spin asymmetry," *Phys. Rev. D*, vol. 79, p. 016003, 2009.
- [178] V. Braun, A. Manashov, and B. Pirnay, "Scale dependence of twist-three contributions to single spin asymmetries," *Phys. Rev. D*, vol. 80, p. 114002, 2009. [Erratum: *Phys.Rev.D* 86, 119902 (2012)].
- [179] Z.-B. Kang, "QCD evolution of naive-time-reversal-odd fragmentation functions," *Phys. Rev. D*, vol. 83, p. 036006, 2011.
- [180] H. Eguchi, Y. Koike, and K. Tanaka, "Twist-3 Formalism for Single Transverse Spin Asymmetry Reexamined: Semi-Inclusive Deep Inelastic Scattering," *Nucl. Phys. B*, vol. 763, pp. 198–227, 2007.

- [181] X. Ji, J.-W. Qiu, W. Vogelsang, and F. Yuan, "A unified picture for single transverse-spin asymmetries in hard processes," *Phys. Rev. Lett.*, vol. 97, p. 082002, 2006.
- [182] Y. Koike, W. Vogelsang, and F. Yuan, "On the Relation Between Mechanisms for Single-Transverse-Spin Asymmetries," *Phys. Lett. B*, vol. 659, pp. 878–884, 2008.
- [183] J. Cammarota, L. Gamberg, Z.-B. Kang, J. A. Miller, D. Pitonyak, A. Prokudin, T. C. Rogers, and N. Sato, "Origin of single transverse-spin asymmetries in high-energy collisions," *Phys. Rev. D*, vol. 102, no. 5, p. 054002, 2020.
- [184] L. Gamberg, Z.-B. Kang, A. Metz, D. Pitonyak, and A. Prokudin, "Left-right spin asymmetry in  $\ell N^\uparrow \rightarrow hX$ ," *Phys. Rev. D*, vol. 90, no. 7, p. 074012, 2014.
- [185] J.-w. Qiu and G. F. Sterman, "Single transverse spin asymmetries in hadronic pion production," *Phys. Rev. D*, vol. 59, p. 014004, 1999.
- [186] C. Kouvaris, J.-W. Qiu, W. Vogelsang, and F. Yuan, "Single transverse-spin asymmetry in high transverse momentum pion production in pp collisions," *Phys. Rev. D*, vol. 74, p. 114013, 2006.
- [187] A. Metz and D. Pitonyak, "Fragmentation contribution to the transverse single-spin asymmetry in proton-proton collisions," *Phys. Lett. B*, vol. 723, pp. 365–370, 2013. [Erratum: *Phys.Lett.B* 762, 549–549 (2016)].
- [188] K. Kanazawa, Y. Koike, A. Metz, and D. Pitonyak, "Towards an explanation of transverse single-spin asymmetries in proton-proton collisions: the role of fragmentation in collinear factorization," *Phys. Rev. D*, vol. 89, no. 11, p. 111501, 2014.
- [189] L. Gamberg, Z.-B. Kang, D. Pitonyak, and A. Prokudin, "Phenomenological constraints on  $A_N$  in  $p^\uparrow p \rightarrow \pi X$  from Lorentz invariance relations," *Phys. Lett. B*, vol. 770, pp. 242–251, 2017.
- [190] V. Barone and P. Ratcliffe, *Transverse spin physics*. 9 2003.
- [191] D. Pitonyak, *Exploring The Structure of Hadrons Through Spin Asymmetries in Hard Scattering Processes*. Ph.d thesis, Temple University, 2013.
- [192] A. Efremov and P. Schweitzer, "The Chirally odd twist 3 distribution  $e(a)(x)$ ," *JHEP*, vol. 08, p. 006, 2003.
- [193] M. Burkardt and Y. Koike, "Violation of sum rules for twist three parton distributions in QCD," *Nucl. Phys. B*, vol. 632, pp. 311–329, 2002.
- [194] F. Aslan and M. Burkardt, "Singularities in Twist-3 Quark Distributions," *Phys. Rev. D*, vol. 101, no. 1, p. 016010, 2020.
- [195] J. Ma and G. Zhang, "On the Singular Behavior of the Chirality-Odd Twist-3 Parton Distribution  $e(x)$ ," 3 2020.
- [196] Y. Hatta and Y. Zhao, "Parton distribution function for the gluon condensate," *Phys. Rev. D*, vol. 102, no. 3, p. 034004, 2020.

- [197] S. Bhattacharya, K. Cichy, M. Constantinou, A. Metz, A. Scapellato, and F. Steffens, "The role of zero-mode contributions in the matching for the twist-3 PDFs  $e(x)$  and  $h_L(x)$ ," 6 2020.
- [198] R. Jaffe and X.-D. Ji, "Chiral odd parton distributions and Drell-Yan processes," *Nucl. Phys. B*, vol. 375, pp. 527–560, 1992.
- [199] H. Avakian, A. Efremov, P. Schweitzer, and F. Yuan, "The transverse momentum dependent distribution functions in the bag model," *Phys. Rev. D*, vol. 81, p. 074035, 2010.
- [200] R. Jakob, P. Mulders, and J. Rodrigues, "Modeling quark distribution and fragmentation functions," *Nucl. Phys. A*, vol. 626, pp. 937–965, 1997.
- [201] P. Schweitzer, "The Chirally odd twist three distribution function  $e^{\alpha}(x)$  in the chiral quark soliton model," *Phys. Rev. D*, vol. 67, p. 114010, 2003.
- [202] M. Wakamatsu and Y. Ohnishi, "The Nonperturbative origin of delta function singularity in the chirally odd twist three distribution function  $e(x)$ ," *Phys. Rev. D*, vol. 67, p. 114011, 2003.
- [203] Y. Ohnishi and M. Wakamatsu, " $\pi$  N sigma term and chiral odd twist three distribution function  $e(x)$  of the nucleon in the chiral quark soliton model," *Phys. Rev. D*, vol. 69, p. 114002, 2004.
- [204] C. Lorcé, B. Pasquini, and P. Schweitzer, "Unpolarized transverse momentum dependent parton distribution functions beyond leading twist in quark models," *JHEP*, vol. 01, p. 103, 2015.
- [205] B. Pasquini and S. Rodini, "The twist-three distribution  $e^q(x, k_{\perp})$  in a light-front model," *Phys. Lett. B*, vol. 788, pp. 414–424, 2019.
- [206] M. Radici, A. Courtoy, A. Bacchetta, and M. Guagnelli, "Improved extraction of valence transversity distributions from inclusive dihadron production," *JHEP*, vol. 05, p. 123, 2015.
- [207] I. Balitsky, V. M. Braun, Y. Koike, and K. Tanaka, " $Q^{*2}$  evolution of chiral odd twist - three distributions  $h(L)(x, Q^{*2})$  and  $e(x, Q^{*2})$  in the large  $N(c)$  limit," *Phys. Rev. Lett.*, vol. 77, pp. 3078–3081, 1996.
- [208] A. V. Belitsky and D. Mueller, "Scale dependence of the chiral odd twist - three distributions  $h-L(x)$  and  $e(x)$ ," *Nucl. Phys. B*, vol. 503, pp. 279–308, 1997.
- [209] Y. Koike and N. Nishiyama, " $Q^{*2}$  evolution of chiral odd twist - three distribution  $e(x, Q^{*2})$ ," *Phys. Rev. D*, vol. 55, pp. 3068–3076, 1997.
- [210] C. Adloff *et al.*, "Inclusive measurement of diffractive deep inelastic ep scattering," *Z. Phys. C*, vol. 76, pp. 613–629, 1997.
- [211] J. Breitweg *et al.*, "Measurement of the diffractive structure function  $F_2(D(4))$  at HERA," *Eur. Phys. J.*, vol. C1, pp. 81–96, 1998.

- [212] J. C. Collins, "Proof of factorization for diffractive hard scattering," *Phys. Rev. D*, vol. 57, pp. 3051–3056, 1998. [Erratum: *Phys.Rev.D* 61, 019902 (2000)].
- [213] A. Berera and D. E. Soper, "Behavior of diffractive parton distribution functions," *Phys. Rev.*, vol. D53, pp. 6162–6179, 1996.
- [214] L. Trentadue and G. Veneziano, "Fracture functions: An Improved description of inclusive hard processes in QCD," *Phys. Lett. B*, vol. 323, pp. 201–211, 1994.
- [215] A. Aktas *et al.*, "Measurement and QCD analysis of the diffractive deep-inelastic scattering cross-section at HERA," *Eur.Phys.J.*, vol. C48, pp. 715–748, 2006.
- [216] S. Chekanov *et al.*, "A QCD analysis of ZEUS diffractive data," *Nucl.Phys.*, vol. B831, pp. 1–25, 2010.
- [217] L. Motyka, M. Sadzikowski, W. Słomiński, and K. Wichmann, "Evidence of quasi-partonic higher-twist effects in deep inelastic scattering at HERA at moderate  $Q^2$ ," *Eur. Phys. J. C*, vol. 78, no. 1, p. 80, 2018.
- [218] M. Klasen, G. Kramer, and S. Salesch, "Photoproduction of jets at HERA: Comparison of next-to-leading order calculation with ZEUS data," *Z. Phys. C*, vol. 68, pp. 113–120, 1995.
- [219] A. Aktas *et al.*, "Tests of QCD factorisation in the diffractive production of dijets in deep-inelastic scattering and photoproduction at HERA," *Eur. Phys. J. C*, vol. 51, pp. 549–568, 2007.
- [220] S. Chekanov *et al.*, "Diffractive photoproduction of dijets in ep collisions at HERA," *Eur. Phys. J. C*, vol. 55, pp. 177–191, 2008.
- [221] V. Guzey and M. Klasen, "Diffractive dijet photoproduction at the EIC," *JHEP*, vol. 05, p. 074, 2020.
- [222] L. Frankfurt, V. Guzey, and M. Strikman, "Leading twist nuclear shadowing phenomena in hard processes with nuclei," *Phys. Rept.*, vol. 512, pp. 255–393, 2012.
- [223] I. I. Balitsky and L. N. Lipatov, "The Pommeranchuk Singularity in Quantum Chromodynamics," *Sov. J. Nucl. Phys.*, vol. 28, pp. 822–829, 1978.
- [224] E. Kuraev, L. Lipatov, and V. S. Fadin, "The Pommeranchuk Singularity in Nonabelian Gauge Theories," *Sov. Phys. JETP*, vol. 45, pp. 199–204, 1977.
- [225] M. Deak, A. M. Stasto, and M. Strikman, "High  $|t|$  diffractive vector meson production at the EIC," 11 2020.
- [226] M. Dasgupta and G. P. Salam, "Event shapes in  $e^+e^-$  annihilation and deep inelastic scattering," *J.Phys.G*, vol. G30, p. R143, 2004.
- [227] E. Farhi, "A QCD test for jets," *Phys. Rev. Lett.*, vol. 39, pp. 1587–1588, 1977.

- [228] S. Catani, G. Turnock, and B. R. Webber, "Jet broadening measures in  $e^+e^-$  annihilation," *Phys. Lett.*, vol. B295, pp. 269–276, 1992.
- [229] R. K. Ellis, D. A. Ross, and A. E. Terrano, "The perturbative calculation of jet structure in  $e^+e^-$  annihilation," *Nucl. Phys.*, vol. B178, p. 421, 1981.
- [230] C. F. Berger, T. Kucs, and G. F. Sterman, "Event shape / energy flow correlations," *Phys. Rev. D*, vol. 68, p. 014012, 2003.
- [231] C. F. Berger and L. Magnea, "Scaling of power corrections for angularities from dressed gluon exponentiation," *Phys. Rev.*, vol. D70, p. 094010, 2004.
- [232] V. Antonelli, M. Dasgupta, and G. P. Salam, "Resummation of thrust distributions in DIS," *JHEP*, vol. 0002, p. 001, 2000.
- [233] I. W. Stewart, F. J. Tackmann, and W. J. Waalewijn, "N-Jettiness: An Inclusive Event Shape to Veto Jets," *Phys. Rev. Lett.*, vol. 105, p. 092002, 2010.
- [234] Z.-B. Kang, S. Mantry, and J.-W. Qiu, "N-Jettiness as a Probe of Nuclear Dynamics," *Phys.Rev.*, vol. D86, p. 114011, 2012.
- [235] D. Kang, C. Lee, and I. W. Stewart, "Using 1-Jettiness to Measure 2 Jets in DIS 3 Ways," *Phys.Rev.*, vol. D88, p. 054004, 2013.
- [236] Z.-B. Kang, X. Liu, and S. Mantry, "1-jettiness DIS event shape: NNLL+NLO results," *Phys.Rev.*, vol. D90, no. 1, p. 014041, 2014.
- [237] S. Catani, L. Trentadue, G. Turnock, and B. R. Webber, "Resummation of large logarithms in  $e^+e^-$  event shape distributions," *Nucl. Phys.*, vol. B407, pp. 3–42, 1993.
- [238] M. Dasgupta and G. P. Salam, "Resummed event shape variables in DIS," *JHEP*, vol. 0208, p. 032, 2002.
- [239] L. G. Almeida, S. D. Ellis, C. Lee, G. Sterman, I. Sung, and J. R. Walsh, "Comparing and counting logs in direct and effective methods of QCD resummation," *JHEP*, vol. 1404, p. 174, 2014.
- [240] C. W. Bauer, S. Fleming, and M. E. Luke, "Summing Sudakov logarithms in  $B \rightarrow X_s \gamma$  in effective field theory," *Phys. Rev.*, vol. D63, p. 014006, 2000.
- [241] C. W. Bauer, S. Fleming, D. Pirjol, and I. W. Stewart, "An effective field theory for collinear and soft gluons: Heavy to light decays," *Phys. Rev.*, vol. D63, p. 114020, 2001.
- [242] C. W. Bauer and I. W. Stewart, "Invariant operators in collinear effective theory," *Phys. Lett.*, vol. B516, pp. 134–142, 2001.
- [243] C. W. Bauer, D. Pirjol, and I. W. Stewart, "Soft-collinear factorization in effective field theory," *Phys. Rev.*, vol. D65, p. 054022, 2002.

- [244] C. W. Bauer, S. Fleming, D. Pirjol, I. Z. Rothstein, and I. W. Stewart, “Hard scattering factorization from effective field theory,” *Phys. Rev.*, vol. D66, p. 014017, 2002.
- [245] R. Abbate, M. Fickinger, A. H. Hoang, V. Mateu, and I. W. Stewart, “Thrust at N<sup>3</sup>LL with Power Corrections and a Precision Global Fit for  $\alpha_s(m_Z)$ ,” *Phys. Rev.*, vol. D83, p. 074021, 2011.
- [246] A. H. Hoang, D. W. Kolodrubetz, V. Mateu, and I. W. Stewart, “State-of-the-Art Predictions for C-parameter and a Determination of  $\alpha_s$ ,” 2015.
- [247] D. Kang, C. Lee, and I. W. Stewart, “DIS Event Shape at N3LL,” *PoS*, vol. DIS2015, p. 142, 2015.
- [248] I. W. Stewart, F. J. Tackmann, and W. J. Waalewijn, “Factorization at the LHC: From PDFs to Initial State Jets,” *Phys. Rev.*, vol. D81, p. 094035, 2010.
- [249] I. W. Stewart, F. J. Tackmann, and W. J. Waalewijn, “The Beam Thrust Cross Section for Drell-Yan at NNLL Order,” *Phys. Rev. Lett.*, vol. 106, p. 032001, 2011.
- [250] I. W. Stewart, F. J. Tackmann, and W. J. Waalewijn, “The Quark Beam Function at NNLL,” *JHEP*, vol. 09, p. 005, 2010.
- [251] J. Gaunt, M. Stahlhofen, and F. J. Tackmann, “The Gluon Beam Function at Two Loops,” *JHEP*, vol. 1408, p. 020, 2014.
- [252] J. R. Gaunt, M. Stahlhofen, and F. J. Tackmann, “The Quark Beam Function at Two Loops,” *JHEP*, vol. 1404, p. 113, 2014.
- [253] J. R. Gaunt and M. Stahlhofen, “The Fully-Differential Quark Beam Function at NNLO,” *JHEP*, vol. 1412, p. 146, 2014.
- [254] G. Korchemsky and A. Radyushkin, “Renormalization of the Wilson Loops Beyond the Leading Order,” *Nucl.Phys.*, vol. B283, pp. 342–364, 1987.
- [255] I. Korchemskaya and G. Korchemsky, “On lightlike Wilson loops,” *Phys.Lett.*, vol. B287, pp. 169–175, 1992.
- [256] S. Moch, J. Vermaseren, and A. Vogt, “The Three loop splitting functions in QCD: The Nonsinglet case,” *Nucl.Phys.*, vol. B688, pp. 101–134, 2004.
- [257] J. M. Henn, G. P. Korchemsky, and B. Mistlberger, “The full four-loop cusp anomalous dimension in  $\mathcal{N} = 4$  super Yang-Mills and QCD,” *JHEP*, vol. 04, p. 018, 2020.
- [258] D. Kang, C. Lee, and I. W. Stewart, “Analytic calculation of 1-jettiness in DIS at  $\mathcal{O}(\alpha_s)$ ,” *JHEP*, vol. 1411, p. 132, 2014.
- [259] G. P. Korchemsky and G. Sterman, “Power corrections to event shapes and factorization,” *Nucl. Phys.*, vol. B555, pp. 335–351, 1999.
- [260] G. P. Korchemsky and S. Tafat, “On power corrections to the event shape distributions in QCD,” *JHEP*, vol. 10, p. 010, 2000.

- [261] A. H. Hoang and I. W. Stewart, "Designing gapped soft functions for jet production," *Phys. Lett.*, vol. B660, pp. 483–493, 2008.
- [262] C. Lee and G. Sterman, "Momentum flow correlations from event shapes: Factorized soft gluons and Soft-Collinear Effective Theory," *Phys. Rev.*, vol. D75, p. 014022, 2007.
- [263] G. Salam and D. Wicke, "Hadron masses and power corrections to event shapes," *JHEP*, vol. 0105, p. 061, 2001.
- [264] V. Mateu, I. W. Stewart, and J. Thaler, "Power Corrections to Event Shapes with Mass-Dependent Operators," *Phys.Rev.*, vol. D87, p. 014025, 2013.
- [265] A. H. Hoang and S. Kluth, "Hemisphere soft function at  $\mathcal{O}(\alpha_s^2)$  for dijet production in  $e^+e^-$  annihilation," 2008.
- [266] H.-M. Chang, M. Procura, J. Thaler, and W. J. Waalewijn, "Calculating Track Thrust with Track Functions," *Phys. Rev. D*, vol. 88, p. 034030, 2013.
- [267] H.-M. Chang, M. Procura, J. Thaler, and W. J. Waalewijn, "Calculating Track-Based Observables for the LHC," *Phys. Rev. Lett.*, vol. 111, p. 102002, 2013.
- [268] R. A. Davison and B. R. Webber, "Non-perturbative contribution to the thrust distribution in  $e^+e^-$  annihilation," *Eur. Phys. J.*, vol. C59, pp. 13–25, 2009.
- [269] R. Abbate, M. Fickinger, A. H. Hoang, V. Mateu, and I. W. Stewart, "Precision Thrust Cumulant Moments at  $N^3\text{LL}$ ," *Phys.Rev.*, vol. D86, p. 094002, 2012.
- [270] T. Gehrmann, G. Luisoni, and P. F. Monni, "Power corrections in the dispersive model for a determination of the strong coupling constant from the thrust distribution," *Eur.Phys.J.*, vol. C73, no. 1, p. 2265, 2013.
- [271] A. H. Hoang, D. W. Kolodrubetz, V. Mateu, and I. W. Stewart, "A Precise Determination of  $\alpha_s$  from the C-parameter Distribution," 2015.
- [272] T. Sjostrand, S. Mrenna, and P. Z. Skands, "A Brief Introduction to PYTHIA 8.1," *Comput. Phys. Commun.*, vol. 178, pp. 852–867, 2008.
- [273] J. de Favereau, C. Delaere, P. Demin, A. Giammanco, V. Lemaître, A. Mertens, and M. Selvaggi, "DELPHES 3, A modular framework for fast simulation of a generic collider experiment," *JHEP*, vol. 02, p. 057, 2014.
- [274] E. D. W. Group, "Detector Matrix,"
- [275] E. A. et al, "Electron-Ion detector requirements and R+D handbook,"
- [276] M. I. Arratia, "Delphes EIC card,"
- [277] M. Cacciari, G. P. Salam, and G. Soyez, "The Anti-k(t) jet clustering algorithm," *JHEP*, vol. 04, p. 063, 2008.

- [278] RooUnfold <http://hepunix.rl.ac.uk/~adye/software/unfold/RooUnfold.html>.
- [279] R. Aaij *et al.*, “Measurement of the track reconstruction efficiency at LHCb,” *JINST*, vol. 10, no. 02, p. P02007, 2015.
- [280] F. Aaron *et al.*, “Jet Production in ep Collisions at Low  $Q^2$  and Determination of  $\alpha(s)$ ,” *Eur. Phys. J. C*, vol. 67, pp. 1–24, 2010.
- [281] U. von Toussaint, “Bayesian inference in physics,” *Rev. Mod. Phys.*, vol. 83, pp. 943–999, Sep 2011.
- [282] J. Kelly, “Simple parametrization of nucleon form factors,” *Phys. Rev. C*, vol. 70, p. 068202, 2004.
- [283] A. Puckett *et al.*, “Polarization Transfer Observables in Elastic Electron Proton Scattering at  $Q^2 = 2.5, 5.2, 6.8,$  and  $8.5 \text{ GeV}^2$ ,” *Phys. Rev. C*, vol. 96, no. 5, p. 055203, 2017. [Erratum: *Phys.Rev.C* 98, 019907 (2018)].
- [284] A. Accardi *et al.*, “ $e^+$ @JLab White Paper: An Experimental Program with Positron Beams at Jefferson Lab,” 7 2020.
- [285] D. Abbott *et al.*, “Phenomenology of the deuteron electromagnetic form-factors,” *Eur. Phys. J. A*, vol. 7, pp. 421–427, 2000.
- [286] D. Abbott *et al.*, “Measurement of tensor polarization in elastic electron deuteron scattering at large momentum transfer,” *Phys. Rev. Lett.*, vol. 84, pp. 5053–5057, 2000.
- [287] A. Parker and D. W. Higinbotham, “Deuteron form factor parameterization,” Oct. 2020. doi:10.5281/zenodo.4074280.
- [288] J. Zhou *et al.*, “Advanced extraction of the deuteron charge radius from electron-deuteron scattering data,” 10 2020.
- [289] M. Bouwhuis *et al.*, “Measurement of  $T(20)$  in elastic electron deuteron scattering,” *Phys. Rev. Lett.*, vol. 82, pp. 3755–3758, 1999.
- [290] D. Nikolenko *et al.*, “Measurement of the tensor analyzing powers  $T(20)$  and  $T(21)$  in elastic electron deuteron scattering,” *Phys. Rev. Lett.*, vol. 90, p. 072501, 2003.
- [291] G. Huber *et al.*, “Charged pion form-factor between  $Q^2 = 0.60\text{-GeV}^2$  and  $2.45\text{-GeV}^2$ . II. Determination of, and results for, the pion form-factor,” *Phys. Rev. C*, vol. 78, p. 045203, 2008.
- [292] T. Vrancx and J. Ryckebusch, “Charged pion electroproduction above the resonance region,” *Phys. Rev. C*, vol. 89, no. 2, p. 025203, 2014.
- [293] A. V. Belitsky and A. V. Radyushkin, “Unraveling hadron structure with generalized parton distributions,” *Phys. Rept.*, vol. 418, pp. 1–387, 2005.

- [294] K. Goeke, M. V. Polyakov, and M. Vanderhaeghen, "Hard exclusive reactions and the structure of hadrons," *Prog. Part. Nucl. Phys.*, vol. 47, pp. 401–515, 2001.
- [295] X. Ji, "Generalized parton distributions," *Ann. Rev. Nucl. Part. Sci.*, vol. 54, pp. 413–450, 2004.
- [296] S. Boffi and B. Pasquini, "Generalized parton distributions and the structure of the nucleon," *Riv. Nuovo Cim.*, vol. 30, p. 387, 2007.
- [297] M. Guidal, H. Moutarde, and M. Vanderhaeghen, "Generalized Parton Distributions in the valence region from Deeply Virtual Compton Scattering," *Rept. Prog. Phys.*, vol. 76, p. 066202, 2013.
- [298] N. Chouika, C. Mezrag, H. Moutarde, and J. Rodríguez-Quintero, "Covariant Extension of the GPD overlap representation at low Fock states," *Eur. Phys. J. C*, vol. 77, no. 12, p. 906, 2017.
- [299] K. Kumericki, S. Liuti, and H. Moutarde, "GPD phenomenology and DVCS fitting: Entering the high-precision era," *Eur. Phys. J. A*, vol. 52, no. 6, p. 157, 2016.
- [300] L. Favart, M. Guidal, T. Horn, and P. Kroll, "Deeply Virtual Meson Production on the nucleon," *Eur. Phys. J. A*, vol. 52, no. 6, p. 158, 2016.
- [301] B. Kriesten and S. Liuti, "Theory of Deeply Virtual Compton Scattering off the Unpolarized Proton," 4 2020.
- [302] A. Belitsky, D. Müller, and A. Kirchner, "Theory of deeply virtual compton scattering on the nucleon," *Nuclear Physics B*, vol. 629, p. 323–392, May 2002.
- [303] E. Berger, M. Diehl, and B. Pire, "Timelike compton scattering: exclusive photoproduction of lepton pairs," *The European Physical Journal C*, vol. 23, p. 675–689, Apr 2002.
- [304] M. Boër, M. Guidal, and M. Vanderhaeghen, "Timelike compton scattering off the proton and generalized parton distributions," *The European Physical Journal A*, vol. 51, p. 103, Aug 2015.
- [305] M. Boër, M. Guidal, and M. Vanderhaeghen, "Timelike compton scattering off the neutron," 2015.
- [306] O. Grocholski, H. Moutarde, B. Pire, P. Sznajder, and J. Wagner, "Data-driven study of timelike Compton scattering," 2019.
- [307] D. Mueller, B. Pire, L. Szymanowski, and J. Wagner, "On timelike and spacelike hard exclusive reactions," *Phys. Rev.*, vol. D86, p. 031502, 2012.
- [308] B. Pire, L. Szymanowski, and J. Wagner, "NLO corrections to timelike, spacelike and double deeply virtual Compton scattering," *Phys. Rev.*, vol. D83, p. 034009, 2011.

- [309] H. Moutarde, B. Pire, F. Sabatie, L. Szymanowski, and J. Wagner, "Timelike and spacelike deeply virtual Compton scattering at next-to-leading order," *Phys. Rev. D*, vol. 87, no. 5, p. 054029, 2013.
- [310] E.-C. Aschenauer, S. Fazio, K. Kumericki, and D. Mueller, "Deeply Virtual Compton Scattering at a Proposed High-Luminosity Electron-Ion Collider," *JHEP*, vol. 09, p. 093, 2013.
- [311] B. Pire, L. Szymanowski, and S. Wallon, "Diffractive deeply virtual Compton scattering," *Phys. Rev. D*, vol. 101, no. 7, p. 074005, 2020.
- [312] D. Y. Ivanov, B. Pire, L. Szymanowski, and O. Teryaev, "Probing chiral odd GPD's in diffractive electroproduction of two vector mesons," *Phys. Lett.*, vol. B550, pp. 65–76, 2002.
- [313] W. Cosyn, B. Pire, and L. Szymanowski, "Diffractive two-meson electroproduction with a nucleon and deuteron target," *Phys. Rev. D*, vol. 102, no. 5, p. 054003, 2020.
- [314] J. Chwastowski, W. Cosyn, M. Defurne, B. Pire, and R. Staszewski in progress.
- [315] R. Boussarie, B. Pire, L. Szymanowski, and S. Wallon, "Exclusive photoproduction of a  $\gamma\rho$  pair with a large invariant mass," *JHEP*, vol. 02, p. 054, 2017. [Erratum: *JHEP*10,029(2018)].
- [316] A. Pedrak, B. Pire, L. Szymanowski, and J. Wagner, "Hard photoproduction of a diphoton with a large invariant mass," *Phys. Rev. D*, vol. 96, no. 7, p. 074008, 2017. [Erratum: *Phys.Rev.D* 100, 039901 (2019)].
- [317] G. Duplančić, K. Passek-Kumerički, B. Pire, L. Szymanowski, and S. Wallon, "Probing axial quark generalized parton distributions through exclusive photoproduction of a  $\gamma\pi^\pm$  pair with a large invariant mass," *JHEP*, vol. 11, p. 179, 2018.
- [318] A. Pedrak, B. Pire, L. Szymanowski, and J. Wagner, "Electroproduction of a large invariant mass photon pair," *Phys. Rev. D*, vol. 101, no. 11, p. 114027, 2020.
- [319] B. Pire, D. Sokhan, L. Szymanowski, and S. Wallon in progress.
- [320] M. Siddikov and I. Schmidt, "Generalized Parton Distributions from charged current meson production," *Phys. Rev.*, vol. D99, no. 11, p. 116005, 2019.
- [321] M. Burkardt, "Impact parameter space interpretation for generalized parton distributions," *Int. J. Mod. Phys.*, vol. A18, pp. 173–208, 2003.
- [322] R. Dupre, M. Guidal, and M. Vanderhaeghen, "Tomographic image of the proton," *Phys. Rev. D*, vol. 95, no. 1, p. 011501, 2017.
- [323] R. Dupré, M. Guidal, S. Niccolai, and M. Vanderhaeghen, "Analysis of Deeply Virtual Compton Scattering Data at Jefferson Lab and Proton Tomography," *Eur. Phys. J.*, vol. A53, no. 8, p. 171, 2017.

- [324] H. Moutarde, P. Sznajder, and J. Wagner, "Border and skewness functions from a leading order fit to DVCS data," *Eur. Phys. J.*, vol. C78, no. 11, p. 890, 2018.
- [325] B. Pasquini and S. Boffi, "Nucleon spin densities in a light-front constituent quark model," *Phys. Lett.*, vol. B653, pp. 23–28, 2007.
- [326] E. C. Aschenauer, S. Fazio, J. H. Lee, H. Mantysaari, B. S. Page, B. Schenke, T. Ullrich, R. Venugopalan, and P. Zurita, "The Electron-Ion Collider: Assessing the Energy Dependence of Key Measurements," *arXiv preprint arXiv:1708.01527*, 2017.
- [327] S. Joosten and Z. Meziani, "Heavy Quarkonium Production at Threshold: from JLab to EIC," *PoS*, vol. QCDEV2017, p. 017, 2018.
- [328] M. V. Polyakov and P. Schweitzer, "Forces inside hadrons: pressure, surface tension, mechanical radius, and all that," *Int. J. Mod. Phys. A*, vol. 33, no. 26, p. 1830025, 2018.
- [329] M. Polyakov, "Generalized parton distributions and strong forces inside nucleons and nuclei," *Phys. Lett.*, vol. B555, pp. 57–62, 2003.
- [330] C. Lorcé, L. Mantovani, and B. Pasquini, "Spatial distribution of angular momentum inside the nucleon," *Phys. Lett.*, vol. B776, pp. 38–47, 2018.
- [331] X.-D. Ji, W. Melnitchouk, and X. Song, "A Study of off forward parton distributions," *Phys. Rev.*, vol. D56, pp. 5511–5523, 1997.
- [332] K. Goeke, J. Grabis, J. Ossmann, M. V. Polyakov, P. Schweitzer, A. Silva, and D. Urbano, "Nucleon form-factors of the energy momentum tensor in the chiral quark-soliton model," *Phys. Rev.*, vol. D75, p. 094021, 2007.
- [333] C. Cebulla, K. Goeke, J. Ossmann, and P. Schweitzer, "The Nucleon form-factors of the energy momentum tensor in the Skyrme model," *Nucl. Phys.*, vol. A794, pp. 87–114, 2007.
- [334] B. Pasquini, M. V. Polyakov, and M. Vanderhaeghen, "Dispersive evaluation of the D-term form factor in deeply virtual Compton scattering," *Phys. Lett.*, vol. B739, pp. 133–138, 2014.
- [335] P. Hagler *et al.*, "Nucleon Generalized Parton Distributions from Full Lattice QCD," *Phys. Rev.*, vol. D77, p. 094502, 2008.
- [336] P. Shanahan and W. Detmold, "Pressure Distribution and Shear Forces inside the Proton," *Phys. Rev. Lett.*, vol. 122, no. 7, p. 072003, 2019.
- [337] F. X. Girod *et al.*, "Measurement of Deeply virtual Compton scattering beam-spin asymmetries," *Phys. Rev. Lett.*, vol. 100, p. 162002, 2008.
- [338] H. S. Jo *et al.*, "Cross sections for the exclusive photon electroproduction on the proton and Generalized Parton Distributions," *Phys. Rev. Lett.*, vol. 115, no. 21, p. 212003, 2015.

- [339] V. D. Burkert, L. Elouadrhiri, and F. X. Girod, "The pressure distribution inside the proton," *Nature*, vol. 557, no. 7705, pp. 396–399, 2018.
- [340] K. Kumerički, "Measurability of pressure inside the proton," *Nature*, vol. 570, no. 7759, pp. E1–E2, 2019.
- [341] H. Moutarde, P. Sznajder, and J. Wagner, "Unbiased determination of DVCS Compton Form Factors," *Eur. Phys. J. C*, vol. 79, no. 7, p. 614, 2019.
- [342] H. Dutrieux, C. Lorcé, H. Moutarde, P. Sznajder, A. Trawiński, and J. Wagner in progress.
- [343] B. Pire and L. Szymanowski, "Hadron annihilation into two photons and backward VCS in the scaling regime of QCD," *Phys. Rev. D*, vol. 71, p. 111501, 2005.
- [344] J. Lansberg, B. Pire, and L. Szymanowski, "Backward DVCS and Proton to Photon Transition Distribution Amplitudes," *Nucl. Phys. A*, vol. 782, pp. 16–23, 2007.
- [345] B. Pire and L. Szymanowski, "QCD analysis of anti-p N  $\rightarrow$  gamma\* pi in the scaling limit," *Phys. Lett. B*, vol. 622, pp. 83–92, 2005.
- [346] J. Lansberg, B. Pire, K. Semenov-Tian-Shansky, and L. Szymanowski, "A consistent model for  $\pi$  N transition distribution amplitudes and backward pion electroproduction," *Phys. Rev. D*, vol. 85, p. 054021, 2012.
- [347] B. Pasquini, M. Pincetti, and S. Boffi, "Parton content of the nucleon from distribution amplitudes and transition distribution amplitudes," *Phys. Rev. D*, vol. 80, p. 014017, 2009.
- [348] B. Pire, K. Semenov-Tian-Shansky, and L. Szymanowski, "Nucleon-to-meson transition distribution amplitudes in impact parameter space," *PoS*, vol. LC2019, p. 012, 2019.
- [349] D. W. Sivers, "Single Spin Production Asymmetries from the Hard Scattering of Point-Like Constituents," *Phys. Rev.*, vol. D41, p. 83, 1990.
- [350] J. C. Collins, "Fragmentation of transversely polarized quarks probed in transverse momentum distributions," *Nucl. Phys. B*, vol. 396, pp. 161–182, 1993.
- [351] M. Anselmino, A. Mukherjee, and A. Vossen, "Transverse spin effects in hard semi-inclusive collisions," *Prog. Part. Nucl. Phys.*, vol. 114, p. 103806, 2020.
- [352] P. Mulders and R. Tangerman, "The Complete tree level result up to order  $1/Q$  for polarized deep inelastic lepton production," *Nucl. Phys. B*, vol. 461, pp. 197–237, 1996. [Erratum: *Nucl. Phys. B* 484, 538–540 (1997)].
- [353] J. Collins, *Foundations of perturbative QCD*, vol. 32. Cambridge University Press, 11 2013.

- [354] M. G. Echevarria, A. Idilbi, and I. Scimemi, "Factorization Theorem For Drell-Yan At Low  $q_T$  And Transverse Momentum Distributions On-The-Light-Cone," *JHEP*, vol. 07, p. 002, 2012.
- [355] I. Scimemi and A. Vladimirov, "Systematic analysis of double-scale evolution," *JHEP*, vol. 08, p. 003, 2018.
- [356] S. Aybat and T. C. Rogers, "TMD Parton Distribution and Fragmentation Functions with QCD Evolution," *Phys. Rev. D*, vol. 83, p. 114042, 2011.
- [357] I. Scimemi and A. Vladimirov, "Analysis of vector boson production within TMD factorization," *Eur. Phys. J. C*, vol. 78, no. 2, p. 89, 2018.
- [358] I. Scimemi and A. Vladimirov, "Non-perturbative structure of semi-inclusive deep-inelastic and Drell-Yan scattering at small transverse momentum," *JHEP*, vol. 06, p. 137, 2020.
- [359] A. Bacchetta, V. Bertone, C. Bissolotti, G. Bozzi, F. Delcarro, F. Piacenza, and M. Radici, "Transverse-momentum-dependent parton distributions up to  $N^3LL$  from Drell-Yan data," *JHEP*, vol. 07, p. 117, 2020.
- [360] M. Derrick *et al.*, "Inclusive charged particle distributions in deep inelastic scattering events at HERA," *Z. Phys. C*, vol. 70, pp. 1–16, 1996.
- [361] C. Adloff *et al.*, "Measurement of charged particle transverse momentum spectra in deep inelastic scattering," *Nucl. Phys. B*, vol. 485, pp. 3–24, 1997.
- [362] R. Asaturyan *et al.*, "Semi-Inclusive Charged-Pion Electroproduction off Protons and Deuterons: Cross Sections, Ratios and Access to the Quark-Parton Model at Low Energies," *Phys. Rev. C*, vol. 85, p. 015202, 2012.
- [363] A. Airapetian *et al.*, "Multiplicities of charged pions and kaons from semi-inclusive deep-inelastic scattering by the proton and the deuteron," *Phys. Rev. D*, vol. 87, p. 074029, 2013.
- [364] C. Adolph *et al.*, "Hadron Transverse Momentum Distributions in Muon Deep Inelastic Scattering at 160 GeV/c," *Eur. Phys. J. C*, vol. 73, no. 8, p. 2531, 2013. [Erratum: *Eur.Phys.J.C* 75, 94 (2015)].
- [365] M. Aghasyan *et al.*, "Transverse-momentum-dependent Multiplicities of Charged Hadrons in Muon-Deuteron Deep Inelastic Scattering," *Phys. Rev. D*, vol. 97, no. 3, p. 032006, 2018.
- [366] A. Ito *et al.*, "Measurement of the Continuum of Dimuons Produced in High-Energy Proton - Nucleus Collisions," *Phys. Rev. D*, vol. 23, pp. 604–633, 1981.
- [367] G. Moreno *et al.*, "Dimuon production in proton - copper collisions at  $\sqrt{s} = 38.8$ -GeV," *Phys. Rev. D*, vol. 43, pp. 2815–2836, 1991.

- [368] P. McGaughey *et al.*, “Cross-sections for the production of high mass muon pairs from 800-GeV proton bombardment of H-2,” *Phys. Rev. D*, vol. 50, pp. 3038–3045, 1994. [Erratum: *Phys.Rev.D* 60, 119903 (1999)].
- [369] C. Aidala *et al.*, “Measurements of  $\mu\mu$  pairs from open heavy flavor and Drell-Yan in  $p + p$  collisions at  $\sqrt{s} = 200$  GeV,” *Phys. Rev. D*, vol. 99, no. 7, p. 072003, 2019.
- [370] T. Affolder *et al.*, “The transverse momentum and total cross section of  $e^+e^-$  pairs in the Z boson region from  $p\bar{p}$  collisions at  $\sqrt{s} = 1.8$  TeV,” *Phys. Rev. Lett.*, vol. 84, pp. 845–850, 2000.
- [371] T. Aaltonen *et al.*, “Transverse momentum cross section of  $e^+e^-$  pairs in the Z-boson region from  $p\bar{p}$  collisions at  $\sqrt{s} = 1.96$  TeV,” *Phys. Rev. D*, vol. 86, p. 052010, 2012.
- [372] B. Abbott *et al.*, “Measurement of the inclusive differential cross section for Z bosons as a function of transverse momentum in  $\bar{p}p$  collisions at  $\sqrt{s} = 1.8$  TeV,” *Phys. Rev. D*, vol. 61, p. 032004, 2000.
- [373] V. Abazov *et al.*, “Measurement of the shape of the boson transverse momentum distribution in  $p\bar{p} \rightarrow Z/\gamma^* \rightarrow e^+e^- + X$  events produced at  $\sqrt{s}=1.96$ -TeV,” *Phys. Rev. Lett.*, vol. 100, p. 102002, 2008.
- [374] V. M. Abazov *et al.*, “Measurement of the Normalized  $Z/\gamma^* \rightarrow \mu^+\mu^-$  Transverse Momentum Distribution in  $p\bar{p}$  Collisions at  $\sqrt{s} = 1.96$  TeV,” *Phys. Lett. B*, vol. 693, pp. 522–530, 2010.
- [375] G. Aad *et al.*, “Measurement of the  $Z/\gamma^*$  boson transverse momentum distribution in  $pp$  collisions at  $\sqrt{s} = 7$  TeV with the ATLAS detector,” *JHEP*, vol. 09, p. 145, 2014.
- [376] G. Aad *et al.*, “Measurement of the transverse momentum and  $\phi_\eta^*$  distributions of Drell-Yan lepton pairs in proton-proton collisions at  $\sqrt{s} = 8$  TeV with the ATLAS detector,” *Eur. Phys. J. C*, vol. 76, no. 5, p. 291, 2016.
- [377] S. Chatrchyan *et al.*, “Measurement of the Rapidity and Transverse Momentum Distributions of Z Bosons in  $pp$  Collisions at  $\sqrt{s} = 7$  TeV,” *Phys. Rev. D*, vol. 85, p. 032002, 2012.
- [378] V. Khachatryan *et al.*, “Measurement of the transverse momentum spectra of weak vector bosons produced in proton-proton collisions at  $\sqrt{s} = 8$  TeV,” *JHEP*, vol. 02, p. 096, 2017.
- [379] R. Aaij *et al.*, “Measurement of the forward Z boson production cross-section in  $pp$  collisions at  $\sqrt{s} = 7$  TeV,” *JHEP*, vol. 08, p. 039, 2015.
- [380] R. Aaij *et al.*, “Measurement of forward W and Z boson production in  $pp$  collisions at  $\sqrt{s} = 8$  TeV,” *JHEP*, vol. 01, p. 155, 2016.
- [381] R. Aaij *et al.*, “Measurement of the forward Z boson production cross-section in  $pp$  collisions at  $\sqrt{s} = 13$  TeV,” *JHEP*, vol. 09, p. 136, 2016.

- [382] A. A. Vladimirov, "Self-contained definition of the Collins-Soper kernel," *Phys. Rev. Lett.*, vol. 125, no. 19, p. 192002, 2020.
- [383] J. C. Collins, "Leading-twist Single-transverse-spin asymmetries: Drell- Yan and Deep-Inelastic Scattering," *Phys. Lett.*, vol. B536, pp. 43–48, 2002.
- [384] A. Efremov and O. Teryaev, "THE TRANSVERSAL POLARIZATION IN QUANTUM CHROMODYNAMICS," *Sov. J. Nucl. Phys.*, vol. 39, p. 962, 1984.
- [385] I. Scimemi, A. Tarasov, and A. Vladimirov, "Collinear matching for Sivers function at next-to-leading order," *JHEP*, vol. 05, p. 125, 2019.
- [386] M. Anselmino, M. Boglione, U. D'Alesio, A. Kotzinian, S. Melis, F. Murgia, A. Prokudin, and C. Turk, "Sivers Effect for Pion and Kaon Production in Semi-Inclusive Deep Inelastic Scattering," *Eur. Phys. J.*, vol. A39, pp. 89–100, 2009.
- [387] M. Bury, A. Prokudin, and A. Vladimirov, "in preparation,"
- [388] A. Airapetian *et al.*, "Azimuthal single- and double-spin asymmetries in semi-inclusive deep-inelastic lepton scattering by transversely polarized protons," 7 2020.
- [389] C. Adolph *et al.*, "Collins and Sivers asymmetries in muonproduction of pions and kaons off transversely polarised protons," *Phys. Lett. B*, vol. 744, pp. 250–259, 2015.
- [390] C. Adolph *et al.*, "Sivers asymmetry extracted in SIDIS at the hard scales of the Drell–Yan process at COMPASS," *Phys. Lett. B*, vol. 770, pp. 138–145, 2017.
- [391] M. Alekseev *et al.*, "Collins and Sivers asymmetries for pions and kaons in muon-deuteron DIS," *Phys. Lett.*, vol. B673, pp. 127–135, 2009.
- [392] X. Qian *et al.*, "Single Spin Asymmetries in Charged Pion Production from Semi-Inclusive Deep Inelastic Scattering on a Transversely Polarized  $^3\text{He}$  Target," *Phys. Rev. Lett.*, vol. 107, p. 072003, 2011.
- [393] M. Aghasyan *et al.*, "First measurement of transverse-spin-dependent azimuthal asymmetries in the Drell-Yan process," *Phys. Rev. Lett.*, vol. 119, no. 11, p. 112002, 2017.
- [394] Ł. Adamczyk *et al.*, "Measurement of the transverse single-spin asymmetry in  $p^\uparrow + p \rightarrow W^\pm / Z^0$  at RHIC," *Phys. Rev. Lett.*, vol. 116, no. 13, p. 132301, 2016.
- [395] A. Airapetian *et al.*, "Single-spin asymmetries in semi-inclusive deep-inelastic scattering on a transversely polarized hydrogen target," *Phys. Rev. Lett.*, vol. 94, p. 012002, 2005.
- [396] A. Airapetian *et al.*, "Effects of transversity in deep-inelastic scattering by polarized protons," *Phys. Lett. B*, vol. 693, pp. 11–16, 2010.
- [397] K. Abe *et al.*, "Measurement of azimuthal asymmetries in inclusive production of hadron pairs in  $e^+ e^-$  annihilation at Belle," *Phys. Rev. Lett.*, vol. 96, p. 232002, 2006.

- [398] R. Seidl *et al.*, “Measurement of Azimuthal Asymmetries in Inclusive Production of Hadron Pairs in  $e^+e^-$  Annihilation at  $s^{*(1/2)} = 10.58\text{-GeV}$ ,” *Phys. Rev. D*, vol. 78, p. 032011, 2008. [Erratum: *Phys.Rev.D* 86, 039905 (2012)].
- [399] J. Lees *et al.*, “Measurement of Collins asymmetries in inclusive production of charged pion pairs in  $e^+e^-$  annihilation at BABAR,” *Phys. Rev. D*, vol. 90, no. 5, p. 052003, 2014.
- [400] J. Lees *et al.*, “Collins asymmetries in inclusive charged  $KK$  and  $K\pi$  pairs produced in  $e^+e^-$  annihilation,” *Phys. Rev. D*, vol. 92, no. 11, p. 111101, 2015.
- [401] M. Ablikim *et al.*, “Measurement of azimuthal asymmetries in inclusive charged dipion production in  $e^+e^-$  annihilations at  $\sqrt{s} = 3.65\text{ GeV}$ ,” *Phys. Rev. Lett.*, vol. 116, no. 4, p. 042001, 2016.
- [402] H. Li *et al.*, “Azimuthal asymmetries of back-to-back  $\pi^\pm - (\pi^0, \eta, \pi^\pm)$  pairs in  $e^+e^-$  annihilation,” *Phys. Rev. D*, vol. 100, no. 9, p. 092008, 2019.
- [403] C. Alexandrou, S. Bacchio, M. Constantinou, J. Finkenrath, K. Hadjiyiannakou, K. Jansen, G. Koutsou, and A. Vaquero Aviles-Casco, “The nucleon axial, tensor and scalar charges and  $\sigma$ -terms in lattice QCD,” 2019.
- [404] A. Courtoy, S. Baeßler, M. González-Alonso, and S. Liuti, “Beyond-Standard-Model Tensor Interaction and Hadron Phenomenology,” *Phys. Rev. Lett.*, vol. 115, p. 162001, 2015.
- [405] T. Liu, Z. Zhao, and H. Gao, “Experimental constraint on quark electric dipole moments,” *Phys. Rev. D*, vol. 97, no. 7, p. 074018, 2018.
- [406] P. J. Mulders and J. Rodrigues, “Transverse momentum dependence in gluon distribution and fragmentation functions,” *Phys. Rev.*, vol. D63, p. 094021, 2001.
- [407] M. G. Echevarria, T. Kasemets, P. J. Mulders, and C. Pisano, “QCD evolution of (un)polarized gluon TMDPDFs and the Higgs  $q_T$ -distribution,” *JHEP*, vol. 07, p. 158, 2015. [Erratum: *JHEP* 05, 073 (2017)].
- [408] M. Buffing, A. Mukherjee, and P. Mulders, “Generalized Universality of Definite Rank Gluon Transverse Momentum Dependent Correlators,” *Phys. Rev. D*, vol. 88, p. 054027, 2013.
- [409] C. Pisano, D. Boer, S. J. Brodsky, M. G. Buffing, and P. J. Mulders, “Linear polarization of gluons and photons in unpolarized collider experiments,” *JHEP*, vol. 10, p. 024, 2013.
- [410] D. Boer, M. G. Echevarria, P. Mulders, and J. Zhou, “Single spin asymmetries from a single Wilson loop,” *Phys. Rev. Lett.*, vol. 116, no. 12, p. 122001, 2016.
- [411] C. Bomhof, P. Mulders, and F. Pijlman, “The Construction of gauge-links in arbitrary hard processes,” *Eur. Phys. J. C*, vol. 47, pp. 147–162, 2006.

- [412] F. Dominguez, C. Marquet, B.-W. Xiao, and F. Yuan, "Universality of Unintegrated Gluon Distributions at small  $x$ ," *Phys. Rev.*, vol. D83, p. 105005, 2011.
- [413] D. Boer, C. Lorcé, C. Pisano, and J. Zhou, "The gluon Sivers distribution: status and future prospects," *Adv. High Energy Phys.*, vol. 2015, p. 371396, 2015.
- [414] D. Boer, S. Cotogno, T. van Daal, P. J. Mulders, A. Signori, and Y.-J. Zhou, "Gluon and Wilson loop TMDs for hadrons of spin  $\leq 1$ ," *JHEP*, vol. 10, p. 013, 2016.
- [415] S. J. Brodsky, F. Fleuret, C. Hadjidakis, and J. P. Lansberg, "Physics Opportunities of a Fixed-Target Experiment using the LHC Beams," *Phys. Rept.*, vol. 522, pp. 239–255, 2013.
- [416] D. Kikoła, M. G. Echevarria, C. Hadjidakis, J.-P. Lansberg, C. Lorcé, L. Massacrier, C. M. Quintans, A. Signori, and B. Trzeciak, "Feasibility Studies for Single Transverse-Spin Asymmetry Measurements at a Fixed-Target Experiment Using the LHC Proton and Lead Beams (AFTER@LHC)," *Few Body Syst.*, vol. 58, no. 4, p. 139, 2017.
- [417] C. Hadjidakis *et al.*, "A Fixed-Target Programme at the LHC: Physics Case and Projected Performances for Heavy-Ion, Hadron, Spin and Astroparticle Studies," 7 2018.
- [418] D. Boer, P. J. Mulders, C. Pisano, and J. Zhou, "Asymmetries in Heavy Quark Pair and Dijet Production at an EIC," *JHEP*, vol. 08, p. 001, 2016.
- [419] D. Boer *et al.*, "Gluons and the quark sea at high energies: Distributions, polarization, tomography," *arXiv preprint arXiv:1108.1713*, 2011.
- [420] T. Burton, "Gluon sivers and experimental considerations for TMDs," *arXiv preprint arXiv:1212.3590*, 2012.
- [421] L. Zheng, E. C. Aschenauer, J. H. Lee, B.-W. Xiao, and Z.-B. Yin, "Accessing the gluon Sivers function at a future electron-ion collider," *Phys. Rev.*, vol. D98, no. 3, p. 034011, 2018.
- [422] D. Boer and C. Pisano, "Polarized gluon studies with charmonium and bottomonium at LHCb and AFTER," *Phys. Rev. D*, vol. 86, p. 094007, 2012.
- [423] J. Ma, J. Wang, and S. Zhao, "Transverse momentum dependent factorization for quarkonium production at low transverse momentum," *Phys. Rev. D*, vol. 88, no. 1, p. 014027, 2013.
- [424] G.-P. Zhang, "Probing transverse momentum dependent gluon distribution functions from hadronic quarkonium pair production," *Phys. Rev. D*, vol. 90, no. 9, p. 094011, 2014.
- [425] J. Ma and C. Wang, "QCD factorization for quarkonium production in hadron collisions at low transverse momentum," *Phys. Rev. D*, vol. 93, no. 1, p. 014025, 2016.

- [426] D. Boer, “Linearly polarized gluon effects in unpolarized collisions,” *PoS*, vol. QCDEV2015, p. 023, 2015.
- [427] R. Bain, Y. Makris, and T. Mehen, “Transverse Momentum Dependent Fragmenting Jet Functions with Applications to Quarkonium Production,” *JHEP*, vol. 11, p. 144, 2016.
- [428] A. Mukherjee and S. Rajesh, “Probing Transverse Momentum Dependent Parton Distributions in Charmonium and Bottomonium Production,” *Phys. Rev. D*, vol. 93, no. 5, p. 054018, 2016.
- [429] A. Mukherjee and S. Rajesh, “Linearly polarized gluons in charmonium and bottomonium production in color octet model,” *Phys. Rev. D*, vol. 95, no. 3, p. 034039, 2017.
- [430] J.-P. Lansberg, C. Pisano, and M. Schlegel, “Associated production of a dilepton and a  $Y(J/\psi)$  at the LHC as a probe of gluon transverse momentum dependent distributions,” *Nucl. Phys. B*, vol. 920, pp. 192–210, 2017.
- [431] J.-P. Lansberg, C. Pisano, F. Scarpa, and M. Schlegel, “Pinning down the linearly-polarised gluons inside unpolarised protons using quarkonium-pair production at the LHC,” *Phys. Lett. B*, vol. 784, pp. 217–222, 2018. [Erratum: *Phys.Lett.B* 791, 420–421 (2019)].
- [432] A. Bacchetta, D. Boer, C. Pisano, and P. Taels, “Gluon TMDs and NRQCD matrix elements in  $J/\psi$  production at an EIC,” *Eur. Phys. J. C*, vol. 80, no. 1, p. 72, 2020.
- [433] U. D’Alesio, F. Murgia, C. Pisano, and P. Taels, “Azimuthal asymmetries in semi-inclusive  $J/\psi + \text{jet}$  production at an EIC,” *Phys. Rev. D*, vol. 100, no. 9, p. 094016, 2019.
- [434] M. G. Echevarria, “Proper TMD factorization for quarkonia production:  $pp \rightarrow \eta_{c,b}$  as a study case,” *JHEP*, vol. 10, p. 144, 2019.
- [435] S. Fleming, Y. Makris, and T. Mehen, “An effective field theory approach to quarkonium at small transverse momentum,” *JHEP*, vol. 04, p. 122, 2020.
- [436] F. Scarpa, D. Boer, M. G. Echevarria, J.-P. Lansberg, C. Pisano, and M. Schlegel, “Studies of gluon TMDs and their evolution using quarkonium-pair production at the LHC,” *Eur. Phys. J. C*, vol. 80, no. 2, p. 87, 2020.
- [437] M. Grewal, Z.-B. Kang, J.-W. Qiu, and A. Signori, “Predictive power of transverse-momentum-dependent distributions,” *Phys. Rev. D*, vol. 101, no. 11, p. 114023, 2020.
- [438] D. Boer, U. D’Alesio, F. Murgia, C. Pisano, and P. Taels, “ $J/\psi$  meson production in SIDIS: matching high and low transverse momentum,” *JHEP*, vol. 09, p. 040, 2020.
- [439] K.-T. Chao, Y.-Q. Ma, H.-S. Shao, K. Wang, and Y.-J. Zhang, “ $J/\psi$  Polarization at Hadron Colliders in Nonrelativistic QCD,” *Phys. Rev. Lett.*, vol. 108, p. 242004, 2012.

- [440] R. Sharma and I. Vitev, "High transverse momentum quarkonium production and dissociation in heavy ion collisions," *Phys. Rev. C*, vol. 87, no. 4, p. 044905, 2013.
- [441] R. F. del Castillo, M. G. Echevarria, Y. Makris, and I. Scimemi, "TMD factorization for di-jet and heavy meson pair in DIS," 8 2020.
- [442] U. D'Alesio, F. Murgia, and C. Pisano, "Towards a first estimate of the gluon Sivers function from  $A_N$  data in pp collisions at RHIC," *JHEP*, vol. 09, p. 119, 2015.
- [443] S. Gliske, A. Bacchetta, and M. Radici, "Production of two hadrons in semi-inclusive deep inelastic scattering," *Phys. Rev. D*, vol. 90, no. 11, p. 114027, 2014. [Erratum: *Phys.Rev.D* 91, 019902 (2015)].
- [444] A. Vossen *et al.*, "Observation of transverse polarization asymmetries of charged pion pairs in  $e^+e^-$  annihilation near  $\sqrt{s} = 10.58$  GeV," *Phys. Rev. Lett.*, vol. 107, p. 072004, 2011.
- [445] D. Boer, R. Jakob, and M. Radici, "Interference fragmentation functions in electron positron annihilation," *Phys. Rev.*, vol. D67, p. 094003, 2003.
- [446] A. Bacchetta, F. A. Ceccopieri, A. Mukherjee, and M. Radici, "Asymmetries involving dihadron fragmentation functions: from DIS to  $e+e-$  annihilation," *Phys. Rev.*, vol. D79, p. 034029, 2009.
- [447] A. Courtoy, A. Bacchetta, M. Radici, and A. Bianconi, "First extraction of Interference Fragmentation Functions from  $e^+e^-$  data," *Phys. Rev. D*, vol. 85, p. 114023, 2012.
- [448] H. H. Matevosyan, A. Bacchetta, D. Boer, A. Courtoy, A. Kotzinian, M. Radici, and A. W. Thomas, "Semi-inclusive production of two back-to-back hadron pairs in  $e^+e^-$  annihilation revisited," *Phys. Rev.*, vol. D97, no. 7, p. 074019, 2018.
- [449] A. Airapetian *et al.*, "Evidence for a Transverse Single-Spin Asymmetry in Lepto-production of  $\pi^+\pi^-$  Pairs," *JHEP*, vol. 06, p. 017, 2008.
- [450] C. Adolph *et al.*, "Transverse spin effects in hadron-pair production from semi-inclusive deep inelastic scattering," *Phys.Lett.*, vol. B713, pp. 10–16, 2012.
- [451] C. Adolph *et al.*, "A high-statistics measurement of transverse spin effects in dihadron production from muon-proton semi-inclusive deep-inelastic scattering," *Phys.Lett.*, vol. B736, pp. 124–131, 2014.
- [452] C. Braun, "COMPASS results on the transverse spin asymmetry in hadron-pair production in SIDIS," *EPJ Web Conf.*, vol. 85, p. 02018, 2015.
- [453] A. Bacchetta, A. Courtoy, and M. Radici, "First glances at the transversity parton distribution through dihadron fragmentation functions," *Phys. Rev. Lett.*, vol. 107, p. 012001, 2011.
- [454] A. Bacchetta, A. Courtoy, and M. Radici, "First extraction of valence transversities in a collinear framework," *JHEP*, vol. 03, p. 119, 2013.

- [455] J. Benel, A. Courtoy, and R. Ferro-Hernandez, "A constrained fit of the valence transversity distributions from dihadron production," *Eur. Phys. J. C*, vol. 80, no. 5, p. 465, 2020.
- [456] A. Bacchetta and M. Radici, "Dihadron interference fragmentation functions in proton-proton collisions," *Phys. Rev.*, vol. D70, p. 094032, 2004.
- [457] L. Adamczyk *et al.*, "Observation of Transverse Spin-Dependent Azimuthal Correlations of Charged Pion Pairs in  $p^\uparrow + p$  at  $\sqrt{s} = 200$  GeV," *Phys. Rev. Lett.*, vol. 115, p. 242501, 2015.
- [458] M. Radici and A. Bacchetta, "First Extraction of Transversity from a Global Analysis of Electron-Proton and Proton-Proton Data," *Phys. Rev. Lett.*, vol. 120, no. 19, p. 192001, 2018.
- [459] T. Harris, G. von Hippel, P. Junnarkar, H. B. Meyer, K. Ottnad, J. Wilhelm, H. Wittig, and L. Wrang, "Nucleon isovector charges and twist-2 matrix elements with  $N_f = 2 + 1$  dynamical Wilson quarks," *Phys. Rev.*, vol. D100, no. 3, p. 034513, 2019.
- [460] N. Hasan, J. Green, S. Meinel, M. Engelhardt, S. Krieg, J. Negele, A. Pochinsky, and S. Syritsyn, "Nucleon axial, scalar, and tensor charges using lattice QCD at the physical pion mass," *Phys. Rev.*, vol. D99, no. 11, p. 114505, 2019.
- [461] N. Yamanaka, S. Hashimoto, T. Kaneko, and H. Ohki, "Nucleon charges with dynamical overlap fermions," *Phys. Rev.*, vol. D98, no. 5, p. 054516, 2018.
- [462] R. Gupta, Y.-C. Jang, B. Yoon, H.-W. Lin, V. Cirigliano, and T. Bhattacharya, "Isovector Charges of the Nucleon from 2+1+1-flavor Lattice QCD," *Phys. Rev.*, vol. D98, p. 034503, 2018.
- [463] C. Alexandrou *et al.*, "Nucleon scalar and tensor charges using lattice QCD simulations at the physical value of the pion mass," *Phys. Rev.*, vol. D95, no. 11, p. 114514, 2017. [erratum: *Phys. Rev.*D96,no.9,099906(2017)].
- [464] G. S. Bali, S. Collins, B. Glaesle, M. Goeckeler, J. Najjar, R. H. Roedl, A. Schaefer, R. W. Schiel, W. Soeldner, and A. Sternbeck, "Nucleon isovector couplings from  $N_f = 2$  lattice QCD," *Phys. Rev.*, vol. D91, no. 5, p. 054501, 2015.
- [465] J. R. Green, J. W. Negele, A. V. Pochinsky, S. N. Syritsyn, M. Engelhardt, and S. Krieg, "Nucleon Scalar and Tensor Charges from Lattice QCD with Light Wilson Quarks," *Phys. Rev.*, vol. D86, p. 114509, 2012.
- [466] D. Boer and P. J. Mulders, "Time reversal odd distribution functions in lepton production," *Phys. Rev.*, vol. D57, pp. 5780–5786, 1998.
- [467] M. Arratia, Y. Song, F. Ringer, and B. Jacak, "Jets as precision probes in electron-nucleus collisions at the Electron-Ion Collider," *Phys. Rev. C*, vol. 101, no. 6, p. 065204, 2020.

- [468] M. Arratia, Y. Makris, D. Neill, F. Ringer, and N. Sato, "Asymmetric jet clustering in deep-inelastic scattering," 6 2020.
- [469] D. Gutierrez-Reyes, I. Scimemi, W. J. Waalewijn, and L. Zoppi, "Transverse momentum dependent distributions with jets," *Phys. Rev. Lett.*, vol. 121, no. 16, p. 162001, 2018.
- [470] X. Liu, F. Ringer, W. Vogelsang, and F. Yuan, "Lepton-jet Correlations in Deep Inelastic Scattering at the Electron-Ion Collider," *Phys. Rev. Lett.*, vol. 122, no. 19, p. 192003, 2019.
- [471] D. Gutierrez-Reyes, I. Scimemi, W. J. Waalewijn, and L. Zoppi, "Transverse momentum dependent distributions in  $e^+e^-$  and semi-inclusive deep-inelastic scattering using jets," *JHEP*, vol. 10, p. 031, 2019.
- [472] D. Gutierrez-Reyes, Y. Makris, V. Vaidya, I. Scimemi, and L. Zoppi, "Probing Transverse-Momentum Distributions With Groomed Jets," *JHEP*, vol. 08, p. 161, 2019.
- [473] Z.-B. Kang, X. Liu, S. Mantry, and D. Y. Shao, "Jet Charge: A Flavor Prism for Spin Asymmetries at the EIC," 8 2020.
- [474] X. Liu, F. Ringer, W. Vogelsang, and F. Yuan, "Lepton-jet Correlation in Deep Inelastic Scattering," 7 2020.
- [475] M. Arratia, Z.-B. Kang, A. Prokudin, and F. Ringer, "Jet-based measurements of Sivers and Collins asymmetries at the future Electron-Ion Collider," 7 2020.
- [476] Z.-B. Kang, K. Lee, and F. Zhao, "Polarized jet fragmentation functions," *Phys. Lett. B*, vol. 809, p. 135756, 2020.
- [477] F. Yuan, "Azimuthal asymmetric distribution of hadrons inside a jet at hadron collider," *Phys. Rev. Lett.*, vol. 100, p. 032003, 2008.
- [478] D. Neill, I. Scimemi, and W. J. Waalewijn, "Jet axes and universal transverse-momentum-dependent fragmentation," *JHEP*, vol. 04, p. 020, 2017.
- [479] Z.-B. Kang, X. Liu, F. Ringer, and H. Xing, "The transverse momentum distribution of hadrons within jets," *JHEP*, vol. 11, p. 068, 2017.
- [480] Z.-B. Kang, F. Ringer, and W. J. Waalewijn, "The Energy Distribution of Subjets and the Jet Shape," *JHEP*, vol. 07, p. 064, 2017.
- [481] Z.-B. Kang, A. Prokudin, F. Ringer, and F. Yuan, "Collins azimuthal asymmetries of hadron production inside jets," *Phys. Lett. B*, vol. 774, pp. 635–642, 2017.
- [482] Y. Makris, D. Neill, and V. Vaidya, "Probing Transverse-Momentum Dependent Evolution With Groomed Jets," *JHEP*, vol. 07, p. 167, 2018.

- [483] D. Neill, A. Papaefstathiou, W. J. Waalewijn, and L. Zoppi, "Phenomenology with a recoil-free jet axis: TMD fragmentation and the jet shape," *JHEP*, vol. 01, p. 067, 2019.
- [484] P. Cal, F. Ringer, and W. J. Waalewijn, "The jet shape at NLL'," *JHEP*, vol. 05, p. 143, 2019.
- [485] P. Cal, D. Neill, F. Ringer, and W. J. Waalewijn, "Calculating the angle between jet axes," *JHEP*, vol. 04, p. 211, 2020.
- [486] A. J. Larkoski, I. Moulton, and B. Nachman, "Jet substructure at the large hadron collider: A review of recent advances in theory and machine learning," *Phys. Rep.*, vol. 841, p. 1, 2020.
- [487] M. Connors, C. Nattrass, R. Reed, and S. Salur, "Review of Jet Measurements in Heavy Ion Collisions," *arXiv preprint arXiv:1705.01974*, 2017.
- [488] P. Newman and M. Wing, "The Hadronic Final State at HERA," *Rev. Mod. Phys.*, vol. 86, no. 3, p. 1037, 2014.
- [489] L. Zheng, E. C. Aschenauer, J. H. Lee, B.-W. Xiao, and Z.-B. Yin, "Accessing the Gluon Sivers Function at a future Electron-Ion Collider," *arXiv preprint arXiv:1805.05290*, 2018.
- [490] Y. Hatta, B.-W. Xiao, and F. Yuan, "Probing the Small- $x$  Gluon Tomography in Correlated Hard Diffractive Dijet Production in Deep Inelastic Scattering," *Phys. Rev. Lett.*, vol. 116, no. 20, p. 202301, 2016.
- [491] H. Mäntysaari, N. Mueller, and B. Schenke, "Diffractive Dijet Production and Wigner Distributions from the Color Glass Condensate," *Phys. Rev.*, vol. D99, no. 7, p. 074004, 2019.
- [492] A. Dumitru, T. Lappi, and V. Skokov, "Distribution of Linearly Polarized Gluons and Elliptic Azimuthal Anisotropy in Deep Inelastic Scattering Dijet Production at High Energy," *Phys. Rev. Lett.*, vol. 115, no. 25, p. 252301, 2015.
- [493] Y. Hatta, N. Mueller, T. Ueda, and F. Yuan, "QCD Resummation in Hard Diffractive Dijet Production at the Electron-Ion Collider," *Phys. Lett. B*, vol. 802, p. 135211, 2020.
- [494] B. Abelev *et al.*, "Measurement of transverse single-spin asymmetries for di-jet production in proton-proton collisions at  $s^{*1/2} = 200$ -GeV," *Phys. Rev. Lett.*, vol. 99, p. 142003, 2007.
- [495] L. Bland *et al.*, "Cross Sections and Transverse Single-Spin Asymmetries in Forward Jet Production from Proton Collisions at  $\sqrt{s} = 500$  GeV," *Phys. Lett. B*, vol. 750, pp. 660–665, 2015.
- [496] L. Adamczyk *et al.*, "Azimuthal transverse single-spin asymmetries of inclusive jets and charged pions within jets from polarized-proton collisions at  $\sqrt{s} = 500$  GeV," *Phys. Rev. D*, vol. 97, no. 3, p. 032004, 2018.

- [497] E.-C. Aschenauer *et al.*, “The RHIC Cold QCD Plan for 2017 to 2023: A Portal to the EIC,” 2 2016.
- [498] D. Krohn, M. D. Schwartz, T. Lin, and W. J. Waalewijn, “Jet Charge at the LHC,” *Phys. Rev. Lett.*, vol. 110, no. 21, p. 212001, 2013.
- [499] D. Neill, F. Ringer, and N. Sato, “Calculating the energy loss of leading jets,” in *10th International Conference on Hard and Electromagnetic Probes of High-Energy Nuclear Collisions: Hard Probes 2020*, 8 2020.
- [500] D. Bertolini, T. Chan, and J. Thaler, “Jet Observables Without Jet Algorithms,” *JHEP*, vol. 04, p. 013, 2014.
- [501] M. Dasgupta, A. Fregoso, S. Marzani, and G. P. Salam, “Towards an understanding of jet substructure,” *JHEP*, vol. 09, p. 029, 2013.
- [502] A. J. Larkoski, S. Marzani, G. Soyez, and J. Thaler, “Soft Drop,” *JHEP*, vol. 05, p. 146, 2014.
- [503] A. Gao, H. T. Li, I. Moulton, and H. X. Zhu, “Precision QCD Event Shapes at Hadron Colliders: The Transverse Energy-Energy Correlator in the Back-to-Back Limit,” *Phys. Rev. Lett.*, vol. 123, no. 6, p. 062001, 2019.
- [504] H. T. Li, I. Vitev, and Y. J. Zhu, “Transverse-Energy-Energy Correlations in Deep Inelastic Scattering,” 6 2020.
- [505] D. Boer, C. Lorcé, C. Pisano, and J. Zhou, “The gluon Sivers distribution: status and future prospects,” *Adv. High Energy Phys.*, vol. 2015, p. 371396, 2015.
- [506] S. Meissner, A. Metz, and M. Schlegel, “Generalized parton correlation functions for a spin-1/2 hadron,” *JHEP*, vol. 08, p. 056, 2009.
- [507] S. Meissner, A. Metz, M. Schlegel, and K. Goetze, “Generalized parton correlation functions for a spin-0 hadron,” *JHEP*, vol. 08, p. 038, 2008.
- [508] C. Lorcé, B. Pasquini, and M. Vanderhaeghen, “Unified framework for generalized and transverse-momentum dependent parton distributions within a 3Q light-cone picture of the nucleon,” *JHEP*, vol. 05, p. 041, 2011.
- [509] C. Lorcé and B. Pasquini, “Structure analysis of the generalized correlator of quark and gluon for a spin-1/2 target,” *JHEP*, vol. 09, p. 138, 2013.
- [510] C. Lorcé and B. Pasquini, “Quark Wigner Distributions and Orbital Angular Momentum,” *Phys. Rev. D*, vol. 84, p. 014015, 2011.
- [511] C. Lorcé and B. Pasquini, “Multipole decomposition of the nucleon transverse phase space,” *Phys. Rev. D*, vol. 93, no. 3, p. 034040, 2016.
- [512] X.-d. Ji, “Viewing the proton through ‘color’ filters,” *Phys. Rev. Lett.*, vol. 91, p. 062001, 2003.

- [513] A. V. Belitsky, X.-D. Ji, and F. Yuan, “Quark imaging in the proton via quantum phase space distributions,” *Phys. Rev.*, vol. D69, p. 074014, 2004.
- [514] Y. Hatta, “Notes on the orbital angular momentum of quarks in the nucleon,” *Phys. Lett. B*, vol. 708, pp. 186–190, 2012.
- [515] C. Lorcé, B. Pasquini, X. Xiong, and F. Yuan, “The quark orbital angular momentum from Wigner distributions and light-cone wave functions,” *Phys. Rev. D*, vol. 85, p. 114006, 2012.
- [516] X. Ji, X. Xiong, and F. Yuan, “Proton Spin Structure from Measurable Parton Distributions,” *Phys. Rev. Lett.*, vol. 109, p. 152005, 2012.
- [517] R. L. Jaffe and A. Manohar, “The G(1) Problem: Fact and Fantasy on the Spin of the Proton,” *Nucl. Phys.*, vol. B337, pp. 509–546, 1990.
- [518] M. Burkardt, “Parton Orbital Angular Momentum and Final State Interactions,” *Phys. Rev. D*, vol. 88, no. 1, p. 014014, 2013.
- [519] Y. Hatta, Y. Nakagawa, F. Yuan, Y. Zhao, and B. Xiao, “Gluon orbital angular momentum at small- $x$ ,” *Phys. Rev. D*, vol. 95, no. 11, p. 114032, 2017.
- [520] X. Ji, F. Yuan, and Y. Zhao, “Hunting the Gluon Orbital Angular Momentum at the Electron-Ion Collider,” *Phys. Rev. Lett.*, vol. 118, no. 19, p. 192004, 2017.
- [521] A. Rajan, A. Courtoy, M. Engelhardt, and S. Liuti, “Parton Transverse Momentum and Orbital Angular Momentum Distributions,” *Phys. Rev. D*, vol. 94, no. 3, p. 034041, 2016.
- [522] S. Bhattacharya, A. Metz, and J. Zhou, “Generalized TMDs and the exclusive double Drell–Yan process,” *Phys. Lett. B*, vol. 771, pp. 396–400, 2017.
- [523] S. Bhattacharya, A. Metz, V. K. Ojha, J.-Y. Tsai, and J. Zhou, “Exclusive double quarkonium production and generalized TMDs of gluons,” 2018.
- [524] Y. Hagiwara, Y. Hatta, R. Pasechnik, M. Tasevsky, and O. Teryaev, “Accessing the gluon Wigner distribution in ultraperipheral  $pA$  collisions,” *Phys. Rev.*, vol. D96, no. 3, p. 034009, 2017.
- [525] T. Altinoluk, N. Armesto, G. Beuf, and A. H. Rezaeian, “Diffractive Dijet Production in Deep Inelastic Scattering and Photon-Hadron Collisions in the Color Glass Condensate,” *Phys. Lett. B*, vol. 758, pp. 373–383, 2016.
- [526] F. Salazar and B. Schenke, “Diffractive dijet production in impact parameter dependent saturation models,” *Phys. Rev. D*, vol. 100, no. 3, p. 034007, 2019.
- [527] R. Boussarie, A. Grabovsky, L. Szymanowski, and S. Wallon, “On the one loop  $\gamma^{(*)} \rightarrow q\bar{q}$  impact factor and the exclusive diffractive cross sections for the production of two or three jets,” *JHEP*, vol. 11, p. 149, 2016.

- [528] R. Boussarie, A. Grabovsky, L. Szymanowski, and S. Wallon, "Towards a complete next-to-logarithmic description of forward exclusive diffractive dijet electroproduction at HERA: real corrections," *Phys. Rev. D*, vol. 100, no. 7, p. 074020, 2019.
- [529] H. Mäntysaari, N. Mueller, F. Salazar, and B. Schenke, "Multi-Gluon Correlations and Evidence of Saturation from Dijet Measurements at an Electron Ion Collider," 2019.
- [530] R. Boussarie, Y. Hatta, L. Szymanowski, and S. Wallon, "Probing the Gluon Sivers Function with an Unpolarized Target: GTMD Distributions and the Odderons," *Phys. Rev. Lett.*, vol. 124, no. 17, p. 172501, 2020.
- [531] J. Zhou, "Transverse single spin asymmetries at small  $x$  and the anomalous magnetic moment," *Phys. Rev. D*, vol. 89, no. 7, p. 074050, 2014.
- [532] C. Adloff *et al.*, "Search for odderon induced contributions to exclusive  $\pi^0$  photoproduction at HERA," *Phys. Lett. B*, vol. 544, pp. 35–43, 2002.
- [533] M. Hattawy *et al.*, "First Exclusive Measurement of Deeply Virtual Compton Scattering off  $^4\text{He}$ : Toward the 3D Tomography of Nuclei," *Phys. Rev. Lett.*, vol. 119, no. 20, p. 202004, 2017.
- [534] M. Hattawy *et al.*, "Exploring the Structure of the Bound Proton with Deeply Virtual Compton Scattering," *Phys. Rev. Lett.*, vol. 123, no. 3, p. 032502, 2019.
- [535] R. Dupré and S. Scopetta, "3D Structure and Nuclear Targets," *Eur. Phys. J. A*, vol. 52, no. 6, p. 159, 2016.
- [536] M. Burkardt, "Impact parameter dependent parton distributions and off forward parton distributions for  $\zeta \rightarrow 0$ ," *Phys. Rev.*, vol. D62, p. 071503, 2000. [Erratum: *Phys. Rev. D* 66, 119903 (2002)].
- [537] E. R. Berger, F. Cano, M. Diehl, and B. Pire, "Generalized parton distributions in the deuteron," *Phys. Rev. Lett.*, vol. 87, p. 142302, 2001.
- [538] W. Armstrong *et al.*, "Partonic Structure of Light Nuclei," 8 2017.
- [539] K. Goeke, V. Guzey, and M. Siddikov, "Leading twist nuclear shadowing, nuclear generalized parton distributions and nuclear DVCS at small  $x$ ," *Phys. Rev.*, vol. C79, p. 035210, 2009.
- [540] M. Rinaldi and S. Scopetta, "Extracting generalized neutron parton distributions from  $^3\text{He}$  data," *Phys. Rev.*, vol. C87, no. 3, p. 035208, 2013.
- [541] F. Cano and B. Pire, "Deep electroproduction of photons and mesons on the deuteron," *Eur. Phys. J.*, vol. A19, pp. 423–438, 2004.
- [542] W. Cosyn and B. Pire, "Transversity generalized parton distributions for the deuteron," *Phys. Rev. D*, vol. 98, no. 7, p. 074020, 2018.

- [543] W. Cosyn, A. Freese, and B. Pire, "Polynomiality sum rules for generalized parton distributions of spin-1 targets," *Phys. Rev. D*, vol. 99, no. 9, p. 094035, 2019.
- [544] S. K. Taneja, K. Kathuria, S. Liuti, and G. R. Goldstein, "Angular momentum sum rule for spin one hadronic systems," *Phys.Rev.*, vol. D86, p. 036008, 2012.
- [545] S. Scopetta, "Generalized parton distributions of He-3," *Phys. Rev.*, vol. C70, p. 015205, 2004.
- [546] S. Scopetta, "Conventional nuclear effects on generalized parton distributions of trinucleons," *Phys. Rev.*, vol. C79, p. 025207, 2009.
- [547] M. Rinaldi and S. Scopetta, "Neutron orbital structure from generalized parton distributions of  $^3\text{He}$ ," *Phys. Rev.*, vol. C85, p. 062201, 2012.
- [548] M. Rinaldi and S. Scopetta, "Theoretical description of deeply virtual Compton scattering off  $^3\text{He}$ ," *Few Body Syst.*, vol. 55, pp. 861–864, 2014.
- [549] A. Del Dotto, E. Pace, G. Salmè, and S. Scopetta, "Light-Front spin-dependent Spectral Function and Nucleon Momentum Distributions for a Three-Body System," *Phys. Rev. C*, vol. 95, no. 1, p. 014001, 2017.
- [550] S. Fucini, S. Scopetta, and M. Viviani, "Coherent deeply virtual Compton scattering off  $^4\text{He}$ ," *Phys. Rev.*, vol. C98, no. 1, p. 015203, 2018.
- [551] S. Liuti and S. K. Taneja, "Generalized parton distributions and color transparency phenomena," *Phys. Rev.*, vol. D70, p. 074019, 2004.
- [552] V. Guzey and M. Strikman, "DVCS on spinless nuclear targets in impulse approximation," *Phys.Rev.*, vol. C68, p. 015204, 2003.
- [553] R. B. Wiringa, V. G. J. Stoks, and R. Schiavilla, "An Accurate nucleon-nucleon potential with charge independence breaking," *Phys. Rev.*, vol. C51, pp. 38–51, 1995.
- [554] B. Pudliner, V. Pandharipande, J. Carlson, and R. B. Wiringa, "Quantum Monte Carlo calculations of  $A \leq 6$  nuclei," *Phys. Rev. Lett.*, vol. 74, pp. 4396–4399, 1995.
- [555] S. Fucini, S. Scopetta, and M. Viviani, "Catching a glimpse of the parton structure of the bound proton," *1909.12261 [nucl-th]*, 2019.
- [556] S. Fucini, S. Scopetta, and M. Viviani, "Incoherent deeply virtual Compton scattering off  $^4\text{He}$ ," 8 2020.
- [557] P. Hoodbhoy, R. Jaffe, and A. Manohar, "Novel Effects in Deep Inelastic Scattering from Spin 1 Hadrons," *Nucl. Phys. B*, vol. 312, pp. 571–588, 1989.
- [558] A. Efremov and O. Teryaev, "ON HIGH P(T) VECTOR MESONS SPIN ALIGNMENT," *Sov. J. Nucl. Phys.*, vol. 36, p. 557, 1982.
- [559] R. Jaffe and A. Manohar, "NUCLEAR GLUONOMETRY," *Phys. Lett. B*, vol. 223, pp. 218–224, 1989.

- [560] F. Close and S. Kumano, "A sum rule for the spin dependent structure function  $b_1(x)$  for spin one hadrons," *Phys. Rev. D*, vol. 42, pp. 2377–2379, 1990.
- [561] S. Kumano, "Tensor-polarized quark and antiquark distribution functions in a spin-one hadron," *Phys. Rev. D*, vol. 82, p. 017501, 2010.
- [562] G. A. Miller, "Pionic and Hidden-Color, Six-Quark Contributions to the Deuteron  $b_1$  Structure Function," *Phys. Rev. C*, vol. 89, no. 4, p. 045203, 2014.
- [563] I. Passchier *et al.*, "Spin momentum correlations in quasielastic electron scattering from deuterium," *Phys. Rev. Lett.*, vol. 88, p. 102302, 2002.
- [564] A. DeGrush *et al.*, "Measurement of the Vector and Tensor Asymmetries at Large Missing Momentum in Quasielastic ( $\vec{e}, e'p$ ) Electron Scattering from Deuterium," *Phys. Rev. Lett.*, vol. 119, no. 18, p. 182501, 2017.
- [565] A. Airapetian *et al.*, "First measurement of the tensor structure function  $b_1$  of the deuteron," *Phys. Rev. Lett.*, vol. 95, p. 242001, 2005.
- [566] K. Slifer, E. Long, D. Keller, O. Rondon, P. Solvignon, N. Kalantarians *et al.*, "The Tensor Structure Function,  $b_1$ ," *JLab PAC40, C12-13-011*, 2013.
- [567] E. Long, D. Keller, K. Slifer, D. Day, P. Solvignon, D. Higinbotham *et al.*, "Measurements of the Quasi-Elastic and Elastic Deuteron Tensor Asymmetries," *JLab PAC44, C12-15-005*, 2016.
- [568] I. C. Cloet, W. Bentz, and A. W. Thomas, "Isovector EMC effect explains the NuTeV anomaly," *Phys. Rev. Lett.*, vol. 102, p. 252301, 2009.
- [569] J.-H. Gao, Z.-t. Liang, and X.-N. Wang, "Nuclear dependence of azimuthal asymmetry in semi-inclusive deep inelastic scattering," *Phys. Rev. C*, vol. 81, p. 065211, 2010.
- [570] Y.-k. Song, J.-h. Gao, Z.-t. Liang, and X.-N. Wang, "Azimuthal asymmetries in semi-inclusive DIS with polarized beam and/or target and their nuclear dependences," *Phys. Rev. D*, vol. 89, no. 1, p. 014005, 2014.
- [571] J. C. Collins, D. E. Soper, and G. F. Sterman, "Factorization of Hard Processes in QCD," *Adv. Ser. Direct. High Energy Phys.*, vol. 5, pp. 1–91, 1989.
- [572] M. Arneodo *et al.*, "The A dependence of the nuclear structure function ratios," *Nucl. Phys. B*, vol. 481, pp. 3–22, 1996.
- [573] D. F. Geesaman, K. Saito, and A. W. Thomas, "The nuclear EMC effect," *Ann. Rev. Nucl. Part. Sci.*, vol. 45, pp. 337–390, 1995.
- [574] J. Gomez *et al.*, "Measurement of the A-dependence of deep inelastic electron scattering," *Phys. Rev. D*, vol. 49, pp. 4348–4372, 1994.
- [575] P. Norton, "The EMC effect," *Rept. Prog. Phys.*, vol. 66, pp. 1253–1297, 2003.

- [576] H. Paukkunen, "Nuclear PDFs in the beginning of the LHC era," *Nucl. Phys.*, vol. A926, pp. 24–33, 2014.
- [577] S. Peigne and A. Smilga, "Energy losses in a hot plasma revisited," *Phys. Usp.*, vol. 52, pp. 659–685, 2009.
- [578] F. Arleo, C.-J. Naim, and S. Platchkov, "Initial-state energy loss in cold QCD matter and the Drell-Yan process," *JHEP*, vol. 01, p. 129, 2019.
- [579] J. Adams *et al.*, "Distributions of charged hadrons associated with high transverse momentum particles in pp and Au + Au collisions at  $\sqrt{s(NN)} = 200$ -GeV," *Phys. Rev. Lett.*, vol. 95, p. 152301, 2005.
- [580] V. Khachatryan *et al.*, "Observation of Long-Range Near-Side Angular Correlations in Proton-Proton Collisions at the LHC," *JHEP*, vol. 09, p. 091, 2010.
- [581] G. Aad *et al.*, "Observation of Long-Range Elliptic Azimuthal Anisotropies in  $\sqrt{s} = 13$  and 2.76 TeV pp Collisions with the ATLAS Detector," *Phys. Rev. Lett.*, vol. 116, no. 17, p. 172301, 2016.
- [582] V. Khachatryan *et al.*, "Measurement of long-range near-side two-particle angular correlations in pp collisions at  $\sqrt{s} = 13$  TeV," *Phys. Rev. Lett.*, vol. 116, no. 17, p. 172302, 2016.
- [583] V. Khachatryan *et al.*, "Evidence for collectivity in pp collisions at the LHC," 2016.
- [584] B. Abelev *et al.*, "Long-range angular correlations on the near and away side in p-Pb collisions at  $\sqrt{s_{NN}} = 5.02$  TeV," *Phys. Lett.*, vol. B719, pp. 29–41, 2013.
- [585] S. Chatrchyan *et al.*, "Observation of long-range near-side angular correlations in proton-lead collisions at the LHC," *Phys. Lett.*, vol. B718, pp. 795–814, 2013.
- [586] G. Aad *et al.*, "Observation of associated near-side and away-side long-range correlations in  $\sqrt{s_{NN}} = 5.02$  TeV proton-lead collisions with the atlas detector," *Phys. Rev. Lett.*, vol. 110, p. 182302, 2013.
- [587] G. Aad *et al.*, "Measurement with the atlas detector of multi-particle azimuthal correlations in p+pb collisions at  $\sqrt{s_{NN}} = 5.02$  TeV," *Phys. Lett.*, vol. B725, pp. 60–78, 2013.
- [588] B. B. Abelev *et al.*, "Multiparticle azimuthal correlations in p-pb and pb-pb collisions at the CERN large hadron collider," *Phys. Rev.*, vol. C90, p. 054901, 2014.
- [589] G. Aad *et al.*, "Measurement of long-range pseudorapidity correlations and azimuthal harmonics in  $\sqrt{s_{NN}} = 5.02$  TeV proton-lead collisions with the ATLAS detector," *Phys. Rev.*, vol. C90, p. 044906, 2014.
- [590] V. Khachatryan *et al.*, "Evidence for Collective Multiparticle Correlations in p-Pb Collisions," *Phys. Rev. Lett.*, vol. 115, no. 1, p. 012301, 2015.

- [591] M. H. Seymour, "The Average number of subjects in a hadron collider jet," *Nucl. Phys. B*, vol. 421, pp. 545–564, 1994.
- [592] R. Kogler *et al.*, "Jet Substructure at the Large Hadron Collider: Experimental Review," *Rev. Mod. Phys.*, vol. 91, no. 4, p. 045003, 2019.
- [593] L. V. Gribov, E. M. Levin, and M. G. Ryskin *Phys. Rept.*, vol. 100, p. 1, 1983.
- [594] A. H. Mueller and J.-W. Qiu, "Gluon Recombination and Shadowing at Small Values of  $x$ ," *Nucl. Phys.*, vol. B268, p. 427, 1986.
- [595] L. D. McLerran and R. Venugopalan *Phys. Rev.*, vol. D49, p. 2233, 1994.
- [596] F. Gelis, E. Iancu, J. Jalilian-Marian, and R. Venugopalan, "The Color Glass Condensate," *Ann. Rev. Nucl. Part. Sci.*, vol. 60, pp. 463–489, 2010.
- [597] I. Balitsky, "Operator expansion for high-energy scattering," *Nucl. Phys.*, vol. B463, pp. 99–160, 1996.
- [598] Y. V. Kovchegov *Phys. Rev.*, vol. D60, p. 034008, 1999.
- [599] J. Jalilian-Marian, A. Kovner, A. Leonidov, and H. Weigert, "The BFKL equation from the Wilson renormalization group," *Nucl. Phys. B*, vol. 504, pp. 415–431, 1997.
- [600] J. Jalilian-Marian, A. Kovner, and H. Weigert, "The Wilson renormalization group for low  $x$  physics: Gluon evolution at finite parton density," *Phys. Rev.*, vol. D59, p. 014015, 1999.
- [601] E. Iancu, A. Leonidov, and L. D. McLerran *Nucl. Phys.*, vol. A692, p. 583, 2001.
- [602] E. Ferreiro, E. Iancu, A. Leonidov, and L. McLerran, "Nonlinear gluon evolution in the color glass condensate. 2.," *Nucl. Phys.*, vol. A703, pp. 489–538, 2002.
- [603] S. Munier and R. B. Peschanski, "Geometric scaling as traveling waves," *Phys. Rev. Lett.*, vol. 91, p. 232001, 2003.
- [604] H. Kowalski, T. Lappi, and R. Venugopalan *Phys. Rev. Lett.*, vol. 100, p. 022303, 2008.
- [605] A. Stasto, K. J. Golec-Biernat, and J. Kwiecinski, "Geometric scaling for the total gamma\* p cross-section in the low  $x$  region," *Phys. Rev. Lett.*, vol. 86, pp. 596–599, 2001.
- [606] I. Balitsky and G. A. Chirilli, "Next-to-leading order evolution of color dipoles," *Phys. Rev. D*, vol. 77, p. 014019, 2008.
- [607] I. Balitsky and G. A. Chirilli, "Rapidity evolution of Wilson lines at the next-to-leading order," *Phys. Rev. D*, vol. 88, p. 111501, 2013.
- [608] A. Kovner, M. Lublinsky, and Y. Mulian, "Jalilian-Marian, Iancu, McLerran, Weigert, Leonidov, Kovner evolution at next to leading order," *Phys. Rev. D*, vol. 89, no. 6, p. 061704, 2014.

- [609] G. Beuf, "Improving the kinematics for low- $x$  QCD evolution equations in coordinate space," *Phys. Rev. D*, vol. 89, no. 7, p. 074039, 2014.
- [610] E. Iancu, J. Madrigal, A. Mueller, G. Soyez, and D. Triantafyllopoulos, "Resumming double logarithms in the QCD evolution of color dipoles," *Phys. Lett. B*, vol. 744, pp. 293–302, 2015.
- [611] B. Ducloué, E. Iancu, A. Mueller, G. Soyez, and D. Triantafyllopoulos, "Non-linear evolution in QCD at high-energy beyond leading order," *JHEP*, vol. 04, p. 081, 2019.
- [612] I. Balitsky and G. A. Chirilli, "Photon impact factor and  $k_T$ -factorization for DIS in the next-to-leading order," *Phys. Rev. D*, vol. 87, no. 1, p. 014013, 2013.
- [613] I. Balitsky and G. A. Chirilli, "Photon impact factor in the next-to-leading order," *Phys. Rev. D*, vol. 83, p. 031502, 2011.
- [614] G. Beuf, "Dipole factorization for DIS at NLO: Loop correction to the  $\gamma_{T,L}^* \rightarrow q\bar{q}$  light-front wave functions," *Phys. Rev. D*, vol. 94, no. 5, p. 054016, 2016.
- [615] G. Beuf, "Dipole factorization for DIS at NLO: Combining the  $q\bar{q}$  and  $q\bar{q}g$  contributions," *Phys. Rev. D*, vol. 96, no. 7, p. 074033, 2017.
- [616] H. Hänninen, T. Lappi, and R. Paatelainen, "One-loop corrections to light cone wave functions: the dipole picture DIS cross section," *Annals Phys.*, vol. 393, pp. 358–412, 2018.
- [617] B. Ducloué, E. Iancu, G. Soyez, and D. Triantafyllopoulos, "HERA data and collinearly-improved BK dynamics," *Phys. Lett. B*, vol. 803, p. 135305, 2020.
- [618] G. Beuf, H. Hänninen, T. Lappi, and H. Mäntysaari, "Color Glass Condensate at next-to-leading order meets HERA data," 7 2020.
- [619] T. Lappi and H. Mäntysaari, "Single inclusive particle production at high energy from HERA data to proton-nucleus collisions," *Phys. Rev. D*, vol. 88, p. 114020, 2013.
- [620] A. H. Mueller, "Soft gluons in the infinite momentum wave function and the BFKL pomeron," *Nucl. Phys. B*, vol. 415, pp. 373–385, 1994.
- [621] J. Jalilian-Marian, A. Kovner, L. D. McLerran, and H. Weigert, "The Intrinsic glue distribution at very small  $x$ ," *Phys. Rev. D*, vol. 55, pp. 5414–5428, 1997.
- [622] Y. V. Kovchegov and A. H. Mueller, "Gluon production in current nucleus and nucleon - nucleus collisions in a quasiclassical approximation," *Nucl. Phys. B*, vol. 529, pp. 451–479, 1998.
- [623] F. Dominguez, A. Mueller, S. Munier, and B.-W. Xiao, "On the small- $x$  evolution of the color quadrupole and the Weizsäcker–Williams gluon distribution," *Phys. Lett. B*, vol. 705, pp. 106–111, 2011.

- [624] A. Dumitru, J. Jalilian-Marian, T. Lappi, B. Schenke, and R. Venugopalan, “Renormalization group evolution of multi-gluon correlators in high energy QCD,” *Phys. Lett. B*, vol. 706, pp. 219–224, 2011.
- [625] F. Dominguez, B.-W. Xiao, and F. Yuan, “kt-factorization for Hard Processes in Nuclei,” *Phys. Rev. Lett.*, vol. 106, p. 022301, 2011.
- [626] D. Kharzeev, E. Levin, and L. McLerran *Nucl. Phys.*, vol. A748, p. 627, 2005.
- [627] L. Zheng, E. C. Aschenauer, J. H. Lee, and B.-W. Xiao, “Probing Gluon Saturation through Dihadron Correlations at an Electron-Ion Collider,” *Phys. Rev.*, vol. D89, no. 7, p. 074037, 2014.
- [628] A. H. Mueller, B.-W. Xiao, and F. Yuan, “Sudakov Resummation in Small- $x$  Saturation Formalism,” *Phys. Rev. Lett.*, vol. 110, no. 8, p. 082301, 2013.
- [629] A. H. Mueller, B.-W. Xiao, and F. Yuan, “Sudakov double logarithms resummation in hard processes in the small- $x$  saturation formalism,” *Phys. Rev.*, vol. D88, no. 11, p. 114010, 2013.
- [630] A. Stasto, S.-Y. Wei, B.-W. Xiao, and F. Yuan, “On the Dihadron Angular Correlations in Forward  $pA$  collisions,” *Phys. Lett.*, vol. B784, pp. 301–306, 2018.
- [631] D. Boer, S. J. Brodsky, P. J. Mulders, and C. Pisano, “Direct Probes of Linearly Polarized Gluons inside Unpolarized Hadrons,” *Phys. Rev. Lett.*, vol. 106, p. 132001, 2011.
- [632] A. Metz and J. Zhou, “Distribution of linearly polarized gluons inside a large nucleus,” *Phys. Rev.*, vol. D84, p. 051503, 2011.
- [633] F. Dominguez, J.-W. Qiu, B.-W. Xiao, and F. Yuan, “On the linearly polarized gluon distributions in the color dipole model,” *Phys. Rev.*, vol. D85, p. 045003, 2012.
- [634] A. Dumitru, V. Skokov, and T. Ullrich, “Measuring the Weizsäcker-Williams distribution of linearly polarized gluons at an electron-ion collider through dijet azimuthal asymmetries,” *Phys. Rev. C*, vol. 99, no. 1, p. 015204, 2019.
- [635] T. Altinoluk, R. Boussarie, and P. Kotko, “Interplay of the CGC and TMD frameworks to all orders in kinematic twist,” *JHEP*, vol. 05, p. 156, 2019.
- [636] R. Boussarie and Y. Mehtar-Tani, “On gauge invariance of transverse momentum dependent distributions at small  $x$ ,” 1 2020.
- [637] P. Kotko, K. Kutak, C. Marquet, E. Petreska, S. Sapeta, and A. van Hameren, “Improved TMD factorization for forward dijet production in dilute-dense hadronic collisions,” *JHEP*, vol. 09, p. 106, 2015.
- [638] A. van Hameren, P. Kotko, K. Kutak, C. Marquet, E. Petreska, and S. Sapeta, “Forward di-jet production in  $p+Pb$  collisions in the small- $x$  improved TMD factorization framework,” *JHEP*, vol. 12, p. 034, 2016. [Erratum: *JHEP* 02, 158 (2019)].

- [639] P. Kotko, K. Kutak, S. Sapeta, A. Stasto, and M. Strikman, “Estimating nonlinear effects in forward dijet production in ultra-peripheral heavy ion collisions at the LHC,” *Eur. Phys. J. C*, vol. 77, no. 5, p. 353, 2017.
- [640] K. Roy and R. Venugopalan, “Inclusive prompt photon production in electron-nucleus scattering at small  $x$ ,” *JHEP*, vol. 05, p. 013, 2018.
- [641] I. Kolbé, K. Roy, F. Salazar, B. Schenke, and R. Venugopalan, “Inclusive prompt photon-jet correlations as a probe of gluon saturation in electron-nucleus scattering at small  $x$ ,” 8 2020.
- [642] K. Roy and R. Venugopalan, “NLO impact factor for inclusive photon+dijet production in  $e + A$  DIS at small  $x$ ,” *Phys. Rev. D*, vol. 101, no. 3, p. 034028, 2020.
- [643] K. Roy and R. Venugopalan, “Extracting many-body correlators of saturated gluons with precision from inclusive photon+dijet final states in deeply inelastic scattering,” *Phys. Rev. D*, vol. 101, no. 7, p. 071505, 2020.
- [644] F. Cougoulic and Y. V. Kovchegov, “Helicity-dependent generalization of the JIMWLK evolution,” *Phys. Rev. D*, vol. 100, no. 11, p. 114020, 2019.
- [645] J. Bartels, B. Ermolaev, and M. Ryskin, “Flavor singlet contribution to the structure function  $G(1)$  at small  $x$ ,” *Z. Phys. C*, vol. 72, pp. 627–635, 1996.
- [646] F. Cougoulic and Y. V. Kovchegov, “Helicity-dependent extension of the McLerran-Venugopalan model,” *Nucl. Phys. A*, vol. 1004, p. 122051, 2020.
- [647] A. Caldwell and H. Kowalski, “Investigating the gluonic structure of nuclei via  $J/\psi$  scattering,” *Phys. Rev. C*, vol. 81, p. 025203, 2010.
- [648] H. Mäntysaari, “Review of proton and nuclear shape fluctuations at high energy,” *Rept. Prog. Phys.*, vol. 83, no. 8, p. 082201, 2020.
- [649] H. Kowalski, T. Lappi, C. Marquet, and R. Venugopalan, “Nuclear enhancement and suppression of diffractive structure functions at high energies,” *Phys. Rev.*, vol. C78, p. 045201, 2008.
- [650] N. N. Nikolaev, B. Zakharov, and V. Zoller, “Unusual effects of diffraction dissociation for multiproduction in deep inelastic scattering on nuclei,” *Z. Phys. A*, vol. 351, pp. 435–446, 1995.
- [651] N. Armesto, P. R. Newman, W. Słomiński, and A. M. Staśto, “Inclusive diffraction in future electron-proton and electron-ion colliders,” *Phys. Rev. D*, vol. 100, no. 7, p. 074022, 2019.
- [652] V. Gribov, “Glauber corrections and the interaction between high-energy hadrons and nuclei,” *Sov. Phys. JETP*, vol. 29, pp. 483–487, 1969.
- [653] V. Gribov and A. A. Migdal, “Properties of the pomeron pole and the branch cuts related to it at low momentum transfer,” *Sov. J. Nucl. Phys.*, vol. 8, pp. 583–590, 1969.

- [654] L. Frankfurt, G. Miller, and M. Strikman, "The Geometrical color optics of coherent high-energy processes," *Ann. Rev. Nucl. Part. Sci.*, vol. 44, pp. 501–560, 1994.
- [655] N. Armesto, A. Capella, A. Kaidalov, J. Lopez-Albacete, and C. Salgado, "Nuclear structure functions at small  $x$  from inelastic shadowing and diffraction," *Eur. Phys. J. C*, vol. 29, pp. 531–540, 2003.
- [656] R. Boussarie, A. Grabovsky, L. Szymanowski, and S. Wallon, "Impact factor for high-energy two and three jets diffractive production," *JHEP*, vol. 09, p. 026, 2014.
- [657] T. Altinoluk, R. Boussarie, C. Marquet, and P. Taels, "Photoproduction of three jets in the CGC: gluon TMDs and dilute limit," *JHEP*, vol. 07, p. 143, 2020.
- [658] N. Armesto, H. Paukkunen, C. A. Salgado, and K. Tywoniuk, "Nuclear effects on the longitudinal structure function at small  $x$ ," *Phys. Lett. B*, vol. 694, pp. 38–43, 2011.
- [659] E. C. Aschenauer, S. Fazio, M. A. C. Lamont, H. Paukkunen, and P. Zurita, "Nuclear Structure Functions at a Future Electron-Ion Collider," *Phys. Rev.*, vol. D96, no. 11, p. 114005, 2017.
- [660] A. Kusina *et al.*, "Impact of LHC vector boson production in heavy ion collisions on strange PDFs," 7 2020.
- [661] R. Abdul Khalek, J. J. Ethier, J. Rojo, and G. van Weelden, "nNNPDF2.0: quark flavor separation in nuclei from LHC data," *JHEP*, vol. 09, p. 183, 2020.
- [662] E. Abbas *et al.*, "Charmonium and  $e^+e^-$  pair photoproduction at mid-rapidity in ultra-peripheral Pb-Pb collisions at  $\sqrt{s_{NN}}=2.76$  TeV," *Eur. Phys. J. C*, vol. 73, no. 11, p. 2617, 2013.
- [663] V. Guzey, E. Kryshen, M. Strikman, and M. Zhalov, "Evidence for nuclear gluon shadowing from the ALICE measurements of PbPb ultraperipheral exclusive  $J/\psi$  production," *Phys. Lett. B*, vol. 726, pp. 290–295, 2013.
- [664] V. Guzey, E. Kryshen, M. Strikman, and M. Zhalov, "Nuclear suppression from coherent  $J/\psi$  photoproduction at the Large Hadron Collider," 8 2020.
- [665] A. Kusina, J.-P. Lansberg, I. Schienbein, and H.-S. Shao, "Gluon Shadowing in Heavy-Flavor Production at the LHC," *Phys. Rev. Lett.*, vol. 121, no. 5, p. 052004, 2018.
- [666] K. J. Eskola, I. Helenius, P. Paakkinen, and H. Paukkunen, "A QCD analysis of LHCb D-meson data in p+Pb collisions," *JHEP*, vol. 05, p. 037, 2020.
- [667] K. J. Eskola, P. Paakkinen, and H. Paukkunen, "Non-quadratic improved Hessian PDF reweighting and application to CMS dijet measurements at 5.02 TeV," *Eur. Phys. J. C*, vol. 79, no. 6, p. 511, 2019.
- [668] A. Accardi *et al.*, "A Critical Appraisal and Evaluation of Modern PDFs," *Eur. Phys. J. C*, vol. 76, no. 8, p. 471, 2016.

- [669] C. Weiss *et al.*, “Nuclear gluons with charm at EIC, Jefferson Lab LDRD Project,” 2017. [https://wiki.jlab.or/nuclear\\_gluons/](https://wiki.jlab.or/nuclear_gluons/).
- [670] Y. Furltova, N. Sato, and C. Weiss, “Probing Nuclear Gluons with Heavy Flavor Production at EIC,” in *Probing Nucleons and Nuclei in High Energy Collisions: Dedicated to the Physics of the Electron Ion Collider*, pp. 295–299, 2020.
- [671] H. Abramowicz *et al.*, “Measurement of charm fragmentation fractions in photo-production at HERA,” *JHEP*, vol. 09, p. 058, 2013.
- [672] K. J. Eskola, P. Paakkinen, H. Paukkunen, and C. A. Salgado, “EPPS16: Nuclear parton distributions with LHC data,” *Eur. Phys. J.*, vol. C77, no. 3, p. 163, 2017.
- [673] R. Baier, Y. L. Dokshitzer, S. Peigne, and D. Schiff, “Induced gluon radiation in a QCD medium,” *Phys. Lett.*, vol. B345, pp. 277–286, 1995.
- [674] B. G. Zakharov, “Radiative energy loss of high-energy quarks in finite size nuclear matter and quark - gluon plasma,” *JETP Lett.*, vol. 65, pp. 615–620, 1997.
- [675] M. Gyulassy, P. Levai, and I. Vitev, “Reaction operator approach to nonAbelian energy loss,” *Nucl.Phys.*, vol. B594, pp. 371–419, 2001.
- [676] X.-F. Guo and X.-N. Wang, “Multiple Scattering, Parton Energy Loss and Modified Fragmentation Functions in Deeply Inelastic eA Scattering,” *Phys. Rev. Lett.*, vol. 85, pp. 3591–3594, 2000.
- [677] P. B. Arnold, G. D. Moore, and L. G. Yaffe, “Photon and gluon emission in relativistic plasmas,” *JHEP*, vol. 06, p. 030, 2002.
- [678] Y. Guo, B.-W. Zhang, and E. Wang, “Parton Energy Loss at Twist-Six in Deeply Inelastic e-A Scattering,” *Phys. Lett. B*, vol. 641, pp. 38–44, 2006.
- [679] I. Vitev, “Non-Abelian energy loss in cold nuclear matter,” *Phys. Rev. C*, vol. 75, p. 064906, 2007.
- [680] W.-t. Deng and X.-N. Wang, “Multiple Parton Scattering in Nuclei: Modified DGLAP Evolution for Fragmentation Functions,” *Phys. Rev.*, vol. C81, p. 024902, 2010.
- [681] L. Apolinário, N. Armesto, J. G. Milhano, and C. A. Salgado, “Medium-induced gluon radiation and colour decoherence beyond the soft approximation,” *JHEP*, vol. 02, p. 119, 2015.
- [682] M. Fickinger, G. Ovanesyan, and I. Vitev, “Angular distributions of higher order splitting functions in the vacuum and in dense QCD matter,” *JHEP*, vol. 1307, p. 059, 2013.
- [683] M. D. Sievert and I. Vitev, “Quark branching in QCD matter to any order in opacity beyond the soft gluon emission limit,” *Phys. Rev. D*, vol. 98, no. 9, p. 094010, 2018.

- [684] M. D. Sievert, I. Vitev, and B. Yoon, "A complete set of in-medium splitting functions to any order in opacity," *Phys. Lett. B*, vol. 795, pp. 502–510, 2019.
- [685] N.-B. Chang, W.-T. Deng, and X.-N. Wang, "Initial conditions for the modified evolution of fragmentation functions in the nuclear medium," *Phys. Rev.*, vol. C89, no. 3, p. 034911, 2014.
- [686] Z.-B. Kang, R. Lashof-Regas, G. Ovanesyan, P. Saad, and I. Vitev, "Jet quenching phenomenology from soft-collinear effective theory with Glauber gluons," *Phys. Rev. Lett.*, vol. 114, no. 9, p. 092002, 2015.
- [687] H. T. Li and I. Vitev, "Inclusive heavy flavor jet production with semi-inclusive jet functions: from proton to heavy-ion collisions," *JHEP*, vol. 07, p. 148, 2019.
- [688] H. T. Li and I. Vitev, "Nuclear matter effects on jet production at electron-ion colliders," 10 2020.
- [689] I. Vitev, S. Wicks, and B.-W. Zhang, "A Theory of jet shapes and cross sections: From hadrons to nuclei," *JHEP*, vol. 0811, p. 093, 2008.
- [690] "Measurement of Jet Nuclear Modification Factor in PbPb Collisions at  $\sqrt{s_{NN}} = 5.02$  TeV with CMS," 11 2019.
- [691] S. Adler *et al.*, "Dense-Medium Modifications to Jet-Induced Hadron Pair Distributions in Au+Au Collisions at  $s(NN)^{1/2} = 200$ -GeV," *Phys. Rev. Lett.*, vol. 97, p. 052301, 2006.
- [692] H. Mäntysaari, B. Schenke, C. Shen, and P. Tribedy, "Imprints of fluctuating proton shapes on flow in proton-lead collisions at the LHC," *Phys. Lett. B*, vol. 772, pp. 681–686, 2017.
- [693] J. Orjuela Koop, A. Adare, D. McGlinchey, and J. Nagle, "Azimuthal anisotropy relative to the participant plane from a multiphase transport model in central p + Au, d + Au, and  $^3\text{He} + \text{Au}$  collisions at  $\sqrt{s_{NN}} = 200$  GeV," *Phys. Rev. C*, vol. 92, no. 5, p. 054903, 2015.
- [694] P. Romatschke, "Azimuthal Anisotropies at High Momentum from Purely Non-Hydrodynamic Transport," *Eur. Phys. J. C*, vol. 78, no. 8, p. 636, 2018.
- [695] A. Kärkela, U. A. Wiedemann, and B. Wu, "Opacity dependence of elliptic flow in kinetic theory," *Eur. Phys. J. C*, vol. 79, no. 9, p. 759, 2019.
- [696] C. Aidala *et al.*, "Creation of quark–gluon plasma droplets with three distinct geometries," *Nature Phys.*, vol. 15, no. 3, pp. 214–220, 2019.
- [697] A. Dumitru, K. Dusling, F. Gelis, J. Jalilian-Marian, T. Lappi, and R. Venugopalan, "The ridge in proton-proton collisions at the LHC," *Phys. Lett.*, vol. B697, pp. 21–25, 2011.

- [698] T. Lappi, B. Schenke, S. Schlichting, and R. Venugopalan, "Tracing the origin of azimuthal gluon correlations in the color glass condensate," *JHEP*, vol. 01, p. 061, 2016.
- [699] K. Dusling, M. Mace, and R. Venugopalan, "Multiparticle collectivity from initial state correlations in high energy proton-nucleus collisions," *Phys. Rev. Lett.*, vol. 120, no. 4, p. 042002, 2018.
- [700] A. Dumitru, F. Gelis, L. McLerran, and R. Venugopalan, "Glasma flux tubes and the near side ridge phenomenon at RHIC," *Nucl. Phys. A*, vol. 810, pp. 91–108, 2008.
- [701] A. Kovner and M. Lublinsky, "Angular Correlations in Gluon Production at High Energy," *Phys. Rev. D*, vol. 83, p. 034017, 2011.
- [702] A. M. Sirunyan *et al.*, "Elliptic flow of charm and strange hadrons in high-multiplicity pPb collisions at  $\sqrt{s_{NN}} = 8.16$  TeV," *Phys. Rev. Lett.*, vol. 121, no. 8, p. 082301, 2018.
- [703] C. Zhang, C. Marquet, G.-Y. Qin, S.-Y. Wei, and B.-W. Xiao, "Elliptic Flow of Heavy Quarkonia in  $pA$  Collisions," *Phys. Rev. Lett.*, vol. 122, no. 17, p. 172302, 2019.
- [704] D. V. Perepelitsa, "Connection between soft and hard probes of small collision systems at RHIC and LHC," *EPJ Web Conf.*, vol. 235, p. 04003, 2020.
- [705] I. Abt *et al.*, "Two-particle azimuthal correlations as a probe of collective behaviour in deep inelastic  $ep$  scattering at HERA," *JHEP*, vol. 04, p. 070, 2020.
- [706] Y. Shi, L. Wang, S.-Y. Wei, B.-W. Xiao, and L. Zheng, "Exploring the Collective Phenomenon at the Electron-Ion Collider," 8 2020.
- [707] R. D. Field and R. P. Feynman, "A Parametrization of the Properties of Quark Jets," *Nucl. Phys.*, vol. B136, p. 1, 1978. [763(1977)].
- [708] H. T. Li and I. Vitev, "Jet charge modification in dense QCD matter," *Phys. Rev. D*, vol. 101, p. 076020, 2020.
- [709] S.-Y. Chen, B.-W. Zhang, and E.-K. Wang, "Jet charge in high energy nuclear collisions," *Chin. Phys. C*, vol. 44, no. 2, p. 024103, 2020.
- [710] A. M. Sirunyan *et al.*, "Measurement of quark- and gluon-like jet fractions using jet charge in PbPb and pp collisions at 5.02 TeV," *JHEP*, vol. 07, p. 115, 2020.
- [711] G. Aad *et al.*, "Measurement of jet charge in dijet events from  $\sqrt{s}=8$  TeV pp collisions with the ATLAS detector," *Phys. Rev.*, vol. D93, no. 5, p. 052003, 2016.
- [712] X. Li, "Heavy flavor and jet studies for the future Electron-Ion Collider," in *10th International Conference on Hard and Electromagnetic Probes of High-Energy Nuclear Collisions: Hard Probes 2020*, 7 2020.

- [713] C.-P. Wong, X. Li, M. Brooks, M. J. Durham, M. X. Liu, A. Morreale, C. da Silva, and W. E. Sondheim, "A Proposed Forward Silicon Tracker for the Future Electron-Ion Collider and Associated Physics Studies," 9 2020.
- [714] B. Schmookler *et al.*, "Modified structure of protons and neutrons in correlated pairs," *Nature*, vol. 566, no. 7744, pp. 354–358, 2019.
- [715] O. Hen, G. Miller, E. Piasetzky, and L. Weinstein, "Nucleon-Nucleon Correlations, Short-lived Excitations, and the Quarks Within," *Rev. Mod. Phys.*, vol. 89, no. 4, p. 045002, 2017.
- [716] L. Weinstein, E. Piasetzky, D. Higinbotham, J. Gomez, O. Hen, and R. Shneor, "Short Range Correlations and the EMC Effect," *Phys. Rev. Lett.*, vol. 106, p. 052301, 2011.
- [717] O. Hen, E. Piasetzky, and L. Weinstein, "New data strengthen the connection between Short Range Correlations and the EMC effect," *Phys. Rev. C*, vol. 85, p. 047301, 2012.
- [718] O. Hen, D. Higinbotham, G. A. Miller, E. Piasetzky, and L. B. Weinstein, "The EMC Effect and High Momentum Nucleons in Nuclei," *Int. J. Mod. Phys. E*, vol. 22, p. 1330017, 2013.
- [719] G. Serman, "Fixed Angle Scattering and the Transverse Structure of Hadrons," in *4th Workshop on Exclusive Reactions at High Momentum Transfer*, pp. 16–25, 2011.
- [720] Z. Tu, A. Jentsch, M. Baker, L. Zheng, J.-H. Lee, R. Venugopalan, O. Hen, D. Higinbotham, E.-C. Aschenauer, and T. Ullrich, "Probing short-range correlations in the deuteron via incoherent diffractive  $J/\psi$  production with spectator tagging at the EIC," 5 2020.
- [721] C. Alexa *et al.*, "Elastic and Proton-Dissociative Photoproduction of  $J/\psi$  Mesons at HERA," *Eur. Phys. J. C*, vol. 73, no. 6, p. 2466, 2013.
- [722] D. Higinbotham, G. A. Miller, O. Hen, and K. Rith, "The EMC effect still puzzles after 30 years," *CERN Cour.*, vol. 53N4, p. 24, 2013.
- [723] W. Cosyn and M. Sargsian, "Nuclear final-state interactions in deep inelastic scattering off the lightest nuclei," *Int. J. Mod. Phys. E*, vol. 26, no. 09, p. 1730004, 2017.
- [724] N. Baillie *et al.*, "Measurement of the neutron F2 structure function via spectator tagging with CLAS," *Phys. Rev. Lett.*, vol. 108, p. 142001, 2012. [Erratum: *Phys.Rev.Lett.* 108, 199902 (2012)].
- [725] H. C. Fenker *et al.*, "BoNuS: Development and Use of a Radial TPC using Cylindrical GEMs," *Nucl. Instrum. Meth. A*, vol. 592, pp. 273–286, 2008.
- [726] L. Mankiewicz, A. Schafer, and M. Veltri, "PEPSI: A Monte Carlo generator for polarized leptoproduction," *Comput. Phys. Commun.*, vol. 71, pp. 305–318, 1992.

- [727] A. Del Dotto, L. Kaptari, E. Pace, G. Salmè, and S. Scopetta, “Final state interactions and the extraction of neutron single spin asymmetries from semi-inclusive deep-inelastic scattering by a transversely polarized  $^3\text{He}$  target,” *Phys. Rev. C*, vol. 96, no. 6, p. 065203, 2017.
- [728] S. Scopetta, “Neutron single spin asymmetries from semi-inclusive deep inelastic scattering off transversely polarized He-3,” *Phys. Rev.*, vol. D75, p. 054005, 2007.
- [729] S. Klein and P. Steinberg, “Photonuclear and Two-photon Interactions at High-Energy Nuclear Colliders,” 5 2020.
- [730] J. A. Crittenden, “Experimental results on the diffractive production of light vector mesons,” *J. Phys. G*, vol. 28, pp. 1103–1112, 2002.
- [731] C. A. Bertulani, S. R. Klein, and J. Nystrand, “Physics of ultra-peripheral nuclear collisions,” *Ann. Rev. Nucl. Part. Sci.*, vol. 55, pp. 271–310, 2005.
- [732] A. Baltz, “The Physics of Ultraperipheral Collisions at the LHC,” *Phys. Rept.*, vol. 458, pp. 1–171, 2008.
- [733] S. Acharya *et al.*, “Coherent  $J/\psi$  photoproduction at forward rapidity in ultra-peripheral Pb-Pb collisions at  $\sqrt{s_{\text{NN}}} = 5.02$  TeV,” *Phys. Lett. B*, vol. 798, p. 134926, 2019.
- [734] M. Lomnitz and S. Klein, “Exclusive vector meson production at an electron-ion collider,” *Phys. Rev.*, vol. C99, no. 1, p. 015203, 2019.
- [735] H. Mäntysaari and R. Venugopalan, “Systematics of strong nuclear amplification of gluon saturation from exclusive vector meson production in high energy electron–nucleus collisions,” *Phys. Lett.*, vol. B781, pp. 664–671, 2018.
- [736] S. P. Jones, A. D. Martin, M. G. Ryskin, and T. Teubner, “Probes of the small  $x$  gluon via exclusive  $J/\psi$  and  $Y$  production at HERA and the LHC,” *JHEP*, vol. 11, p. 085, 2013.
- [737] S. R. Klein, “Ultra-peripheral collisions and hadronic structure,” *Nucl. Phys. A*, vol. 967, pp. 249–256, 2017.
- [738] C. A. Flett, S. P. Jones, A. D. Martin, M. G. Ryskin, and T. Teubner, “Exclusive production of heavy quarkonia as a probe of the low  $x$  and low scale gluon PDF,” 2019.
- [739] S. P. Jones, A. D. Martin, M. G. Ryskin, and T. Teubner, “The exclusive  $J/\psi$  process at the LHC tamed to probe the low  $x$  gluon,” *Eur. Phys. J.*, vol. C76, no. 11, p. 633, 2016.
- [740] C. A. Flett, S. P. Jones, A. D. Martin, M. G. Ryskin, and T. Teubner, “How to include exclusive  $J/\psi$  production data in global PDF analyses,” 2019.
- [741] S. Klein and J. Nystrand, “Exclusive vector meson production in relativistic heavy ion collisions,” *Phys. Rev. C*, vol. 60, p. 014903, 1999.

- [742] M. L. Good and W. D. Walker, "Diffraction dissociation of beam particles," *Phys. Rev.*, vol. 120, pp. 1857–1860, 1960.
- [743] S. R. Klein and H. Mäntysaari, "Imaging the nucleus with high-energy photons," *Nature Rev. Phys.*, vol. 1, no. 11, pp. 662–674, 2019.
- [744] T. Toll and T. Ullrich, "Exclusive diffractive processes in electron-ion collisions," *Phys. Rev.*, vol. C87, no. 2, p. 024913, 2013.
- [745] L. Adamczyk *et al.*, "Coherent diffractive photoproduction of  $\rho^0$  mesons on gold nuclei at 200 GeV/nucleon-pair at the Relativistic Heavy Ion Collider," *Phys. Rev. C*, vol. 96, no. 5, p. 054904, 2017.
- [746] S. R. Klein, "Dipion photoproduction and the  $Q^2$  evolution of the shape of the gold nucleus," *PoS*, vol. DIS2018, p. 047, 2018.
- [747] H. Mäntysaari and B. Schenke, "Evidence of strong proton shape fluctuations from incoherent diffraction," *Phys. Rev. Lett.*, vol. 117, no. 5, p. 052301, 2016.
- [748] H. Mäntysaari and B. Schenke, "Probing subnucleon scale fluctuations in ultraperipheral heavy ion collisions," *Phys. Lett.*, vol. B772, pp. 832–838, 2017.
- [749] S. R. Klein, "Heavy ion beam loss mechanisms at an electron-ion collider," *Phys. Rev. ST Accel. Beams*, vol. 17, no. 12, p. 121003, 2014.
- [750] A. Metz and A. Vossen, "Parton Fragmentation Functions," *Prog. Part. Nucl. Phys.*, vol. 91, pp. 136–202, 2016.
- [751] V. Bertone, S. Carrazza, N. P. Hartland, E. R. Nocera, and J. Rojo, "A determination of the fragmentation functions of pions, kaons, and protons with faithful uncertainties," *Eur. Phys. J. C*, vol. 77, no. 8, p. 516, 2017.
- [752] N. Sato, J. Ethier, W. Melnitchouk, M. Hirai, S. Kumano, and A. Accardi, "First Monte Carlo analysis of fragmentation functions from single-inclusive  $e^+e^-$  annihilation," *Phys. Rev. D*, vol. 94, no. 11, p. 114004, 2016.
- [753] W. Braunschweig *et al.*, "Pion, Kaon and Proton Cross-sections in  $e^+e^-$  Annihilation at 34-GeV and 44-GeV Center-of-mass Energy," *Z. Phys. C*, vol. 42, p. 189, 1989.
- [754] K. Abe *et al.*, "Production of  $\pi^+$ ,  $K^+$ ,  $K^0$ ,  $K^{*0}$ ,  $\phi$ ,  $p$  and  $\Lambda^0$  in hadronic  $Z^0$  decays," *Phys. Rev. D*, vol. 59, p. 052001, 1999.
- [755] R. Akers *et al.*, "Measurement of the production rates of charged hadrons in  $e^+e^-$  annihilation at the  $Z^0$ ," *Z. Phys. C*, vol. 63, pp. 181–196, 1994.
- [756] P. Abreu *et al.*, " $\pi^+$ ,  $K^+$ ,  $p$  and anti- $p$  production in  $Z^0 \rightarrow q \text{ anti-}q$ ,  $Z^0 \rightarrow b \text{ anti-}b$ ,  $Z^0 \rightarrow u \text{ anti-}u$ ,  $d \text{ anti-}d$ ,  $s \text{ anti-}s$ ," *Eur. Phys. J. C*, vol. 5, pp. 585–620, 1998.
- [757] D. Buskulic *et al.*, "Inclusive  $\pi^+$ ,  $K^+$  and ( $p$ , anti- $p$ ) differential cross-sections at the  $Z$  resonance," *Z. Phys. C*, vol. 66, pp. 355–366, 1995.

- [758] H. Aihara *et al.*, “Pion and kaon multiplicities in heavy quark jets from  $e^+e^-$  annihilation at 29-GeV,” *Phys. Lett. B*, vol. 184, pp. 299–304, 1987.
- [759] H. Aihara *et al.*, “Charged hadron inclusive cross-sections and fractions in  $e^+e^-$  annihilation  $\sqrt{s} = 29$  GeV,” *Phys. Rev. Lett.*, vol. 61, p. 1263, 1988.
- [760] G. Abbiendi *et al.*, “Leading particle production in light flavor jets,” *Eur. Phys. J. C*, vol. 16, pp. 407–421, 2000.
- [761] J. Lees *et al.*, “Production of charged pions, kaons, and protons in  $e^+e^-$  annihilations into hadrons at  $\sqrt{s}=10.54$  GeV,” *Phys. Rev. D*, vol. 88, p. 032011, 2013.
- [762] M. Leitgab *et al.*, “Precision Measurement of Charged Pion and Kaon Differential Cross Sections in  $e+e-$  Annihilation at  $s=10.52$  GeV,” *Phys. Rev. Lett.*, vol. 111, p. 062002, 2013.
- [763] A. Adare *et al.*, “Inclusive cross-section and double helicity asymmetry for  $\pi^0$  production in  $p + p$  collisions at  $s^{*(1/2)} = 200$ -GeV: Implications for the polarized gluon distribution in the proton,” *Phys. Rev.*, vol. D76, p. 051106, 2007.
- [764] B. Abelev *et al.*, “Strange particle production in  $p+p$  collisions at  $s^{*(1/2)} = 200$ -GeV,” *Phys. Rev. C*, vol. 75, p. 064901, 2007.
- [765] B. B. Abelev *et al.*, “Production of charged pions, kaons and protons at large transverse momenta in  $pp$  and  $Pb-Pb$  collisions at  $\sqrt{s_{NN}} = 2.76$  TeV,” *Phys. Lett. B*, vol. 736, pp. 196–207, 2014.
- [766] G. Agakishiev *et al.*, “Identified hadron compositions in  $p+p$  and  $Au+Au$  collisions at high transverse momenta at  $\sqrt{s_{NN}} = 200$  GeV,” *Phys. Rev. Lett.*, vol. 108, p. 072302, 2012.
- [767] I. Arsene *et al.*, “Production of mesons and baryons at high rapidity and high  $P(T)$  in proton-proton collisions at  $s^{*(1/2)} = 200$ -GeV,” *Phys. Rev. Lett.*, vol. 98, p. 252001, 2007.
- [768] L. Adamczyk *et al.*, “Neutral pion cross section and spin asymmetries at intermediate pseudorapidity in polarized proton collisions at  $\sqrt{s} = 200$  GeV,” *Phys. Rev. D*, vol. 89, no. 1, p. 012001, 2014.
- [769] C. Adolph *et al.*, “Multiplicities of charged kaons from deep-inelastic muon scattering off an isoscalar target,” *Phys. Lett. B*, vol. 767, pp. 133–141, 2017.
- [770] R. Hernández-Pinto, M. Epele, D. de Florian, R. Sassot, and M. Stratmann, “Global extraction of the parton-to-pion fragmentation functions at NLO accuracy in QCD,” *J. Phys. Conf. Ser.*, vol. 761, no. 1, p. 012037, 2016.

- [771] R. Hernández-Pinto, M. Epele, D. de Florian, R. Sassot, and M. Stratmann, “Global extraction of the parton-to-kaon fragmentation functions at NLO in QCD,” *J. Phys. Conf. Ser.*, vol. 912, no. 1, p. 012043, 2017.
- [772] D. de Florian, R. Sassot, and M. Stratmann, “Global analysis of fragmentation functions for pions and kaons and their uncertainties,” *Phys. Rev.*, vol. D75, p. 114010, 2007.
- [773] M. Adams *et al.*, “Lambda and anti-lambda polarization from deep inelastic muon scattering,” *Eur. Phys. J. C*, vol. 17, pp. 263–267, 2000.
- [774] A. Airapetian *et al.*, “Longitudinal Spin Transfer to the Lambda Hyperon in Semi-Inclusive Deep-Inelastic Scattering,” *Phys. Rev. D*, vol. 74, p. 072004, 2006.
- [775] M. Alekseev *et al.*, “Measurement of the Longitudinal Spin Transfer to Lambda and Anti-Lambda Hyperons in Polarised Muon DIS,” *Eur. Phys. J. C*, vol. 64, pp. 171–179, 2009.
- [776] A. Bravar *et al.*, “Spin transfer in inclusive Lambda<sup>0</sup> production by transversely polarized protons at 200-GeV/c,” *Phys. Rev. Lett.*, vol. 78, pp. 4003–4006, 1997.
- [777] B. Abelev *et al.*, “Longitudinal Spin Transfer to Lambda and anti-Lambda Hyperons in Polarized Proton-Proton Collisions at  $s^{*}(1/2) = 200\text{-GeV}$ ,” *Phys. Rev. D*, vol. 80, p. 111102, 2009.
- [778] J. Adam *et al.*, “Improved measurement of the longitudinal spin transfer to  $\Lambda$  and  $\bar{\Lambda}$  hyperons in polarized proton-proton collisions at  $\sqrt{s} = 200\text{ GeV}$ ,” *Phys. Rev. D*, vol. 98, no. 11, p. 112009, 2018.
- [779] J. Adam *et al.*, “Transverse spin transfer to  $\Lambda$  and  $\bar{\Lambda}$  hyperons in polarized proton-proton collisions at  $\sqrt{s} = 200\text{ GeV}$ ,” *Phys. Rev. D*, vol. 98, no. 9, p. 091103, 2018.
- [780] D. de Florian, M. Stratmann, and W. Vogelsang, “QCD analysis of unpolarized and polarized Lambda baryon production in leading and next-to-leading order,” *Phys. Rev. D*, vol. 57, pp. 5811–5824, 1998.
- [781] W. Lu and B.-Q. Ma, “The Strange quark spin of the proton in semiinclusive Lambda lepton production,” *Phys. Lett. B*, vol. 357, pp. 419–422, 1995.
- [782] B.-Q. Ma, I. Schmidt, J. Soffer, and J.-J. Yang, “Lambda, anti-Lambda polarization and spin transfer in lepton deep inelastic scattering,” *Eur. Phys. J. C*, vol. 16, pp. 657–664, 2000.
- [783] B.-Q. Ma, I. Schmidt, J. Soffer, and J.-J. Yang, “Helicity and transversity distributions of nucleon and Lambda - hyperon from Lambda fragmentation,” *Phys. Rev. D*, vol. 64, p. 014017, 2001. [Erratum: *Phys.Rev.D* 64, 099901 (2001)].
- [784] C.-x. Liu, Q.-h. Xu, and Z.-t. Liang, “Hyperon polarization in semiinclusive deeply inelastic lepton nucleon scattering at high-energy,” *Phys. Rev. D*, vol. 64, p. 073004, 2001.

- [785] J. R. Ellis, A. Kotzinian, and D. V. Naumov, "Intrinsic polarized strangeness and Lambda<sup>0</sup> polarization in deep inelastic production," *Eur. Phys. J. C*, vol. 25, pp. 603–613, 2002.
- [786] J. R. Ellis, A. Kotzinian, D. Naumov, and M. Sapozhnikov, "Longitudinal Polarization of Lambda and anti-Lambda Hyperons in Lepton-Nucleon Deep-Inelastic Scattering," *Eur. Phys. J. C*, vol. 52, pp. 283–294.
- [787] S.-s. Zhou, Y. Chen, Z.-t. Liang, and Q.-h. Xu, "Longitudinal polarization of hyperon and anti-hyperon in semi-inclusive deep-inelastic scattering," *Phys. Rev. D*, vol. 79, p. 094018, 2009.
- [788] G. Bunce *et al.*, "Lambda<sup>0</sup> Hyperon Polarization in Inclusive Production by 300-GeV Protons on Beryllium," *Phys. Rev. Lett.*, vol. 36, pp. 1113–1116, 1976.
- [789] L. Schachinger *et al.*, "A Precise Measurement of the  $\Lambda^0$  Magnetic Moment," *Phys. Rev. Lett.*, vol. 41, p. 1348, 1978.
- [790] K. J. Heller *et al.*, "Polarization of  $\Sigma^0$  and Lambda Hyperons produced by 400-GeV/c protons," *Phys. Rev. Lett.*, vol. 51, pp. 2025–2028, 1983.
- [791] B. Lundberg *et al.*, "Polarization in Inclusive  $\Lambda$  and  $\bar{\Lambda}$  Production at Large  $p_T$ ," *Phys. Rev.*, vol. D40, pp. 3557–3567, 1989.
- [792] B. Yuldashev *et al.*, "Neutral strange particle production in p Ne-20 and p N interactions at 300-GeV/c," *Phys. Rev. D*, vol. 43, pp. 2792–2802, 1991.
- [793] E. Ramberg *et al.*, "Polarization of Lambda and anti-Lambda produced by 800-GeV protons," *Phys. Lett. B*, vol. 338, pp. 403–408, 1994.
- [794] V. Fanti *et al.*, "A Measurement of the transverse polarization of Lambda hyperons produced in inelastic p N reactions at 450-GeV proton energy," *Eur. Phys. J. C*, vol. 6, pp. 265–269, 1999.
- [795] I. Abt *et al.*, "Polarization of Lambda and anti-Lambda in 920-GeV fixed-target proton-nucleus collisions," *Phys. Lett. B*, vol. 638, pp. 415–421, 2006.
- [796] G. L. Kane, J. Pumplin, and W. Repko, "Transverse Quark Polarization in Large  $p(T)$  Reactions,  $e^+e^-$  Jets, and Leptonproduction: A Test of QCD," *Phys. Rev. Lett.*, vol. 41, p. 1689, 1978.
- [797] A. D. Panagiotou, " $\Lambda^0$  Polarization in Hadron - Nucleon, Hadron - Nucleus and Nucleus-nucleus Interactions," *Int. J. Mod. Phys. A*, vol. 5, p. 1197, 1990.
- [798] W. G. Dharmaratna and G. R. Goldstein, "Single quark polarization in quantum chromodynamics subprocesses," *Phys. Rev. D*, vol. 53, pp. 1073–1086, 1996.
- [799] M. Anselmino, D. Boer, U. Dalesio, and F. Murgia, " $\lambda$  polarization from unpolarized quark fragmentation," *Phys. Rev.*, vol. D63, p. 054029, 2001.

- [800] M. Anselmino, D. Boer, U. D'Alesio, and F. Murgia, "Transverse lambda polarization in semiinclusive DIS," *Phys. Rev. D*, vol. 65, p. 114014, 2002.
- [801] D. Boer, Z.-B. Kang, W. Vogelsang, and F. Yuan, "Test of the Universality of Naive-time-reversal-odd Fragmentation Functions," *Phys. Rev. Lett.*, vol. 105, p. 202001, 2010.
- [802] D. Boer, "Transverse Lambda polarization at high energy colliders," *PoS*, vol. DIS2010, p. 215, 2010.
- [803] L. Gamberg, Z.-B. Kang, D. Pitonyak, M. Schlegel, and S. Yoshida, "Polarized hyperon production in single-inclusive electron-positron annihilation at next-to-leading order," *JHEP*, vol. 01, p. 111, 2019.
- [804] G. Aad *et al.*, "Measurement of the transverse polarization of  $\Lambda$  and  $\bar{\Lambda}$  hyperons produced in proton-proton collisions at  $\sqrt{s} = 7$  TeV using the ATLAS detector," *Phys. Rev. D*, vol. 91, no. 3, p. 032004, 2015.
- [805] K. Ackerstaff *et al.*, "Polarization and forward - backward asymmetry of Lambda baryons in hadronic Z0 decays," *Eur. Phys. J. C*, vol. 2, pp. 49–59, 1998.
- [806] Y. Guan *et al.*, "Observation of Transverse  $\Lambda/\bar{\Lambda}$  Hyperon Polarization in  $e^+e^-$  Annihilation at Belle," *Phys. Rev. Lett.*, vol. 122, no. 4, p. 042001, 2019.
- [807] J. C. Collins and D. E. Soper, "Back-To-Back Jets in QCD," *Nucl. Phys. B*, vol. 193, p. 381, 1981. [Erratum: *Nucl.Phys.B* 213, 545 (1983)].
- [808] D. Boer, R. Jakob, and P. Mulders, "Asymmetries in polarized hadron production in  $e^+e^-$  annihilation up to order  $1/Q$ ," *Nucl. Phys. B*, vol. 504, pp. 345–380, 1997.
- [809] U. D'Alesio, F. Murgia, and M. Zacccheddu, "First extraction of the  $\Lambda$  polarizing fragmentation function from Belle  $e^+e^-$  data," *Phys. Rev. D*, vol. 102, no. 5, p. 054001, 2020.
- [810] D. Callos, Z.-B. Kang, and J. Terry, "Extracting the Transverse Momentum Dependent Polarizing Fragmentation Functions," *Phys. Rev. D*, vol. 102, no. 9, p. 096007, 2020.
- [811] H. H. Matevosyan, A. Kotzinian, and A. W. Thomas, "Accessing Quark Helicity through Dihadron Studies," *Phys. Rev. Lett.*, vol. 120, no. 25, p. 252001, 2018.
- [812] H. H. Matevosyan, A. Kotzinian, and A. W. Thomas, "Dihadron fragmentation functions in the quark-jet model: Longitudinally polarized quarks," *Phys. Rev. D*, vol. 96, no. 7, p. 074010, 2017.
- [813] H. H. Matevosyan, A. Kotzinian, and A. W. Thomas, "Dihadron fragmentation functions in the quark-jet model: Transversely polarized quarks," *Phys. Rev. D*, vol. 97, no. 1, p. 014019, 2018.

- [814] X. Luo, H. Sun, and Y.-L. Xie, "Single spin asymmetry  $A_{UL}^{\sin(\phi_h - \phi_R)}$  in dihadron semi-inclusive DIS," *Phys. Rev. D*, vol. 101, no. 5, p. 054020, 2020.
- [815] M. Dasgupta, F. Dreyer, G. P. Salam, and G. Soyez, "Small-radius jets to all orders in QCD," *JHEP*, vol. 04, p. 039, 2015.
- [816] D. J. Scott and W. J. Waalewijn, "The leading jet transverse momentum in inclusive jet production and with a loose jet veto," *JHEP*, vol. 03, p. 159, 2020.
- [817] L. G. Almeida, S. J. Lee, G. Perez, G. F. Sterman, I. Sung, and J. Virzi, "Substructure of high- $p_T$  Jets at the LHC," *Phys. Rev. D*, vol. 79, p. 074017, 2009.
- [818] S. D. Ellis, C. K. Vermilion, J. R. Walsh, A. Hornig, and C. Lee, "Jet Shapes and Jet Algorithms in SCET," *JHEP*, vol. 11, p. 101, 2010.
- [819] A. Hornig, Y. Makris, and T. Mehen, "Jet Shapes in Dijet Events at the LHC in SCET," *JHEP*, vol. 04, p. 097, 2016.
- [820] Z.-B. Kang, K. Lee, and F. Ringer, "Jet angularity measurements for single inclusive jet production," *JHEP*, vol. 04, p. 110, 2018.
- [821] E.-C. Aschenauer, K. Lee, B. Page, and F. Ringer, "Jet angularities in photoproduction at the Electron-Ion Collider," *Phys. Rev. D*, vol. 101, no. 5, p. 054028, 2020.
- [822] J.-W. Qiu, F. Ringer, N. Sato, and P. Zurita, "Factorization of jet cross sections in heavy-ion collisions," *Phys. Rev. Lett.*, vol. 122, no. 25, p. 252301, 2019.
- [823] K. M. Burke *et al.*, "Extracting the jet transport coefficient from jet quenching in high-energy heavy-ion collisions," *Phys. Rev. C*, vol. 90, no. 1, p. 014909, 2014.
- [824] G.-Y. Qin and X.-N. Wang, *Jet quenching in high-energy heavy-ion collisions*, vol. 24, p. 1530014. 10 2015.
- [825] J.-P. Blaizot and Y. Mehtar-Tani, "Jet Structure in Heavy Ion Collisions," *Int. J. Mod. Phys. E*, vol. 24, no. 11, p. 1530012, 2015.
- [826] A. Majumder and M. Van Leeuwen, "The Theory and Phenomenology of Perturbative QCD Based Jet Quenching," *Prog. Part. Nucl. Phys.*, vol. 66, pp. 41–92, 2011.
- [827] R. Kunnawalkam Elayavalli and K. C. Zapp, "Medium response in JEWEL and its impact on jet shape observables in heavy ion collisions," *JHEP*, vol. 07, p. 141, 2017.
- [828] Y. He, S. Cao, W. Chen, T. Luo, L.-G. Pang, and X.-N. Wang, "Interplaying mechanisms behind single inclusive jet suppression in heavy-ion collisions," *Phys. Rev. C*, vol. 99, no. 5, p. 054911, 2019.
- [829] A. Airapetian *et al.*, "Hadronization in semi-inclusive deep-inelastic scattering on nuclei," *Nucl. Phys.*, vol. B780, pp. 1–27, 2007.

- [830] J. Adams *et al.*, "Pion, kaon, proton and anti-proton transverse momentum distributions from  $p + p$  and  $d + Au$  collisions at  $\sqrt{s_{NN}} = 200\text{GeV}$ ," *Phys. Lett. B*, vol. 616, pp. 8–16, 2005.
- [831] S. S. Adler *et al.*, "Centrality dependence of  $\pi^0$  and eta production at large transverse momentum in  $s(NN)^{1/2} = 200\text{-GeV}$   $d + Au$  collisions," *Phys. Rev. Lett.*, vol. 98, p. 172302, 2007.
- [832] R. Sassot, M. Stratmann, and P. Zurita, "Fragmentations Functions in Nuclear Media," *Phys. Rev. D*, vol. 81, p. 054001, 2010.
- [833] A. Airapetian *et al.*, "Quark fragmentation to  $\pi^{\pm}$ ,  $\pi^0$ ,  $K^{\pm}$ ,  $p$  and anti- $p$  in the nuclear environment," *Phys. Lett. B*, vol. 577, pp. 37–46, 2003.
- [834] E. Wang and X.-N. Wang, "Jet tomography of dense and nuclear matter," *Phys. Rev. Lett.*, vol. 89, p. 162301, 2002.
- [835] F. Arleo, "Quenching of hadron spectra in DIS on nuclear targets," *Eur. Phys. J. C*, vol. 30, pp. 213–221, 2003.
- [836] A. Accardi, V. Muccifora, and H.-J. Pirner, "Hadron production in deep inelastic lepton nucleus scattering," *Nucl. Phys. A*, vol. 720, pp. 131–156, 2003.
- [837] B. Z. Kopeliovich, J. Nemchik, E. Predazzi, and A. Hayashigaki, "Nuclear hadronization: Within or without?," *Nucl. Phys.*, vol. A740, pp. 211–245, 2004.
- [838] W. K. Brooks and J. A. Lopez, "Estimating the Color Lifetime of Energetic Quarks," 4 2020.
- [839] T. Falter, W. Cassing, K. Gallmeister, and U. Mosel, "Hadron attenuation in deep inelastic lepton-nucleus scattering," *Phys. Rev. C*, vol. 70, p. 054609, 2004.
- [840] H. T. Li, Z. L. Liu, and I. Vitev, "Heavy meson tomography of cold nuclear matter at the electron-ion collider," 7 2020.
- [841] X. Li *et al.*, "A New Heavy Flavor Program for the Future Electron-Ion Collider," *EPJ Web Conf.*, vol. 235, p. 04002, 2020.
- [842] H. T. Li and I. Vitev, "Inverting the mass hierarchy of jet quenching effects with prompt  $b$ -jet substructure," *Phys. Lett. B*, vol. 793, pp. 259–264, 2019.
- [843] H. Fritzsche, "Producing Heavy Quark Flavors in Hadronic Collisions: A Test of Quantum Chromodynamics," *Phys. Lett. B*, vol. 67, pp. 217–221, 1977.
- [844] F. Halzen, "Cvc for Gluons and Hadroproduction of Quark Flavors," *Phys. Lett. B*, vol. 69, pp. 105–108, 1977.
- [845] C.-H. Chang, "Hadronic Production of  $J/\psi$  Associated With a Gluon," *Nucl. Phys. B*, vol. 172, pp. 425–434, 1980.

- [846] G. T. Bodwin, E. Braaten, and G. Lepage, "Rigorous QCD analysis of inclusive annihilation and production of heavy quarkonium," *Phys. Rev. D*, vol. 51, pp. 1125–1171, 1995. [Erratum: *Phys.Rev.D* 55, 5853 (1997)].
- [847] S. Aid *et al.*, "Elastic and inelastic photoproduction of  $J/\psi$  mesons at HERA," *Nucl. Phys. B*, vol. 472, pp. 3–31, 1996.
- [848] J. Breitweg *et al.*, "Measurement of inelastic  $J/\psi$  photoproduction at HERA," *Z. Phys. C*, vol. 76, pp. 599–612, 1997.
- [849] F. Aaron *et al.*, "Inelastic Production of  $J/\psi$  Mesons in Photoproduction and Deep Inelastic Scattering at HERA," *Eur. Phys. J. C*, vol. 68, pp. 401–420, 2010.
- [850] S. Chekanov *et al.*, "Measurements of inelastic  $J/\psi$  and  $\psi'$  photoproduction at HERA," *Eur. Phys. J. C*, vol. 27, pp. 173–188, 2003.
- [851] C. Adloff *et al.*, "Inelastic photoproduction of  $J/\psi$  mesons at HERA," *Eur. Phys. J. C*, vol. 25, pp. 25–39, 2002.
- [852] H. Abramowicz *et al.*, "Measurement of inelastic  $J/\psi$  and  $\psi'$  photoproduction at HERA," *JHEP*, vol. 02, p. 071, 2013.
- [853] S. Chekanov *et al.*, "Measurement of  $J/\psi$  helicity distributions in inelastic photoproduction at HERA," *JHEP*, vol. 12, p. 007, 2009.
- [854] C. Adloff *et al.*, "Charmonium production in deep inelastic scattering at HERA," *Eur. Phys. J. C*, vol. 10, pp. 373–393, 1999.
- [855] C. Adloff *et al.*, "Inelastic lepton production of  $J/\psi$  mesons at HERA," *Eur. Phys. J. C*, vol. 25, pp. 41–53, 2002.
- [856] S. Chekanov *et al.*, "Measurement of inelastic  $J/\psi$  production in deep inelastic scattering at HERA," *Eur. Phys. J. C*, vol. 44, pp. 13–25, 2005.
- [857] M. Krämer, "QCD corrections to inelastic  $J/\psi$  photoproduction," *Nucl. Phys. B*, vol. 459, pp. 3–50, 1996.
- [858] M. Butenschoen and B. A. Kniehl, "Complete next-to-leading-order corrections to  $J/\psi$  photoproduction in nonrelativistic quantum chromodynamics," *Phys. Rev. Lett.*, vol. 104, p. 072001, 2010.
- [859] C. Flore, J.-P. Lansberg, H.-S. Shao, and Y. Yedelkina, "Large- $P_T$  inclusive photoproduction of  $J/\psi$  in electron-proton collisions at HERA and the EIC," 9 2020.
- [860] S. Fleming, A. K. Leibovich, and T. Mehen, "Resummation of Large Endpoint Corrections to Color-Octet  $J/\psi$  Photoproduction," *Phys. Rev. D*, vol. 74, p. 114004, 2006.
- [861] Y. Hatta, A. Rajan, and D.-L. Yang, "Near threshold  $J/\psi$  and  $Y$  photoproduction at JLab and RHIC," *Phys. Rev. D*, vol. 100, no. 1, p. 014032, 2019.

- [862] B. Gittelmann, K. Hanson, D. Larson, E. Loh, A. Silverman, and G. Theodosiou, "Photoproduction of the  $\psi$  (3100) Meson at 11-GeV," *Phys. Rev. Lett.*, vol. 35, p. 1616, 1975.
- [863] L. Frankfurt and M. Strikman, "Two gluon form-factor of the nucleon and  $J/\psi$  photoproduction," *Phys. Rev. D*, vol. 66, p. 031502, 2002.
- [864] R. Kishore, A. Mukherjee, and S. Rajesh, "Sivers asymmetry in the photoproduction of a  $J/\psi$  and a jet at the EIC," *Phys. Rev. D*, vol. 101, no. 5, p. 054003, 2020.
- [865] M. G. Echevarria, Y. Makris, and I. Scimemi, "Quarkonium TMD fragmentation functions in NRQCD," 7 2020.
- [866] M. Beneke, I. Rothstein, and M. B. Wise, "Kinematic enhancement of nonperturbative corrections to quarkonium production," *Phys. Lett. B*, vol. 408, pp. 373–380, 1997.
- [867] S. Fleming and A. K. Leibovich, "The Resummed Photon Spectrum in Radiative Upsilon Decays," *Phys. Rev. Lett.*, vol. 90, p. 032001, 2003.
- [868] S. Fleming, A. K. Leibovich, and T. Mehen, "Resumming the color octet contribution to  $e^+e^- \rightarrow J/\psi + X$ ," *Phys. Rev. D*, vol. 68, p. 094011, 2003.
- [869] A. K. Leibovich and X. Liu, "The Color-singlet contribution to  $e^+e^- \rightarrow J/\psi + X$  at the endpoint," *Phys. Rev. D*, vol. 76, p. 034005, 2007.
- [870] Z. Cui, M. Hu, and J. Ma, "Gluon GPDs and exclusive photoproduction of quarkonium in forward region," *Eur. Phys. J. C*, vol. 79, no. 10, p. 812, 2019.
- [871] Z.-Q. Chen and C.-F. Qiao, "NLO QCD corrections to exclusive electroproduction of quarkonium," *Phys. Lett. B*, vol. 797, p. 134816, 2019. [Erratum: *Phys. Lett. B*, 135759 (2020)].
- [872] Y. Makris and I. Vitev, "An Effective Theory of Quarkonia in QCD Matter," *JHEP*, vol. 10, p. 111, 2019.
- [873] I. Z. Rothstein, P. Shrivastava, and I. W. Stewart, "Manifestly Soft Gauge Invariant Formulation of vNRQCD," *Nucl. Phys. B*, vol. 939, pp. 405–428, 2019.
- [874] S. Aronson, E. Borrás, B. Odegard, R. Sharma, and I. Vitev, "Collisional and thermal dissociation of  $J/\psi$  and  $Y$  states at the LHC," *Phys. Lett. B*, vol. 778, pp. 384–391, 2018.
- [875] G. Ovanessian and I. Vitev, "An effective theory for jet propagation in dense QCD matter: jet broadening and medium-induced bremsstrahlung," *JHEP*, vol. 06, p. 080, 2011.
- [876] Y.-T. Chien and I. Vitev, "Jet Shape Resummation Using Soft-Collinear Effective Theory," *JHEP*, vol. 12, p. 061, 2014.

- [877] Y. Akamatsu, "Heavy quark master equations in the Lindblad form at high temperatures," *Phys. Rev. D*, vol. 91, no. 5, p. 056002, 2015.
- [878] N. Brambilla, M. A. Escobedo, J. Soto, and A. Vairo, "Heavy quarkonium suppression in a fireball," *Phys. Rev. D*, vol. 97, no. 7, p. 074009, 2018.
- [879] X. Yao and T. Mehen, "Quarkonium in-medium transport equation derived from first principles," *Phys. Rev. D*, vol. 99, no. 9, p. 096028, 2019.
- [880] Y. Akamatsu, "Quarkonium in Quark-Gluon Plasma: Open Quantum System Approaches Re-examined," 9 2020.
- [881] X. Yao and T. Mehen, "Quarkonium Semiclassical Transport in Quark-Gluon Plasma: Factorization and Quantum Correction," 9 2020.
- [882] M. Leitch *et al.*, "Measurement of  $J/\psi$  and  $\psi'$  suppression in p-A collisions at 800-GeV/c," *Phys. Rev. Lett.*, vol. 84, pp. 3256–3260, 2000.
- [883] B. Alessandro *et al.*, " $J/\psi$  and  $\psi'$  production and their normal nuclear absorption in proton-nucleus collisions at 400-GeV," *Eur. Phys. J. C*, vol. 48, p. 329, 2006.
- [884] F. Arleo, P. Gossiaux, T. Gousset, and J. Aichelin, "Charmonium suppression in p-A collisions," *Phys. Rev. C*, vol. 61, p. 054906, 2000.
- [885] S. L. Olsen, T. Skwarnicki, and D. Zieminska, "Nonstandard heavy mesons and baryons: Experimental evidence," *Rev. Mod. Phys.*, vol. 90, no. 1, p. 015003, 2018.
- [886] J. Crittenden, "Exclusive production of neutral vector mesons at the electron - proton collider HERA," 4 1997.
- [887] S. J. Brodsky, J. Rathsman, and C. Merino, "Odderon-Pomeron interference," *Phys. Lett. B*, vol. 461, pp. 114–122, 1999.
- [888] I. Ginzburg, I. Ivanov, and N. Nikolaev, "Possible odderon discovery via observation of charge asymmetry in the diffractive  $\pi^+\pi^-$  production at HERA," *Eur. Phys. J. direct*, vol. 5, no. 1, p. 002, 2003.
- [889] I. Ginzburg and I. Ivanov, "How to measure the pomeron phase in diffractive dipion photoproduction," *Eur. Phys. J. C*, vol. 45, pp. 193–200, 2006.
- [890] P. Hägler, B. Pire, L. Szymanowski, and O. Teryaev, "Hunting the QCD-Odderon in hard diffractive electroproduction of two pions," *Phys. Lett. B*, vol. 535, pp. 117–126, 2002. [Erratum: *Phys.Lett.B* 540, 324–325 (2002)].
- [891] P. Hagler, B. Pire, L. Szymanowski, and O. Teryaev, "Pomeron - odderon interference effects in electroproduction of two pions," *Eur. Phys. J. C*, vol. 26, pp. 261–270, 2002.

- [892] M. Diehl, T. Gousset, B. Pire, and O. Teryaev, "Probing partonic structure in  $\gamma^* \gamma \rightarrow \pi \pi$  near threshold," *Phys. Rev. Lett.*, vol. 81, pp. 1782–1785, 1998.
- [893] M. V. Polyakov and C. Weiss, "Two pion light cone distribution amplitudes from the instanton vacuum," *Phys. Rev. D*, vol. 59, p. 091502, 1999.
- [894] M. Diehl, T. Gousset, and B. Pire, "Exclusive production of pion pairs in  $\gamma^* \gamma$  collisions at large  $Q^2$ ," *Phys. Rev. D*, vol. 62, p. 073014, 2000.
- [895] J.-M. Laget, "Exclusive Meson Photo- and Electro-production, a Window on the Structure of Hadronic Matter," *Progress in Particle and Nuclear Physics*, vol. 111, p. 103737, 2020.
- [896] M. Derrick *et al.*, "Measurement of elastic omega photoproduction at HERA," *Z. Phys. C*, vol. 73, pp. 73–84, 1996.
- [897] A. Stanek and S. Klein. personal communication.
- [898] K. Park *et al.*, "Hard exclusive pion electroproduction at backward angles with CLAS," *Phys. Lett.*, vol. B780, pp. 340–345, 2018.
- [899] W. B. Li *et al.*, "Unique Access to  $u$ -Channel Physics: Exclusive Backward-Angle Omega Meson Electroproduction," *Phys. Rev. Lett.*, vol. 123, no. 18, p. 182501, 2019.
- [900] I. I. Strakovsky, L. Pentchev, and A. Titov, "Comparative analysis of  $\omega p$ ,  $\phi p$ , and  $J/\psi p$  scattering lengths from A2, CLAS, and GlueX threshold measurements," *Phys. Rev. C*, vol. 101, no. 4, p. 045201, 2020.
- [901] R. F. Lebed, R. E. Mitchell, and E. S. Swanson, "Heavy-Quark QCD Exotica," *Prog. Part. Nucl. Phys.*, vol. 93, pp. 143–194, 2017.
- [902] A. Esposito, A. Pilloni, and A. Polosa, "Multiquark Resonances," *Phys. Rept.*, vol. 668, pp. 1–97, 2017.
- [903] N. Brambilla, S. Eidelman, C. Hanhart, A. Nefediev, C.-P. Shen, C. E. Thomas, A. Vairo, and C.-Z. Yuan, "The XYZ states: experimental and theoretical status and perspectives," *Phys. Rept.*, vol. 873, pp. 1–154, 2020.
- [904] X.-H. Liu, Q. Zhao, and F. E. Close, "Search for tetraquark candidate  $Z(4430)$  in meson photoproduction," *Phys. Rev. D*, vol. 77, p. 094005, 2008.
- [905] J. He and X. Liu, "Discovery potential for charmonium-like state  $Y(3940)$  by the meson photoproduction," *Phys. Rev. D*, vol. 80, p. 114007, 2009.
- [906] Q.-Y. Lin, X. Liu, and H.-S. Xu, "Charged charmoniumlike state  $Z_c(3900)^\pm$  via meson photoproduction," *Phys. Rev. D*, vol. 88, p. 114009, 2013.
- [907] S. R. Klein and Y.-P. Xie, "Photoproduction of charged final states in ultraperipheral collisions and electroproduction at an electron-ion collider," *Phys. Rev. C*, vol. 100, no. 2, p. 024620, 2019.

- [908] S. Adhikari *et al.*, “The GlueX Beamline and Detector,” 5 2020.
- [909] V. Burkert *et al.*, “The CLAS12 Spectrometer at Jefferson Laboratory,” *Nucl. Instrum. Meth. A*, vol. 959, p. 163419, 2020.
- [910] C. Adloff *et al.*, “Diffractive photoproduction of  $\psi(2S)$  mesons at HERA,” *Phys. Lett. B*, vol. 541, pp. 251–264, 2002.
- [911] C. Adloff *et al.*, “Elastic photoproduction of  $J/\psi$  and Upsilon mesons at HERA,” *Phys. Lett. B*, vol. 483, pp. 23–35, 2000.
- [912] S. Chekanov *et al.*, “Exclusive photoproduction of Upsilon mesons at HERA,” *Phys. Lett. B*, vol. 680, pp. 4–12, 2009.
- [913] M. Aghasyan *et al.*, “Search for muoproduction of  $X(3872)$  at COMPASS and indication of a new state  $\tilde{X}(3872)$ ,” *Phys. Lett. B*, vol. 783, pp. 334–340, 2018.
- [914] C. Adolph *et al.*, “Search for exclusive photoproduction of  $Z_c^\pm(3900)$  at COMPASS,” *Phys. Lett. B*, vol. 742, pp. 330–334, 2015.
- [915] M. Albaladejo, A. H. Blin, A. Pilloni, D. Winney, C. Fernández-Ramírez, V. Mathieu, and A. Szczepaniak, “XYZ spectroscopy at electron-hadron facilities: Exclusive processes,” 8 2020.
- [916] M. Arneodo *et al.*, “Transverse Momentum and Its Compensation in Current and Target Jets in Deep Inelastic Muon - Proton Scattering,” *Phys. Lett. B*, vol. 149, pp. 415–420, 1984.
- [917] M. Arneodo *et al.*, “Studies of Quark and Diquark Fragmentation Into Identified Hadrons in Deep Inelastic Muon - Proton Scattering,” *Phys. Lett. B*, vol. 150, p. 458, 1985.
- [918] M. Arneodo *et al.*, “Investigation of the  $w$  and  $q^2$  dependence of charged pion distributions in  $\mu p$  scattering,” *Z. Phys. C*, vol. 31, p. 1, 1986.
- [919] M. Adams *et al.*, “Production of charged hadrons by positive muons on deuterium and xenon at 490-GeV,” *Z. Phys. C*, vol. 61, pp. 179–198, 1994.
- [920] M. Derrick *et al.*, “Properties of the Hadronic System Resulting from anti-Muon-neutrino  $p$  Interactions,” *Phys. Rev. D*, vol. 17, p. 1, 1978.
- [921] P. Allen *et al.*, “Transverse Momentum Distributions of Hadrons in Deep Inelastic Neutrino - Proton Scattering,” *Nucl. Phys. B*, vol. 188, pp. 1–10, 1981.
- [922] P. Allen *et al.*, “An Investigation of Quark and Diquark Fragmentation in Neutrino  $p$  and Anti-neutrino  $p$  Charged Current Interactions in {BEBC},” *Nucl. Phys. B*, vol. 214, p. 369, 1983.
- [923] S. Chekanov *et al.*, “Leading proton production in deep inelastic scattering at HERA,” *JHEP*, vol. 06, p. 074, 2009.

- [924] V. Andreev *et al.*, "Measurement of Feynman- $x$  Spectra of Photons and Neutrons in the Very Forward Direction in Deep-Inelastic Scattering at HERA," *Eur. Phys. J. C*, vol. 74, no. 6, p. 2915, 2014.
- [925] C. Alexa *et al.*, "Measurement of Charged Particle Spectra in Deep-Inelastic ep Scattering at HERA," *Eur. Phys. J. C*, vol. 73, no. 4, p. 2406, 2013.
- [926] F. A. Ceccopieri, "QCD analysis of forward neutron production in DIS," *Eur. Phys. J. C*, vol. 74, no. 8, p. 3029, 2014.
- [927] J. Lee, M. Ruspa, A. Stasto, M. Strikman, and C. Weiss, "CFNS AdHoc Workshop on Target Fragmentation Physics with EIC," 2020. <https://indico.bnl.gov/event/9287/>.
- [928] M. Strikman and L. Frankfurt, "Deep Inelastic Processes as a Tool to Study the Structure of Nucleons and Nuclei and the Nature of Nuclear Forces," *Yad. Fiz.*, vol. 25, pp. 1177–1184, 1977.
- [929] F. A. Ceccopieri and D. Mancusi, "QCD analysis of Lambda hyperon production in DIS target-fragmentation region," *Eur. Phys. J. C*, vol. 73, p. 2435, 2013.
- [930] P. Schweitzer, M. Strikman, and C. Weiss, "Intrinsic transverse momentum and parton correlations from dynamical chiral symmetry breaking," *JHEP*, vol. 01, p. 163, 2013.
- [931] E. C. Aschenauer, T. Burton, T. Martini, H. Spiesberger, and M. Stratmann, "Prospects for Charged Current Deep-Inelastic Scattering off Polarized Nucleons at a Future Electron-Ion Collider," *Phys. Rev.*, vol. D88, p. 114025, 2013.
- [932] Y. Zhao, A. Deshpande, J. Huang, K. Kumar, and S. Riordan, "Neutral-Current Weak Interactions at an EIC," *Eur. Phys. J. A*, vol. 53, no. 3, p. 55, 2017.
- [933] C. S. Wood, S. C. Bennett, D. Cho, B. P. Masterson, J. L. Roberts, C. E. Tanner, and C. E. Wieman, "Measurement of parity nonconservation and an anapole moment in Cesium," *Science*, vol. 275, no. 5307, pp. 1759–1763, 1997.
- [934] D. Androic and *et al.*, "First determination of the weak charge of the proton," *Physical Review Letters*, vol. 111, Oct 2013.
- [935] D. Wang *et al.*, "Measurement of Parity-Violating Asymmetry in Electron-Deuteron Inelastic Scattering," *Phys. Rev. C*, vol. 91, no. 4, p. 045506, 2015.
- [936] J. P. Chen, H. Gao, T. K. Hemmick, Z. E. Meziani, and P. A. Souder, "A White Paper on SoLID (Solenoidal Large Intensity Device)," 2014.
- [937] S. M. Berman and J. R. Primack, "Weak neutral currents in electron and muon scattering," *Phys. Rev. D*, vol. 9, pp. 2171–2173, Apr 1974.
- [938] X. Zheng, R. Michaels, P. Reimer, and *et al.*, " $\bar{e}$ - $^2$ h pvdis at 6 gev," *Jefferson Lab E08-011*, 2008.

- [939] A. Argento and et al., “Electroweak asymmetry in deep inelastic muon-nucleon scattering,” *Physics Letters B*, vol. 120, no. 1, pp. 245 – 250, 1983.
- [940] Y. Furltova and S. Mantry, “Using polarized positrons to probe physics beyond the standard model,” *AIP Conf. Proc.*, vol. 1970, no. 1, p. 030005, 2018.
- [941] M. R. Buckley and M. J. Ramsey-Musolf, “Precision Probes of a Leptophobic  $Z'$  Boson,” *Phys. Lett.*, vol. B712, pp. 261–265, 2012.
- [942] M. González-Alonso and M. J. Ramsey-Musolf, “Leptophobic  $Z'$  Boson and Parity-Violating eD Scattering,” *Phys. Rev. D*, vol. 87, no. 5, p. 055013, 2013.
- [943] A. Czarnecki and W. J. Marciano, “Electroweak radiative corrections to polarized muon/muon scattering asymmetries,” *Physical Review D*, vol. 53, p. 1066–1072, Feb 1996.
- [944] A. CZARNECKI and W. J. MARCIANO, “Parity violating asymmetries at future lepton colliders,” *International Journal of Modern Physics A*, vol. 13, p. 2235–2244, Jun 1998.
- [945] A. CZARNECKI and W. J. MARCIANO, “Polarized muon scattering asymmetries,” *International Journal of Modern Physics A*, vol. 15, p. 2365–2375, Jun 2000.
- [946] A. Ferroglia, G. Ossola, and A. Sirlin, “The electroweak form factor  $\hat{\kappa}(q^2)$  and the running of  $\sin^2 \hat{\theta}_w$ ,” *The European Physical Journal C*, vol. 34, p. 165–171, May 2004.
- [947] K. Kumar, S. Mantry, W. Marciano, and P. Souder, “Low Energy Measurements of the Weak Mixing Angle,” *Ann. Rev. Nucl. Part. Sci.*, vol. 63, pp. 237–267, 2013.
- [948] H. Davoudiasl, H.-S. Lee, and W. J. Marciano, ““dark” implications for parity violation, rare meson decays, and higgs physics,” *Physical Review D*, vol. 85, Jun 2012.
- [949] H. Davoudiasl, H.-S. Lee, and W. J. Marciano, “Muon anomaly and dark parity violation,” *Physical Review Letters*, vol. 109, Jul 2012.
- [950] P. Jean *et al.*, “Early SPI / INTEGRAL measurements of 511 keV line emission from the 4th quadrant of the Galaxy,” *Astron. Astrophys.*, vol. 407, p. L55, 2003.
- [951] O. Adriani *et al.*, “An anomalous positron abundance in cosmic rays with energies 1.5-100 GeV,” *Nature*, vol. 458, pp. 607–609, 2009.
- [952] S. Barwick *et al.*, “Measurements of the cosmic ray positron fraction from 1-GeV to 50-GeV,” *Astrophys. J. Lett.*, vol. 482, pp. L191–L194, 1997.
- [953] J. Beatty *et al.*, “New measurement of the cosmic-ray positron fraction from 5 to 15-GeV,” *Phys. Rev. Lett.*, vol. 93, p. 241102, 2004.
- [954] M. Aguilar *et al.*, “Cosmic-ray positron fraction measurement from 1 to 30-GeV with AMS-01,” *Phys. Lett. B*, vol. 646, pp. 145–154, 2007.
- [955] M. Tanabashi *et al.*, “Review of Particle Physics,” *Phys. Rev. D*, vol. 98, no. 3, p. 030001, 2018.

- [956] R. Litchfield, "Muon to electron conversion: The COMET and Mu2e experiments," in *Interplay between Particle and Astroparticle physics*, 12 2014.
- [957] D. Wiedner, H. Augustin, S. Bachmann, N. Berger, M. Kiehn, A.-K. Perrevoort, and I. Peric, "A Novel Experiment Searching for the Lepton Flavor Violating Decay  $\mu \rightarrow eee$ ," *PoS*, vol. Vertex2012, p. 033, 2013.
- [958] P. Wintz, "Results of the SINDRUM-II experiment," *Conf. Proc. C*, vol. 980420, pp. 534–546, 1998.
- [959] M. Lee, "COMET Muon Conversion Experiment in J-PARC," *Front. in Phys.*, vol. 6, 2018.
- [960] A. Baldini *et al.*, "The design of the MEG II experiment," *Eur. Phys. J. C*, vol. 78, no. 5, p. 380, 2018.
- [961] A. van der Schaaf, "SINDRUM II," *J. Phys. G*, vol. 29, pp. 1503–1506, 2003.
- [962] F. Aaron *et al.*, "Search for Lepton Flavour Violation at HERA," *Phys. Lett. B*, vol. 701, pp. 20–30, 2011.
- [963] S. Chekanov *et al.*, "Search for lepton-flavor violation at HERA," *Eur. Phys. J.*, vol. C44, pp. 463–479, 2005.
- [964] A. Aktas *et al.*, "Search for lepton flavour violation in ep collisions at HERA," *Eur. Phys. J.*, vol. C52, pp. 833–847, 2007.
- [965] M. Gonderinger and M. J. Ramsey-Musolf, "Electron-to-Tau Lepton Flavor Violation at the Electron-Ion Collider," *JHEP*, vol. 1011, p. 045, 2010.
- [966] P. Taxil, E. Tugcu, and J. M. Virey, "Search and identification of scalar and vector leptoquarks at HERA with polarization," *Eur. Phys. J.*, vol. C14, pp. 165–178, 2000.
- [967] A. Aktas *et al.*, "First measurement of charged current cross sections at HERA with longitudinally polarised positrons," *Phys. Lett. B*, vol. 634, pp. 173–179, 2006.
- [968] A. Filippi and M. De Napoli, "Searching in the dark: the hunt for the dark photon," *Rev. Phys.*, vol. 5, p. 100042, 2020.
- [969] M. Fabbrichesi, E. Gabrielli, and G. Lanfranchi, "The Dark Photon," 5 2020.
- [970] "Search for a narrow resonance decaying to a pair of muons in proton-proton collisions at 13 TeV," 8 2019.
- [971] B. Batell, T. Ghosh, T. Han, and X. Keping, "Bsm physics at the electron ion collider: Searching for heavy neutral leptons," *Letter of Interest submitted to the Snowmass 2021 Energy Frontier*, 2020.
- [972] P. Minkowski, " $\mu \rightarrow e\gamma$  at a Rate of One Out of  $10^9$  Muon Decays?," *Phys. Lett. B*, vol. 67, pp. 421–428, 1977.

- [973] T. Yanagida, "Horizontal gauge symmetry and masses of neutrinos," *Conf. Proc. C*, vol. 7902131, pp. 95–99, 1979.
- [974] M. Gell-Mann, P. Ramond, and R. Slansky, "Complex Spinors and Unified Theories," *Conf. Proc. C*, vol. 790927, pp. 315–321, 1979.
- [975] S. Glashow, "The Future of Elementary Particle Physics," *NATO Sci. Ser. B*, vol. 61, p. 687, 1980.
- [976] R. N. Mohapatra and G. Senjanovic, "Neutrino Mass and Spontaneous Parity Non-conservation," *Phys. Rev. Lett.*, vol. 44, p. 912, 1980.
- [977] J. Schechter and J. Valle, "Neutrino Masses in  $SU(2) \times U(1)$  Theories," *Phys. Rev. D*, vol. 22, p. 2227, 1980.
- [978] T. Asaka and M. Shaposhnikov, "The  $\nu$ MSM, dark matter and baryon asymmetry of the universe," *Phys. Lett. B*, vol. 620, pp. 17–26, 2005.
- [979] E. K. Akhmedov, V. Rubakov, and A. Smirnov, "Baryogenesis via neutrino oscillations," *Phys. Rev. Lett.*, vol. 81, pp. 1359–1362, 1998.
- [980] J. Beacham *et al.*, "Physics Beyond Colliders at CERN: Beyond the Standard Model Working Group Report," *J. Phys. G*, vol. 47, no. 1, p. 010501, 2020.
- [981] R. Boughezal, F. Petriello, and D. Wiegand, "Removing flat directions in standard model EFT fits: How polarized electron-ion collider data can complement the LHC," *Physical Review D*, vol. 101, Jun 2020.
- [982] D. Colladay and V. Kostelecky, "Lorentz violating extension of the standard model," *Phys. Rev. D*, vol. 58, p. 116002, 1998.
- [983] V. Kostelecky, "Gravity, Lorentz violation, and the standard model," *Phys. Rev. D*, vol. 69, p. 105009, 2004.
- [984] D. Colladay and V. Kostelecky, "CPT violation and the standard model," *Phys. Rev. D*, vol. 55, pp. 6760–6774, 1997.
- [985] E. Lunghi, "Lorentz Violation in Deep Inelastic Electron-Proton Scattering," in *7th Meeting on CPT and Lorentz Symmetry*, pp. 165–168, 2017.
- [986] E. Lunghi and N. Sherrill, "Lorentz violation and the electron-ion collider," *Phys. Rev. D*, vol. 98, no. 11, p. 115018, 2018.
- [987] V. A. Kostelecký, E. Lunghi, N. Sherrill, and A. Vieira, "Lorentz and CPT Violation in Partons," *JHEP*, vol. 04, p. 143, 2020.
- [988] L. Alvarez-Ruso *et al.*, "NuSTEC 1 1 Neutrino Scattering Theory Experiment Collaboration <http://nustec.fnal.gov>. White Paper: Status and challenges of neutrino-nucleus scattering," *Prog. Part. Nucl. Phys.*, vol. 100, pp. 1–68, 2018.

- [989] B. Abi *et al.*, “Deep Underground Neutrino Experiment (DUNE), Far Detector Technical Design Report, Volume II DUNE Physics,” 2 2020.
- [990] K. Abe *et al.*, “Hyper-Kamiokande Design Report,” 5 2018.
- [991] R. Petti, “Precision Measurements of Fundamental Interactions with (Anti)Neutrinos,” in *Proceedings, 27th International Workshop on Deep Inelastic Scattering and Related Subjects (DIS 2019): Torino, Italy, April 8-12, 2019*, 2019.
- [992] P. Bernardini *et al.*, “Enhancing the lbnf/dune physics program,” European Particle Physics Strategy Update 2018-2020, contribution # 131.
- [993] G. Adamov *et al.*, “Precision measurements with (anti)neutrinos at lbnf,” LoI submitted to Snowmass 2021, contribution # 122 to neutrino physics frontier.
- [994] R. Petti, “Precision (anti)neutrino scattering off nucleons and nuclei,” *9th International Conference on Physics Opportunities at an Electron-Ion-Collider, LBNL, Berkeley, USA, September 21, 2019*.
- [995] K. Winter, ed., *Neutrino physics (2nd Edition)*, vol. 14. 2000.
- [996] A. Cooper-Sarkar, P. Mertsch, and S. Sarkar, “The high energy neutrino cross-section in the Standard Model and its uncertainty,” *JHEP*, vol. 08, p. 042, 2011.
- [997] S. Kumano, “Neutrino physics and EIC,” *Pre-DIS EIC workshop, Kobe, Japan, April 15, 2018*.
- [998] S. Kumano, “High-energy neutrino-nucleus interactions,” *EPJ Web Conf.*, vol. 208, p. 07003, 2019.
- [999] S. Nakamura *et al.*, “Towards a Unified Model of Neutrino-Nucleus Reactions for Neutrino Oscillation Experiments,” *Rept. Prog. Phys.*, vol. 80, no. 5, p. 056301, 2017.
- [1000] S. A. Kulagin and R. Petti, “Neutrino inelastic scattering off nuclei,” *Phys. Rev. D*, vol. 76, p. 094023, 2007.
- [1001] M. Hirai, S. Kumano, and T.-H. Nagai, “Determination of nuclear parton distribution functions and their uncertainties in next-to-leading order,” *Phys. Rev.*, vol. C76, p. 065207, 2007.
- [1002] K. Kovarik *et al.*, “nCTEQ15 - Global analysis of nuclear parton distributions with uncertainties in the CTEQ framework,” *Phys. Rev. D*, vol. 93, no. 8, p. 085037, 2016.
- [1003] D. de Florian, R. Sassot, P. Zurita, and M. Stratmann, “Global Analysis of Nuclear Parton Distributions,” *Phys. Rev. D*, vol. 85, p. 074028, 2012.
- [1004] H. Khanpour and S. Atashbar Tehrani, “Global Analysis of Nuclear Parton Distribution Functions and Their Uncertainties at Next-to-Next-to-Leading Order,” *Phys. Rev. D*, vol. 93, no. 1, p. 014026, 2016.

- [1005] S. Kulagin and R. Petti, "Nuclear parton distributions and the Drell-Yan process," *Phys. Rev. C*, vol. 90, no. 4, p. 045204, 2014.
- [1006] H. Duyang, B. Guo, S. Mishra, and R. Petti, "A Novel Approach to Neutrino-Hydrogen Measurements," 9 2018.
- [1007] H. Duyang, B. Guo, S. Mishra, and R. Petti, "A Precise Determination of (Anti)neutrino Fluxes with (Anti)neutrino-Hydrogen Interactions," *Phys. Lett. B*, vol. 795, pp. 424–431, 2019.
- [1008] L. Alvarez-Ruso *et al.*, "Neutrino scattering measurements on hydrogen and deuterium," LoI submitted to Snowmass 2021, contribution # 165 to neutrino physics frontier.
- [1009] O. Samoylov *et al.*, "A Precision Measurement of Charm Dimuon Production in Neutrino Interactions from the NOMAD Experiment," *Nucl. Phys. B*, vol. 876, pp. 339–375, 2013.
- [1010] M. Goncharov *et al.*, "Precise Measurement of Dimuon Production Cross-Sections in  $\nu_\mu$  Fe and  $\bar{\nu}_\mu$  Fe Deep Inelastic Scattering at the Tevatron.," *Phys. Rev. D*, vol. 64, p. 112006, 2001.
- [1011] S. Alekhin, J. Blümlein, S. Kulagin, S.-O. Moch, and R. Petti, "Strange and non-strange distributions from the collider data," *PoS*, vol. DIS2018, p. 008, 2018.
- [1012] S. Alekhin, J. Blümlein, and S. Moch, "Strange sea determination from collider data," *Phys. Lett. B*, vol. 777, pp. 134–140, 2018.
- [1013] S. Alekhin, J. Blumlein, L. Caminadac, K. Lipka, K. Lohwasser, S. Moch, R. Petti, and R. Placakyte, "Determination of Strange Sea Quark Distributions from Fixed-target and Collider Data," *Phys. Rev. D*, vol. 91, no. 9, p. 094002, 2015.
- [1014] R. D. Young, J. Roche, R. D. Carlini, and A. W. Thomas, "Extracting nucleon strange and anapole form factors from world data," *Phys. Rev. Lett.*, vol. 97, p. 102002, 2006.
- [1015] L. Ahrens *et al.*, "Measurement of Neutrino - Proton and anti-neutrino - Proton Elastic Scattering," *Phys. Rev. D*, vol. 35, p. 785, 1987.
- [1016] G. Garvey, W. Louis, and D. White, "Determination of proton strange form-factors from neutrino p elastic scattering," *Phys. Rev. C*, vol. 48, pp. 761–765, 1993.
- [1017] W. Alberico, M. Barbaro, S. M. Bilenky, J. Caballero, C. Giunti, C. Maieron, E. Moya de Guerra, and J. Udias, "Strange form-factors of the proton: A New analysis of the neutrino (anti-neutrino) data of the BNL-734 experiment," *Nucl. Phys. A*, vol. 651, pp. 277–286, 1999.
- [1018] A. Aguilar-Arevalo *et al.*, "Measurement of the Neutrino Neutral-Current Elastic Differential Cross Section on Mineral Oil at  $E_\nu \sim 1$  GeV," *Phys. Rev. D*, vol. 82, p. 092005, 2010.

- [1019] S. F. Pate, "Determination of the strange form-factors of the nucleon from  $\nu p$ , anti- $\nu p$ , and parity violating polarized- $e p$  elastic scattering," *Phys. Rev. Lett.*, vol. 92, p. 082002, 2004.
- [1020] S. F. Pate, D. W. McKee, and V. Papavassiliou, "Strange Quark Contribution to the Vector and Axial Form Factors of the Nucleon: Combined Analysis of G0, HAPPEX, and Brookhaven E734 Data," *Phys. Rev. C*, vol. 78, p. 015207, 2008.
- [1021] S. L. Adler, "Tests of the Conserved Vector Current and Partially Conserved Axial-Vector Current Hypotheses in High-Energy Neutrino Reactions," *Phys. Rev.*, vol. 135, pp. B963–B966, 1964.
- [1022] D. Allasia *et al.*, " $Q^2$  Dependence of the Proton and Neutron Structure Functions from Neutrino and anti-neutrinos Scattering in Deuterium," *Z. Phys.*, vol. C28, p. 321, 1985.
- [1023] D. J. Gross and C. H. Llewellyn Smith, "High-energy neutrino - nucleon scattering, current algebra and partons," *Nucl. Phys.*, vol. B14, pp. 337–347, 1969.
- [1024] J. Kim *et al.*, "A Measurement of  $\alpha(s)(Q^2)$  from the Gross-Llewellyn Smith sum rule," *Phys. Rev. Lett.*, vol. 81, pp. 3595–3598, 1998.
- [1025] S. Larin and J. Vermaseren, "The  $\alpha_s^3$  corrections to the Bjorken sum rule for polarized electroproduction and to the Gross-Llewellyn Smith sum rule," *Phys. Lett. B*, vol. 259, pp. 345–352, 1991.
- [1026] A. L. Kataev and A. V. Sidorov, "The Jacobi polynomials QCD analysis of the CCFR data for  $xF_3$  and the  $Q^2$  dependence of the Gross-Llewellyn-Smith sum rule," *Phys. Lett. B*, vol. 331, pp. 179–186, 1994.
- [1027] G. Zeller *et al.*, "A Precise Determination of Electroweak Parameters in Neutrino Nucleon Scattering," *Phys. Rev. Lett.*, vol. 88, p. 091802, 2002. [Erratum: *Phys.Rev.Lett.* 90, 239902 (2003)].
- [1028] S. Kumano, "Modified Paschos-Wolfenstein relation and extraction of weak mixing angle  $\sin^2 \theta(W)$ ," *Phys. Rev. D*, vol. 66, p. 111301, 2002.
- [1029] M. Hirai, S. Kumano, and T.-H. Nagai, "Nuclear modification difference between  $u(v)$  and  $d(v)$  distributions and its relation to NuTeV  $\sin^2 \theta(W)$  anomaly," *Phys. Rev. D*, vol. 71, p. 113007, 2005.
- [1030] A. Martin, R. Roberts, W. Stirling, and R. Thorne, "Parton distributions incorporating QED contributions," *Eur. Phys. J. C*, vol. 39, pp. 155–161, 2005.
- [1031] W. Bentz, I. Cloet, J. Londergan, and A. Thomas, "Reassessment of the NuTeV determination of the weak mixing angle," *Phys. Lett. B*, vol. 693, pp. 462–466, 2010.
- [1032] S. A. Kulagin, "Paschos-Wolfenstein relationship for nuclei and the NuTeV  $\sin^2(\theta(w))$  measurement," *Phys. Rev. D*, vol. 67, p. 091301, 2003.

- [1033] S. Kumano, Q.-T. Song, and O. Teryaev, "Hadron tomography by generalized distribution amplitudes in pion-pair production process  $\gamma^*\gamma \rightarrow \pi^0\pi^0$  and gravitational form factors for pion," *Phys. Rev. D*, vol. 97, no. 1, p. 014020, 2018.
- [1034] B. Pire, L. Szymanowski, and J. Wagner, "Hard exclusive neutrino production of a light meson," *Phys. Rev. D*, vol. 95, no. 11, p. 114029, 2017.
- [1035] H. Dembinski *et al.*, "Report on Tests and Measurements of Hadronic Interaction Properties with Air Showers," *EPJ Web Conf.*, vol. 210, p. 02004, 2019.
- [1036] F. Fenu, "The cosmic ray energy spectrum measured using the Pierre Auger Observatory," *PoS*, vol. ICRC2017, p. 486, 2018.
- [1037] D. Ivanov, "Energy Spectrum Measured by the Telescope Array," *PoS*, vol. ICRC2019, p. 298, 2020.
- [1038] D. Ivanov, "Report of the Telescope Array - Pierre Auger Observatory Working Group on Energy Spectrum," *PoS*, vol. ICRC2017, p. 498, 2018.
- [1039] A. di Matteo *et al.*, "Full-sky searches for anisotropies in UHECR arrival directions with the Pierre Auger Observatory and the Telescope Array," *PoS*, vol. ICRC2019, p. 439, 2020.
- [1040] A. Aab *et al.*, "Inferences on mass composition and tests of hadronic interactions from 0.3 to 100 EeV using the water-Cherenkov detectors of the Pierre Auger Observatory," *Phys. Rev. D*, vol. 96, no. 12, p. 122003, 2017.
- [1041] D. Bergman and T. Stroman, "TA 10 Year Stereo Composition Measurement," *PoS*, vol. ICRC2019, p. 191, 2020.
- [1042] G. K. Mezek, "Mass composition of cosmic rays with energies from  $[10^{17.2}]eV$  to  $[10^{20}]eV$  using surface and fluorescence detectors of the Pierre Auger Observatory," *EPJ Web Conf.*, vol. 191, p. 08008, 2018.
- [1043] S. Müller, "Direct Measurement of the Muon Density in Air Showers with the Pierre Auger Observatory," *EPJ Web Conf.*, vol. 210, p. 02013, 2019.
- [1044] M. Aartsen *et al.*, "Cosmic ray spectrum and composition from PeV to EeV using 3 years of data from IceTop and IceCube," *Phys. Rev. D*, vol. 100, no. 8, p. 082002, 2019.
- [1045] R. Abbasi *et al.*, "Lateral Distribution of Muons in IceCube Cosmic Ray Events," *Phys. Rev. D*, vol. 87, no. 1, p. 012005, 2013.
- [1046] D. Soldin, "Atmospheric Muons Measured with IceCube," *EPJ Web Conf.*, vol. 208, p. 08007, 2019.
- [1047] M. Aartsen *et al.*, "Observation of High-Energy Astrophysical Neutrinos in Three Years of IceCube Data," *Phys. Rev. Lett.*, vol. 113, p. 101101, 2014.

- [1048] T. K. Gaisser, K. Jero, A. Karle, and J. van Santen, "Generalized self-veto probability for atmospheric neutrinos," *Phys. Rev. D*, vol. 90, no. 2, p. 023009, 2014.
- [1049] A. Bhattacharya, R. Enberg, M. H. Reno, I. Sarcevic, and A. Stasto, "Perturbative charm production and the prompt atmospheric neutrino flux in light of RHIC and LHC," *JHEP*, vol. 06, p. 110, 2015.
- [1050] M. Aartsen *et al.*, "IceCube-Gen2: The Window to the Extreme Universe," 8 2020.
- [1051] A. Connolly, R. S. Thorne, and D. Waters, "Calculation of High Energy Neutrino-Nucleon Cross Sections and Uncertainties Using the MSTW Parton Distribution Functions and Implications for Future Experiments," *Phys. Rev. D*, vol. 83, p. 113009, 2011.
- [1052] S. R. Klein, S. A. Robertson, and R. Vogt, "Nuclear effects in high-energy neutrino interactions," *Phys. Rev. C*, vol. 102, no. 1, p. 015808, 2020.
- [1053] M. Aartsen *et al.*, "Measurements using the inelasticity distribution of multi-TeV neutrino interactions in IceCube," *Phys. Rev. D*, vol. 99, no. 3, p. 032004, 2019.
- [1054] A. Garcia, R. Gauld, A. Heijboer, and J. Rojo, "Complete predictions for high-energy neutrino propagation in matter," *JCAP*, vol. 09, p. 025, 2020.
- [1055] S. R. Klein, *Probing high-energy interactions of atmospheric and astrophysical neutrinos*, pp. 75–107. 2020.
- [1056] M. Aartsen *et al.*, "Measurement of the multi-TeV neutrino cross section with IceCube using Earth absorption," *Nature*, vol. 551, pp. 596–600, 2017.
- [1057] A. Bhattacharya, R. Enberg, M. H. Reno, and I. Sarcevic, "Charm decay in slow-jet supernovae as the origin of the IceCube ultra-high energy neutrino events," *JCAP*, vol. 06, p. 034, 2015.
- [1058] R. Angeles-Martinez *et al.*, "Transverse Momentum Dependent (TMD) parton distribution functions: status and prospects," *Acta Phys. Polon.*, vol. B46, no. 12, pp. 2501–2534, 2015.
- [1059] F. Dominguez, C. Marquet, A. M. Stasto, and B.-W. Xiao, "Universality of multiparticle production in QCD at high energies," *Phys. Rev. D*, vol. 87, p. 034007, 2013.
- [1060] P. Sun, B.-W. Xiao, and F. Yuan, "Gluon Distribution Functions and Higgs Boson Production at Moderate Transverse Momentum," *Phys. Rev. D*, vol. 84, p. 094005, 2011.
- [1061] T. Liou, "Color-neutral heavy particle production in nucleus-nucleus collisions in the quasi-classical approximation," *Nucl. Phys.*, vol. A897, pp. 122–140, 2013.
- [1062] J. Collins and J.-W. Qiu, " $k_T$  factorization is violated in production of high-transverse-momentum particles in hadron-hadron collisions," *Phys. Rev. D*, vol. 75, p. 114014, 2007.

- [1063] T. C. Rogers and P. J. Mulders, “No Generalized TMD-Factorization in Hadro-Production of High Transverse Momentum Hadrons,” *Phys. Rev. D*, vol. 81, p. 094006, 2010.
- [1064] F. Gelis, T. Lappi, and R. Venugopalan, “High energy factorization in nucleus-nucleus collisions. II. Multigluon correlations,” *Phys. Rev. D*, vol. 78, p. 054020, 2008.
- [1065] F. Gelis, T. Lappi, and R. Venugopalan, “High energy factorization in nucleus-nucleus collisions,” *Phys. Rev. D*, vol. 78, p. 054019, 2008.
- [1066] F. Gelis, T. Lappi, and R. Venugopalan, “High energy factorization in nucleus-nucleus collisions. 3. Long range rapidity correlations,” *Phys. Rev. D*, vol. 79, p. 094017, 2009.
- [1067] R. Abdul Khalek, J. J. Ethier, and J. Rojo, “Nuclear parton distributions from lepton-nucleus scattering and the impact of an electron-ion collider,” *Eur. Phys. J. C*, vol. 79, no. 6, p. 471, 2019.
- [1068] R. Aaij *et al.*, “Study of prompt  $D^0$  meson production in  $p$ Pb collisions at  $\sqrt{s_{NN}} = 5$  TeV,” *JHEP*, vol. 10, p. 090, 2017.
- [1069] I. Helenius, K. J. Eskola, and H. Paukkunen, “Probing the small- $x$  nuclear gluon distributions with isolated photons at forward rapidities in  $p$ +Pb collisions at the LHC,” *JHEP*, vol. 09, p. 138, 2014.
- [1070] “Letter of Intent: A Forward Calorimeter (FoCal) in the ALICE experiment,” 6 2020.
- [1071] Z. Citron *et al.*, *Report from Working Group 5: Future physics opportunities for high-density QCD at the LHC with heavy-ion and proton beams*, vol. 7, pp. 1159–1410. 12 2019.
- [1072] Y. Akiba *et al.*, “The Hot QCD White Paper: Exploring the Phases of QCD at RHIC and the LHC,” 2 2015.
- [1073] J. E. Bernhard, J. S. Moreland, and S. A. Bass, “Bayesian estimation of the specific shear and bulk viscosity of quark–gluon plasma,” *Nature Phys.*, vol. 15, no. 11, pp. 1113–1117, 2019.
- [1074] S. Schlichting and P. Tribedy, “Collectivity in Small Collision Systems: An Initial-State Perspective,” *Adv. High Energy Phys.*, vol. 2016, p. 8460349, 2016.
- [1075] T. Altinoluk and N. Armesto, “Particle correlations from the initial state,” *Eur. Phys. J. A*, vol. 56, no. 8, p. 215, 2020.
- [1076] C. Marquet, E. Petreska, and C. Roiesnel, “Transverse-momentum-dependent gluon distributions from JIMWLK evolution,” *JHEP*, vol. 10, p. 065, 2016.
- [1077] G. Aad *et al.*, “Centrality and rapidity dependence of inclusive jet production in  $\sqrt{s_{NN}} = 5.02$  TeV proton-lead collisions with the ATLAS detector,” *Phys. Lett. B*, vol. 748, pp. 392–413, 2015.

- [1078] A. Adare *et al.*, “Centrality-dependent modification of jet-production rates in deuteron-gold collisions at  $\sqrt{s_{NN}}=200$  GeV,” *Phys. Rev. Lett.*, vol. 116, no. 12, p. 122301, 2016.
- [1079] R. Neufeld, I. Vitev, and B.-W. Zhang, “A possible determination of the quark radiation length in cold nuclear matter,” *Phys. Lett. B*, vol. 704, pp. 590–595, 2011.
- [1080] H. Xing, Y. Guo, E. Wang, and X.-N. Wang, “Parton Energy Loss and Modified Beam Quark Distribution Functions in Drell-Yan Process in p+A Collisions,” *Nucl. Phys. A*, vol. 879, pp. 77–106, 2012.
- [1081] F. Arleo and S. Peigne, “ $J/\psi$  suppression in p-A collisions from parton energy loss in cold QCD matter,” *Phys. Rev. Lett.*, vol. 109, p. 122301, 2012.
- [1082] Z.-B. Kang, I. Vitev, and H. Xing, “Effects of cold nuclear matter energy loss on inclusive jet production in p+A collisions at energies available at the BNL Relativistic Heavy Ion Collider and the CERN Large Hadron Collider,” *Phys. Rev. C*, vol. 92, no. 5, p. 054911, 2015.
- [1083] Y.-T. Chien and I. Vitev, “Towards the understanding of jet shapes and cross sections in heavy ion collisions using soft-collinear effective theory,” *JHEP*, vol. 05, p. 023, 2016.
- [1084] I. Vitev, “Jet quenching at intermediate RHIC energies,” *Phys. Lett. B*, vol. 606, pp. 303–312, 2005.
- [1085] J.-w. Qiu and I. Vitev, “Transverse momentum diffusion and broadening of the back-to-back dihadron correlation function,” *Phys. Lett. B*, vol. 570, pp. 161–170, 2003.
- [1086] J. Arrington, D. Higinbotham, G. Rosner, and M. Sargsian, “Hard probes of short-range nucleon-nucleon correlations,” *Prog. Part. Nucl. Phys.*, vol. 67, pp. 898–938, 2012.
- [1087] C. Ciofi degli Atti, “In-medium short-range dynamics of nucleons: Recent theoretical and experimental advances,” *Phys. Rept.*, vol. 590, pp. 1–85, 2015.
- [1088] A. Tang *et al.*, “n-p short range correlations from (p,2p + n) measurements,” *Phys. Rev. Lett.*, vol. 90, p. 042301, 2003.
- [1089] E. Piasetzky, M. Sargsian, L. Frankfurt, M. Strikman, and J. Watson, “Evidence for the strong dominance of proton-neutron correlations in nuclei,” *Phys. Rev. Lett.*, vol. 97, p. 162504, 2006.
- [1090] R. Subedi, R. Shneor, P. Monaghan, B. Anderson, K. Aniol, *et al.*, “Probing Cold Dense Nuclear Matter,” *Science*, vol. 320, pp. 1476–1478, 2008.
- [1091] N. Fomin *et al.*, “New measurements of high-momentum nucleons and short-range structures in nuclei,” *Phys. Rev. Lett.*, vol. 108, p. 092502, 2012.

- [1092] I. Korover *et al.*, “Probing the Repulsive Core of the Nucleon-Nucleon Interaction via the  ${}^4\text{He}(e, e'pN)$  Triple-Coincidence Reaction,” *Phys. Rev. Lett.*, vol. 113, no. 2, p. 022501, 2014.
- [1093] O. Hen *et al.*, “Momentum sharing in imbalanced Fermi systems,” *Science*, vol. 346, pp. 614–617, 2014.
- [1094] M. Duer *et al.*, “Probing high-momentum protons and neutrons in neutron-rich nuclei,” *Nature*, vol. 560, no. 7720, pp. 617–621, 2018.
- [1095] M. Duer *et al.*, “Direct Observation of Proton-Neutron Short-Range Correlation Dominance in Heavy Nuclei,” *Phys. Rev. Lett.*, vol. 122, p. 172502, 2019.
- [1096] J. Arrington and N. Fomin, “Searching for flavor dependence in nuclear quark behavior,” *Phys. Rev. Lett.*, vol. 123, no. 4, p. 042501, 2019.
- [1097] X. Wang, A. Thomas, and W. Melnitchouk, “Do short-range correlations cause the nuclear EMC effect in the deuteron?,” 4 2020.
- [1098] V. Khachatryan *et al.*, “Coherent  $J/\psi$  photoproduction in ultra-peripheral PbPb collisions at  $\sqrt{s_{NN}} = 2.76$  TeV with the CMS experiment,” *Phys. Lett. B*, vol. 772, pp. 489–511, 2017.
- [1099] B. Abelev *et al.*, “Coherent  $J/\psi$  photoproduction in ultra-peripheral Pb-Pb collisions at  $\sqrt{s_{NN}} = 2.76$  TeV,” *Phys. Lett. B*, vol. 718, pp. 1273–1283, 2013.
- [1100] G. A. Miller, M. D. Sievert, and R. Venugopalan, “Probing short-range nucleon-nucleon interactions with an Electron-Ion Collider,” *Phys. Rev. C*, vol. 93, no. 4, p. 045202, 2016.
- [1101] E. Aschenauer, M. Baker, W. Chang, J. Lee, Z. Tu, *et al.*, “BeAGLE: a Tool to Refine Detector Requirements for eA Collisions EIC R&D; Project eRD17,” 2017. <https://wiki.bnl.gov/eic/index.php/BeAGLE>.
- [1102] L. L. Frankfurt, M. M. Sargsian, and M. I. Strikman, “Feynman graphs and Gribov-Glauber approach to high-energy knockout processes,” *Phys. Rev.*, vol. C56, pp. 1124–1137, 1997.
- [1103] M. M. Sargsian, “Selected topics in high energy semiexclusive electronuclear reactions,” *Int. J. Mod. Phys.*, vol. E10, pp. 405–458, 2001.
- [1104] J. Laget, “The Electro-disintegration of few body systems revisited,” *Phys. Lett. B*, vol. 609, pp. 49–56, 2005.
- [1105] K. Egiyan *et al.*, “Experimental study of exclusive  $\text{H-2}(e, e'p)n$  reaction mechanisms at high  $Q^2$ ,” *Phys. Rev. Lett.*, vol. 98, p. 262502, 2007.
- [1106] M. M. Sargsian, “Large  $Q^2$  Electrodisintegration of the Deuteron in Virtual Nucleon Approximation,” *Phys. Rev. C*, vol. 82, p. 014612, 2010.

- [1107] W. Boeglin *et al.*, “Probing the high momentum component of the deuteron at high  $Q^2$ ,” *Phys. Rev. Lett.*, vol. 107, p. 262501, 2011.
- [1108] R. Cruz-Torres *et al.*, “Probing few-body nuclear dynamics via  $^3\text{H}$  and  $^3\text{He}$  ( $e, e'p$ )pn cross-section measurements,” *Phys. Rev. Lett.*, vol. 124, p. 212501, 2020.
- [1109] G. A. Miller, “A Light front treatment of the nucleus implications for deep inelastic scattering,” *Phys. Rev. C*, vol. 56, pp. 8–11, 1997.
- [1110] G. Miller and R. Machleidt, “Infinite nuclear matter on the light front: Nucleon-nucleon correlations,” *Phys. Rev. C*, vol. 60, p. 035202, 1999.
- [1111] R. Machleidt, “The high-precision, charge-dependent Bonn nucleon-nucleon potential (CD-Bonn),” *Phys. Rev.*, vol. C63, p. 024001, 2001.
- [1112] E. Epelbaum, H.-W. Hammer, and U.-G. Meissner, “Modern Theory of Nuclear Forces,” *Rev. Mod. Phys.*, vol. 81, pp. 1773–1825, 2009.
- [1113] R. Machleidt and D. Entem, “Chiral effective field theory and nuclear forces,” *Phys. Rept.*, vol. 503, pp. 1–75, 2011.
- [1114] J. R. Cooke and G. A. Miller, “Ground states of the Wick-Cutkosky model using light front dynamics,” *Phys. Rev. C*, vol. 62, p. 054008, 2000.
- [1115] J. Vary, H. Honkanen, J. Li, P. Maris, S. Brodsky, A. Harindranath, G. de Teramond, P. Sternberg, E. Ng, and C. Yang, “Hamiltonian light-front field theory in a basis function approach,” *Phys. Rev. C*, vol. 81, p. 035205, 2010.
- [1116] B. R. Barrett, P. Navratil, and J. P. Vary, “Ab initio no core shell model,” *Prog. Part. Nucl. Phys.*, vol. 69, pp. 131–181, 2013.
- [1117] J. Hiller, “Nonperturbative light-front Hamiltonian methods,” *Prog. Part. Nucl. Phys.*, vol. 90, pp. 75–124, 2016.
- [1118] J.-W. Chen, W. Detmold, J. E. Lynn, and A. Schwenk, “Short Range Correlations and the EMC Effect in Effective Field Theory,” *Phys. Rev. Lett.*, vol. 119, no. 26, p. 262502, 2017.
- [1119] S. Bogner, R. Furnstahl, and R. Perry, “Similarity Renormalization Group for Nucleon-Nucleon Interactions,” *Phys. Rev. C*, vol. 75, p. 061001, 2007.
- [1120] S. D. Glazek and K. G. Wilson, “Renormalization of Hamiltonians,” *Phys. Rev. D*, vol. 48, pp. 5863–5872, 1993.
- [1121] S. Bogner and D. Roscher, “High-momentum tails from low-momentum effective theories,” *Phys. Rev. C*, vol. 86, p. 064304, 2012.
- [1122] Snowmass 2021, <https://snowmass21.org/loi>.
- [1123] Snowmass 2021, <https://snowmass21.org/submissions/start>.

- [1124] S. Fazio *et al.*, “Hadronic Tomography at the EIC and the Energy Frontier.” a Letter of Interest submitted to the Snowmass 2021 Theory Frontier, 2020.
- [1125] M. Arratia and p. others, “Jet Physics at the Electron Ion Collider.” a Letter of Interest submitted to the Snowmass 2021 Theory Frontier, 2020.
- [1126] M. Abdolmaleki *et al.*, “Heavy flavors at the EIC.” a Letter of Interest submitted to the Snowmass 2021 Theory Frontier, 2020.
- [1127] M. Arratia *et al.*, “EW and BSM physics at EIC.” a Letter of Interest submitted to the Snowmass 2021 Theory Frontier, 2020.
- [1128] S. J. Brodsky, D. S. Hwang, and I. Schmidt, “Final-state interactions and single-spin asymmetries in semi-inclusive deep inelastic scattering,” *Phys. Lett.*, vol. B530, pp. 99–107, 2002.
- [1129] S. Aoki *et al.*, “FLAG Review 2019,” 2019.
- [1130] P. Zyla *et al.*, “Review of Particle Physics,” *PTEP*, vol. 2020, no. 8, p. 083C01, 2020.
- [1131] X. Ji, “Parton Physics on a Euclidean Lattice,” *Phys. Rev. Lett.*, vol. 110, p. 262002, 2013.
- [1132] X. Ji, “Parton Physics from Large-Momentum Effective Field Theory,” *Sci. China Phys. Mech. Astron.*, vol. 57, pp. 1407–1412, 2014.
- [1133] X. Ji, Y.-S. Liu, Y. Liu, J.-H. Zhang, and Y. Zhao, “Large-Momentum Effective Theory,” 4 2020.
- [1134] K.-F. Liu and S.-J. Dong, “Origin of difference between anti-d and anti-u partons in the nucleon,” *Phys. Rev. Lett.*, vol. 72, pp. 1790–1793, 1994.
- [1135] K. F. Liu, S. J. Dong, T. Draper, D. Leinweber, J. H. Sloan, W. Wilcox, and R. M. Woloshyn, “Valence QCD: Connecting QCD to the quark model,” *Phys. Rev.*, vol. D59, p. 112001, 1999.
- [1136] K.-F. Liu, “Parton degrees of freedom from the path integral formalism,” *Phys. Rev.*, vol. D62, p. 074501, 2000.
- [1137] W. Detmold and C. J. D. Lin, “Deep-inelastic scattering and the operator product expansion in lattice QCD,” *Phys. Rev.*, vol. D73, p. 014501, 2006.
- [1138] V. Braun and D. Mueller, “Exclusive processes in position space and the pion distribution amplitude,” *Eur. Phys. J.*, vol. C55, pp. 349–361, 2008.
- [1139] Y.-Q. Ma and J.-W. Qiu, “Extracting Parton Distribution Functions from Lattice QCD Calculations,” *Phys. Rev.*, vol. D98, no. 7, p. 074021, 2018.
- [1140] Y.-Q. Ma and J.-W. Qiu, “QCD Factorization and PDFs from Lattice QCD Calculation,” *Int. J. Mod. Phys. Conf. Ser.*, vol. 37, p. 1560041, 2015.

- [1141] Y.-Q. Ma and J.-W. Qiu, "Exploring Partonic Structure of Hadrons Using ab initio Lattice QCD Calculations," *Phys. Rev. Lett.*, vol. 120, no. 2, p. 022003, 2018.
- [1142] A. Radyushkin, "Nonperturbative Evolution of Parton Quasi-Distributions," *Phys. Lett.*, vol. B767, pp. 314–320, 2017.
- [1143] A. J. Chambers, R. Horsley, Y. Nakamura, H. Perlt, P. E. L. Rakow, G. Schierholz, A. Schiller, K. Somfleth, R. D. Young, and J. M. Zanotti, "Nucleon Structure Functions from Operator Product Expansion on the Lattice," *Phys. Rev. Lett.*, vol. 118, no. 24, p. 242001, 2017.
- [1144] C. Monahan, "Recent Developments in  $x$ -dependent Structure Calculations," *PoS*, vol. LATTICE2018, p. 018, 2018.
- [1145] K. Cichy and M. Constantinou, "A guide to light-cone PDFs from Lattice QCD: an overview of approaches, techniques and results," *Adv. High Energy Phys.*, vol. 2019, p. 3036904, 2019.
- [1146] M. Constantinou, "The  $x$ -dependence of hadronic parton distributions: A review on the progress of lattice QCD," 10 2020.
- [1147] H.-W. Lin, W. Melnitchouk, A. Prokudin, N. Sato, and H. Shows, "First Monte Carlo Global Analysis of Nucleon Transversity with Lattice QCD Constraints," *Phys. Rev. Lett.*, vol. 120, no. 15, p. 152502, 2018.
- [1148] J. Bringewatt, N. Sato, W. Melnitchouk, J.-W. Qiu, F. Steffens, and M. Constantinou, "Confronting lattice parton distributions with global QCD analysis," 10 2020.
- [1149] J. Aubert *et al.*, "The ratio of the nucleon structure functions  $F_{2,n}$  for iron and deuterium," *Phys. Lett. B*, vol. 123, pp. 275–278, 1983.
- [1150] J.-W. Chen and W. Detmold, "Universality of the EMC effect," *Phys. Lett. B*, vol. 625, pp. 165–170, 2005.
- [1151] J. R. Smith and G. A. Miller, "Polarized quark distributions in nuclear matter," *Phys. Rev. C*, vol. 72, p. 022203, 2005.
- [1152] I. Cloet, W. Bentz, and A. W. Thomas, "Spin-dependent structure functions in nuclear matter and the polarized EMC effect," *Phys. Rev. Lett.*, vol. 95, p. 052302, 2005.
- [1153] W. Detmold, M. Illa, D. J. Murphy, P. Oare, K. Orginos, P. E. Shanahan, M. L. Wagman, and F. Winter, "Lattice QCD constraints on the parton distribution functions of  $^3\text{He}$ ," 9 2020.
- [1154] F. Winter, W. Detmold, A. S. Gambhir, K. Orginos, M. J. Savage, P. E. Shanahan, and M. L. Wagman, "First lattice QCD study of the gluonic structure of light nuclei," *Phys. Rev. D*, vol. 96, no. 9, p. 094512, 2017.
- [1155] P. Shanahan, A. Thomas, and R. Young, "Charge symmetry breaking from a chiral extrapolation of moments of quark distribution functions," *Phys. Rev. D*, vol. 87, no. 9, p. 094515, 2013.

- [1156] A. Keshavarzi, D. Nomura, and T. Teubner, "Muon  $g - 2$  and  $\alpha(M_Z^2)$ : a new data-based analysis," *Phys. Rev. D*, vol. 97, no. 11, p. 114025, 2018.
- [1157] A. Afanasev, P. Blunden, D. Hasell, and B. Raue, "Two-photon exchange in elastic electron-proton scattering," *Prog. Part. Nucl. Phys.*, vol. 95, pp. 245–278, 2017.
- [1158] B. Henderson *et al.*, "Hard Two-Photon Contribution to Elastic Lepton-Proton Scattering: Determined by the OLYMPUS Experiment," *Phys. Rev. Lett.*, vol. 118, no. 9, p. 092501, 2017.
- [1159] O. Tomalak, B. Pasquini, and M. Vanderhaeghen, "Two-photon exchange contribution to elastic  $e^-$ -proton scattering: Full dispersive treatment of  $\pi N$  states and comparison with data," *Phys. Rev. D*, vol. 96, no. 9, p. 096001, 2017.
- [1160] D. Yennie, S. C. Frautschi, and H. Suura, "The infrared divergence phenomena and high-energy processes," *Annals Phys.*, vol. 13, pp. 379–452, 1961.
- [1161] L. W. Mo and Y.-S. Tsai, "Radiative Corrections to Elastic and Inelastic  $e p$  and  $\mu p$  Scattering," *Rev. Mod. Phys.*, vol. 41, pp. 205–235, 1969.
- [1162] T. Liu, W. Melnitchouk, J.-W. Qiu, and N. Sato, "Factorized approach to radiative corrections for inelastic lepton-hadron collisions," 8 2020.
- [1163] F. Bloch and A. Nordsieck, "Note on the Radiation Field of the electron," *Phys. Rev.*, vol. 52, pp. 54–59, 1937.
- [1164] J. Kripfganz, H. Mohring, and H. Spiesberger, "Higher order leading logarithmic QED corrections to deep inelastic  $e p$  scattering at very high-energies," *Z. Phys. C*, vol. 49, pp. 501–510, 1991.
- [1165] J. Blumlein and H. Kawamura, "Universal higher order singlet QED corrections to unpolarized lepton scattering," *Eur. Phys. J. C*, vol. 51, pp. 317–333, 2007.
- [1166] R.-D. Bucoveanu and H. Spiesberger, "Second-Order Leptonic Radiative Corrections for Lepton-Proton Scattering," *Eur. Phys. J. A*, vol. 55, no. 4, p. 57, 2019.
- [1167] P. Banerjee, T. Engel, A. Signer, and Y. Ulrich, "QED at NNLO with McMule," *SciPost Phys.*, vol. 9, p. 027, 2020.
- [1168] A. Kwiatkowski, H. Spiesberger, and H. Mohring, "Heracles: An Event Generator for  $ep$  Interactions at {HERA} Energies Including Radiative Processes: Version 1.0," *Comput. Phys. Commun.*, vol. 69, pp. 155–172, 1992.
- [1169] K. Charchula, G. Schuler, and H. Spiesberger, "Combined QED and QCD radiative effects in deep inelastic lepton - proton scattering: The Monte Carlo generator DJANGO6," *Comput. Phys. Commun.*, vol. 81, pp. 381–402, 1994.
- [1170] M. Meziane *et al.*, "Search for effects beyond the Born approximation in polarization transfer observables in  $\vec{e}p$  elastic scattering," *Phys. Rev. Lett.*, vol. 106, p. 132501, 2011.

- [1171] I. Akushevich and A. Ilyichev, “Lowest order QED radiative effects in polarized SIDIS,” *Phys. Rev. D*, vol. 100, no. 3, p. 033005, 2019.
- [1172] J. C. Bernauer, *Measurement of the elastic electron-proton cross section and separation of the electric and magnetic form factor in the  $Q^2$  range from 0.004 to 1 (GeV/c) $^2$* . PhD thesis, Mainz U., Inst. Kernphys., 2010.
- [1173] I. Akushevich, O. Filoti, A. Ilyichev, and N. Shumeiko, “Monte Carlo Generator ELRADGEN 2.0 for Simulation of Radiative events in Elastic ep-Scattering of Polarized Particles,” *Comput. Phys. Commun.*, vol. 183, pp. 1448–1467, 2012.
- [1174] A. Gramolin, V. Fadin, A. Feldman, R. Gerasimov, D. Nikolenko, I. Rachek, and D. Toporkov, “A new event generator for the elastic scattering of charged leptons on protons,” *J. Phys. G*, vol. 41, no. 11, p. 115001, 2014.
- [1175] S. Hoeche, S. Schumann, and F. Siegert, “Hard photon production and matrix-element parton-shower merging,” *Phys. Rev. D*, vol. 81, p. 034026, 2010.
- [1176] A. Buckley *et al.*, “General-purpose event generators for LHC physics,” *Phys. Rept.*, vol. 504, pp. 145–233, 2011.
- [1177] J. Bernauer *et al.*, “OLYMPUS: First measurement of the charge-averaged elastic lepton-proton scattering cross section,” 8 2020.
- [1178] D. Rimal *et al.*, “Measurement of two-photon exchange effect by comparing elastic  $e^\pm p$  cross sections,” *Phys. Rev. C*, vol. 95, no. 6, p. 065201, 2017.
- [1179] I. Rachek *et al.*, “Measurement of the two-photon exchange contribution to the elastic  $e^\pm p$  scattering cross sections at the VEPP-3 storage ring,” *Phys. Rev. Lett.*, vol. 114, no. 6, p. 062005, 2015.
- [1180] “CFNS ad-hoc workshop on Radiative Corrections,” Jul 2020. <https://indico.bnl.gov/event/8844/>, proceedings in preparation.
- [1181] D. Wang, *Measurement of the Parity-Violating Asymmetry in Deep Inelastic Scattering at JLab 6 GeV*. PhD thesis, Virginia U., 2013.
- [1182] S. Alekhin *et al.*, “HERAFitter,” *Eur. Phys. J. C*, vol. 75, no. 7, p. 304, 2015.
- [1183] J. Blumlein, “The Theory of Deeply Inelastic Scattering,” *Prog. Part. Nucl. Phys.*, vol. 69, pp. 28–84, 2013.
- [1184] D. Glazier *et al.* <https://github.com/dglazier/elSpectro>.
- [1185] E. Perez, L. Schoeffel, and L. Favart, “MILOU: A Monte-Carlo for deeply virtual Compton scattering,” 11 2004.
- [1186] R. Akhunzyanov *et al.*, “Transverse extension of partons in the proton probed in the sea-quark range by measuring the DVCS cross section,” *Phys. Lett. B*, vol. 793, pp. 188–194, 2019.

- [1187] K. Kumericki, D. Mueller, and K. Passek-Kumericki, "Towards a fitting procedure for deeply virtual Compton scattering at next-to-leading order and beyond," *Nucl. Phys.*, vol. B794, pp. 244–323, 2008.
- [1188] K. Kumericki and D. Mueller, "Deeply virtual Compton scattering at small  $x(B)$  and the access to the GPD  $H$ ," *Nucl. Phys.*, vol. B841, pp. 1–58, 2010.
- [1189] K. Kumerički, D. Müller, and M. Murray, "HERMES impact for the access of Compton form factors," *Phys. Part. Nucl.*, vol. 45, no. 4, pp. 723–755, 2014.
- [1190] M. Cuic, K. Kumericki, and A. Schafer, "Separation of Quark Flavors using DVCS Data," 6 2020.
- [1191] S. Goloskokov and P. Kroll, "Vector meson electroproduction at small Bjorken- $x$  and generalized parton distributions," *Eur. Phys. J. C*, vol. 42, pp. 281–301, 2005.
- [1192] S. Goloskokov and P. Kroll, "The Role of the quark and gluon GPDs in hard vector-meson electroproduction," *Eur. Phys. J.*, vol. C53, pp. 367–384, 2008.
- [1193] S. Goloskokov and P. Kroll, "An Attempt to understand exclusive  $\pi^+$  electroproduction," *Eur. Phys. J. C*, vol. 65, pp. 137–151, 2010.
- [1194] B. Berthou *et al.*, "PARTONS: PARTonic Tomography Of Nucleon Software: A computing framework for the phenomenology of Generalized Parton Distributions," *Eur. Phys. J. C*, vol. 78, no. 6, p. 478, 2018.
- [1195] J. Botts and G. Sterman, "Hard elastic scattering in qcd: Leading behavior," *Nuclear Physics B*, vol. 325, no. 1, pp. 62 – 100, 1989.
- [1196] M. Alexeev *et al.*, "Measurement of the cross section for hard exclusive  $\pi^0$  muoproduction on the proton," *Phys. Lett. B*, vol. 805, p. 135454, 2020.
- [1197] S. Jadach and P. Sawicki, "mFOAM-1.02: A Compact version of the cellular event generator FOAM," *Comput. Phys. Commun.*, vol. 177, pp. 441–458, 2007.
- [1198] S. Joosten, *Argonne I/A-event Generator*, 2020.
- [1199] O. Gryniuk, S. Joosten, Z.-E. Meziani, and M. Vanderhaeghen, "Y photoproduction on the proton at the Electron-Ion Collider," *Phys. Rev. D*, vol. 102, no. 1, p. 014016, 2020.
- [1200] N. Davidson, T. Przedzinski, and Z. Was, "PHOTOS interface in C++: Technical and Physics Documentation," *Comput. Phys. Commun.*, vol. 199, pp. 86–101, 2016.
- [1201] T. Abe, "GRAPE dilepton (Version1.1): A Generator for dilepton production in  $e p$  collisions," *Comput. Phys. Commun.*, vol. 136, pp. 126–147, 2001.
- [1202] K. Kauder, *eic-smear detectors*, 2020.
- [1203] P. Sznajder, *TCS generator for EIC*, 2020.

- [1204] E.-C. Aschenauer *et al.*, “Electron-ion collider detector requirements and R&D handbook,” 2020. =[http://eicug.org/web/sites/default/files/EIC\\_HANDBOOK\\_v1.2.pdf](http://eicug.org/web/sites/default/files/EIC_HANDBOOK_v1.2.pdf).
- [1205] T. Toll and T. Ullrich, “The dipole model Monte Carlo generator Sartre 1,” *Comput. Phys. Commun.*, vol. 185, pp. 1835–1853, 2014.
- [1206] B. Sambasivam, T. Toll, and T. Ullrich, “Investigating saturation effects in ultraperipheral collisions at the LHC with the color dipole model,” *Phys. Lett. B*, vol. 803, p. 135277, 2020.
- [1207] H. Kowalski, L. Motyka, and G. Watt *Phys. Rev.*, vol. D74, p. 074016, 2006.
- [1208] S. Chekanov *et al.*, “Exclusive photoproduction of  $J/\psi$  mesons at HERA,” *Eur. Phys. J. C*, vol. 24, pp. 345–360, 2002.
- [1209] W. Li *et al.*, “Backward-angle Exclusive  $\pi^0$  Production above the Resonance Region,” 8 2020.
- [1210] B. Singh *et al.*, “Experimental access to Transition Distribution Amplitudes with the PANDA experiment at FAIR,” *Eur. Phys. J. A*, vol. 51, no. 8, p. 107, 2015.
- [1211] B. Pire, L. Szymanowski, and J. Wagner, “Exclusive neutrino-production of a charmed meson,” *Phys. Rev.*, vol. D95, no. 9, p. 094001, 2017.
- [1212] T. K. Choi, K. J. Kong, and B. G. Yu, “Pion and proton form factors in the Regge description of electroproduction  $p(e, e' \pi^+)n$ ,” *J. Korean Phys. Soc.*, vol. 67, no. 7, pp. 1089–1094, 2015.
- [1213] S. Basnet *et al.*, “Exclusive  $\pi^+$  electroproduction off the proton from low to high- $t$ ,” *Phys. Rev. C*, vol. 100, no. 6, p. 065204, 2019.
- [1214] I. Helenius and C. O. Rasmussen, “Hard diffraction in photoproduction with Pythia 8,” *Eur. Phys. J. C*, vol. 79, no. 5, p. 413, 2019.
- [1215] M. Derrick *et al.*, “Diffractive hard photoproduction at HERA and evidence for the gluon content of the pomeron,” *Phys. Lett. B*, vol. 356, pp. 129–146, 1995.
- [1216] M. Derrick *et al.*, “Observation of events with a large rapidity gap in deep inelastic scattering at HERA,” *Phys. Lett. B*, vol. 315, pp. 481–493, 1993.
- [1217] T. Ahmed *et al.*, “Deep inelastic scattering events with a large rapidity gap at HERA,” *Nucl. Phys. B*, vol. 429, pp. 477–502, 1994.
- [1218] N. Fomin, D. Higinbotham, M. Sargsian, and P. Solvignon, “New Results on Short-Range Correlations in Nuclei,” *Ann. Rev. Nucl. Part. Sci.*, vol. 67, pp. 129–159, 2017.
- [1219] J. D. Osborn, “Requirements, Status, and Plans for Track Reconstruction at the sPHENIX Experiment,” 6 2020.
- [1220] IAEA, *Live Chart of Nuclides*, 2020.

- [1221] C. Weiss *et al.*, “Jefferson Lab 2014/2015 Laboratory-directed Research and Development Project,” 2014. <https://www.jlab.org/theory/tag/>.
- [1222] S. Agostinelli *et al.*, “GEANT4: A Simulation toolkit,” *Nucl. Instrum. Meth.*, vol. A506, pp. 250–303, 2003.
- [1223] H. Jung, “Hard diffractive scattering in high-energy  $e p$  collisions and the Monte Carlo generator RAPGAP,” *Comput. Phys. Commun.*, vol. 86, pp. 147–161, 1995.
- [1224] L. Gonella, “EIC Silicon Vertex and Tracking: Technology survey,” *1<sup>st</sup> EIC Yellow Report Workshop at Temple University*, 19 March 2020.
- [1225] G. Contin *et al.*, “The STAR MAPS-based PiXeL detector,” *Nucl. Instrum. Meth. A*, vol. 907, pp. 60–80, 2018.
- [1226] B. Abelev *et al.*, “Technical Design Report for the Upgrade of the ALICE Inner Tracking System,” *J. Phys. G*, vol. 41, p. 087002, 2014.
- [1227] G. Aglieri Rinella, “The ALPIDE pixel sensor chip for the upgrade of the ALICE Inner Tracking System,” *Nucl. Instrum. Meth. A*, vol. 845, pp. 583–587, 2017.
- [1228] R. Schimassek, A. Andreazza, H. Augustin, M. Barbero, M. Benoit, F. Ehrler, G. Iacobucci, A. Meneses, P. Pangaud, M. Prathapan, A. Schöning, E. Vilella, A. Weber, M. Weber, W. Wong, H. Zhang, and I. Perić, “Test results of ataspix3 — a reticle size hvcmos pixel sensor designed for construction of multi chip modules,” *Nuclear Instruments and Methods in Physics Research Section A: Accelerators, Spectrometers, Detectors and Associated Equipment*, vol. 986, p. 164812, 2021.
- [1229] K. Moustakas *et al.*, “CMOS Monolithic Pixel Sensors based on the Column-Drain Architecture for the HL-LHC Upgrade,” *Nucl. Instrum. Meth. A*, vol. 936, pp. 604–607, 2019.
- [1230] R. Cardella *et al.*, “MALTA: an asynchronous readout CMOS monolithic pixel detector for the ATLAS High-Luminosity upgrade,” *JINST*, vol. 14, no. 06, p. C06019, 2019.
- [1231] M. Dyndal *et al.*, “Mini-MALTA: Radiation hard pixel designs for small-electrode monolithic CMOS sensors for the High Luminosity LHC,” *JINST*, vol. 15, no. 02, p. P02005, 2020.
- [1232] W. Snoeys *et al.*, “A process modification for CMOS monolithic active pixel sensors for enhanced depletion, timing performance and radiation tolerance,” *Nucl. Instrum. Meth. A*, vol. 871, pp. 90–96, 2017.
- [1233] M. Munker, M. Benoit, D. Dannheim, A. Fenigstein, T. Kugathasan, T. Leitner, H. Pernegger, P. Riedler, and W. Snoeys, “Simulations of CMOS pixel sensors with a small collection electrode, improved for a faster charge collection and increased radiation tolerance,” *JINST*, vol. 14, no. 05, p. C05013, 2019.

- [1234] P. Allport, L. Gonella, P. Jones, P. Newman, and H. Wennl f, "eRD18 report and presentation," *EIC Generic Detector R&D Advisory Panel Meeting*, January 2020.
- [1235] A. Collaboration, "Letter of Intent for an ALICE ITS Upgrade in LS3," *CERN-LHCC-2019-018. LHCC-I-034*, January 2020.
- [1236] L. Gonella, L. Greiner, P. Jones, I. Sedgwick, E. Sichtermann, and H. Wennl f, "eRD25 proposal," *EIC Generic Detector R&D Advisory Panel Meeting*, July 2020.
- [1237] L. Greiner, "Silicon material projections," *2<sup>nd</sup> EIC Yellow Report Workshop at Pavia University*, 21 May 2020.
- [1238] G. Pellegrini *et al.*, "Technology developments and first measurements of low gain avalanche detectors (LGAD) for high energy physics applications," *Nuclear Instruments and Methods in Physics Research Section A: Accelerators, Spectrometers, Detectors and Associated Equipment*, vol. 765, pp. 12 – 16, 2014. HSTD-9 2013 - Proceedings of the 9<sup>th</sup> International Hiroshima Symposium on Development and Application of Semiconductor Tracking Detectors.
- [1239] R. Padilla, C. Labitan, Z. Galloway, C. Gee, S. Mazza, F. McKinney-Martinez, H.-W. Sadrozinski, A. Seiden, B. Schumm, M. Wilder, Y. Zhao, H. Ren, Y. Jin, M. Lockerby, V. Cindro, G. Kramberger, I. Mandiz, M. Mikuz, M. Zavrtanik, R. Arcidiacono, N. Cartiglia, M. Ferrero, M. Mandurrino, V. Sola, and A. Staiano, "Effect of deep gain layer and carbon infusion on LGAD radiation hardness," *Journal of Instrumentation*, vol. 15, pp. P10003–P10003, oct 2020.
- [1240] Y. Jin *et al.*, "Experimental study of acceptor removal in UFSD," *Nuclear Instruments and Methods in Physics Research Section A: Accelerators, Spectrometers, Detectors and Associated Equipment*, vol. 983, p. 164611, Dec 2020.
- [1241] N. Cartiglia, A. Staiano, V. Sola, R. Arcidiacono, R. Cirio, F. Cenna, M. Ferrero, V. Monaco, R. Mulargia, M. Obertino, F. Ravera, R. Sacchi, A. Bellora, S. Durando, M. Mandurrino, N. Minafra, V. Fadeyev, P. Freeman, Z. Galloway, E. Gkoukousis, H. Grabas, B. Gruey, C. Labitan, R. Losakul, Z. Luce, F. McKinney-Martinez, H.-W. Sadrozinski, A. Seiden, E. Spencer, M. Wilder, N. Woods, A. Zatserklyaniy, G. Pellegrini, S. Hidalgo, M. Carulla, D. Flores, A. Merlos, D. Quirion, V. Cindro, G. Kramberger, I. Mandi c, M. Mikuz, and M. Zavrtanik, "Beam test results of a 16ps timing system based on ultra-fast silicon detectors," *Nuclear Instruments and Methods in Physics Research Section A: Accelerators, Spectrometers, Detectors and Associated Equipment*, vol. 850, pp. 83 – 88, 2017.
- [1242] A. Apresyan, W. Chen, G. D'Amico, K. F. Di Petrillo, G. Giacomini, R. Heller, H. Lee, S. Los, C.-S. Moon, and A. Tricoli, "Measurements of an AC-LGAD strip sensor with a 120 GeV proton beam," *JINST*, vol. 15, no. 09, p. P09038, 2020.
- [1243] H. Pernegger, R. Bates, C. Buttar, M. Dalla, J. van Hoorne, T. Kugathasan, D. Maneuski, L. Musa, P. Riedler, C. Riegel, C. Sbarra, D. Schaefer, E. Schioppa, and W. Snoeys, "First tests of a novel radiation hard CMOS sensor process for depleted

- monolithic active pixel sensors," *Journal of Instrumentation*, vol. 12, pp. P06008–P06008, jun 2017.
- [1244] I. Berdalovic *et al.*, "Monolithic pixel development in towerjazz 180 nm cmos for the outer pixel layers in the atlas experiment," *JINST*, vol. 13, p. C C01023, 2018.
- [1245] B. Hiti *et al.*, "Development of the monolithic "MALTA" CMOS sensor for the ATLAS ITK outer pixel layer," *PoS*, vol. TWEPP2018, p. 155, 2019.
- [1246] R. Schimassek, A. Andreatza, H. Augustin, M. Barbero, M. Benoit, F. Ehrler, G. Iacobucci, A. Meneses, P. Pangaud, M. Prathapan, A. Schöning, E. Vilella, A. Weber, M. Weber, W. Wong, H. Zhang, and I. Perić, "Test results of ATLASPIX3 — a reticle size HVCMOS pixel sensor designed for construction of multi chip modules," *Nuclear Instruments and Methods in Physics Research Section A: Accelerators, Spectrometers, Detectors and Associated Equipment*, vol. 986, p. 164812, 2021.
- [1247] F. Sauli, "GEM: A new concept for electron amplification in gas detectors," *Nucl. Instrum. Meth.*, vol. A386, no. 2, pp. 531–534, 1997.
- [1248] Y. Giomataris, P. Rebourgeard, J. Robert, and G. Charpak, "Micromegas: a high-granularity position-sensitive gaseous detector for high particle-flux environments," *Nuclear Instruments and Methods in Physics Research Section A: Accelerators, Spectrometers, Detectors and Associated Equipment*, vol. 376, no. 1, pp. 29 – 35, 1996.
- [1249] G. Bencivenni, R. D. Oliveira, G. Morello, and M. P. Lener, "The micro-resistive WELL detector: a compact spark-protected single amplification-stage MPGD," *Journal of Instrumentation*, vol. 10, pp. P02008–P02008, feb 2015.
- [1250] C. Altunbas, M. Caprignans, K. Dehmelt, J. Ehlers, J. Friedrich, I. Konorov, A. Gandi, S. Kappler, B. Ketzer, R. D. Oliveira, S. Paul, A. Placci, L. Ropelewski, F. Sauli, F. Simon, and M. van Stenis, "Construction, test and commissioning of the triple-gem tracking detector for compass," *Nucl. Instrum. Meth.*, vol. A490, no. 1, pp. 177 – 203, 2002.
- [1251] K. Gnanvo, X. Bai, C. Gu, N. Liyanage, V. Nelyubin, and Y. Zhao, "Performance in test beam of a large-area and light-weight GEM detector with 2D stereo-angle (UV) strip readout," *Nucl. Instrum. Meth.*, vol. A808, pp. 83–92, 2016.
- [1252] A. A. *et al.*, "The clas12 micromegas vertex tracker," *Nuclear Instruments and Methods in Physics Research Section A: Accelerators, Spectrometers, Detectors and Associated Equipment*, vol. 957, p. 163423, 2020.
- [1253] W. Xiong and *et al.*, "A small proton charge radius from an electron–proton scattering experiment," *Nature*, vol. 575, p. 147–150, 2019.
- [1254] M. Collaboration, "The moller experiment: An ultra-precise measurement of the weak mixing angle using møller scattering," 2014.
- [1255] J. P. Chen, H. Gao, T. K. Hemmick, Z. E. Meziani, P. A. Souder, and the SoLID Collaboration, "A white paper on solid (solenoidal large intensity device)," 2014.

- [1256] E. Aschenauer, B. Azmoun, V. Bhopatkar, T. Burton, H. Caines, A. Camsonne, K. D. A. Deshpande, A. Drees, S. Fazio, A. Franz, C. Gal, H. Ge, K. Gnanvo, J. W. Harris, T. Hemmick, M. Hohlmann, P. Kline, M. Lamont, A. Lebedev, B. Lewis, N. Liyanage, R. Majka, V. and R. Pak, R. Pisani, M. Purschke, M. Rosati, K. Saenboonruang, E. Sichtermann, N. Smirnov, M. Staib, S. Stoll, B. Surrow, S. Taneja, T. Ullrich, T. Videbaek, C. Woody, and S. Yalcin, "Proposal for detector R&D towards an EIC detector," 2012.
- [1257] B. Stelzer, "The New Small Wheel Upgrade Project of the ATLAS Experiment," *Nuclear and Particle Physics Proceedings*, vol. 273-275, pp. 1160–1165, Apr. 2016.
- [1258] "The STAR Forward Calorimeter System and Forward Tracking System beyond BES-II." <https://drupal.star.bnl.gov/STAR/starnotes/public/sn0648>.
- [1259] A. Abusleme, C. Bélanger-Champagne, A. Bellerive, Y. Benhammou, J. Botte, H. Cohen, M. Davies, Y. Du, L. Gauthier, T. Koffas, S. Kuleshov, B. Lefebvre, C. Li, N. Lupu, G. Mikenberg, D. Mori, J. P. Ochoa-Ricoux, E. P. Codina, S. Rettie, A. Robichaud-Véronneau, R. Rojas, M. Shoa, V. Smakhtin, B. Stelzer, O. Stelzer-Chilton, A. Toro, H. Torres, P. Ulloa, B. Vachon, G. Vasquez, A. Vdovin, S. Viel, P. Walker, S. Weber, and C. Zhu, "Performance of a full-size small-strip thin gap chamber prototype for the ATLAS new small wheel muon upgrade," *Nuclear Instruments and Methods in Physics Research Section A: Accelerators, Spectrometers, Detectors and Associated Equipment*, vol. 817, pp. 85–92, May 2016.
- [1260] C. Yang and Q. Yang, "The STAR Detector Upgrades for the BES-II and at Forward Rapidity," *J. Inst.*, vol. 15, pp. C07040–C07040, July 2020.
- [1261] "Fun4All." [https://wiki.bnl.gov/sPHENIX/index.php/EIC\\_SPHENIX\\_FUN4ALL](https://wiki.bnl.gov/sPHENIX/index.php/EIC_SPHENIX_FUN4ALL). Accessed: 2020-06-16.
- [1262] C. Pinkenburg, "Analyzing ever growing datasets in PHENIX," *J. Phys. Conf. Ser.*, vol. 331, p. 072027, 2011.
- [1263] C. Pinkenburg, "Online Monitoring and online calibration/reconstruction for the PHENIX experiment," in *14th International Conference on Computing in High-Energy and Nuclear Physics*, pp. 127–129, 2005.
- [1264] "sPHENIX Technical Design Report." [https://indico.bnl.gov/event/5905/contributions/32455/attachments/25084/37388/sphenix\\_tdr\\_20191015.pdf](https://indico.bnl.gov/event/5905/contributions/32455/attachments/25084/37388/sphenix_tdr_20191015.pdf).
- [1265] "BeAST Magnetic Field." [https://eic.github.io/software/beast\\_magnetic\\_field.html](https://eic.github.io/software/beast_magnetic_field.html).
- [1266] "A dedicated eRHIC Detector Design." <https://indico.desy.de/indico/event/12482/session/7/contribution/259/material/slides/0.pptx>.
- [1267] "A. Y. Kiselev." Private communication.
- [1268] "E. Cisbani." Private communication.

- [1269] “erd25: “a compact all-silicon central tracker concept for eic”.” <https://indico.bnl.gov/event/8231/>. open-mic session at the 2<sup>nd</sup> EIC Yellow Report Workshop at Pavia University.
- [1270] E. C. Aschenauer *et al.*, “eRHIC Design Study: An Electron-Ion Collider at BNL,” *arXiv preprint arXiv:1409.1633*, 2014.
- [1271] B. Abelev *et al.*, “Technical design report for the upgrade of the ALICE inner tracking system,” *Journal of Physics G: Nuclear and Particle Physics*, vol. 41, p. 087002, jul 2014.
- [1272] I. Berdalovic *et al.*, “Monolithic pixel development in towerjazz 180 nm cmos for the outer pixel layers in the atlas experiment,” *JINST*, vol. 13, p. C C01023, 2018.
- [1273] B. Abelev, J. Adam, D. Adamová, M. M. Aggarwal, G. Aglieri Rinella, M. Agnello, A. Agostinelli, N. Agrawal, Z. Ahammed, N. Ahmad, A. Ahmad Masoodi, I. Ahmed, S. U. Ahn, and M. More, “Technical Design Report for the Upgrade of the ALICE Inner Tracking System,” Tech. Rep. CERN-LHCC-2013-024. ALICE-TDR-017, Nov 2013.
- [1274] eRD6, “eRD6 Progress Report,” *EIC Generic Detector R&D Advisory Panel Meeting*, July 2020.
- [1275] F. Barbosa, H. Fenker, S. Furletov, Y. Furletova, K. Gnanvo, N. Liyanage, L. Pentchev, M. Posik, C. Stanislav, B. Surrów, and B. Zihlmann, “A new Transition Radiation detector based on GEM technology,” *Nuclear Instruments and Methods in Physics Research A*, vol. 942, p. 162356, Oct. 2019.
- [1276] G. Visser, D. Abbot, F. Barbosa, C. Cuevas, H. Dong, E. Jastrzembski, B. Moffit, and B. Raydo, “A 72 channel 125 msp/s analog-to-digital converter module for drift chamber readout for the gluex detector,” in *IEEE Nuclear Science Symposium Medical Imaging Conference*, pp. 777–781, 2010.
- [1277] B. Azmoun, S. Aune, K. Dehmelt, A. Deshpande, W. Fan, P. Garg, T. K. Hemmick, M. Kebbiri, A. Kiselev, I. Mandjavidze, H. Pereira-Da-Costa, C. E. Perez-Lara, M. L. Purschke, M. Revolte, M. Vandenbroucke, and C. Woody, “Design Studies of High-Resolution Readout Planes Using Zigzags With GEM Detectors,” *IEEE Transactions on Nuclear Science*, vol. 67, pp. 1869–1876, Aug 2020.
- [1278] B. Azmoun, P. Garg, T. K. Hemmick, M. Hohlmann, A. Kiselev, M. L. Purschke, C. Woody, and A. Zhang, “Design Studies for a TPC Readout Plane Using Zigzag Patterns With Multistage GEM Detectors,” *IEEE Transactions on Nuclear Science*, vol. 65, no. 7, pp. 1416–1423, 2018.
- [1279] L. Greiner, “<https://www.jlab.org/indico/event/400/contribution/18/material/slides/0.pdf>,” *Silicon pixel-based particle vertex and tracking detectors towards the US Electron Ion Collider Workshop*, 2 September 2020.
- [1280] J. Repond, “TOPSiDE: Concept of an EIC Detector,” *PoS*, vol. DIS2018, p. 179, 2018.

- [1281] B. Aubert *et al.*, “The BaBar detector,” *Nucl. Instrum. Meth. A*, vol. 479, pp. 1–116, 2002.
- [1282] B. Aubert *et al.*, “The BABAR Detector: Upgrades, Operation and Performance,” *Nucl. Instrum. Meth. A*, vol. 729, pp. 615–701, 2013.
- [1283] L. Aphecetche *et al.*, “PHENIX calorimeter,” *Nucl. Instrum. Meth. A*, vol. 499, pp. 521–536, 2003.
- [1284] D. Britton, M. Ryan, and X. Qu, “Light collection uniformity of lead tungstate crystals for the CMS electromagnetic calorimeter,” *Nucl. Instrum. Meth. A*, vol. 540, pp. 273–284, 2005.
- [1285] S. Diehl, D. Bremer, K.-T. Brinkmann, V. Dormenev, T. Eissner, R. W. Novotny, C. Rosenbaum, and H.-G. Zaunick, “Measurement and optimization of the light collection uniformity in strongly tapered PWO crystals of the PANDA detector,” *Nucl. Instrum. Meth. A*, vol. 857, pp. 1–6, 2017.
- [1286] C. Aidala *et al.*, “Design and Beam Test Results for the 2D Projective sPHENIX Electromagnetic Calorimeter Prototype,” 3 2020.
- [1287] R. Wigmans, “New developments in calorimetric particle detection,” *Prog. Part. Nucl. Phys.*, vol. 103, pp. 109–161, 2018.
- [1288] D. Acosta *et al.*, “Results of Prototype Studies for a Spaghetti Calorimeter,” *Nucl. Instrum. Meth. A*, vol. 294, pp. 193–210, 1990.
- [1289] A. Antonelli *et al.*, “Construction and performance of the lead scintillating fiber calorimeter prototypes for the KLOE detector,” *Nucl. Instrum. Meth. A*, vol. 354, pp. 352–363, 1995.
- [1290] T. D. Beattie *et al.*, “Construction and Performance of the Barrel Electromagnetic Calorimeter for the GlueX Experiment,” *Nucl. Instrum. Meth. A*, vol. 896, pp. 24–42, 2018.
- [1291] P. Abbon *et al.*, “The COMPASS Setup for Physics with Hadron Beams,” *Nucl. Instrum. Meth. A*, vol. 779, pp. 69–115, 2015.
- [1292] H. Shimizu, Y. Sakamoto, T. Hashimoto, K. Abe, Y. Asano, T. Kinashi, T. Matsumoto, T. Matsumura, H. Yoshida, and H. Okuno, “Performance of a PbWO<sub>4</sub> crystal calorimeter for 0.2-GeV to 1.0-GeV electrons,” *Nucl. Instrum. Meth. A*, vol. 447, pp. 467–475, 2000.
- [1293] G. Conesa, H. Delagrangé, J. Diaz, M. Ippolitov, Y. Kharlov, D. Peresunko, and Y. Schutz, “Performance of the ALICE photon spectrometer PHOS,” *Nucl. Instrum. Meth. A*, vol. 537, pp. 363–367, 2005.
- [1294] P. Abbon *et al.*, “The COMPASS experiment at CERN,” *Nucl. Instrum. Meth. A*, vol. 577, pp. 455–518, 2007.

- [1295] Y. Kharlov *et al.*, "Performance of a fine-sampling electromagnetic calorimeter prototype in the energy range from 1-GeV to 19-GeV," *Nucl. Instrum. Meth. A*, vol. 606, pp. 432–438, 2009.
- [1296] J. Allen *et al.*, "Performance of prototypes for the ALICE electromagnetic calorimeter," *Nucl. Instrum. Meth. A*, vol. 615, pp. 6–13, 2010.
- [1297] S. Inaba, M. Kobayashi, M. Nakagawa, T. Nakagawa, H. Shimizu, K. Takamatsu, T. Tsuru, and Y. Yasu, "A Beam test of a calorimeter prototype of PWO crystals at energies between 0.5-GeV and 2.5-GeV," *Nucl. Instrum. Meth. A*, vol. 359, pp. 485–491, 1995.
- [1298] G. Alexeev *et al.*, "Studies of lead tungstate crystal matrices in high-energy beams for the CMS electromagnetic calorimeter at the LHC," *Nucl. Instrum. Meth. A*, vol. 385, pp. 425–434, 1997.
- [1299] H. Mkrtchyan *et al.*, "The lead-glass electromagnetic calorimeters for the magnetic spectrometers in Hall C at Jefferson Lab," *Nucl. Instrum. Meth. A*, vol. 719, pp. 85–100, 2013.
- [1300] T. Awes *et al.*, "High-energy beam test of the PHENIX lead scintillator EM calorimeter," 2 2002.
- [1301] C. Aidala *et al.*, "Design and Beam Test Results for the sPHENIX Electromagnetic and Hadronic Calorimeter Prototypes," *IEEE Trans. Nucl. Sci.*, vol. 65, no. 12, pp. 2901–2919, 2018.
- [1302] A. Benvenuti *et al.*, "A shashlik calorimeter with longitudinal segmentation for a linear collider," *Nucl. Instrum. Meth. A*, vol. 461, pp. 373–375, 2001.
- [1303] Y. Qiang, C. Zorn, F. Barbosa, and E. Smith, "Radiation Hardness Tests of SiPMs for the JLab Hall D Barrel Calorimeter," *Nucl. Instrum. Meth. A*, vol. 698, pp. 234–241, 2013.
- [1304] B. Biró *et al.*, "A Comparison of the Effects of Neutron and Gamma Radiation in Silicon Photomultipliers," *IEEE Trans. Nucl. Sci.*, vol. 66, no. 7, pp. 1833–1839, 2019.
- [1305] I. Chirikov-Zorin *et al.*, "Performance of the COMPASS II shashlyk calorimeter ECAL0 read out by SiPMs," *Nucl. Instrum. Meth. A*, vol. 936, pp. 141–143, 2019.
- [1306] N. Anfimov *et al.*, "Novel micropixel avalanche photodiodes (MAPD) with super high pixel density," *Nucl. Instrum. Meth. A*, vol. 628, pp. 369–371, 2011.
- [1307] G. Alexeev *et al.*, "Beam test results of a PbWO-4 crystal calorimeter prototype," *Nucl. Instrum. Meth. A*, vol. 364, pp. 307–310, 1995.
- [1308] D. Aleksandrov *et al.*, "A high resolution electromagnetic calorimeter based on lead-tungstate crystals," *Nucl. Instrum. Meth. A*, vol. 550, pp. 169–184, 2005.
- [1309] P. Adzic *et al.*, "Results of the first performance tests of the CMS electromagnetic calorimeter," *Eur. Phys. J. C*, vol. 44S1, pp. 1–10, 2006.

- [1310] M. Kubantsev, I. Larin, and A. Gasparian, "Performance of the PrimEx electromagnetic calorimeter," *AIP Conf. Proc.*, vol. 867, no. 1, pp. 51–58, 2006.
- [1311] C. Rosenbaum *et al.*, "Performance of Prototypes for the Barrel Part of the ANDA Electromagnetic Calorimeter," *J. Phys. Conf. Ser.*, vol. 742, no. 1, p. 012015, 2016.
- [1312] M. Kavatsyuk *et al.*, "Performance of the prototype of the electromagnetic calorimeter for PANDA," *Nucl. Instrum. Meth. A*, vol. 648, pp. 77–91, 2011.
- [1313] I. Balossino *et al.*, "The HPS electromagnetic calorimeter," *Nucl. Instrum. Meth. A*, vol. 854, pp. 89–99, 2017.
- [1314] A. Acker *et al.*, "The CLAS12 Forward Tagger," *Nucl. Instrum. Meth. A*, vol. 959, p. 163475, 2020.
- [1315] T. Horn *et al.*, "Scintillating crystals for the Neutral Particle Spectrometer in Hall C at JLab," *Nucl. Instrum. Meth. A*, vol. 956, p. 163375, 2020.
- [1316] T. Sumiyoshi *et al.*, "Performance of the Venus Lead Glass Calorimeter at Tristan," *Nucl. Instrum. Meth. A*, vol. 271, p. 432, 1988.
- [1317] K. Ahmet *et al.*, "The OPAL detector at LEP," *Nucl. Instrum. Meth. A*, vol. 305, pp. 275–319, 1991.
- [1318] Y. Prokoshkin and A. Shtannikov, "Energy resolution calculation of the PWO calorimeter, comparison with the beam tests," *Nucl. Instrum. Meth. A*, vol. 362, pp. 406–409, 1995.
- [1319] H. Avakian *et al.*, "Performance of F101 radiation resistant lead glass shower counters," *Nucl. Instrum. Meth. A*, vol. 378, pp. 155–161, 1996.
- [1320] S. Sedykh *et al.*, "Electromagnetic calorimeters for the BNL muon (g-2) experiment," *Nucl. Instrum. Meth. A*, vol. 455, pp. 346–360, 2000.
- [1321] T. Armstrong *et al.*, "The E864 lead-scintillating fiber hadronic calorimeter," *Nucl. Instrum. Meth. A*, vol. 406, pp. 227–258, 1998.
- [1322] O. Tsai *et al.*, "Results of \& on a new construction technique for W/ScFi Calorimeters," *J. Phys. Conf. Ser.*, vol. 404, p. 012023, 2012.
- [1323] S. Barsuk, "The LHCb Calorimeter Performance and its Expected Radiation-Induced Degradation," *IEEE Trans. Nucl. Sci.*, vol. 57, no. 3, pp. 1447–1453, 2010.
- [1324] I. Chirikov-Zorin, Z. Krumshtein, and A. Olchevski, "The design of a photodetector unit of a new Shashlyk EM calorimeter for COMPASS II," *Nucl. Instrum. Meth. A*, vol. 824, pp. 674–677, 2016.
- [1325] G. Atoian *et al.*, "An Improved Shashlyk Calorimeter," *Nucl. Instrum. Meth. A*, vol. 584, pp. 291–303, 2008.

- [1326] A. Semenov *et al.*, “Electromagnetic Calorimeter for MPD Spectrometer at NICA Collider,” *JINST*, vol. 15, no. 05, p. C05017, 2020.
- [1327] G. Avoni *et al.*, “The electromagnetic calorimeter of the HERA-B experiment,” *Nucl. Instrum. Meth. A*, vol. 580, pp. 1209–1226, 2007.
- [1328] N. Anfimov *et al.*, “Shashlyk EM calorimeter prototype readout by MAPD with superhigh pixel density for COMPASS II,” *Nucl. Instrum. Meth. A*, vol. 718, pp. 75–77, 2013.
- [1329] N. Anfimov *et al.*, “Tests of the module array of the ECAL0 electromagnetic calorimeter for the COMPASS experiment with the electron beam at ELSA,” *Phys. Part. Nucl. Lett.*, vol. 12, no. 4, pp. 566–569, 2015.
- [1330] E. Bernardi *et al.*, “Performance of a Compensating Lead Scintillator Hadronic Calorimeter,” *Nucl. Instrum. Meth. A*, vol. 262, p. 229, 1987.
- [1331] R. Wigmans, “Sampling calorimetry,” *Nucl. Instrum. Meth. A*, vol. 494, pp. 277–287, 2002.
- [1332] G. Drews *et al.*, “Experimental Determination of Sampling Fluctuations in Uranium and Lead Hadronic Calorimeters,” *Nucl. Instrum. Meth. A*, vol. 290, p. 335, 1990.
- [1333] D. Acosta *et al.*, “Electron, pion and multiparticle detection with a lead / scintillating - fiber calorimeter,” *Nucl. Instrum. Meth. A*, vol. 308, pp. 481–508, 1991.
- [1334] R. Wigmans, “Quartz fibers and the prospects for hadron calorimetry at the 1% resolution level,” in *7th International Conference on Calorimetry in High-Energy Physics (ICCHEP 97)*, pp. 182–193, 1997.
- [1335] R. Wigmans, *Calorimetry: Energy measurement in particle physics*, vol. 107. 2000.
- [1336] C. Leroy and P. Rancoita, “Physics of cascading shower generation and propagation in matter: Principles of high-energy, ultrahigh-energy and compensating calorimetry,” *Rept. Prog. Phys.*, vol. 63, pp. 505–606, 2000.
- [1337] A. Benaglia, E. Auffray, P. Lecoq, H. Wenzel, and A. Para, “Space-Time Development of Electromagnetic and Hadronic Showers and Perspectives for Novel Calorimetric Techniques,” *IEEE Trans. Nucl. Sci.*, vol. 63, no. 2, pp. 574–579, 2016.
- [1338] G. Giacomini, W. Chen, F. Lanni, and A. Tricoli, “Development of a technology for the fabrication of Low-Gain Avalanche Diodes at BNL,” *Nucl. Instrum. And Meth. in Phys. Res. A*, vol. 934, pp. 52–57, 2019.
- [1339] N. Moffat, R. B. ans M. Bullough, L. Flores, D. Maneuski, L. Simon, N. Tartoni, F. Dohertya, and J. Ashbya, “Low gain avalanche detectors (LGAD) for particle physics and synchrotron applications,” *JINST*, vol. 13, p. C 03014, 2018.
- [1340] CMS Collaboration, “Technical Proposal for a MIP timing detector in the CMS experiment phase 2 upgrade,” Tech. Rep. CERN-LHCC-2017-027. LHCC-P-009, CERN, Geneva, Dec 2017.

- [1341] A. Collaboration, "Technical Proposal: A High-Granularity Timing Detector for the ATLAS Phase-II Upgrade," Tech. Rep. CERN-LHCC-2018-023. LHCC-P-012, CERN, Geneva, 6 2018.
- [1342] I. Bejar Alonso and L. Rossi, "HiLumi LHC Technical Design Report: Deliverable: D1.10," Nov 2015.
- [1343] L. Rossi and O. Bruning, "High Luminosity Large Hadron Collider: A description for the European Strategy Preparatory Group," Geneva, Aug 2012.
- [1344] M. Mandurrino, R. Arcidiacono, M. Boscardin, N. Cartiglia, G. F. D. Betta, M. Ferrero, F. Ficorella, L. Pancheri, G. Paternoster, F. Siviero, V. Sola, A. Staiano, and A. Vignati, "Analysis and numerical design of resistive ac-coupled silicon detectors (rsd) for 4d particle tracking," *Nucl. Inst. Meth. A*, vol. 959, p. 163479, 2020.
- [1345] G. Giacomini, W. Chen, G. D'Amen, and A. Tricoli, "Fabrication and performance of ac-coupled lgads," *JINST*, vol. 14, p. P09004, 2019.
- [1346] M. Mandurrino, R. Arcidiacono, M. Boscardin, N. Cartiglia, G. F. Dalla Betta, M. Ferrero, F. Ficorella, L. Pancheri, G. Paternoster, F. Siviero, and M. Tornago, "Demonstration of 200-, 100-, and 50-  $\mu$  m pitch resistive ac-coupled silicon detectors (rsd) with 100% fill-factor for 4d particle tracking," *IEEE Electron Device Letters*, vol. 40, no. 11, 2019.
- [1347] A. Sharma, I. A. Asensi, I. Berdalovic, D. Bortoletto, R. Cardella, F. Dachs, V. Dao, T. Hemperek, B. Hiti, T. Kugathasan, K. Moustakas, H. Pernegger, P. Riedler, C. Riegel, P. Rymaszewski, C. Solans Sanchez, E. J. Schioppa, W. Snoeys, C. A. M. Tobon, T. Wang, N. Vermes, and L. S. Argemi, "The MALTA CMOS pixel detector prototype for the ATLAS Pixel ITk," *PoS*, vol. VERTEX2018, p. 014. 11 p, 2019.
- [1348] A. Collaboration, "A Forward Calorimeter (FoCal) in the ALICE experiment," tech. rep., CERN, Oct 2019.
- [1349] T. Horn, "A  $\text{PbWO}_4$ -based Neutral Particle Spectrometer in Hall C at 12 GeV JLab," *J. Phys. Conf. Ser.*, vol. 587, no. 1, p. 012048, 2015.
- [1350] W. B. Atwood, A. A. Abdo, M. Ackermann, W. Althouse, B. Anderson, M. Axelsson, L. Baldini, J. Ballet, D. L. Band, G. Barbiellini, and et al., "The large area telescope on the fermi gamma-ray space telescope mission," *The Astrophysical Journal*, vol. 697, p. 1071?1102, May 2009.
- [1351] "Joint Zero Degree Calorimeter Project." <http://jzcap.physics.illinois.edu/pages.html>.
- [1352] Y. Kharzheev, "Radiation Hardness of Scintillation Detectors Based on Organic Plastic Scintillators and Optical Fibers," *Phys. Part. Nucl.*, vol. 50, no. 1, pp. 42–76, 2019.
- [1353] P. Achenbach *et al.*, "In-beam tests of scintillating fibre detectors at MAMI and at GSI," *Nucl. Instrum. Meth. A*, vol. 593, pp. 353–360, 2008.

- [1354] C. Ayerbe Gayoso, *The scintillating fiber focal plane detector for the use of Kaos as a double arm spectrometer*. PhD thesis, Mainz U., Inst. Kernphys., 2012.
- [1355] F. Blanc, “Scintillating Fiber Trackers: recent developments and applications,” Sep 2013.
- [1356] “Electron-Ion Collider Detector Requirements and R&D Handbook (version 1.1),” Jan 2019. [http://eicug.org/web/sites/default/files/EIC\\_HANDBOOK\\_v1.1.pdf](http://eicug.org/web/sites/default/files/EIC_HANDBOOK_v1.1.pdf).
- [1357] Z. Tu, A. Jentsch, M. Baker, L. Zheng, J.-H. Lee, R. Venugopalan, O. Hen, D. Higinbotham, E.-C. Aschenauer, and T. Ullrich, “Probing short-range correlations in the deuteron via incoherent diffractive  $j/\psi$  production with spectator tagging at the eic,” *Physics Letters B*, 2020.
- [1358] U.S. Department of Energy Office of Science, *Reaching for the horizon: The 2015 Long Range Plan for Nuclear Science*.
- [1359] U. Amaldi, ed., *Study of an ep Facility for Europe DESY, Hamburg, April 2-3, 1979.*, vol. 790402, (Hamburg, Germany), Deutsches Electron Synchrotron / European Committee for Future Accelerators, 1979.
- [1360] Zeus Luminosity Monitor, [http://www-zeus.desy.de/zeus\\_det\\_papers/zeus\\_det\\_papers.html](http://www-zeus.desy.de/zeus_det_papers/zeus_det_papers.html).
- [1361] H1 Luminosity Monitor, <http://www-h1.desy.de/h1/www/h1det/lumi/>.
- [1362] F. D. Aaron *et al.*, “Determination of the Integrated Luminosity at HERA using Elastic QED Compton Events,” *Eur. Phys. J.*, vol. C72, p. 2163, 2012. [Erratum: *Eur. Phys. J.*C74,2733(2012)].
- [1363] T. Haas and V. Makarenko, “Precision calculation of processes used for luminosity measurement at the ZEUS experiment,” *Eur. Phys. J. C*, vol. 71, p. 1574, 2011.
- [1364] J. Adam, “eic-lgen event generator,”
- [1365] K. Aulenbacher, E. Chudakov, D. Gaskell, J. Grames, and K. D. Paschke, “Precision electron beam polarimetry for next generation nuclear physics experiments,” *Int. J. Mod. Phys. E*, vol. 27, no. 07, p. 1830004, 2018.
- [1366] J. Hansknecht and M. Poelker, “Synchronous photoinjection using a frequency-doubled gain-switched fiber-coupled seed laser and ErYb-doped fiber amplifier,” *Phys. Rev. ST Accel. Beams*, vol. 9, p. 063501, 2006.
- [1367] A. Narayan *et al.*, “Precision Electron-Beam Polarimetry at 1 GeV Using Diamond Microstrip Detectors,” *Phys. Rev. X*, vol. 6, no. 1, p. 011013, 2016.
- [1368] N. Vansteenkiste, P. Vignolo, and A. Aspect, “Optical reversibility theorems for polarization: application to remote control of polarization,” *J. Opt. Soc. Am. A*, vol. 10, pp. 2240–2245, Oct 1993.

- [1369] B. Sobloher, R. Fabbri, T. Behnke, J. Olsson, D. Pitzl, S. Schmitt, and J. Tomaszewska, "Polarisation at HERA - Reanalysis of the HERA II Polarimeter Data -," *HERA Internal Note*, 1 2012.
- [1370] A. Camsonne, J. Hoskins, *et al.*, "eRD15: R&D for a Compton Electron Detector," *EIC R&D Progress Report*, June 2017.
- [1371] A. Camsonne, J. Hoskins, *et al.*, "eRD15: R&D for a Compton Electron Detector," *EIC R&D Progress Report*, January 2016.
- [1372] F. Méot *et al.*, "eRHIC EIC: Plans for Rapid Acceleration of Polarized Electron Bunch at Cornell Synchrotron," in *9th International Particle Accelerator Conference*, p. MOPMF013, 2018.
- [1373] W. B. Schmidke *et al.*, "Rhic polarization for runs 9-17," Tech. Rep. BNL-209057-2018-TECH, C-A/AP/609, Brookhaven National Laboratory, 2018. <https://technotes.bnl.gov/PDF?publicationId=209057>.
- [1374] A. A. Poblaguev, A. Zelenski, G. Atoian, Y. Makdisi, and J. Ritter, "Systematic error analysis in the absolute hydrogen gas jet polarimeter at RHIC," *Nucl. Instrum. Meth. A*, vol. 976, p. 164261, 2020.
- [1375] A. Zelenski *et al.*, "Absolute polarized H-jet polarimeter development, for RHIC," *Nucl. Instrum. Meth. A*, vol. 536, pp. 248–254, 2005.
- [1376] W. Fischer and A. Bazilevsky *Phys. Rev. ST Accel. Beams*, vol. 15, p. 041001, 2012.
- [1377] C. Aidala *et al. Phys. Rev. Lett.*, vol. 120, p. 022001, 2018.
- [1378] G. Mitsuka *Phys. Rev.*, vol. C95, p. 044908, 2017.
- [1379] N. H. Buttimore, B. Kopeliovich, E. Leader, J. Soffer, and T. Trueman, "The spin dependence of high-energy proton scattering," *Phys. Rev. D*, vol. 59, p. 114010, 1999.
- [1380] A. A. Poblaguev *et al.*, "Precision Small Scattering Angle Measurements of Elastic Proton-Proton Single and Double Spin Analyzing Powers at the RHIC Hydrogen Jet Polarimeter," *Phys. Rev. Lett.*, vol. 123, no. 16, p. 162001, 2019.
- [1381] G. Atoian, A. Zelenski, and A. Poblaguev, "Precision absolute polarimeter development for the  $3\text{He}^{++}$  ion beam at 5.0–6.0 MeV energy," *PoS*, vol. PSTP2019, p. 045, 2020.
- [1382] A. Adare *et al.*, "Concept for an Electron Ion Collider (EIC) detector built around the BaBar solenoid," 2 2014.
- [1383] "An EIC Detector Built Around The sPHENIX Solenoid - A Detector Design Study," 10 2018.
- [1384] M. Bodlak, V. Frolov, V. Jary, S. Huber, I. Konorov, D. Levit, J. Novy, R. Salac, M. Virius, and S. Paul, "FPGA based data acquisition system for COMPASS experiment," *J. Phys. Conf. Ser.*, vol. 513, p. 012029, 2014.

- [1385] J. Alves, A. Augusto *et al.*, “The LHCb Detector at the LHC,” *JINST*, vol. 3, p. S08005, 2008.
- [1386] T. Colombo *et al.*, “The LHCb Online system in 2020: trigger-free read-out with (almost exclusively) off-the-shelf hardware,” *J. Phys. Conf. Ser.*, vol. 1085, no. 3, p. 032041, 2018.
- [1387] P. Moreira *et al.*, “The GBT Project,” in *Topical Workshop on Electronics for Particle Physics*, 2009.
- [1388] J. A. *et al.*, “SAMPA chip: the new 32 channels ASIC for the ALICE TPC and MCH upgrades,” *Journal of Instrumentation*, vol. 12, no. 04, p. C04008, 2017.
- [1389] J. Anderson, K. Bauer, A. Borga, H. Boterenbrood, H. Chen, K. Chen, G. Drake, M. Dönszelmann, D. Francis, D. Guest, B. Gorini, M. Joos, F. Lanni, G. L. Miotto, L. Levinson, J. Narevicius, W. P. Vazquez, A. Roich, S. Ryu, F. Schreuder, J. Schumacher, W. Vandelli, J. Vermeulen, D. Whiteson, W. Wu, and J. Zhang, “FELIX: a PCIe based high-throughput approach for interfacing front-end and trigger electronics in the ATLAS upgrade framework,” *Journal of Instrumentation*, vol. 11, no. 12, p. C12023, 2016.
- [1390] M. L. Purschke, “RCDAQ, a lightweight yet powerful data acquisition system.” <https://github.com/SPHENIX-Collaboration/rcdaq>, 2012.
- [1391] S. Ritt, “The PSU+I DRS4 Evaluation Board.” <https://www.psi.ch/en/drs/evaluation-board>.
- [1392] “CERN SRS Home Page.” <https://espace.cern.ch/rd51-wg5/srs/default.aspx>.
- [1393] M. Favaro, T. Chiarusi, F. Giacomini, M. Manzali, A. Margiotta, and C. Pellegrino, “The Trigger and Data Acquisition System for the KM3NeT-Italia towers,” *EPJ Web Conf.*, vol. 116, p. 05009, 2016.
- [1394] D. Lawrence, A. Boehnlein, N. Brei, and D. Romanov, “JANA2: Multithreaded Event Reconstruction,” *J. Phys. Conf. Ser.*, vol. 1525, no. 1, p. 012032, 2020.
- [1395] F. Barbosa, C. Hutton, A. Sitnikov, A. Somov, S. Somov, and I. Tolstukhin, “Pair spectrometer hodoscope for Hall D at Jefferson Lab,” *Nucl. Instrum. Meth. A*, vol. 795, pp. 376–380, 2015.
- [1396] M. Frank, F. Gaede, C. Grefe, and P. Mato, “DD4hep: A Detector Description Toolkit for High Energy Physics Experiments,” *J. Phys. Conf. Ser.*, vol. 513, p. 022010, 2014.
- [1397] R. Brun, A. Gheata, and M. Gheata, “The ROOT geometry package,” *Nucl. Instrum. Meth. A*, vol. 502, pp. 676–680, 2003.
- [1398] G. Amadio *et al.*, “GeantV Alpha Release,” *J. Phys. Conf. Ser.*, vol. 1085, no. 3, p. 032037, 2018.

- [1399] X. Ai, "Acts: A common tracking software," *arXiv: Instrumentation and Detectors*, 2019.
- [1400] J. Rauch and T. Schlüter, "GENFIT — a Generic Track-Fitting Toolkit," *J. Phys. Conf. Ser.*, vol. 608, no. 1, p. 012042, 2015.
- [1401] G. Barrand *et al.*, "GAUDI - A software architecture and framework for building HEP data processing applications," *Comput. Phys. Commun.*, vol. 140, pp. 45–55, 2001.
- [1402] M. Clemencic, H. Degaudenzi, P. Mato, S. Binet, W. Lavrijsen, C. Leggett, and I. Belyaev, "Recent developments in the LHCb software framework Gaudi," *J. Phys. Conf. Ser.*, vol. 219, p. 042006, 2010.
- [1403] E. Tejedor, E. Bocchi, D. Castro, H. Gonzalez, M. Lamanna, P. Mato, J. Moscicki, and D. Piparo, "Facilitating collaborative analysis in SWAN," *EPJ Web Conf.*, vol. 214, p. 07022, 2019.
- [1404] S. Höche and S. Prestel, "The midpoint between dipole and parton showers," *Eur. Phys. J. C*, vol. 75, no. 9, p. 461, 2015.
- [1405] F. Dulat, S. Höche, and S. Prestel, "Leading-Color Fully Differential Two-Loop Soft Corrections to QCD Dipole Showers," *Phys. Rev. D*, vol. 98, no. 7, p. 074013, 2018.
- [1406] G. Schuler and H. Spiesberger, "DJANGO: The Interface for the event generators HERACLES and LEPTO," in *Workshop on Physics at HERA*, pp. 1419–1432, 1991.
- [1407] L. Barion *et al.*, "RICH detectors development for hadron identification at EIC: design, prototyping and reconstruction algorithm," *JINST*, vol. 15, no. 02, p. C02040, 2020.
- [1408] E. Cisbani *et al.*, "AI-optimized detector design for the future Electron-Ion Collider: the dual-radiator RICH case," *JINST*, vol. 15, no. 05, p. P05009, 2020.
- [1409] W. Anderson *et al.*, "Design, Construction, Operation and Performance of a Hadron Blind Detector for the PHENIX Experiment," *Nucl. Instrum. Meth. A*, vol. 646, pp. 35–58, 2011.
- [1410] J. Agarwala *et al.*, "The MPGD-Based Photon Detectors for the upgrade of COMPASS RICH-1 and beyond," *Nucl. Instrum. Meth. A*, vol. 936, pp. 416–419, 2019.
- [1411] M. Blatnik *et al.*, "Performance of a Quintuple-GEM Based RICH Detector Prototype," *IEEE Trans. Nucl. Sci.*, vol. 62, no. 6, pp. 3256–3264, 2015.
- [1412] B. Azmoun *et al.*, "Results from a Prototype Combination TPC Cherenkov Detector with GEM Readout," *IEEE Trans. Nucl. Sci.*, vol. 66, no. 8, pp. 1984–1992, 2019.
- [1413] S. N. White, "R&D for a Dedicated Fast Timing Layer in the CMS Endcap Upgrade," *Acta Phys. Pol. B Proc. Suppl.*, vol. 7, p. 743, 2014.

- [1414] N. Cartiglia *et al.*, “Design optimization of ultra-fast silicon detectors,” *Nucl. Instrum. Meth. A*, vol. 796, p. 141, 2015.
- [1415] D. Breton *et al.*, “Measurements of timing resolution of ultra-fast silicon detectors with the SAMPIC waveform digitizer,” *Nucl. Instrum. Meth. A*, vol. 835, p. 51, 2016.
- [1416] N. Minafra *et al.*, “Test of Ultra Fast Silicon Detectors for Picosecond Time Measurements with a New Multipurpose Read-Out Board,” *Nucl. Instrum. Meth. A*, vol. 867, p. 88, 2017.
- [1417] A. Apresyan *et al.*, “Studies of Uniformity of 50  $\mu\text{m}$  Low-Gain Avalanche Detectors at the Fermilab Test Beam,” *Nucl. Instrum. Meth. A*, vol. 895, p. 158, 2018.
- [1418] C. Collaboration, “A MIP Timing Detector for the CMS Phase-2 Upgrade,” Tech. Rep. CERN-LHCC-2019-003. CMS-TDR-020, CERN, Geneva, 3 2019.
- [1419] M. Jadhav, W. Armstrong, I. Cloet, S. Joosten, S. Mazza, J. Metcalfe, Z.-E. Meziani, H. Sadrozinski, B. Schumm, and A. Seiden, “Picosecond Timing Resolution Measurements of Low Gain Avalanche Detectors with a 120 GeV Proton Beam for the TOPSiDE Detector Concept,” 2020.
- [1420] O. Tsai *et al.*, “Development of a forward calorimeter system for the STAR experiment,” *J. Phys. Conf. Ser.*, vol. 587, no. 1, p. 012053, 2015.
- [1421] S. Trentalange *et al.*, “T-1018: UCLA Spacordion Tungsten Powder Calorimeter,” tech. rep., Fermilab, 12 2013.
- [1422] T. Polakovic, W. Armstrong, V. Yefremenko, J. Pearson, K. Hafidi, G. Karapetrov, Z.-E. Meziani, and V. Novosad, “Superconducting nanowires as high-rate photon detectors in strong magnetic fields,” *Nucl. Instrum. Meth. A*, vol. 959, p. 163543, 2020.
- [1423] “Doe basic research needs study on high energy physics detector research and development, report of the office of science workshop on basic research needs for hep detector research and development,” 2019 (December 11-14, 2019). [https://science.osti.gov/-/media/hep/pdf/Reports/2020/DOE\\_Basic\\_Research\\_Needs\\_Study\\_on\\_High\\_Energy\\_Physics.pdf](https://science.osti.gov/-/media/hep/pdf/Reports/2020/DOE_Basic_Research_Needs_Study_on_High_Energy_Physics.pdf).
- [1424] “High precision timing distribution project.” <https://espace.cern.ch/HighPrecisionTiming>.
- [1425] C. E. P. Department, “Strategic r&d programme on technologies for future experiments,” 2018. [https://ep-dep.web.cern.ch/sites/ep-dep.web.cern.ch/files/Report%20final\\_0.pdf](https://ep-dep.web.cern.ch/sites/ep-dep.web.cern.ch/files/Report%20final_0.pdf).
- [1426] “Cern GBT project.” <http://cern.ch/proj-gbt>.
- [1427] “Cern dcdc project.” <http://project-dcdc.web.cern.ch>.
- [1428] S. Bentvelsen, J. Engelen, and P. Kooijman, “Reconstruction of  $(x, Q^2)$  and extraction of structure functions in neutral current scattering at HERA,” pp. 23–42, 1 1992.